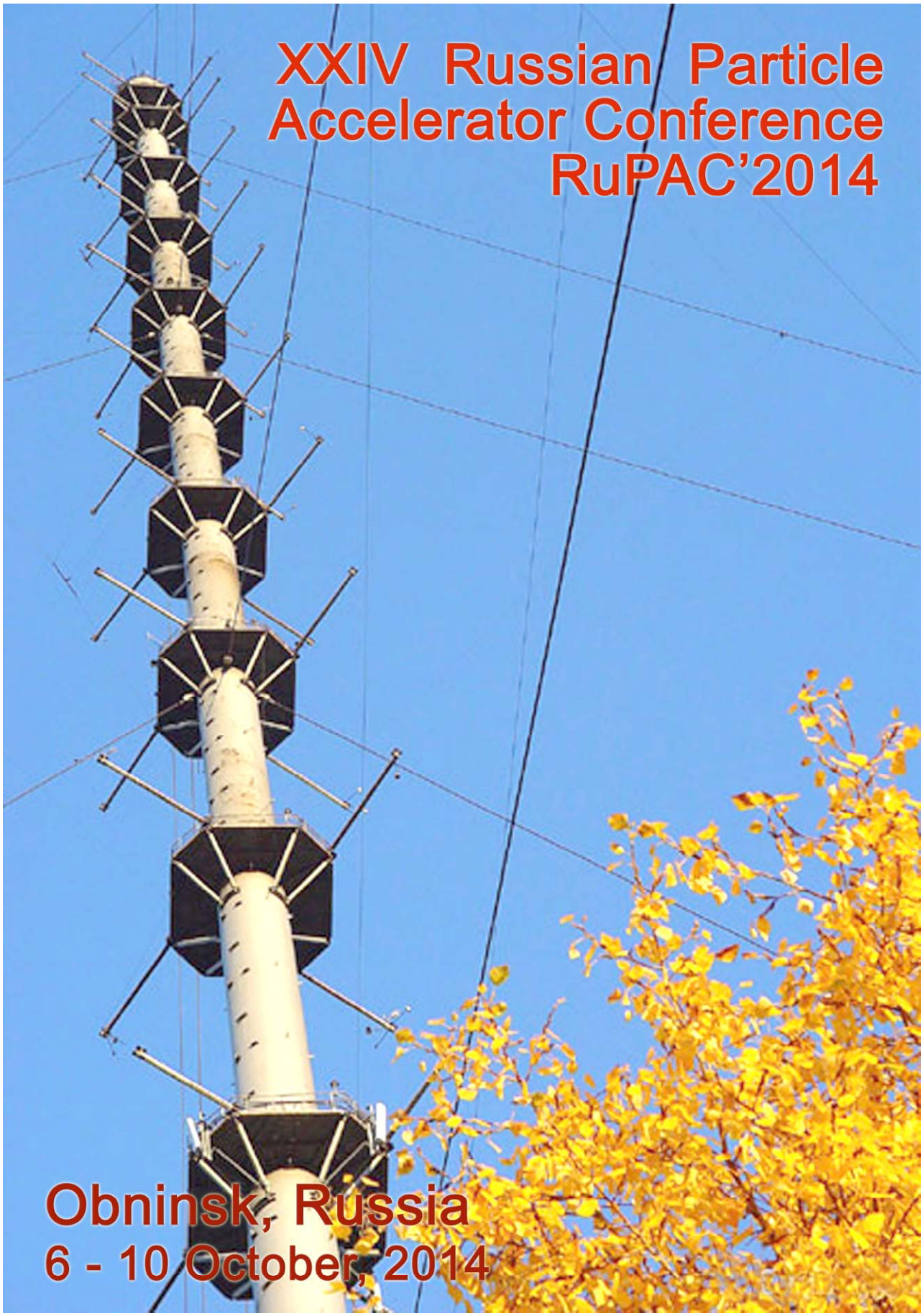
XXIV Russian Particle
Accelerator Conference
RuPAC'2014
Obninsk, Russia
6 - 10 October, 2014

PREFACE

The 24-th Russian Particle Accelerator Conference (RuPAC-2014) was held in Obninsk, Kaluga Region, October 6–10, 2014. It was organized by State Scientific Center of the Russian Federation — A.I. Leipunski Institute of Physics and Power Engineering (IPPE), State Atomic Energy Corporation ROSATOM, Russian Academy of Sciences, Scientific Council for Accelerators of Russian Academy of Sciences and was hosted by Advanced Research Division of IPPE.

This RuPAC event provided a forum for exchange of new information and discussions in the field of accelerator science and engineering: particle beam physics, new projects of particle colliders, new accelerator designs and upgrades of the existing accelerator facilities for basic research and applications. The scientific program scope covered traditionally the topics to follow:

- Modern trends in accelerators
- Colliders
- Particle dynamics in accelerators and storage rings, cooling methods
- New methods of acceleration
- High intensity cyclic and linear accelerators
- Heavy ion accelerators
- Synchrotron radiation sources and free electron lasers
- Magnetic and vacuum systems, power supplies
- Superconducting accelerators and cryogenics
- RF power structures and systems
- Control and diagnostic systems
- Ion sources and electron guns
- Medical and industrial applications
- Radiation problems in accelerators

More than 140 participants took part at the RuPAC-2014 from 29 institutions and companies, mostly the interior ones. The Accelerator Prizes for young physicists and engineers for the best work presented at the Conference were nominated. The First Prize was awarded to I. Zemlyansky (BINP, Novosibirsk) who presented the papers “Electron and Positron Beams Transportation Cannels to who presented the papers BINP Colliders” and the Second Prizes – to Roman Klopenkov (NIIEFA, St. Petersburg) who presented the papers “System for Remote Replacement of Targets of the Target System for CC-Cyclotrons” and “Automated Control System of Target System for Production of PET-radionuclides“, and to Konstantin Mitrofanov (IPPE, Obninsk) for the paper “Experimental Study of the Time Dependence of the Activity of Delayed Neutrons in the Fission of 235U by Neutrons from the Reaction 7Li(p, n) at the Electrostatic Accelerator EG-1”.

Processing of the electronic files of the contributions in course of and after the Conference was accomplished by Maxim Kuzin and the BINP (Novosibirsk) editorial team, a member of the Joint Accelerator Conferences Website (JACoW) collaboration.

The Conference was supported in part by the Russian Foundation for Basic Research and the Ministry of Education and Science of the Russian Federation.

The accomplishment of the RuPAC-2014 Conference is due to the efforts of the Organizing and Program Committees, the local staff of the host Institute – IPPE, and, naturally, due to all of the participants thus involved.

Andrey Goverdovsky, Chair of RuPAC-2014 Organizing Committee

Sergey Ivanov, Chair of Program Committee

Contents

Preface i
Foreword . . . iii
Contents . . . v
Committees . . . ix
Pictures . . . x

Papers 1
TUX02 – Accelerator Complex U70 of IHEP: Status and Upgrades . . . 1
TUY01 – Status and Perspectives of the VEPP-2000 Complex . . . 6
TUY02 – Status of Injection Complex VEPP-5 . . . 11
TUCA01 – Commissioning 2 MeV Cooler in COSY and Novosibirsk . . . 14
TUCA02 – On the Way to a Relativistic Electron Cooler . . . 17
TUCA04 – Mechanism of Compression of Positron Clouds in the Surko Trap of the LEPTA Facility . . . 20
TUCB01 – Ultrahigh Vacuum in Superconducting Synchrotrons . . . 23
TUCB02 – RF System of the Booster of NICA Facility . . . 26
TUZ01 – Particle and Accelerator Physics at the VEPP-4M Collider . . . 29
TUZ02 – Accelerator Technologies Development at ITEP . . . 34
TUPSA02 – Superconducting Unclosed Shields in High Energy Physics . . . 39
TUPSA04 – Operating Frequency and Accelerating Structure Geometry Chose for the Travelling Wave Compact Electron Linear Accelerator . . . 42
TUPSA05 – Three Electrode Electron Gun with the Decreased Anode Voltage Geometry Optimization . . . 45
TUPSA06 – Beam Dynamics Calculation in the Induction Linear Accelerator . . . 48
TUPSA07 – Transit Code for Beam Dynamic Simulation . . . 51
TUPSA09 – Beam Dynamics Calculations in the Multi-Beam Generator Cavity . . . 54
TUPSA10 – Advanced Optimization of an Low-energy Ion Beam Dynamics at Linac Front-end with RF Focusing 57
TUPSA12 – The User Friendly Interface for BEAMDULAC-RFQ Code . . . 60
TUPSA13 – The Interactive Computer Environment for Designing and Tuning of Charged Particle Beams Transport Channels . . . 63
TUPSA14 – Mathematical Optimization Model of Longitudinal Beam Dynamics in Klystron-Type Buncher . . . 66
TUPSA15 – Second Order Method for Beam Dynamics Optimization . . . 69
TUPSA16 – Electron Gun with Adiabatic Plasma Lens . . . 72
TUPSA17 – Axial Injection to a Compact Cyclotron with High Magnetic Field . . . 75
TUPSA18 – Complex Shunt Impedance and Beam-RF Cavity Interaction . . . 77
TUPSA20 – Output Energy Variation in the SC Linac for the Proton Radiotherapy . . . 80
TUPSA23 – LEPTA - the Facility for Fundamental and Applied Research . . . 83
TUPSA24 – Project of Electron Cooler for NICA Collider . . . 85
TUPSA25 – Acceleration of the Oppositely Charged Particles in the Single Stream . . . 88
TUPSA26 – Electrodes Form Optimization of RF Deflecting System Wobbler for FAIR Project . . . 91
TUPSA27 – The First Design of Medium Resolution Mass Spectrometer (MRMS) High Voltage Platform in a SPES Project . . . 94
TUPSA28 – The Advanced Nanostructure Steel Modification by Gas Ions Beams . . . 97
TUPSA29 – Method of Broadband Stabilization of the VEPP-4M Main Field . . . 100
TUPSA31 – Magnetic System of Isochronous Cyclotron F250 for Proton Therapy Applications . . . 103
TUPSA32 – Magnetic Field Design and Calculation for the FLNR DC-280 Cyclotron . . . 105
TUPSA34 – The Power Supply System of Electrostatic Deflecting Plates for Accelerating Complex NICA . . . 108
TUPSA35 – Virtual Laboratory of Vacuum Technique . . . 110
TUPSA36 – Measurement of the Dose Rate and the Radiation Spectrum of the Interaction of 2 MeV Proton Beam with a Variety of Structural Materials . . . 113
TUPSA37 – Measurement of the Spatial Distribution of Gamma Radiation at Tandem Accelerator with Vacuum Insulation . . . 116
TUPSA38 – Estimation of the Efficiency of Biological Shielding for the Circular Hall of U-70 Accelerator at IHEP 118
WEX01 – Development of Accelerator Facilities at FSUE SSC RF – IPPE . . . 120
WEX03 – Production of Accelerating Equipment for Nuclear Medicine in NIIEFA. Potentialities and Prospects . 125
WECA02 – Radiobiological Research with Charged Particles Beams in ITEP . . . 128
WECA04 – Accelerator Hadron Therapy Technique Developed at JINR . . . 131

WECA05 – Operation and Development of the BINP AMS Facility . . . 134
WECA06 – Extended Scope of Application of Industrial ELV Accelerator . . . 137
WECA07 – LIA-2 and BIM Accelerators as Part of Radiographic Complex at RFNC-VNIITF . . . 140
WECA08 – Main Parameters and Operational Experience with New Generation of Electron Accelerators for Radiography and Cargo Inspection . . . 143
WECA09 – Dedicated DC-110 Heavy Ion Cyclotron for Industrial Production of Track Membranes . . . 146
WECA11 – CC-18/9M Cyclotron System . . . 149
WECA12 – SEE Testing Facilities at FLNR Accelerators Complex: State of the Art and Future Plans . . . 152
WEPSB01 – Modernization the Modulator of the RF-Generator Ion Linear Accelerator LU-20 . . . 155
WEPSB02 – Modernization the Modulators Klystrons Accelerating Stand of the Electron Linear Accelerator LINAC-800 . . . 157
WEPSB03 – System Power Microwave Impulse Compression Based on Double Forming Line . . . 159
WEPSB04 – Field Optimization Technique of the Multigap H-mode Resonators . . . 162
WEPSB05 – Optimization of Electric Field Distribution Inside Multi-gap CH-Resonator . . . 164
WEPSB06 – The Optimization of the Buncher at 145.2 MHz to Reduce Multipactor Effect . . . 166
WEPSB07 – MultP-M Code Geometry Import Module Performance Optimization . . . 169
WEPSB08 – Multi-beam Generator Cavity for the Proton Linear Accelerator Feeding System on 991 MHz Frequency Geometry Optimization . . . 171
WEPSB09 – Comparision of Higher Order Modes Damping Techniques for Array of Single Cell Cavities . . . 174
WEPSB11 – Test Results of 433 MHz Deuteron Linac (RFQ) . . . 177
WEPSB12 – Cascade Interference Switches for Active Microwave Compressors . . . 180
WEPSB13 – Oversized Interference Switches of Active Microwave Pulse Compressors . . . 183
WEPSB15 – The Utilization of Standard DC Accelerator ELV for The Tomography . . . 186
WEPSB16 – Studying of the Accompanying Charged Particles in the Tandem Accelerator with Vacuum Insulation 189
WEPSB17 – Development of the Injector for Vacuum Insulated Tandem Accelerator . . . 191
WEPSB18 – Modification of the Argon Stripping Target of the Tandem Accelerator . . . 194
WEPSB19 – First Results of Experiments with the Extracted Carbon Beam at the U-70 Accelerator . . . 197
WEPSB20 – Experimental Study of the Time Dependence of the Activity of Delayed Neutrons in the Fission of 235U by Neutrons from the Reaction 7Li(p, n) on the Electrostatic Accelerator EG-1 . . . 200
WEPSB21 – Registration of Gamma Rays from the Reaction 16O(n, p)16N on the Direct Neutron Beam of Cascade Generator KG-2.5 . . . 203
WEPSB22 – Conditioning and Monitoring of Cleanliness of High Voltage System with Gesous Insulation . . . 206
WEPSB23 – Set-up for Measurements of Delayed Neutron Characteristics in Interaction of Heavy Nuclei with Relativistic Protons of the Synchrocyclotron PINP Gatchina . . . 209
WEPSB24 – Comparison of Biological Impact of Proton and Ion Beams in Radiation Treatment . . . 211
WEPSB25 – PRIOR Proton Microscope . . . 214
WEPSB26 – Study of Possibility of Industrial Application of Ion Injector I-3 . . . 217
WEPSB27 – Design of Multifunctional Facility Based on ECR Ion Source for Material Science . . . 220
WEPSB29 – The Induction Synchrotron with a Constant Magnetic Field . . . 223
WEPSB30 – The Compact Induction Accelerator of Electrons for Radiation Technologies . . . 226
WEPSB31 – Project of Demonstration Center of the Proton Therapy at DLNP JINR . . . 228
WEPSB32 – Positron Annihilation Spectroscopy at LEPTA Facility . . . 231
WEPSB33 – Development of the Equipment for the Prototype of a Complex of Radiotherapy at the Nuclotron-M 234
WEPSB35 – Thermal Simulations of the Biperiodical Accelerating Structure with the Operating Frequency 27 GHz 237
WEPSB36 – A prototype of a Phased Array for Deep Thermoradiotherapy . . . 240
WEPSB37 – Interdisciplinary Glossary – Particle Accelerators and Medicine . . . 243
WEPSB38 – Multifunctional Extraction Channel Development Heavy Ion RFQ (Radio Frequency Quadrupole) . 245
WEPSB39 – Industrial Prototype of Compact CW Linac . . . 248
WEPSB40 – Design of a Linear Accelerator with a Magnetic Mirror on the Beam Energy of 45 MeV . . . 251
WEPSB41 – The X-ray System with Sub-system of Shaping of Fun-Shaped Beam and its Application in the Custom Inspection Systems . . . 254
WEPSB42 – Histogram Based Bremsstrahlung Radiation Source Model for the CyberKnife Medical Linear Accelerator . . . 256
WEPSB43 – Magnetic Buncher Accelerator UELV-10^{-10}-T-1 for Studying Fluorescence and Radiation-Physical Researches . . . 259
WEPSB44 – Neutron Radiation Monitoring of the Therapeutic Proton Beam Transportation . . . 262

WEPSB45 – Small-Size High-Performance ARSA Accelerators for On-Line Testing for ECB for Radiation Hardness 264
WEPSB47 – Depth Dose Distribution of the Bremsstrahlung Generated by the Betatron OB-4 in Different Environments . . . 266
WEPSB48 – Status of Experiments on Surface Modification of Materials on the Accelerator HIP-1 . . . 269
WEPSB49 – Method of Measuring Fast Neutron Fluence Using the Planar Silicon Detectors . . . 272
THX01 – Results of LIA-2 Operation . . . 275
THX02 – Experience in Research, Development, Construction and Commissioning of Normally Conducting Accelerating Structures . . . 278
THX03 – Status of the Nuclotron . . . 283
THCA01 – Accelerator Complex Based on DC-60 Cyclotron . . . 287
THY02 – The Status of the Facilities of Kurchatov's Synchrotron Radiation Source . . . 290
THCB01 – The NSLS-II Booster Development and Commisioning . . . 293
THZ01 – Superconducting Multipole Wigglers for Generation of Synchrotron Radiation . . . 296
THZ03 – Production of Superconducting Equipment at IHEP . . . 301
THCE01 – INR RAS Linac Proton Injector 100 Hz PRR Operation Mode . . . 306
THCE02 – CW 100 keV Electron RF Injector for 40 mA Average Beam Current . . . 309
THPSC01 – Status of Linacs with High-frequency Quadrupole Focusing LU-30 and LU-30M in IHEP . . . 312
THPSC02 – Geometry of Quadrupole Magnet for the U-3.5 Accelerator in the OMEGA Project . . . 315
THPSC03 – Study of Superconducting Accelerating Structures for Megawatt Proton Driver Linac . . . 318
THPSC04 – Study of Normal Conducting Accelerating Structures for Megawatt Proton Driver Linac . . . 321
THPSC05 – Study of Possibility of 600-1000 MeV and 1 MW Proton Driver Linac Development in Russia . . . 324
THPSC06 – Development and Testing of Powerful High-voltage Electron Accelerator for Energy-intensive Industries 327
THPSC07 – Single Frequency High Intensity High Energy Normal Conducting Hadron Linac . . . 330
THPSC08 – The Project of the HV Axial Injection for the DC-280 Cyclotron at the FLNR JINR . . . 333
THPSC09 – The Project of Beam Transportation Lines for the DC-280 Cyclotron at the FLNR JINR . . . 336
THPSC10 – Magnets of Injection and Extraction Systems of Cyclotron DC280 . . . 339
THPSC11 – NSLS-II Booster Vacuum System . . . 342
THPSC12 – Effect of the Vertical Velocity Component on Properties of Synchrotron Radiation . . . 345
THPSC13 – Horizontal Emittance Regulation at SIBERIA-2 . . . 347
THPSC14 – Electron Emission and Trapping in Non-Uniform Fields of Magnet Structure and Insertion Devices at SR Source Siberia-2 . . . 350
THPSC16 – Analysis of High Order Modes Damping Techniques for 800 MHz Single Cell Superconducting Cavities 353
THPSC17 – Higher Order Modes Damping for 9-cell Structure with Modified Drift Tubes . . . 356
THPSC18 – Suppression of Mechanical Oscillations in Quarterwave 10^6 MHz Resonator . . . 359
THPSC19 – Influence of the Different Geometric Parameters of Superconducting Elliptical Cavities on the Multipactor . . . 362
THPSC20 – Multipactor in Elliptical Cavities 800 MHz . . . 365
THPSC23 – Upgrade of BPM System at VEPP-4M Collider . . . 368
THPSC25 – Extending VEPP-5 Control System by Middleware for Injection/extraction Automation . . . 371
THPSC26 – Distributed Beam Loss Monitor Based on the Cherenkov Effect in Optical Fiber . . . 374
THPSC27 – Modernization of VEPP-2000 Control System . . . 377
THPSC28 – Development of Automation System of the Ion Source . . . 380
THPSC29 – Controller for RF Stations for Booster of NICA Project . . . 383
THPSC31 – Media Server for Video and Audio Exchange between the U-70 Accelerator Complex Control Rooms 386
THPSC32 – U-70 Accelerator Complex: Centralized Access to IP-Devices with Embedded Web-Server . . . 389
THPSC33 – Digital Signal Processing Algorithms for Linac Low-Level RF Systems . . . 392
THPSC34 – A Digital Low-Level RF System for Resonant Beam Deflector of LAPLAS Experiment . . . 395
THPSC35 – Quench Detector for Superconducting Elements of the NICA Accelerator Complex . . . 398
THPSC36 – Experimental Study of the Scattering of 7.4 Mev Electrons Intersecting a Foil at an angle of 5–60 degree to its Surface . . . 401
THPSC37 – A Pulse Generator of X-Ray Quants for Remote Radiation Monitoring . . . 404
THPSC38 – Development of the Software for the Accelerating Fields in Linear Structures Measurement . . . 407
THPSC39 – Control Systems for Radiography and Cargo Inspection RF Accelerators . . . 410
THPSC40 – Automated Control System of Target System for PET radionuclids Production . . . 413
THPSC41 – System for Remote Replacement of Targets of the Target System for CC-Cyclotrons . . . 415

THPSC42 – Modernization of the Automated Control System of Kurchatov Synchrotron Radiation Source Using Citect SCADA . . . 417
THPSC43 – Electrostatic Pick-ups for Debunched Beams at INR Linac . . . 420
THPSC44 – Development of Remote Control System for H-minus Ions Source of INR LINAC . . . 423
THPSC45 – Use of Fast Magnetic Beam Raster System for INR Isotope Production Facility . . . 426
THPSC46 – Simulation and Optimization of Ion Optical Extraction, Acceleration and H-minus Ion Beam Matching Systems . . . 429
THPSC47 – Production of Metal Ion Beams from ECR Ion Sources by MIVOC Method . . . 432
THPSC48 – Hydrogen Nuclides Acceleration from Laser Plasma in the Diode with Magnetic Insulation of Electrons 435
THPSC49 – Hydrogen Nuclides Removing From Pulse Plasma Formations . . . 438
THPSC50 – Neutron Accelerating Tubes with Microwave Deuterons Source Using Electron-cyclotron Resonance Effect . . . 441
THPSC51 – Ion Source Deuteron Beam Acceleration in Gas-filled Ion-optic System . . . 444
THPSC52 – Dynamics of Plasma-Beam Formations in the Acceleration Gap of the Pulse Neutron Generator-based Vacuum Neutron Tube . . . 447
THPSC53 – The NG-10 Neutron Generator for Production of Neutron Fluxes in Continuous and Pulse Modes . 450
THPSC55 – Improvement of the Beam Transmission in the Central Region Of Warsaw U200P Cyclotron . . . 453
FRCA01 – Cooling Storage Ring CR of the FAIR Facility - Status and Perspectives . . . 456
FRCA02 – Time Dependence of Ion Beam Transverse Phase-Space Portrait Orientation During Linac Proton Injector Pulse . . . 459
FRCA03 – Electron and Positron Beams Transportation Channels to BINP Colliders . . . 462
FRCB01 – Problems and Prospects of the Tandem Accelerator with Vacuum Insulation . . . 465
FRCB02 – Dynamics of Processes in Subcritical Reactor Driven by Linear Accelerator . . . 467
FRCB03 – Accelerators Application for Radiation Processing of Foodstuffs . . . 470

Appendices **473**
List of Authors . . . 473
Institutes List . . . 481
Participants List . . . 489

PROGRAM COMMITTEE

Chairman	S. Ivanov	(SSC IHEP NRC “Kurchatov Institute”)
Co-Chairman	I. Meshkov	(JINR)
Scientific Secretary	S. Bazhal	(SSC RF – IPPE)

A. Ageyev	(SSC IHEP NRC “Kurchatov Institute”)	F. Komarov	(BSU, Belarus)
		L. Kravchuk	(INR RAS)
		E. Levichev	(BINP SB RAS)
N. Alexeev	(SSC RF ITEP)	D. Ovsyannikov	(SPbSU)
N. Vinokurov	(BINP SB RAS)	V. Parkhomchuk	(BINP SB RAS)
M. Vorogushin	(NIIEFA)	V. Romanov	(SSC RF – IPPE)
A. Goverdovski	(SSC RF – IPPE)	A. Skrinsky	(BINP SB RAS)
A. Golubev	(SSC RF ITEP)	G. Trubnikov	(JINR)
V. Glukhikh	(NIIEFA)	B. Sharkov	(FRRC/FAIR)
A. Dovbnya	(NSC KIPT, Ukraine)	Yu. Shatunov	(BINP SB RAS)
		G. Shirkov	(JINR)
N. Zavyalov	(RFNC-VNIIEF)		
M. Zdorovets	(INP, Kazakhstan)		

ORGANIZING COMMITTEE

Chairman	A. Goverdovski	(SSC RF – IPPE)
Co-Chairmen	O. Grudzevich	(SSC RF – IPPE)
	V. Romanov	(SSC RF – IPPE)
Secretary	K. Mitrofanov	(SSC RF – IPPE)

S. Ivanov	(SSC IHEP NRC “Kurchatov Institute”)	D. Ovsyannikov	(SPbSU)
		O. Patarakin	(ROSATOM)
		A. Razbash	(Cyclotron Co., Ltd.)
M. Kuzin	(BINP SB RAS)	V. Smirnov	(CJSC NII)
I. Meshkov	(JINR)	V. Khryachkov	(SSC RF – IPPE)

WORKING GROUP

Chairman	V. Borisov	(SSC RF – IPPE)
Co-Chairman	V. Rudnikov	(SSC RF – IPPE)

A. Glotov	(SSC RF – IPPE)	K. Rezvykh	(SSC RF – IPPE)
T. Vereshchagina	(SSC RF – IPPE)	S. Stozhilov	(SSC RF – IPPE)
D. Kolesnikov	(SSC RF – IPPE)	A. Troshina	(SSC RF – IPPE)
A. Lebezov	(SSC RF – IPPE)	Yu. Chalyi	(SSC RF – IPPE)
P. Penkov	(SSC RF – IPPE)		


RUPAC 2014

ACCELERATOR COMPLEX U70 OF IHEP: STATUS AND UPGRADES

S. Ivanov, on behalf of the U70 staff#
Institute for High Energy Physics (IHEP) of NRC "Kurchatov Institute"
Protvino, Moscow Region, 142281, Russia

Abstract

The report overviews present status of the Accelerator Complex U70 of IHEP–Protvino. It is a sequel to prior status reports [1] delivered to RuPAC-2008, -2010, -2012, and outlines the recent machine-related activity and upgrades in run-by-run chronological ordering.

GENERALITIES

Layout of the entire Accelerator Complex U70 of IHEP–Protvino is shown in Fig. 1. It comprises four machines — 2 linear (I100, URAL30) and 2 circular (U1.5, U70) accelerators.

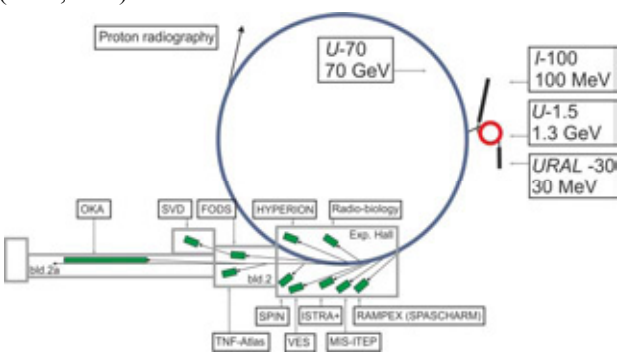

Figure 1: Accelerator Complex U70, beam transfer line network and fixed-target experimental facilities included. Proton mode (default) — cascade of URAL30–U1.5–U70, light-ion (carbon) mode — that of I100–U1.5–U70.

The points of attraction to the efforts spent during the period under report to be spotted in the scheme above are:

- Quality of stochastic slow extraction of 50–60 GeV protons to BTL#21 and the OKA facility;
- Extractions of the top-energy (24.1 GeV/u) carbon ions to BTL#22 (which is also an incidental fragment separator) and the FODS or SVD facilities;
- Stochastic slow extraction of the intermediate-energy (456 MeV/u ca) carbon ions via the new BTL#25 to the Interim Radio-Biological Work-bench;
- Launching beam-commissioning of the new Proton Radiography Facility (along the upward arrow, via a fast extraction);
- Re-equipment of the U-70 ring magnet main power supply plant with the up-to-date static thyristor AC-DC convertors.

N. Tyurin, Yu. Fedotov, O. Zyatkov, A. Minchenko, A. Maksimov, A. Afonin, E. Ludmirsky, O. Lebedev, D. Demihovskiy, V. Lapygin, A. Ermolaev, Yu. Milichenko, I. Tsygankov, I. Sulygin, N. Ignashin, S. Sytov, Yu. Antipov, D. Hmaruk, and G. Kuznetsov.

The light-ion program proceeds smoothly. Its advances are listed in Table 1.

Table 1: Light-ion program milestones

	Deuterons $^{2}H^{1+}$	Carbon $^{12}C^{6+}$
U1.5	16.7–448.6 MeV/u March 30, 2008	16.7–455.4 MeV/u December 08, 2010
U70	23.6 GeV/u April 27, 2010	34.1 GeV/u April 24, 2011
		Slow extraction at 455 MeV/u April 24, 2011
		24.1 GeV/u (300 GeV full) in BTL#22 and the FODS facility April 27, 2012
		Validation tests of all top-energy extractions with the ion beam April 24, 2013

STATISTICS

Since RuPAC-2012, the U70 complex operated for five runs in total. Table 2 lists their calendar data. There were two runs in a row during the spring of 2014, which is uncommon.

Figure 2 shows beam availability data during machine development (MD) and fixed-target experimental physics program (XPh) with averages accumulated over 2002–13. The extracted beam is delivered to experimental facilities with the 82.2% availability, on average.

Runs 2013-2 and 2014-1, 2 are all excluded from the statistics since these were the MD runs entirely, without a pronounced top-energy physical program.

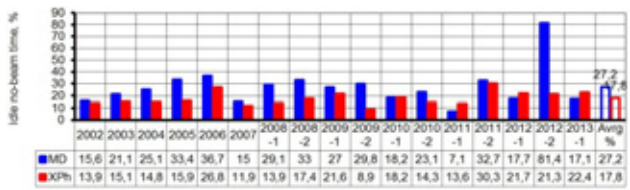

Figure 2: Beam availability statistics.

Details of the routine operation and upgrades are given on a run-by-rum basis in what follows.

RUN 2012-2

As it can be seen from Fig. 2, the unfortunate feature of this run was a failed MD program followed by a squeezed

ISBN 978-3-95450-170-0

tuning time for the machines prior to delivering proton beam to the fixed-target physics. (Say, the U70 PS had only 36 hr left for the machine studies and tuning.) The culprit to blame was an ageing HV equipment of RF power supply of the URAL30 linac. Its poor performance was aggravated by a delayed shipment of components and consumables due to adoption of a novel contracting regulation.

Still, all the problems thus involved were absorbed by the MD time thus yielding sustained beam availability for the fixed-target physics that is well commeasurable to the 10-year average expectation value.

Table 2: Five runs of the U70 in between RuPAC-2012 and -2014

Run	2012-2	2013-1	2013-2	2014-1, 2
Launching linac URAL30, booster U1.5 and U70 sequentially	October, 08	February, 25	November, 11	March, 11
Proton beam in the U70 ring since	November, 01	March, 11	November, 26	March, 28
Fixed-target physics program with extracted top-energy beams	November, 08 – December, 14, 35 days	March, 22 – April, 22 31 day	n/a	n/a
No. of multiple beam users (of which the 1st priority ones)	11 (9)	9 (8)	1	2(2)
MD sessions and R&D on beam and accelerator physics, days	8	7	21	21 ½
Light-ion acceleration MD program	December, 14–18, 3½ days	April, 24–27, 3½ days	December, 16–25, 8½ days	April ,08–25, 17½ days

To the final end, state of the entire complex was found to be adequate providing top manageable operational intensity of $1.05 \cdot 10^{13}$ ppp with only 4% beam losses over a cycle, refer to Fig. 3.

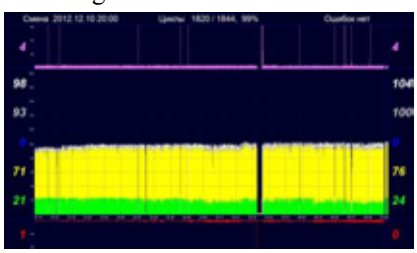

Figure 3: Screenshot of the on-line monitoring over the U70 operation. Time interval (abscissa) extends over 3 hr, or 1000 cycles. Yellow trace slows intensity of slow stochastic extraction, green trace — operation of internal targets and crystal deflectors. The bottom (red) trace indicates spent beam remains dumped onto an internal absorber. The top (purple) ray indicates beam losses.

The top-energy slow stochastic extraction has fed the OKA facility with $7–7.6 \cdot 10^{12}$ protons per a low-ripple spill (1.26 s long) at the 1st half of flattop, see Fig. 4.

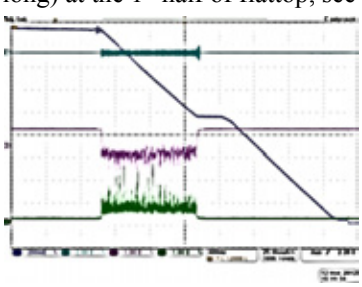

Figure 4: Slow stochastic extraction. The first (top) trace is intensity of waiting beam monitored with a DCCT. The second trace is AM-modulated phase noise of the 200 MHz carrier The third ray is the feedback signal that modulates the noise. The fourth ray shows slowly extracted beam monitored with a BLM at ES-septum.

Still, a persisting critical issue related to the stochastic extraction was left unhandled. The in-out transfer ratio of the extracted beam fraction was as low as 85–87% (occasionally, up to 90%) with a clear trend to lower values at higher beam intensities, above $7 \cdot 10^{12}$ ppp. There was no separation gap observed between the waiting and extracted beams at the upstream deflecting magnet #24 resulting in over-irradiating its septum. This problem was resolved in the run to follow.

Switching over to the carbon nuclei mode went on smoothly.

The I100 linac has provided 12–14 mA of pulsed current. Each emitting point on the graphite block inside the laser ion source survived for 4 300 laser pulses per spot which was equivalent to comfortable 9.5 hr of a non-stop operation, refer to Fig. 5.

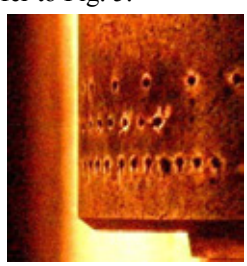

Figure 5: Graphite target of the laser ion source. The lower compact row of spent emitting spots stands for the present, optimised operation.

The booster synchrotron U1.5 operated with 9% overall beam availability and provided up to $6.5 \cdot 10^9$ ipp.

The main ring U70 accelerated $5 \cdot 10^9$ ipp (cycle period 8.3 s) to 24.1 GeV/u, the beam being extracted to BTL#22 terminated by the FODS facility. Research activity has been focused on the beam diagnostics and extraction procedure conditioning per se. The in-out transparency of the BTL#22 was recorded as 0.82 for test protons and 0.77 for carbon nuclei. These exercises have allowed for acquiring practical experience in handling composite

ISBN 978-3-95450-170-0

multi-nucleon projectiles with an existing inventory adapted to protons by its design.

RUN 2013-1

Prior to this run, the upstream part of the new BTL#25 has been manufactured and assembled, see Fig. 6. The reference top beam rigidity is 6.9 T·m. The beam line is 18 m long and has 3 dipoles, 4 quads and 2 vertical correctors. The line is fed from the septum magnet #34 facing the waiting beam coasting around the U70. The BTL#25 had to transport the beam towards the inner radiation-shielding wall of the ring hall (bld. 1) just upstream of the would-be radio-biological workbench.

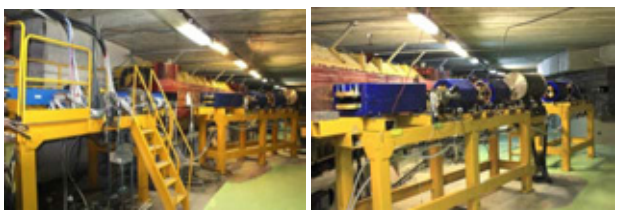

Figure 6: Upstream part of the new BTL#25 adjacent to and directed inwards the U70 ring. View along the beam.

To this end, the run was launched in a very uncommon sequence with the U-70 operating, first, in a beam storage and stretcher ring mode with 1.32 GeV protons. Such a beginning pursued the double goal:

1. To condition the URAL30 proton linac under beam in the aftermath of a crash program to restore its functionality during the shutdown.
2. To tune, align and commission with the (more affordable and intense) proton beam the aforesaid BTL#25 so as to ensure its readiness to accept the same-rigidity carbon nuclei beam scheduled by end of the run.

Both these goals were attained. Say, the linac ultimately turned out inoperative for only 8 hr 40 min (of which 6 hr 15 min were spend to replace 3 depleted high power generating tubes) which should be compared to some 320 idle hours during the run 2012-2. The linac had safely provided 35 mA of pulsed current thus enabling a few hours of the U1.5 booster running with $8{\cdot}10^{11}$ ppp, the cruise intensity being $4–5{\cdot}10^{11}$ ppp. The U70 itself yielded (max) $9.5{\cdot}10^{12}$ and (on average) $4.6{\cdot}10^{12}$ ppp limited by beam user demand.

In course of the U70 machine tune-up, one has spotted and eliminated a malfunction in the $B \propto x^2$ (octupolar) correction system of the magnetic guide field. The outcome was the long sought-for radical improvement of the slow stochastic extraction. It has attained a sustained in-out transfer ratio of 90–94% in the intensity range of $1–6.5{\cdot}10^{12}$ ppp, see Fig. 7.

With a diffusive (stochastic) actuation of the waiting beam outskirts onto the 3rd order betatron resonance, the spills used to reveal a pronounced DC content and a low-ripple structure free of cut-offs, see Fig. 8. Duty factor of such spills $\langle F\rangle^2/\langle F^2\rangle$ could go as high as to 0.81–0.82.

Both these two features allow for concluding that the U70 has ultimately got the effective low-ripple lasting slow extraction of an intensive proton beam.

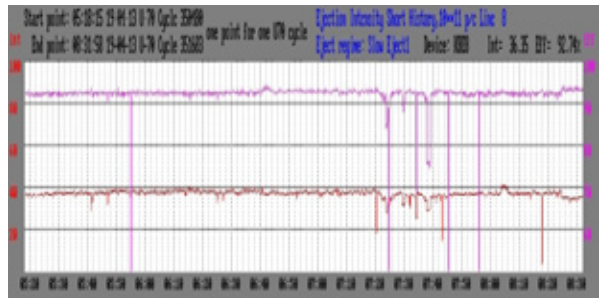

Figure 7: Screenshot of the on-line slow extraction monitor. The upper ray is in-out transfer ratio that safely goes above the 90% grid line intercepting rightmost ordinate axis. The lover ray traces the slowly extracted beam intensity (a bit lower than $4{\cdot}10^{12}$ ppp here).

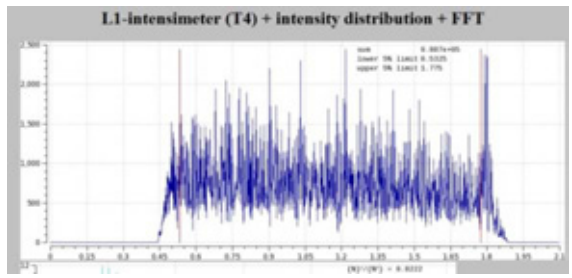

Figure 8: Beam slow spill monitored with head counters of the OKA experimental facility and broadcasted real-time via technological web-network for a control purpose.

During the run, a triple sequential beam splitting at the flattop was also implemented. The regime was found to be operational but not convenient due to an inevitable loss of the valuable flattop time for interfacing in-between the three extraction windows.

There were also the two outcomes of beam slow extractions with bent crystal deflectors worth mentioning:

1. Feeding the TNF-Atlas facility with a proton beam of intensity ranging from $1{\cdot}10^6$ to $4{\cdot}10^{11}$ ppp (i.e., varying by more than 5 orders of magnitude!).
2. Exercises with a new path of 700 ms long extraction of the 24.1 GeV/u carbon beam with the crystal deflector in straight section #22 and minimal spill intensity of $1.5{\cdot}10^7$ ipp. Still, even less intensive spills are demanded for. The work will be continued with a due analysis of the unwanted en-route fragmentation, if any.

The major outcome of the ion program was a successful commissioning of the new BTL#25 (Fig. 6) with a carbon beam, see Fig. 9.

RUN 2013-2

This run, like the run 2014-1 to follow, were the MD runs entirely, without acceleration of protons to the top energy of 50–60 GeV. By the summer of 2013, the former

ISBN 978-3-95450-170-0

out-of-date power supply system (rotating machine generators) of the 1.5 km long U70 ring magnet had been stopped and dismantled. Instead, the new one based on static thyristor AC-DC convertors was being installed thus precluding any conventional operation of the machines.

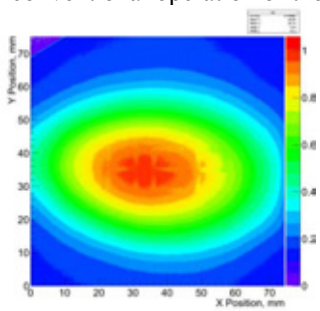

Figure 9: The first-in-record footprint of the slowly extracted carbon beam at the inner wall of the ring hall (bld. 1), i.e., at the end of upstream section of BTL#25.

To this end, the U70 magnet lattice was toggled to a stand-alone DC power supply unit yielding 130 A (field 353.7 Gs) and enabling operating the U70 as a beam storage and stretcher ring for 1.32 GeV (protons) or 455.7 MeV/u (carbon nuclei), which the U1.5 booster serves as the full-energy injector to.

The intermediate-energy runs pursued a double goal:

1. To provide a hot backup run-through and conditioning of all the technological sub-systems except for the top-energy magnet power supply, water-cooling of the U70 ring magnet, and powerful magnetic optics of the top-energy extractions.
2. To provide more time for studies and finer tuning of beam circulation, the new stochastic slow extraction of the intermediate-energy protons (a test beam) and carbon nuclei, and the new BTL#25 terminated by a radio-biological workbench.

The carbon-nuclei mode was turned-on smoothly. Pulsed current form the I100 linac reached 20 mA in 6 μs at base. The U1.5 booster accelerated 10^{10} ipp, the main ring U70 accepting around $5{\cdot}10^{9}$ ipp. In-out transfer ratio of the slow extraction was around 35%, and the external target got up to $1.7{\cdot}10^{9}$ ipp shaped into a tightly focused beam, see Fig. 10.

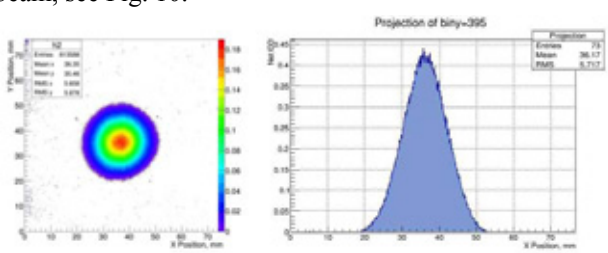

Figure 10: Carbon beam footprint at the entry window through radiation shielding of the workbench. Diameter 3 cm at 90% population level.

Given such a beam, the Interim Radio-Biological Workbench has been for the first time run legally as a self-sufficient experimental setup, short-named the IRBW, having got all the formal permissions thus prescribed. It constituted a noticeable step towards launching the topical applied-research activity there.

RUN 2014-1

The activity proceeded under the same restrictions and along the same guidelines as during the previous run. Finer alignment of the upstream magnets of the BTL#25 backed-up by a horizontal λ/2-bump compensation of the beyond-septum dipole stray field adverse effect on the circulating (waiting) beam has allowed raising the in-out ratio of the slow extraction to

- 8–10% for test protons which constitutes a gain ×2½ w.r.t. outcome of the run 2013-2, top expected limit being around 30% according to calculations;
- 45–50% (occasionally, to 57%) for carbon nuclei with expected calculated limit of around 80%.

Temporal and spatial portraits of the carbon beam extracted from the U70 are summarized in Fig. 11.

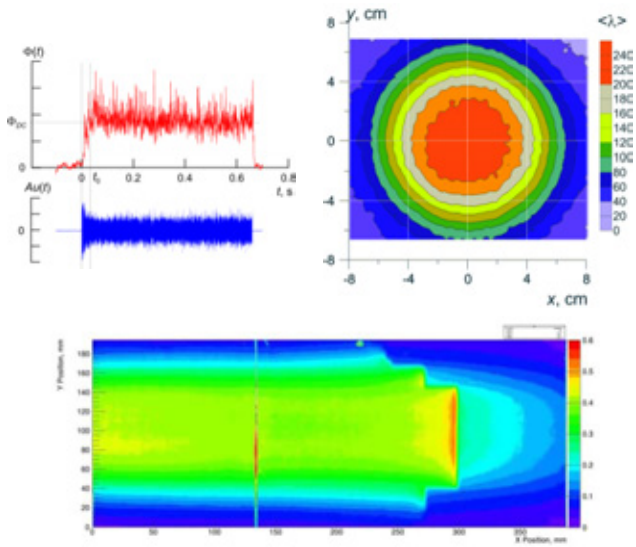

Figure 11: Structure of carbon beam from the U70. Top left — temporal *t*-pattern (0.6 s long low-ripple spill via feedback-controlled slow stochastic extraction). Top right — spatial transverse (*x*, *y*)-pattern (flattened paraxial dose field with a diameter 6 cm of <5% non-uniformity via a PM rotating electromechanical wobbler). Bottom — spatial longitudinal *s*-pattern (30 cm of stopping range in a water phantom with the Bragg's peak visible).

The temporal structure is drawn with a slow stochastic extraction system employing λ/2-phase-advance 2-stage Piccioni-Wright scheme, controlled horizontal noise-induced beam diffusion and dedicated beam fe edback circuit closed over "extraction flux – amplitude of colored-noise random carrier" path, just commissioned. Square-wave spills of 0.6–1.0 s duration are obtained routinely.

Transversally-flat paraxial dose distributions are obtained with a fixed-radius circular sweeping of the primary beam with the purpose-built PM rotating electro-mechanical wobbler. The device employs two third-party

ISBN 978-3-95450-170-0

cylindrical dipole Halbach structures and imposes the net deflection of about 6.5 mrad. Rotation frequency 30–50 Hz is compliant to the spill duration.

Longitudinal dose distribution is governed by the natural Bragg's law for 455.7 MeV/u carbon projectiles in water.

Such beam parameters were found adequate to launch the first-in-U70-record (17.04.2014) radiobiological exercises with biological substances that were accomplished by a team from the Medical Radiological Research Center of the Russian Ministry of Health (Obninsk, Kaluga Region).

RUN 2014-2

It was an extra ad hoc one-month long run dedicated to the two sequential and pressing tasks:

1. The first proof-of-workability ramps to 50 GeV (protons) with the new power supply plant of the U70 ring magnet.
2. Pre-commissioning with the fast-extracted 50 GeV protons of the new Proton-Radiographic Facility.

Both the tasks were accomplished successfully.

Deep upgrading the power supply plant of the U70 ring magnet from rotating machine generators to static thyristor convertors called for 1.5-year long persistent efforts from IHEP and the LLC "NIIEFA–Energo" (St.-Petersburg). These were spent to accomplish design, contracting, manufacturing and shipping the equipment followed by assembly operations on the site.

Figure 12 shows a few pieces of equipment thus acquired.

Figure 12: Direct connecting to an electric power transmission line 220 kV with a commercially available insulating gas (sulfur hexafluoride) electricity distribution switchgear (ABB) followed by a new step-down (10 kV) 108 ton transformer (left). Five sets of (static) thyristor AC-DC convertors designed and manufactured by the LLC "NIIEFA–Energo" (St.-Petersburg) (right).

In despite of quite a new-fangled dynamical and ripple performance of the guide field, the proton beam has been successfully captured at the flat bottom, accelerated to 50 GeV and then transferred to the extraction flattop, see Fig. 13.

Actuating all the control entries foreseen and finer tuning and conditioning of the new power supply plant are planned for the run 2014-3 scheduled for October–December, 2014. Still, quality of the 50 GeV proton beam attained was adequate to deliver fast extracted beam to the Proton Radiographic Facility.

This newly-built 50–70 GeV Proton-Radiographic Facility is a joint venture by IHEP and RFNC–VNIIEF (Sarov, N. Novgorod Region) that was launched in 2010. The facility has been designed to attain a ∅200 mm field-of-view and a sub-mm resolution for > 450 g/cm^2 optical density objects.

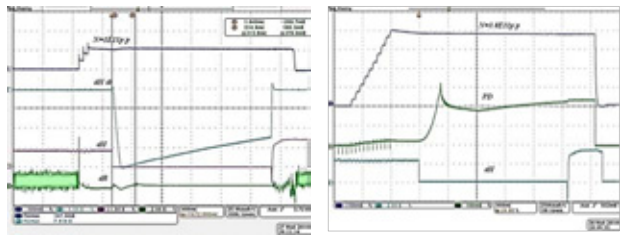

Figure 13: Oscilloscope screenshots of ramping to 50 GeV (protons) with a new power supply plant of the U70 ring magnet. Rays: *N* – beam intensity; *dH*/*dt* – magnetic-field ramping rate; *PD* – read-outs of beam peak-current detector inversely proportional to bunch length (spike at transition crossing); *dR* – radial excursion of rotating beam w.r.t. the reference orbit; *dH* – feedback signal to stabilize flat-bottom and flattop guide fields.

The core of the facility constitutes a triad of 180°FODOFODO quadruplets assembled of 24 paired side-by-side wide-aperture (hole ∅300 mm) quadrupole lenses with the top field gradient 6.7 T/m, see Fig. 14, all the lenses being designed and manufactured by IHEP.

During the run, the fast extracted 50 GeV proton beam from the U70 has been for the first time safely tracked and detected on-axis throughout the entire facility. There were no bottlenecks fond to preclude a further progress.

Figure 14: Wide-aperture quadrupole lenses of the new Proton Radiographic Facility at IHEP.

CONCLUSION

Accelerator Complex U70 of IHEP-Protvino is a subject to an ongoing upgrade program aimed at extending the machine functionality for fixed-target research, both fundamental and applied, with protons and carbon nuclei of high and intermediate energies, slowly or fast extracted.

REFERENCES

[1] S. Ivanov, on behalf of the U70 staff, Proc. of RUPAC-2008, Zvenigorod, 2008, p. 130–133; Proc. of RUPAC-2010, Protvino, 2010, p. 27–31. Proc. of RUPAC-2012, St.-Petersburg, 2012, p. 85–89.

ISBN 978-3-95450-170-0

STATUS AND PERSPECTIVES OF THE VEPP-2000 COMPLEX*

Yu.A. Rogovsky#, D.E. Berkaev, I.A. Koop, E.A. Perevedentsev, Yu.M. Shatunov, D.B. Shwartz,
BINP SB RAS and Novosibirsk State University, Novosibirsk, Russia

A.S. Kasaev, A.N. Kyrpotin, A.P. Lysenko, V.P. Prosvetov, A.L. Romanov, A.I. Senchenko,
P.Yu. Shatunov, A.N. Skrinsky, I.M. Zemlyansky, Yu.M. Zharinov,
BINP SB RAS, Novosibirsk,Russia

Abstract

The VEPP-2000 is a modern electron-positron collider at BINP. Last season in 2012–2013 was dedicated to the energy range of 160÷520 MeV per beam. The application of round colliding beams concept along with the accurate orbit and lattice correction yielded the high peak luminosity of $1.2 \cdot 10^{31}$ cm^{-2}s^{-1} at 500 MeV with average luminosity of $0.9 \cdot 10^{31}$ cm^{-2}s^{-1} per run. The peak luminosity limited only by beam-beam effects, while average luminosity – by present lack of positrons in whole energy range of 160÷1000 MeV. To perform high luminosity at high energies with small dead time the top-up injection is needed. At present new electron and positron injection complex at BINP is commissioned and ready to feed VEPP-2000 collider with intensive beams with energy of 450 MeV. Last calendar 2014 year was dedicated to the full/partial upgrade of complex's main parts.

VEPP-2000 OVERVIEW

The VEPP-2000 collider [1] exploits the round beam concept (RBC) [2]. This approach, in addition to the geometrical factor gain, should yield the significant beam–beam limit enhancement. An axial symmetry of the counter-beam force together with the X–Y symmetry of the transfer matrix between the two IPs provide an additional integral of motion, namely, the longitudinal component of angular momentum $M_z = x'y - xy'$. Although the particles' dynamics remains strongly nonlinear due to beam–beam interaction, it becomes effectively one-dimensional.

The RBC at VEPP-2000 was implemented by placing two pairs of 13 T superconducting final focusing solenoids into two interaction regions (IR) symmetrically with respect to collision points. There are several combinations of solenoid polarities that satisfy the RBC requirements, with different type of eigenmodes of betatron oscillations. Finally it was found that only 'flat' combinations (+− +− or +− −+) provide enough dynamic aperture (DA) for effective collider operation. This optics satisfies the RBC approach if the betatron tunes lie on the coupling resonance $\nu_1 - \nu_2 = 2$ to provide equal emittances via eigenmodes coupling.

The layout of the VEPP-2000 complex as it worked until 2013 is presented in Fig. 1. The complex consisted of the injection chain (including the old beam production system and Booster of Electrons and Positrons (BEP) with an energy limit of 800 MeV) and the collider itself with two particle detectors, Spherical Neutral Detector (SND) and Cryogenic Magnetic Detector (CMD-3), placed into dispersion-free low-beta straights. The main design collider parameters are listed in Table 1.

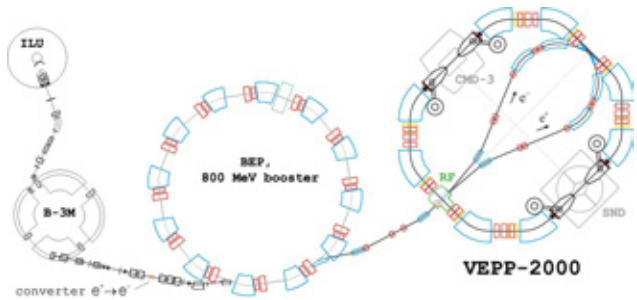

Figure 1: VEPP-2000 complex layout.

Table 1: VEPP-2000 main parameters @ E = 1 GeV.

Parameter	Value
Circumference (C)	24.3883 m
Energy range (E)	200÷1000 MeV
Number of bunches	1×1
Number of particles per bunch (N)	1×10^{11}
Betatron functions at IP ($\beta^*_{x,y}$)	8.5 cm
Betatron tunes ($\nu_{x,y}$)	4.1, 2.1
Beam emittance ($\varepsilon_{x,y}$)	1.4×10^{-7} m rad
Beam–beam parameters ($\xi_{x,y}$)	0.1
Luminosity (L)	1×10^{32} cm^{-2} s^{-1}

The density of magnet system and detectors components is so high that it is impossible to arrange a beam separation in the arcs. As a result, only a one-by-one bunch collision mode is allowed at VEPP-2000.

BEAM DIAGNOSTICS

Diagnostics is based on 16 optical CCD cameras that register the visible part of synchrotron light from either end of the bending magnets and give full information about beam positions, intensities and profiles. In addition to optical beam position monitors (BPM) there are also four electrostatic pickups in the technical straight sections, two photomultipliers for beam current measurements via the synchrotron light intensity, and one beam current transformer as an absolute current monitor.

*Work is supported by: 1) the Ministry of Education and Science of the Russian Federation, Nsh-4860.2014.2; 2) the RFBR grant 14-02-31501
#rogovsky@inp.nsk.su

ISBN 978-3-95450-170-0

During last season VEPP-2000 was equipped with two phi-dissectors [3] – stroboscopic image dissector with electrostatic focusing and deflection, that gives information about e^+/e^- longitudinal distribution of particles and bunch length.

EXPERIMENTAL RUNS

VEPP-2000 started data-taking with both detectors installed in 2009 [4]. The first runs were dedicated to experiments in the high-energy range, while during the last 2012 to 2013 run the scan to the lowest energy limit was done. Apart from partial integrability in beam-beam interaction the RBC gives a significant benefit in the Touschek lifetime when compared to traditional flat beams. This results in the ability of VEPP-2000 to operate at an energy as low as 160 MeV — the lowest energy ever obtained in e^+e^- colliders.

The averaged over 10% of best runs luminosity obtained by CMD-3 detector during the last three seasons is shown in Fig. 2 with red points. The red lines overestimate the hypothetically achievable peak luminosity. The blue dashed line shows the beam–beam limited luminosity for a fixed machine lattice (energy scaling law $L \propto \gamma^4$). It was successfully exceeded due to β^* reduction to 4÷5 cm available at low energies.

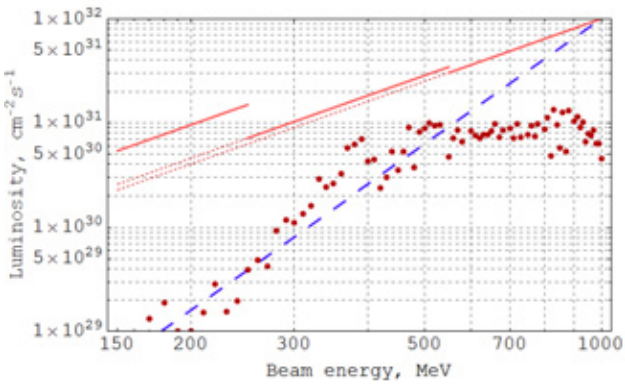

Figure 2: VEPP-2000 luminosity.

At high energies (>500 MeV) luminosity was limited mostly by an insufficient positron production rate. At energies over 800 MeV the necessity of energy ramping in the collider storage ring additionally restricts the luminosity. Only for middle energy range 300÷500 MeV the luminosity is really limited by the beam–beam effects, especially by the flip-flop [5]. At the lowest energies the main limiting factors are the small DA, IBS, and low beam lifetime.

BEAM–BEAM PARAMETER

We can define the 'achieved' beam–beam parameter as:

$$\xi_{\text{lumi}} = \frac{N^- r_e \beta^*_{\text{nom}}}{4\pi\gamma\sigma^{*2}_{\text{lumi}}}, \qquad (1)$$

where the beta function is nominal while the beam size is extracted from the fairly measured luminosity.

In Fig. 3 the correlation between achieved and nominal beam-beam parameters is shown for the full data at the given energy $E = 392.5$ MeV. 'Nominal' parameter defined as (1) but with unperturbed nominal beam size, thus being the measure of beam current. After thorough machine tuning the beam–beam parameter achieves the maximal value of $\xi \sim 0.09$ during regular work (magenta dots in Fig. 3).

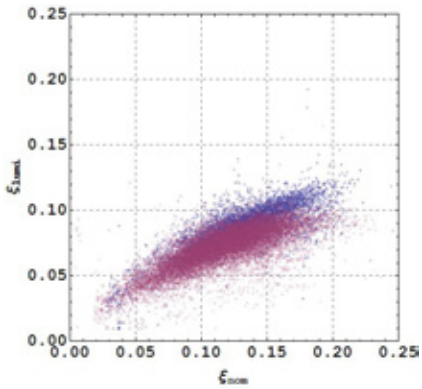

Figure 3: Achieved beam–beam parameter at 392.5 MeV.

LONG BUNCH

While studying the dependence of beam–beam threshold on bunch length at relatively low energy of 392.5 MeV it was found that the RF voltage decrease from 30 kV to 17 kV gives a significant benefit in the maximal value of ξ (blue dots in Fig. 3) up to $\xi \sim 0.12$ per IP. The cross-check for beam–beam parameter measurement is the analysis of the coherent beam oscillation spectrum.

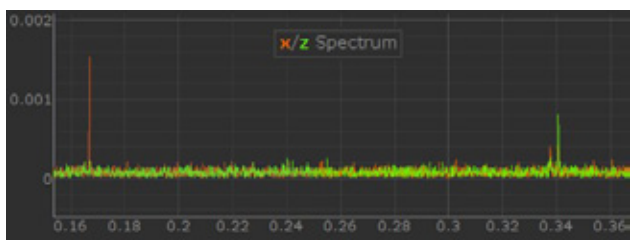

Figure 4: Beam-beam tune-shift @ 392.5 MeV.

In Fig. 4 one can find two pairs of σ- and π-modes tunes equal to 0.165 and 0.34, respectively. The total tune shift of $\Delta\nu = 0.175$ corresponds to ξ per one IP equal to:

$$\xi = \frac{\cos(\pi\nu_\sigma) - \cos(\pi\nu_\pi)}{2\pi\sin(\pi\nu_\sigma)} = 0.124\,. \qquad (2)$$

The Yokoya factor here is taken to be equal to 1 due to the fact that oscillations with very small amplitude (~5 μm = 0.1 σ^*) were excited by a fast kick and the spectrum was investigated for only 8000 turns. During this short time beam distribution is not deformed by an oscillating counter beam and remains Gaussian [6].

ISBN 978-3-95450-170-0

The observed beam-beam limit enhancement correlated with bunch lengthening firstly believed to be an experimental evidence of predictions [7] of beam-beam interaction mitigation for the bunch slightly longer than β^* due to second integral of motion arrival. The bunch lengthening in our particular case comes not only from the RF voltage decrease itself, but also from microwave instability, which was observed at low energies with a low RF voltage above a certain bunch intensity. Later it was shown in simulations [8] that finite synchrotron oscillations should demolish full integrability of beam-beam interaction.

Bunch lengthening

The length of an electron bunch in a storage ring depends on the peak current of the bunch. The two effects which alter the length are potential well distortion and microwave instability. For potential well distortion the bunch length varies due to the electro-magnetic fields induced by the electrons modify the RF voltage as seen by the bunch. This effect is present even at very low currents. The second effect, microwave instability, is only observed after a certain threshold current has been reached. Above this threshold the energy spread of the beam increases until the peak current of the bunch reduces to equal the threshold current again.

Direct observation of the onset of microwave instability in the VEPP-2000 was possible at an intermediate energy. Measurements have been carried out for electrons with intensities up to 50 mA at energy equal to 478 MeV with different values of RF voltages in presence of positrons with infinitesimal intensity. In these experiments all three beam dimensions were recorded as a function of bunch current. A subsequent experiments for positrons shows the same dependencies as for electrons.

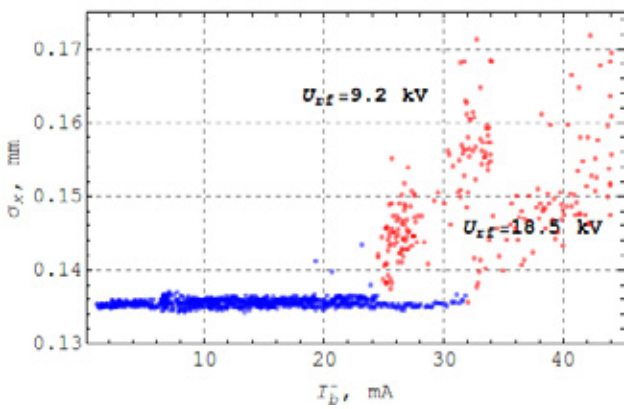

Figure 5: Horizontal beam size on 4M1L CCD (in place with non zero dispersion) as a function of beam current @ E=480 MeV.

Throughout the experiment σ_x remained constant below certain threshold (see Fig. 5, where blue dots show bunch size below threshold, red ones – above), confirming that the beam was indeed below the threshold of microwave instability. The variation of the bunch length with the beam current is given in Fig. 6. The microwave instability threshold appears at around 24.5 mA and 32 mA for RF voltages equal 9.2 kV and 18.5 kV respectively.

The bunch length data below threshold has been fitted to the model [9] described by equation:

$$\sigma_z^3 - \sigma_{z0}^2 \sigma_z = \frac{\alpha_p \left| Z/n \right|_{eff} R^3}{\sqrt{2\pi}(E/e)\nu_s^2} I_b, \qquad (3)$$

where I_b is the average beam current, e is the electron's charge, R is the ring average radius, E is the beam energy and ν_s is the synchrotron tune. The magnitude of the effect depends on the reactive part of the effective longitudinal coupling impedance |Z/n|. The dashed lines on the figure is a curve derived using (3) for |Z/n| = 2.32 Ohm.

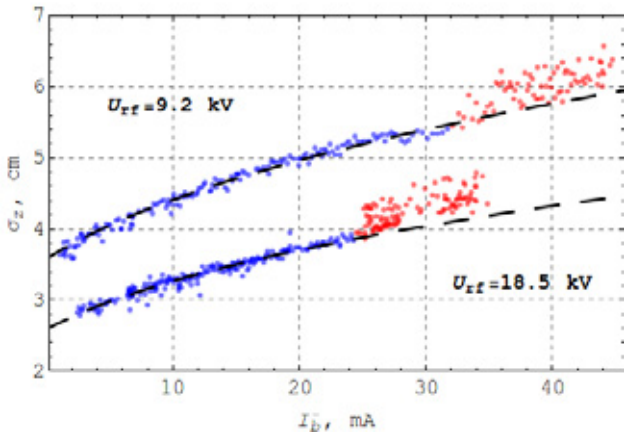

Figure 6: Bunch length as a function of beam current @ E=480 MeV.

Our capabilities do not allow to measure the energy spread directly, but estimation can be done by methods developed [10] during VEPP-2000 operations. This methods based on measurements of beam transverse sizes along the ring with further fitting the emittances end effective beta functions to known optical model of the ring assuming that there is no focusing perturbations other than those caused by collisions. In Fig. 7 one can find beam energy spread is estimated in such a way.

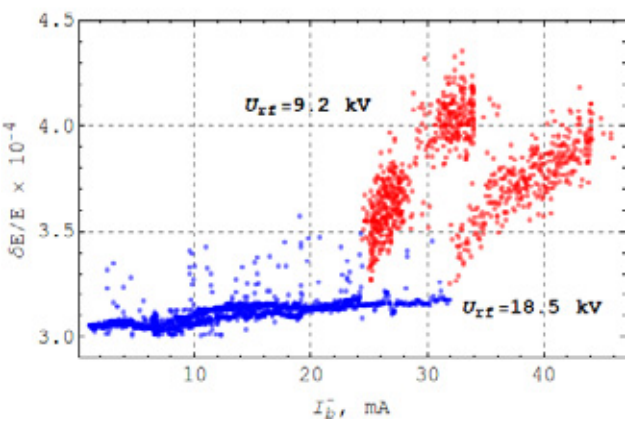

Figure 7: Beam energy spread as a function of beam current @ E=480 MeV.

ISBN 978-3-95450-170-0

The synchronous phase shift is being determined as a difference between phase of beam longitudinal distribution centre of mass and phase of RF system reference signal. Dependence of synchronous phase on beam current allow to determine a value of a bunch coherent energy loss. Results are shown in Fig. 8, where dashed line corresponds to coherent energy loss caused only by RF cavity HOM frequencies. As one can see from the pictures the contribution of the RF cavity is comparable (or slightly less) with the contribution of all the vacuum chamber in the ring.

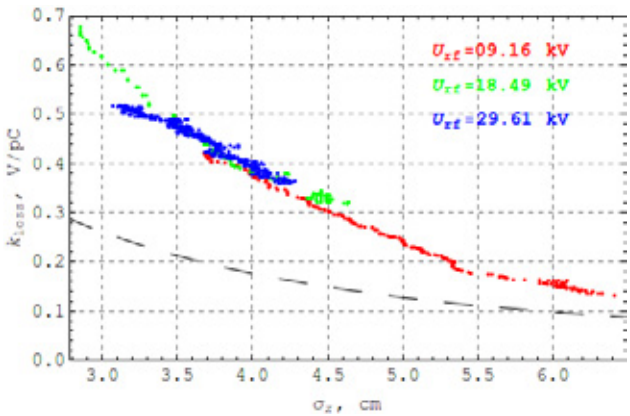

Figure 8: Longitudinal loss factor @ E=480 MeV.

UPGRADE MOTIVATION

VEPP-2000 electron positron collider was commissioned and spent three successful runs 2010-2013 collecting data at whole energy range of 160÷1000 MeV per beam [10]. During this work VEPP-2000 used the injection chain of its predecessor VEPP-2M [11]. That machine worked at lower energy (< 700 MeV) and showed luminosity 30 time lower than designed value of 10^{32} $cm^{-2}s^{-1}$ for VEPP-2000 at 1 GeV. As a result the positron production rate was not enough to achieve beams intensity limited only by beam-beam threshold. This restriction will be cured by link up via 250 m beamline K–500 [12] to the new injection complex VEPP-5 [13] capable to produce intensive electron and positron high quality beams at energy of 450 MeV (see Fig. 9).

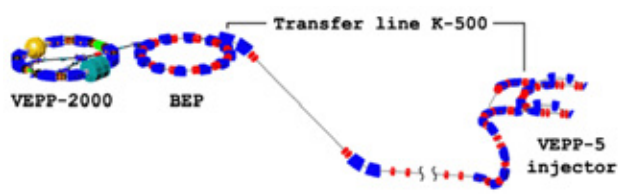

Figure 9: VEPP-2000 accelerator complex after upgrade.

Another VEPP-2000 efficiency limitation comes from maximal energy of the booster ring BEP [14] limited at the value of 800 MeV. Even with unlimited beams production rate beam-beam parameter being at the threshold after injection inevitably decrease after acceleration in the collider ring $\xi \propto 1/\gamma^2$. In addition dead time during acceleration process and the complexity of acceleration of colliding beams close to the threshold mean the necessity of the top-up injection.

BEP OVERVIEW

Booster synchrotron BEP dedicated to capture, cooling and storage of hot 125 MeV positrons from conversion system operated since 1991. It consists of 12 FODO cells. Each cell houses 30° sector dipole, two quads and straight, used for RF-cavity, kickers, injection/extraction septum, diagnostics, vacuum pumping. Booster layout is presented in Fig. 10, main parameters of BEP after upgrade are listed in Table 2.

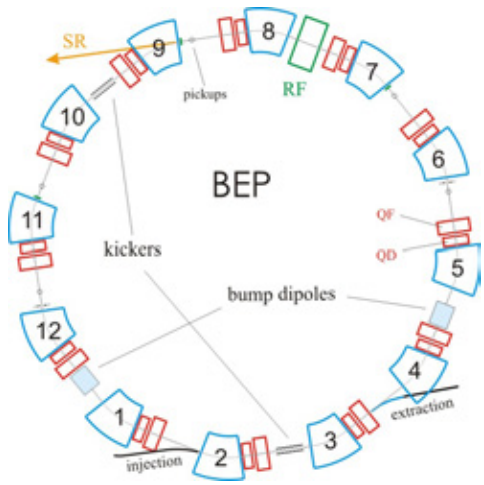

Figure 10: Booster synchrotron BEP layout.

Table 2: Modified BEP Main Parameters @ E = 1 GeV.

Parameter	Value
Perimeter, Π	22.35 m
Revolution frequency, f_0	13.414 MHz
Bending radius, r_0	128 cm
RF harmonic, q	13
Synchrotron radiation loss	70 KeV/turn
Emittances, ε_x, ε_y	$8.6 \cdot 10^{-6}$, 10^{-8} cm
Betatron tunes, ν_x, ν_y	3.4, 2.4
Momentum compaction, α_p	0.06

BEP UPGRADE STATUS

Magnetic system

To achieve the target beam energy all magnetic elements should be significantly strengthened [15]. The main idea of magnets upgrade is the use of existing coils, power supplies and whole infrastructure. Fields increase arises both from iron reshaping with aperture reduction and feeding current boost up to 10 kA.

Prototype dipole magnet was produced at the end of 2013. It's measured field distribution is shown in Fig. 11. Main efforts of quadrupole modification were

ISBN 978-3-95450-170-0

aimed to reproduce strongly non-linear saturation curve of dipole.

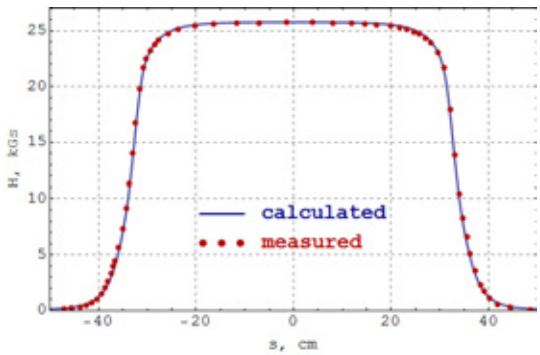

Figure 11: Field longitudinal distribution $B_y(s)$ at 9.9 kA.

Vacuum system

One cell vacuum chamber consists of extruded aluminium segment inside dipole and focusing doublet and stainless steel chamber with pumping equipment port. To use the old system after components modernization aluminium chamber (a) deformed locally inside dipole magnet (b) and small quad QD (c) (see Fig. 12). In order to decrease QD strength and reduce deformation the BEP working point was moved from (3.46, 2.85) to (3.4, 2.4).

Figure 12: Vacuum chamber cross-section.

RF system

Since the energy loss increases at higher energy and achieves 70 KeV/turn new copper RF cavity was manufactured in BINP workshops. It will operate with 174.376 MHz frequency and 110 kV voltage.

Injection / extraction

New injection septum magnet is needed to receive 450 MeV beams from VEPP-5. 25° pulsed magnet with 10 mm aperture and field value of 34 kGs is completed and will be installed after magnetic measurements. Extraction system remains completely unchanged.

Slow-pulsed closed orbit distortion of ~25 mm in horizontal direction (so called "bump") is needed for beam extraction. Old system of additional windings in 4 dipoles becomes very ineffective at high energy due to strong iron saturation. Instead two 30 cm pulsed (2.5 ms) laminated C-shape magnets will be installed with 1.7 kGs field.

TRANSFER LINE BEP-VEPP

The transport of accelerated to 1 GeV bunches from BEP to VEPP-2000 collider needs significant modernization of transfer line. The most important one is the manufacturing of new bending magnets (17.2°, 41.2°) with the same radius and field as BEP dipoles but smaller gap of 12.8 mm and 2 turns/pole coil instead 5 turns/pole in BEP dipoles. Fed in series with BEP magnets channel's ones should have the same field-current dependence.

CONCLUSION

Round beams give a serious luminosity enhancement. The achieved beam-beam parameter value at middle energies amounts to $\xi \sim 0.1$–0.12. VEPP-2000 is successfully taking data with two detectors across the whole designed energy range of 160÷1000 MeV with a luminosity value two to five times higher than that achieved by its predecessor, VEPP-2M [10]. At present the VEPP-2000 booster BEP is disassembled and passing through deep modernization to achieve top energy of 1 GeV, provide top-up injection and designed luminosity of the electron-positron collider.

REFERENCES

[1] Yu. Shatunov et al., "Project of a New Electron-Positron Collider VEPP-2000", EPAC'2000, Vienna, Austria, p.439.
[2] V.V. Danilov et al. “The Concept of Round Colliding Beams”, Proc. EPAC’96, Sitges, p. 1149 (1996).
[3] E.I. Zinin, PhD Thesis, Budker Institute of Nuclear Physics, 1984 (un Russian)
[4] M.N. Achasov et al., “First Experience with SND Calorimeter at VEPP-2000 Collider”, Nucl. Instrum. Meth. A 598 (2009) 31–32.
[5] D.B. Shwartz et al., “Recent Beam–Beam Effects and luminosity at VEPP-2000”, Proc. IPAC’14, Dresden (2014)
[6] P.M. Ivanov et al. “Experimental Studies of Beam–Beam Effects at VEPP-2M”, Proc. Workshop on Beam–Beam Effects in Circular Colliders, Fermilab, p. 36 (2001).
[7] V.V. Danilov and E.A. Perevedentsev. “Two Examples of Integrable Systems with Round Colliding Beams”, Proc. PAC’1997, Vancouver, Canada, p. 1759 (1997).
[8] A. Valishev et al. “Beam-Beam Limit in an Integrable System”, Proc. NaPAC’13, Pasadena, p. 77 (2013).
[9] A. Hoffman and J.R. Maidment, “Current dependent phenomena in LEP”, CERN, LEP Note-168 (1979).
[10] A. Romanov et al. “Status of the Electron-Positron Collider VEPP-2000”, Proc. NaPAC’13, Pasadena, p. 14 (2013).
[11] G.M. Tumaikin et al., HEACC'1977, Serpukhov, USSR, p.443.
[12] I. Zemlyansky et al., "Electron and Positron Beams Transportation Channels to BINP Colliders", these proceedings (FRCA03).
[13] A. Starostenko et al., "Status of Injection Complex VEPP-5", these proceedings (TUY02).
[14] V.V. Anashin et al., "Damping Ring for Electrons and Positrons BEP", BINP preprint 84-114, Novosibirsk, 1984.
[15] D.B. Shwartz et al., “Booster of Electrons and Positrons (BEP) Upgrade to 1 GeV”, Proc. IPAC’14, Dresden (2014)

ISBN 978-3-95450-170-0

STATUS OF INJECTION COMPLEX VEPP-5

P. Logatchev, A. Petrenko, D. Bolkhovityanov, D. Nikiforov, A.Levichev, A.Barnyakov, A.Novikov, V. Gambaryan, K. Astrelina, Budker INP, Novosibirsk, Russia
A.Starostenko, F.Emanov, Budker INP, Novosibirsk; NSU, Novosibirsk, Russia

Abstract

The VEPP-5 Injection Complex [1] will supply BINP RAS colliders with electron and positron beams. Primary launch have been performed: electron and positron beams were obtained, injection to damping ring have been done, as well as storage of electrons and positrons. Now both transport channel to the electron/positron colliders VEPP-2000 and VEPP-4M are fully assembled and therefore test extractions of electron beam with energy of 360 MeV into beam lines to users are being performed. Main users require a reliable and trouble proof source of particles, thus reliability and stability of operation are a paramount tasks.

INTRODUCTION

VEPP-5 Injection Complex consists of 270 MeV driving electron linac, 510 MeV positron linac and damping ring (See Fig.1). Both linear accelerators are based on four accelerating modules, each one feeds by one SLAC klystron (5045). Two first modules have three accelerating structures and second two — four structures. First accelerating structures of both linacs have an enhanced average acceleration gradient of 20 MeV/m and other regular sections up to 17–20 MeV/m. Both linacs can operate up to 50 Hz repetition rate. Dumping ring stores and cools down both electron and positron beams (See Figure 3). It is equipped with 50 Hz injection system.

Figure 2: Linear accelerators.

Figure 3: Damping ring.

Table 1: Designed parameters of Injection Complex

Maximum Beam Energy (MeV)	510
Max. number of electrons in the beam	$2 \cdot 10^{10}$
Max. number of positrons in the beam	$2 \cdot 10^{10}$
Energy spread in the beam (%)	0.07
Longitudinal beam sigma (mm)	4
Vertical emittance (mm mrad)	0.005
Horizontal emittance (mm mrad)	0.023
Dumping times vert./horis. (ms)	17/11
Extraction rate (Hz)	1

Designed parameters of VEPP-5 Injection Complex are presented in Table 1. At the parameters listed above Injection Complex will be able to cover all needs of BINP e+ e- colliders for nearest future. This will greatly improve the VEPP-2000 and VEPP-4M performance, because of significant increase of positron production rate and will help to reach their maximum luminosity.

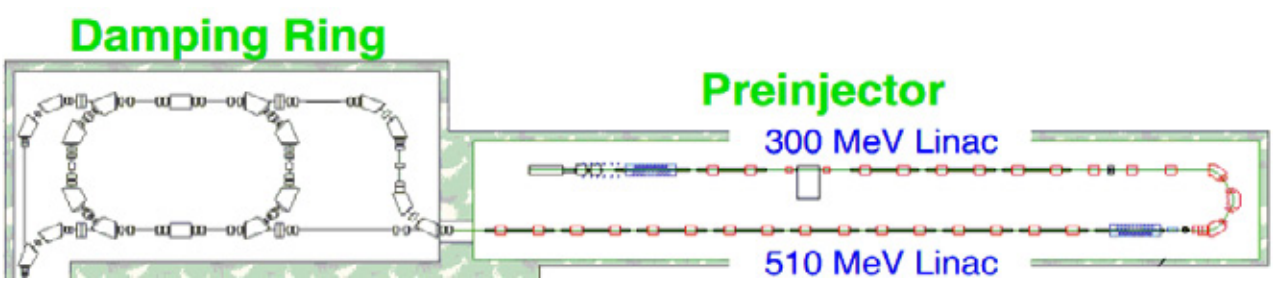

Figure 1: Injection complex.

ISBN 978-3-95450-170-0

COMMISSIONING PLANS AND TECHNIC

Commissioning Results

The VEPP-5 Injection Complex should be running with project parameters in the near future. Damping ring of the Complex stores the electron beams of 350 MeV today. Storage rate is $3 \cdot 10^9$ electrons per pulse and maximum store current is 160 mA, which exceeds design parameters. Beam transfer line to the BINP colliders is completely assembled and ready for beam accepting. The Damping ring optics were tuned to improve the Complex stability. Also new beam diagnostics were installed to ease beam injection in the Damping ring.

Measurement of Injection Angle

To improve the parameters of storage rate it is necessary to perform matching of the injection system and damping ring. Injection scheme use vertical DC Lambertson type septum magnet biased from an equilibrium orbit in the radial direction and kicker. Septum magnet directs the beam to the median plate and then by means of kicker beam is shifted to closed orbit. In this system injection angle must tend to zero. To determine the transverse coordinate of the beam in the septum and injection angle we can measure the beam position as a function of some quadruple lens strength after septum magnet (See Figure 4). In this experiment, transverse coordinate x of the injected beam recorded by means of phosphor screen LK4, furthermore 3D2 lens and kicker plate were switched off (See Figure 5). Beam displacement on the phosphor screen is performed via a current variation in the 3F3 lens (See Figure 6). Coordinate value and angle on the phosphor screen (x, x') and in the septum magnet (x_0, x_0') is associated via transport matrix R :

$$\begin{pmatrix} x \\ x' \end{pmatrix} = \begin{pmatrix} R_{11} & R_{12} \\ R_{21} & R_{22} \end{pmatrix} \begin{pmatrix} x_0 \\ x_0' \end{pmatrix}$$

Thus by means of known coordinates for two values of current in a lens it is possible to obtain system of the equations for (x_0, x_0'):

$$\begin{cases} R_{11}(I_1)x_0 + R_{12}(I_2)x_0' = x_1 \\ R_{11}(I_2)x_0 + R_{12}(I_2)x_0' = x_2 \end{cases}$$

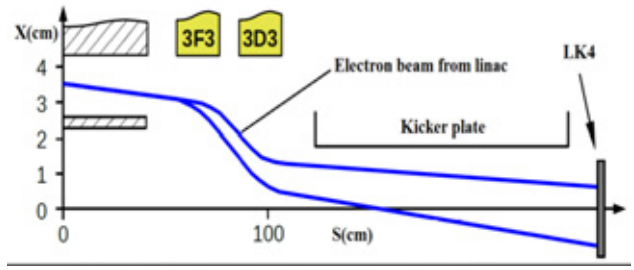

Figure 5: Scheme of angle measurement experiment.

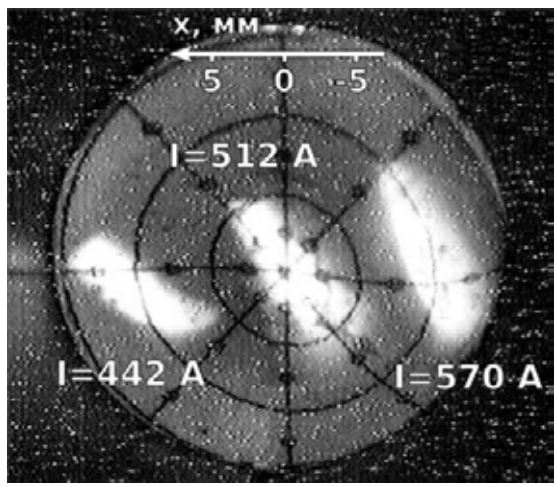

Figure 6: Beam shifting depends on the 3F3 current.

For measurement on the Figure 7 following values for x coordinate and x' angle were obtained: $x \approx 3cm$, $x' \approx -3mrad$. After precision geodetic installation of septum magnet and after repeated measurements the next values were obtained: $x \approx 3.5cm$, $x' \approx -0.08mrad$.

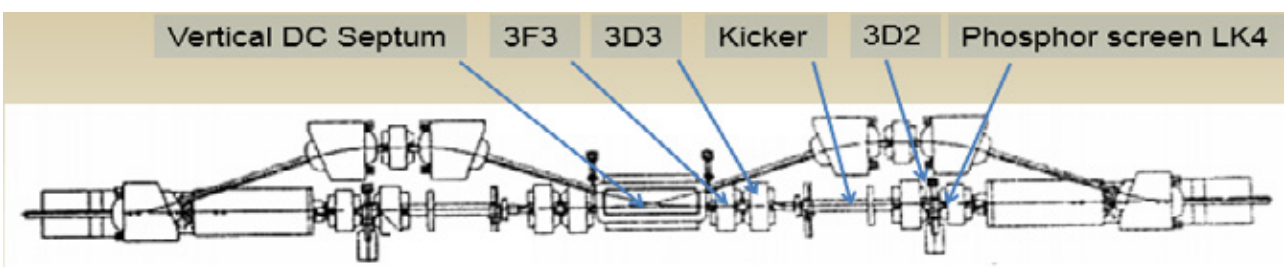

Figure 4: Injection transport line. 3F3, 3D3, 3D2 – quadruple lenses after septum magnet.

ISBN 978-3-95450-170-0

Damping Ring Lattice and Closed Orbit Correction

One of the most crucial issues arising during launching the dumping ring is a presence of optical parameters in accuracies in a real structure. Thus, detection and removal of such inaccuracies are tasks of highest priority in achieving the stable functioning of the complex.

First betatron tunes were set to the project values. After that software "sixdsimulation" developed for VEPP-2000 [2] was applied to correct linear lattice and closed orbit. It took 4 iterations to correct linear lattice by fitting the model to the experimental data composed of closed orbit responses to the all dipole correctors, dispersion, and betatron tunes. After last iteration, the fitted model didn't show significant variation from the ideal configuration (See Fig. 7).

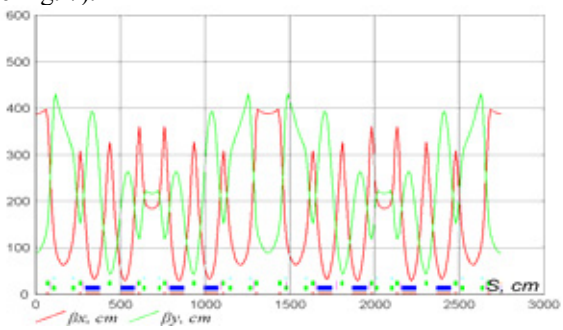

Figure 7: Beta functions for project optics in VEPP-5 dumping ring.

Closed orbit correction was done with respect to the quadruple magnetic centers (See Fig. 8-9). To do so closed orbit responses to the gradient variations of the individual quadruples [3].

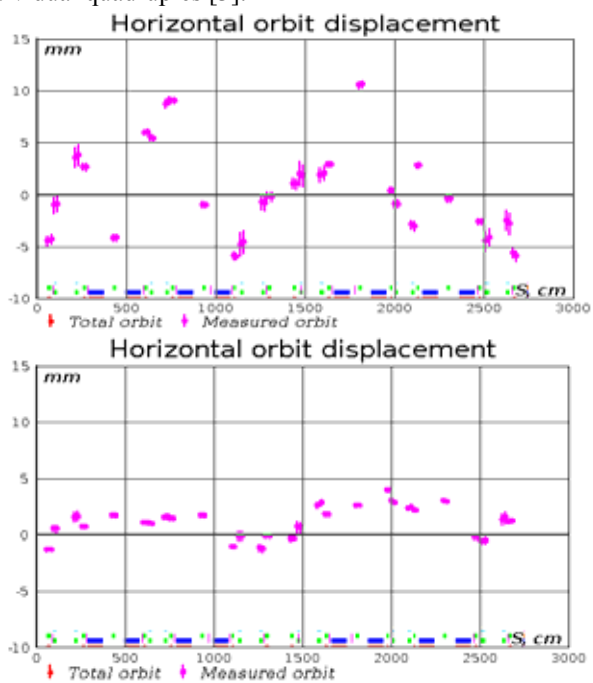

Figure 8. Closed orbit correction. Top – befor correction, bottom – after.

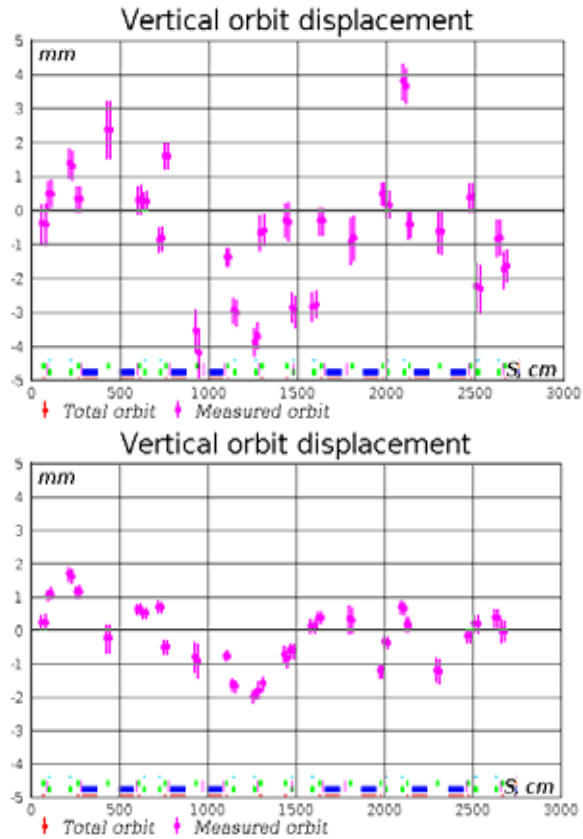

Figure 9: Closed orbit correction. Top – befor correction, bottom – after.

CONCLUSION

During the season 2013/2014 following results were achieved: number of e^- on conversion target - $1.5 \cdot 10^{10}$ per pulse, energy of e^- on conversion target- 275Me, energy of e^+ at the end of linac – 420 MeV, number of e^+ at the end of linac - $6 \cdot 10^+$ per pulse, maximum current of e^+ in dumping ring - 70 mA (number - $4 \cdot 10^{10}$), maximum current of e^- in dumping ring -160 mA (number - $9 \cdot 10^{10}$), injection rate - 12.5 Hz. Maximum storage rate of electron is $9.3 \cdot 10^9$ per pulse. Maximum storage rate of electron is $5 \cdot 10^8$ per pulse.

REFERENCES

[1] P.V.Logatchev et al, "Status of VEPP-5 Injection Complex",Proc. RuPAC-2006

[2] A. Romanov et al., Round Beam Lattice Correction using Response Matrix at VEPP-2000, Conf. Proc. IPAC-2010, THPE014 (2010).

[3] *J. Safranek*. Experimental Determination of Storage Ring Optics Using Orbit Response Measurements, Nucl. Instr. And Meth. A388, (1997) p. 27.

ISBN 978-3-95450-170-0

COMMISSIONING 2 MEV COOLER IN COSY AND NOVOSIBIRSK

V. B. Reva, V.V. Parkhomchuk, BINP, Novosibirsk, and NSU, Novosibirsk, Russia
M.I. Bryzgunov, A.V. Bubley, A.D. Goncharov, V.M. Panasyuk, BINP, Novosibirsk, Russia
Vsevolod Kamerdzhiev, FZJ, Jülich, Juergen Dietrich, HIM, Mainz

Abstract

The 2 MeV electron cooling system for COSY-Julich was proposed to further boost the luminosity in presence of strong heating effects of high-density internal targets. The 2 MeV cooler is also well suited in the start up phase of the High Energy Storage Ring (HESR) at FAIR in Darmstadt. It can be used for beam cooling at injection energy and for testing new features of the high energy electron cooler for HESR. The COSY cooler is designed on the classic scheme of low energy coolers like cooler CSRm, CSRe, LEIR that was produced in BINP before. The electron beam is transported inside the longitudinal magnetic field along whole trajectory from an electron gun to a collector. The 2 MeV electron cooler was installed in the COSY ring in the spring 2013. Electron beam commissioning and first studies using proton and deuteron beams were carried out. Electron cooling of proton beam up to 1662 MeV kinetic energy was demonstrated. Maximum electron beam energy achieved so far amounted to 1.25 MeV. Voltage up to 1.4 MV was demonstrated. The cooler was operated with electron current up to 0.5 A.

SETUP DESCRIPTION

Electron cooling is very useful technique for obtaining high-quality ion beams with high-intensity and low momentum spread [1]. In this method, the phase-space density of an ion beam is increased with a Coulomb interaction of a “hot” ion beam with a “cold” electron beam. Therefore, the ion beam repeatedly transfers its thermal energy to the electron beam moving with the same velocity.

There are many experiments and theoretical calculation that shows the useful of the magnetized cooling. These experiments and calculation was done in the different scientific centres in the world. The 2 MeV cooler at COSY is the first device utilizing the idea of magnetized cooling in this energy range, being an important step towards relativistic electron cooling required for the HESR at FAIR. Furthermore, it has been shown, that the 2 MeV cooler, if installed in the HESR, can be used without changes for the heavy ion operation modes [2,3].

First ideas was formulated in 2003 and a first report was published in 2005 [4].The construction of the 2 MeV electron cooler for COSY began at the Budker Institute of Nuclear Physics (BINP) in 2009 and ended 2012. In spring 2013 the cooler was installed in the COSY ring. First beam cooling results were obtained in October 2013 by the joint BINP-COSY team. Further beam cooling experiments followed during a two-week period of dedicated beam time beginning of 2014. At that time a first attempt to use electron and stochastic cooling in the same machine cycle was made. Furthermore, electron cooling of proton/deuteron beam into a barrier bucket was demonstrated. The design of the cooler and its main parameters are described in [5].

The schematic design of the setup is shown in Fig.1. The electron beam is accelerated by an electrostatic generator that consists of 33 individual sections connected in series. Each section has two high-voltage power supplies with maximum voltage 30 kV and current 1 mA. The electron beam is generated in electron gun immersed into the longitudinal magnetic field. After that the electron beam is accelerated, moves in the transport line to the cooling section where it will interact with protons of COSY storage ring. After interaction the electron beam returns to electrostatic generator where it is decelerated and absorbed in the collector.

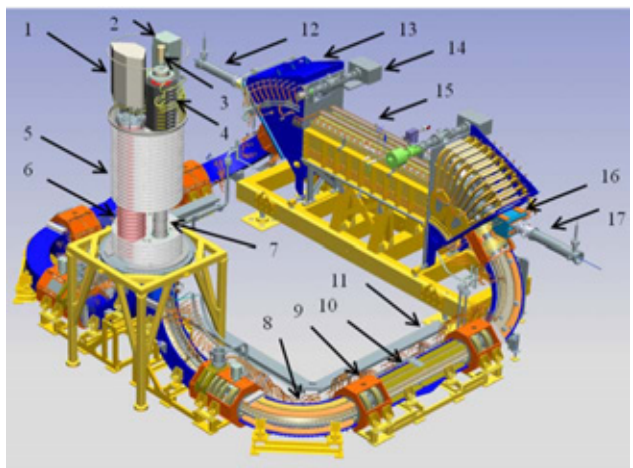

Figure 1: 3D design of 2 MeV COSY cooler. Collector PS is 1, SGF system is 2, ion pump of collector is 3, collector with magnetic system is 4, HV section is 5, cascade transformer is 6, acceleration tube is 7, bend 90 degrees is 8, straight section is 9, line section is 10, cable path is 11, input of the proton beam is 12, toroid 45 is 13, vacuum pump is 14, cooling section is 15, ion dipole is 16, output of the ion beam is 17.

The optics of 2 MeV cooler for COSY is designed close to the classical low-energy coolers. The motion of the electron beam is magnetized (or close to magnetized conditions) along whole trajectory from a gun to a collector. This decision is stimulated by requirement to operate in the wide energy range from 25 keV to 2 MeV. So, the longitudinal field is higher then transverse component of the magnetic fields. The bend magnets and linear magnets of the cooler are separated by a section

ISBN 978-3-95450-170-0

with large coils for the location of the BPMs, pumps and a comfort of the setup assembling. The length of the linear magnets is defined by the necessity to locate the electrostatic generator outside the shield area of the storage ring.

The vacuum chamber is pumped down by ion and titanium sublimation pumps. The typical diameter of the vacuum chamber is 100 mm and the aperture in the transport channel and cooling section is close to this value. The diameter of the accelerating tube is 60 mm.

HIGH-VOLTAGE AND RECUPERATION STABILITY

The final of the electron beam commissioning in Novosibirsk was stay during 6 days and nights at the energy 1 MeV and currents 200 mA. Figure 2 shows the example of the long-term training regime. Sometimes the recuperation breakdown occurs often and some time rarely. It seems that this behaviour can be improved by a training procedure. The physical nature of breakdowns isn't clear because any precursors weren't observed before breakdown. The spontaneous recuperation breakdowns were observed also at low energy (30 kV for example). Today the main hypothesis concerned with the fast changing of the vacuum condition in the accelerator tubes. It can be induced by some dust particle evaporation or the accumulation of the secondary ions. The ions can be trapped in the potential well formed by the electron beam. After reaching a threshold value the accumulated ions fast escape from the trap region to the vacuum chamber and accelerating tube which has negative potential respect to the ground. The pumping of the secondary ions with special device slightly improves the situation with breakdowns but it doesn't solve this problem completely. The typical vacuum value is a few 10^{-8} mbar.

More accurate vacuum assembling and careful vacuum baking procedure make it possible to obtain the vacuum 10^{-9}-10^{-10} in whole electron cooler in Juelich. The situation with spontaneous breakdown was improved but the detail investigation wasn't done. Figure 3 shows the example of the operation with high-voltage in COSY.

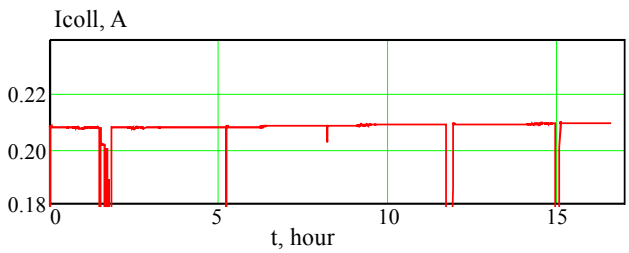

Figure 2: Electron current versus time. Fragment of training regime with electron beam in BINP.

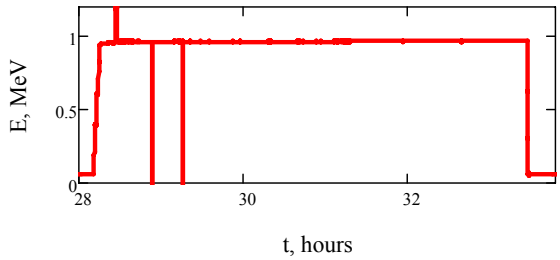

Figure 3: Example of the operation with high-voltage in COSY.

FIRST COOLING EXPERIMENTS

The first electron cooling experiments was done with electron energy 109 kV and the proton energy 200 MeV. The longitudinal magnetic field in the cooling section is 530 G.. The choice of such energy is avoidance of the problem with electron beam tracing. Such electron energy is small enough for the strong adiabatic motion of the electron along its trajectory, but the proton beam life is higher as compared with the injection energy. Because the observing of the electron cooling effects is easy at small value of the electron friction force until the situation when all parameters are acquiring the optimum values.

Figure 4 shows the parameters of the proton beam versus time. One can see that the sizes of the proton beam decrease from 5÷7 mm to 1 mm. The losses of the proton beam are small enough.

Increasing of proton beam intensity leads to growth of the proton beam losses. At initial proton current 3.7 mA the intensity of the proton beam decreases in factor 3 during cooling procedure.

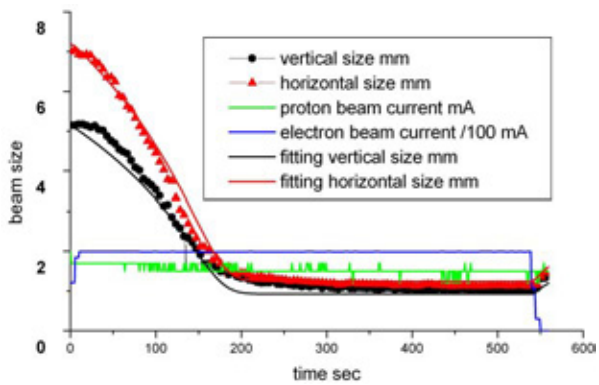

Figure 4: Parameters of the proton beam versus time during the electron cooling process

JOINT ACTION OF ELECTRON AND STOCHASTIC COOLING

The storage ring COSY is equipped by the system of the stochastic cooling. In time of the electron cooling experiments the stochastic system was tuned on the energy corresponding to the energy of the electron beam 908 kV and it was operated in the vertical direction only. The experiment with joint action of the different cooling

ISBN 978-3-95450-170-0

systems was done at this energy. Figure 5 shows the sizes of the proton beam at the different conditions.

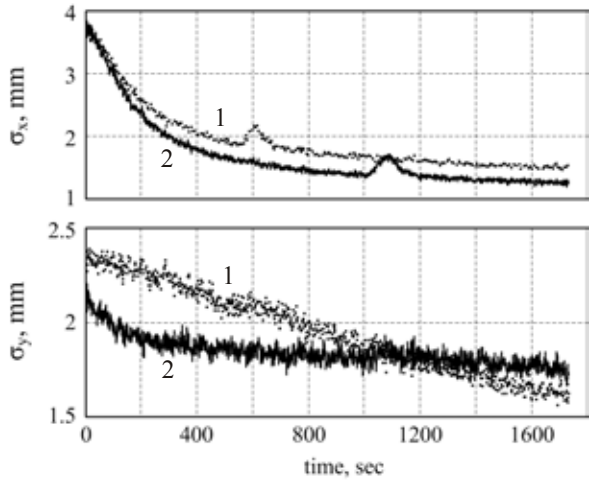

Figure 5: Sizes of the proton beam versus time at the different condition of the experiments. The action of electron beam only is 1, the joint action of the electron and stochastic cooling in vertical direction is 2.

One can see that the joint action of the cooling systems makes it possible more deep shrinking of the proton beam in the horizontal direction. The dynamics of the vertical size is different essentially. The vertical size of the proton beam decreases very fast in initial time but the action of the electron cooling system only enables to receive smallest size of the proton beam in compare with joint action of the cooling systems. This effect may be explained by the excitation of a coherent instability. The signal from the Schotky pick-ups showed strong oscillation when the proton beam was cooled significantly. The vertical size increases in this moment, the horizontal size remains same. The electron cooling force is enough for preserving of the horizontal size but the excitation is absent.

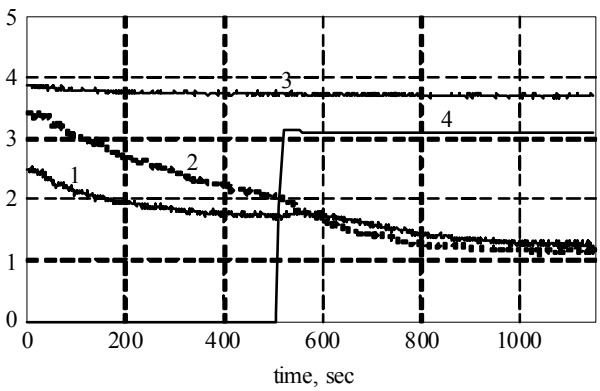

Figure 6: Parameters of the proton beam versus time. The vertical size is 1, the horizontal size is 2, the proton current is 3 (in unit 100 uA), the electron current is 4 (in unit 100 mA).

Figure 6 shows the dynamics of the proton beam in machine cycle with action of both cooling systems. In first moment the stochastic cooling was used only. In the middle of cycle the electron cooling was added. The rate of the cooling in the transverse direction became higher.

The experiments with joint action of the electron and stochastic cooling is very important because the stochastic cooling is very effective at large amplitude of the betatron oscillation, but the electron cooling is effective at small betatron amplitudes.

SUMMARY

The key problems of the electron cooler 2 MeV (modular approach of the accelerator column, the cascade transformer, the compass base probe located in the vacuum chamber, the design of the electron gun with 4-sectors control electrode) is experimentally verified during commissioning in Novosibirsk.

The first successful experiment was carried out in COSY with 2 MeV electron cooling device. The large range of the cooling energy for operation makes it possible to cool the proton beam with energy from 200 MeV to 1.66 GeV. The experimental results show usefulness the electron cooling device with strong longitudinal magnetic field for improving quality of the proton beam.

AKNOWLEGMENTS

This work us supported by the Ministry of Education and Science of the Russian Federation, NSh-4860.2014.2

REFERENCES

[1] 1. A.N.Skrinsky, V.V.Parkhomchuk. Physics of elementary particle and atomic nucleus. v.12 (1981), N.3, p. 557-613.

[2] Th. Stöhlker et al., “SPARC Experiments at the HESR: A Feasibility Study”; https://www.gsi.de/fileadmin/SPARC/documents/SPARC@HESR_FS_V26.pdf”.

[3] T. Katayama et al., “Electron Cooling of Heavy Ions Interacting with Internal. Target at HESR of FAIR”, , IPAC2013, Shanghai, China, May 2013, MOPEA017; http://www.JACoW.org

[4] V. Bocharov et al., “Budker INP Proposals for HESR and COSY electron cooler systems” COOL’05, Galena, September 2005, p. 308-316; AIP Conference Proceedings, v.821.

[5] V. B. Reva, N.I. Alinovskiy, T. V. Bedareva et al. Proc. “Commissioning COSY cooler with electron beam at Novosibirsk”. COOL-13, Murren, Switzerland, 2013, P.79-83.

ISBN 978-3-95450-170-0

ON THE WAY TO A RELATIVISTIC ELECTRON COOLER

J. Dietrich#, TU Dortmund and Helmholtz Institut Mainz, Germany
K. Aulenbacher, M. Bruker, A. Hofmann, Helmholtz-Institut Mainz, Germany
V. Kamerdzhiev, Forschungszentrum Jülich, Germany
M. Bryzgunov, V. Parkhomchuk, V. Reva, BINP SB RAS, Novosibirsk, Russia

Abstract

A 4-8 MeV relativistic electron cooling system for the HESR storage ring, which is part of the future GSI facility FAIR, is needed to further boost the luminosity even with strong heating effects of high-density internal targets. In addition, the upgrade to 8 MeV of the relativistic electron cooler is essential for the future Electron Nucleon Collider (ENC at FAIR) project. Using the experience of the 2 MeV electron cooler at COSY, which has the highest energy of all coolers that were made based on the idea of magnetised cooling and transport of the electron beam up to now, a new concept for powering the solenoids at high voltage is proposed.

INTRODUCTION

The use of electron coolers in the range of electron beam energy lower 400 keV is well established and state of the art. For higher electron energies there exists up to now only one machine – the Recycler Electron Cooler (REC) of Fermilab with a terminal voltage of 4.4. MV [1]. The cooler was installed into the Recycler during the summer of 2005 and was operating until the end of 2011 when the Tevatron was shut off. The cooling opened the possibility for several times higher, record luminosities. The REC overcame not only the great challenge of operating 4.4 MV pelletron accelerator in the recirculation mode with up to 1A beams, but also resolved the hard issue of high quality beam transport through non-continuous magnetic focusing beamline [2]. The next unique high energy electron cooler -the 2 MV COSY electron cooler- was commissioned in 2013 at Juelich [3]. Development of high energy electron coolers is a technical challenge due to the engineering problems like high voltage generation, power transmission to the gun and collector in the accelerator "head" and the power transmission to the magnetic coils at the accel/decel tubes for magnetised electron beam transport. Today there is a need for further development. In the high energy storage ring HESR for antiprotons at the FAIR facility in Darmstadt a 4.5 MV electron cooler is planed [4]. The proposed concept of the polarised Electron-Nucleon Collider (ENC) integrates the 15 GeV/c HESR of the FAIR project for protons/deuterons and an additional 3.3 GeV electron ring [5]. A new 8.2 MV electron cooler is an essential part in this concept. In the NICA collider project of JINR Dubna a 2.5 MV electron cooler is foreseen with one electron beam per each ring of the collider [6]. There are some special features of high energy cooling. The cooling rate decreases with $\beta^{-4}\gamma^{-5}$ [7]. To obtain a maximum friction force the "waveiness" of the magnetic force line should be as small as possible to get a smaller contribution to the effective electron velocity [8]. To get a high cooling rate magnetised electron cooling is necessary. All low-energy (3-400 keV) electron coolers are based on magnetised cooling. The electron beam transport and alignment of electron and ion beam is done with continuous magnetic field. Strong magnetic field completely suppresses transverse temperature of electron beam, so that effectiveness of cooling is determined by a very low longitudinal temperature of electrons. Non-magnetised cooling relies on the fact that rms velocity spread of electrons is comparable or smaller than the one of ions which need to be cooled. For the REC (non-magnetised case) cooling times of about one hour was sufficient. The new coolers for COSY and the new future projects should provide a few orders of magnitude more powerful longitudinal and transverse cooling. This requires new technical solutions. The basic idea of the 2MeV COSY cooler and for the future HESR and NICA collider coolers is to use a high magnetic field along the orbit of the electron beam from the electron gun to the collector. Faster cooling times are essential for the future projects. The technical problems for electrostatic accelerator at 8-10 MV and needed electron beam currents up to 3 A is a great challenge. An alternative can be a low frequency linac with bunched electron beam. Today this system achieved electron peak currents of about 10 A [9].

In order to solve critical technical issues of a future relativistic electron cooler based on an electrostatic accelerator the Helmholtz-Institut Mainz promotes collaborations with other Institutes such as Forschungszentrum Juelich (FZJ), Budker Institute of Nuclear Physics Novosibirsk (BINP), Russia and Lehrstuhl fuer Technische Thermodynamik und Transportprozesse, University Bayreuth. One of the challenges in case of the electrostatic accelerator is the powering of HV-solenoids for the magnetised electron beam transport. The HV-solenoids are located on different electrical potentials inside a high voltage vessel, which is why they needed a floating power supply. A novel idea from Budker institute is to use small turbines for high voltage generation, for power of the magnetic coils in-side the high voltage vessel and for powering of

#juergen.dietrich@tu-dortmund.de

ISBN 978-3-95450-170-0

gun and collector in the HV terminal. At the moment, two different concepts are being discussed. In the first design, many small HV-solenoids are powered by a cascade transformer, which is powered by turbo generators. In the second proposal, few big HV-solenoids are powered directly by turbo generators.

HIGH VOLTAGE ACCELERATOR-VESSEL

An important element of the electron cooler device is the high voltage vessel, whose principal design is illustrated in Figure 1.

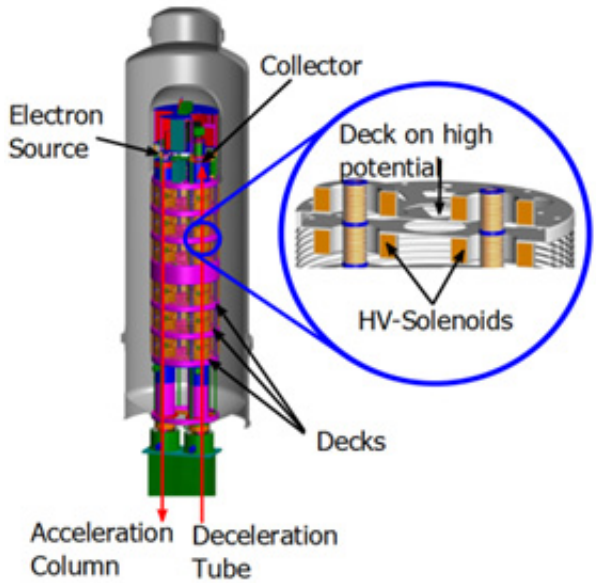

Figure 1: Principal design of the high voltage vessel [10].

The main components are the DC-thermionic electron source, the collector, the acceleration and deceleration tubes. The acceleration/deceleration voltage is provided by a high voltage column, which is built in a modular way and consists of decks. Every deck has a defined electrical potential. To guide the electrons from the gun to the interaction section, where the cooling process takes place, and back to the collector, a homogeneous magnetic field is necessary. It is generated with solenoids, the so-called HV-solenoids, which are mounted on the decks. This results in various requirements to the power supply for the HV-solenoids. Because the decks are on a fixed electrical potential, the power supply for the HV-solenoids must not be grounded. A high reliability of the powering system for the HV-solenoids is a must. In addition to the HV-solenoids, there are more devices on the HV deck, which also need powering, e.g. vacuum pumps.

POWERING OF THE HV-SOLENOIDS

Currently, two different concepts are being discussed, which were proposed by the BINP in a frame of a design study [11]. In both concepts, the power supply should be built in a modular way. While the 2MeV COSY cooler serves as a basis for the first concept, for the second concept the Swedish design, which had originally been planned by the Svedberg Laboratory, Uppsala University [9], was taken as a model.

Cascade Transformer

A well known and tested technology to power the HV-solenoids is a cascade transformer, which is already in use at the COSY cooler. to power the HV-solenoids and to generate a potential difference of 60kV between the individual decks.

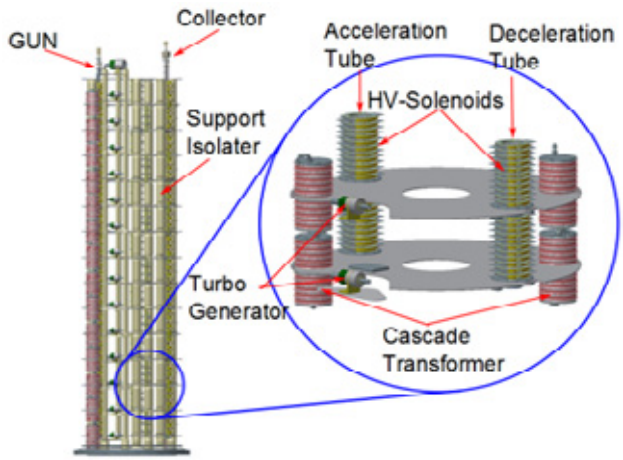

Figure 2: Powering the HV-solenoids with a cascade transformer. The left image shows the whole modular power supply, the right drawing shows two modules. The magnetic field is generated by several small HV-solenoids that are mounted along the acceleration/deceleration tube. The HV-solenoids are powered by a cascade transformer. A second cascade transformer generated the acceleration/deceleration voltage. Both cascade transformers are feeded by a turbo generator, an assembly of a turbine and a generator.

The turbine is powered by a gas under high pressure, consequently driving the generator. An advantage which is obtained with the use of turbo generators is that the expanded gas from the turbine can be used for cooling the HV-solenoids.

High-Voltage Column with Unit Elements

In this approach, the power supply should also be built in a modular way, but instead of a cascade transformer which distributes the power to many small decks (or HV-solenoids respectively), only one deck, a so-called Separation Box, per module should be used (Figure 3). Each Separation Box sits on a defined electrical potential. The potential difference between two Separation Boxes is 600kV, the distance is 0.7m. Every Separation Box contains all the electronics of a module. Furthermore, two HV-solenoids are mounted per Separation Box. In this design, the HV-solenoids are composed of four coils. To smooth the variations of the magnetic field, the coils are surrounded with iron. But also in this design, a floating power supply is necessary to feed the HV-solenoids. As in the first design proposal, turbo generators should be

ISBN 978-3-95450-170-0

used. But in contrast to the first approach, the turbo generators feed the HV-solenoid and all the other electronics inside the Separation Box directly. For the generation of the acceleration/deceleration voltage a Cockcroft-Walton generator can be considered.

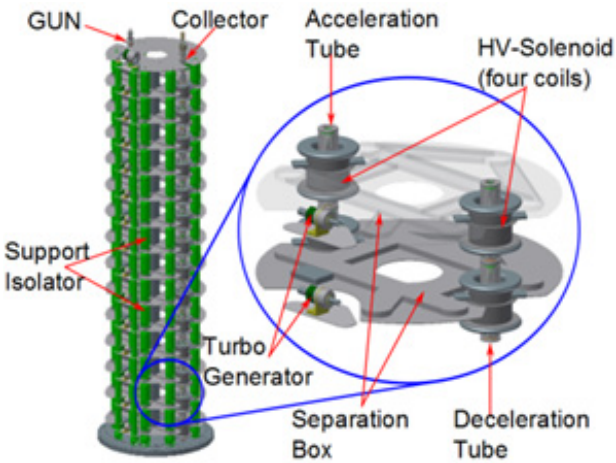

Figure 3: Direct powering of the HV-solenoids with a turbo generator. The left image shows a drawing of the entire module with electron gun and collector. On the right two modules, consisting of a Separation Box and two HV-solenoids are shown.

The second design approach allows easier construction and maintenance. Disadvantages are higher power consumption and the arrangement of the HV-solenoids that demands more attention to the beam optics due to small variations of the magnetic field along the beam axis.

GREEN ENERGY TURBINE

For both concepts, a suitable turbo generator is essential. A research for proper turbo generators has identified the GREEN ENERGY TURBINE (GET) (Figure 4) form the company DEPRAG [12] as a potential candidate, which works with dry air. Further properties of the GET are listed in the Table.

Table: Properties of the GET

Power	5 kW
Pressure (in)	4 bar
Pressure (out)	1 bar
Mass Flow	4 m3/min

A critical point in both concepts is the generation of the pressurised gas. As the high voltage vessel is filled with sulphur hexafluoride, the preferred gas is SF_6, since this reduces the problems e.g. in the case of leaks. Based on the data of the GET, the efficiency was roughly estimated to 12.5% for a compressor power (air) of 40kW. If we assume the same specification of the GET for SF_6 as driving gas, a compressor power of 28kW is required. This results in an efficiency of 18%, but that is probably an overestimation. However, a low efficiency means high operational cost. Alternatively an Organic Ranking Cycle (ORC) like process could be applied in the case of SF_6 [13].

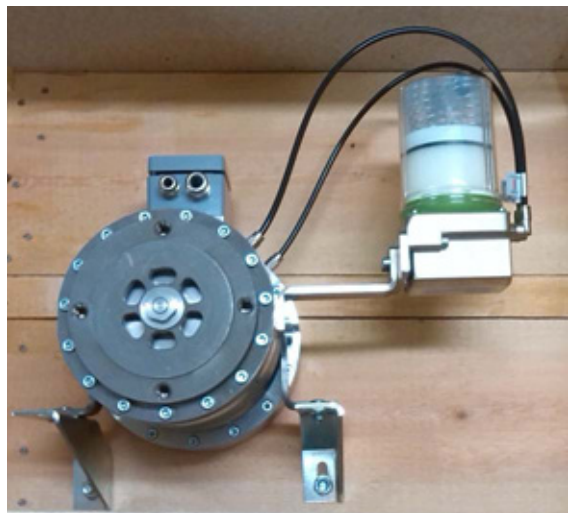

Figure 4: GET turbine with lubrication unit.

CONCLUSION

To investigate the pros and contras of the different approaches a test bench is necessary, where e.g. the reliability, temperature regime, efficiency of the turbine can be studied. Other problem to study is the magnetic field quality dependent on the magnetic coil design.

REFERENCES

[1] S. Nagaitsev et al., Phys. Rev. Lett. **96**, 044801 (2006).
[2] A. Burov et al., Phys. Rev. ST-AB **3**, 094002 (2000).
[3] V.B.Reva et al., COSY 2MeV Cooler: Design, Diagnostic and Commissioning, , IPAC2014, Dresden, p. 777 (2014).
[4] R. Maier, The High Energy Storage Ring (HESR), PAC 2011, New York, p. 2104 (2011).
[5] Andreas Lehrach, Polarized Electron-Nucleon Collider ENC at FAIR, Beam Dynamics Newsletter, No. 58, p.29 (2012).
[6] E.V. Ahmanova et al., Electron Cooler for NICA collider, COOL'11, Alushta, p. 125 (2011).
[7] M. Bryzgunov, privat communication.
[8] V.V. Parkhomchuk, New insights in the theory of electron cooling, Nuclear Instruments and Methods in Physics Research A 441 (2000) 9-17.
[9] V.V. Parkhomchuk et al., Electron Cooling for RHIC, C-A/AP/47, BNL, Upton (2001).
[10] "HESR Electron Cooler Design Study", University Uppsala, 2009.
[11] Report: Design Study for a Power Supply Test Modul for a 4-8 MeV Electron Cooler, BINP Novosibirsk, (2014).
V.V. Parkhomchuk et al., Conceptual Project Relativistic Electron Cooler for FAIR/HESR, IPAC2014, Dresden, p.774 (2014).
[12] www.deprag.com
[13] A. Hofmann et al., Turbo Generators for Powering the HV Solenoids at the HESR Electron Cooler, IPAC2014, Dresden, p.492 (2014).

ISBN 978-3-95450-170-0

MECHANISM OF COMPRESSION OF POSITRON CLOUDS IN THE SURKO TRAP OF THE LEPTA FACILITY*

E. Ahmanova, A. Kobets, I. Meshkov, O. Orlov, A. Sidorin, S. Yakovenko , JINR, Dubna, Russia
M.K. Eseev#, NAFU after name M.V. Lomonosov, Arkhangelsk, Russia

Abstract

Results from experimental studies of plasma storage in the Surko trap at the LEPTA facility are presented. The number of stored particles is found to increase substantially when using the so-called "rotating wall" (RW) method, in which a transverse rotating electric field generated by a cylindrical segmented electrode cut into four pairs is applied to the positrons storage region.

The conditions of transverse compression of the plasma bunch under the action of the rotating field and buffer gas are studied. The optimal storage parameters are determined for these experimental conditions. Mechanisms of the action of the rotating field and buffer gas on the process of positron clouds storage are presented.

INTRODUCTION

Experiments with antimatter required the development of methods of storage, confinement and manipulate of clouds of antiparticles. For these purposes, generally used a electromagnetic trap. One method of increasing the efficiency of storage: increase in the lifetime of charged clouds inside the trap in a rotating electric field. The effect of «The Rotating Wall» (RW) was detected in experiments on the storage of a plasmoid ions [1]. Then, similar results were obtained for both the electron and positron plasma [2, 3]. The method of the rotating field is used to generate antihydrogen in projects ATHENA/ALPHA [4, 5]. Successful use of this method allowed us to begin the study of the properties of antimatter and exotic atomic and molecular systems. Determining if there is storage of the frequency and the direction of rotation of the field in a plane transverse to the axis of the trap. The dependence of the efficiency savings from RW-field parameters is resonant. There are several mechanisms [6-9] action of the rotating field compression and holding a bunch of charged particles trapped. Until now, the explanation of this phenomenon causes a heated discussion.

THE SURKO TRAP OF THE LEPTA FACILITY

The LEPTA facility [10] is designed for generating high flow orthopositronium opportunity to carry out precision measurements of the characteristics of positronium. In the storage ring can be made of two kinds of particles injection. The electron beam creates an electron gun to clear the circulating electron beam collector exists, positron beam is injected from the source of positrons passing through positron trap. Optimization of the process of accumulation of positrons in the trap is one of the basic conditions of work. This is an open the trap Malmberg-Penning type with a longitudinal magnetic field. Retention of charged particles in the longitudinal direction of the accumulation is carried out by the electrostatic field created by trap electrodes. With the storage of positrons injection from the source (^{22}Na) of a continuous stream necessary to ensure the selection of the energy of motion for the "rolling" in the potential well inside the trap. For these purposes, Surko [11] proposed the use of a buffer gas. Thus modified trap began to wear his name. It is used to the LEPTA facility (see Fig. 1).

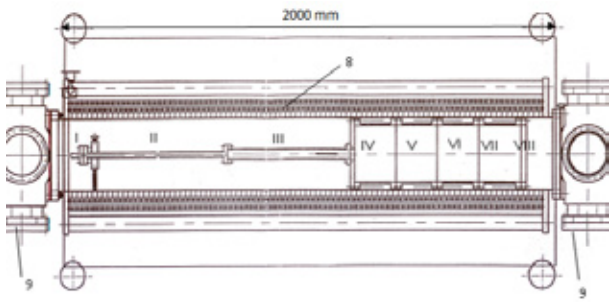

Figure 1: Scheme the Surko traps (longitudinal section). I - VIII - electrodes 8 - solenoid 9 - Vacuum posts.

MECHANISM OF COMPRESSION OF POSITRON CLOUDS

In [12] proposed a mechanism of the effect of a RW-field on the transverse size and lifetime of the storage trapped cloud based 3D model of the dynamics of charged particles. The exteriments datas were presented on research independion frequency of the rotating field with a longitudinal oscillation bounce-frequency, which show the validity of this model. The essence of the proposed mechanism is reduced to the necessity of matching the frequency of the rotating field f_{RW}, frequency magnetron motion of particles in the trap f_- and the frequency of the longitudinal oscillations of the bounce f_z :

$$f_{RW} = Nf_- = Lf_z . \quad (1)$$

Here N, L — integers. The values of the longitudinal oscillation frequency bounce-determined depth and size of the potential well, retaining particles within the area of accumulation. The values of the magnetron frequency is

*Work supported by grant RFBR №12-02-00072
#m.eseev@narfu.ru

ISBN 978-3-95450-170-0

defined as the electrode potential and the space charge accumulated particles. The resonance condition (see Eq. 1) provides a systematic effect of the rotating field, which can reduce the drift of particles to the walls of the trap due to the pressure of the buffer and the residual gas.

EXPERIMENTAL RESULTS: POSITRON STORAGE

In 2013-2014 he was modernized equipment [13] on the LEPTA facility. In particular, as the trapped vacuum stations are installed cryogenic pump and the turbomolecular pump. This allowed to disconnect during storage ion pump, improve almost an order of magnitude (up to 10-9 torr) vacuum inside the base of the trap. In addition to quantitative changes in vacuum conditions and this has led to qualitative changes in the conditions of storage. The adsorption of large organic molecules, which give large cross sections of positron annihilation in the cryopump has significantly raised the lifetime and efficiency of accumulation of positrons. Results were obtained by accumulation of electrons in the trap. Found resonances of storage electrons on the frequency of the rotating field, which agreed well with the calculations (see Eq. 1) for the given parameters.

Experiments were performed to generate the positron annihilation with a detector PMT. Were obtained depending on the number of storage positrons in low-density mode of the frequency of the rotating field (see Fig. 2).

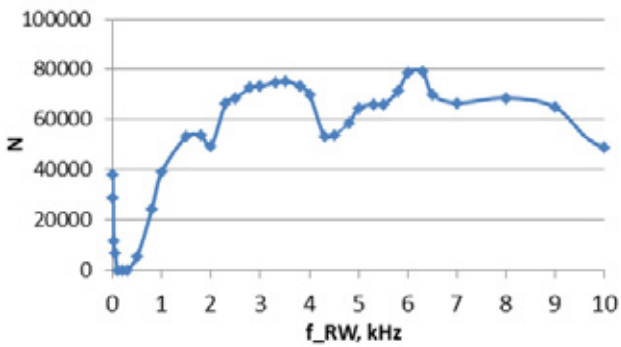

Figure 2: Dependence of the number of positrons in the cloud on the frequency of the rotating field.

Emphasis is placed on the resonances at low frequencies. The dynamics of the accumulation process when turning the rotating field at resonance shows a significant increase in the number of accumulated positrons at low frequencies (see Fig. 3).

With movable collector were obtained transverse size positron clouds when turning the rotating field (see Fig. 4).

Data from these experiments show that the increase in the lifetime and the reduction of the transverse size of the cloud of positrons trapped possible at low frequencies of the rotating field, which are far from the bounce frequency oscillations (about 1 MHz).

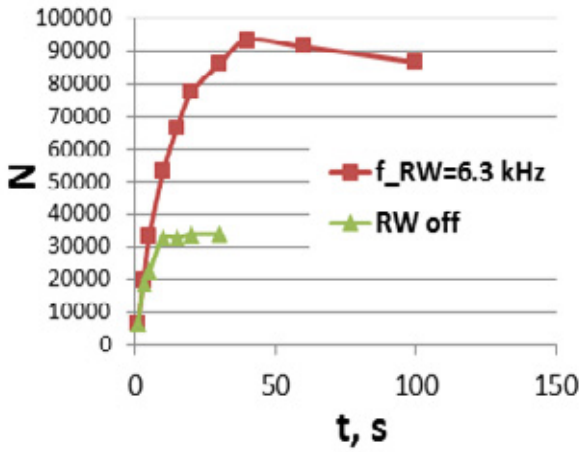

Figure 3: Dependence of the number of positrons in the clouds from the storage time.

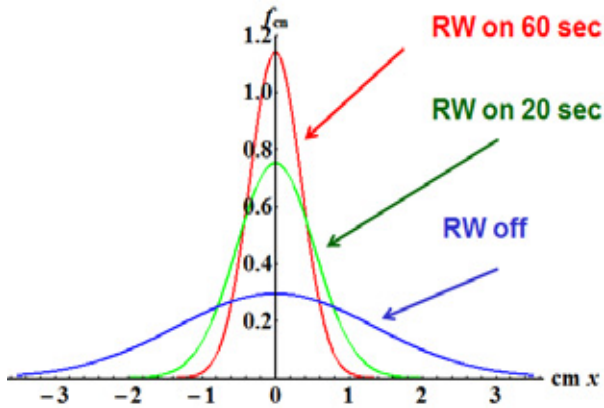

Figure 4: The dependence of the size of the positron cloud working time of the RW field: RW frequency equal 6.3 kHz.

Simultaneously, the frequency of the rotating field does not fall into resonance with the frequency of the magnetron motion of positrons at low densities (about 60 Hz). Moreover, the harmonization of the magnetron frequency with the frequency of the field allows RW under the proposed mechanism to explain the effect of RW-field on the ыещкфпу of positrons. Our hypothesis is that the missing space charge positrons in this case is supplemented with the positive charge of the ions produced in the ionization positrons buffer gas molecules (nitrogen). To test this hypothesis, we need careful measurement of the amount of positive ions in the trap.

CONCLUSION

- «The Rotating Wall» method was studied experimentally at LEPTA injector and a high efficiency of particle storage with RW application has been obtained.
- Optimal the Surko trap parameters have been found.

ISBN 978-3-95450-170-0

- It was found that the RW mechanisms compression of positron clouds were discussed at the LEPTA Trap parameters.
- Methods of optimization of the particle storage and bunch compression in the Surko trap has been obtained.
- Experimental results of positron storage in the LEPTA trap have been presented. A hypothesis about the effect of positive ions on the storage of positrons in the low-density regime.

REFERENCES

[1] X.P. Huang, F. Anderegg, E.M. Hollmann, C.F. Driscoll, and T. M. O'Neil, Phys. Rev. Lett. 78, 875 (1997).
[2] R.G. Greaves and C.M. Surko, Phys. Rev. Lett. 85, 1883 (2000).
[3] J.R. Danielson and C.M. Surko, Phys. Plasmas 13, 055706 (2006).
[4] C. Amole, M.D. Ashkezari, M. Baquero-Ruiz et al., Nature (London) 483, 439 (2012).
[5] N. Kuroda, S. Ulmer, D.J. Murtagh et. al., Nature Commun. 5, 3089 (2014).
[6] J.R. Danielson and C.M. Surko, Phys. Plasmas 13, 055706 (2006).
[7] R.G. Greaves and J.M. Moxom , Phys. Plasmas 15, 072304 (2008).
[8] C.A. Isaac, C.J. Baker, T. Mortensen , D.P. van der Werf, and M. Charlton, Phys. Rev. Lett. 107, 033201 (2011).
[9] C.A. Isaac, Phys. Rev. A. 87, 043415 (2013).
[10] E.V. Akhmanova, M.K. Eseev, A.G. Kobets et. al., Phys. Part. Nucl. Lett. 9, 373 (2012).
[11] C.M. Surko, M. Leventhal, and A. Passner, Phys. Rev. Lett. 62, 901 (1989).
[12] M.K. Eseev, A.G. Kobets, I.N. Meshkov et. al., Plasma Phys. Rep. 39, 787 (2013).
[13] E. Akhmanova, V.M. Drobin, P. Horodek et al., Proceedings this conference.

ISBN 978-3-95450-170-0

ULTRAHIGH VACUUM IN SUPERCONDUCTING SYNCHROTRONS

A.M.Bazanov, A.V.Butenko, A.R.Galimov, A.V.Nesterov, A.V.Smirnov#
JINR, Dubna, 141980, Russia

Abstract

The achievement of ultrahigh vacuum conditions in the range of 10^{-10} – 10^{-12} Torr is a very complicate task for charged particle accelerators. For the superconducting accelerators the main rest gas is the hydrogen which does not freeze effectively on the chamber wall even under the liquid helium temperature. A fast ramp of the magnetic field in the superconducting synchrotrons leads to the heating of the vacuum chamber and the additional evaporation of the hydrogen from the vacuum wall. Non-evaporable getters under the liquid nitrogen temperature are planned to the pumping of the hydrogen and achievement of the necessary vacuum conditions in the new accelerator complex of the NICA project at JINR.

VACUUM GAS COMPOSITION

In the atmosphere conditions the main gas components are nitrogen and oxygen. Other gases like water, argon, CO_2 occupy less than 1% of the air volume. The gas composition at vacuum condition is varied depending on many factors: choice of material, cleaning, baking, pumping system design, type of pumps, temperature, photon, electron or ion bombardment of the surface and many others.

Water is the main gas in unbaked metal chambers. The water outgassing does not depend significantly on the nature of metals, on surface treatments and on temperature (for temperatures lower than 110° C). At present no methods, except heating, exist to remove water from unbaked metals.

At the ultrahigh vacuum condition H is the main gas desorbed by baked metals. The outgassing of hydrogen is an intrinsic property of metals and the value of the outgassing rate of hydrogen is stable at room temperature. The diffusion model predicts values for the hydrogen outgassing that are in accord with experimental observations. Firing decreases the hydrogen outgassing rate by more than 2 orders of magnitude.

Gas molecules are dissolved into the bulk of materials during the production processing and during their permanence in air. In vacuum, the lighter molecules diffuse and, after reaching the surface, they are released. Only hydrogen atoms have enough mobility in metals to attain the surface where they recombine to form H_2. The models that take into account all the steps in the outgassing process are quite complicate and, in general, they give only asymptotic solution for limit conditions.

#smirnov@jinr.ru

PUMPING SYSTEMS

Different pumping systems are used for the achievement of ultrahigh vacuum conditions in particle accelerators. Ion sputter pump cannot effectively remove hydrogen from the rest gas and can be used in the combination with other pumping systems. Turbomolecular pumps has a minimum limit about 10^{-11} Torr and can be used as preliminary pumping system only. Titanium sublimation pumps require the periodical activation at high temperature and cannot be used with superconducting accelerators at the cryogenic temperature.

Cryosorption pumps are the most popular pumping systems for the achievement of the ultrahigh vacuum conditions at superconducting accelerators. Cyocondensation is based on the mutual attraction of similar molecules at low temperature. The key property is the saturated vapour pressure, i.e. the pressure of the gas phase in equilibrium with the condensate at a given temperature. It limits the attainable pressure. Only Ne, H_2 and He have saturated vapour pressures higher than 10^{-11} Torr at 20 K (Figure 1). The vapour pressure of H_2 at 4.3 K is in the 10^{-7} Torr range, at 1.9 K lower than 10^{-12} Torr.

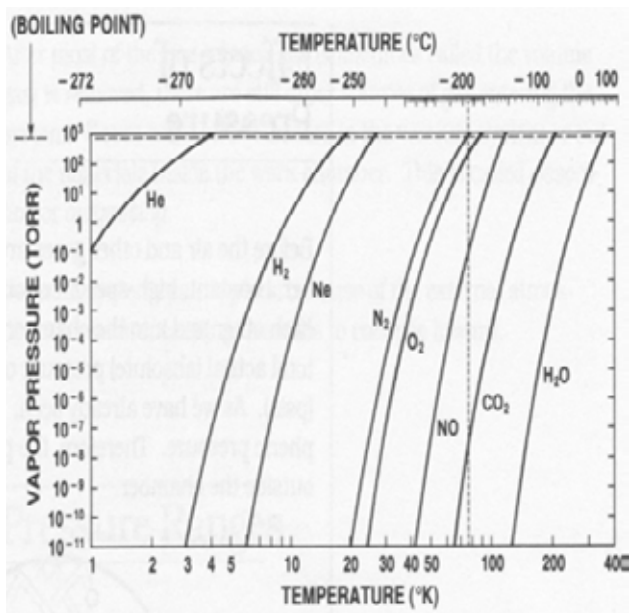

Figure 1: Vapour pressure of common gases.

Cryosorption is based on the attraction between molecules and substrate. This interaction is much stronger than that between similar molecules. Gas molecules are pumped at pressures much lower than the saturated vapour pressure providing the adsorbed quantity is lower than one monolayer. Porous materials in cryosorption

ISBN 978-3-95450-170-0

pumps are used to increase the specific surface area; for charcoal about 1000 m^2 per gram are normally achieved. The important consequence is that significant quantities of H_2 can be pumped at 20 K and He at 4.3 K.

NON EVAPORABLE GETTERS

Non evaporable getters (NEG) are usually used at the room temperature. Gases diffuse into the interior of the getter material. Gases are categorized into four families based on their interactions with NEGs:
- hydrogen and its isotopes - sorbed reversibly;
- CO, CO_2, O_2, and N_2 - sorbed irreversibly;
- H_2O, C_xH_y - sorbed in a combination of two processes;
- rare gases - not sorbed at all.

The dissolution of the oxide layer is possible only in metals having very high oxygen solubility limit, namely the elements of the 4th group: Ti, Zr and Hf. NEG materials are produced industrially by powder technology. Small fragments are sintered to form pellets, discs or plates [SAES]. The powder can also be pressed at room temperature on metallic ribbon. NEG pump can be used in combination with ion pumps.

An activation temperature is a function of the activation time and depends on the NEG material (Figure 2). NEG partially activated during bakeout at T ~ 250°C. Full pumping speed is obtained after heating at 400°C for 45 min or 300°C for 24 hours; activation pressure is $P < 10^{-5}$ Torr. NEG pumps can be activated more than 50 times without significantly losing of its characteristics.

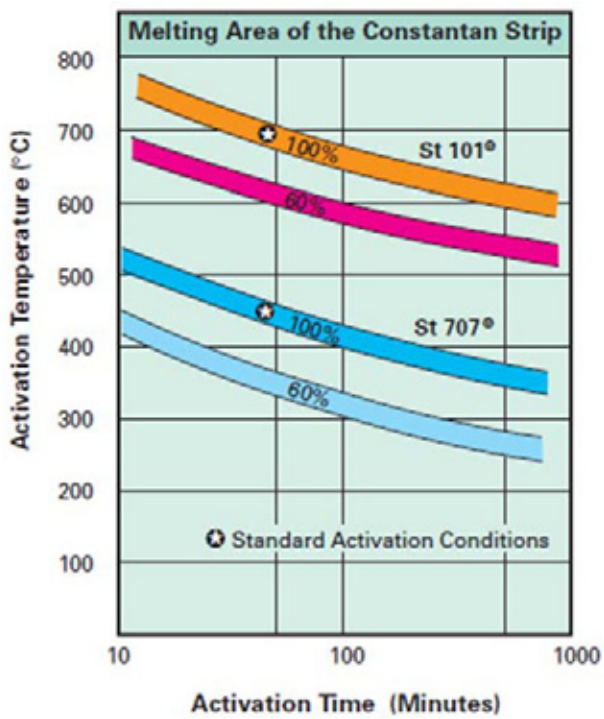

Figure 2: The dependence of the activation temperature on the activation time for different NEG pumps. St707® [1]: 70% Zr, 24.6% V, 5.4% Fe.

Up to now NEG don't used under cryogenic temperatures. Nevertheless NEG still have good pumping speed for H_2 close to liquid nitrogen temperature (Figure 3).

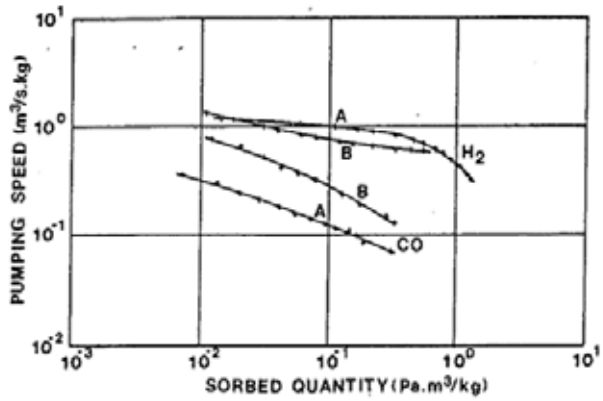

Figure 3: H_2 and CO sorption characteristics for Zr-V-Fe getter alloy at (A) room and (B) LN_2 temperature after activation at 400°C for 300 min [2].

SUPECONDUCTING ACCELERATOR

A few superconducting particle accelerators over the world operate at ultrahigh vacuum conditions. Large Hadron Collider (LHC) at CERN (Switzerland) has 27 km circumference with ultrahigh vacuum conditions about 10^{-12} Torr. Cryogenic chambers have the temperature of the liquid helium at 1.9 K that permits very effectively freeze hydrogen on the chamber wall. A special beam screen is used in the beam pipe to prevent the heating of the outer shell which is kept the helium temperature [3].

All camber walls which are operated under room temperature were coated with NEG pumps. CERN's NEG coating facility was constructed for this purpose. More than 1300 chambers coated with TiZrV NEG for the LHC. Standard chambers are 7 m long, 80 mm diameter [4].

The superconducting synchrotron SIS100 will be constructed in frame of the new FAIR project (Germany) [5]. Total length of SIS100 is 1083.6 m (82% cold, 18% warm), basic structure is hexagonal - six straights and six arcs, 25 warm sections (24 x 9.1 m long, 1x 3.3 m), 25 cold sections (6 long arcs: 5x 135m, 1x 122.6m), 19 short straight sections (18 x 4.3m, 1 x 9.2m).

The inner beam pipe wall will be used as expanded cold surface of an efficient cryopump with practically infinite capacity for nearly all condensable gas species. Static vacuum pressure inside the chamber is about 10^{-12} Torr, under dynamic conditions less than 10^{-11} Torr. Due to the fast magnet ramping eddy currents heat up the chamber wall to temperatures > 20 K [6].

10 cryosorption pumps per arc (each 13 m) and one per short quadrupole doublet in the straight sections are planned for vacuum chamber under cryogenic temperature. Cryosorption pump consists of several round cryopanels (copper disks coated with charcoal) which are cooled down to T ~ 4.5K [7].

ISBN 978-3-95450-170-0

NICA PROJECT

General goal of the NICA project [8] is to study of hot and dense strongly interacting QCD matter and search for possible manifestation of signs of the mixed phase and critical endpoint in heavy ion collisions. The Nuclotron-based Ion Collider fAcility (NICA) and the Multi Purpose Detector (MPD) are proposed for these purposes.

In the frame of the project a few superconducting accelerators will be operated as an accelerator chain. Superconducting booster synchrotron will be used for the accumulation and acceleration of the gold ions from the linear accelerator. Next step particles are injected from Booster to the superconducting synchrotron Nuclotron, where particles are bunched and accelerated up to experimental energy. Finally particles are injected bunch per bunch from Nuclotron to superconducting collider rings.

Vacuum conditions in circular accelerators are defined by the beam life during accumulation and acceleration processes. The vacuum condition at Booster and Collider was estimated on the level of 10^{-11} Torr, at Nuclotron the necessary vacuum value is about 10^{-9} Torr. During 2007 – 2011 years the Nuclotron vacuum system was upgraded and at the present time Nuclotron operates with vacuum value about 10^{-9}-10^{-8} Torr [9].

The Booster optics structure permits to install the standard vacuum station each 9 m (Figure 4). The problem is that the cross section of the beam chamber is too small (ellipse 130 x 69 mm) and the vacuum conductance of the such pipe is not enough to reach the necessary vacuum condition.

To resolve this problem NEG pumps which operates under temperature close to the liquid nitrogen were proposed. NEG pumps can be installed in each free space between dipoles and quadrupoles.

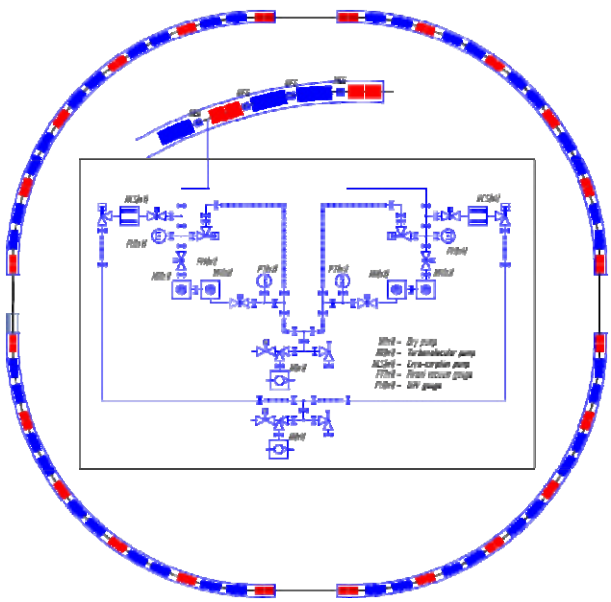

Figure 4: Scheme of Booster optics structure and pumping station: red is quadrupoles, blue – dipoles.

It means that vacuum chambers inside superconducting magnets will operate under temperature close to the liquid helium but vacuum chambers between superconducting magnets can operate under temperature close to the liquid nitrogen. This idea can significantly decrease the cost of the pumping system in the comparison with cryosorption pumps which have more complicate construction and the own cryogenic system.

Next year a special cryogenic test bench will be assembled at JINR for the testing of vacuum chambers and NEG pumps under cryogenic temperatures.

This year in the collaboration with Vakuum Praha company [10] the vacuum test bench was assembled at JINR for the testing of vacuum chambers under the room temperature. After baking procedure during 30 hours with 280°C the vacuum was reached value about 10^{-11} Torr (Figure 5). The ultrahigh vacuum was reached with the combination of the ion pump and titanium sublimation pump with the nitrogen trap.

Figure 5: JINR vacuum test bench under the room temperature.

REFERENCES

[1] http://www.saesgroup.com
[2] Boffito et al., Gettering in cryogenic applications, J. Vac. Sci tech. A, 5 (6), 3442 (1987).
[3] I. Collins, P. Cruikshank, B. Jenninger and N.Kos, “Beam Screens for the LHC Arc Magnets”, Functional Specification LHC-VSS-ES-0001 rev. 1.0
[4] C. Benvenuti et al., Vacuum 60 (2001) 57-65.
[5] A. Krämer, M.C. Bellachioma, H. Kollmus, H. Reich-Sprenger. The Vacuum System of FAIR Accelerator Facility. Proceedings of EPAC 2006, Edinburgh, Scotland.
[6] A. Krämer. Challenges of the FAIR Vacuum System. 3rd ASPERA Technology Forum Industry meets Academia: Vacuum & Cryogenics (2012).
[7] St.Wilfert, T.Hackler, M.Wengentorh. Development of cryosorption pumps for SIS100 cryogenic vacuum system. GSI Scientific Report PHN-FAIR-16 (2012).
[8] http://nica.jinr.ru
[9] A.Averichev, et al. The results of 42nd and 43th Nuclotron runs. JINR Preprint P9-2011-72 (2011).
[10] http://www.vakuum.cz

ISBN 978-3-95450-170-0

RF SYSTEM OF THE BOOSTER OF NICA FACILITY

G.Ya.Kurkin#, A.M.Batrakov, S.A.Krutikhin, Ya.G.Kruchkov, S.V.Motygin, A.M.Pilan,
Budker Institute of Nuclear Physics, SB RAS, Novosibirsk, Russia
G.A.Fatkin, Budker Institute of Nuclear Physics, Novosibirsk State University, Novosibirsk, Russia

Abstract

The project NICA is being constructed in JINR, Dubna to provide collisions of heavy ion beams in the energy range from 1 to 4.5 GeV/u at the luminosity level of $1 \cdot 10^{27}$ $cm^{-2} \cdot s^{-1}$. One of the elements in the collider injection chain is the Booster – a cycling accelerator of ions $^{197}Au^{32+}$. The injection energy of particles is 6.2 MeV/u, extraction energy is 600MeV/u.

Two RF station are to provide 10 kV of acceleration voltage. Frequency range of operation of the stations in the injector chain is from 634 kHz to 2400 kHz [1, 2]. The provisions are made for autonomous mode of operation in the frequency range of 0.5 – 5.5 MHz at the same accelerating voltage. Amorphous metal rings produced in Russia are used in the RF cavities.

RF stations are created in the Budker Institute of Nuclear Physics, SB RAS, Novosibirsk. The stations are tested in the operative mode and have been delivered to the customer in September 2014. Main design features and parameters of RF cavity power generator and control system of the stations are described in the paper.

INTRODUCTION

Acceleration of particles in the Booster will be made in two stages.

- Adiabatic capture and acceleration at the fourth harmonic of revolution frequency up to the energy of electronic cooling of 100 MeV/U.
- Acceleration of particles at the first harmonic up to energy of 600 MeV/U.

Between the acceleration stages the electronic cooling of beam is made for a time of ~1sec with RF switched off.

During both acceleration stages the operational frequency range lays within the limits of 0.5 - 2.5 MHz.

On the customer request for autonomous operation of Booster the frequency range is extended to 0.5 - 5.5 MHz at the same gap voltage of 10 kV. The duration of the acceleration cycle in this mode is 1.5 sec, the repetition time of a cycle is 6 sec. It is supposed, that after acceleration of ions their slow extraction from Booster for physical experiments will be carried out.

THE ACCELERATING CAVITY

The accelerating cavity is formed by two pieces of the short-circuited coaxial lines divided by the accelerating gap (Fig.1). A vacuum-tight ceramic insulator 6 is installed in the gap. Only the stainless steel beam pipe and the gap ceramic are under vacuum, the remaining cavity is operated in air.

Main parameters of RF cavity are given in table 1.

Table 1: RF station main parameters

Parameter	Value
Frequency range, MHz	0.5 – 5.5
Gap voltage, kV	5.0
Beam pipe diameter, mm	160
Residual gas pressure, Torr	$< 5.5 \cdot 10^{-11}$
Outside station diameter, m	1.2
Installation length, m	1.4
Real part of conductance at the cavity gap, Ohm	> 1000

To increase the shunt impedance of RF cavities in the frequency range from hundreds kilohertz and in excess of ten megahertz a space between conductors of the coaxial is filled with a material with large magnetic permeability.

The choice usually is between ferrites and amorphous magnetic alloys. The last material is used in modern designs more often.

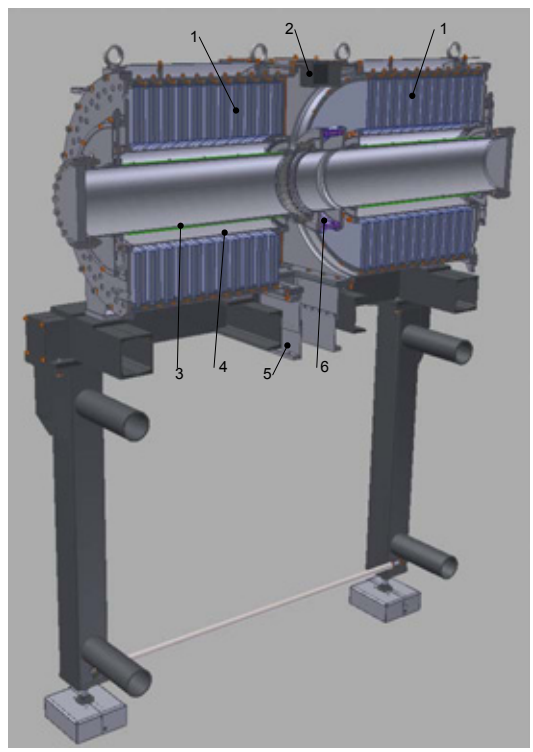

Figure 1: Accelerating cavity of RF station. 1. Amorphous alloy rings. 2. Gap voltage pickup. 3. Beam pipe. 4. Coaxial inner conductor. 5. Connecting nipple. 6. Ceramic insulator.

ISBN 978-3-95450-170-0

In case if ferrite are used the design needs a power supply for ferrite biasing and a feedback loop to keep tuning of the cavity to resonance [3, 4]. RF cavity with amorphous material does not need these elements and flux density is much higher than that of ferrite therefore it is used in modern design more often [5,6].

In our stations the amorphous material of Russian production based on iron are used. Type of the material is 5B-M. Rings are produced by Asha Metal Works. The sizes of rings are D x d x h = 500 x 250 x 15 mm. For use in RF cavity the technology of the standard material 5B has been modified. As the reference parameter for the factory a requirement to have modulus of relative magnetic permeability (μr) above 2000 at frequency of 1 MHz had been defined. This requirement has been realized. 90 such rings were supplied to BINP by the factory.

The rings in the cavity are glued up together by pairs and fixed in the holders attached to external cylindrical wall of the cavity. There is a gap of 10 mm between neighbor pairs for cooling air. A part of airflow from the fan cooling generator tubes is used.

Air passes from RF generator compartment through the connecting nipple 5 and goes further between an internal conductor of a coaxial 4 and an internal surface of rings, being distributed between gaps.

Having passed a gap in the radial direction, air leaves the cavity through apertures in external cylindrical and face walls of the cavity.

The average power dissipation in the rings during operation in regular mode is 3 kW. Through the nipple 5 the connection is made between output stage of RF generator and RF cavity.

Vacuum parts of the cavity – beam pipe and ceramic insulator are baked out at temperature of 300°C for reaching the designed vacuum. As a result the vacuum $3 \cdot 10^{-11}$ Torr have been obtained.

RF POWER AMPLIFIER

The output stage of the power amplifier employs two tetrodes GU-36B-1 produced by the Joint-Stock Company " S.E D.-SPb", St.-Petersburg, Russia.

The tubes are driven in push-pull mode in the common cathodes schematic. Air-cooling of the tubes is used.

Anodes of tubes are connected directly to an accelerating gap of the cavity through the blocking capacitors Cb (Fig. 2). The anode power supply voltage Va = +4.5kV is connected to anodes through the inductance choke. The choke is made of two ferrite rings with dimensions of 180 x 110 x 20 mm. Magnetic permeability of rings material is 1000. The type of the used winding also allows suppressing even harmonics of the accelerating voltage at the cavity accelerating gap. A semi-conductor preamplifier with the peak output power of 500 W drives the tubes. Maximum input power of the preamplifier is 1W. During testing of the stations maximum output power of the preamplifier did not exceed 200 W.

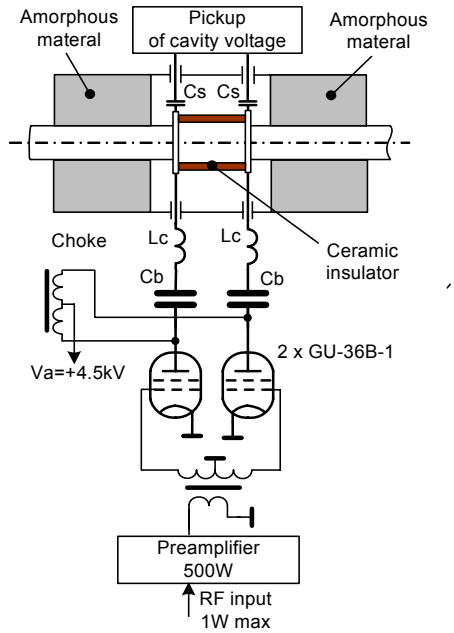

Figure 2: Block diagram of RF power amplifier.

To reduce nonlinear distortions of the accelerating voltage, tubes operate in a cycle close to class A. In a pause between cycles the tubes should be in off state for reduction of the average anode power dissipation.

The modulus of the tubes loads impedance changes in the frequency range almost twice. For reduction of average anodes power dissipation a DC component of the anode current in the acceleration cycle is controlled programmatically by a feedback. On frequencies with smaller load impedance the DC component being increased. The reference voltage for this circuit provides a DAC in the control system.

The impedance of the cavity at the accelerating gap is defined substantially by the distributed capacity of the coaxial line filled by rings and by capacity of the insulator. Therefore, on the higher side of the frequency range of 5.5 MHz this capacity shunts accelerating gap of the cavity heavily and anode current of a tube appears to be insufficient for maintenance of the necessary RF voltage.

The problem is fixed by correction of the impedance at anodes of tubes in the given frequency range. For this purpose the inductance Lc of 10 μH is inserted in series between anodes and blocking capacitances Cb (see Fig. 2). As a result, the maximum DC component of the anode current does not exceed 8A at 3.3 MHz and it is less than 5A on both sides of the frequency range. The average anodes power dissipation of the tubes is 4.9 kW for maximum rating of 15 kW.

CONTROL SYSTEM

Low level signal circuits of the control system of both stations are placed in the SCHROFF rack. The circuits

ISBN 978-3-95450-170-0

control the amplitude of the accelerating voltage, a DC component of anode current of the tubes by means of feedback loops and protect powerful elements of stations and personnel in emergencies.

The pickup of the accelerating voltage in the cavity is a capacitive divider.

The output voltage of the pickup comes to an amplitude detector. Its output signal together with a reference voltage from a DAC comes to an error amplifier (EA). EA output controls the amplitude of RF voltage, which drives the preamplifier. A response time of this feedback loop is 150 μs.

The DC component of the anode current is measured by a probes based on the Hall sensor. Probes signals from each tube together with a reference voltage from a DAC come separately into two EA. Their outputs control biasing of the tubes control grid.

A reference voltage from DAC is common for both feedback loops, so DC anode currents of the tubes are always equal. It also prevents saturating of ferrite of the Choke. A response time of the loop is 1ms.

An intellectual controller and tester modules are installed in the same rack [7]. They are connected to Booster ring control system by Ethernet network.

The controller operates master frequency of the stations, which depends on the value of the accelerator leading magnetic field. In addition, this frequency could be corrected by signals from beam position monitors of the accelerator ring. The frequency is generated by 2-channel DDS, each of the channels driving one station. It is possible to control phase shift between output signals of the channels to provide correct phasing of accelerating voltages for any mutual position of RF stations in the ring of Booster.

Controller has DAC's that produce reference voltages to control the accelerating voltage and DC component of anode currents. It also employs ADC's for measurement of operating regimes of the stations. Two I/O registers are provided for control and monitoring of operating modes of stations.

Tester module allows to disconnect RF stations controller from Booster signals (magnetic field sensor and synchronization pulses) and provide corresponding imitation or to through-pass these signals. This functionality is intended to provide for on-site RF Stations testing.

DESIGN OF THE STATION

The cavity rests upon 4 supports (See Fig.3). A generator box is placed under the cavity with all its power supplies and control units. A SCHROFF rack contains the low level control electronics and computer control.

CONCLUSION

Two RF accelerating stations are created in Novosibirsk Institute of Nuclear Physics for Booster, NICA project, JINR in Dubna. The stations are tested in operating modes. The designed accelerating voltage in the frequency range of 0.5 – 5.5 MHz is obtained. In the end of September, 2014 the stations have been sent to the customer. Test of stations at the customer's site is planned in November.

Figure 3: RF station on the test bench.

REFERENCES.

[1] Alexey V. Eliseev, Oleg I. Brovko, Igor N. Meshkov, Anatoly O. Sidorin, Grigoriy V. Trubnikov, JINR, Dubna, Moscow Region Russia; Grigory Y. Kurkin, Victor M. Petrov, BINP SB RAS, Novosibirsk, Russia. RF SYSTEMS AND BUNCH FORMATION AT NICA Proceedings of IPAC2011, San Sebastián, Spain WEPS014

[2] A.V.Eliseev, I.N.Meshkov, V.A.Mikhailov, A.O.Sidorin. Dinamic of Longitudinal Beam Motion in the Injection Chain of NICA Collider. Letter to ECHAYA, 2010. V7, #7(163). P.777-780.

[3] G.Ya.Kurkin et al. Accelerating RF Station for HIRFL-CSR, Lanzhou, China. (RUPAC 2004) Dubna, October 4-8 2004.:Proceedings of the XIX Russian Particle Accelerator Conference.-Dubna ,2005 p. 332-334.

[4] G.Ya.Kurkin et al. RF Station for Ion Beam Stacking in HIRFL-CSR. (RUPAC 2004) Dubna, October 4-8 2004.: TUGO04.PDF

[5] M. Kanazawa et al. RF CAVITY WITH CO-BASED AMORPHOUS CORE. Proceedings of EPAC 2006, Edinburgh, Scotland, TUOCFI03

[6] C.Ohmori et al. A MAGNETIC ALLOY LOADED RF CAVITY SYSTEM FOR EMMA. Proceedings of IPAC'10, Kyoto, Japan. THPEA017.

[7] G.A.Fatkin at al. CONTROLLER FOR RF STATIONS FOR BOOSTER OF NICA PROJECT. This Conference. October 6 – 10, 2014, Dubna, Russia.

ISBN 978-3-95450-170-0

PARTICLE AND ACCELERATOR PHYSICS AT THE VEPP-4M COLLIDER

V. Kiselev for the VEPP-4 team [1]
BINP, Novosibirsk 630090, Russia

Abstract

VEPP-4M electron-positron collider is now operating with KEDR detector for high-energy physics experiments in the 1.5−4.0 GeV beam energy range to study production of hadrons in continuum and for precise measurement of R constant. In parallel with these experiments, the VEPP-4M scientific team carries out a number of accelerator physics investigations. Here are some of them: stabilization of the guide field of VEPP-4M with an accuracy of 10^{-6} using a special feedback system, development of the method of RF orbit separation of electron and positron beams at VEPP-4M instead of usual electrostatic orbit separation for CPT-theorem testing experiment, finding ways to increase luminosity of VEPP-4M. The paper discusses the recent results, present status and prospective plans for the facility.

INTRODUCTION

The VEPP-4M is the modernized VEPP-4 collider, which was commissioned for the first time in 1977. At present, the complex [2] includes (Fig. 1) a Positron injector, VEPP-3 booster accumulator with beam energy in the range from 350 MeV to 2 GeV, VEPP-4M electron–positron collider with beam energy E in the range from 0.9 to 5.5 GeV (Table 1), and KEDR universal magnetic detector [3].

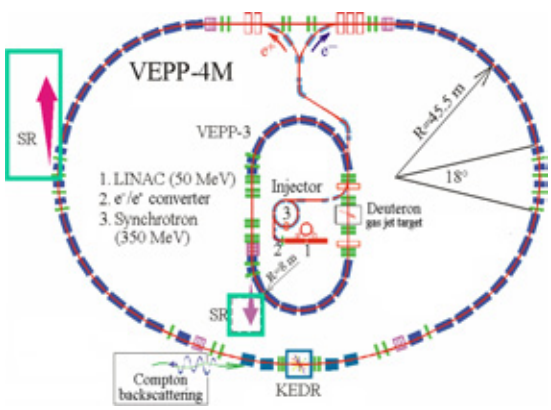

Figure 1. The layout of the VEPP-4 complex.

In addition to the KEDR detector, the experimental spacing of the collider contains a system for registering scattered electrons and positrons for two-photon physics. The VEPP-3 and VEPP-4 facilities are equipped with user stations for studies on the extracted SR beams. A Deuteron unit with the internal polarized gas target for nuclear physics experiments is operating at VEPP-3. Some physical technical characteristics of the complex make it possible to design experiments that are unique not only for Russia but for the world as a whole.

Table 1: Main Parameters of VEPP-4M

Parameters	Values	Units
Circumference	366	m
Tunes Q_H/Q_V	8.54/7.58	
Mom. compaction	0.017	
Max. energy	5.5	GeV
Nat. chromaticity C_H/C_V	-13/-20	
RF-frequency	181.8	MHz
Harmonic number	222	
RF power	0.3	MW
RF voltage	5	MV
No. of bunches per beam	2	
Interaction point		
β_V function	0.05	m
β_H function	0.75	m
D_H function	0.80	m

HIGH-ENERGY PHYSICS

The luminosity of VEPP-4M is a bit lower than the corresponding value in new-generation colliders. For this reason, the KEDR physical program is directed at precision measurements of the parameters of fundamental particles. The following advantages are used in this case: a broad energy range of the center of mass at the complex ($2E$ = 2–10 GeV), the methods and techniques that have been developed for the precision determination of the beam energy [4, 5], the fine energy and spatial resolution in a LKr calorimeter (3.5% and 1 mm, E =1.8 GeV), and the high resolution in the system of scattered electrons (10^{-2}). A number of HEP experiments have been carried out at the VEPP-4 complex over the years of its operation since 1980: spectroscopy of the *c* and *b* states, including precision measurements of the masses of fundamental particles (the particles from J/ψ_, $\psi(2S)$_, $\psi(3770)$ and *Y*_families, and *D*_mesons), as well as of the lepton masses and total widths of narrow resonances (Γee and Γtot); measurement of the tau_lepton mass proceeding from the threshold behavior of the production cross section (near E =1777 MeV); the unique measurement of fundamental parameter R in the wide energy range of $2E$ = 2–10 GeV at one facility; and studies of two-photon physics (full cross section of the $\gamma\gamma \rightarrow$ hadrons process and charge parity states) [6-12].

ISBN 978-3-95450-170-0

Here are some recent results:

1) A high-precision determination of the main parameters of the ψ(2S) and ψ (3770) resonances has been performed [13-14]. Fitting the energy dependence of the multihadron cross section in the vicinity of the ψ (2S) has also been carried out (Fig.2, left)

2) The ratio of the electron and muon widths of the J/ψ meson has been measured using direct J/ψdecays (Fig.2, right). The result Γe+e (J/ψ)/Γμ+μ (J/ψ) =1.0022 ± 0.0044 ± 0.0048 is in a good agreement with the lepton universality [15].

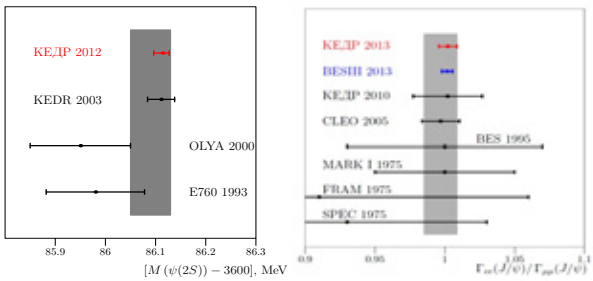

Figure 2. On the left: the compilation of the results on ψ(2S) mass. The relative accuracy of the KEDR result is about $2*10^{-6}$. On the right: the measurement result Γe+e /Γμ+μ .

The following experiments are planned for 2014: scanning at energy 2E = 3.1-4.0 GeV for the measurement of R and collection of statistical data at the peak of the ψ (3770) meson to measure the mass D_mesons.

NUCLEAR PHYSICS

The electro-nuclear experiments with internal targets at the electron-positron storage ring VEPP – 3 have been performed by BINP for several years [16]. During this time the data on the tensor analyzing power in reactions with deuteron have been obtained, the two-photon exchange contribution in (ep) -scattering have been measured.

Further progress of experiments is connected with introduction into VEPP-3 a quasi-real photon tagging system, which will allow performance of a series of measurements of the polarization observables in various reactions with photon energy of up to 1.5 GeV. Creation of the tagging system will be an important stage in development of the technique of experiments with internal targets at the VEPP-3 storage ring. The system will considerably simplify process of event reconstruction of different reactions. Moreover, a significant part of the photons is determined by their transverse polarization that enables to carry out experiments with double polarization.

New experimental section "Deuteron", including the tagging system, differs essentially from the previous one. The new section, in addition to a storage cell, elements of vacuum pumping and quadrupole lenses, comprises three new dipole magnets and a scattered electron registration system (Fig. 3).

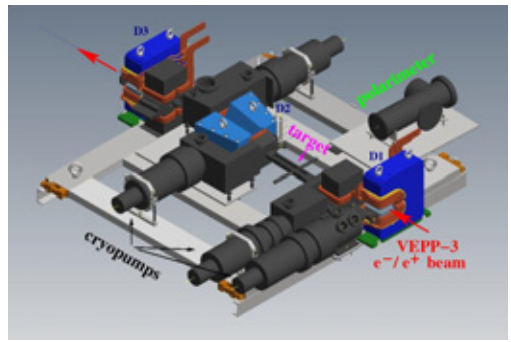

Figure 3. Layout of a new experimental section "Deuteron".

In 2013 the tagging system was introduced into VEPP-3 ring and tested with electron and positron beams. The spectra of the bremsstrahlung and the annihilation radiation were detected at zero angle of the tagging system (Fig.4).

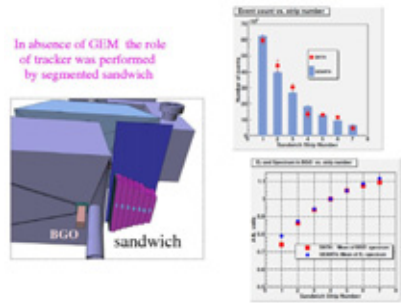

Figure 4. Test of the photon tagging system trigger.

SR EXPERIMENTS

Experiments with synchrotron radiation have been carried out at VEPP-3 for more than 30 years and few years ago at VEPP-4M. Fifteen stations are installed in the experimental halls providing study on X-ray lithography, high pressure and time resolving diffractometry, EXAFS, X-ray fluorescence analysis, X-ray microscopy, small-angle scattering and others.

More than 60 works performed at the VEPP-3 and VEPP-4M storage rings were presented at the XXth National Conference on Synchrotron Radiation "SR - 2014" held recently in Novosibirsk [17]. Installation of a new 7-polar electromagnetic wiggler with a 1.2 T field has provided a increase of radiation intensity by an order of magnitude and reduction of wave length. This has extended possibilities to study the fast processes proceeding in a detonation wave, at the front of a shock wave, and to begin a new program of experiments in diffractometry with a very high time resolution. Thus, for example, the method of acquisition of phase-contrast images with use of X-ray Talbot interferometer, produced

ISBN 978-3-95450-170-0

in BINP, has been implemented. Monochromatic radiation with a 0,3 Å wave length was chosen for testing. A fruit of hautbois strawberry (Fragaria moschata) with a low absorption contrast at the specified wave length (Fig. 5) was taken as a research subject.

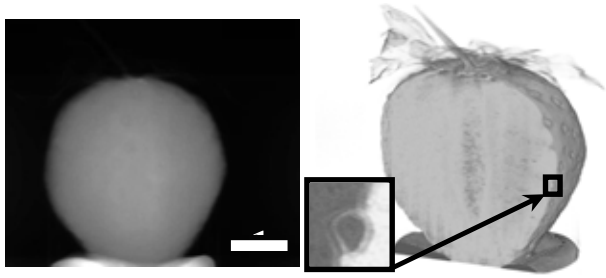

(a) (b)

Figure 5. (a) – Absorption contrast, (b) – Tomographically reconstructed three-dimensional structure of a strawberry from a set of phase projections.

Small low-contrast details, such as a stalk, leaves and seeds which are not distinguishable at absorption contrast are well visible. The Talbot interferometer, created at VEPP-4M and used for solving problems of a computer X-ray tomography and microscopy, opens up possibilities for research in such science fields as: geology, materials technology, archeology, biology and are especially important for medical research.

MODERNIZATION OF THE VEPP-4M PICK-UPS

A BINP-developed wideband beam position monitor (BPM) electronics as been installed at the VEPP-4M electron-positron collider [14]. VEPP-4M operates with two electron and two positron bunches. Wide bandwidth of new electronics (210 MHz) allows separation of the measurements of electron and positron bunches with the time interval between the bunches of up to 20 ns. 15 of 54 collider BPMs located near four meeting points are supplied with new electronics. The electronics can measure the position of each of four bunches. BPM system works in two modes: slow closed-orbit measurements and turn-by-turn measurements (Fig.6). With new electronics the accuracy of closed orbit measurements (~3 μm) and turn-by-turn measurements (~ 15 μm) has increased significantly.

HIGH-FREQUENCY SEPARATION OF ORBITS

At the beginning of 2013, we tested a system for separation of electron and positron orbits in the parasitic collision point that had been recently suggested and developed at the Institute of Nuclear Physics [15]. It is designed to be used instead of traditional electrostatic separation of orbits in the precision experiment on verifying the CPT invariance by comparison of the electron and positron spin frequencies by the RD method [4].

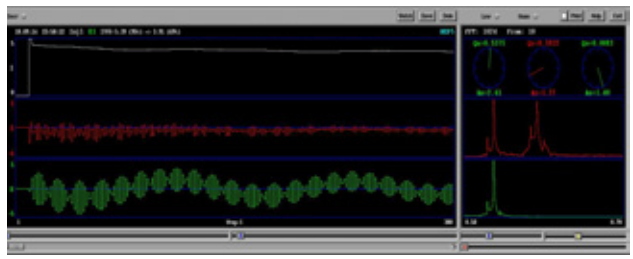

Figure 6. The example of the turn-by-turn measurement of the intensity, vertical (the middle plot) and horizontal (the lower plot) oscillations of the injected beam. The spectra of the oscillations and the calculated deviations of the injection conditions from the optimal values are shown on the right.

In this experiment, the electrostatic method can give a systematic error of about 10^{-6} at the required value of 10^{-9} The alternative method is based on the application of a high-frequency radial electric field with a frequency strictly equal to half of the circulation frequency of a particle in the collider ($f0$ = 819 kHz). The plates on which the above-mentioned field is generated are located on the same azimuth with the parasitic collision point. The electron and positron beams in this case circulate on the common orbit, closing after two turns (Fig. 7)

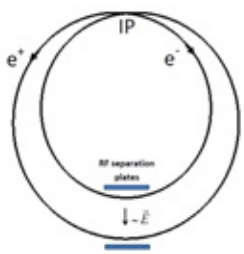

Figure 7. A schematic two-turn orbit in the form of a plane Pascal's snail.

Hence, the systematic error of the CPT experiment connected with the difference in the integrals of a magnetic field along the electron and positron orbits is minimized. The radial bias of the orbit on the high frequency separation azimuth is expressed as follows:

$$X = \frac{\theta\beta}{2\sin 2\pi\nu_X}(\cos 2\pi\nu_X - 1)$$

where θ is the angle of deflection in the field of the plates and β is the local value of the horizontal β_X function. Near the integer frequency values of the radial betatron oscillations, $\nu_X \to n$, we have $X \to 0$. Near the half-integer values, $\nu_X = (2n + 1)/2 + \varepsilon$, the X bias becomes significant ($\varepsilon \ll 1$): $X \approx \theta\beta/(2\pi\varepsilon)$. According to the performed numerical simulation of the collision effects, it

ISBN 978-3-95450-170-0

is necessary to separate the orbits, $2X \geq 7\sigma_X$ (σ_X is the radial beam size). The system of high-frequency separations includes a controllable amplitude-phase modulator for the generation of a self-tuning sinusoidal signal of 409 kHz and a 200 W power amplifier and resonance circuit connected to two deflecting plates with a length of 130 cm. A few experiments in the 1 x 1 collision mode with the use of the above-mentioned system have been performed. The critical beam current unacceptably drops (at 1.85 GeV from 3 to 0.3 mA) in the absence of any separation of orbits in the parasitic collision point. Figure 8 illustrates the experiment, in which the system of electrostatic separation is completely deactivated, but the high -frequency separation is actuated in the parasitic collision point.

Figure 8. An image of colliding beams on screens of the SR monitors, i.e., a 1.1 mA electron (on the left) and 0.3 mA positron (on the right) beam; the voltage amplitude on the high-frequency separation plates is 6.5 kV (E = 1.85 GeV), and two positions of the two-turn orbit are visible.

The electron beam current reaches the range of the operating values in this case, and the collision effects are suppressed. Later, we intend to optimize the mode of colliding beams with high-frequency separation and proceed to comparison of the electron and positron spin frequencies under the new conditions.

GUIDING FIELD STABILIZATION SYSTEM

To increase time stability of the VEPP-4M guiding field, the feedback loop was implemented into the power supply control [21]. The field is measured by a precise NMR magnetometer and the error signal is used to correct the power supply current. With the feedback the field ripples are suppressed in the band of 0-0.1 Hz. The long term non-stability of the field was reduced to 10^{-6}. Fig. 9 shows the NMR magnetometer data with the feedback off and on.

The field values in Oersteds approximately correspond to the beam energy in MeV. With the closed feedback loop, the day-to-day beam energy drift is of an order of 1 keV as it has been. For the frequency range 1 ÷ 100 Hz decisive contribution to the instability is made by powerful parts of the main field power supply IST. For these frequencies instabilities are not determined by NMR feedback and control voltage quality. In this regard, it was proposed to investigate the possibility of suppressing high-frequency ripples with an induction method.

Figure 9: The VEPP-4M guide field stabilization.

The essence of the proposal was measuring the field ripples by the induction sensor to adjust the current in the magnet with the help of parallel connected to IST current generator, which is opposite to the measured ripples. Fig. 10. shows the spectra of the magnetic field fluctuations in terms of ΔB / B, when the broadband compensation is off (upper curve) and on (lower curve). The graph shows that at a frequency of 5 Hz suppression of ripples is more than by 10 times, at a frequency of 10 Hz - 3 times, at a frequency of 30 Hz - 2 times. Attempts to obtain a more effective suppression of magnetic field fluctuations in the band above 50 Hz result in system instability.

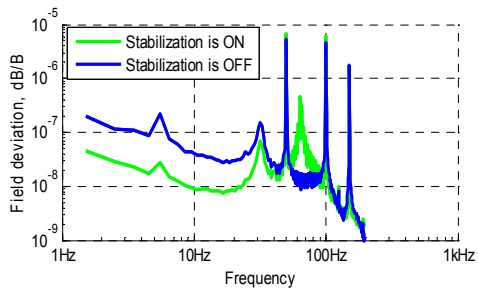

Figure 10: Spectra of magnetic field ripples in the frequencies of 1-100Hz.

In the near future it is planned to achieve the suppression of magnetic ripples in a broad frequency band, as well as to combine the suppression system based on the induction method and the NMR stabilization method. More details of these works are presented in the report [22].

POSSIBILITY OF LUMINOSITY ENHANCEMENT

In early 2014, we performed an experiment in order to increase the luminosity of the collider VEPP_4M at a low energy (<2 GeV). The radial β-function, βx, in the collision point has been reduced by two times for this purpose, this has correspondingly increased the monochromatization parameter:

ISBN 978-3-95450-170-0

$$\lambda_m = \frac{\sigma_{xs}}{\sigma_{x\beta}} = \frac{\eta_x \sigma_E}{\sqrt{\varepsilon_x \beta_x}}$$

i.e., the ratio of the synchrotron and betatron contributions to the radial beam size, where η_X is the radial dispersion function, σ_E is the relative energy spread, and ε_X is the radial beam emittance. The initial value of this parameter at VEPP-4M is about 2. The physical meaning contained in the λm parameter is most obvious in the limit $\lambda m \rightarrow \infty$, when the betatron contribution to this value is negligibly small. The dependence of the vertical action on the particle from the side of the colliding beam on the horizontal betatron oscillations of the particle itself (x) is eliminated in this case. Thus, the effect of coupling resonances is suppressed. If an increase in the λm value is a finite quantity, then the critical current will increase due to a decrease in the linear radial frequency shift at the collision effects,

$$\xi_x = \frac{N r_e}{2\pi\gamma} \cdot \frac{\beta_x^*}{\sigma_x^2},$$

and the critical frequency shift by the vertical direction

$$\xi_y = \frac{N r_e}{2\pi\gamma} \cdot \frac{\beta_y^*}{\sigma_y^* \cdot \sigma_x}$$

will increase due to the suppression of coupling resonances. Numerical simulation [23] of the collision effects shows an increase in the critical current from 3 to 5 mA in the case of reducing the value by two times (Fig. 11). An appreciable luminosity enhancement proportional to the product of the beam current and critical vertical frequency shift is expected.

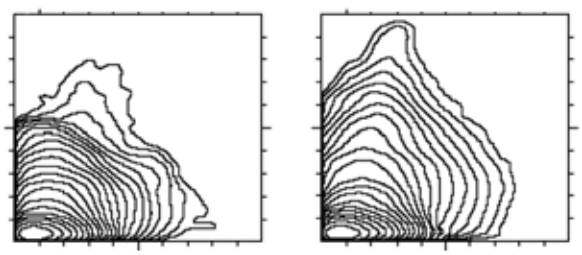

Figure 11**.** The equilibrium distribution of the normalized betatron amplitudes on a plane in two cases that differ in the values of the beam current, functions, and the resulting parameter ξy (E = 1.85 GeV). On the left: I = 3 mA, βx = 65 cm, ξy = 0.036. On the right: I = 5 mA, βx = 32.5 cm, ξy = 0.053.

The experiment, after double decrease of βx at the interaction point, resulted in increasing of a threshold current (collision effects) by half, accompanied by βx beating at the ring though. After studying the problem, experiments will be continued.

ACKNOWLEDGMENTS

This work was supported by the Ministry of Education and Science of the Russian Federation and the Russian Foundation for Basic Research (grants nos.10_02_00645, 11_02_01064, 11_02_01422, and 10_02_00904) and the Siberian Branch of the Russian Academy of Sciences (integration grant no. 103).

REFERENCES

[1] A. Aleshaev, V. Anashin, O. Anchugov, A.Batrakov, E. Behtenev, V. Blinov, A Bogomyagkov, D. Burenkov, S. Vasichev, S. Glukhov, Yu. Glukhovchenko, O. Gordeev, V. Erokhov, K. Zolotarev, V. Zhilich, A. Zhmaka, A. Zhuravlev*, V. Kaminsky, S. Karnaev, G. Karpov, V. Kiselev, G. Kulipanov, E. Kuper, K. Kuper, G. Kurkin, O. Meshkov, S. Mishnev, I. Morozov, N. Muchnoi, V. Neifeld, I. Nikolaev, D. Nikolenko, I. Okunev*, A. Onuchin, A. Pavlenko, V.Petrov, P. Piminov* , O. Plotnikova, A. Poyansky, Yu. Pupkov, V. Sandyrev, V .Svistchev, I. Sedliarov, E. Simonov, S. Sinyatkin*, A. Skrinsky, E. Starostina, Yu. Tikhonov, D. Toporkov, K. Todyshev, G. Tumaikin, A. Shamov, D. Shatilov, D. Shvedov, E. Shubin, S. Nikitin.
* Novosibirsk State Technical University
[2] V.Anashin et al., BINP Preprint 2011-20, 136 pages.
[3] V.V. Anashin et al., Physics of particles and nuclei, Vol.44 No.4 (2013) 657-702.
[4] V.E. Blinov et al., NIM A 494 (2002) 81.
[5] V.E.Blinov et al. NIM, A598(2009)23.
[6] O.Anchugov, et al. Instr. Exp. Tech. **53**, no. 1, 15 (2010).
[7] V.E.Blinov et al.Yader.Fizika 72, N 3, p. 1-6 (2009).
[8] V.Anashin et al. JETP, 2009, V.109, N4, pp. 590–601
[9] V.E.Blinov et al. Nuclear Physics B 189(2009)21-23.
[10] V.E.Blinov et al. Phys.Letters B 686 (2010) 84-90.
[11] V.E.Blinov et al. Phys.Letters B 685 (2010) 134-140
[12] V.E.Blinov et al. Phys.Letters B703 (2011)543-546.
[13] V.Anashin et al. Physics Letters B711(2012)280-291
[14] V.Anashin et al Physics Letters B711(2012)292-300.
[15] V.M. Aulchenko et al. Phys. Lett. B731 (2014) 227.
[16] D.M. Nikolenko et al Phys.Atom.Nucl. 73 (2010) 1322-1338.
[17] http://ssrc.inp.nsk.su/conf/SR2014
[19] E.Behtenev et al. Upgrade of BPM system at VEPP-4M collider, these Proceedings.
[20] V. E. Blinov et al, BINP,Preprint 2013-12, 18 pages
[21] V.E.Blinov, et al., ICFA Beam Dynamics Newsletters, No. 48, April 2009, pp. 209-217.
[22] A. Pavlenko et.al. Method of Broadband Stabilization of the VEPP-4M Main Field, these Proceedings.
[23] D. Shatilov, Particle Accelerators 52, 65–93 (1996).

ISBN 978-3-95450-170-0

ACCELERATOR TECHNOLOGIES DEVELOPMENT AT ITEP

N.N.Alexeev, V.A.Andreev, A.A.Golubev, A.A.Kolomiets, A.M.Kozodaev, T.V.Kulevoy, V.I.Nikolaev, Ju.A.Satov, V.A.Schegolev, A.V.Shumshuruv, A.B.Zarubin,
ITEP, B. Cheremushkinskaya 25, 117218, Moscow, Russia

Abstract

Restart of scientific activity at ITEP associated with join it to the pilot project of NRC "Kurchatov Institute" is the occasion for summing up of intermediate results and existing capability of accelerator physics and technologies development in the institute. School of accelerators construction at ITEP has old traditions and refers on studying, invention, mastering and implementation to operation of technological features of proton and ion beams generation, transportation, acceleration, accumulation, extraction and space-time formation for usage of accelerated beams in physical experiments and applied research works. Historical survey and current state of accelerator science activity at ITEP are presented.

INTRODUCTION

The heyday of the accelerator areas in the country can be attributed to the mid 70-ies of the last century, when the proton synchrotron U-70 in Protvino occupied a leading position in the world and attempts were made to maintain this leading position in almost all areas of development accelerator science and technology. It was difficult to find such physical Institute, which would not have or were not going to have an accelerator facility for experiments in nuclear physics and physics of elementary particles or the practical use of the accelerated beams for applied purposes. In ITEP at that time, it was reconstructed the country's first alternating gradient synchrotron U-7, was created new experimental setups, was implemented proton therapy, were studied and begin to be realised new ideas for creating a linear accelerator with radio-frequency quadrupole focusing of the accelerated beam, were developed intensively technology of ion sources, was discussed actively the idea of creating high-current accelerators for use in electronuclear installations and in experiments on heavy ion fusion. Created in those years in ITEP scientific-technical potential, technology base and high school for training of specialists were allowed to retain up to the present time the leading position of the Institute in the development of accelerator science and technology, despite the constantly changing not for the better conditions for the development and implementation of promising projects.

Historical analysis of distance travelled from emergence of accelerator subjects in ITEP to the current state of Affairs and possible directions in the future use and development of existing scientific and practical groundwork is the basis for the search of optimal ways of combining the efforts of stakeholders in the revival of the accelerator industry in the country to a new level of technological development and expansion of the practical use of charged particle beams

FIRST ACCELERATOR IN ITEP

The first accelerator appeared at ITEP in 1948, three years after the establishment of the Institute It was a cyclotron capable of accelerating protons to an energy of 6.2 MeV, deuterons up to 12.5 MeV and the α-particle up to 24 MeV, with relatively high current of the accelerated beam: current of deuteron at work on the inner target was reached 600 μA, the current of extracted beam was 70 μA. The cyclotron has successfully operated more than 20 years and was dismantled in 1972. If it was known then, where we will come in 40 years, it would have to be preserved.

HISTORY OF THE FIRST ALTERNATING GRADIENT SYNCHROTRON IN RUSSIA

In Russia the principle of alternating gradient focusing became aware of the messages that appeared in the October 1952 American popular science magazine Scientific American. On the initiative M.S.Kozodaev, drew attention to the importance of this message and entrusted to A.A.Tyapkina to check the correctness of this idea, in early January 1953, a meeting was organized in the office of the Minister of medium machine building M.G.Pervukhina [1], which was attended by all the leading accelerator scientists at that time in the country: V.I.Veksler, A.A.Kolomensky, M.S.Rabinovich, V.V.Vladimirsky, and other. In spite of serious doubts as to the correctness of this principle, expressed at the meeting, it was approved the proposal of V.V.Vladimirsky to build on the territory of the ITEP proton synchrotron U-7 on energy 7 GeV to check the beam stability at alternating gradient focusing , and, if successful, to begin the design of the 70 GeV accelerator U-70 and finding a place for its construction.

Design of U-7 (Fig.1) and U-70 began under the leadership V.V.Vladimirsky in 1953, and in 1961 the U-7 was put into operation with electrostatic injector [2].

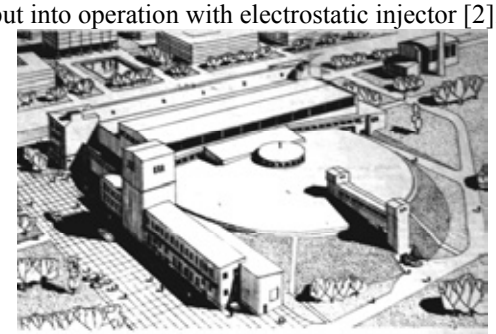

Figure 1: General view of U-7 Accelerator in ITEP

ISBN 978-3-95450-170-0

The main role in actually opening new directions for the development of accelerator science and technology in Russia belongs to the Director of ITEP academician A.I.Alikhanov, which, due to the high personal authority, has made the Government's decision to build two proton AGS synchrotrons - U-7 in Moscow, and U-70 in Protvino, city, whose existence is also obliged A.I.Alikhanov.

CONSTRUCTION OF PROTON LINEAR INJECTORS

Projects of proton synchrotrons ITEP (U-7) and IHEP (U-70) were designed for operation with injected beam current of about 100 mA. Available at that time, the experience of linac construction with grid focusing (KIPT and JINR) could not be used directly, since it was possible to obtain the output current of the proton beam not higher than 1 mA.

The design of linear injectors I 2 on the energy 25 MeV for U-7 and I-100 (100 MeV) for U-70 began in 1958, under the leadership I.M.Kupchinsky. Design, development and construction of both of these injectors were carried out under the general guidance of V.V.Vladimirsky and academician A.L.Mintz, head of RTIAS. The work involved several dozen research institutes and industrial enterprises of the country.

Obtained in the laboratory of I.M.Kupchinsky calculations have allowed to develop a theoretical justification and to determine the parameters of the injectors I-2 and I-100 [3,4]. The launch of accelerator I-2 (Fig.2) took place on 2 November 1966 [5], when it was obtained a record beam current of 135 mA, which was later increased to 250 mA.

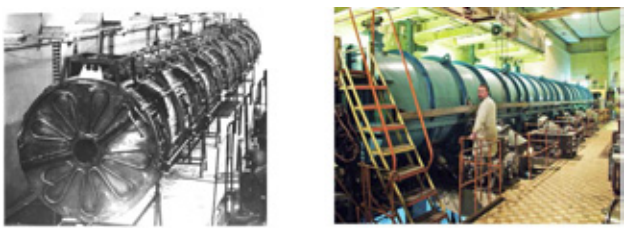

Figure 2: Resonator and tank of linac I-2

The project energy 100 MeV was achieved on the accelerator I-100 28 July 1967 at the current of the accelerated beam 5 mA. By the end of 1967, the output current of the I-100 beam was raised to 60 mA, which enables the injection of the beam during physical launch of synchrotron U-70. Shortly after starting up the machine all work on I-100 moved fully to the staff of IHEP

RECONSTRUCTION OF U-7

Reconstruction of the U-7 synchrotron was carried out in 1973 [6]. In addition to the change of the ring lattice were reconstructed virtually all systems of the circular accelerator: the accelerating tubes were replaced with ferrite resonators, the vacuum system was completely replaced, lamp low voltage electronics was replaced by transistor one, it was created new main power supply, and entirely new distribution system for secondary beams on experimental installations, computer control began to be implemented.

The main result of the reconstruction: the increase in the intensity of the secondary beams more than tenfold. The intensity of the accelerator has exceeded the level of 10^{12} particles per pulse and reached the value of 1.5×10^{12}.

PROTON THERAPY IN ITEP

The ITEP medical proton facility has been working since 1969 [7]. Energy value was regulated in the range 70-200 MeV by the time of beam ejection from the synchrotron on the ramp of magnetic cycle. One bunch from the four accelerated was used for medicine. The remaining 3 bunches were accelerated further to be used by physicists. Four treatment installations placed in three treatment rooms were used: that for stereotactic multidirectional irradiations of intracranial targets, that for eye and orbit tumors irradiations, that for urogynecological tumors, and that for general oncology.

Up to 1988, 8000 patients has been proton treated in the world, 2500 of them in the USSR. There were 3 proton therapy facilities in Russia: in Moscow (ITEP), in Leningrad (LNPI) and in Dubna (LNP. JINR), 77% of Russia-treated patients had been irradiated in Moscow, 20% in Leningrad, and 3% in Dubna.

DEVELOPMENT OF HIGH CURRENT LINACS

Acceleration of high current beams of proton or ions requires strong focusing of the beam at the initial stage of acceleration to compensate Coulomb forces in the beam. This problem has been solved by V.V,Vladimirsky, I.M.Kapchinsky and V.A.Teplyakov inventing SHQF – Specially Homogenous Quadrupole Focusing (1968) [8], renamed later Radio Frequency Quadrupole (RFQ) [9].

The first accelerator based on this principle was implemented by Teplyakov in 1974 as 2H resonator [10].

In ITEP, the first high-current proton RFQ-1 was developed under the guidance of I.M.Kapchinsky in the period 1976-1982 as four vane resonator [11, 12]. Fig, 3 shows a detail of a vane machined with a constant radius of curvature. This RFQ-1 accelerated protons from 88 keV to 3 MeV with beam pulse current 250 mA.

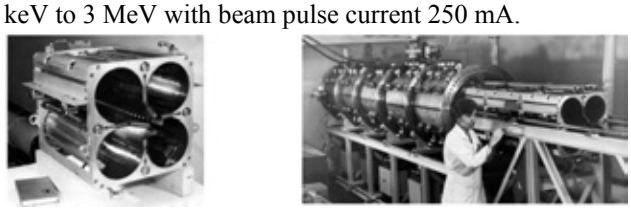

Figure 3: Inlet section of 4-vane resonator and assembled one with vacuum shell

However, RFQ-1 was found to have some drawbacks, main among which was insufficient heat sink for operation with a maximum average beam current

ISBN 978-3-95450-170-0

An improved version of RFQ2 (Fig.4) was developed and implemented in 1998 [14]. The design of the sections and scheme of cooling channels allow to receive the average beam current up to 5 mA.

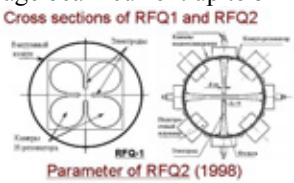

Parameter of RFQ2 (1998)

Injection energy, keV	81
Output energy, MeV	3
RF, MHz	148.5
Repetition rate, Hz	25
Pulsed beam current, mA	200
Average beam current, μA	500
Resonator length, m	4.5
Resonator diameter, mm	449
Transmission, %	>90

Figure 4: Design and parameters of RFQ-2

The RFQ-2 structure was to be used in the accelerator ISTRA56 on the energy of 56 MeV and beam current of 500 μA. It consists of the RFQ followed by an Alvarez linac with permanent magnetic quadrupole focusing (Fig.5). The planned linac had to serve as an new injector to synchrotron U-10 replacing the old linac I-2 and to be used for applications [15].

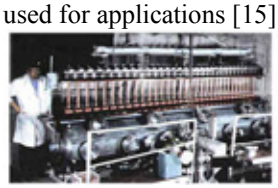

Figure 5: Drift tube line of resonator DTL1 and PMQ

A new version of 90° – apart-stem RFQ structure, has been proposed by V.A.Andreev [16], hence–forth called "4-ladder ", which combines the merits of 4-vane and 4-rod RFQ's, has been developed in the frame-work of a collaboration between ITEP and INFN-LNL. It has good RF efficiency (quite reliable mode separation and field distribution) and maintains such merits of a 4-vane structure as simplicity of manufacture and mechanical stability. Upgraded version of "4-ladder" RFQ successfully operates since 2001 at a frequency of 27 MHz on the accelerator of heavy ions TIPr (Fig.6). This RFQ designed to accelerate 15 mA of U^{4+} ions from 1.5 to 110 keV/u. Combination of quadrupole and coaxial modes is excited in the structure and provides a reliable separation between operating mode and dipole ones [17].

Ring-connected RFQ

Z/A of ions	1/60
Injection energy, keV/u	1.5
Output energy, keV/u	110
RF, MHz	27
Length of resonator tank, m	12
Inner tank diameter, m	1.2
Aperture radius, mm	6.4
Shunt-impedance, MΩ m	1.49
Transmission at 15 mA, %	96
Beam pulse width, μs	400
Average beam current, μA	5

Figure 6: Prototype of heavy ion driver for inertial fusion

ITEP-TWAC FACILITY

The task of creating heavy ion accelerating-storage complex for experiments of ion beams on physics of high energy density in matter began to be solved at the ITEP accelerator complex on the proposal D.G.Kochkarev and B.Ju.Sharkov in 1996. For generation of high-current beams of multiply charged ions, it was assumed to use laser ion source (LIS) with powerful pulsed CO_2 laser. Available in the ITEP two magnetic rings, synchrotron U-10 and the retaining ring UK, are allowed to consider the scheme of obtaining the maximum intensity and, accordingly, high power beam using technology of multiple charge-exchange injection of heavy ions into the storage ring [18].

During execution of this work, it were resolved following main tasks:

It was developed and brought into practical use in accelerators new technology of generation and formation of high-current beams of multiply charged ions in LIS with using of high power pulsed CO_2 laser.

It was developed and mastered the technology of multiple charge-exchange injection of heavy ions and accumulation of nuclei beams that monotonically increase of particles density in phase space to reach the extreme nuclei intensity in the circulating beam.

On the basis of the developed technology, it has been created a unique heavy ion complex ITEP-TWAC [19], and implemented acceleration up to relativistic energies of ions with mass number up to 100, including ions Ag^{19+} up to 10 GeV with intensity $2.5x10^7$ and nuclei Fe^{26+} (200 GeV, $2x10^8$). In the U-10 Ring, it has been received stripping accumulation of nuclei C, Al, Si, Fe in the energy range of 200-300 MeV/u with factor of beam stacking up to 70 (Fig.7).

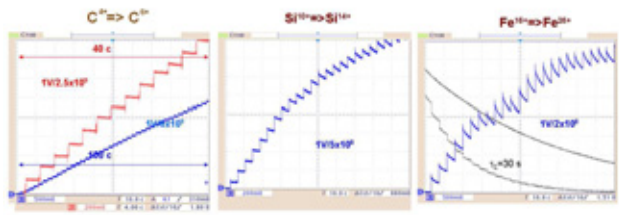

Figure 7: Stacking of nuclei C, Si and Fe in U-10 Ring

PROJECT OF MULTIPURPOSE ACCELERATOR COMPLEX

Created structure of the accelerating-storage complex ITEP-TWAC [20] focused on fundamental and applied research using accelerated beams of protons and ions can be considered as the basis for creating multi-purpose proton-ion accelerating-storage complex (MAC) that meets the needs of many interested in the use of proton and all types of ions beams of intermediate energies areas of modern science, engineering and technology, and to be able with maximum efficiency to meet these needs.

The main areas of MAC includes [21]:

- fundamental and applied research with relativistic proton and ion beams in the energy range from 1

ISBN 978-3-95450-170-0

GeV/u up to 10 GeV for protons and 5 GeV/u for ions;
- applied research with proton and ion beams in the energy range from 10 MeV/u up to 1000 MeV/u in industry, biology and medicine;
- fundamental and technological research with high power stacked nuclei beams in the energy range of <1 GeV/u;
- technological research for generation, acceleration, accumulation, compression, extraction and sharp focusing of high charge state and high intensity heavy ion beams;
- expansion of scientific and educational activity in the areas of nuclear technologies.

Practical implementation of MAC in ITEP is based on:
- high current proton and ion linacs development;
- extending of accelerated ions up to A~200;
- cardinal increase of intensity for accelerated ion beams in UK Ring on a base of ion injector and synchrotron upgrade;
- cardinal increase of intensity for stacked nuclei beams in U-10 Ring on a base of charge exchange injection technology improvement;
- expansion and development of machine experimental area;
- mastering of multimode machine operation in parallel with proton and ion beams for maximal efficiency jf machine operation.

The basis of MAC parameters is upgraded injection complex of circular accelerators. Three independent injectors for protons, heavy ions and light ions provide enhanced opportunities for multi-use machine operation.

Upgrade of proton injector I 2 will allow raising of beam intensity to empower applied use of the beam. The new injection channel from I-2 to UK will allow accelerating in this Ring not only ions but protons too.

Upgrade of I-3 (Fig.8) will raise the beam energy to 12 MV and accelerating frequency from 2.5 to 5 MHz. This accelerator will be used with laser L-100 for acceleration of heavy ions in wide range of charge to mass ratio.

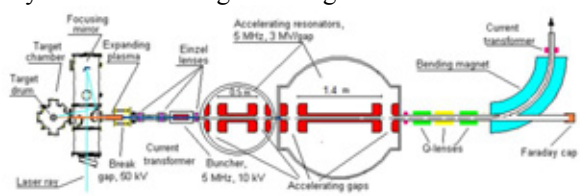

Accelerating ions, A/Z	3-10	Parameter	R1	R2
Injection energy, kV	50	Height, mm	2500	2970
Resonance frequency, MHz	5	Diameter, mm	1500	1985
Accelerating voltage, MV	12	Spiral diameter, mm	700	700
Trans. acceptance, π· mm mrad	1000	Spiral length, mm	1000	1500
Output momentum spread, Δp/p,%	1	Length of drift tube, mm	500	1400
Transmission factor, %	>50	Aperture, mm	70	
Quality	~6000	Width of accelerating gap, mm	250	

Figure 8: Layout and parameters of upgraded linac I-3

New high current injector I-4 is designed for the acceleration of light ions with a current up to 100 mA and will be used with laser L20 (Fig.9). The beam intensity of linac I-4 is limited by LIS on the level of ~10^{11} particles per pulse

Upgrade of the booster synchrotron UK is aimed before all at reducing the loss of accelerated ions due to the cardinal improvement of the vacuum system and increase the rate of beam acceleration. The result of UK upgrade should be getting vacuum <10^{-11} Torr and a doubling of the magnetic field ramp that will minimize particle losses during acceleration.

Parameters

RF - (~80 MHz)
Energy - 5÷7 MeV/u
Z/A - ≤1/3
Imax - up to 100 mA

RFQ section for the energy of 1,6 MeV/u

Parameters of RFQ section

RF, MHz	81.5
Z/A	≤1/3
Energy, MeV/u	0.02/1.57
Voltage, kV	182.5
Input emittance, mm mrad	3.27·π
Output emittance, mm mrad	2.3·π
Beam current, mA	до 100
Repetition rate, Hz	до 1
Beam pulse width, μ	100
Beam energy spread, %	±1.5
Resonator length, m	6.258
Resonator diameter, m	0.564
Quality	11000

Figure 9: RFQ section and parameters of linac I-4

New system of beam slow extraction will be created to extend the use of this ring for applied purposes.

Intensity of ion beams accelerated in the synchrotron UK is limited LIS with laser L20 for I-4 and L100 for I-3. Since the beam intensity, however, is quite high (Fig.10), we do not consider now the possibility of using other types of ion sources.

Accelerated beam parameters with injector I-4
A/Z≤3, U_{inj}=7 MV/u, β_{inj}=0,122, F_{acc}=0.7÷10 MHz, T_{UK}=6.1 μs, p_{max}=4 GeV/c

A/Z	3(C^{4+})	2.8(Si^{10+})	2.45(Al^{11+})	2.4(C^{5+})	2.33(Si^{12+})	2 (C^{6+})
E_{max}, MeV/u	668	744	910	941	981	1229
N_{max}, p/p	8,1x10^{11}	3,0x10^{11}	2,4x10^{11}	5,2x10^{11}	2,1x10^{11}	3,6x10^{11}
N_{exp}, p/p	3.0x10^{11}	1.4x10^{11}	1.3x10^{11}	1.4x10^{11}	1.3x10^{11}	2.0x10^{11}

Accelerated beam parameters with injector I-3M
A/Z≥3, U_{inj}=(1÷3.5)MV/u, β_{inj}=(0.05÷0.09), F_{acc}=0.7÷10 MHz, T_{UK}=9÷16 μs

A/Z	10(U^{24+})	9(U^{28+})	8(Au^{25+})	7(Ta^{20+})	6(Ag^{19+})	5(Ag^{22+})	4(Fe^{16+})	3(Ni^{18+})
E_{max}, MeV/u	78	95	120	154	204	283	417	668
N_{max}(T_b=5 μs)	2x10^{10}	1.7x10^{10}	2.4x10^{10}	2.8x10^{10}	3.5x10^{10}	2.4x10^{10}	4.3x10^{10}	5.1x10^{10}
N_{exp}, p/p	6.0x10^{9}	5.5x10^{9}	6.0x10^{9}	6.0x10^{9}	8.0x10^{9}	7.0x10^{9}	9.0x10^{9}	8.5x10^{9}

Figure 10: Ion beams accelerated in synchrotron UK

Upgrade of the U-10 rings is focused on three main objectives: 1) creating opportunities to accelerate any type of ions to relativistic energies; 2) improvement of technology for stripping accumulation of ions; 3) creation system of combined (fast and slow) extraction of the beam for protonography and nuclear physics.

Modification of charge-exchange injection scheme for the range of Z/Z_o variation from 0.27 to 0.87 will allow to accelerate in U-10 Ring any type of ions. The parameters of light and heavy ions accelerated in the U-10 Ring up to relativistic energies are shown on Fig.11.

Upgrade of charge exchange stacking system is aimed at the real achievement of terawatt power level for stacked beam of nuclei with energies <GeV and includes improvement of one turn bump system and stripping

ISBN 978-3-95450-170-0

targets mechanics for increase of injection efficiency up to absolute value, and implementation of new systems for dynamic expanding of accumulator acceptance at beam stacking to 100 π mm mrad and stochastic cooling of stacked beam which will eliminate the disturbance of the circulating beam after injection of another portion of the particles. The expected result should be an increase of stacked beam intensity up to $>10^{13}$ (for C^{6+}, 0.9 GeV/u) and $>10^{12}$ (for Co^{27+}, 0.5 GeV/u).

Parameters of injected light ions

A/Z≤3, E_{inj} =(200÷300) MeV/u, p_{inj}=2Z GeV/c, T_{inj} =1.5 μs, h=2, F_{inj} =1.4÷1,7 MHz,

Overcharge	$_{12}C^{4+}$=>C^{6+}	$_{28}Si^{10+}$=>Si^{14+}	$_{27}Al^{11+}$=> Al^{13+}
E_{inj}, MeV/u	214	242	306
E_{max}, MeV/u	4250	4250	4060
N_{exp} with I-4, p/p	$3.0x10^{11}$	$1.4x10^{11}$	$1.3x10^{11}$
N_{exp} with I-3, p/p	$2.0x10^{11}$	$7x10^{10}$	$3x10^{10}$

Parameters of injected heavy ions

A/Z>3,E_{inj}=(100÷250) MeV/u, p_{inj}=(2÷4)Z GeV/c, T_{inj} <2 μs, h=2, F_{inj} =1.0÷1,5 MHz

Overcharge	U^{28+}=>U^{92+} U^{28+}=>U^{90+}	Au^{25+}=>Au^{79+}	Ag^{22+}=>Ag^{47+}	Fe^{16+}=>Fe^{26+}
E_{inj}, MeV/u	105	121	179	242
E_{max}, MeV/u	2960	3180	3240	3800
N_{exp}, p/p	$2x10^{9}$	$4.0x10^{9}$	$6.0x10^{9}$	$8.0x10^{9}$

Figure 11: Ions accelerated in U-10 Ring

Experimental area of MAC is shown on Fig.12. the complex infrastructure compactly arranged for extraction of protons and ions beams and placement of experimental installations and test stands. BEH is divided into two areas: the protected area of the extracted beams of high intensity and momentum up to 10Z GeV/c and the area of secondary beams, combined with zone of slow extracted beams of low intensity for radiation testing of electronics. MH and TH is used for applications and experiments on physics of high energy density in matter. All of the experimental installations and stands are supplied with protons and ions. Linear accelerators are also equipped with stands for applied purposes.

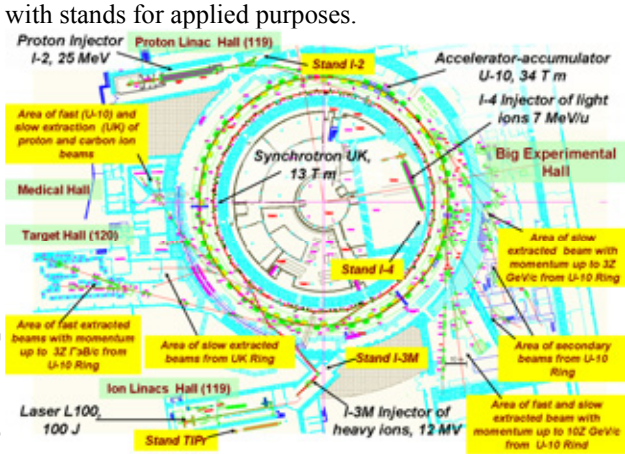

Figure 12: Layout of Multi-purpose Accelerator Complex

CONCLUSION

More than sixty-year history of the development in the thematic areas of accelerator science and technology in ITEP marked a number of significant stages of elaboration and implementation of ideas and projects that helped create accelerator facility: U-7, I-2, I-100, U-70, U10, RFQ1, RFQ2, HIP1, ISTRA10, ISTRA36, TIPr, I-3, UK, ITEP-TWAC.

Accumulated in ITEP scientific and technical potential has allowed to create the technological base and scientific school for training of highly qualified engineers and scientists in the field of physics of charged particle beams and accelerator technology.

Construction of accelerator facilities at ITEP has always been focused on the development of the experimental base of the Institute, on carrying out fundamental and applied research with beams of protons and ions of intermediate energies, as well as studying and elaboration of promising technologies for generation, acceleration and accumulation of protons and heavy ions beams for accelerators and experimental facilities of future generations.

The proposed project of Multi-purpose Accelerator Complex created on the basis of ITEP Ring Accelerators with using of existing technological reserves will ensure continuous improvement of technical and scientific level of the research in line with the growing requirements of the physical experiment in the composition of the world's leading heavy ion complexes of intermediate energies .

Solid and reliable foundation for the creation in the ITEP experimental area on the basis of the upgraded accelerator complex ITEP is in demand in various fields of fundamental and applied research and the perspective of effective use of accelerated beams of protons and ions generated in a wide range of operating parameters.

REFERENCES

[1] A.Tjapkin, .http://bourabai.ru/tyapkin/publications.
[2] PTE №4 (1962)
[3] V.K.Plotnikov et al. Preprint ITEP, N389, 1965
[4] I.M.Kapchinsky et al. Preprint IHEP, 67-38, 1967
[5] PTE, N5 (1967)
[6] N.N.Alexeev, et.al Proc. of VI Rus. Acc. Conf. v.1, p.327 (1975)
[7] V.S.Khoroshkov, et al.. Int. J. Rad. Onc. Biol. Phys., 15, N4 (1988)
[8] V.V.Vladimirsky et al., Avt. svid. USSA № 265312. Bjull. OIPOTS, N10, p. 75 (1970)
[9] I.M.Kapchinsky et al. Proc. of VII Int. Part. Acc. Conf., v.1, p.153 (1970)
[10] V.A.Teplyakov et al. Proc.of VI Int. Part. Acc. Conf. p.125 (1967)
[11] I.M.Kapchinsky et al. PTE, №2, 1970, p.19.
[12] B.L.Ioffe et al., Proc. of VI Rus. Acc. Conf. v.1, p.236 (1978)
[13] E.M. Pottmeyer. Proc. of VI Rus. Acc. Conf. v.1, p.264, (1978)
[14] V.S.Artemov et al., Proc. of XVI Rus. Acc. Conf. v.1, 1998, p.223,
[15] A.I.Balabin et al. Preprint ITEP, № 157, (1989)
[16] V.A.Andreev, G.Parisi. Proc. of the 1993 Part. Acc. Conf., Washington D.C., (1993)
[17] D.Kashinsky et al.. Proc. of EPAC'00, p.854, (2000)
[18] N.N.Alexeev et al. Let. of JETP, v.77-3, p.149 (2003)
[19] N.N.Alexeev et al. Atomic Energy, v..93, p.474 (2002)
[20] N.Alexeev, et al., IPAC'11, p.2193-2195, (2011)
[21] N.Alexeev, et al., RuPAC'12, p.112 (2012

ISBN 978-3-95450-170-0

SUPERCONDUCTING UNCLOSED SHIELDS IN HIGH ENERGY PHYSICS

E. Kulikov, G. Dorofeev, V. Drobin, H. Malinovski, A. Smirnov, JINR, Dubna, Russia

Abstract

This paper presents the experimental and theoretical results of studying the unclosed shields made from LTS (low temperature superconductor) and HTS (high temperature superconductor) materials to obtain a homogeneous magnetic field in solenoids. There is a comparison of LTS and HTS shields, the construction peculiarities are described. HTS shield was proposed to obtain the required magnetic field homogeneity (about 10^{-5}) in the 6 meters length solenoid of the electron cooling section which will be installed in the heavy ion collider of the NICA project (JINR, Russia).

INTRODUCTION

The main requirement at the development of the electron cooling system for charged-particle beams of the NICA collider is to form a highly homogeneous magnetic field [1,2]. At the same time the electron cooling system solenoid will be multisectional with a magnetic field up to 0.2 T. Generation of a highly homogeneous magnetic field using unclosed superconducting shields is the most promising direction to solve this problem.

It is known that low-temperature superconductors can be used for these purposes [3,4,5]. Still, the need of cooling to the liquid helium temperature (4.2 K) forms a major disadvantage of the shield and raises exploitation costs.

For this reason the idea of an HTS shield, which works under 77K, is even more attractive. This paper presents the comparison between conventional LTS shields and HTS shields requiring a fundamentally different winding technology, their construction peculiarities are described as well. It also contains data on characteristic homogeneity of magnetic fields which appear in HTS shield in the gap between two magnetic dipoles.

LTS SHIELD

Investigations on unclosed shields were first carried out in the 1970s; the shields were made of low temperature NbTi alloy superconductor [3]. First papers lacked a clear physical model and had pure experimental nature. Thus there was no unified approach like the one described in our papers [4,5] to the problem of unclosed superconducting shields.

The LTS shield structure is formed by multilayer winding of superconducting foil on a cylindrical frame [4,5] (Fig.1).

A characteristic property of the technology is cross arrangement of superconducting foil pieces to the frame. Shield layers are isolated with condenser paper.

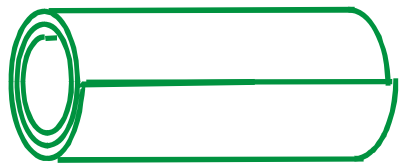

Figure 1: The scheme of spiral winding.

The carried out experiments and numeric researches proved high efficiency of conventional LTS shield usage to improve the magnetic field homogeneity in a straight solenoid [5]. Data analysis showed that the existence of an area with the homogenous magnetic field longitudinal component resulted from screening the external field's radial component by the superconducting unclosed shield.

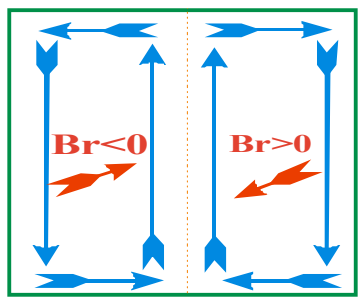

Figure 2: The unfolded shield with effective shielding currents on its surface.

In particular on the end of the shield the shielding currents flow in the same direction as the major solenoid currents, while in the center they have an opposite direction which explains the formation of typical homogenous field areas. (See in Fig.2.)

The derived results formed a basis for works upon the next technical solution – the unclosed HTS shield.

2-G HTS SHIELD

A 12-mm wide 2-G HTS (Re)BCO produced by Super Power and SuperOx was used as a base element of the construction. Its critical current – up to 300 A (i.e. 2.5×10^6 A/sm^2), the field of one tape full magnetization is about 25 mT.

Figure 3: Structure of 2-G HTS tape (Re)BCO.

ISBN 978-3-95450-170-0

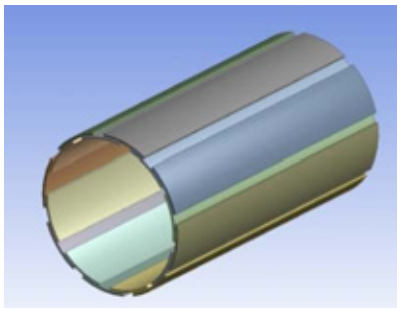

Figure 4: The unclosed HTS shield in the form of the lengthwise winding.

However the HTS material has several drawbacks: permissible minimum bending radius as the superconductor is hyperfine ceramics (Fig.3) and anisotropy of tape-wide physicotechnical properties, which causes undesirable edge effect. For this reason lengthwise shield winding technology was offered, when the HTS tape is laid along the frame (Fig.4.). At the same time control over the critical current distribution inhomogeneity on tape length is required. (See in Fig.5.)

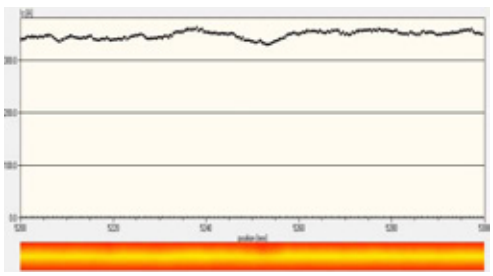

Figure 5: Critical current distribution along the tape length.

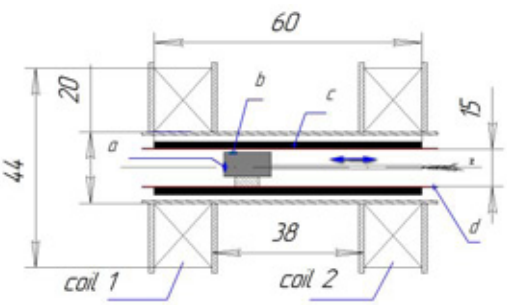

Figure 6: Experimental set-up with HTS shield. **a**- Hall sensor to measure the longitudinal field component , **b**– Hall sensor to measure the radial field component, **c** – HTS share shield, **d** - non-magnetic steel tube.

Paper [6] explored the effect of HTS shield on the coaxial coil system magnetic field. The experimental set-up is shown in Fig.6. A lengthwise shield eliminated the dip of the longitudinal component in the gap between magnetic dipoles; it was determined that its "tile" structure (see in Fig.4) performed as a uniform piece of the LTS foil. In that way the principal possibility to use the existing HTS tape for unclosed shields was shown.

Let's estimate the slope angle of lines of force to the longitudinal axis of the magnetic system according to the results of the mentioned paper. It is clearly shown that the slope ratio is delivered by the formula

$$tg(\varphi) = \frac{B_\rho}{B_Z} \quad (1)$$

Using $\varphi << 1$, we get

$$\varphi \approx \frac{B_\rho}{B_Z} \quad (2)$$

The absolute value of this angle is called characteristic magnetic field homogeneity.

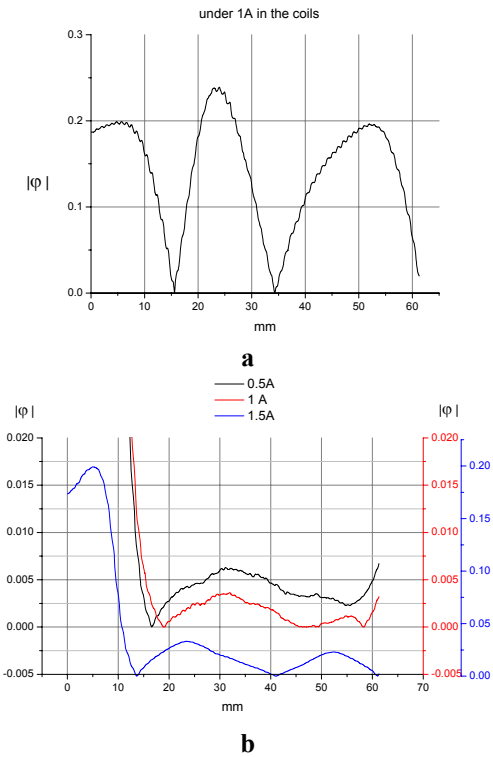

Figure 7: Characteristic homogeneity of the magnetic fields: **a**- without shield; **b**- with shield under different currents in the dipoles.

The graphs (Fig. 7a vs. Fig 7b) show that HTS shield reduces the maximum angle between the magnetic field lines and the longitudinal axis of dipoles up to 100 times. This is a significant value for the electronic cooling technique as dissipative friction force strongly depends on angles [2].

The magnetic field was measured with Hall probes in all presented papers. The accuracy of the magnetic field measurements was about $\Delta B/B \sim 10^{-3}$, which was basically determined by the stability of its power supply. Actually,

ISBN 978-3-95450-170-0

this is the maximum precision available for magnetic field measurements in this methodology. This is the reason why a totally different approach is needed to measure fields with 10^{-5}-10^{-6} accuracy. For example, an optical-mechanical method with magnet-sensitive "compass" element offered by our Novosibirsk colleagues [7].

FUTURE PLANS

In October 2014 shield prototypes experiments start. These shields are planned to be used for charged-particle beam electron cooling within the NICA project. The authors of this paper have developed and produced a test bench for large-dimension HTS shields.

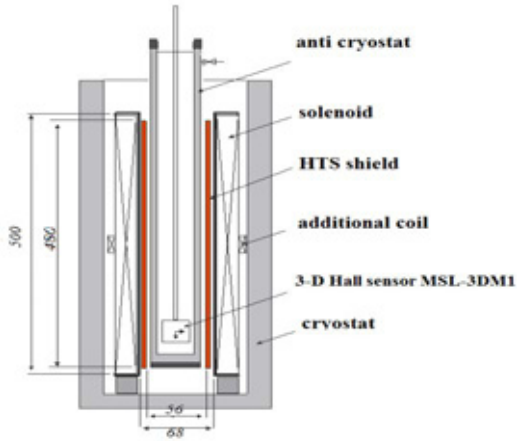

Figure 8: Test bench for large-scale HTS shields.

The bench consists of:

1. solenoid which is made of a copper wire with ø = 1.4 mm
2. additional coil which forms inhomogenious areas of the magnetic field to emulate intersection junctions or defects of winding. It has an individual power supply
3. MSL-3DM1 Hall probe for 3-D magnetic field measurements
4. anti cryostat which holds the operating temperature for the MSL-3DM1 by means of compressor and heaters (20 ±0.5 ^{0}C)
5. foam-plastic cryostat with liquid nitrogen. The magnetic system with HTS shield sinks into it.
6. HTS shield

The solenoid generates maximum magnetic field up to 0.2 T. The magnetic field homogeneity length with 10^{-3} level is about 150 mm. Instrumental resolution of the MSL-3DM1 is 0.1 mT; precision of the magnetic field measurement is 0.5% in the range of 0.1 – 0.35 T.

We hope that the existing HTS shield will improve the solenoid magnetic field homogeneity two orders up from 10^{-3}. At the moment an electron cooling system for booster is being constructed at BINP, consisting of a 2 m solenoid with a magnetic field of 0.2 T [8]. The unclosed superconducting shield is also planned to be installed for the investigation of its parameters.

REFERENCES

[1] E. Ahmanova et al.,"Application of Cooling Methods To NICA Project", COOL`09, Lanzhou, August 2009,MOM2MCIO02,p.16(2010);http://www.JACoW.org

[2] A.V. Fedotov et al., New J. of Phys. 8 (2006) 283.

[3] Yu.F. Bychkov, *Metallurgy and Metal Science of Pure Metals vol.14*, (Moscow: Atomizdat,1980), 53.

[4] N. N. Agapov et al., Phys. Part. Nucl. Lett. 9 (2012) 422.

[5] E. Kulikov et al.,"Superconducting Unclosed Shields for Improving Homogeneity of the Magnetic Field in Magnetic Systems", Proc. 12th IIR Int. Conf. on Cryogenics, Dresden, Germany (2012).

[6] E. Kulikov et al., J. of Phys. Conf. Ser. (JPCS) 507(3) (2014) 032028

[7] V. Bocharov et al., Instruments and Experimental Techniques, 48(6) (2005), p.772.

[8] M. Bryzgunov et al.,"Low Energy Cooler for NICA Booster", these proceedings, RuPAC2012, Saint-Petersburg, September 2012, TUPPB034, p.391; http://www.JACoW.org.

ISBN 978-3-95450-170-0

OPERATING FREQUENCY AND ACCELERATING STRUCTURE GEOMETRY CHOSE FOR THE HYBRID TRAWELLING WAVE ELECTRON LINEAR ACCELERATOR

I.D. Sokolov, R.Yu. Alekhanov, E.A. Savin, National Research Nuclear University MEPhI (Moscow Engineering Physics Institute), Moscow, Russia

Abstract

For the compact electron linear accelerating structure based on the hybrid scheme which consists from SW biperiodic structure buncher and TW DLS with magnetic couple TW accelerating part, the best option for the operating frequency and cells geometry has been chosen. Comparative calculations for the DLS cells with magnetic couple and without it, on the different operating frequencies and with the different couple coefficient were carried out. The best option will be manufactured, measured and used in the accelerator structure.

ELECTRO-DYNAMICS PARAMETERS

In this paper we use some specified parameters to describe the efficiency of the accelerating structures [1].

Coupling coefficient – describes the width of the dispersion curve $k_c = \frac{|f_\pi - f_0|}{f_{\frac{\pi}{2}}}$, where $f_\pi, f_0, f_{\pi/2}$ – are the frequencies π, 0, π/2 respectively;

Phase velocity $v_{ph} = \frac{\omega}{k_z}$, where ω is the circular frequency and k_z is the longitudinal wave number;

Group velocity $v_{gr} \frac{d\omega}{dk_z}$;

Shunt Impedance per unit length $r_{sh} = \frac{\left(\int_0^z Ezdz\right)^2}{Ploss*l}$;

T – transit time factor ;

Q - quality factor $Q = \frac{\omega W}{Ploss}$, where W-is the stored energy and Ploss –is the dissipated power in walls;

α – attenuation coefficient $\alpha = \frac{\omega}{2v_{gr}Q}$;

Normalized electric field strength $\frac{E_z\lambda}{\sqrt{P}} = \sqrt{\frac{2\pi\lambda r_{sh}}{Q\beta_{gr}}}$.

DIAPHRAGM-LOADED STRUCTURE

Diaphragm – loaded structure (DLS) [2] (see Fig.1) is the most common geometry type for using it in travelling wave electron linear accelerator. But the disadvantage of this geometry is small coupling coefficient and small group velocity i.e. structure filling time. But the shunt impedance is relatively high.

For working mode 2π/3 (D=βλθ/2π) electro dynamical parameters of the DLS with different a/λ at S band – 2997.2 MHz were calculated [3] and compared (see Table 1.). All data are in this table are matched with the DLS catalogue [4].

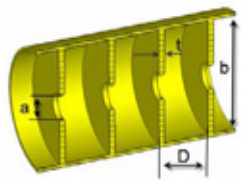

Figure 1: DLS geometry.

Table 1. S band different DLS geometry

Parameter	Value			
a/λ	0.06	0.08	0.1	0.12
k_c, %	0.008	0.03	0.09	0.19
r_{sh}, MOhm/m	111	106	102	96
Q	13800	13800	13800	13800
T	0.61	0.62	0.63	0.64
E_{acc}, MV/m	37	36	35	34
β_{gr}	0.00007	0.0002	0.0008	0.0016
α, м $^{-1}$	33	11	2.8	1.5
K_E	2.22	2.33	2.46	2.59
$E\lambda/P^{1/2}$, $Ohm^{1/2}$	8500	4900	2400	1700

From the Table 1 results we can see, that the group velocity is very small, i.e. it is needed to increase coupling coefficient by inventing a magnetic coupling.

MAGNETIC COUPLED DIAPHRAGM-LOADED STRUCTURE

By putting radial slits in the maximum magnetic field concentration area we increase the connection between the cells [5] thereby obviously we increase the value of the coupling coefficient. Construction and dimensions of DLS-M are presented on Fig. 2. DLS-M was constructed and tuned for S-band -2997.2 MHz and L-band -1818 MHz, working on $2\pi/3$ mode. To design a linac that uses DLS-M as an accelerating structure it is necessary to find its optimal dimensions in order to obtain the best electro-dynamic parameters (EDP). The most significant parameters are: shunt impedance per unit length rsh, normalized electric field strength $E\lambda/P^{1/2}$ and overvoltage K_E. These parameters dependencies from coupling coefficient, group velocity and a/λ are presented on Fig. 3 and Figure 4 for different frequencies. Data calculations are present in Tables 2-5 for the S-band and L-band. On the Fig.5 is shown the comparison of the dispersion

ISBN 978-3-95450-170-0

curves for S band DLS and DLS-m structure. The coupling coefficient was tuned by phi changing.

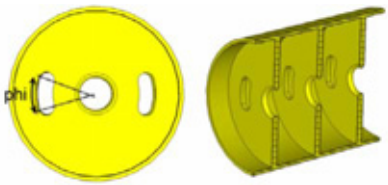

Figure 2: Magnetic coupling.

Table 2. EPD for DLS S-band (upper number) and L-band (lower number) at constant k_c=1%

Parameter	Value				
a/λ	0.04	0.06	0.08	0.1	0.12
k_c, %			1.00		
r_{sh}, MOhm/m	116.5 71	111 68	106 62	100 52	95 42
Q	13600 17830	13400 17820	13400 16298	13300 15695	13200 14551
T	0.60 0.65	0.61 0.68	0.62 0.5	0.63 0.5	0.63 0.6
E_{acc}, MV/m	38.1 16.62	37.3 16.28	36.4 15.22	35.5 14.19	34.5 13.15
β_{gr}	0.01 0.009	0.009 0.009	0.009 0.005	0.009 0.005	0.01 0.005
α, м $^{-1}$	0.24 0.12	0.26 0.12	0.27 0.24	0.27 0.23	0.24 0.3
K_E	2.5 2.73	2.6 2.78	2.6 2.79	2.8 3	3.3 3.2
$E\lambda/P^{1/2}$, Ohm$^{1/2}$	735 1000	720 942	705 858	690 799	675 687

Table 3. EPD for DLS S-band (upper number) and L-band (lower number) at constant k_c=1.5%

Parameter	Value				
a/λ	0.04	0.06	0.08	0.1	0.12
k_c, %			1.50		
r_{sh}, MOhm/m	113 70	109 95	104 60	99 50	93 42
Q	13000 17560	13000 17170	13000 15753	13000 15220	12900 14670
T	0.61 0.65	0.60 0.68	0.64 0.5	0.63 0.5	0.63 0.5
E_{acc}, MV/m	38.2	37.5	36.6	35.6	34.6
β_{gr}	0.014 0.013	0.014 0.013	0.014 0.007	0.013 0.007	0.014 0.005
α, м $^{-1}$	0.18 0.08	0.18 0.08	0.18 0.17	0.19 0.17	0.19 0.2
K_E	2.8 2.55	2.8 2.72	2.9 2.9	3.0 3.2	3.1 3.3
$E\lambda/P^{1/2}$, Ohm$^{1/2}$	625 842	615 797	600 737	605 696	570 587

Table 4. EPD for DLS S-band (upper number) and L-band (lower number) at constant k_c=2%

Parameter	Value				
a/λ	0.04	0.06	0.08	0.1	0.12
k_c, %			1.00		
r_{sh}, MOhm/m	111 72	107 61	102 58	95 48	91 38
Q	12700 16880	12700 16390	12700 15348	12400 14740	12600 13640
T	0.64 0.66	0.65 0.67	0.66 0.5	0.67 0.5	0.69 0.6
E_{acc}, MV/m	38.3 17.17	37.6 16.14	36.7 15.15	35.7 14.09	34.6 13
β_{gr}	0.018 0.018	0.018 0.018	0.017 0.01	0.017 0.01	0.018 0.01
α, м $^{-1}$	0.14 0.06	0.14 0.06	0.15 0.13	0.15 0.14	0.15 0.15
K_E	2.8 2.36	2.9 2.69	3.0 2.8	3.1 3.2	3.2 3.6
$E\lambda/P^{1/2}$, Ohm$^{1/2}$	550 770	540 666	545 659	530 614	500 603

Table 5. EPD for for DLS S-band (upper number) and L-band (lower number) at constant β_{gr} =0.01

Parameter	Value				
a/λ	0.04	0.06	0.08	0.1	0.12
β_{gr}			0.01		
r_{sh}, MOhm/m	104 77.5	95 70	84 62	72 54	61 44
Q	13200 16160	13500 16200	13500 16382	13100 16100	12400 16000
T	0.57 0.57	0.58 0.58	0.59 0.59	0.59 0.59	0.58 0.6
E_{acc}, MV/m	27 12	26 11	25 10	24 9	23 9
k_c, %	1 1.14	1.1 1.15	1.15 1.16	1.21 1.18	1.3 1.18
α, м $^{-1}$	0.24 0.12	0.23 0.14	0.23 0.18	0.24 0.2	0.25 0.21
K_E	1.52 2.76	1.71 2.89	1.9 3.2	2.18 3.4	2.5 3.5
$E\lambda/P^{1/2}$, Ohm$^{1/2}$	700 945	665 823	625 700	585 588	555 531

ISBN 978-3-95450-170-0

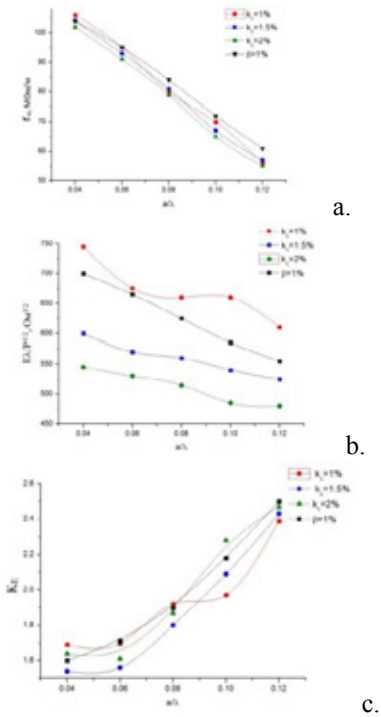

Figure 3: Electro dynamical parameters dependencies on aperture radius for S-band: a)Shunt impedance per length, b) Normalized electric field strength, c) Overvoltage.

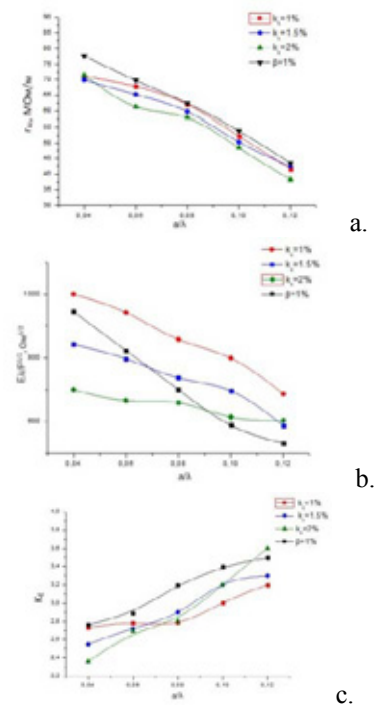

Figure 4: Electro dynamical parameters dependencies on aperture radius for L-band: a)Shunt impedance per length, b) Normalized electric field strength, c) Overvoltage.

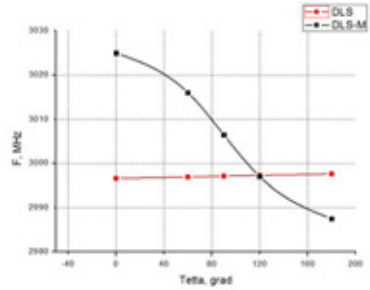

Figure 5: Dispersion curves for the S-band DLS (red) and DLS-m (black).

CONCLUSION

The best results were shown by S – band DLS-m structure with a/λ=0.08 and K=1% (see Table 6). This geometry has the appropriate shunt impedance, small fabrication sizes (speaking about frequency) and overvoltage smaller than 3.

Table 6. EDP of the chosen cell

r_{sh}, MOhm/m	Q	T	E_{acc}, MV/m
104	13000	0.64	36.6
β_{gr}	α, м $^{-1}$	K_E	$E\lambda/P^{1/2}$, $Ohm^{1/2}$
0.014	0.18	2.9	600

REFERENCES

[1] Kaminskiy V.I., lalayan M.V., Sobenin N.P., Accelerating structures, MEPhI 2005
[2] N.P. Sobenin, O.S. Milovanov, RF technique, M:Energoatomizdat,2007
[3] http://www.cst.com
[4] Diaphragme-loaded structures catalogue O.A. Waldner, N.P. Sobenin, B.V. Zverev, I.S Shchedrin, M:Energoatomizdat,1991
[5] S. Kutsaev et. al., Design of of hybrid linac with standing wave buncher and travelling wave structure, Nuclear Instruments and methods in Physics Research A, Vol. 636, Issue 1, p.13-30

ISBN 978-3-95450-170-0

THREE ELECTRODE ELECTRON GUN WITH THE DECREASED ANODE VOLTAGE GEOMETRY OPTIMIZATION

S.V. Matsievskiy, E.A. Savin, National Research Nuclear University MEPhI
(Moscow Engineering Physics Institute), Moscow, Russia

Abstract

With the rapid growth of demand for compact particle accelerators, used in number of different fields (medicine, security, etc.), there is a need for more compact and simple in production particle accelerator parts. One of such parts, electron gun injector for linear accelerator, is considered in this paper.

Modifications to the initial design, such as anode potential decrease and change of geometrical properties of cathode are described, optimal operating mode is calculated.

INITIAL MODEL CALCULATION

On figure 1 an existing electron gun with buncher cell are shown. In this case, buncher cell has an electric potential and acting as anode. Potential difference between anode and heated cathode forces electrons to emit from cathode. Control electrode is used to focus electron beam from cathode and to control electron emission intensity by altering electric field value near the cathode surface.

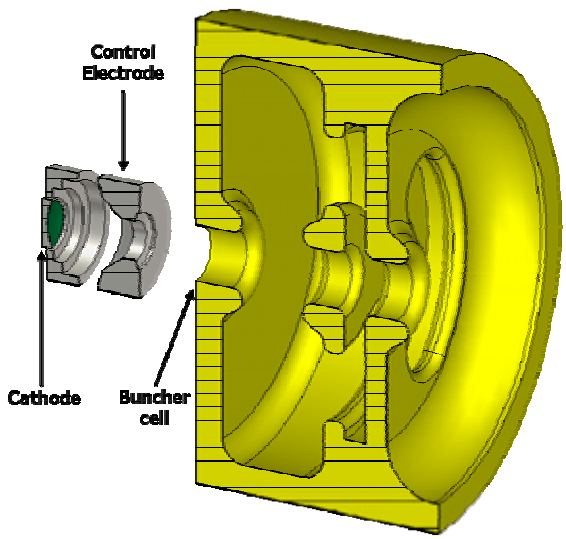

Figure 1: Cross-section of electron gun with buncher cell.

To validate the calculation method of electron gun, model of existing one was built. It consisted of spherical cathode with potential set to zero, control electrode with potential of 12.9 kV and 50 kV anode. On the figure 2 calculation output data is presented. Purple lines represent equipotential lines of electric field inside of the gun. Green lines are the electron trajectories.

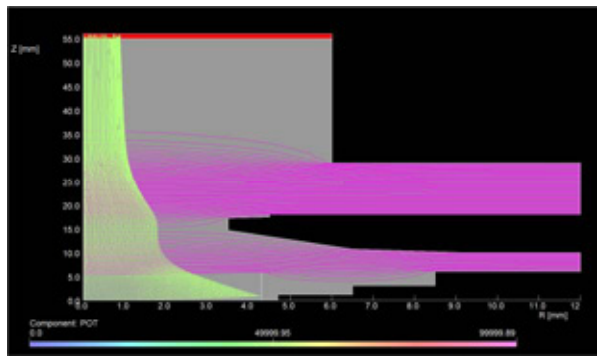

Figure 2: Initial model output data.

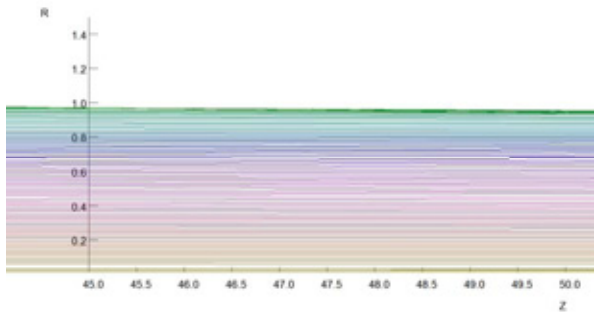

Figure 3: Electron trajectories near crossover.

Calculation results of existing gun model coincided with beam parameters measurement. Calculation method is suitable for modified gun calculations.

MODEL WITH DECREASED ANODE VOLTAGE

Beam width in the crossover dependence of anode potential was investigated. The plot of beam radius r over anode potential U_1 is shown on the figure 4.

As shown on figure 4, beam width is decreasing in reverse ratio to anode potential. For simplification of electron gun design due to the isolation requirement reduction, compromise potential of 30 kV on the anode was chosen.

ISBN 978-3-95450-170-0

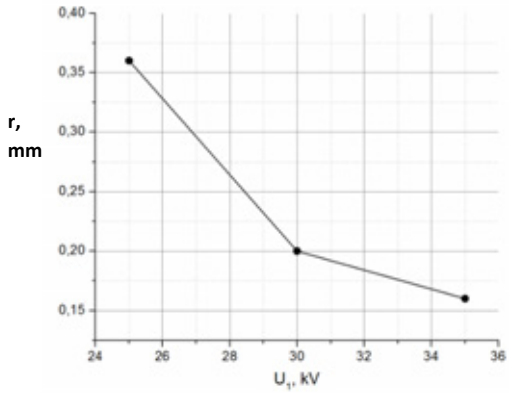

Figure 4: Beam radius over anode potential.

On the figure 5 plot of beam width in the center of the cell over control electrode potential is presented.

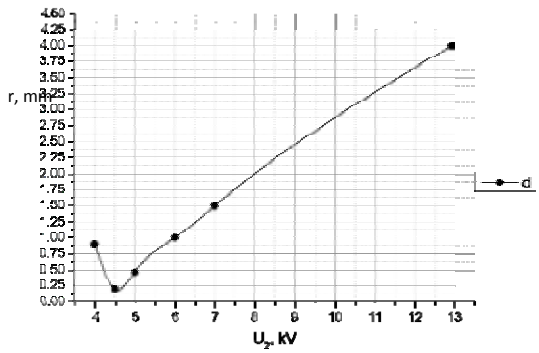

Figure 5: Beam width over control electrode potential for model with decreased anode potential.

Set of electrode potentials, corresponded to the smallest width of beam, is shown in the table 1.

Table 1: Electrode potentials for model with decreased anode potential .

Cathode	0
Anode	30 kV
Control electrode	3.5 kV

Equipotential lines of electric field and electron trajectories for model with decreased anode potential (electrode potential values are presented in table 1) are shown on the figure 6.

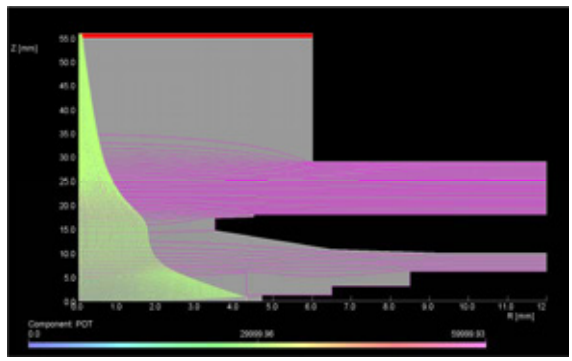

Figure 6: Electric field equipotential lines and electron trajectories for model with decreased anode potential.

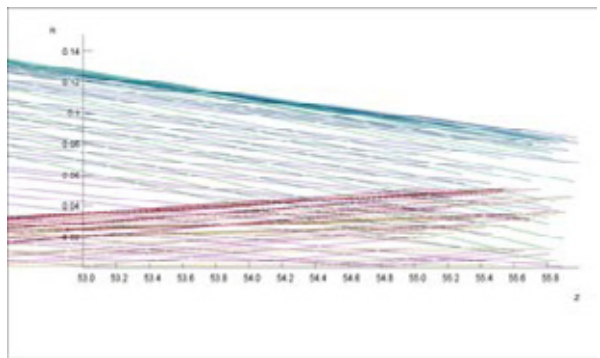

Figure 7: Electron trajectories near crossover.

MODEL WITH MODIFIED CATHODE GEOMETRY

For increasing cathode lifetime and technological reasons original cathode was changed to the bigger and more frequently used one. To fit new cathode to the form-factor of initial gun, geometry of control cathode was altered.

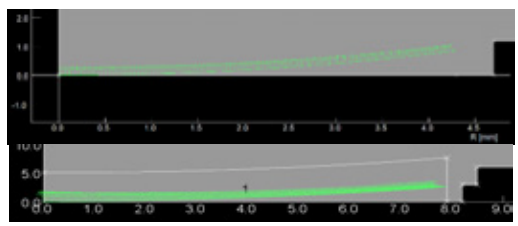

Figure 8: Emitting area for initial 8.6mm cathode model (a) and modified 15.8mm cathode model (b).

For a new gun model geometry beam width dependence on control electrode potential was investigated (Figure 9). Optimal electrode potentials are presented in table 2.

ISBN 978-3-95450-170-0

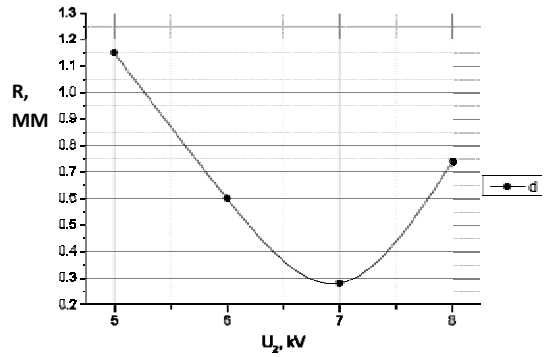

Figure 9: Beam crossover radius over control electrode potential plot.

Table 2. Electrode potentials for model with modified geometry.

Cathode	0
Anode	30 kV
Control electrode	7 kV

For modified geometry model with electrode potentials, shown in table 2, electric field and electron trajectories were calculated (Figure 9).

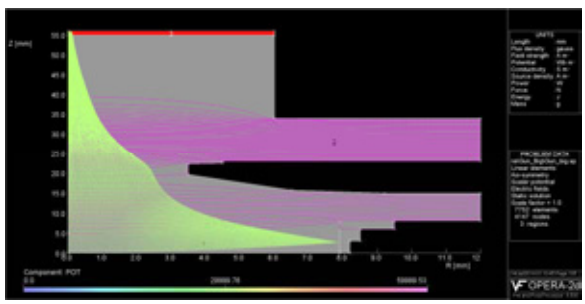

Figure 10: Electric field equipotential lines and electron trajectories for model with modified geometry.

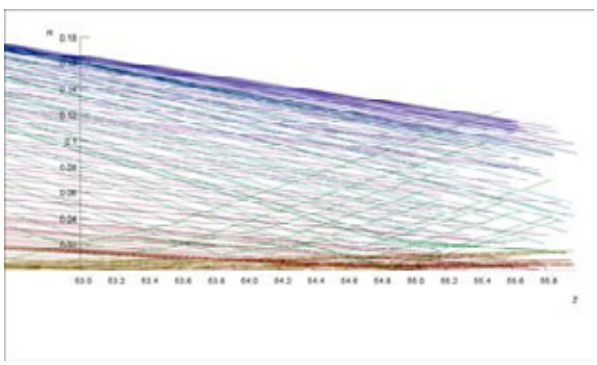

Figure 11: Electron trajectories near crossover.

CONCLUSION

Three electrode gun, consisting of spherical cathode, control electrode and anode, has been designed. Anode potential was varying between 30kV and 50kV. For the each potential the control electrode potential has been chosen to achieve the smallest beam crossover in the middle of the first accelerator cell. Calculations was based on the initial model of the already existing gun – electron injector in the linear accelerator. All calculations for the different anode voltages has been repeated for the bigger cathode, which imply different cathode electrode geometry. The result, usable in the further accelerator calculations has been achieved.

REFERENCES

[1] N.P. Sobenin, O.S. Milovanov, RF technique, M:Energoatomizdat,2007
[2] I.V. Aliamovskiy, Electron beams and electron guns, M:USSR Radio 1966
[3] http://www.cst.com

ISBN 978-3-95450-170-0

BEAM DYNAMICS CALCULATION IN THE INDUCTION LINEAR ACCELERATOR

D.S. Bazyl, E.A. Savin, National Research Nuclear University "MEPhI", Moscow, Russia
A.A. Zavadtsev, D.A. Zavadtsev, OOO "NANO INVEST", Moscow, Russia

Abstract

The geometry of the linear induction electron accelerator (LIA), which will be used for high current acceleration, has been calculated. For the different currents values the optimum focusing magnetic field and has been obtained. Also a current in the compensative coil near the cathode has been calculated. The cathode electrode geometry was changing to achieve minimum beam oscillations during the acceleration.

INTRODUCION

Electric field which is created by ferromagnetic rings having windings mounted along the beam axis is used for the acceleration of particles in this type of machine. As soon as the accelerating field structure excited in the tubes is similar to the electrostatic field excited by applying a potential difference between the span tubes, to simplify the calculation in this model fields is excited by an electrostatic field.[1] Schematic version of model of the accelerator is shown on the Figure 1. Basic parameters of the accelerator are shown in Table 1.

Injector is a flat grid-controlled cathode, located in the first accelerating gap. Grid voltage is up to 200 V. Voltage on the grid draws electrons which are then accelerated in the first gap. One inductor is connected to each accelerating gap. The pulse duration of the accelerating field is ~10 ns. The modules will contain a delay pulse-matching acceleration. The calculation was carried out in a constant acceleration field.

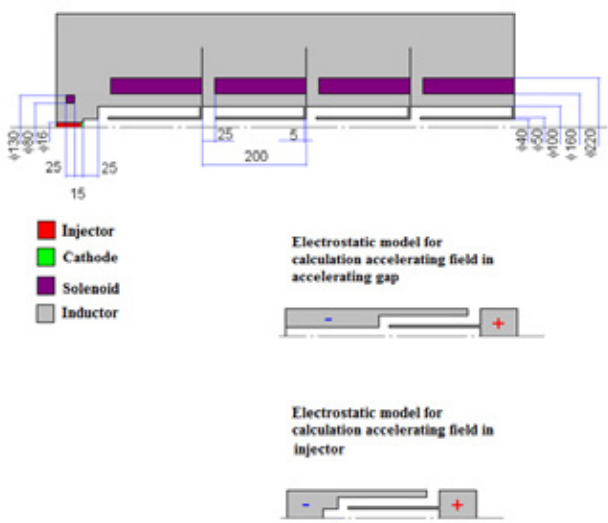

Figure 1: Schematic model for calculating the induction accelerator.

Table 1: Parameters of the accelerator.

Energy of the accelerated electrons, MeV	8
Injection energy, eV	200
The injection current, A	10
The diameter of the injected beam, mm	16
Accelerating voltage in each gap, kV	100

The calculations have started with a small number of modules but with further simulations their number was gradually increased.

Each inductor comprises one focusing coil. The compensating coil is positioned in the injector. The purpose of this coil is to compensate the field at the cathode. Its current is selected so that the total magnetic field at the cathode is zero.

SIMULATIONS

Several electro dynamical parameters were found by using simulations in CST PIC solver.

Simulations of the Electric Fields

When appropriate boundary conditions [2] are installed, the distribution of electric fields in the injector (Figure 2,3), corresponding to reality.

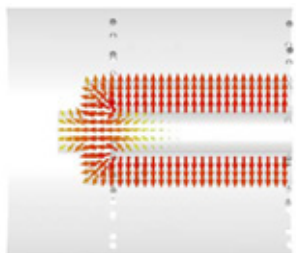

Figure 2: accelerating field in the injector.

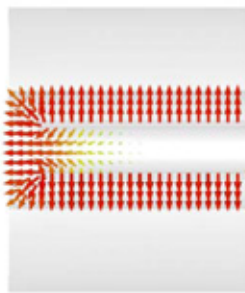

Figure 3: accelerating field in the accelerating gap.

ISBN 978-3-95450-170-0

Further, these fields are imported into the layout, consisting of four gaps (Figure 4) and four coils.

The magnetic field on the axis of each of the four focusing coils power 0.1T = 1000 Oe field in the injector (right on schedule from the "cathode") will nullify the compensating coil.

Figure 4: Structure with four accelerating gaps.

Compensating Coil

To compensate the magnetic field at the cathode (Figure 5), the structure was examined with an additional solenoid.

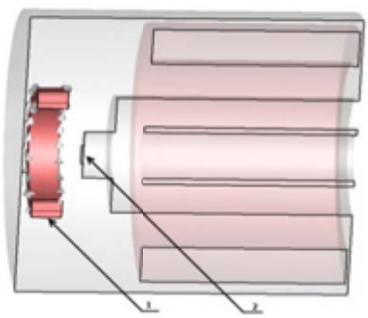

Figure 5: Model with compensating solenoid. (1-compensating coil; 2-cathode).

Direction of the current in the compensating solenoid was chosen the opposite to the direction of the current in the focusing solenoid. During the calculation was obtained the following current value at which the field at the cathode offset: Icomp. = -2900.05A

Table 2: Values of the current and magnetic fields.

The current in the focusing solenoid, A	29500
Current in the compensating solenoid, A	-2900
The magnetic field at the cathode, T	-0,00005
The maximum magnetic field on the axis, T	1
The current in the focusing solenoid, A	29500

Further, three sections with the accelerating gap was added to the structure, the field at the cathode was not changed. Figure 6 represents the distribution of the magnetic field on the axis of propagation of the electron beam

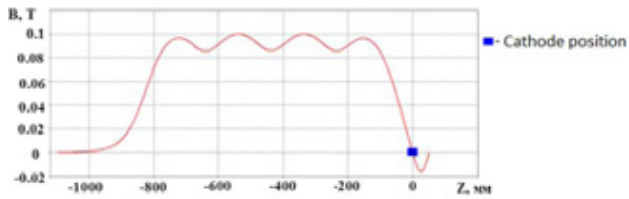

Figure 6: The magnetic field on the central axis of the structure.

Calculation of the Dynamics for Different Currents

LIA was considered with a beam current I = 10 A and a voltage of the first module U = 100 kV. It was further suggested to consider the dynamics of the injected beam at higher current values. However, for example, for the value of the current I = 50 A, using the current values of the magnetic (B = 0.1 T) and electrical (voltage module 100 kV) fields to obtain acceptable beam dynamics in the accelerating structure is not possible, because by increasing the beam current is observed shielding effect near the cathode (Figure 7,8)

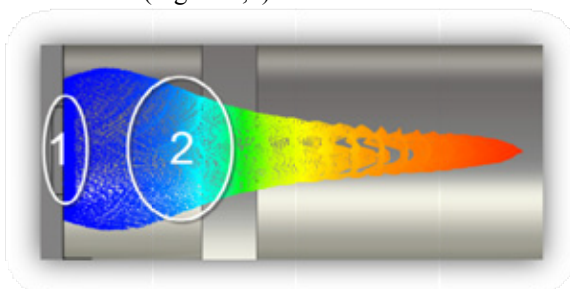

Figure 7: Dynamics of the beam, taking into account the emerging phenomenon.

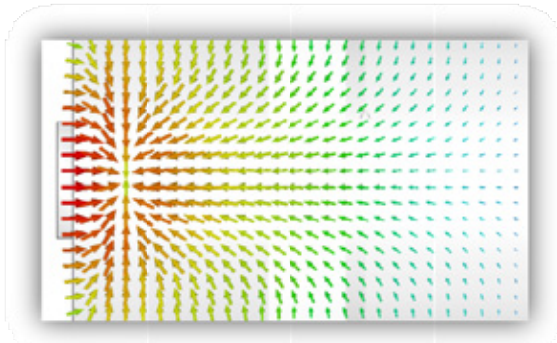

Figure 8: electric field in the event of this effect.

At some point the electric field of electrons from the region 2 (Fig. 7) adopts a configuration as depicted in Fig.11. This prevents subsequent emission of electrons which subsequently accumulates near the cathode (region 1, Fig. 7).

This phenomenon can be eliminated in two ways:

1) Increase the value of the electric field gradient in the accelerating gap

2) Reduce the distance from the cathode to the first accelerating module.

ISBN 978-3-95450-170-0

The first way worked out well but high voltage was required. Fine beam dynamics appeared when the voltage on each accelerating gap was U=1 MV, which is quite a lot, as soon it's proposed to have 80 sections. So we can say that first way showed to be impossible to make it practically by economical and practically.

Due to the fact that an increase in the voltage at the first accelerating module is irrational solution to the problem of screening near the cathode, it was decided to study the behaviour of the particle dynamics depending on the position of the cathode ΔL relative to the first accelerating module.

To eliminate these effects, a series of calculations, the results of which were set to the optimal value of the magnetic field at the center of the first module, the value of which was: B = 0.2 Tesla.

Figure 9 shows the dynamic of the beam for the above parameters of the magnetic field B = 0.2 T; the voltage at the first module U = 100 kV, the distance between the cathode and accelerating gap ΔL = 28.39 mm, and the beam current I = 50 A.

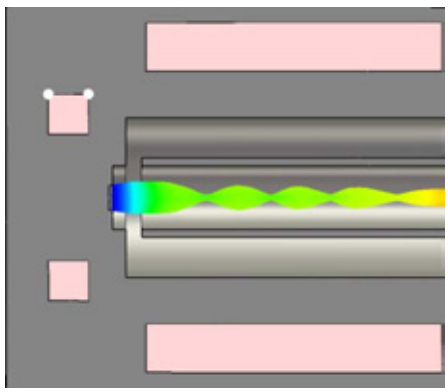

Figure 9: Dynamics of the beam at ΔL = 28.39 mm, I = 50A, U = 100 kV, B = 0.2 Tesla.

THE ENERGY OF THE OUTPUT BEAM FOR THE EIGHT ACCELERATING MODULES

Besides the beam dynamics, output energy of the electrons was also calculated. The results are shown in Table 3, also this table presents other settings that allow to present an complete picture of the dependencies between the different parameters:

Table 3: Results of the calculations.

I, A	E, eV*10^5	B, T	ΔL, mm
10	8,11	0,1	28.39
20	8,16	0,1	28.39
50	8,32	0,2	28.39

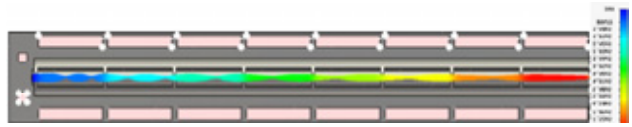

Figure 10: Beam dynamics for eight accelerating gaps.

CONCLUSION

Accelerating structure has been optimized, taking into account any adverse events. While increasing the value of the beam current, at some point there was an effect of screening in the vicinity of the cathode. It was proposed to solve the problem in two ways: to change the distance between the cathode and the first module or increase the voltage. Increased tension in the first gap proved unsustainable way. The problem was solved by approaching the cathode to the first module. The optimal distance between the cathode and the first accelerating module was found and was ΔL = 28.39 mm. For a beam with a current I = 10 A and I = 20 A, the value of the magnetic field was B = 0.1 T (based on previous calculations). For a beam with a current I = 50 A, the value of the magnetic field was chosen B = 0.2 T. With the parameters described above, there is an acceptable beam dynamics in the accelerating structure.

The energy of the output beam of the structure is linearly dependent on the number of modules and to the accelerating voltage. This report described the dynamics of the beam in the structure of the eight modules. For a beam with a current of I = 50 A value of the output energy was E = 8,32 * 105 eV, and hence for the module 80 is equal to the energy E ~ 8 MeV and 100 units - E ~ 10 MeV.

REFERENCES

[1] A.N. Lebedev, A.V. Shalnov, “Basic physics and accelerator technology. Linear accelerators” Moscow, Energoatomizdat, (1983).

[2] N.P. Sobenin, O.S. Mylovanov "RF technics". Moscow, Energoatomizdat, (2007)

ISBN 978-3-95450-170-0

TRANSIT CODE FOR BEAM DYNAMIC SIMULATION

A.A. Kolomiets, A.S. Plastun, T.E. Tretyakova, FSBI «SSC RF ITEP», Moscow, Russia

Abstract

Multiparticle computer code TRANSIT for simulation of intense ion beams in linacs and transport systems is presented. The code is based on experience in design of ion linacs in ITEP. TRANSIT summarizes the most actual and modern methods and algorithms for integration of motion equations including space charge forces. It is being used in ITEP for design and simulation of conventional RFQs, spatially periodic RF focusing linacs, beam transport systems, RF deflectors, etc. The paper presents general description of TRANSIT code and some achieved results.

INTRODUCTION

Development of codes for beam dynamic simulation in ITEP has been started in the early 80s [1]. It was concerned with design of first RFQ proton linacs in ITEP [2]. The simulation code was a tool for study of high intensity beam dynamics in RFQ linacs. It had to describe motion of beam particles accurately and in the most natural approach. Initially external field of RFQ channel was approximated by 2-term 3-D potential, but self-field of the beam was calculated by combined "particle-particle" (PP) and "particle-in-cell" (PIC) method. It was expected as the most adequate method for beam interaction solver, but it was replaced by conventional PIC method in following versions due to technique difficulties. Coulomb field of each macroparticle was expressed by Lienard–Wiechert potentials. The beam had initial truncated normal (gaussian) distribution of space charge density as the most natural. Macroparticle motion solver was operated on predictor-corrector scheme. This code was called PROTON.

Further upgrades of the code allow user to choose PP or PIC methods, simulate multi-component ion beams with different charge-to-mass ratios in different elements of the channel: RFQ cells, quadrupoles, drift spaces, drift tube linacs, etc. External fields can be based on 3-D interpolation of data from ASCII files. The code POLE [x] was used to simulate 3-D field in RFQ cells and the code ALFIL - to simulate 3-D field in DTL cells. These upgrades were caused by application of the code for simulations of UNILAC [3]. This upgraded code was called DYNAMION. Thus it was able to simulate beam dynamics from plasma border inside the ion source up to the end of the linac.

Further versions of the code have been developed in GSI [4] and ITEP independently due to separate applications. To avoid a confusion the code developing in ITEP was called TRANSIT. This paper presents general description of TRANSIT code and some achieved results.

MOTION SOLVER

Motion Equations

One of the most important effect in linear accelerators is emittance growth of accelerated ion beam. It is mainly expressed by redistribution of space-charge density of the beam and halo formation due to nonlinear external and self fields. Unfortunately finite difference approximation of particle motion can produce the artificial emittance growth. The rate of artificial growth is defined by resolution of finite difference approximation (i.e. integration step) and order of numeric method. There are methods that doesn't cause the artificial growth - symplectic methods [5]. The most simple and natural one is "symplectic Euler method", which is used in TRANSIT. Symplectic Euler methods is shown below:

$$\vec{v}_{i+1} = \vec{v}_i + \Delta t \cdot \vec{A}(\vec{v}_{i+1}, \vec{r}_i),$$

$$\vec{r}_{i+1} = \vec{r}_i + \Delta t \cdot \vec{v}_{i+1},$$

$$\vec{A} = \frac{q}{m}\sqrt{1-\frac{v^2}{c^2}}\left\{\vec{E} + \frac{1}{c}\left[\vec{v}\vec{H}\right] - \frac{1}{c^2}\vec{v}\left(\vec{v}\vec{E}\right)\right\}.$$

Here $\vec{v}$ is vector of particle velocity, $\vec{r}$ - radius-vector of a particle, $\vec{A}$ - acceleration vector, q - particle charge, m - particle mass, E and H - vectors of external and self electromagnetic field, c - speed of light.

In addition elementary transfer matrices of every particle are evaluated for each integration step during simulation. The multiplication of elementary matrices defines common transfer matrix of focusing lattice. It provides the analysis of beam dynamics proposed in [6].

Beam frame

TRANSIT is able to simulate beam dynamics through the channel consisted from various number of elements. Element is a part of a channel with specifically defined field distribution (3-D mapping, series, etc.) or drift space.Length and aperture radius (especially for self-field calculations) have to be defined for each element.

To reduce calculating time for multi-element channel the moving frame has been proposed for TRANSIT. Beam frame is 3-D space domain around the reference particle. Frame has length of βλ and transverse sizes equal to aperture radius. Frame moves with reference particle during simulation. Beam frame can include only part of all elements. of a channel at every moment of time. Special algorithm of interaction between lost particles and beam frame has been proposed for accurate and authentic simulation.

External Fields

One of the most important feature of TRANSIT code is 3-D mapping of external field from ASCII file. Motion

ISBN 978-3-95450-170-0

solver performs 3-D quadratic interpolation of imported field in turn. Files with external field distribution can be exported from any code of electrostatic or microwave simulation. Measured 3-D field distribution can be used for simulation as well.

A package of additional 3D electrostatic solvers has been developed for the most demanded linacs to provide field maps for TRANSIT. PreRFQ is a code for calculating field in RFQ cells with sinusoidal or trapezoidal modulation. PreRFQ builds the cell from two halves with different parameters as shown in Figure 1.

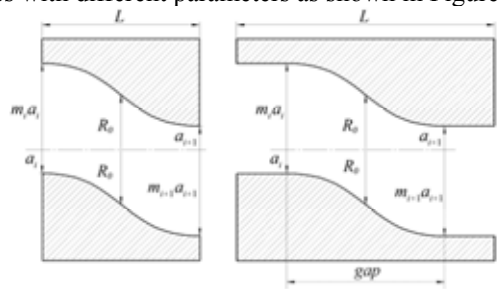

a *b*

Figure 1: RFQ cell (*a* - sinusoidal, *b* - trapezoidal) geometry for PreRFQ code.

ALFIL code is used to simulate field in DTL cells with round drift tubes with or without quadrupole lenses. TUBE-RFQ code is used for spatially – periodic structures where accelerating gaps are formed between RF quadrupoles and cylindrical drift tubes (Figure 2). All these codes export 3D distribution of field or potential to ASCII files.

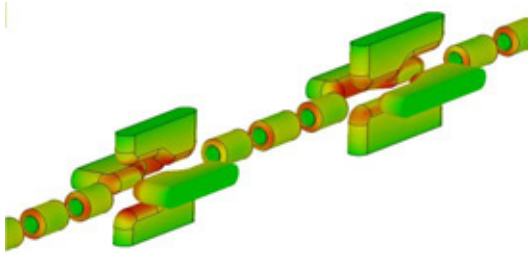

Figure 2: Spatially - periodic structure.

Self-field

Like most beam dynamics codes TRANSIT uses conventional PIC method [7] for self-field calculation. Charge weighting scheme used in PIC method is volume weighting or so-called Cloud-in-Cell (CIC) which is 1st order scheme.

Self-field of the beam is calculated from 3-D charge density distribution with fast Fourier transformation (FFT) algorithm.

Upgrade of PIC method to combined PIC and PP method (called "Particle-Particle - Particle-Mesh" or P^3M [7]) is scheduled in following versions of the code.

Initial Distribution

TRANSIT has an external random generator for initial distribution of macroparticles. Binomial algorithm used in this generator can simulate various kinds of distributions: KV, waterbag and truncated normal (gaussian) distribution with specified truncation parameter. For the most applications truncated normal distribution with truncation parameter 2.5σ (full emittance is 2.5^2 = 6.25 RMS emittance) is useful.

Graphical User Interface

One of significant difference of TRANSIT code from DYNAMION is presence of Graphical User Interface (GUI). GUI is a single window application with several tabs (Figure 3):

- initial beam parameters,
- phase-plots of input and output beam,
- linac structure,
- transverse envelopes,
- phase-space density of the beam,
- log & project files.

Moreover GUI is able to show field distribution along the linac, modify parameters of the main solver and run the simulation, calculate emittance values and Twiss parameters of the beam, export plots into graphical files, etc. For example, phase-plots in Figure 3 correspond to exit of the structure shown in Figure 2 as well as electric field along the structure near the longitudinal axis is shown in Figure 4.

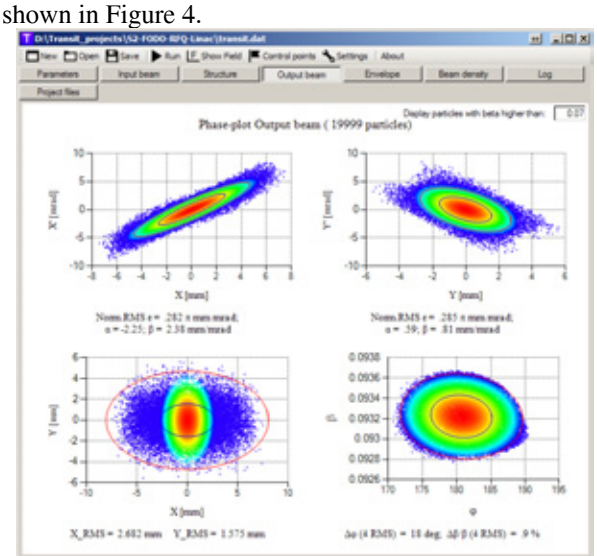

Figure 3: Main window of TRANSIT GUI.

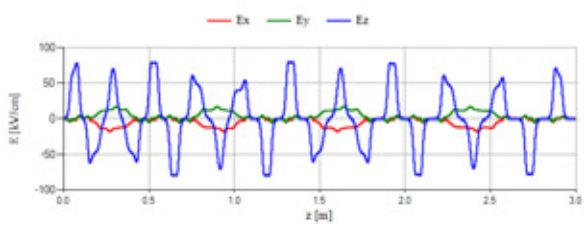

Figure 4: Field distribution along the linac.

TRANSIT solver operation is displayed as beam phase-plots and transverse envelopes online during simulation (Figure 5, that corresponds to simulation of the structure shown in Figure 2).

ISBN 978-3-95450-170-0

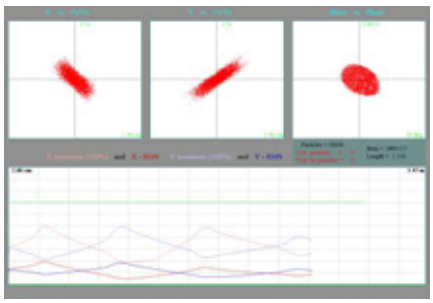

Figure 5: Phase-plots and transverse envelopes during simulation.

POSTPROCESSING

TRANSIT calculates only main beam parameters. For detailed analysis of beam dynamics TRANSIT is able to export coordinates and velocity components of beam particles to ASCII file at any position along the linac or periodically through several integration steps. It allows user to analyze and plot results at any time without new run with special programs, like PAW (Physics Analysis Workstation) [8], Gnuplot [9], PlotWin [10], etc.

Figure 6 illustrates PAW histograms for transverse phase advance of particles in 352 MHz DTL section with FOFODODO focusing lattice. Figure 6*a* presents phase advance distribution for lattice without accelerating field and zero beam current. Figure 6*b* present phase advance distribution of accelerating beam with zero current, and figure 6*c* - phase advance distribution of accelerating beam with 40 mA current.

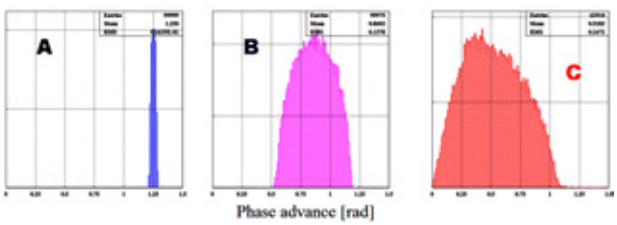

Figure 6: Transverse phase advance distribution. *a* - no acceleration of beam with zero current, *b* - accelerating beam with zero current, *c* - accelerating beam with 40 mA current.

APPLICATION OF THE CODE

TRANSIT code is being used in ITEP for design and simulation of conventional RFQs, spatially periodic RF focusing linacs, beam transport systems, RF deflectors, etc. List of some applications of the code is presented below.

- Ion RFQ injector for ITEP-TWAC project [11],
- Some variants of second section of ion injector for ITEP-TWAC project [12, 13, 14],
- High intensity proton 7.4 MeV RFQ with trapezoidal modulation [15],
- RF deflector for hollow beam formation [16],
- Single frequency high intensity high energy normal conducting hadron linac [17],
- Compact proton injector for synchrotrons [18].

REFERENCES

[1] E.S. Galpern, V.N. Lyahovitskiy, “Calculation for evolution of self-consistent ion beam in a section of linear accelerator with spatially homogeneous quadrupole focusing”, Preprint ITEP-130, 1983.
[2] A.I. Balabin et al., “Main parameters of proton linac “ISTRA”, Preprint ITEP-157, 1989.
[3] A.A. Kolomiets, S.G. Yaramishev, Ju. Klabunde et al., “DYNAMION - The code for beam dynamics simulations in high current ion linac”, THP04F, Proceedings of EPAC98, Stockholm, Sweden, 1998.
[4] A. Orzhekhovskaya, W. Barth, S. Yaramyshev, “An effective space charge solver for DYNAMION code”, TUO2A02, Proceedings of HB2010, Morschach, Switzerland, 2010.
[5] E. Hairer, C. Lubich, G. Wanner. Geometric Numerical Integration, Springer, 2006. 644 p.
[6] A. A. Kolomiets, S. G. Yaramishev, P. R. Zenkevich et al., “The study of nonlinear effects influenced by space charge in high intensity linac”, TPA052, Proceedings of PAC95, Dallas, USA, 1995.
[7] R.W. Hockney, J.W. Eastwood, Computer simulation using particles, IOP Publishing Ltd, 1989, 523 p.
[8] http://paw.web.cern.ch/paw/
[9] http://www.gnuplot.info/
[10] PlotWin, CEA Saclay.
[11] V.A. Andreev, N.N. Alexeev, A.A. Kolomiets et al. “First beam test of 81.5 MHz RFQ for ITEP-TWAC”, weps056, Proceedings of IPAC11, San Sebastián, Spain, 2011.
[12] A.S. Plastun, A.A. Kolomiets, “RFQ with improved energy gain”, supb016, Proceedings of LINAC12, Tev-Aviv, Israel, 2012.
[13] V. Andreev, A. Kolomiets, A. Plastun et al. “Novel DTL section for ITEP-TWAC heavy ion injector”, weppc013, Proceedings of RuPAC12, Saint-Petersburg, Russia, 2012.
[14] A.A. Kolomiets, A.S. Plastun, “Spatially periodic RF quadrupole linac”, SUPG013, Proceedings of LINAC14, Geneva, Switzerland, 2014.
[15] A.S. Plastun, “RFQ as a second section of front end of ion linac”, article_2013_6_109, Problems of atomic science and technology, Series: Nuclear Physics Investigations, №6(88), 2013.
[16] A. Golubev, T. Kulevoy, A. Sitnikov et al., “Simulation of hollow ion beam formation line”, tuppb018, Proceedings of RuPAC12, Saint-Petersburg, Russia, 2012.
[17] V. Paramonov, A. Kolomiets, A. Dourkine et al., “Single Frequency High Intensity High Energy Normal Conducting Hadron Linac”, Proceedings of RuPAC14, Obninsk, Russia, 2014.
[18] A. Kovalenko, A. Kolomiets, A. Plastun et al., “Compact proton injector for synchrotrons”, MOPP099, Proceedings of LINAC14, Geneva, Switzerland, 2014.

ISBN 978-3-95450-170-0

BEAM DYNAMICS CALCULATIONS IN THE MULTI-BEAM GENERATOR CAVITY

S.V. Matsievskiy, E.A. Savin, N.P. Sobenin, National Research Nuclear University MEPhI (Moscow Engineering Physics Institute), Moscow, Russia
A.A. Zavadtsev, OOO "Nano Invest", Moscow, Russia

Abstract

In the previously designed, calculated and tuned structure of the compact generator-cavity the beam dynamics for the different geometry options has been calculated. The influence of injected beam parameters to the output power value has been overviewed. Also the geometry of the beam tubes and couple coefficient between cavity and the output waveguide has been optimized to reach the maximum output power value.

INTRODUCTION

The inductive output tube klystrod combine two superior characteristics of gridded tube and high-frequency klystron. A grid is used to provide simple control of electron beam. Cavity of klystrod couple bunches of modulated beam to the RF field. This combination makes a smaller, lower cost, high-frequency, high-power tube. To increase power of device without significant size change multiple electron beams coupled to one RF cavity.

RESONATOR TUNING

RF power is generated is multi-beam klystrod by drawing power from the electron beams, and storing it in cylindrical resonator, operating on TM020 mode at 2856 MHz. Beam drift tubes are located in maximums of electrical field. Electrical field distribution in resonator model is shown on figures 1 and 2.

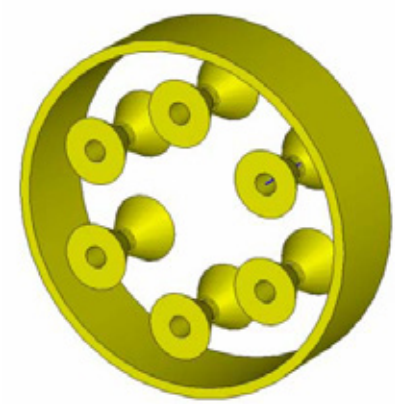

Figure 1: Resonator of multi-beam klystrod.

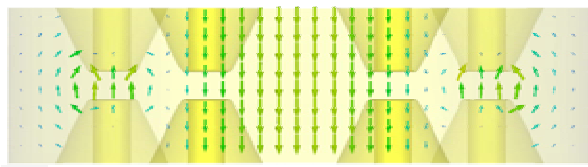

Figure 2: Electric field distribution in multi-beam klystrod resonator (side view).

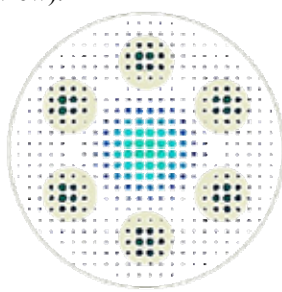

Figure 3: Electric field distribution in multi-beam klystrod resonator (top view).

For this resonator geometry, shunt impedance on the axis of each beam tube is 2.95 MOhm/m, which gives a total impedance of the model 17.7 MOhm/m.

WAVEGUIDE IRIS TUNING

For power input, standard waveguide 72.1mm x 34mm is used.

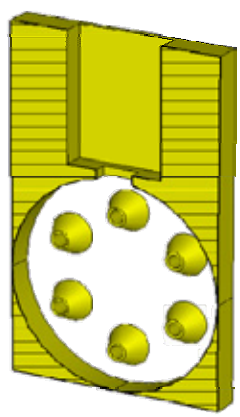

Figure 4: Multi-beam klystrod resonator and waveguide, connected by iris.

Maximum power transition from resonator to waveguide was acquired by tuning waveguide iris. On the figure 6 plot of normalized output port power over iris

ISBN 978-3-95450-170-0

width il (output power was normalized to the maximum achieved output power). On the figure 5 iris geometrical parameters are shown.

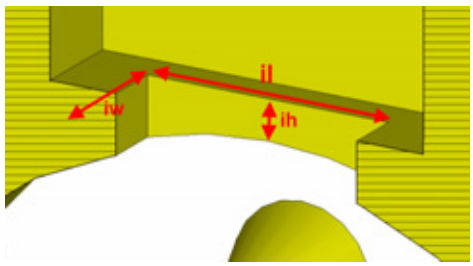

Figure 5: Iris geometrical parameters.

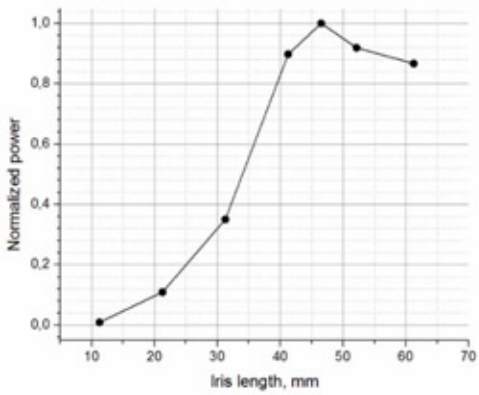

Figure 6: Normalized power over iris width plot.

Optimal iris parameters, which provide maximum output power, are presented in table 1.

Table 1 Iris parameters

ih	7.53 mm
iw	20 mm
il	46.5 mm

POWER OUTPUT TUNING

For power generation modulated electron beam is used. This beam is provided by electron gun with control grid, its parameters are shown in table 2.

Table 2 Electron beam parameters

Electron energy	$1 \cdot 10^5$ eV
Beam diameter	3 mm

In the table 3 parameters of beam modulation are presented. Explanation of bunch parameters can be found of the figure 7.

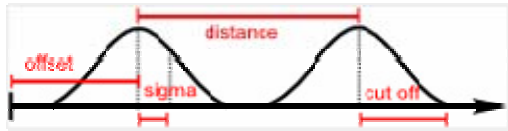

Figure 7: Beam bunches parameters scheme.

Table 3 Beam bunch modulation parameters set

Offset	0
Sigma	60 ps
Distance	350 ps
Cut off	70 ps

Output signal amplitude dependence of beam tube gap. Output power dependence of gap length g plot is presented on the figure 9.

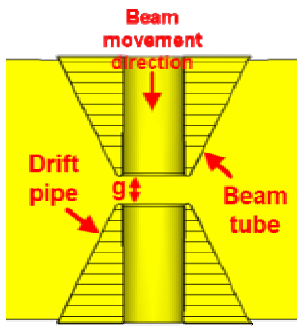

Figure 8: Resonator geometry parameters.

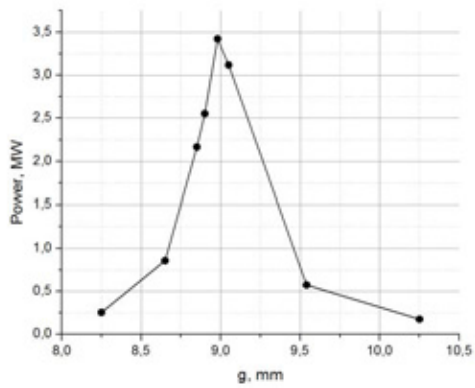

Figure 9: Output rms power over gap length g between beam tube and drift pipe plot.

After tuning, power generation was simulated. Electron beams with parameters, shown in tables 2 and 3 were launched to the centers of the beam tubes and coupled to the resonator RF field. From the resonator RF power was transmitted to the waveguide. This power was calculated shown on the figure 10. Klystrod reaches 90% output power level in 100 ns.

ISBN 978-3-95450-170-0

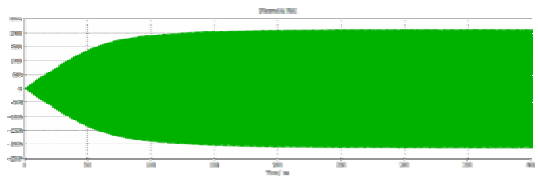

Figure 10: Multi-beam klystron output rms power over time plot.

Device efficiency was estimated by dividing output RF power on the electron beam bunch power. Presented parameters were achieved with total electron beams power of 4.3 MW. On the maximum output power level 3.4 MW of multi-beam klystrod efficiency is 73%.

KLYSTROD APPLICATION

Tuned multi-beam klystrod will be installed as a power source for electron accelerator. On the figure 11 presented a model of 8 cell acceleration structure, connected to the klystrod. Tuning of this accelerating structure is still in progress.

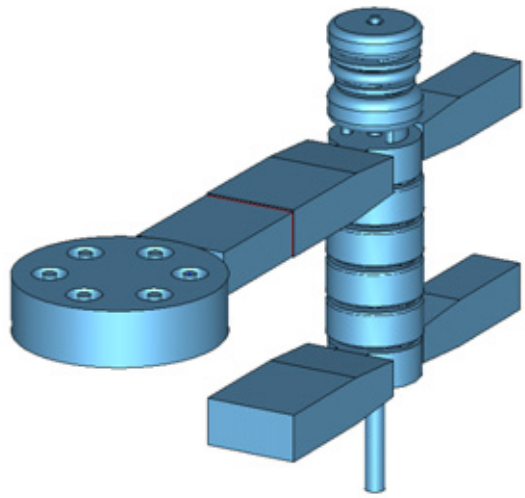

Figure 11: Multi-beam klystrod, connected to the accelerating structure.

REFERENCES

[1] N.P. Sobenin, O.S. Milovanov, RF technique, M:Energoatomizdat,2007
[2] Morten Jensen, High Power RF Sources for the ESS RF Systems, Linac 2014
[3] http://www.cst.com
[4] Jerry C. Whitaker, The Electronics Handbook

ISBN 978-3-95450-170-0

ADVANCED OPTIMIZATION OF AN LOW-ENERGY ION BEAM DYNAMICS AT LINAC FRONT-END WITH RF FOCUSING

V.S. Dyubkov,*
National Research Nuclear University "MEPhI", Moscow, Russian Federation

Abstract

A design and development of a linac front-end, that guaranties the required beam, quality is an issue of the day. A linac with RF focusing by means of the accelerating field spatial harmonics is suggested as an alternative to RFQ system. Simulation results of the low-energy proton beam dynamics at linac, that takes into account main linac parameter optimization, based on advanced dynamical acceptance calculation, are presented and discussed.

INTRODUCTION

Projects based on accelerator driven systems are developed in about twenty countries around the world. In order to ensure the safety and stability of this systems it is used well-tried and proven engineering solutions. The initial part of a linear accelerator-driver is a section with spatially homogeneous quadrupole focusing (RFQ), as a general rule. However, a grave drawback of classical RFQ structures is the relatively low acceleration rate that often leads to an increase of the accelerator driver total length. In addition, main losses of the particles typically occur in initial parts of the RFQ sections.

Proton and ion accelerators with RF focusing by means of field spatial harmonics are offered as almost only adequate alternative to the well-proven and reliable RFQ systems for many years [1–3]. Analytical method to control the beam envelope at linac with RF focusing was developed previously to minimize particle losses [4]. The goals of this work are to present results of beam dynamics advanced optimization, which allows one to define main parameters of structure with RF focusing by means of nonsynchronous spatial harmonic which guarantee high acceleration rate under high current transmission.

ANALYTICAL RESULTS

Let's present some results obtained earlier in [4]. One first expresses RF field in an axisymmetric periodic resonant structure as Fourier's representation by spatial harmonics of a standing wave assuming that the structure period is a slowly varying function of a longitudinal coordinate z

$$E_z = \sum_{n=0}^{\infty} E_n I_0(k_n r) \cos\left(\int k_n\, dz\right)\cos\omega t,$$

$$E_r = \sum_{n=0}^{\infty} E_n I_1(k_n r) \sin\left(\int k_n\, dz\right)\cos\omega t,$$

where E_n is the nth harmonic amplitude of RF field on the axis; $k_n = (\mu + 2\pi n)/D$ is the propagation wave number for the nth RF field spatial harmonic; μ is the phase advance per D; D is the resonant structure geometric period; ω is the RF frequency; I_0, I_1 are modified Bessel functions of the first kind.

On averaging over rapid oscillation period one can present the motion equation in the smooth approximation in the following matrix form

$$\ddot{\Upsilon} + \Lambda\dot{\Upsilon} = -L\Phi_{\text{ef}}, \qquad (1)$$

where the dot above stands for differentiation with respect to the independent longitudinal coordinate ξ and

$$\Upsilon = \begin{pmatrix}\psi\\ \delta\end{pmatrix}, \qquad \Lambda = \begin{pmatrix}3\varkappa & 0\\ 0 & \varkappa\end{pmatrix}, \qquad L = \begin{pmatrix}\frac{\partial}{\partial\psi}\\ \frac{\partial}{\partial\delta}\end{pmatrix}.$$

Here $\psi = \tau - \tau^*$ ($\tau = \omega t$, τ^* is a normalized motion time of the reference particle at the laboratory coordinate system), $\xi = 2\pi z/\lambda$, $\delta = 2\pi r/\beta_s\lambda$, $\varkappa = \ln'_\xi \beta_s$. Φ_{ef} plays role of an effective potential function (EPF) describing a beam interaction with the polyharmonical field of the system subject to the incoherent particle oscillations.

For example, we consider there are two spatial harmonics at the linac. One of it is the synchronous harmonic with $s = 0$, and another one is the nonsynchronous (focusing) with $n = 1$. In this case one has

$$\begin{aligned}\Phi_{\text{ef}} = {} & \frac{e_0}{2\beta_s}\left[I_0(\delta)\sin(\psi+\varphi^*) - \psi\cos\varphi^* - \sin\varphi^*\right]\\ & + \frac{e_0^2}{64}\left[I_0^2(\delta) + I_1^2(\delta) - 1\right]\\ & + \frac{5e_1^2}{256}\left[I_0^2(3\delta) + I_1^2(3\delta) - 1\right]\\ & - \frac{e_0^2}{32}\left[I_0(\delta)\cos\psi - 1\right] - \frac{5e_1^2}{128}\left[I_0(3\delta)\cos\psi - 1\right]\\ & - \frac{e_0e_1}{32}\{[I_0(\delta) + I_0(3\delta)]\cos(\psi+2\varphi^*) - 2\cos 2\varphi^*\}\\ & + \frac{e_0e_1}{32}\{[I_0(\delta)I_0(3\delta) + I_1(\delta)I_1(3\delta)]\cos 2(\psi+\varphi^*)\\ & - \cos 2\varphi^*\},\end{aligned}$$

where $e_n = eE_nZ\lambda/2\pi\beta_s^2 m_0c^2$, φ^* is the reference particle phase.

In order to guarantee effective acceleration under small particle loss it is necessary to optimize a changing of synchronous particle phase & field amplitude so that the Eq. 1 has stable solution for a number of initial conditions.

* vsdyubkov@mephi.ru

ISBN 978-3-95450-170-0

NUMERICAL RESULTS

Linac parameters with RF focusing by means of one non-synchronous spatial harmonic were optimized by using numerical self-consistent low-energy proton beam dynamics simulation after beam dynamics optimization in one particle approximation on the basis of obtained analytical results. Self-consistent beam dynamics simulations were performed by using a version of the specialized computer code BEAM-DULAC–ARF based on CIC technique to calculate beam self-space-charge field. Special optimization of the field change law was done & it was based on the supposition that channel acceptance is a nondecreasing function of the longitudinal beam coordinate. Therefore, taking into account the equation of motion for the equilibrium particle, the law of the synchronous harmonic amplitude variation at a field increasing length can be written as

$$\frac{d\widehat{e}_s}{d\xi} = \frac{\widehat{e}_s}{\ell}\frac{d\ell}{d\xi} - \frac{\widehat{e}_s}{\varsigma}\frac{d\varsigma}{d\xi} - \frac{\widehat{e}_s{}^3\cos\varphi_s}{\beta_s(0)\widehat{e}_s(0)\varsigma(0)}\frac{\varsigma}{\ell} - \frac{\chi\,\widehat{e}_s{}^{\frac{9}{2}}\sin 2\varphi_s}{8\beta_s{}^8(0)\widehat{e}_s{}^{\frac{3}{2}}(0)\varsigma^{\frac{3}{2}}(0)}\frac{\varsigma^{\frac{3}{2}}}{\ell^{\frac{3}{2}}}, \quad (2)$$

where ς is a longitudinal acceptance phase width; ℓ is a certain function of ξ and it can be found by numerical optimization in every given case, $\widehat{e}_s = e_s\beta_s^2$. χ is the amplitude ratio, that is e_1/e_s. In the accelerating parts of the structures $\widehat{e}_s$ is equal to the constant.

Main linac parameters are listed in Table 1. A variation of the linac parameters are shown in Fig. 1.

Table 1: Basic parameters of linac

Parameter	Value
Operational frequency, MHz	176.1
Total linac length, m	2.0
Bunching length, m	1.7
Input equilibrium particle phase	−90.0°
Output equilibrium particle phase	−25.7°
Input synchronous harmonic amplitude, kV/cm	0.3
Amplitude ratio	7.4
Linac half-aperture, mm	5.0

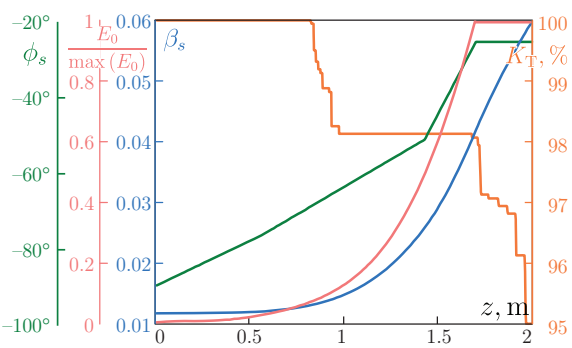

Figure 1: Main linac parameters after optimization.

A calculation of E_0 was performed by using separatrix width calculated for conservative approximation (see curve 1 in Fig. 2) at first. Based on this calculation, particle capture region phase width was found for the non-conservative approximation (curve 2 in Fig. 2). After that, it was used to refine solution of Eq. (2). Finally, numerical simulation was carried out for the found solution above.

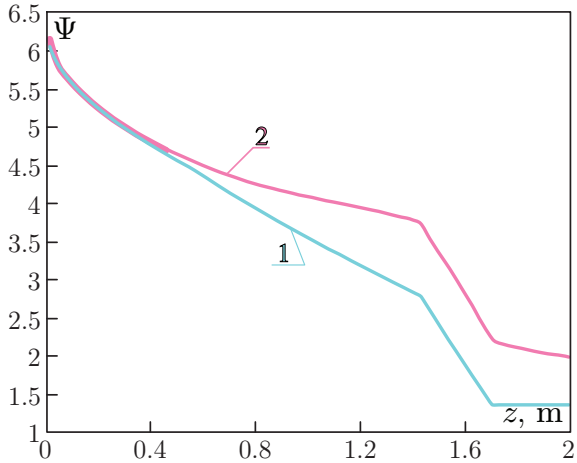

Figure 2: Phase width of longitudinal capture region.

For example, summarized in Table 2 beam parameters were used for computer simulation.

Table 2: Beam parameters @ linac input

Parameter	Value
Particle	p
Input energy, keV	65
Input energy spread, %	1
Input radius, mm	2.5
Input transversal emittance, π•mm•mrad	18
Input beam current, mA	10

Obtained numerical results are presented in Fig. 3-5.

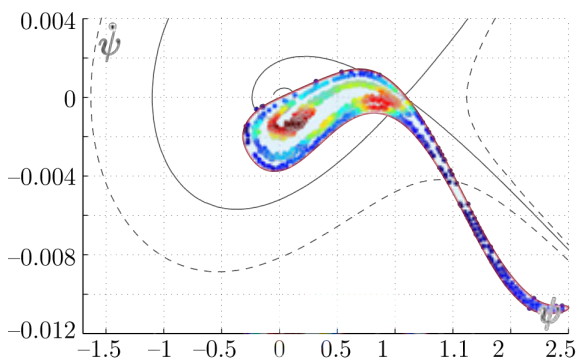

Figure 3: Output longitudinal beam particles distribution.

Output beam energy is equal to 1.7 MeV. Other beam parameters can be estimated by means of presented figures.

Furthermore, halo parameter calculated in accordance with [5] is presented in Fig. 6.

ISBN 978-3-95450-170-0

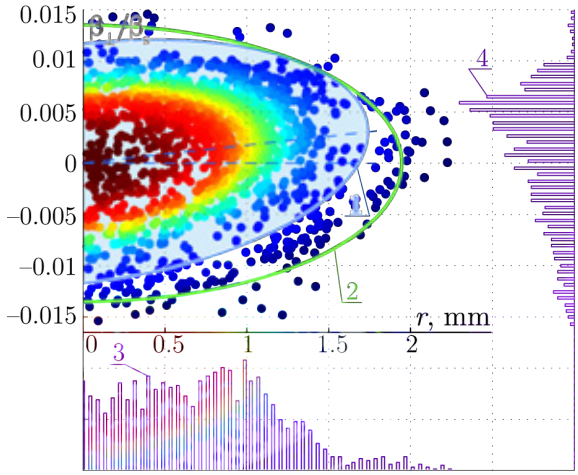

Figure 4: Output transversal beam particles distribution: RMS emittance (1); Floquet ellipse (2); particle distribution by radii (3); particle distribution by $\beta_\perp$ (4).

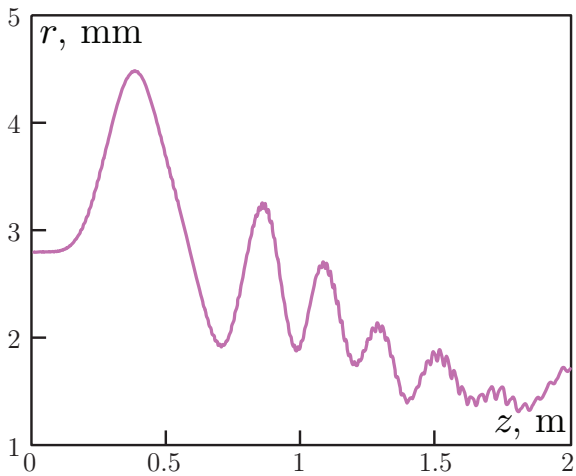

Figure 5: RMS beam radius vs longitudinal coordinate.

Bandwidth of calculated linac channel as a function of injected beam current is shown in Fig. 7.

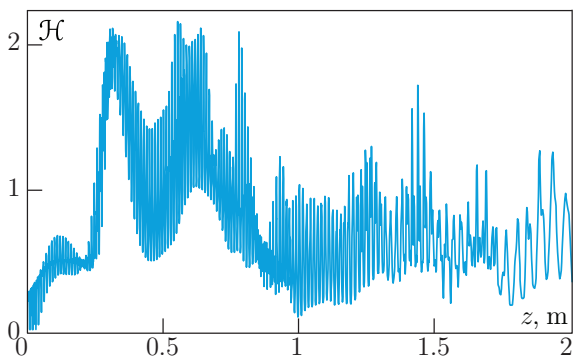

Figure 6: Halo parameter behaviour.

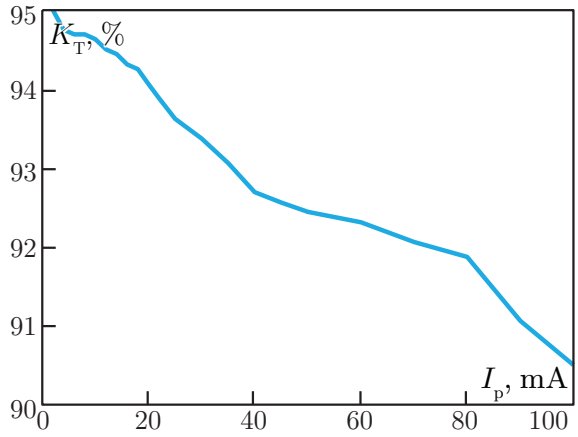

Figure 7: Current transmission vs input beam current.

CONCLUSION

It was shown that advanced optimization allows one to increase current transmission up to 95% under high enough acceleration rate. The main parameters of linac front-end were chosen. There are no beam envelope overgrowth and significant halo formation under chosen parameters at the linac output. Numerical simulation of self-consistent beam dynamics confirmed the analytical results.

REFERENCES

[1] E.S. Masunov, N.E. Vinogradov, Phys. Rev. ST Accel. Beams 4, 070101 (2001).

[2] E.S. Masunov et al., "RF focusing methods for heavy ions in low energy accelerators", PAC'03, Portland, May 2003, RPAG035 (2003).

[3] V.S. Dyubkov, E.S. Masunov, Int. J. Modern Physics A, 24 (5), P. 843 (2009).

[4] V.S. Dyubkov, S.M. Polozov, "Vestnik of St. Petersburg univ.". Ser. 10: Applied math. Comp. sci. Control proc., 1, P. 135 (2011) (in Russian).

[5] C.K. Allen, T.P. Wangler, Phys. Rev. ST Accel. Beams 5, 124202 (2002).

ISBN 978-3-95450-170-0

THE USER FRIENDLY INTERFACE FOR BEAMDULAC-RFQ CODE

P.O. Larin, S.M. Polozov, National Research Nuclear University MEPhI (Moscow Engineering Physics Institute), Moscow, Russia

Abstract

The BEAMDULAC [1] beam dynamics simulation code is under development at MEPhI Department of Electrophysical Facilities since 1999. Such code includes versions for beam dynamics study in a number of accelerating structures as RFQ, DTL, APF, transport channels, ets. The motion equation for each particle is solved self-consistently in the external fields and the inter-particle Coulomb field simultaneously. The BEAMDULAC code utilizes the cloud-in-cell (CIC) method for accurate treatment of the space charge effects. The external field can be represented analytically, as a series or on the grid. The absence of user-friendly interface was the main disadvantage of the code. Last year such interface was developed and will present in the report.

INTRODUCTION

A number of codes for beam dynamics study as DYNAMION, TRACE, PARMELA, COBRA and etcetera are well known. Any one of codes has own field of use, own abilities and disabilities, a different methods for motion equation and Poisson equation solving are used.

The BEAMDULAC code is developing at Department of Electophysical Facilities of MEPhI by E.S. Masunov, N.E. Vinogradov and S.M. Polozov through 1999. This code was early designed for self-consistent beam dynamics study in RF focusing linacs as axisymmetric radio frequency focusing (ARF, [2]), ribbon radio frequency focusing (RRF, [3]) accelerators and undulator linear accelerators (UNDULAC, [4-8]). 2D and 3D versions were developed for axisymmetric structures and for ribbon beams respectively.

Later new code versions were developed to simulate the beam dynamics in RFQ or DTL linacs, transport channels [1]. Especially versions for electron linacs were designed. The beam dynamics taking into account beam loading and Coulomb field can be studied with the help of these codes [9].

But all code versions have one serious disadvantage. They are compiled as dos operation system application and have not user friendly interface. Now we start so solve such problem and the interface for BEAMDULAC-RFQ version was modified first.

BEAMDULAC CODE AND USED ALGORITHMS AND METHODS

The BEAMDULAC code utilizes the cloud-in-cell (CIC) method for accurate treatment of the own beam space charge effects that are especially important for high-intensity beams. The motion equation of each particle is solved in the external fields and the inter-particle Coulomb field simultaneously. The charge density is deposited on the grid points using the CIC technique. To determine the potential of the Coulomb field the Poisson equation is solved on the grid with periodic boundary conditions at both ends of the domain in the longitudinal direction. The aperture of the channel is represented as an ideally conducting surface of rectangular or circular cross-section. Therefore the Dirichlet boundary conditions are applied in transverse boundaries of the simulation domain. In such approach the interaction of the bunch space charge with the accelerating channel boundaries is taken into account. This allows considering of the shielding effect which is sufficiently important for transverse focusing in the narrow channel. The fast Fourier transform (FFT) algorithm is used to solve the Poisson equation on a 3D grid. The Fourier series for the space charge potential obtained can be analytically differentiated and thus each component of the Coulomb electrical field can be found as a series with known coefficients. The Coulomb defocusing force is the main factor limiting the beam current in high-intensity linacs. In our code the space charge field can be calculated with the same precision as the Coulomb potential without numerical differentiation. Time is used as an independent variable and standard fourth-order Runge-Kutta method is applied for integration of the motion equation. The external fields in BEAMDULAC code can be represented by three different methods: analytically, as a series of space harmonics (the field amplitude is representing as a polynomial coefficient series) and in a “real field” which can be defined on 2D or 3D grid by electrodynamics simulation codes or experimental measurement [10].

Especially versions of code were developed to study the ion beam dynamics with different charge to mass ratio in low energy transport systems, RF bunchers and linacs, as an example for simultaneous acceleration of positive and negative ions and beam space charge neutralization study [1, 8].

The RF field induced by the beam in the accelerating structure depends on the beam velocity as well as the current pulse shape and duration. The influence of the beam loading can reduce the external field amplitude and induce the irradiation in the wide eigen frequency modes. Therefore we should to solve the motion equations simultaneously with Maxwell’s equations for accurate simulation of beam dynamics. The method of beam loading effect treatment was developed by E.S. Masunov [11]. It provides to define eigen modes amplitude variation equations in stationary and transient cases for standing and traveling wave periodical structures. Such technique was used for BEAMDULAC-BL code version development [9].

ISBN 978-3-95450-170-0

The BEAMDULAC-RFQ code versions were developed for beam dynamics study in RFQ linacs. The linac channel parameters can be defined by two ways. The preliminary simulations could be done using synchronous phase, electrodes modulation, aperture size and ets. defined as slow functions of longitudinal coordinate into accelerator channel. The second way is to define the structure parameters period-to-period. An example of beam dynamics simulation results for 2 MeV RFQ is presented in [12].

INTERFACE AND NEW ABILITIES OF BEAMDULAC-RFQ

The developed code with graphical user interface is an improvement for BEAMDULAC-RFQ code. It is a convenient tool for handling simulation process, data visualization and constructing a simulating structure. It uses BEAMDULAC-RFQ code as a simulator engine and some own algorithms for complex structure simulation.

The main window is shown in Figure 1. The top part (it is marked as "A") contains a ribbon panel with separated tabs for adjusting initial beam parameters, simulation settings and selected structure item properties. The simulation conditions sets by "INJECTION" and "SIMULATION" tabs. The "INJECTION" tab sets initial beam parameters: ions charge, energy, separatrix size, average velocity, Twiss-parameters and particles distribution functions. The "SIMULATION" tab sets beam parameters and cloud-in-cell mesh. In addition, top panel contains an "ELEMENTS" tab arranges the content of extendable accelerator elements library for under simulation structure constructing.

One of the program abilities is a constructing of arbitrary simulating structure. Each structure item is a special library entity and can be designed independently of main program code. Each item is an accelerator element model and defines the equations of particle moving in its electromagnetic field. At the moment, there are RFQ and PMQ elements in library. The structure layout is carried out using the area marked as *"B"*. This is an RFQ section example in the picture. The panel marked as *"C"* shows the computed data during simulation runtime. This panel arranges the beam envelopes, phase portraits and channel configuration parameters. An example of beam dynamics in RFQ section simulation results is shown in Figure 1. Such section is designed as first 2 MeV section of high-power CW linac [12]. The first tab named "Envelopes" shows longitudinal dependencies of beam parameters such as emittance, transverse sizes and particles number. The second data tab named "Phase portraits" shown in Figure 2 arranges a beam phase portraits in different longitudinal direction coordinates. The channel configuration characteristics arranged by third tab named "Channel configuration". These characteristics are presented as longitudinal dependencies of synchronous velocity and aperture (Fig. 3).

CONCLUSION

The results of modern interface development for BEAMDULAC-RFQ code were presented. The new program was designed using conventional BEAMDULAC Fortran codes for simulation and visual possibilities of .NET Framework 4.5. An example of test simulation illustrates the new code abilities.

REFERENCES

[1] S.M. Polozov. Problems of Atomic Science and Technology. Series: Nuclear Physics Investigations, 3 (79), 2012, pp. 131-136.

[2] E.S. Masunov, N.E. Vinogradov. Phys. Rev. ST Accel. Beams, 2001, No 7, 070101.

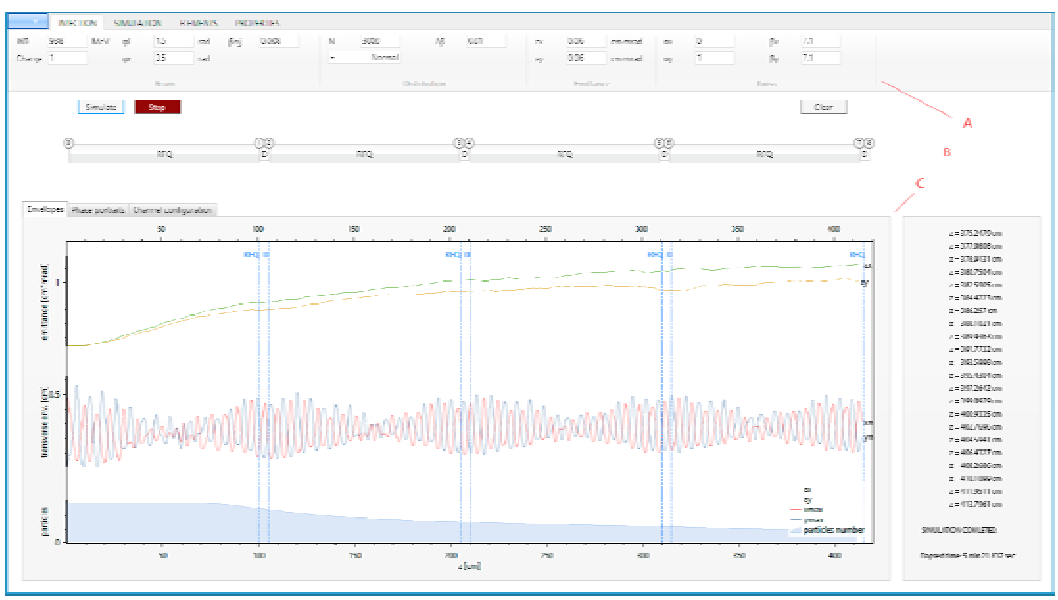

Figure 1: Main window of the new BEAMDULAC-RFQ code interface.

ISBN 978-3-95450-170-0

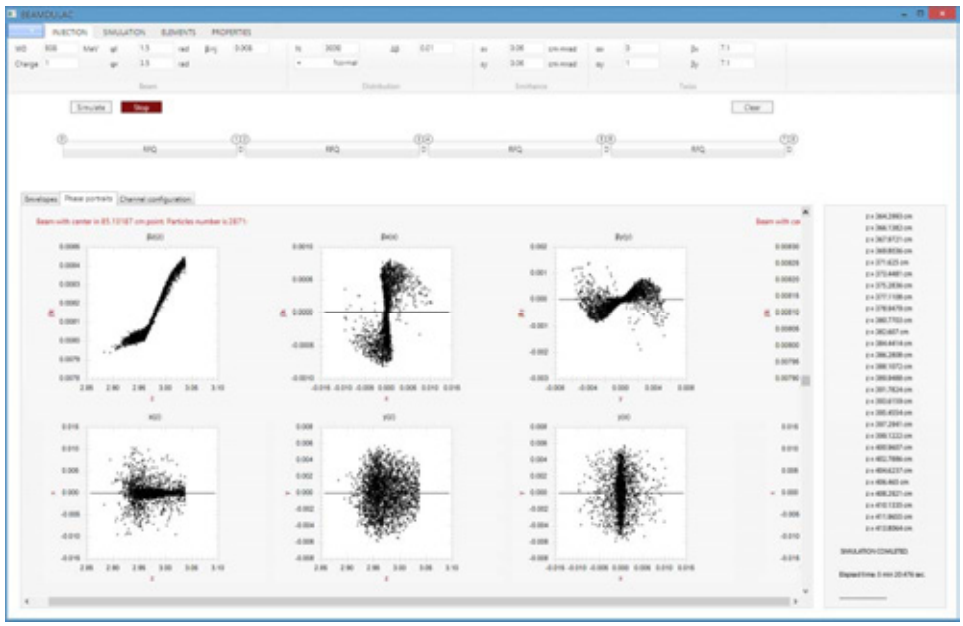

Figure 2: Main window: phase portraits.

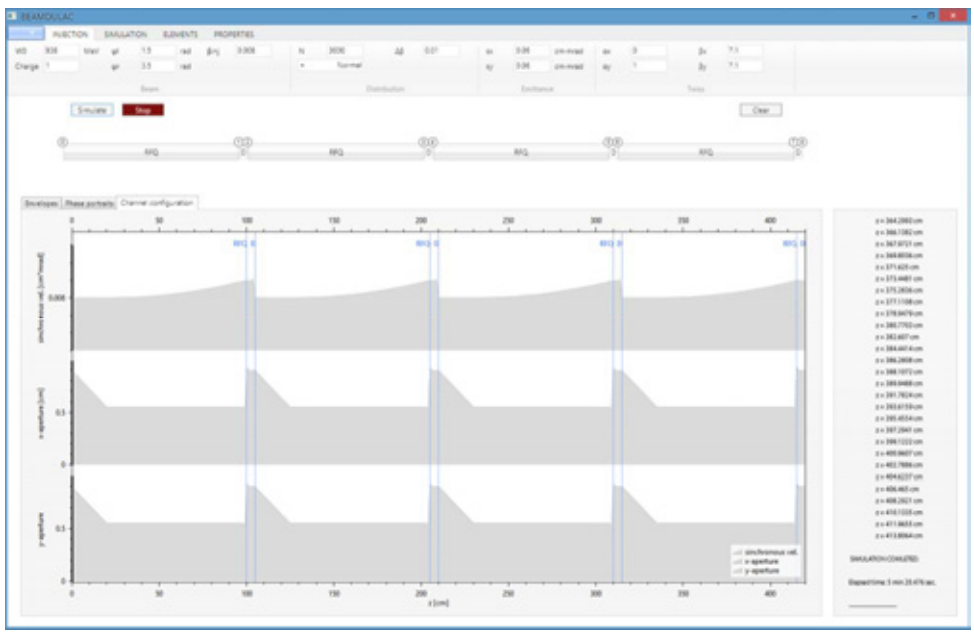

Figure 3: Main window: structure configuration.

[3] E.S. Masunov, S.M. Polozov, N.E. Vinogradov. Problems of atomic science and technology. Series "Nuclear Physics Investigations", 5 (39), 2001, pp. 71 – 73.
[4] E.S. Masunov, S. M. Polozov, A.S. Roshal. Radiation Physics and Chemistry, 2001, v. 61, pp. 491-493.
[5] E.S. Masunov, S. M. Polozov. Problems of atomic science and technology. Series "Nuclear Physics Investigations", 2 (43), 2004, pp. 141-143.
[6] E.S. Masunov, S.M. Polozov. NIM A, 558. 2006, p. 184–187.
[7] E.S. Masunov, S.M. Polozov. Phys. Rev. ST AB (11), 2008, 074201.
[8] E.S. Masunov, S.M. Polozov. Problems of atomic science and technology. Series "Nuclear Physics Investigations", 5 (50), 2008, pp.136-139.
[9] T.V. Bondarenko, E.S. Masunov, S.M. Polozov. Problems of Atomic Science and Technology. Series: Nuclear Physics Investigations, 6 (88), 2013, pp. 114-118.
[10] E.S. Masunov, S.M. Polozov. Problems of Atomic Science and Technology. Series Nuclear Physics Investigations, 3 (47). 2006, pp. 119-121.
[11] E.S. Masunov, V.I. Rashchikov. Accelerators, Atomizdat, Issue 17, 1977, p. 96 (in Russian).
[12] A.Y. Aksentyev, S.M. Polozov, T.V. Kulevoy. Proc. of IPAC'14, 2014, pp. 3286-3288.

ISBN 978-3-95450-170-0

THE INTERACTIVE COMPUTER ENVIRONMENT FOR DESIGNING AND TUNING OF CHARGED PARTICLE BEAMS TRANSPORT CHANNELS

G.P. Averyanov[1], Yu. A. Bashmakov[1,2], V.A. Budkin[1], V.V. Dmitrieva[1], I.O. Osadchuk[1]
[1]National Research Nuclear University «MEPhI», Moscow, Russia
[2]P.N. Lebedev Physical Institute of RAS, Moscow, Russia

Abstract

This paper considers the application package that simulates transport channel of relativistic charged particles. The package provides an interactive mode for the user. It is possible to observe the main parameters of the beam crossing the channel on the PC screen such as envelope and cross-section of the beam at different sections of the channel while changing the main control parameters of the real channel. Enabling of procedures of mathematical programming provides express optimization of control parameters of the channel. The designed package is compact, has a modular structure and can be easily adapted to different software platforms. MATLAB integrated environment is used as instrumental environment, which has a freeware version of this system - SCILAB. Package testing was carried out on the electron synchrotron “Pakhra” during the recalibration of the channel of the accelerator working in different modes, which are determined by conducted experiments.

INTRODUCTION

A simulation model of the channel is created on the basis a MATLAB environment and its open-source counterpart SCILAB. One of the main advantages of these software environments is the programming efficiency of matrix operations, which are the basic mathematical tools for calculating the magneto-optical systems. In this environment is developed KATRAN representing an integrated modular open structure, adaptable to the calculation of a specific transportation channel of relativistic charged particles [2].

KATRAN STATE DIAGRAM

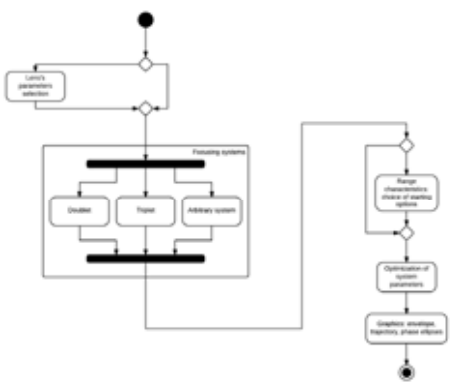

Figure 1: KATRAN state diagram.

The complete cycle of study of the properties and the calculation of the focusing system begins with the selection of the quadrupole lens. Preliminary review of its envelop characteristics will allow in further calculations to select working variant the system parameters. In general, this process is iterative by nature. You must select a variant of the system fully provide the required launch parameters, using perhaps more "weak" lenses. Module KATRAN named "Range characteristics" allows consider depending focal lengths of the system (the lens, doublet, triplet, etc.) one by one. Building a envelop characteristics provides a visual representation of the degree of influence of the individual parameters of the system on its focusing properties. Figure 2 shows, as an example, the dependence of the focal length of the triplet from the first lens's magnetic field with a parameter - the distance between the first and second lenses. As can be seen from the figure, the focus of the charged particles at the same time in the two transverse planes (vertical and horizontal) is possible in a limited range of parameters of quadrupole lenses and system as a whole (the focal lengths in both planes have positive values).

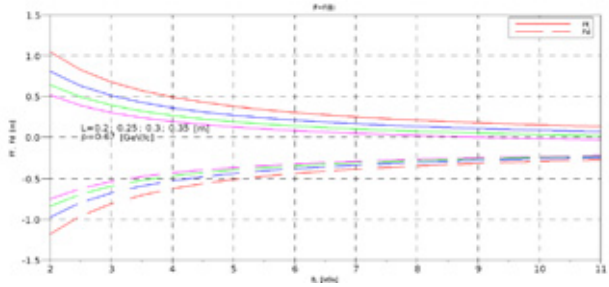

Figure 2: Dependency of focal lengths of the triplet from magnetic field of the first lens with a parameter - the distance between the first and second lenses.

KATRAN allows us to consider these characteristics of the various focusing systems. When considering the envelop characteristics of focusing systems and calculation of parameters of the transport channel numerical methods used for finding optimal solutions (search simplex method).

In general, the objective function Ft, used for the calculation of the magneto-optical system can be written as

$$\mathrm{Ft} = \sqrt{\sum_n a_i((\phi_i(\bar{x}) - x_i^c)/x_i^{norm})^2}\,. \qquad (1)$$

ISBN 978-3-95450-170-0

where $\phi_i(\bar{x})$ - current value of the parameter, x_i^c - target value of the parameter, x_i^{norm} - normalization coefficient of the parameter, a_i- weighting coefficient of the parameter, $\bar{x}$ - vector of search parameters space.

Normalization coefficient x_i^{norm} is chosen so that the value of objective function component of this parameter was close to unity and become dimensionless. This operation is scaling of the objective function, i.e. the contribution of all components in the objective function to get about the same. Weighting factor of x_i^c parameter reflects the priorities of achievements of goal parameters of one or another component of the objective function.

Graphical tools of MATLAB (or SCILAB) allow us to show the focusing properties of the transportation channel in the form of the trajectories of individual particles, beam envelopes and phase portraits of the beam in the horizontal and vertical planes. This information is sufficient for operative channel setup to the new operating mode.

SIMULATION BY KATRAN

As an example, was considered by the transport channel of existing synchrotron “Pakhra” [1].

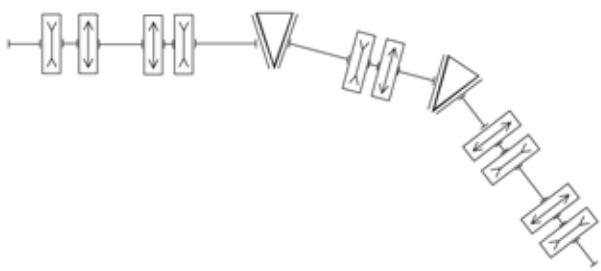

Figure 3: Scheme of transportation channel of “Pakhra” synchrotron.

Figures 4 and 5 show the graphic results of the calculation of the current channel KATRAN transportation in “Pakhra” synchrotron.

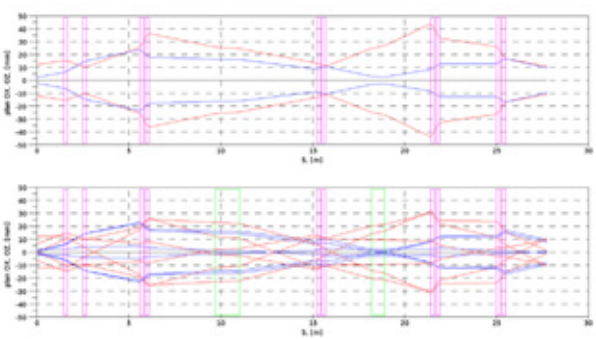

Figure 4: Envelopes (upper figure) and particle trajectories (lower figure) of existing transport channel of “Pakhra” synchrotron.

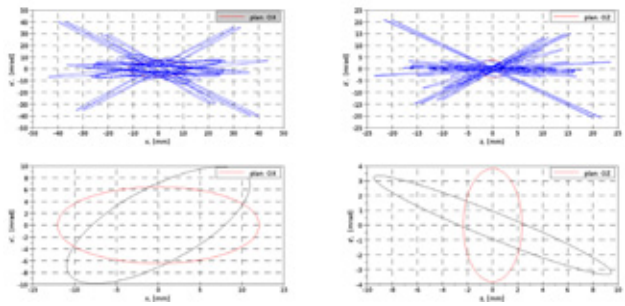

Figure 5: Upper figure - phase portraits of the beam after passing each element of the transport channel in the horizontal and vertical planes, bottom figure - phase portraits of the beam at the input (red line) and output (black line) transport channel in existing transport channel of “Pakhra” synchrotron.

Figures 6-9 presents options for optimizing the transport channel of “Pakhra” synchrotron.

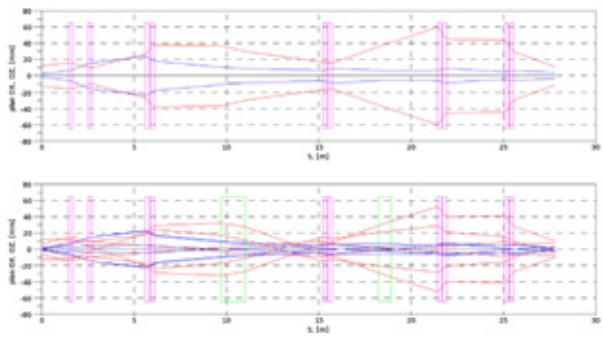

Figure 6: Envelopes (upper figure) and particle trajectories (lower figure) of existing transport channel of “Pakhra” synchrotron.

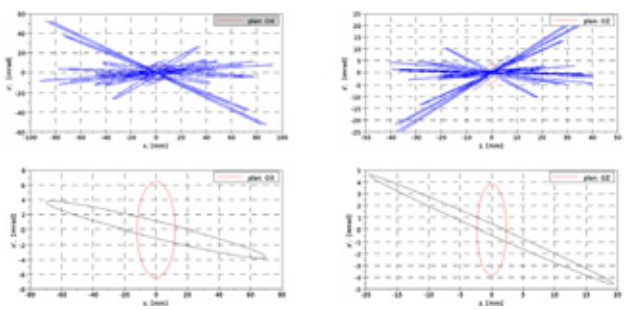

Figure 7: Upper figure - phase portraits of the beam after passing each element of the transport channel in the horizontal and vertical planes, bottom figure - phase portraits of the beam at the input (red line) and output (black line) transport channel in existing transport channel of “Pakhra” synchrotron.

ISBN 978-3-95450-170-0

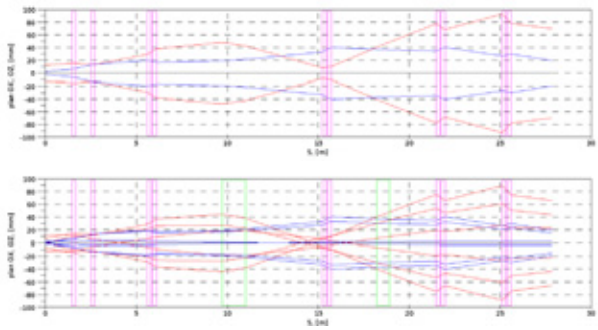

Figure 8: Envelopes (upper figure) and particle trajectories (lower figure) of existing transport channel of "Pakhra" synchrotron.

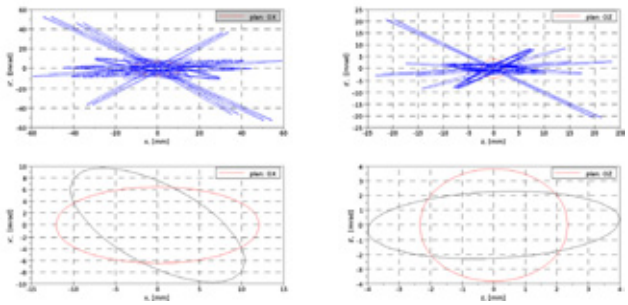

Figure 9: Upper figure - phase portraits of the beam after passing each element of the transport channel in the horizontal and vertical planes, bottom figure - phase portraits of the beam at the input (red line) and output (black line) transport channel in existing transport channel of "Pakhra" synchrotron.

The main problem of the transport channel of "Pakhra" accelerator is large particle loss during the passage of the transport channel. Increasing the size of the beam occurs due to the influence of the magnetic field (~ 4 kG) accelerator magnets and Coulomb scattering of electrons by dural plate output window of the accelerator and in the air [1]. At the inlet of the transportation channel the beam has an elliptical cross section. The semimajor axis of the ellipse is 12 cm, and a small is 4 cm. Diameter of the transportation channel is 40 mm. Small diameter leads to a significant loss of beam intensity already at the inlet of transportation channel. As can be seen, in a number of elements of the channel cross-sectional dimensions of the beam is larger than the diameter of the transportation channel. This is due not only to the large linear dimensions of the beam in the transverse plane, but with large divergence angles of the particles (6.45 mrad and 3.82 mrad) in the horizontal and vertical planes. In this regard, the current transportation channel includes two collimators that limit the size of the beam. Attempts to improve the beam parameters have shown that the optimal parameter search of the channel by changing the parameters of the field focusing elements, and their arrangement along the length of the channel leading to a change in the dynamics of the particles but do not solve the problem of the loss of particles along the channel length. This is largely due to the formulation of the problem: it is necessary to fit into the geometric dimensions of the room and only use existing lens, doublets and bending magnets.

KATRAN allows us to consider the structure of transportation channel with individual focusing systems (doublets, triplets, ect) and with the whole channel either. Necessary parameters of the particle beam is provided by specifying the respective values of the elements of the transformation matrix in the horizontal and vertical planes. To find the values of the elements of transformation matrix extreme search methods are used. The dimension of the search area is determined by the number of elements of the channel and the number of their geometry and field parameters. In our calculations the search for optimal parameters of the focusing system was considered by varying from 10 to 15 parameters.

When choosing a transportation channel focusing system, there are two main problems: providing the required size of the beam at the output of the channel and the channel transparency. The first problem is solved by using of extreme search methods, in which the objective function is based on the transformation matrix of the beam. The second problem is related to the construction of the phase space acceptance of the the channel, which is constructed on the basis of transformation matrices of individual elements of the channel in its exit plane. Transformation of the output acceptance to the input plane of transportation channel allows to evaluate the consistency of the beam parameters at the exit of the accelerator with the possibility of passing without loss along the entire length of the channel.

FINAL REMARKS

The calculations show that to improve the conductivity of the beam is necessary to build a transport channel at a more short focusing lenses. This will reduce the length of the intervals between, making the main contribution to the increase in the transverse dimensions of the beam. Due to specified size of the room, the number of lenses must be increased.

REFERENCES

[1] V.I. Alekseev, V.A. Karpov, V.V. Kim, S.V. Mishin, V.I. Sergienko, V.A. Hablo, "Sistema diagnostiki vyvedennogo jelektronnogo puchka na uskoritele "Pakhra". FIAN, Moscow, 2000. (in Russian)

[2] G.P. Averyanjv, Yu.A. Bashmakov. V.A. Budkin, V.V. Dmitrieva, I.O. Osadchuk. Transportation channels calculation method in MATLAB. Problems of atomic science and technology (PAST), 2014, №3.

ISBN 978-3-95450-170-0

MATHEMATICAL OPTIMIZATION MODEL OF LONGITUDINAL BEAM DYNAMICS IN KLYSTRON-TYPE BUNCHER*

I.D. Rubtsova#, SPbSU, Saint-Petersburg, Russia

Abstract

The paper presents recurrent integral-differential beam evolution model. This model is convenient for mathematical description of specific dynamic processes with due account of particle interaction and electric fields excitation by moving beam. On the basis of this model the problem of beam dynamics optimization is formalized as trajectory ensemble control problem. Analytical expression for quality functional gradient is obtained. Theoretical results are applied for solving problem of beam dynamics optimization in klystron-type buncher.

RECURRENT INTEGRAL-DIFFERENTIAL BEAM EVOLUTION MODEL

Let us consider beam dynamics description by recurrent system of integral-differential equations. Finite iteration process is introduced. At every iteration beam evolution is described by the equations of the following form:

$$\frac{d\mathbf{x}^{(k)}}{d\tau} = \mathbf{f}^{(k)}\left(\tau,\mathbf{x}^{(k)},\mathbf{u},\mathbf{H}^{(k-1)}(\mathbf{u})\right) = \mathbf{f}_1\left(\tau,\mathbf{x}^{(k)},\mathbf{u},\mathbf{H}^{(k-1)}(\mathbf{u})\right) + \int\limits_{M_{\tau,\mathbf{u}}^{(k)}} \mathbf{f}_2\left(\tau,\mathbf{x}^{(k)},\mathbf{y}_\tau^{(k)}\right)\rho^{(k)}\left(\tau,\mathbf{y}_\tau^{(k)}\right)d\mathbf{y}_\tau^{(k)}, \quad (1)$$

$$\frac{\partial\rho^{(k)}}{\partial\tau} + \frac{\partial\rho^{(k)}}{\partial\mathbf{x}^{(k)}}\mathbf{f}^{(k)}\left(\tau,\mathbf{x}^{(k)},\mathbf{u},\mathbf{H}^{(k-1)}(\mathbf{u})\right) + \rho^{(k)} div_{\mathbf{x}}\mathbf{f}^{(k)}\left(\tau,\mathbf{x}^{(k)},\mathbf{u},\mathbf{H}^{(k-1)}(\mathbf{u})\right) = 0 \quad (2)$$

with initial conditions

$$\mathbf{x}^{(k)}(0) = \mathbf{x}_0 \in M_0,\ \rho^{(k)}(0,\mathbf{x}) = \rho_0(\mathbf{x}). \quad (3)$$

Here $\tau \in [0,T]$ is independent variable; T is fixed; k is iteration number $(1 \le k \le K)$; $\mathbf{x}^{(k)}$ (or $\mathbf{y}^{(k)}$) is n-vector of phase coordinates; $\mathbf{u}(\tau)$ is r-vector of control; $\mathbf{f}_1\left(\tau,\mathbf{x}^{(k)},\mathbf{u},\mathbf{H}^{(k-1)}(\mathbf{u})\right)$ and $\mathbf{f}_2\left(\tau,\mathbf{x}^{(k)},\mathbf{y}^{(k)}\right)$ are n-vector functions; $\mathbf{H}^{(k-1)}(\mathbf{u})$ is the matrix containing the values $H_{sj}^{(k-1)}(\mathbf{u})$, $s=\overline{1,S}$, $j=\overline{J_1,J_2}$ of functionals defined on beam trajectories at previous iteration; $\rho^{(k)}\left(\tau,\mathbf{x}^{(k)}\right)$ is phase density corresponding to dynamic system (1); $M_{\tau,\mathbf{u}}^{(k)} = \left\{\mathbf{x}_\tau^{(k)} = \mathbf{x}^{(k)}\left(\tau,\mathbf{x}_0,\mathbf{u}\right) : \mathbf{x}_0 \in M_0\right\}$, M_0 is open bounded initial phase domain; $\rho_0(\mathbf{x})$ is initial phase density; it is supposed $\int\limits_{M_0}\rho_0(\mathbf{x}_0)d\mathbf{x}_0 = 1$.

The components of every matrix $\mathbf{H}^{(l)}$, $l=\overline{1,K}$ are the values of functionals

$$H_{sj}^{(l)}(\mathbf{u}) = \int\limits_0^T \int\limits_{M_{\tau,\mathbf{u}}^{(l)}} C_{sj}(\tau,\mathbf{x}_\tau^{(l)},\bar{\mathbf{x}}^{(l)}(\tau),\mathbf{u})\rho^{(l)}\left(\tau,\mathbf{x}_\tau^{(l)}\right)d\mathbf{x}_\tau^{(l)}d\tau, \quad (4)$$

$s=\overline{1,S}$, $j=\overline{J_1,J_2}$; here $\bar{\mathbf{x}}^{(l)}(\tau) = \int\limits_{M_{\tau,\mathbf{u}}^{(l)}} \mathbf{x}_\tau^{(l)}\rho\left(\tau,\mathbf{x}_\tau^{(l)}\right)d\mathbf{x}_\tau^{(l)}$ is average phase vector at l-th iteration. Note that $\mathbf{H}^{(0)} = \mathbf{0}$.

The resulting beam evolution is to be achieved at the last iteration number K.

Beam evolution model suggested is based on formalization and generalization of iterative method of beam dynamics simulation in floating-drift klystron with due account of Coulomb repulsion and RF fields excitation in resonators. According to this method excited fields are represented via induced current Fourier decomposition [1]. Vector-function $\mathbf{f}_1\left(\tau,\mathbf{x}^{(k)},\mathbf{u},\mathbf{H}^{(k-1)}(\mathbf{u})\right)$ is determined by the method of RF fields description. Functional values (4) represent induced current Fourier harmonics in resonators (excluding modulator) and are used to express excited fields at next $(l+1)$-th iteration and thus to determine vector-function $\mathbf{f}_1\left(\tau,\mathbf{x}^{(l+1)},\mathbf{u},\mathbf{H}^{(l)}(\mathbf{u})\right)$ in dynamics equation (1). Vector function $\mathbf{f}_2\left(\tau,\mathbf{x},\mathbf{y}\right)$ is defined by particle interaction accounting (in view of space-charge forces representation given in [2]).

It should be noted that model (1)-(4) may be convenient for wide class of beam evolution iterative descriptions with due account of beam dynamics dependence on the functionals defined on beam trajectories at previous iteration. These functionals approximate the fields generated by moving beam itself.

Beam evolution modeling with due account of the fields mentioned (in particular, Coulomb forces) may be performed in different ways [2-14]. Analytical representation of these fields allows to formalize beam dynamics optimization problem and to obtain quality criterion gradient analytical expression [2,11,12].

OPTIMIZATION PROBLEM

Let us introduce quality criterion of the dynamic process (1)-(4) as a function of functionals defined on beam trajectories at finite iteration:

*Work supported by St. Petersburg State University, grant 9.38.673.2013
#rubtsova05@mail.ru

ISBN 978-3-95450-170-0

$$\Gamma(\mathbf{u}) = F\left(\Gamma_1(\mathbf{u}), \Gamma_2(\mathbf{u}), \ldots, \Gamma_N(\mathbf{u})\right), \quad (5)$$

$$\Gamma_i(\mathbf{u}) = \int_0^T \int_{M^{(K)}_{\tau,\mathbf{u}}} \Phi_i\left(\tau, \mathbf{x}^{(K)}, \mathbf{u}, \mathbf{A}_i(\mathbf{u})\right) \rho^{(K)}\left(\tau, \mathbf{x}^{(K)}_\tau\right) d\mathbf{x}^{(K)}_\tau d\tau, \quad (6)$$

$i = \overline{1,N}$. Here $F(\Gamma_1, \ldots \Gamma_N)$, $\Phi_i(\tau, \mathbf{x}, \mathbf{u}, \mathbf{A}_i)$, $i = \overline{1,N}$ are smooth functions; $\mathbf{A}_i(\mathbf{u})$, $i = \overline{1,N}$ are M-vectors of values of integral functionals

$$A_{im}(\mathbf{u}) = \int_0^T \int_{M^{(K)}_{\tau,\mathbf{u}}} V_{im}\left(\tau, \mathbf{x}^{(K)}, \mathbf{u}\right) \rho^{(K)}\left(\tau, \mathbf{x}^{(K)}_\tau\right) d\mathbf{x}^{(K)}_\tau d\tau, \quad (7)$$

$i = \overline{1,N}$, $m = \overline{1,M}$, with smooth integrands. The expressions (7) may be interpreted as particle characteristics averaged over the device spatial cross-sections (when τ is the time or its analogue).

So beam dynamics optimization problem is reduced to hill-climbing problem with objective functional (5)-(6). This problem is investigated on the basis of mathematical methods suggested by D.A. Ovsyannikov and widely used for treatment different beam dynamics optimization problems [2,3,7,11,12]. Analytical expression of criterion functional (5)-(6) variation is derived in terms of auxiliary functions satisfying the special equations on dynamic system trajectories. This expression allows to obtain objective functional gradient and to apply directed optimization methods. The results obtained may be used for beam dynamics optimization in different structures.

BEAM DYNAMICS IN BUNCHER: MODELING AND OPTIMIZATION

Model (1)-(4) is used for beam evolution description in klystron buncher. In this case independent variable is $\tau = ct$, where c is the velocity of light, t is the time; $[0, T]$ is independent variable segment sufficiently large for any particle to pass the structure; $n = 2$; $\mathbf{x}^{(k)} = (x_1^{(k)}, x_2^{(k)}) = (z^{(k)}, p^{(k)})$, where z is longitudinal coordinate, p is reduced impulse of electron. RF fields in resonators (except modulator) are simulated on the basis of induced current first harmonics [1, 11];

$$f_{1,1}(\mathbf{x}) = x_2 \Big/ \sqrt{1 + x_2^2}\ ;\ S = 2,\ J_1 = 2,\ J_2 = J\ ;$$

$$f_{1,2}(\tau, \mathbf{x}, \mathbf{u}, \mathbf{H}) = -\frac{e}{m_0 c^2}\left[\frac{U_1}{d_1}\widetilde{E}_1(x_1 - \xi_1)\sin(2\pi\tau/\lambda + \Phi_1) + \right.$$
$$\left. + \sum_{s=1}^{2}\sum_{j=2}^{J} B_{sj}(\tau, \mathbf{x}, \mathbf{u}) H_{sj}\right];$$

$$B_{sj}(\tau, \mathbf{x}, \mathbf{u}) = \rho_j Q_j / d_j\, \widetilde{E}_j(x_1 - \xi_j)\cos\theta_j \eta_s(2\pi\tau/\lambda + \theta_j),$$

$$C_{sj}(\tau, \mathbf{x}, \bar{\mathbf{x}}, \mathbf{u}) = \frac{2I}{d_j}\frac{x_2}{\sqrt{1 + x_2^2}}\widetilde{E}_j(x_1 - \xi_j) \times$$
$$\times \Pi_\varepsilon\left(\bar{x}_1 - \xi_j, 0.5\lambda\bar{x}_2 \Big/ \sqrt{1 + \bar{x}_2^2}\right)\eta_s(2\pi\tau/\lambda),$$
$$s = \overline{1,2},\ j = \overline{2,J};$$
$$\eta_1(\xi) = \cos(\xi)\ ;\ \eta_2(\xi) = \sin(\xi)\ .$$

Here J is total number of resonators; e is absolute value of electron charge; m_0 is electron rest-mass; λ is RF field wavelength; U_1 and Φ_1 are prescribed amplitude and initial phase of RF field voltage in first resonator (modulator); j is resonator number; ρ_j and Q_j are wave resistance and Q-factor; d_j is electrical gap length; ξ_j is resonator center coordinate; smooth bell-shaped function $\widetilde{E}_j(\eta)$ presents electric field intensity distribution along the gap axis; θ_j is the mismatch angle; $\theta_j = arctg(2Q_j\,\Delta f_j / f_0)$; $\Delta f_j / f_0$ is resonator mismatch with respect to basic frequency $f_0 = c/\lambda$; $\Pi_\varepsilon(\xi, h)$ is smooth approximation of the step function $\Pi(\xi, h) = U(\xi + h)U(h - \xi)$, where $U(\eta)$ is Heaviside function; $\mathbf{u}$ is the vector of control parameters: $\mathbf{u} = (\Delta f_2 / f_0, \ldots, \Delta f_J / f_0, \xi_2, \ldots, \xi_J, \xi_{ex})$, where ξ_{ex} is device exit coordinate; I is average beam current.

Electron beam is considered to have constant radius R and to move inside the conducting channel of radius a. Model particles are supposed to be disks-clouds (cylinders) with radius R and thickness 2Δ. To describe Coulomb forces we use the analytical expression for electric field intensity [6]. Thus,

$$f_{2,1} = 0\ ;\ \ f_{2,2}(\tau, \mathbf{x}, \mathbf{y}) = \frac{e}{m_0 c^2}\frac{I\lambda a^2}{2\pi\varepsilon_0 c\Delta^2 R^2} \times$$
$$\times \sum_{m=1}^{\infty}\frac{J_1^2(\mu_m R/a)}{\mu_m^4 J_1^2(\mu_m)} G_m\left(\sqrt{1 + y_2^2}(x_1 - y_1)\right);$$
$$G_m(\eta) = \left[2g_m(\eta) - g_m(\eta + 2\Delta) - g_m(\eta - 2\Delta)\right];$$
$$g_m(\eta) = sign(\eta)\left(1 - e^{-\mu_m|\eta|/a}\right),$$

where ε_0 is electric constant; $J_l(\eta)$ is Bessel function of the l-th order; $\mu_m, m = 1,2,\ldots$ are the roots of Bessel function $J_0(\eta)$.

It should be mentioned, that numerical experiments confirm the iteration process convergence. The criterion of iteration process completion is the coincidence (with necessary accuracy) of the corresponding values of functionals (4) on two successive iterations.

Mathematical optimization method presented above is applied for solving problem of bunching efficiency maximization. Quality criterion K_B is defined as the proportion of particles getting required phase domain at buncher exit: $|\varphi - \overline{\varphi}| \le \Delta\varphi$, $|W - \overline{W}| \le bW_0$. Here φ and

ISBN 978-3-95450-170-0

W are correspondingly the phase and kinetic energy of particle at device exit, $\overline{\varphi}$ and $\overline{W}$ are mean values of the quantities mentioned; $\Delta\varphi$ and b are given constants; W_0 is initial energy of particles. This criterion is approximated by the functional of the form (6), where

$$\Phi(\tau, \mathbf{x}, \mathbf{u}, \mathbf{A}) =$$

$$= \Pi_\varepsilon\left(\frac{2\pi\tau}{\lambda} - A_1, \Delta\varphi\right)\Pi_\varepsilon\left(\sqrt{1+x_2^2} - A_2, b\gamma_0\right)S_\varepsilon(x_1 - \xi_{ex}),$$

$$S_\varepsilon(\xi) = \frac{1}{2\varepsilon}\begin{cases}\cos(\pi\xi/\varepsilon)+1, & |\xi| < \varepsilon \\ 0, & |\xi| \geq \varepsilon\end{cases},$$

$A_i(\mathbf{u})$ are the functionals of the form (7) introduced to approximate average values of phase and energy at buncher exit; ε is sufficiently small constant to provide required approximation accuracy. Quality functional gradient with respect to parameters (mismatches and positions of resonators) is obtained.

Gradient optimization of device parameters is performed for klystron buncher with following main characteristics: $W_0 = 500\,\text{keV}$; $I = 10\,\text{A}$; $a = 0.006\,\text{m}$; $R = 0.003\,\text{m}$; $\lambda = 0.125\,\text{m}$; input power $P_{ent} = 1\,\text{kVt}$. The device contains four resonators with electric gap length 0.027 m. The required phase and energy intervals at buncher exit are as follows: $|\varphi - \overline{\varphi}| \leq 2\pi/9$, $|W - \overline{W}| \leq 0.1W_0$. After the optimization bunching efficiency K_B increased from 0.34 until 0.67.

The numerical experiments performed confirm the efficiency of developed mathematical methods of beam dynamics modeling and optimization. It should be noted, that these methods may be successfully applied for investigation of longitudinal and transverse beam dynamics in klystron-type buncher.

REFERENCES

[1] B.P. Murin, A.P. Durkin, O.Ju. Shlygin, "Relativistic Electron Beams Bunching in Microwave Generator of Quasi-continuous Action", in collection of papers: Theory and Techniques of Relativistic Microwave Generators, 1988, Moscow, Radio Engineering Institute, pp.76-83.

[2] D.A. Ovsyannikov, Modeling and Optimization of Charged Particle Beam Dynamics. (Leningrad: Leningrad State University, 1990), 312.

[3] D.A. Ovsyannikov, "Mathematical Modeling and Optimization of Beam Dynamics in Accelerators", RuPAC'12, St. Petersburg, Russia, September 2012, pp. 68-72 (2012); http://www.JACoW.org

[4] D.A. Ovsyannikov, N.S. Edamenko, "Modeling of Charged Particle Beam Dynamics", Vestnik St. Petersburg University, Ser. 10: Applied Mathematics, Informatics, Control Processes, 2013, No 2, pp. 61-66.

[5] D.A. Ovsyannikov, A.D. Ovsyannikov, I.V. Antropov, V.A. Kozynchenko, "BDO-RFQ Code and Optimization Models," 2005 International Conference on Physics and Control (PhysCon 2005), Proceedings, Art. No 1513994, pp. 282-288 (2005).

[6] D.A. Ovsyannikov, I.D. Rubtsova, V.A. Kozynchenko, Some Problems of Intense Charged Particle Beams Modeling in Linear Accelerators, (SPb: VVM publishing, 2013), 144.

[7] A.D. Ovsyannikov, D.A. Ovsyannikov, A.P. Durkin, S.-L. Chang, "Optimization of Matching Section of an Accelerator with a Spatially Uniform Quadrupole Focusing", Technical Physics, The Russian Journal of Applied Physics, 2009, Vol. 54, No 11, pp. 1663-1666.

[8] B. Bondarev, A. Durkin, Y. Ivanov, I. Shumakov, S. Vinogradov, A. Ovsyannikov, D. Ovsyannikov, "The LIDOS.RFQ.DESIGNER Development", Proceedings of the IEEE Particle Accelerator Conference 2001, Chicago, IL, 2001, pp. 2947-2949 (2001).

[9] O.I. Drivotin, D.A. Ovsyannikov, "Modeling of Self-consistent Distributions for Longitudinally Non-uniform Beam", Nuclear Instruments and Methods in Physics Research, Section A: Accelerators, Spectrometers, Detectors and Associated Equipment, 2006, Vol. 558, No 1, pp 112-118.

[10] O.I. Drivotin, D.A. Ovsyannikov, "Self-consistent Distributions for Charged Particle Beam in Magnetic Field", International Journal of Modern Physics, Section A, 2009, Vol.24, No 5, pp. 816-842.

[11] I.V. Olemskoy, I.D. Rubtsova, "Modeling and Optimization of Beam Dynamics in Resonance Bunching and Decelerating Systems", First International Workshop: Beam Dynamics & Optimization, St. Petersburg, Russia, 1994, pp. 143-153 (1995).

[12] I.D. Rubtsova, E.N. Suddenko, "Investigation of Program and Perturbed Motions of Particles in Linear Accelerator", RuPAC'12, St. Petersburg, Russia, September 2012, pp. 367-369 (2012); http://www.JACoW.org

[13] I.D. Rubtsova, "On Quasiperiodic Beam of Interacting Particles Dynamics Modeling", Vestnik St. Petersburg University, Ser. 10: Applied Mathematics, Informatics, Control Processes, 2014, No 1, pp. 104-119.

[14] I.D. Rubtsova, "Integral-differential Model of Quasi-periodic Beam Longitudinal Dynamics", Beam Dynamics & Optimization (BDO), 2014 20th International Workshop, June-July 2014, St. Petersburg, Russia, Proceedings, IEEE, p. 144 (2014).

ISBN 978-3-95450-170-0

SECOND ORDER METHOD FOR BEAM DYNAMICS OPTIMIZATION *

O.I. Drivotin, D.A. Starikov, St. Petersburg State University, St. Petersburg, Russia

Mathematical methods of beam dynamics optimization was developed in the works of D.A. Ovsyannikov (see [1]). These methods are based on numerical calculation of the first derivatives on accelerator structure parameters of functional estimating quality of a beam. They allow to find accelerator structures with satisfactory parameters and also to improve existing structures. The present paper is devoted to new method based on numerical calculation of the second derivatives of the functional. This method can be considered as an extension of the methods of first order.

BEAM DYNAMICS CONTROL PROBLEM

Consider a beam describing by the particle distribution density $\varrho(x)$ in the phase space Ω, $x \in \Omega$. Let at the initial moment t_0 the particle distribution density [2] is given on some p-dimensional surface $S : \varrho(t_0, x) = \varrho_{(0)}(x) = \varrho_{(0)\,1\ldots p}(x)\, dx^1 \wedge \ldots \wedge dx^p$, $p \le \dim \Omega$, where x^i, $i = \overline{1,p}$, are coordinates on S_0 which can be taken also as some of coordinates in the phase space.

Assume that the particle trajectories are described by the differential equation

$$\frac{dx}{dt} = f(t, x, u),$$

where t is trajectory parameter, $t \in [t_0, T]$, u is control function, $u(t) \in U \subset R^r$. Assume that vector f is defined in a domain $[t_0, T] \times \Omega \times U$, and that the solution of the Cauchy problem for this equation with initial condition $x(t_0) = x_0$ uniquely exists for any x_0 under consideration.

Let introduce functional characterizing quality of the controlled process

$$\Phi(u) = \int\limits_{\Omega} g(x_T)\varrho(T, x_T), \qquad (1)$$

where $g(x)$ is a piecewice continuous function, and integral on Ω means in fact integration over image of initial surface S_0 of corresponding differential form satisfying to the Vlasov equation [2]. The problem of minimizing of functional (1) on control function u from U is called the terminal problem of beam control with account of particle distribution density.

METHOD FORMULATION

Equation for the first variation of x has the form

$$\frac{d\delta x^i}{dt} = \frac{\partial f^i}{dx^j}\delta x^j + \delta_u f^i, \qquad \delta x^i(t_0) = 0, \qquad (1)$$

where

$$\delta_u f^j = \frac{\partial f^j}{\partial u^k}\delta u^k$$

(summation is meant on coincident indices). The solution of the problem (1) can be written as

$$\delta x^i(t) = \int\limits_{t_0}^{t} G^i_j(t, t')\delta_u f^j(t')dt',$$

where $G(t, t')$ is the Green matrix of the system (1), satisfying to the equation

$$\frac{dG^i_j(t, t')}{dt} = \frac{\partial f^i}{\partial x^k}G^k_j(t, t'),$$

and to the condition $G(t, t) = E$, where E is identity matrix.

Then variation of the functional (1) can be written in the form

$$\delta_u \Phi = \int\limits_{t_0}^{T}\int\limits_{\Omega} \frac{\partial g}{\partial x}G(T, t')\delta_u f(t, x)\varrho(t, x)\, dt. \qquad (1)$$

Let introduce the differential form

$$\psi(t, x) = -\frac{\partial g}{\partial x}|_{x=x_T}G(T, t),$$

satisfying to equation and condition

$$\frac{d\psi}{dt} = -\psi\frac{\partial f}{\partial x}, \qquad \psi(T) = -\frac{\partial g}{\partial x}|_{x=x_T}.$$

Then the functional variation (1) takes the form

$$\delta_u \Phi = -\int\limits_{t_0}^{T}\int\limits_{\Omega} \psi(t, x)\delta_u f(t, x)\varrho(t, x)\, dt.$$

Assume that u is a piecewise constant vector function

$$u = u_i, \quad t \in [t_{i-1}, t_i), \quad i = \overline{1, M}, \quad t_M = T.$$

Then fuctional (1) can be considered as function of rM control parameters. The derivatives on these parameters are

$$\frac{\partial \Phi}{\partial u^k_i} = -\int\limits_{t_0}^{T}\int\limits_{\Omega} \psi(t, x)\frac{\partial \delta_u f(t, x)}{\partial u^k_i}\varrho(t, x)\, dt. \qquad (1)$$

Passing to the summation on macroparticles within the framework of the method of macroparticles, write the functional derivatives in the form

$$\frac{\partial \Phi}{\partial u^k_i} = -\int\limits_{t_0}^{T}\sum_{j=1}^{N} \psi(t, x_{(j)}))\frac{\partial \delta_u f(t, x_{(j)})}{\partial u^k_i}\, dt,$$

* Work supported by St. Petersburg State University grant #9.38.673.2013

ISBN 978-3-95450-170-0

where $x_{(j)}$ denotes position in the phase space of the j-th particle.

Consider second derivatives of the functional on the control parameters. For simplicity assume that $r = 1$ (one scalar control function). Let us consider second derivatives only on the same parameters $\partial^2\Phi/\partial u_i^2$. As

$$\frac{\partial x^j}{\partial u_i}(t) = \int\limits_{t'}^{t} G_k^j(t,t')\frac{\partial \delta_u f^k}{\partial u_i}(t')\,dt', \qquad (1)$$

the expression (1) can be rewriteen in the form

$$\frac{\partial \Phi}{\partial u_i} = \int\limits_{\Omega} \frac{\partial \Phi}{\partial x^j}\frac{\partial x^j}{\partial u_i}(T)\varrho(T). \qquad (1)$$

Assume also that $\partial^2\Phi/(\partial x^i \partial x^j) = 0$ if $i \neq j$. Then

$$\frac{\partial^2 \Phi}{\partial u_i^2} = \int\limits_{\Omega} \varrho(T)\left[\frac{\partial \Phi}{\partial x^j}\frac{\partial^2 x^j}{\partial u_i^2}(T) + \frac{\partial^2 \Phi}{\partial (x^j)^2}[\frac{\partial x^j}{\partial u_i}(T)]^2\right].$$

Passing to the summation on macroparticles we get

$$\frac{\partial^2 \Phi}{\partial u_i^2} = \sum_{k=1}^{N}\left[\frac{\partial \Phi}{\partial x^j}\frac{\partial^2 x^j_{(k)}}{\partial u_i^2}(T) + \frac{\partial^2 \Phi}{\partial (x^j)^2}[\frac{\partial x^j_{(k)}}{\partial u_i}(T)]^2\right],$$

where the first derivatives are expressed by (1).

It can be shown that when f^j are linear on control parameters u_i, second variation of x has the form

$$\delta^2 x^j(t) = \int\limits_{t_0}^{t}(D_{kl}^j(t,t')\delta_u f^k(t') + G_k^j(t,t')\delta_u(\frac{\partial f^k}{\partial x^l})|_{t'})\times$$

$$\times(\int_{t_0}^{t'} G_m^l \delta_u f^m(t'')\,dt'')\,dt',$$

where components of the tensor D satisfy to the system of differential equations

$$\frac{\partial D_{lk}^i(t,t')}{\partial t'} = -2D_{lm}^i(t,t')\frac{\partial f^m}{\partial x^k}(t') + G_m^i(t,t')\frac{\partial^2 f^m}{\partial x^l \partial x^k}(t')$$

and the condition

$$D_{lk}^i(t,t) = 0, \quad i,j,k = \overline{1,m}.$$

Then

$$\frac{\partial^2 x^j}{\partial u_i^2}(t) = \int\limits_{t_{i-1}}^{t_i}\left[D_{kl}^j(t,t')\frac{\partial \delta_u f^k}{\partial u_i}(t') + \right.$$

$$\left. + G_k^j(t,t')\frac{\partial}{\partial u_i}\left(\delta_u(\frac{\partial f^k}{\partial x^l})\right)|_{t'}\right]\times$$

$$\times \int\limits_{t_{i-1}}^{t'} G_m^l(t',t'')\frac{\partial \delta_u f^m}{\partial u_i}(t'')\,dt''\,dt'.$$

Numerical optimization process can be implemented as a sequence of steps of numerical calculation of first and second derivatives of the functional, and changing of control parameters according to the expression

$$\delta u_i = -\frac{\partial \Phi/\partial u_i}{\partial^2 \Phi/\partial u_i^2.} \quad i = \overline{1,M}$$

while the functional is decreasing. If at some step it will be turned out that $\partial^2\Phi/\partial u_i^2 = 0$ for some i, one should combine this method with method of gradient descent or another first order method.

OPTIMIZATION OF RFQ CANNEL

Assume that longitudinal component of electric field in the RFQ channel is

$$E_z = U_0\frac{4kT}{\pi}\cos\eta\cos\omega t, \quad \eta(z) = \int\limits_{z_0}^{z} k(z')\,dz', \quad (1)$$

Here $2U_0$ is intervane voltage, ω is frequency of the field oscillations, a is aperture of the cell, $k = \pi/L$, L is the cell length, which varies along the channel, $\eta(z)$ is the phase of electrode modulation, T is acceleration efficiency.

Within the framework of this model, the longitudinal motion does not depend of the transverse motion. It allows us to consider logitudinal motion separately. For simplicity, consider optimization problem accounting only longitudinal motion.

Take reduced energy γ and phase of the particle $\varphi = \omega t$ as the phase coordinates. Initial distribution in the phase space of longitudinal motion can be set in various manner. For example it can be taken in the form $\varrho_{(0)\,\varphi} = (2\pi)^{-1}$, $\varphi_0 \in [-2\pi, 0]$, $\gamma = \gamma_0$. Here $\varrho_{(0)\,\varphi}$ is $\varphi-$component of the initial distribution density, φ_0 and γ_0 are initial phase and energy of a particle.

Consider the difference between phase of the synchronous particle φ_s and the phase of space modulation η

$$\Phi_s = \varphi_s - \int \overline{k}\,d\zeta. \qquad (1)$$

Here $\zeta = z/\lambda$, $\overline{k} = \lambda k$, $\lambda = 2\pi c/\omega$. Take function $u_1(\zeta) = d\Phi_c/d\zeta$ as the first control function. Let T be the second control function: $u_2(\zeta) = T(\lambda\zeta)$.

The equation of longitudinal dynamics for low intensity beam can be written in the form

$$\frac{d\varphi}{d\zeta} = 2\pi\gamma(\gamma^2 - 1)^{-1/2}, \qquad (1)$$

$$\frac{d\gamma}{d\zeta} = C_L(2\pi\gamma_s(\gamma_s^2 - 1)^{-1/2} - u_1)u_2\cos\eta\cos\varphi, \quad (1)$$

where $C_L = 2eU_0/(\pi mc^2)$. Equation for η has form [3]

$$\frac{d\eta}{d\zeta} = 2\pi\gamma_s(\gamma_s^2 - 1)^{-1/2} - u_1.$$

ISBN 978-3-95450-170-0

Then equations for ψ can be written in the form

$$\frac{d\psi_\eta}{d\zeta} = \sum_{i=1}^{N} \psi_{(i)\gamma} C_L \overline{k} u_2 \sin\eta\cos\varphi_i,$$

$$\frac{d\psi_{(s)\gamma}}{d\zeta} = \psi_\eta \frac{2\pi}{(\gamma_s^2-1)^{3/2}} +$$

$$+\psi_{(s)\varphi}\frac{2\pi}{(\gamma_s^2-1)^{3/2}}\sum_{i=1}^{N}\psi_{(i)\gamma}\frac{2\pi}{(\gamma_s^2-1)^{3/2}} C_L u_2\cos\eta\cos\varphi_i,$$

$$\frac{d\psi_{(i)\varphi}}{d\zeta} = C_L\,\psi_{(i)\gamma}\overline{k}T\cos\eta\sin\varphi_i, \qquad i=\overline{1,N},$$

$$\frac{d\psi_{(i)\gamma}}{d\zeta} = \psi_{(i)\varphi}\frac{2\pi}{(\gamma_i^2-1)^{3/2}}, \qquad i=\overline{1,N}.$$

Here i is number of a macroparticle. It is written in parenthesis at ψ to avoid confuse with indices. Let control functions are constant inside cells: $u_i(\zeta) = u_{ij}$, $\zeta \in [\zeta_{j-1}, \zeta_j)$, $j = \overline{1,M}$. Then

$$\frac{\partial\Phi}{\partial u_{1j}} = \int\limits_{\zeta_{j-1}}^{\zeta_j} (\psi_\eta + \sum_{i=1}^{N}\psi_{(i)\gamma} C_L u_2\cos\eta\cos\varphi_i)\,d\zeta,$$

$$\frac{\partial\Phi}{\partial u_{2j}} = \int\limits_{\zeta_{j-1}}^{\zeta_j}\sum_{i=1}^{N}\psi_{(i)\gamma} C_L\overline{k}\cos\eta\cos\varphi_i\,d\zeta.$$

Restrict ourselves to the case of one scalar control function $u = T$. Then equation for Green functions and for components of tensor D are

$$\frac{dG_\varphi^\varphi}{d\zeta} = -G_\gamma^\varphi C_L\overline{k}T\cos\eta\sin\varphi, \frac{dG_\gamma^\varphi}{d\zeta} = G_\varphi^\varphi\frac{2\pi}{(\gamma^2-1)^{3/2}},$$

$$\frac{dG_\varphi^\gamma}{d\zeta} = -G_\gamma^\gamma C_L\overline{k}T\cos\eta\sin\varphi, \frac{dG_\gamma^\gamma}{d\zeta} = G_\varphi^\gamma\frac{2\pi}{(\gamma^2-1)^{3/2}},$$

$$\frac{\partial D_{\varphi\varphi}^\varphi(\zeta,\zeta')}{\partial\zeta'} = (2D_{\varphi\gamma}^\varphi\sin\varphi - G_\gamma^\varphi\cos\varphi)C_L\overline{k}T\cos\eta,$$

$$\frac{\partial D_{\varphi\varphi}^\gamma(\zeta,\zeta')}{\partial\zeta'} = (2D_{\varphi\gamma}^\gamma\sin\varphi - G_\gamma^\gamma\cos\varphi)C_L\overline{k}T\cos\eta,$$

$$\frac{\partial D_{\varphi\gamma}^\varphi(\zeta,\zeta')}{\partial\zeta'} = -\frac{4\pi D_{\varphi\varphi}^\varphi}{(\gamma^2-1)^{3/2}} + 2D_{\gamma\gamma}^\varphi C_L\overline{k}T\cos\eta\sin\varphi,$$

$$\frac{\partial D_{\varphi\gamma}^\gamma(\zeta,\zeta')}{\partial\zeta'} = -\frac{4\pi D_{\varphi\varphi}^\gamma}{(\gamma^2-1)^{3/2}} + 2D_{\gamma\gamma}^\gamma C_L\overline{k}T\cos\eta\sin\varphi,$$

$$\frac{\partial D_{\gamma\gamma}^\varphi(\zeta,\zeta')}{\partial\zeta'} = -\frac{4\pi D_{\varphi\gamma}^\varphi}{(\gamma^2-1)^{3/2}} - G_\varphi^\gamma C_L\overline{k}T\cos\eta\cos\varphi,$$

$$\frac{\partial D_{\gamma\gamma}^\gamma(\zeta,\zeta')}{\partial\zeta'} = -\frac{4\pi D_{\varphi\gamma}^\gamma}{(\gamma^2-1)^{3/2}} - G_\gamma^\gamma C_L\overline{k}T\cos\eta\cos\varphi.$$

Second derivatives of the functional are $\partial^2\Phi/\partial T_j^2 =$

$$= \sum_{i=1}^{N}\Big\{\frac{\partial^2\Phi}{\partial\varphi^2}\Big[\int\limits_{\zeta_{j-1}}^{\zeta_j} G_\gamma^\varphi(\zeta_M,\zeta')\overline{k}\cos\eta(\zeta')\cos\varphi(\zeta')\,d\zeta'\Big]^2 +$$

$$+\frac{\partial^2\Phi}{\partial\gamma^2}\Big[\int\limits_{\zeta_{j-1}}^{\zeta_j} G_\gamma^\gamma(\zeta_M,\zeta')\overline{k}\cos\eta(\zeta')\cos\varphi(\zeta')\,d\zeta'\Big]^2 +$$

$$+\frac{\partial\Phi}{\partial\varphi}\int\limits_{\zeta_{j-1}}^{\zeta_j} D_{\gamma\varphi}^\varphi(\zeta_M,\zeta')\overline{k}\cos\eta(\zeta')\cos\varphi(\zeta')\times$$

$$\times\Big[\int\limits_{\zeta_{j-1}}^{\zeta'} G_\gamma^\varphi(\zeta',\zeta'')\overline{k}\cos\eta(\zeta'')\cos\varphi(\zeta'')\,d\zeta''\Big]\,d\zeta'$$

$$+\frac{\partial\Phi}{\partial\varphi}\int\limits_{\zeta_{j-1}}^{\zeta_j} D_{\gamma\gamma}^\varphi(\zeta_M,\zeta')\overline{k}\cos\eta(\zeta')\cos\varphi(\zeta')\times$$

$$\times\Big[\int\limits_{\zeta_{j-1}}^{\zeta'} G_\gamma^\gamma(\zeta',\zeta'')\overline{k}\cos\eta(\zeta'')\cos\varphi(\zeta'')\,d\zeta''\Big]\,d\zeta'$$

$$+\frac{\partial\Phi}{\partial\gamma}\int\limits_{\zeta_{j-1}}^{\zeta_j} D_{\gamma\varphi}^\gamma(\zeta_M,\zeta')\overline{k}\cos\eta(\zeta')\cos\varphi(\zeta')\times$$

$$\times\Big[\int\limits_{\zeta_{j-1}}^{\zeta'} G_\gamma^\varphi(\zeta',\zeta'')\overline{k}\cos\eta(\zeta'')\cos\varphi(\zeta'')\,d\zeta''\Big]\,d\zeta'$$

$$+\frac{\partial\Phi}{\partial\gamma}\int\limits_{\zeta_{j-1}}^{\zeta_j} D_{\gamma\gamma}^\gamma(\zeta_M,\zeta')\overline{k}\cos\eta(\zeta')\cos\varphi(\zeta')\times$$

$$\times\Big[\int\limits_{\zeta_{j-1}}^{\zeta'} G_\gamma^\gamma(\zeta',\zeta'')\overline{k}\cos\eta(\zeta'')\cos\varphi(\zeta'')\,d\zeta''\Big]\,d\zeta'\Big\}C_L^2.$$

Particle number i at G, D, φ, γ is omitted for brevity. Analogous expressions can be obtained in 6-dimensional general case with 3 control functions [3].

REFERENCES

[1] D.A. Ovsyannikov, O.I. Drivotin "Modeling of Intensive Charge Particle Beams" St.Petersburg: Publ.Comp. of St.Petersburg State Univ., 2003.

[2] O.I. Drivotin "Covariant Formulation of the Vlasov equation" IPAC'2011, San-Sebastian, Sept.2011, accelconf.web.cern.ch/accelconf/IPAC2011/papers/wepc114.pdf

[3] O.I. Drivotin, et.al. "Mathematical Models for Accelerating Structures of Safe Energetical Installation" EPAC'98, June 1998, Stockholm, Sweden.

ISBN 978-3-95450-170-0

ELECTRON GUN WITH ADIABATIC PLASMA LENS

A. Drozdovsky, A.Bogdanov, S. Drozdovsky, R. Gavrilin, A. Golubev, I. Roudskoy, S. Savin, V. Yanenko, SSC RF Institute of Theoretical and Experimental Physics, Moscow, Russia

Abstract

For researches on plasma physics has been designed and constructed the electronic gun with the cold cathode on energy to 300 кэВ. The gun have the parameters: time width of pulses -100 ns, current amplitude - 100 A. The adiabatic plasma lens is developed for transportation and compression of the received electron beam. Results of researches are presented.

INTRODUCTION

The electron beam with energy in hundreds кэВ is necessary for carrying out researches in the field of plasma physics - studying of formation of Z-pinch [1]. For these purposes the electron beam has to have the following parameters: current amplitude > 100 A, front duration ~ 10 nanoseconds, energy of electrons > 200 keV. The experimental installation is shown on fig. 1. The electron beam is entered through foil into the experimental channel with pressure ~ 1 mbar. The beam size is reduced in the adiabatic plasma and then is injected in the camera for Z-pinch formation. For creation of the required accelerating voltage form was accepted the scheme of the generator on cable lines with use of the double forming line of Blumlein (DFL) and the cable transformer of Lewis [2].

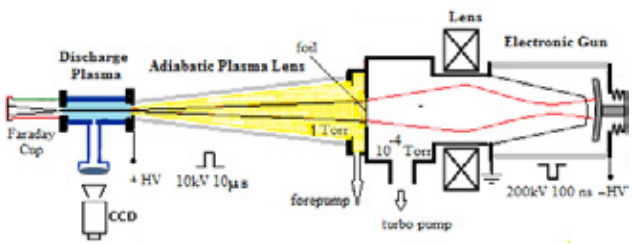

Figure 1: Set up of the adiabatic plasma lens with the ITEP electron gun.

THE GUN INSTALLATION

The gun installation (fig. 2) consists of actually electron gun with magnetic lens, surveillance camera with the scintillators located in it. Vacuum pumping of an electronic gun is made by the turbomolecular pump, and of plasma part of installation - the roughing-down pump. The appropriate volumes are separated from each other by a mylar film. The desorption emitter was used for reduction of requirements to vacuum. Such long-lasting emitter was developed in ITEP [3]. The gun emitter of an electron beam (fig. 2) is located in the center of a cathode. The desorption emitter represents a set of thin plates of mica and copper. The emitter diameter is 50mm, diameter of a cathode electrode is 110 mm. The gap width is about 50 mm.

Fig. 3 represents simulation results of the electron beam propagation from cathode (C) to adiabatic magnetic lens. Emission current of 100 A and 50 mm cathode-anode gap under voltage of 200 kV were assumed during calculation.

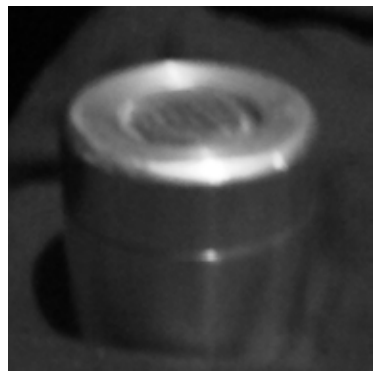

Figure 2: The cathode assemble.

The simulation was performed using numerical code PICSIS-2D [4] based on use of system of the equation of Vlasov-Boltsman with calculation of collisions of particles by Monte-Carlo method. The program enables to calculate a transportation of relativistic charged particles in arbitrary 2D electromagnetic fields taking into account its space charge and self-magnetic field.

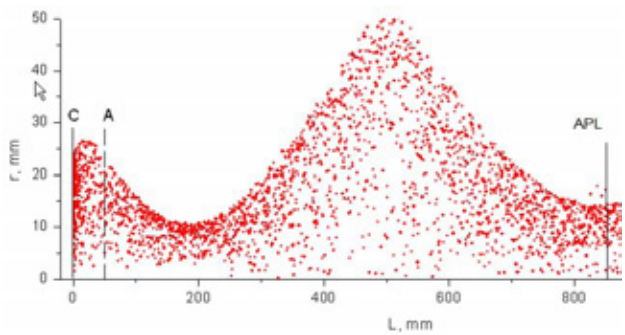

Figure 3: Electron beam propagation; I=100A, U=200kV.

PULSE MODULATOR

For creation of the accelerating voltage was accepted the scheme (fig. 4) of the generator on cable lines with use of the double forming line of Blumlein (LB) and the cable transformer of Lewis (TL). Generators of this kind were realized [5] and on them voltage about 300 kV impulses were received. For switching of the LB was used by "pseudospark switches" TPI1-10k/50. The forming line was executed from 18 couples 10-meter RC-50 cables. It is loaded from a high-voltage source through R_h resistance. To reduce communication between an exit

* Work supported by the Russian Foundation for Basic Research (grant № 12-02-00866-a)

ISBN 978-3-95450-170-0

of the transformer of Lewis and the forming line, the last unites to the earth through decoupling inductance of L_{dec}. The cable transformer consists of nine 20-meter cables, each of which contain two inductivity decouplings (permalloy and ferrite). For compensation of distortions of a form of an impulse the L_c, C_c and R_c elements are entered into the scheme. The control signal is removed from a low-voltage shoulder of R_d of a divider of the accelerating tension.

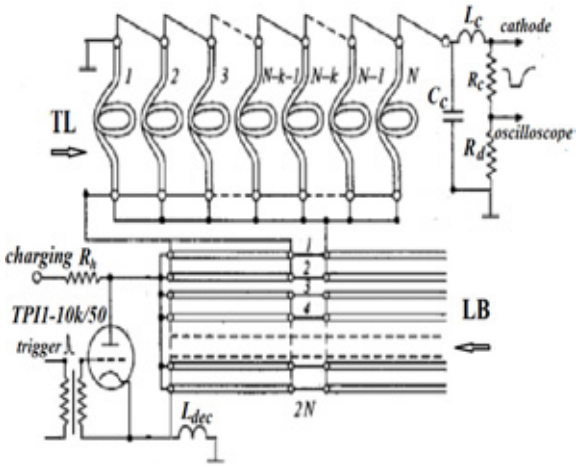

Figure 4: Pulse modulator.

ELECTRON DIAGNOSTICS

The Kuraray company scintillators are used for obtaining of a beam density distribution. A scintillators luminescence are registered by CCD television cameras. The last together with operating computer are in the iron boxing providing an electromagnetic shielding. Information to the central computer is transferred on optical communication.

An electron beam current was measured by the current transformer which has been built in the transport channel. All measuring systems, as well as start systems, are equipped with fiber-optical devices [1].

Figure 5 shows waveforms of the beam current and DFL voltage pulse at of 25 kV. The peak current of 50 A and the beam time width of 60 nsec.

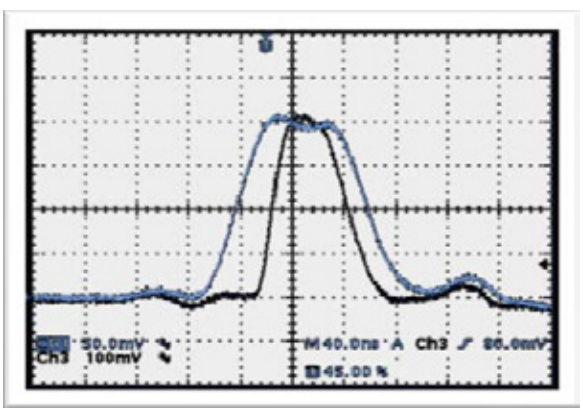

Figure 5: The electron beam current (black curve) and DFL voltage pulse signals.

The measurements of a electron beam energy spectrum on the magnetic analyzer were taken (fig. 6). Width of recession of a spectrum above a maximum is defined by the value of angular dispersion which exceeds 0.01 rad.

Characteristics of an electron beam were close to design values.

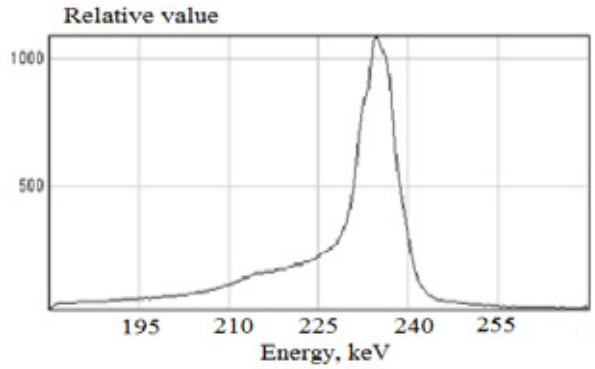

Figure 6: Electron beam energy spectrum for charging voltage 28 kV.

ADIABATIC PLASMA LENS

Focusing of an charge particle beam in a plasma lens is carried out as follows (fig. 7): the z-discharge plasma current creates an azimuthal magnetic field which focuses a beam passing through the discharge tube. If a discharge tube conic, density of current and a magnetic field increase with reduction of a tube diameter. That plasma z-discharge can be used to reduce the beam size in a way increasing of the focusing strength along the lens [5]. The focusing strength increase reduces the betatron wavelength and at the same time the amplitude of the betatron oscillation and thus results in a reduction of the beam envelope radius. That is different from the traditional "coherent focusing". This of focusing can be achieved by a slow, or 'adiabatic'.

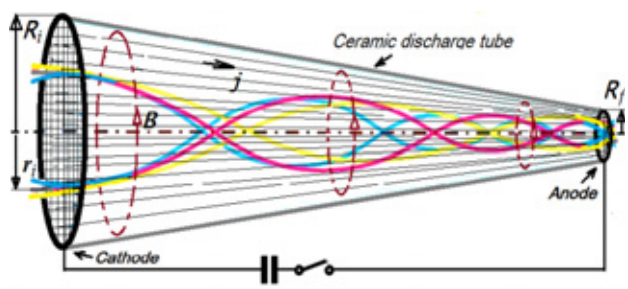

Figure 7: Schematic drawing of the principle and geometry of an adiabatic plasma lens.

Reduction ratio of the final beam radius r_f to the initial beam radius r_i depends on the increase of focusing strength along the lens:

$$r_f / r_i = (R_f / R_i)^{1/2}$$

ISBN 978-3-95450-170-0

where R_f /Ri is the reduction ratio of final to initial diameter of discharge tube. The first studying of an adiabatic plasma lens were performed in Berkeley [6]. The researches were conducted with use of a beam ions K^+ of 1.5 MeV energy.

Now research and adjustment works on creation of the adiabatic plasma lens (APL) are carried out. The pulse generator with thyratron TDI1-150/25 as the switchboard on current to 30 kA was created. As current impulse rather long (20 microsec), the discharge current fills all section of a tube, and distribution of the current closely to the uniform where a beam passes. Therefore it is possible the adiabatic formula will correctly define change of the size of a bunch in our lens.

Because of technological problems decided to replace a conic discharge tube with a set of cylindrical tubes. The set of tubes has length of 120 cm and their diameter decreases from 100 to 10 mm. The lens was tested on initial part 60 cm long, where diameter decreases from 100 to 50 mm (see fig. 8).. The steady discharge happens with a pressure less than 0.5 Torr. According to Paschen's curve for the full length lens pressure will need to be reduced to 0.2 Torr.

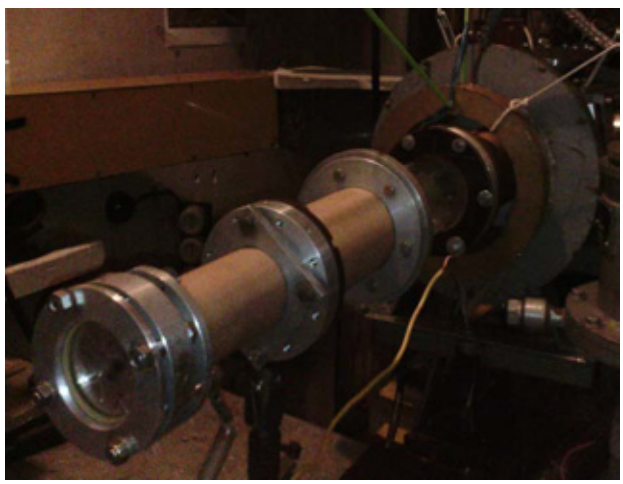

Figure 8: The adiabatic plasma lens (initial part).

The first tests were carried out for a electron beam with energy 200 кэВ and current 30 A. The fig. 9 show a scintillators luminescence for the lens entrance and exit. The corresponding sizes of a beam section are 50 mm and 40 mm. Of course, quality of conducting of a beam leaves to wish much the best, but, nevertheless, the beam size didn't increase on a drift interval 60 cm. Further it allows to hope to achieve the demanded results.

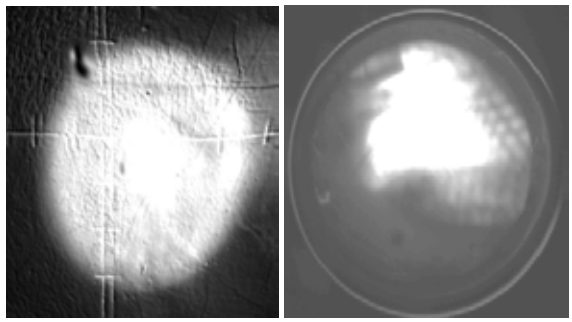

Figure 9: Scintillators luminescence for the lens entrance and exit.

CONCLUSION

Measurements of parameters of a beam showed their good compliance to projected values. Reliable work of installation speaks about operability of the made technical solutions.

The developed generator for an adiabatic plasma lens provides stable implementation of the plasma discharge.

The carried out tests of an adiabatic plasma lens with an electron beam allow to hope for the successful solution of objectives.

REFERENCES

[1] A.A.Drozdovsky, A.V.Bogdanov, R.O.Gavrilin, A.A.Golubev, S.A.Drozdovsky, A.V.Kantsyrev, E.M.Ladygina, I.V. Roudskoy, S.M.Savin, V.V.Yanenko. Electronic Gun for Physical Researches, Physics of Particles and Nuclei Letters, 2014, Vol. 11, No. 5, pp. 577–580. © Pleiades Publishing, Ltd., 2014.

[2] A. I. Pavlovskii and G. V. Sklizkov, “Generation ofhigh_voltage rectangular pulses,” Prib. Tekh.Eksp.,No. 4, 36 (1979).

[3] E. N. Danil’tsev and V. I. Pershin, “Pulsed DesorptionSlot Cathode,"Prib. Tekh.Eksp., No. 4, 36 (1979).

[4] I. Roudskoy, T.V. Kulevoy, S.V.Petrenko et al. “Bernas ion source discharge simulation”, Rev. Sci. Instrum., 2008, v. 79, p. 02B313.

[5] P. Chen, K. Oide, A.M. Sessler, S.S. Yu, ’Plasma-Based Adiabatic Focuser’, Phys. Rev. Lett. **64**, 1231-1234, 1990.

[6] A. Tauschwitz, S.S. Yu, R.O. Bangerter, J. Barnard, S. Eylon, T.J. Fessenden, S. Eylon, D.H.H. Hoffmann, J. Kwan, W. Leemans, M. de Magistris, C. Peters, L. Reginato, W.M. Sharp, ’Adiabatic Focusing and Channel Transport for Heavy Ion Fusion’, Proc. Int. Conf. on Laser Int. and Rel. Plasma Phen., Monterey, CA, AIP Conference Proceedings **406**, 251-258, 1997.

ISBN 978-3-95450-170-0

AXIAL INJECTION TO A COMPACT CYCLOTRON WITH HIGH MAGNETIC FIELD

V. L. Smirnov, S. B. Vorozhtsov
Joint institute for nuclear research, Dubna, Russia

Abstract

One of advantages of a compact cyclotron over other type accelerators is a small size mainly defined by the facility's bending magnetic field. In such cyclotrons an application of an external injection is required in some cases. But for high magnetic field of the cyclotrons (over 4-5 T) there appears a severe problem to make the 1st turns in the machine with external injection of accelerated particles. This paper describes a proposal of a new central region structure of a compact cyclotron that permits one to successfully solve the problem of the axial injection into such a facility using a spiral inflector.

INTRODUCTION

To reach the smallest accelerator size, application of an as high as possible magnetic field of the machine is required. In the compact cyclotron with high magnetic field its magnitude is mainly limited by the minimal focusing available. Thus, in sector structures with large spiral angles of 60-70 degrees and maximal possible deep valleys the practically reachable limit for the central field would be 4-5 T. In a cyclotron with external ion source the particle injection in the accelerator central region is one of the main problems. A design of the cyclotron central region is a key moment for such accelerators. An application of a conventional spiral inflector [1] leads to substantial particle losses on the first turns in the magnetic field.

A possible way to increase the particle transmission through the central region is the application of a higher dee voltage and increasing the number of the dees [2]. Such approach contradicts the main requirement to the modern compact accelerators – the minimum power consumption at their use. Application of higher particle injection energy also can help in solving the problem [3]. But the modern ion sources have restrictions on the maximal possible particle energy at the level of 25-30 keV for the singly charged ions. Besides, at high energies the inflector voltage also should be higher that essentially complicates development of the machine. Miniaturization of the central region structure [4] can also be a solution. This approach in the spiral inflector with minimum size implies very complicated structure of the cyclotron center.

In this report the authors propose a very different approach to the cyclotron central region configuration. In the suggested structure the trajectories of the injected particles on the first turns in the magnetic field and RF are axially separated from the inflector external surfaces [5].

CENTRAL REGION STRUCTURE

The particle trajectory curvature in the high magnetic field is smaller than the spiral inflector external dimensions. Therefore, the injected particles get lost on the inflector case during their initial turn. To prevent those particle losses it is proposed to inject them under some angle with the accelerator median plane at the inflector exit. Such particles make the first turns with some offset to the median plane excluding in this way their collision with the inflector outside surface. The further consideration deals with some hypothetic compact cyclotron having the central magnetic field of 4.5 T. Simulations were performed by the SNOP program of particle tracing [6] in three-dimensional fields of the main magnet, the spiral inflector and the accelerating dees calculated in the Tosca\Opera3D program. As a test particle H^- ion injected from axial line with energy 25 keV was used.

As mentioned above in the proposed method the particle trajectory radius on the first turn should not be larger than the effective inflector half-size. To provide required inclination of the particle trajectory to the median plane at the inflector exit, inflector electrodes should be cut off at its exit by some small angle defined by calculations. In our case 20 degrees was chosen to cut (Fig. 1).

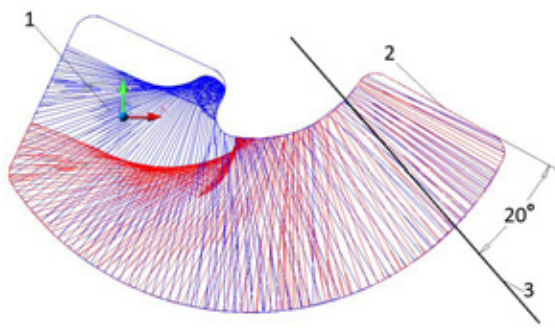

Figure 1: Spiral inflector cut: 1 – inflector entrance, 2 – inflector exit, 3 – cutting plane.

In this case the particle trajectory makes ~ 6 degree angle with the median plane, and the radius of curvature of the particle trajectory is 5.5 mm. Due to axial separation of the particle trajectory with the inflector they do not intersect despite larger effective radius of the inflector of 9 mm. To minimize the axial size of the inflector case the lower electrode is set at ground potential and connected electrically to the inflector case. The upper electrode is under the potential of +10 kV (Fig. 2).

ISBN 978-3-95450-170-0

Calculations show that 3.7 mm axial shift of the inflector from the median plane is necessary to provide sufficiently small amplitude of the axial oscillations of particles on the first turns.

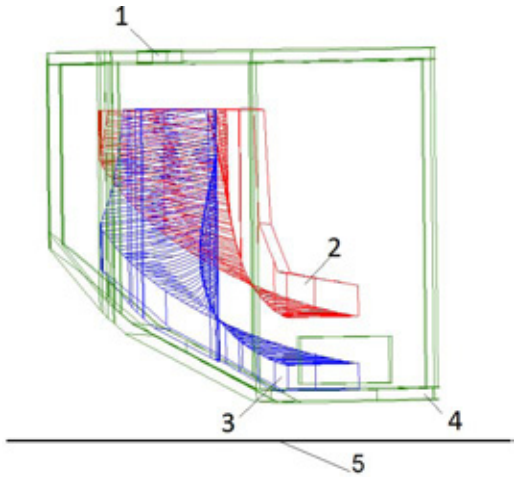

Figure 2: Inflector structure: 1 – inflector entrance, 2 – upper electrode, 3 – lower electrode, 4 – inflector RF shield, 5 – median plane.

Particle motion simulation using three-dimensional distribution of the electric field of one 180 degree dee confirmed stability of the axial oscillations of particles. The proposed method of the cyclotron central region construction allows application of rather small dee voltage. In our case 30 kV voltage with dee to dummy dee gap of 2.5 mm was chosen.

The structure of dee tip was chosen, such as to provide maximal electric focusing of particles on initial turns. The positive RF phase was provided when crossing with particles of the accelerating gaps, creating thereby conditions for quickly damped oscillations about the median plane. The calculations above showed that despite increasing an axial aperture of the dee structure required in the method, it is possible to create a central region with stable axial oscillations of the particles with their further capture in the acceleration process (Fig. 3, 4).

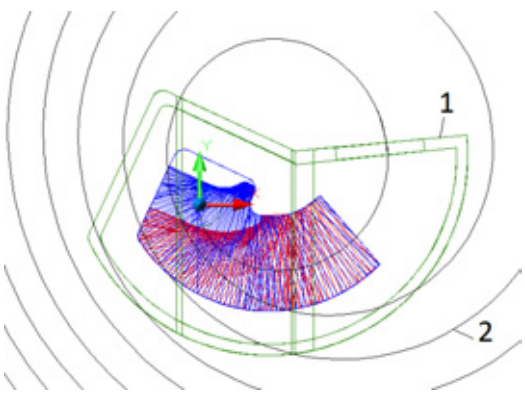

Figure 3: Particle trajectory in the central region: 1 – inflector RF shield, 2 – particle trajectory, 3 – dee, 4 – dummy dee.

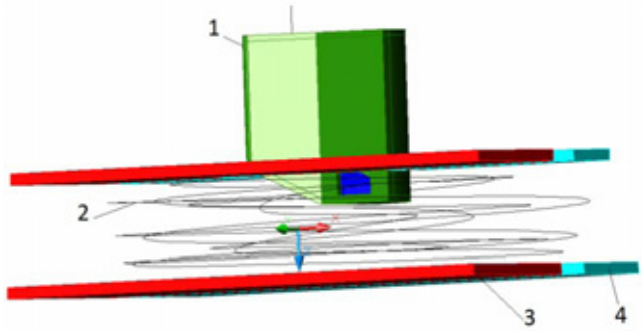

Figure 4: Central region structure: 1 – inflector RF shield, 2 – particle trajectory, 3 – dee, 4 – dummy dee.

CONCLUSION

In this study a new structure of the central region of the compact cyclotron that allows us to solve a basic problem of cyclotron physics – axial injection from the external ion source in the cyclotron with a high magnetic field – was proposed. The new method of particle injection is based on innovative idea of axial separation of a trajectory of the injected particles with the inflector geometry. The described structure is rather simple in realization and doesn't demand a high dee and inflector voltages. The proposed injection can be applied in the design of accelerators with external injection and the highest magnetic field, like those described in reference [2].

REFERENCES

[1] J. L. Belmont and J. L. Pabot, IEEE Trans. Nucl. Sci. NS-13, 191 (1966).
[2] D. Campo, L. Calabretta, M. Maggiore, L.A.C. Piazza, “Beam injection and extraction of SCENT300, a superconducting cyclotron for hadrontherapy”, Proc. of EPAC08, Genoa, Italy.
[3] V. S. PANDIT, “Study on using high injection voltage and spiral inflector in the central region of VEC”, PRAMANA journal of physics, Indian Academy of Sciences, Vol. 59, No. 6, pp. 1019-1024, 2002.
[4] A. Garonna, “Cyclotron designs for ion beam therapy with cyclinacs”, PhD Thesis, Ecole Polytechnique Federale de Lausanne, 2011.
[5] V.L. Smirnov and S.B. Vorozhtsov, “Axial injection to a compact cyclotron with an ultrahigh magnetic field”. Patent application RU 2014103854, 04.02.2014.
[6] V.L. Smirnov and S.B. Vorozhtsov, “SNOP – Beam Dynamics Analysis Code for Compact Cyclotrons”. Proc. of RuPAC’12, September 24 - 28, 2012, St. Petersburg, Russia.

ISBN 978-3-95450-170-0

COMPLEX SHUNT IMPEDANCE AND BEAM-RF CAVITY INTERACTION

V.G.Kurakin, Lebedev Physical Institute, Moscow, Russia

Abstract

Two approaches usually are used to describe beam-cavity interaction in accelerator based applications. The first one is electro dynamical and uses Maxwell equations to derive appropriate equations, field modes expressions being necessary to calculate field amplitudes excited by moving charges in the cavity. The other one uses LC circuit to derive appropriate equations for voltage amplitude induced in cavity by accelerated bunches, thin accelerating gap to some extent being not fully correctly defined representation in such approach. In this paper, the expressions are derived that describe beam-RF cavity interactions in terms of so called complex shunt impedance, strict electro dynamical approach being used in calculations. It is shown that complex shunt impedance module coincides completely with usual shunt impedance definition that up to now is used widely to describe rf cavity efficiency. The physical sense of its phase is given in the paper as well. Both complex shunt impedance module and its phase can be calculated or measured experimentally.

INTRODUCTION

To analyze the processes resulting from beam-cavity interaction two approaches are used mainly. The first one is based on Maxwell equations solving. Cavity eigen functions for vector potential are found that together with differential equations for fields amplitudes form the basis for following analysis. In other approach mentioned the RF cavity is replaced with the electrical circuit containing active resistance, capacitance and inductance, their values are chosen in such a way to have the resonance frequency, quality factor and shunt impedance the same for the RF cavity and for the circuit. In this approach one has an analytical representation so necessary for analysis but the questions concerning approach justification and some uncertainness arise.

In this paper we use strict field approach based on Maxwell equation to derive the equation for field amplitude that might be suitable for processes analysis in accelerator containing RF cavity. Complex shunt impedance concept have been introduced and this appeared be fruitful for beam-cavity interaction processes description in RF accelerator based applications problems.

ELECTRODYNAMICS OF RF CAVITY-BEAM INTERACTION

To find out the fields that induces moving charge in a RF cavity, we will use the method that had been developed in [1]. Vortex electrical $\vec{E}(\vec{r},t)$ and magnetic $\vec{H}(\vec{r},t)$ fields are represented as derivatives of vector potential $\vec{A}(\vec{r},t)$ on time t and space $\vec{r}$ coordinates:

$$\vec{E}(\vec{r},t) = -\frac{\partial \vec{A}(\vec{r},t)}{\partial t}, \quad \vec{H}(\vec{r},t) = \frac{1}{\mu_0} rot\vec{A}(\vec{r},t) \quad (1)$$

where μ_0 is magnetic permeability of free space. Here and later SI units are used. Vector potential satisfies the wave equation

$$\Delta\vec{A}(\vec{r},t) - \frac{1}{c^2}\frac{\partial^2 \vec{A}(\vec{r},t)}{\partial t^2} = -\mu_0 \vec{j}(\vec{r},t) \quad (2)$$

$\vec{j}(\vec{r}.t)$, c being current density and the light velocity.

To find out the expressions for vector potential we will use the most direct way. Namely, we represent vector potential as an expansion on the infinite sum of RF cavity eigen functions $\vec{A}_\lambda(\vec{r})$ with time dependent coefficients $g_\lambda(t)$:

$$\vec{A}(\vec{r},t) = \sum_{\lambda=1}^{\infty} g_\lambda(t)\vec{A}_\lambda(\vec{r}) \quad (3)$$

with the boundary conditions $\vec{A}_\lambda|_\Sigma = 0$ on cavity surface.

Starting from the equation (2) and taking into account (3) one can easily obtain the equations for cavity vector eigen functions and appropriate time dependent coefficients (fields amplitudes):

$$\Delta\vec{A}_\lambda(\vec{r}) + k_\lambda{}^2\vec{A}_\lambda(\vec{r}) = 0 \quad (4)$$

$$\frac{d^2 g_\lambda(t)}{dt^2} + \omega_\lambda{}^2 g_\lambda(t) = \int_V \vec{j}(\vec{r},t)\vec{A}_\lambda(\vec{r})dV \quad (5)$$

Here $k_\lambda = \omega_\lambda / c$ are eigen values of boundary values problems (4), the specific solutions for RF cavities are called cavity modes, ω_λ being the eigen angular frequencies of appropriate modes, c is light velocity. Integration in formula is assumed to be performed over cavity volume V. Last equation can be generalized up to the next one

$$\frac{d^2 g_\lambda(t)}{dt^2} + \frac{\omega_\lambda}{Q_\lambda}\frac{dg_\lambda}{dt} + \omega_\lambda{}^2 g_\lambda(t) = \int_V \vec{j}(\vec{r}.t)\vec{A}_\lambda(\vec{r})dV \quad (6)$$

if losses in cavity and outside are taking into account. Here Q_λ stands for cavity quality factor:

$$Q_\lambda = \frac{\omega_\lambda W_\lambda}{P_\lambda} \quad (7)$$

ISBN 978-3-95450-170-0

where W_λ is the electromagnetic energy in the mode λ, stored in cavity volume and P_λ represents the total RF power losses that besides ohm losses in cavity walls includes the external losses due to cavity coupling with external circuits. It is supposed that eigen functions are normalized by the condition

$$\int_V A_\lambda^2 = \mu_0 c^2 = 1/\varepsilon_0 \quad (8)$$

Here μ_0 and ε_0 are magnetic and electric permeability respectively.

For the analysis followed we will use the cavity excitation equation in the form with small RF losses, and this has no any influence on generality of results to be obtained. Then, all calculations will be made for a single charged particle with charge value q of zero dimensions in all directions entering cavity at moment $t = 0$. In such a case the total current density

$$\vec{j}(\vec{r},t) = q\vec{v}(\vec{r},t)\delta(x,y,vt)), \quad (9)$$

where $\vec{v}(\vec{r},t)$ stands for particle velocity being assumed constant within the cavity, and $\delta()$ is Dirac delta function: $\delta(x) = \infty$ for $x = 0$, $\delta(x) = 0$ for $x \neq 0$

$$\int_{-\infty}^{\infty} \delta(x)dx = 1 \quad (10)$$

We suppose also the case that is the most interesting for accelerator based applications – the particle moves along cavity axis where

$$x = 0, y = 0, z = vt \quad (11)$$

In such assumptions:

$$\frac{d^2 g(t)}{dt^2} + \omega^2 g(t) = \int_0^L \delta(z - vt) qvA(z)dz \quad (12)$$

From here and to the paper end we omit mode indexes that does not lead to ambiguity. It follows from last relation that

$$\frac{d^2 g(t)}{dt^2} + \omega^2 g(t) = J(t), \; J(t) = qvA(vt)\eta(t)\eta(L - vt) \quad (13)$$

were $A(z) = A_z(0,0,z)$ and $\eta()$ is Heaviside step function

$\eta(x) = 1$ for all $x \geq 0$, $\eta(x) = 0$ for all $x < 0$ (14)

The solution of the equation (13) that satisfies initial conditions $g(0) = \dot{g}(0) = 0$ (corresponding equal to zero electric and magnetic components of induced field) can be represented in the form [2]:

$$g(t) = \frac{1}{\omega}\int_0^{L/v} J(\tau)\sin\omega(t-\tau)d\tau = \frac{\sin\omega t}{\omega}J_1 - \frac{\cos\omega t}{\omega}J_2 \quad (14)$$

Here

$$J_1 = \int_0^{L/v} J(\tau)\cos\omega\tau\, d\tau, \quad J_2 = \int_0^{L/v} J(\tau)\sin\omega\tau\, d\tau \quad (15)$$

Note that solution for field amplitude in the form (14) is valid for time interval $t > L/v$.

INDUCED VOLTAGE OVER CAVITY EXTERNAL PARAMETERS

Let us find out probe particle with charge e energy gain after passage of the cavity assuming field amplitude being $g(t) = a\sin(\omega t + \varphi)$, where a is constant. One can derive easily:

$$\mathrm{E}(\varphi) = -e\int \dot{g}(t)A(z)dz = -\frac{ea\omega}{q}\cos\varphi J_1 + \frac{ea\omega}{q}\sin\varphi J_2 \quad (16)$$

Representing rf cavity in the form of equivalent thin gap of zero length (accelerating gap) with applied rf voltage one can conclude that appropriate voltage amplitude U_m is equal to

$$U_m = \frac{\mathrm{E}}{e} = \frac{a\omega}{q}\left(J_1^2 + J_2^2\right)^{1/2} \quad (17)$$

This can be expressed in terms of cavity shunt impedance R and cavity quality factor Q:

$$R = \frac{U_m^2}{P_0}, \; Q_0 = \frac{\omega W}{P_0} \quad (18)$$

where P_0 stands for cavity walls power losses and W is electromagnetic energy stored in the cavity volume.

$$W = \frac{\varepsilon_0}{2}\int_V E_m^2 dV = \frac{a^2\omega^2\varepsilon_0}{2}\int_V A^2(\vec{r})dV \quad (19)$$

Taking into account normalization condition one arrives finally at relations

$$W = \frac{a^2\omega^2}{2}, \; J_1^2 + J_2^2 = \frac{R}{Q_0}\frac{\omega q^2}{2} \quad (20)$$

Let us calculate energy loss for the particle traversing cavity filled with the field induced by previous charge, both radiating charge and probe particle being spaced by time interval equal to period of rf oscillations.

$$\mathrm{E}_{lost} = -ev\int_0^{L/v}\dot{g}(t)A(vt)dt = -ev\int_0^{L/v}\left[\int_0^{L/v} J(\tau)\cos(\omega t - \omega\tau)d\tau\right]A(vt)dt = -\frac{e}{q}\left(J_1^2 + J_2^2\right) \quad (21)$$

Together with last expression this gives

$$\mathrm{E}_{lost} = -\frac{eq\omega}{2}\frac{R}{Q_0} \quad (22)$$

ISBN 978-3-95450-170-0

In terms of thin gap this means that bunch with charge q induces rf voltage of amplitude

$$U = \frac{q\omega}{2}\frac{R}{Q_0} \quad (23)$$

and rf phase π. Furthermore, taking into account field damping we arrive finally to the next expression for rf field, induced by charged bunch on equivalent thin gap

$$U = -\frac{q\omega}{2}\frac{R}{Q_0}\exp(-\omega t/2Q)\cos\omega t \quad (24)$$

Very often, current value I averaged over RF period is used instead of charge value

$$U = -\pi I\frac{R}{Q_0}\exp(-\omega t/2Q)\cos\omega t \quad (25)$$

RF CAVITY COMPLEX SHUNT IMPEDANCE CONCEPT

It follows from (14) that the phase of oscillating depends on two quantities J_1 and J_2, and these two quite different functionals can not be expressed over one quantity. These parameters might be used for detailed description of beam-cavity interaction and the outlook on relation (14) prompts to represent it in the form

$$g(t) = \frac{\sin\omega t}{\omega}J_1 - \frac{\cos\omega t}{\omega}J_2 = \frac{D}{\omega}\left(\sin\omega t\sin\psi - \cos\omega t\cos\psi\right) \quad (26)$$

where

$$D = \sqrt{J_1^2 + J_2^2},\ \sin\psi = \frac{J_1}{D}, \cos\psi = \frac{J_2}{D} \quad (27)$$

and formula takes the form:

$$g(t) = -\frac{D}{\omega}\cos(\omega t + \psi) \quad (28)$$

Thus, the pare of quantities J_1 and J_2 or D and ψ is needed for detailed description of beam-cavity interaction, and this pare, as it followes from formulae written above, might be considered as the real and imaginary parts or the module and the phase of complex quantity:

$$\hat{D} = \mathrm{Re}\,D + i\,\mathrm{Im}\,D = D\exp i\psi \quad (29),$$

where i is imaginary unit. D is expressed over cavity shunt impedance, and finally expression for field amplitude looks like

$$g(t) = -q\sqrt{\frac{R}{2\omega Q_0}}\cos(\omega t + \psi) \quad (30)$$

It is often much more convenient to deal with complex quantities remembering that physical sense has its real part. Then, denoting

$$Z = R\exp(i2\psi)\ , \quad (31)$$

we arrive at relation

$$g(t) = -\mathrm{Re}\,q\sqrt{\frac{Z}{2\omega Q_0}}\exp i\omega t \quad (32)$$

In these notations, it is quite natural to refer to Z as complex shunt impedance. Its module coincides with usual cavity shunt impedance. To establish physical sense its phase let us rewrite expression (16) for energy gain for the probe particle entering a cavity at $t = 0$ using ψ definition:

$$U(\varphi) = \frac{a\omega}{qv}D(-\cos\varphi\sin\psi + \sin\varphi\cos\psi) = \frac{a\omega}{qv}D\sin(\varphi - \psi) \quad (33)$$

Complex cavity shunt impedance can be calculated for any particular mode according formulae above or established experimentally. To measure R and ψ the following experiment has to be done. RF cavity installed on probe beam path is fed with power P. Cavity RF phase is adjusted to have the maximum energy gain U_m at its exit. Appropriate combination (18) of values obtained gives cavity shunt impedance module. Adjusting phase shifter to position corresponding zero energy gain at cavity exit one gets information concerning phase ψ .

CONCLUSION

The concept of complex shunt impedance has been introduced to the problem under attention, and solution for field amplitude had been expressed in terms of this cavity parameter. The physical sense both for the module and the phase as well of complex shunt impedance has been clarified. The first one is simply cavity shunt impedance in widely used sense, while the other fixes the phase at which the probe particle, entering cavity, traverses it without additional energy gain. It had been shown, that complex shunt impedance components can be calculated or measured experimentally.

ACKNOWLEDGMENT

The author dedicates this work to Svetlana Kurakina. For many years this beautiful and very nice woman was the wife and the best friend supporting in all initiatives.

The author is grateful to Dr. Korchuganov from Kurchatov Scientific Center in Moscow for fruitful discussions

REFERENCES

[1] V.M.Lopukchin. Excitation of electromagnetic oscillations and waves by electron flows. .Gostekchizdat, 1953. 324 pp., in Russian.

[2] V.V.Stepanov. Kurs differencialnikch uravneniy, Moscow, KomKniga, 2006. 468 pp., in Russian.

ISBN 978-3-95450-170-0

OUTPUT ENERGY VARIATION IN THE SC LINAC FOR THE PROTON RADIOTHERAPY

I.A. Ashanin, S.M. Polozov, A.V. Samoshin, National Research Nuclear University MEPhI (Moscow Engineering Physics Institute), Moscow, Russia

Abstract

Current success of the superconducting linear accelerators based on independently phased SC cavities gives a seriously reason to consider such structure in proton radiotherapy. Superconductivity allow to solve at once some problems concerned with a low rate of energy gain, high length, higher capacity losses and higher cost of the proton linear accelerator subsequently. One of the traditional aims of such facilities is receiving of the beam energy about 240 MeV with possibility of fluently regulation in range from 150 to 240 MeV that responds to irradiate the tumors located at different depth. The possibility of beam energy variation by means of RF field phase in last resonators and number of the resonator turn-off becomes the major advantage of the proton SC linac.

The optimal choice of accelerator parameters and the beam dynamics simulation results with using BEAMDULAC-SCL code will presented [1]. Methods of the output energy variation with beam quality preservation in the proton SC linac will discussed.

INTRODUCTION

The very high procedure cost caused by accelerator and its engineering systems cost is main factor limiting proton therapy application and ideas to reduce the cost are very actual.

The proton beam basically receives in proton synchrotrons or cyclotrons [2]. The proton beam can be accelerated also in linac but main limitation is a low rate of the energy gain that involves increasing the accelerator length. Superconductivity allows essentially reduce the linac length, that is important by economic and technical aspects. Contemporary progress in SC linacs development allows proposing their using for medical application [3]. Such facilities satisfy to all standard demands for medical using. It's energy of the beam about 240 MeV with fluently regulation, possibility of control of beam envelope up to 6 mm, intensity of the beam not less than 10^9 p/s. Besides SC linacs have some significantly advantages. It's a very high rate of energy gain for the period of the structure that allows reducing the facilities length and low requirement in RF power feeding. Also the possibility of easily beam energy variation by means of a number of the resonator turn-off (deeply variation) or RF field phase in last resonators (slow variation).

Beam focusing can be provided with the help of SC solenoids following each cavity or with the help of RF focusing [4]. Using a solenoid into focusing period will allow to make optimal choice of main accelerator parameters and to provide the transverse and longitudinal beam motion stability.

Beam dynamics simulation directed to produce the fluently tuning of the beam energy in range 150-240 MeV with preserving beam quality will discuss. Such tuning of energy can be realized in the hardware way without use of padding filters by means of voltage change on cavities or of input phase variation in cavities.

GEOMETRIC CHARACHTERISTICS

It is advisable to divide accelerator into several groups, consists of cavities having identical geometry. A slipping of the particles relative to the accelerating wave presents in such SC structure. The slipping value must not exceed an acceptable value. The number of cavities should be limited and the number of groups should be minimal. The geometrical velocity β_g of the RF wave is constant for any group of cavities and the number of such groups in linac should be minimized to reduce the accelerator cost [5].

So in our case the phase slipping factor was limited by 18 %. The accelerator will be divided into four groups of cavities with geometric velocity of cavities β_g = 0.09, 0.18, 0.31 and 0.49 respectively. The first two groups consist of cavities with two accelerating gaps and the third and the fourth would consist of three gap cavities (see Fig. 1).

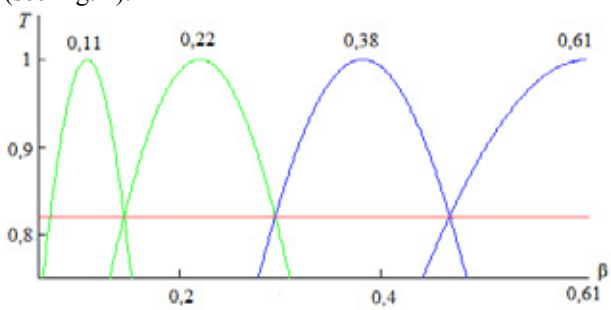

Figure 1: Slipping factor value depending on β.

BEAM DYNAMICS SIMULATION IN POLYHARMONIC FIELD

Beam dynamics simulation results for the last group having the beam energy range from 123.2 to 240 MeV will present below. The electric field amplitude for each cavity is equal 14.20 MV/m, the length of each cavity 0.386 m, the particle phase into RF field -25º and operating frequency f = 702 MHz, magnetic field B = 3 T.

Beam dynamics simulation results in polyharmonic field in the last part are shown in Figure 2.

ISBN 978-3-95450-170-0

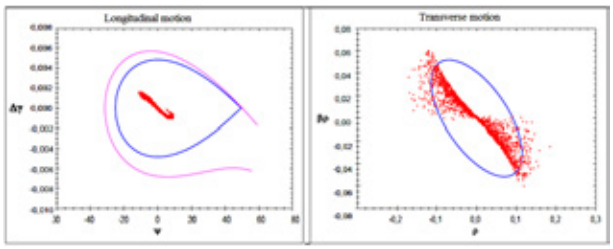

Figure 2: Longitudinal and transverse phase space in the fourth part.

Parameters of all groups of cavities optimized by the same principle are presented in the Table 1.

Table 1: Main accelerator parameters and beam dynamics simulation results

Parameter	Value			
Energy range	1	2	3	4
Injection energy, W_{in}, MeV, (β_{in})	2.4 (0.07c)	10.4 (0.15c)	43.6 (0.29c)	123.2 (0.47c)
Output energy, W_{out}, MeV (β_{out})	10.4 (0.15c)	43.6 (0.29c)	123.2 (0.47c)	240 (0.61c)
Frequency, f, MHz	176	176	352	704
Geometric phase velocity, β_g	0.09	0.18	0.31	0.49
Length of resonator, L_{res}, m	0.184	0.374	0.487	0.386
Phase, φ, °	-25	-25	-25	-25
Electric field amplitude, E, MV/m	3.21	5.96	8.87	14.2
Magnetic field, B, T	1.25	1.7	2.3	3
Number of periods, N_{per}	16	18	22	24
Length, L, m	9.344	13.932	19.514	18.864

OUTPUT ENERGY VARIATION

Different values of energy allow irradiating tumors with various depths. So the energy range 150 – 240 MeV need to irradiate tumors deeper than 15 cm. Basic methods of energy variation are considered below.

The first method concluded in voltage variation on cavities (deeply variation). Some resonators may be turned off to realize this method.

Beam dynamics simulation results in polyharmonic field in the last part varying value of the electric field amplitude at preservation of other parameters, exactly B = 3 T, φ = -25°, f = 702 MHz, N_{per} = 24 are presented below. The electric field amplitude for each cavity is equal 9.84 MV/m, that according to output energy of 200 MeV (β_{out} = 0.57).

Beam dynamics simulation results with set parameters are shown in Figure 3. The transmission efficiency is equal 100%.

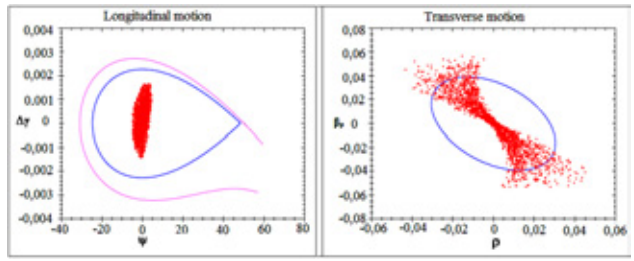

Figure 3: Longitudinal and transverse phase spaces in the fourth part with energy 200 MeV.

Beam dynamics simulation results in case when the electric field amplitude for each cavity is equal 3.34 MV/m, that according to output energy of 150 MeV (β_{out} = 0.51) are shown in Figure 4. The transmission efficiency is equal 100% but the bunch has higher phase space.

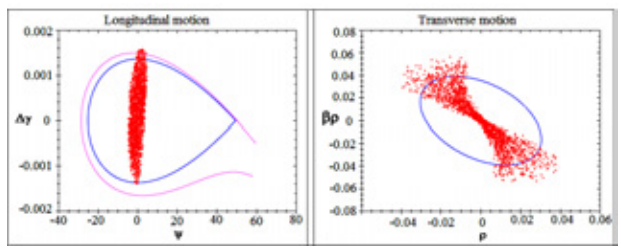

Figure 4: Longitudinal and transverse phase spaces in the fourth part with energy 150 MeV.

By the similar way the beam dynamics simulation was done with over energy values and varying of the corresponding electric field amplitude. Other parameters relating to this method of energy variation with accelerating field amplitude variation are presented in [6].

Note that the beam longitudinal phase volume decrease negligible and transverse emittance changes insignificantly and with the chosen accelerator parameters the beam motion is stable and it is possible to keep a beam quality.

The second way of output energy variation concluded in changing of RF field phase in a number of last resonators (slowly variation).

Beam dynamics simulation in polyharmonic field in the fourth part varying value of RF field phase in last 6 cavities at preservation of other parameters, exactly B = 3 T, E = 14.2 MV/m, f=702 MHz are discussed below.

The particle phase into RF field is equal -45°, than according to output energy of 200 MeV (β_{out} = 0.572). Beam dynamics simulation results in polyharmonic field with these parameters are presented in Figure 5. The transmission efficiency is equal 100%.

Other parameters relating to this method are presented in Table 2.

ISBN 978-3-95450-170-0

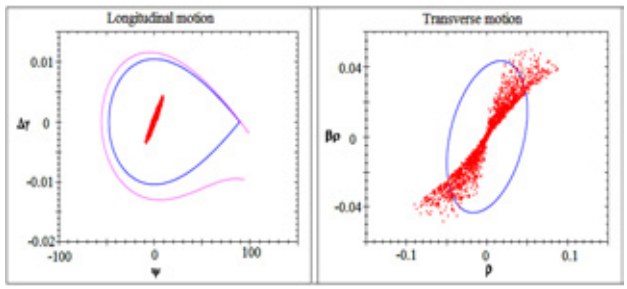

Figure 5: Longitudinal and transverse phase spaces in the fourth part with energy 200 MeV after phase variation.

Table 2: Beam output energy variation versus RF field phase in last 6 resonators

Phase into RF field, φ, °	Output phase velocity, β_{out}	Output energy, W_{out}, MeV
-25	0.605	240
-30	0.596	230
-35	0.588	220
-40	0.579	210
-45	0.572	200

The method to achieve more slowly variation is presented below. It's mean to varying of RF field phase in each cavity in each period in the last group in eligible range. It allows to receive the most exactly values of energy at irradiation of the tumors thus preserving of the beam quality.

Let's we consider the case with N_{per} = 22 and φ = -25 ° according to energy 222 MeV (β_{out} = 0.592), φ = -30 ° to W_{out} = 218 MeV (β_{out} = 0.586) and φ = -35 ° to W_{out} = 214 MeV (β_{out} = 0.582). RF-field phase values range was from -25 ° to -35 ° because at such parameters the most motion stability is provided.

Beam dynamics simulation results in polyharmonic field with φ = -35 ° and W_{out} = 214 MeV are presented in Figure 6. The transmission efficiency is equal 100%.

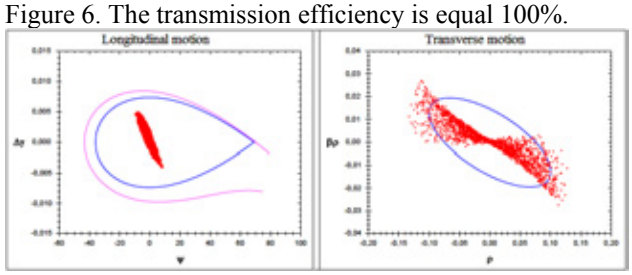

Figure 6: Longitudinal and transverse phase spaces in the fourth part with energy 214 MeV after phase variation.

Further it's possible to reduce the number of turned on resonators to 20 and receive values of energy 212, 208 and 200 MeV according to RF-field phase values φ=-25°, -30 ° and -35 ° respectively and to less values.

Beam dynamics simulation results in polyharmonic field with N_{per} = 20, φ = -35 ° and W_{out} = 200 MeV are presented in Figure 7. The transmission efficiency is equal 100%.

Other parameters relating to this method of energy variation are presented in Table 3. In all cases beam transmission efficiency is equal 100% and only when RF-field phase φ exceeds -45 ° this value decreases to 98-97%, beam motion insignificantly worsens and it can lead to cavities failure.

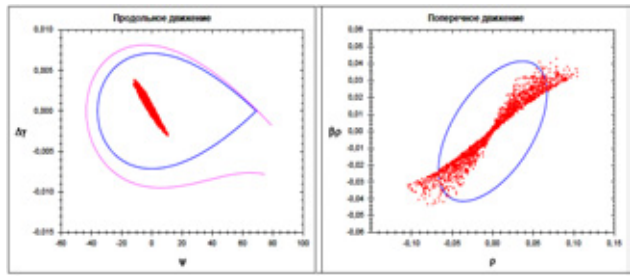

Figure 7: Longitudinal and transverse phase spaces in the fourth part with energy 200 MeV after phase variation.

Table 3: Beam output energy variation with RF field phase in different number of periods

N_{per}	RF-field phase, φ, °	Phase velocity, β_{out}	Output energy, W_{out}, MeV
20	-25	0.580	212
	-30	0.578	208
	-35	0.572	200
18	-25	0.570	198
	-30	0.568	194
	-35	0.562	190
16	-25	0.560	188
	-30	0.558	186
	-35	0.554	182
14	-25	0.550	180
	-30	0.547	177
	-35	0.544	173
12	-25	0.540	170
	-30	0.536	166
	-35	0.533	160

CONCLUSION

Choice of optimal parameters and it's optimization for SC linac structure with energy up to 240 MeV was done. Beam transverse and longitudinal motion stability study was made. Two base methods of the energy variation with beam quality preservation were proposed. The beam quality preservation with energy variation was achieved by correct accelerating system tuning.

REFERENCES

[1] A.V. Samoshin. Proc. of LINAC2012, Tel-Aviv, Israel, TUPB069, p. 630 - 632
[2] Holovkov V.M. Proton and ion radiotherapy: actual status and opportunities. Tomsk. April, 2013.
[3] S.M. Polozov, A.V. Samoshin. Proc. of LINAC'12, pp. 633-635.
[4] E.S. Masunov, A.V. Samoshin, Ion Beam Dynamic Investigation in Superconducting Linac, Atomic Energy 108 (2) (2010), p. 141.
[5] A.V. Samoshin. Proc. of LINAC2012, Tel-Aviv, Israel, TUPB070, p. 633 - 635.
[6] I.A. Ashanin, S.M. Polozov, A.V. Samoshin, Proc. of LINAC2014, Geneva, Switzerland, TUPP103

ISBN 978-3-95450-170-0

LEPTA - THE FACILITY FOR FUNDAMENTAL AND APPLIED RESEARCH

E. Ahmanova, V. Drobin, P. Horodek, I. Meshkov, O. Orlov, A. Rudakov,
V.Seleznev, A.A. Sidorin, S. Yakovenko, JINR, Dubna, Russia
A. Kobets# JINR, Dubna and Institute of Electrophysics and Radiation Technologies, NAS of Ukraine
M. Eseev JINR, Dubna and M.V. Lomonosov Pomor State University, Russia

Abstract

The project of the Low Energy Positron Toroidal Accumulator (LEPTA) is under development at JINR. The LEPTA facility is a small positron storage ring equipped with the electron coolin system. The project positron energy is of 2 – 10 keV. The main goal of the facility is to generate an intense flux of positronium atoms – the bound state of electron and positron.

Storage ring of LEPTA facility was commissioned in September 2004 and is under development up to now. The positron injector has been constructed in 2005 ÷ 2010, and beam transfer channel – in 2011. By the end of August 2011 experiments on injection into the ring of electrons and positrons stored in the trap have been started. The recent results are presented here.

LEPTA RING DEVELOPMENT

The Low Energy Particle Toroidal Accumulator (LEPTA) is designed for studies of particle beam dynamics in a storage ring with longitudinal magnetic field focusing (so called "stellatron"), application of circulating electron beam to electron cooling of antiprotons and ions and positronium in-flight generation.

For the first time a circulating electron beam was obtained in the LEPTA ring in September 2004 [1]. First experience of the LEPTA operation demonstrated main advantage of the focusing system with longitudinal magnetic field: long life-time of the circulating beam of low energy electrons. At average pressure in the ring of 10^{-8} Torr the life-time of 4 keV electron beam of about 170 ms was achieved that is by several orders of magnitude longer than in usual strong focusing system. However, experiments showed a decrease of the beam life-time at increase of electron energy. So, at the beam energy of 10 keV the life time was not longer than 12 ms. The possible reasons of this effect are the magnetic inhomogeneity and resonant behavior of the focusing system.

Diagnostic System Development

Previous PU system was connected to amplifier by using the cable of near 3 meters length. That reduced significantly sensitivity for all system. New amplifier was designed, manufactured and mounted (Fig. 1). It locates directly at connector exits from vacuum chamber. Sensitivity of new system is of 1,1 mV/μA.

#kobets@jinr.ru

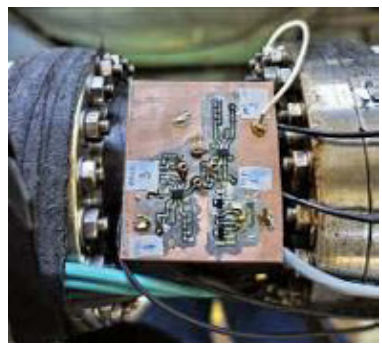

Figure 1: The new PU amplifiers.

For fine tuning of the trajectory and control of circulating positron beam aperture probe based on semiconductor gamma detector has been designed (Fig.2), fabricated, mounted and tested with positrons injected into the ring.

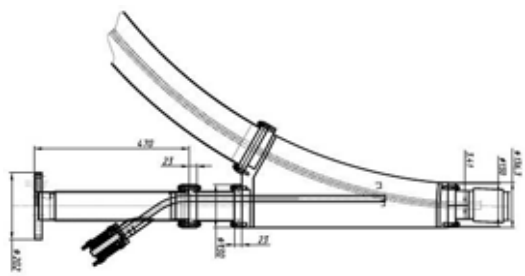

Figure 2: The circulating e^+ beam detector.

THE POSITRON INJECTOR

In summer 2010 the slow positron source and the trap have been assembled. The first attempts of slow positron storage were performed and stored positrons were extracted to the diagnostic collector.

Vacuum System Development

New vacuum chamber for transport channel was manufactured and mounted to minimize losses during injection. Aperture was increased from 3,2 cm to 6,5 cm.

Spectrometric studies were carried out of the residual gas in the trap. As a result, it was found the presence in the vacuum volume of compounds with atomic number of 68-69 (Fig. 3).

ISBN 978-3-95450-170-0

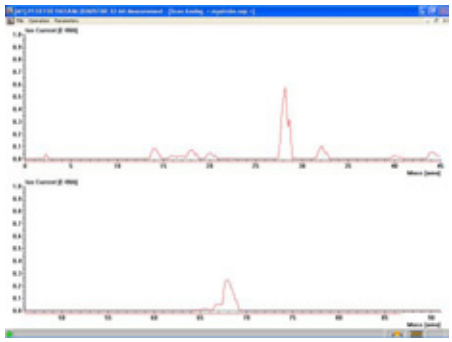

Figure 3: The residual gas spectrum.

For improvement of the vacuum conditios in the storage area the vacuum chamber was disassembled and cleaned. Also instead of Ion Pump (Pos.9 on positron injector picture) was set cryopump VCP160 CF-F. On the opposite side of the trap was installed turbomolecular pump of the capacity of 350 I/s.

e^- Injection and Circulation

Circulation of electron beam accumulated and extracted from the trap was received in March 2013. Electron energy was of 4 keV (Fig. 4).

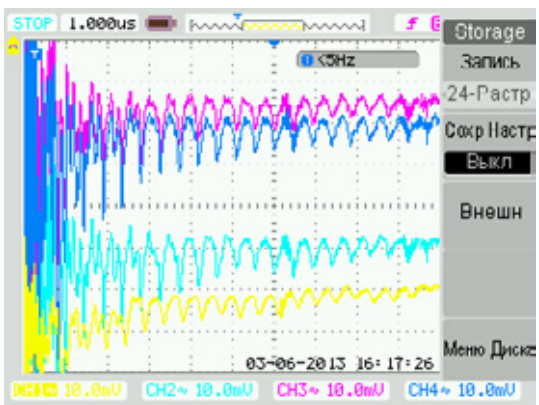

Figure 4: The oscillogram of electron circulation.

e^+ Accumulation and Injection

For tuning of positron trajectory in the ring we have used scintillation counter operated in analog signal mode (Fig.5). The positrons extracted from the trap, passed through the transfer channel and after completion of single turn were deflected to the vacuum chamber wall. Finally, single turn regime of positron extraction/injection has been found. Photoelectron multiplier tube has been calibrated by etalon 22Na source that allows to measure accumulated e+ beam. Its sensitivity is 10^3 e^+/Volt.

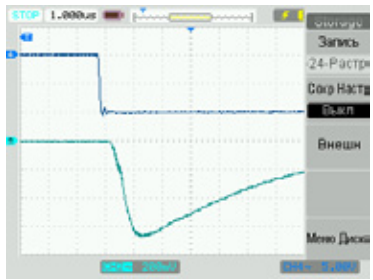

Figure 5: Pulse from photomultiplier tube.

The new generator "rotating wall“ (RW) was installed to improve the accumulation process. As result more accurately measured the size of the accumulated e+ bunch (Fig. 6).

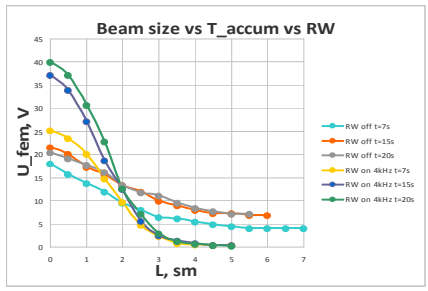

Figure 6: The beam size.

CONCLUDING REMARKS

The development of the LEPTA project is approaching the stage of experiments with circulating positron beam. All main elements of the ring and the injector are ready and have been tested.

All works supported by RFBR grant №12-02-00072.

REFERENCES

[1] A.Kobets, et. al., Status of the LEPTA project, Proc. of COOL'05 AIP Conference Proceedings, 2006, v.821, p.95-102

[2] M. Amoretti et al., The ATHENA antihydrogen apparatus, Nucl. Inst.Meth. Phys. Res. A 518 (2004) 679-711

[3] C.M.Surko, R.G.Greaves, Radial compression and inward transport of positron plasmas using a rotating electric field, Phisics of plasmas, 8 (2001), 1879-1885.

ISBN 978-3-95450-170-0

PROJECT OF ELECTRON COOLER FOR NICA COLLIDER

E. V. Ahmanova, I. N. Meshkov, O. S. Orlov, A. Y. Rudakov, V. I. Shokin, A. A. Sidorin#,
S. L. Yakovenko, JINR, Dubna
A. G. Kobets, Joint Institute for Nuclear Research, Russia, Institute of Electrophysics and Radiation Technologies, NAS of Ukraine
M. P. Kokurkin, N. Y. Lysov, M. M. Pashin, All-Russian Lenin Electrotechnical Institute, Moscow

Abstract

Electron cooling system (ECS) of the NICA collider is designed to form the required parameters of the ion beam at energy of the experiment in the range of 1 - 4.5 GeV/amu that requires energy cooling electrons from 0.5 to 2.5 MeV. To achieve the required energy of the electrons all elements of ECS are placed in tanks filled with sulfur hexafluoride (SF_6) under pressure of 6 atm. For testing items ECS elements the test bench "Recuperator" is used . This paper presents the results of testing the prototype elements of the ECS and the first results of technical design of ECS.

ELECTRON COOLING SYSTEM OF THE NICA COLLIDER

High voltage elements must be placed in three tanks due to the requirements to ECS parameters (Fig. 1). ECS NICA collider has two independent electron beams. Therefore tanks 1 and 3 (Fig. 1, 2) contain a devices for generating and formation of electron beams, the acceleration of the electrons, and after passing through the cooling section, deceleration of the electrons and their energy recuperation. Tank 2 (Fig. 2) contains a high-voltage generator voltage up to 2.5 MW. Inside tanks 1 and 3 are placed solenoids of the superconducting magnetic system (the field up to 2 kGs) for transporting electron beams, so the material for these tanks could be a magnetic steel that allows using the tanks walls as magnetic shield for magnetic flux "return". All three tanks are filled with the insulating gas SF6 («sulfur hexafluoride") under pressure of 6 atm.

Electrons of the two beams are accelerated by electrostatic voltage in a longitudinal magnetic field and when get the necessary energy transported in a longitudinal magnetic field into the cooling section (Fig. 3). In this part of the trajectory electrons and ions circulating in the collider ring, are merged.

Table 1: Parameters of ECS for NICA.

Parameter	Value
Electron energy, MeV	0,5 - 2,5
Electron beam current, A	0,1 - 1
Electron beam diameter, mm	10 - 20
Magnetic field of SC solenoids, T	0,1 – 0,2
Relative current losses at recuperation	3×10^{-4}
Elegas (FS_6) pressure, bar	6

sidorinalexsey@gmail.com

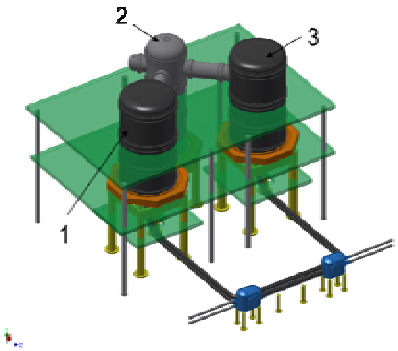

Figure 1: Scheme 1,3 - acceleration tanks, 2 - tank of the high-voltage generator.

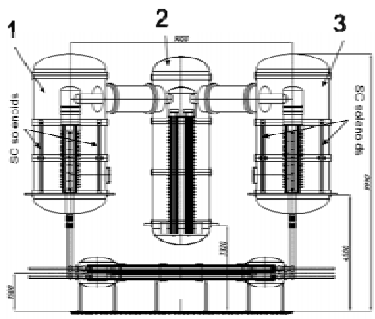

Figure 2: Tanks 1,3 - acceleration tanks, 2 - tank of the high-voltage generator.

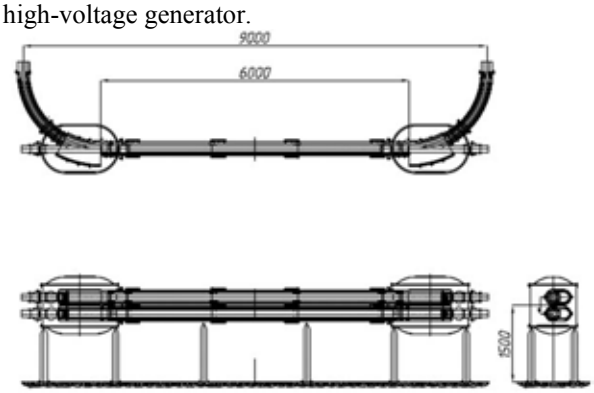

Figure 3: Transportation and cooling sections.

TEST BENCH "RECUPERATOR" AND PROTOTYPING ECS

Test bench "Recuperator" (Fig. 4, 5 and Table 2) is a model of the electron cooling system. It has linear vacuum chamber of a length of about 4 m and a diameter of 10 to 30 cm, immersed in a longitudinal magnetic field

ISBN 978-3-95450-170-0

from 0.3 to 0.6 kGs. The electron beam is generated by an electron gun of variable perveances. Electrons pass drift section (model of the cooling section) and enters the electron collector whose potential is of 1-2 kV (Fig. 4) higher than the potential of the gun cathode (electron energy recuperation mode).

The cooling water system for the collector cooling was designed, assembled and tested. It consists of a water tank, two radiators and the pump driving water inside the system. Water circulates through collector, the connecting hoses and two radiators (connected in series), where it is cooled. Test had shown efficiency of the system sufficient for cooling the collector at the power of the recuperating beam up to 0.5 kW.

Table 2: Main Parameters of the Test Bench "Recuperator".

Parameter	Value
Electron energy, keV	up to 4
Beam current, mA	up to 400
Cathode diameter, mm	10
Residual gas pressure, Torr	2×10^{-3}
Magnetic field, Gs	up to 400

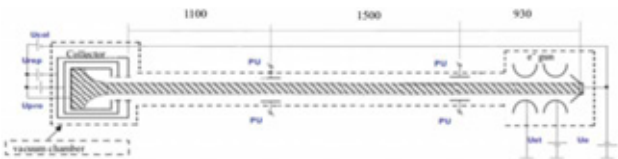

Figure 4: Scheme of test bench "Recuperator".

Figure 5: Test bench "Recuperator".

DESIGN PROJECT OF THE NICA ECS

The first concept NICA ECS has been developed jointly by JINR and All-Russian Electrotechnical Institute (VEI, Moscow) on the basis of the voltage generator of the Dynamitron type. Its maximum DC voltage is of 2.5 MV and current of 1 mA (sufficient in recuperation regime).

In each of the **two acceleration tanks** of high-voltage accelerator – recuperator are placed two accelerating structures of the seven high-voltage sections each one of a total length of 2.14 m. They are placed vertically (Fig. 1, 2). In the upper part of the accelerating structure on the magnetic screen which maintained by four columns of the sections of insulators are mounted electron gun and a water-cooled collector, both covered by electrostatic screen.

The main peculiarity of ECS design is application of **superconducting solenoids (SC)** placed inside acceleration tanks under pressure of 6 atm. Such solution allows to reduce significantly the tank diameter and magnetic steel. The value of the saturation field for the material of the tank walls is chosen of 1.5 T. The diameter of SC solenoid cryostat is of 2370 mm that gives the tanks' wall thickness is of 67mm. The tank height is of 2.8 m and the weight of each accelerator tank is of 40 t.

Tank of the high-voltage generator has an internal diameter of 2.3 m and height of 7.3 m. In the tank are placed three assembly of capacitors in the form of vertical columns which are positioned around the supporting tube of a dielectric material and rest on the lower mounting platform inside the tank. Columns of capacitors are surrounded by metallic guard rings, which are having outer diameter of 1200 mm. Two transformers and two electric motors of capacity of 5 kW equipped with reducers are placed at the bottom of the tank. Electric motors are intended to drive two generators located on the upper platform of the tank under high potential and connected with motors mechanically by shafts of a dielectric material (glass-reinforced plastic) and rotating inside the tubes serving as support for capacitor columns. Auxiliary equipment powering electron gun and collector, vacuum pumps and other devices are also located on the upper platform of the generator tank within the high voltage accelerators tanks. Power/voltage transmission lines connecting the high-voltage generator tank with accelerator tanks by two high voltage feed-through which inner tubes are used as electrostatic screen for low voltage supplying electric power to guns and collectors.

Two beam transfer lines are equipped with SC solenoids as well, which have straight and toroidal sections (Fig.3). The last ones have curvature radius of 1.5m. The solenoids transport electrons from the acceleration tube exit through cooling section and to the entrance of deceleration tube. Each SC solenoid is placed inside own cryostat. The total length of each transfer line is of 12m.

Cooling section located in the Collider tunnel has length of 6 m. It consists of two vacuum cryostats of dimensions of 1500x900x1200 (h) mm which contain SC magnetic coils and magnetic shields, correctors for steering electron beams and pick-up stations for positioning both electron and ion beams.

ELECTRON BEAM RECUPERATION EXPERIMENT

To reduce losses in the recuperation process has been put forward the idea of using a contrary magnetic field on the back wall of the collector. In our tests, to generate the magnetic field has been proposed to use permanent magnets. Calculations and simulations of magnetic fields

ISBN 978-3-95450-170-0

in the collector for the NICA was done. Simulation was made for two versions: without (Fig. 6a) and with magnets (Fig. 6b). In simulation, primary electron energy 60 keV, collector voltage was -58 kV, beam current was 1 A, magnetic field was 1 kGs and magnets had field of 100 Gs.

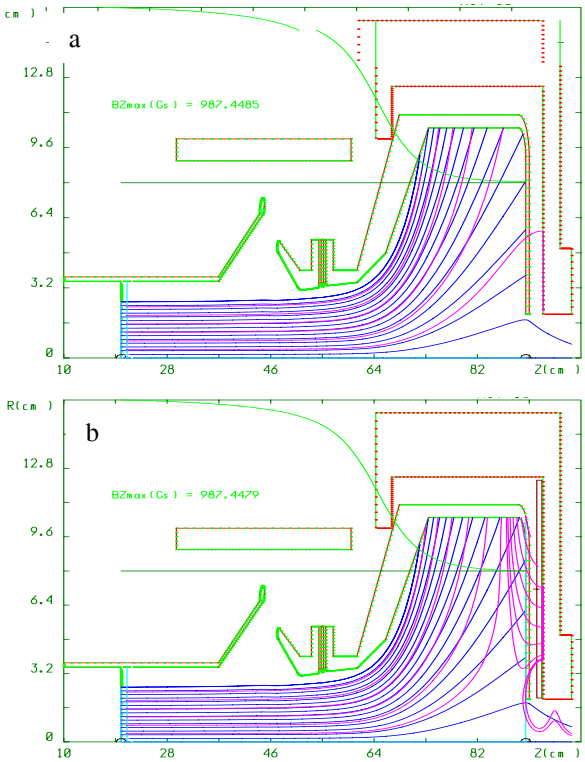

Figure 6: Distribution of magnetic field and primary electron trajectories in collector without(a) and with(b) permanent magnets.

Results were obtained with weak test magnets and experiments have shown that the magnets decrease the collector losses (Fig. 7, 8). It means that experiments with more powerful magnets are needed. Full current was bigger at maximum electron energy (what we can obtain) but losses were bigger too (Fig. 7, 8). Maximum current was obtained 330 mA at electron energy of 3.5 keV, collector potential relatively to cathode was of 1.22 kV and losses were $3.6 \cdot 10^{-4}$.

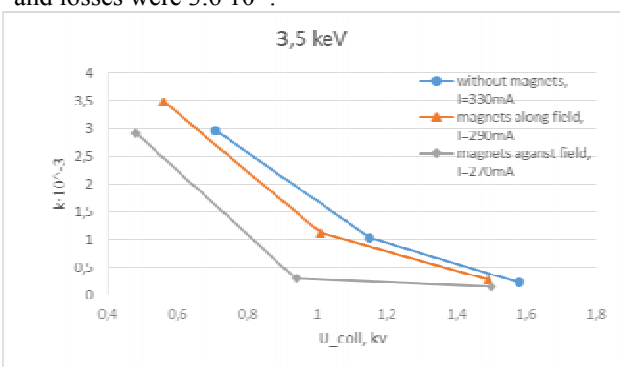

Figure 7: Losses versus collector voltage at different magnets` position.

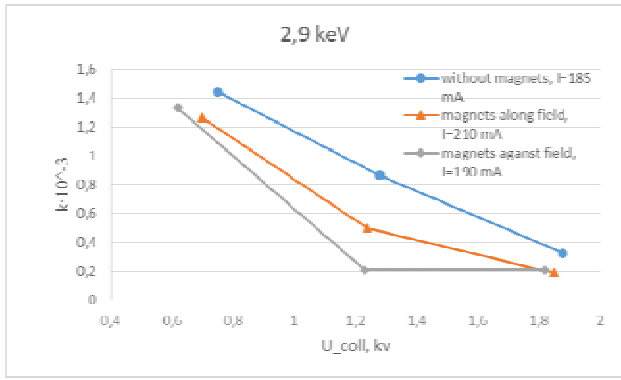

Figure 8: Losses versus collector voltage at different magnets` position.

CONCLUSION

Project Status:

- technical design ECS for NICA Collider is in a progress;
- test experiment on electron recuperation at the test bench “Recuperator” is in active stage of research;
- conceptual project of HV generator is completed by group of All-Russian Electrotechnical Institute (Moscow) ;
- preliminary agreement is achieved on fabrication of high pressure tanks - with Geliymash company (Moscow) and on
- procurement of equipment for SF6 gas system of ECS– with DILO company (Germany).

Commissioning of startup version of NICA is planned for 2019.

In nearest future we plan to develop at the test bench “Recuperator":

- the electron gun with the adiabatic optics and dispenser cathode of diameter of 50mm;
- the electron collector of high recuperation efficiency;
- a stable DC electron beam with a current up to 1 Amp at high recuperation efficiency.

All works supported by RFBR, grant №12-02-00072a.

ISBN 978-3-95450-170-0

ACCELERATION OF THE OPPOSSITELY CHARGED PARTICLES IN THE SINGLE STREAM

A.S.Chikhachev, All-Russian Electrotechnical Institute, Moscow, Russia

Abstract

One of the problems arising at extraction of heavy ions from plasma is removal of electrons from a stream of particles. Therefore possibility of simultaneous acceleration in one direction as ions (electric field), and electrons (pressure gradient) is represented rather interesting. In work when using the hydrodynamic description in the accelerating interval conditions of cold ions and hot electrons are studied. Possibility of excess by ions of speed of an ionic sound is shown, and the ratio of sizes of streams of electrons and ions can be any.

INTRODUCTION

In work [1] acceleration of heavy ions in the presence of a counter flow of electrons was studied. Thus streams of charged particles were considered equal in size. We will note, however, that flows oppositely charged particles can be accelerated in one direction if electrons except force from electric field are affected by rather big force caused by pressure gradient.

MAXWELLIAN DISTRIBUTION OF THE ELECTRONS

Let at there is a source of electrons at $x = 0$ and once ionized ions, and potential $\phi(x)|_{x=0} = \phi_0$. Ions are considered cold, that is $T_i \to 0$ and them only force affects, from electric field, electrons, except a field pressure gradient ΔP works. In the stationary mode of the equation, describing system, have an appearance:

$$M\frac{\upsilon^2}{2} = -e\phi + M\frac{\upsilon_0^2}{2}, \tag{1}$$

$$m\upsilon_e\frac{d\upsilon_e}{dx} = e\frac{d\phi}{dx} - \frac{1}{n_e}\frac{dP}{dx}. \tag{2}$$

Here M - the mass of an ion, m - the mass of an electron, υ_i, υ_e - speeds of ions and electrons, respectively,υ_0 - the initial speed of ions, P - pressure of electronic gas. In an isothermal case,$P = nT, T \equiv const$ - temperature of electronic gas. The equation (2) can be integrated:

$$m\frac{\upsilon_e(x)^2}{2} - e\phi(x) + T\ln\frac{n_e(x)}{n_*} = 0, \tag{3}$$

where n_* - any constant, dimensional density. We will put that there is a stream of ions Γ and a stream of electrons $\Gamma_e = g\Gamma$. Then follows from the equations of a continuity $\upsilon_e = \frac{g\Gamma}{n_e}$ and $\upsilon_i = \frac{\Gamma}{n_i}$. We will designate $\frac{e\phi}{T} = \varphi$ and will set entry conditions: at $x = 0 n_e = n_i = n_0, \varphi = \varphi_0$ Then $\Gamma = n_0\upsilon_0$, where υ_0 - the speed of ions at x =0. From (3) follows: $\varphi - \varphi_0 = \ln\left(\frac{n_e}{n_0}\right) - \frac{\upsilon g^2}{M}\frac{\upsilon_0^2}{2\upsilon_s^2}\left(1 - \frac{n_0^2}{n_e^2}\right)$. Poisson's equation has an appearance:

$$\frac{d^2\phi}{dx^2} = 4\pi(n_i - n_e). \tag{4}$$

Using the expression for potential following from (3), we will receive from (4) equation containing only density of electrons. Passing to dimensionless variables $y = \frac{x}{\lambda}, \lambda^2 = \frac{T}{8\pi e^2 n_0}, \eta = \frac{n_e}{n_0}$ and having designated $a = \frac{m}{M}\frac{\upsilon_0^2}{\upsilon_s^2}g^2, S(\eta) = 1 - 2\frac{\upsilon_s^2}{\upsilon_0^2}\left(\ln\eta + a\frac{\upsilon_s^2}{\upsilon_0^2}\right)$, we will receive:

$$2\frac{d}{dy}\left[\frac{1}{y}\frac{d\eta}{dy}\left(1 - \frac{a}{\eta^2}\right)\right] = \eta - \frac{1}{\sqrt{S(y)}}. \tag{5}$$

Speed of a stream of ions from the above-stated expressions is defined as $\upsilon_i = \upsilon_0\sqrt{S(\eta)}$. The equation (5) has integral of the following look:

$$\left[\frac{1}{\eta}\frac{d\eta}{dy}\left(1 - \frac{a}{\eta^2}\right)\right]^2 = C_0 + \left(\frac{a}{\eta} + \eta\right) + \\ + \frac{\upsilon_0^2}{\upsilon_s^2}\sqrt{1 - 2\frac{\upsilon_0^2}{\upsilon_s^2}\left(\ln\eta + \frac{a}{2\eta^2}\right) + a\frac{\upsilon_0^2}{\upsilon_s^2}}. \tag{6}$$

At a zero stream of electrons (i.e. at $g = 0$) the integral (7) passes into the integral used in [2] for studying of criterion Bohms. The system of the equations describing particles a field according to definition [2], is the Hamilton, having integral system of the equations. This property remains and for more difficult case in the presence of nonzero stream of electrons. We will enter a new variable:$\eta = \exp(-z)$ also we will construct dependence

$$q(z) = a\exp(z) + \exp(-z) + \\ + \frac{\upsilon_0^2}{\upsilon_s^2}\sqrt{1 - 2\frac{\upsilon_s^2}{\upsilon_0^2}\left(-z + \frac{a}{2}\exp(2z)\right) + a\frac{\upsilon_s^2}{\upsilon_0^2}}.$$

At $a = 10^{-6}, \upsilon_0 = 0.1\upsilon_s$ this dependence has the appearance represented in fig. 1. The phase trajectory, the equation for which follows from (5):

$$\frac{dz}{dy} = \frac{\sqrt{C_0 + q(z)}}{|1 - 10^{-6}\exp(2z(y))|}, \tag{7}$$

at $C_0 = -0.2935$, it is represented in fig. 2. We will note that value of a constant C_0 is chosen we conceal in a way that the phase trajectory concerned an axis $\dot{z} = 0$. If $C_0 < -0.2935$, the phase trajectory breaks up to two

ISBN 978-3-95450-170-0

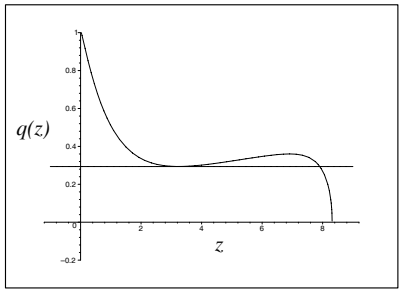

Figure 1: Dependence $q(z)$ at $a = 10^{-6}, \upsilon_0 = 0.1\upsilon_s$.

not connected areas that doesn't allow to translate a stream from small speeds to rather big. At the chosen value C_0 the initial field is minimum.

We will bring, further dependence $z(y)$, following from the decision (7) under a condition $z(0) = 0$. Because of existence of feature in the equation (5) dependence finds a characteristic break a rupture of a derivative. In compliance with this dependence density of electrons $n_e = n_0 \exp(-z)$ very quickly exponential decreases with growth of value of coordinate.

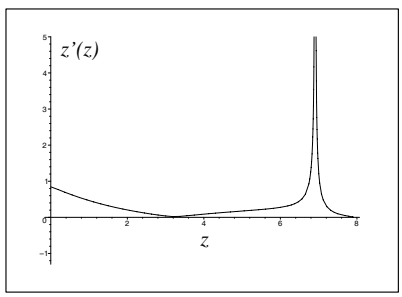

Figure 2: The phase trajectory $z'(z)$ at $C_0 = -0.2935$.

We will provide the schedule of the dependence $u(y) = \frac{\upsilon_i}{\upsilon_s} = 0.1\sqrt{S(\eta(y))}$, determining the speed of a stream of ions (fig. 3). Existence of a break at $y \approx 60$ is also explained by feature in (5) at $z \approx 8$. In this point the stream speed relation to the speed of a sound maximum and equally, i.e. the speed of a stream of ions by ≈ 3.5 times exceeds ion-sound speed.

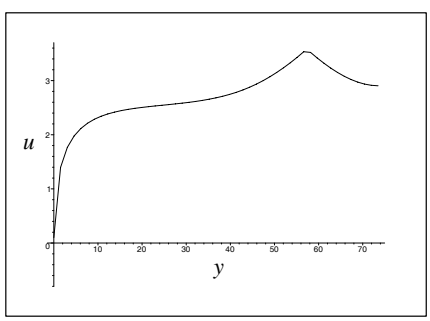

Figure 3: Dependence of ion velocity from coordinate.

We will note importance of creation of certain entry conditions for streams of particles here. Size g is the relation of initial speeds and is defined by entry conditions. Parameter a meets a condition $a << 1$ in wide area of parameters, including at $g = 1$, i.e. at equality of streams of ions and electrons. Thus, it is shown that perhaps simultaneous acceleration of ions and electrons in a flat interval ions electric field, and electrons pressure gradient at rather big difference of electronic density, and the speed of ions can surpass ion-sound speed.

ADIABATIC DISTRIBUTION OF THE ELECTRONS

Unlike the previous section, we will consider the cold ions and electrons which are characterized by adiabatic distribution here. In work [2] acceleration of heavy ions at counter flows of ions and electrons was studied, and electrons were characterized by the isothermal equation of a state $P = n_e T$, where p - pressure,T - temperature of electrons,n_e - density of electrons. In the section states with the electrons characterized by the adiabatic equation of a state will be considered, considering that streams of particles coincide in size and the direction. We will consider electrons as the one-nuclear ideal gas described by the state equation:

$$P = Cn_e^{\gamma}. \tag{8}$$

where γ - an adiabatic curve indicator. For one-nuclear gas $\gamma = 5/3$. It is convenient to Constant Still there are fair equations (1), (2) and (4), and instead of (3) will receive:

$$\frac{m\upsilon_e^2}{2} - e\varphi + T_0\left[\left(\frac{n_e}{n_0}\right)^{\gamma-1} - \kappa\right] = 0. \tag{9}$$

In (9) size κT_0 is an integration constant. From the equations (1), (2), (4) and (9) we will receive at $\upsilon_0 = 0$ and at equality of streams of ions and electrons:

$$\frac{e}{T}\frac{d^2\varphi}{dx^2} = y - \sqrt{\frac{M}{2m}}\frac{1}{\sqrt{\kappa - \left(\frac{y}{y_0}\right)^{\gamma-1} - \frac{1}{2y^2}}}. \tag{10}$$

Substituting $\frac{e\varphi}{T_0}$ from (9) we come to the equation wich has the integral similar (7):

$$\left[\frac{dy}{dx}\left(\frac{1}{y^2} - \frac{\gamma-1}{y_0}\left(\frac{y}{y_0}\right)^{\gamma-2}\right)\right]^2 = C_* + \left(\frac{1}{y} - \frac{\gamma-1}{\gamma}\left(\frac{y}{y_0}\right)^{\gamma}\right) + \sqrt{\frac{2M}{m}}\sqrt{\kappa - \left(\frac{y}{y_0}\right)^{\gamma-1} - \frac{1}{3y^2}}. \tag{11}$$

We will solve further (11) considering $\gamma = 5/3, y_0 = 10, \kappa = 1$, and assuming that $\sqrt{\frac{2M}{m}} \approx 697$, i.e. considering plasma of once ionized xenon. We will study behavior

ISBN 978-3-95450-170-0

of the right member of equation (11) at these values of parameters and at $C_* = 0$. Fig. 4. shows behavior of function $G(y)$:

$$G(y) = \frac{\sqrt{F(y)}}{\frac{1}{y^2} - \frac{\gamma-1}{y_0}\left(\frac{y}{y_0}\right)^{\gamma-1}},$$

where $F(y) = \left(\frac{1}{y} - \frac{\gamma-1}{\gamma}\left(\frac{y}{y_0}\right)^{\gamma}\right) + \sqrt{\frac{2M}{m}}\sqrt{\kappa - \left(\frac{y}{y_0}\right)^{\gamma-1} - \frac{1}{3y^2}}$.

From drawing it is possible to see that in the equation (11) there is a gap at $y \approx 2.1$,, and y decreases from size $y = 9.92$.

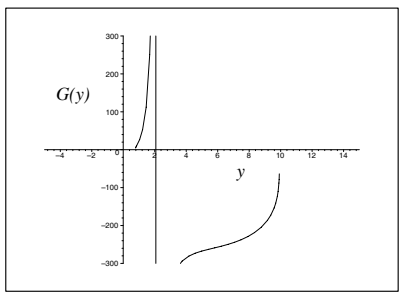

Figure 4: Dependence $G(y)$ at $C_* = 0$.

Fig. 5 shows the solution of the equation (11) with initial value. The curve of I shows behavior of electronic density, and the curve of II represents 10^{-3} density of ions. The gradient of pressure accelerates electrons in the same direction in which electric field accelerates ions. The size of a gradient of pressure is sufficient to exceed the slowing-down force from electric field. Density of ions in all interval significantly exceeds electrons.

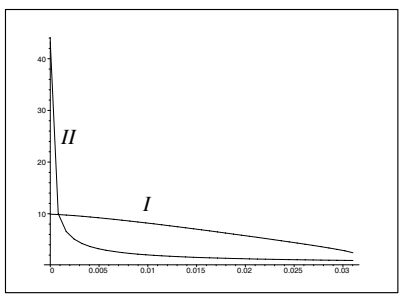

Figure 5: Dependence of the electron density from coordinate (I) and ion density$\times 10^{-3}$ from coordinate (II).

According to an equation of a state of ideal gas temperature of an electronic stream is function of coordinate: $T_e = T_0\frac{\gamma-1}{\gamma}\left(\frac{y(x)}{y_0}\right)^{\gamma-1}$. Speed of an ionic stream is defined by expression:

$$v_i(x) = \sqrt{\frac{2T_0}{M}}\sqrt{1 - \left(\frac{y(x)}{y_0}\right)^{2/3} - \frac{1}{2y(x)^2}}$$

For comparison of ion-sound speed with the speed of an ionic stream in Fig.6 dependences $v_i(x)\sqrt{\frac{M}{2T_0}}$ (a curve of I) and $\sqrt{\frac{T_e}{T_0}}$ are shown (a curve of II). Speed of an ionic stream grows and reaches ion-sound speed at the end of an accelerating interval.

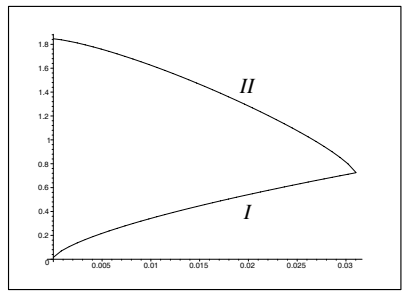

Figure 6: Dependence of the ion speed and temperature from coordinate.

CONCLUSION

Thus, it is shown that, both in case of isothermal distribution and in case of the electrons described by adiabatical distribution perhaps simultaneous acceleration of streams of particles of an opposite sign of a charge in one direction. The described problems were studied in works [3], [4] earlier.

REFERENCES

[1] 1. Yu.A.Kovalenko, T. V. Chernyshev, A. S. Chikhachev, News of the Russian Academy of Sciences, Energy drink series, 2011, No. 4, page 24-28

[2] 2.N.Sternberg, V. Godyak//IEEE Transaction on Plasma Science, Vol. 35, No 5. October 2007.

[3] 3. Yu.A.Kovalenko, T. V. Chernyshev, A. S. Chikhachev, ZhTF, 2013, T.83, No. 4, page 142-145.

[4] 4.A.S.Chikhachev, Journal of Modern Physics, 2011, 2, 1550-1552

ISBN 978-3-95450-170-0

ELECTRODES FORM OPTIMIZATION OF RF DEFLECTING SYSTEM WOBBLER FOR FAIR PROJECT

A. Sitnikov, T. Kulevoy, S. Vysotskiy, A. Golubev, FSBI SSC RF ITEP, Moscow, Russia

Abstract

The new method for high energy density states in matter investigation, which based on irradiation of combined target by hollow high energy heavy ion beam was proposed in the Institute for theoretical and experimental physics (ITEP). The target consists of a sample of matter at the center and a hollow shell around it [1]. The experiment of high energy density states generation will be carry on at FAIR project. The RF deflecting system (Wobbler) for hollow high energy heavy ion U_{238}^{28+} beam with kinetic energy W_k = 1 GeV/n formation is developing at ITEP [2].

The current results of electrodes form optimization for RF deflecting system (Wobbler) which is developing at ITEP for FAIR project are shown in this paper.

INTRODUCTION

The electrodes form of RF deflecting system influence to homogeneity heavy ions U_{238}^{28+} beam with kinetic energy W_k = 1 GeV/n deflection was investigated. The deflecting system developed for ITEP TWAC project was taken as basis [3]. The length of deflecting cell could be defined by $D = \beta\lambda/2$, where D – cell`s length, $\beta$ – relative speed of particles, $\lambda$ – wavelength of RF electromagnetic field. According to that, for particles with kinetic energy $W_k$ = 1 GeV/n and resonant frequency $f_0$ = 352 MHz the cell`s length should equal to D = 373 mm.

RESULTS

The model of one deflecting cell for FAIR project is presented on Fig. 1. In order to increase self quality factor of the deflecting cavity the area of the electrodes stems was increased [4] as well as electrodes deflecting plates form was also changed (compared to cavity developed for ITEP TWAC project).

The method of electrodes form optimization was the same as it described in [5]. During electrodes form optimization the width of plate (EW parameter) as well as height (EH parameter) of edges were varied.

According to electrodes form optimization it was found that particles deflection homogeneity not better than 1.9% at EH = 6 mm; at EH = 10 mm and 12 mm deflection homogeneity was equal to 1.1% and 1% correspondently. The particles deflection homogeneity equaled to 0.9% was achieved at EH = 8 mm and EW = 130 mm (see Fig. 2). The cavity`s self quality factor was also increased to Q_0 = 20000 which on 30% greater than Q_0-factor of the deflecting cavity for ITEP TWAC project.

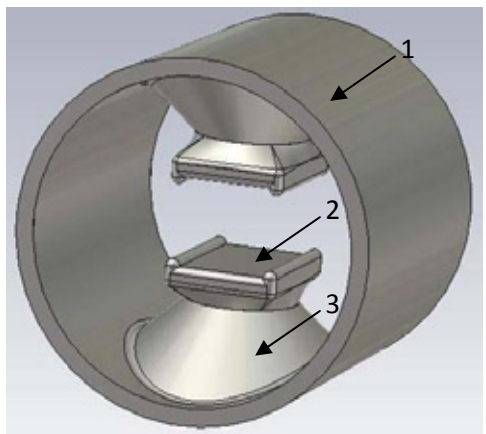

Figure 1. The model of one deflecting cell, where 1 – cavity`s shell; 2 – electrode; 3 – electrode`s stem.

The maximum intensity of the electric field on electrodes surface (E_{max}) is located on plates edges and greater than the maximum electric field intensity at axis (E_0) up to E_{max}/E_0 ≈3.7 times. The typical electric field distribution on the electrodes surface is presented on Fig. 3. In order to reduce the maximum electric field intensity on the electrodes surface the electrodes edges was rounded (see Fig. 4) [6]. From Fig. 4 one can see that E_{max}/E_0 has a sharp increasing up to ≈ 4.4 at rounding radius El_R = 5 mm. The following increasing of El_R parameter leads to decreasing E_{max}/E_0 as well as worsening a particles homogeneity deflection (see Fig. 5). The cavity`s self quality factor Q_0 vs. El_R is presented on Fig. 6.

ISBN 978-3-95450-170-0

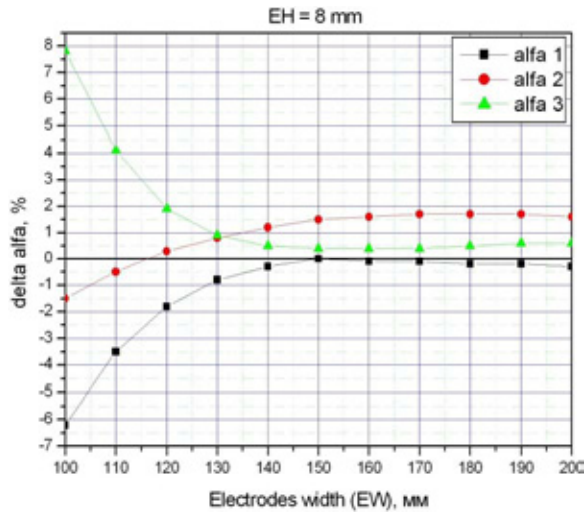

Figure 2. The dependence of deflecting homogeneity on electrodes geometrical sizes. (the angle number corresponds to [5]).

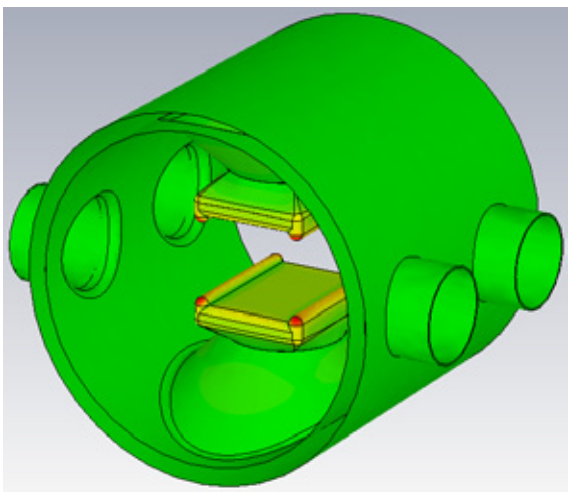

Figure 3. The electric field intensity on electrodes surface.

According to results presented on Fig. 2, 4-6 the following parameters of the deflecting cavity were chosen: the cell length D – 373 mm; the cell diameter – 368 mm; the width of deflecting electrodes EW – 130 mm; the height of electrodes edges EH – 8 mm; the rounding radius of electrodes edges El_R – 15 mm. The particles deflection homogeneity at this parameters of the cavity is equaled to $\delta\alpha$ = 1.1%, the self quality factor Q_0 = 20700 and E_{max} / E_0 = 3.1.

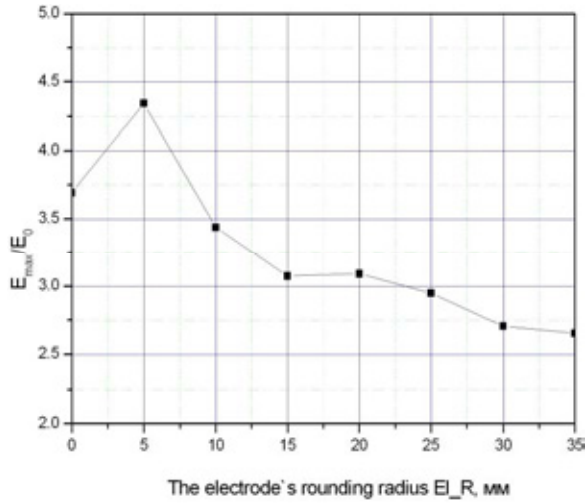

Figure 4. The dependence of E_{max} / E_0 on electrode`s rounding radius.

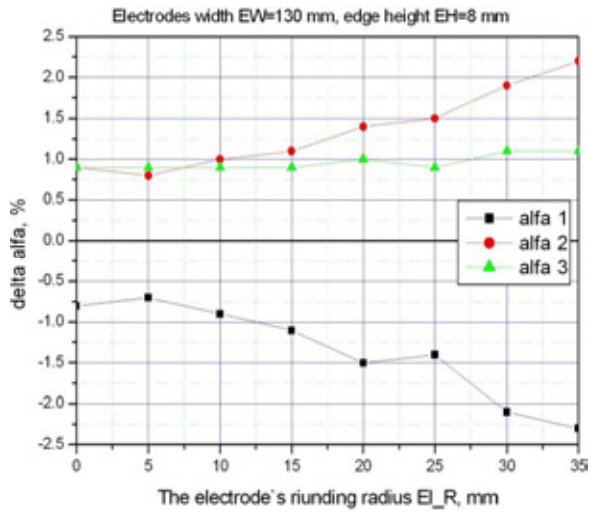

Figure 5. The dependence of deflecting homogeneity on electrode`s rounding radius El_R.

According to particle dynamics simulation the maximum intensity of the deflecting electric field at the axis should equal to E_0 = 10 MV/m, the cavity should be feeding by RF power P = 403 kW/cell. The maximum intensity of the electric field on the electrodes surface in this case will be lower than 31 MV/m. It equals to ≈ 1.6 $E_{кл}$, where $E_{кл}$ – intensity of the electric field by Kilpatrick criteria and equals to $E_{кл}$ ≈ 19 MV/m [7] at frequency f_0 = 352 MHz.

ISBN 978-3-95450-170-0

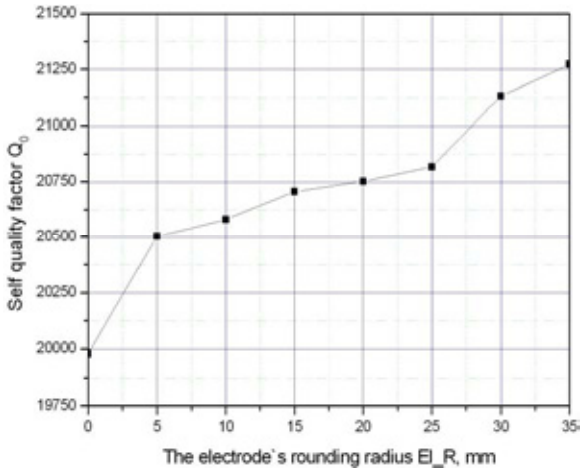

Figure 6. The dependence of self quality factor Q_0 on electrode`s rounding radius El_R.

CONCLUSION

The electrodes form optimization of the deflecting cavity for FAIR project LAPLAS experiment was carried out. The new form of deflecting electrodes which provide the particles deflection homogeneity not worse than 1.1% was found. Also this electrodes form increases the self quality factor up to 20700 as well as decreases the intensity of the electric field on electrodes surface to $E_{max} / E_0 = 3.1$.

REFERENCE

[1] Prospects of heavy ion fusion in cylindrical geometry, Basko M.M., Churazov M.D., Aksenov A.G., Laser and Particle Beams, 20, 2002;
[2] S. Minaev, et al., Nucl. Instr. and Meth. A (2010);
[3] Introduction of radio-frequency power into the cell of a former of a high-energy beam heavy ion beam , A.L. Sitnikov, V.G. Kuz'michev, A.A. Golubev, A.M. Kozodaev, Yu.B. Stasevich, T.V. Kulevoi, S.A. Minaev, YFEN, 2011, vol 2, № 4, pp. 355–358;
[4] Private communication with Dr. V.V. Paramonov, Institute for Nuclear Research RAS, Troitsk, Moscow, Russia;
[5] Formation of a quasi-hollow beam of high-energy heavy ions using a multicell resonance RF deflector, S. A. Minaev, A.L. Sitnikov, A.A. Golubev, T.V. Kulevoy, Technical Physics, 2012, Vol. 57, No. 9, pp. 1251–1256.;
[6] Private communication with Dr. A.A. Kolomiets, Institute for Theoretical and Experimental Physics, Moscow, Russia;
[7] Issledovanie vozmozhnosti sozdaniya nachal`noi chasti uskoritelya (NCHU) nepreryvnogo rezhima na energiu 5 MeV, report, V.A. Teplyakov;

ISBN 978-3-95450-170-0

THE FIRST DESIGN OF MEDIUM RESOLUTION MASS SPECTROMETER (MRMS) HIGH VOLTAGE PLATFORM IN A SPES PROJECT

S. Andrianov, ITEP, Moscow, Russia
M.F.Moisio, C.Roncolato, LNL, Legnaro, Italy

Abstract

A new project of 130 kV high voltage platform (HVP) is developed in a Laboratori Nazionali di Lagnaro as part of SPES (Selective Production of Exotic Species) project for the production of the multiply charged rare ion beams (RIB). The HVP will be located after ECR ion source charge breeder [1]. Medium resolution mass spectrometer (MRMS) is installed at the platform to provide high purity beams with mass resolution about 1/1000. The Draft of platform design including all beamline elements is discussed. It is proposed a several way of equipment feeding on HVP, required engineering services parameters (vacuum system, cooling system, power system and etc) were defined. Some safety measures are proposed.

MRMS IN SPES FACILITY

Selective Production of Exotic Species (SPES) project is under development. The result of SPES operation should be production of the multiply charged rare ion beams (RIB) by ISOL technique which using the proton induced fission on a Direct Target of UCx. The proton driver is a Cyclotron with variable energy (15-70 MeV) and a maximum current of 0.750 mA. The RIB separate in HRMS platform and transport to charge breeder. The charge breeder is a device that accepts RIB ions coming from the Target-Ion source complex with charge state $+1$ and it transforms their charge states to $+n$. The last separator (MRMS) will be installed after the charge breeder to avoid the contamination of the selected beam by the stable contaminant introduced by the charge breeder itself [2].

The beam will transport from charge breeder to 130 kV MRMS platform, which will separate ions with mass resolution about 1/1000. The Potential of 130 kV is necessary for high mass resolution.

The beam will be transported to MRMS high voltage platform (HVP) through an 130 kV accelerate tube, ions will be focused by electrostatic lenses and after that, the ions with different mass will be selected by magnetic dipole. The beam orbit will be rotated at 90 degrees by each dipole. Separated ions will be refocused ones more in electrostatic lenses and then slows down to the initial speed (same ions speed before MRMS platform) by deaccelerating tube.

The beam line elements will be located on the platform according figure 1. MRMS platform will be enclosed in Faraday cage and will set on insulators columns.

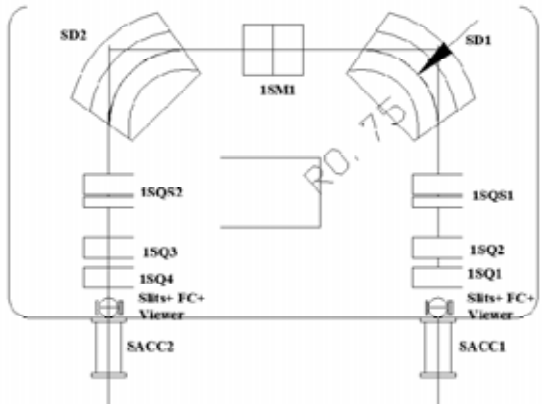

Figure 1: layout of main elements on the MRMS platform. SD1, SD2- magnetic dipoles; 1SQS1, 1SQS2 - sestupole electrostatic lenses; 1SQ1, 1SQ2, 1SQ3, 1SQ4 - quadrupole electrostatic lenses, SACC1 –accelerating tube, SACC2 – deaccelerating tube.

The platform should be located in experimental hall with sizes according figure 2 and further than 0.9 m to the nearest surface of the building. It is important to avoid electrical breakdowns. The Platform height will be 5 meters or less it for the crane movement will be free over the HVP.

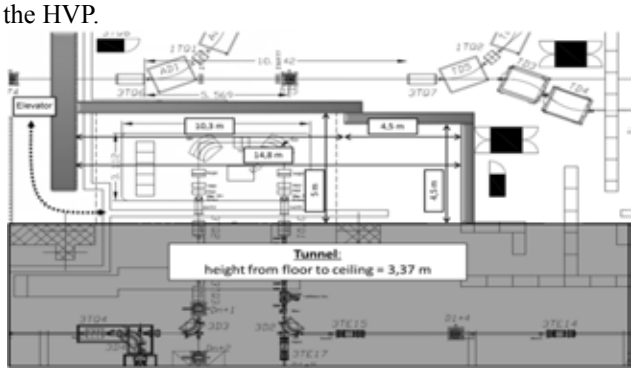

Figure 2: layout of experimental hall.

Secondary Faraday cage locating around the platform at a distance for 0.9 m.

Successful HVP design is necessary several calculations and circuits:

- power system calculations and circuit of power board;
- water cooling and ventilation system should be provided;
- radioactive and fire security should be provided;
- vacuum scheme and appropriate calculation, residual pressure should be less than 10^{-8} mbar;
- HV power supply will be defined according leakage currents;

ISBN 978-3-95450-170-0

- way of equipment feeding on the HVP should be defined.

The platform needed following locks: doors, power supplies and secondary Faraday cage around the HVP (HVP zone) for safe operation.

PLATFORM DESIGN AND PLACEMENT OF EQUIPMENT ON IT

130 kV high voltage platform have one level, with sizes 5400x3110 mm. 130 kV is made HV power supply which will locate in HVP zone. Power of HV power supply should be more than leakage currents. Total leakage current from HPV will be less than 1.3 mA.

The Faraday cage will be installed around HVP area with height 2800 mm. This cage must be made of light and strong materials, with a door and removable upper cover for easiness of installation of different equipment's. The cage consists of aluminums panels, which must be mounted on frame. HVP shape must be a rounded (on all corners), we use a 14 cm radius for sides and vertices. This radius calculated by formula 1 [3].

$$R := \left(\frac{\sqrt{8} \cdot V2}{3 \cdot E} \right)^3 \cdot \frac{1}{b^2} \quad . \qquad (1)$$

The false floor will be located under floor with equipment. Electrics and others cables should be located in false floor as is shown in figure 3.

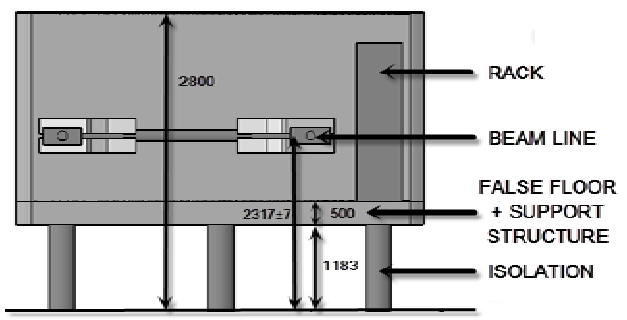

Figure 3: The front view of model HVP.

Height of beamline is 2317±7 mm (over floor of experimental hall). Height of insulation column should be less than 1200mm because false floor and beam line base necessary about 1150mm. The HVP will be standed on 9 insulating support columns, withstand 130 kV+20% Voltage. Metallic ring should be mounted in the middle of the insulator and bottom side isolators. It is important that the equipotential V=0 and half-potential (V/2) will be defined by metal rings, potential is distributed along the columns by two 750 MΩ resistors. Bottom part of insulators should be grounded.

Electrostatic and magnetic components are located along beam line. These components must be mounting on adjustable supports. Equipment inside racks must be located on a HVP. As well other engineering services must be locating on a HVP: vacuum pumps, diagnostic boxes, water cooling, lighting, interlocks and different alarms. Description thereof will be in the following chapters.

POWER SYSTEM

Equipment (load about 50 kVA) on a HVP can be powered by three ways:

1. Indoor Isolating transformer:

In case of dry type isolating transformer will be purchased, it will enable to install transformer in the experimental hall.

2. Outoor Isolating transformer:

In case of isolating transformer with oil will be purchased, it should be located on the outside of the building in the up special room. Transformer will be supplied power through the high voltage cables to HVP.

3. Motor-generator (figure 4).

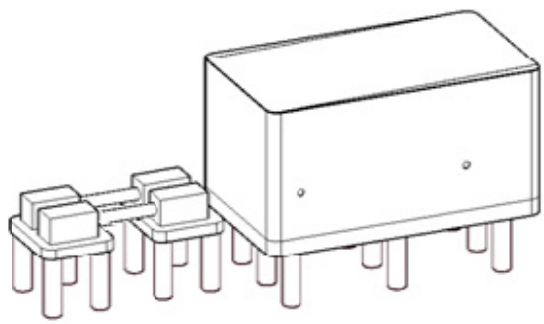

Figure 4: The front view of model HVP.

2 motors and 2 generators installed horizontally and connected by plexiglass shaft (1 motor-generator is spare), which acts as insulator. Motor and generator will be located on 2 platforms at the same level. Platform with generators will be connected to the main high-voltage potential platform. The generator will be located on a separate platform with insulating columns to eliminate vibrations.

The choice of power system depends on the power of finite resources of the project.

In any cases electric power should be distribute in power board with differential and overload breakers.

Grounding circuitry on HVP will be carried out by IT scheme [5]. In an IT system neutral of power supply should be isolate from earth or earthed via instruments or apparatus having high resistance, and the exposed conductive parts are earthed.

CONTROL UNITS

Control units should be operating the equipment on HVP remotely from the console. Also they will be indicated important values for safe operations on the HVP like leakage currents, pressure, powerboard status etc.

Two consoles will be used to control the platform and equipment installed on it:

ISBN 978-3-95450-170-0

- A main console will be located in the main control room;
- Service console will be located closed to the platform, outside the secondary Faraday cage

Consoles will be connected with a platform by optical cables.

COOLING SYSTEM

Water from the central water delivery system can use for cooling equipment on HVP. The central conduit pressure is 8 bars. The equipment on the platform requires a cooling water flow about 40 l/min. Leakage currents by plastic tubes should be less than 1 mA. Tubes with L=20 m d=0.03 m provide necessary level of leakage currents and water flow at same time. Calculation of water flow by Darcy-Weisbach formula [6] is satisfying the requirements.

Racks will be cooled by air flow. Roof of HVP consist of grid blocks, for good heat air outlet.

SAFETY SYSTEM AND INTERLOCKS

HVP must have several locks and alarms for safe startup and operation of theplatform. For safety start up the HV power supply it must have positive status of doors interlocks, disconnectors interlocks, vacuum interlocks and ronda.

The ronda is a system of protection the presence people on the platform from HV generator startup. When you perform a technique (until 5 min) to bypass the platform, Ronda set a positive status and enables HV generator.

HV automatically disconnector position depends on the HV generator.

All equipment and RACK must be grounded to the housing platform. Also be placed on the platform and fire alarm sensors.

Emergency stop button should be installed near to console. This button can turn off all equipment on the platform, including UPS.

Also radioactive and fire security should be involved on the HVP.

VACUUM SYSTEM

The residual gas in the beam line will be removed by a small number of Turbo Molecular Pumps (TMPs). A rough estimation on the pumps installed is 4 TMPs assisted by 2 Primary Pumps (PP) (see. Figure 4).

Additional Ion Pumps (IPs) are planned as extension of the system to increase further the performance of the line. This type of pumps use the principle of the evaporable getters, i.e.

Compressed air is used to operate the vacuum valves, whereas nitrogen is used for venting the beam line before opening. Both these fluids are distributed to the valves on the HVP from a unique pressure gas panel (PGP).

The PNG collects the air compressed and nitrogen inlet lines from the III Experimental Hall. For the former there is one tank positioned below the PNG (approx. 10 lt) that is used as a reservoir for closing the valves even if the inlet is out of service. For the nitrogen line there is a pressure reducer. A mechanical sensor for gauging the pressure is installed in both the lines of the PNG.

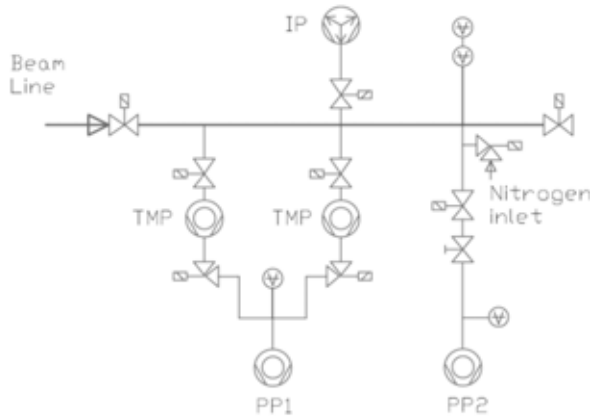

Figure 5: Diagram of the beam pipe with two pumping stations. The pumping station is composed of a TMP a Gate Valve (GV) and a Ion Pump (IP) as further option. The Primary Pumps (PPs) send the gas to the exhaust line.

The gas from the two PPs have the different contamination level. Thus two different pumping lines are used.

Indeed, the pumping of the exhaust gases with low contamination level can be achieved keeping into account the precaution that all the flow is sent to the air ventilation pipe, but for a gas with high contamination level this is no longer true. The gas must be stored in a tank since the radiation level is decreased and afterwards released to the air ventilation pipe.

REFERENCES

[1] G. Prete, A. Covello “SPES Project Technical Design Report” INFN-LNL-223 (2008)

[2] G. Prete, A. Covello “SPES Executive Summary” INFN-LNL-224 (2008)

[3] M. Cavenago, T. Kulevoy, G. Abrioni, S. Canella, F. Cervellera, “The Legnaro ECR ion source platform” Heavy ion Accelerator Technology: Eighth International Conference, (1999).

[4] Kuchling H. Physics. VEB Fachbuchverlag, Leipzig (1980).

[5] Guldbrand A., “Industrial Electrical Engineering and Automation”, Lund University (2006).

[6] De Nevers (1970), Fluid Mechanics, Addison–Wesley, ISBN 0-201-01497-1

ISBN 978-3-95450-170-0

THE ADVANCED NANOSTRUCTURE STEEL MODIFICATION BY GAS IONS BEAMS

R.P Kuibeda, S.L Andrianov, P.A Fedin, B.K. Kondratiev, A.V. Kozlov, A.A. Nikitin, B.B Chalih, A.L. Sitnikov, S.V. Rogozhkin, T.V. Kulevoy ITEP, Moscow, Russia

Abstract

New construction materials are under developing for the nuclear energy sector. They will provide energy production, store and transportation with high efficiency and ecology safety. The nanostructures steels like a consolidation oxide dispersion strengthened (ODS) as well as ferritic-martensitic steel (for example EK-181) are the most promising materials for new generation of nuclear reactors. The experimental program for investigation of the steel nanocluster generation and growth under ion beam irradiation is ongoing in ITEP at the accelerator complex "Heavy ion prototype-1" (HIPr-1). The duoplasmatron ion source provides gas ion beams for experimental program. The source installation and it's power systems development are presented. As well the results of charge state distribution measurements for nitrogen ion beam generated by the duoplasmatron and the first results of ODS materials irradiation by gas ions are described and discussed.

INTRODUCTION

The changes in chemical composition of structural steels which occur under irradiation can cause changes in their mechanical characteristics. To investigate the steel structure changes under irradiation, in ITEP experimental works for structural materials irradiation by metal ion beams are carried out since 2007 [1]. However, the investigation of materials irradiated by both gas ion beams and combination of gas and metal ion beams can significantly enlarge the experimental potential of ITEP research program.

At the accelerator "heavy ions-prototype-1" (HIPr-1) a gas ion source duoplasmatron was installed, tested, tuned and put under operation. The procedure of materials irradiation with gas ions was tested. Nitrogen ion beam with a current of 150 mA was obtained at the outlet of the injector. The results of charge state distribution measurements for nitrogen ion beam generated by the duoplasmotron as well as the first experimental data obtained for ODS steel irradiated by the nitrogen beam are presented and discussed.

EXPERIMENTAL FACILITY

Experiments on the structural steels modification are performed at the accelerator TIPr-1, which shown on figure 1. Injector system (1) consists of ion source, extraction system and accelerator tube with high voltage up to 100 kV. The beam current at the injector output is measured by beam transformer (2). The experimental chamber (3) is used for steel samples irradiation by low-energy ion beams. Electrostatic lenses (4) provide beam matching with the input to RFQ (5). The chamber (6) has a beam detector for accelerated beam current measurements. Three magnetic quadruples (7) forms at the targets the beam profile needed for experiments. In chamber (8) the target assembly for material samples irradiation by the ion beam accelerated in TIPr-1 is installed. The target construction enables the irradiation experiments with samples heated to the temperature up to 700ºC.

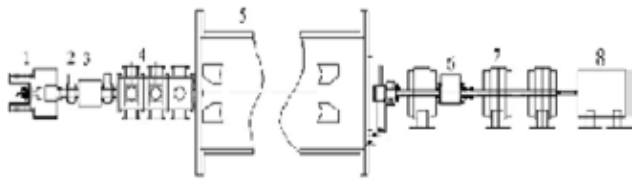

Figure 1: Scheme of accelerator TIPr-1.

Duoplasmatron, which is a regular source for proton beam generation at the injector I-2 at ITEP, was installed in TIPr-1 injector system. The pulse valve mounted at discharge chamber output significantly reduces the gas load in the injector and enables the cold cathode operation mode [2]. A system of the power supply for duoplasmatron was developed. It provides the production of an ion beam with a duration of 60 microseconds and a pulsce repetition rate of 1/3 pps.

The power supply circuit of the ion source is shown at figure 2. The main elements of this circuit are a pulse discharge generator (PDG), a power supply (PSIV) for the inlet valve; power supply for duoplasmatron magnet (PSM). This circuit located on the high voltage platform.

TEST OF ION SOURCE WITH NITROGEN BEAM

Duoplasmatron was tested under operation with nitrogen ion beam. The time-of-flight method was used for charge state distribution (CSD) measurements of nitrogen ion beam generated by duoplasmatron [3]. CSD and beam current were measured for two different discharge currents: I_{arc}=213 A and I_{arc}=173 A. The CSD behavior during the beam pulse for discharge current of 173 A is shown in Figure 3. The measured distribution of different ions in total beam current are shown in Table 1.

ISBN 978-3-95450-170-0

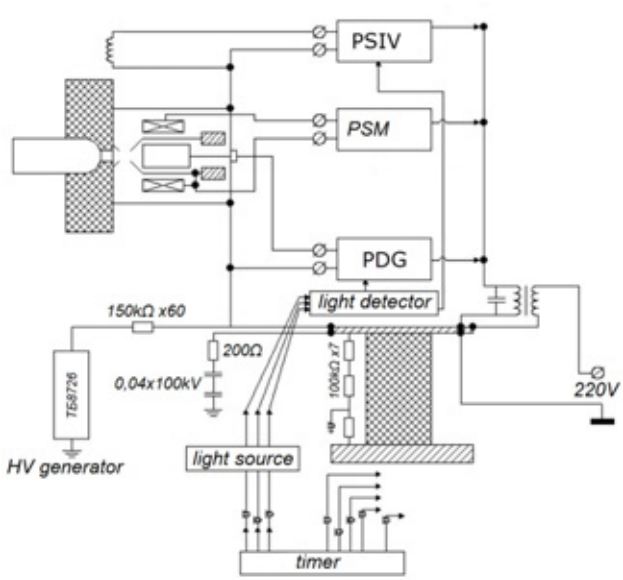

Figure 2: Circuit of duoplasmatron power supply.

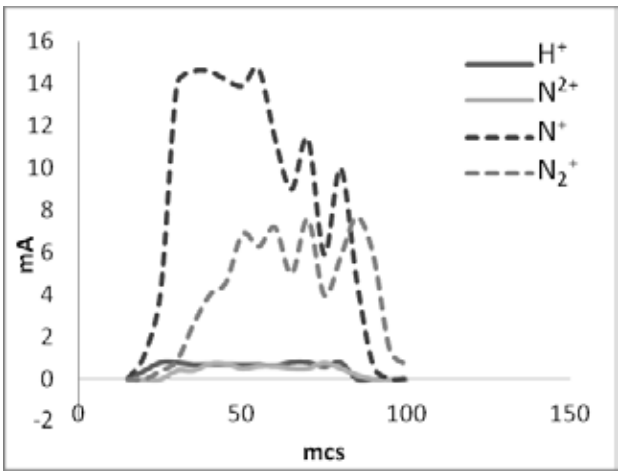

Figure 3: Charge ion distribution in duoplasmatron beam.

Table 1: Charge distribution of the ions in the beam from duoplasmatron.

Ions	I_{arc}=173 A	I_{arc}=213 A
H^+	4,0%	11,5%
N^{2+}	1,4%	4,9%
N^+	63,2%	73,1%
N_2^+	31,4%	10,5%

RESULTS

For simulation experiments, the samples in the form of needle with tip thickness of about hundred nanometers were used. They were mounted in a chamber (p.3. Figure. 1) at the injector output and were adjusted so that the needle tips are located close to the centre of the beam axis. During experiemnts the pressure in the chamber was $P=5\cdot10^{-6}$ torr. The ion source was adjusted to the operation with a current density of ~1 mA/cm^2. The oxide dispersion strengthened (ODS) Eurofer steel and ferritic-martensitic precipitation-aging steel EK-181 were used for experiments. Their chemical compositions before irradiation are given in Table. 2. Two sets of samples from those materials were irradiated by different beams. One of them was irradiated by the titanium ion beam and another one by nitrogen ion beam. The flux of 10^{15} particles/cm^2 for both experiments was achieved. The research of the irradiated samples were performed on an optical tomographic atom probe microscope [4].

Table 2: Chemical compositions before irradiation, at %.

	Eurofer ODS, at %	EK-181, at%
Cr	9.65	11.9
Mn	0.38	0.95
Si	0.16	0.73
C	0.51	0.64
N	0.03	0.16
O	0.37	-
V	0.38	0.31
Y	0.25	-

The peaks corresponding to the evaporated Ti^+ and N^+ ions were found in the mass spectrum of the irradiated samples. According simulation the concentrations of these elements in irradiated samples should be increased by 0.2 at. %. Data with experimental values are shown in Table 3. Comparing Tables 3 and 2 one can see that experimental data for nitrogen don't correlate with the calculated ones. The discrepancy between the results may be due to the migration of the implanted nitrogen from the irradiation zone to the sample surface.

It is necessary to note that the clusters in the samples under nitrogen beam irradiation not changed however clusters in the samples irradiated by Ti beam changed significantly.

Table 3: Chemical compositions after irradiation.

The test sample	Chemical Element	Concentration after ion irradiation to a dose of 10^{15} particle/cm^2	Estimated value of the concentration particle/cm^2
Eurofer ODS	N	0.06±0.01	0.2
EK-181	N	0.04±0.01	0.2
Eurofer ODS	Ti	0.23±0.07	0.2
ЭК-181	Ti	0.21±0.05	0.2

ISBN 978-3-95450-170-0

CONCLUSION

The gas ions source (duoplasmatron) was installed at the accelerator HIPr-1, to provide the investigation of material modification under gas ion implantation into the prospective steels for nuclear reactor manufacture. The power supply circuit, gas pipeline and related tools were developed for the ion source, to provide gas ion beam generation with pulse length of 60 μs and repetition rate of 1/3 pps and beam current up to 100-200 mA. Nitrogen ion beam with a current of 150 mA –was generated and used for the experiments.

The charge state distribution of the nitrogen ion beam during the discharge time in duoplasmatron was measured by the time-of-flight method.

The samples of EK-181 and ODS were irradiated by nitrogen ion beam with energies up to 60 keV. Results were compared with the ones obtained after the titan ions implantation.

For nitrogen beam, irradiation changes in chemical composition of the samples did not coincide with the simulated ones thanks to the migration of implanted nitrogen atoms to the sample surface. As a next step we plan to carry out the irradiation of the same steel samples first by the titanium beam and then by the nitrogen beam.

REFERENCES

[1] Rogozhkin S.V., Kulevoy T.V., Iskandarov N.A., Orlov N.N., Chalykh B.B., Aleev A.A., Grachev N.Y., Kujbeda R.P., Nikitin A.A., Fertman A.D., Shishmarev V.B."Simulation experiment on study in the radiation resistance of advanced ferrite-martensite steel hardened by disperse inclusions". Atomic Energy. 2013. T. 114. № 1.C. 14-20.

[2] V.A Batalin, A.A. Kolomiec, B.K. Kondrat'ev, R.P. Kujbeda. “Duoplazmatron s holodnym katodom dlja inzhektora linejnogo uskoritelja protonov.” PTJE №2 1975 (In Russian).

[3] Batalin V.A., Kondrat'ev B.K., Turchin V.A. “Ionno-opticheskaja sistema istochnika tjazhelyh ionov dlja vremja-proletnyh izmerenij”.\\ PTJE, N 4, 1987g., str.34. (In Russian).

[4] S.V. Rogozhkin, A.G. Zaluzhnyj, A.A. Aleev, A.V. Karpov, O.N. Makeev “Tomograficheskaja Atomno-zondovaja mikroskopija nanoctrukturirovannyh materialov” ISBN 5-7262-0633-9. NAUCHNAJA SESSIJA MIFI-2006. Tom 9 (In Russian).

ISBN 978-3-95450-170-0

METHOD OF BROADBAND STABILIZATION OF THE VEPP-4 MAIN FIELD

A. Pavlenko, BINP SB RAS; NSU, Novosibirsk, Russia
A. Batrakov, G. Karpov, I. Nikolaev, V.Svishchev, BINP SB RAS, Novosibirsk, Russia

Abstract

The stability of the main field has great influence on precision experiments on particle physics which are performed on VEPP-4M facility currently. A method of broadband stabilization of the VEPP-4M main field allowing us to achieve field stability better than 0.5 ppm over DC - 50Hz frequency range is presented. The method combines NMR stabilization and feedback loop using induction signal.

INTRODUCTION

It is necessary to know the beam energy of cycling accelerators in the particle physics experiments. At VEPP-4M experiment of CPT-invariance test by comparison of spin precession frequencies of electron and positron simultaneously circulating in VEPP-4M storage ring with accuracy 10^{-8} is planned [1]. The error of this experiment directly depends on stability of guiding magnetic field therefore long-term stability and field ripples are of the great importance. Long-term (hours) stability 10^{-6} allow one to find optimal parameter for the measurements. High-frequency ripples (up to 5 Hz) results in broadening of resonance spin precession frequency. This effect increases statistical error of the experiment. The frequencies more 10 Hz result to side spin resonance harmonic and could be excluded by optimal experiment parameters choice. Furthermore field instability induces beam orbit pulsation which has negative influence on count rate of Touschek polarimeter and increases the systematic error of the experiment. So, detrimental influence of filed pulsation in a range from 0.01 to 10 Hz on statistic and systematic error in this experiment requires wide range stabilization system of guiding field of VEPP-4M storage ring.

THE VEPP-4M MAIN FIELD QUALITY

The VEPP-4M magnetic structure containing about 100 bending magnets are supplied by high current power supply IST. The main field varies in the range from 0.15 T at injection energy to approximately 0.55 T at maximum energy [2]. All magnets are connected in series, and current is changed from 2 kA to 5.5 kA. Long-term stability of supply current stays at 10^{-5} relative level. In series with the bending magnets, there is "out of ring" additional calibration magnet which is fully identical to bending magnets.

The precision NMR magnetometer [3] is used to measure absolute value of the VEPP-4M main field in the calibration magnet. Full measurement cycle consists a few elementary cycles. Each cycle includes only one excitation RF pulse and one NMR response signal. Typical NMR signal duration for the VEPP-4M dipole magnet in the field range 0.15-0.2 T is ~5 ms. Time interval between elementary cycles T_e is defined by NMR working substance relaxation time. For VEPP-4M NMR probe $T_e \approx 0.08$ s. So, during full busy time real measurement is performed only within short interval ~5 ms separated with 0.08 s, where no NMR signal presents. To improve measurement accuracy the accumulation of NMR response signals is used (usually 8 – 16 elementary cycles).

To increase stability of the VEPP-4M main field, the feedback loop was implemented into the power supply control using data given by NMR magnetometer. The difference between set point and measured field is converted to an additive to be added to value measured with DCCT. That "via-DCCT" way allows correcting the power supply current. The integral term of PID controller is used with integral gain approximately equals to 0.5. Higher gain value results in feedback loop instability. The correction rate is about 1 s, providing field correction in the band from 0 Hz up to 0.1 Hz. Fig. 1. presents the NMR magnetometer data with the feedback off and on.

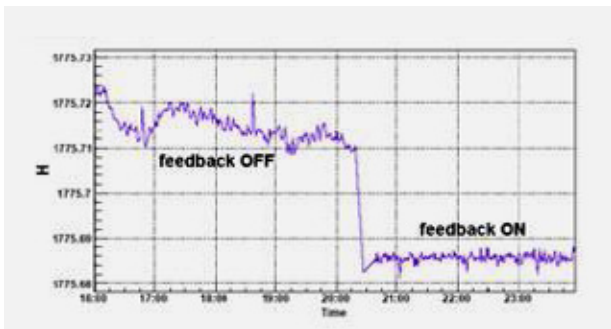

Figure 1: The NMR stabilization efficiency.

The long-term instability is about 1 ppm (RMS). However, NMR measurements don't provide information about amplitude and frequency content of field instability for frequencies higher than 1 Hz. In order to measure high frequency ripples it was used the induction sensor placed into calibration magnet. The sensor is equipped with electrostatic shield which suppresses coupling with power supply rails. The sensor has magnetic area $wS = 7.7\ m^2$. Its output voltage is recorded by the multimode digital integrator VsDC3 [4] and these data are processed to get Fourier transform. The spectral components are divided by $2\pi F \cdot wS \cdot B$ factor giving magnetic field ripple amplitude relative to mean value B at frequency F. Fig. 2 (blue plot) presents the VEPP-4M field ripple spectrum.

ISBN 978-3-95450-170-0

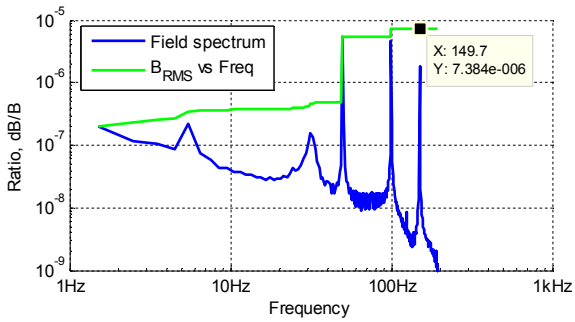

Figure 2: Ripple spectrum (blue) in terms dB/B and dB/B vs on band of observation (green).

There are spectrum peaks at 5 Hz and 30 Hz because of magnets mechanical vibration. Such system as vacuum, air-conditioning or cooling water pumps can provide it. Spectral components which are multiple of AC frequency (50 Hz, 100 Hz and so on) are influenced by IST power stage. Note that despite the fact that bending magnets have not laminated iron yoke the field spectrum contains significant components up to 150 Hz. Green plot in Fig. 2 represents dB/B rms depend on band of observation. One can see that dB/B rms level increases from $8 \cdot 10^{-7}$ at 5 Hz to $7 \cdot 10^{-6}$ at 150 Hz. This fact leads us to develop the stabilization system for frequencies higher than 1 Hz in addition to NMR stabilization.

THE BROADBAND STABILIZATION SYSTEM

To solve this task the following technique was proposed. By measuring instantaneous value of magnetic field variation with induction sensor, compensate it by adding directly into the magnetic structure a current of opposite polarity. The structure of the fast suppression system proposed is presented in the Fig. 3.

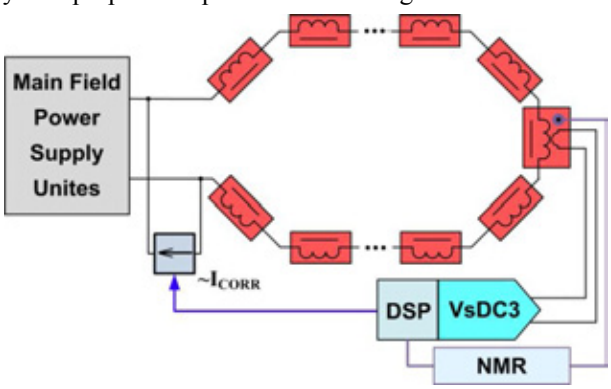

Figure3: The structure of the fast stabilization system.

The system consists of VsDC3 integrator and correction current generator, which is connected in parallel with IST. The distance between devices is about 200 m and they are connected via RS485 digital link. The achieved correction code computing rate equals to 2 kHz. The experimental results of fast suppression system testing are presented in Fig. 4.

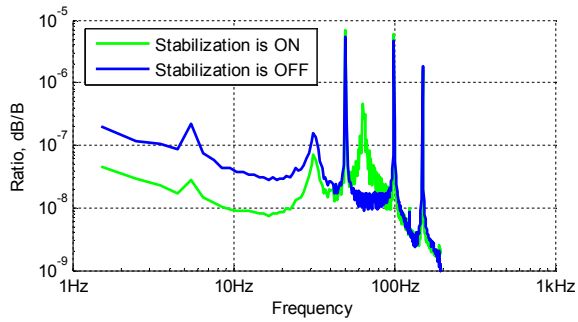

Figure 4: Ripple spectrum for stabilization is OFF (blue) and ON (green).

The blue plot represents typical magnetic field ripple spectrum with fast stabilization is off and green plot corresponds to on-state. The graph shows that at a frequency of 5 Hz suppression of ripples is about 10 times, at a frequency of 10 Hz - 3 times, at a frequency of 30 Hz - 2 times. However, the system demonstrates a lack of performance at 50 Hz and significant loop response rise at approximately 65 Hz. The reason for such system behavior is due to falling of IST output impedance and increasing of magnetic structure impedance with frequency. The measured ratio of magnetic structure current to correction current is presented in Fig. 5.

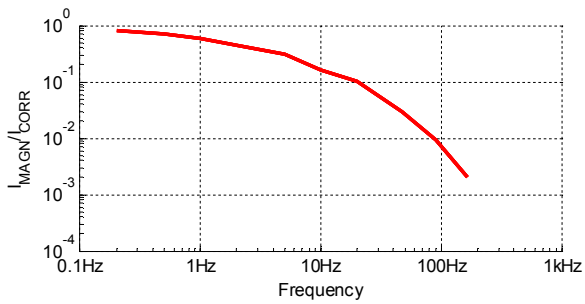

Figure 5: Ratio $I_{magnet}/I_{correction}$ vs frequence.

Less than tens part of correction current is flown into magnetic structure at 50 Hz. As a result the amplitude and phase response of correction current transfer function leads the system to fall in efficiency at frequencies higher than 50 Hz. At the same time attempts to obtain a higher suppression of field ripples in the band above 50 Hz results in unstable operation of the system.

Let us consider open loop response of the fast feedback system in order to demonstrate these statements. The simplified fast feedback loop signal chain is presented in Fig. 6. The digital integrator path gives magnetic flux increments $\Delta\Phi_n$ at 1/Ts sample rate. These $\Delta\Phi_n$ are accumulated in S(z) element giving instant magnetic field values Φ_n. The accumulator S(z) has relaxation time constant (1-δ) which determines low frequency level of the loop operation. Calculated field values are multiplied by gain constant G and pass through the optional five order loop filter H(z). Calculated values are transmitted to correction generator and converted into current using calibration constant α_C. All parameters such as relaxation

ISBN 978-3-95450-170-0

constant δ, gain G or loop filter H(z) coefficients are remotely tunable.

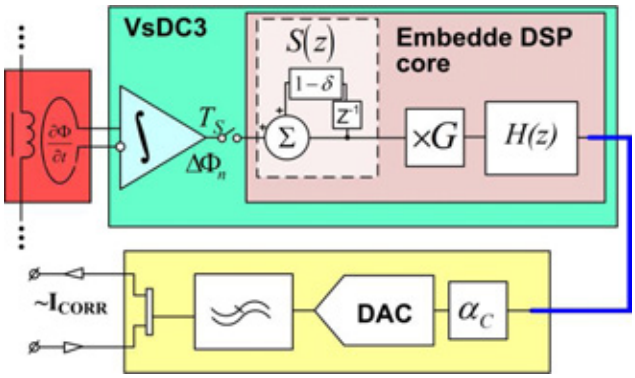

Figure 6: The simplified fast feedback signal chain.

Considering this the signal processing in feedback loop elements can be expressed a follows:

$$I_{CORR}(z) = \left\{ \frac{1 - z^{-1}}{1 - (1-\delta) z^{-1}} \cdot G \cdot H(z) \right\} \cdot \alpha_C \cdot \Phi(z)$$

The numerator of the first term corresponds to z-transform of the sampled flux Φ(z) measurement process, denominator represents S(z) term. Magnetic flux value multiplied by calibration constant α_C approximates ripple current value so the term inside braces represents the gain of the feedback loop. This expression multiplied by measured ratio I_{magn}/I_{corr} (Fig. 5.) gives the model of the system behaviour which is presented in Fig. 7.

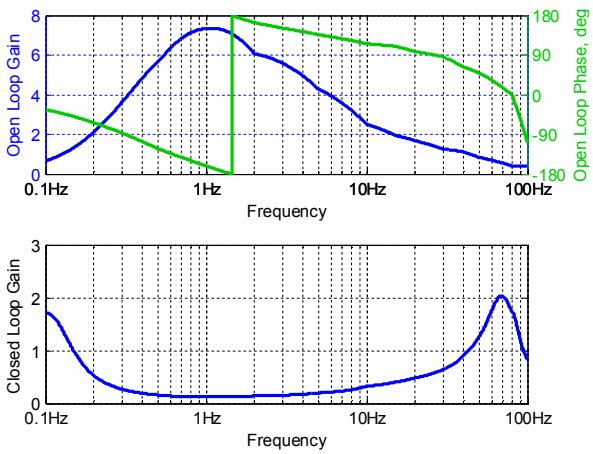

Figure 7: Amplitude and phase response for the case of closed and open-loop feedback.

The maximum stable loop gain G is chosen. The presented model demonstrates good agreement with experimental results: the suppression level and the high limit of working bandwidth match to Fig.4. The low level bandwidth limit is at approximately 0.1 Hz. This limit is determined by VsDC3 noise floor and is tunable via parameter δ.

The integration of broadband stabilization and NMR-stabilization is done by summing correction values from the NMR feedback and the fast feedback. An expected close loop gain is shown in Fig.8. Accordingly the way of slow stabilization "via DCCT" should be disabled.

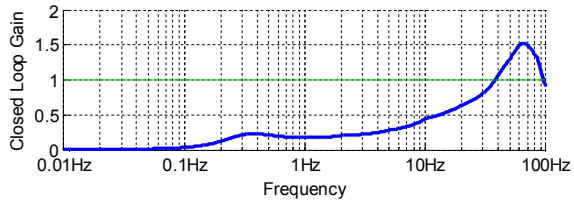

Figure 8: Typical induction signal of pulsed magnetic field and error source of "direct" digital integration technique.

The DSP block of the VsDC3 is able to receive and process NMR and broadband measurements. Up to now standalone operation of NMR stabilization via broadband system was implemented and tested while shared algorithm of stabilization is under development.

Main task in achieving this goal is to increase the NMR measurement rate by decreasing elementary cycle accumulation number. In addition, ways should be found to extend bandwidth of suppression system operation by finding optimal configuration of the loop filter.

SUMMARY

The method of reducing the magnetic field ripples in a band up to 50 Hz is described. In this band the proposed method improves the stability of the VEPP-4 main field in 3-5 times, reaching the level $3\text{-}5 \cdot 10^{-7}$. These new features should increase quality of future VEPP-4M CPT-invariance test experiments.

The nearest plans are to integrate the NMR and broadband stabilizations and try to increase the band of the ripple suppression using a faster feedback loop.

ACKNOWLEGMENT

The work is is supported by the Ministry of Education and Science of the Russian Federation, NSh-4860.2014.2.

REFERENCES

[1] V.E. Blinov at al. "Study of the possibility of increasing the accuracy of CPT Invariance. Test at electron-positron storage rings", ICFA Beam Dynamics Newsletter V48 p.207-217 (2009)

[2] V.E Blinov at al. "The status of VEPP-4". Physics and technique of accelerators, Vol 11 No.5 p620-631 (2014)

[3] G.V.Karpov et al. "Precise magnetometers on base of pulsed NMR techniques", Proc. of the RuPAC-2006, Novosibirsk, p.58-60.

[4] A.Batrakov et al. "Multimode digital integrator for precision magnetic measurements", Proc. of the RuPAC-2012, Saint Petersburg, p.617-619.

ISBN 978-3-95450-170-0

MAGNETIC SYSTEM OF ISOCHRONOUS CYCLOTRON F250 FOR PROTON THERAPY APPLICATIONS

Yu. G.Alenitsky#, N.L.Zaplatin, E.V.Samsonov,
V.P.Dzhelepov Laboratory of Nuclear Problems, JINR, Dubna, Russia

Abstract

Possibility of the isochronous cyclotron F250 creation with protons energy ~250 MeV on the basis of magnet with pole diameter 6 m, which is used for the synchrocyclotron (Phasotron), is examined in the JINR Laboratory of Nuclear Problems (LNP). The proposed cyclotron F250 will make it possible to strongly decrease the electric power of magnet and to avoid the need of beam degradation from 680 MeV to 250 MeV.

For creating the required magnetic field of the cyclotron F250 it is necessary to change the form of steel spiral shims and disks, located inside a vacuum chamber of synchro-cyclotron. The basic parameters of the magnetic system of the cyclotron F250 with the condition of retaining the vacuum chamber and the magnet yoke of synchrocyclotron are given.

INTRODUCTION

The basis of the experimental base for JINR Laboratory of Nuclear Problems (LNP) until 1979 served the first accelerator of Dubna - synchrocyclotron. As a result of a number of improvements this accelerator for a long time remained one of the most powerful installations of this type [1].

In (1967 -1970) the project [2] of reconstruction the synchrocyclotron into a small meson factory with the energy of protons 680 MeV was developed. In (1979 - 1984) this project was realized with the maximum intensity of the internal beam of protons 7 mkA and with the efficiency of extraction ~50%. The obtained parameters of accelerator made it possible to substantially enlarge the program of physical and applied works on the accelerator [3].

At present a medico - biological complex operates in LNP for treating the oncologic sick with the use of protons at energies 160-250 MeV. For determining the required energy of protons the information about the mean free path of protons in the correspondence for the position of Bragg's peak in each case is used. Necessary energy of protons is obtained by means of degrader system providing a retarding the extracted beam of protons with 680 MeV to 250 MeV and less. In this case the utilized for medical purposes intensity of beam does not exceed 50 nA.

The successes achieved in the last decade in the proton therapy led to development and creation of the specialized accelerators for this purpose. The considerable progress in this direction is achieved in the creation of isochronous cyclotrons [4, 5].

#alen@jinr.ru

The considerable progress in this direction is achieved in the creation of isochronous cyclotrons [4, 5]. However, the cost of construction as well as the operating costs of such cyclotrons comprises the rather great values.

In connection with the foregoing it looks appropriate to develop a project with a partial use of magnetic, high-frequency and other systems of working accelerator for creation on their basis an isochronous cyclotron for proton therapy.

The decommissioning of the JINR Phasotron will allow in the shortest possible time with minimal capital expenditure to create an isochronous cyclotron for protons up to 250 MeV with an intensity of the extracted beam about 50 mkA.

CALCULATION OF MAGNETIC FIELD

General view of F250 magnetic system, including the magnet of the working JINR Phasotron and the lids of vacuum chamber with the system of spiral shims of new configuration is shown in Figure 1. Position of the main elements of the magnetic system in the gap between poles of the electromagnet (Ø=6000 mm, d =1540 mm), that provide the desired field in the mid-plane is shown in Fig. 2.

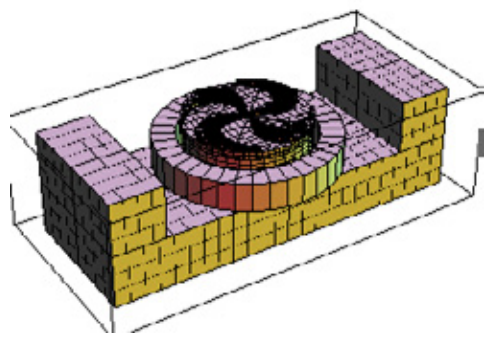

Figure 1: General view of FC250 magnetic system.

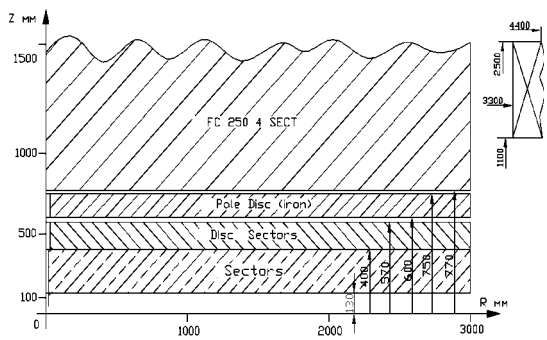

Figure 2: Scheme of the main elements location on vertical cross section.

ISBN 978-3-95450-170-0

Pole disk and disk with sectors form the lids of the vacuum chamber of cyclotron.

Geometry of the steel disks and spiral shims has been chosen by the help of code Radia [6] which computes 3D magnetic fields in the system of Mathematica [7].

The calculations were carried out at a current in the magnet coil IW=165 kA, which corresponds to the power consumed by the magnet P= 100 kWt.

The selected configuration of sectors (Figure 3) provides the required radial dependencies of average magnetic field (Figure 4) and both spiral angle and flutter (Figure 5).

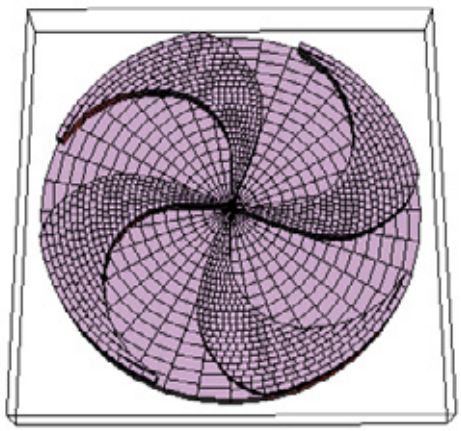

Figure 3: Configuration of the magnetic sectors.

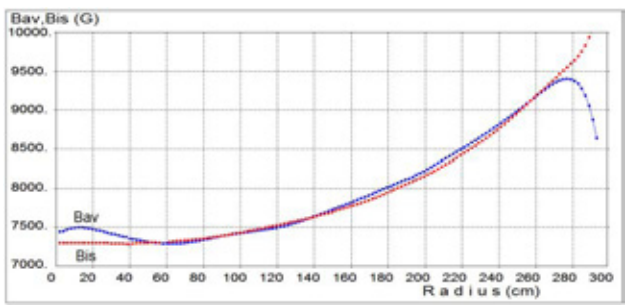

Figure 4: Average magnetic field Bav and isochronous one Bis versus radius.

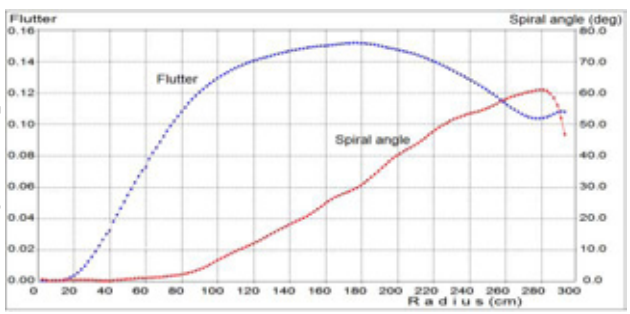

Figure 5: Flutter and spiral angle of the field versus radius

As can be seen from Figure 4 the deviation of the average magnetic field from the isochronous one in central region of the accelerator (r < 40 cm) is not larger than 250 G, and in the interval r =(40-270) cm does not exceed 50 Gauss. Off course, tight trimming of the average field in a main acceleration region is needed up to a level ±2-3 Gs deviation from the isochronous one. This can be provided by changing azimuthal width of the sectors.

Betatron tunes Qr and Qz are shown in Figure 6 versus orbital radius. Axial focusing by means of magnetic field begins from radius 15 cm. To provide focusing at radii less than 15 cm a corresponding change of the field bump in this place is needed. Some increase of the axial focusing due to electric field should also be taken into account in the very center of cyclotron

It is seen that the frequency of axial oscillations decreases from Qz=0.35 at radius r =230 cm to Qz=0.0 at radius r= 268 cm, which corresponds to maximal attainable proton energy W=260 MeV in this cyclotron (see Figure 7).

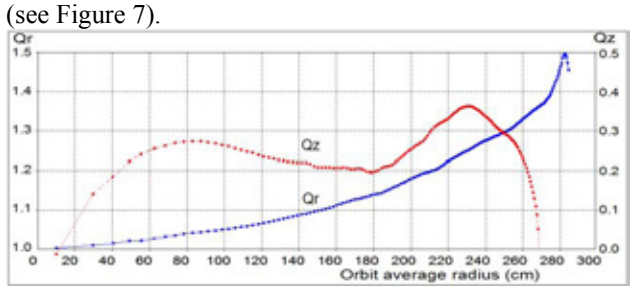

Figure 6: Frequencies of axial Qz and radial Qr oscillations versus orbit average radius.

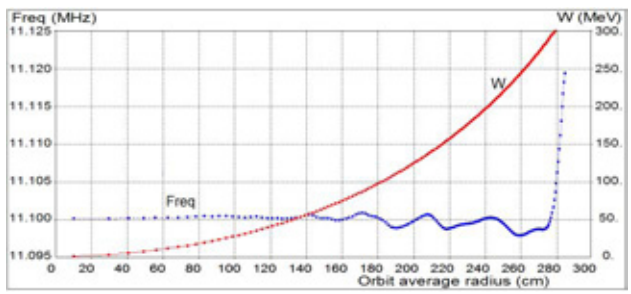

Figure 7: Orbital frequency Freq and energy of central proton W in isochronous field versus orbit average radius.

REFERENCES

[1] V.P.Dzhelepov, et al., Six-meter synchrocyclotron of Institute for Nuclear Problems of USSR Academy of Science, Atomic Energy, N4, 1956, p. 5. (in Russian).

[2] A.A.Glazov, et al., Proceedings of International Conference on Accelerators, Moscow, 1963, p.547, (in Russian).

[3] A.A.Glazov, et al., Synchrocyclotron with magnetic field variation (installation F), preprint of JINR, 9-3211, 1967, (in Russian).

[4] http://www.iba-worldwide.com/ruut.hd/index.html;

[5] Yu.G.Alenitcky, et al. , Cyclotron for beam therapy, preprint of JINR, P9-2005-32, (in Russian).

[6] http://www.esrf.fr/machine/groupe/insertion-devices/Codes/Radia/Radia.html

[7] Elleaume P., Chubar O., Chavanne J., Computing 3D Magnetic Field from Insertion Devices// Proc. of the PAC97 Conference. May 1997 P.3509-3511.

ISBN 978-3-95450-170-0

MAGNETIC FIELD DESIGN AND CALCULATION FOR FLNR DC-280 CYCLOTRON

B.Gikal, G.Gulbekian, I.Ivanenko, J. Franko, JINR, Dubna, 141980, Russia
T.Belyakova V.Kukhtin, E.Lamzin, S.Sytchevsky, ERIEA, St. Petersburg, 189631, Russia

Abstract

The isochronous cyclotron DC-280 is intended to accelerate the ion beams with A/Z from 4 to 7 up to the energy 8 – 4 MeV/nucleon. The wide range of the magnetic field levels from 0.64T till 1.32T allows to make a smooth variation of the beam energy over the range ± 50% from nominal. For operational optimization of the magnetic field the 11 radial and 4 pairs of harmonic correcting coils are used. The numerical formation of the magnetic field is carried out. The problems and solutions of DC-280 magnetic field design are described.

INTRODUCTION

The new isochronous cyclotron DC-280 is now under construction in Laboratory of Nuclear Reactions (FLNR, JINR, Dubna). The cyclotron is intended for accelerating the beams of heavy ions from Carbon to Uranium of the energies from 4 to 8 MeV/nucleon [1]. The cyclotron has a H-shape main magnet with 4 meter pole diameter. The magnetic structure allows to carry out the smooth adjustment of the beam energy over the range ± 50 % from nominal by means of variation of the average magnetic field level at the range from 0.64T till 1.32T. The isochronous field is formed by 4 pair of 45-degrees sectors The operational correction of the magnetic field is realized by means of 11 radial and 4 pairs of harmonic correcting coils. The betatron frequencies lies on the range $1.005<Qr<1.02$ and $0.2<Qz<0.3$.

Table 1: Main parameters of the DC-280 cyclotron

Main size of the magnet, [mm]	8760×4080×4840
Weight of the magnet [t]	1100
Maximal power, [kWt]	≈ 280
Diameter of the pole, [mm]	4000
Distance between the poles, [mm]	500
Number of the sectors pairs	4
Sector angular extent (spirality)	45° (0°)
Sector height, [mm]	111
Distance between the sectors (magnet aperture), [mm]	208
Distance between the sector and pole (for correcting coils), [mm]	35
Number of radial coils	11
Number of azimuthal coils	4

NUMERICAL FORMATION OF DC-280 CYCLOTRON MAGNETIC FIELD

The numerical 3D formation of DC-280 magnetic field was made in some stages using the KOMPOT program package [2-4]. At the first stage the optimization of magnet yoke was carried out. The criteria of optimization is the magnetic field inside yoke elements should not exceed 1.5 – 1.6 T. In this case the efficiency of the magnetic system stays in linear area, figure 2.

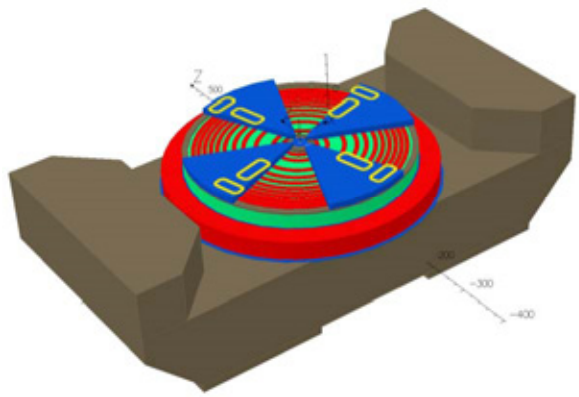

Figure 1: The model of DC-280 magnetic system.

The important problem of DC-280 magnet yoke optimization was the decreasing of the fringe field level over the magnet, where ECR ion source and axial injection line are placed. The special form of the upper (and lower for symmetry) balk of yoke and usage of the magnetic shield platform lets to decrease the fringe field down to acceptable level about 40Gs near ECR ion source and horizontal elements of beam injection line.

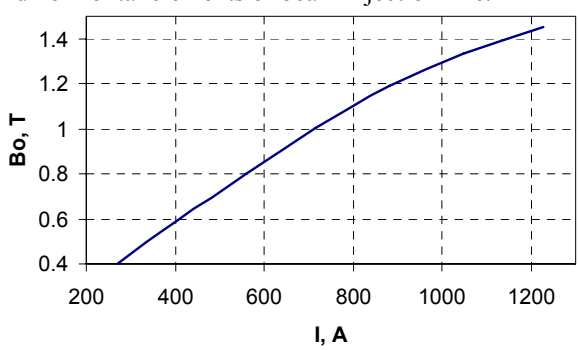

Figure 2: The current of main coil and the magnetic field level for DC-280 magnetic system.

The distance in 500-mm between poles was chosen to place the high–voltage (up to 130kV) RF system and the independent Flat-Top system. The isochronous form of the magnetic field is formed by 4 pairs of sectors. The

ISBN 978-3-95450-170-0

sectors has no spirality and equipped with removable edge shims, placed on the both sides of each sector. The shims has the form of straight plates with 10-mm wide and are intended for final formation of the magnetic field.

THE STEEL MAGNETIC PROPERTIES

At the first stage of the magnetic field calculations the test steel magnetic properties from the program database were used. As soon as the real steel magnetic properties were measured, it was used in the final calculations. Wherein the average magnetic field decreases at 29±4 Gs for 0.64T, 81±3 Gs for 1.05T and 89±9 Gs for 1.32T.

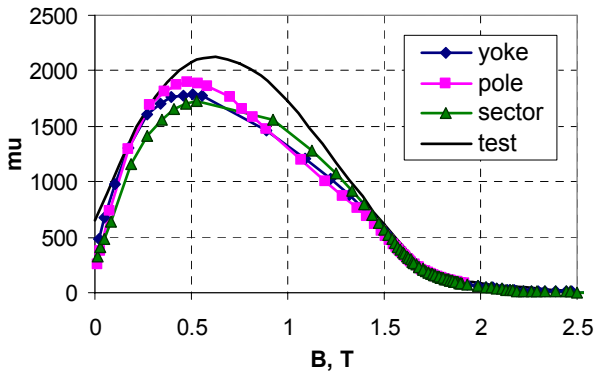

Figure 3: The test and real steel magnetic properties.

THE CORRECTING COILS

To form the isochronous accelerating modes, presented by the working diagram, the DC-280 cyclotron has eleven radial correcting coils. The radial coils are placed between pole and sectors, figure 1. The maximum power consumption of all eleven coils with the current 25A is no more then 2×8kW. Each coil has 2×78 turns. It is enough to produce the required sum contribution of the radial coils about ±1000Gs to form the accelerating modes of the DC-280 cyclotron. 3th and 10th trim coils have a separate power supplies for upper and lower sub coils and could be used for correction of the beam vertical position. At the figure 4 the contributions of DC-280 trim coils with 25A current supply is presented.

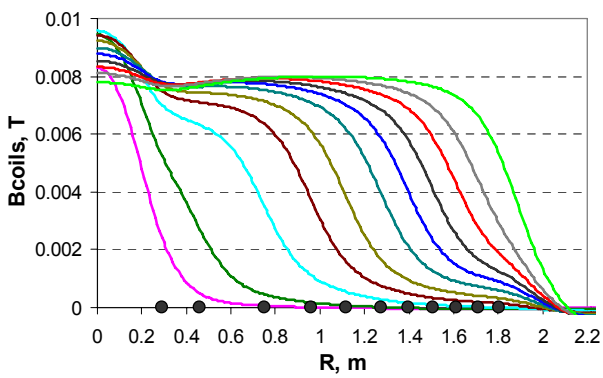

Figure 4: The contributions of the radial coils at the average magnetic field level 1.32T.

Four pairs of azimuhal coils are intended for correction of first harmonic of magnetic field and for adjust beam orbit centring. Azimuthal coils are placed on the sectors at the side of working area, figure 1. One pair of azimuthal coils can create up to 0.0025T of amplitude of the first harmonic, figure 5. Two pairs of azimuhal coils are placed perpendicular one to another in two rows at radiuses:

- R=1.5m, coils are intended for common correction;
- R=1.78m, coils are intended to correct the beam position before extraction.

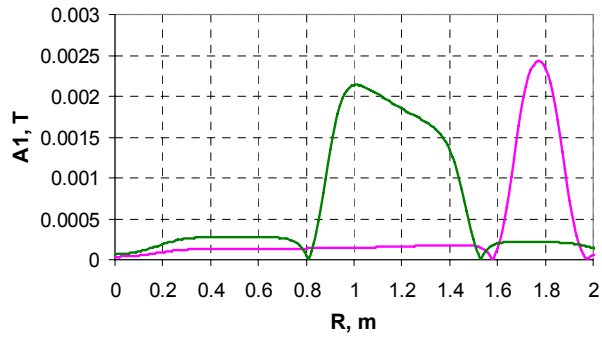

Figure 5: The amplitude of the first harmonic, created by one pair of azimuhal coil.

MAGNETIC FIELD AT CENTRE REGION

Because DC-280 cyclotron magnetic field is varied in a wide range of levels, 0.64 – 1.32T, the magnetic structure is saturated unevenly. It leads to a non uniform changing of magnetic field for different levels. Especially it is dramatic at the central region [2,3].

Thus the formation of the magnetic field at cyclotron centre consists of two interrelated problems:

- formation of the isochronous field
- minimization of non uniform changing of magnetic field for different levels.

For DC-280 cyclotron both problems were solved by finding the special form of central region elements: sector noses, centre plugs and shims.

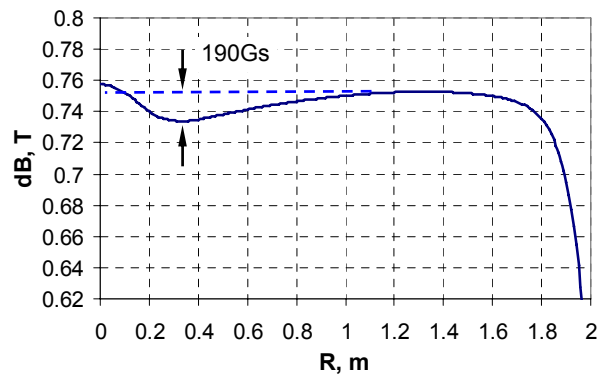

Figure 6: The difference between the average magnetic fields at the high, 1.32T and low, 0.64T levels.

ISBN 978-3-95450-170-0

The form of the difference between the average magnetic fields at the high, 1.32T and low, 0.64T levels was taken as a criteria of the magnetic field formation. In ideal case this difference at the centre must be a flat form. For DC-280 the best difference was found about 190Gs, figure 6. The payment for this was some difference of the formed magnetic field from isochronous, figure 7. This difference can be partially compensated by trim coils. At figure 7 the example of formation of 48Ca8+ acceleration mode by trim coils is presented. The "calculated" field presents the "iron" formed magnetic field, and "formed" field is a result of trim coil usage. As a result, the phase shifting of accelerated beam at the "formed" magnetic field is not more then ±3°.

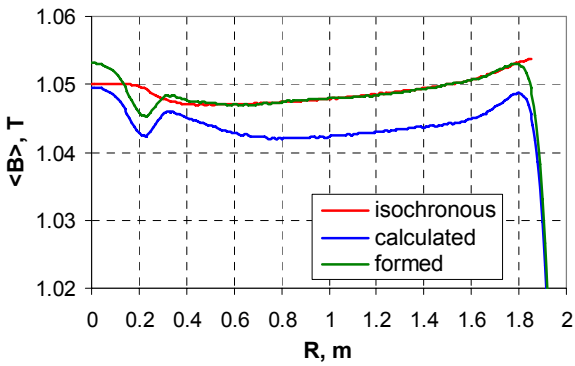

Figure 7: The isochronous, calculated and formed with trim coils magnetic field for 48Ca8+ acceleration mode.

MAGNETIC CHANNEL INSTALATION

DC-280 extraction system is equipped with the passive magnetic channel, placed at the extraction radius in the vertical gap between pair of sectors, figure 8.

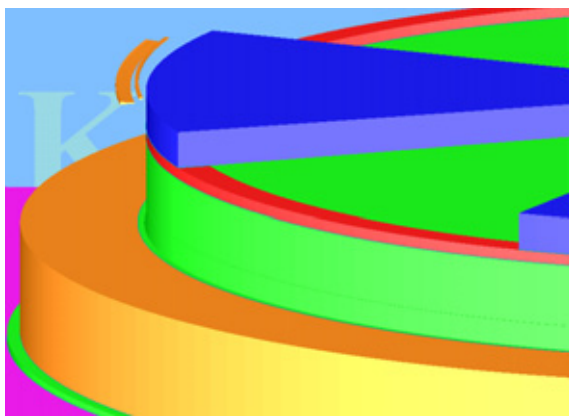

Figure 8: The passive magnetic channel installation at the computer model of DC-280 magnet.

The calculation of the magnetic field with the passive magnetic channel was carried out on the computer model with 1/2 geometry of the cyclotron magnet (360° on the azimuth). At the figure 9 the perturbation of the magnetic field after channel installation is shown. The calculations has shown, that up to the extraction radius 1.78m, the average magnetic field is changed not more than 2Gs from initial form and the amplitude of induced first harmonic less than 4Gs. The compensation of the passive magnetic channel influence will be held during magnetic field measurements by means of the sector shims [4].

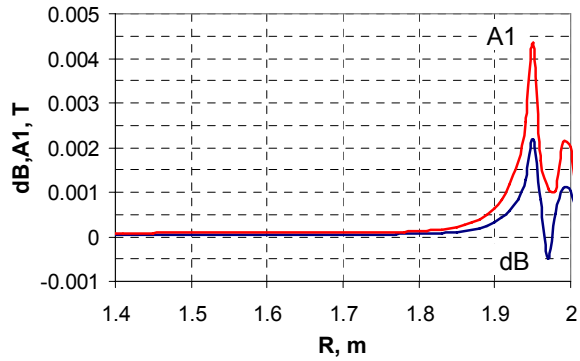

Figure 9: The average magnetic field perturbation and first harmonic amplitude after magnetic channel installation.

PRESENT STATUS

At present time the magnet is manufactured and wait for transportation to Dubna, figure 10.

Figure 10: DC-280 magnet at the manufacture.

REFERENCES

[1] G.Gulbekian, "Status of DC-280 cyclotron project", These proceedings, RuPAC-14, October 2014, Obninsk, Russia.

[2] B.N.Gikal et al., "Magnetic Field Design and Calculation for the FLNR U400R Cyclotron", In: Proceedings of EPAC-11, June 2008, Italy, p.p. 2359 – 2361.

[3] B.N.Gikal et al., "The method and results of formation of the DC-60 cyclotron magnetic field", In: Proceedings of the 18th Conference on Cyclotrons and Their Applications, October 2007, Giardini Naxos, Italy.

[4] B.Gikal, et al., "The procedure and results of magnetic field formation at the cyclotron with the magnetic channel of the beam extraction system", ECPM-12, May 2012, PSI, Switzerland.

ISBN 978-3-95450-170-0

THE POWER SUPPLY SYSTEM OF ELECTROSTATIC DEFLECTING PLATES FOR ACCELERATING COMPLEX NICA.

V.A.Bulanov, A.A. Fateev, E.V. Gorbachev, N.I. Lebedev, Joint Institute for Nuclear Research, Dubna, 141980, Russia

Abstract

Three pairs of electrostatic deflecting plates will be placed in the booster ring. They will provide injection of heavy ion beam into the Booster. The power supply system for one plate providing all necessary parameters including suppression of the afterpulses is described in the report. The calculated and experimental results are also presented.

INTRODUCTION

Development and construction of the NICA ion collider [1] is underway at the Joint Institute for Nuclear Research. The booster in which the ion beam is preaccelerated and cooled is one of the main facilities of the complex.

The booster injection system presupposes the use of the electrostatic septum and of three deflecting devices [2]. Electric plates are expected to be used as the actuating elements. Hydrogen thyratrons are used as a switches.

CHARACTERISTICS OF ELECTRIC PULSES

All electrical plates are fed with identical pulses that differ only by the amplitude of the applied voltage. Main characteristics of electric pulse with maximum amplitude are shown in Table 1.

Table 1: Main characteristics of electric pulse.

Maximum electrical potential on the plate	60 kV
Charging time	< 50 ms
Duration of pulse plateau at least	30 us
Nonuniformity of voltage on the plateau	≤ 1%
The discharge time	≤ 0,1 us
Residual voltage	≤ 0,5 kV
The number of pulses in a row	1 ÷ 3
The pulse repetition frequency	10 Hz

The parameter values given in Table 1 are generally achieved without major difficulties, but the residual voltage value stands out as an exception to this generalization.

This issue was given special attention. The measurements showed that the voltage at the thyratron (and, consequently, at the plate) nears zero by the time the thyratron is switched off and starts increasing after that. This may be attributed to the response of multiplication and filter circuits of the controlled power supply and the relaxational polarization of dielectrics (e.g., in the lead cables). One possible solution to this problem consists in implementing the "afterburning" (i.e., maintaining the discharge current through the thyratron with the use of an additional low voltage power supply). Such a system is presently used at the Nuclotron accelerator. The arc-burning voltage naturally depends on the thyratron model and operating regime and usually falls within the range from 100 V to several hundred volts.

THE SUPPLY SCHEME

To reduce residual voltage and improve reliability of high voltage components, it was decided to use a pulse charging.

The PSPICE model of the power supply circuit is presented in Fig.1.

The initial pulse of the thyristor generator is applied to the primary winding of the step-up transformer. We use industrial measuring transformer GE-36. Near the top of the pulse when the current in the primary winding of the transformer crosses zero value thyratron is triggered.

The discharge chain C_2, R_3, R_4 maintains the discharge current through the thyratron in a few tens of microseconds, thereby preventing fast afterpulses. Slow processes are suppressed by leakage of charges through the secondary winding of transformer.

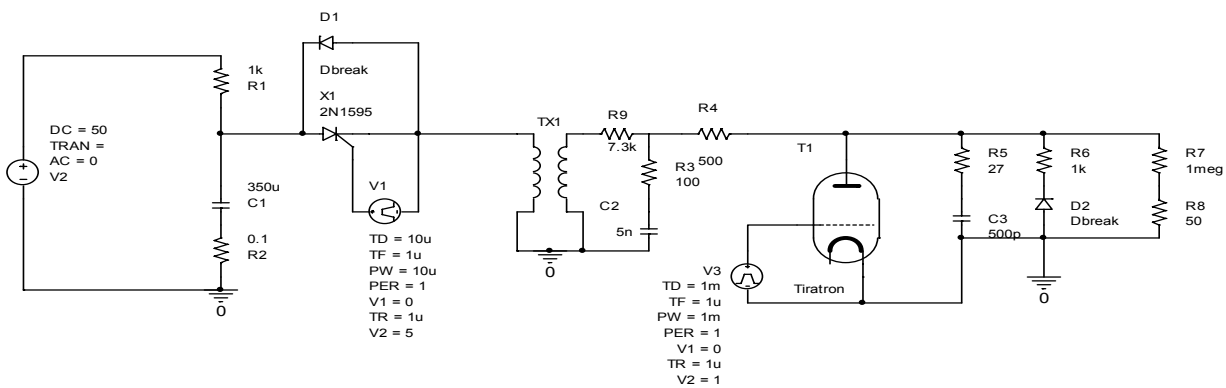

Figure1: PSPICE model of the power supply circuit.

ISBN 978-3-95450-170-0

The result of calculation with program SPICE is presented in Fig.2. Voltage scale is reduced. Prototyping measurement results are presented in Fig.3.

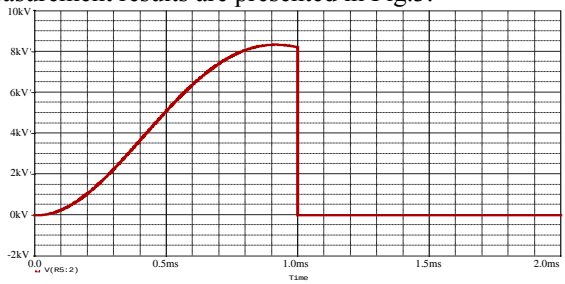

Figure 2: Shape of the voltage pulse on the plate simulated with PSPICE.

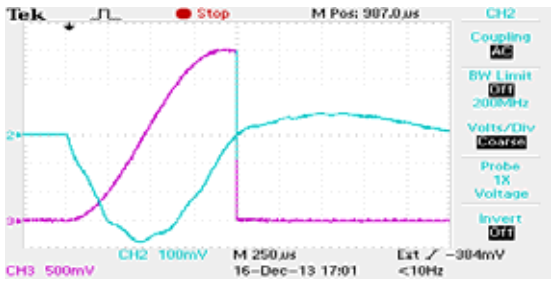

Figure 3: Prototyping measurement results. Voltage (10 kV/div) at the equivalent capacitance and input current (40 A/div) of the transformer.

CONCLUSIONS

Selected approach and scheme of the power supply for deflecting plates were simulated with PSPICE and compared with experimental results on equivalent load. The test results allow to take this scheme as a prototype for booster injection system.

ACKNOWLEDGMENT

Authors express thanks Petrov Viktor Aleksandrovich for seminal discussion and useful remarks.

REFERENCES

[1] NICA (Nuclotron based Ion Collider fAcility) accelerating–storage complex. Preliminary design, Ed. By I. N. Meshkov and A. O. Sidorin (2009). http://nucloweb.jinr.ru/nica/index1.htm.

[2] A Conceptual Design of a Power Supply System of Deflecting Plates for Multivariate Injection into the NICA Accelerator Complex Booster, V. A. Bulanov, E. V. Gorbachev, N. I. Lebedev at al., ISSN 1547-4771, Physics of Particles and Nuclei Letters, 2014, Vol. 11, No. 5, pp. 695–698.

ISBN 978-3-95450-170-0

VIRTUAL LABORATORY OF VACUUM TECHNIQUE

G.P. Averyanov, V.V. Dmitriyeva, V.L. Shatokhin,
National Research Nuclear University (Moscow Engineering Physics Institute)
Moscow, Russia

Abstract

The report considers the interactive computer modeling of vacuum systems. Operation of real vacuum systems is modeled by simulating computer code. It is possible to assemble virtual installation, to choose the necessary pumps (from the database of low-vacuum and high-vacuum ones), to select the vacuum connecting pipes with the required parameters. The vacuum chamber volume and its internal surfaces characteristics (roughness, types of preliminary processing), defining outgassing from these surfaces are set.

INTRODUCTION

Vacuum Technique virtual laboratory is part of a complex of similar Electrophysics Laboratories, developed at the Department of Electrophysical Facilities (EF) of NRNU MEPhI. Computer modelling and simulation of individual components and entire electrophysical systems is a promising and in some cases the only possible way to replace the full-scale simulation. The creation of computer-based simulators is used in various fields of technology, including nuclear physics field (i.e. nuclear power reactors management simulators). The development of the set of laboratory exercises for Electrophysics solves the following tasks:

- acquire technology skills in assembly and maintenance of various subsystems and systems of EF (as simulator);
- to investigate the structure and the main characteristics of the EF devices and different modes of their work;
- gain experience in EF designing and master the methods of their calculation.

The vacuum system is an essential specialty of any accelerator. In this regard, the "Vacuum Technique" educational laboratory has existed since the founding of the Department of EF. Real vacuum systems of accelerators can have a very large extent, complex structure, and the procedure for their pumping (including heating of system) can take many days. Therefore, the development of computer workshop was a logical continuation of the vacuum practical work, significantly expanding its functionality.

VACUUM SYSTEMS MODELING THEORY

The simulation program algorithm is based on the following basic theoretical principles of vacuum technology [1, 2]. The number of gas molecules in the vacuum system is reducing by means of vacuum pumps, which create a volume flow Q, determined by the speed with which pressure p in the vacuum system of constant volume V decreases with time t:

$$Q = \frac{\mathrm{d}(pV)}{\mathrm{d}t} = V \cdot \frac{\mathrm{d}p}{\mathrm{d}t} \quad . \tag{1}$$

In reality, there is a lower limit of pressure below that pumping of the system is impossible - the ultimate residual pressure p_r. The amount of gas in the vacuum system depends on the ratio of gas flow entering the system - Q_{in} and pumping - Q_p: $Q = Q_p - Q_{in}$. The magnitude of the gas flow entering the system depends on the quality of manufacture of the vacuum system, that is, the values of leakage flow Q_l and outgassing flows Q_{gf} from inner surfaces. When the limit of the residual pressure in the vacuum system is reached mode is set to dynamic quasi-equilibrium: $Q_p = Q_{in}$. Pumped flow is equal $Q_\mathrm{p} = Sp$, where S is pumping speed. Equation (1) takes the form:

$$p \cdot S - Q_l - Q_{gf} = V \cdot \frac{\mathrm{d}p}{\mathrm{d}t} \, . \tag{2}$$

Thus $p_r = (Q_l + Q_{gf})/S$. The result of the solution of equation (2) for the total pressure will be the dependence:

$$p(t) = \frac{Q_\Sigma}{S} + \left(p_{st} - \frac{Q_\Sigma}{S} \right) \cdot \mathrm{e}^{-t/\tau} \quad ,$$

where $\mathrm{Q}_\Sigma = \mathrm{Q}_{gf} + \mathrm{Q}_l$; p_{st} - initial pressure in the vacuum system, $\tau = V/S$. Similar dependences can be obtained for each partial gas component $p_i(t)$. Furthermore, the system pressure cannot be obtained under the pump ultimate pressure. In case of the continues pumping flow $Q = S_p p_p = S_{ef} p$, where S_p and p_p - the pumping speed and the pressure at the pump inlet, S_{ef} - effective pumping speed of the vacuum chamber. The presence of the connecting pipelines leads to the fact that between the vacuum pump and the vacuum chamber arises a pressure differential: $p - p_p = Q/U$, U - the pipeline conductivity. Thus, the pumping of the vacuum chamber is carried out with some S_{ef}, lower than S_p.

Considering these equations, we come to the pumping model determined by the ordinary differential equations with initial conditions (Cauchy problem). The solution to this problem has been realized by the Runge-Kutta method of fourth order.

VACUUM ELEMENTS MODELS

Each of the pumps designed to operate over a certain pressure range with approximately constant pumping speed - S_0. The ultimate pump pressure p_0 determined by

ISBN 978-3-95450-170-0

the balance between entering and going out gas flows of the pump. Magnitude of the going out flow can be approximately given in this form $Q_{out} = S_0 \cdot p_0$, thus $Q_p = S_0 \cdot p - S_0 \cdot p_0 = S_p \cdot p$. With pressure decrease in the inlet of the pump to a value p_0, pumping flow becomes zero. The dependence of the pumping speed from the inlet pressure expressed by the equation: $S_p = S_0(1 - p_0/p)$. Actual pumping speed dependence is much more complicated and can be found empirically, but this equation quite accurately describes this dependency and can be used in the calculations. The pumping speed at pressures in the pump inlet above the operating range depends on operation principle of the pump.

Calculation of parameters of pipelines is a separate task. Since the various vacuum components have a rather complicated internal geometrical shape, it is necessary to use Monte-Carlo method for calculation of the conductivity of such element in the molecular or viscose gas flow mode. In a simplified version, pipeline conductance in a wide range of pressures can be determined by the following formula (Knudsen equation): $U = U_v + K \cdot U_M$, where U_v and U_M - conductance in the viscous and molecular gas flow modes respectively; K - coefficient, depending of the pressure in the pipeline.

Leakage occurs in areas with inadequate tightness of the vacuum system. Leakage flow $Q_l = \sigma (p_a - p)$. Here σ - total conductance determining the aggregate bandwidth of all leaks. Valid leakage flow is considered a flow, in which is possible to obtain the desired pressure p in the system: $Q_l \le p \cdot S$.

The level of initial outgassing rate q_0 and the total surface area A determine the flow rate from the inner surfaces of the vacuum chamber $Q_{gf} = A \cdot q_0 \cdot k \cdot \exp(-kt)$. Value of Q_0 depends on the material and the roughness of vacuum chamber surface. Degassing coefficient k is mainly acquired experimentally. It increases with rising temperature of the vacuum system, which leads to increase the outgassing rate and simultaneously to more rapid decay time $\sim\exp(-kt)$. Therefore, to accelerate the process of obtaining a high vacuum the temperature heating of the vacuum chamber is applied.

THE SOFTWARE STRUCTURE

Virtual laboratory software has a unified structure. In the present representation each software module of Electrophysics laboratory can be represented as interrelated functional blocks, which when necessary may be upgraded independently of each other. The most conservative components of the system (almost independent of the operating environment implementation, etc.) are the configuration file that defines the structure of the system and its mathematical description (mathematical model). All other components of the structure are highly dependent on the level of information technology and tools for their development.

Brief description of the main functional elements.

1) Graphical environment. In the graphic design of any software package that simulates electrophysical facilities and their individual subsystems can distinguish five basic elements:
- Data input element. Used to set the numerical values of a specific physical quantity.
- Graphs display element. The main function of this display is static or dynamic picture of the physical process.
- Elements reflecting an installation diagram.
- Reflection element help (HELP).
- Grouping elements to create pop-up windows, tabs or simply dividing lines.

2) The configuration file. Is a description of the components and their position in the formatted file as an XML document.

3) Mathematics module. Exchange protocol. Mathematical module is a separate executable file, which is called as a system call command.

4) The core is the basic infrastructure of the project, provides a coherent libraries and interfaces that defines communication protocols and the structure of the configuration files.

USER INTERFACE

The structure of the user interface is designed for all virtual laboratories by the same cathedral rules and determined by the main purpose of the laboratory. Assumes the solution of the following main tasks within this laboratory:
- study of the vacuum system and the influence of various factors and components on its characteristics;
- design of the vacuum system (in extracurricular time), its virtual assembly and check for compliance with the technical task.

Laboratories environment consists of two main (working) modules (the window) and a number of additional. The main working window (see Fig. 1) is given the structure of the vacuum system containing the necessary components to ensure high vacuum in the required volume and panels with setting of parameters of the pumping system. This window consist buttons that define the range of parameters of vacuum chamber and pumping unit (based on the manufacturers' data). The characteristics of pumped chamber (material, the quality of treatment of the inner surface, the initial level of surface outgassing) are entered.

When selecting vacuum pumps popup window represent their nomenclature and features. As a result of the choice of an industrial vacuum pump its parameters (ultimate pressure, pumping speed, inlet sizes) are recorded in the right pane of the window (see Fig. 1). Arbitrarily adjustable pump is selectable and its parameters can be varied within wide limits. The panel also contains pumping system parameters (pipelines), which are specified in the design of the vacuum system.

ISBN 978-3-95450-170-0

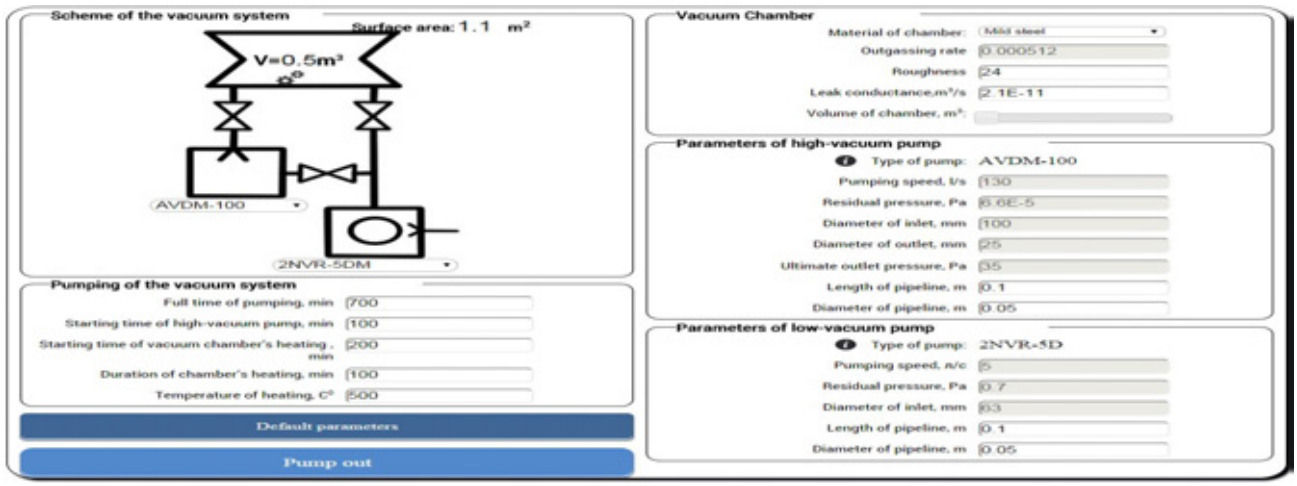

Figure 1: Simulation of vacuum system parameters.

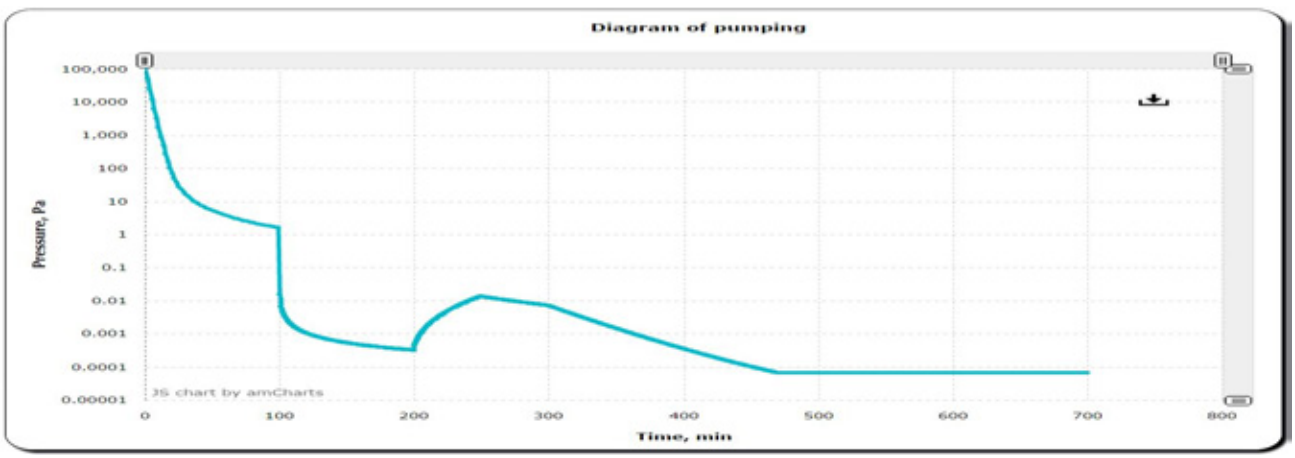

Figure 2: Dynamics of vacuum chamber pumping.

In the left pane of the main window (see Fig. 1) "pumping on" and the management of pumping process are performed. Here you set the timing diagram of pumping and all process total time. It's possible to select only preliminary pumping (low vacuum), or connect thermal degassing phase at high vacuum pumping.

The second working window displays the dynamics of the pumping process in time for given characteristics of the vacuum system (see Fig. 2). There is a possibility of a detailed study of the pumping process at different time stages. As a result of the analysis of the results an adjustment of the characteristics of the elements of the pumping system is performed to achieve the desired parameters.

Additional windows contain the traditional set of features of virtual laboratories - theoretical principles of developed topic, guidelines for carrying out the works, individual assignments, and tests for self-control.

CONCLUSION

Developed virtual environment provides a choice of means of pumping and traditional elements of vacuum systems, the choice of material of pumped volume, its pre-treatment, monitoring the process of pumping, registration, analysis of the data and making changes to complete system in order to obtain the desired results. It becomes possible in a short time (with the assessment of real-time) to pass through full cycle of the technologies to reach high vacuum state and to estimate the necessary time. Modeling of vacuum systems significantly expands the functional capabilities of vacuum laboratory.

REFERENCES

[1] L.N. Rozanov, *Vacuum Technique*, (Moscow: V. shkola, , 2007), 391.

[2] K. Demihov et al., *Vacuum Technology. Handbook*, (Moscow: Mashinostroenie, 2009), 590.

ISBN 978-3-95450-170-0

MEASUREMENT OF THE DOSE RATE AND THE RADIATION SPECTRUM OF THE INTERACTION OF 2 MeV PROTON BEAM WITH A VARIETY OF STRUCTURAL MATERIALS*

D. Kasatov#, A. Makarov, S. Taskaev, I. Schudlo
BINP SB RAS, Novosibirsk, Russia,

Abstract

At the BINP, a pilot epithermal neutron source is now in use. It is based on a compact Vacuum Insulation Tandem Accelerator (VITA) and uses neutron generation from the reaction ^{7}Li(p,n)^{7}Be. Irradiation experiments using various structural materials were carried out. The results of measuring the intensity and the spectra of the γ and X-ray radiation are discussed in the present work. This work is a part of a plan to create a therapeutic beam and strategies for the use of the accelerator for clinical application.

INTRODUCION

Presently, Boron Neutron Capture Therapy (BNCT) [1] is considered to be a promising method for the selective treatment of malignant tumors. The results of clinical tests, which were carried out using nuclear reactors as neutron sources, showed the possibility of treating brain glioblastoma and metastasizing melanoma not curable by other methods [2, 3]. The broad implementation of the BNCT in clinics requires compact inexpensive sources of epithermal neutrons. At the BINP the source of epithermal neutrons based on 2 MeV Vacuum Insulation Tandem Accelerator (VITA) and neutron generation through ^{7}Li(p,n)^{7}Be reaction was proposed [4] and created.

General view of the accelerator is shown in Fig. 1. Negative hydrogen ions are injected and accelerated up to 1 MeV by potential applied to the electrodes, then H^- turn into protons in the stripping target and at last the protons are accelerated up to 2 MeV by the same potential. Pumping of the gaseous stripping target is carried out by cryogenic and turbomolecular pumps through the jalousies. The potential of the high-voltage and five intermediate electrodes is supplied by a high-voltage source through the insulator which has a resistive divider.

Presented work is aimed on measurement of lithium target radiation hazard and to find materials for high-energy beam transporting channel and for substrate of neutron producing target with minimum radiation emission during proton bombardment. There were studied different materials.

EXPERIMENTAL LAYOUT

Generation of γ- rays was carried out by directing the proton beam on targets made of various materials. The target is a disc of 100 mm diameter and thickness from 1 mm to 10 mm depending on the material mounted on a cooled copper substrate. Gamma spectra were detected by BGO spectrometer. BGO spectrometer was located at a distance of 75 cm from the target along the beam axis and was covered by a lead shielding having thickness of 50 mm with collimation hole 25 mm in diameter. The spectrometer was calibrated using the isotopes ^{137}Cs and ^{60}Co taking into account the background radiation from the accelerator [5]. After irradiation the target was extracted and induced radioactivity was measured. For this purpose we used NaI and BGO detectors.

Dose rate measurements were carried out by an automatic system based on ionization chambers. In some cases the neutron yield was registered by the lithium glass detector.

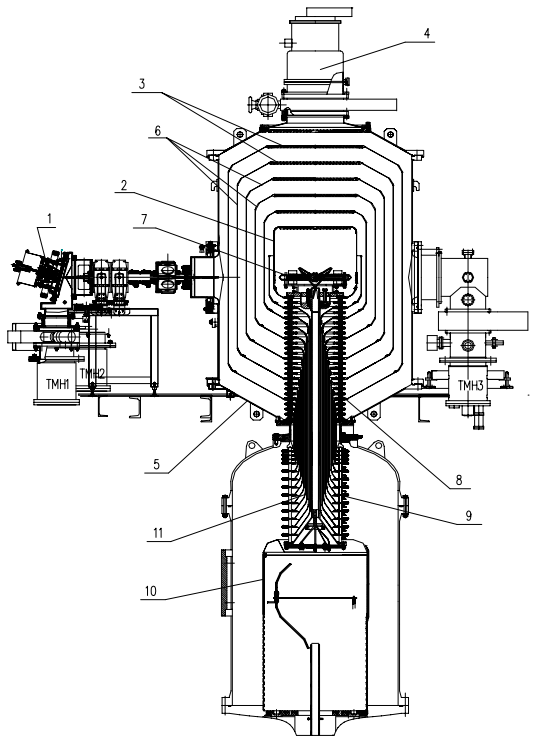

Figure 1: High-current vacuum insulation tandem accelerator: 1 –ion source (H-); 2 – high voltage electrode; 3 – electrode shutters; 4 – cryo pump; 5 – accelerator vacuum volume; 6 – intermediate electrodes; 7 – stripping target; 8 – feedthrough insulator (vacuum part); 9 – feedthrough insulator (gas part); 10 – high voltage source; 11 – coaxial feeding tubes.

* The study was performed by a grant from the Russian Science Foundation (Project No.14-32-00006) with support from the Budker Institute of Nuclear Physics.
# kasatovd@gmail.com

ISBN 978-3-95450-170-0

EXPERIMENTAL RESULTS

Gamma-ray Generation

Various materials (Li, C, Al, Si, Ti, V, Fe, Cu, Mo, Ta) were bombarded by 2 MeV protons. The average proton current was 400 mkA. Gamma spectra normalized to the current and time are shown in Fig. 2.

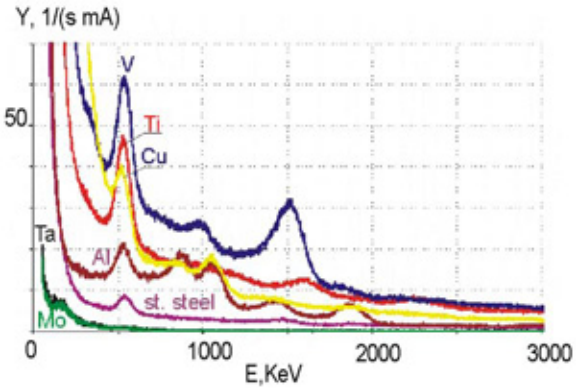

Figure 2: Gamma spectra of different materials under proton beam.

Titanium and graphite showed significant activation by the proton beam (Fig.2 and Fig.3). In other cases activation dropped fast before the target was retrieved. Target retrieving time was about 15 minutes.

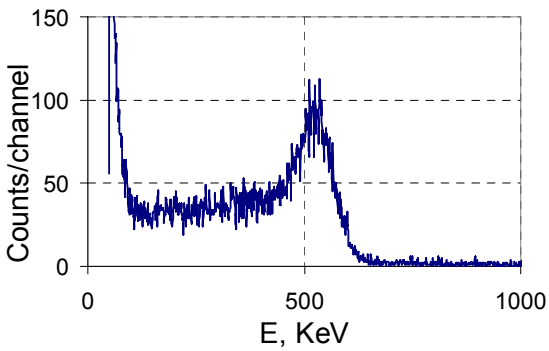

Figure 3: Gamma spectrum of $^{12}C(p)^{13}N \rightarrow \beta+(10\ min) \rightarrow {}^{13}C$ (dose rate 0.5 μSv/h).

Also irradiation experiments were carried out using a proton beam deposited on lithium fluoride and barium fluoride as an attempt of generating positrons in reaction $^{19}F(p,\alpha e^{+}e^{-})^{16}O$. Spectra are shown in Fig. 5. In case of lithium fluoride the positron line is superimposed with 478 KeV line which is produced in $^{7}Li(p,n)^{7}Be$ reaction.

Neutron Generation

At energy of 2 MeV protons on some materials (Ti, V, LiF_2 and stainless steel) experienced significant neutron flux. For them, the neutron yield was measured at a lower energy proton beam.

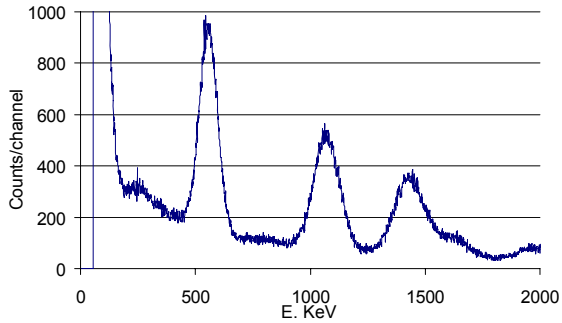

Figure 4: Gamma spectrum of activated natural titanium 3 days after irradiation (dose rate 4.6μSv/h).

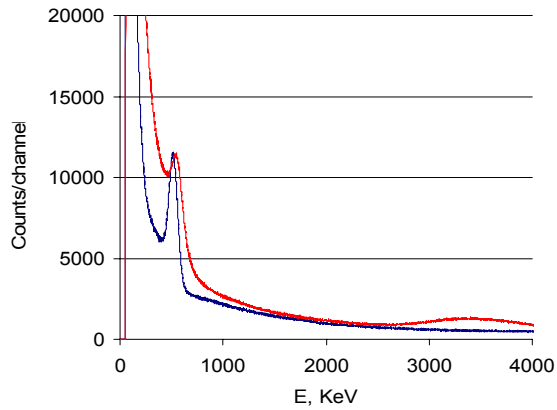

Figure 5: Gamma spectra of lithium fluoride (red) and barium fluoride (blue).

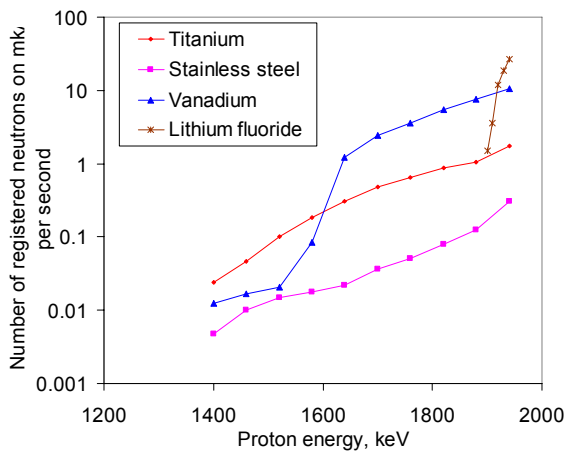

Figure 6: Neutron yield for different materials.

SUMMARY

Bombardment of C, Al, Si, Ti, V, Cu and stainless steel by 2 MeV protons leads to intense γ-ray emission. Bombardment of stainless steel, titanium, vanadium and lithium fluoride by 2 MeV protons leads also to neutron generation. Therefore the best materials for minimizing of gamma-rays radiation under 2 MeV protons are tantalum and molybdenum.

ISBN 978-3-95450-170-0

REFERENCES

[1] G. Locher, Am. J. Roentgenol. Radium Ther. 36 (1936) 1.
[2] H. Hatanaka, Basic Life Sci. 54 (1990) 15.
[3] H. Hatanaka, and Y. Nakagawa, Int. J. Radiat. Oncol. Biol. Phys. 28 (1994) 1061.
[4] B. Bayanov, et al., NIM A 413 (1998) 397.
[5] I. Sorokin, et. al., "X-ray Radiation of the High-Voltage Elements of the Tandem-Accelerator with Vacuum Insulation", MOPPA030, these proceedings.

ISBN 978-3-95450-170-0

MEASUREMENT OF THE SPATIAL DISTRIBUTION OF GAMMA RADIATION AT TANDEM ACCELERATOR WITH VACUUM INSULATION *

I. Schudlo#, D. Kasatov, A. Makarov, S. Taskaev
Budker Institute of Nuclear Physics SB RAS, Novosibirsk, Russia

Abstract

The experiments on generating 2 MeV proton beam with the current of 1.6 mA were carried out at BINP. During the experiments the spatial distribution of the bremsstrahlung dose rate was studied. According to the experimental results the suggestion of the reasons for the radiation appearance and ways to reduce it were made.

INTRODUCTION

At the BINP, the source of epithermal neutrons for boron neutron capture therapy of malignant tumors based on the tandem accelerator with vacuum insulation and a lithium target is created and put in operation [1]. The circuit source is shown at Fig. 1. The proton beam energy of 2 MeV and a current of 1.6 mA is obtained at the accelerator-tandem with vacuum insulation, marked by rapid acceleration - 25 kV/cm. Generation of neutrons occurs as a result of the threshold reaction ^{7}Li(p,n)^{7}Be while dumping the proton beam onto the thin lithium target with intense cooling.

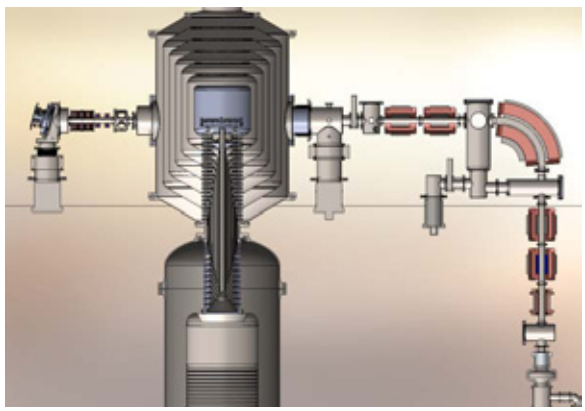

Figure 1: High-current vacuum insulation tandem accelerator.

To conduct BNCT it is required to increase the proton beam current at least up to 3 mA. But the increase in the injected current accelerator leads to unstable operation of the accelerator and requires research to ascertain the causes of the current limit. It was assumed that one of the beam current limitations is presence of accompanying electrons in the accelerator channel. The electrons are produced by the interaction of low energy beam of H^- ions with the residual gas in the input node of the accelerator. The electrons are accelerated to the full energy according the accelerator voltage and absorbed in the construction materials of the accelerator generating intense bremsstrahlung radiation. To investigate the electron current the experiment was conducted on measurement of the angular distribution of the accelerator gamma radiation.

EXPERIMENTAL LAYOUT

During the experiment, the beam of accelerated protons with a current of 0.5 mA is measured by the Faraday cup, located at the accelerator output. Measurements of gamma dose are carried out using two dosimetry detectors Berthold LB-112. One detector is placed at a distance of three meters from the center of the accelerator at a 90 degree angle to the beam axis, the measurements with the second detector were carried out at different angles to the beam axis at the same distance to the accelerator. The detectors are located at the horizontal plane with the acceleration tract.

EXPERIMENTAL RESULTS

The measured gamma dose distributions are presented at Fig. 2 and 3.

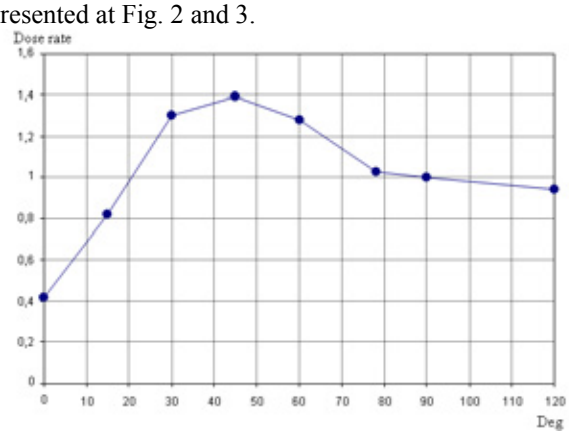

Figure 2: A gamma dose rate in dependence on the radiation emission angle. The value is normalized to the reading of the detector mounted at an angle of 90° to the beam axis.

The dose rate lowering at the angles 0°-30° is the result of gamma attenuation by the construction elements: the stripping tube and output pumping volume are located between the detector and the gamma source area. Actual trend should have higher values according to Fig. 3. Such a dose distribution having the preferred direction coinciding with the accelerated beam could be explained if the bremsstrahlung radiation is caused by the relativistic electrons.

* The study was performed by a grant from the Russian Science Foundation (Project No.14-32-00006) with support from the Budker Institute of Nuclear Physics.
# Cshudlo.i.m@gmail.com

ISBN 978-3-95450-170-0

Forward direction of radiation can be attributed to the direction of flow of electrons incident on the materials of the facility construction. The most probable process is the following: negative hydrogen ions injected into the accelerator ionize the residual and stripping gas at the entrance of the accelerator with high efficiency because the velocity of the injected particles is small. Arising in the area with the accelerator electric field, electrons are accelerated to the full energy by 1 MV voltage and thereof the appreciable part of electrons reaches the end of the stripping tube installed inside the high voltage electrode. Such a directed high-energy electrons flow causes the directed flow of the bremsstrahlung while absorbing in the construction metals.

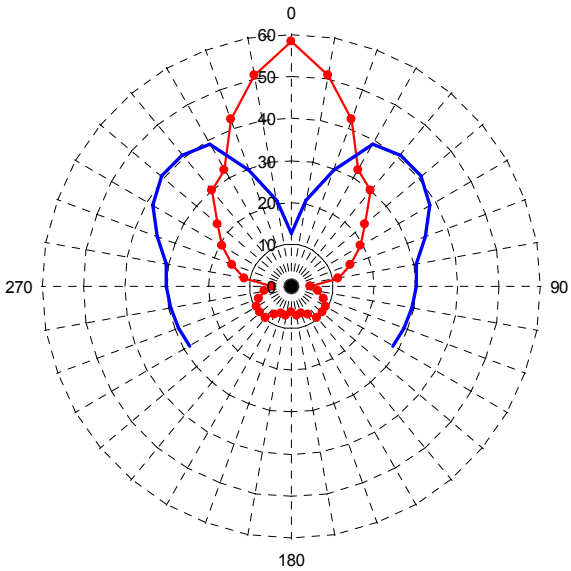

Figure 3: Angle distribution of gamma radiation. Blue line – experimental results, red line – theoretical dependence for the case of 1 MeV electrons dumped onto an iron [2].

SUMMARY

The measurements of the spatial distribution of the X and gamma radiation dose rate were carried out at the tandem accelerator with vacuum insulation. Directional effect of bremsstrahlung is discovered, which is described as radiation of 1 MeV electrons. This result confirms the assumption that a significant current in the accelerating gap is a result of the interaction of the injected and accelerated beam of charged particles with a residual and the stripping gas. The understanding of the processes allows one to propose suggestions for the modernization of the accelerator in order to obtain 3 mA proton beam.

REFERENCES

[1] D. Kasatov, A. Koshkarev, A. Kuznetsov, A. Makarov, Yu. Ostreinov, I. Sorokin, I. Shchudlo, S. Taskaev, “Problems and prospects of the Tandem Accelerator with Vacuum Insulation”, these proceedings.

[2] Hygienic requirements for the placement and operation of electron accelerators with energies up to 100 MeV. Sanitary rules and norms SanPiN 2.6.1.2573-10, 2010.

ISBN 978-3-95450-170-0

ESTIMATION OF THE EFFICIENCY OF BIOLOGICAL SHIELDING FOR THE CIRCULAR HALL OF U-70 ACCELERATOR AT IHEP

G. Britvich, M. Kostin, V. Pikalov, O. Sumaneev, IHEP, Moscow Region, Russia

Abstract

Report presents estimation of biological shielding efficiency for annular hall of U-70 accelerator. Distribution of neutron flux in concrete shielding of proton accelerator measurements carried out by method of long-lived isotopes specific activity determination. The experimental data may be compared with Monte-Carlo simulation.

INTRODUCTION

During construction of the new medical channel for carbon ions beam extraction the side concrete shielding of the accelerator was disclosed. We have got a good opportunity to measure depth distribution of the gamma-activity of the shielding on the height of 10 cm from the beam orbit plane. Such measurement allows us to estimate efficiency of the neutron radiation attenuation in the biological shielding of accelerator.

GEOMETRY OF MEASUREMENTS AND BOUNDARY CONDITIONS

Cross-section of the U-70 side shielding is shown in Fig.1. This shielding was partly disclosed for the new channel construction. Point M corresponds to the internal target 35/1 of channel #18. This target was working during previous run of U-70 since 09 to 21.04.2012. Berillium target (with 3×3 mm2 cross-section and 30 mm length) was irradiated by 5×1011 protons with 50 GeV energy during every 9.7 sec cycle. Induced radioactivity was measured along lines 1-4 in the Fig. 1. Measurements were done on the surface of concrete blocks at the level of 2 m from the floor. Beam orbit is laying at the level of 2.15 m from the floor. Blocks were removed from the shielding for the measurements to improve background conditions. One can see measurement points marked, detector and its shielding.

GAMMA-SPECTROMETER

Scintillation gamma-spectrometer with NaI(Tl) crystal was used for the measurements. Crystal size is 40×40 mm2, it was equipped with PMT XP 2212. Parameters were measured in operational conditions, with 50 m cable and rate ~ 103 Hz. 43 calibration sources were used.

GAMMA-ACTIVITY OF THE CONCRETE

Measurements were done in two concrete blocks along lines 1-4 (see in Fig. 1) in set of points placed in 25.4 cm from each other. Typical gamma spectrum is shown in Fig. 2. Two isotopes – ^{22}Na and ^{54}Mn – could be easily identified. ^{22}Na is created by the fast neutrons with energy threshold 13 MeV in the reaction ^{23}Na(n, 2n)^{22}Na, and ^{54}Mn in the reactions ^{55}Mn(n, 2n)^{54}Mn with 11 MeV threshold and ^{54}Fe(n, p)^{54}Mn with 1.5 MeV threshold [1-2]. ^{24}Na is presented in cement, ^{55}Mn and ^{54}Fe are presented in cement, gravel and steel fixtures.

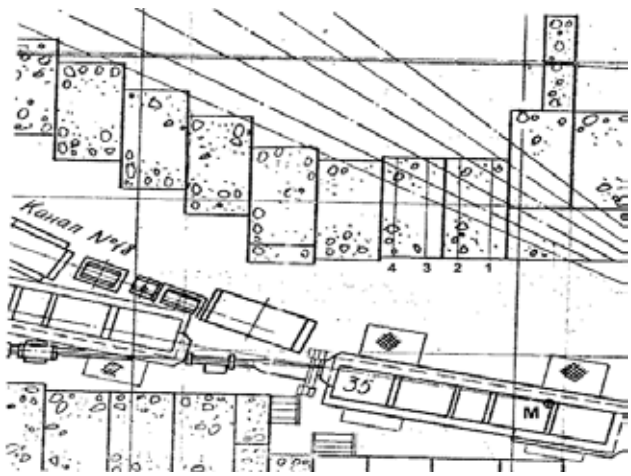

Figure 1: Accelerator equipment and shielding layout in the U-70 circular hall in the region of 34, 35 and 36th magnet blocks.

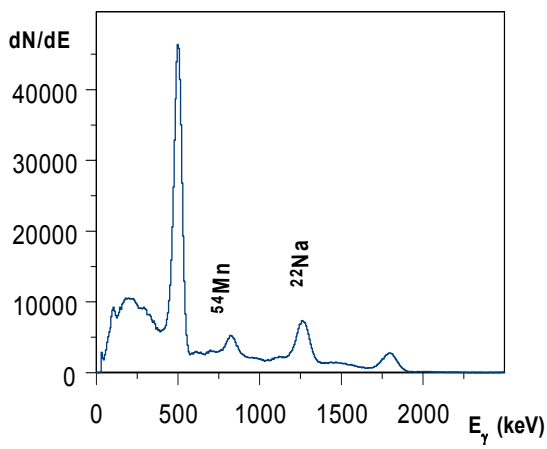

Figure 2: Gamma-spectrum measured on the concrete surface.

ABSOLUTE ACTIVITY OF ^{22}NA AND ^{54}MN ISOTOPES IN CONCRETE

Detector is placed on the concrete surface and measure number of gamma rays (N_γ) in the point from the semi-infinite layer of concrete.

ISBN 978-3-95450-170-0

If specific activity of the concrete (q, in Bq/kg) can be treated as a constant in the vicinity of the point of measurement, Nγ value is equal to 2π×q/μ, where μ is the linear coefficient of gamma rays attenuation in the concrete. Practically detector can "see" semi-spherical volume of the concrete with radius equal to 1/μ.

For ^{22}Na (E_γ = 511 keV) L is equal to 4.87 cm, for ^{22}Na (E_γ = 1274.537 keV) L is equal to 7.53 cm, and for ^{54}Mn (E_γ = 834.838 keV) L is equal to 6.15 cm. Activity measurements with E = 511 keV is most suitable for coordinate resolution, because in this case detector can see less volume of concrete. ^{22}Na is a positron-active nucleus with positron mean energy ~ 200 keV. Range of such e^+ in concrete is near 250 um [3], therefore point of 511 keV photon generation is coincides with ^{22}Na nucleus. Measurements of such photon in the spectrometric mode indicates that this photon does not interact between generation point and detector.

Number of pulses in the total absorption peak for E_γ = 511 keV at all points of measurements are presented in Appendix 1. The same data are presented in the normalized form as a distribution of specific ^{22}Na activity along the side concrete shielding.

CONCLUSION

Result of the measurements can be used for the estimation of U-70 accelerator shielding residual radioactivity, and for the tests of shielding codes.

REFERENCES

[1] Table of Radioactive isotopes. E.Browne and R.B. Firestone. 1980

[2] Table of Isotopes. Seventh ed. By C.M. Lederer and V.S. Shirley, 1978

[3] J.H. Hubbel. Photon mass attenuation and energy-absorption coefficients from 1 keV to 20 MeV. Int. J. Appl. Radiat. Isot. Vol.33, pp.1269 to 1290, 1982

APPENDIX

Table 1: Counts rate in the full absorption peak for Eγ = 511 keV. Measurements along the Line #1.

point	file	L, (cm)	L, (g/cm^2)	S, puls/s	Uncer-tainty,%
1	act157	25.4	59.7	32.06	4
2	act158	50.8	119.4	15.00	4
3	act159	76.2	179.1	7.96	7
4	act160	101.6	238.8	4.34	6
5	act161	127.0	298.5	2.34	7
6	act162	152.4	358.1	1.43	11
7	act163	177.8	417.8	0.79	11
8	act164	203.2	477.5t	0.42	23

Table 2: Counts rate in the full absorption peak for Eγ = 511 keV. Measurements along the Line #2.

point	file	L, (cm)	L, (g/cm^2)	S, puls/s	Uncer-tainty,%
1	act147	25.4	59.7	43.78	3
2	act148	50.8	119.4	20.43	4
3	act149	76.2	179.1	10.59	5
4	act150	101.6	238.8	6.35	5
5	act151	127.0	298.5	2.81	8
6	act152	152.4	358.1	1.80	12
7	act153	177.8	417.8	1.08	12
8	act154	203.2	477.5t	0.63	23

Table 3: Counts rate in the full absorption peak for Eγ = 511 keV. Measurements along the Line #3.

point	file	L, (cm)	L, (g/cm^2)	S, puls/s	Uncer-tainty,%
1	act124	25.4	59.7	61.94	3
2	act125	50.8	119.4	31.67	6
3	act126	76.2	179.1	15.57	6
4	act127	101.6	238.8	9.96	12
5	act128	127.0	298.5	4.14	10
6	act130	152.4	358.1	2.65	15
7	act131	177.8	417.8	1.59	25
8	act132	203.2	477.5t	0.93	40

Table 4: Counts rate in the full absorption peak for Eγ = 511 keV. Measurements along the Line #4.

point	file	L, (cm)	L, (g/cm^2)	S, puls/s	Uncer-tainty,%
1	act137	25.4	59.7	68.92	2
2	act138	50.8	119.4	28.34	4
3	act139	76.2	179.1	16.02	6
4	act140	101.6	238.8	8.48	7
5	act141	127.0	298.5	4.62	7
6	act142	152.4	358.1	2.66	7
7	act143	177.8	417.8	1.37	10
8	act144	203.2	477.5t	0.92	16

ISBN 978-3-95450-170-0

DEVELOPMENT OF ACCELERATOR FACILITIES AT SSC RF – IPPE

V.A. Romanov, S.V. Bazhal, A.I. Glotov and K.A. Rezvykh, SSC RF – IPPE, Obninsk, Russia

Abstract

Short overview of status and operation of accelerator facilities of the SSC RF – IPPE for various applications in nuclear science and technologies is given. Some results obtained as well as prospect of development of the accelerator facilities are described.

INTRODUCTION

An infrastructure for experimental research in nuclear physics based on high-voltage accelerators has been developed at the SSC RF-IPPE for more than half a century. The results obtained have made significant contribution to the solution to problems of fission physics, solid-state physics and studies of materials under radiation, as well as to the build-up of nuclear data for development of fast neutron reactors and to some other fields of basic and applied research.

At the present time scientific research on the accelerators at the SSC RF-IPPE is carried out in the following main fields:

- Low and intermediate energy nuclear physics. Nuclear data for nuclear power engineering. Closed fuel cycle. Safe handling of radioactive waste and spent fuel [1-4].
- Solid state physics. Physics of radiation damage and studies of materials under radiation [5-7].
- Nuclear microanalysis. Analysis of composition and structure of materials [8-10].
- Basic research on dusty plasma physics [11-13].
- Development of technology of membranes [14].
- Nuclear medicine [15-16].

Experimental facilities based on six electrostatic accelerators were constructed at the institute. The EGP-15 tandem accelerator (Fig. 1), the largest electrostatic accelerator in Russia, is among those six machines. This tandem accelerator was designed and manufactured at the Institute for Physics and Power Engineering in close cooperation with many Russian scientific organizations.

The accelerator facilities provide a wide spectrum of species of accelerated ions (H, He, Li, C, O, F, Al, Si, Cl, Fe, Ni, Zr) formed in the continuous or pulsed ion beams with current in the range 10^{-8} A to 10^{-3} A and energy varying from several hundred keV to tens of MeV. The main operational characteristics of the accelerators are given in Table 1.

The following factors determining interest in electrostatic accelerators can be mentioned among the others:

- high uniformity of energy of accelerated beam;
- broad range of accelerated ions;
- possibility of quick alteration of species of accelerated particles;
- intensity of ion beams produced at the accelerators of this type are in the range 10^{-8} A to 10^{-3} A;

Figure 1: The EGP-15 tandem electrostatic accelerator.

Table 1. The main operating characteristics of accelerator facilities of the SSC RF-IPPE

Model	Ion Energy, MeV	Ion species	Beam Mode	Beam Current μA
EG-2.5	0.2÷3.1	P, D	continuous	0.1÷30
		He, N, Ar, O		0.01÷10
EG-1	0.9÷4.5	P, D	continuous	1.0÷20
			pulsed	2000
KG-2.5	0.3÷2.2	P, D	continuous	100÷2000
EGP-15	4÷12 (P)	P, D	continuous	5
			pulsed	400
		heavy ions	continuous	0.01÷1.0
EGP-10 (temporarily closed)	3.5÷9.0	P, D	continuous	0.01÷10
			pulsed	400
KG-0.3 (temporarily closed)	0.3	P, D	continuous	10÷2000
			pulsed	5000

ISBN 978-3-95450-170-0

- smooth adjustment of energy of accelerated ions from several hundred keV to several tens of MeV;
- simplicity of service, reliability, small energy consumption (power consumption - some tens of kW).

Wide use of these accelerators in the world as tools for basic and applied research, as well as for beam technologies is caused by the features mentioned above.

Ion sources of various types, accelerating tubes, charging systems, ion-optical devices, high voltage power supplies, special electronic systems for the accelerators, as well as beam control instruments were developed and implemented at the accelerator facilities of the Institute for Physics and Power Engineering. Vacuum systems, beam lines and cooling systems of the accelerators were upgraded. Many of the developments are protected by copyright certificates and patents.

ACCELERATING TUBES FOR ELECTROSTATIC ACCELERATORS

Research-and-development activities aimed at designing, production and comprehensive studies of the accelerating tubes for the electrostatic accelerators have been carried out at the Institute for Physics and Power Engineering for more than 50 years. For many years of research, development and operation of the accelerating tubes a wide range of activities was fulfilled, including:

- identification of features of discharge processes determining the level of electric strength of the individual accelerating gaps and accelerating tubes in general;
- development of techniques of high-voltage tests of accelerating gaps;
- development of method of manufacture of accelerating tubes;
- elaboration of the criteria of electric strength that must be taken into account in the manufacturing of accelerating tubes designed for operating gradient over 1.2 MV/m;
- studies of the gaps of accelerating tubes depending on surface area and the shape of electrodes, as well as material of insulating rings and the shape of their vacuum-side surface;
- development of ion-optical calculation techniques as applied to the accelerating tubes with straight and inclined fields;
- calculation analysis of dynamics of multiply charged heavy ions in the inclined field accelerating tubes of the tandem accelerators;
- development of various designs of the accelerating tubes with straight and inclined fields, as well as their full-scale testing.

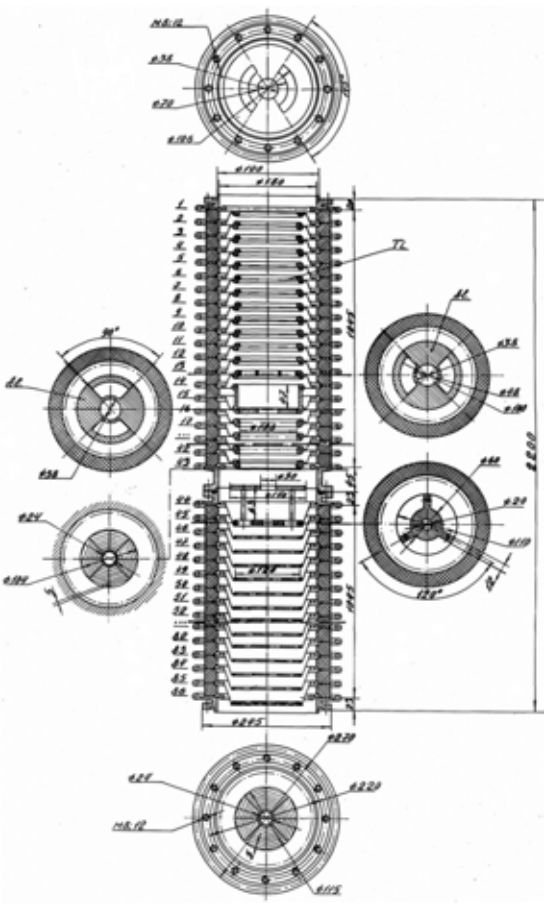

Figure 2: Design of accelerating tube of the EG-2.5 electrostatic accelerator.

A design of the accelerating tube of the EG-2.5 electrostatic accelerator is shown in Fig. 2 as an example of the developments carried out at the Institute for Physics and Power Engineering.

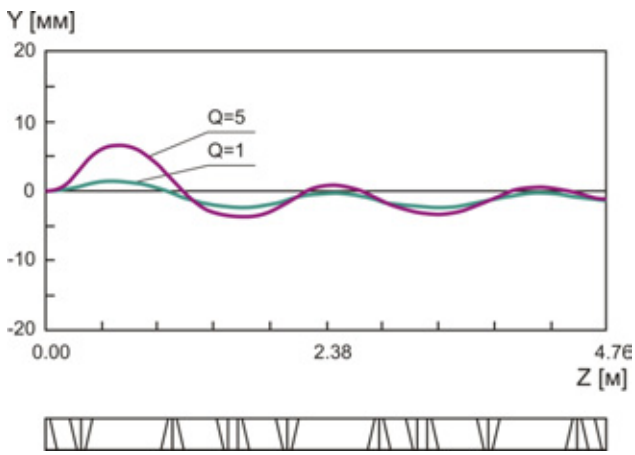

Figure 3: Trajectories of ions with charge states of 1 and 5 in high-energy inclined field tube of the EGP-15 tandem accelerator.

Fig. 3 shows the motion of multiply charged heavy ions in the inclined field tube of the EGP-15 tandem accelerator. This accelerating tube was designed and produced at the SSC RF-IPPE as well. A feature of the inclined field accelerating tubes in the mode of acceleration of multiply charged heavy ions is dispersion of the ion trajectories depending on their charges. The dispersion is caused by change of the ion charges from -e

ISBN 978-3-95450-170-0

to +Qe occurring in the stripper. An electrode structure for the inclined field tube of the EGP-15 tandem accelerator making it possible to minimize the dispersion of ion beams with different charge states was selected on the basis of calculation results [17].

CHARGING SYSTEMS FOR ELECTROSTATIC ACCELERATORS

Until recently, one of the most unreliable units of the electrostatic accelerators was the charging system based on the belt conveyor of charges. The main disadvantages of the previous charging belts were their short lifetime and high degree of wear of the working surface. Limited lifetime of the belt prevented from efficient use of the expensive equipment and resulted in additional costs of purchase of the insulating gas mixture. Increased wear of the belt led to the dust pollution of insulating gas and elements of the high-voltage structure that caused significant decrease of electric strength of the accelerator.

Activities aimed at development of the reliable belt conveyor of charges for the electrostatic accelerators have been carried out at the SSC RF – IPPE for many years. Previously used belts produced on the basis of cotton fabric had short lifetime (300-1000 hours) and high degree of wear of the rubber coating. Many types of synthetic and cotton fabrics, as well as their various combinations have been tested.

The new KBN-1591-RD conveyor of charges produced on the basis of combined polyester cotton fabric with the use of butadiene-nitrile rubber was developed in cooperation with the experts of JSC "Jaroslavrezinotehnika" [18]. This belt conveyor of charges is characterized by high electrical and mechanical properties and high wear-resistance. Production of two-layer and four-layer belts with thickness from 1.2 mm to 3 mm and width up to 800 mm has been organized. The lifetime of belt conveyors of this type is more than 10000 hours.

HIGH-VOLTAGE STRUCTURES

A computer code for optimization of high-voltage accelerator structures was developed at the Accelerator department of the SSC RF – IPPE [19-24]. The “Modulus of electric strength” calculation model now in use allows finding the breakdown voltage of elements of rather complicated systems such as accelerators solely by analytical techniques. The model has no analogs in the world practice in terms of simplicity and calculation accuracy (2-3%).

Upgrade of the high-voltage structures of the EG-2.5 electrostatic accelerator and the EGP-15 tandem accelerator was carried out on the basis of calculations. The modernized column of the EG-2.5 accelerator is shown in Fig. 4. Some results of high-voltage tests of the column are given in [24].

Operational voltage exceeding the nominal value by 24 % was achieved as a result of implementation of the “Twice orientated oval” engineering solution at the EG-2.5 accelerator.

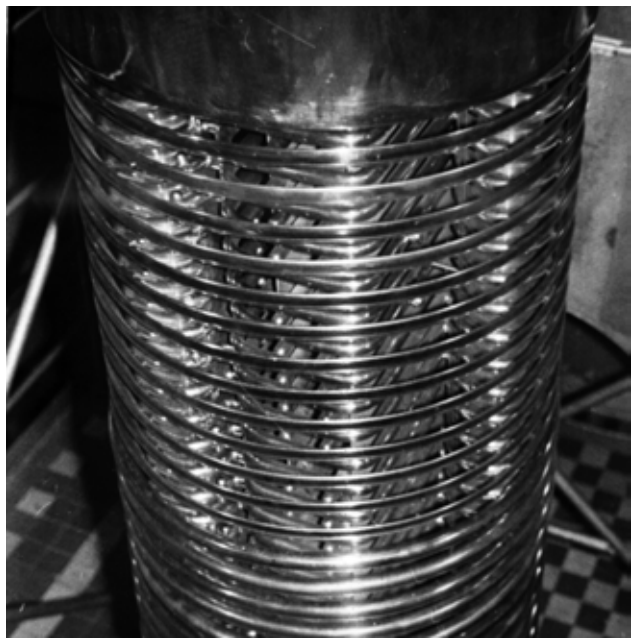

Figure 4: High-voltage column of the EG-2.5 electrostatic accelerator after upgrading.

ION SOURCES

Several designs of RF-ion sources developed at the Institute for Physics and Power Engineering are widely used at the electrostatic accelerators in Russia and abroad. The main features of these sources are low gas flow rate and high content of atomic ions (more than 80%) in the extracted beam. Characteristics of some RF-ion sources designed at the institute are given in Table 2.

Table 2. Characteristics of the RF-ion sources

Model #	Beam Current, μA	Gas Flow Rate, cm^3/h	Cathode Lifetime, h
1	200	1.5	1000
2	2000	2.5	500

The MISS-790 Cs-sputter negative-ion source designed at Helmholtz-Zentrum Dresden-Rossendor, Germany is used at the EGP-15 tandem electrostatic accelerator to produce negatively charged heavy ion beams.

To ensure required energy of injection of the negative ion beams into the EGP-15 tandem accelerator, a pre-acceleration tube with improved electric strength of the vacuum insulation was designed and manufactured at the SSC RF – IPPE. In spite of the possibility of penetration of cesium vapour to vacuum volume of pre-acceleration tube from working chamber of the ion source, the tube is able to withstand required high-voltage for the long period of time.

ISBN 978-3-95450-170-0

ION OPTICS AND BEAM TRANSPORT

Work performed at the SSC RF – IPPE in the field of ion optics and charged beam transport reflects the specifics of high-voltage accelerators, namely: a) predominance of devices in which static fields are used for acceleration, focussing and transport of charged beams; b) close interrelation between the process of ion acceleration and phenomena in the accelerating channel leading to breakdown of vacuum electric strength of the accelerator; c) wide range of accelerated particles: from single-charged ions of the hydrogen isotopes to multiply charged heavy ions; d) need for efficient change of the acceleration mode (for example, change of ion species or beam energy).

In the framework of the research, analytical and numerical methods of computation of the straight and inclined field tubes were developed [17, 25]. The results obtained were used in designing, modernization and running of accelerating tubes of the accelerator facilities.

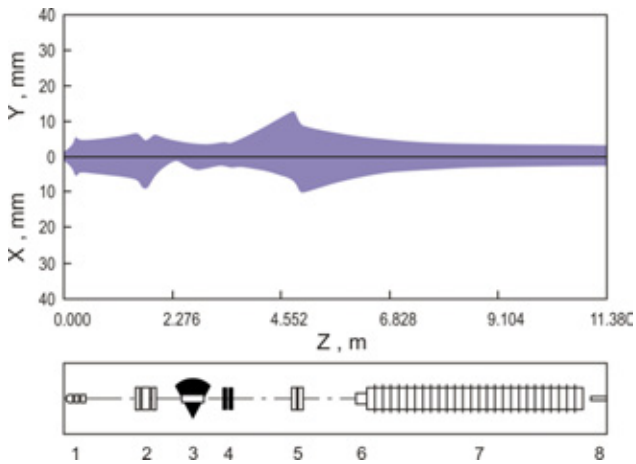

Figure 5: Beam envelopes in low-energy stage of the EGP-15 tandem accelerator calculated for Ni^- ions: 1 – ion source lens; 2 – electrostatic quadrupole triplet; 3 – magnetic analyzer; 4 – electromagnetic quadrupole doublet; 5 - electrostatic quadrupole doublet; 6 – gridded lens; 7 – accelerating tube; 8 – stripper.

Considerable attention was paid to the development of the system of injection of negatively charged heavy ions into the EGP-15 tandem accelerator. This accelerator was designed to accelerate the beams of light ions, first of all, ions of hydrogen isotopes. This circumstance, in particular, determines application of electromagnetic quadrupole lenses in the injection channel. During transition to the modes of acceleration of heavy ions, such as Ni ions, it was found that the optical power of the electromagnetic quadrupole lenses was insufficient to transport beams of singly charged negative heavy ions from the ion source to the entrance to the accelerating tube, as well as to ensure the appropriate conditions for matching of the injected beam to the accelerating channel.

The first stage of modernization of the injection channel including the replacement of two electromagnetic quadrupole lenses by the electrostatic quadrupoles was performed on the basis of the ion-optical calculations [26]. This, in particular, allowed increasing current of the beam injected into the accelerating tube from 2.5 μA to 7.0 μA and more for Ni^- ions and from 0.2 μA to 1.5 μA for ZrH^- ions. The calculated envelopes of the beam of negatively charged Ni ions in the injection channel and the low energy accelerating tube of the EGP-15 tandem accelerator are shown in Fig. 5.

In more detail this ion-optical studies (the calculation methods and their applications) are described in the papers [27-31].

PROSPECTS OF DEVELOPMENT OF THE ACCELERATOR FACILITIES

With a view to enhancement of the unique accelerator facilities it was decided to purchase a new commercially available tandem accelerator with potential of the high-voltage terminal up to 3.3 MV.

It is assumed that experimental research on nuclear physics, solid state physics, studies of materials under radiation, nuclear microanalysis and high-energy ion implantation will be carried out at this new accelerator.

To ensure optimal conditions of the experimental research the ion beams will be extracted to the existing experimental chamber of the KG-2.5 high-current cascade accelerator. This allows performing experiments on two ion beams obtained simultaneously from two accelerators.

REFERENCES

[1] B.D. Kuz'minov et al., "Use of Electrostatic Accelerators in Nuclear-Physics Research," Soviet Atomic Energy, 55 (1983) 661; http://link.springer.com/article/10.1007/BF01124128

[2] B.D. Kuz'minov "The Role of Accelerator Complex of SSC RF-IPPE in Providing Nuclear Data for Nuclear technologies," Proc. of XIII Int. Conf. on Electrostatic Accelerators and Beam Technologies, Obninsk, May 25-28, 1999, p. 5 (in Russian).

[3] V.A. Khrachkov et al., "Measurement of the Cross Section for the Reaction 20Ne(n, α)17O in the Neutron-Energy Between 4 and 7 MeV," Physica of Atomic Nuclei, ISSN: 1063-7788,75 (2012) 404.

[4] V. A. Khrachkov et al., "Experimental Studies of (n, α) Reaction Cross-Sections Performed at the Institute for Physics and Power Engineering," Bulletin of the Russian Academy of Science: Physics, ISSN: 1062-8738, 76 (2012) 486.

[5] V.A. Stepanov et al., "Electrostatic Accelerator Based Fundamental and Applied Research on Material Science," Proc. of XIII Int. Conf. on Electrostatic Accelerators and Beam Technologies, Obninsk, June 6-9, 2001, p. 29 (in Russian).

[6] Yu.V. Konobeev et.al., "The Dependence of Void Swelling Bias Factor on Iron Concentration in V-Fe Alloys," J. Nucl. Mater., 233-237 (1996) 1070.

ISBN 978-3-95450-170-0

[7] V.A. Pechenkin et al. "An Analysis of Void Swelling Dose Dependence in Ion Irradiated V-Fe Alloys," J. Nucl. Mater., 271-272 (1999) 266.
[8] S.L. Molodtsov et al., "Accurate Ion Beam Analysis in the Presence of Surface Roughness," J. Phys. D: Appl. Phys. 41 (2008) 205303.
[9] D. Abriola, et al., "Proton Elastic Scattering Differential Cross-Sections for 12C," Nucl. Instr. Meth., B269 (2011) 2011.
[10] A.F. Gurbich et al., "Measurements and Evaluation of the Cross-Section for Helium Elastic Scattering from Nitrogen," Nucl. Instr. Meth. B269 (2011)40.
[11] V.E. Ftorov et al., "Self-Organization of Dusty Particles in Plasma of Proton Beam," Prikladnaya Fizika, 1 (2009) 46, (in Russian).
[12] L.V. Deputatova et al., "Ordered Structures in Nuclear-Track Dusty Plasma for Potential and Nonpotential Forces of Interparticle Interaction» // Proc. of XIII Internat. Conf. on Physics of Non-Ideal Plasma, Chernogolovka, 2009, p.96.
[13] V.S. Filinov et al., "Influence of Potential and Non Potential Forces of Interparticle Interaction on Stability of Nuclear Excited Dusty Plasma," Contrib. Plasma Phys. 49 (2009) 446.
[14] G.S. Zhdanov et al., "Track Membranes as Promising Materials with New Optical Properties," Proc. of XIII Int. Conf. on Electrostatic Accelerators and Beam Technologies, Obninsk, June 6-9, 2001, p. 103 (in Russian).
[15] V. Kononov et al., "Accelerator Based Neutron Sources for Medicine," Proc. of Int. Symp. on BNCT, Novosibirsk, July 2004,. BINP 2004–50 (2004) p. 62.
[16] V.N. Kononov et al., "Accelerator-Based Fast Neutron Source for Neutron Therapy," Nucl. Instr. Meth., A564 (2006) p. 525.
[17] S.V. Bazhal, V.A. Romanov, "Dynamics of Multiply Charged Ions in Inclined Accelerating Tubes at the Tandem Accelerators," Proc. of XIV Conf. on Charged Particle Accelerators, Protvino, 1 (1994) 81, (in Russian).
[18] V.A. Romanov, N.A. Demidova, Patent of RF # 2443031.
[19] K.A. Rezvykh., V.A. Romanov "An Analytical Estimation of Systematic Errors of Gradient of Potential in Calculation by the Finite Difference Technique," Elektrichestvo, 6 (2004) 17, (in Russian).
[20] K.A. Rezvykh., V.A. Romanov "A Device for Increasing the Insulating Strength of Electrostatic Accelerator Column," Nucl. Instr. Meth., 216 (1983) 11.
[21] K.A. Rezvykh, V.A. Romanov, "Increase of the Reliability of an Electrostatic Accelerator at the Highest Possible Operating Potential," Proc. of SNEAP XXXIV, Lund, Sweden, Krontrick AB, Eslöv, Sweden: 2002, p. 89.
[22] K.A. Rezvykh, V.A. Romanov," Gases Breakdown Voltage Calculation for the Case of Accelerator Nonuniform Fields by the Method of Base," Nucl. Instr. Mewth., A423 (1999) 203.
[23] K.A. Rezvykh et al., "Calculation Technique for High-Voltage Equipment in Gas," Box 1 in "Electrostatic Accelerators. Fundamentals and Applications," (Springer Verlag, Berlin - Heidelberg: 2005), 84.
[24] K.A. Rezvykh, V.A. Romanov, "Conditioning and Check of Cleanliness of Gaseous Insulation of High Voltage System," WEPSB22, these proceedings.
[25] S.V. Bazhal, V.A. Romanov, "An Accelerating Tube of Electrostatic Accelerator with Improved Efficiency of Suppression of the Secondary Charged Particles," Proc. of XV Conf. on Charged Particle Accelerators, Protvino, 1 (1996) 196, (in Russian).
[26] S.V. Bazhal, V.A. Romanov, "An Upgrade of Ion Optics of Injection System of the EGP-15 Tandem Accelerator," Proc. of XVI Int. Conf. on Electrostatic Accelerators and Beam Technologies, Obninsk, June 6-8, 2006, p. 108 (in Russian).
[27] S.V. Bazhal, V.A. Romanov "On Application of an Electrostatic Zoom Lens for Matching of Ion Beam to Optical Channel of Low-Energy Stage of the Tandem Accelerator," Proc. of XV Conf. on Charged Particle Accelerators, Protvino, 1 (1996) 201, (in Russian).
[28] R. Hellborg et al., "A High Resolution AMS-Injector for the Pelletron in Lund // Pramana, Journal of Physics," 59 (2002) 1061.
[29] M. Faarinen et al.,"^{26}Al at the AMS facility in Lund," Nucl. Instr. Meth., B 223-224 (2004) 130.
[30] S. Bazhal, R. Hellborg, "Beam Envelope Techniques for Ion-Optical Calculations," Chapter 14 in "Electrostatic Accelerators. Fundamentals and Applications," (Springer Verlag, Berlin - Heidelberg: 2005), 299.
[31] S.V. Bazhal, V.A. Romanov, "Calculation Analysis of the Beam Transport of Multiply Charged Heavy Ions at The EGP-15 Tandem Accelerator," Proc. of XVIII Int. Conf. on Electrostatic Accelerators and Beam Technologies, Obninsk, Oct. 19-22, 2010, p. 99 (in Russian).

ISBN 978-3-95450-170-0

PRODUCTION OF ACCELERATING EQUIPMENT FOR NUCLEAR MEDICINE IN NIIEFA. POTENTIALITIES AND PROSPECTS

M.F. Vorogushin#, Yu. N. Gavrish, A. P. Strokach
JSC "D.V. Efremov Institute of Electrophysical Apparatus", St. Petersburg, Russia

Abstract

The D.V. Efremov Institute (NIIEFA) is the leader in Russia in designing and manufacturing of the accelerating equipment for medicine. About one hundred of linear accelerators for the beam therapy and more than forty cyclotrons for production of radiopharmaceuticals have been designed, manufactured and delivered to clinics of Russia and some foreign countries.

The equipment designed and manufactured in NIIEFA in its technical characteristics is on a par with foreign analogs and sufficiently cheaper in expenditures for personnel training, hardware and software compatibility, warranty and post-warranty service, delivery of spare parts and updating.

In accordance with Federal Targeted Programs on the development of medical and pharmaceutical industries up to 2020, the production facilities, material and technical resources have been prepared for the organization of serial production of cyclotrons and gamma tomographs.

A leap forward in the nuclear medicine, understood as the introduction of nuclear–physical technologies into medicine, is directly connected with a broad application of charged particle accelerators. This is most distinctly manifested in diagnostics and treatment of the most dangerous and widely spread oncologic and cardiovascular diseases, which rate of mortality mainly defines an average age of human life in Russia.

A single-photon emission computer tomograph «EFATOM» [1] has been designed in NIIEFA for radionuclide diagnostics. It is used to visualize images obtained by using special radiopharmaceuticals. This method allows the anatomy and functioning of various organs to be studied as well as, osteal pathologies to be diagnosed. A wide range of available radiopharmaceuticals and methods makes possible diagnostics practically of any organ. The information obtained is used in oncology, cardiology, nephrology, neurology, endocrinology, traumotology, hematology, gastroenterology, in cases of cerebrum brain diseases, etc. A package of clinical programs was developed in cooperation with the staff of the State St. Petersburg University for diagnostics of the aforementioned scope of diseases. It was tested in leading clinics of Russia and was awarded the top assessment. Radionuclide examinations with emission tomographs are one of the main diagnostic methods all over the world. In developed countries, tens of millions radionuclide examinations are carried out annually, and this number increases by 10-12% each year.

#vorogushin@luts.niiefa.spb.su

Upon completing clinical tests, the «EFATOM» (see Fig.1) was included on the State Register of RF Medical Products, and in 2011 it was included on the List of products intended for serieal production. More than 15 thousand examinations have been performed with the «EFATOM» in clinical hospital № 83, Moscow.

The main features of the «EFATOM» are as follows. Analog signals are transformed in the digital detection block at the output of each photomultiplier with a subsequent processing by a ditgital processor. This allows the maximum resolution to be realized. The gantry provides fixing of two detection units and their travel along radial, axial and angular coordinates. Detectors' positioning is computer-controlled. Patient's support system provides patient's fixation in the lying position and its travel in vertical and horizontal planes. Both manual and computer control is possible.

Further progress of this diagnostic method can be facilitated by application of the gamma-tomograph together with a computer tomograph, which realizes a technology combining the functional sensitivity of the single emission tomography with a high anatomic resolution of CT. Designing and construction of such a combined apparatus is a near-future aim of NIIEFA in the field of diagnostics.

Figure 1: The «EFATOM» gamma-tomograph.

The accumulated clinical experience shows that nearly in 20% of cases more exact diagnostics with the positron-emission tomography (PET) using ultra-short-lived isotopes is required after the gamma-tomograph examination. PET allows the visualization of biological processes behavior in organs and tissues of a human-being on the molecular level, and both quantitative and qualitative assessments of the information obtained. For example, the accuracy of a malignant tumour detection,

ISBN 978-3-95450-170-0

including metastases of any localization, is up to 95-97%. In cardiology, PET allows the detection of the myocardium viability with a high accuracy. Early treatment along with a possibility to choose proper methods for treatment and to observe the dynamics of the process will significantly increase chances for recovery.

To produce medical isotopes directly in clinics, a series of compact cyclotrons [2] has been designed and manufactured in NIIEFA. The main technical characteristics of these machines are given in Table 1.

Table 1: Main Characteristics of Compact Cyclotrons.

Technical Characteristics	Cyclotron Model		
	CC-12	CC-18/9 M	MCC-30/15
Accelerated ions	H^-	H^-/D^-	H^-/D^-
Beam energy, MeV	12	12…18/ 6…9	18…30/ 9…15
Beam current, μA	50	150/70	200/100
Power consumption, kW	30	70	100
Shielding magnet weight, t	10	34	41
RF generator power, kW	15	20	25

Distinctive features of compact cyclotrons of the new generation are**:** shielding type magnet with the vertical median plane; vacuum chamber of the cyclotron made as a part of the magnet; resonance system completely located inside the vacuum chamber; possibility to move apart the movable part of the magnet to a distance of up to 800 mm to give an easy access to the in-chamber devices; system for external injection of hydrogen and deuterium negative ions; acceleration of negative ions of hydrogen and deuterium at one frequency of the RF field (the 2nd and 4th harmonics, respectively); extraction of beams of accelerated protons and deuterons by stripping negative ions on carbon foils practically with no loss of intensity; completely automated control of all cyclotron systems from a computerized operator workstation.

Figure 2 shows the CC-12 cyclotron at a test-facility in NIIEFA. Two CC 18/9 cyclotrons are operated in Russia; CC-18/9 and MCC-30/15 machines are in service in PET centers in Finland.

Over the last two years, the CC-18/9 machine was updated to vary the final energy of protons and deuterons and to increase the output beam current up to 150 and 70 μA respectively. In addition, target devices for production of F-18 (see Fig.3) and C-11 (see Fig.4) radionuclides have been designed for cyclotrons of the CC series. An automated system for remote replacement of targets allows one from five available targets to be placed under the beam at the operator option. The equipment of the CC—18/9 M cyclotron together with the target system has been manufactured and delivered to the JSC «NIITFA», Moscow and now it is under final acceptance tests [3].

Figure 2: The CC-12 cyclotron.

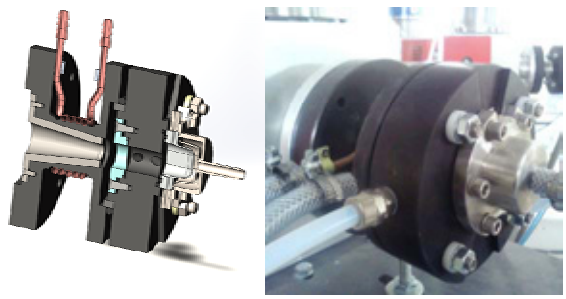

Figure 3: Target device for production of F-18.

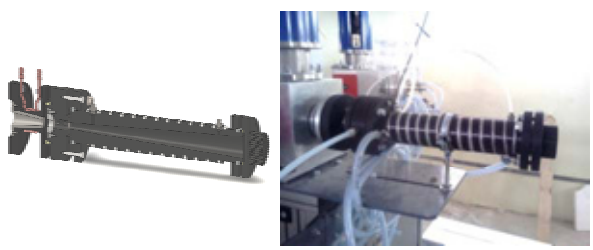

Figure 4: Target device for production of C-11.

In future, it seems reasonable to update the CC-12 cyclotron to equip it with an internal ion source instead of the external injection system and a local radiation shielding. Highly promising may be designing and manufacturing of a 70 MeV proton cyclotron with a beam current of about 200 μA intended for production of a more comprehensive set of radionuclides and for neutron and proton therapy of superficial tumors. NIIEFA is ready to take part in designing and manufacturing of a number of units of a medical cyclotron intended for proton, neutron and hadron therapy.

However, to the present day the radiotherapy with electron beams and X-rays still takes the main part among radiation methods in the vast majority of clinics all over the world. In the late 1990s, within the frames of cooperation with the «PHILIPS MEDICAL SYSTEMS. RADIOTHERAPY» firm (Great Britain), NIIEFA

ISBN 978-3-95450-170-0

pioneered in Russia in the small-scale production of 6 MeV medical accelerators for radiotherapy (SL-75-5M). Sixty similar machines were delivered to clinics of Russia; part of these accelerators have been operated till now.

Recently, an accelerator of new generation «ELLUS - 6M» with a set of additional medical equipment has been designed and manufactured in NIIEFA. This accelerator is an isocentric radiation facility intended for 3-D beam therapy with 6MeV X-rays in multi-static and arc modes. It is equipped with a multi-leaf collimator, portal vision system and patient-support system [4].

In 2012 in the N.I. Petrov Scientific Research Institute of Oncology of the RF Ministry of Health (St. Petersburg), clinical tests of «ELLUS-6M» were successfully completed. The accelerator was integrated into a radiotherapeutical system with a standard set of technological processes [5]:

- analysis of obtained diagnostic results on a tumor, in particular, its biological type, stage of a disease and choice of radiotherapy method to be applied;
- topometric preparation including the choice of a patient's treatment position and immobilization means on the therapeutic coach; reconstruction of 3-D volumes of anatomical structures and a tumor on the basis of the X-ray tomograph data;
- treatment planning including preparation of treatment prescriptions, calculation of dose field distributions for a chosen configuration, and a set of control programs for the accelerator;
- treatment simulation and verification. The accelerator control program is simulated on the simulator, which X-ray verification system compares projection images of a patient in the treatment position with projection images calculated by the planning system;
- treatment. The treatment basic method is built upon formation of a dose field with a multi-leaf collimator. The position of the collimator leaves for a particular field is preset from a file of data of the accelerator control computer. The portal vision system fixes parameters of a dose field in the process of treatment. Data for a passed treatment session are transferred through a local network to the information system of the radiotherapeutical system.

The results of performed medical tests have shown that the «ELLUS-6M» accelerator designed and manufactured in NIIEFA completely meets the requirements for modern therapeutic facilities with an X-ray energy of 6 MeV.

Progress in the field of radiotherapy is associated with a need for creation of domestically produced 3-D tomograph-simulators and treatment planning systems, high-energy (up to 25 MeV) radiation sources and mobile radiation sources for operational theatres. To solve these problems within reasonable periods of time and with lower costs, organization of joint manufacturing with the participation of foreign firms seems reasonable. The experience gained in NIIEFA proves that this measure will allow the compatibility of both hardware and software with the equipment available in clinics to be ensured and the matters of delivery of unique technologies and completing parts as well as servicing of the equipment to be solved.

In conclusion I wish to draw your attention that in accordance with the Federal targeted program «Development of Pharmaceutical and Medical Industry up to 2020 and Further», NIIEFA has performed works on the reconstruction and technical re-equipment of production rooms with a total area of about 3500 m^2 to organize serial production of medical cyclotrons and gamma-tomographs. Design documentation was worked out, production areas with engineering support for installation works and tests of equipment were prepared, and commissioning works of new machine tools and processing equipment, totally 60 in amount, were carried out. As a result, production facilities and processing equipment necessary for a planned annual production output of 10 CC cyclotrons with target devices and 20 «EFATOM» gamma-tomographs are provided.

However, until now the questions of procurement and introduction of domestic equipment for nuclear medicine, training of attending personnel, designing and construction of specialized areas to house radiation-dangerous equipment, its maintenance/repair and updating are still open. These problems can be solved by working out an inter-ministerial Program of Nuclear Medicine Development, including all the stages of creation, introduction and operation of equipment.

REFERENCES

[1] M.A. Arlychev et al., "EFATOM two-detector one-proton emission gamma tomograph". Technical Physics 54, pp. 1539-1537 (2009).

[2] O.G. Filatov, A.P. Strokach, M.F. Vorogushin, "Status and Progress of the Accelerating Equipment in NIIEFA», VANT, series: Electrophysical Apparatus, №.5 (31), pp.3-11 (2010).

[3] A.P. Strokach et al., "The CC-18/9M Cyclotron System", these proceedings, RuPAC'2014, October 6-10, Obninsk, Russia (2014).

[4] M.F. Vorogushin "NIIEFA Accelerators for Industry and Medicine" XXII Russian Rarticle Accel. St. Petersburg, Proceedings of RuPAC-2012, pp.167-172 (2012).

[5] S.V. Kanaev et al. "Problems of Transition to Modern Radiation Technologies in Russian Clinics", Medical Physics, №. 4 (48), pp. 17-27 (2010).

ISBN 978-3-95450-170-0

RADIOBIOLOGICAL RESEARCH WITH CHARGED PARTICLES BEAMS IN ITEP

N. Markov#, A. Kantsyrev, I. Roudskoy, ITEP, Moscow, Russia
A. Colubev, ITEP, Moscow, Russia and MEPhI, Moscow, Russia

Abstract

Radiobiological researches with heavy ions have been started at ITEP in 2006 on unique heavy ion accelerating facility ITEP-TWAC. The main purpose of these researches is study of the biological efficiency of carbon ions for different types of biological objects, such as tumor and normal cells, in the framework of the development of heavy ion therapy for cancer treatment in Russia. Another possible area of application of this research is the space radiobiology, studying stochastic and deterministic effects of ionizing radiation in the space environment on human. In this work the experimental setup for radiobiological research with heavy ions in ITEP, the dosimetry system for dose measurements and the results of the radiobiological researches with carbon ions are presented.

INTRODUCTION

In the last few decades there is a tendency in the increasing of the number of hadron (protons and heavy ions) therapy centers, that are in general hospital-based facilities in versus the previous times when the treatments were performed in nuclear physics research centers. For today, hadron therapy in Russia is only represented by proton therapy, that is carried out in three scientific research centers in ITEP (Moscow), JINR (Dubna) and PNPI (Gatchina). Research in the field of carbon ion therapy is at the very beginning and currently several projects of the new facilities construction, mainly based on the particle accelerators for nuclear physics research, are under discussion.

In 1997 the project for the reconstruction of ITEP U-10 proton synchrotron (TWAC-ITEP project) was started. The aim of this project was to create new facility for heavy-ion acceleration up to relativistic energies and ion accumulation with energies up to several hundreds of MeV/u [1]. In 2004 realization of the first stage of the TWAC-ITEP project has been completed and as one of the results a possibility to accelerate and accumulate carbon ions C^{6+} with energy suitable for therapy application was shown [2]. After several years radiobiological research program with carbon ions was initiated in ITEP. Since then in collaboration with biophysicist and radiation oncologist from JINR and Russian Cancer Research Centre various kind of radiobiological experiments (surviving of irradiated cells, chromosome aberration, mutagenic influence of heavy ions) with cancer and normal cells, as well as with other types of biological systems have been carried out.

#markov@itep.ru

EXPERIMENTAL SETUP

For radiobiological research at the TWAC-ITEP accelerator facility an experimental setup was organized at the end of the 511 beam-line (fast extraction beam-line from accelerator-storage ring U-10) in the building 120. Layout of the experimental setup is illustrated in Fig. 1

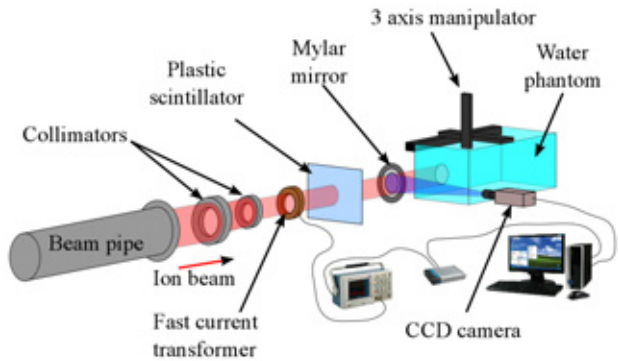

Figure 1: Layout of the experimental setup.

Formation of the dose fields with characteristic transverse dimensions of 20-100 mm was performed by system of magnetic elements, defocusing the ion beam at a considerable distance from the place of exposure and passive collimating system, located in the immediate vicinity of the irradiated target. Homogeneity of the field was controlled by the intensity of the luminescence of the plastic scintillator (Bicron BC412). The image of the beam on the scintillator was transferred to the CCD camera by means of a mirror from metalized Mylar, placed at an angle of 45 degrees to the beam axis.

For measurements of spatial distributions of the absorbed dose to water, as well as alignment of the biological targets during irradiation, was developed and produced water-phantom with the established three-axis manipulator. For readout and analysis of the signals from the detectors and instruments used in the experiment, as well as for operation of the manipulator, developed in ITEP hardware-software complex was used [3].

DOSE-FIELD MEASURMENTS

In the study a beam of carbon ions, accelerated to energy of 215 MeV/amu in the booster synchrotron UK was used. The level of ion accumulation in a storage ring U-10 varied the number of particles per pulse. As in these experiments it was possible to use only ion beam pulses, generated in fast extraction mode, with single pulse width approximately 800 ns (FWHM), firstly questions of the carbon ions dosimetry have been considered. Due to the

ISBN 978-3-95450-170-0

possible height ionization densities in short time period, caused by short width of ion beam pulse and high particle fluence per pulse, additional uncertainties in adsorbed dose determination can occur when widely accepted in clinical dosimetry detectors, such as ionization chambers, are used. To eliminate this problem a method of absorbed dose determination, based on information about particle fluence, measured with fast current transformer, and relative dose distribution in water phantom, measured with point-like silicon detector (SSD), was realized [4]. As an example, Fig. 2 shows the relative depth dose distribution of monoenergetic carbon ion beam in water, measured with the SSD.

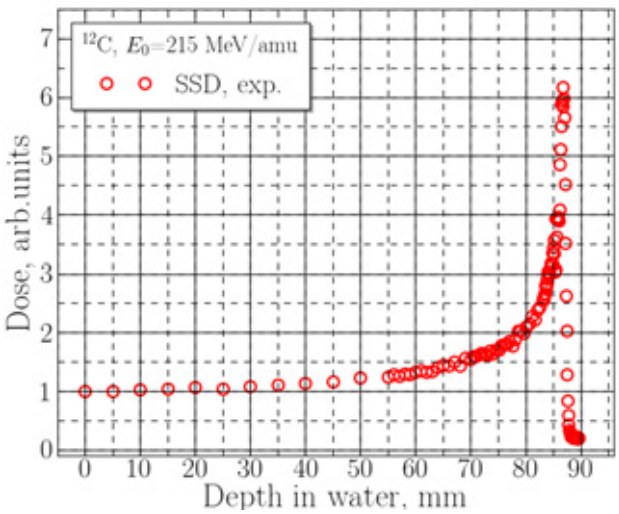

Figure 2: Depth-dose curve.

Although this approach showed reasonable results, with uncertainty not more than 5 %, it is only employed for determination of the ion beam characteristic, e.g. particle fluence, energy and angular distributions, as well as for commissioning of the dose fields required, for biological target irradiation. At the same time for the biological results assurance additional information about dose field homogeneity in target volume is essential. For that purpose radiochromic films were used.

For research was chosen radiochromic film GafChromic MD-V2-55, allowing measurments of the absorbed dose in the range from 1 to 100 Gy. Calibration measurements on a beam of photons with energy of 6 MV, as well as a series of irradiation experiments with carbon ions were carried out. To quantify the observed effect of reducing the sensitivity of the type of films with increasing ions LET, on the basis of the obtained data the dependence of the relative sensitivity of the films as a function of the ion energy was determined. Subsequently, the obtained dependence was used for reconstruction of the iso-dose distributions in the transverse plane to the beam direction based on the measured distribution of the optical density of the exposed film. Dose distribution, measured with GafChromic MD-V2-55 radiochromic film for beam field size with diameter 12 mm at the depth 80 mm in water, is shown in Fig. 3.

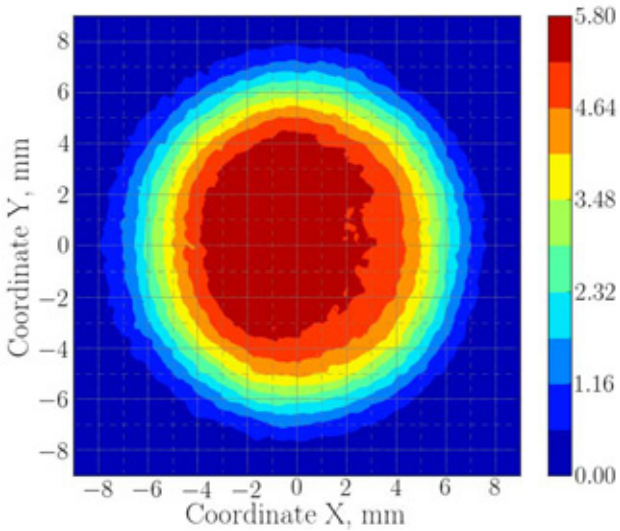

Figure 3: Dose distribution in transverse plane.

RESULTS OF RADIOBIOLOGICAL EXPERIMENTS

"In vitro" Experiments

A series of radiobiological experiments "in vitro" by irradiation with carbon ions of different types of cells, such as tumor and normal. In particular, irradiation was carried out in human peripheral blood lymphocytes (HPBL), mammary cells adecarcinoma Cal51, Chinese hamster cells CHO-K1 and melanoma cells B16F10.

Depending on the size of the target in the preparatory phase prior to the experiments were formed homogeneous dose fields with diameter of 45 mm and 80 mm (inhomogeneity of the field did not exceed 5%). All studies were conducted using a monoenergetic beam of carbon ions with an initial energy of 215 MeV/amu. Irradiation of cells were carried out at two points located at different depths in a water phantom, corresponding to different LET values, with the exception of lymphocytes, irradiated only in the plateau region.

To assess the biological effect of carbon ions in the investigated cell types used two methods. In the case of irradiation of HPBL and Cal51 cell biological efficiency was determined based on the method of analysis of chromosomal aberrations in dividing cells - the so-called metaphase method of analysis of chromosomal aberrations. In the case of irradiation of B16F10 and CHO-K1 cells efficiency of carbon ions was determined by cell survival. As a general method for determining the number of surviving cells a test for colony formation was used. It has to be mentioned, that the results of HPBL irradiation were used as biological method of dosimetry and they were compared with the data of HPBL irradiation with different heavy ions (LET range from 11 to 3160 keV/mkm) in GSI (Darmstadt, Germany) [5]. Table 1 summarizes the results of experiments on the irradiation of the four types of cells held within the reported studies, where RBE is the relative biological

ISBN 978-3-95450-170-0

effectiveness of carbon ions in comparison with x-rays or ^{60}Co photons.

Table 1: Results of the radiobiological experiments

Cell type	Depth in water, mm	LET, keV/mkm	Dose range, Gy	RBE (x-ray)	RBE (^{60}Co)
HPBL	0	16	0-8	1.53	1.77
Cal51	0	16	0-4	-	2.02
	82	40	0-4	-	3.63
B16F10	23	20	0-10	-	1.45
	85	44	0-8	-	2.46
CHO-K1	0	16	0-8	1.65	-
	82	40	0-5	2.27	-

"In vivo" Experiments

In addition to the "in vitro" radiobiological research were conducted several experiments on irradiation of laboratory animals with carbon ions. The study used a laboratory mouse lines C57BL/6 with inoculated melanoma B16F10 tumor.

For the formation of the depth-dose distribution (so-called spread-out Bragg peak), allowing the irradiation of an extended target a comb filters, developed in the Department of Medical Physics in ITEP, were used. Fig. 4 shows the measured with SSD depth-dose distribution for one of the comb filters. The graph shows that the length of the modified peak is about 10 mm, wherein the peak-to-plateau dose ratio corresponds to 1.7.

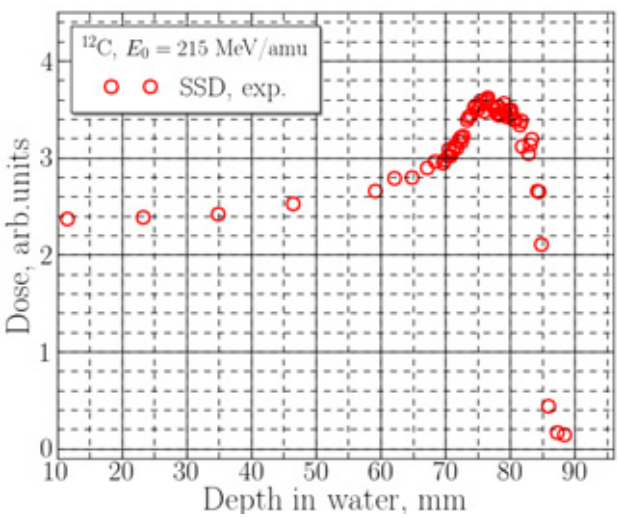

Figure 4: Spread-out Bragg peak.

Based on these results the thickness of the water-equivalent plastic, required for conformal positioning of the spread-out Bragg peak within the tumor location, was calculated. To adjust the position of the tumor relative to the axis of the beam using a system consisting of two semiconductor lasers (Fig. 5).

Further analysis of the results of irradiation showed that for laboratory animals irradiated with carbon ions observed tumor growth delay compared to control animals not exposed to radiation. It was thus demonstrated in principle the possibility of "in vivo" studies on the basis of established in ITEP experimental setup.

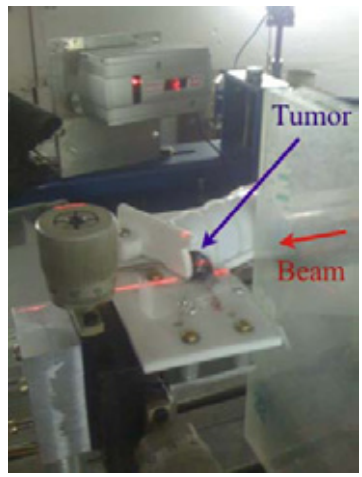

Figure 5: Irradiation of the laboratory animals.

CONCLUSION

An experimental setup for radiobiological research with pulsed heavy ion beams, including corresponding dosimetry system, was created in ITEP. A series of radiobiological research for irradiation of different biological targets were carried out. The further research will be focused on the investigation of various radiobiological aspects of the low-energy protons in the linear accelerator I-2 in ITEP.

REFERENCES

[1] D.G. Koshkarev et al., ITEP Accelerator Facility Upgrade, XV Workshop on Charged Accelerator, Protvino, v.2 (1996) p.319.
[2] N.N. Alexeev et al., Accumulator-Accelerator ITEP-TWAC. Particle and Nuclei Letters. 2004. No 3(120), 78-87.
[3] A. Kantsyrev et al., Instruments and Experimental Techniques, 2010, vol. 53, No. 5, pp 663-674.
[4] N Markov et al., Instruments and Experimental Techniques, 2014, vol. 57, No. 1, pp 55-61.
[5] R. Lee et al., Radiat. Environ. Biophys., 2011, vol. 50, no. 3. pp 371-381.

ISBN 978-3-95450-170-0

ACELERATOR HADRON TERAPY TECHNIQUE DEVELOPED AT JINR

E.M. Syresin, Joint Institute for Nuclear Research, Dubna, Russia

Abstract

Accelerator hadron therapy technique is one of applied researches realized at JINR. The JINR-IBA collaboration has developed and constructed the C235-V3 cyclotron for Dimitrovgrad hospital center of the proton therapy. Proton transmission in C235-V3 from radius 0.3m to 1.03 m is 72% without beam cutting diaphragms; the extraction efficiency is 62%. The main advantage of this cyclotron in comparison with serial commercial cyclotrons of IBA is related to higher current of the extracted beam.

The cancer treatment is realized in JINR on the phasotron proton beam. More than 1000 patients were treated there. A project of the demonstration center of the proton therapy is discussed on base of a superconducting 230 MeV synchrocyclotron. The superconducting synchrocyclotron is planned to install instead of phasotron in Medical Technical Complex of DLNP.

The project of the medical carbon synchrotron together with superconducting gantry was developed in JINR. The basis of this medical accelerator is the superconducting JINR synchrotron – Nuclotron. One important feature of this project is related to the application of superconducting gantry.

PROTON CYCLOTRON C235-V3

The JINR-IBA collaboration has developed and constructed the C235-V3 proton cyclotron (Fig.1) for Dimitrovgrad hospital proton center. The C235–V3 cyclotron, superior in its parameters to the IBA C235 medical proton cyclotron, has been designed and manufactured by the JINR-IBA collaboration. This cyclotron is a substantially modified version of the IBA C235 cyclotron.

Modification of the extraction system is the main aim of the new C235-V3 cyclotron [1-2]. The main feature of the cyclotron extraction system is a rather small gap (9 mm) between the sectors in this area. The septum surface consists of several parts of circumferences of different radii. The septum thickness is linearly increased from 0.1 mm at the entrance to 3 mm at the exit. The proton extraction losses considerably depend on the septum geometry. In the septum geometry proposed by JINR, where the minimum of the septum thickness is placed at a distance of 10 cm from the entrance, the losses were reduced from 25% to 8%. Together with the optimization of the deflector entrance and exit positions it leads to an increase in the extraction efficiency to 80%. The new extraction system was constructed and tested at the IBA C235 cyclotron. The experimentally measured extraction efficiency was improved from 60% for the old system to 77% for the new one.

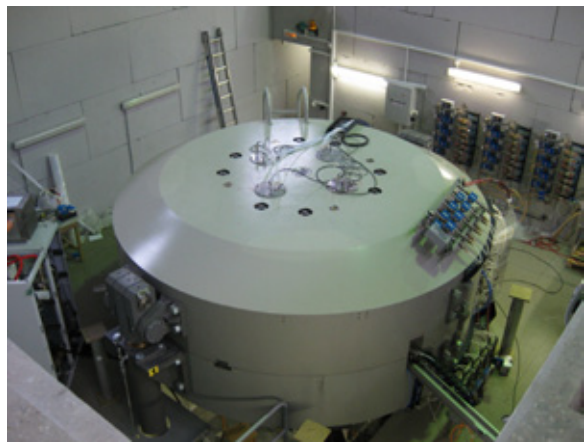

Figure 1: Cyclotron C235-V3 in JINR engineering center.

Another difference in the structure of the magnetic field for the C235–V3 cyclotron compared to an IBA C235 serial cyclotron is related to the value of the radial component of magnetic field in the median plane, bump parameters, and the minimal value of the vertical betatron frequency in the central area of the cyclotron.

The bump of magnetic field B_z in the center is used in many cyclotrons for axial focusing during the first turns, when the B_z variation is low. When the decreasing field of the bump passes to the increasing isochronous one, the dip in the axial betatron frequency Q_z could appear. In the C235-V3, Q_z decreases at a radius of 10 cm down to ~0.04–0.05.

The presence in the area of the Q_z minimum of the mean radial component of the magnetic field B_r with a level of 5 G and gradient of 5 G/cm in the median plane (Fig.2) results in the transformation of coherent motion of the center of gravity of the beam in this area into the noncoherent oscillations of individual particles and coherent oscillations of the center of gravity. The simulated axial r.m.s. ($\pm 2\sigma$) size (Fig.3) is equal to 6 mm at B_r=0, it increases up to 12 mm at B_r corresponded to shimm thickness of 2mm (Fig.2) and 8 mm at optimized shimm thickness of 1.7 mm. In the C235-V3, the B_r component was optimized using the establish of shim correctors at the sectors.

In experiment, the r.m.s. vertical size of the beam (2σ) (Fig.4) at the radii of 15–20 cm is ~17–18 mm and becomes comparable with the vertical aperture of the accelerator of 20 mm determined by the interdee gap.

ISBN 978-3-95450-170-0

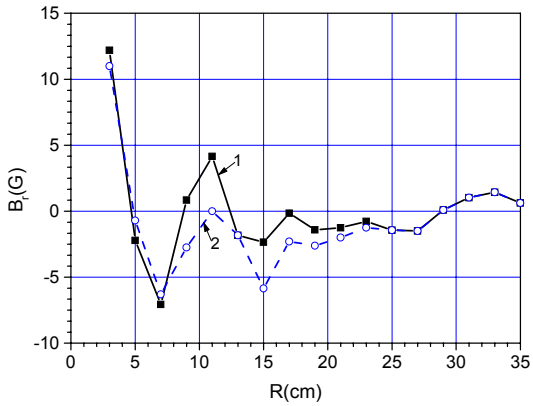

Figure 2: Distribution of average radial component in cyclotron median plane at shim thickness 2 mm (curve 1) and shim thickness 1.7 mm (curve 2).

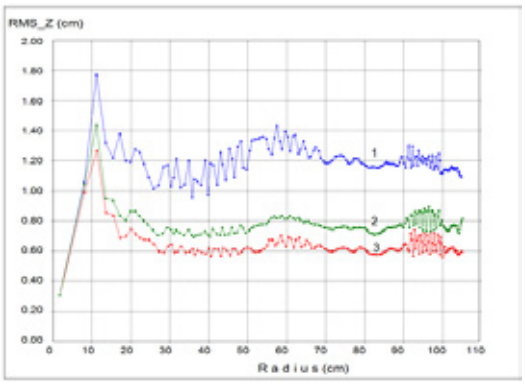

Figure 3: Simulated dependence of axial r.m.s. (±2σ) size on radius: curve 1 at B_r (curve 1in Fig.2), curve 2 at B_r (curve 2 in Fig.2), curve 3 at B_r=0.

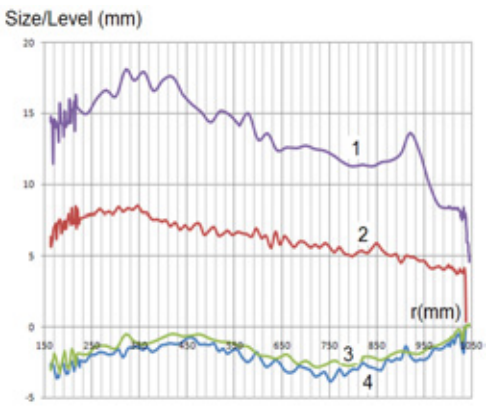

Figure 4: Experimental dependence of axial r.m.s. size (1, 2) and beam center gravity (3, 4) on radius 1, 3 – before magnet field optimization, 2, 4 after optimization.

During the further acceleration of protons in the area of large radii, where the aperture of the accelerator decreases, the appearance of the radial field in the median plane leads to beam losses because of the large amplitude of noncoherent oscillations occurring in the central area of the accelerator.

After shimm optimization, the axial size of the proton beam at radii of 15–20 cm was reduced by a factor of two and was ~7–8 mm (Fig. 4). This led to the efficiency of acceleration in the C235–V3 cyclotron being increased to 72% without the establishment of restrictive diaphragms.

DEMONSTRATION CENTER OF PROTON THERAPY

The final stage of the project is creation of the Dubna hospital center of proton therapy on basis of superconducting synchrocylotron and rotating gantry.

The first stage of the project is related to the construction of demonstration center of proton therapy on base of a superconducting 230 MeV synchrocyclotron.

The superconducting synchrocyclotron [3] is planned to install instead of phasotron in Medical Technical Complex of DLNP. The new transport channel is designed for beam delivery to the JINR medical cabin. The equipment of demonstration center of proton therapy and realized here technologies will be lay in the base of the Dubna hospital center of the proton therapy.

Figure 5: Scheme of synchrocyclotron with beam delivery channel and modernized medical cabin in demonstration center of proton therapy.

The synchrocyclotron S2C2 [3] (Table 1) has diameter of 2.3m. Main peculiarity of synchrocyclotron is connected with its superconducting magnets with magnetic field in hills and valleys of 5.64/5.24 T, correspondently. Four Sumitomo cryocoolers are used at realization of superconducting regime.

ISBN 978-3-95450-170-0

Table 1. Parameters of synchrocyclotron S2C2.

Irradiation	Active
Diameter, m	2,3
Weight, t	50
Magnet	Superconducting
Average field, center/extract., T	5,64/5.24
Voltage of dee-electrodes, kV	14
RF–frequency, MHz	90-61.5
Frequency of beam pulses, kHz	1
Average current, nA	20
Proton energy, MeV	230
Energy spread, 2σ, MeV	2,5

The peculiarity of synchrocyclotron S2C2 is relatively low average current of extracted beam. At present time this current is equal to 20 nA.

SUPERCONDUCTING SYNCHROTRON FOR CARBON THERAPY

A project of the medical superconducting synchrotron (Fig.5) dedicated for the carbon therapy has been designed in JINR [4]. The basis of this medical accelerator is the superconducting JINR synchrotron – Nuclotron. The Nuclotron type straight dipole magnets were adopted for the optic of the medical synchrotron and beam delivery system. The superconducting magnets permit to reduce the accelerator electrical consumption, the size and weight of the accelerator and the carbon gantry.

The superconducting electron string ion source is planed to use for $^{12}C^{4+}$ injection in the carbon linac. The compact IH linac will apply as synchrotron injector.

The FODO structure is more preferable for injection and extraction schemes and corrections of the closed orbit distortions. The synchrotron magnetic system [4] consists of 4 superperiods, which involves 8 straight dipole magnets, 8 quadrupole lenses and multipole correctors. The maximum magnetic field in dipole magnets corresponds to 1.8 T. The multiturn injection is realized at fulfilling of the horizontal acceptance during 10-15 ion turns. The stored beam intensity is equal to 10^{10} ions C^{6+} per pulse. The working point corresponds to betatron tunes $Q_{x,z}$ ≈3.25. Nonlinear 3 order resonance $3Q_x=10$ is used for slow beam extraction. The intensity of extracted beam is equal to 10^9 pps.

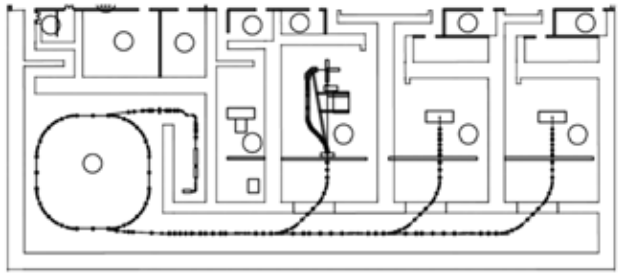

Figure 6: Layout of the carbon therapy hospital center on the basis of superconducting synchrotron.

One important feature of this project is related to the application of superconducting gantry. The superconducting magnets of low aperture (about 120 mm) are used in the gantry. The gantry consists of two 67.5° and one 90^0 bending sections, each including similar dipole magnets.

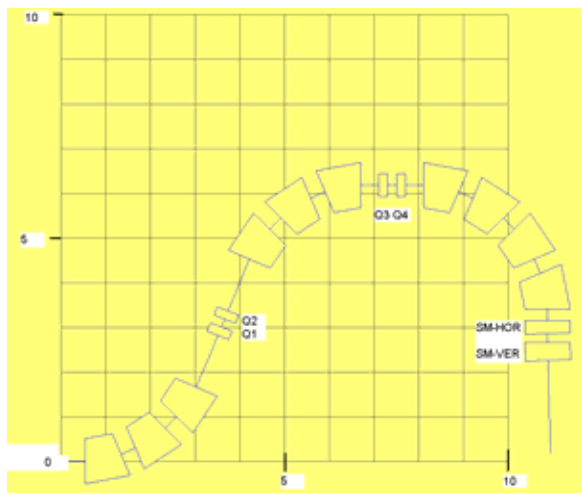

Figure 7: Layout of the JINR superconducting carbon ion gantry.

REFERENCES

[1] E.M. Syresin et al, IPAC11, S-Sebastian, (2011) 2706.
[2] S. Kostromin, E. Syresin, Physics of Particles and Nuclei Letters, v. 10, No.7 (2013) 833.
[3] W. Kleeven et al, Proceedings of Cyclotrons 2013, Canada, MO4PB02.
[4] E. Syresin et al, Particle and Nuclei Letters, v.9 (2012) 328.

ISBN 978-3-95450-170-0

OPERATION AND DEVELOPMENT OF THE BINP AMS FACILITY

S.A. Rastigeev, V. V. Parkhomchuk, BINP SB RAS, Novosibirsk, and NSU, Novosibirsk, Russia
A.R. Frolov, A.D. Goncharov, V. F. Klyuev, E.S. Konstantinov, A.V. Petrozhitskii, BINP SB RAS, Novosibirsk, Russia
L. A. Kutnykova, IAE SB RAS, Novosibirsk, Russia

Abstract

The BINP AMS facility is the accelerator complex for accelerator mass spectrometry. The most distinguishing features of BINP AMS is the use of the middle energy separator of ion beams, the magnesium vapors target as a stripper and time-of-flight telescope for accurate ion selection. Present status and development of AMS complex for extension of applications are reviewed.

INTRODUCTION

The accelerator mass spectrometry is an ultra-sensitive method of isotopic analysis for archaeology, biomedical, environment science and for another field. It's based on measurements of the ratio between isotopes. The ratio between isotopes in sample can be less than 10^{-14}. So, the counting methods are used for detection of such low radiocarbon concentration [1-3]. The AMS system consists of the ion source, low energy channel, tandem accelerator and high-energy channel [4-6]. The tandem accelerator is a folded type vertical machine. The low energy beam line is used for initial isotopes selection. The tandem accelerator is applied for rejection of the molecular ions and of course for obtaining necessary beam energy for radioisotopes detector. The high-energy beam line is used for the subsequent ions selection and for radioisotopes detection.

The most distinguishing features of our AMS machine are the use of the middle energy ions separator. The middle energy electrostatic separator is located inside the tandem terminal. It can essentially decrease the ion background [7,8]. The next important distinguishing feature is the magnesium vapors stripper [9] instead of the gaseous one. The molecular destruction and ion recharging by magnesium are localized into the hot tube of the stripper. Moreover, the moment of time for ion detection can be registered with 16 μs channel width by TOF detector [10,11]. This data is used for calculation of number of detected ions per unit time, allowing filtering the background ions from electrical breakdowns.

The accelerator mass spectrometer created at BINP SB RAS is installed at CCU "Geochronology of the Cenozoic era" for sample dating by the ^{14}C isotope and recently upgraded for biomedical applications. Over the past year have been analyzed more then 500 samples. Given the interest in using AMS in the biomedical field, the first biomedical researches are started jointly with biologists [12].

ION SOURCE

The multi-cathode (for 23 samples) sputter ion source is used for AMS analysis. The typical current of negative carbon ions is about 10 uA for analyzed samples. The negative ions are produced by bombarding the graphite target with positive cesium ions. The vapor is formed by heating of the reservoir with cesium. Then the vapor via the pipe rises from the reservoir to the ionizer. The positive charged Cs ions are produced on a hot tantalum ionizer. The cesium ion beam is focused on the carbon sample placed on the cathode, because the working surface of ionizer is a spherical-shape cup. The copper sample holder has the inner diameter of 2 mm. The sample after AMS analysis is present at the Fig.1. As seen, the sputtering region of the sample is about 0.5 mm in diameter.

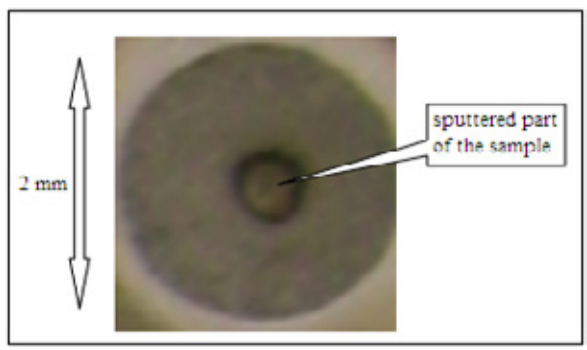

Figure 1: The sample in the ion source sputtered by cesium beam.

ION SELECTION

The sensitivity and reliability of radiocarbon measurement is limited by ion background.The nitrogen ions have the same mass as radiocarbon ones, but they are filtered by BINP AMS complex. The negative nitrogen ions are unstable, but the negative molecular NH^- ions can rich high voltage terminal. The positive nitrogen ions are produced from the breakup of NH^- ions after passing through the stripper. The energies for nitrogen from NH molecules are always less than the radiocarbon ions energy into tandem terminal, because nitrogen ion gets only a part of the molecule's energy. The BINP AMS complex has the electrostatic filter into tandem terminal for effective filtration of the different energy ions.

To test such selection, the NH molecular ions was accelerated and passed through 180^0 electrostatic bend which was set for ions energy 14/15 and charge state 3+

ISBN 978-3-95450-170-0

for a good passing through of nitrogen ions. The terminal voltage was increased so that the energy of nitrogen ion was same as usual radiocarbon energy at the exit of AMS. Thus, the time-of-flight of nitrogen and radiocarbon ions become the same, as shown at Fig.2.a. But the energy loss by passing the film is different for nitrogen and radiocarbon ions. The time-of-flights of such ions after passing through 2.5 um Mylar film are present at Fig.2.b. As seen, radiocarbon beam at the exit of AMS is clean without nitrogen additive. The 180^0 electrostatic bend is very effective for the isobaric background filtration.

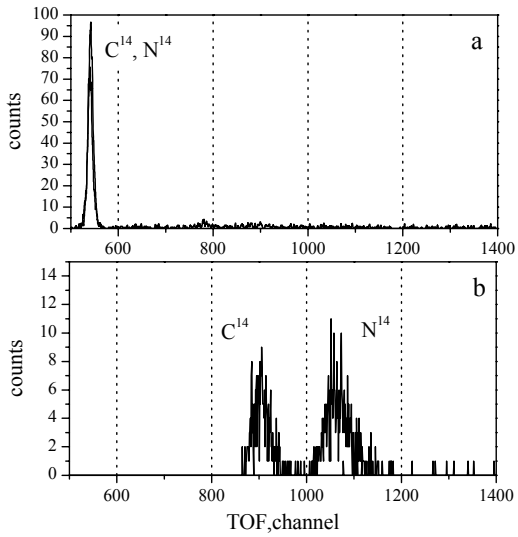

Figure 2: The time-of-flight of ions at the exit of AMS (a) and same, but after passing through 2.5um Mylar film (b).

AMS ANALYSIS

Now, during the routine measurements of user samples, the injection energy of radiocarbon beam was 25 keV. The terminal voltage of tandem accelerator was 1 MV. The 180° electrostatic bend was set to transmit the ions with charge state 3+.

The 20 graphitized samples are setted in the ion source sample wheel to measure the concentration of radiocarbon. Furthermore, the 3 control sample with a known concentration of radiocarbon is setted in ion source sample wheel for control and normalization of the measurement samples. Typically, this sample are two carbon fiber with a carbon concentration on the natural content of modern plants and one sample of graphite MPG with radiocarbon concentration at $2*10^{-3}$ compared to modern plants. It should be noted that the control samples did not require the procedure of graphitization and setted in the sample wheel in natural form.

When measuring the concentration of radiocarbon in the samples, the switching algorithm is used. The isotope ^{14}C is detected by TOF telescope and ^{13}C currents are measured at the exit of AMS. For switching algorithm the high voltage of ion source is changed. The energy of the cesium ions remains constant. The electrostatic lens and correctors at the exit of the ion source are changed for each isotope. Thus, the passage of isotopes is carried out through a first dipole magnet, without changing the magnetic field. The magnetic field in high energy magnet is not changed to, because the radial aperture is wide enough for passing radiocarbon ions to TOF detector and ^{13}C ions to shifted FC.

Now, the cycle of AMS-analysis of samples is represented as follows. For each sample, the ^{14}C ions are twice counted (20 seconds each) and twice the ^{13}C currents are measured. After that, the samples wheel is turned to the next sample for process repetition. Measuring of whole sample wheel (23 samples) takes about 20 minutes. For a set of statistics the wheel are moving to the second turn, third, etc. Typically, the measurement will take approximately 10 hours, with a statistical error of measurement for modern samples of approximately 2%. Typically, the next day the cycle repeats. The data from different days are compared. If they are within the statistical spread, the final result is given as a set of data for all measurements of these samples. The process of isotope measuring and sample changing (wheel rotation) is fully automated. The measured radiocarbon concentrations in samples are normalized to the radiocarbon concentration in carbon fiber (1.045 PMC).

The contamination level in the samples during the sample preparation procedure estimated by the radiocarbon content in graphite after combustion and graphitization (the radiocarbon concentration in graphite is insignificant before this procedure). Typically, the quantity of pollution (radiocarbon concentration) composes approximately 1% of the concentration level in the modern plants. The typical radiocarbon concentration of graphite MPG with and without sample preparation are shown at Fig. 3.

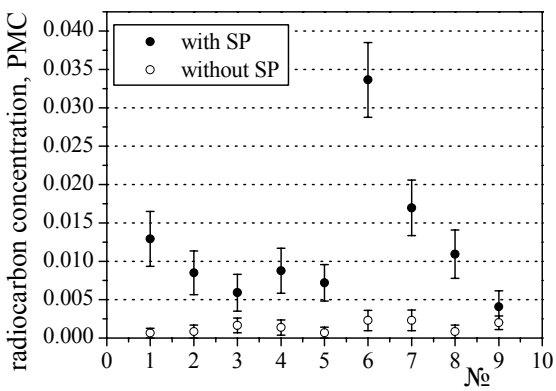

Figure 3: The radiocarbon concentration in graphite MPG samples with and without sample preparation procedure.

As an example of AMS-analysis, the data from archeological samples - peat deposits near Lake Baikal , depending on the depth from surface level (samples of Bezrukova EV, IAET SB RAS), presented in Fig. 4 . Such analyzes are necessary to obtain a timescale for peat deposits. Such results are quite revealing, since in the

ISBN 978-3-95450-170-0

absence of mixings deposits should be observed dependence - the deeper the ancient.

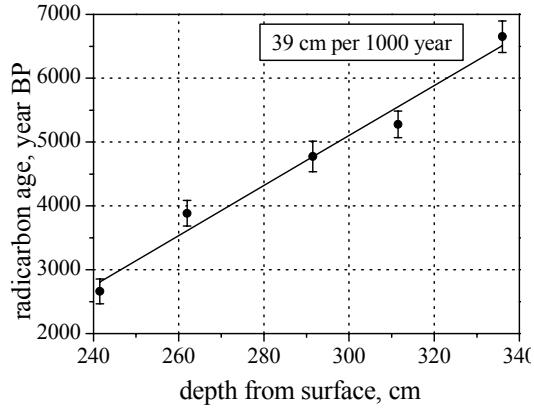

Figure 4: The radiocarbon age of peat deposits, depending on the depth from surface level.

Now, jointly with NSU (Gulyaeva LF et al.), the biomedical researches are started. As an example, the radiocarbon concentrations in the mice kidney versus time after injection of methanol with (20 Bq/mouse) and without ^{14}C labels for each individual are present at Fig. 5. As seen, the radiocarbon concentration in the labeled mice significantly lager, than the concentration in the control mice. The range of radiocarbon concentration values for individual animals is considerably greater than the statistical error of AMS analysis. Radiocarbon concentration in samples without ^{14}C label is independent of time and corresponds to the natural level.

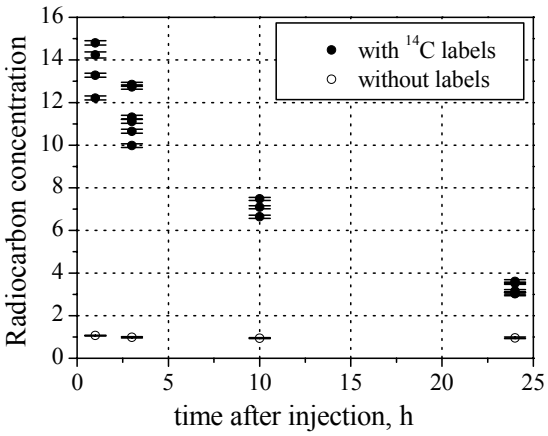

Figure 5: The radiocarbon concentrations in the mice kidney versus time after injection of methanol with and without ^{14}C labels.

SUMMARY

The BINP AMS with additional ion selection properties has demonstrated the good radiocarbon ions identification. The process of AMS analysis was described. The BINB AMS is used for radiocarbon dating, and more recently for biomedical applications.

ACKNOWLEDGMENT

This work is supported by the Ministry of Education and Science of the Russian Federation, NSh-4860.2014.2

REFERENCES

[1] S.A. Rastigeev et al, “First radiocarbon measurements at BINP AMS“, Proceedings of RuPAC-2010, Protvino, Russia, 2010, p. 309.

[2] S.A. Rastigeev et al, Accelerator mass spectrometer SB RAS // Problems of Atomic Science and Technology/ Series “Nuclear Physics Investigation”. 2013, №6(88), p. 16.

[3] Parkhomchuk, V. V., Rastigeev S.A., Accelerator mass spectrometer of the center for collective use of the Siberian Branch of the Russian Academy of Sciences // Journal of Surface Investigation. X-ray, Synchrotron and Neutron Techniques, 2011, V. 5, Issue: 6, p.1068

[4] N.I. Alinovskii et al, Accelerator mass spectrometer for the Siberian Branch of the Russian Academy of Sciences. // Technical Physics, 2009, Vol. 54, No 9, p 1350.

[5] S.A. Rastigeev et al, Development of the BINP AMS complecs at CCU SB RAS. // Problems of Atomic Science and Technology/ Series “Nuclear Physics Investigation”. 2012, №3(79), p. 188.

[6] S.A. Rastigeev et al, Recent results in accelerator mass spectrometer construction at BINP. // Problems of Atomic Science and Technology/ Series “Nuclear Physics Investigation”. 2008, №5, p. 8.

[7] Parkhomchuk, V. V., Rastigeev S.A., Ion selection in accelerator mass spectrometer at the Budker institute of nuclear physics // Physics of Particles and Nuclei Letters, 2012, V. 9, Issue 4-5, p. 406

[8] V.V. Parkhomchuk and S.A. Rastigeev, Analysis of the ion background in an acceleration mass spectrometer of the Siberian Division of the Russian Academy of Sciences. // Technical Physics, 2009, Vol. 54, No. 10, p 1529.

[9] V.F. Klyuev, V. V. Parkhomchuk, S.A. Rastigeev, A magnesium vapor charge-exchange target for an accelerator mass spectrometer. // Instruments and Experimental Techniques, 2009, Vol. 52, No. 2, p. 245.

[10] N.I. Alinovskii et al, A time-of-flight detector of low-energy ions for an accelerating mass-spectrometer. // Experimental Techniques, 2009, Vol. 52, No. 2, p. 234.

[11] V. V. Parkhomchuk et al, Thin-film detector for ion registration in accelerator mass spectrometers // Physics of Particles and Nuclei Letters, 2012, V. 9, Issue 4-5, p. 448

[12] S.A. Rastigeev et al,., Acceleration Mass Spectrometer of the Budker Institute of Nuclear Physics for Biomedical Applications // Physics of Particles and Nuclei Letters, 2014, V. 11, № 5, p. 642

ISBN 978-3-95450-170-0

EXTENDED SCOPE OF APLICATION OF INDUSTRIAL ELV ACCELERATOR

N.K. Kuksanov, Yu.I. Golubenko, P.I.Nemytov, R.A. Salimov, S.N. Fadeev,
A.I. Korchagin, D.A. Kogut, E.V. Domarov, A.V. Lavruchin, V.G. Cherepkov, V.A. Semenov,
Budker INP, Novosibirsk, Russia

Abstract

ELV accelerators are DC machines, designed and manufactured by Budker Institute of Nuclear Physics of Siberian Branch of Russian Academy of Science. These machines are well known in the world. They are operating from Germany in West to Indonesia and Malaysia in East. Main application of these accelerators is the treatment of polymers. New development of ELV accelerators is concerning the low energy range and design of self-shielded accelerators. There are the set of self-shielded accelerators. The lowest energy is 150 - 200 kV. These machines are unified with usual ELV accelerators and extend their application area. For industrial tomography based ELV4 accelerator was developed with low values of ripple current (≤2%) and the instability of energy (≤5%) of the electron beam.

INTRODUCTION

Radiation-chemical technology with the use of electron accelerators as the sources of ionizing radiation had been widely developed. Budker Institute of Nuclear Physics of the Siberian Branch of Russian Academy of Sciences is one of the world leaders in the development, design, production and delivery to the industry of electron accelerators of different types (i.e. continuous accelerators based on high-voltage rectifier, high frequency, pulse, etc.), covering a wide range of accelerated electrons energy and power. ELV accelerators hold a specific place in the range of equipment manufactured by the Institute. Compact dimensions and high operational qualities have allowed BINP take a leading position in the market of industrial accelerators, both in Russia and abroad. The ELV accelerators series has the range of accelerated electrons energy from 0.3 to 2.5 MeV, maximum beam power for separate machines from 20 to 100 kW and maximum beam current up to 100 mA. The special accelerator was designed and manufactured for ecological and research purposes with a beam power 400 kW.

DEVELOPMENT OF ELV ACCELERATORS FAMILY

ELV accelerators high voltage source is a generator with a cascade of parallel inductive links. HV rectifier column is installed inside the primary winding. The primary winding is powered by a frequency converter on the base of IGBT transistors. The secondary winding of the coil have the maximum induced voltage of about 20 kV. This voltage is rectified by voltage doubling circuit. Rectifier unit connected in series or series-parallel to form the column of HV rectifier, ending with the high-voltage electrode. The injector control unit is located inside the high-voltage electrode. Accelerator tube is placed inside the rectifier column and the top of the tube is connected with the high-voltage electrode. All these elements are placed inside the pressure vessel filled with insulating gas (SF6). This design reduces the overall dimensions of ELV accelerators and makes them the most compact among the devices of this class. The accelerator is supplied with gas system that enables to save SF6 gas during maintenance and repair. Vacuum systems and the extraction device are attached to the bottom of the vessel. The cathode is placed at the upper end of the accelerator tube. The electrons emitted by the cathode have the full energy at the exit of the accelerator tube. They are passing through the system of scanning magnets that evenly distribute electrons on the foil window. The electron beam is scanned in 2 directions along and across the window. The material moves under the window in the transverse direction and is treated by extracted electrons. The beam position inside window is monitoring. The accelerator control is equipped with an automated system that enables not only to make the operator's job easy, but to synchronize the process equipment and the accelerator, or combine them into one complex.

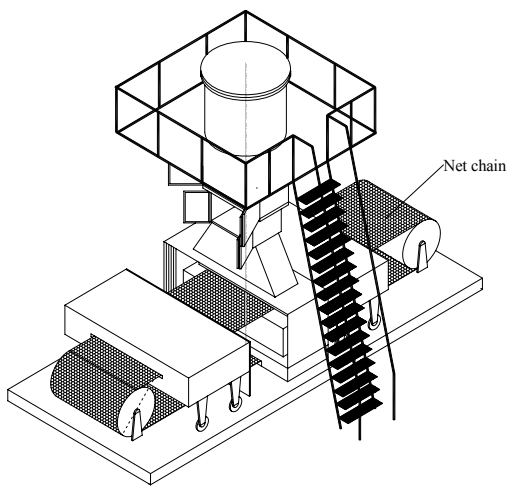

Figure1: 0.3 MeV*100 mA accelerator for tire industries.

The analysis of demands for accelerators (a market for accelerators) was made in 2011. As a result, the in-demand accelerators are distributed evenly for maximum energy from 1 MeV up to 2.5 MeV. Concerning the beam power – all queries on the boosters had 100 kW beam

ISBN 978-3-95450-170-0

power. In accordance with the results of the analysis of ELV family was supplemented by accelerators with the maximum current up to 100 mA in the range 0.5-1.0 MeV, with max. current 80 mA in the range of 0.8-1.2 MeV, max. current 67 mA - in the range of 1.0-1.5 MeV.

For the range of energy 1.0-2.5 MeV max. current is the same as previous - 50 mA. Maximum beam power for all of the accelerators is 100 kW.

Analysis of last years' activity concludes the increasing requests of low-voltage machines (range 0.3-0.7 MeV). In all these settings, it was the wish of the local radiation protection. It should be noted that the increasing interest in low-voltage accelerators is caused by the mobile accelerators, among others. This mobile accelerator was developed together with our South Korea partner EB-TECH Co Ltd. The main purpose of this machine is to demonstrate the advantages of electron beam technology for environmental purposes (Fig. 2).

Figure 2: Mobile accelerator.

As a result of the carried out research the Institute offers a series of accelerators in the local protection of overlapping energy range of 0.25-0.7 MeV. The value of the maximum current depends on the design of the extraction devices (length of foil windows, one window, two windows) and can reach up to 150 mA.

Figure 3: Accelerator for producing of foamed polyethylene was upgrade in 2012.

The accelerator for rubber industry 0.3 MeV*100 mA is shown in Fig.1. The new concept enables to upgrade accelerators produced by other manufacturers. Figure 3 shows the accelerator which was manufactured by Efremov Electro-physical Institute (Russia) in 1970 and modernized by BINP in 2012. The exhaust system of the electron beam to the atmosphere has been remained non-upgraded, the system scans the beam was changed to the original for ELV accelerators.

UTILIZATION OF ELV ACCELERATOR FOR TOMOGRAPHY

Electron beam tomography is highly attractive as an imaging tool for technical flow studies, because it is fast and gives a good spatial resolution of one millimetre or better. Furthermore, this technology is very versatile, that is, electron beam scanning can be adapted to complex object shapes and can be extended to multi-slice and three-dimensional imaging . One particular problem associated with technical multiphase flow studies is associated with the fact that multiphase flows do often occur in vessels of complex geometries, with thicker

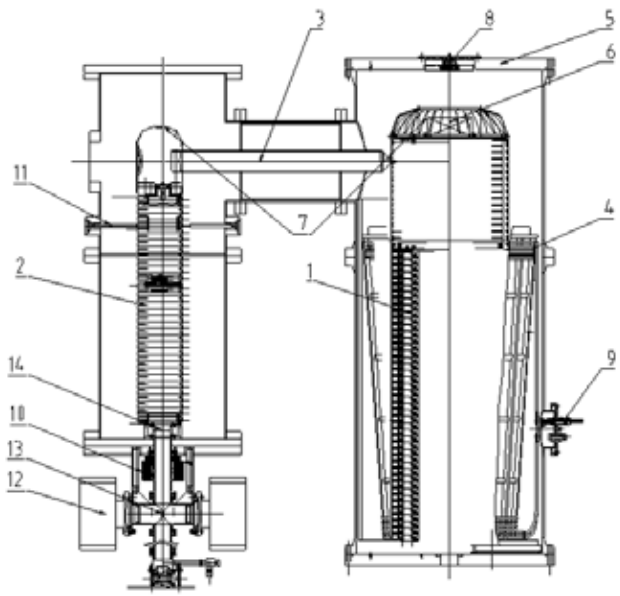

Figure 4: Common design of accelerator: Common design of accelerator: 1 - column rectifying sections; 2 - accelerating tube; 3 - gas feeder; 4 - the primary winding; 5 - the case of the pressure vessel; 6 -block injector control; 7, high voltage electrodes; 8 - the optical elements of the beam current control system; 9 entries of the primary winding; 10 - lens; 11 - supports to support tube; 12 - ion pump vacuum system; 13 - docking port of the vacuum system; 14 - bellows for fixing the accelerating tube.

metal walls and internals. Examples are pressurized pipes and reactors with steel walls, heat exchangers, rod bundles or chemical reactors with packings, stirrers, injectors, heaters, coolers and other internals. Spatial

ISBN 978-3-95450-170-0

resolution in X-ray tomography images is mainly limited by the focal spot size of the X-ray source due to the fan-beam geometry. The permissible spot size in electron beam tomography depends on many parameters. One is the focusability of the beam, which decreases with increasing beam emittance, increasing beam current due to space charging effects and decreasing electron energy. Another limit is the permissible power density in the spot, which is determined by the melting/sublimation point of the target material, the beam power and the scanning speed. For fast scanning of several hundred meters per second focal spot speed, the main limitation comes from beam emittance, which is inherent to the accelerator design. The ELV accelerators may achieve spot sizes well below one millimeter.

If the application of ELV accelerators for radiation modification of materials related with ensuring the required level of uniformity of the radiation dose [3], the use of ELV accelerators for the tasks of industrial tomography is associated with the need to fulfill the following requirements on the parameters of the injected beam:

- energy pulsing at the level E = 1,0 MeV ≤±5%;
- current ripple at the level I_{beam} = 100 mA ≤±2%.

To solve these problems and meet the specific requirements of design-based accelerator ELV4 was developed and is now in the process of installing the accelerator for fast imaging (Fig. 4).

Figure 5: Modified accelerating tube.

To reduce the ripple current and energy, a series of experiments were conducted on a standard accelerator ELV-4 as a simplified model of the accelerator for tomography. The main difference is that the high-voltage rectifier has a lower output capacitance, and the accelerating tube is positioned within the high-voltage rectifier.

As a result, has reduced volatility in energy of up to ± 5% at a beam current of 100 mA. To reduce the ripple current divider resistances in parallel tubes were placed additional capacity (Fig. 5). It is possible to reduce the instability of current to ± 0.14%.

Currently the accelerator for industrial tomography has been assembled at the customer's site and is subjected to adjustment tests (Fig. 6).

Figure 6: Assembled accelerator for tomography.

ELV accelerators continuously adapted for use in a variety of processes of radiation in industry and can be used for research into and development of new techniques and materials by electron irradiation.

REFERENCES

[1] N.K. Kuksanov, R.A. Salimov (BINP SB RAS, Novosibirsk), B.S.Han, W.G.Kang, S.M.Kim EB TECH Co. Ltd., Daejeon, Republic of Korea «High Voltage ELV Accelerators for Industrial Application (Family of Accelerators and Tendency of Development) » Proceeding of RuPAC-2012, Peterhof, Russia, 2012.

[2] Kuksanov N. K., Fadeev S. N., Golubenko Yu. I., Kogut D. A., Korchagin A. I., Lavrukhin A. V., Nemytov P. I., Salimov R. A., Domarov E. V. Development of the model range and improve performance accelerators ELV. Probl. At. Sci. Tech. 2012. Issue 3. P. 15-18.

[3] U. Hampel, Y. Bärtling, D. Hoppe Feasibility study for MeV electron beam tomography, Institute of Safety Research, Helmholtz-Zentrum Dresden-Rossendorf, Dresden, Germany, 2012

[4] Kuksanov N.K. Fadeev S.N., Kogut D.A. Improving Of Uniformity Of The Electron-Beam Treatment Of Materials By Elv Accelerators //Proceeding of RuPAC-2012, Saint Petersburg, Russia, 2012

ISBN 978-3-95450-170-0

LIA-2 AND BIM ACCELERATORS AS PART OF RADIOGRAPHIC COMPLEX AT RFNC-VNIITF

A. Akhmetov, S. Khrenkov, P. Kolesnikov, E. Kovalev, O. Nikitin, D. Smirnov, Russian Federal Nuclear Center — Zababakhin All-Russian Scientific Research Institute of Technical Physics (RFNC-VNIITF), Snezhinsk, Russian Federation

Abstract

The paper describes installations included in the radiographic complex at RFNC-VNIITF, their purpose, composition, and principle of operation. The paper presents the synchronizing system for the betatron complex based on BIM pulse air-cored betatrons and LIA-2 linear induction accelerator, as well as the synchronizing circuit and functioning algorithm in the mode of BIM and LIA-2 combined operation. This combined mode of operation was tested and results of this testing are also provided.

COMPOSITION OF THE RADIOGRAPHIC COMPLEX

The radiographic complex includes the betatron complex consisting of two pulse air-cored betatrons BIM (further – betatron complex) and linear induction accelerator LIA-2 (further – LIA-2). The betatron complex ensures two-direction recording of dynamic objects at 90° between directions. Each betatron in the betatron complex can generate from one to three radiation pulses in one gas-dynamic experiment. LIA-2 is placed between betatrons and can generate up to two radiation pulses.

The betatron complex and LIA-2 are independent units.

The betatron complex is intended study high-speed processes in gas-dynamic experiments using the pulse shadow X-ray diffraction technique. Main technical characteristics of the betatron complex are given in table 1 [1].

Table 1: Main technical characteristics of the betatron complex

Parameter (Units)	Value
Boundary energy of bremsstrahlung spectrum (MeV)	65
Penetrability in Pb (mm)	165
Radiation source size (mm)	2.5x6
Duration of γ-radiation pulse in the mode of one radiation peak generation (ns)	100
Max. number of successive pulses	3
Time interval between γ-radiation pulses in the mode of three radiation peaks generation (μs)	0.5-5

Penetrability of the betatron complex was estimated based on a X-ray diffraction image of a lead test object ”wedge” [2] positioned at the 4-m distance from a target. Maximum thickness of the test object was 100 mm with the 10-mm step. Two more lead blocks with the total thickness of 100 mm were placed in front of the test object. The recording unit was immediately adjacent to the “wedge”. The maximum penetrability of the betatron complex was 180 mm. The X-ray diffraction image of the “wedge” is given in Fig. 1.

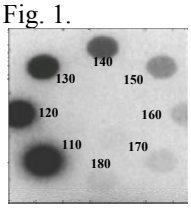

Figure 1: X-ray diffraction image of test object “wedge”.

The radiation source size was estimated based on the X-ray diffraction image given by the pinhole camera positioned at the distance of 1 m from the target. The recording unit was positioned at the 3-m distance. The radiation source size was measured at 0.5 blackening density minus background. Blackening density distribution after X-raying of the pinhole camera is given in Fig. 2.

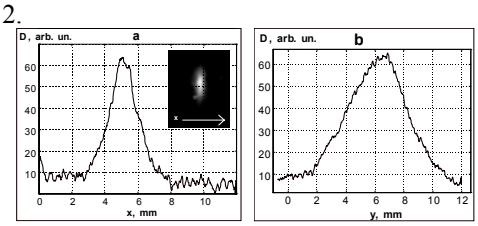

Figure 2: Blackening density distribution after X-raying of the pinhole camera.

Electrons are deflected onto the target either in one pulse or in portions with the formation of up to three X-ray pulses with a certain intensity relation between them depending on a particular task. For this purpose, installation is equipped with generators that deflect the electron beam onto the target. Usually, total energy is distributed as follows: 1-st pulse takes 10-15%, 2-nd pulse – 30%-40%, and 3-d pulse – 50%-60%.

LIA-2 is a high-quality injector of a large-scale linear induction accelerator LIA-20 intended for small-direction X-ray tomography complex. Thanks to high-quality of the formed electron beam, LIA-2 is used as an independent X-ray installation. Main technical characteristics LIA-2 are given in table 2 [3].

Table 2: Main technical characteristics of LIA-2

Parameter (Units)	Value
Max. beam energy (MeV)	2.0
Max. beam current (kA)	2.0

ISBN 978-3-95450-170-0

Min. beam spot size on the target in all modes (mm)	1.5
Current pulse length (ns)	180
Max. number of successive pulses	2
Time interval between pulses (μs)	3-20

LIA-2 penetrability is determined with the help of the test lead "wedge" positioned at the distance of 1.5 m from the target. Maximum thickness of the "wedge" was 100 mm.

Fig. 3 shows the X-ray diffraction image of the lead "wedge" with the electron energy of 1.1 MeV. LIA-2 penetrability at the observability limit is 60 mm in lead when Image Plate is used for recording.

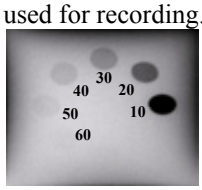

Figure 3: Penetrability determination at 1.1MeV electron energy.

Fig. 4 shows the X-ray diffraction image of the lead "wedge" with the electron energy of 1.3 MeV. With this electron energy, LIA-2 penetrability equals 70 mm.

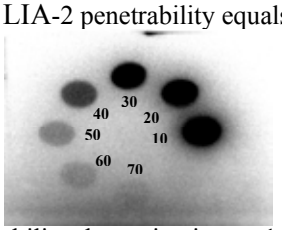

Figure 4: Penetrability determination at 1.3MeV electron energy.

Fig. 5 shows the X-ray diffraction image of the lead "wedge" with the electron energy of 1.5 MeV. With this electron energy, LIA-2 penetrability equals 70 mm.

X-radiation source size was estimated based on the X-ray diffraction image of the pinhole camera positioned at the 1.5-m distance from the target.

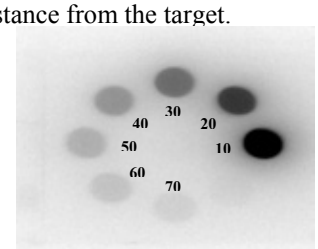

Figure 5: Penetrability determination at 1.5MeV electron energy.

The recording unit was positioned at the 3-m distance. The radiation source size was measured at 0.5 blackening density minus background. Fig. 6 shows X-ray diffraction image of the pinhole camera.

Figure 6: X-ray diffraction image of the pinhole camera.

Blackening density distribution after X-raying of the pinhole camera is given in Fig. 7.

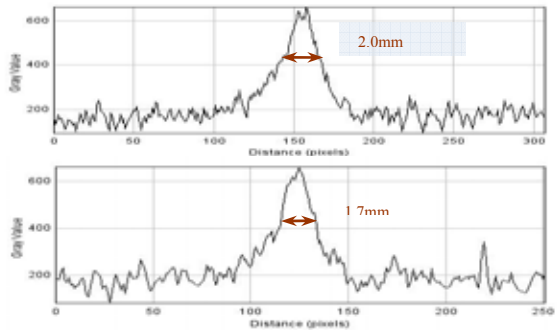

Figure 7: Blackening density distribution over the horizontal and vertical axes, respectively.

SYNCHRONIZING SYSTEM

Analysis of time diagrams for technological processes in the betatron complex and LIA-2 in the independent operational mode demonstrated that physical implementation of the synchronizing system is possible. Installations are synchronized through "wedging-in" of the LIA-2 start-up into the betatron complex functioning, i.e. after the switch-on and charging stage and before the injection stage and the acceleration cycle. Duration of the technological process in LIA-2 is ~57 ms, duration of the switch-on and charging stage for the betatron complex is 60 seconds, duration of the injection stage and the acceleration cycle is ~0.4 ms.

Synchronization diagram for the betatron complex and LIA-2 is given in Fig. 8 (numbers denote the sequence of signals formation).

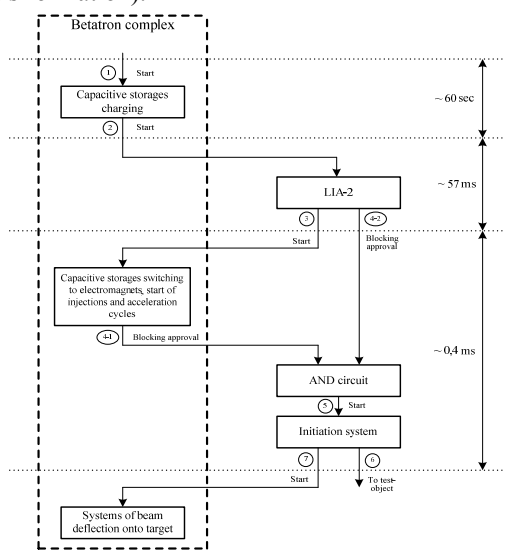

Figure 8: Synchronization diagram for the betatron complex and LIA-2.

Fig. 9 shows the synchronization algorithm block-diagram for the betatron complex and LIA-2 operation.

ISBN 978-3-95450-170-0

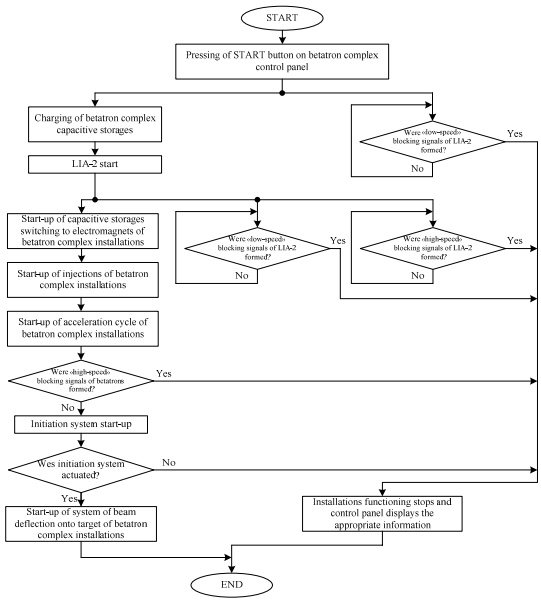

Figure 9: Synchronization algorithm block-diagram for the betatron complex and LIA-2 operation.

Pressing the button START on the control panel of the betatron complex initiates start of the betatron complex and LIA-2 in the mode of combined synchronized operation. Then, all capacitive storages of the betatron complex are charged.

Then, functional parts and systems of LIA-2 are started up; time delays of their start-up are preliminarily adjusted on the LIA-2 control panel [4]. Somewhere about 300-450 μs prior to the γ-radiation pulse generation, the LIA-2 control system forms the signal to continue BIM start.

In parallel, operation of all LIA-2 units and systems, as well as of the betatron complex is controlled. In the case of any discrepancies in the technological process, an appropriate blocking signal is formed to stop betatron complex functioning; the control panel displays the appropriate information.

In the normal mode of initiation system actuation, the system of beam deflection onto the target of each installation of the betatron complex is initiated and γ-radiation pulses are generated. Fig. 10 shows the time diagram for the combined synchronized operation of the betatron complex and LIA-2.

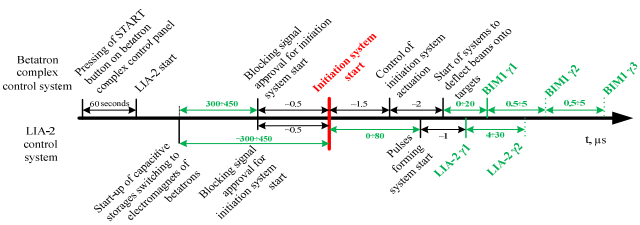

Figure 10: Time diagram for the combined operation of installations.

TESTING

Testing of the combined mode of betatron complex and LIA-2 operation included a series of start-ups with the registration of γ-radiation pulses. These tests allowed us to record γ-radiation pulses of the betatron complex and LIA-2. Time delays in the recorded γ-radiation pulses were observed to correspond to those specified. A typical oscilloscope record of γ-radiation pulses recorded during a technological start-up of the betatron complex and LIA-2 in the combined operation mode is given in Fig. 11 where: channel 1 – is the signal of the initiation system start; channels 2 and 3 – are signals of γ-radiation pulses from installations of the betatron complex; channel 4 – are signals of γ-radiation pulses of the betatron complex and LIA-2.

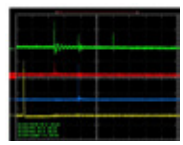

Figure 11: Oscilloscope record of γ-radiation pulses.

CONCLUSION

Nowadays, the radiographic complex at RFNC-VNIITF includes a number of up-to-date installations that can successfully meet challenges of gas dynamic testing.

By now, the combined operation mode was tested for the betatron complex and LIA-2 with the generation of γ-radiation pulses at a specified instant.

Radiographic installations capable of generating both soft and hard radiation spectra will allow one to solve a wider range of tasks during the same explosive experiment. Combined operation of the betatron complex and LIA-2 will also provide X-ray diffraction images in 3 directions during the same explosive experiment.

Development of appropriate recording systems will allow realization of inherent potential and, on the whole, increase operation efficiency of the radiographic complex at RFNC-VNIITF.

REFERENCES

[1] Y Kuropatkin, V Mironenko, V. Tsyberev, A. Kostin, V. Kotilevskiy, "Technical description of the installation BIM for X-ray radiography of high-speed processes," R&D report (intermediate), VNIIEF, 2000.

[2] Y. Kuropatkin, S. Voronov, V. Suvorov, V. Mironenko, D. Grishin, V. Tsyberev, A. Kostin, V. Kotilevskiy, "Radiographic characteristics of installation BIM to study high-speed processes," R&D report (intermediate), VNIIEF, 2001.

[3] P. Logachev, A. Batrakov, A. Pavlenko, V. Sazanskiy, G. Fatkin, "Automation system for the linear induction accelerator of the radiographic complex," Vestnik NGU (Reporter of Novosibirsk State University), Novosibirsk, 2010.

[4] P. Logachev, P. Bak, A. Batrakov, R. Kadyrov, A. Pavlenko, A. Panov, V. Sazanskiy, G. Fatkin, "Control system for the linear induction accelerator of the radiographic complex: structure, hardware, trial operation results," Novosibirsk, 2011.

ISBN 978-3-95450-170-0

MAIN PARAMETERS AND OPERATIONAL EXPERIENCE WITH NEW GENERATION OF ELECTRON ACCELERATORS FOR RADIOGRAPHY AND CARGO INSPECTION

A.N. Ermakov[a,b #], A.S. Alimov[a,b], B.S. Ishkhanov[a,c], I.A. Frejdovich[d], A.N. Kamanin[a,b], V.V. Klementiev[b], V.V. Khankin[a,b], S.V. Lamonov[d], L.Yu. Ovchinnikova[b,c], N.I. Pakhomov[a,b], Yu.N. Pavshenko[b,d], A.S. Simonov[b,d], I.V. Shvedunov[b], N.V. Shvedunov[a,b], V.I. Shvedunov[a,b], I.Yu. Vladimirov[b,c], D.S. Yurov[a,b]

[a)]Skobeltsyn Institute of Nuclear Physics, Lomonosov Moscow State University
[b)]Laboratory of Electron Accelerators MSU, Ltd.
[c)]Physics Department, Lomonosov Moscow State University
Leninskie Gory, 119992 Moscow, Russia
[d)]"Research and Production Enterprise "Toriy", Obrucheva 52, 117393 Moscow, Russia

Abstract

We describe main parameters and operational experience with new generation of electron accelerators for radiography and cargo inspection developed with participation of scientists, engineers and technologists from Lomonosov Moscow State University and "Research and Production Enterprise "Toriy". Two accelerators are described: accelerator for radiography UELR-8-2D with beam energy regulated in the range 3-8 MeV and dose rate from 0.5 to 15 Gy/min and accelerator for cargo inspection UELR-6-1-D-4-01 with pulse to pulse energy switching between 3.5 and 6 MeV, with repetition rate 400 Hz and dose rate 4 Gy/min. Both accelerators use klystron as an RF source, which is fed by a solid state modulator.

INTRODUCTION

Main directions for perfection of electron accelerators for radiography are connected with the possibility of regulating the accelerated beam energy and dose rate of bremsstrahlung in a wide range to achieve optimum conditions for defects visualization for different thicknesses of material; with minimization of the electron beam spot size at bremsstrahlung target in order to improve spatial resolution; with extended life of the bremsstrahlung target; reduction in weight and size characteristics of the accelerator; increasing its resource; simplifying the operator work and servicing; in reducing parasitic radiation.

Electron accelerator for modern cargo inspection complex capable to recognize the effective atomic number of the contents of the container [1] in addition to the features listed above must be able to switch the energy of the accelerated beam from pulse to pulse between two or more values; must ensure high stability of the beam energy and dose rate; must have a short transient time after switching on X-rays; must be able to generate packages of closely spaced pulses of different energy [2], following with a high repetition rate.

The above requirements are the basis for the design of accelerators described in this report.

a_ermak1978@mail.ru

COMMON FEATURES

Developed accelerators for radiography and cargo inspection have several common features. In particular, the change of the energy of the accelerated beam in both cases is done by changing the level of the accelerating field. To ensure the high quality of the beam at more than twice change of the energy the standing wave on-axis coupled accelerating structure was optimized in order to produce the transverse and longitudinal beam focusing with capture efficiency more than 60% in the whole range of the accelerating field variation. The sealed-off design of the accelerating system, consisting of an accelerating structure with RF antenna, electron gun, vacuum RF window, ion and getter pumps and intensively cooled bremsstrahlung target, is used. The electron gun is attached to the accelerating structure using Conflat joint that facilitates the repair in the case of cathode filament failure. Exterior view of the accelerating system is shown in Fig. 1.

Figure 1: Accelerating system.

Accelerating structure is fed by the pulse multi-beam klystron KIU-168 [3] operating under reduced high voltage. To power klystron and electron gun solid state modulator [4] is used. The parameters of the modulator

ISBN 978-3-95450-170-0

provide the maximum output pulsed power of the klystron 3.5 MW.

Both accelerators have similar design of the radiation shielding, which provides precise positioning of the accelerating structure, shielding the electron beam from stray magnetic fields and allows for quick replacement of the structure. To reduce parasitic radiation a combination of lead and tungsten is used. The dose rate of the bremsstrahlung at a distance of 1 m from the bremsstrahlung target in all directions except the working area is reduced by 10^4 times for radiographic accelerator and 10^5 times for cargo inspection as compared to the dose rate on the axis.

The dose rate measurement is done by built-in ionization chamber. The pressure of the insulating gas in the waveguide is automatically maintained constant by means of the gas system, including besides other parts also a vacuum pump, pumping out waveguide before filling by gas. X-ray head and modulator are combined into a single module.

Both accelerators have the same principle of the control system. Control of the individual subsystems of the accelerator is produced by controllers coupled to the control computer via Ethernet. All controllers and control computer are located in the X-ray head cabinet in the vicinity of controlled objects. The remote control panel is connected to the control computer also using Ethernet. Control of the accelerator operation is done by the original software. The system of the accelerator interlocks ensures safe operation in accordance with the applicable rules. Control of the accelerator operation and fault diagnostic can be performed via remote access. Details of control system are described in [5].

ACCELERATOR FOR RADIOGRAPHY

Photo of accelerator for radiography is shown in Fig. 2, the basic parameters are given in Table 1. During accelerator commissioning its calibration is carried out. Built-in ionization chamber is calibrated by an external camera. Beam energy is determined by attenuation of bremsstrahlung by barrier. For each of the energy values in a fixed range of 3 to 8 MeV, following with steps of 1 MeV, parameters of RF system operation are calculated using theoretical models and measured data. The parameters of RF system such as the frequency of the RF generator, pulse repetition rate, the output power of the klystron depend on the set energy, dose rate, and the temperature of the coolant. In the operation of the accelerator parameters for the selected mode of operation, are installed automatically. Also the process of the accelerator on and off is fully automated.

Measurement of the size of the electron beam focal spot at the bremsstrahlung target is illustrated by Fig. 3 (a). Lead diaphragm (2) which is 10 mm thick with d = 2 mm hole is placed at distance s = 0.18 m from the target (1). Bremsstrahlung beam spot is registered by X-ray film (3) placed at L = 3 m from the target. Electron beam focal spot diameter in this geometry is defined by the:

$$d_b = \frac{S}{L} D_1 - d \quad (1)$$

Beam image recorded by film, is shown in Fig. 3(b) Image diameter can be estimated as, $D_1 \approx 38$ mm, hence electron beam focal spot diameter at target is $d_b \approx 0.28$ mm, which well correlate with spot diameter measured directly using transition radiation during accelerator design stage.

Figure 2: Accelerator for radiography.

Table 1: Radiographic accelerator parameters

Parameter	Value
Beam energy	3 - 8 MeV
Dose rate	1 – 15 Gy/min
Beam spot size	< 1 mm
Dimensions W×L×H	640×1090×1460
Weight	1025 kg

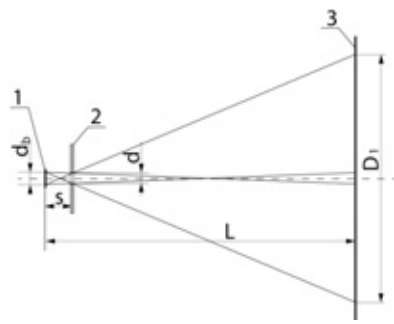

(a)

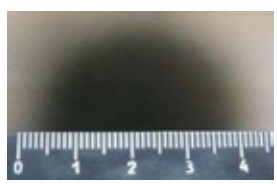

(b)

Figure 3: (a) Geometry for electron beam focal spot size measurements. (b) Bremsstrahlung beam spot registered by X-ray film.

ISBN 978-3-95450-170-0

ACCELERATOR FOR CARGO INSPECTION

Photo of the accelerator for cargo inspection is shown in Fig. 4, the main parameters are listed in Table 2.

Figure 4: Accelerator for cargo inspection..

Table 2: Cargo inspection accelerator parameters.

Parameter	Value
Beam energy	3.5/6 MeV
Energy stability	0.5 %
Dose rate	4 Gy/min
Dose rate stability	2 %
Repetition rate	2×200 Hz
Beam spot size	< 1 mm
Dimensions W×L×H	640×1090×1460
Weight	1250 kg

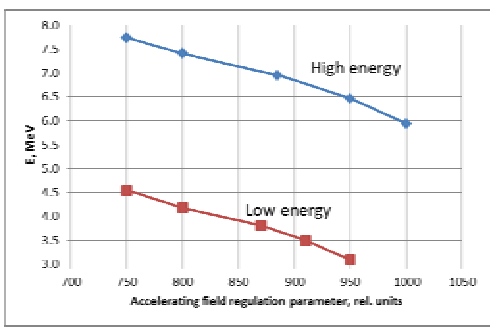

Figure 5: Low and high beam energy regulation.

Presented here accelerator is a fundamental modification of the accelerator prototype described in [6]. The accelerator can operate in a low-energy or high-energy mode with a pulse repetition rate up to 400 Hz, or in energy switching mode with a repetition rate of pairs of closely spaced pulses of 200 Hz. The interval between a pair of pulses in energy switching mode can be adjusted in the range of 200-600 μs [2]. The values of the low and high energy can be regulated independently over a wide range, as shown in Fig. 5.

Important for cargo inspection accelerators is reduced transient time after the X-rays switching on. To compensate for changes in the energy and dose rate caused primarily by thermal processes, we have developed a model describing the behavior of accelerating structure in the transient period taking into account a load by beam current, which is different for low and high energies. Based on this model and measurements the control algorithm for RF system was developed to compensate for changes in the energy and dose rate. Fig. 6 shows example of time dependencies of the values of the low and high energy when operating in the energy switching mode without and with compensation mechanism. To measure beam energy the detector line [1] was used.

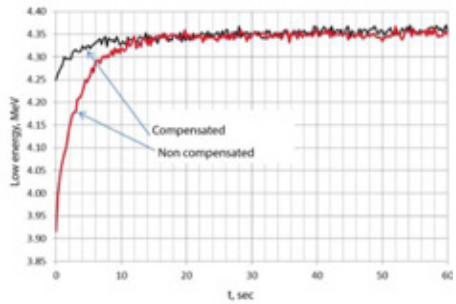

(a)

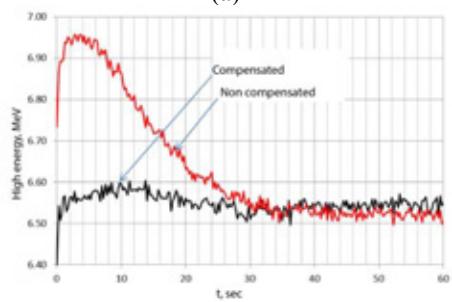

(b)

Figure 6: Time dependencies of low (a) and high (b) energies in energy switching mode with compensating mechanism switched off and on.

CONCLUSION

We have developed a new generation of accelerators for radiography and cargo inspection. The authors are grateful to Mr. A.V. Nalivaev for support of this work and Dr. S.A. Ogorodnikov for measurements of the cargo inspection accelerator parameters.

REFERENCES

[1] S. Ogorodnikov et al., in Proc. IPAC13, p.3699
[2] M. Arlichev et al., RF patent UM-31998/RU-NF
[3] I.A. Frejdovich et al, in Proc. RuPAC06, p. 100
[4] www.sc-nova.com
[5] A.N.Ermakov et al., in these Proc.
[6] O.Yu. Maslennikov et al., RF patent RU 2452143 C2

ISBN 978-3-95450-170-0

DEDICATED DC-110 HEAVY ION CYCLOTRON FOR INDUSTRIAL PRODUCTION OF TRACK MEMBRANES

B.N.Gikal, S.N.Dmitriev, G.G.Gulbekian, P.Yu.Apel, S.L.Bogomolov, O.N.Borisov, V.A.Buzmakov, A.A.Efremov, I.A.Ivanenko, N.Yu.Kazarinov, V.I.Kazacha, I.V. Kalagin, V.N.Melnikov, V.I.Mironov, S.V.Pashchenko, O.V.Semchenkova, V.A.Sokolov, N.F.Osipov, A.V.Tikhomirov, A.A.Fateev, M.V.Khabarov, FLNR JINR, Dubna, Russia

Abstract

In the Laboratory of nuclear reactions JINR dedicated accelerator complex on the basis of the heavy ion cyclotron DC-110 for the industrial track membrane production has been developed and created. The isochronous cyclotron DC-110 accelerates the ions Ar, Kr and Xe with a fixed energy of 2.5 MeV/nucleon and intensity of 10-15 μA. The cyclotron is equipped with ECR ion source - DECRIS-5 (18 GHz) and axial injection system. The pole diameter of the magnet is 2m. Isochronous magnetic field formed by shimming sectors on the level of 1.67 T. Accelerated ions $^{40}Ar^{6+}$, $^{86}Kr^{13+}$, $^{132}Xe^{20+}$ have close mass-to-charge ratio, which allows changing particles without changing the operation mode of the cyclotron. Accelerator complex DC-110 is capable of producing up to 2 million square meters of track membranes per the year.

INTRODUCTION

A series of heavy-ion accelerators for applied purposes have been developed and created at the Laboratory of Nuclear Reactions of the Joint Institute for Nuclear Research. The IC-100 cyclotron was put into operation in 1985 and upgraded in 200-2002 [1,2]. In 2004-2006 the DC-60 cyclotron was created for the Interdisciplinary Research Center of the Gumilev Eurasian National University (Astana, Kazakhstan) [3,4]. The accelerator beams are successfully used for solid state physics research, and track membrane production. Based on the technological solutions and experience of operating the IC-100 and DC-60 accelerators there has been developed the project of the DC-110 cyclotron [5,6]. The accelerator complex produces intense Ar, Kr, and Xe ion beams with a fixed 2.5 MeV/nucleon energy, which allows the production of track membranes on the basis of up to 30 μm thick polymer films.

The accelerator complex includes:
- the DC-110 cyclotron,
- ECR ion source and axial beam injection system,
- accelerated beam transport channel equipped with technological equipment for irradiating the polymer film,
- vacuum system,
- electrical supply and control system,
- cooling system.

The accelerator is furnished with one polymer film irradiation channel. The possibility of installing a switching magnet and assembly of a second channel is provided for increasing the productivity of the equipment by simultaneous irradiation of film on one channel and preparing for installation on the other.

The cyclotron magnet has a 2m pole diameter. The ions being accelerated are $^{40}Ar^{6+}$, $^{86}Kr^{13+}$ и $^{132}Xe^{20+}$ with close mass-to-charge ratios of 6.667, 6.615, and 6.600, which allows realizing an acceleration regime practically at a fixed frequency of the accelerating system and fixed magnetic field.

The DC-110 accelerator does not provide for ion energy variation and changes in the mass-to-charge ratio of accelerated particles. This concept is characterized by increased reliability and by simplicity of controlling the complex.

ION SOURCE

The 18 GHz DECRIS-5 ion source was developed on the basis of sources of the DECRIS-4 (14 GHz) series with copper windings created at LNR (JINR, Dubna) [7] by intensifying the magnetic structure and changing to a new type of microwave oscillator. The DECRIS-5 ion source created for industrial application is characterized by increased reliability.

To ensure the design parameters of the beams accelerated on the DC-110, the ion source should generate intensities of $^{40}Ar^{6+}$, $^{86}Kr^{13+}$ and $^{132}Xe^{20+}$ ion beams of not less than 85μA, 150 μA and 150 μA, respectively. After assembling the ECR source and axial injection system, thorough adjustment of all systems of the source and axial injection channel was carried out. Beams of Ar, Kr, and Xe ions were produced from the source. The possibility of producing maximum Ar, Kr, and Xe ion beam intensity was investigated, the results are given in Table 1.

Table 1. Maximum ion beam intensities obtained from DECRIS-5 source in μA (Z - ion charge).

Z	8+	9+	11+	15+	18+	19+	20+
Ar	1200	750	300				
Kr				325	182	120	70
Xe							220

BEAM AXIAL INJECTION SYSTEM

For transporting the ion beam of the ECR source to the center of the cyclotron, beam axial injection system is used, which is composed of:
- 3 focusing elements, 2 correcting elements,
- analyzing magnet,
- diagnostic elements of the injected beam,

ISBN 978-3-95450-170-0

- linear buncher located 2450 mm away from median,
- sinusoidal buncher located 800 mm away from median plane,
- vacuum system based on turbomolecular pumps and cryogenic pumps,
- electrostatic inflector located in the center of the cyclotron for deflecting the injected beam from the vertical channel into the cyclotron median plane.

The 20 kV injection voltage was selected for the optimal conditions of beam dynamics in the cyclotron center.

CYCLOTRON MAGNETIC STRUCTURE

The DC-110 magnetic structure is created on the basis of an electromagnet with a 2m pole diameter.

The use of radial correction coils is not provided for in the DC-110 cyclotron; the isochronous magnetic field is formed by iron structure. Azimuthal correction coils are installed in the valleys of the cyclotron for correcting the first harmonic.

In the working gap of the magnet there are four pairs of sectors with straight boundaries fastened at the magnet's pole. Each sector is equipped with lateral detachable shims. Azimuthal or vertical processing of the lateral sector shims was used for correcting the magnetic field when forming the isochronous acceleration conditions and also for compensating the effect of the magnetic channel used for focusing the beam in the cyclotron's beam extraction system. A compensating channel identical in design to the main channel is installed in the cyclotron centrally-symmetrically to the focusing magnetic channel for suppressing odd harmonics of the magnetic field. The main parameters of the magnet of the DC-110 cyclotron are given in Table 2.

Table 2. Main parameters of DC-110 cyclotron magnet.

Pole diameter, [mm]	2000
Number of sector pairs	4
Angular length of sector (helicity)	52^o (0^o)
Number of radial correction coils	0
Number of sets of azimuthal correction coils	2
Electromagnet weight [tons]	250
Isochronous magnetic field at center, T	1.67

RADIO FREQUENCY SYSTEM OF CYCLOTRON

A resonance system consisting of the following components is used in the DC-110 isochronous cyclotron for producing a dee-accelerating voltage:

- two quarter-wave coaxial resonators, which are stainless-steel tanks plated inside with copper,
- two copper dees with an angular span of 40°,

The characteristics of the RF system are given in Table 3.

Table 3. General characteristics of RF system.

Resonance frequency of resonators	7.494 - 7.806 MHz
Acceleration harmonic	2
Dee voltage	55 kV
Maximum power of RF generator	20 kW

BEAM EXTRACTION

An electrostatic system based on a deflector with a 50–60 kV/cm and focusing magnetic channel is used at the DC-110 cyclotron for extracting accelerated beam. The deflector is located in the valley. A passive magnetic channel is used in the cyclotron chamber for focusing the beam during extraction.

BEAM CHANNELS FOR IRRADIATION OF POLYMER MATERIALS

The DC-110 cyclotron complex (Fig.1) has one channel for transporting accelerated ion beams with the possibility of installing a switching magnet and assembling a second channel.

The horizontal heavy ion beam scanning system is created on the basis of a magnet supplied by a sawtooth current. Vertical scanning is accomplished by an electrostatic deflector with a sawtooth voltage of 15 kV. The scanning system provides irradiation of a 600×200 mm^2 stationary target with uniformity not worse than ±10% and irradiation of a moving film up to 600 mm wide at a speed from 0.05 to 1 m/s.

Figure 1: DC-110 cyclotron.

ISBN 978-3-95450-170-0

CYCLOTRON OPERATING REGIMES AND ACCELERATED IONS

To accelerate $^{40}Ar^{6+}$, $^{86}Kr^{13+}$, $^{132}Xe^{20+}$ ions have a small difference in the mass-to-charge ratio (6.667, 6.615, and 6.600), it was decided to use an acceleration regime with a fixed magnetic field. The frequency of the accelerating system should be changed in conformity with Table 4.

Table 4. Optimal frequency values of RF system (F_{RF}) and magnetic field (B_0) .

Ion	A/Z	B_0, T	F_{RF}, MHz	Frequency difference, kHz
$^{40}Ar^{6+}$	6.6667	1.6612	7.653	23
$^{86}Kr^{13+}$	6.6154	1.6612	7.712	-18
$^{132}Xe^{20+}$	6.6000	1.6612	7.730	0

The acceleration regime indicated in Table 6 doesn't require a change in any parameters of the accelerator systems when changing the type of ions being accelerated except for tuning the frequency of the resonance system.

The phase acceptance of the DC-110 cyclotron is about 30°; a beam bunching system is used for increasing capture efficiency of the injected beam into acceleration. The efficiency of capturing the beam into acceleration and the coefficient of the beam intensity increase compared to the unbunched beam are shown in Table 5.

An increase of the capture coefficient to 48% at a low injected beam intensity of 6 μA, is related not only to a decrease of the space charge effect in the beam but mainly to a decrease of beam emittance at a low intensity from the ion source.

Table 5. Capture coefficient of injected beam into acceleration in different regimes.

I_{inj}, μA	Capture coefficient into acceleration in %			
	without bunching	Lin-on. Sin-off.	Sin-on. Lin-off.	Sin+Lin – on.
6	9.3	23.2	25.8	48.2
18.4	8.7	15.6	25.0	38.0
49	9.1	15.7	25.7	36.7
103	8.7	14.1	24.8	34.0

The main tuning of the DC-110 cyclotron to achieve the design parameters was done with the use of a $^{86}Kr^{13+}$ ion beam. During accelerator tuning, a regime was found with a high beam transmission coefficient from the ion source to the polymer film irradiation device at an injected beam intensity close to the maximum, 150 μA.

In a working regime, the pressure in the cyclotron chamber as at the moment of commissioning was $2.4 \cdot 10^{-7}$ Torr (without the beam, $1.7 \cdot 10^{-7}$ Torr). Losses of $^{86}Kr^{13+}$ ions during acceleration from radius 140 mm to radius 890 mm were about 37% both in the case of a bunched beam and in the case of disconnected bunchers, of which vacuum losses amount to about 30%. In 2013 as a result of vacuum training of the cyclotron chamber internal surfaces there was achieved a pressure of $\sim 1 \cdot 10^{-7}$ Torr in the acceleration mode. Vacuum losses in this case decreased by a half.

Works on creating the DC-110 cyclotron complex began in August 2009. In 2012, assembly and adjustment of the cyclotron equipment were carried out in the building of the BETA research and industrial complex and beams of accelerated Ar, Kr, and Xe ions were obtained.

Table 6 presents design and experimentally obtained parameters of ion beams after the completion of commissioning. There was carried out the irradiation of a polymer film of 12μm thickness with ions of Kr. The non-uniformity of pore density in the manufactured track membranes was better than ±10%.

Table 6. Ion beam parameters of the DC-110 cyclotron.

Ion	ECR beam intensity, μA	Extracted beam intensity, μA		Ion energy, MeV/nucleon
		design	obtained	
$^{40}Ar^{6+}$	94	6	13	2.5
$^{86}Kr^{13+}$	150	13	14.5	2.5
$^{132}Xe^{20+}$	190	10	10.9	2.5

REFERENCES

[1] B.N.Gikal et al. Modernization of cyclic implanter IC-100. Preprint JINR E9-2003-121 (Dubna, 2003).

[2] B.N.Gikal et al. IC-100 Accelerator Complex for Scientific and Applied Research. Physics of Particles and Nuclei Letters. 2008. V5. No1(143). P. 59-85.

[3] B.N.Gikal et al. DC-60 Heavy Ion Cyclotron Complex: First Beams And Project Parameters. Physics of Particles and Nuclei Letters, 2008. V.5. No.7(149). P. 160-165.

[4] B.N.Gikal et al. DC-60 cyclotron complex for scientific and applied research and commercial applications in nanotechnology. At. Energy. 2007. V103. No 6. P. 357-364.

[5] B.N.Gikal et al. Heavy ion DC_110 cyclotron for industrial applications and applied studies in nanotechnologies. Physics of Particles and Nuclei Letters. 2010. V.7. No7(163). P.891-896.

[6] B.N.Gikal et al. FLNR Heavy Ion Cyclotrons for investigation in the field of Condensed Matter Physics Industrial Applications. In Proc. of RUPAC-2012. Saint-Petersburg, Russia. 2012. P.172-175.

[7] S.Bogomolov, V.Bekhterev, A.Efremov, B.Gikal, G.Gulbekian, Yu.Kostukhov, A.Lebedev,V.Loginov, N.Yazvitsky. Recent Development in ECR Ion Sources at FLNR JINR. In Proc. of RUPAC2012. Saint-Petersburg, Russia. 2012. P.203-207.

[8] B.N.Gikal et al. Heavy Ion Cyclotron Beam Scanning System of DC-110 Accelerator. Physics of Particles and Nuclei Letters. 2010. V.7. No.7(163). P. 1-4.

ISBN 978-3-95450-170-0

CC-18⁄9M CYCLOTRON SYSTEM

A.P. Strokach, O.L. Veresov, Yu.N. Gavrish,A.V. Galchuck, S.V. Grigorenko, V.I. Grigoriev,
M.A. Emeljanov, M.L. Klopenkov, A.N. Kuzhlev, V.G. Mudroliubov, G.V. Muraviov,
V.I. Nikishkin, V.I. Ponomarenko, Yu.I. Stogov, S.S. Tsygankov,
JSC "D.V. Efremov Institute of Electrophysical Apparatus", St. Petersburg, Russia

Abstract

The CC-18/9M cyclotron system has been designed, manufactured and delivered to NIITFA, Moscow. The system consists of an updated CC-18⁄9M cyclotron and a targets system. The cyclotron is intended to produce accelerated proton and deuteron beams with an energy of 12-18/6-9 MeV and current up to 150/70 μA, respectively. For this purpose, a shielding-type electromagnet and a resonance system have been afresh designed. The target system for the production of F-18 and C-11 radionuclides for PET has been designed in NIIEFA for the first time.

The CC-18⁄9M cyclotron system was designed for the delivery to JSC «NIITFA», Moscow with a view to creating a pilot PET center. The cyclotron system consists of an updated CC-18⁄9M cyclotron and a target system. This cyclotron is a new version of three CC-18⁄9 machines manufactured previously and delivered to PET centers of the University in Turku, Finland, Russian Research Center for Radiology and Surgical Technologies, Pesochny, St. Petersburg and «VNIITF », Snezhinsk town, Chelyabinsk region, Russia. To widen the possibilities of application and increase the marketability of the CC-18⁄9M cyclotron, the energy of accelerated proton and deuteron beams is made variable in the range of 12-18 and 6–9 MeV, respectively. Simultaneously, the design current of protons and deuterons is increased by one and a half in comparison with the original model, i.e. up to 150 и 70 μA, respectively.

The new version of the cyclotron keeps the continuity in the main engineering solutions proven in CC-18⁄9 and MCC-30⁄15 machines [1, 2]:

- shielding-type electromagnet with a limited number of holes in the shielding,
- vertical median plane to give an easy access to in-chamber devices by moving apart the movable part of the magnet along the guides,
- the vacuum chamber of the cyclotron made as a part of the electromagnet,
- the resonance system located completely inside the vacuum chamber of the electromagnet [3],
- extraction of beams of accelerated protons and deuterons by stripping negative ions on carbon foils practically with no loss of intensity,
- an external injection system, which significantly reduces the working gas admittance from the source to the vacuum chamber, facilitates production of high vacuum and consequently reduces the losses of ions in the acceleration process by molecules of the residual gas [4],
- acceleration of negative ions of hydrogen and deuterium at one fixed frequency of the RF field (the 2nd and 4th harmonics, respectively),
- installation of movable shims in special recesses to correct the magnetic field topology and to ensure isochronous field when changing the type of ions to be accelerated,
- extraction of proton and deuteron beams through 3 windows made in the vacuum chamber. Two windows are intended for installation of targets directly onto the magnet ("near" targets) and the third window is used to transport the beam to remote targets,
- simultaneous extraction of beams with a max energy to one of remote and one of near targets,
- standard set of components of a beamline transporting the beam to remote targets: matching magnet, 2 correcting magnets, doublet of quadrupole lenses and switching magnet making possible the beam transport to 3 target devices,
- compete automatic control of the cyclotron system.

In the process of designing, the following principal modifications were made, which significantly improved the conditions of service and maintenance/repair compared to the original model:

- A new resonance accelerating system consisting of 2 mirror-symmetrical resonators has been designed. In CC-18⁄9 cyclotrons, one resonator was used, the central conductor of which consisted of two dees, two stems, which had a common part with a shorting flange. The new design allowed the loss power to be reduced from 18 to 13 kW. Due to the resonance system symmetry, was reduced the effect of thermal deformations, which in the original machine limited the beam current in the continuous mode. The operating frequency of the new resonance system of 40.68 MHz (38.2 MHz -in the original model) coincides with the operating frequency used in the MCC-30⁄15 cyclotron., so in both models identical RF power supply systems can be used.
- The new cyclotron design allowed 2 cryogenic pumps to be installed on the vacuum chamber, which provided more uniform distribution of pressure and, as a consequence, lower losses of ions in the acceleration by molecules of the residual gas.

ISBN 978-3-95450-170-0

- The main magnet of the cyclotron was designed anew taking into account modifications in the resonance and vacuum pumping systems. Manufacturing of the whole magnet yoke at one enterprise, the Novokramatorsky machine-building plant, starting from steel making to metal finishing treatment, allowed the beam, pillar and pole of each half-yoke to be made as an integral element. Such a design provides uniform magnetic properties (steel of one melting cycle), makes significantly easier the magnet yoke assembly and increases the accuracy of critical dimensions.
- A new system of shims similar to that used in the MCC-30/15 cyclotron has been designed (4 shims instead of 16 used in the original model), which made much more simpler shims' manufacturing and change of the magnetic field topology when the type of accelerated ions is changed. Shims are located in valleys not occupied with resonance system dees [5].
- New constructions of stripping devices, probe and AFT trimmer has been designed. Due to the use of standard articles, linear translators, which ensure their travel in vacuum, less labor efforts and time were spent for manufacturing the aforementioned equipment in the NIIEFA production department.
- It was for the first time in the NIIEFA practice, that a cyclotron was delivered together with a target system. Design and operational documentation for the target system of the cyclotron has been worked out. The target system consists of a target station with systems for fore-vacuum pumping, water and helium cooling; liquid and gas targets; control system and system for target loading[6].

The main characteristics of cyclotron are given in Table1.

Table1: Main characteristics of the cyclotron

System, parameter	Characteristics, value
Accelerated ions	H-/D-
Extractedions	H^+/D^+
Beam energy, variable, MeV	12-18/6-9
Beam current, μA	150/70
Electromagnet	
- type	shielded-type
- pole diameter, cm	1150
- mass, t	34
Resonance system	
- operating frequency, MHz	40.68
- dee number	2
- RF voltage amplitude,kV	38
RF power,kW	20
Ion source	external
Operating mode	continuous/pulse
Total power consumption, not more, kW	
- beam on target	90
- stand-by mode	15

The cyclotron system has been designed, delivered and installed in the laboratory building in JSC «NIITFA», Moscow. Fig.1 demonstrates the layout of the cyclotron system equipment in rooms with radiation shielding. At the forefront, diagnostic units with target devices are shown, under which units for targets' loading with target materials are placed. Fig.2 demonstrates the movable half-yoke of the main electromagnet moved apart and in-chamber units can be seen. The target station rack is given in Fig.3.

Figure 1: Cyclotron system.

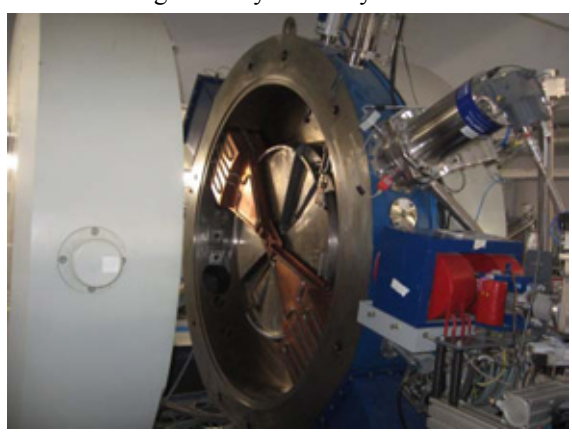

Figure 2: Electromagnet with open vacuum chamber.

Figure 3: Target station rack.

To date, the adjustment works have been finished, and the design ranges of proton energy and extracted beam current have been attained. Final acceptance tests have

ISBN 978-3-95450-170-0

been performed with extraction of proton beams to targets. Tests of the target system with production of F-18 and C-11 and their transport to modules of radiopharmaceuticals' synthesis have been done.

REFERENCES

[1] P.V. Bogdanov, M.F. Vorogushin, V.P. Kukhtin, E.A. Lamzin, A.P. Strokach, S.E. Sychevsky. RF Patent №2373873 H05H «Isochronous Cyclotron for Acceleration of Several Species of Charged Particles». Bulletin № 32, 20.11.2009

[2] P.V. Bogdanov, I.N. Vasilchenko, M.F. Vorogushin, A.V. Galchuck, S.V. Grigorenko, V.G. Mudrolyubov, A.P. Strokach, S.E. Sychevsky, "New Compact Cyclotrons for Radionuclides Production, Proceed. of RuPAC'08.

[3] P.V. Bogdanov, V.G. Mudrolyubov, S.A. Silaev, "Specific Features of Accelerating Systems of CC-18/9, CC-12 and MCC-30/15 Compact Cyclotrons', Voprosy Atomnoi Nauki i Tekhniki, series «Electrofizicheskaya Apparatura», №.5, St. Petersburg, 2010, pp. 65-74.

[4] P.V. Bogdanov, I.N. Vasilchenko, O.L. Veresov, S.V. Grigorenko, Yu.V. Zuev, M.T. Козиенко, V.G. Mudrolyubov, A.P. Strokach, S.S. Tsygankov, "Systems for External Injection of Negative Ions for Compact Cyclotrons", Voprosy Atomnoi Nauki i Tekhniki, series «Electrofizicheskaya Apparatura», №.5, St. Petersburg, 2010, pp. 74-83.

[5] P.V. Bogdanov, A.A. Budtov, I.N. Vasilchenko, M.F. Vorogushin, S.V. Grigorenko, V.G. Mudrolyubov, S.A. Silaev, Yu.I. Stogov, A.P. Strokach, S.E. Sychevsky, N.F. Shilkin, "The MCC-30/15 Medical Compact Cyclotron with Variable energy of Accelerated Ions", Voprosy Atomnoi Nauki i Tekhniki, series «Electrofizicheskaya Apparatura», №.5, St. Petersburg, 2010, pp. 32-48.

[6] E.N. Abramov, Yu.N. Gavrish, P.A. Gnutov, B.N. Zabrodin, M.L. Klopenkov, R.M. Klopenkov, K.A. Kravchuck, A.N. Kuzhlev, A.A. Melnikov, G.V. Muraviov, A.V. Regel, A.P. Strokach, "Target System for the CC-series Cyclotrons Designed and Manufactured in NIIEFA", Problems of Atomic Science and Technology, 2013, V. 6(88), Series "Nuclear Physics Investigation" (61), Pp. 201-204.

ISBN 978-3-95450-170-0

SEE TESTING FACILITIES AT FLNR ACCELERATORS COMPLEX: STATE OF THE ART AND FUTURE PLANS*

S. Mitrofanov, B. Gikal, G. Gulbekyan, I Kalagin, V. Skuratov, Y. Teterev, N.Osipov, S. Paschenko
JINR, Dubna, Moscow Region, Russia
V. Anashin, United Rocket and Space Corporation, Moscow, Russia

Abstract

The Russian Space Agency (Roscosmos) utilizes U400 and U400M cyclotrons at accelerator complex of the Flerov Laboratory of Nuclear Reactions (FLNR) of the Joint Institute for Nuclear Research (JINR) in Dubna for heavy ion SEE testing. The ions up to the Xe and Bi with the energy up to 40 AMeV are available for the users. The detailed overview of the facility and the features of diagnostic set-up used for ion beam parameters evaluation and control during SEE testing are discussed. The road map for the strategic development of this field in FLNR is presented.

INTRODUCTION

Since becoming discovery in 1975 [1], intensive investigations of single-event effects (SEE) in electronic devices have resulted test method and facility developments. As known, the ion energy for such experiments should be high enough as 3 MeV/nucleon. Therefore, heavy ion beams in this energy range are delivered from large accelerators. Usually they are located at basic physics research laboratories. Currently, there are several major heavy ion beam facilities in the U.S. and Europe that are available for SEE testing [2]. The Russian Space Agency (Roscosmos) utilizes U400 and U400M cyclotrons at accelerator complex of Flerov Laboratory of Nuclear Reactions (FLNR) of Joint Institute for Nuclear Research (JINR) in Dubna for heavy ion testing. U400 cyclotron has been in operation since 1978 and delivers ion beams of atomic masses 4÷209 at energies of 3÷29 MeV/nucleon [3]. U400M cyclotron has been in operation since 1991. This cyclotron was originally intended for acceleration of ion beams with A/Z=3÷3.6 (A- atomic weight of the accelerated ion; Z - ion charge when accelerated) at energies of 34-50 MeV/nucleon. The beam is extracted from cyclotron using stripping foil. In 2008 the U400M possibilities have been extended by addition of the ion beams with A/Z=8÷10 at energies of 4.5-9 MeV/nucleon to carry out the experiments on synthesis the new super heavy elements as well as applied researches [3]. Last few decades the SEE testing have been carried out using ion beam transport lines designed for nuclear physics experiments. However, specific requirements to ion beam parameters, like uniformity over large irradiating area, beam intensity variation from units to hundred thousands of particles per second and etc., could not be realized in full by these facilities.

* This work was sponsored by the Russian Federal Space Agency by special agreement between Institute of Space Device Engineering and Joint Institute for Nuclear Research.

To reproduce the effects of a heavy component of cosmic radiation for the SEE testing one should use the low-intensity (10^3 - 10^6 cm^{-2} s^{-1}) heavy ion beams with the LET range in silicon, typical for ion energies of 50-200 MeV/nucleon. But, keeping in mind to test the real DUT which are in metal and plastic housings, as well as ready-to-use electronic boards, the heavy ion beams with energies in the range 5 - 50 MeV/nucleon must be used in experiments.

The main purpose of this report is to describe heavy ion beam lines specialized for SEE testing at FLNR JINR accelerator complex. Originally these facilities were designed to meet demands of EIA/JESD57 and ESCC BS 25100. Since becoming operational in 2010, the low energy beam (3÷6 MeV/nucleon) facility has been available to users. The facility for the SEE testing at high energy (20÷40 MeV/nucleon) was successfully commissioned in January'14. The third line is based on U400 and after modernization of this cyclotron in 2015 there will be the possibility to make the SEE testing with the fluent energy variation for every ion [3].

ION BEAM LINE WITH ENERGIES OF 3-6 MEV PER NUCLEON AT U400M.

The ion beam line for SEE testing is a part of the U400M cyclotron. This beam line contains: ion beam transportation system, beam monitoring system, energy measurement system and user's vacuum test chamber with a mounting and positioning assembly to hold the sample in the irradiation field. The photograph of the experimental set up showing its components is given in Fig. 1. The beam leading line is separated from a bending magnet (1) by vacuum gate valve (2). The next transport element is two-coordinate beam-positioning magnet (3) guiding the beam through variable size diaphragm placed in entrance of the 50 Hz X-Y magnetic scanning system (4). Scanning system provides exposure over the target area 200x200 mm with inhomogeneity better 30% in the flux range of $1 \div 10^5$ particles/cm^2s. To choose appropriate ion energy and the LET value we use a degrader with tantalum foils of 5, 9, 12.5, 14, 19, 22.5, 25 of 27 microns thickness. A driver of foils holder is designated as (5) in Fig. 1. Energy of particles passed through the foils as well as initial ion energy is measured by time-of-flight (TOF) method. Ions with 3÷9 MeV/nucleon energy pass the distance between two pick up electrodes (8), 1.602 m, during 39÷67 ns. These parameters were chosen to register the time of passage of one bunch according to the beam time structure at U-400M cyclotron - the duration

ISBN 978-3-95450-170-0

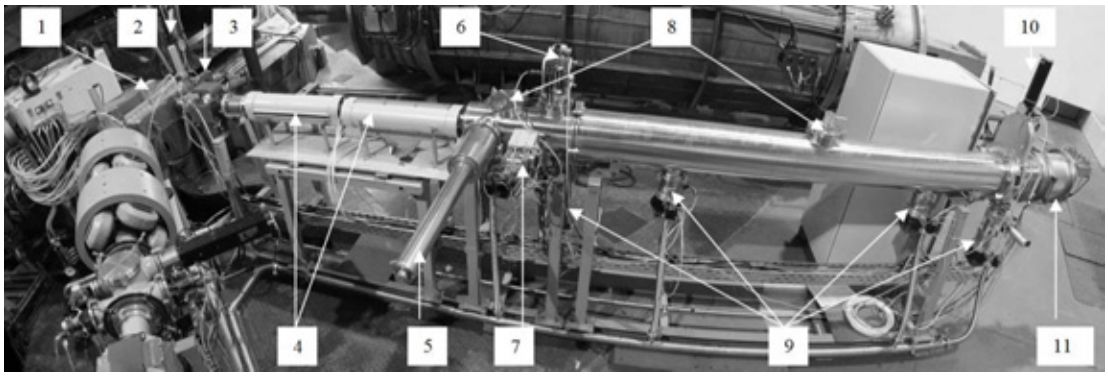

Figure 1: General view of the ion beam transport line and experimental set up for SEE testing at U400M cyclotron. See explanations in text.

of a pulse is 6÷7 ns and frequency 15÷15.5 MHz. The accuracy of ion energy measurements is no worse than 1%. Diagnostic elements such as Faraday cup (6) and luminophor holder (7) are used during beam adjusting and tuning at high intensity. The beam line is pumped by three turbo molecular pumps (9). The user target chamber (11), the out – and inside photographs of which are given in Fig. 2, is separated from the ion transport line by vacuum gate valve (10) and is equipped with own vacuum system. This system is fast enough to pump down in less than 10 minutes. The pumping system is fully interlocked for ease of use and safety of the equipment.

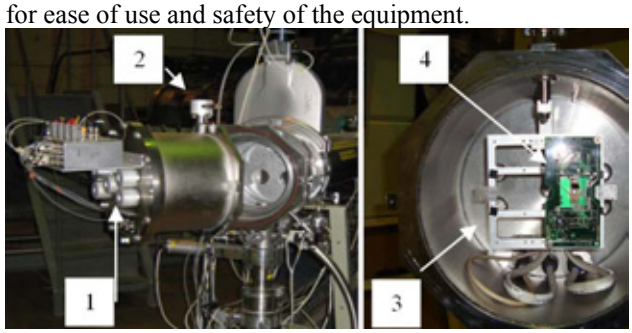

Figure 2: Target chamber for SEE testing.

The internal diameter of a chamber having shape of a barrel is 28 cm, the depth is 30 cm. The beam diagnostic elements (1) and user connectors are placed on the end flange of the chamber. Testing targets (4) are mounted on the frame (3) which can be tilted to the ion beam direction within 0÷75 degrees using turning gear (2).

Table 1. Ion beam parameters used for the low energy SEE testing

Accelerated ion	Extracted ion	Energy, MeV	LET, MeV/(mg/cm^2)	Ion flux, cm^{-2}s^{-1}
$^{16}O^{2+}$	$^{16}O^{8+}$	56±3	4.5	1 ÷ 10^5
$^{22}Ne^{3+}$	$^{22}Ne^{10+}$	65±3	7	1 ÷ 10^5
$^{40}Ar^{5+}$	$^{40}Ar^{16+}$	122±7	16	1 ÷ 10^5
$^{56}Fe^{7+}$	$^{56}Fe^{23+}$	213±3	28	1 ÷ 10^5
$^{84}Kr^{12+}$	$^{84}Kr^{32+}$	240±10	41	1 ÷ 10^5
$^{136}Xe^{18+}$	$^{136}Xe^{46+}$	305±12	67	1 ÷ 10^5
$^{209}Bi^{22+}$	$^{209}Bi^{58+}$	490±10 (820±20)	95 (100)	1 ÷ 10^5

Ion beam parameters used for SEE testing, like ion type and energy, the LET and ion flux range, are listed in Table 1.

ION BEAM LINE WITH ENERGIES UP TO 40 MEV PER NUCLEON

In order to cover the necessary energy range (up to 40 MeV/nucleon) for the SEE testing the high energy beam line was created.

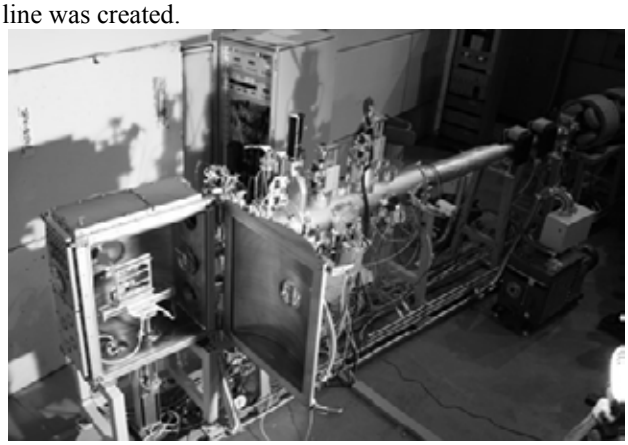

Figure 3: The user target chamber. Outside view.

The beam line was named A1S and consists of a part of existing physical channel for the ion beams extraction and transportation and the new part by using. The line has length about 6 meters. The scheme of the experimental equipment is given in Fig. 4. The beam leading line is separated from a last bending magnet M4 by vacuum the gate valve (1). The two- magnetic quadrupole lenses (2) provide exposure over the target area with uniformity better 20% in the flux range of 1÷10^5 particles/cm2s. After lenses two steering magnets (3) are places for the vertical beam correction. The A1S beam line consists of: ion beam transportation system (is pumped by three turbo molecular pumps (4)), beam monitoring system (5, 6,8,10, and 11), energy measurement system (to measure the ion energy the TOF technique is used(7)) and DUT's chamber (12) with a mounting and positioning assembly to hold the sample in the irradiation field. The user target chamber (Fig.3), is separated from the ion transport line

ISBN 978-3-95450-170-0

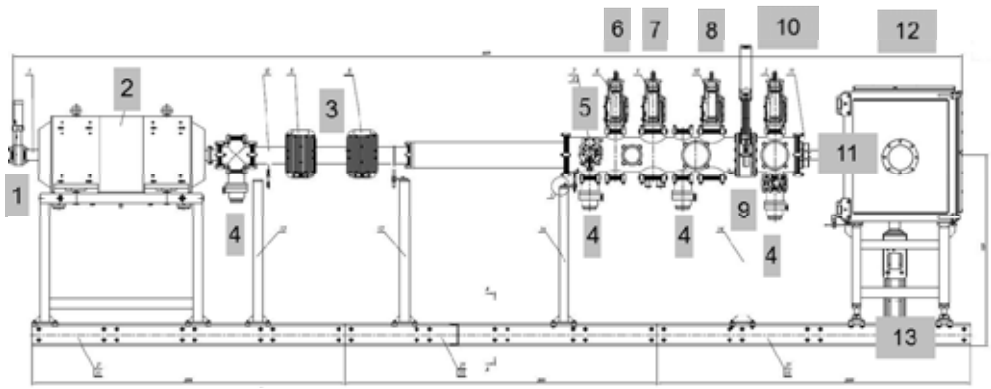

Figure 4: General scheme of the high energy ion beam transport line and the experimental set up for SEE testing at U400M cyclotron. See explanations in text.

by the vacuum gate valve (9) and is equipped with own vacuum system. This system is fast enough to pump down in less than 2 minutes. The pumping system is fully interlocked for ease of use and safety of the equipment. The target chamber provides two operational modes: at atmospheric (ATM) pressure and at vacuum (VAC) of 10 mbar. To provide the ATM mode shaped ion beam extracted from beam-line to the chamber through a stainless steel foil of 12.6 μm thickness with diameter up to 60 mm (the extraction window). The DUT frame has possibility to move remotely (13) in X-Y directions (to place the DUT into beam spot area with accuracy 0.1 mm) and can be tilted to the ion beam direction within 0÷90 degrees using turning gear.

ION BEAM DIAGNOSTIC

The wide range of beam control systems are used during beam run. To catch the beam movable probes inside the U400M are used. Diagnostic elements such as the luminophor and the Faraday cup are used during rough beam adjusting at high intensity. For the fine beam tuning, double side Si strip detector (Fig.5) and arrays of proportional counter are installed. The last one provide on-line control of beam flux with air ambient as working gas. The choice for this type of counters was done due to their operation simplicity, radiation-resistant and almost infinite resource. The beam uniformity and flux are determined using an array of five active particle detectors. Two kind of active detectors can be utilized in the diagnostic system - proportional counters and scintillation detectors. The four detectors are placed in corners (for the ion beam halo control) of DUT irradiating area and the fifth in its center. To increase the reliability of ion fluence measurements, total number of ions which hit the target is controlled additionally by using polycarbonate or polyethylene terephthalate track detectors placed in close vicinity of any testing device in all irradiation sessions. The efficiency of swift heavy ion registration by such detectors is close to 100%. Besides of ex situ monitoring of accumulated ion fluence, polymer track detectors are used also for precise determination (with accuracy no worse than 5%) of the beam uniformity over the irradiating area after change from one ion to another.

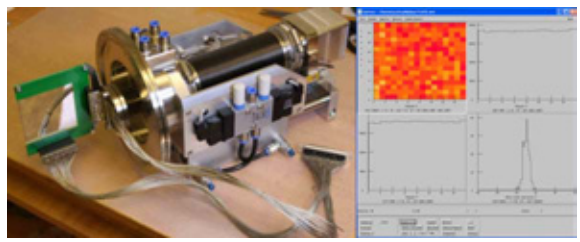

Figure 5: Double-side Si strip detector. Dual axes (X-Y) orthogonal beam detection Kr beam profile as example.

CONCLUSION

The only facility in Russian Federation dedicated for the SEE testing with heavy ions up to 40 MeV/ nucleon is open for the users. The LET range 4.5÷100 MeV/(mg/cm^2) meet in full the requirements for SEE testing experiments. Since becoming operational in 2010, more than 500 devices have been tested (10000 hours of heavy ion beam operation time). All needed infrastructure was created in the way to provide to the users the friendliest atmosphere during the irradiation procedure.

ACKNOWLEDGMENT

The authors would like to thank the excellent technical support from the FLNR JINR cyclotrons staff.

REFERENCES

[1] D. Binder, E. C. Smith, and A. B. Holman, “Satellite Anomalies from Galactic Cosmic Ray”, IEEE Trans. Nucl. Sci., vol. NS-22, p .2675, 1975.

[2] Robert A. Reed et al, “Single-Event Effects Ground Testing and Orbit Rate Prediction Methods: The Past, Present and Future”, IEEE Trans. Nucl. Sci., vol. 50, pp. 622-634, 2003.

[3] B. Gikal, I.Kalagin, G. Gulbekyan, S. Dmitriev, “Status of the FLNR JINR cyclotrons”. Proceedings of PAC09, Vancouver, BC, Canada FR5REP099, pp. 5011-5013. [4] H. Koivisto, J. Drentje, M. Nurmia, Rev. Sci. Instrum., 69, (2). 1998, p. 785.

ISBN 978-3-95450-170-0

MODERNIZATION THE MODULATOR OF THE RF-GENERATOR ION LINEAR ACCELERATOR LU-20

A.V. Butenko, A.I. Govorov, D.E. Donets, V.V. Kobets,
V.A. Montchinsky, A.O. Sidorin, Dubna, Russia

Abstract

The report discusses the replacement of the lamp switch the modulator semiconductor. A schematic of the modulator and a semiconductor switch scheme protection against voltage surges in the generator lamp. Replacing the lamp switch it possible to increase the output power generator.

INTRODUCTION

Modulator frequency generator ion linac LU-20 was commissioned at the beginning of 70th years. Currently modulator lamps GMI-34B used in this modulator, taken out of production and the existing stock has long worn out and due to the increase of the internal resistance of these lamps, the anode voltage on the generator lamps significantly decreased and the generator does not produce RF-power required to normal operation of the accelerator. It was therefore decided to replace the modulator lamps solid state switch HTS 501-80-LC2 firm "BEHLKE" Germany. This decision was implemented.

THE MODULATOR

RF-generator supplying linear accelerator LU-20 was launched in 1970. It provides a nominal power level in the cavity of the accelerator. Eventually all aging occurred generator elements. In the 90 years has stopped the release of modulator tubes GMI-34B used as a key modulator of the generator. I had to work on finding a used lamps. To ensure the total anodic current generator tubes 220 A key is a four connected in parallel modulator tubes GMI-34B (Fig. 1). Since the lamp old internal resistance from them several times the rated and thereon a high voltage drop is applied to the anodes generator tubes. As a result, the output power of the generator is insufficient to provide desired accelerating voltage in the resonator of the accelerator.

Figure 1: Modulator of the RF-generator.

It was decided to replace the modulator tubes semiconductor switches. The switches were ordered us "BEHLKE" Germany. The first experience of replacement bulbs semiconductor switches proved unsuccessful. After working the switches was breakdown.

SIMULATION OF THE MODULATOR

After analyzing the causes of the breakdown of the switch modeling work was conducted modulator using Micro-cap 9. The modeling was made for the lamp and the semiconductor switch. Several schemes have been analyzed with a semiconductor switch. The modeling was assembled circuit protection semiconductor switch and then on the simulator breakdowns in generator lamps were tested semiconductor switch and perfected the technique of working as part of a key generator in normal mode and circuit protection from breakdowns in key generator lamps and from spontaneous elongation of the anode pulse. Fig. 2 is a schematic diagram of the modulator on which to carry out simulation of the modulator. Figure 3 shows the simulation results.

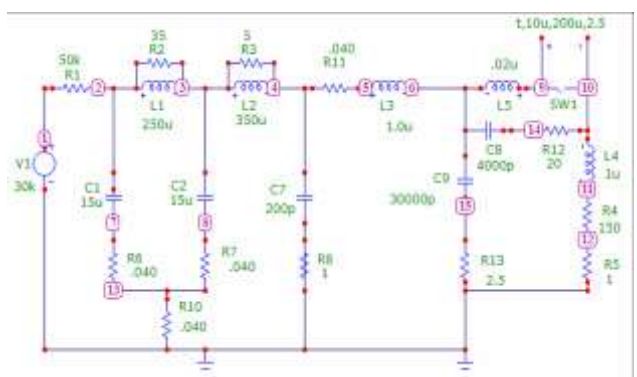

Figure 2: Scheme of the modulator.

ISBN 978-3-95450-170-0

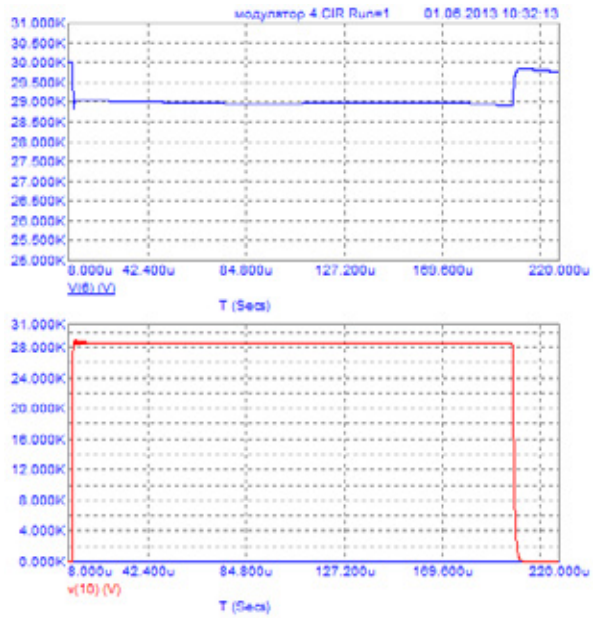

Figure 3: The results simulation of the modulator.

After testing a semiconductor switch and protection circuits (Figure 4, 5) modulator lamps were replaced by a switch (Figure 6) and has been successfully operated at the Nuclotron session.

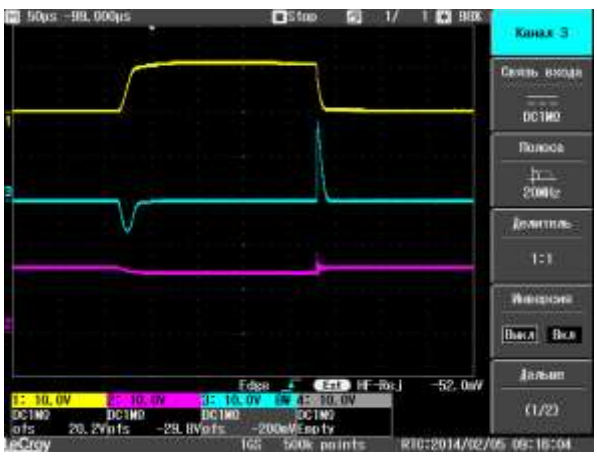

Figure 4: Oscillograms of the protection scheme.

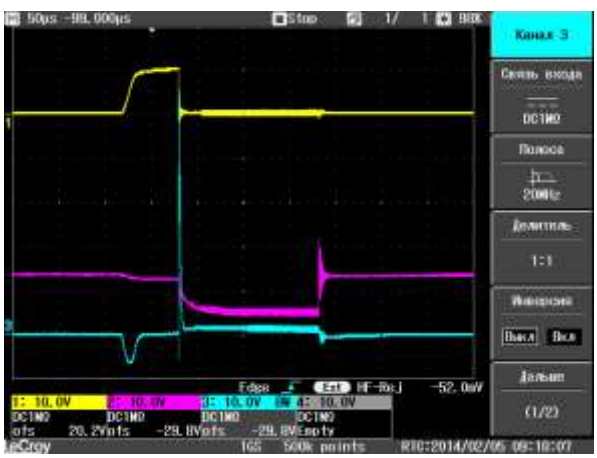

Figure 5: Oscillograms of the protection scheme.

Figure 5: The modulator with semiconductor switche.

CONCLUSION

As a result of the work done modulator tubes were replaced by semiconductor switches HTS 501-80-LC2 firm "BEHLKE" Germany, which led to a successful work session at the Nuclotron[1] and provide work of Nuclotron on the carbon the fourth charge states.

REFERENCES

[1] A.S. Averichev et al., Results of the 46th and 47th sessions Nuclotron. Posts JINR, R9-2013-140, Dubna, 2013.

ISBN 978-3-95450-170-0

MODERNIZATION THE MODULATORS KLYSTRONS ACCELERATING STAND OF THE ELECTRON LINEAR ACCELERATOR LINAK-800

V.V. Kobets, N.I. Balalykin, P.P. Zhuravlyv, A.G. Kobets, V.G. Shabratov,
G.D. Shirkov, A.G. Sorokin, JINR, Dubna, Russia

Abstract

The report presents the work on the modernization of the modulator klystron second accelerating station of the acceleration stand on the basis of electron linear accelerator LINAC-800. The analysis of the modulator first accelerating station and made suggestions for improving the management system modulator. The functional circuit blocks control the modulator.

INTRODUCTION

Equipment for control of the modulator klystron 1-st accelerator accelerating station of the acceleration stand on the basis of a linear electron accelerator LINAC-800 was based on the so-called "hard" logic and provides a fixed control algorithm modulator.[1] Operational management of the klystron power level produced a local manual closing desired number of sections modulator (PFN modules). Also carried out manually switching frequency modulator battery life and modulator switching trigger from an external clock source. In the operation of the modulator identified the need provide both local manual control modulator and local indication of the state of the modulator, and the potential control modulator using computational tools and providing top-level to the top level of operational information section operation modulators.

To implement the requirements set forth above new algorithms have been developed management of the modulators klystrons of the accelerating stations the linear electron accelerator of the acceleration stand and new hardware requirements. They are as follows.

Instead, the pulse generator to the "hard" logic was applied management controller specifically designed for this task. Due to the need to develop specific requirements regarding management of the modulator, the implementation of the user interface and the input and output channels of information.

Instead, the control unit on the PFN "hard logic" used block-based 8-bit microcontroller.

To increase the reliability of electronic components and diminishing the amount of electronic components instead of discrete active components and chips low degree of integration applied chips with medium and high level of integration, applied to surface mounting technology instead of mounting holes. This reduced the size of the nodes, which reduced the level of interference from the pulse amplifier and improve noise immunity of the whole device.

To organize the cable connections between control units PFN and PFN modules was introduced patch panel, allowing to increase the reliability of connections and reduce errors when connecting modules.

For communication with the top management level was selected RS-485 interface. Selection of the interface due to the fact that the requirements on the speed of information exchange with the upper level is initially low (not more than several packets per second) on the one hand and on the other - to the requirements of simplicity and reliability of the interface RS-485 fully satisfies.

FUNCTIONAL BLOCK DIAGRAM OF THE CONTROL MODULATOR

As a result, the control circuit is a modulator of a multiprocessor system with one master controller and several slave controllers (Fig. 1).

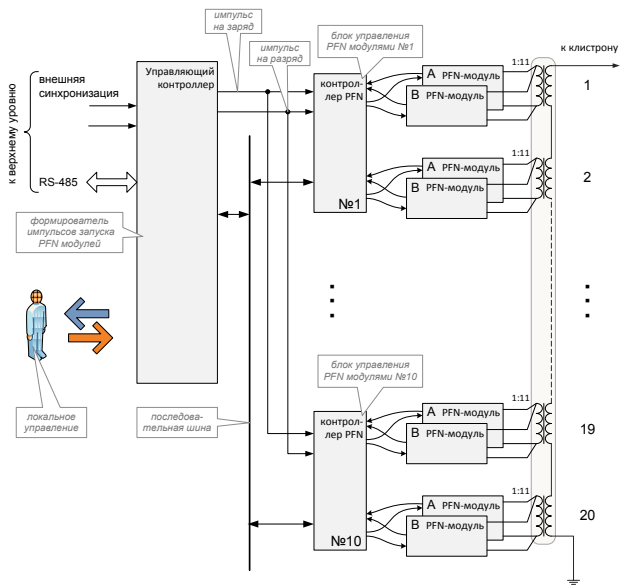

Figure 1: Functional diagram of the control unit modulator.

The control unit by a modulator consists of the control controller which generates pulses start modules PFN, and ten controllers PFN, which form the charge and discharge pulses modules PFN, PFN modules include team-master controller and the controller sends control information on the charging and discharging storage modules PFN. Operator on the master controller is set startup frequency modulator with local work or run mode from the external clock. Is defined as the number of units involved PFN to obtain the required RF power. Next, the master controller generates control pulses to the general charge and discharge of storage modules PFN and sends serial

ISBN 978-3-95450-170-0

commands to turn on or off the required modules PFN. PFN controllers confirm their activation or deactivation, the impulse to run their modules PFN and on request of the control of the controller provide information on the real events charge and discharge of a particular module. PFN is controlled by the controller as a fact of physical cable connections to the modules PFN. In the master controller laid excess computing power for a possible modulator control system modernization. For the same purposes are reserved 8 input logic signals with levels 0..24V, 8 input logic signals with levels 0..5V 7 output logic signals with levels 0..5V and 8 analog signals that may be involved either directly or through additional normalizing signal conditioners.

FUNCTIONAL OF THE PULSE START OF THE PFN-MODULES

Functional diagram of the pulse start PFN is shown below in Fig. 2. The microcontroller generates a local charge and discharge pulses drive the modulator controls the switch clock to supply pulses of charge (\ LTR) and discharge (\ OTR) for PFN either from its own clock, or galvanically separated from the external clock. Diagrams indicating pulses control the corresponding LEDs on the front panel. Character OLED display and encoder are also located on the front panel and provide operator feedback. Through the driver «serial TTL» microcontroller communicates with the slave controller PFN modules, and through the RS-485 driver microcontroller can communicate with the upper level. In the EEPROM stores the current settings and the settings of the control unit modulator, correction factors and other service information.

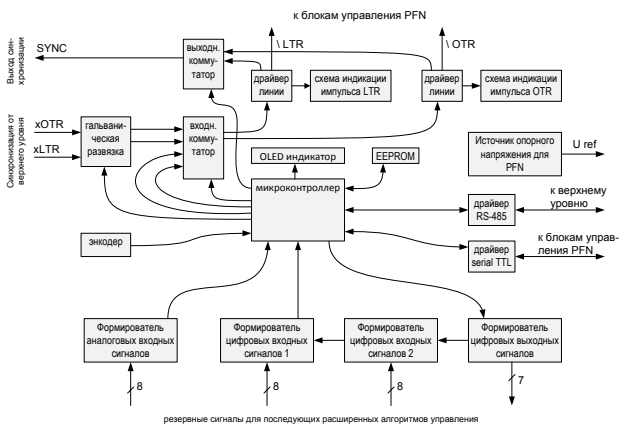

Figure 2: Functional diagram of the control of the controller.

FUNCTIONAL DIAGRAM OF THE CONTROL UNIT PFN-MODULES

Functional diagram of the control unit PFN modules is shown below in Fig. 3. MCU control unit PFN modules enables or disables the pulse amplifier, run the module PFN. The microcontroller provides control of two pairs of PFN modules. The signals on the prohibition or authorization of the microcontroller module control unit PFN module receives from the master controller. Pulses supporting charging and discharging PFN module supplied to an amplitude discriminator is processed by microcontroller and serial controller transmits control on request. Also transmits information about the physical connection PFN modules. When the real presence of the pulse charge and discharge is displayed flashes of the LED display circuit pulses. It also displays the fact physical connection PFN module and enable signal operation.

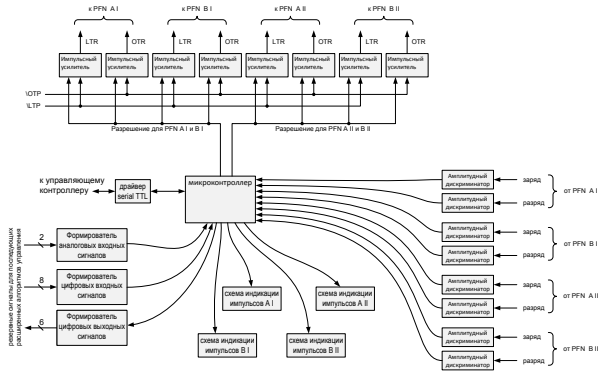

Figure 3: Functional diagram of the control unit PFN modules.

The output current of the accelerating section of the induction sensor and the measured Faraday (Fig. 3) cup energy through 45-degree bending magnet. Electron beam with a current of 5 mA was accelerated to an energy of 20 MeV. Further work continued to increase in the current and began assembling the undulator infrared. After installation of the undulator (Fig. 4) the accelerated electron beam was conducted through an undulator and outlet undulator registered the infrared radiation with a wavelength of 14 microns. Studies over the undulator radiation were stopped in order to continue the work on the second accelerator station. Was upgraded modulator the klystron second accelerating station mounted klystron and the waveguide system. Obtained working vacuum in the accelerating sections and waveguide tract (Fig. 5). Are currently under commissioning in the second accelerator station.

CONCLUSION

As a result of this work has been offered a new concept of management of the modulator klystron, designed and created functional circuit control unit modulator. Are currently under commissioning at the modulator.

REFERENCES

[1] N.I. Balalykin et al., Start modulator klystron VA938D 1-st accelerating station electron linear accelerator LINAC-800; JINR, Dubna, RuPAC 2012 Conf., S.-Peterburg.

ISBN 978-3-95450-170-0

SYSTEM POWER MICROWAVE IMPULSE COMPRESSION BASED ON DOUBLE FORMING LINE

G.O. Buyanov, A.P. Klachkov, A.A. Osipov, A.G. Ponomarenko, National Research Nuclear University «MEPhI», Moscow, 115409 Russia

Abstract

In this article presents the results of an electrodynamic modeling and optimization of the design of the compressor based on double forming line (DFL), proposed new structure to effectively accumulate and output energy from a multimode resonator with working mode $H^{\square}_{01}$.

THE PRINCIPLE OF OPERATION OF THE COMPRESSOR BASED ON DFL

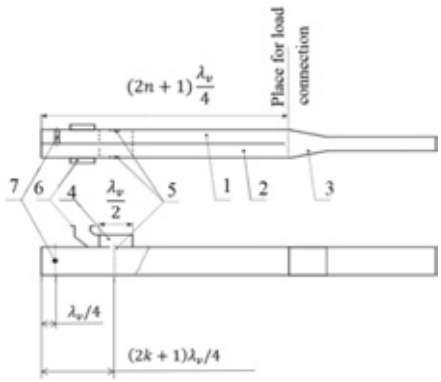

Figure 1: Compressor based on DFL.

In the compressor which bases of the double forming line (DFL) resonator-energy accumulator (see Fig. 1) consists of two waveguides 1, 2 long odd number of quarter-wave [1,2]. On the one hand, these waveguides are shorted, and with the opposite side waveguide 3 is connected to these waveguides, whose height in this location is twice the height of the waveguide drive. A standing wave is excited in the drive so that throughout the process of accumulation of the field in the two waveguides are strictly antiphase. Due to this fact and because of the special choice of the length of the waveguide cross-sectional load connection antinode of the electric field is realized. The waveguide load is excited at the same time load the fields of the two waveguides drive in opposite to the load and the energy does not go (see. Fig. 2 a).

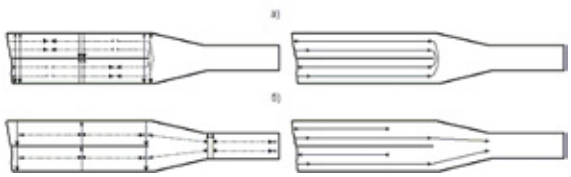

Figure 2: The field structure and scheme of wave propagation in a compressor with DFL. a-accumulation, б-output after $t=l/v_{gr.}$

Switchboard (position 7 in Fig. 1) is placed inside of any waveguides spaced at the distance $\lambda_e/4$ from the shorted end. Its inclusion leads to the fact that the phase of the wave reflected from the left end, changes to π. After a time, l/v_g (see Fig. 2, b), this wave reaches the section connecting the load, radically changes the conditions for the excitation of the waveguide 3, now the waveguide load is exciting in phase by two waves arriving here on the left, both of them rush to the load without reflection. So, the reflected waves in waveguides formed by the trailing edge of the drive, which section returns to the load after a time $2l/v_g$. At this moment all the electromagnetic energy originally stored in two sections of the resonator drive is transmitted to the load.

COMPRESSOR DFL BASED ON MULTIMODE WAVEGUIDES.

Previously worked on the design of single-mode waveguides [3,4,5,6]. The aim of this work is to study the compressor to work with oversized waveguides mode $H^{\square}_{01}$. Compressor design built on the single-mode waveguides have large losses, low dielectric strength, which significantly limits the maximum compression ratio and power of the compressed pulse. The performance parameters of the compressor can be improve by using multimode waveguides with a working mode $H^{\square}_{01n}$. For example, cross-section waveguides increases from 28,5 × 12,6 mm to 72 × 34 mm allows you to raise the compression ratio in 2.65 times and the maximum output power in 6.3 times.

The device power output (see Fig. 3) is H-tee matched two inductive pins.

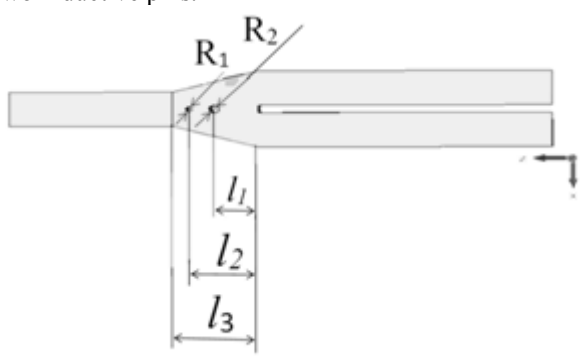

Figure 3: Sketch of the microwave - compressor l_1=53.4 mm; l_2=42.5 mm; l_3=27 mm; R_1=2 mm; R_2=3.2 mm

It is known that in the output device power have to use nonstandard waveguide section 72 × 28,5 mm at the

ISBN 978-3-95450-170-0

operating frequency of 8568 MHz for suppressing parasitic oscillation modes. As the result of optimization of the geometry of the H - tee reflection coefficient on the operating frequency is -35 dB (see Fig. 4). Due to reducing the height of the waveguide to a value of 28.5 mm wave excitation of higher type does not occur in the vicinity of the operating frequency.

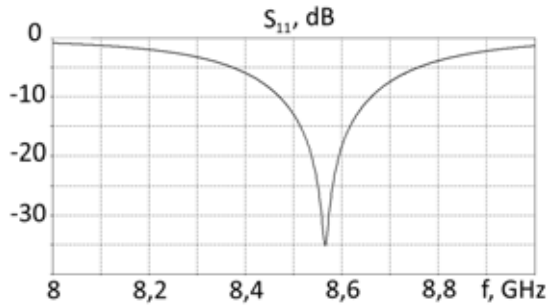

Figure 4. Dependence of the parameter of the scattering matrix S_{11} in the frequency range 8000-9000 MHz using waveguides 72 × 28.5 mm.

Fig. 5. shows the device of power input.

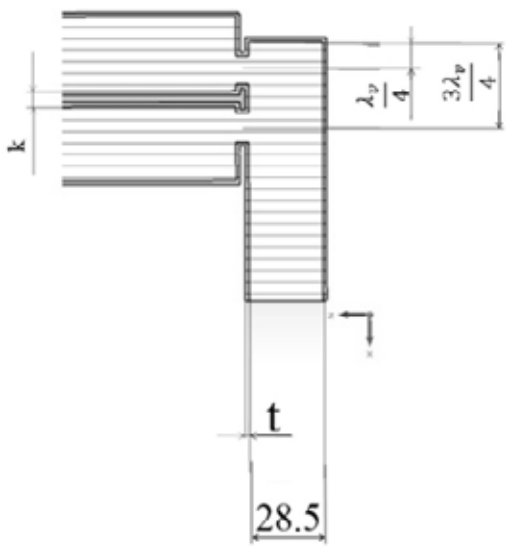

Figure 5: Input device of power. t=0.5 mm; k=6 mm; $\lambda_v = 22.2$ mm.

As can be seen from the calculated distribution of the electric field (see Fig. 6) ,(see Fig. 7) there is modulation of the field of the working modes of waves $H^{\square}_{01p}$ higher types in the resonator – accumulator along the trajectory. A significant part of the energy in the resonator - accumulator is stored in the form of spurious waves.

Figure 6: Trajectory along which investigated the electric field distribution.

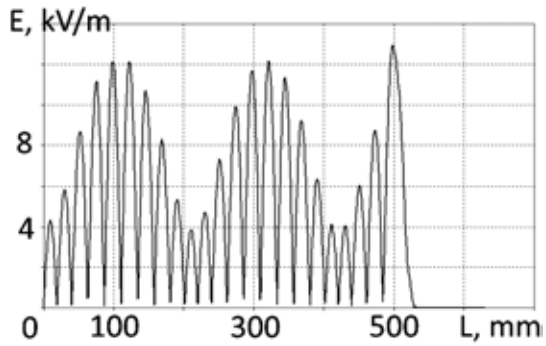

Figure 7: The distribution of the electric field in the resonator - storage along the trajectory.

There were carried out a series of calculations of various designs compressor microwave for suppressing parasitic oscillation modes and reducing the operating wave modulation field $H^{\square}_{01}$.

Figure 8: Compressor design I. The curve along which the electric field distribution was investigated.

Figure 9: Compressor design II. Curve along which the electric field distribution was investigated.

Modulation ratio of the amplitude of the electric field in the first construction is M = 1.01. In the second structure it is M = 1.08.

For next structures, with another device of exciter, were stored the energy for two lengths (968 and 2,300 mm) was calculated in the waves of higher types, as well as the modulation factor of the amplitude of the electric field.

Design II was examined in two versions: with E-tee on the output waveguide section and section 28.5x12.6 mm 23x10 mm. Also considered the design based on III-E tee on waveguides 28.5x12.6 mm with step-smooth transition.

Fig. 10 shows one of the designs of the compressor. For the design I was used to study the dependence of the modulation M on the distance d between the plates (see Fig. 11).

ISBN 978-3-95450-170-0

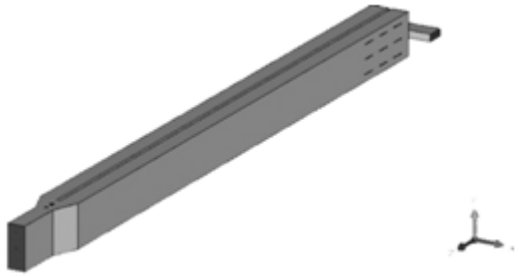

Figure 10: Compressor design I.

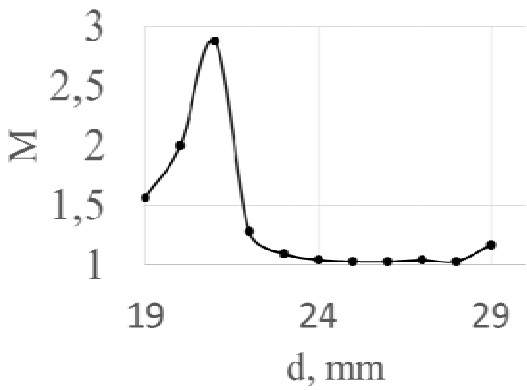

Figure 11: The dependence of the modulation M on the distance d between the rows of plates.

The diagram shows that the optimal distance d between the plates for the design length of 2,387 mm (Figure 10), is equal to 25 mm.

Table 1: Comparison of compressor designs

Type of construction	The modulation index	Stored energy in the parasites, %	Stored energy in the wave of the type $H^{\square}_{01}$, %	Length of the resonator-storage l, mm
I	1,047	0,06	99,94	2386,98
II 28.5x12.5	1,027	0,01	99,99	968
	1,043	0,02	99,98	2387
II 23x10	1,056	0,22	99,78	969,88
	1,083	0,14	99,86	2386
III	1,026	0,01	99,99	968
	1,040	0,02	99,98	2386
I with 9 rows	1,011	0,05	99,95	968

This chart shows that the design of the compressor with the E-tee on the output waveguides 23x10 mm proved to be worse than others, due to the fact that the transition from the waveguides 23x10 mm to the waveguides 72x34 mm waveguide resonator has a large reflection coefficient (-10 dB). It also shows that the modulation factor and the stored energy in the parasitic forms of oscillations have the lowest values in the design of Design III with a smoothly-step transition. (M=1.04, W_{par}=0.02%W_{full}).

REFERENCES

[1] B.J. Bogdanovich, V.E. Kalyuzhny, E.S. Masunov, A.V. Nesterovich, A.G. Ponomarenko, V.A. Senyukov. The concept of a mobile source of a focused gamma radiation. "Problems of Atomic Science and Technology", Ser. "Physics of radiation effects on electronic equipment", issue 2. Moscow, 2009, p. 73-80.

[2] A.G. Ponomarenko. Device temporal pulse compression of microwave energy. Patent RU № 2293404 since 10.02. 2007.

[3] A.A. Osipov, A.G. Ponomarenko. Device for Time Compression of Microwave Energy Pulses. Patent RU № 2293404 since 10.01. 2013..

[4] A.A. Osipov, A.G. Ponomarenko. Modelling of the process of withdrawal of energy from the microwave radio pulse compressor based on DFL. "Nuclear Physics and Engineering", 2010, vol.1, №5, p. 438-449.

[5] A.A. Osipov, A.G. Ponomarenko, V.A. Senyukov. The equivalent circuit of the plasma column in the microwave cavity. // Scientific session MEPHI - 2010 Collection of scientific papers. - 2010 - Volume 1: Nuclear Physics and Power Engineering. - S. 180-181

[6] B.J. Bogdanovich, A.V. Nesterovich, A.G. Ponomarenko, V.A. Senyukov. Create highly mobile electron accelerators with high acceleration rate. "Nuclear Physics and Engineering", 2010, №2.

ISBN 978-3-95450-170-0

FIELD OPTIMIZATION TECHNIQUE OF THE MULTIGAP H-MODE RESONATORS

A.B. Buleyko, M.V. Lalayan, S.E. Toporkov, National Research Nuclear University MEPHI (Moscow Engineering Physics Institute), Moscow, Russia

Abstract

High frequency optimization of multigap IH-/CH-resonators involves the number of problems to be solved. It is important to obtain high values of effective shunt impedance and uniform accelerating field distribution along the axis. To reach both of these goals design of H-mode resonators contains flat vanes (pylons). This article presents the results of electrodynamic modelling of CH- and IH-resonators in case of zero gap between end walls of the vanes and resonator sidewall [1]. The values of the optimized shunt impedances, Q-factor and field flatness for IH- and CH-designs are presented.

INTRODUCTION

Investigated IH- and CH- cavities were designed for the beam velocities $\beta = 0.1$. The operating frequency of the inter-digital structures is equal to $162MHz$. Whereas, CH-resonators operate in 324 MHz band since they are excited at higher operating mode H_{210}. Each cavity type works on π-mode. Cavity design in either case features constant period D along axis and acceleration gap between drift tubes $t = D/2$. Whole structure consists of 9 RF gaps with beam aperture diameter $D_a = 15mm$.

To estimate the field flatness following factor was used:

$$K = \frac{E_{min}}{E_{max}} \cdot 100\%,$$

where E_{min} and E_{max} – on-axis minimal and maximal accelerating field strengths.

ELECTRODYNAMIC MODEL

CH-resonator

As it was mentioned the CH-cavity design includes flat vanes (see fig.1.). Each pylon has one rectangular hole cut out at the last drift tube end. The opposite pylon part is flat but its position is variable and defined by parameter L_{gap}.

First step of the field flatness optimization consists in selection of correct start length of holding rods l_{stem} and correct vane height h_{vane}. It should be mentioned that each l_{stem} value (e. g. $l_{stem} = 35, 40, 45, 50$ mm) could be associated with different pylon geometries defined by h_{vane}. Almost all of these combinations could be tuned to the operating frequency by appropriate geometry of the pylon hole choice. But during selection the necessary geometry from all possible designs the field flatness also needs to be considered: in our case initial K values should lie in the range from 85% to 95%. Dimensions of possible holes could be different: for long rods ($l_{stem} =$ 45,50mm) the longitudinal length reaches 110mm (which is quite large regarding $D = 46.3$ mm), for short rod length ($l_{stem} = 35$ mm) they become compact (as it shown at fig.1.). Maximum value of shunt impedance among all l_{stem}values stays unchanged. Thus there was chosen the geometry with short holding rods $l_{stem} = 35mm$, large vane h_{vane}~100 mm and compact holes in it.

At the fig.2 the dependence of the field flatness during parametric sweep of L_{gap} is presented. All another geometric dimensions stay fixed.

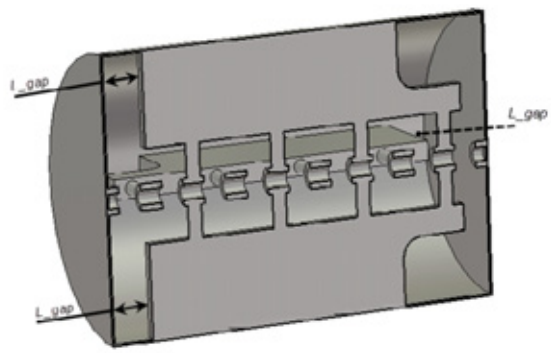

Figure 1: The designed layout. Each vane contains 1 rectangular hole and 1 movable sidewall (positioned by L_{gap}).

From the graph it could be found out that the best field flatness is observed in case of zero gap $L_{gap} = 0$ mm. According to the magnetic field distribution inside such geometry four separated magnetic fluxes around each vane combine in one common flux. Absolute value of magnetic field distribution is presented at fig. 3: the flux turns around the vane at point A, then goes through plane B to point C, makes another turn around vane and then continues the propagation to the point D in similar way.

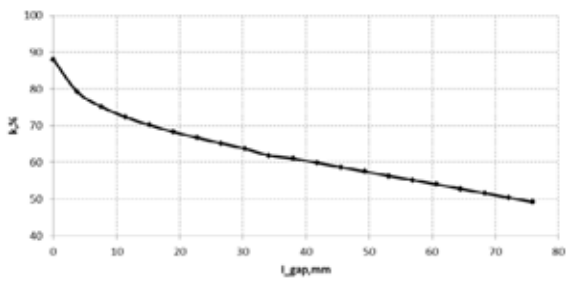

Figure 2: Dependence of the field flatness vs. distance L_{gap}.

Also it should be noted that during parametric sweep resonant frequency and shunt impedance had negligible changes: frequency was shifted from 324MHz

ISBN 978-3-95450-170-0

(L_{gap} = 0 mm) to 328MHz (L_{gap} = 60 mm), effective shunt impedance was changed from 86 MΩ/m (L_{gap} = 0 mm) to 82 MΩ/m (L_{gap} = 60 mm). According to this results it is clear that for such type of resonator the case L_{gap} = 0 mm is preferable.

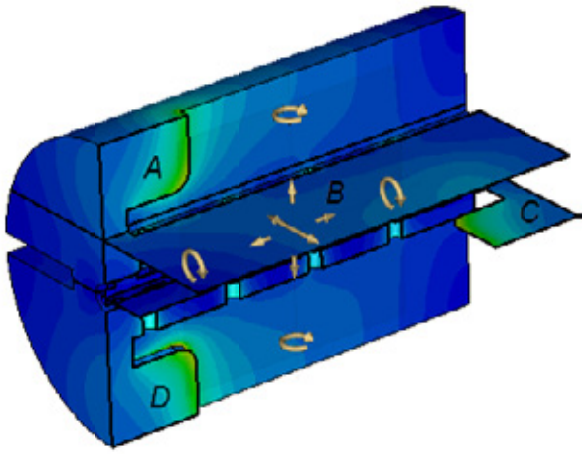

Figure 3: Magnetic field distribution inside CH-resonator.

After preliminary design the final adjustment of the field distribution and electrodynamic characteristics should be performed. That was achieved by optimizing the holes inside the pylons. Right geometry allows one to get 15% increase of shunt impedance with field flatness better than 95%. Elecrodynamic characteristics and the field distribution are presented at the table 1 and figure 4 correspondingly.

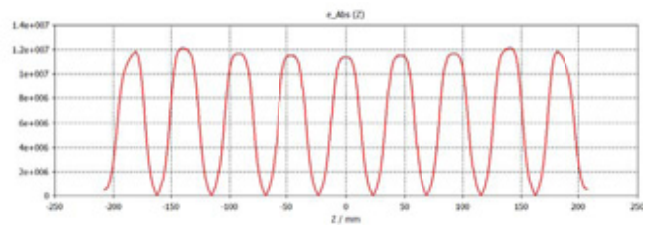

Figure 4: E-field distribution on the axes of CH-resonator.

IH-resonator

The same technique was used for the field tuning on the axis of interdigital structure. The example of final layout is presented at fig.5. Dependence of the field flatness from the parameter has the same behavior as CH-structure (see fig.2.)

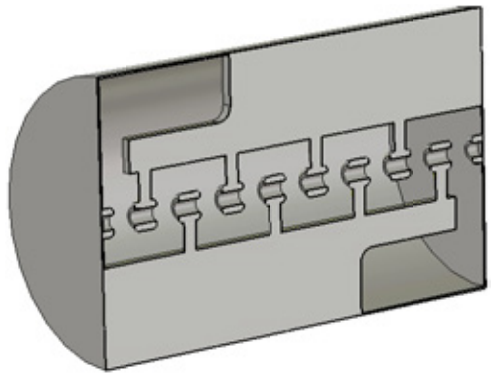

Figure 5: Final IH-cavity layout.

Final tuning was performed by hole in the vane design optimization. Elecrodynamic characteristics and the field distribution are presented at the table 1 and figure 6 correspondingly. It should be noted that for IH-resonators operating frequency and field flatness stay fixed with addition or removal of two RF gaps.

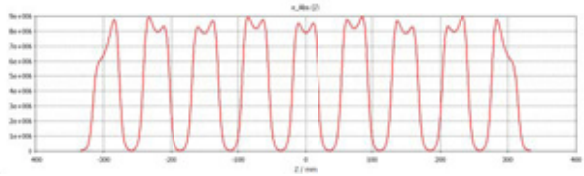

Figure 6: Field distribution on the axes of IH- resonator.

Table 1. Electrodynamic characteristics of CH-/IH-structures.

Parameter	Value	
Type of resonator	CH-	IH-
Operating frequency, MHz	324	162
Number of periods	9	9
Length of the resonator, mm	323,85	647,70
Effective shunt impedance, MOhm/m	91	125
Transit time factor	0,843	0,850
Q – factor	14700	17250
Field flatness, %	95	98

CONCLUSION

Electrodynamic parameters optimization technique for H-mode resonator was developed. Results of numerical modelling are presented.

REFERENCES

[1] P.N. Ostroumov, A. Barcikowski, B. Clifft et al. High power test of A 57-MHz CW RFQ. Proc. of LINAC'06, THP079.

ISBN 978-3-95450-170-0

OPTIMIZATION OF ELECTRIC FIELD DISTRIBUTION INSIDE MULTI-GAP CH-RESONATOR

S.E. Toporkov, National Research Nuclear University MEPHI (Moscow Engineering Physics Institute), Moscow, Russia

Abstract

RF H-mode resonators are frequently used in the most modern proton accelerators. For instance crossbar H-mode (CH) [1] resonators could be mentioned. For this cavity type the task of accelerating field flatness tuning is quite important. This paper presents the results of the electric field adjustment on the beam axis for different CH-geometries.

INTRODUCTION

The main goal during investigation was to achieve the even accelerating field distribution for the different geometries of CH-resonator. Main variable parameters are presented at table 1.

Table 1: The designed parameters

Number of periods	7; 9; 11;
Aperture diameter, mm	15; 20; 30
Beam velocity β=v/c	0,07; 0,08; 0,09; 0,10

The layout of the 7 and 9-gap CH- cavities is presented in Fig. 1-2. All CH-cavity designs considered operate at 324MHz and have a constant period D=βλ/2. Acceleration gap between drift tubes t=D/2.

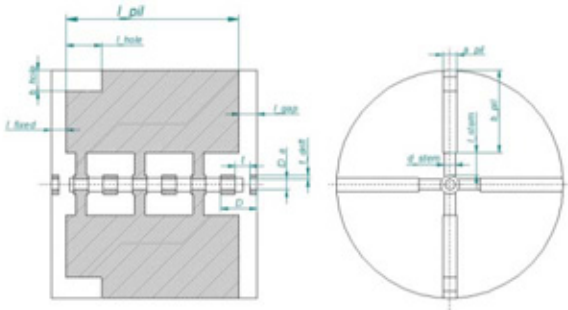

Figure 1: The designed layout.

To estimate the field flatness the uniformity factor was used:

$$k = \frac{E_{\min}}{E_{\max}} \cdot 100\%,$$

where E_{min} - minimal accelerating field amplitude, E_{max} - maximal accelerating field amplitude.

FIELD FLATNESS TUNING TECHNIQUE

To optimize both electric field distribution and effective shunt impedance geometry includes flat vanes (see Figs.1, 2.). Each vane (pylon) has one rectangular hole made on downstream pylon side. The opposite pylon part is flat but its position is variable and defined by parameter L_{gap}.

The tuning task consists of several steps. First the optimal start value of holding rod length l_{stem} and its optimal relation with the pylon height (b_{pil} / l_{stem} see Fig.1.) should be chosen for specified beam velocity, aperture diameter and number of periods. It determines initial values of field flatness (it should be better than 15-20%) and optimal values of effective shunt impedance

Then the most significant improvement on the field distribution is introduced by the length L_{gap} (see Fig.2.) between end walls of the tank and the pylon. Dependence of the field uniformity vs. this length is presented in the Fig.3. It could be mentioned that the best field flatness was obtained in case of zero gap (L_{gap}=0 mm). For such cavity geometry magnetic field distribution differs from the classical CH – resonator, it transforms in one common magnetic flux like in split-coaxial cavities [2]. According to the magnetic field distribution inside such geometry four separated magnetic fluxes around each vane combine in one common flux.

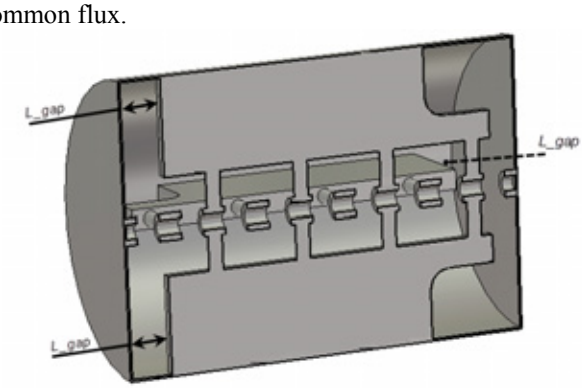

Figure 2: 3D-view of the CH-resonator. Each vane contains 1 rectangular hole and 1 movable sidewall (position defined with L_{gap} value).

It should be noted that resonant frequency and effective shunt impedance have some changes with L_{gap} variation: frequency shifts to 1-3% and effective shunt impedance changes to 5-15% depending on aperture diameter, number of periods etc.

ISBN 978-3-95450-170-0

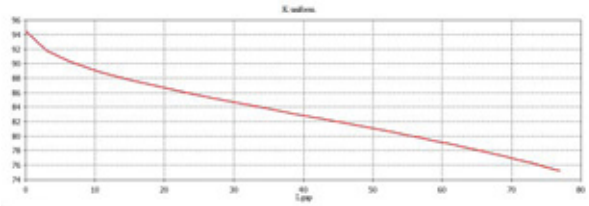

Figure 3: Dependence of the field flatness vs. L_{gap}.

DIFFERENT GEOMETRIES OPTIMIZATION

The case of zero gap between end walls of the tank and the pylon was used to tune the field uniformity for all investigated CH-geometries. In examples discussed below field flatness k is better 95%.

At the figure 4 the dependence of effective shunt impedance vs. particle velocity for the 7-gap model is presented. It should be mentioned that period D was changed according to particle velocity β. To achieve necessary field flatness for low β cases the holding stems were shortened.

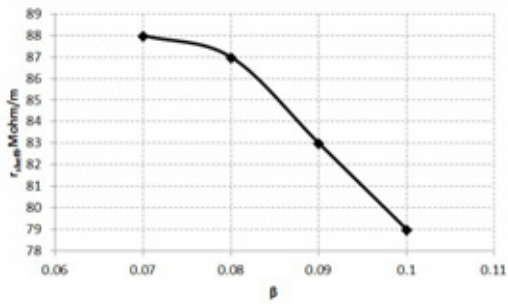

Figure 4:Dependence of effective shunt impedance vs. particle velocity.

The dependence of effective shunt impedance vs. aperture diameter D_a is presented in figure 5. Results were obtained for 7 gap cavities and two different particle velocities β. To optimize field flatness in case D_a=30mm correct rounding of the drift tube outer wall was used.

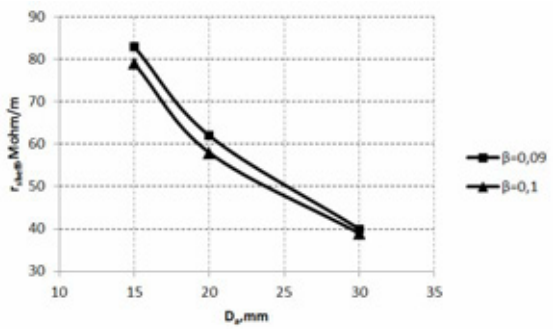

Figure 5: Dependence of effective shunt impedance vs. aperture diameter.

The uniform field distribution was also reached for the cavities with different number of accelerating gaps.

The results of optimization are presented in Fig.6 for two different particle velocities β.

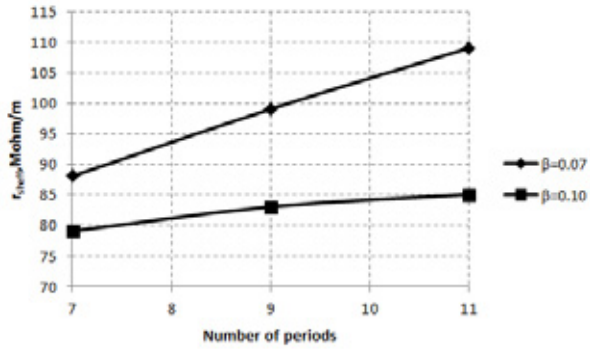

Figure 6: Dependence of effective shunt impedance vs. number of periods.

The flat field distribution could be obtained for different holding vanes geometries (see Fig.1.). The dependence of main electrodynamic characteristics from the vane geometry and tuning hole dimension is presented at the table 2:

Table 2: Dependence of the main eletrodynamic characteristics from the vane geometry.

Parameter	Value			
b_{pil}, mm	87.5	91	94.5	98
b_{hole}, mm	45	50	60	65
r_{sheff}, MOhm/m	63	67	74	77
T	0.841	0.840	0.840	0.840
Q – factor	11680	12150	13000	13400
Field flatness, %	4.6	3.7	3.3	3.2

CONCLUSION

Field flatness tuning technique for CH cavities development is employed. This method allows one to find right cavity dimensions resulting cavity with flat field distribution and good elecrodynamic characteristics. Application to the multigap CH-resonators with EDCs obtained using computer simulation are presented.

REFERENCES

[1] Podlech H., Bechtold A., Busch M., Klein H., Liebermann H., Ratzinger U. DEevelopment of the superconducting CH-cavity and applications to proton and ion acceleration.. Proc. of SRF2007, Peking Univ., Beijing, China. pp. 48 – 54.

[2] Schrage D., Ostroumov P., Barcikowski A., et.al. A 57-MHz CW RFQ for the AEBL Project, Journal of the Korean Physical Society, Vol. 50, No. 5, May 2007, pp. 1363 – 1367.

ISBN 978-3-95450-170-0

THE OPTIMIZATION OF THE BUNCHER AT 145.2 MHZ TO REDUCE MULTIPACTOR EFFECT

M.A. Gusarova, I.I. Petrushina, S.M. Polozov, National Research Nuclear University «MEPhI», Moscow, Russia
A.S. Plastun, T.V. Kulevoy, FSBI «SSC RF ITEP», Moscow, Russia

Abstract

The results of the 145.2 MHz single gap buncher cavity in order to reduce multipacting discharge influence are presented in this paper. Resonant voltages, impact energies and corresponding particle trajectories are obtained. The ways of cavity design modifications to reduce multipacting discharge effects are considered.

INTRODUCTION

The proposed cavity is a single gap buncher of medium energy beam transport system (MEBT) for linear injector of Nuclotron-NICA project (JINR) [1-2]. The cavity shape is a modified E_{010} pillbox. The modifications are performed in order to decrease the cavity size and to place MEBT quadrupoles near the cavity, according to the general layout. 3D model of the buncher cavity before the optimization is presented in Figure 1.

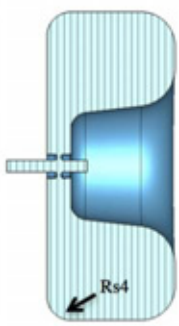

Figure 1: Side-view of the buncher cavity.

Computer simulations of the multipacting dischegre were performed using MultP-M [3] and CST PS [4] software. The possibility of multipacting discharge was concluded from the percentage growth rate of secondary electrons number inside the cavity, the shapes of resonant electron trajectories and the energy of impact with the cavity surface. Secondary emission coefficients for copper surface that were used in simulation are taken from [5].

MULTIPACTING DISCHARGE SIMULATIONS OF THE NON-OPTIMIZED CAVITY

Electric field and voltage values presented in this paper are normalized to 1 J of energy stored in the cavity. Initial computer simulation with MultP-M code was performed in order to identify the most dangerous levels of normalized voltage in the range U_N = 0 - 5, which can induce the progress of multipacting. The operating voltage of 150 kV corresponds to the normalized voltage of $U_N = 0.45$, and the operating voltage of 337 kV corresponds to $U_N = 1.0$. Figure 2 illustrates the number of particles percentage growth rate after 10 RF periods for U_N levels from 0 to 5.

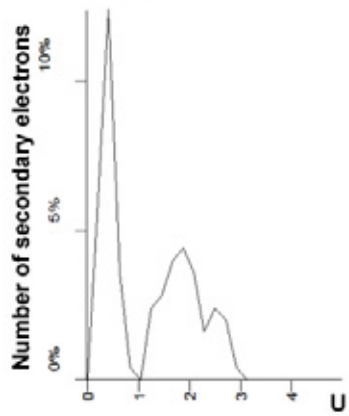

Figure 2: Number of particles percentage growth rate of after 10 RF periods for U_N levels from 0 to 5.

Figure 2 shows the possibility of multipacting at U_N voltage levels from 0 to 3 with two or three peaks, which correspond to several different multipacting spatial domains. The detailed analysis has detected these three spatial domains of multipacting discharge, which are presented in Figure 3 along with particle trajectories. In the range of $U_N = 0.001$ - 0.018 (Figure 3*a*), the number of particles growth rate peak is observed at $U_N = 0.015$. Multipacting discharge shifts outside from accelerating gap and totally attenuates after 40 RF periods.

The trajectories in the range of $U_N = 0.063$ - 0.461 is shown in Figure 3*b*. Secondary electrons return to the cavity surface every single RF period, so this discharge is of the 1st order. Simulation has shown stable electron trajectories in the whole range of $U_N = 0.063$ - 0.461 during 50 - 200 RF periods. The number of particles growth rate peak is observed at $U_N = 0.417$, which is close to the operating value. In this case, the discharge remains stable for more than 200 RF periods. The impact energy is 800 eV at $U_N = 0.14$, while at $U_N = 0.424$ it is 1400 eV. Analysis of secondary emission coefficient variation has shown that the surface quality and polishing are very important for discharge attenuation.

ISBN 978-3-95450-170-0

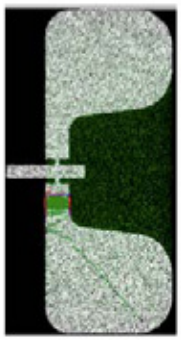

a: U_N = 0.001 - 0.018

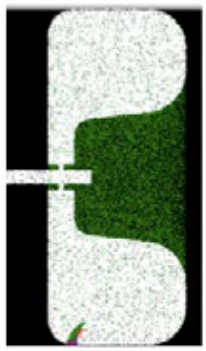

b: U_N = 0.063 - 0.461

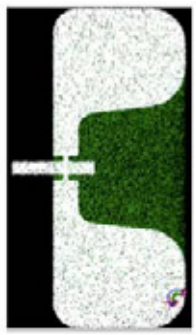

c: U_N = 0.424 - 2.992

Figure 3: Spatial domains of multipacting trajectories.

The multipacting discharge in the range of U_N = 0.424 - 2.992 is shown in Figure 3*c*. This range overlaps with the previous one shown in Figure 3*b*. Thus, multipacting can occur in both 3*b* and 3*c* spatial domains in the voltage range of U_N = 0.424 - 0.461.The most dangerous voltage level is U_N = 2.5. It provides a stable 1st order multipacting discharge with the impact energy of 1400 eV. Higher voltage levels are dangerous only for dirty copper surfaces. Fortunately, U_N level of 2.5 is significantly higher than the operating level.The first peak shown in Figure 2 corresponds to multipacting discharge in the domain shown in Figure 3b and, probably, Figure 3c. The Second and the third peaks correspond to multipacting discharge in the domain shown in Figure 3c.

Computer simulation of multipacting discharge in the cavity were also performed in CST Particle Studio. The results of these simulations are in agreements with the MultP-M code results. . Figure 4 illustrates the domain of discharge avalanche at U_N = 0.45 and the increase of particles number in time.

As mentioned above, the multipacting discharge can occur in the spatial domains, shown in Figures 3b and 3c, at operating voltage level of 150 kV or U_N = 0.45. Therefore, the cavity geometry optimization has been done to avoid multipacting discharge progress. Blending radius *Rs* (shown in Figure 1) was increased and the parallel surfaces near the accelerating gap were replaced with conical.

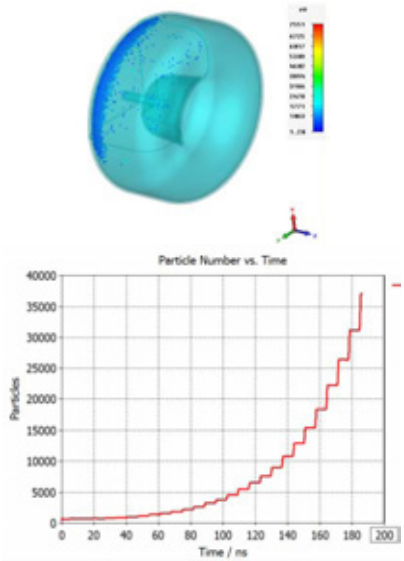

Figure 4: Multipacting discharge area and an increase of particle number in time.

MULTIPACTING DISCHARGE SIMULATION OF THE OPTIMIZED CAVITY

The side-view of the optimized cavity is presented in Figure 5*b*.

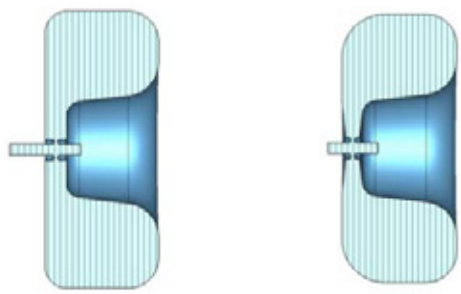

a *b*

Figure 5: Geometry of the cavity (a) before and (b) after optimization.

Simulation show that the increase the blending radius *Rs* from 60 mm to 120 mm, allows us avoiding the resonant conditions at U_N = 0.45. But multipacting isn't totally suppressed – the trajectories remain stable during 5 to 15 RF periods.

Figure 6 presents the number of particles percentage growth rate of for 100 initial electrons in the voltage range of U_N = 0 - 1 at the step of 1/400 of RF period during 100 RF periods. The plot illustrates the contribution to this growth only from particles which had more than 25 hits with cavity surface.

ISBN 978-3-95450-170-0

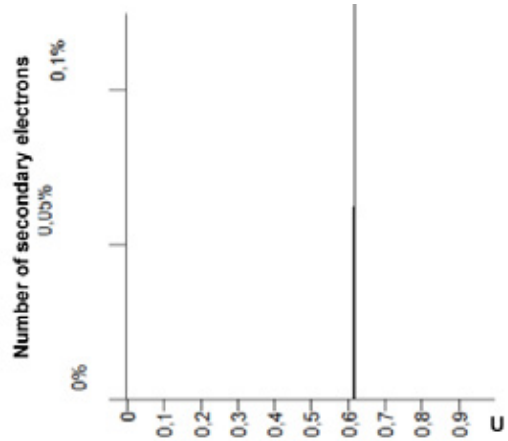

Figure 6: Percentage growth rate of number of particles in optimized cavity after 100 RF periods of simulation for U_N levels from 0 to 5.

Further increase of the blending radius Rs doesn't change the result - multipacting trajectories remain stable during 5 -10 RF periods.,The surface cleaning and the longtime RF conditioning of the cavity should be performed in order to avoid the progress of multipacting discharge.

Conical or V-shape surfaces near the accelerating gap provide multipacting suppression in spatial domain shown in Figure 3*a* at low voltages of U_N from 0.009 to 0.016. Strong resonant conditions don't remain active during multipacting discharge, but also don't suppress the discharge totally (see Figure 7).

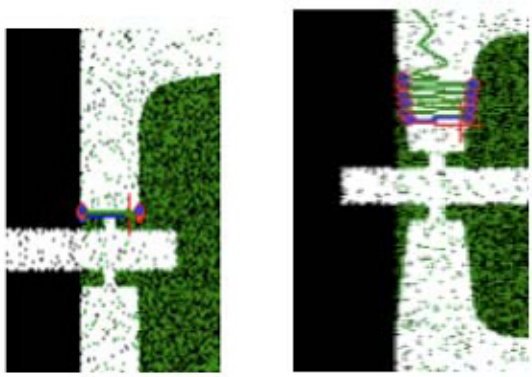

a *b*

Figure 7: Electrons trajectories for (a) parallel and (б) V-shape surfaces.

The results of the computer simulations of multipacting sicharge in domains, illustrated in Figure 7s, done in CST Particle Studio, are in agreement with the results achieved in MultP-M code. The optimized geometry is presented in Figure 8.

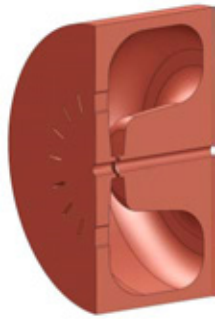

Figure 8: The optimized geometry of the single gap buncher cavity.

SUMMARY

In order to reduce the multipacting discharge effect, the , the 145.2 MHz single gap buncher cavity shape was optimized. . The threshold values of the accelerating gradient when the discharge may occur in these structures have been calculated. Several ways of the cavity design that help to reduce multipacting discharge effect were considered.

REFERENCES

[1] A.V.Butenko et al., DEVELOPMENT OF NICA INJECTION COMPLEX, Proceedings of IPAC2014, Dresden, Germany

[2] V.A. Andreev et al., RECONSTRUCTION OFLIGHT AND POLARIZED ION BEAM INJECTION SYSTEM OF JINR NUCLOTRON NICA ACCELERATOR COMPLEX, BAHT. 2013. No 6 (88). P.8.

[3] M.A. Gusarova, S.V. Kutsaev, V.I. Kaminsky, "Multipacting simulation in accelerator RF structure", Nuclear Instrument and Methods in Physics Research A, 599. P. 100-105, 2009

[4] www.cst.com

[5] V. Baglin et al. The secondary electron yield of technical materials and its variation with surface treatments. EPAC 2000, Vienna, Austria

ISBN 978-3-95450-170-0

MULTP-M CODE GEOMETRY IMPORT MODULE PERFORMANCE OPTIMISATION

S.A. Khudyakov, M.A. Gusarova, M.V.Lalayan, National research nuclear university MEPhI, Moscow, Russia

Abstract

Introduces the new features of the module import geometry for three-dimensional modeling program multipactor MultP-M. On an example, consider an increase in the speed and accuracy of the calculation using a new algorithm for calculating the use of loading geometry format STL.

INTRODUCTION

Earlier [1] new module of geometry import for multipactor discharge simulation code MultP-M implementation and testing results were presented. This upgrade allows device under investigation geometry to be directly imported as STL file. Previously device under simulation shape was described using Boolean operations on basic geometry primitives like brick, torus, sphere etc. Results obtained using this code were compared and found coincident with known numeric, analytical and experimental data. Figure 1 shows geometry import module interface developed.

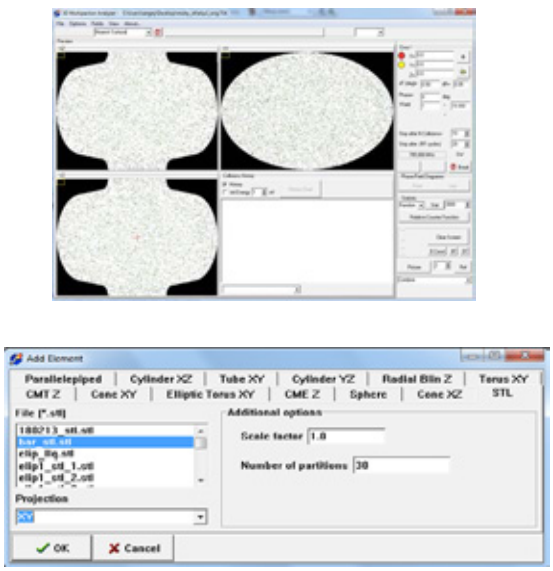

Figure 1: STL import module interface.

Tests showed [1] that new module operates correctly and could be used instead of preceding one with practically the same accuracy as it is illustrated in Figure 2. However despite of pretty effective algorithms and numeric models implementation it was found that computation time significantly grows for fine mesh models. This paper reports the simulation algorithm optimization solutions developed for MultP-M code that allow it to operate faster without detriment to accuracy.

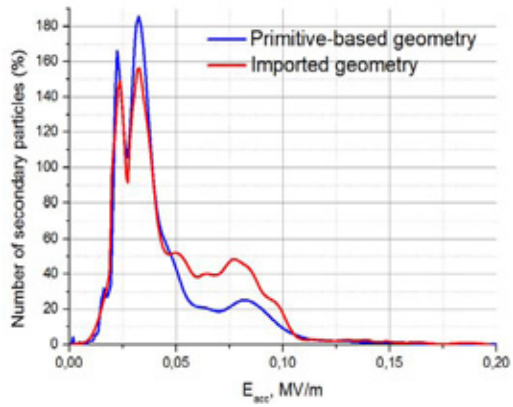

Figure 2: Simulation accuracy test.

MULTP-M AND STL FILE

While MultP-M multipactor discharge simulation code runs the main task to be solved is to determine each electron location with respect to model confines, i.e. to decide whether particle is inside the model boundaries or not. In case of boundaries defined as set of geometric primitives this task could easily solved using simple math. STL file describes 3D objects by their facets thus making this math much more complicated.

Geometry import module developed incorporates ray tracing algorithm [2] in order to get point position with coordinates (x, y, z) relative to facets specified 3D body.

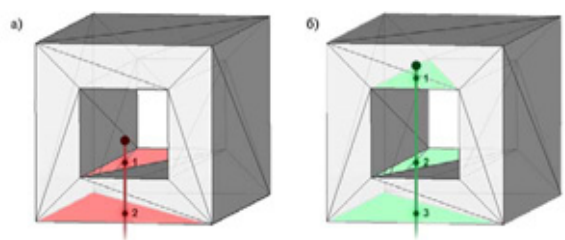

Figure 3: Different point and body collocation: a – point is outside body, ray has even number of boundary crosses; b – point is inside body, odd crosses number.

This algorithm demands 3D body under consideration to be closed. STL standard also sets the same requirement to all objects described.

So one has to develop algorithm that calculates number of ray and boundary crossings. This algorithm is

ISBN 978-3-95450-170-0

to be accurate and effective with respect to code performance.

Net crossings number is calculated by searching for possible ray intersection with every facet. In case ray crosses the plane of facet one should check whether the point lies inside facet or not. In case of STL file triangle facets are used therefore known intersection theory for barycentric (areal) coordinate system [3] suits well.

However for facets number exceeding 20,000 severe computation speed drop was noted despite of powerful algorithms implemented for checking of ray and plane intersection and if cross point belongs to facet triangle.

Thorough algorithm performance analysis and its efficacy for different facets number it was stated that ray traced form every point crosses just a few facets. Crossings number is appreciably less than total facets amount and it seldom exceeds 5 to 6. Obviously algorithm computation rate increases with diminishing facets considered number. This could be done if only facets in some area close to ray are considered.

Basic idea of algorithm developed is to split whole body into equal areas (Figure 4). First the area consisting ray source point with coordinates (x, y, z) is considered. Then algorithm checks for crossings of ray and facets only from selected area. In case of triangle facet partially lies in several adjacent areas it is simultaneously attributed to the both because only triangles of single selected area are considered.

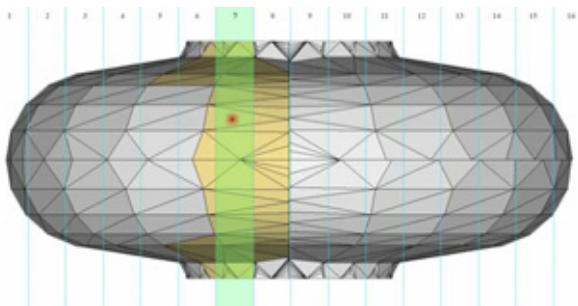

Figure 4: Area selection scheme.

Algorithm developed will run correctly in case the following conditions are met:

1. projection plane (XY, XZ, YZ) for the whole model division in areas is to be chosen;
2. ray traced from given point is to be perpendicular to the chosen projection axis.

These conditions are caused by the fact that in order to evaluate ray traced from the point and surface crossing number all facets are to be checked. Figure 5 shows computation time dependence on triangles number for two algorithms, one without optimization and the second with optimization at 50 areas.

It is clear that non-optimized algorithm run time has liner dependence on triangles number. Optimization leads to noticeable run time growth only for large models having 250,000 triangles.

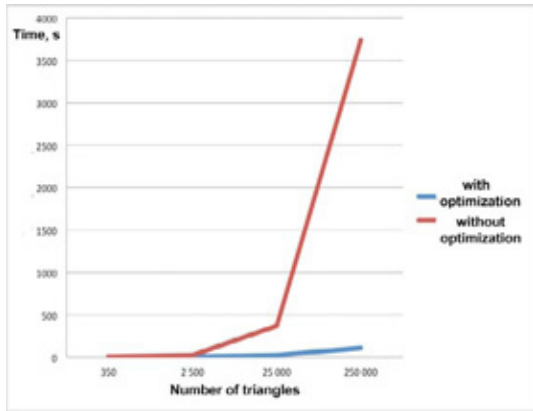

Figure 5: Different algorithms run time vs. triangles number.

It should be mentioned however that is triangles number in every area increases with total triangles number growth, so areas number is also to be increased. This fact is illustrated by the dependence of run time vs. areas number for model having 250,000 triangles shown in Figure 6.

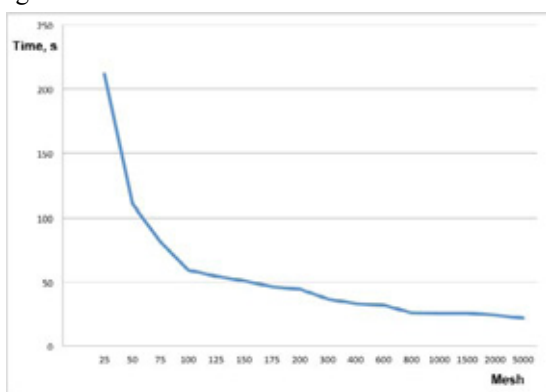

Figure 6: Computation time vs. areas number for model of 250000 triangles.

CONCLUSION

Model import module algorithm of computer simulation code MultP-M was done. This upgrade made simulated task preparation time shorter and more convenient.

REFERENCES

[1] Gusarova M.A., Petrushina I.I., Khuduakov S., The new possibility of MultP-M code, Proceedings of IPAC'14.

[2] Eric Haines, Point in Polygon Strategies. http://erich.realtimerendering.com/ptinpoly/. 2001.

[3] Steve Marschner. Ray-Surface Intersection. Cornell CS417 Spring. 2003.

ISBN 978-3-95450-170-0

MULTI BEAM GENERATOR CAVITY FOR THE PROTON LINEAR ACCELERATOR FEEDING SYSTEM ON 991 MHz FREQUENCY GEOMETRY OPTIMIZATION

E.A. Savin, S.V. Matsievskiy, N.P. Sobenin, National Research Nuclear University MEPhI (Moscow Engineering Physics Institute), Moscow, Russia
A.A. Zavadtsev, OOO "Nano Invest", Moscow, Russia

Abstract

For the proton linear accelerator feeding system 800 kW input power value is required [1]. The system consists from pillbox cavity with six beam tubes connected to the rectangular waveguide as a power output system is designed. In case of using high voltage gun with modulated six-bunch injection, this system allows to transform the energy of electron bunches, which flies throw beam tubes, to accelerating section feeding power. Different types of the structure geometry were calculated. The whole structure consists both from generator cavity and accelerating structure, has been designed [2].

ACCELERATING STRUCTURE

Proton linear accelerator is based on the diaphragm-washers loaded structure [3]. The accelerating mode is E_{020} (see Fig.1). This kind of structure has a coupling coefficient bigger than in DLS or biperiodic accelerating structure (see Table 1).

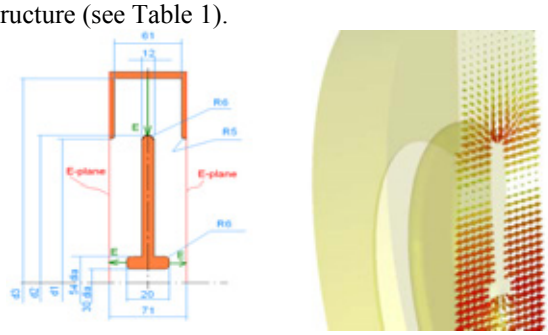

Figure 1.Accelerating structure geometry and field lines in it.

Table 1: Accelerating structure parameters

Parameter	Value
Q0	21376
rsh.ef, MOhm/m	19.16
rsh.ef/Q, KOhm/m	896
T	0.79
Ploss, kW	125
Eacc, MV/m	5.23
Emax/Eacc	1.85

THE CHOICE OF THE GENERATOR CELL GEOMETRY

E_{020} mode [3] was chosen as an operating mode in the resonator. This mode provides one field main maximum in the center of a pillbox cavity and local maximum across the perimeter (see Fig. 2).

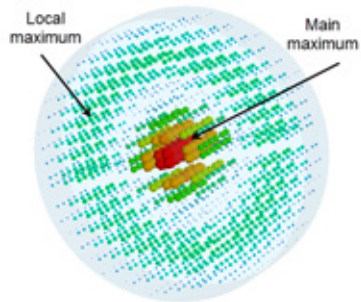

Figure 2: E_{020} mode field lines in a pillbox cavity.

By inserting beam channels in these maximums we can obtain local maximums centered in each channel (see Fig. 3).

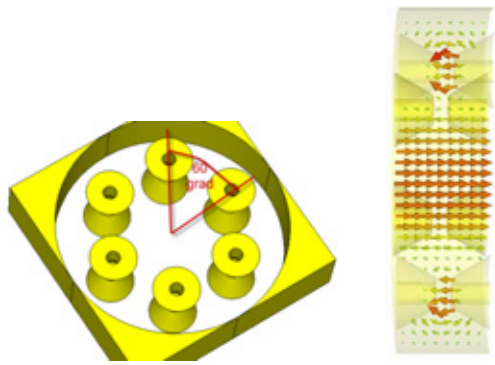

Figure 3: Modified structure.

Second geometry type is the geometry based on E_{310} mode (see Fig.4). On this mode the parasite center main maximum doesn't exist, thus all energy goes to the local maximums (see Fig.5) that will increase shunt impedance. The difference of shunt impedances along beam channels for these two most efficient structures is shown in the table 2.

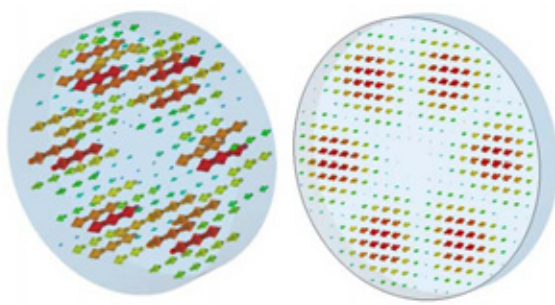

Figure 4: E_{310} field lines in the pillbox cavity.

ISBN 978-3-95450-170-0

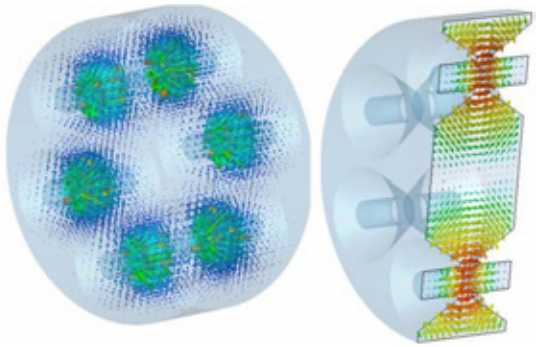

Figure 5: E_{310} lines in the tuned cavity.

Table 2: Different modes operating structures comparison

Cavity type	E_{020}	E_{310}
diameter, mm	466	341
rsh, MOhm/m	1.96	4.74

From the table 2 we see that the E_{310} mode based structure has a bigger efficiency. Another method of the shunt impedance increasing along the channels – is to put the coaxial core in the center of a resonator (see Fig. 6). By varying the diameter d3 of this core it is possible to obtain maximum shunt impedance in beam channels (see Fig. 7).

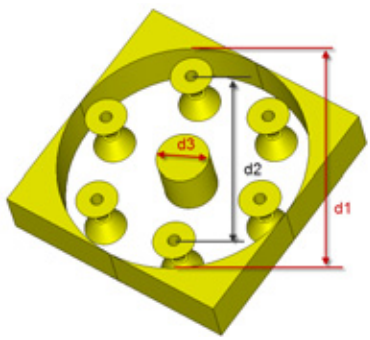

Figure 6: The geometry with a coaxial core.

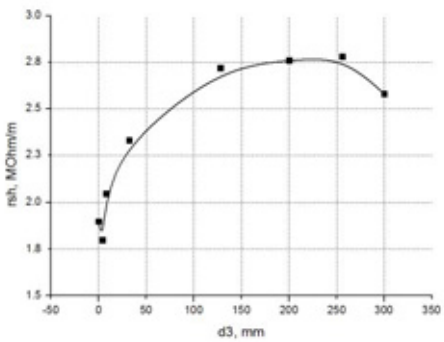

Figure 7: Rsh dependence from the core diameter.

From the Fig. 7 it is easy to see, that the maximum shunt impedance that it is possible to obtain in this geometry is equal to 2.8 MOhm/m, but the diameter of the resonator is so big: 737 mm. It means. that E_{310} based structure has the best efficiency and is the most suitable to be used in the accelerator feeding system. Now it is needed to calculate the power input in the accelerator to connect it with the generator cell.

POWER INPUT TUNING

This resonator is connected to the accelerating structure throw rectangular waveguide (see Fig. 8). The required coupling was obtained by changing window width w and the resonator radius.

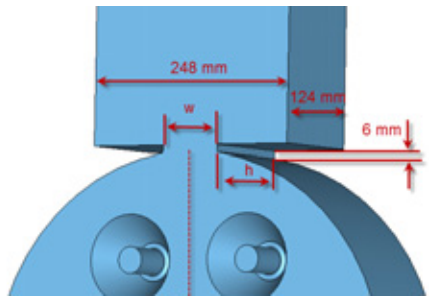

Figure 8: Waveguide to resonator connection

CONNECTING TO THE ACCELERATING STRUCTURE

On the Fig. 9 the connection between waveguide and accelerating structure is shown.

Coupling was tuned by coupling hole angle phi and by changing sizes d and z of the recess in the coupling cell. The dependence of the resonant peak from the recess diameter d with z=5mm and phi=29 grad is shown on the Fig. 10. There we can see that further increasing of the size d is unjustified, that's why next tuning step was changing recess depth z (see Fig.11).

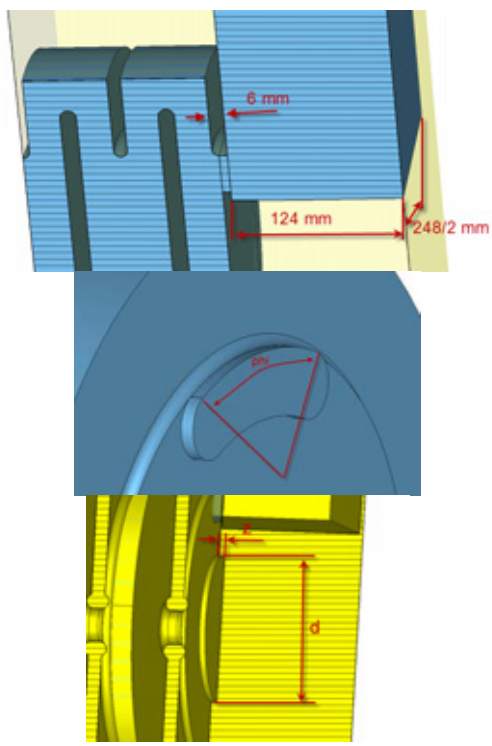

Figure 9: waveguide to accelerating structure connection.

ISBN 978-3-95450-170-0

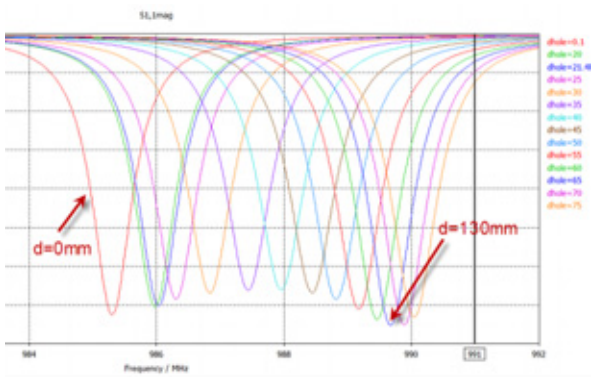

Figure 10: recess diameter variation.

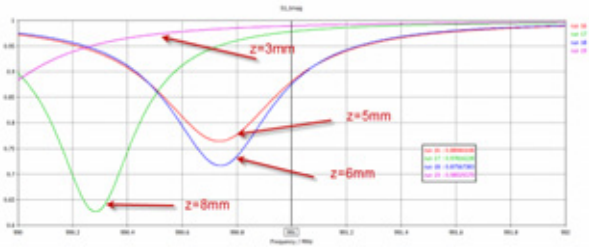

Figure 11: recess depth variation.

After the final tuning we can see the asymmetric field distribution in the accelerating structure (see Fig. 12).

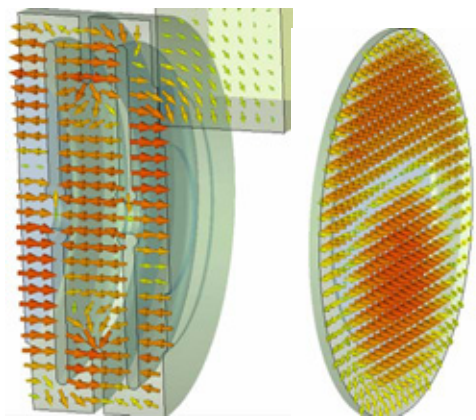
Figure 12: Asymmetric field.

The field symmetry was obtained (see Fig. 13) by increasing the diameter of the coupling cell of the accelerating structure and further coupling tuning.

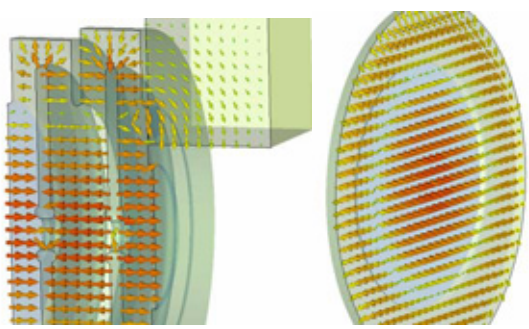
Figure 13: Tuned symmetrical field.

REFERENCES

[1] L.A. Frejdovich et.al., Multi-Beam Klystrons With Reverse Permanent Magnet Focusing System As The Universal RF Power Sources For The Compact Electron Accelerators, Proceedings of RuPAC 2006, Novosibirsk, Russia.
[2] http://www.cst.com
[3] N.P. Sobenin, O.S. Milovanov, RF technique, M:Energoatomizdat,2007.

ISBN 978-3-95450-170-0

COMPARSION OF HIGHER ORDER MODES DAMPING TECHNIQUES FOR AN ARRAY OF SINGLE CELL CAVITIES

Ya.V. Shashkov, N.P. Sobenin, National Research Nuclear University MEPhI
(Moscow Engineering Physics Institute), Moscow, Russia
M.M. Zobov, LNF-INFN, Frascati (Rome), Italy

Abstract

The LHC High Luminosity upgrade program considers an option of using additional cavities, operating at multiplies of the main RF system frequency of 400 MHz. Such harmonic cavities should provide a possibility to vary the length of colliding bunches. In order to supply the required harmonic voltage several single cell superconducting cavities are to be used. It is desirable to house more cavities in a single cryostat to reduce the number of transitions between "warm" and "cold" parts of the cryogenic system. In this paper we study electromagnetic characteristics of a chain of the single cell superconducting cavities coupled by drifts tubes. In order to reduce the influence of Higher order modes (HOM) excited in the structure on the beam stability and to minimize eventual power losses we analyze the HOM parameters and calculate the wake potential decay rates due to application of different HOM damping devices. In particular, the methods of HOM damping with rectangular waveguides connected to the drift tubes, the loads placed in the fluted and ridged drift tubes, as well as combinations of these methods are compared.

INTRODUCTION

In the frameworks of High Luminosity LHC upgrade [1] an application of additional second harmonic cavities with the operating frequency of 800 MHz is currently under discussion. It is desired to combine more such cavities in a single cryostat in order to avoid multiple transitions between cryogenic and warm areas. However, connecting several cavities in a chain can create parasitic higher order modes (HOM) that may affect the stability of circulating beams and lead to excessive power loss. In order to reduce the influence of HOM excited in the structure by passing beams their electromagnetic characteristics were calculated and the decay rates of the induced wake potential in the chain of cavities with different HOM damping devices were analyzed. In particular, the methods of HOM damping with rectangular and ridged waveguides attached to the beam pipes, usage of fluted and ridged beam pipes, as well as combinations of these methods were considered and compared.

ARRAY OF TWO CELLS

HOM extraction from superconducting cavities could be realised in different ways. The most common HOM damping technique is the HOM extraction with couplers. These devices are effective but they also have some disadvantages. They break the cylindrical symmetry of operating mode leading to appearance of the transverse potential (kick-factor); they are subjects to all kinds of pollutions and multipactor discharge [2]. Another method implies HOM extraction to the load placed outside of a cryogenic system. The load can be made of ferrites or in a form of resistive material on an inner surface of the drift tube. In this case, it is necessary to have frequencies of these HOM higher than cut-off frequencies of drift tube in order to provide conditions for HOM propagation toward the load.

In [3, 4] HOM damping technique for the structure with fluted beam pipe was considered. Such beam pipe provides conditions for HOM propagation toward the load. In this structure a high speed of wake field decay was observed that is why it was decided to consider the option of a chain of two such resonators (Fig 1a).

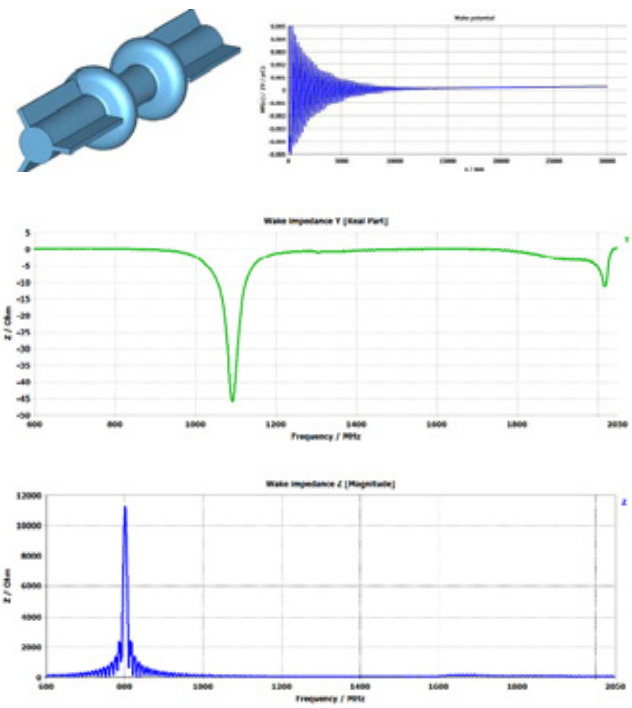

Figure 1: a). Array of 2 cells with fluted beam pipe; b). Dipole wakefield; c). Transverse impedance; d). Longidtudinal impedance.

Fig 1b shows that the wake potential falls almost to zero at a distance comparable to the bunch separation in LHC. The high decay rate could be achieved due to the

*Work supported by RFBR grant 13-02-00562/14 and by the EU FP7 HiLumi LHC - Grant Agreement 284404

ISBN 978-3-95450-170-0

low cut-off frequencies of H_{11} and H_{21} waves in the fluted beam pipe. Nevertheless, E_{01} cut off frequency is high enough to keep operating mode trapped in cavity preventing its dissipation in the load.

In [3, 4] the HOM damping technique for the structure with ridged beam pipe was also considered. Such beam pipe also provides conditions for HOM propagation toward the load. In this structure a high speed of wake field decay was observed so that it was decided to conduct the same calculations (Fig 2a) as for the 2 cell array of structure with fluted beam pipe.

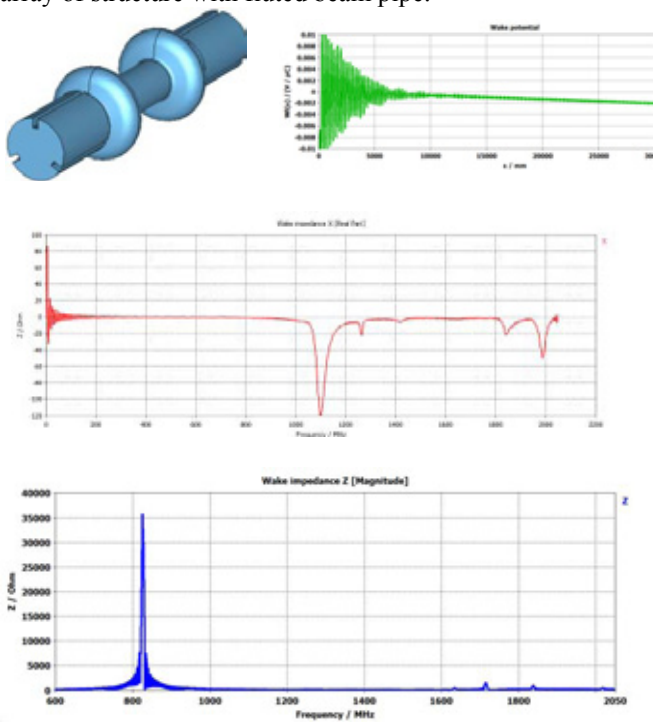

Figure 2: a). Array of 2 cells with ridged beam pipe; b). Wake potential; c). Transverse impedance; d). Longitudinal impedance.

From Fig. 2b it is seen that the wake potential decays very fast. Respectively, there also no sharp peaks corresponding to HOM with Q_{ext} higher than 100 on the graph of the transverse impedance (Fig. 2c) and longitudinal impedance (Fig. 2d)

HOM DAMPING WITH WAVEGUIDES

We can conclude that in an array of two cavities HOM damping is not a problem. But if we want to increase the number of cells we will face a problem of damping modes trapped between the cells in a drift tube. So we have to study methods to suppress these modes. HOM extraction of the trapped modes could be obtained with waveguides attached to the connecting drift tubes (Fig. 3a). Such a solution with "wings" has proven to be effective in extraction of fields propagating along the beam pipes [5]. At a certain length of the connecting drift tube and the waveguide the high rate of decay of the wake potential is provided (Fig. 3b) and the absence of sharp peaks in the graph of the transverse impedance is observed (Fig. 3c). However, the longitudinal impedance exhibits several peaks that can be potentially dangerous. These peaks correspond to the monopole HOM. The extraction of this HOM is complicated by the fact that the wave that they excite in the waveguide does not propagate through, since the cut-off frequency of this wave is much higher than the frequency of these HOM.

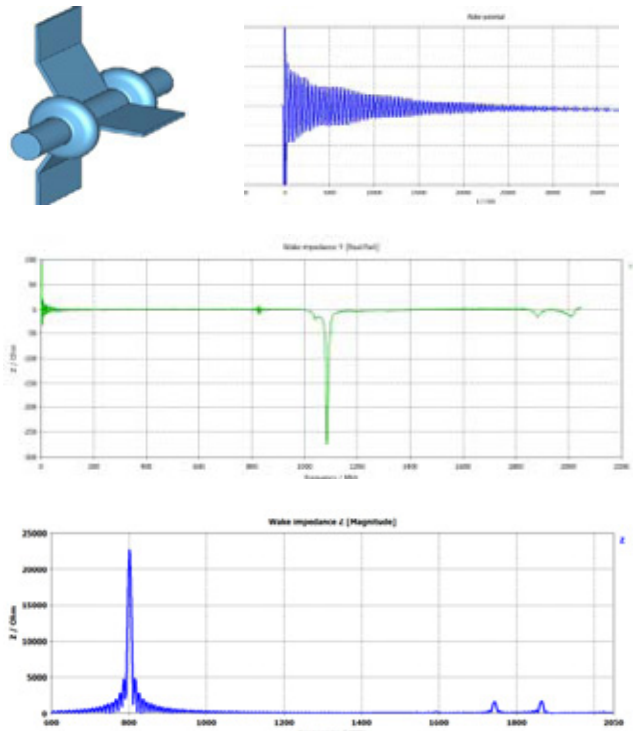

Figure 3: a). Array of 2 cells with attached waveguide; b). Wake potential; c). Transverse potential; d). Longitudinal impedance.

In order to provide conditions for monopole modes damping the waveguides with increased height were attached to the structures with the ridged beam pipe (Fig. 4a). A number and amplitude of peaks on longitudinal impedance graph decreased (Fig 4b).

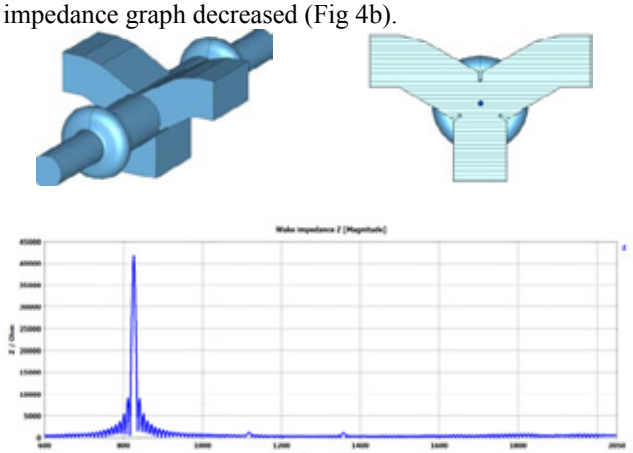

Figure 4: Array of 2 cells with attached wide waveguide and Longitudinal impedance.

ISBN 978-3-95450-170-0

Unfortunately, application of such large waveguide structures could break the cylindrical symmetry of the operating mode; lead to an excitation of the transverse potential and could be difficult in manufacturing. That is why it was decided to add “teeth” to these waveguides (Fig 5a) that decrease the cut-off frequency for the monopole and other HOMs. This will allow us to decrease sizes of the waveguides.

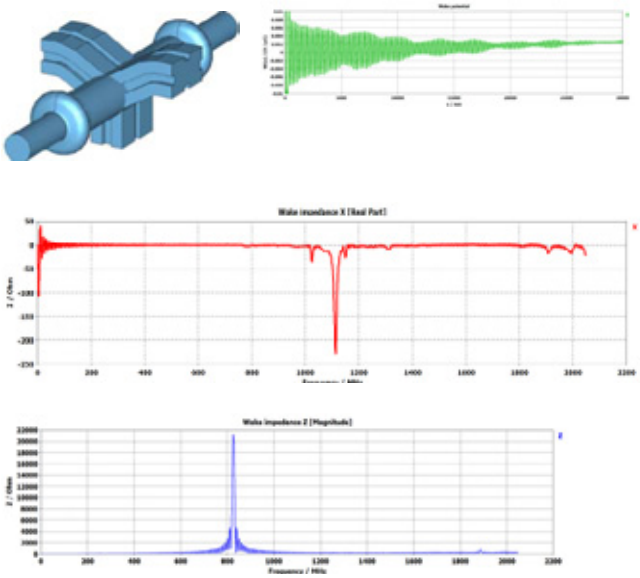

Figure 5: a). Array of 2 cells with ridged waveguides; b). Wake potential; c). Transverse potential; d). Longitudinal impedance.

In such a structure, the fast wake decay was achieved (Fig. 5b). The absence of sharp peaks was obtained for both the transverse (Fig. 5c) and the longitudinal (Fig. 5d) impedance.

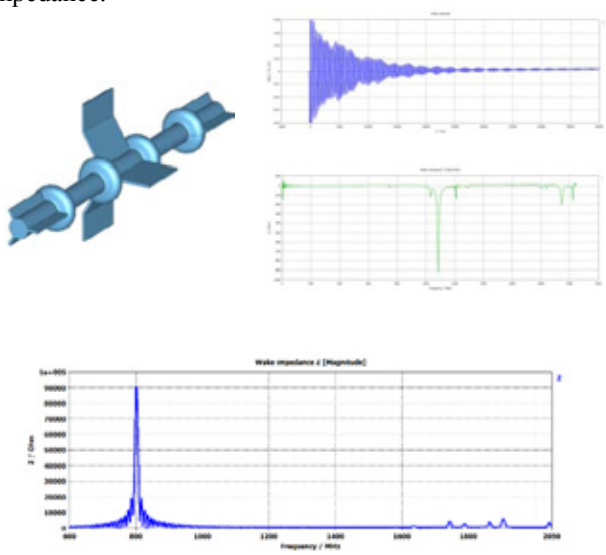

Figure 6: a). Array of 4 cells with waveguides; b). Wake potential; c). Transverse impedance; d). Longitudinal impedance.

4 CELL ARRAY

As long as the structures shown in Fig 1a and Fig 3a have demonstrated good results the calculations for an array of four cells (Fig 6a) have been conducted. As expected, the wake potential decays reasonably fast (Fig 6b) and the transverse and longitudinal impedances (Fig 6c, 6d) do not reveal strong HOMs. For the array of 6 and 8 cavities the dependences shows similar behaviour.

The same calculations have been performed for the combination of structures shown in Fig 2a and 5a. The obtained results are presented in Fig 7a.

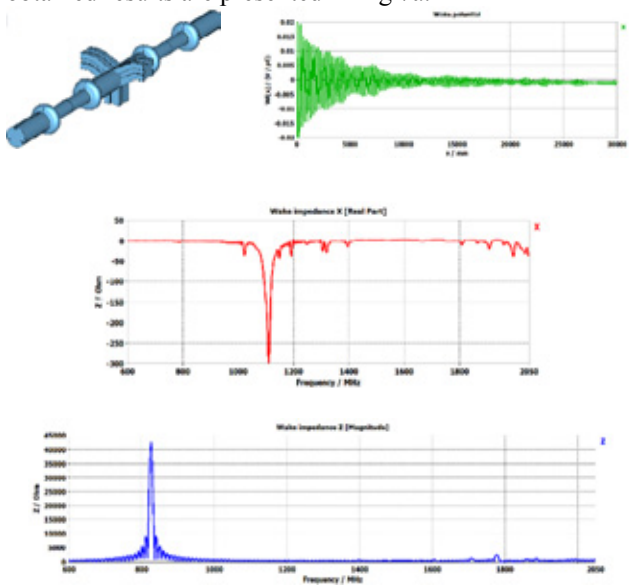

Figure 7: a). Array of 4 cells with ridged waveguide; b). Wakepotential; c). Transverse impedance; d). Longitudinal impedance.

The results (Fig 7b-7d) are the similar to those for the structure in Fig 5a.

CONCLUSIONS

The simulation results and the following analyses show that all options with two cavities connected by the drift tube have no problems with HOM damping. In turn, the HOM damping in arrays of 4 cavities could also be efficient with the help of waveguides.

REFERENCES

[1] L. Rossi, LHC upgrade plans: options and strategy, IPAC2011, p.908

[2] D. Kostin, Multipacting in HOM couplers at the 1.3 GHz 9-cell TESLA type SRF cavity, Proceedings of SRF2011, Chicago, IL USA

[3] Ya. V. Shashkov et al. “Comparison of high order modes damping techniques for 800 MHz single cell superconducting cavities”, Proceedings of IPAC2014, p 2258-2261

[4] Ya. V. Shashkov et al. “Comparison of higher order modes damping techniques for 800 MHz single cell superconducting cavities”, Nuclear Instruments and Methods in Physics Research A, v. 767, 2014, p 271–280

[5] Y. Suetsugu et al., “Development of wing-type HOM damper for KEKB”, Nuclear Instruments and Methods in Physics Research A, v. 533, 2004, p. 295–304

ISBN 978-3-95450-170-0

TEST RESULTS OF 433 MHZ DEUTRON LINAC (RFQ)

O.L. Veresov, S.V. Grigorenko, Yu.V. Zuev, A.N. Kuzhlev, A.K. Liverovskij,
I.I. Mezhov, A.A. Ryaskov, Yu.A. Svistunov, A.P. Strokach, V.F. Tsvetkov,
JSC "NIIEFA", 196641 Saint-Petersburg, Russia

Abstract

The results of bench tests of an RF-frequency deuteron accelerator (RFQ) with an output energy of 1 MeV and operating frequency of 433 MHz are presented. The paper describes specific features of the RFQ construction and assembly, RF power supply system and test procedures. Parameters of the facility when operating with a beam energy analyzer and Be target are given.

INTRODUCTION

Starting from 2005, JSC "NIIEFA" carried out R&D works on the creation of compact accelerating structures with RFQ and APF. These structures can be used in contraband detection systems, ADS, medical facilities for BNCT, or carbon therapy [1]-[3]. In the paper we consider an RFQ structure designed for use as a part of a small-scale facility for neutron production. The main design parameters of the structure are shown in Table 1. Specificity of operation at a frequency of 433 MHz and problems in the manufacturing of an RFQ with a precise channel for the beam acceleration are discussed in [4].

FEATURES OF DESIGN AND ASSEMBLY

Four massive parts with space-modulated vanes made of oxygen-free copper serve as a base of the RFQ construction, Fig.1. When assembling, the components are joined together in pairs like a sandwich, and adjusting copper spacers are set between the parts. The rigidity of the construction is provided by bolting the parts with numerous connecting rods placed along the vanes from the outer side. Bolting power is used for additional tuning of operating frequency. The longitudinal alignment of modulated vanes consists in a small shifting of supporting parts and control of their mutual position. In case of the vane-tip damage, a 10-20μm layer can be removed from the tip surface with a corresponding decrease in spacers height to remain unchanged the operating frequency.

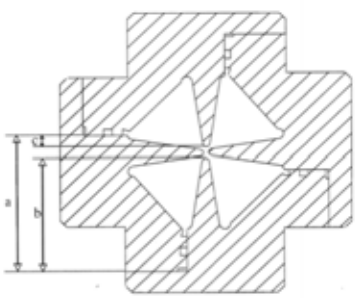

Figure 1: Structure cross-section.

Table 1: RFQ Design Parameters

Parameter	Value
Type of resonator	4-vane
Accelerated particles	$D^{\pm}$
Operating frequency, MHz	433
Beam injection energy, keV	25
Beam output energy, MeV	1
Current pulse length, μs	100
Pulse repetition rate, Hz	10
Intervane voltage, kV	50
Average channel radius, mm	1.8
Minimal channel radius, mm	1.18
Peak surface electric field, Kilpatrick	≤ 2
Input beam synchronous phase, degrees	-90
Output beam synchronous phase, degrees	-23
RFQ acceptance (norm.), π·mm · mrad	0.89
Vane length, mm	1090
RFQ resonator length, mm	1300

The modulation of each vane was checked in twenty points with a precision calibrated ruler of black granite and a linear encoder for sub-micron measurements. The results have shown that deviations in the modulation amplitude were not more than 8 μm. A difference in the distance between neighboring vanes, which disturbs the channel quadrupole symmetry, was not more than 10 μm. High quality of the RFQ manufacturing and assembly made unnecessary special tuners reserved for the equalization of the RF field along the resonator length.

ELECTRODYNAMIC CHARACTERISTICS OF RFQ RESONATOR

The measured Q-factor of the resonator was 6800. The results of measuring the magnetic field distribution along the resonator are shown in Fig.2. Fig.3 demonstrates the intervane voltage as a function of measured RF power. The RFQ intervane voltage corresponding to different levels of RF power was determined from the endpoint of the bremsstrahlung spectrum [5]. To make the spectral analysis, a measuring system [6] with a scintillation detector was used. The results of the detector calibration by reference to Am-241 are shown in Fig.4. The FWHM–to-maximum position ratio is 21keV/59.5keV, consequently, the detector energy resolution is 0.35.

ISBN 978-3-95450-170-0

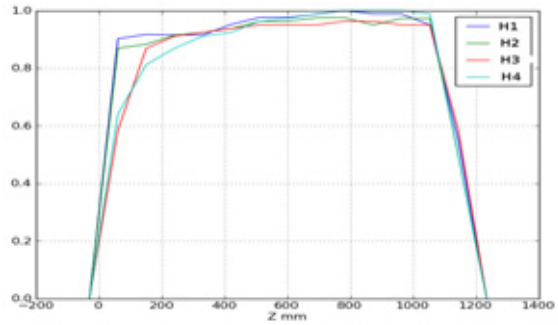

Figure 2: Distribution of a normalized magnetic field along RFQ quadrants.

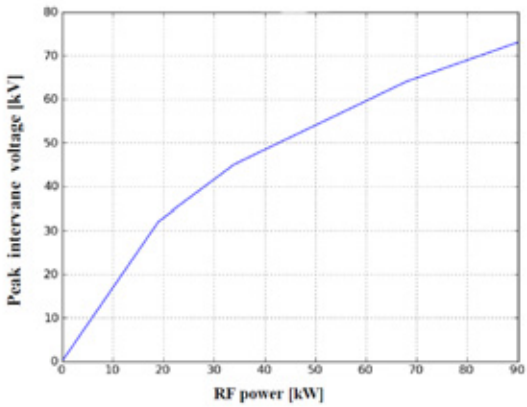

Figure 3: Peak intervane voltage versus RFQ resonator power.

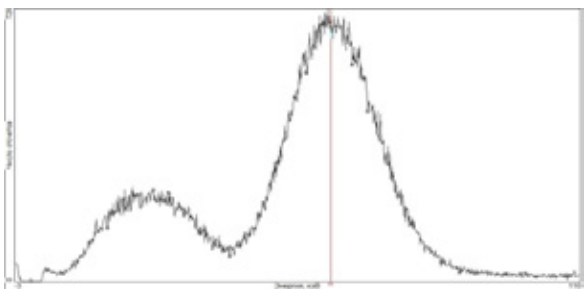

Figure 4: Energy spectrum of Am-241 at the spectrometer output.

DESCRIPTION OF THE TEST-FACILITY

The RF power was supplied to the RFQ from an amplifying system comprising a low-power master-oscillator, preamplifier with an output power of 2 kW and final amplifier with an output power of up to 450 kW per pulse. An endotron-type device, "Colesso", was used as the final amplifier; its functional diagram is given in Fig.5. To protect amplifiers against overloads under breakdown in the RFQ cavity, a ferrite circulator was installed between the endotron and accelerating structure. Pulsed voltages of 2kV and 12 kV were fed to amplifiers from a common modulator.

Operation of the RFQ under the beam load was studied on a facility shown in Fig.7. An injector unit of the facility consists of a multi-cusp source of charged ions, two einzel (unipotential) lenses and two steering magnets. The einzel lenses were used for transport and matching the beam with the RFQ acceptance. The first step of the beam forming was done by the multi-cusp source. In the continuous mode the source can produce a weakly divergent H^- beam with a current of up to 2 mA and normalized emittance of 0.3 π· mm mrad [7]. Phase characteristics of a pulsed beam were not measured. D^- current at the output of the source vacuum chamber was measured with a movable Faraday cup. In addition, the beam intensity was controlled with two beam current transformers (BCTs) at the RFQ input and output.

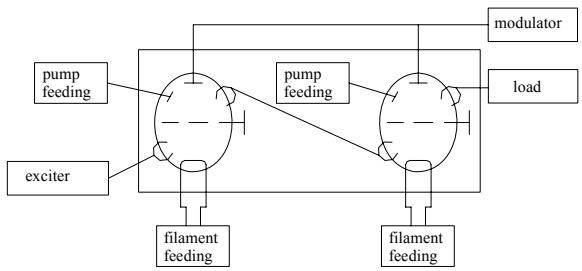

Figure 5: Functional diagram of the endotron.

MEASUREMENT OF BEAM CURRENT AND ENERGY SPECTRUM

To measure the energy spectrum and current of the accelerated particles we used either a standard magnetic analyzer with a set of lamellae or a foil analyzer (a set of Al foils of a fixed thicknesses installed in front of a beam collector). Fig.6 presents experimental data on the collector current as a function of the RFQ intervane voltage, which (in contrast to Fig.3) was found taking into account the energy resolution of the x-ray analyzer. The same figure shows the results of an end-to-end simulation of the beam dynamics under the experiment conditions. The simulation was started from the beam source with a measured beam current of 1.7мА and assumed phase distribution of particles; potentials of the 1st and 2nd einzel lenses were -16kV and -23.8kV respectively. The blue (top) curve corresponds to the calculated current of all particles at the RFQ output. The red line with crosses shows the current of particles with an energy more or equal to 1 MeV. The black line with circles describes the data obtained experimentally. The measured and calculated data are in agreement. The simulation explains the beam current losses at nominal intervane voltage by mismatch of the beam and RFQ in angle characteristics of particles. Similar conclusions were drawn in [8].

TEST RESULTS WITH BERYLLIUM TARGET

In addition to the experiments described above, the accelerator was tested when operating with a Be target of 5mm thickness. The target is intended to produce

ISBN 978-3-95450-170-0

neutrons by the $^{9}Be(d,n)^{10}B$ reaction. Cylindrical form of the target was designed for the beam power of 10 kW per pulse. The target is sited on a water-cooled 1 mm-thick copper disk.

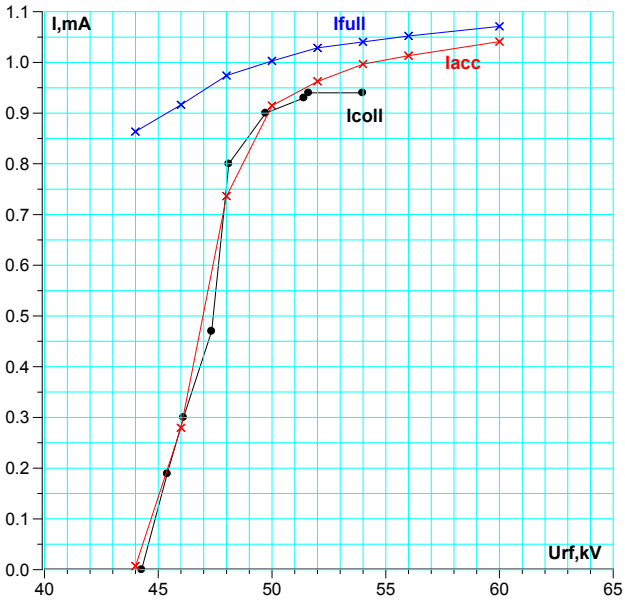

Figure 6: Beam current at the RFQ output as a function of the intervane voltage: I_{full} is the total current (calc.), I_{acc} is the current of accelerated particles (calc), I_{coll} is the current on the beam collector (measur.).

Neutron fluxes were measured in two stages by the personnel from FSUE «D.I. Mendeleyev Institute for Metrology (VNIIM)». First, direct measurements of the neutron flux at a minimum ion current of 0.033mA were done with a calibrated all-wave detector OVS-3M. Then, relative measurements were carried out with indium activation detectors at ion current values of 0.033 mA and 1.0 mA. In direct measurements, the neutron flux density was measured at angle 0° with respect to the direction of the accelerated ion beam. Contribution of the scattered radiation was estimated by the "shadow cone" method in accordance with ISO-8582. The obtained neutron flux value of 10^8 n/s correlates well with previously published data for a beam current of 1 mA.

ACKNOWLEDGMENT

The authors would like to thank our colleagues Z.Andreeva, G.Voronin, V.Ershov, V.Korobov, V.Petrov and S.Silaev for useful discussions and help in experimental researches.

REFERENCES

[1] Yu.A.Svistunov, M.F.Vorogushin, Yu.N.Gavrish, A.P.Strokach et al., // ICAA'05, St.Petersburg, pp.406-409 (2005)

[2] Yu.A.Svistunov, M.F.Vorogushin, G.P.Vedernikov et.al. // ICAA'05, St.Petersburg, pp. 263-266 (2005)

[3] Yu.Svistunov, M.Vorogushin, D.Semenov, B.Vodennikov // LINAC 2006, Knoxville, pp.475-477 (2006)

[4] Yu.A.Svistunov, Yu.V.Zuev, D.A.Ovsyannikov, A.D. Ovsyannikov // Vestnik St. Petersburg University. Ser. 10, pp.14-23 (2010).

[5] G.O. Bolme et al. // LINAC90, Albuquerque, p.219 (1990).

[6] Yu.N. Gavrish, V.G.Mudrolyubov, A.V. Sidorov et al. // NIIEFA P-0951 (1996)

[7] P.V.Bogdanov, I.N.Vasilchenko, O.L.Veresov, S.V.Grigorenko et.al. // VANT. Series "Electrofizicheskaya Apparature", №.5 (31), pp.74-83 (2010).

[8] Yu.A. Svistunov, A.P.Durkin, A.D. Ovsyannikov // RUPAC-2012, St.Petersburg, pp.82-84 (2012)

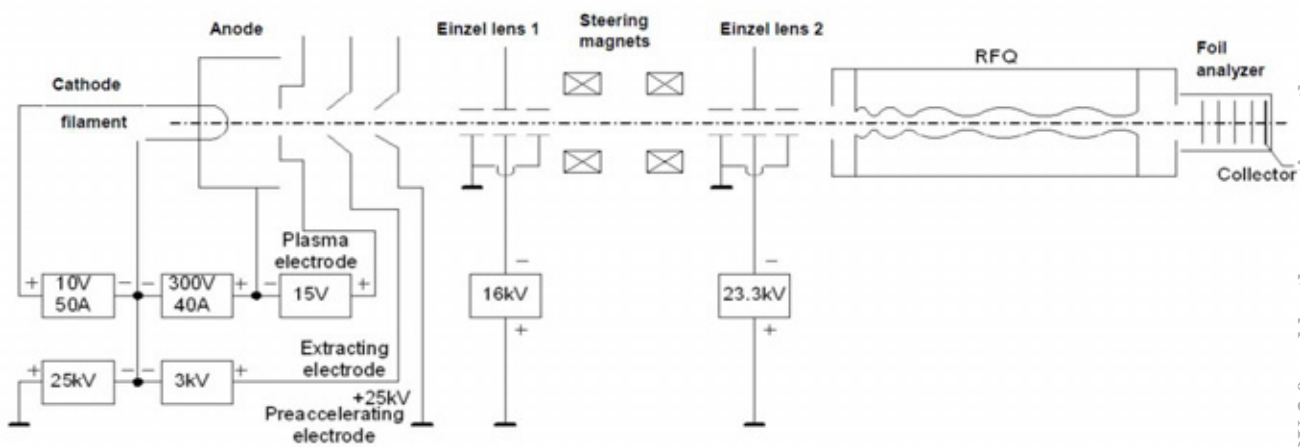

Figure 7: The test-facility schematically.

ISBN 978-3-95450-170-0

CASCADE INTERFERENCE SWITCHES IN ACTIVE MICROWAVE COMPRESSORS*

S.Gorev, S.Artemenko, V.Avgustinovich, V.Igumnov, V.Kaminsky, S.Novikov, Yu.Yushkov#,
Tomsk Polytechnic University, Tomsk, 634050, Russia

Abstract

The switching element is usually located in the area of maximum electric field strength and the desire to put it in the area of lower field strength, but keeping the same efficiency and steadiness, of operation is quite understood. Presumably a cascade switch might provide the required way of operation. Two designs of cascade switches were examined. The first one was formed by waveguide tees connected in a way when a direct input arm of a next tee is connected to a side arm of a preceding tee. The second was a set of tees connected in series through their direct arms. It was shown that the considerable decrease of the switched power value and the increase of the output power and stability of the output pulse parameters can be provided.

INTRODUCTION

Requirements applicable to high power microwave sources are diverse. The sources in particle accelerator technique should have high efficiency, beside high pulse power values, steady phase and oscillation frequency and also rectangular envelope of output pulses. The possibility of meeting most of requirements in resonant microwave compressors [1] is strongly influenced by operating quality of the switch controlling the coupling between a cavity and a load and being, factually, a device of energy extraction. Precisely this device determines the output power level, repetition rate and steadiness of output pulse parameters. Taking strict requirements for switch operation into account it is one of the most troubled elements of a compressor. The trigatron type of a gas-filled microwave switch is usually used as the energy extraction device. Its electric strength is normally lower than one of the cavity volume as it is located in an area of high electric field strength. Therefore the electric strength of the switch determines the compressor limiting output power and steadiness of output pulse power.

The way of a power increase and output pulse steadiness improvement when the energy is extracted through the H-tee waveguide interference switch is considered in the report. The main idea of the element operation is that the switched power is distributed between several switches connected by a certain manner [2,3]. The cascade of tees connected as “side arm – direct arm” and series connection “direct arm – direct arm” may serve as main designs. Conditions enabling the considerable electric field strength decrease in arms of the switching tees along keeping field strength in the volume of the storage cavity are considered as well.

CASCADE OF TEES IN SIDE ARM

In the cascade of tees in the side arm of the switch a direct arm at each sequential tee is connected with a side arm of the proceeding one. Other direct arms of tees are short circuited. The switching arm is the side short circuited arm of the last tee. In this arm the microwave switching gap is located at quarter of the waveguide wavelength from the short circuiting end plate. Input direct arms of the tees have lengths equal to half wavelength in a waveguide and output short circuited ones – quarter of the wavelength. This configuration of tees provides mode “closed” to the switch. The tees are opened in sequence starting with the lost tee. Once the microwave switch gap for the lost tee is closed this tee is getting opened and the half wavelength of its input arm changes into the quarter wavelength of the total section of input direct arms. This results in sequential opening of all tees.

The power decrease is obtained due to matching each tee from the side arm. It is well known the power in the side arm in tees of this type is half as much as the power fed by the direct arm [4]. This means the switched power is decreased by the factor of 2^3, which is equal to eight times, when three tees are used in the circuit design.

The main switch characteristic – the transition attenuation in storage and extraction modes of operation and the wave amplitude amplification in the cavity volume and the side tee arm of the storage mode – can be easily obtained by using of scattering matrix method. The results of calculation are presented as plots on Fig.1.

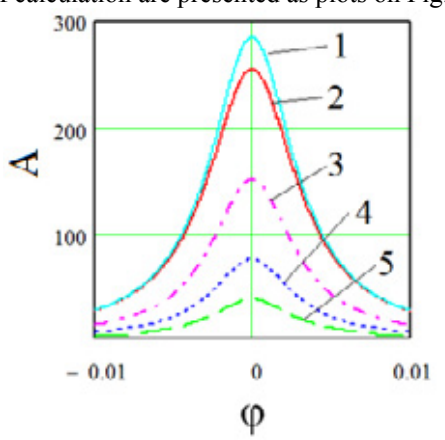

Figure 1: wave amplitude amplification A in the cavity volume and side arms of tees against the phase shift at discharge gap operation.

* The work was supported by The Ministry of Education and Science of Russian Federation within the program “Nauka”, project N 1814.
#yuyu@tpu.ru

ISBN 978-3-95450-170-0

Following marks are used in Fig. 1: 1 – cavity amplification factor with the ordinary switch; 2 – three sequential tee switches; 3,4,5 – amplification in the volumes of side arms of consecutive tees. The curves are plotted for the compressor tested experimentally with the attenuation constant along the cavity $\alpha \approx 1.5\times10^{-3}$ and for other elements 5×10^{-4}. The attenuation constant values here derived from the Q-factor value determined experimentally. As the comparison of curves 1 and 2 shows the amplification of the cavity with the ordinary switch is higher than one for the cavity with the cascade switch by 0.5dB. The reason of the difference is the additional energy losses for field excitation the cascade of tees. Obviously the cascade switch is suited in a greater degree for compressors with cavities of large volumes. The plots of Fig.1 prove that the switched power can be decreased by the factor of 2^3 in the switched combined of three tees and so, if the amplification in the cavity volume is 24dB, the amplification in the switching tee arm does not exceed 16dB.

The experimental tests were made with the microwave S-band compressor at the operational frequency f_0 of 2800MHz. The energy was extracted through different interference switches – through the ordinary switch with one tee only, through cascade switches with two and three tees. The tees were made of circular waveguides of 90mm cross section diameter. The copper cylindrical cavity with the diameter of 120mm and length of 55cm was used as an energy accumulator. The cavity was matched with the switch by the smooth matching transition. The total length of the cavity was 710mm. The working oscillation mode was $H_{11(8)}$, its measured intrinsic Q-value Q_0 was 3×10^4, the estimated time T_1 of H_{11} wave mode round trip along the cavity was about 5ns. The maximum estimated amplification factor G of the compressor with the output pulse width equal to T_1 was $G = Q_0/2\pi f_0 T_1 \approx 25$dB. Two perspectives of the external view of the microwave compressors with the two tees incorporated into the switch by connecting to side arms are shown in Fig.2.

Figure 2: Microwave resonant compressor with the cascade switch based on two H-tees in side arms.

The microwave magnetron generator with the pulse power of 0.8..2MW and the pulse width of 3μs was used as a source of input pulses. The estimated efficiency of storing reached 0.47 and the amplification factor 24.5dB. So the estimated maximum output power of the compressor was 480 MW at the output pulse width of 5ns. The electric field strong in the switching arm of the ordinary switch was close to the value 185 kV/cm. In the cascade switch with two tees it decreases down to the value 130 kV/cm and with three tees – down to the value 90 kV/cm.

Before the characteristics of the cascade switch were determined the pilot experiment with the compressor including the ordinary switch was made. The blown through quartz tube was used to confine the discharge area of the microwave switch. The tube was positioned diametrically along the electric field line of the working H_{11} mode and had the triggering spark gap at one of the ends [5]. The compressor with such a switch provided pulses of 300MW pulse power at the amplification factor 22dB and pulse width of 4.8ns. The typical envelope of the output pulse is presented in Fig.3. When the tube was filled with argon steady spontaneous breakdowns occurred at the input pulse power of 1MW and corresponding output power of 150MW. The occurrence of steady spontaneous breakdowns was the sign of reaching the limiting working power of the switch.

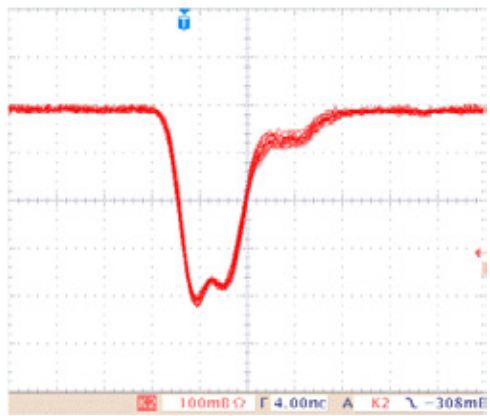

Figure 3: Oscillogram of output pulse envelopes of microwave compressor with the ordinary switch.

There were three stages of experimental tests of the cascade switch. The first stage was investigation of the tee cascade when tees were mismatched from directions of the side arms. The wave power values in the storage volume and the switching arm are practically equal for this type of design. The tees wave matched from the direction of side arms at the second stage but that mismatched the compressor output. The third stage involved matching the compressor output line with the cascade switch having tees matched from the directions of side arms. That required installing the additional matching element at the output. The principal result of the experiments is presented by the oscillogram in Fig.3 displaying the figure of output pulse envelope of the compressor with the two tees switch. The amplification was lower than 21dB and that is 1dB less than the amplification value of the compressor with an ordinary switch. But the discharge area of the tube was filled with argon only at the excess pressure at 0..0.5bar, the input

ISBN 978-3-95450-170-0

pulse power could be increased to 2MW, the output pulse power reached 250MW and all that proved the decrease of the switched power and potential opportunity for the further output power increase.

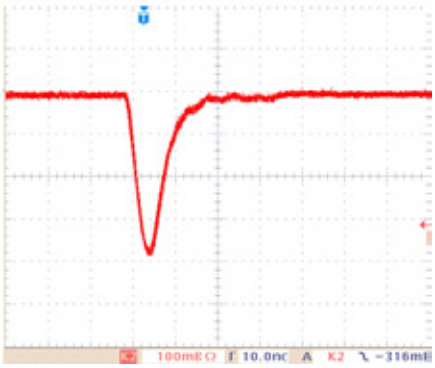

Figure 4: Oscillogram of output pulse envelopes of microwave compressor with the cascade switch including two tees.

The three tees cascade switch was tested at the final stages of the experiments. The experiments exhibited the stored energy exerted the noticeable effects on the output parameters such as steadiness, shape, pulse width and amplitude. So it should be perspectives of these type of switches in microwave compressors with big volume cavities.

SIERIES DIRECT ARM CONNECTION

Experimental studies of the compressor with a serial cascade switch were performed at the same laboratory bench. The difference was only in design of the cascade switch. The cascade of two tees was used. External view of the compressor with the switch is presented in Fig.5.

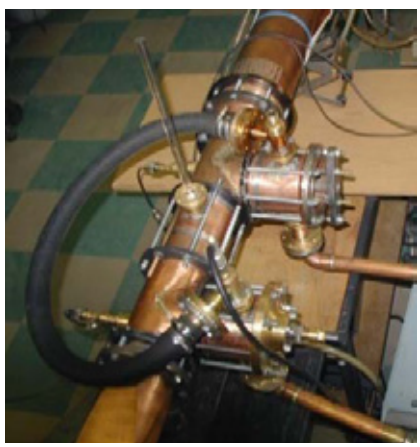

Figure 5: External view of the cascade with “direct arm – direct arm connection.

The formation of two types of pulses due to precedence in acting of switches was observed. One of the switches was controlled by external triggering, the other switch acted spontaneously. Therefore, in both cases, the main pulse is usually preceded by a pre-pulse. The prepulse associated with either energy extraction of the waveguide section between the tees when the second switch was externally triggered or by leakage of the second tee and the delayed of starting of spontaneous breakdown this tee when the first tee switch is controlled. This is the reason the main pulse is shorter in the first case and has higher power while the second is longer. Alternating triggering tees alternately generates pulses of both types. When the spontaneous breakdown formation time coincides with the transmission time of the line between the waveguide tees the output pulse is short and has maximum amplitude. Significant prepulse amplitude due to the comparability of the lengths of the side shoulder tees and a segment of the waveguide between the tees with long storage cavity. A consistent cascade switches allowed to increase the working capacity of the compressor switched in argon in half, bringing it to a level of about 150 MW. A lower power level compared to the power compressor cascade tees lateral shoulder due to the use of the cascade tees not approved by the lateral arm, and energy losses due to the pre-pulse. To reduce losses in the pre-pulse is necessary to use a larger cumulative cavity.

CONCLUSION

Possibility of making the output parameters higher in the microwave compressor with the energy extraction through the waveguide H-tee was proved. Practically it can be brought about by making the switching side arm as a cascade of H-tees. This design is especially effective in compressors when the energy extraction period is bigger than the time of wave travelling along the storage microwave structure. The cascade switches could be useful for compressors with solid state switches which level of the switched power is considerably lower than one of the gaseous switches and electron beam switches. It is seems quite possible to decrease the switched power to the level acceptable for a semiconducting switch. The cascade switches will be functionally operative if they are made of oversized tees [4] or in the figure of a packet of standard tees with the oversized switching arm [5].

REFERENCES

[1] A.N.Didenko et al., Powerful microwave pulses of nanosecond pulse duration, (Moscow: Energoatomizdat, 1984), 112 (in Russian).
[2] S.G. Tantawi, The design and analysis of multi-megawatt distributed single pole double throw (SPDT) microwave switches. AIP Conference Proceedings (1999) 959; doi: 10.1063/1.58890.
[3] S.N. Artemenko. Izv. Vuz. Fiz., 56(2013) 238 (in Russian).
[4] J. L. Altman, *Microwave Circuits,* (D. Van Nostrand Company, Inc. 1964) 114.
[5] V. Avgustinovich et al., Instrum Exp Tech+, 52, 4 (2009) 547.
[6] V. Avgustinovich et al. Tech. Phys. Lett., 39 (2013) 492.
[7] S.N.Artemenko et al. Tech. Phys. Lett., 39 (2013) 1040.

ISBN 978-3-95450-170-0

OVERSIZED INTERFERENCE SWITCHES IN MICROWAVE PULSE COMPRESSORS*

S.Artemenko, V.Avgustinovich, S.Gorev, V.Igumnov, V.Kaminsky, S.Novikov, Yu.Yushkov#
Tomsk Polytechnic University, Tomsk, 634050, Russia

Abstract

Oversized interference switches in resonant microwave compressors have high electrical strength. The switches of two types with a gaseous discharge gap were studied experimentally. The first type was developed on basis of the oversized rectangular waveguide H-tee with the H_{01} operation mode. The output pulse power of 2.8MW and pulse width of 3.5ns were obtained. The second type was a compact packet of common single mode switches incorporating the five identical waveguide tees. Synchronous operation of the switches was provided by the gas discharge plasma formed in the mutual side arm of the packet.

INTRODUCTION

Microwave resonant compressors (MRC) produce pulses by accumulating energy in a resonant cavity during a relatively long time and subsequent rapid extraction of the energy into a load. The ultimate output power of a MRC is equal to a power of the travelling wave component in a resonant volume. The coupling between a cavity and a load is controlled by the phase shift between the waves radiating from the cavity and from the side arm of the tee. The phase is inverted by the gaseous microwave switch having the trigatron type triggering. The limited cross section of a single waveguide limits the electrical strength of the elements and the output power value. An increase of gas pressure leads to big energy losses in the discharge plasma and a decrease of efficiency. For example the output pulse power for switches located in S-band waveguides of the cross section 72×34 mm^2 does not usually exceed 200 MW [1] and the efficiency is within the range of 0.2-0.3 at the losses value in the switch of 2-3dB. The switching in oversized cavities involving mode transformation increases the limiting output power [2,3]. This report presents the study of switch designs based on oversized waveguides but intended for fast energy extraction and keeping high values of amplification.

OVERSIZED INTERFERENCE SWITCH

It was assumed the strong coupling between the output line and the switching resonator and the necessary frequency change are enough for developing an effective interference switch no matter what operational wave mode is used.

Switching resonators made of single mode waveguides were connected to storage volumes by T-junctions or bridge junctions and demonstrated high switching efficiency. Although the cross section limited by the cut-off frequency value limits the electric strength and the output power.

One possible solution of increasing a waveguide cross section is the use of rectangular waveguides with H_{01} operational wave mode [4]. Corresponding elements in a tee or bridge manner keep the switching parameters of single mode analogs, does not require the special mode transformation into the primary mode of an output waveguide and make the maximum output peak power greater by several-fold. These oversized switches, besides usual requirements to the level of multimode transformation, raise some specific conditions to be provided for effective operation of the switch and the compressor. In order to provide switching over to extraction the phase of wave reflected from the tee should be changed by about 180^0 along with the change of the frequency beyond the resonance curve by value of $\delta f \approx nf / Q_a$, where $n \geq 3$ and Q_a - quality factor of the tee arm. Although it was found the dimensions of switching arm should be less some value determined by the ratio of the volume parameter transient time to the time of two ways wave travelling along the storage cavity.

The expression for the limit of the oversized waveguide wall size at the given arm length of $L_{arm} \approx \lambda_w / 2$ was derived:

$$b_{\max} < \frac{z_0 Q_{arm} l^3}{90 n a L_{arm} \lg\left(\frac{2l}{r}\right)} = \frac{z_0 Q_{arm} \left(0.2 L v_{pl} / v_g\right)^3}{90 n a L_{arm} \lg\left(\frac{0.4 L v_{pl} / v_g}{r}\right)} \quad (1)$$

where v_g – wave group velocity, v_{pl} – plasma propagation velocity, $L_{arm} \approx T v_g / 2$, l – length of the plasma spark channel, r – cross section radius of the plasma channel. As is clear from (1) the size is proportional to $f^{1.5}$. This means the switches are more efficient for higher frequencies of the microwave band when the relative increase of the wall size is higher at given T.

Experimental study was made in X-band and the tee waveguides had the cross section of 58×25 mm^2. External view of the tee is shown in Fig.1. The longitudinal section of the tee is identical to the single mode one. So when dimensions are precise and operational mode H_{01} is not converted the switch of this type operates similarly to the common switch as there are no physical causes impeding that. It was proved by measuring the transition attenuation in the switch close state. The attenuation was 41±2 dB in

*The work was partially supported by the state order "Nauka" of RF Education and Science Ministry, project 1814.
uyuy@tpu.ru

ISBN 978-3-95450-170-0

the frequency range 8800-9500 MHz and that corresponded to the attenuation of a common tee.

Figure 1: Interference switch on the basis of oversized rectangular waveguide.

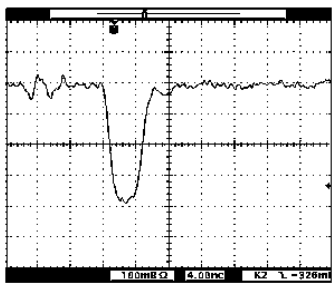

Figure 2: Envelope of the formed microwave pulse.

The tee with H_{01}-mode came to the open state by a slight change of the short-circuited arm parameters. It was verified as well when the switch was installed in the compressor. The calculated double time interval of wave travelling along the storage cavity was 4 ns at the quality factor of 1.6×10^4. That gave the calculated power gain of about 20dB. The measured gain value was 17.5dB at the pulse width of 3.5ns. The primary exciting microwave source was the pulse magnetron generator with the power of 50 kW and so the output pulse power reached 2.8 MW. The switch was triggered by illumination of the discharge gap by the electric discharge spark or by the light beam of the nitrogen laser. The switch discharge was formed in argon at atmospheric pressure in a waveguide volume or in a quartz tube located in the area of maximum electric field and aligned along the electric flux. The typical output pulse envelope is shown in Fig. 2. As the figure shows the energy extraction time is equal to the double time of wave travelling along the cavity that is similarly to operation parameters of a singlemode switch.

PACK OF SYNCHRONIZED SWITCHES

Several synchronized switches connected to a single cavity can enable the energy extraction time close to the double time of wave travelling along the cavity volume. The extraction time decreased with increase in the number of switches but the spread of switch triggering was compared to the output pulsewidth recorded at a single switch output [5]. High-level synchronization was reached when the switches were arranged closely to each other i.e. they formed a packet of parallel switches [6]. External view of the switch packet in a rectangular waveguide of the tee, the short-circuit plate is disconnected, is shown in Fig. 3.

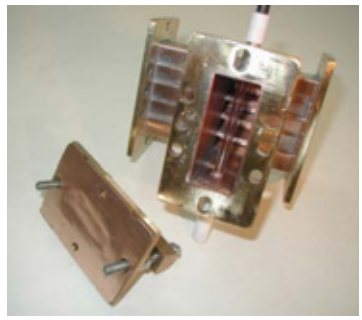

Figure 3: Packet of switches with mutual side arm.

The key problem of synchronous power extraction is maintaining identical switching conditions in each gap. First, the electric field strength values in the gaps should be equal and this condition depends on the cavity geometrical arrangement, the type of the wave working mode, the waveguide interior surface quality, the coupling between switches and the cavity. For the proposed design the H_{01} mode of a prismatic cavity is most acceptable. The E-field strength along the larger wall is constant and this contributes to equality of field strength values in the switches. The wave modes H_{01} and H_{10} are easily transformed into each other and so combining the energy extracted through all switches is not difficult.

The second issue is the quantity of switches in the packet which affects the compressor limiting power. The effective switching corresponds to the switching time less than T and if t_f is a characteristic time of the discharge development then the maximum number of switches is given by $n < T/t_f$. For example, in X-band the acceptable number is in the range 2…5 at T = 5ns and $t_f \approx 2ns$ that is the number is not so great. For higher frequencies the usage of the packet may be efficient as $t_f < 1ns$ and, keeping the same T value, the allowable switch number is larger.

The larger number of switches requires hard locking of discharge triggering. The mutual switching area as a joint oscillation system was supposed to be realized as a mutual switching tee arm. The switching process should be controlled by a single discharge and should not be a need for special synchronization of switches. But the resonant frequency of the arm should be withdrawn beyond the resonant curve during the time interval about T. It may be executed by the discharge having the spark channel length much less than the total length of channels when switching proceeds in uncoupled arms. The wave traveling time along the mutual arm is less than the discharge formation time so the phase inversion of waves reflected by the arm is synchronous and so the switches of the packet come to open state also synchronously. The maximum number of switches is estimated by $n < L/b$, where b- size of the narrow wall of the tee waveguide.

ISBN 978-3-95450-170-0

Experimental tests in X-band proved that the strong coupling between the switching arms is the requirement for synchronous operation. The coupling in the packet was introduced by different ways e.g. by holes in adjoining switch walls, by slots between the short-circuit and flat ends of side arms and by integrating the side arms into a mutual side arm in the form of an oversized regular waveguide section. The level of synchronism rose with increase of the coupling between the arms. The packet with coupled not in full arms is responsible for unsteady process of energy extraction characterized by the spread of output pulses as shown in Fig. 4.

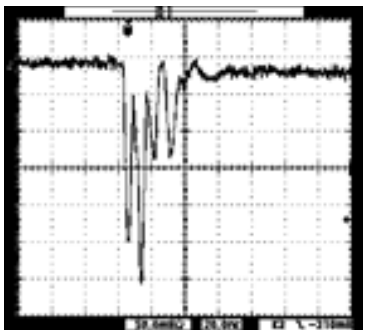

Figure 4: Output pulse envelope when separate side arms are coupled not in full.

The simultaneous energy extraction during the double transmission time along the cavity is reached with the strong coupling. The strong coupling is reached by integrating the side arms of tees of the packet into a section of a regular rectangular oversized waveguide. The power gain of the compressor with the oversized storage cavity and the mutual oversized side arm of 58x25 mm^2 cross section was 16.5dB at the pulsewidth of 3.5 ns and the corresponding peak power of 2.2MW. The envelope of the output pulse is shown in Fig. 5. According to estimate the energy extraction through a packet with 5…7 switches can form pulses with the peak power of 0.1GW in X-band and the peak power 1GW to 2GW in S-band.

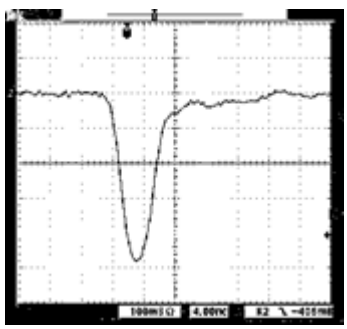

Figure 5: Output pulse envelope with switching in the mutual oversized side arm.

The packet of interference switches may combine parallel resonant cavities fed by different sources into a single high power compression system.

CONCLUSION

Thus, we demonstrated that microwave power can rapidly be extracted from a set of cavities through a packet of synchronized switches based on *H* tees. It was established that the commuting arms of the tee junctions should be strongly coupled to obtain complete synchronization. The limiting number of switches in the packet is proportional to the ratio of the cavity length to the small wall dimension of H- tee waveguide. Therefore, the use of a packet is most efficient for short microwaves at a specified cavity length. For example, according to estimates, in the case of X- band, power extraction through a packet containing five to seven switches can provide formation of pulses with a power up to 0.1 GW. In the 10_cm range, a system similar to the investigated one can generate 1 to 2GW pulses. A packet with single mode cavities and uncoupled commuting arms can be used to form nanosecond microwave pulses with a high repetition frequency. This packet can also be used to increase the pulse energy of resonant microwave compressors with large accumulating volumes, fed from different sources and coupled via a packet.

REFERENCES

[1] R A. Alvarez et al., Rev. Sci. Instrum. 57 (1986) 2475.
[2] A. Gorbachev et al., Tech. Phys. Letters 24 (1998) 791.
[3] A. Vikharev et al., Radiophysics and Quantum Electronics 51 (2008) 597.
[4] V. Avgustinovich et al., Tech. Phys. Letters 39 (2013) 492.
[5] V. Avgustinovich et al., Tech. Phys. Letters 45 (2000) 1475.
[6] S. Artemenko et al., Tech. Phys. Letters 39 (2013) 1014.

ISBN 978-3-95450-170-0

THE UTILIZATION OF STANDARD DC ACCELERATOR ELV FOR THE TOMOGRAPHY

N.K. Kuksanov, R.A. Salimov, P.I.Nemytov, S.N. Fadeev, E.V. Domarov, K.A. Bryazgin, D.A. Kogut, Budker INP, Novosibirsk, Russia

Abstract

ELV accelerators have been developed at the Institute of Nuclear Physics, Siberian Branch of the Russian Academy of Sciences and occupy a special place in the spectrum of the equipment produced by the Institute. These machines are widely used for radiation modification of polymers and worked well in a variety of processes in many countries of the Eurasian continent. Using serial ELV accelerators for industrial tomography opens up new possibilities for industrial technologies. This increases the requirements on the stability parameters of the injected electron beam.

The article formulates the requirements for electron accelerator ELV for tomographic studies, pulsation energy and beam current. Described Schottky effect affects to the shape and size of the ripple current, and the method for increasing the stability of the beam parameters. These machines are unified with conventional accelerators ELV and expand the scope of their utilization.

INTRODUCTION

Budker Institute of Nuclear Physics of the Siberian Branch of Russian Academy of Sciences is one of the world leaders in the development, design, production and delivery to the industry of electron accelerators based on high-voltage rectifier, covering the energy range from 0.3 to 2.5 MeV, maximum beam power for separate machines from 20 to 100 kW and maximum beam current up to 100 mA. These properties, as well as compact dimensions and high operational qualities have allowed BINP take a leading position in the market of industrial accelerators, both in Russia and abroad. But if the application of ELV accelerators for radiation modification of materials is related with ensuring the required level of uniformity of the radiation dose [1], the use of ELV accelerators for the tasks of industrial tomography is associated with the need to fulfill the following requirements on the parameters of the injected beam:

- energy pulsing at the level E = 1,0 MeV ≤±5%;
- current ripple at the level Ibeam = 100 mA ≤±2%.

These conditions were formulated as a result of a number of experiments on the industrial 100-kW accelerator of the ELV type, whose special features are the high electron energy (1.4 MeV) and the possibility of extracting the focused electron beam directly into atmosphere.

The Design of the Accelerator

To conform to these requirements and to take to account specific requirements of design, ELV4-based accelerator has been developed (Figure 1).

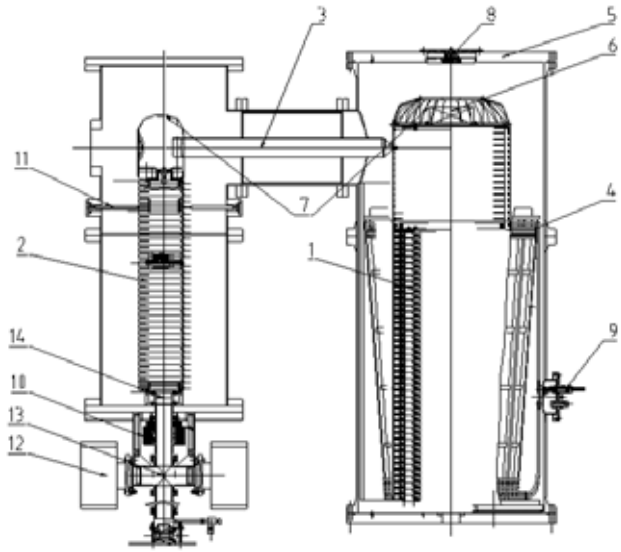

Figure 1: Common design of accelerator: Common design of accelerator: 1 - column rectifying sections; 2 - accelerating tube; 3 - gas feeder; 4 - the primary winding; 5 - the case of the pressure vessel; 6 -block injector control; 7, high voltage electrodes; 8 - the optical elements of the beam current control system; 9 entries of the primary winding; 10 - lens; 11 - supports to support tube; 12 - ion pump vacuum system; 13 - docking port of the vacuum system; 14 - bellows for fixing the accelerating tube.

Energy Pulsing

To reduce the energy pulsing, the series of experiments was carried out on a standard accelerator ELV-4. Energy was measured by the sensor circuit shown on Figure 2.

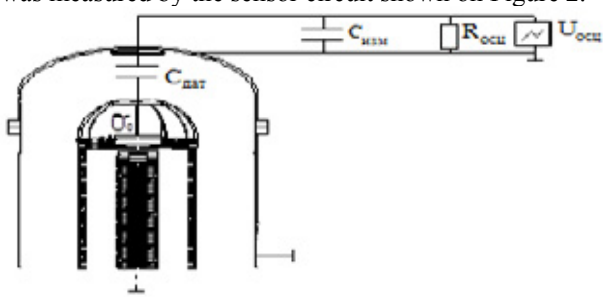

Figure 2: Sensor circuit for measuring pulsation energy.

The pulsing of energy measured by this sensor and the spectral decomposition of the signal is shown in Figure 3.

It shows three distinct peaks:

ISBN 978-3-95450-170-0

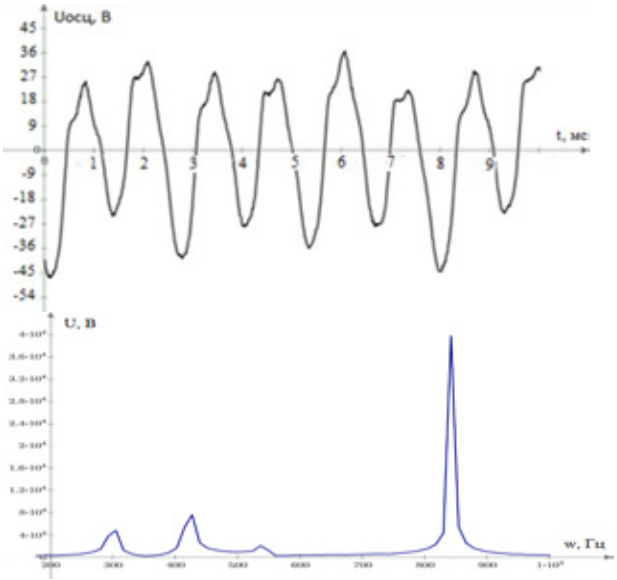

Figure 3: Waveform pulses with energy(up) and the spectrum of the signal pulses(down), E = 1 MeV IBeam = 100 mA.

- The peak frequency of 300 Hz is due to ripple voltage mains rectifier inverter. At the input of the inverter is installed six-phase rectifier with the filter capacitance $C_ф$. Ripple voltage of the rectifier with a frequency of 300 Hz will contribute to accelerating voltage ripple. Increasing the filter capacitance at the input of the frequency converter giving energy to further reduce ripple of ± 5% when a beam current of 100 mA at an energy of 1 MeV (Figure 4).

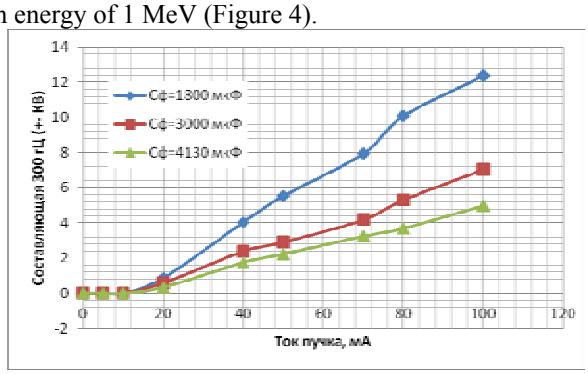

Figure 4: 300 Hz ripple component at different $C_ф$ depending on the beam current

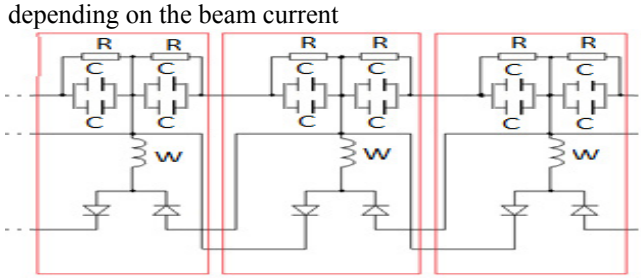

Figure 5: Series-parallel circuit connection rectifying sections.

- peak at a frequency of 840 hertz (main) is due to a full-wave mode of operation of high-voltage rectifier. Using an electric circuit with a series-parallel connection rectifying sections (Fig.5), allowing to limit the ripple HV column.
- third peak has a frequency of 420 Hz voltage. His appearance associated with fact that capacitors rectifying sections in different half-lives are fed from different windings. The voltage distribution on the secondary windings is not entirely uniform, it slightly decreases from the center of the column to its upper end. Therefore the half cycle when the capacitors are charged from the upper winding, they get smaller charge and, conversely, when charged from an underlying winding, produced a larger amount, i.e. appears with frequency ripple voltage.

Current Pulsing and Schottky Effect

Measurement beam current ripple produced by a special discharge device used for generating x-rays radiation, which fully absorbs the electron beam (Figure 7).

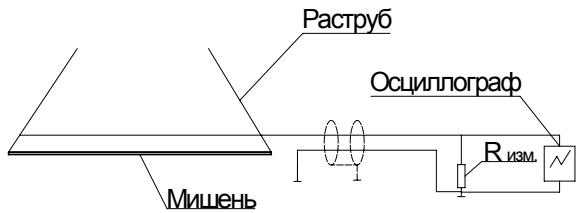

Figure 7: Scheme of the measurement current ripple.

Measurements of beam current showed the presence of pulsations correlated with the ripple voltage on the upper rectifying sections. Schottky effect is that when the electric field around the cathode current changes its saturation. If the electric field will have a variable component, the saturation current will also pulsate with the same frequency. Figure 8 shows the appearance of the variable component of the electric field near the cathode in the accelerator.

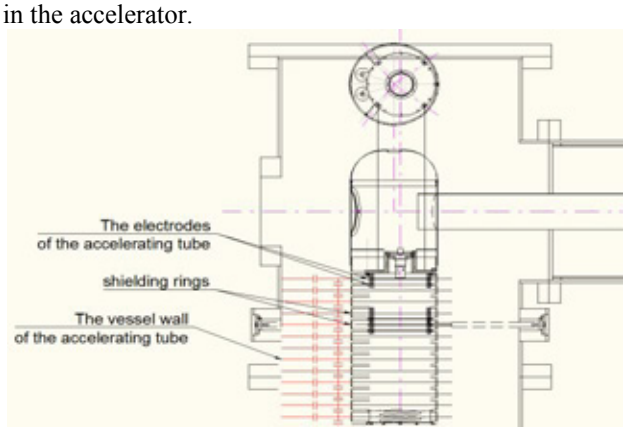

Figure 8: The upper part of the accelerator.

All capacitance shown in Fig. 8 form a complex capacitive divider, so there is a variable voltage component in the capacitance between the cathode and the first electrode to the accelerating tube. Increasing the capacitance (Fig. 9) causing it to fall the value of the variable component, thereby reducing the pulsation of the beam current.

ISBN 978-3-95450-170-0

The table 1 shows the results of measurements of different plug to the electrodes of the tube containers, where 30 pF is standard capacitance between the electrodes without additional connections.

Figure 9: Modified accelerating tube.

As a result, has reduced volatility in energy of up to ± 5% at a beam current of 100 mA. To reduce the ripple current the additional capacity were placed in parallel the divider resistances of tube. It reduces the instability of current to ± 0.14%.

Figure 10: Assembled accelerator for tomography.

CURRENT STATUS

Currently the accelerator for industrial tomography has been assembled at the customer's site and is subjected to adjustment tests (Fig. 10).

ELV accelerators continuously adapted for use in a variety of processes of radiation in industry and can be used for research into and development of new techniques and materials by electron irradiation.

Table 1.The dependence of the pulsation energy and beam current from the interelectrode capacitance.

The capacitance between electrodes	30 pF	310 pF	590 pF
Ripple of the beam current	± 6%	± 1.3%	± 0.8%
Pulsation of the electric field near the cathode	± 21%	± 1.2%	± 0.7%
$(\frac{\delta I}{I})/(\frac{\delta E}{E})$	0,29	1,08	1,14

REFERENCES

[1] N. Kuksanov, S. Fadeev, Y. Golubenko, D. Kogut et al, «High Power ELV Accelerators for Industries Application» // Proceeding of RuPAC-2010, Protvino, Russia, 2010

[2] S. Fadeev, Salimov R., et al, "Underbeam equipment to expand technological capabilities ELV accelerators", Proceedings of the X International Workshop on the Application of Charged Particle Accelerators in industry and medicine, St. Petersburg, October 1-4, 2001. 68. See also Bulletin "Radteh - Eurasia", Novosibirsk, 2002. p. 8.

[3] N. Kuksanov, S. Fadeev, et al, BINP SB RAS, Novosibirsk, “The development of the model range and the improvement of the performance accelerators”, VANT №3 March 2012, p. 15 (1996); http://vant.kipt.kharkov.ua

ISBN 978-3-95450-170-0

STUDYING OF THE ACCOMPANYING CHARGED PARTICLES IN THE TANDEM ACCELERATOR WITH VACUUM INSULATION*

D. Kasatov, A. Makarov#, I. Shchudlo, S. Taskaev,
Budker Institute of Nuclear Physics, Novosibirsk, Russia

Abstract

On the tandem accelerator with vacuum insulation in a steady long mode it was obtained 1.6 mA current of protons with 2 MeV energy. It was studied the one of the possible reasons of current limitation – the appearance of accompanying charged particles during acceleration of the ion beam.

The paper presents and discusses the results of the accompanying beam measurement using a special detector. The detector registered an opposite positive current in the range of 80-170 μA, which is directly dependent on vacuum conditions in the accelerator. Also it was measured the dependence of the dose rate on the total current in the accelerating gap. These measurements confirmed that injected H^- beam ionizes residual and stripping gas mainly in the area before the first electrode and two proposals were made to minimize the accompanying current.

INTRODUCTION

Presently, Boron Neutron Capture Therapy (BNCT) is considered to be a promising method for the selective treatment of malignant tumours [1]. The results of clinical trials, which were carried out using nuclear reactors as neutron sources, showed the possibility of treating brain glioblastoma and metastasizing melanoma incurable by other methods. The broad implementation of the BNCT in clinics requires compact inexpensive sources of epithermal neutrons. At BINP the source of epithermal neutrons based on Vacuum Insulation Tandem Accelerator (VITA) and neutron generation through $^7Li(p,n)^7Be$ reaction was proposed [2] and launched [3,4].

For providing BNCT it is required a high flux of epithermal neutrons which is dependent on proton current and energy. Now on VITA it is obtained 1.6 mA current of protons with 2 MeV energy in a steady long mode [5]. These parameters are sufficient for *in vitro* [6] and *in vivo* studies, but not enough for treating people. In this work it was investigated the one of the possible reasons of current limitation – the appearance of accompanying charged particles in the accelerating channel. There were proposed several origins of these spurious particles: ionization of the residual gas, ionization of the stripping gas in the accelerating channel and positive argon ions coming out of the charge-exchange target.

* Work is financially supported by the Russia through the Ministry of Education and Science of Russia (project RFMEFI60414X0066)
# A.N.Makarov@inp.nsk.su

EXPERIMENTAL SETUP

In order to register and measure the accompanying current the special detector was constructed and installed in the input flange of the accelerator tank. It is mounted in such a way that H^- particles can not reach it, and only positive particles that are going from the opposite direction to H^- beam can hit the detector (Fig. 1).

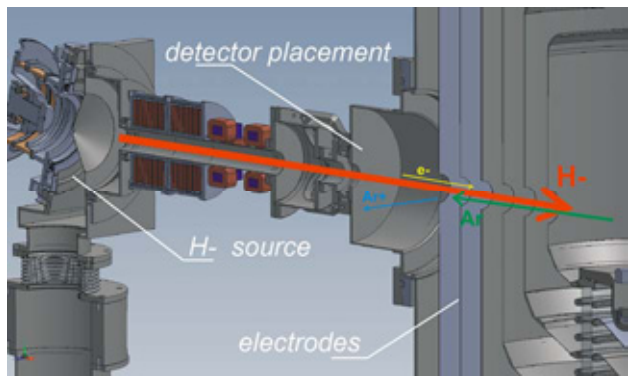

Figure 1: Placement of the argon detector.

The choice of this location for the detector is made due to previously registered modification of the surface of rotating diaphragm, which was mounted in the input flange of the accelerator tank. During the planned disassembly of the accelerator it was found the distinct imprint on the diaphragm presumably left by outgoing positive beam. Surface modification of the imprint was confirmed by scanning electron microscope Jeol JCM-5700 and energy dispersive X-ray analyzer of elemental composition IncaEnergy.

The detector consists of two insulated rings (with diameters 52 – 90 mm and 92 – 138 mm) surrounding the beam transporting channel and covered with suppressing grid under -40 V potential (Fig. 2). For convenience the square of the inner disk is twice as much as the aperture square; the square of the outer disk is twice as much as the inner disk square.

MEASUREMENTS

Fig. 3 shows that the positive current in the range of 80-170 μA measured by the detector is a direct function of the vacuum conditions in the accelerator. It can be seen that once the gate of the cryogenic pump was opened (1400 s) – the positive argon current has immediately decreased by 5 times and no breakdowns happened after that. In the same time the output proton current stayed almost unchanged. It can also be seen that argon current

ISBN 978-3-95450-170-0

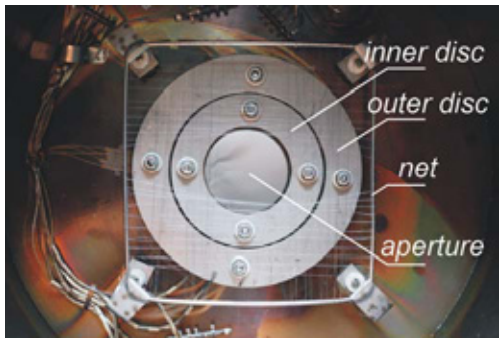

Figure 2: Photo of the argon detector mounted in the input flange of the accelerator tank.

depends very little on argon puffing in the stripping target. This means that argon is ionized mainly in the accelerating gaps, producing an opposite Ar^+ beam and an electron beam (which is accelerated toward the central electrode, causing intense braking radiation production).

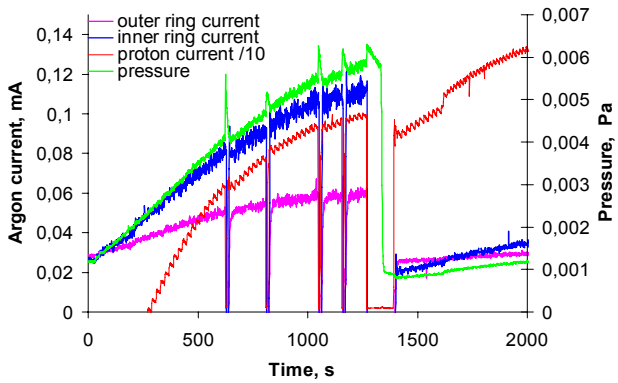

Figure 3: The time dependence of the argon current, proton current (divided to 10 for convenience) and vacuum conditions.

Fig. 4 shows that the increase in argon puffing leads to an increase in current in the accelerating gap and increase of the braking radiation (Bremsstrahlung). Measurements were made without cryogenic pump. Approximation the graph to zero gives the value of the input current, excluding the impact of residual gas.

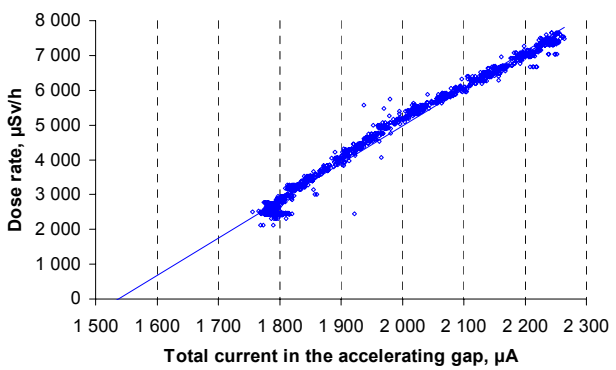

Figure 4: The dependence of the dose rate on the total current in the accelerating gap.

CONCLUSIONS

It is confirmed that injected H^- beam ionizes residual and stripping gas mainly in the area before the first electrode. In this area electrons are born and accelerated to the full voltage of 1 MV and absorbed by construction materials leading to significant braking radiation emission [7]. At the same time positive argon ions are born and accelerated in the opposite direction. They were registered by the special argon detector mounted on inlet flange of the accelerator. The magnitude of the current of accompanying charged particles reaches 25 % of the current of the accelerated ion beam. Probably, it is the presence of a beam of charged particles in the accelerating gap that limits high voltage reliability of the gap and does not allow increasing of the proton beam current.

To reduce the flow of charged particles and to improve the vacuum conditions, two solutions are proposed.

The first proposal is to install a cooling aperture and to use a cryogenic pump at the input of the accelerator. This will allow reducing significantly the gas flow from the ion source to an accelerating gap.

The second proposal is to reduce the gas flow to the accelerating gap from the gas stripping target. It is proposed to tilt the stripping target, to place permanent magnets in the space between the target and the input aperture of the high voltage electrode [8] and to put the turbo molecular pump inside the high-voltage electrode. This will make it possible not only to reduce the gas flow into the accelerating gap, but also to reduce the ultraviolet radiation and suppress the flow of positive argon ions from weakly ionized plasma inside the stripping tube.

REFERENCES

[1] Neutron Capture Therapy: Principles and Applications. Eds.: W. Sauerwein, A. Wittig, R. Moss, Y. Nakagawa. Springer, 2012, 533 p.
[2] B. Bayanov, et al., NIM A 413 (1998) 397.
[3] A. Kuznetsov, et al., Tech. Phys. Lett. 35 (2009) 346.
[4] A. Kuznetsov, et al., NIM A 606 (2009) 238.
[5] D. Kasatov, et al., "Obtaining of 2 MeV 1.6 mA proton beam on a tandem accelerator with vacuum insulation", JINST (2014).
[6] L. Mostovich, et al., Bulletin of Experimental Biology and Medicine 151 (2011) 264.
[7] D. Kasatov, A. Makarov, I. Shchudlo, S. Taskaev, "Measurement of the spatial distribution of gamma radiation on accelerator-tandem with vacuum insulation", these proceedings.
[8] A. Makarov, Yu. Ostreinov, S. Taskaev, P. Vobly, "Modification of the argon stripping target of the tandem accelerator", these proceedings.

ISBN 978-3-95450-170-0

DEVELOPMENT OF THE INJECTOR FOR VACUUM INSULATED TANDEM ACCELERATOR

A. Kuznetsov, A. Ivanov, A. Koshkarev, D. Kasatov, M. Tiunov, BINP SB RAS, Novosibirsk, Russia

Abstract

The new beam injector of negative hydrogen ions was designed for modernization of the epithermal neutron source based on the tandem accelerator with vacuum insulation. The parameters of the ion source used in the injector construction allow one to increase the H^- current from 5 mA to 15 mA. Preliminary acceleration of the injecting beam can provide more reliable operation of the facility when changing the parameters of the injecting beam or the tandem accelerator voltage. Realization of this injector will make the next step towards the creation of a compact source of epithermal neutrons for boron neutron capture therapy of malignant tumors in clinics. The paper presents the injector design and computer simulations of the beam transportation.

INTRODUCTION

The tandem accelerator with vacuum insulation of electrodes (VITA) [1, 2] built at BINP is designed specifically for the development of the AB-BNCT concept [3]. The epithermal neutrons generation reaction is $^7Li(p,n)^7Be$, and the estimated proton current for minimal therapeutic neutron flux should be higher than 3 mA @ 2.5 MeV energy [4] meanwhile about 10 mA required for comfortable BNCT treatment.

The VITA facility design is shown at Fig. 1. The particles acceleration takes place in two stages in a tandem accelerator. At the first stage the negative hydrogen ions are accelerated by the high voltage electrode potential to the half of required energy, and then the ions meet the gas stripping target to be converted into protons and accelerated again by the same potential to the full beam energy. Several innovative ideas were realized in the accelerator design to allow for stable acceleration of intense beam in a compact facility.

The initial ion beam is produced by the injector composed of the ion source, low energy beam line and magnetic elements providing focusing and correction of the beam. Series of investigations have revealed the limitations of injecting current. The main problems are the ions loss due to high residual gas concentration and the ability of the stripping gas to rich the injector and corrupt the stability of the ion source [4]. To provide a reliable H- beam for clinical application of the facility the new injector is designed. The paper presents the design scheme of the injector and the results of calculations performed.

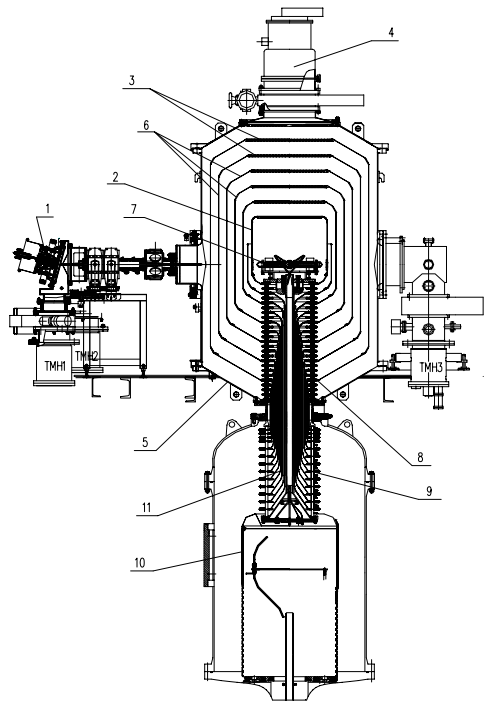

Figure 1: Scheme of the VITA facility. 1–ion source (H^-); 2 – high voltage electrode; 3 – electrode shutters; 4 – cryo pump; 5 – accelerator vacuum volume; 6 – intermediate electrodes; 7 – stripping target; 8 – feedthrough insulator (vacuum part); 9 – feedthrough insulator (gas part); 10 – high voltage source; 11 – coaxial feeding tubes.

EXISTING INJECTOR CONSTRUCTION

The scheme of the existing injector is shown at Fig. 2. The surface-plasma ion source with Penning discharge and with hollow cathode is used to generate the beam of negative hydrogen ions with the energy of 21 keV and the current up to 5 mA. The output aperture of the ion source has the diameter of 3 mm and the beam angular divergence is about ±100 mrad. The magnet required for Penning discharge turns the beam to the angle of 15°, and the cone diaphragm passes the axial part of the beam into the transport channel through the aperture with 28 mm diameter. Then the beam is focused by two magnetic solenoids and directed to the accelerator through the beam diagnostics chamber. The beam transport channel is a long tube with 50 mm diameter that limits the pumping speed significantly and does not provide the appropriate vacuum level resulting in up to 50% of generated ions loss due to interaction with the residual gas.

ISBN 978-3-95450-170-0

In addition, the is a back streaming of the stripping gas ionized by the H^- beam and accelerated to an energy of 1 MeV. A strong electrostatic input lens of the accelerator makes the beam transportation to be very sensitive to the range of parameters: the alignment of the magnetic elements of the low-energy beam line, the adjustment of the accelerating voltage and H^- beam parameters.

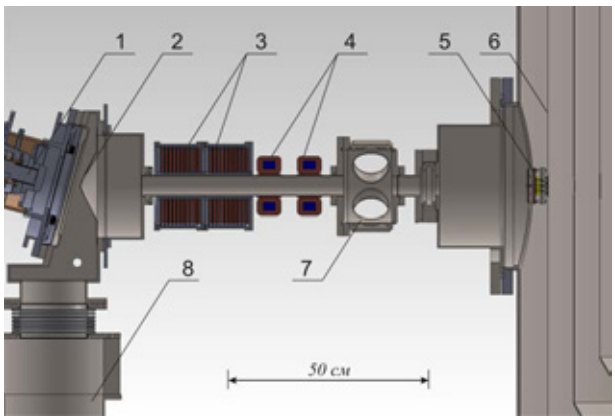

Figure 2: The scheme of existing injector: 1 – H^- ion source; 2 – cone diaphragm; 3 – focusing solenoids; 4 – magnetic beam corrector; 5 – beam aperture; 6 – first accelerator electrode; 7 – beam diagnostics; 8 – turbomolecular pump.

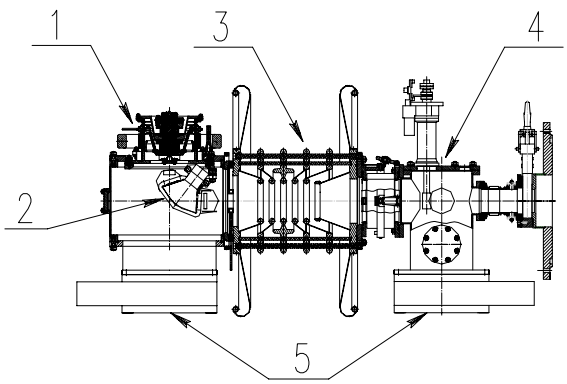

Figure 3: The new injector for BNCT facility: 1 –H^- ion source; 2 – bending and focusing magnet; 3 – accelerating tube; 4 – beam diagnostics; 5 – valves for turbomolecular pumps.

PROPOSED INJECTOR CONSTRUCTION

To raise the injecting current and to improve the beam quality the new injector is proposed and designed. The scheme of the injector is presented at Fig. 3.

The construction implements the new ion source with the current increased up to 15 мА [5-7]. The bending magnet is placed inside the vacuum chamber to direct the beam into the electrostatic tube for preliminary acceleration. The magnet is designed to provide additional beam focusing and ensure axially symmetric round beam profile in the output (Fig. 4). The vacuum chamber has several inputs and windows to hold the beam probes and to improve the construction elements adjustment using a laser. To provide high vacuum level and to reduce particle loss the turbomolecular pump of 3000 l/s pumping speed is used. The acceleration tube and diagnostic chamber are pumped by separate pump with the same pumping speed.

The ion source with vacuum chamber and the cabinet with power supply and control electronics are placed on the isolated platform with Faraday cage. This platform can be at high potential while being supplied by an external power source. With the preliminary acceleration the injector can produce the beam of 120-200 keV energy that provides more stable operations with adjustable accelerator voltage and beam parameters.

The trajectories simulation made by MAGEL code proves the effective transportation of the beam through the acceleration system (Fig. 5, 6).

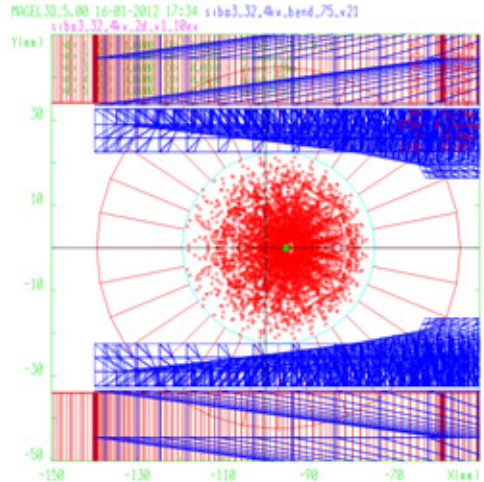

Figure 4: Beam profile at the bending magnet exit.

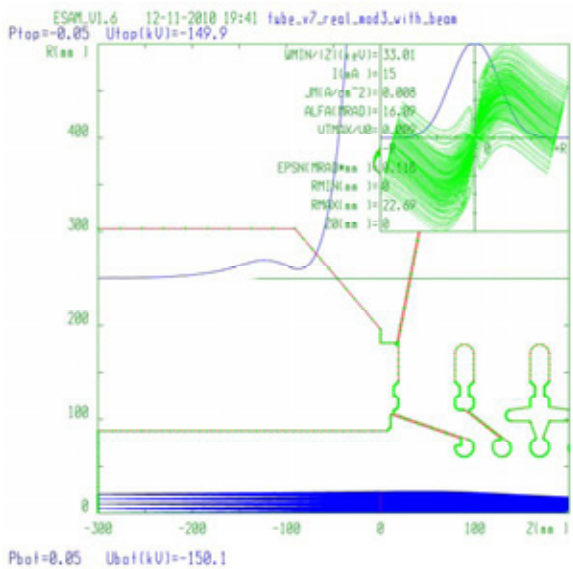

Figure 5: The ion beam transportation through the pre-acceleration tube.

ISBN 978-3-95450-170-0

a)

b)

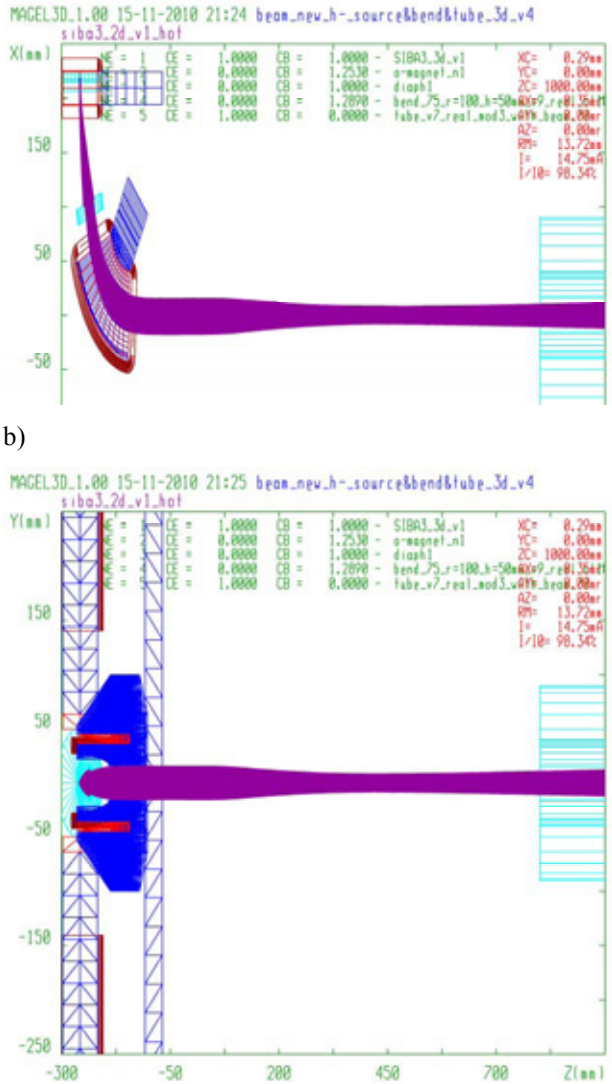

Figure 6: The ion beam transportation through the low energy beam line, 1-st stage of tandem acceleration and stripping target.

SUMMARY

The new injector was developed to modernize the epithermal neutron source based on the Vacuum Insulated Tandem Accelerator. This injector designed to produce H^- beam of 15 mA current and energy of 120-200 keV. Better vacuum condition, more stable operation and effective beam transportation provide the ability to generate high power proton beam with VITA and create compact facility for clinical AB-BNCT.

Applied research is carrying out with the financial support of the Russian Federation represented by the Ministry of Education and Science of Russia (unique identifier RFMEFI60414X0066).

REFERENCES

[1] V. Aleynik, A. Bashkirtsev, et al., Current progress and future prospects of the VITA based neutron source. Applied Radiation and Isotopes 88 (2014) 177-179.

[2] B.F.Bayanov, V.P.Belov, et al. Accelerator based neutron source for the neutron-capture and fast neutron therapy at hospital. Nuclear Instr. and Methods in Physics Research A 413/2-3 (1998) 397-426.

[3] Wolfgang A. G. Sauerwein et al., Neutron Capture Therapy Principles and Applications. Springer-Verlag Berlin Heidelberg 2012; DOI: 10.1007/978-3-642-31334-9

[4] A.Kuznetsov, V.Aleynik, et al., Raising the generating current in the VITA neutron source for BNCT. 4 International Particle Accelerator Conference, 12-14 May 2013, Shanghai, China, p. 3693-3695.

[5] Yu. Belchenko, A. Sanin, and A. Ivanov. A 15 mA CW H Source for Accelerators. AIP Conference Proceedings 1097, 214 (2009); doi: 10.1063/1.3112515

[6] Yu. I. Belchenko, A. I. Gorbovsky, et al. Upgrade of CW negative hydrogen ion source. AIP Conference Proceedings 1515, 448 (2013); doi: 10.1063/1.4792815

[7] Yu. I. Belchenko, A. I. Gorbovsky, et al. The 25 mA continuous-wave surface-plasma source of H ions. Review of Scientific Instruments 85, 02B108 (2014); doi: 10.1063/1.4828373

ISBN 978-3-95450-170-0

MODIFICATION OF THE ARGON STRIPPING TARGET OF THE TANDEM ACCELERATOR

A. Makarov, S. Taskaev, P. Vobly, Budker Institute of Nuclear Physics, Novosibirsk, Russia
Yu. Ostreinov, Novosibirsk State Technical University, Russia

Abstract

Presented work is aimed on modernization of the gas stripping target that is used in the Vacuum Insulated Tandem Accelerator (VITA) to recharge negative hydrogen ions into protons. The target construction was modernized to get higher efficiency of the beam transportation, suppressing gas flow into the acceleration channel, and to raise the current of the accelerated proton beam. The design of the modernized stripping target, the calculated data on the magnetic fields and particle trajectories are presented.

INTRODUCTION

The Vacuum Insulated Tandem Accelerator (VITA) was developed in the Budker Institute of Nuclear Physics [1] to produce epithermal neutrons for boron neutron capture therapy in the ^{7}Li(p,n)^{7}Be reaction. The parameters of the generated radiation allow us to carry out in vitro and in vivo investigations of BNCT. In present moment the modernization of the facility elements is carrying out to meet the parameters required for clinical usage.

The design of the VITA facility is shown at figure 1. The principle of the tandem accelerating scheme is accelerating of the negative hydrogen ions to the 1 MeV energy determined by the high voltage electrode potential, recharging the ions into protons in the gas stripping target and then accelerating to the 2 MeV energy by the same accelerating potential. Stripping target is made as a tube 16 mm in diameter and 400 mm long with the supply of the stripping gas (argon) in the middle (figure.2).

When studying the dependence of beam stripping on the argon pressure we have found an effect that can be explained by the appearance of the additional flow of positively charged ions of the stripping gas in accelerating channels. The interaction of the injected ion beam with the gas in the stripping target leads to ionization of the argon and to appearance of a low-ionized plasma with a positive potential. Under the influence of this potential part of positive argon ions comes out of the stripping target, enters into the acceleration channel where it is accelerated. This effect causes an additional load of power source, deterioration of the high-voltage strength in the vacuum gap and limiting of the proton beam current.

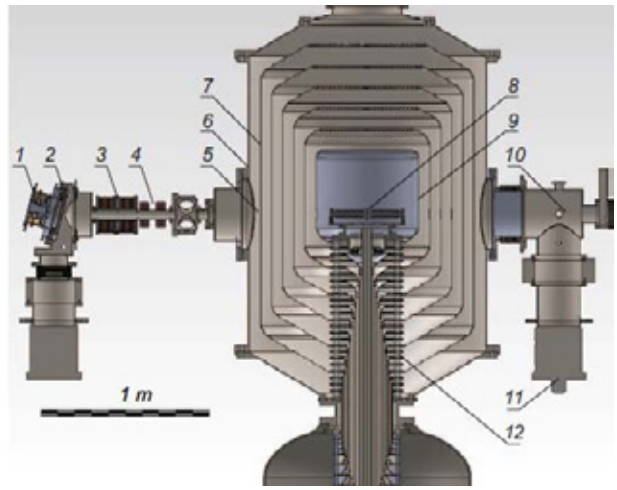

Figure 1: High-current vacuum insulation tandem accelerator. 1—H ion source, 2—diaphragm, 3—magnetic lenses, 4—corrector, 5—a temporary location of thebeam detector, 6—accelerator, 7—electrodes, 8—stripper, 9—high voltage electrode,10—high energy beam transport, 11—turbo molecular pumps, 12—insulator.

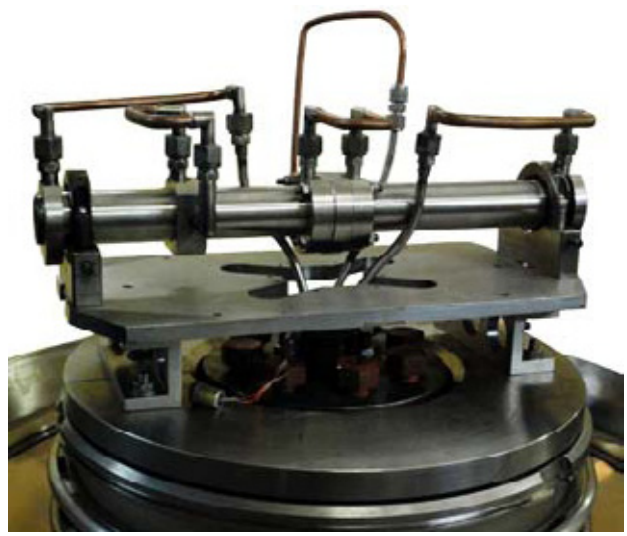

Figure 2: Ø16-mm stripping target placed on the feedthrough insulator.

ISBN 978-3-95450-170-0

TARGET CONSTRUCTION

Suppression of the ion flux of the stripping gas is proposed using a magnetic field applied in the region between the stripping target and the apertures in the high-voltage electrode. The idea of the target modification is the following. Inside the high-voltage electrode just behind inlet aperture it is proposed to apply 0.4 T magnetic field using a two-pole permanent magnets (NdFeB). In this field is performed rotation at a small angle of the injected beam of negative hydrogen ions. Similar magnets at the exit of the stripping target return proton beam back to the axis of accelerator channel.

In this geometry not only significant suppression of ion penetration of the stripping gas into the accelerating channel can be achieved, but also a significant improvement of vacuum conditions in the accelerating channel and reduction of the ultraviolet radiation from the plasma in the stripping target. Stripping target modification scheme is shown in Figure 3.

COMPUTER SIMULATION

Simulation of the considered system is executed in a software package COMSOL Multiphysics. The first step was to obtain distribution and value of the magnetic fields for proposed construction. Maximum value of the field in the magnet's gap was 0.35 T, the value of the field penetrating into the stripping target is insignificant and it doesn't influence on the beam angular divergence. The field distribution along the beam trajectory is shown in Figure 4.

The second step was the calculation of the beam's trajectory and its the cross profile change. Transverse displacement of the beam after passing through the dipole magnets was 74 mm (Figure 5.). Desired rotation angle of the target was 8 degrees. Beam passage in the dipole magnet field is accompanied by focusing on one coordinate, and defocusing in the other. In the simulation, it is assumed that the initial beam is flat and parallel to that with good accuracy correspond to reality[1]. The beam profile produced at the output of the second magnet is shown in Figure 6.

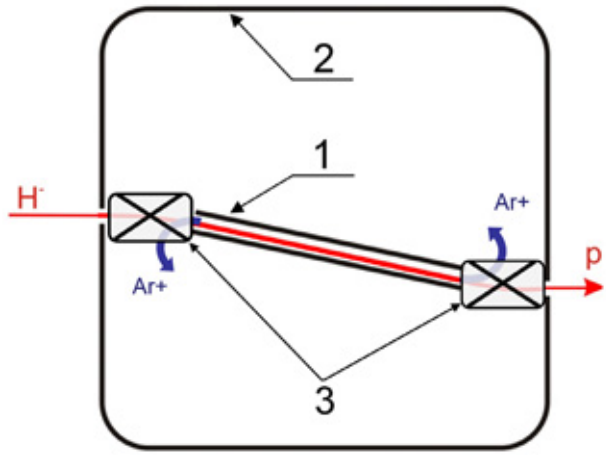

Figure 3: Concept of rotated stripping target with a magnetic field. 1–Stripping target; 2–Central electrode; 3–Permanent magnet.

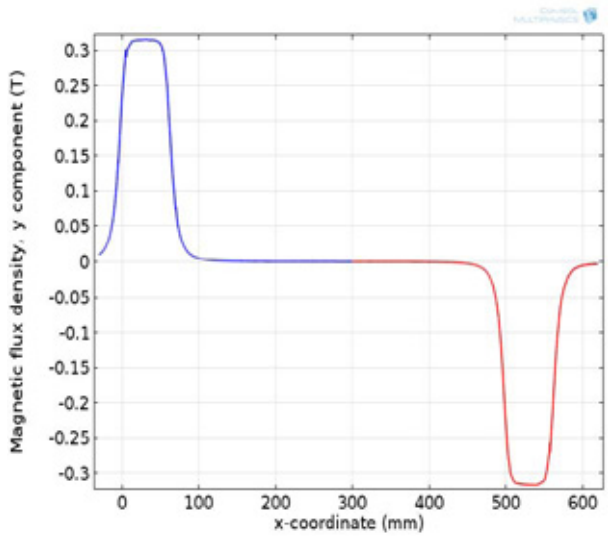

Figure 4: Transverse component of the magnetic flux density along the beam trajectory.

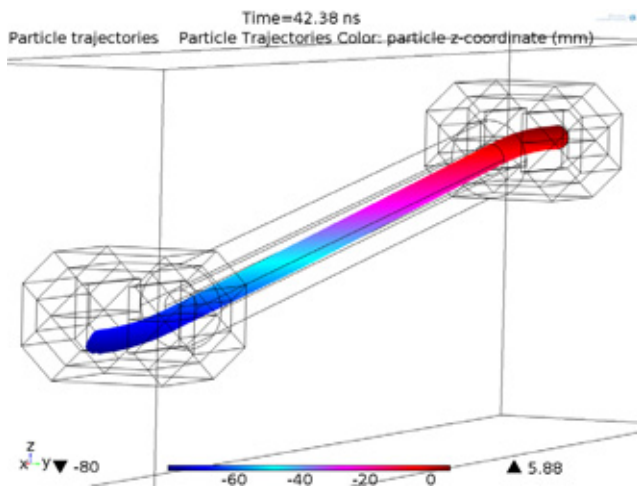

Figure 5: Results of particle trajectories calculations.

ISBN 978-3-95450-170-0

SUMMARY

To provide recharging of the negative hydrogen ions to protons in the Vacuum Insulated Tandem Accelerator the stripping target is used, that is an oil-cooled tube with length 400 mm and diameter 16 mm with gas injection in the middle of the tube.

In the paper the calculated data on the beam components and current in dependence on the linear target density was presented alone with the experimental results on output current measuring in dependence on the gas flow rate. The method of regulation of the gas flow rate using the residual pressure measurements to get the required negative hydrogen ions recharging is tested. All experimental measurements are in good agreement with calculations. The residual pressure in the accelerating channel is estimated.

The study was performed by a grant from the Russian Science Foundation (Project No.14-32-00006) with support from the Budker Institute of Nuclear Physics.

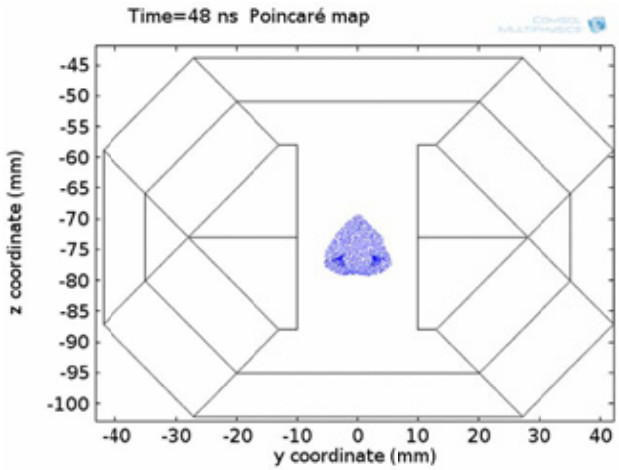

Figure 6: Cross-section of beam after passing through the magnetic system.

REFERENCES

[1] A.S. Kuznetsov, V.I. Aleynik, I.M. Shchudlo, I.N. Sorokin, S.Yu. Taskaev, M.A. Tiunov. Calibration Testing of the Stripping Target of the Vacuum Insulated Tandem Accelerator. Proceedings of XXIII Russian Particle Accelerator Conference RUPAC2012, September, 24 - 28, 2012, Saint-Petersburg, Russia, p. 560-562.

ISBN 978-3-95450-170-0

FIRST RESULTS OF EXPERIMENTS WITH THE EXTRACTED CARBON BEAM AT THE U-70 ACCELERATOR

G. Britvich , S. Gorokhov, N. Ivanova, V. Kalinin, M. Kostin, A. Koshelev, A. Lukyantsev, S. Makonin, A. Matyushin, A. Maximov, V. Milyutkin, A. Ostankov , V. Pikalov, M. Polkovnikov, V. Seleznev, A. Sotnikov, IHEP, Moscow Region, Russia
E. Beketov, S. Koryakin, A. Lychagin, M. Troshina, S. Ulyanenko, MRRC, Obninsk, Russia

Abstract

The scheme of the C ions beam production with energy 455 MeV/nucleon from the U-70 accelerator was described briefly. The equipment facilities for the radiobiology experiments were shown. Experimental parameters of the carbon beam were described. The first experimental results were shown.

INTRODUCTION

Carbon beam program at IHEP has been started at 2001. The goal is to create an Ion beam therapy Center.
Project state. For today we have finished:
- Laser based carbon ions source;
- Acceleration of carbon ions in the I-100 linac;
- Transfer line between I-100 and U-1.5 booster;
- Modernization of U-1.5 and U-70 equipment;
- Stable acceleration of carbon ions in U-1.5 and U-70;
- Slow extraction of the carbon beam from U-70 with parameters appropriate for the medical practice;
- U-70 biological shielding was modified to build radiobiological extraction line (Channel #25) in the experimental hall;
- Magnetic elements for the head part of the Channel #25 mounting (four dipoles and four quadrupoles);
- Slow extraction of the carbon beam with 450 MeV/A energy into the temporary radiobiological setup (VRBS) at the Channel #25;
- Three runs of the VRBS with the carbon beam at 450 MeV/A.

Carbon ions are accelerated up to the 450 MeV/A in U-1.5 booster, and then are transferred into the U-70 synchrotron. Carbon beam is not accelerated in the U-70. Carbon ions are collected in the U-70 and then are transferred by means of slow extraction scheme into the VRBS region.

Parameters of the extracted carbon beam and background conditions were measured, and VRBS was qualified for the radiobiological studies.

EXPERIMENTS WITH EXTRACTED CARBON BEAM

Experimental studies with extracted carbon beam at VRBS were done during three last runs of U-70. Water phantom with 3D system of detector movement. This phantom is installed in the VRBS zone. It has 15 mm thick side walls and 30 mm front wall made from polycarbonate.

Bragg peak position was measured in this phantom by means of:
- Clinical dosimeter with natural diamond detector;
- Clinical dosimeter with TM-30013 ionization chamber with graphite walls;
- Radiochromic film Gafchromic EBT3.

Thin ionization chambers were used to measure intensity of the extracted carbon beam. These chambers were designed and produced at IHEP. Chamber with 200x200 mm2 cross-section was used for general beam intensity measurements. To measure transversal distribution of the extracted beam density 2D multicellular chamber was used. One cell has 1x1 cm2 size, number of cells is 64 (8x8) wall.

Ionization chambers were calibrated with activation detectors data. Pure carbon discs 40 mm in diameter and 5 mm thickness were used as activation detectors. Detectors were placed on the flange of OM-1 magnet in between OM-1 and OM2 magnets. Measurements data are shown in Table 1.

Table 1: Activation detectors calibration

Date	Particles	Cycling	Intensity by cycle
30.03.2014	Proton E=1,3 GeV	7	$1{,}9\times10^{10}$
04.04.2014	Proton E=1,3 GeV	7	$1{,}3\times10^{10}$
04.04.2014	Carbon E=455 MeV/nucleon	7	$4{,}5\times10^{8}$
21.04.2014	Carbon E=455 MeV/nucleon	7	$1{,}5\times10^{9}$

Extracted beam composition was studied. For this goal detecting setup was combined from three 1 mm thick and 1 cm2 square scintillation detectors, dE/dx ion-implanted Si detector with 450 um thickness and 1 cm2 square, and full absorption BGO detector. Time-of-flight, amplitude analysis and 2D amplitude analysis methods were used. As a result of measurements it was found that extracted carbon beam at VRBS has 11% of admixtures, which corresponds to the amount of matter crossed by beam upstream of the VRBS.

ISBN 978-3-95450-170-0

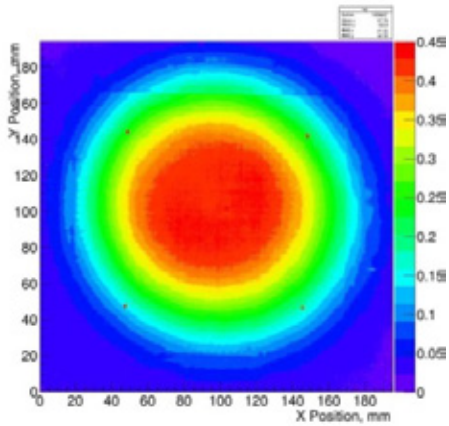

Figure 1: Dose distribution measured around the irradiation point.

For the radiobiological studies one needs to have heterogeneity of the carbon field not worse than 5% in the VRBS region. Method of the longitudinal transversely flat paraxial dose field production was developed for this. Carbon ions beam was slowly extracted during the lower plateau of the U-70 synchrotron magnetic field. Dose field is produced by compact electromechanical wobbler using rotating constant di-pole magnets. As a result we have got uniform irradiation field with diameter 60 mm for the first radiobiological experiments. Dose distributions around the irradiation point, measured by the radiochromic film Gafchromic EBT3, are shown in Fig.1.

Irradiation of the biological objects by carbon ions beam was performed. Culture of cells of the mouse melanoma B-16 was used as an experimental biological test-system. Cells were received from Moscow institute of medical ecology. Culture was cultivated in monolayer according by standard method and was irradiated in the late log-phase. Irradiation of the cells monolayer was done at a room temperature in vials totally filled with RPMI-1640 medium with addition of 2% of embryonic veal serum. There are three sets of irradiation were performed – through up to the Bragg peak ("on the cross"), in the Bragg peak and be-hind the Bragg peak. Positioning of the vials is shown in Fig. 2.

Doses of irradiation are shown in Table 2. Standard gamma-irradiation for the comparison was performed on the isotope gamma-setup "Luch" (Co60, E = 1.25 MeV) with dose rate 1.04 Gy/min. Residual clonogenic activity of cells was determined in standard way after irradiation. Experimental curves for "dose-effect" are shown in Fig. 3. Experimental data was approximated by the linear-quadratic model:

$$\log\left(\frac{1}{S}\right)=\alpha D+\beta D^2, \qquad (1)$$

where S is a fraction of survived cells, D – irradiation dose in Gy, α and β – coefficients equal to the probability of lethal damages in tracks of one or different particles.

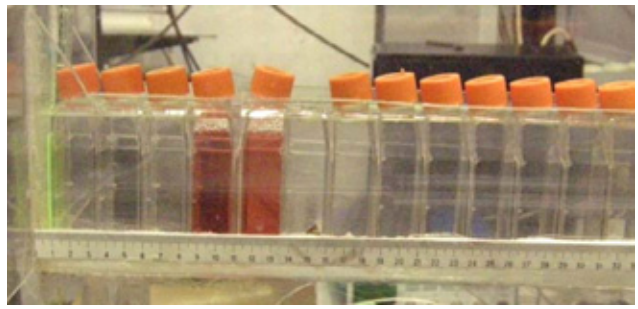

Figure 2: Irradiation of the vials with monolayer of melanoma B-16 in the region of the Bragg peak. First veal is sitting in the region of the peak, second – behind the peak. Beam is hitting from the right side.

Table 2: Radiation dose.

Namber	Dose , Gr	Errors	Cycling	Time
602	1,97	0,14	67	10 min.
603	1,53	0,11	52	6 min.
604	1,10	0,04	33	5 min.
605	0,54	0,04	14	2 min.
606	1,65	0,04	126	18 min.
607	2,55	0,07	133	19 min.
608	3,81	0,10	223	31 min.
609	5,05	0,15	251	33 min.

The coefficient of the relative biological effectiveness (RBE) was determined according to the level of 10% survival of cells:

$$\mathrm{RBE}=\frac{D_\gamma}{D_c}, \qquad (2)$$

where Dγ – dose of standard γ-irradiation, D_C – dose of the carbon beam irradiation. RBE value was calculated equal to 2.7 in the Bragg peak position and 1.7 at "on the cross" irradiation.

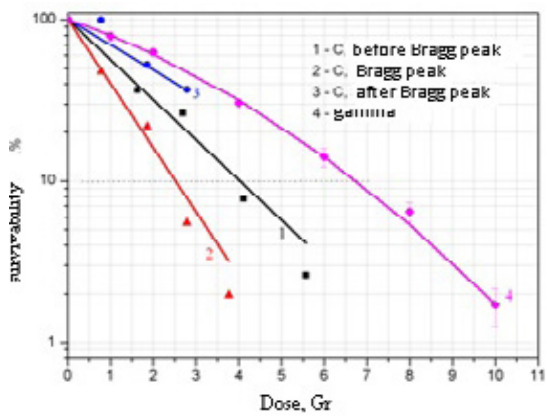

Figure 3: Survival probability curves for mouse melanoma cells B-16 after gamma-irradiation (4) and carbon irradiation (1 – 3).

ISBN 978-3-95450-170-0

Experimental date presented in the Fig. 3 does not contradict to the published date and support attraction of the carbon beams to goals of radiation therapy.

CONCLUSION

1. Carbon beam with parameters suitable for radio-biological studies was extractive into VRBS region.
2. Beam diagnostics equipment was tested.
3. Experimental data for the future development of wobbler magnet were obtained.
4. First irradiations of biological objects were performed.
5. Future development of dosimetry approaches is required.

ISBN 978-3-95450-170-0

EXPERIMENTAL STUDY OF THE TIME DEPENDENCE OF THE ACTIVITY OF DELAYED NEUTRONS IN THE FISSION OF ^{235}U BY NEUTRONS FROM THE REACTION ^{7}LI(P, N) ON THE ELECTROSTATIC ACCELERATOR EG-1

K.V. Mitrofanov, V.M. Piksaikin, A.S. Egorov, V.F. Mitrofanov, D.E. Gremyachkin, B.F. Samylin,
State Scientific Center of Russian Federation Institute of Physics and Power Engineering,
Obninsk, Russia

Abstract

In the present work the installation created on the basis of the accelerator EG-1 (IPPE) for the experimental studies of the time dependence of delayed neutron activity from neutron induced fission of ^{235}U is described. Measurements were carried out with neutron beam generated with the help of the ^{7}Li(p,n) reaction. The lower limit of the investigated time range was governed by the proton beam switching system that was 20 ms. It was shown that the temporary characteristics of delayed neutrons from the fission of ^{235}U by epithermal neutrons is consistent with the time dependence which at present is recommended as a standard. In case of the fast neutron induced fission of ^{235}U the measured decay curve of delayed neutrons shows excess of counting rate in the time interval 0.01-0.2 s as compared with the decay curve corresponding to the recommended data.

Experiment was carried out at the accelerator IPPE EG-1. Block scheme of the experimental setup is shown in Figure 1.

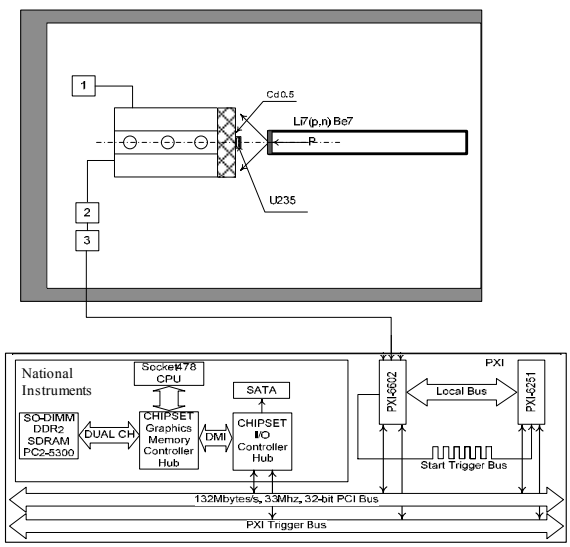

Figure 1: Block scheme of the experimental setup is performed on the basis of the system of accumulation of National Instruments. 1 – high voltage source; 2 – preamplifiers of signals from the counters SNM-18; 3 – summator of signals from the preamplifier of detector counters.

The neutron detector is an assembly of three counters SNM-18 (working gas: a mixture of 97% He-3 + 3% Ar. The pressure of 405 kPa) mounted in a polyethylene box. Signals from the counters SNM-18 received consistently to preamplifiers, amplifiers and conditioners. TTL signals received on the adder were formed at the output of the last, combined into a single digital stream of information transmitted by electronic analysis system and accumulation.

In this work, the neutron detector was set up, in which the effect of the distortion of the counting characteristics was absent at the initial time after irradiation session. In addition, the counting characteristics of the detector is not distorted even during irradiation intense beam of neutrons generated in the lithium target under the action of protons. The neutron source was a lithium target irradiated by a proton beam. The current in the experiment was 10 μA. The proton energy was 2.6 MeV.

There were two types of experiments. In the first experiment, the irradiated sample was placed on a side surface of a neutron detector. In a second experiment, a ^{235}U sample was placed in cadmium cover and a lead shield was placed between the detector and the sample. Obviously, in the first experiment, the neutron spectrum is significantly softer than the case of experiment №2, because the direct beam of the neutrons from the target is added the neutrons scattered by the material of the neutron detector. In the second experiment, a sample of ^{235}U is at a distance of 5 cm from the detector, and the scattered neutron at the detector are intensity absorbed by cadmium filter. Lead filter is designed to shield the detector from the possible detection of delayed gamma rays from the sample ^{235}U. A sample of ^{235}U is a metal disk of 3 mm thickness and 41 mm in diameter, located in a metal shell. Measurements in the experiments were carried out for two different irradiation times – 180 s and 15 s. The experimental method used in this experiment based on the cyclic irradiation of fissile samples in a neutron flux of Li(p,n) reaction and the measurement of the time dependence of the delayed neutron activity [2].

THE FIRST EXPERIMENT

To verify the correct operation of all the experimental equipment (neutron detector with a registration tract, the electronic data storage system) the obtained data were processed to evaluate the time parameters of the delayed neutron. The estimation of parameters of the delayed

ISBN 978-3-95450-170-0

neutron performed by an iterative least-squares method [3]. The evaluation was carried out as part a 6-group model of time parameters of the delayed neutron. The obtained data are presented in Table 1. The table shows the analogous data from Kipin work [5]. The value of the average half-life obtained in the present work is the same as the corresponding recommended data [4].

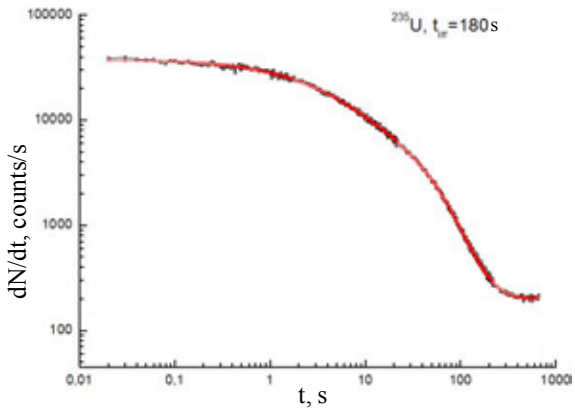

Figure 2: Time dependence of the activity of the ^{235}U sample obtained in experiments №1 with irradiation time of the sample tirr = 180 s, presented as a count rate.

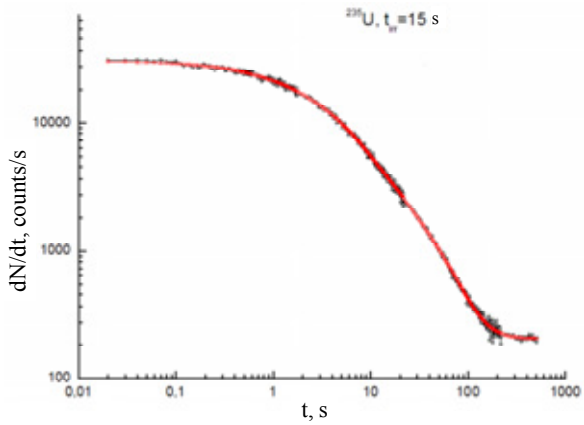

Figure 3: Time dependence of the activity of the ^{235}U sample obtained in experiments №1 with irradiation time of the sample tirr = 15 s, presented as a count rate.

The Figures 2 and 3 show that in this configuration the experimental data for the time of irradiation tirr = 15 do not show a significant excess of delayed neutron activity at the lower boundary of the investigated time range (0.01-0.5 s) as in the case of long irradiation (tirr = 180).

THE SECOND EXPERIMENT

Figure 4 shows that data of experiment №2 indicate the excess of count numbers in the low times in relation to the recommended data [4]. Similar results were obtained in experiments with a configuration corresponding to a fast spectrum of primary neutrons for the irradiation time of the sample tirr = 15 s. These data are presented as the count rate of pulses from a neutron detector in Figure 5. It is seen that there is an increase the count rate of delayed neutrons in the times region up to 0.12 s compared with the data obtained on the basis of the recommended data. The recommended data were measured in the time range starting from 0.1 s.

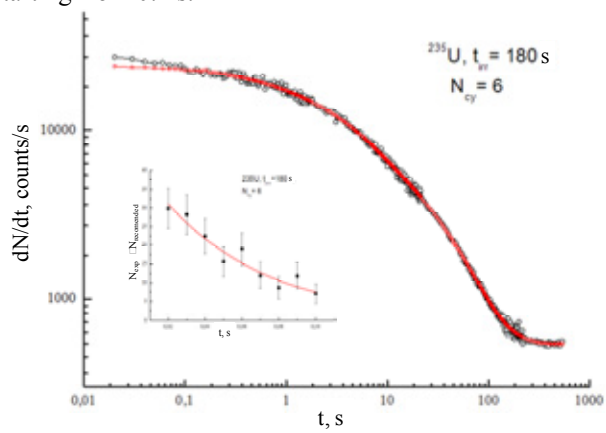

Figure 4: Time dependence of the activity of the ^{235}U sample obtained in experiments №2 with irradiation time of the sample tirr = 180 s, presented as a count rate.

Thus, it was shown in the experiment that the measured time dependence of delayed neutron activity for soft neutrons agrees with the recommended one. As for the fast spectrum of primary neutrons the excess of count numbers is observed on the decay curve in the time range of 0.01 - 0.2 s as compared to the decay curve corresponding to the recommended data.

Table 1. Relative yields and periods of delayed neutrons in the fission of ^{235}U by neutrons from the reaction ^{7}Li (p, n).

№		1	2	3	4	5	6	$T_{1/2}$ ср
^{235}U (present work, fast spectrum)	a_i	0.03950 ± 0.00131	0.20823 ± 0.00692	0.19670 ± 0.00881	0.38126 ± 0.01501	0.14655 ± 0.00692	0.02776 ± 0.00139	8.90932 ± 0.48652
	T_i	54.12201 ± 1.01994	22.38173 ± 0.29337	6.09608 ± 0.22313	2.2432 ± 0.05674	0.45424 ± 0.02208	0.17896 ± 0.00894	
^{235}U Kipin (fast)	a_i	0.038	0.213	0.188	0.407	0.128	0.026	8.83
	T_i	54.51	21.84	6.0	2.23	0.496	0.179	

ISBN 978-3-95450-170-0

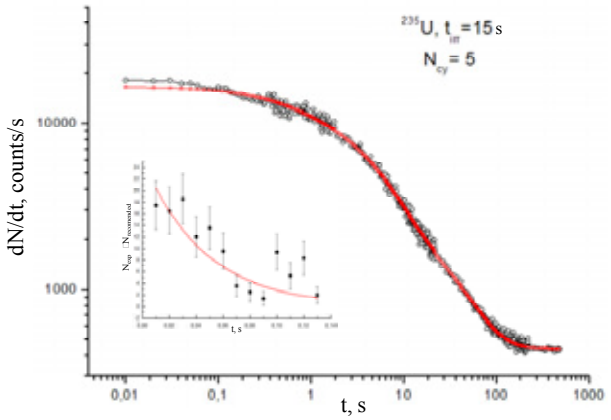

Figure 5: Time dependence of the activity of the ^{235}U sample obtained in experiments №2 with irradiation time of the sample tirr = 15 s, presented as a count rate.

In this work, the set-up was created on the basis of the accelerator EG-1 IPPE allowing to measure the activity of delayed neutrons of fission of heavy nuclei in the time range, which the lower limit is determined by the speed of the charged particle beam interruption. It was shown in the experiments that the measured time dependence of delayed neutron activity in the fission of ^{235}U on the soft spectrum of primary neutrons agrees with the recommended one. As for the fast spectrum of primary neutrons the excess of count numbers is observed on the decay curve in the time range of 0.01 - 0.2 s as compared to the decay curve corresponding to the recommended data.

The microscopic approach using the data on the probability of emission of delayed neutrons and cumulative yields of fission products for 368 nuclei precursors also indicates the existence of short-lived component ($T_{1/2}$ <0.2 s) in the decay curve of activity of delayed neutrons emitted in the fission of ^{235}U.

REFERENCE

[1] http://www.ni.com/pdf/products/us/4daqsc386-393_386-387.pdf

[2] V.M. Piksaikin, N.N. Semenova. “A method and setup for studying the energy dependence of delayed neutron characteristics in nuclear fission induced by neutrons from the T(p, n), D(d, n), and T(d, n) reactions.” Nuclear experimental technique, Vol. 49, pp. 765-777, 2006.

[3] V.M. Piksaikin, L.E. Kazakov. “Energy dependence of relative abundances and periods of delayed neutrons from neutron-induced fission of ^{235}U, ^{238}U, ^{239}Pu in 6- and 8-group model representation.” Progress in nuclear energy, Vol. 41, pp. 203-222, 2002.

[4] G. Spriggs, J. Campbel, V. Piksaikin. “An 8-group delayed neutron model based on a consistent set of half-lives.” Progress in nuclear energy. Vol. 41, pp. 223-251, 2002.

[5] G.R. Kipin “Physical basis of the kinetics of nuclear reactors”. Atomizdat, 1967.

ISBN 978-3-95450-170-0

REGISTRATION OF GAMMA RAYS FROM THE REACTION $^{16}O(N,P)^{16}N$ ON THE DIRECT NEUTRON BEAM OF CASCADE GENERATOR KG-2.5

K.V. Mitrofanov, V.M. Piksaikin, A.S. Egorov, B.F. Samylin,
State Scientific Center of Russian Federation Institute of Physics and Power Engineering,
Obninsk, Russia

Abstract

In the present work the results of analysis of the oxygen content in the water with the help of gamma-rays registration from the reaction 16O(n, p)16N is described. The samples were installed permanently on the direct beam of neutrons generated by the reaction 7Li(d, n) in the cascade generator KG-2.5 (IPPE). A comparison was carried out with experimental data obtained by the activation method in similar experimental conditions.

The method of determination of oxygen in the samples is based on the reaction $^{16}O(n,p)^{16}N(\beta-)$. A beam of neutrons generated in the reaction ^{7}Li (d,n) on the cascade generator KG-2.5 was used for irradiation of the sample. The energy distribution of neutrons from the target in the case of deuterons with an energy of 0.7 MeV is shown in Figure 1. There is a homogeneous group of neutrons in the region of 14 MeV (the channel of reaction $^{7}Li(d,n)^{8}Be$) and a continuous spectrum of neutrons with energies ranging from very small up to 14 MeV. The total neutron yield from this reaction for deuterons with an energy of 1 MeV and a thick target is about $3\cdot10^{7}$ neutrons/μA/sr.

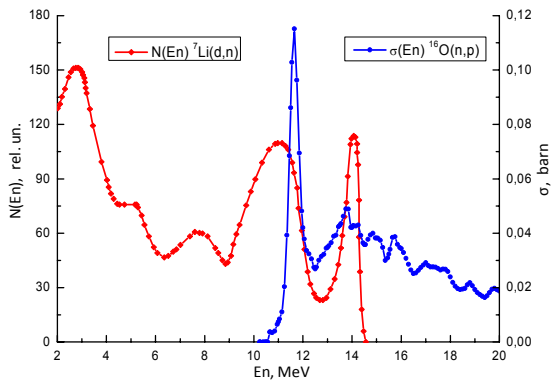

Figure 1: The energy spectrum of neutrons in the $^{7}Li(d,n)$ at an angle $\theta=0^{0}$ at Ed=0,7 MeV and a cross section of reaction $^{16}O(n,p)^{16}N$.

The same figure shows a cross section of the reaction $^{16}O(n,p)^{16}N$. It is seen that only a small fraction of the total neutron spectrum is effective for generating reaction $^{16}O(n,p)$ (~ 15%). The rest of the neutrons generates the background component of the resulting gamma-spectra, which is caused by the reactions (n,γ), (n,2n), (n,α), (n,p) of setup constructional materials (including detector materials), which generate a spectrum of gamma rays in the range of 0-3 MeV. There is an opportunity to distinctly register gamma rays with energies 7.12 and 6.13 MeV produced by beta decay of ^{16}N. [1]

Methodical difficulty of this experiment is the intensity of gamma background caused by the above reactions. These gamma rays produce a large load electronic path of the spectrometer. It leads to a distortion of the response function of the spectrometer and bandwidth of gamma spectroscopy system.

One of the consequences of high load detector is, for example, blocking the registration of high-energy gamma rays. The parameters of the electron spectrometric channel and of the detector shielding was optimized to solve this problem (choosing the correct amplifier and its mode of operation, the choice of parameters for the formation and registration of signals). There was also selected the optimum exposure time mode irradiation of samples and recording the spectra of gamma-ray induced activity.

The water was selected as a sample. The permanently installed water sample was irradiated for 10 s. Time of measurement of the induced activity was 100 s. The experimental scheme for the case of a stationary target is presented in Figure 2.

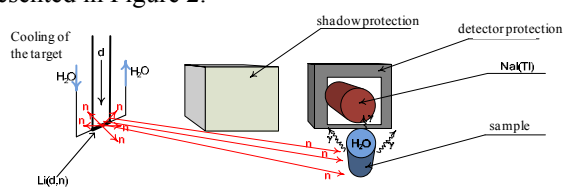

Figure 2: The experimental scheme for the identification of oxygen on the direct beam accelerator. NaI(Tl) - 100x100.

A similar experiment was carried out in the absence of the sample (background measurement). The results are shown in Figure 3.

ISBN 978-3-95450-170-0

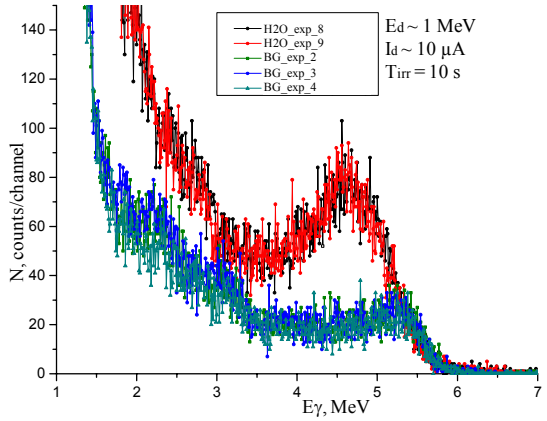

Figure 3: The energy distribution of gamma rays in the range of 0-20 s registered after irradiation the sample H_2O by neutrons from the reaction ^{7}Li(d,n) for 10 s. NaI(Tl) -100x100.

The figure shows that the number of gamma rays corresponding to the double peak emission of gamma rays is significantly higher than the number of pulses background. High-energy gamma rays in the background spectrum is due to the reactions of the isotopes of oxygen, which is part of the atmosphere and the reflector (MgO_2) crystal NaI(Tl) [2]. The selection of the time dependence of pulses belonging to the energy range 3.5-6 MeV was conducted to determine the decay rate of activated nuclei ^{16}N. The resulting decay curve for one cycle of measurements is shown in Figure 4.

The resulting decay curve of gamma activity was processed to evaluate the half-life of the induced activity. The processing of decay curves showed that the half-life of accumulated activity is 7.14 ± 0.39 s and belongs to the nuclei of ^{16}N.

For demonstration of the possible use of this method for practical applications was carried out continuous irradiation of the pipeline through which water moves from the target to the neutron detector.

Figure 5 shows the scheme of an experiment to determine the induced activity of water moving in the pipe from the accelerator target to the neutron detector.

The results of the experiment are shown in Figure 6. The difference in the number of counts in the peak is due to the fact that the curves are not normalized to the total neutron flux. Some difference may also be due to the fluctuation of water flow in the pipeline. One of the curves was obtained at a reduced flow rates.

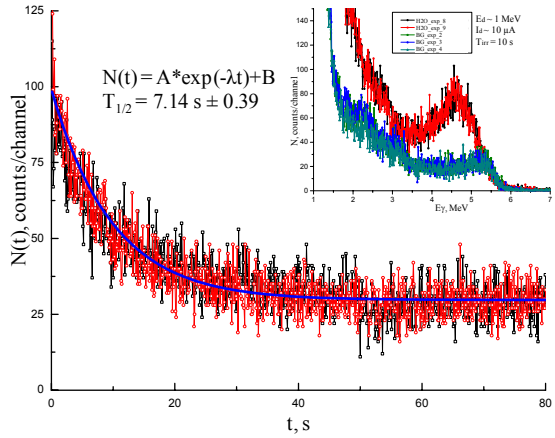

Figure 4: The decay curves of gamma-activity of nuclei ^{16}N accumulated in the reaction ^{16}O(n,p)^{16}N. Energy window: 3.5-6 MeV. NaI (Tl) -100x100.

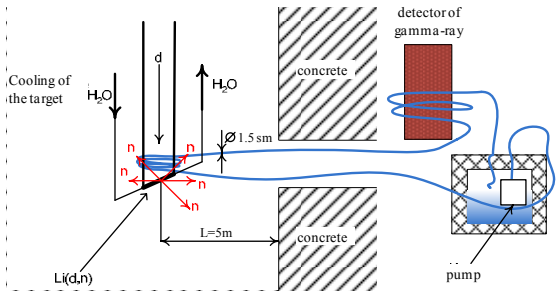

Figure 5: Scheme of the experiment to determine the induced activity of water in the pipeline. NaI (Tl) -100x100.

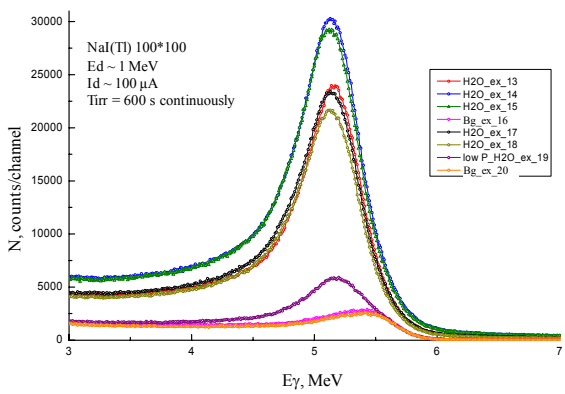

Figure 6: The energy distribution of gamma rays registered during continuous irradiation of water flow by neutrons from the reaction ^{7}Li(d,n). The irradiation time of 600 seconds. NaI(Tl) -100x100.

Figure 6 shows that there is a significant excess of the number of counts of reaction ^{16}O(n,p)^{16}N in the sample over the count number of background. The effect will be greatly enhanced in the case of detectors with higher energy resolution - BGO or lanthanum bromide.

This method may obtain application in actual practical applications, not only in the nuclear industry, but also in the oil and gas industry. A compact 14 MeV neutron

ISBN 978-3-95450-170-0

generator is used as the neutron source - neutrons generated by the reaction T(d,n). Currently, these generators are produced by the domestic industry. The intensity of the neutron flux is approximately 10^9-10^{10} neutrons/s.

The following are the possible practical applications related to the registration of induced activity ^{16}N:

- ✓ Creating a device for determining the velocity and flow rate (oil and gas) in pipelines. (Contents of oxygen. Flow rate and liquid).
- ✓ Source of High-Energy Gamma-rays (2.75, 6.13 and 7.11 MeV) for the calibration of the energy scale of gamma spectrometers.
- ✓ Monitoring the spatial distribution of oxygen in the fuel rods.
- ✓ Certification of the chemical composition of irradiated fuel rods, which must be disposed.

It should be noted that the present measurements were carried out in the presence of a large background of gamma radiation. A similar situation will occur with irradiated fuel.

REFERENCE

[1] http://www.nndc.bnl.gov/endf/b7.1/download.html

[2] N.A. Vartanov, P.S. Samoilov. “Practical methods of scintillation gamma spectrometry”. Atomizdat, Moscow, 1964.

ISBN 978-3-95450-170-0

CONDITIONING AND MONITORING OF CLEANNESS OF HIGH VOLTAGE SYSTEM WITH GASEOUS INSULATION

K.A. Rezvykh and V.A. Romanov, SSC RF – IPPE, Obninsk, Russia

Abstract

New effective technique of conditioning of gaseous insulation of electrostatic accelerator is described. To achieve stable breakdown voltage, accelerator conditioning procedure would take 7-8 hours (volume of pressure tank is 9 m^3). Three methods of monitoring cleanness of gaseous insulation are proposed.

HIGH UNSTABLE VOLTAGE

The paper is devoted to preliminary tests of accelerator without tubes. Cleanness of the system is usually achieved by step-like increasing of gas pressure ("from low to high pressure" method). Breakdowns are repeated until the breakdown voltage rise stops. The method is ineffective since it disregards the second source of instability of breakdown voltage, namely: presence of free solid particles in the vessel space.

Influence of particles was evidently found when testing the EG-2.5 and the EG-3 accelerators without tubes with positive voltage polarity. N_2/CO_2 gas mixture always contained 20% of CO_2. Tests were carried out by step-like decreasing of gas pressure ("from high to low pressure" method). High unstable breakdown voltage first appeared under gas pressure of 1 MPa during fourth breakdown after the start of the experiment. Then the breakdown voltage gradually decreased down to about 0.8 of high unstable value and increased again up to 1.09 of this value in the thirteenth breakdown.

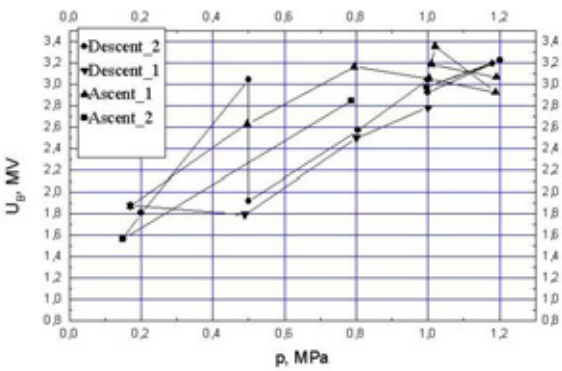

Figure 1: Breakdown voltage of the EG-2.5 accelerator before conditioning versus vessel pressure measured in descending and ascending series of tests. Descent_1 curve corresponds to "low unstable breakdown voltage" mode, Descent 2 curve corresponds to "stable" and "high unstable voltage" modes. Ascent_1 and Ascent_2 curves correspond to "high unstable breakdown voltage" modes.

After that we replaced the whole amount of insulation gas and obtained "four parallel lines" picture (Fig. 1), i.e. four voltage values corresponding to the same pressure. No special gas conditioning was conducted. The first descending series of tests started with 1 MPa pressure in "low unstable voltage" mode and it was converted into "high unstable voltage" mode upon pressure decrease down to 0.17 MPa. In the first ascending series of tests, "high unstable voltage" mode was stopped upon reaching 1.0 MPa pressure and it was converted into "the low unstable voltage" mode starting from 1.2 MPa pressure.

The abrupt change of the average stable breakdown voltage to high unstable value was observed in the second descending series of tests under 0.5 MPa pressure (after the fifth breakdown) with multiplicity of 1.9 relative to its value. It should be noted that high unstable breakdown voltage naturally arose under constant N_2/CO_2 gas pressure maintained within 0.1–1 MPa operating range and it was kept during the second ascending series of tests.

"High unstable voltage" mode is slightly mentioned in [2].

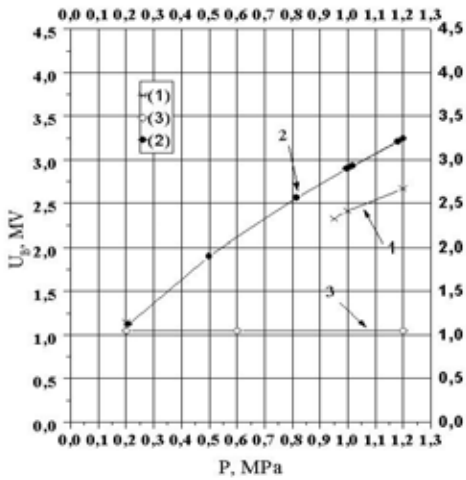

Figure 2: Breakdown voltage of the EG-2.5 accelerator versus vessel pressure before and after "from high to low pressure" conditioning. Curves 1 and 2 correspond to "low unstable" and "stable" modes, and curve 3 corresponds to "conditioning without breakdowns" technique (to remove light particles from the vessel).

NEW CONDITIONING TECHNIQUE

It is experimentally found that polished electrodes have the most relative increase of breakdown voltage, i.e. the highest conditioning effect [3]. Therefore one can consider free solid particles as the main cause of insulation deterioration. The particles arise and start

ISBN 978-3-95450-170-0

moving between the electrodes under high voltage. Besides, accelerators operating experience showed that particle traps installed in the gap were ineffective. As a result of a breakdown trap is shaken and particles are returned to the gap space.

The new technique [4] combines high voltage application to the system electrodes and pumping out insulation gas from the vessel in order to completely remove particles instead of their trapping.

Diagrams in Figs. 3 and 4 are made on the common time scale.

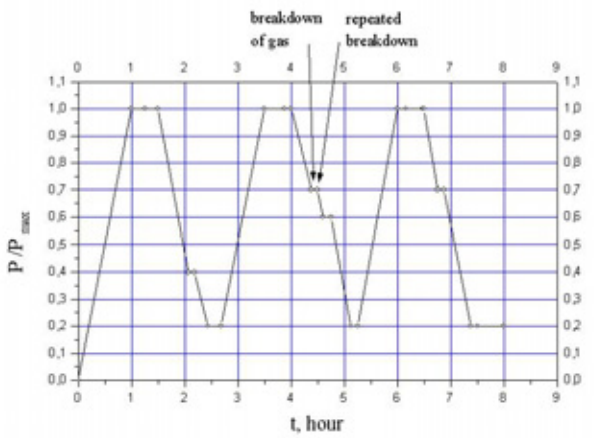

Figure 3: Vessel pressure change versus time.

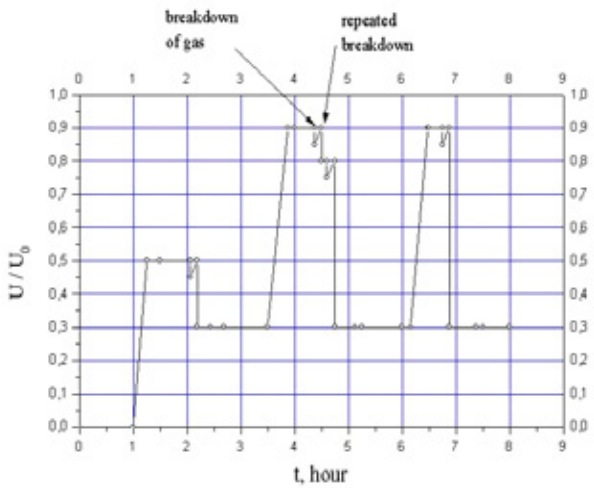

Figure 4: Electrodes voltage change versus time.

In the initial stage, dust filter with pores of 1 μm is installed in the vicinity of the gas main inlet to the vessel, insulation gas is dried to humidity of 30-50 ppm and pumped to the vessel up to the max permissible pressure $p_{\max}$ (Fig. 3).

System cleanness degree is determined by the stable breakdown voltage value for the clean system, e.g. U_{max}. To estimate anticipated $U_{\max}$ voltage the following procedures are conducted as the second step: rise of static voltage on the electrodes to about haft of maximum anticipated breakdown voltage value (Fig. 4); gas pumping out from the vessel to reserve tank until the occurrence of the first breakdown of gas; pressure change stop; voltage decrease followed by its slow increase until repeated breakdown occurs; and calculation of anticipated voltage value using the following relationship:

$$U_{\max} = k_{cl}^{-1} \cdot (p_{\max} / p_{in})^{X_p} \cdot U_{in}, \quad (1)$$

where $U_{\max}$ is the stable breakdown voltage under maximum pressure in the clean system: $U_{\max} = U_B(p_{\max})$, U_{in} is the breakdown voltage measured under initial gas pressure in the vessel; $p_{\max}$ and p_{in} are, respectively, maximum and initial values of absolute gas pressure reduced to 20°C temperature; X_p is exponent, k_{cl} is an empirical cleanness coefficient: $k_{cl} = U_{in} / U_{stbl}$; and U_{stbl} is gas breakdown voltage under the same pressure in the clean system.

The third step implies decrease of electrode voltage and vessel pressure to the minimum level corresponding to electric field strength on gap electrodes not lower than 0.5 kV/mm value.

The fourth step includes cleaning cycles repeated till the min fluctuations of breakdown voltage under max pressure are achieved. Results of "from high to low pressure" conditioning technique application for rare breakdowns [4, 7] are presented using least-square method as follows:

$$U_B = A \cdot p^{X_p}, \quad (2)$$

where U_B is breakdown voltage of the gap, MV; p is gas pressure (MPa) reduced to 20˚C temperature; A and X_p – constants. Thus Eq. (2) can be used for calculations on, respectively, EG-2.5 and EG-3 accelerators as follows:

$$U_B = 2.901 \cdot p^{0.609}, MV, \sigma = 4.2\%, p = 0.21 - 1.2 \text{ MPa}, \quad (3)$$

$$U_B = 3.613 \cdot p^{0.677}, MV, \sigma = 5.0\%, p = 0.21 - 1.2 \text{ MPa}, \quad (4)$$

where σ – standard deviation of the experimental values from the curve.

The "MNK_one" code written in Pascal for calculation of A and X_p constants in Eq. (2) was published [7]. Absence of high unstable breakdown voltage and coincidence of $U_B(p_{\max})$ values provide the strict proof of cleanness of tested systems.

CHECKING SYSTEM CLEANNESS

Two simple criteria of conditioning completion and three methods of conditioning obtained recently are listed below.

(1) Independence of breakdown voltage of its serial number.

(2) Change of the average breakdown voltage values is insignificant for two successive series of 5-10 breakdowns [3].

ISBN 978-3-95450-170-0

The above two criteria assume the use of "from low to high pressure" testing method and conditioning by successive breakdowns. Both criteria are ineffective in "high unstable voltage " mode.

(3) Conditioning by "from high to low pressure" technique with applied voltage and rare breakdowns provides reliable cleanness checking with small fluctuations of voltage $U_B(p_{\max})$ and without high unstable voltage.

(4) Eq. (2) can also be used for verification of experimental data. It is known that pressure increase results in non-linearity of breakdown voltage / pressure dependence due to the rough electrode surface. Condition of $X_p \le 1$ in Eq. (2) with $p_{\min} \le 0.2$ MPa corresponds to the "stable" test mode.

Let us calculate parameters of Eq. (2) using code from [7]. For this purpose data file length is varied several times by successive decrease of maximum pressure $p_{\max}$ in the data file. If X_p parameter approaches 1 asymptotically, then the breakdown voltages are stable. Otherwise the experimental data contains a systematic error caused by unfinished conditioning.

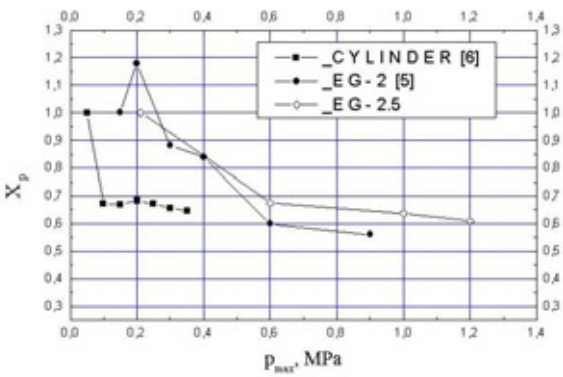

Figure 5: Exponent X_p in Eq. (2) versus maximum pressure in the $U_B(p)$ file.

Thus EG-2.5 curve in Fig. 5 characterizes dependence 2 from Fig. 2 of this paper; it is related to polished electrodes and stable voltages. EG-2 curve shows the presence of low or high unstable breakdown voltage under 0.2 MPa pressure in the preliminary tests of the other accelerator [5] with $N_2 / CO_2 / SF_6$ gas mixture.

It is in the case of CYLINDER for coaxial cylinders in SF_6 gas [6, Fig.3] that exponent X_p does not approach 1 apparently due to the rough surface of electrodes having arithmetic mean profile deviation $R_a = 10 \mu m$.

(5) If conditions of the base experiment and input data of calculation are taken into account, then mathematical model described in [1, 7] extrapolates result of the base experiment to the calculated breakdown voltage of the object. If the base breakdown voltage is stable (e.g. that in MP, EG-2.5 and EG-3 accelerators), then calculated breakdown voltage for the object would also correspond to the stable performance accurate to $\pm(2-3)\%$. Hence the calculated breakdown voltage determines reachable limit of electric object's strength.

CONCLUSION

1. "High unstable" breakdown voltage mode arises within operating range of N_2 / CO_2 gas pressure indicating deterioration of the system insulation.

2. In contrast to the unsafe "from low to high pressure" technique based on repeated breakdowns with step-like pressure changes, "from high to low pressure" method with limited number of breakdowns allows to effectively remove free solid particles from the gap.

3. Quantitative criteria of insulation cleanness, namely: maximum voltage $U_B(p_{\max})$, exponent X_p, and calculated breakdown voltage U_{B_CALC} make it possible to determine electrical strength of a system, its shortcomings and reserves.

REFERENCES

[1] K.A. Rezvykh and V.A. Romanov, Nucl. Instr. Meth. A423 (1999) 203-212.

[2] D.I. Blokhintsev et al., Journal Tech. Phys., 10 (1940) No. 5, p. 357-368 (in Russian).

[3] I.M. Bortnik, Physical characteristics and electric strength of hexafluoride of sulphur, (Moscow: Energoatomizdat, 1988), 29 (in Russian).

[4] K.A. Rezvykh and V.A. Romanov, A technique of cleaning of a gas insulated high voltage equipment, patent of RF No. 2 443 031, publ.20.02.2012, bull.No.5 (in Russian).

[5] L.P. Batvinov et al., VANT, Series: Techn. Phys. Exper., Kharkov: (1985) No. 1(22), p. 26-28 (in Russian).

[6] V.N. Borin, Electricity (1972) No. 11, p. 67-72 (in Russian).

[7] K.A. Rezvykh and V.A. Romanov, "Features of the "An asymptotic breakdown gradient" mathematical model of breakdown voltage of gaseous and vacuum elements of accelerators" Proc. XVII Int. Conf. ESACCEL, Obninsk, October 2008, (Obninsk: SSC RF IPPE, 2010), p. 127 (in Russian).

ISBN 978-3-95450-170-0

SET-UP FOR MEASUREMENTS OF DELAYED NEUTRON CHARACTERISTICS IN INTERACTION OF HEAVY NUCLEI WITH RELATIVISTIC PROTONS OF THE SYNCHROCYCLOTRON PINP GATCHINA

A.S. Egorov, V.M. Piksaikin, V.F. Mitrofanov, B.F. Samylin, State Scientific Center of Russian Federation Institute of Physics and Power Engineering, Obninsk, Russia

Abstracts

In present paper the method and set-up for measurements of delayed neutron characteristics in interaction of heavy nuclei with relativistic protons are described. On the basis of this method the time dependence of delayed neutron activity has been measured from interaction of ^{238}U sample with 1 GeV pulsed proton beam of the synchrocyclotron of the Petersburg Institute of Nuclear Physics, Gatchina. The measured data was analyzed in frame of 8-group precursor's model with a consistent set of half-lives. Obtained results on the fractional yields of delayed neutron precursors are compared with an appropriate data from the fast neutron induced fission of ^{238}U.

EXPERIMENTAL METHOD AND SET-UP

The measurements of delayed neutron decay from the fission of ^{238}U induced by relativistic protons were carried out on the set-up installed at the synchrocyclotron of the Petersburg Institute of Nuclear Physics, Gatchina. The synchrocyclotron is a pulsed accelerator with a 1 GeV proton beam intensity of about 10^{10} protons/cm^2·s in the location of sample. The width of proton pulses in the ^{238}U experiment was 0.008 s with the repetition time of 0.02 s

The experimental method employed in the measurements of delayed neutron decay curves is based on cyclic irradiations of the ^{238}U samples by protons followed by the registration of the time dependence of accumulated delayed neutron activity.[1]

Block diagram of the experimental setup is presented on figure 1.

The detector is shielded against the neutron background by borated polyethylene and cadmium sheets. The amplifier (A) and pulse discriminator (D) were used for two sets of counters – outer and inner as related to incident neutrons. The output signals from these electronic channels are fed to a mixing module (Σ) coupled with DAQ electronic system. The dead time of neutron detector is 2.3±0.2 μs.

The pneumatic transfer system is capable to transport the sample for the time short enough to measure the delayed neutron yields with the shortest half-lives. Two electromagnetic valves are responsible for the sample transportation route. The stainless steel tube with inner diameter of 12 mm and wall thickness of 1 mm serves as a pneumatic flight guide (3). The positions of the sample in the neutron detector and irradiation location are fixed by the plugs with adjustable central hole which provides the excessive pressure in front of the moving sample and smoothes the contact between the sample and the plug. The information on the sample location is obtained from sample position detector (6). Time of flight of the sample is about 150 ms.

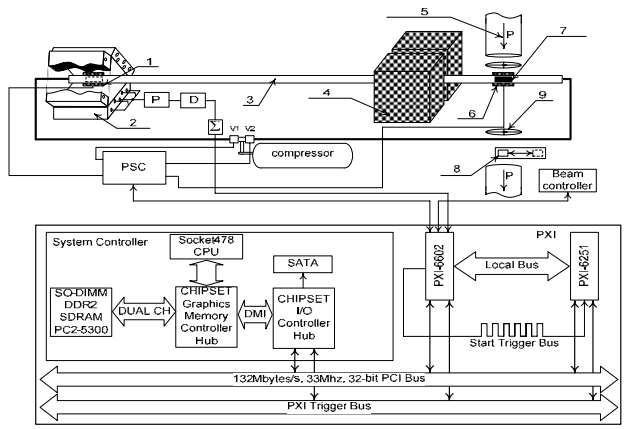

Figure 1: Block diagram of the experimental setup: 1,6-sample position detector; 2-neutron detector; 3-pneumatic transfer system; 4-neutron detector shield; 5-beam line; 7-sample of ^{238}U; 8,9 Laser positioning device; (P) preamplifier, (D) pulse discriminator; (Σ) summator; (PSC) Pneumatic System Controller; In the bottom of the fig.1 is presented Data Acquisition system by National Instruments based on Labview.

RESULTS AND DISCUSSION

Composite decay curves which were measured in interaction of 1 GeV pulsed beam of protons with ^{238}U with irradiation times 15 and 180 s is presented on fig.2. The original scale of time analyzer (0.0001 s/channel) were transformed in scale of 0.1 s/channel. The obtained data were also corrected for the degradation effect of counting response of neutron detector placed in a high intensity fields of neutrons and gamma rays during irradiation time [2].

The accumulated decay curves were analyzed in the 8-group model approximation [3] with the help of the iterative least-squares method [4]. The relative abundances for ^{238}U were obtained on the basis of experimental data which were measured with different irradiation times. In the analysis of the delayed neutron time-dependence the data with irradiation time of 180 s were used to obtain the group constants for the first, second and third group of delayed neutrons. Group constants for the fourth to the eighth groups were

ISBN 978-3-95450-170-0

obtained from the data measured in the experiment with the irradiation time of 15 s. The group constants obtained from the long time irradiation data were fixed in the analysis of short time irradiation data.

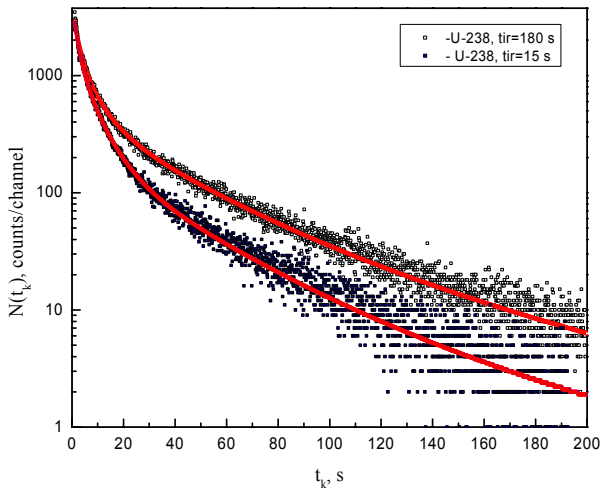

Figure 2: Composite delayed neutrons curves measured from interaction of 1 GeV pulsed beam of protons with ^{238}U with irradiation times 15 and 180 s. Solid lines – results of delayed neutron parameters estimation. Time-channel width – 0.1 s.

In the course of data processing two additional groups of delayed neutron precursors were introduced to take into consideration decay ^{16}C and ^{17}N with half-life 0.747 и 4.17 s respectively. These nuclides are produced in interaction of 1 GeV proton with ^{238}U with high probability [5]. It is allowed to take into account a contribution of the fragmentation channel in the composite delayed neutron decay curve. Thus the obtained fractional yields of delayed neutron precursors are corresponding mainly to the fission channel of the investigated interaction. The average half-life of delayed neutron precursors was obtained on the basis of the relative abundances and half-lives of their precursors according to formula $<T>=\Sigma T_j \cdot a_j$ (j=1-8). Obtained results on the fractional yields of delayed neutron precursors and their average half-life calculated on the basis of these data are presented in Table 1.

REFERENCE

[1] V. M. Piksaikin, N. N. Semenova, V. I. Mil'shin, V. A. Roshchenko and G. G. Korolev. "A Method and Setup for Studying the Energy Dependence of Delayed Neutron Characteristics in Nuclear Fission Induced By Neutrons From the T(p, N), D(d, N), and T(d, N) Reactions". Nuclear Experimental Technique 49, No. 6 (2006), p. 765-777.

[2] V. A. Roshchenko, V. M. Piksaikin, L. E. Kazakov and G. G. Korolev "Relative yield of delayed neutrons and half-life of their precursor nuclei with fissioning of ^{239}Pu by 14.2–17.9 MeV neutrons" Atomic Energy Vol. 101, Number 6(2006), p. 897-900.

[3] G.D. Spriggs, J.M. Campbell, and V.M. Piksaikin. "An 8-Group Delayed Neutron Model Based on a Consistent Set of Half-Lives". Progress in Nuclear Energy Vol. 41, no. 1-4 (2002), p. 223-251.

[4] I. Dostrovsky, R. Davis, Jr., A. M. Poskanzer, and P. L. Reeder "Cross Sections for the Production of ^{9}Li, ^{16}C, and ^{17}N in Irradiations with GeV-Energy Protons" . Phys. Rev. 139, (1965), p. B1513–B1524.

[5] V.M.Piksaikin, L.E. Kazakov, S.G. Isaev, M.Z. Tarasko, V.A. Roshchenko, R.G. Tertytchnyi, G.D. Spriggs, and J.M. Campbell. "Energy Dependence of Relative Abundances and Periods of Delayed Neutrons From Neutron-Induced Fission of U-235, U-238, Pu-239 in 6- and 8-Group Model Representation". Progress in Nuclear Energy 41, no. 1-4 (2002), p. 203-222.

Table 1. Fractional yields of delayed neutron precursors and their average half-life from fission of ^{238}U by 1 GeV protons.

Target, proton energy	Group number, half-life and predominant precursors of delayed neutrons								Average half-life, s $<T>=\sum_{j=1}^{8} T_j \cdot a_j$
	1 55.6 c ^{87}Br	2 24.5 c ^{137}I	3 16.3 c ^{88}Br	4 5.21 c ^{138}I, ^{93}Rb, ^{89}Br	5 2.37 c ^{94}Rb, ^{139}I, ^{85}As, ^{98m}Y	6 1.04 c ^{93}Kr, ^{144}Cs, ^{140}I	7 0.424 c ^{91}Rb, ^{95}Rb	8 0.195 c ^{96}Rb, ^{97}Rb	
^{238}U 1 GeV	0.023 ±0.004	0.139 ±0.004	0.050 ±0.001	0.365 ±0.010	0.263 ±0.010	0.102 ±0.002	0.035 ±0.001	0.023 ±0.015	8.15 ±0.25

ISBN 978-3-95450-170-0

COMPARISON OF BIOLOGICAL IMPACT OF PROTON AND ION BEAMS IN RADIATION TREATMENT

Mark Kats, ITEP, 25, B.Cheremushkinskaya, Moscow, Russia

Abstract

The work contains the comparison of biological doses' distribution calculated for treatment of the same targets by proton and ion beams. Advantages of the ion beam are shown for targets with different sizes and with different depths.

We made an attempt to compare the distribution of the biological dose for treating same targets with proton and ion beams. The research [1] based on the calculations performed with TRIM program [2] contained the evaluation of the integral distribution of the physical dose D and biological dose BD = D * RBE in water environment with a single-direction irradiation using the target scan with the thin beam for different target sizes (a cylinder with the diameter d and the size along the beam d) and with varying depth within the body L. The number of layers for the scanning was determined by the allowance for the consistency of irradiation (±5%). It was assumed for the calculation purposes that the beam has impulses' discrepancy of dP/P = ±0.5% (where P is the particle's impulse), the initial angle divergence (±2 mrad), the lateral dimensions equal to the size of the target (in accordance with the target's scan) and that it is directed at a patient with such variable energy that Bragg's peak would be at a depth of the layer required for the irradiation. The calculations included the particles' diminution caused by the nuclear interaction, the impact of repeated Coulomb's dispersion, the statistical dispersal of range's size and the dependency of relative biological efficiency RBE of particles with the given energy at the current depth within the body.

This dependency is not known authentically. The amount of RBE strongly depends on dE/dx [KeV/mkm], from the type of cells, from the organ that is being irradiated, from the method of measurement and from the size of a single dose. The curve shown on Figure 1, taken from the source [3] and from Figuress 1.2, 4.1, 4.2 and from source [4] was used to evaluate the amount of RBE, depending on dE/dx.

The calculations were made for the target sizes d from 1cm to 16cm with the depth of target's deposition from L≥ 1cm to (L+d)=30 cm. The research [1] shows that the basic distribution of the integral BD in relation to depth can be approximately (with the accuracy of ±10%) described as a constant in the target (BD = 1.0) and as a plateau until the target with BD= K, with the transitional zone of 3 cm (see table 1 and Fig. 2). Tailings in the zone's distribution, which appear during ions' fragmentation, were not accounted for.

Additionally, there are zones of irradiation on the side of the target, related to the secondary particles' dispersion in the body, and beyond the target, related to particles' scattering within the beam with impulses dP/P and with the statistical dispersion of ranges. The sizes of these zones depend on the depth and can be estimated through the calculations utilizing the THRIM program.

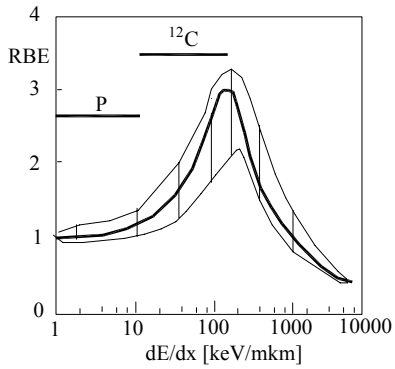

Figure 1: Dependence of RBE from dE/dx.

Table 1. The evaluation of K (the relation of BD on the plateau until the target to BD in the target), depending on the target's size, during target's irradiation in the water environment, using the single-direction scanning with ion and proton beams.

Target cylinder, diameter d [cm]; its size d in depth	1	2	4	8	16
Protons K	0.55 ±0.10	0.60 ±0.10	0.70 ±0.08	0.80 ±0.07	0.95 ±0.05
Carbon ions K	0.28 ±0.05	0.38 ±0.05	0.51 ±0.05	0.70 ±0.05	0.95 ±0.05

Ion beams additionally irradiate the healthy tissues behind the target. This is related to potential nuclear interactions and with the possible disintegration of ions into charged particles and neutrons (fragmentation). Newly created particles have varying directions and energies, which is why they don't have the maximum energy release at the same place, where the initial ions have Bragg's peak. The distribution of the physical dose beyond Bragg's peak was calculated and measured multiple times (Fig. 2 [5]). The lower the depth of the target is, the smaller are the ranges of the ions, the less nuclear interactions take place. For the depth of 30 cm, the level of the physical does immediately beyond the target's volume is 15% of the does within the target, lowering with the depth. This means that the level of the biological dose beyond the target is always below 8% from BD within the target, due to fragmentation.

ISBN 978-3-95450-170-0

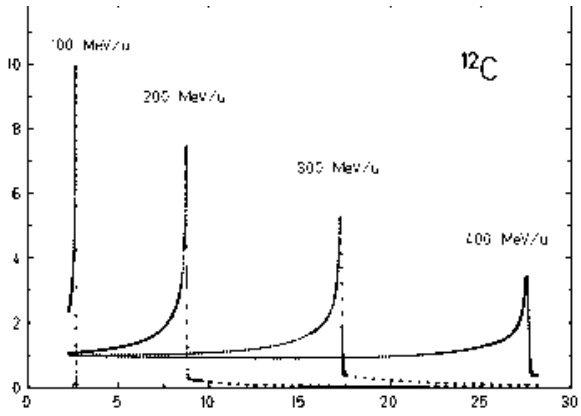

Figure 2: Examples of distribution of physical dose along the direction of carbon ions' beam, depending on their energy (MeB per one nucleon) [5].

There is a dependence of the biological impact on the irradiated cells from the biological dose. This dependence is shown schematically on Fig. 3 for three different types of cells. Two important data points are visible on all graphs. The first one is BD1, which indicates the 90% probability of suppressing cells' life (and higher with increased doses). This level is used during the therapy. With lower doses, the probability of suppression is reduced in an approximately linear pattern; in data point BD2, it becomes around 10%. With even lower doses, the probability of suppression is reduced more flatly and the irradiation virtually doesn't suppress the cells [5].It's important to notice that the ratio of doses in points BD1and BD2 does not exceed 5 and that the lower is Bragg's peak depth, the lower is the impact of fragmentation. Therefore, the impact of fragmentation is not high for the evaluation of the biological dose distribution beyond the target with the 15% accuracy, despite the significant space being irradiated [5].

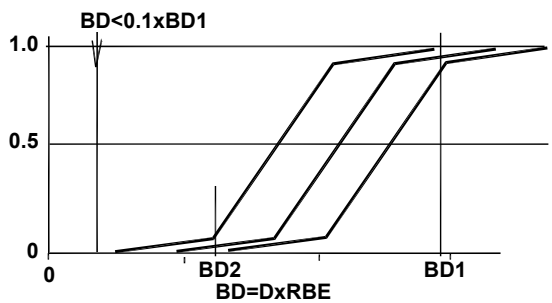

Figure 3: The dependence of the biological impact from the biological dose.

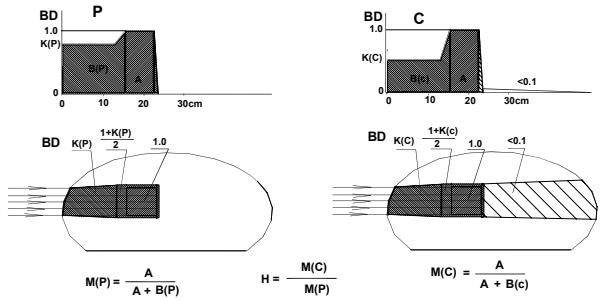

Figure 4: The scheme of the distribution of the biological dose BD for the irradiation of the target with size d, which is positioned on depth L.
A – Useful integral BD within the target;
B – Harmful integral BD emitted by the beam within the body outside the volume of the target;
(A+B) - total integral biological dose emitted by the beam in the body;
M=A/(A+B) – the share of the useful biological dose within the total biological dose emitted by the beam in the body;
H = M(C)/M(P) – by how many times the ion beam distributes the biological dose in a more useful way.

In order to get the same therapeutic effect using proton and ion beams, the target should be irradiated with the same biological dose. The integral of the biological dose within the target is labeled A, while the integral of the biological does outside the target is labeled B. The size of B depends on the particles' type – protons B(P) or ions B(C). It is suggested to characterize the quality of irradiation by the relation of M(P)=A/(A+B(P)) and M(C)=A/(A+B(C)), the integrals of the biological dose A distributed within the target (the useful effect of the beam), to the total biological dose emitted by the beam in the body – A+B(p) for the protons and A+B(C) for the ions. Correlation H = M(C)/M(P) indicates by how many times the application of the ion beam is more effective than the use of the proton irradiation with the same targets. The results of the calculations are presented in table 2. It's obvious that this correlation will be close to 1,0 for the irradiation of surface targets (L=0), without taking into consideration beam's scattering within the target.

Because the accuracy of estimating the distribution of BD in relation to depth was close to ±10% [1], the accuracy of the calculations being conducted does not exceed ±15%, but they do provide the general understanding of the degree to which the use of more expensive ion beams, instead of traditional proton beams, is justified.

Similar estimates can be used for the multi-directional irradiation of a target, setting a specific target depth L for every direction and the size of a target in a given direction d.

ISBN 978-3-95450-170-0

Table 2. Comparison of the biological impact of ion and proton beams for different target sizes and depths.

L см **d** см		1	2	4	8	12	18	26
1	M(P) M(C) H	**0.51** **0.59** **1.2**	**0.35** **0.42** **1.2**	**0.23** **0.30** **1.3**	**0.14** **0.22** **1.5**	**0.10** **0.17** **1.7**	**0.07** **0.13** **1.9**	**0.05** **0.10** **2.0**
2	M(P) M(C) H	**0.64** **0.72** **1.1**	**0.50** **0.57** **1.1**	**0.36** **0.43** **1.2**	**0.24** **0.32** **1.3**	**0.18** **0.25** **1.4**	**0.13** **0.19** **1.5**	**0.10** **0.15** **1.5**
4	M(P) M(C) H	**0.76** **0.82** **1.1**	**0.63** **0.70** **1.1**	**0.50** **0.57** **1.1**	**0.36** **0.43** **1.2**	**0.28** **0.35** **1.2**	**0.21** **0.28** **1.3**	**0.15** **0.20** **1.3**
8	M(P) M(C) H	**0.82** **0.88** **1.1**	**0.74** **0.80** **1.1**	**0.63** **0.69** **1.1**	**0.49** **0.55** **1.1**	**0.40** **0.46** **1.1**	**0.32** **0.37** **1.2**	
12	M(P) M(C) H	**0.84** **0.90** **1.1**	**0.79** **0.81** **1.1**	**0.70** **0.75** **1.1**	**0.57** **0.62** **1.1**	**0.48** **0.53** **1.1**	**0.39** **0.43** **1.1**	
16	M(P) M(C) H	**0.86** **0.92** **1.1**	**0.81** **0.87** **1.1**	**0.73** **0.79** **1.1**	**0.62** **0.66** **1.1**	**0.53** **0.57** **1.1**		

CONCLUSION

Table 2 shows that the ion beam always irradiates healthy tissues less then the proton beam. This advantage is significant for deep targets (L≥ 4cm) with small sizes (d≤ 4cm). However, despite the sharper Bragg's peak, up to 3 times higher RBE (in maximum of dE/dx) and 20 times higher LET of ions, for many targets, the difference between the quality of irradiation with ion beams and with proton beams is small – below 10%.

These conclusions could be expected, based upon several basic characteristics of BD distribution in water by proton and ion beams. First: the bigger is the target size d, the closer is the BD plateau before the target K to the dose within the target (see [1] and table 1) and the difference between the application of the ion beam and the proton beam is reduced. Second: the smaller the depth of the target is, the lower is the volume of health tissues that are being irradiated, and the closer are the results of proton and ion irradiation. Third: the bigger the depth of the target L is, the higher is the impact of healthy tissues' irradiation due to the repeated Coulomb's scattering, especially, for small targets. Ions' angles of scattering are 4 times less than those of protons.

The presented estimates may be useful for a rough comparison of multi-directional irradiation plans, where L and d values can be determined for every direction, and also for the planning of the new ion and proton irradiation centres' development.

It is very useful to repeat those calculations with more high precision by using well known system for planning of irradiation.

REFERENCES

[1] Kats M.M.; Druzhinin B.L. A simple method for estimating the distribution of the biological effect for the three-dimensional scanning of the target with a narrow proton or ion beam. Medical Physics; 2004; 4; Pages 20 – 25.

[2] Biersack J.P. and J.F. Ziegler J.F. Calculation from TRIM //Version -95, 1995.

[3] Jong Seo Chai (KIRAMS) Medical Application of the heavy Ion accelerator. // Report on Asian Particle Accelerator Conference, 2004.

[4] IAEA, TRS -. 461 VIENNA, 2008. // Relative biological effectiveness in ion beam therapy international atomic energy agency.

[5] Schardt D., Elsasser T., Schultz-Ertner D. Heavy-Ion tumor therapy: Physical and radiobiological benefits. // Review of Modern Physics, v.82, 1-3.2010.

ISBN 978-3-95450-170-0

PRIOR PROTON MICROSCOPE

A.V. Kantsyrev, A.A. Golubev, A.V. Bakhmutova, A.V. Bogdanov, V.A. Panyushkin,
Vl.S. Skachkov, N.V. Markov, A. Semennikov, ITEP, 117218, Moscow, Russia
D. Varentsov, P. Lang, M. Rodionova, L. Shestov, K. Weyrich, GSI, 64291, Darmstadt, Germany
S. Udrea, TUD, 64277, Darmstadt, Germany
C. Barnes, F. Mariam, F. Marrill, C. Wilde, LANL, NM 87545, Los Alamos, USA
S. Efimov, Y. Krasik, O. Antonov, Technion, 3200003, Haifa, Israel

Abstract

The new proton radiography facility PRIOR[2] (Proton microscope for FAIR) was developed at SIS-18 accelerator at GSI (Darmstadt, Germany). PRIOR setup is designed for measurement, with high spatial resolution up to 10 μm, of density distribution of static and dynamic objects by using a proton beam with energy up to 4.5 GeV. In the first experiments with static objects with 3.6 Gev proton, was demonstrated a spatial resolution of 30 μm. Dynamic commissioning was performed with target based on underwater electrical wires explosion with electrical pulse with current amplitude of ~200 kA and rise time ~1 μs.

INTRODUCTION

The study of high-energy-density (HED) matter generated by the impact of intense heavy ion beams dense targets is one of the most challenging and interesting topics in modern physics [1]. Measurement of density distribution, with good spatial and temporal resolution, of matter is important task for fundamental understanding of dynamic material properties in extreme states. High-energy proton radiography exceeds X-Ray diagnostic method in many ways, because it has more transmission ability and high spatial and density resolution. The best spatial resolution was obtained by means of high-energy proton microscopy technique [2]. Novel high-energy proton microscope called PRIOR (Proton Microscope for FAIR)[3] will be the key diagnostic instrument for HED research program of HEDgeHOB collaboration at FAIR. (HIHEX and LAPLAS experiments)

EXPERIMENTAL SETUP

The magnetic system of the PRIOR beam-line consists of two sections (fig. 1). The first, matching section, contains electromagnetic-quadruple lenses and provides formation of a proton beam for the objects imaging task (beam size, angular distribution). The second section is a magnification section (K ~4) that consists of four Permanent Magnet Quadruples (PMQ) lenses. Length of the two PMQ lenses 144 mm and 288 mm the other two, magnetic field on pole is 1.83T, aperture 30 mm, magnetic material NdFeB. Tungsten collimators (with elliptical hole), installed at central plane of magnification section, provide regulation of contrast of the proton-radiographic images.

Figure 1: Photo and scheme of PRIOR proton microscope. 1- electromagnetic quadrupoles (matching section), 2- quadrupole lenses on permanent magnets PMQ (magnification section), 3-scintillator, 4- fast current transformer, 5- mylar foil mirror, 6- vacuum or water target chamber, 7- target, 8- target manipulator, 9- beam position/profile monitor (Bicron scintillator), 10- collimators, 11- beam position monitor, 12- linear actuators, 13- fast CCD cameras, 14- CCD cameras for beam tune

Investigated object installed in vacuum chamber between first and second section. The registration system for static experiments consists of CsI scintillator and plastic scintillator (Bicron BC-412) for dynamic one with two types of intensified CCD cameras PCO DiMAX and PCO DicamPro.

STATIC COMISSIONNING

The aim of first experiments at PRIOR was an adjustment of matching and magnification sections of ion optical scheme of setup to achieve best spatial resolution of proton-radiography images. Static objects were used to measure spatial and density resolutions and to estimate chromatic aberration. Primarily the setup was expected to run with 4,5 GeV proton beam. However due to radiation damage of the magnetic material of PMQ lenses (falling gradient and an increase the amplitude of the high-order harmonics of magnetic field) static commissioning of

ISBN 978-3-95450-170-0

facility has been carried out at lower proton energy 3.6 GeV. The object of tungsten, width 20 mm, with polished rolled edge (rounded radius 500 mm) was used to measure the spatial resolution limit. The spatial resolution was measured as a standard deviation of profile approximated function of image of sharp edge of object. The best spatial resolution, according to the preliminary estimates of proton radiography images, is 30 μm. The tantalum step wedge was used to determine contrast sensitivity of facility. Fig. 2 shows the proton radiography image and transmission/areal density diagram of tantalum steps wedge (thickness 0.56, 2, 4, 6, 8 mm), image was obtained by using collimator with acceptance angle of 2 mrad.

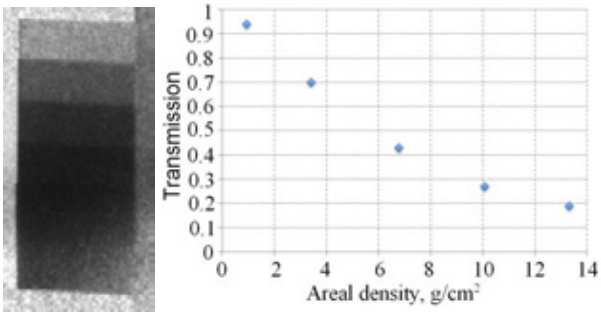

Figure 2: Proton radiography image of tantalum steps wedge and transmission/areal density diagram.

Fig. 3 shows a photo of static object (quartz watch) and its proton radiography image. One can see the main parts of the mechanism, such as a battery, a stepping mechanism, and hands.

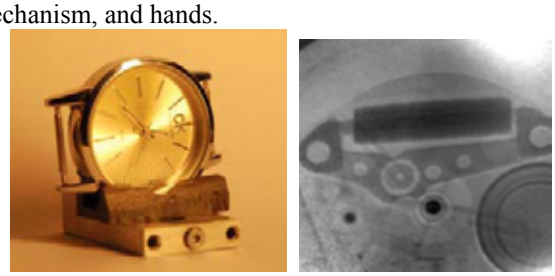

Figure 3: Photo and proton radiography image of quartz watch.

DYNAMIC COMISSIONNING

One of the proposed experiments for PRIOR facility is studying of time- and space-resolved density distribution of different underwater exploding wires (UEWE). First dynamic experiments with UEWE has been carried out using compact high-current generator (fig. 4) producing ~200kA electrical pulse with rise time of ~1μs. The external 10 μF capacitor unit with charge voltage of up to 50 kV controlled by Marx trigger generator is used to generate electrical pulse. Charging of capacitor unit and trigger generator is performed by two high-voltage generator TDK-Lambda 402-50.

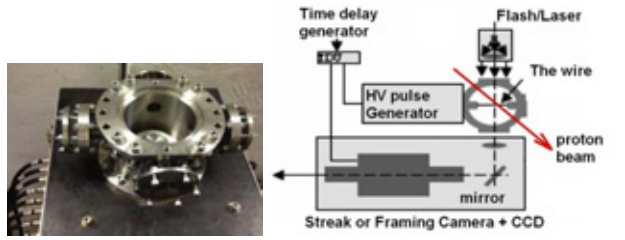

Figure 4: Photo and scheme of underwater electrical wire explosion target.

Fig. 5 shows the photo and proton radiography image of tantalum wire in water with diameter of 0.8 mm. Right part of fig. 5 shows dymanic image of wire which was obtained with electrical pulse of 36 kV voltage.

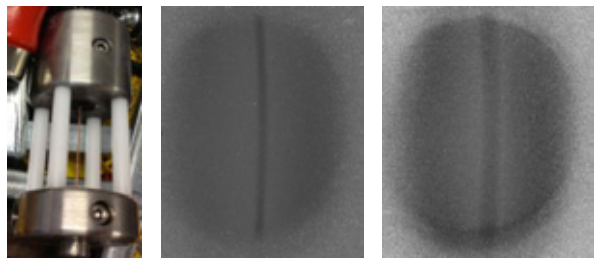

Figure 5: Photo and proton radiography images of tantalum wire.

Fig. 6 shows lineout through the 0.8 mm diameter Ta wire showing that there is sufficient sensitivity and resolution to measure the areal density of the wire.

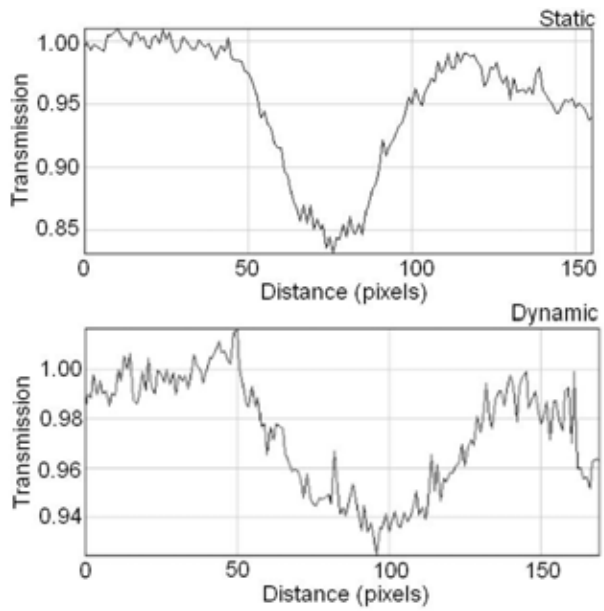

Figure 6: Profile of static and dynamic images of Ta wire.

ISBN 978-3-95450-170-0

ACKNOWLEDGMENT

Funding for this work was provided by the Joint Helmholtz-ROSATOM FAIR-Russia Research Centre and German-Israel foundation grant between GSI and Technion.

REFERENCES

[1] V.E. Fortov, D. Hoffmann, B.Yu. Sharkov, UFN, 2008, vol. 178, No. 2, p.113-138
[2] Merrill F.E. et al., AIP Conf. Proc. 1195, 2009, p.667
[3] A. V. Kantsyrev, A.A. Golubev et al., IET, (2014), No. 1, pp. 5-14.

ISBN 978-3-95450-170-0

STUDY OF POSSIBILITY OF INDUSTRIAL APPLICATION OF ION INJECTOR I-3

P. N. Alekseev, ITEP, Moscow, Russia

Abstract

Ion injector I-3 of the ITEP-TWAC accelerator complex consists of a buncher, two-gap accelerating cavity and a beam transport line. Laser ion source is used to generate ions for the injector. Possibility of application of the injector to dope semiconductor materials with variable energy ions is considered. Results of beam parameters optimization by numerical simulation to produce uniform distribution of particles density and required energy spread on the target are presented.

INTRODUCTION

Layout of the ion injector [1] is shown on Fig. 1. A solid-state target is placed at the target chamber of Laser Ion Source (LIS). The chamber is under potential of 50 kV. Laser pulse focused on the target produces plasma. The ion beam is formed at the extractor then is focused by means of electrostatic lenses, passes through the buncher and accelerated in the two gap resonator at the voltage of up to 2 MV per gap. Resulting beam energy is up to 4 MV per charge. It is possible to accelerate ions with A/Z from 2 to 5. The injector is able to produce ions of carbon, aluminium, silicon, iron and silver with intensity up to 5×10^{11} particles per pulse and repetition rate of 1 Hz.

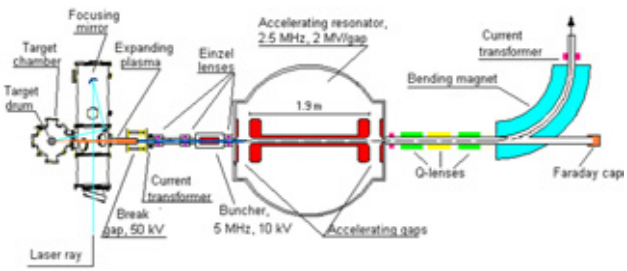

Figure 1: Layout of I-3.

Parameters of the accelerator allow considering it for industrial application in the area of doping of semiconductor materials [2]. Energies of ions in range of hundreds keV to units of MeV allows to provide a deep or a mid-deep ion implantation.

One of the possibilities of such application is production of buffer zone of Soft Punch Through (SPT) IGBT [3]. Fig. 2 shows the cross section of such SPT IGBT and concentration of the doping which should be produced to provide required electric field distribution inside the wafer [4]. Different technologies require different thickness of the buffer layer. To create the buffer layer some n-type particles, such as Phosphorus, should be implanted with a dose higher then 5×10^{12} cm^{-2}. Required particles energy is up to 2÷4 MeV per nucleus, or even more. Silicon wafers have diameter of 150±1 mm and base slice of 57±2 mm and thickness of 120÷700 um. Deviation of irradiation dose over the surface should not exceed 20%.

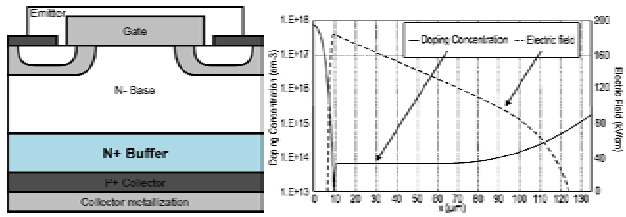

Figure 2: Structure of SPT IGBT.

SOURCE OF IONS

LIS generates ions of different charge states at the same time. These ions are presented in the accelerated beam in different concentrations depending on configuration of the ion source and the accelerator.

An experiment on production of phosphorus ions on LIS is in the beginning stage. Fig. 3 shows structure of silicon beam on the outlet of the accelerator that was produced by LIS with L-100 laser in 2011 [5].

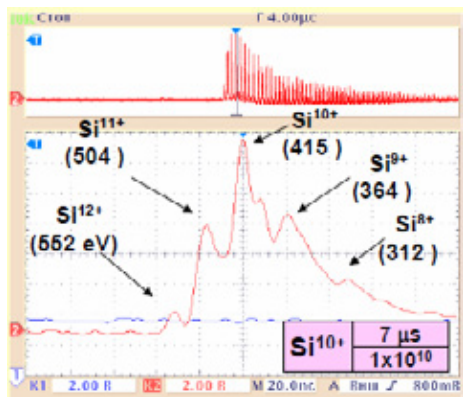

Figure 3: Structure of Si-beam produced by L-100.

Closeness of silicon and phosphorus atoms and similarity of their ionization potentials [6] allows assuming that the structure of phosphorus beam produced by L-100 will include ions of charge 8, 9, 10 and even 11, produced by L-20 - from 4 to 8.

By means of laser's power tuning and positioning of the target it is possible to achieve domination of the particles with required value of ion charge in the beam.

THE SIMULATION

While the accelerator is used as an injector of synchrotron it typically operates at maximum possible energy of ions. But in case of doping of semiconductor

ISBN 978-3-95450-170-0

materials exactly required energy distribution and maximum intensity of the beam should be provided.

Simple mathematical model of an accelerating gap which assumes constant amplitude of acceleration field was used for the simulation, but values of the amplitudes and geometry of the buncher and the accelerator was chosen by approximation of accelerating field calculated by solving of Poisson equations [7]. The model was tested on different types of ions and the results are in good agreement with the experimental data available.

It should be noted that beam loss results listed below were obtained considering only phase motion of particles and they are not involve space charge effects which are dominant prior to the first accelerating gap of the resonator. It was shown in work [7] space charge effects causes beam losses of about 70% of 50 mA and about 80% of 100 mA.

Fig. 4 shows dependence of the transfer factor and the beam energy from the phase of the buncher for different ion charges of phosphorus.

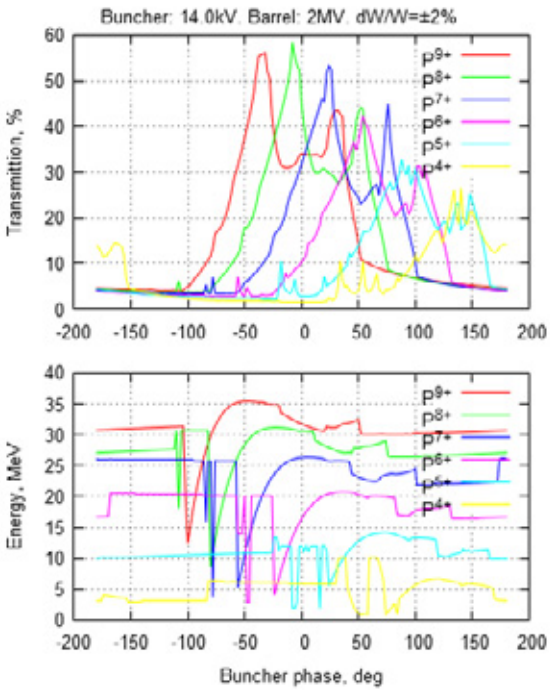

Figure 4: Transferring of phosphorus.

Acceleration efficiency of low charge ions is not high but the energies are in the required range for the implantation. Using of ions with different charge without separation by the energy allows providing smooth variation of doping concentration. Fig. 5a shows the results of the simulation of irradiation of silicon target by the beam composed of phosphorus ions of various charge state. The simulation was performed by SRIM [8] software.

Irregularity of the distribution may be simply eliminated by varying of accelerating voltage during of irradiation (Fig. 5b).

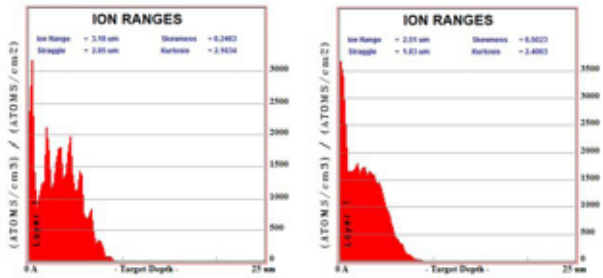

Figure 5: Irradiation of Si-target by P-beam at 1 MV (a), 0.8÷1 MV (b).

More complicated variations of beam parameters that are besides may occur spontaneously during long irradiation process will allow providing high quality of the distribution.

Simulation of longitudinal motion in the accelerator I-3 shows that it is possible to vary the energy of the beam by varying accelerating voltage of the resonator in a wide range. Fig. 6 shows dependence of the beam energy from the accelerating voltage.

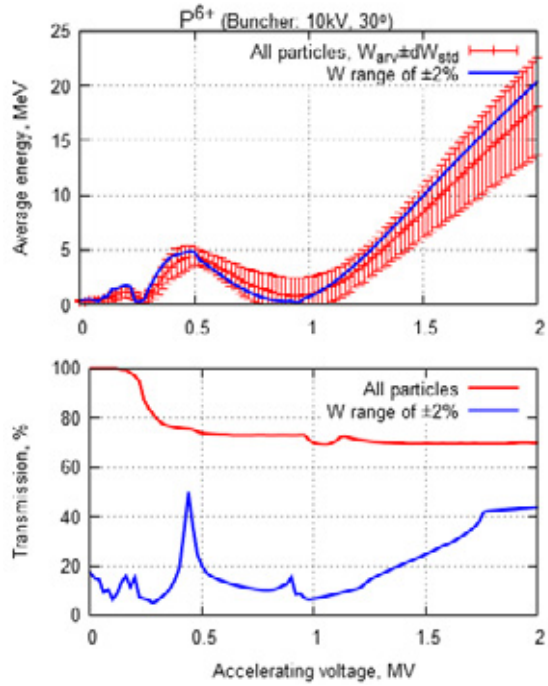

Figure 6: P^{6+} beam energy and transmission factor vs. accelerating voltage.

Transverse motion

Space charge effects are dominant in the transverse motion of particles before the acceleration begins. These effects are not considered in this work. So, transverse motion was simulated only after the acceleration while initial data for the simulation was extracted from [7] where space charge effects were involved.

ISBN 978-3-95450-170-0

Triplet of the quadruples in the beamline allows focusing the beam on the target. If necessary, the analyzing magnet may be used to select required energy of particles.

SCANNING OF THE WAFER

Technology of scanning of the wafer by the beam should be used to produce uniform particles density on the surface. Technical details of this task are out of this work. Only the method of varying of beam coordinates relative to the target to provide uniform dose and minimize time of the irradiation is described.

In case of using I-3 with present parameters to provide required particles density on the target of mentioned size thousands of pulses should be performed. Uniform density distribution may be achieved by simple regular shifting of the beam along the target. The beam should be focused to reduce particle losses on the edges of the target.

In case of increased beam intensity the distribution of the particles inside the beam becomes important. It looks a good idea to use triangular mesh for positioning the beam along the wafer (or vise versa). Minimal number of pulses that provide irradiation of round wafer of radius R with the beam of η particles to produce a dose of ρ may be written as (1).

$$n_{\min} = \frac{\pi \cdot R^2 \cdot \rho}{\eta} \tag{1}$$

Allowable number of nodes of the concentric triangle mesh is defined by expression (2).

$$3k^2 + 3k + 1, \tag{2}$$

where k - is the number of concentric hexagonal layers forming the mesh. Equating expressions (1) and (2) we get the expression for the number of layers (3).

$$K = \left[\sqrt{\frac{4n_{\min} - 1}{12}} - \frac{1}{2} \right] \approx \left[R\sqrt{\frac{\rho}{\eta}} \right] \tag{3}$$

Therefore step of the mesh may be expressed by (4).

$$a = \frac{R}{K} \approx \sqrt{\frac{\eta}{\rho}} \tag{4}$$

Using these expressions we will get that to provide particles density of 5×10^{12} см$^{-1}$ by the beam with 1×10^{11} particles we need about 9 thousands pulses, the step of the mesh is about 1.4 mm and it takes about three hours. These values are acceptable for initial experiments. But to become an industrial machine we need to increase the beam intensity. If we get an order of magnitude then the irradiation of a wafer will take about 15 minutes with step of the mesh about 4.5 mm.

It should be noted that in case of transverse beam size significantly exceeds the step of the mesh additional pulses must be provided outside of the wafer to compensate particles losses on the edges of the wafer. Total number of layers needed may be expressed as (5).

$$K_T \approx \left[(R + r)\sqrt{\frac{\rho}{\eta}} \right], \tag{5}$$

where r - is the radius of the beam. Taking into account (5) it is reasonable to provide good focusing of the beam.

CONCLUSION

The investigation shows that application of ion linac I-3 as independent industrial device may be reasonable. The accelerator may be tested as a machine for doping semiconductor devices particularly for implantation of phosphorus ions in accordance with SPT technology.

Main trouble on the way of industrial application of the accelerator is relatively low intensity of the beam generated by the laser ion source and as the result long irradiation time and low productivity. The way to solve this problem is to optimize parameters of the laser ion source (this work is in progress now) or to use an alternate source of ions such as ECR.

REFERENCES

[1] N.N. Alexeev et al., "Upgrade concept of multipurpose ITEP-TWAC accelerator complex", in Proc. of AccApp'2013, Bruges, Belgium

[2] S.B. Felch et al., "Ion implantation for semiconductor devices: the largest use of industrial accelerators", in Proc. of PAC'2013, Pasadena, CA, USA

[3] A. Wintrich et al., "Application Manual Power Semiconductors", ISBN 978-3-938843-66-6, SEMIKRON International (2011)

[4] M. Rahimo et al., Patent № WO2011058035 A3 "Punch-through semiconductor device and method for producing same", 2011

[5] N.N. Alexeev et al., "ITEP-TWAC Progress Report", in Proc. of IPAC'2011, Kursaal, San Sebastian, Spain

[6] A. Kramida et al., "NIST Atomic Spectra Database", National Institute of Standards and Technology, Gaithersburg, MD, http://physics.nist.gov/asd

[7] A. Balabin et al., "Numerical Study of Beam Current Limit in the I-3 Ion Injector", these proceedings, TUPSA08, RuPAC'2014, Obninsk, Russia

[8] http://www.srim.org/

ISBN 978-3-95450-170-0

DESIGN OF MULTIFUNCTIONAL FACILITY BASED ON ECR ION SOURCE FOR MATERIAL SCIENCE

S. Andrianov, B. Chalykh, M. Comunian, G. Kropachev, R. Kuybeda, T. Kulevoy, A. Ziiatdinova,
ITEP, Moscow, Russia; LNL-INFN, Legnaro (PD), Italy; NRNU "MEPhI", Moscow, Russia

Abstract

The traditional experimental method for new materials radiation resistance investigation is a reactor irradiation. However, there are some difficulties during steel exposure in reactor. Simulationmethod based on ion irradiation allows accelerating the defect generation in the material under investigation. Also a modification of materials by ion beams represents the great practical interest for modern material science. The design of the test-bench based on ECR ion source and electrostatic acceleration is presented. This paper describes the results of beam dynamics simulation in the transport channels of the test-bench. Simulation was carried out in the "real" fields. Continuous ion beam achievable at the test-bench enables beam fluence on the target up to 10^{16} p/m^2.

INTRODUCTION

The creation of new high-tech energy systems is associated with the use of new radiation-resistant materials. A necessity emerges to study and test the new materials. Neutron flux irradiation of samples occurs in the reactor. Certain difficulties arise when steel is exposed to radiation in the reactor. These problems are primarily associated with the time it takes to reach required doses. Even in fast reactors the exposure to the required doses may take years. There is a need to take into account the complexity and high cost of reactor-based systems and, consequently, of the tests themselves. High level of induced radioactivity of the materials is another factor which complicates their study. It emerges in the course of long-term irradiation in the reactor core and makes it difficult to further study the irradiated samples. Low-energy ions can be used to model the process of kicking out atoms formed in the course of neutron irradiation. Ion beams irradiation is an express analysis method which was offered in the 80-s[1]. This method allows to accelerate the process of defect emergence in irradiated materials due to the speeding up of dose accumulation. It must be taken into account that the speeding up of the dose accumulation during the simulation may lead to discrepancies in the results as compared to the real condition that exist in the reactor. Hence, it is considered necessary to reproduce the conditions of the reactor as closely as possible. The process of defect formation depends on the temperature, so the irradiatiated target will be specially heated. Now, experiments are carried out using a pulse beam on HIP-1 RFQ [2]. Oscillation of samples temperature must not exceed 1-3 degrees Celsius. This criterion is very hard to achieve when using a pulse beam.

In order to be able to reproduce the processes in the reactor with greater accuracy our target will not only be heated but defect containing area will be implanted with ions of hydrogen and helium. This will be done with the intention to model the accumulation of He and H in the reactor wall under the influence of the neutron flux.

Besides radiation-resistant material research, modification of materials by high energy ion beams is of great practical interest. Vanadium, chromium, tungsten ions beams can be used for this purpose. A great increase in durability and surface strength can be achieved by irradiation with powerful beams[3].

TEST-BENCH SET-UP

It is planned that apart from material science related tests experiments to study the interaction of the ion beam with plasma and metal vapor targets will be carried out as well. For plasma target and material modification experiments ion beams of 1-2 MeV are necessary. In order to achieve this installation of electrostatic accelerating tube has been planned.

ITEP is developing a multifunctional facility which will make possible the ion beam experiments that will allow to investigate materials by means of express analysis based on imitation of damages materials sustain in the reactor.

The test-bench is designed to have four experimental channels:

1. For experiments simulating of damage caused by neutrons
2. For both modifications of material surfaces and simulation experiments
3. For plasma target experiments
4. For injection of ion beam into accelerating structure

Experimental channels will exit the bending magnet at 90°, 60°, 30°, 0° angles correspondingly.

Specifications of the last two channels are still being discussed. So modeling of their beam dynamics will be carried out at a later date.

Geometry and tract elements of the test-bench were chosen on the basis of beam dynamics modeling.

It had two stages:

1. Modeling of beam dynamics in approximation to “ideal” fields[4].

2. Modeling of beam dynamics in approximation to “real” fields.

Modeling for Fe^{10+}, H^+, He^+ ions was done in both channels.

In order to minimize the possible effects of chemical reactions on the experiment it is best to use the ions of the same element of which the target is built. In this case the Fe ions are going to be used as it is the main constituent of construction steel. A modern ECR ion source can

ISBN 978-3-95450-170-0

generate highly charged particles and when working with Fe^{10+}a continuous ion beam with a current of 50-70 μA can be reached [6].

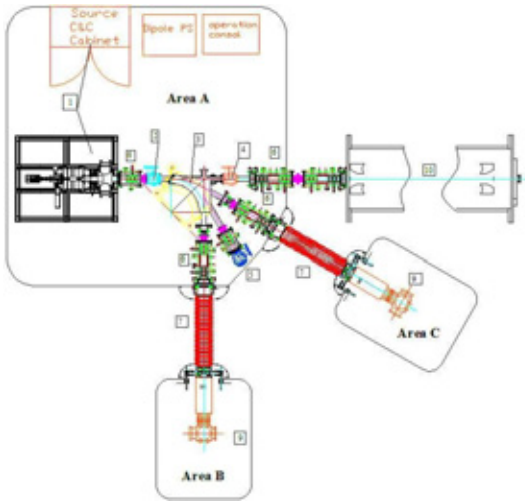

Figure 1: Principal scheme of the multifunction test-bench. 1-ECR ion source and its control cabinet, 2-focusing system, 3-bending magnet, 4-Faraday cup, 5-target assembly for specimen irradiation for atom probe analysis, 6-focusing elements, 7-accelerating tubes, 8,9-target assembly for high-energy experiments, 10-linac [5].

As has been mentioned the area in which the defects appeared when it is bombarded by the main beam is implanted with H and He ions.

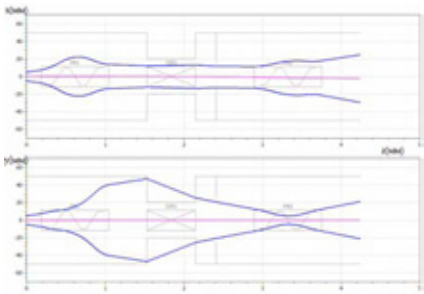

Figure 2: Fe^{10+} ion beam envelope in 60° channel.

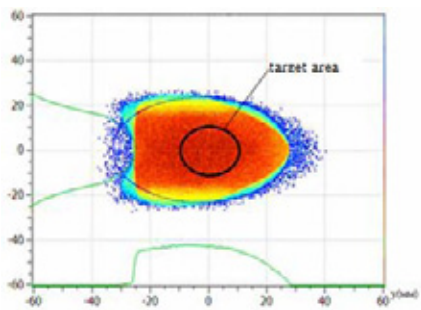

Figure 3: Fe^{10+} ion beam form in output of 60° channel.

For samples placed in the channel turning 60 degrees energies on the order of 150 keV are necessary. In order to reach such energy for Fe^{10+}a voltage of 15 kV has to be applied at the source. This may lead to a decrease of beam intensity as max voltage is 25 kV. For this reason modeling for Fe^{6+}has also been done in this channel. The final decision will be made after the facility is commissioned.

During the initial modeling which was done in order choose the type of the focusing system for the channel that would enable the passage of the beam through the bending magnet with no losses. As a result the system of triplets of quadruple electrostatic lenses was chosen. After the simulation in approximation of "ideal" fields triplet of quadruple electrostatic lenses model was created in CST STUDIO. This was done to calculate the distribution of the "real" fields generated by the lenses.

MODELING OF BEAM DYNAMICS IN APPROXIMATION TO "REAL" FIELDS FOR 60 DEGREES CHANNEL

The date received from the above simulation was used to generate a more realistic picture of the influence of the field distribution on the trajectories of the particles.

The envelope of the beam and the beam profile at the outputs for Fe^{10+} and Fe^{6+} are shown on the fig. 2 and 3.

N, C, O, Fe of different charges may be present inside the beam due to residual gases and ion generation technologies. Below is the Table 1 for the most "dangerous" ions whose mass/charge relation is closest to that of the working ions.

Table 1: Energy for mass/charge relation like Fe^{10+}/ Fe^{6+}

Element	Ion	A/Z	Energy, keV
Iron(56)	Fe^{10+}	5,6	150
	Fe^{11+}	5,1	165
	Fe^{9+}	6,2	135
	Fe^{6+}	9,3	150
	Fe^{5+}	11,2	125
	Fe^{7+}	8	175
Oxygen(16)	O^{3+}	5,3	45
	O^{2+}	8	30
	O^{1+}	4	60
Carbon(12)	C^{1+}	12	25
	C^{2+}	6	30
	C^{3+}	4	45
Nitrogen(14)	N^{1+}	14	25
	N^{3+}	4,6	45
	N^{2+}	7	30

Also, the quality of the separation system's operation was estimated under the parameters from the computer simulation described above. In order to ensure the efficiency of mass separator the modeling of the working and the "contaminated" beams was carried out simultaneously.

For Fe^{10+} it also indicated that ions O^{3+} and C^{2+} partially stopped by the magnet and the diaphragm. 17% of oxygen ions and 2% of carbon ions reached the end of

ISBN 978-3-95450-170-0

the tract, but they don't hit the target. The profile of the beam at the output is shown on the fig. 4 and 5.

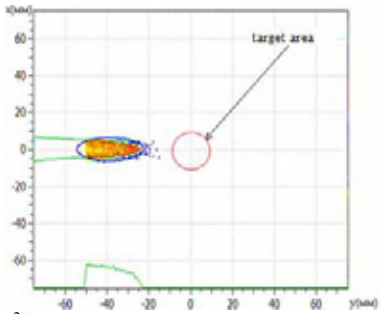

Figure 4: O^{3+} ion beam form in output of 60° channel at joint calculation with Fe^{10+}.

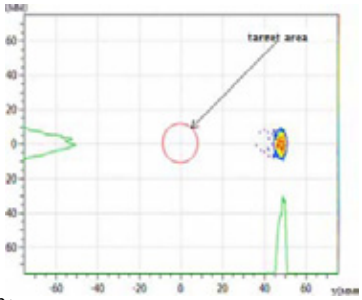

Figure 5: C^{2+} ion beam form in output of 60° channel at joint calculation with Fe^{10+}.

MODELING OF BEAM DYNAMICS IN APPROXIMATION TO "REAL" FIELDS FOR 90 DEGREES CHANNEL

The same kind of simulation was done for the 90 degrees channel. Fig 6 and 7 show envelope and the profile of the Fe^{10+} beam. As well a similar simulations were done for Va, Ti and Cr ions under the same parameters.

The efficiency of the separation system was checked. It showed that all non-working ions were stopped by the separator.

CONCLUSION

As a result of the beam dynamic simulation the geometry of the two channels has been developed and its constituent elements parameters for planned experiments were determined. The formation of the necessary beam profile, uniform distribution of the ions in the point of the samples location as well as the purity of the ion flux have all been achieved.

The results of the simulation became the basis for the engineering project. As of now the measurements of the room that is going to house the facility have been completed. The preliminary blueprints of test-bench installation have also been developed.

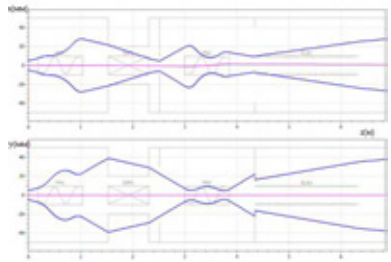

Figure 6: Fe^{10+} beam envelope in 90° channel.

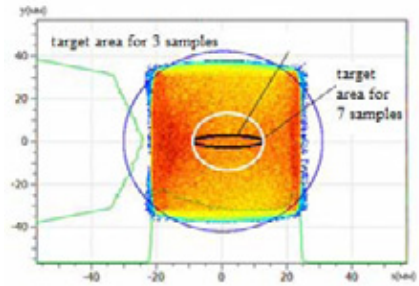

Figure 7: Fe^{10+} ion beam form in output of в 90° channel.

REFERENCES

[1] Nelson R.S., Mazey D.J. // The use of ion accelerations to simulate fast neutron-induced in metals / J.Nucl.Mater. – 1970. – V.37. – P. 1-12.

[2] V.Batalin, Y. Volkov, T. Kulevoy, S.Petrenko, "Report on ITEP MEVVA Development"Proc. WorkshoponVacuumArcIonSources, Berkeley, USA. – 1996.–P.37-39

[3] Shulov V.A. "Modification of the properties of high-temperature alloys continuous and pulsed ion beams" abstract, Minsk, Belarus. – 1995. 42 p.

[4] T. V. Kulevoy, B. B. Chalykh, R. P. Kuibeda, G. N. Kropachev, and A. V. Ziiatdinova "Project of electro-cyclotron resonance ion source test-bench for material investigation", Rev. Sci. Instrum. 85, 02A910 (2014); doi: 10.1063/1.4824642

[5] B.B. Chalykh, R.P. Kuybeda, T.V. Kulevoy, A.V. Ziyatdinova //Designe of the accelerator stand with the ECR-source for simulatuion experiments on the radiation damage of the steels of the nuclear industry/ ISSN 1562-6016. VANT. 2014. №3(91).

[6] H. Koivisto, P. Heikkinen, V. Hänninen, A. Lassila, H. Leinonen, V. Nieminen, J. Pakarinen, K. Ranttila, J. Ärje and E. Liukkonen // The First Results with the New JYFL 14 GHz ECR ion source /Department of Physics, University of Jyväskylä, P.O. Box 35, FIN-40351,Jyväskylä, Finland.

ISBN 978-3-95450-170-0

THE INDUCTION SYNCHROTRON WITH A CONSTANT MAGNETIC FIELD

G.V. Dolbilov#, Joint Institute for Nuclear Research, Dubna, 141980, Russia

Abstract

In this paper the possibility of accelerating charged particles in a "nearly constant" orbit in a constant magnetic field is discussed.

The trajectories of the accelerated particles are formed by set azimuthally short bending magnets in which the deflection angle is independent of the particle energy.

Focusing of the beam is carried out by the alternating field bending magnets and quadrupole lenses.

The particles are accelerated by the electric field induction sections. Stability of longitudinal oscillations is determined by the shape of the top of the accelerating pulse.

INTRODUCTION

- Features Traditional cyclic accelerators:

1. Accelerators with a constant magnetic field.
   - High ranges of change in orbital radius.
   - Heavy weight of magnets.
2. Accelerators with a constant radius of an equilibrium orbit
   - Magnetic strengths depends on energy of ions.
   - Resonant frequencies of the HF-field depends on energy of particles (cyclic frequency).

- The Induction Synchrotron with Constant Magnetic Field

1. The Magnetic field is constant in time.
   - The Orbital radius $r \sim r_{max}$
   - Particle trajectories – arc chords.
   - $\Delta r = r_{max} - r \leq r_{max}(\pi/N)^2$, N - arc chord number.
2. The Induction accelerating electric field:
   - Isn't present resonant systems with a variable frequency.
   - Synchronization is carried out by sync pulses.

Scheme accelerator with a constant magnetic field is shown in Fig. 1.

MAGNETIC SYSTEM OF THE SYNCHROTRON

1. Special sections of magnetic dipoles form the near-circular orbit with $r \simeq r_{max}$ radius.

- Each dipole of section (Fig.2) deflects the accelerated beam on $\Delta\Theta/2$ angle.
- This angle doesn't depend on energy of particles if the internal border of dipoles corresponds to equality

$$x = \pm\left[(r_{max} - r)\sin\frac{\Delta\Theta}{2} + x_0\right]$$

x - distance of internal border of dipoles to bisector of angle $\Delta\Theta$

x_0 - the size determined by a concrete design of section

r , r_{max} -the current and maximum radiuses determined by energy of a particle.

2. The focusing forces of magnetic section.

- Magnetic fields of section focus the accelerated particles in the horizontal plane.
- Magnetic forces of section defocus the accelerated particles in the vertical plane.
- Additional lenses on an entrance and an exit of magnetic section are required.

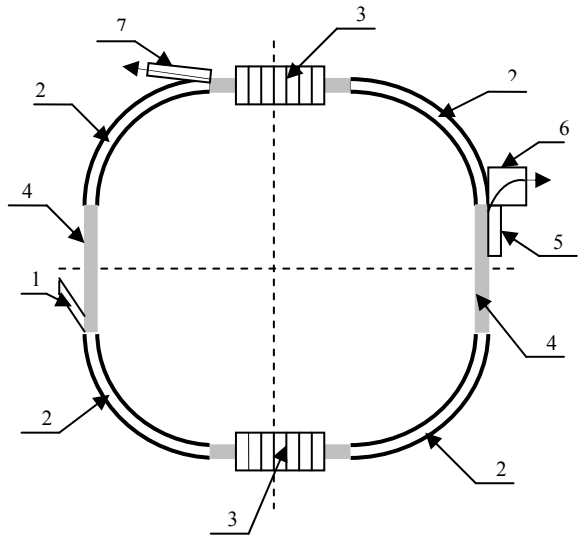

Figure 1: Scheme accelerator with a constant magnetic field. 1 - Injector; 2 - Set of special sections of magnetic dipoles; 3 - Induction accelerating sections; 4 - Straight-line segments; 5-7 - System of fast and slow beam extraction.

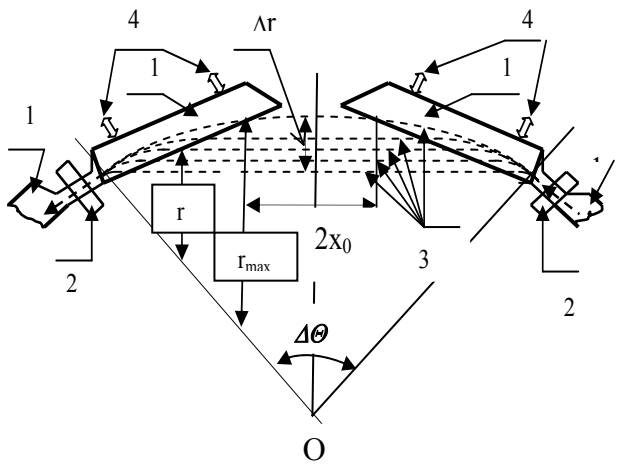

Figure 2: The warrant of the bending magnetic section using dipoles with a uniform field. 1 - Dipoles with a uniform field; 2 – Additional focusing lenses; 3 – Beam trajectories; 4 - System tuning the beam trafctores, 5 – ΔΘ - The center angle of a beam deflection.

ISBN 978-3-95450-170-0

DYNAMICS OF PARTICLES IN MAGNETIC SECTION

Vertical Plane of Section

- Matrix of magnetic section

$$[M_z]=[f_1][m_z][f_z][x][f_z][m_z][f_1]$$

$[f_1]=\begin{bmatrix}1 & 0\\ -1/f_{1z} & 1\end{bmatrix}$ – Matrix of additional lenses

$[m_z]=\begin{bmatrix}1 & m\\ o & 1\end{bmatrix}$ – Matrix of magnetic dipoles $m = r\Delta\Theta/2$

$[f_z]=\begin{bmatrix}1 & 0\\ 1/f & 1\end{bmatrix}$ – Matrix of a fringing field of dipoles $f = rtg\Delta\Theta/4$, [3]

$[x]=\begin{bmatrix}1 & 2x\\ 0 & 1\end{bmatrix}$ – Matrix of drift of particles between dipoles

$$x=\left[(r_{\max}-r)\sin\frac{\Delta\Theta}{2}+x_0\right]$$

Horizontal Plane of Section

- Matrix of magnetic section

$$[M_r]=[f_2][m_r][f_r][x][f_r][m_r][f_2]$$

$[f_2]=\begin{bmatrix}1 & 0\\ -1/f_{2r} & 1\end{bmatrix}$ – Matrix of additional lenses

$[m_r]=\begin{bmatrix}\cos\Delta\Theta/2 & r\sin\Delta\Theta/2\\ -\frac{1}{r}\sin\Delta\Theta/2 & \cos\Delta\Theta/2\end{bmatrix}$ – Matrix of magnetic dipoles

$[f_r]=\begin{bmatrix}1 & 0\\ -1/f & 1\end{bmatrix}$ – Matrix of a fringing field of dipoles $f = rtg\,\Delta\Theta/4$

Of special interest is the case where the focal lengths for additional input and output bending magnetic section are:

$$f_{1z}=(f+m) \quad \text{- for } z\text{-plane} \qquad (1)$$

$$f_{2r}=f \quad \text{- for } r\text{ –plane} \qquad (2)$$

In this case, the matrices M_z and M_r are equivalent drift matrices:

$$[M_z]=\begin{bmatrix}1 & L_z\\ 0 & 1\end{bmatrix}$$

$$L_z=2(1+m_z/f)[m_z+x(1+m_z/f)]$$

$$[M_r]=\begin{bmatrix}1 & L_r\\ 0 & 1\end{bmatrix}$$

$$L_r=2\left[x-f\left(1+\cos\Delta\Theta/2\right)\right]$$

Using on an entrance and an exit of bending sections a combination of a symmetric lens with focal length

$$f_S=2f\frac{(m_z+f)}{m_z+2f}$$

and a quadrupole lens with focal length

$$f_q=\pm 2f\frac{(m_z+f)}{m}$$

we will receive the demanded parameters of a combination of lenses

$$\frac{1}{f_S}-\frac{1}{|f_q|}=\frac{1}{f_1} \qquad \frac{1}{f_S}+\frac{1}{|f_q|}=\frac{1}{f_2}$$

and the simultaneous fulfillment of condition (1) and (2).

5. At small angles of $\Delta\Theta$, when $tg\frac{\Delta\Theta}{4}\cong\frac{\Delta\Theta}{4}$

$$f_S=\frac{3}{8}r\Delta\Theta \qquad f_q=\pm\frac{3}{4}r\Delta\Theta$$

FOCUSING OF A BEAM AT ACCELERATION OF PARTICLES

- The ***FODO*** mode of focusing can be used at acceleration of particles. A focusing period matrix for the case where the conditions (1) and (2) are satisfied

$$[N_{z,r}]=\begin{bmatrix}1 & L_{z,r}\\ 0 & 1\end{bmatrix}\cdot\begin{bmatrix}1 & 0\\ 1/f_{z,r} & 0\end{bmatrix}\cdot\begin{bmatrix}1 & L_{z,r}\\ 0 & 1\end{bmatrix}\cdot\begin{bmatrix}1 & 0\\ -1/f_{z,r} & 1\end{bmatrix}=\begin{bmatrix}N_{11}^{z,r} & N_{12}^{z,r}\\ N_{21}^{z,r} & N_{22}^{rr}\end{bmatrix}$$

$$N_{11}^{z,r}=1-\left(L_{z,r}/f_{z,r}\right)^2-L_{z,r}/f_{z,r}$$

$$N_{12}^{z,r}=\left(2+L_{z,r}/f_{z,r}\right)\cdot L_{z,r}$$

$$N_{21}^{z,r}=-L_{z,r}/f_{z,r}^2$$

$$N_{22}^{z,r}=1+L_{z,r}/f_{z,r}$$

- Change of a phase of betatron fluctuations for one period of the focusing system is defined by a ratio

$$\cos\sigma_{z,r}=\frac{1}{2}\left(N_{11}^{z,r}+N_{22}^{z,r}\right)=1-\frac{1}{2}\left(\frac{L_{z,r}}{f_{z,r}}\right)^2$$

or

$$\sin\frac{\sigma_{z,r}}{2}=\frac{1}{2}\frac{L_{z,r}}{f_{z,r}}$$

ISBN 978-3-95450-170-0

CONCLUSION

- Frequencies of betatron oscillations

At $f_r \approx f_z = 4.5\left[r_{\max}\Delta\Theta + 2x_0\right]$

$2\Delta\Theta = 30^0$; $r_{\max}\Delta\Theta >> 2x_0$

frequency range of betatron oscillations during acceleration is shown in Table 1

Tab.1 frequency range of betatron oscillations during acceleration

$\nu_{z,r}$	$P << P_{\max}$ $r << r_{\max}$	$P = 0{,}5P_{\max}$ $r = 0.5r_{\max}$	$P = P_{\max}$ $r = r_{\max}$
ν_z	6	9.2	10.7
ν_r	11.6	12	12.8

- For 200MeV proton accelerator, B = 1T (NdFeB-magnet), $r_{\max} = 2.15$m, $\Delta r = r_{\max} - r_{\min} = 2.2$cm
- At beam emittance $\varepsilon = 30\pi mm.mrad$ equibrium radius, about which varies the beam envelopes are:

$$a_{z,r} = \sqrt{\varepsilon r_{\max}/\nu_{z,r}} = 2.2 - 3.3mm$$

- The duration of the accelerating pulses of induction system [4]:

$$\tau_{ind} \le 0.5\tau_c = \pi r_{\max}/v_{\max} = 40ns$$

- Azimuthal stability is provided with an inclination of a table of the accelerating induction impulses (See Fig.3)

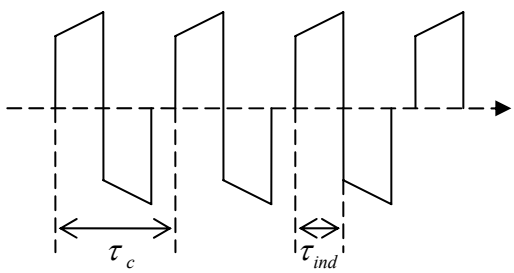

Figure 3: The accelerating induction pulses

τ_c – the acceleration cycle duration,

τ_{ind} – the induction pulse duration.

REFERENCES

[1] G.V. Dolbilov, “Method of cyclic acceleration of charged particles", Patent JINR, №2451435

[2] G.V. Dolbilov, "The cyclic accelerator of charged particles", PatentJINR, №2477936

[3] J. Livingood,”Principle of cyclic particle accelerators”,Argonne National Lababoratory

[4] G.V. Dolbilov, S.I. Tyutyunnikov, ”Method of induction acceleration of ions", Patent JINR №2420045

ISBN 978-3-95450-170-0

THE COMPACT INDUCTION ACCELERATOR OF ELECTRONS FOR RADIATION TECHNOLOGIES

G.V. Dolbilov#, Joint Institute for Nuclear Research, Dubna, 141980, Russia

Abstract

The electron accelerator with energy <10 MEV uses a rectangular pulse of the accelerating induction voltage and a trapezoidal pulse of a leading magnetic field. To preserve the equilibrium orbit radius constant special relationship between the amplitude and temporal characteristics of the magnetic induction and the accelerating voltage inductors are made. It is possible to maintain an orbit close to constant in a constant magnetic field in time. The accelerator contains alternating-sign focusing in dipole magnets and rectilinear accelerator parts.

INTRODUCTION

For receiving electron beams with energy of 0.5-10 MeV the cyclic accelerator in which particles are accelerated by linear induction section can be used [1,2].

For formation of the closed equilibrium orbit of electrons two methods can be used:

1 - a method with the magnetic field growing at acceleration;

2 - a method with a magnetic field, constant on time;

In a both cases the accelerator contains alternating-sign focusing in magnets and rectilinear accelerator parts.

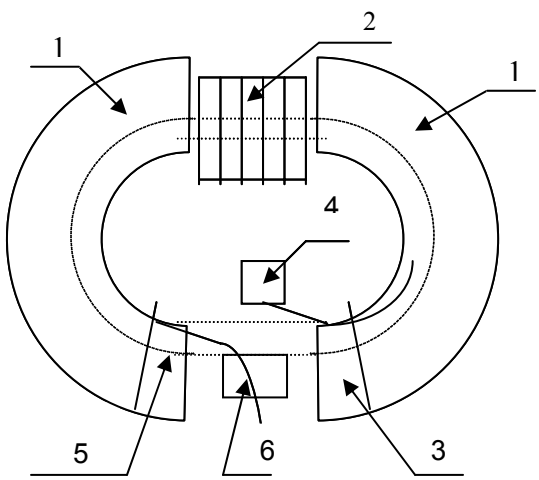

Figure 1: The scheme of the accelerator. 1 - the magnetic system with alternating focusing; 2 - the linear induction accelerating system; 3-6 - systems of input and output of electrons.

THE ELECTRON ACCELERATOR WITH A VARIABLE MAGNETIC FIELD [3]

For $R(t) = R_0$ =Const, the following condition has to be carried out

$$\frac{dB}{dt} = \frac{nU_{ind}}{LR_0}$$

where n – number of inductors; U_{ind} – inductor voltage; L – orbit perimeter.

Energy of electrons 0.5-10MeV can be reached for one pulse T_1 - duration

$$T_1 = 10^{-4} - 10^{-6}\, s$$

To this end total cross-section of inductors of accelerating section is equal to

$$S = \frac{WL}{\Delta Bc}$$

where W - energy of electrons, L - perimeter of an orbit, $\Delta B \leq 2B_s$, B_s - induction of saturation of inductors, c-velocity of light.

Diagram of magnetic induction, B(t), and the accelerating pulse of induction section, U(t), shown in Fig. 2.

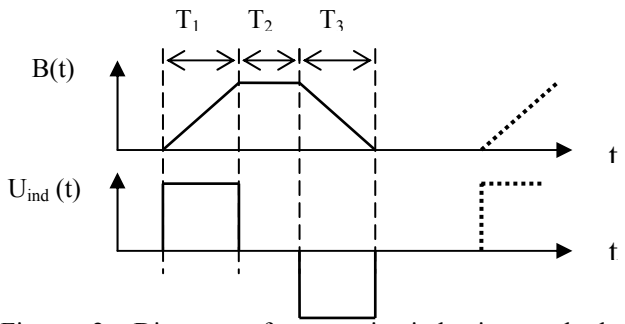

Figure 2: Diagram of magnetic induction and the accelerating pulse of induction section. T_1 – Time of acceleration of electrons, T_2 - Beam extraction time, T_3 - Time of magnetic reversal of inductors of section.

THE ELECTRON ACCELERATOR WITH A CONSTANT MAGNETIC FIELD

The magnetic system of the accelerator is a set of special sections of magnets (Fig.3). The section contains two dipoles. Each dipole deflects the beam at the predetermined angle of ΔΘ/2 which doesn't depend on energy of the accelerated particles.

- The beam trajectory with the maximum energy is r_{max} radius circle;
- The beam trajectory with energy of injection is $\Delta\Theta$ angle chord.

$$\Delta r = r_{max} - r_{min} = r_{max}\left(1 - \cos\frac{\Delta\Theta}{2}\right)$$

$$\Delta r \approx R_{max}\frac{1}{2}\left(\frac{\Delta\Theta}{2}\right)^2$$

ISBN 978-3-95450-170-0

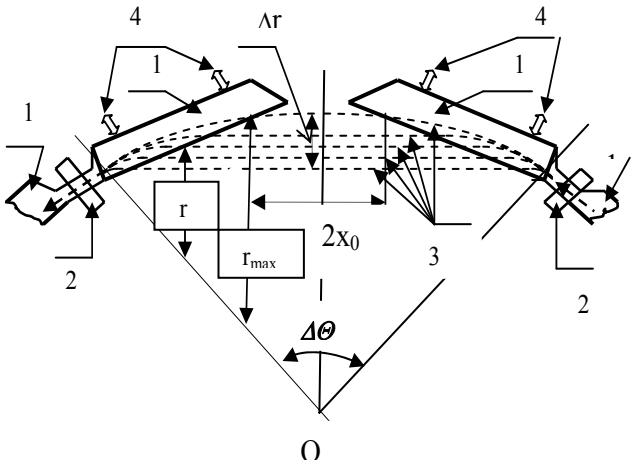

Figure 3: Special section of magnetic system. 1 - Magnetic dipoles with a uniform field, 2 - combination of quadrupole and symmetric lenses, 3 - Beam trajectories with various energy of particles, 4 - System tuning the beam trafctores.

- Amplitude and duration of pulses of the accelerating voltage is

$$U_{acc}T_1 = \Delta BnS$$

U_{acc} – accelerating voltage,
T_1 – pulse duration,
ΔB < 2Bs, Bs - induction of saturation of the inductor core,
n - number of inductors, S - cross-sectional area inductor

- Total cross section of the inductors

$$nS = \frac{WL}{\Delta B v_a}$$

W - the final energy of the electrons;
L - периметр равновесной орбиты;
v_a - the average velocity of the electrons, $v_a \simeq c$

- The radial cross-sectional size of inductors is

$$\Delta r_S = \frac{W}{\Delta Bc}\frac{L_p}{L_{ind}}$$

where L_p and L_{ind} - the perimeter of the equilibrium orbit and length of the induction section.

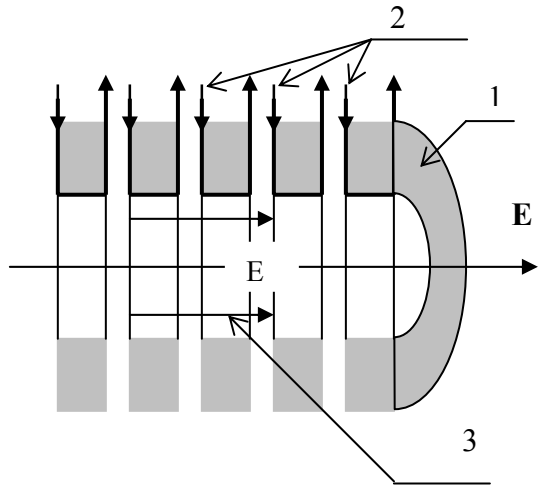

Figure 4: Shematic diagram of induction accelerating section. 1 – Ferromagnetic cores of inductors, 2 – Exciting loops of inductors, 3 - The accelerating electric field.

CONCLUSION

- The maximum energy of the electrons, which can be achieved in the excitation inductors single rectangular pulse, depends only on:
  1. $\Delta B \leq 2Bs$, Bs - Saturation induction inductors;
  2. Δr_s - Radial dimension of the cross section of inductors
  3. $Lp / Lind$ - The ratio of the perimeter of the orbit to the length of the induction section.
- When W = 5 MeV, ΔB = 0.5 T and $Lp/Lind$ = 2 parameters of the accelerator is:
  1. $\Delta r_s \simeq 6$ sm
  2. $U_{ind} = 10^2 - 10^4$V
  3. $T_1 = 10^{-4} - 10^{-6}$s

- When a magnetic field on the orbit equal to 0.1T and $W = 5MeV$

r_{max} = 17 cm

- If $B(t)$ = Const, $\Delta\Theta = 30^0$

$r_{max} - r_{min}$ = 0.6 cm

REFERENCES

[1] G.V. Dolbilov, «The Compact Iduction Circular Accelerator for Radiation Technologies», Proceedings of APAC 2007, Raja Ramanna Centre for Advanced Technology(RRCAT), Indore, India, p.p. 628-629
[2] G.V. Dolbilov, "Induction cyclic electron accelerator", Patent JINR, №25245716, 2014.
[3] G.V. Dolbilov, "Method for induction accelerating of electrons", Patent JINR №2513034, 2014.

ISBN 978-3-95450-170-0

PROJECT OF DEMONSTRATION CENTE R OF THE PROTON THERAPY AT DLNP JINR

E.M. Syresin, G.A. Karamysheva, M.Y. Kazarinov, N.A. Morozov, G.V. Mytzin, N.G. Shakun
Joint Institute for Nuclear Research, Dubna, Russia
J. Bokor, Faculty of Electrical Engineering and Information Technology, Slovak University of Technology, Bratislava, Slovakia

Abstract

JINR is one of the leading proton therapy research centers of the Russia. The modern technique of 3D conformal proton radiotherapy was first effectuated in Russia in this center, and now it is effectively used in regular treatment sessions. A special Medico-Technical Complex was created at JINR on the basis of the phasotron used for proton treatment. About 100 patients undergo a course of fractionated treatment here every year. During last 14 years were treated by proton beams more than 1000 patients.

A project of the demonstration center of the proton therapy is discussed on base of a superconducting 230 MeV synchrocyclotron. The superconducting synchrocyclotron is planned to install instead of phasotron in Medical Technical Complex of DLNP. The new transport channel is designed for beam delivery to the JINR medical cabin.

PROJECT OF DEMONSTRATION CENTER OF PROTON THERAPY

The pioneering proton therapy researches began at JINR in 1967 [1]. The phasotron with the proton energy of 660 MeV and current of 2 μA is used for medical applications [1-3]. More than 1000 patients were treated at JINR by the proton beams. During the last years around 100 patients per year got the proton treatment there.

The superconducting synchrocyclotron is planned to install instead of phasotron in Medical Technical Complex of DLNP. The new transport channel is designed for beam delivery to the JINR medical cabin. The equipment of the demonstration center of the proton therapy and realized here technologies will be lay in the base of the future Dubna hospital center of the proton therapy. The final stage of the project is creation of the Dubna hospital center of the proton therapy on basis of the superconducting synchrocylotron and the rotating gantry (Fig.1). The first stage of this project is related to the construction of the demonstration center of the proton therapy on base of a superconducting 230 MeV synchrocyclotron.

High magnetic field of 5T is used in the superconducting synchrocyclotron where the requirement of isochronism is unnecessary and weak focusing is obtained from the negative gradient of the rotationally symmetric magnetic field. The synchrocylotron has following peculiarities in comparison with the isochronous cyclotron: the RF frequency is periodically modulated and the beam is pulsed; the longitudinal dynamics becomes a major aspect of the beam physics with energy-phase oscillations bound by a separatrix; the beam is captured at injection only during a limited time window; the regenerative extraction is needed to recover the beam which has a very small turn separation at extraction; the extracted beam has a relatively low intensity of 20 nA; the central region is strongly reduced in size compared to an equivalent isochronous cyclotron.

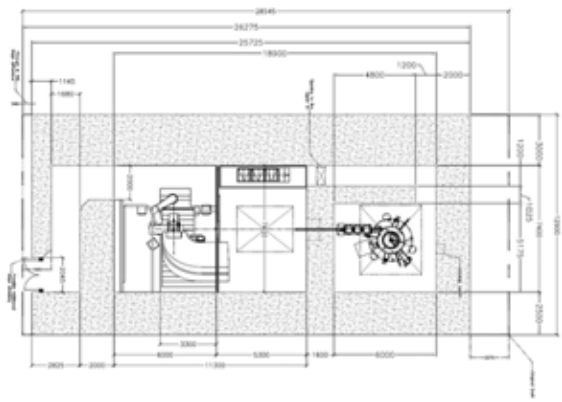

Figure 1: Scheme of Dubna hospital center of proton therapy.

Figure 2: Scheme of synchrocyclotron with beam delivery channel and modernized medical cabin in demonstration center of proton therapy.

ISBN 978-3-95450-170-0

The synchrocyclotron S2C2 [4] (Table.1) has diameter of 2.3m. Main peculiarity of synchrocyclotron is connected with its superconducting magnets with magnetic field in hills and valleys of 5,64/5,24 T, correspondently. Four Sumitomo cryocoolers are used at realization of the superconducting regime.

Table 1. Parameters of synchrocyclotron S2C2.

Irradiation	Active
Diameter, m	2,3
Weight, t	50
Magnet	Superconducting
Average field, center/extract., T	5,64/5.24
Voltage of dee-electrodes, kV	14
RF–frequency, MHz	90-61.5
Frequency of beam pulses, kHz	1
Average current, nA	20
Proton energy, MeV	230
Energy spread, 2σ, MeV	2,5
Horisontal/vertical emittance, π·mm·mrad	23.1/4.1

Figure 3: View of synchrocyclotron S2C2.

Many aspects were considered at optimization of the synchrocylotron magnetic system [4]: optimization of the pole-gap profile; definition of the pole radius and the 230 MeV extraction radius; optimization of coil current density and dimensions; dimensioning of the yoke to reasonably balance the outside stray fields; dimensioning and placement of all horizontal and vertical yoke penetrations; the optimization of the extraction system the shielding required for external systems such as the rotco and the cryo-coolers; the influence of the external iron systems on the accelerated beam; the influence of the fringe field on the external beam line; median plane errors introduced by the vertical asymmetry in the magnetic design and compensation of these errors; magnetic forces acting on the return yoke, the coils, the extraction system elements, external components.

Rf–frequency is changed from 90 MHz to 61.5 MHz, to compensate variation of the revolution period at acceleration caused by increase of the proton relativistic mass and reduction of the magnetic field. The RF resonator operates as a half-wave transmission line terminated on one side by the 180^0 dee and on the opposite side by the rotco. The 8-fold symmetry allows excellent mechanical stability and very good reproducibility of the RF pulse. It rotates at 7500 rpm giving 1 kHz repetition rate.

The central region is extremely compact with a first turn radius less than 2.5 mm and the first 100 turns within a radius of about 3 cm. Calculations show that particles with RF-phases in the range of [-60; +10]° are successfully accepted in synchrotron regime of stable acceleration. Pulse duration of particles captured in acceleration is equal to 7 us, the repetition frequency of beam pulses is 1 kHz, the duty factor corresponds to 0.7 %. Quantitative analysis of losses at injection and during a period of one synchrotron oscillation was carried out to estimate capture as a function of injection time relative to moment when the RF-frequency equals to the revolution frequency of the particles in the centre. Capture efficiency for the synchrocyclotron with driving magnetic field of ~5 Tesla was simulated [5]. Obtained results give capture efficiency of $8 \cdot 10^{-4}$.

Fast and precise pencil beam scanning requires a high dynamic range (a factor 100) in the charge per pulse and also good pulse repeatability. A cold-cathode PIG source is used because of its fast response, long cathode life-time and good pulse stability. The source is pulsed during 50 μsec, in synchrony with the RF.

Regenerative extraction based on $2Q_h = 2$ resonance is used. The regenerator creates a strong bump which locally increases the radial focusing and locks Q_h to 1. Extraction sets at this condition and a displacement of the beam towards the extraction channel steadily builds up. Correctors are used to compensate the undershoots of the regenerator and the extraction channel. A 3-bar corrector guides the beam through the fringe field. A permanent magnet quadrupole in the return yoke matches the cyclotron to the beam line.

In frame of JINR-IBA collaboration are planned to perform special research program oriented on formation of high average current of 100 nA as it was done for proton cyclotron C235-V3.

The simulation of the beam delivery was done from synchrocyclotron to the entrance in the treatment room. The beam is focused to the waist at the entrance of the energy degrader (Fig.4) with a small sizes of 1.95/1.3 mm in order to decrease a growth of the beam geometrical emittances after passing through the energy degrader.

After proton deceleration to energy of 180 MeV at passage through carbon degrader with thickness of 54 mm the beam energy spread corresponds to 4.5 MeV (3σ) and horizontal/vertical beam emittances increase up 36.9/19.3 π·mm·mrad.

ISBN 978-3-95450-170-0

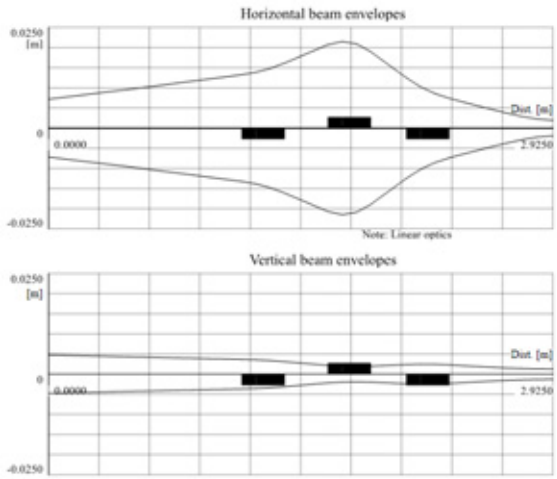

Figure 4: Beam transportation from cyclotron to degrader.

The energy spread (2.4%) is almost 4 times higher after passing the energy degrader than in the case of the extracted beam at the exit of the S2C2 accelerator. To decrease this energy spread and improve the energy distribution quality a momentum slit is placed in the beam line (Fig.5). The momentum slit is placed downstream the dipole magnets to such position where the horizontadispersion function is 1.6 m.

A collimator with a horizontal gap of 10 mm was chosen as a momentum slit. After passing the beam through this slit the energy spread is decreased from 2.4% to 1.6%. Beam transmission of the momentum slit corresponds to 42%.

The horizontal and vertical beam envelopes for the last part of the beam line from the exit of the momentum slit to the final focal point at the entrance to the treatment room are shown in the Fig.6. At the focal plane the horizontal/vertical beam sizes are equal to 9.6/9.7 mm. The horizontal/vertical beam emittance corresponds to 18.3/19 π·mm·mrad.

Two wobbling magnets will be installed to form the uniform dose distribution with transverse size of 15×15 cm in double scattering scheme. The efficiency of beam formation in double scattering scheme is about 30%. As result the average current on tumor target is about 2.4 nA at proton energy of 180 MeV.

At deceleration of proton beam in degrader to energy of 140 MeV it has the energy spread of 2.7 % (3σ) in focal plane, the horizontal/vertical beam size of 11/11.5 mm, horizontal and vertical beam emittances of 26.7/29.2 π·mm·mrad. The efficiency of momentum slit corresponds to 42% at slit gap of 15 mm.

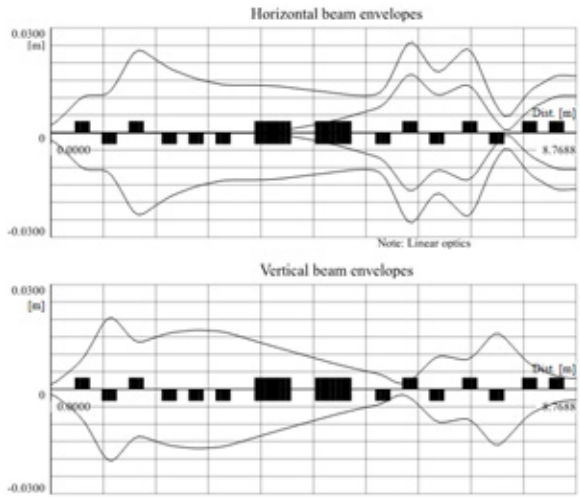

Figure 5: Beam transportation from degrader to momentum slit.

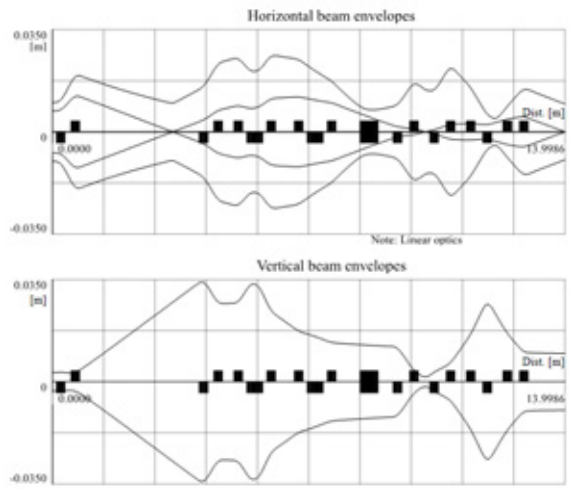

Figure 6: Beam delivery from momentum slit to entrance of treatment room.

REFERENCES

[1] O.V. Savchenko, J. Medical physics (2007), № 3-4.
[2] E.M. Syresin et al, Particle and Nuclei Letters, v.8, 635 (2011).
[3] S.A. Kostromin, E.M. Syresin Particle and Nuclei Letters, v.10, 1346 (2013).
[4] W. Kleeven et al, Proceedings of Cyclotrons 2013, Canada, MO4PB02.
[5] S.Kostromin et al, Proceedings of Cyclotrons 2013, Canada, WEPPT015.

ISBN 978-3-95450-170-0

POSITRON ANNIHILATION SPECTROSCOPY AT LEPTA FACILITY

P. Horodek, Institute of Nuclear Physics PAN, Krakow, Poland
A.G. Kobets, Institute of Electrophysics and Radiation Technologies NAS, Kharkov, Ukraine
I. N. Meshkov, O.S. Orlov, A.A. Sidorin, JINR, Dubna, Russia

Abstract

Positron Annihilation Spectroscopy (PAS) is a sensitive method dedicated to detection of open-volume type of defects in materials. Nowadays, this technique is of a great interest due to the practical character of obtained results. New devices using monoenergetic positron beams are built. The poster presents progress in this field at LEPTA project at Joint Institute for Nuclear Research in Dubna, present and future directions of works.

INTRODUCTION

Positron Annihilation Spectroscopy (PAS) is a great method for detection open-volume defects on the atomic level. It is applied in the field of solid body physics as well as in the material research. It gives interesting results as the independent method or the complementary technique for other methods such as Rutherford Back Scattering (RBS) or Mossbauer Spectroscopy.

PAS is based on the special properties of positron – electron annihilation process. Positron annihilates with its antiparticle – electron and as a result in 99.8 % cases two gamma quanta with energy of about 511 keV are emitted. [1] The annihilation process does not take place immediately, but positron spends some time in the matter on the thermalization and diffusion stages. [2] This time depends on the electron concentration in the structure. If the lattice includes defects the electron density is lower in comparison to a non-defected area and in this was positron life time will be longer. The positron life time means the time between positron emission eg. from the ^{22}Na isotope and annihilation. Because the electron momenta inside traps are also lower in comparison to the bulk, it also finds a reflect in the annihilation characteristics. In this way the energy of gamma quanta will be changed as a result of Doppler effect according to formula

$$E_\gamma \cong mc^2 + E_B \pm \frac{p_{\parallel} c}{2} \qquad (1)$$

where E_b is the energy of positron-electron pair coupling and $p_{\parallel}$ is a perpendicular component of the positron-electron pair's momentum. This effect is observed as the broadening of annihilation line 511 keV. The broadening always appears in this case but for positrons trapped in the defects will be smaller considering the lower electron mementa. It should be noticed that the momentum of thermalized positron can be negligible. Thus the registration 511 keV line gives information about momentum state of electrons taking part in annihilation process. It is the role of Doppler Broadening of Annihilation Gamma Line (DB) technique.

DOPPLER BROADENING OF ANNIHILATION GAMMA LINE TECHNIQUE (DB)

The formula describing the changing of gamma energy can be also expressed as following

$$E_\gamma \cong mc^2 \pm \sqrt{\frac{1}{2} mc^2 E} \ . \qquad (2)$$

If the energy of an annihilating positron equals e.g. 7eV (Fermi energy for copper), then a change of energy of annihilating gamma quantum, according to the above formula, will equal 1,34 keV. Thus, the total broadening of annihilation line will equal 2,68 keV.

Observation of such broadening requires using detectors of a high energetic resolution. Currently available germanium detectors allow to take measurements with resolution equal to 1-2 keV around 511 keV energy.

Doppler broadening of annihilation line technique is used to detect concentrations of defects such as vacancies and their accumulations. A signal from annihilation of a trapped positron gives broadening of the 511 keV line accordingly smaller than the one that would occur in case of annihilation with nucleus electrons. In other words, less defected sample gives smaller broadening of the 511 keV line.

In practice, the broadening of 511 keV line is not calculated but the analysis is limited to evaluating of two characteristic parameters, the so-called S- and W-parameters (see Fig. 1). [3,4]

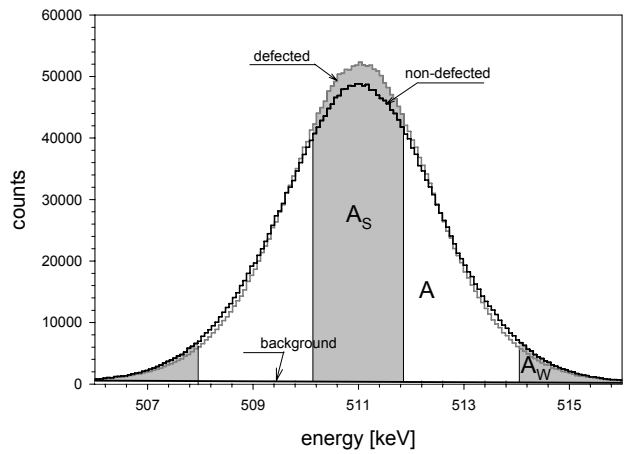

Figure 1: 511 keV lines for defected and nondefected samples.

S parameter defines proportion of annihilation of positrons with low-momentum electrons. It is closely related to concentration of defects in a material. It is

ISBN 978-3-95450-170-0

defined as ratio of surface area under the central part of the 511 keV line to total surface area under this line. Areas are usually selected so that their ratio approximated 0.5. Bigger S parameter value means bigger concentration of defects.

The second parameter, the so called W parameter is defined as a ratio of surface area under the wing part of 511 keV line to total surface area. It is related to annihilation of positrons with high-momentum electrons and it provides information about chemical environment of the defect. Value of this parameter is also selected arbitrarily – it tends to be smaller than 0.01.

Both S and W parameters are calculated after the background reduction. Calculations are made by special computer software. As stated above, the analysis of results of Doppler broadening of annihilation line is based on calculating S and W parameters, changes of which provide information about changes in concentration of defects.

SLOW POSITRON BEAM AT LEPTA FACILITY

The PAS can be realized in two ways. As the standard experiments when positrons emitted directly from the source eg. ^{22}Na are used or using the so called slow positron beam. In the first case positrons have continuous energy spectrum from zero to some maximal energy characterized for chosen isotope eg. 545 keV for ^{22}Na and 1.89 MeV for ^{68}Ge. In this way the mean implantation depth is a few dozen micrometers in dependency on the kind of material. Changes in the structure near the surface are invisible. The second solution allows slowing-down positron to the energy of abou 50 eV and accelerating to the chosen energies - in practice not higher than 40 keV. It is possible to use special moderators based on the W foil or frozen Ne gas. This approach makes the detection of defects in the range up to a few micrometers under the surface possible.

Since the year 2000 at JINR in Dubna project LEPTA has been realized. Its main aim is to acquire a positronium atom in flight [5]. A positron beam (see Fig. 2) constructed for this aim can also be used for PAS.

The idea of producing the beam is following. Positrons emitted from ^{22}Na go through a moderator, which is a condensed Ne source. As a result of elastic scatterings on gas particles some electrons lose their energy. Those two types of particles are separated by the use of perpendicular magnetic fields. Fast positrons are stopped at diaphragm, while the slow ones are slaloming and are then formed into a beam and accelerated by negative potential to needed energies. Currently available beam's parameters are given in Table 1.

Table 1: Parameters of Positron Beam at LEPTA Facility

Feature	Value
activity of ^{22}Na isotope	25 mCi
moderator	frozen Ne (7K)
longitudinal magnetic field	100 Gs
vacuum conditions	10^{-9} Torr
intensity	3×10^{5} e^{+}/s
energy range	50 eV ÷ 35 keV
diameter of the flux	3 mm

EXAMPLE OF APPLICATION

The problem of formation of oxide films on surfaces of stainless steel 304 AISI annealed for 2, 3 and 8 hours at 800 ˚C in vacuum of 6×10^{-6} mbar, air and in flow N_2 of 0.35cm^3/s atmospheres was studied using slow positron beam.

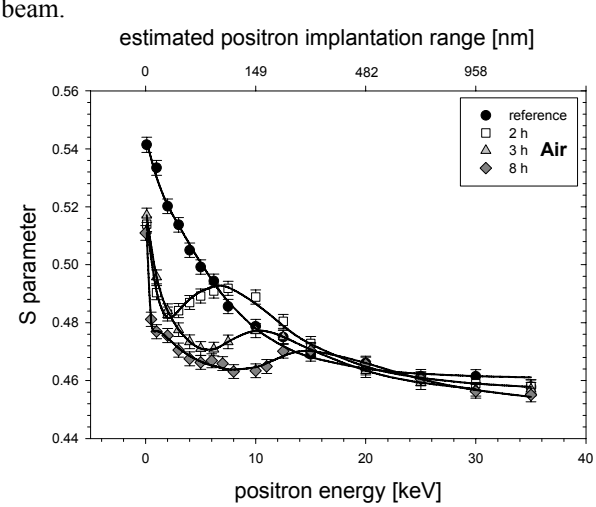

Figure 3: S parameter on dependency the positron implantation energy for studied samples. The solid lines represent the best fits of model function using VEPFIT code. [6]

ISBN 978-3-95450-170-0

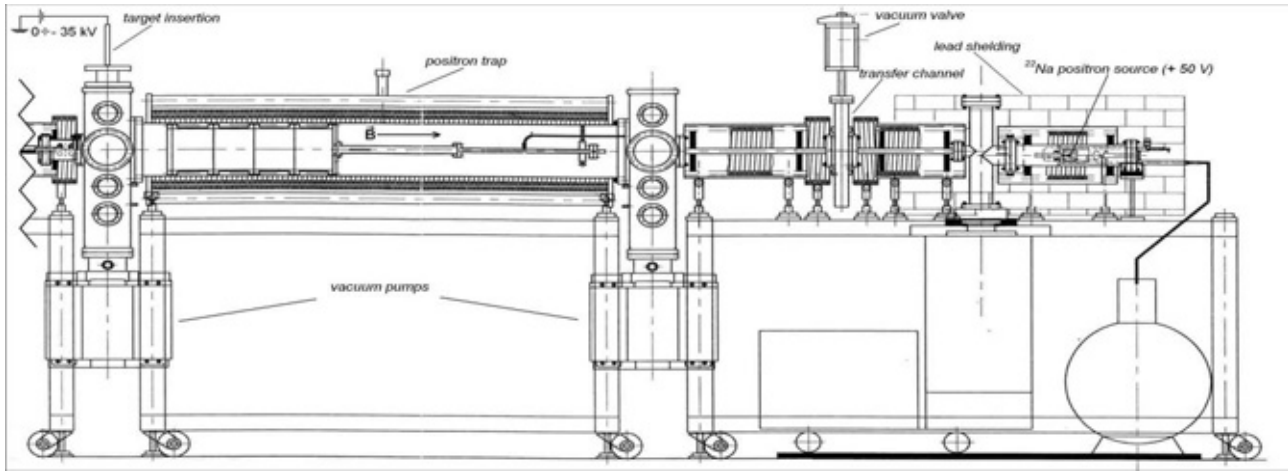

Figure 2: The scheme of slow positron beam at lepta facility.

The S- parameter profiles in dependency on the positron implantation are presented in Fig. 3. The creation of multilayer systems of oxides on the surface after annealing in air and N_2 conditions was confirmed. The fitting procedure [6] of obtained S parameter profiles allowed to find the thicknesses of oxide layers. The S-parameter profiles in dependency on the positron implantation are presented in Fig. 3.

The creation of multilayer systems of oxides on the surface after annealing in air and N_2 conditions was confirmed. The fitting procedure [6] of obtained S parameter profiles allowed to find the thicknesses of oxide layers.

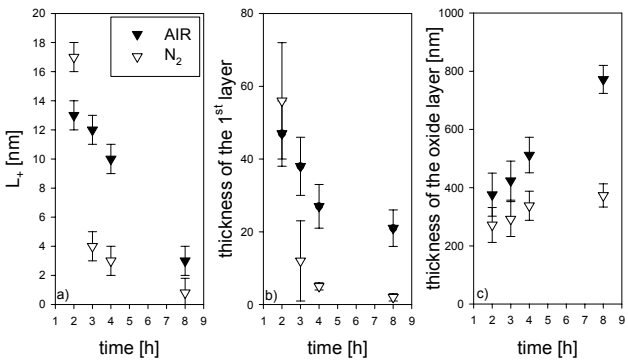

Figure 4: The time-dependencies of parameters obtained from fitting profiles presented in Fig. 3

The information about formation of duplex oxide on the surface, where α-F_2O_3 is created in the outermost layer before the inner spinel rich in chromium up to temperature of 850 ˚C is given in the literature [7]. There is no information about the thickness of these layers. The time-dependencies of parameters obtained from fitting profiles presented in Fig. 3 are presented in Fig. 4.

In the case of sample annealed in vacuum the positron diffusion length in the 4.2±0.9 nm thick oxide layer was 8±1nm, while in the bulk it was 94±3 nm. The thickness of the oxide layer depends on the kind and time of annealing atmosphere. The shield atmosphere of N_2 in flow does not protect the material before oxidation.

CONCLUSIONS

The standard version of DB spectrometer works at LEPTA facility at JINR in Dubna. The first results confirm the beam works in an appropriate way. The research is going to concern mostly materials engineering, both in metals and semi-conductors. The main research is going to include studies on the influence of surface treatment processes on the defecting of the surface layer in materials which are commonly used in industry, such as stainless steel. Furthermore, plans are made to conduct research oriented around thin layers and layers created by ion implantation. In further perspective there are plans to develop the equipment to automatize the measurements and using Surko trap for bunching signal in the aim of building pulsed positron beam for life time measurements.

APPENDIX

All works were supported by RFBR grant No. 12-02-00072.

REFERENCES

[1] S. Adachi, et al., “Phys. Rev. Lett. 65” (1990) 2634.
[2] J. Dryzek, et al., “Mat. Sci. Forum 666” (2011) 10.
[3] R. Krause-Rehberg et al., “Positron Annihilation in Semiconductors: Defect Studies”, (Berlin: Springer-Verlag, Berlin Heidelberg, 2003), 18.
[4] P. Horodek, et al., “Tribol. Lett. 45” (2012) 341.
[5] E. Akhmanova, et al., “Phys. Part. Nucl. Lett. 9” (2012), 373.
[6] A. van Veen et. al, “Appl. Surf. Sci. 85” (1995), 216.
[7] K. Nomura, “J. Mat. Sci.” 25 1990, 1745.

ISBN 978-3-95450-170-0

DEVELOPMENT OF THE EQUIPMENT FOR THE PROTOTYPE OF A COMPLEX OF RADIOTHERAPY AT THE NUCLOTRON-M

I.P. Yudin*, A,M, Makankin, V.A. Panacik, S.I. Tyutyunnikov, S.E. Vasilev, A.V. Vishnevskiy,
Joint Institute for Nuclear Research, Dubna, Russia
K.K. Laktionov, D.I. Yudin, Russian Cancer Research Center them. Blokhin, Moscow, Russia

Abstract

The report deals with the construction of the carbon beam transport line for biomedical research at the Nuclotron accelerator complex, JINR, Dubna. We have studied the scheme and modes of magneto-optical elements of the channel. Used electronics described. We are discussed the compilation and realization of the plan of treating a tumor located at a depth up to 30 cm. Choice of beam scanning schemes and their optimization are shown.

INTRODUCTION

One direction in the development of the Joint Institute for Nuclear Research (JINR) accelerator complex is the design of a test bench for medicobiological research based on the JINR Nuclotron [1].

While designing the test bench, the general technique for manufacturing the hadronic therapy complex is tested.

In this work we present a calculation procedure for the optics of the charge particle transport channel of the hadronic therapy complex. This channel is intended for the transportation of the $^{12}C^{+6}$ carbon ions with an intensity of ~2 × 10^9 and an energy of 100–550 MeV/nucleon.

Figure 1 shows the circuit of the primary transport channel from the Nuclotron to experimental hall 205. An additional channel starts near the F3 focus of the primary channel.

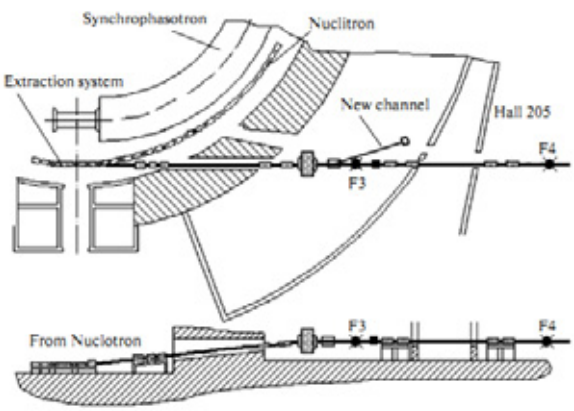

Figure 1: Layout of the primary transport channel from the Nuclotron. Top and side view. A branch of the designed channel before the F3 focus is shown.

PROBLEM STATEMENT

Mathematical Statement

To describe an envelope during beam transportation, one can use the matrix formalism:

$$X_{out} = M_N \cdot \ldots \cdot M_2 \cdot M_1 \cdot X_{in} , \quad (1)$$

where X_{out} and X_{in} are the column vectors ($X = (\beta, \alpha, \gamma)^T$) of the terminal and initial conditions (consisting of the parameters of Twiss matrix) describing the beam; M_1, … M_N are the transformation matrices of channel elements, i.e., drift gaps and quadrupole lenses. The thick lens approximation is used for the quadrupole elements. All transformation matrices are nonlinear with respect to the channel parameters, i.e., geometrical sizes of the elements and lens gradients.

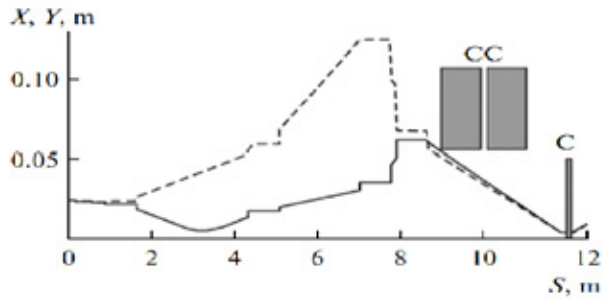

Figure 2: Position of the scanning system of magnets on a beam (CC). The scanning region in the beam focus (C).

The initial conditions for beam transport in the additional channel are taken as current values of the beam parameters from the Nuclotron primary channel. They should satisfy the conditions

$$M_{drift} \cdot X_{in} = X_{F3} , \quad (2)$$

where X_{in} is the initial conditions from Eq. (1), X_{F3} is the beam parameters in the F3 focus of the primary channel, and M_{drift} is the matrix of transformation from the additional channel branching point to the F3 focus.

The output transport values X_{out} should satisfy the focus conditions, i.e., the zero derivative of the beam envelope with respect to the transport coordinate:

$$\alpha_{x.out} = \alpha_{y.out} = 0 , \quad (3)$$

where $\alpha_{x.out}$ and $\alpha_{y.out}$ are the α components of the Twiss matrix in the focus of the additional channel.

The size of the beam envelope in the focus F_k of the additional channel is close to the possible minimum satisfying the geometrical limits of the setup. The envelope minimum is considered known and determined

*yudin@jinr.ru

ISBN 978-3-95450-170-0

by the relative position of the scanning system and the scan region.

Thus, the problem is reduced to a determination of the parameters of transformation matrices from Eq. (1) belonging to the region of setup geometry and corresponding to the minimum envelope size in the additional channel focus (3) at specified parameters of the F3 focus of the primary channel.

Setup Restrictions

Additional restrictions of the transport problem arise in the use of specific optical elements and their mounting in the experimental hall. The following optical elements are used in the channel: dipole and deflecting magnets (SP-94) and a magnetic lens (ML-17).

The length of the transport channel is 12 m. The designed channel starts from a dipole magnet mounted in the primary transport channel at a distance of 5.25 m in front of the F3 focus (Fig. 1). Optical elements (quadrupole lenses) are located over the channel. There is a beam trap at the end of the channel, the test bench in F_k is right before the trap, and the beam scanning system is before the test bench. The scanning system consists of two similar deflecting magnets rotating at an angle of 90° around the axis relative each other.

One natural restriction of beam transportation is that the diameter of the vacuum pipeline is equal to 0.25 m, which passes through all the quadupole elements of the system. A magnet aperture of 0.3 × 0.13 m is a restriction at the final stage of the scanning system. The mutual position of the scan region and the system of scanning magnets is fixed.

The maximum current is limited for each quadrupole lens; this results in a limitation of the coefficient K <1.5 m^{-2} used for calculating the phase incursion on the lens at a preset energy range of 100–550 MeV/nucleon.

The beam cross section in the F3 focus of the primary transport channel is a circle 0.04 m in diameter [2], which makes it possible to define the initial conditions of beam propagation.

Horizontal and vertical emittances of the beam are assumed equal in the calculations [3, 4]; values of 25π mm mrad and 50π mm mrad were used [3].

The space region around the focus in the form of a cube with a side of 0.1 m is planned for the experiments. When scanning the region, the transport channel length changes. Correspondingly, the prolongation of the transport problem solution to the whole scan region should exist with fixed parameters of the channel geometry. That is, in addition to geometrical restrictions, conditions of the existence of a solution to the problem in the vicinity of scanning the final focus are imposed on the problem.

SOLUTION

Minimum Beam Size in Focus and Beam Emittance

The position of the scanning system relative to a target (Fig. 2) specifies the minimum beam size in focus restricted by the scanning system aperture. In view of the emittance formula $E = x'x$, the minimum beam size in focus can be estimated with good accuracy. Here, x' is the mean slope of the envelope at a segment before the focus and x is the envelope value in the focus.

For a preset aperture and the magnet arrangement, we have:

(i) a minimum focus diameter of 2.8 mm for an emittance of 25π mm mrad;
(ii) a minimum focus diameter of 5.6 mm for an emittance of 50π mm mrad.

Geometrical Restrictions to a Scan Region Normal to the Beam

The region of target scanning is restricted by an aperture of two successive magnets in a plane normal to the beam. The magnet aperture is 0.3 × 0.13 m for a specific channel; this agrees with the planned scan region of 0.1 × 0.1 m.

Results Obtained: Beam Envelope

Solutions have been found for emittances of 25π mm mrad and 50π mm mrad based on the above specified restrictions. The beam cross section in the focus F_k is close to the minimum for the given scanning system geometry:

(i) 3.0 × 3.0 mm for an emittance of 25π mm mrad;
(ii) 5.6 × 6.0 mm for an emittance of 50π mm mrad.

BEAM CONTROL

Beam Spreading and Additional Lens Focusing Suring Scanning along the Beam

Deviating along a beam from a focusing point, the beam spreads. The change in the beam size depends on the focus size for a fixed geometry of the scanning system. The change is as follows :

(i) 20% for a beam 3 mm in diameter (emittance of 25π mm mrad), i.e., 0.6 mm;
(ii) 6% for a beam 5.8 mm in diameter (emittance of 50π mm mrad), i.e., 0.35 mm along a beam over a scan region of ±0.05 m.

The beam spreading can be compensated by means of correcting the tuning of optical elements simultaneously with motion over the scan region. The maximum correction value is about 2%.

Features of Energy Absorption

The clearly pronounced feature of the energy absorption peak (Bragg peak) is used during target irradiation; therefore, the value of beam defocusing compensation increases when deviating from the central position during scanning.

The beam control function is chosen from the way target scanning and tolerance of the experiments is chosen.

ISBN 978-3-95450-170-0

CONFIGURATION VARIANTS

The Number of Magnetic Lenses

To choose a specific configuration of the transport channel, variants of different numbers of focusing elements were considered.

We did not find solutions satisfying the initial and boundary conditions of the physical setup for the simplest configurations consisting of one or two quadrupole elements. The resulting envelops for configurations of three and four elements are shown below. These variants differ in size and focus shape; i.e., when increasing the number of lenses, an elliptical focus can be changed to a circular one.

The beam cross section in the focus F_k (emittance of 50π mm mrad) is as follows:

(i) 5.6 × 12.0 mm for a configuration of three lenses;

(ii) 5.6 × 6.0 mm for a configuration of four lenses.

A more complicated configuration of four lenses can be used when two lenses are mounted in the additional channel and two lenses are mounted in the primary one. In this case, the tuning of the lenses from the primary channel should be controlled for the beam transport.

Initial Conditions

To check the existence of a solution in other operating modes, other initial conditions of beam propagation in an additional channel were considered. The beam cross section in the F3 focus acts as a parameter determining these initial conditions.

In addition to a solution with a focus on the primary channel target of 0.04 × 0.04 m, we considered the solution for a focus of 0.1 × 0.12 m [4]. The beam envelopes are shown in Fig. 3 for both solutions.

The beam cross section in the focus on a target for configurations with initial conditions corresponding to different beam sizes in the F3 focus of the primary channel (the emittance is 50π mm mrad) is equal to

(i) 5.6 × 6.3 mm for the focus 0.1 × 0.12 m

(ii) 5.6 × 6.0 mm for the focus 0.04 × 0.04 m.

EQUIPMENT OF THE ADDITIONAL CHANNEL

We suggest the following equipment for the additional channel:

(i) magnetic lenses ML-17;

(ii) scanning and dipole magnets SP-94;

(iii) the pixel chamber and the wire chamber and read out electronics (see Fig.3).

CONCLUSIONS

The possibility in principle of designing an optical system for beam transport with different numbers of optical elements has been shown in the work. The correction values for the beam scanning function have been found.

The choice of parameters of the optical system is determined by the operating mode of the primary channel of the Nuclotron and the requirements of the medicobiological experiments that were conducted.

The choice of the temporal control functions of magnetic elements is determined by the planning problems of the experiment, i.e., the way the beam energy was controlled, the type of target scanning, etc.

The view of distribution of beam can see on fig.4 for on-line monitoring of the carbon beam (as one example).

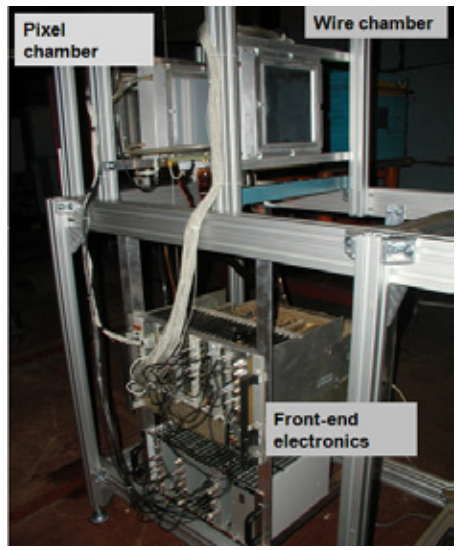

Figure 3: The pixel chamber and the wire chamber and read out electronics which were developed for on-line monitoring of the ”intensive” extracted carbon beams.

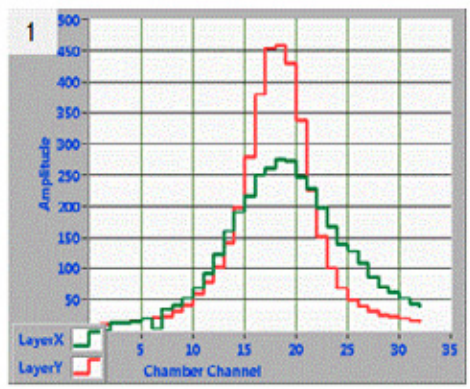

Figure 4: The view of distribution of beam is for on-line monitoring of the carbon beam.

REFERENCES

[1] N.A. Barteneva et al., “A System of Beam Transport from the Synchrophasotron and Nuclotron to the Experimental Setups in Building No. 205,” JINR Preprint No. P1-90-75 (Dubna, 1990), http://nucloserv.jinr.ru/.

[2] A. Safronova et al., , “Investigation of 4 GeV Deutron Beam Parameters at the Nuclotron,” in Proceedings of the 3rd International Conference on Current Problems in Nuclear Physics and Atomic Energy, NPAE-Kyiv 2010, June 7–12, 2010 (Kiev, 2010), p. 113.

[3] V.I. Volkov, private commun.

[4] J. Adam et al., “Transmutations of Th and U with Neutrons Produced in Pb Target and U-Blanket System by Relativistic Deuterons,” JINR Preprint No. E15-2008-118 (Dubna, 2008).

ISBN 978-3-95450-170-0

THERMAL SIMULATIONS OF THE BIPERIODICAL ACCELERATING STRUCTURE WITH THE OPERATING FREQUENCY 27 GHZ

Yu.D. Kliuchevskaia, S.M. Polozov National Research Nuclear University MEPhI (Moscow Engineering Physics Institute), Moscow, Russia

Abstract

Biperiodical accelerating structure (BAS) represents a system based on disk loaded waveguide (DLW) with π/2 operation mode. The 1 cm band structure will have very compact transverse size. Such characteristics give it perspective to use in medical accelerators. The results of beam dynamics simulation and electrodynamics study was discussed early [1]. It will important to study the BAS electrodynamics taking into account thermal processes in structure and to design the cooling system. It is important because of the high pulse RF power (about 1.5 MW) necessary for the beam acceleration. The simulation results which are defined using CST code will presented in report. Calculation and definition of the thermal coefficient depending on speed, temperature and the water flow direction will make.

INTRODUCTION

Many medical applications need to design a compact electron accelerator. Compactness of accelerating structure can be reached by increase of the accelerating RF field frequency (frequency ranges of 6, 10 GHz are widely used and 17 and 30 GHz are also possible). Besides these accelerating structures demand lesser RF-power due to smaller internal volume and surface area. The effective medical accelerators operating on S-and H-bands are well-known [2-4]. The design of 17 GHz linear accelerator was offered [5]. BAS represents a modified structure on the π/2 mode in which case the accelerating cells length increase and coupling cells length decrease. The main aim of simulation was geometry definition providing the operating frequency 27 GHz. General view of the accelerating structure is shown in Figure 1. As a result of tuning the cell geometry with optimal characteristics was defined and they are presented in Table 1.

Table 1: Optimal parameters values of the BAS

Parameter	Value
Operating mode	π/2
Length of accelerating cell, mm	4.5
Length of accelerating system, mm	55
Frequency, GHz	27
Length of wave, mm	10
Radius of the drift tube, mm	4.5
Radius windows coupling, mm	0.8
Radius of the accelerating cell, R_{cell}, mm	8.8
Radius of blending sidewall, R_{lc}, mm	1
Radius of coupling cell, mm	3.8
Length of coupler, mm	50

High power pulse gyrotrons are one of possible power sources types in 30 GHz band. The power system of proposed linac will differ from conventional C-band medical linac therefore gyrotrons can produce the long pulses (hundreds of μs) with low repetition rate. High-efficiency pulse and CW gyrotrons of frequency range 27–30 GHz have been developed at the Institute of Applied Physics of Russian Academy of Sciences. Pulse power reaches to 15 MW at the efficiency of 50 % in gyrotrons with the high operating voltage 500 kV [6]. Accordingly to preliminary estimations based on the gyrotron theory and experimental results pulse and average power of the order the gyrotron is capable of producing 2 MW peak RF power in pulses with pulse duration 400 μs and a repetition rate of 10 Hz.

The combination of high electromagnetic fields and long RF pulse in resonators on operating frequency leads to temperature increase on the surface, to thermal deformations and to noticeable change the resonator characteristics during the RF pulse [7]. The thermal analysis was performed for such structure due to. Thermal calculations to define the frequency shift depending on temperature of cooling liquid were done.

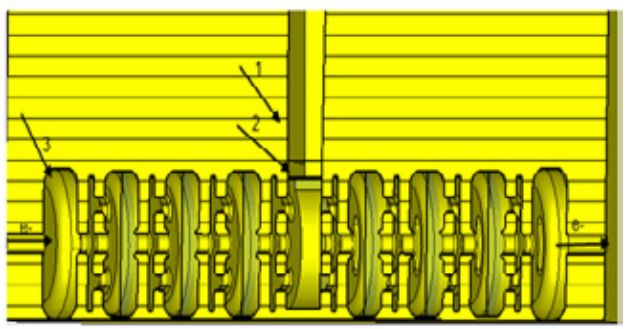

Figure 1: General view of the accelerating structure, 1 – coupler, 2 – power feeding waveguide, 3 – regular accelerating cell.

COOLING SYSTEM FOR BIPERIODICAL STRUCTURE AT 27 GHZ

The simulation of BAS thermal characteristics was done using the model consisting of one accelerating cell and one coupling cell operating on frequency of 27 GHz. The geometry of the BAS cell is shown in Figure 2. The copper BAS based on the DLW with magnetic coupling was studied, it operates on the standing wave. The high operating frequency 27 GHz is the feature of this structure

ISBN 978-3-95450-170-0

which is much higher than the standard frequency used for electron accelerators (2856, 2898 or 5712 MHz).

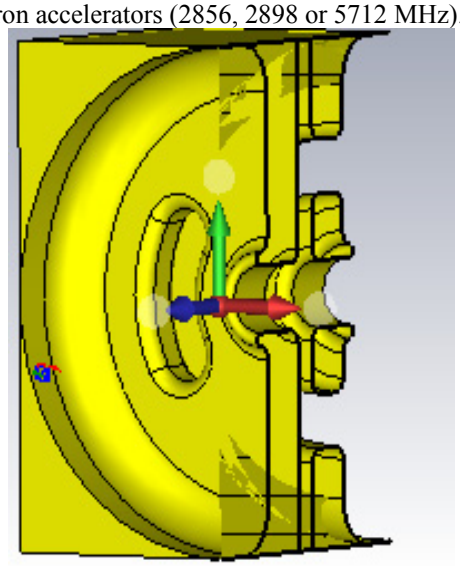

Figure 2: The geometry of the BAS cell, the shell material – copper.

The influence of pulse high-frequency heating effects for accelerating structure with magnetic coupling both negative dispersion and rejecting structure with bores in walls of cells was investigated, the methodology was described in [8]. Modeling was performed using the three-dimensional electrodynamics code CST STUDIO SUITE [9].

Eight water tubes oriented along of the BAS and spaced radially from cells were added to the model (see Fig. 3). The diameter of tubes is equal to 8 mm.

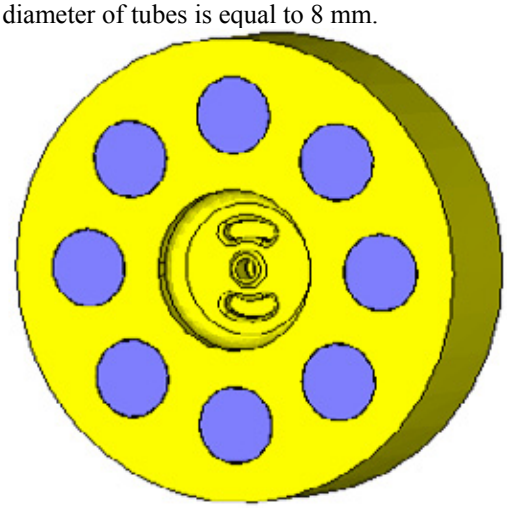

Figure 3: View of the BAS cell with cooling system.

Adiabatic boundary conditions were used at all structure cell's walls before start of the thermal analysis. The water temperature in the cooling tubes was defined equal to 20 C.

Microwave power losses in structure wall's were defined with:

$$P = \frac{\omega W}{Q} \quad (1)$$

where ω – frequency, W – storaged energy, Q – Q-factor.

The calculation of a water flux is one of important aims at developing of cooling system also. It is determined by the equation:

$$G = U\pi d^2 \quad (2)$$

where U – liquid of the velocity, d – diameter of the tube.

Thermal analysis of structure includs continuous process of structure heating simulation and it's cooling by water flux study. As it was defined by electrodinamics simulations that the value of pulse power loses in structure walls are equal to 1.05 MW. Average power loses are equal to 2.7 kW per one period with pulse length 400 μs and pulse repetition 10 Hz.

Distributions of frequency shift and maximal temperature in structure versus water flux are presented in Figures 5-6. It was shown that water flux should be equal to 0.33 l/s for one channel to limit the maximum temperature into the cell by 34 °C. The frequensy shift is negligible with such temperature in the structure. The temperature distribution in structure with water flux and temperature of 0.3 l/s and 34 °C accordingly is shown in Figure 7. At the obtained parameters the maximum temperature in structure reaches 40 °C and gives the frequency shift of 290 kHz down.

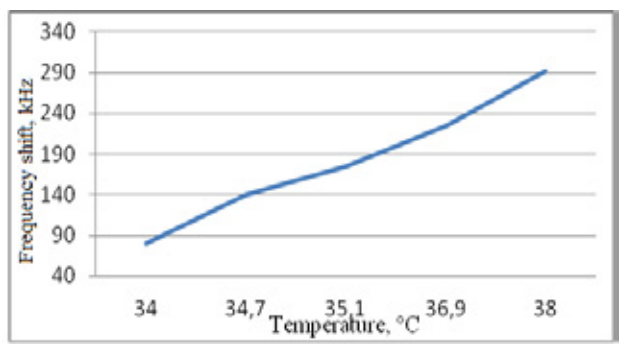

Figure 4: Frequency shift versus on temperature.

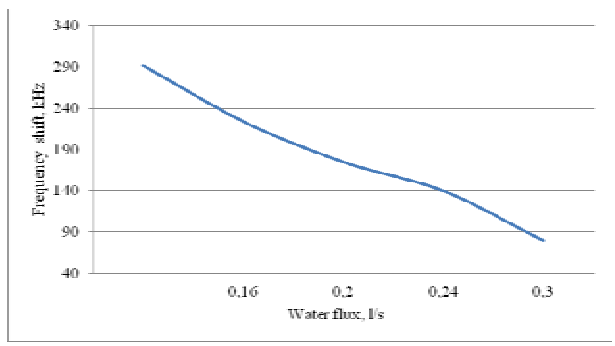

Figure 5: Frequency shift versus of water flux.

ISBN 978-3-95450-170-0

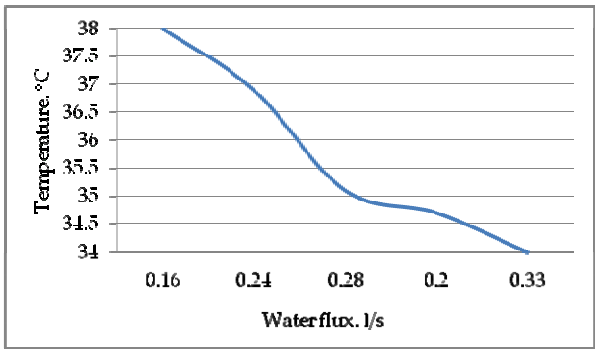

Figure 6: Maximal temperatue versus of water flux.

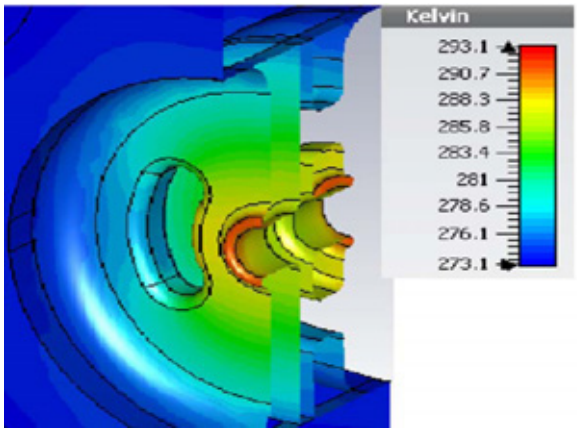

Figure 7: The view of the BAS section and temperature distribution ,water flux equal 0.3 l/s.

ACKNOWLEDGMENT

Especial thanks to Dr. A.S. Plastun for consultation in modeling, fruitful discussions and support.

CONCLUSION

The BAS was designed and tuned on 27 GHz operating frequency. The optimal geometrical parameters of the BAS necessary for π/2 mode were defined by means of accelerating and coupling cell tuning. The high power gyrotron was discussed as a perspective power source on 27 GHz. Numerical simulations of accelerating structure thermal characteristics were carried out. By the results of thermal calculations necessary parameters of cooling system were defined to limit the maximal temperature by 34 °C in which case the frequency shift is negligible. Liquid flux value should be equal to 0.33 l/s per each cooloing tube and the frequency shift will limited by 80 kHz in this case.

REFERENCES

[1] T. Bondarenko, Yu. Kliuchevskaia, S.M. Polozov, V. I. Rashchikov. Proc. of IPAC 2014, p 2191.
[2] S.M. Hanna. Proc. of PAC'99, p. 2516.
[3] http://www.accuray.com/solutions.
[4] N. H. Quyet, M. Uesaka, H. Iijima et al. Proc. of EPAC'04, p. 2670.
[5] F. Rack, F. Black. Fundamentals of heat transfer / Per. Translated from English. M.: "Mir", 1983.
[6] D.A. Zavadtsev. Calculation of Thermal Transient Condition in Biperiodical Accelerating Structure // Problems of Atomic Science and Technology. Series "Nuclear Physics Investigations" (43). 2004, №2, pp.87-89.
[7] M.A. Gusarova, I.V. Isaev, R.A. Kostin. Journal of Applied Physics, 2013, Vol. 83, no. 4, pp. 134-140.
[8] V. Paramonov, A. Skosirskiy, K. Flottmann, F. Stephan. Study of the effects of pulsed RF heating in normal conducting resonators tures of L-band. Problems of atomic science and technology, 2008, Vol 3, pp.51-54.
[9] https://www.cst.com/

ISBN 978-3-95450-170-0

A PROTOTYPE OF A PHASED ARRAY FOR DEEP THERMORADIOTHERAPY

S.M. Polozov, A.M. Fadeev, A.A Blinnikov, S.M. Ivanov, National Research Nuclear University MEPhI (Moscow EngineeringPhysics Institute), Moscow, Russia

Abstract

It is proven that hyperthermia increases radiation and chemotherapy efficiency. In oncology, the generation of a higher temperature at a tumor-involved region of the body is called hyperthermia. The thermoradiotherapy is widely and effective uses. A phased array of eight dipoles for the hyperthermia treatment of deep-seated tumors is proposed earlier. The power and phase coherently delivered to the radiating elements can be varied, so that the electromagnetic field is increased at the tumor location and decreased in the normal tissues. The prototype of the phased array of two dipoles and the RF power scheme are presented and results of experiments are discussed. Measured and simulated temperature distributions along the line connecting two dipoles are discussed in this paper.

INTRODUCTION

Hyperthermia is an efficient adjuvant for the common modalities such as surgery, radiation and chemotherapy. Many researches have shown that hyperthermia temperature can damage and kill tumor cells, thus reduces tumor size. However the main advantage is that hyperthermia is a promising approach to increase efficiency of chemotherapy or radiation therapy. Under hyperthermia temperature some tumor cells become more sensitive to the radiation and anticancer drugs. The effect on surviving fraction depends both on the temperature increase and on the duration of the expose [1, 2]. Treatment requires that temperatures within tumor remain above 43 °C during 30-60 min, while maximum temperature in normal tissues have to be lower than 42°C.

In previous papers the phased array for deep hyperthermia was suggested [3, 4]. This phased array consists of eight dipole antennas arranged on an inner side of a cylindrical dielectric tank. Dipoles are surrounding the patient body and the amplitudes and phases of each antenna are under control of the operator as shown in Figure 1. Necessary distribution of E-field can be reached by means of independent feeding of each dipole that permits us to vary amplitudes and phases of electromagnetic field. In other words we can concentrate absorption energy of E-field and deliver therapeutic heat in tumor and at the same time prevent extra heating of normal tissues.

Deionized water filling space between patient and array is for cooling outer side of body and for better matching. The E-field energy is extremely concentrated in the inner side of a shell due to the electric field energy density inside the shell is higher by a factor ε (the relative dielectric constant of the medium) than outside the shell.

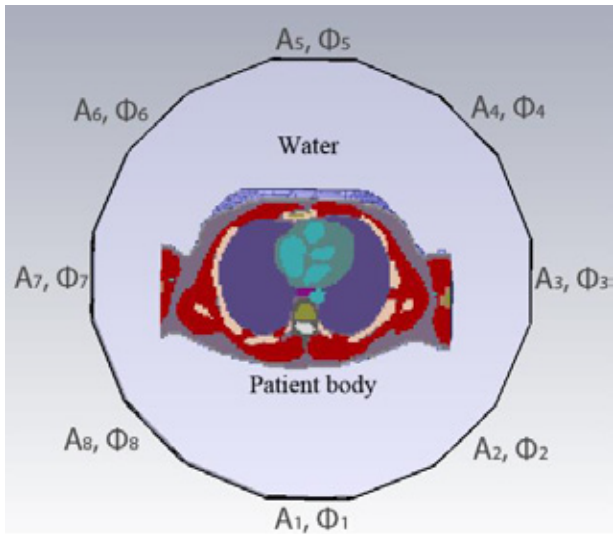

Figure 1: Patient body surrounded by phased dipoles array. Dipole antennas have amplitudes $A_1 \ldots A_8$ and phases $\Phi_1 \ldots \Phi_8$ respectively.

EXPERIMENTAL SETUP

In this paper the prototype of the phased array of two dipoles is presented. The RF power system schematic layout of this prototype is shown in Figure 2, where 1 – driving generator Agilent N5181A, 2 – preamplifier Analog Device 5545 (fixed gain 25 dB, 30 MHz-6 GHz, 5 V), 3 – Wilkinson power divider, 4 – phaseshifter Mini-Circuit JSPHS-150 (100-150 MHz, 0-12 V), 5 – amplifier Toshiba S-AV32A (134-174 MHz, 12.5 V, 60 W), 6 – matching circuit. Single phaseshifter is enough to produce any phase lag between two dipoles. The operating principle of such layout is the following. The RF signal at 150 MHz from signal source splits into two channels by microstrip power divider. Then by means of controlled one phase shifters and two solid state amplifiers we can adjust phase and amplitude of every signal. Due to these adjustments peak temperature moving is available. Solid state RF amplifier Toshiba S-AV32A is simple and stable in operation but it needs intensive cooling system.

For impedance measurements a commercial network analyzer system Agilent Technologies E5061A was used. Impedance matching is provided with short circuit stub. The stub is positioned a distance from the load. This distance is chosen so that at that point the resistive part of the load impedance is made equal to the resistive part of the characteristic impedance by impedance transformer action of the length of the main line. The length of the stub is chosen so that it exactly cancels the reactive part of the presented impedance. Return loss plot for one

ISBN 978-3-95450-170-0

single channel after matching is depicted in Figure 3. The operating frequency is about 150 MHz.

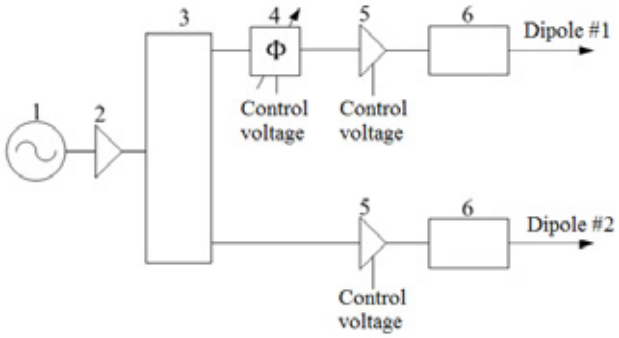

Figure 2: RF power schematic layout.

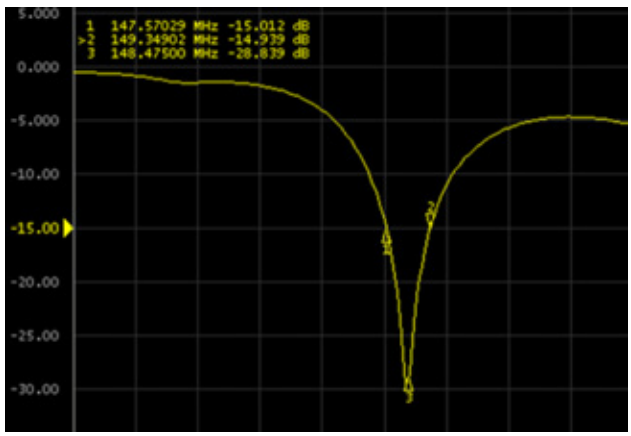

Figure 3: Return loss plot after matching with short circuit stub for one single channel.

As it noted above this phased array consist of two dipoles, thus temperature peak can move along the line connecting these dipoles. Water is used as an absorbing medium because it has dielectric properties and density similar with the muscle tissue. A number of dielectric tubes were positioned along the line connecting dipoles like it is shown in Figure 4 to prevent water blending during heating. These tubes were also filled by water and temperature measurements were carried out inside tubes. Tubes are made of aluminum oxide (permittivity ε=9.4 and density ρ=3990 kg/m^3). Tubes diameter is 10 mm and wall thick is 2 mm.

Thermocouple-sensing element ATE-9380 was used to perform temperature measurement. Whereas it has metallic compounds TSE introduce alternations in electric distribution when RF is on. Thus temperature measurement was carried out after switching RF off.

In these experiments, all channels were driven separately with a power of 15 W. Initially water temperature inside shell and tubes was equal. After switching RF on temperature starts to increase. In the first series of experiments dipoles have equal phases. Phase lag became 60° to move temperature peak. That was the second set of experiments.

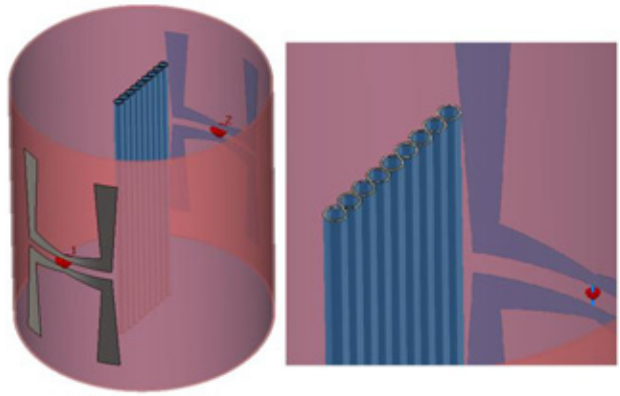

Figure 4: Experimental setup schematic view.

RESULTS

Experimental results were compared with simulation one. Simulations results are performed by CST Studio Suite [5]. Both dielectric and thermal properties of plastic enclosure, water, dielectric tubes were included. The simulations are performed with CST Microwave Studio which uses the Finite Element Method (FEM). Their solvers feature curved elements of arbitrary order. These elements enable a conformal representation of the geometry which improves the simulation accuracy. In combination with the unstructured FEM grid, which can resolve small structure details very efficiently, it can increase the simulation performance dramatically.

Temperature distributions are shown in Figure 5. Red line is for experimental data and black line is for simulation results. “0” in Figure 5 is the midway between dipoles. Initial water temperature was equal 23.4°C. When phases stay equal the temperature peak is situated in the middle tube. After 12 minutes of in-phase excitation temperature in the middle tube has reached 24.4°C.

When phase lag is equal 60 the temperature maximum is moved away from the dipole that has phase delay and after 20 minutes maximum temperature was situated in the third tubes at the left and it equal to 25.2°C.

Also cross section temperature distributions for both cases are presented in Figure 6. As it expected peak temperature is observed in the middle tube when phases are equal (Fig. 6a). Peak is moved away from the center when phase lag is 60° (Fig. 6b). According this picture we can conclude that dipole №2 has the phase delay, because the temperature maximum shifted away from this dipole. Since this array consist of two dipoles, the resulting temperature distribution is spread out and the peak is not so clearly identified as it could be if we would use eight dipoles.

ISBN 978-3-95450-170-0

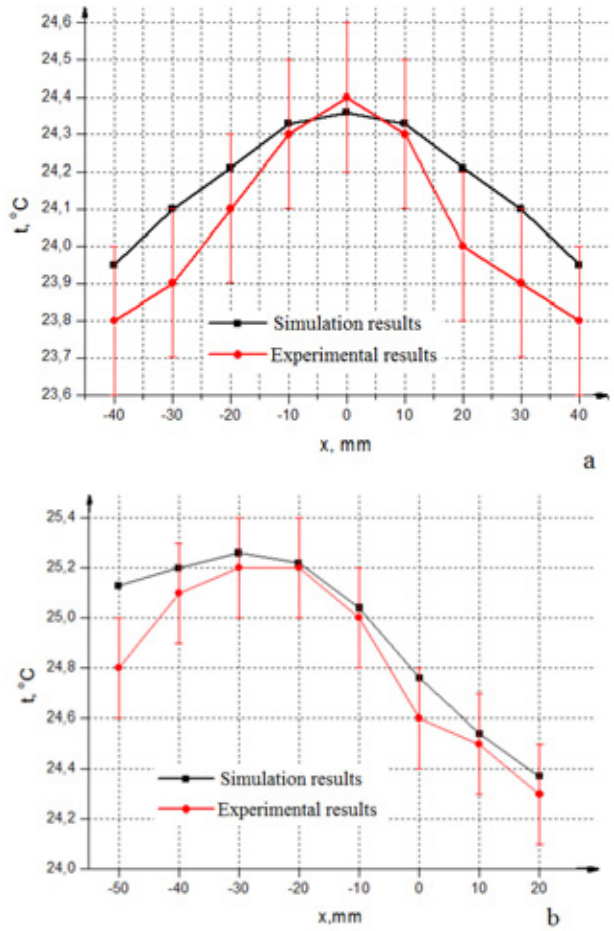

Figure 5: Temperature distribution along the line connecting two dipoles for a) in-phase excitation b) phase lag 60°.

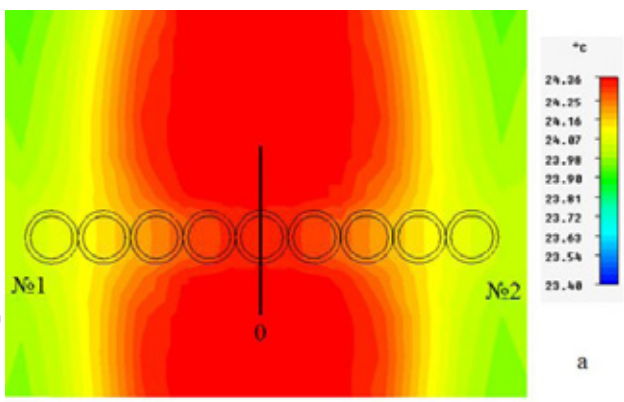

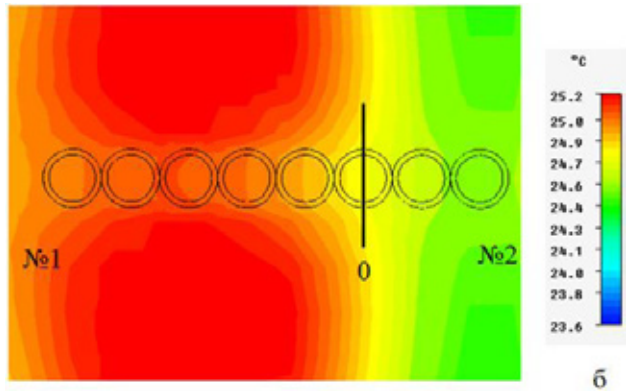

Figure 6: Cross-section temperature distributions for a) in-phase excitation and b) phase lag 60°.

CONCLUSION

To heat deep-seated tumor without overheating of healthy tissues is a complex technical challenge. Heating of deep-seated tumors can be realized by means of focusing of radiofrequency energy inside the patient body. The phased array was suggested to create desirable temperature distribution inside patient body. The first step in realization of this facility was done. The prototype of the phased array of two dipoles has been shown. Experimental and simulation results on water heating are presented. It is proved that the phased array can produce temperature gradient by introducing phase lag between dipoles. Experimental and simulation results agree within the experimental error.

The phased array prototype of eight dipoles construction and software developing for the hyperthermia planning system are the further steps in our project.

REFERENCES

[1] S.B. Field, J.W. Hand, *An Introduction to the Practical Aspects of Clinical hyperthermia*, (New York: Taylor & Francis, 1990), 293.

[2] S.A. Sapareto, W.C. Dewey. Thermal dose determination in cancer therapy. lnt J Radiat Oncol Biol Phys, 1984;10, p. 787-800.

[3] Fadeev A.M., Polozov S.M., V.N. Belyaev et al., “Cylindrical phased dipoles array for hyperthermia of deep-situated tumors“, Proc. of RuPAC2012, p.521-523 (2012);

[4] Fadeev A.M., Polozov S.M., E.A. Perelstein E.A., et al. Facility for the electromagnetic hyperthermia based on the phased array. Problems of Atomic Science and Technology. Series: Nuclear Physics Investigations. v.6(88), p. 220-224, 2013.

[5] CST official website: https://www.cst.com/

ISBN 978-3-95450-170-0

INTERDISCIPLINARY GLOSSARY — PARTICLE ACCELERATORS AND MEDICINE

V.V. Dmitrieva*, V.S. Dyubkov†, V.G. Nikitaev, S.E. Ulin,
National Research Nuclear University "MEPhI", Moscow, Russian Federation

Abstract

A general concept of a new interdisciplinary glossary, which includes particle accelerator terminology used in medicine, as well as relevant medical concepts, are presented. Its structure and usage rules are described. An example, illustrating the quickly searching technique of relevant information in this Glossary, is considered. A website address, where one can get an access to the Glossary, is specified. Glossary can be refined and supplemented.

INTRODUCTION

Number of fields of science as well as its applications are founded and evolved swiftly today. It results in new concepts, professional terminology, which can significantly complicate an understanding and information perception by specialists in the interdisciplinary fields. In particular this situation takes place in the case of specialist cooperation from medicine and particle accelerator fields. Particle accelerators, in that case, are effectively used for disease diagnostics and therapy.

Special problems appear when students and postgraduates study special medicine and particle accelerator courses at Universities, in which rather difficult, and often impossible, to teach courses simultaneously on physics and medicine at the highest level [1].

Interdisciplinary Glossary was made up with the aim of improving the knowledge in the field of particle accelerators and medicine. We hope that Interdisciplinary Glossary will be useful for students,technologists, scientists & users of key facilities.

GLOSSARY STRUCTURE

High-tech nuclear medicine centres are built up for the provision of high quality medical diagnostics and therapy in Russia today, where experts in various scientific fields and application areas work together with doctors.

Interdisciplinary Glossary, which includes a set of hard and electronic copies as well as database of Glossary and contains terminology and explanation in genetics, biology, radio-biology, radiochemistry, radiation safety, radiopharmaceutical, oncology, information technology, particle accelerators, physical methods and means of radiation for medical imaging, is required to provide communication between all members on issues concerning common activity in the field of application of methods and tools for nuclear medicine and radiation therapy for cancer diagnostics and treatment.

* vvdmitrieva@mephi.ru
† vsdyubkov@mephi.ru

In particular, particle accelerators are used for radioactive isotope production as well as radio-diagnostics and oncological diseases therapy, sterilization of medical instruments and transplant tissues.

Particle accelerators for medicine are classified into linear and cyclic on the one hand and into electron and proton/ion on the other hand. Generally, electron linear and cyclic accelerators are used for radiotherapy, whereas proton and ion accelerators are mainly used for nuclear medicine purposes [2, 3]. It is well known that different types of ionizing radiation (photons, electrons, protons, ions, neutrons, π-mesons) are used in radiation therapy. The type and energy of ionizing radiation in complex treatment are determined by a stage and malignant neoplasm prevalence [4].

Interdisciplinary Glossary includes about 1000 terms and explanations, namely:

— 180 on particle accelerators,
— 200 on oncology,
— 200 on computing,

and other terms and explanations that concern radio-biology, radiochemistry, radiation safety, radio-pharmaceutical etc.

Glossary content has been edited by experts of the corresponding fields of knowledge. Glossary content is sorted by subject and alphabet.

Glossary is based on relational database management system (DBMS) MySQL platform. Operation principle of the DBMS MySQL is similar to any other DBMS operation principle that uses SQL as the command language for creating/deleting databases, tables, replenishing the tables with a data, sampling data [5].

phpMyAdmin was installed for easy data management. phpMyAdmin is a LAMP (**L**inux, **A**pache, **M**ySQL, and **P**HP) application specifically written for administering MySQL servers. phpMyAdmin has tools for visual table creation, and also allows one to create, modify and delete tables by means of the SQL toolkit.

Flowchart of the developed application is shown in Fig. 1.

An *administrator* interface consists of:

- category management that allows one to create, delete, and modify Glossary categories/subcategories;
- article management that allows one to create, delete, and edit articles included in all Glossary categories/subcategories;
- user management that allows one to assign/remove user rights to certain categories.

A *moderator* interface consists of:

- category management that allows one to create, delete, and modify Glossary categories/subcategories, which is assigned with administrator rights;

ISBN 978-3-95450-170-0

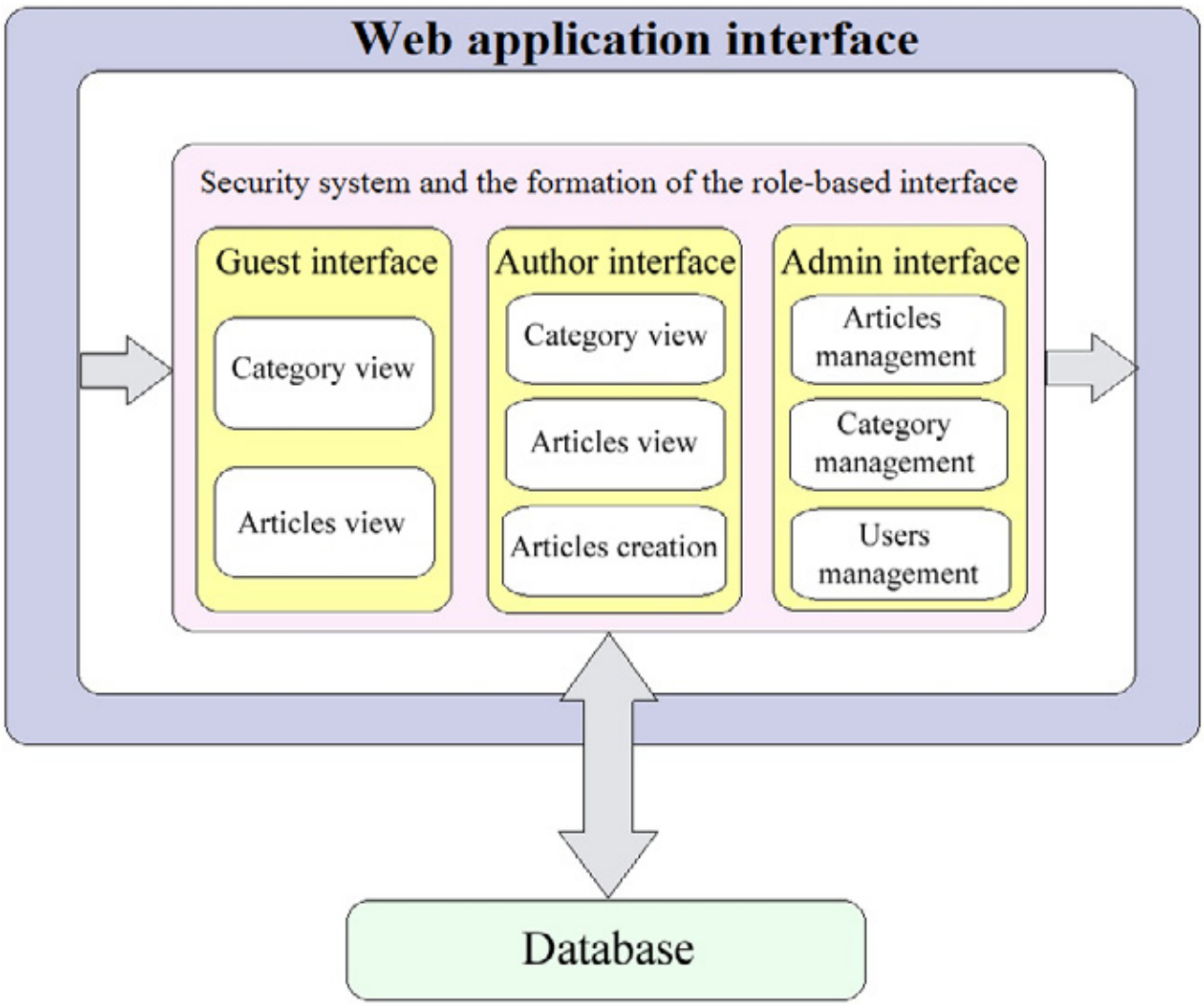

Figure 1: Web-application structure.

- article management that allows one to create, delete and edit articles included in Glossary category/subcategory, to which the moderator has access.

An author interface allows an author to add and edit his articles. A guest interface allows a guest to view articles of all existing categories.

CONCLUSION

Modern trends in technologies, the availability of information technologies and task complexity force researchers to involve other specialists in different fields of science into investigations.

In order to provide interdisciplinary interactions, printed reference books, that contain terms of a special field of knowledge, are usually used [6, 7]. However, it takes a lot of time to find required information in that case.

Multimedia interdisciplinary Glossary on nuclear medicine and radiation therapy, which was developed in NRNU MEPhI and based on information technology, allows one to overcome such difficulties. Finally, Glossary allows one to get the modern scientific and technological information effectively.

REFERENCES

[1] S.E. Ulin et al., *Physical methods of medical imaging*, (Moscow: MEPhI publisher, 2009), 308 (in Russian).

[2] A.P. Chernyaev, *Particle accelerators in the modern world*, (Moscow: Moscow University press, 2013), 368 (in Russian).

[3] C.J. Karzmark, C.S. Ninan, E. Tanabe, *Medical electron accelerators*, (New York: McGraw-Hill, 1993), 332.

[4] E.B. Podgoršak, *Radiation Physics for Medical Physicists*, (Berlin: Springer-Verlag, 2010), 772.

[5] D.N. Kolisnichenko, *PHP5/6 and MySQL 6. Development of Web applications*, (St. Petersburg: bhv-Petersburg, 2010), 560 (in Russian).

[6] *English-Russian dictionary on particle accelerators*, edited by V.P. Dmitrievskiy, (Moscow: Soviet encyclopedia, 1965) (in Russian).

[7] *Charged particles acceleration. Terminology*, (Moscow: Nauka, 1977) (in Russian).

ISBN 978-3-95450-170-0

MULTIFUNCTIONAL EXTRACTION CHANNEL DEVELOPMENT HEAVY ION RFQ (RADIO FREQUENCY QUADRUPOLE)*

E.Khabibullina#, R.Gavrilin, B. Chalykh, G. Kropachev, R. Kuibeda, S.Visotski, T. Kulevoy, A.Golubev, ITEP, Moscow, Russia
M. Comunian, LNL-INFN, Legnaro (PD), Italy
E.Khabibullina#, T. Kulevoy, NRNU "MEPhI", Moscow, Russia

Abstract

In the ITEP the Heavy Ion RFQ HIP-1 (heavy Ion Prototype) has to provide ion beams for two different experimental programs. The first one, aimed to irradiation resistance investigation of reactor construction materials, is successfully ongoing. Samples of new materials for reactors were irradiated by beams of iron, vanadium and titanium ions accelerated by the RFQ. The irradiated materials were investigated by both transmission electron microscope and atom-probe tomography. The second one is under development and it is aimed to investigation of ion beam interaction with plasma and metal vapour targets. For this program a wide range of beams (both gas ions and metal ones) accelerated in the RFQ can be used. Based on beam dynamics simulation the design of new RFQ output beam line enabling both experiments realization was developed. Details of beam dynamics simulation and output line design are presented and discussed in this paper.

INTRODUCTION

In the ITEP the Heavy Ion RFQ (Fig.1) provides irradiation resistance investigation of reactor construction materials. The HIP-1 is a heavy ion RFQ linac accelerating ion beams generated by either MEVVA ion source or duoplasmatron. It provides accelerated beam of ions from C^+ to U^{4+} with energy of 101keV/n and several mA of current[1].

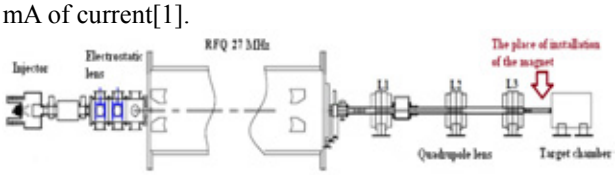

Figure 1: The Heavy Ion Prototype.

For project realization the special target chamber providing sample heating up to desired temperature from range of 20ºC to 700ºC was developed. A set of experimental works for reactor material resistance investigation were carried out already [2].

The experiments of heavy ion beam interaction with plasma and metal vapor target can't be carried out simultaneously with ones for reactor resistance investigation at the existing RFQ output beam line. The existing output beam channel of TIPr-1 can't be used for both targets, for reactor materials investigation and for plasma-beam interaction. The target for imitation experiments with reactor materials is nontransparent. The target for plasma and metal vapor interaction with ion beam is transpired but a considerable amount of intensity (more than 90%) is lost during beam passage through plasma target diaphragms.

According to theoretical models the plasma (ionized gas) has a higher stopping power for ion beam with energy of about 100 keV/n compare to both gas target and even metal one [3]. The design of new beam line is under development now. The results of simulation are presented and discussed.

PLASMA TARGET

The plasma target device generates plasma by an electric discharge igniting in two collinear quartz tubes, each of 5 mm in diameter and 78 mm long. The capacitor bank of ~3 μF provides the discharge at voltage up to 5 kV and produces the electrical current flowing in two opposite directions in both quartz tubes. Such a design for the plasma target enables suppression the well-known effect of the plasma lens caused by the magnetic field of the discharge current. The focusing effect of the first discharge tube is compensated for the defocusing effect of the second one. Symmetry of the discharge ensures by special inductivity coils, included into the discharge circuit, with two wires for the two current branches wind in the opposite directions (Fig.2).

An ultimate vacuum obtained in the target is $1.6 * 10^{-7}$ mbar. During experiments the target pressure may be varied by inlet valve in the range from 1 to 10 mbar. It allows plasma production with variation of both an electron density and a of ionization rate [4].

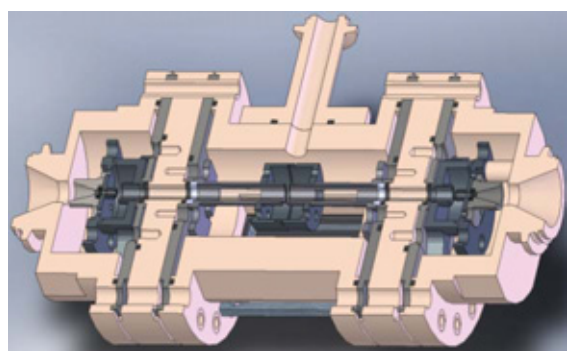

Figure 2: Cross-section view of the plasma target device.

ISBN 978-3-95450-170-0

Therefore to enable two experiments realization with ion beam accelerated in ITEP, it is necessary to develop two correlated beam channels at the RFQ structure output for imitation experiments target and plasma target.

SIMULATION

The multifunctional RFQ output line for both targets was designed on the base of beam dynamic simulation carried out by TraceWin code [5]. The elements which can be transported throughout the channel and provide the required beam parameters at the targets were selected. Moreover, the system described has to fit the experimental hall. For beam transportation to the plasma target, the bending magnet constructed in frame of ADS program [6] for proton beam energy of 36 MeV (Fig.3) was selected thanks to its maximum magnetic field and bending radius. The magnet has magnetic field up to1.3 T, bending radius 670 mm and 30 mm aperture. The quadruple lenses have a 70 mm aperture and can provide up to 12 T/m maximum gradient. It provides the delivering of the ions with mass-to-charge ratio up to 20 to the plasma target.

Figure 3: The dispending magnet.

Since for reactor material irradiation the iron ion beam is used the straight line should be used for this experiment program. The Al^{2+} beam was chosen for experiments at the plasma target, because the maximum field in bending magnet can provide Al beam delivering to the plasma target. The beam initial parameters are determined by Twiss-parameters that were obtained as a result of Al^{2+} and Fe^{2+} ion beams simulation in RFQ channel with the use of Dynamion program [7].

Table 1: The Twiss-parameters

Magnitude	x	y	z
α	-0.238	0.057	0.106
β, mm/π•mrad	0.31	0.022	14.855
γ, π•mm•mrad	0.0248	0.0258	1.008

The simulation was carried out with 4 mA beam current and 10^6 particles in transportation channel. The cross-section of ion beam at the RFQ output is showed in Fig.4.

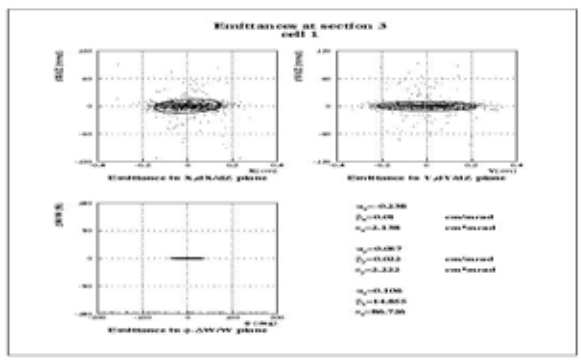

Figure 4: The beam phase characteristics of RFQ structure output.

At first stage, the simulation of existent channel for reactor material target at the HIP-1 output was performed with the quadrupole parameters that are used for ongoing experiments. The obtained results were compared to the experimental data for evaluation of afore-mentioned model and changes made during channel modernization.

Two beam focusing variations at the location of sample installation were considered during the simulation: the elliptical and the circular beam cross-section. The simulation showed the good agreement with the experimental parameters.

At the next step, the similar simulation but taking into account the bending magnet installation between last quadruple lens and the target was carried out. The magnet installation changes the location of the target. The gradient magnitudes were selected in such a way, as to achieve the same values of beam impact on the target, as without magnet installation. The result of simulation is shown in Fig. 5.

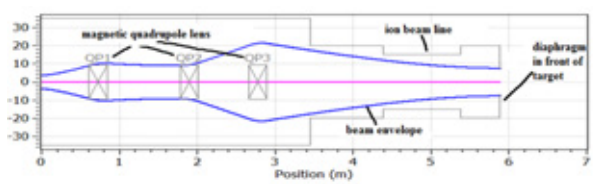

Figure 5: The beam dynamic simulation from RFQ output to target for irradiation resistance investigation of reactor construction materials with magnet ion guide

ISBN 978-3-95450-170-0

As the next stage the beam transport simulation to the plasma target was carried out for the channel with beam bending to 34°. During the simulation the line parameters optimisation to reach the maximum beam passed throughout two 1-mm diaphragms fixed on the input and output on plasma target were carried out. Beam loses will be inevitable, because the beam emittance is several times larger than target acceptance. For best focusing and beam passage through plasma target the magnet quadrupole triplet between bending magnet and target was used. The triplet consist of similar lens were installed at the HIP-1. It was found that more than 2% of beam accelerated in RFQ can be delivered to the detector after the plasma target. It means that the channel provides the beam transportation needed for the experimental works (Fig.6, Tab.2)

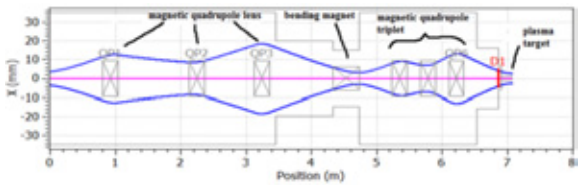

Figure 6: The beam dynamic simulation from RFQ output to plasma target.

Table 2: Channel parameters for transport of Al^{2+}ions

Parameter (units of measurement)	
DRIFT(mm)	613
QUAD, G (T/m)	**3.55**
DRIFT (mm)	935
QUAD, G (T/m)	**-3.9**
DRIFT (mm)	645
QUAD, G (T/m)	**3.95**
DRIFT (mm)	1491
BEND(°)	**34**
DRIFT (mm)	200
QUAD, G (T/m)	**6.4**
DRIFT (mm)	200
QUAD, G (T/m)	**-8.3**
DRIFT (mm)	200
QUAD, G (T/m)	**7.23**
DRIFT (mm)	773

CONCLUSIONS

As a result of this work the magnetic and focusing elements providing realization of two independent experiments at the HIP-1 output channel are selected. The construction is based on the bending magnet and triplet of quadruple lenses.

On the basis of beam dynamic simulation of Fe^{2+} ions in channel for experiments aimed to irradiation investigation of reactor construction materials and Al^{2+} ions in channel for experiments with plasma target in the approximation of ideal fields the channel was designed. The quadruple lenses gradients providing the necessary beam parameters on the targets are determined.

Thus, the base configuration of transport channel at HIP-1 linac was designed for two experiments realization on the plasma target and on metal vapour target (Fig.7).

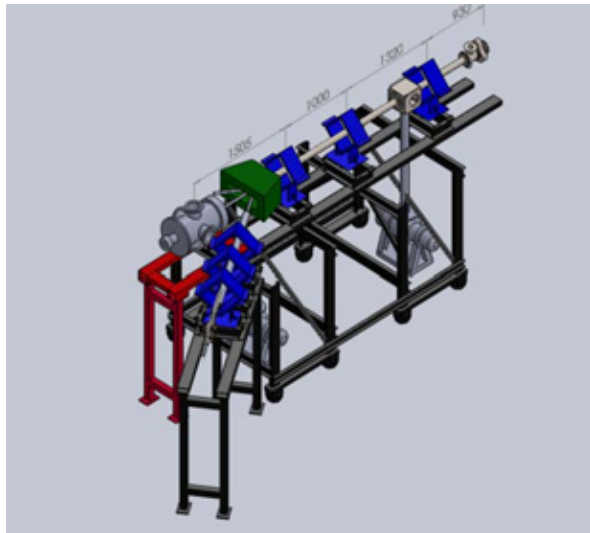

Figure 7: The general view of multifunction channel on the metal vapor target and on the plasma target at the HIP-1.

REFERENCES

[1] D. Kashinsky, A. Kolomiets, T. Kulevoy, R. Kuybida, V. Kuzmichov, S. Minaev, V. Pershin, B. Sharkov, R. Vengrov, S. Yaramishev, “Commissioning of ITEP 27 MHz heavy ion RFQ”, EPAC, 2000, Proc.

[2] T. Kulevoy, R. Kuibeda, G. Kropachev, A. Kozlov, B. Chalyh, A. Aleev, A. Fertman, A. Nikitin, S. Rogozhkin, “ITEP MEVVA ion beam for reactor material investigation”, Review of Scientific Instruments, 2010.

[3] V.E. Fortov, D.H. Hoffmann, B.Yu. Sharkov, “Intense ion beams for generating extreme states of matter”, PHYS-USP, 2008, 51 (2), 109–131

[4] V.P. Dubencov, S.A. Visotski, V. Koshelev.,T.Yu. Mutin, A.D. Fertman, T.V. Kulevoy, R.P. Kuybeda, V.I. Pershin,“The new experimental channel for the HIP-1”, Instrumentals and Experemental Techniques,2005, №4, 1-5.

[5] SACM website:http://irfu.cea.fr/Sacm/logiciels/index3.php.

[6] A .Kozodaev, O. Shvedov, P. Bogdanov, A. Drozdovsky, N.D. Gavrilin, M. Igumnov, V. Konev, N. Lazarev, D. Liakin, A. Raskopin, V. Seliverstov, G. Shimchuk, V. Skachkov, E. Volkov, “Construction of Small-Scale Multipurpose ADS at ITEP”, Proc. of the Second Asian Particle Accelerator Conference, Beijing, China, 2001, 887-889.

[7] A. Kolomiets, I. Vorobyov, S. Yaramishev, “DYNAMION - the New Code for Beam Dynamics Simulation in High Current Ion Linac”, EPAC, June 1998, Stockholm, Proc., 1201-1203, 22-26

ISBN 978-3-95450-170-0

INDUSTRIAL PROTOTYPE OF COMPACT CW LINAC*

D.S. Yurov, A.S. Alimov, B.S. Ishkhanov, N.I. Pakhomov, V.P. Sakharov, V.I. Shvedunov,
Skobeltsyn Institute of Nuclear Physics, Lomonosov Moscow State University, 119992 Moscow, Russia

Abstract

A compact continuous-wave linear accelerator for industrial applications with an output electron energy of 1 MeV and design average beam current of 25 mA is described. The results of beam dynamics, accelerating structure, and RF system simulation are presented, accelerator construction and first results of its commissioning are described.

INTRODUCTION

1 MeV RF CW electron accelerator [1] with a maximum beam current of 25 mA for radiation technologies is being developed at SINP MSU. Accelerator commissioning started in the falls, 2013. At present accelerator is being operated for testing radiation influence at the materials properties and for investigating the radiation degradation of solar cells and circuit boards properties, designed for space operation.

ACCELERATOR DESCRIPTION

The accelerator scheme is shown in Fig. 1.

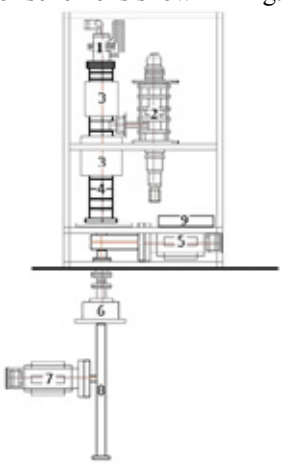

Fig. 1. The accelerator scheme.

An electron gun (1 in Fig. 1) with two focusing electrodes and an operating cathode voltage of -15 kV is located directly at the input flange of the accelerating structure (4). Focusing electrode voltage controls an output gun current from 0 to 250 mA. On-axis coupled biperiodic accelerating structure operates at a frequency of 2450 MHz. A klystron with a maximum output power of 50 kW [2] supplies the accelerating structure with RF power through the central accelerating cavity. Similar high voltage allows to use a common power supply for the klystron and the electron gun. The klystron operates in a self-oscillating mode provided by a low-power RF system (9) which fixes out a positive feedback loop between the klystron and accelerating structure. Magnetic shielding (3) is installed above the structure. Steering coils and solenoidal lens are located in between the structure and magnetic shielding. The accelerator vacuum is provided by an ion pump (5) and a sputter-ion pump of the electron gun. Depending on beam applications different systems can be installed at the output of the accelerating structure. To measure high power beam parameters a Faraday cup with water cooling is placed at the output, provided with vacuum system comprising a rough pump and a turbomolecular pump. The beam scanning system, consisting of a beam divergence camera (8), bending magnet (6) and an ion pump (7) is used for materials irradiation. The bending magnet is powered by the voltage with an amplitude and shape required for the formation of a uniform radiation field over the entire surface of the output window with 5x70 cm^2 dimensions. Accelerator operating volume is separated from atmosphere by 50 microns titanium foil fixed at the beam divergence camera output flange. The accelerating structure and the klystron are cooled with distilled water. A total water consumption of accelerator cooling system is 120 l/min.

The accelerator operation is managed by the control system based on programmable microcontrollers (PMC). The system provides control of all accelerator systems via the remote terminal and information on their operation status. The control system is equipped with a set of emergency – red buttons, and operational interlocks - accelerator hall open door, poor ventilation level, bad vacuum, insufficient structure and klystron water flow, unlocked accelerator case, as well as klystron beam and body overcurrents.

Accelerator photo with the beam scanning system is shown in Fig. 2.

Fig. 2. Photo of the accelerator with the beam scanning system.

ISBN 978-3-95450-170-0

ACCELERATOR SYSTEMS CALCULATION

Accelerating Structure Simulation

Since we have used a common power supply for the gun and the klystron, our electron gun beam energy is 15 keV. To make our accelerator compact, we eliminated the traditional bunching system, drift space, and focusing elements and mounted the gun directly to the accelerator structure. Injecting a 15 keV direct current gun beam into the accelerating structure cells places large demands on the beam dynamics [3]. Electron velocities significantly vary in consequent structure cells, therefore the cells lengths vary too. Besides, to provide high capture efficiency, I_{out}/I_{gun}, we use the initial structure cell as a pre-buncher. To accomplish this we must provide the maximum bunching parameter at the second cell (the first accelerating cell) center.

Electromagnetic fields and beam dynamics in the accelerating structure were calculated with SUPERFISH [4] and PARMELA [5] codes. Electron gun calculations were carried out with EGUN [6] code for different focusing electrodes voltages. An example of particle trajectories for focusing electrodes voltages 500 V and 2500 V with respect to the cathode potential for beam current 53 mA is shown in Fig. 3 Calculated beam spot and phase space at the structure output with 19.1 kW RF power dissipated in the walls are shown in Fig. 4. In this case the capture efficiency, I_{out}/I_{gun}, is 38%.

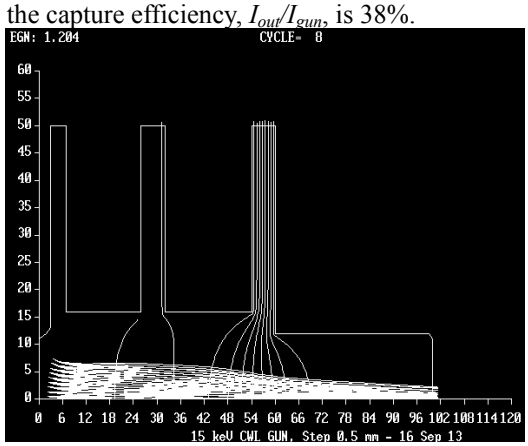

Fig. 3. Calculated particle trajectories in the electron gun for focusing electrodes voltages 500 V and 2500 V with respect to the cathode potential.

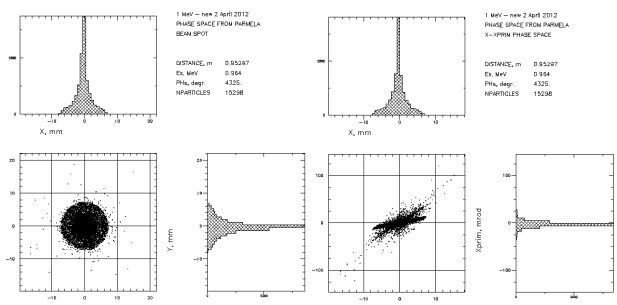

Fig. 4. Calculated beam spot and phase space at the structure output.

RF System Design

Accelerator RF system schematic is shown in Fig. 5.

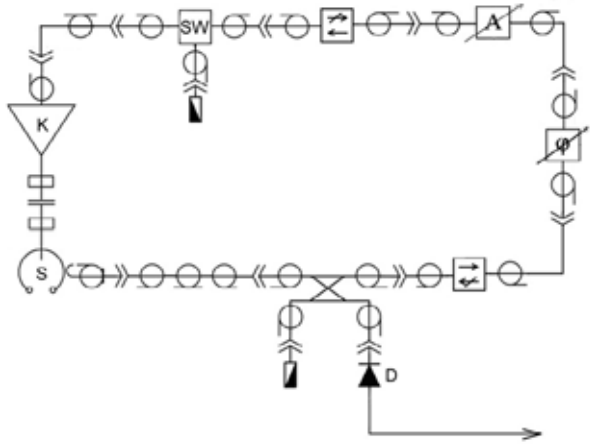

Fig. 5. Accelerator RF system schematic.

We use a 50 kW CW klystron (*K*) to drive the accelerating structure (*S*). Some 22 kW of the klystron power is dissipated in the structure walls providing the accelerating field and, depending on beam current, up to 25 kW goes into the beam. When operating in the self-excited mode, the system oscillates at the structure resonant frequency, which the klystron frequency automatically follows. A RF probe provides the structure signal that passes through electrically driven phase-shifter (φ) and attenuator (*A*), and then enters the klystron. The self-excitation phase conditions are chosen by the phase-shifter while the feedback attenuator regulates the klystron output power and, consequently, the accelerating field amplitude. This amplitude is controlled by a diode (*D*). To start/stop oscillations a RF switch (*SW*) is used.

To define optimum attenuation of the feedback we made calculations of accelerator parameters on beam loading for different values of feedback attenuation.

RF power dissipated in the structure walls P_w and beam energy E are connected with structure coupling β, beam current I, output klystron power P_{kl}, effective shunt impedance Z_{ef} and structure length L by relations [7]:

$$P_w = \frac{4P_{kl}\beta}{(1+\beta)^2}\left(1 - \sqrt{\frac{I^2 Z_{ef} L}{4P_{kl}\beta}}\right)^2$$

$$E = \frac{\sqrt{4P_{kl}\beta Z_{ef} L} - IZ_{ef}L}{1+\beta}$$

Reflected power P_r is defined as $P_r = P_{kl} - P_b - P_w$, where $P_b = EI$.

Amplitude characteristics of the klystron was approximated by the square of the 1-st order Bessel function, normalized in such a way, that maxima of the Bessel function and of amplitude characteristics of the klystron approximately coincided.

Results of the calculation for optimum feedback attenuation of 39 dB, 1.22 coupling value, 53 MΩ/m effective shunt impedance, and 0.84 m structure length are shown in Fig. 6.

ISBN 978-3-95450-170-0

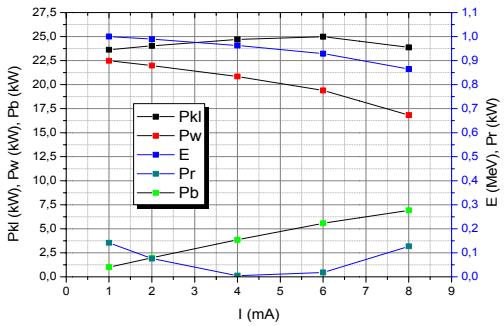

Fig. 6. Results of the RF system calculation.

BEAM SPECTRA MEASUREMENTS

To determine beam energy, current, and power dependence on RF power losses in the structure walls, spectra measurements using a magnetic spectrometer were carried out. Magnetic spectrometer includes a 45^0 bending magnet with its power supply, slit collimator, fixed in the focal plane of the magnet at an angle of 45^0, two isolated beam collectors - Faraday cups, placed at the angles 0^0 and 45^0, and its own vacuum system. The collectors are connected to ground through precise ground resistors for measuring the collectors electron currents.

Measurements were made at a beam current of 500 mA for different values of RF power losses in structure walls. Figure 7 shows measured and calculated spectra for 19.1 kW RF power losses. Figure 8 shows measured dependence of spectrum peak energy on different values of RF power losses in the walls.

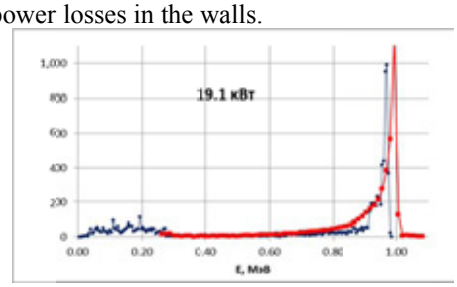

Fig. 7. Measured (red) and calculated (blue) beam spectra for 19.1 kW RF power losses in the walls.

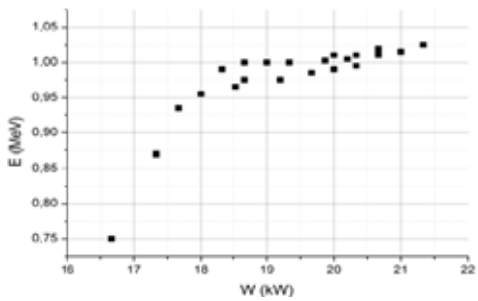

Fig. 8. Spectrum peak energy dependence on RF power losses in the walls.

Beam energy varies slightly when RF power losses in the structure walls are above 18.5 kW. Changing a magnitude of the electromagnetic field in the structure in this range mainly affects the capture efficiency.

HIGH POWER BEAM EXPERIMENTS

The accelerating structure was tuned to a coupling value of 1.22. It corresponds to the minimum of the reflection from the structure at a beam current of ~ 4.3 mA. In the absence of a circulator between the klystron and the structure a deviation from the optimal current affects the reflected wave influence on the klystron output cavity, reducing its operation stability and efficiency.

To obtain and measure a high power beam we installed a copper collector with water cooling at the output of the accelerating structure. The cooling circuit of the collector was connected with a measuring system, which allowed to measure electron beam power by temperature difference between the cooling water input and output temperatures and its flow. For pumping beam line at high beam currents a vacuum system, comprising a rough pump and a turbomolecular pump, was installed at the collector input. In such a configuration, currents up to 6.1 mA with RF power losses in the walls of 19.5 kW were obtained.

CONCLUSION

We have constructed the compact and reliable CW LINAC with 1 MeV output electron energy, thereby validating our design goals. In the first beam tests, our accelerator has provided a 1 MeV, 6 mA, 6 kW electron beam at a 18 mA gun current, thus demonstrating 30% capture efficiency and design beam energy. The accelerator tests are now in progress. Increasing the beam current to 25 mA and capture efficiency to 50% will require tuning the coupling between the structure and the klystron, some modification of the beam collector and vacuum system to improve vacuum conditions in the accelerator.

REFERENCES

[1] A.S. Alimov et al, “Status of 1 MeV 25 kW CW Electron Accelerator”, Proceedings of RuPAC’12, St.-Petersburg, Russia (2012), pp. 541-543.
[2] I.A. Frejdovich, P.V. Nevsky, V.P. Sakharov et al, Proceedings of IVEC-IVESC 2006, Report N13.5.
[3] A.S. Alimov et al. “Low-injection energy continuous linear electron accelerator”. US Patent 8,169,166. May 1, 2012.
[4] K. Halbach, R.F. Holsinger, “SUPERFISH – a Computer Program for Evaluation of RF Cavities with Cylindrical Symmetry”, Particle Accelerators Vol. 7 (1976).
[5] J.H. Billen, L.M. Young, PARMELA, Los Alamos National Laboratory Report, LA-UR-96-1835 (1996).
[6] W.B. Herrmannsfeldt, “EGUN, An Electron Optics and Gun Design Program”, SLAC-331 (1988).
[7] A.N. Ermakov, V.I. Shvedunov, “RF-systems and pulsed racetrack microtron current instabilities”, Nucl. Instr. and Meth. A 550 (2005) 82.

ISBN 978-3-95450-170-0

DESIGN OF A LINEAR ACCELERATOR WITH A MAGNETIC MIRROR ON THE BEAM ENERGY OF 45 MeV

A.N. Ermakov, B.S. Ishkhanov, A.N. Kamanin, V.V. Khankin, L.Yu. Ovchinnikova#,
N.I. Pakhomov, I.V. Shvedunov, N.V. Shvedunov, V.I. Shvedunov, I.Yu. Vladimirov, D.S. Yurov,
Skobeltsyn Institute of Nuclear Physics, Moscow State University, Leninskie Gory 1, 119992 Moscow, Russia
A.I. Karev, V.G. Raevsky, P.N. Lebedev Physical Institute, RAS, Leninsky prospect 53, 117924 Moscow, Russia

Abstract

The results of calculation and optimization of pulsed linear accelerator with magnetic mirror on the beam energy, adjustable in the range of 20 - 45 MeV, designed for explosives detection and other applications are presented. The accelerator consists of an electron gun with an off-axis placed cathode with a beam hole on axis; of about 1.6 m long section of standing wave bi-periodic accelerating structure, operating at 2856 MHz, which is optimized to achieve the capture coefficient of more than 50% and of the energy spectrum width of about 2%; of a movable dispersion free magnetic mirror made with rare earth permanent magnet material. Accelerator provides acceleration of the beam with a pulse current of 100 mA to an energy of 45 MeV with RF power consumption less than 10 MW.

INTRODUCTION

Electron accelerators with energies of the accelerated beam in the range of 20-30 MeV to 100 MeV can be used for medical isotope production, activation analysis, radiation therapy, as the injector for the storage rings, used for basic research in nuclear physics.

One of the promising and new applications of electron accelerators in this energy range is the detection of explosives by photonuclear reactions [1-3]. For the practical implementation of this technique a compact, easy to operate accelerator generating pulses of accelerated beam with an energy of about 45 - 50 MeV, with a charge per pulse of about 1 μC with a repetition rate of 50 -100 Hz is required. Sufficiently high charge per pulse is necessary to provide high sensitivity of the detection method.

Previously, as such an accelerator - pulsed race-track microtrons (RTMs) with energy of 70 MeV [4] and 55 MeV [5] were considered. Advantages of the RTM as compared with linac for the energy range above 20-30 MeV are compactness and low cost. However, operating experience with these RTMs showed that practically attainable accelerated pulse current is limited to about 10 mA, besides there is serious problem associated with the high level of beam losses during acceleration, resulting in high level of induced activity in the elements of the accelerator.

lub.ovch@yandex.ru

As a compromise, in this paper we consider a single-section standing wave linac with a magnetic mirror. A linac with magnetic mirror – linotron - was proposed in [6]. The practical implementation of the accelerator based on this principle with maximum beam energy of 25 MeV – reflexotron - was described in [7].

Here we present a design of the electron linear accelerator with a magnetic mirror for maximum beam energy of 45 MeV.

ACCELERATOR SCHEME

A schematic view of the accelerator is shown in Fig. 1, its main parameters are listed in Table 1. Electron beam from an electron gun (1) is injected into an accelerating structure (2) and is accelerated up to energy 22.5 MeV. Than the beam is reflected back by a magnetic mirror (6) and accelerated once more to the final energy 45 MeV. To provide beam passage through the accelerating structure with minimal losses steering coils (3) and a quadrupole lens (5) are used. An accelerating field in the accelerating structure of a required level is produced by an RF system (8), which is fed by a high voltage modulator (9). A cooling system (10) is used to remove heat from the RF system, the modulator, the accelerating structure, the magnetic mirror. The steering coils and quadrupole lens are fed by current sources (11). Parts of accelerator are also: a gun power supply (7), vacuum system (12), mirror position control (13). Beam current at different points is measured by beam current monitors (4). Accelerator operation is controlled by a control system (14).

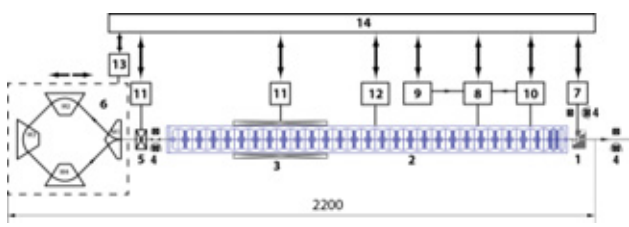

Figure 1: Accelerator scheme.

Table 1: Accelerator parameters

Parameter	Value
Max. beam energy	45 MeV
Max. pulse current	100 mA
Pulse duration	10 μs
Max. repetition rate	100 Hz
Operating frequency	2856 MHz
Max. pulsed RF power	10 MW

ISBN 978-3-95450-170-0

The main features of the accelerator are the next. Since the accelerated beam with energy of 45 MeV comes from the accelerating structure in the direction of the electron gun, for its unhindered passage we use gun with an off-axis placed cathode and the transit hole on the axis. The gun is similar to that described in [8], but is optimized to produce a beam with a current of ~200 mA at a voltage of 25 kV.

To accelerate the beam we use bi-periodic on-axis coupled standing wave accelerating structure operating at 2856 MHz with the beam hole diameter of 10 mm. The parameters of the first three accelerating cells have been optimized to obtain high values of the capture coefficient, a narrow energy spectrum and beam focusing with a crossover, located near the exit of the structure.

To reduce the cost and to simplify the accelerator configuration and operation it is essential to have a linear accelerator, consisting of only one section and powered by a single klystron. RF power required to produce the accelerating field and to accelerate the beam should not exceed ~ 10 MW in order to be able to use commercially available RF equipment, including the klystron, circulator, vacuum RF window and other waveguide elements. In this context, the choice of the number of accelerating cells of the regular part of the structure required to achieve 22.5 MeV, is determined by compromise between the length of the accelerating structure, the complexity of its manufacturing and tuning on the one hand, and amount of the RF power on the other.

As a result of analysis the number of the accelerating cells of a regular part was chosen to be 26, so the total number of accelerating cells is 29, the electrical length of the accelerating structure is 1460 mm, and the pulsed RF power required to create an accelerating field is 4.6 MW. Pulsed power of the accelerated beam is 4.5 MW. So, taking into account the loss of RF power in the waveguide and beam current loss, the output RF power of the klystron should be about 10 MW.

Narrow energy spectrum and the small size of the beam after the first passage through accelerating structure reduce requirements to the parameters of the magnetic mirror from viewpoint of aberrations and thereby simplify the magnets design. We have selected a magnetic mirror consisting of four dipoles. Bending radii, the distance between the magnets and the pole face rotation angles have been optimized in the first order to reach zero-dispersion and negative unite transfer matrix in horizontal and vertical planes. The magnets are designed using a rare earth permanent magnet material as the source of field. Use of permanent magnets with fixed and stable field will simplify tuning of the accelerator.

The parameters of the quadrupole lens installed between the accelerating structure and the magnetic mirror, through which the beam passes in the forward and backward direction, are optimized so as to focus the beam in vertical and horizontal planes.

BEAM DYNAMICS

Beam dynamics simulation was performed using the PARMELA [9] with electromagnetic fields, calculated by SUPERFISH [10], and the parameters of the mirror magnets, found with TRANSPORT [11].

Optimal distribution of the electric field on the axis of the accelerating structure is shown in Fig. 2. Amplitudes of the field and the length of the first three accelerating cells are selected from the conditions of beam bunching, focusing and pre-acceleration.

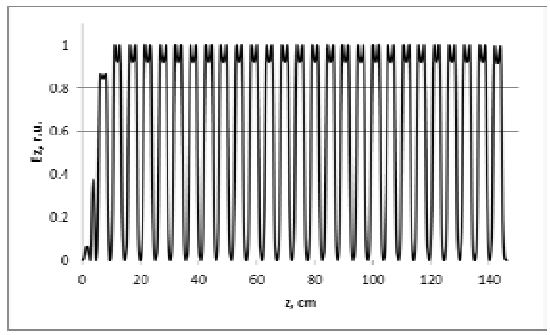

Figure 2: Optimal electric field distribution on accelerating structure axis.

Parameters of the magnetic mirror are shown in Table 2 in accordance with the notation of Fig. 3.

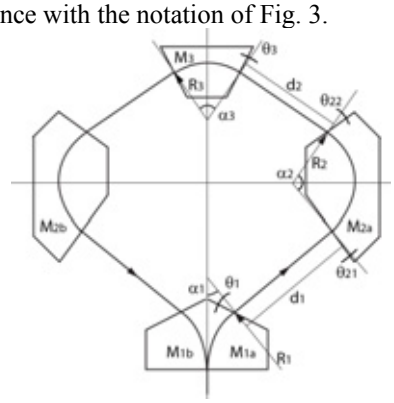

Figure 3: Notations for magnetic mirror.

Table 2: Mirror magnets parameters

Parameter	M_{1a}	M_{1b}	M_{2a}	M_{2b}	M_3
R, mm	76.6	76.6	63.6	63.6	58.7
Magnetic field B, T	1.0	1.0	1.2	1.2	1.3
α, deg.	50.3	50.3	105.9	105.9	68.9
Entrance θ, deg.	0	23.0	-3.5	19.5	6.9
Exit θ, deg.	23.0	0	19.5	-3.54	6.9

The behavior of the rms beam envelope along accelerator is shown in Fig. 4 (a). Fig. 4 (b) shows the relative loss of beam current during acceleration. The number of particles reaching the structure output after the first acceleration is about 74%. The magnetic mirror is positioned in the range 1570 - 2250 mm, by passing mirror additionally ~10% of low-energy particles are lost. Accelerator output reaches ~62% of the particles. The rms beam size in horizontal and vertical planes at output are respectively 1.9 mm and 1.2 mm.

ISBN 978-3-95450-170-0

Calculated spectra of the beam after first acceleration and at output of the accelerator are shown in Fig. 5.

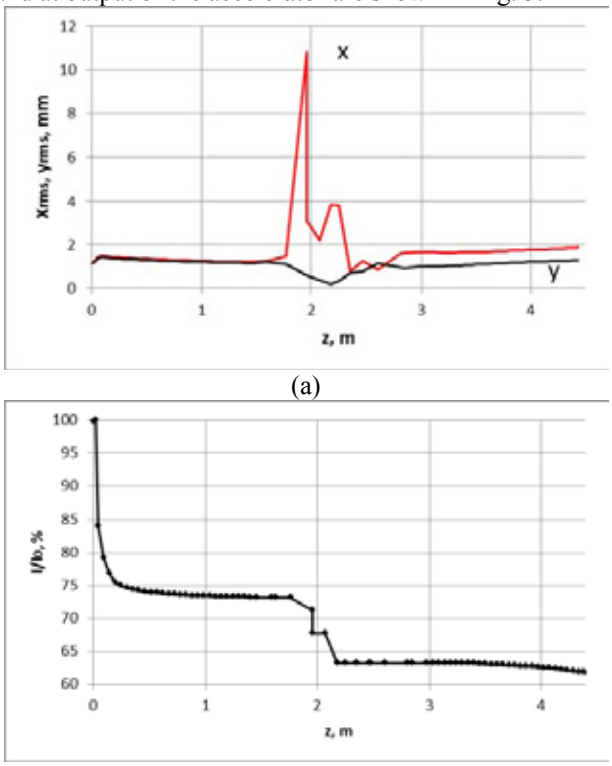

(a)

(b)

Figure 4: (a) Rms beam envelope in x- and y-planes and (b) beam current decrease along the accelerator.

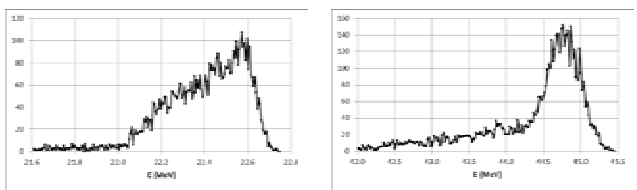

(a) (b)

Figure 5: Beam energy spectra (a) after magnetic mirror and (b) at accelerator output.

RF SYSTEM

Stable values of beam energy and current of the accelerator with the magnetic mirror can be achieved, first of all, due to the high stability of the accelerating field. Instability of the field can be caused by fluctuations in the output power of the klystron, and the change in the resonance frequency of the accelerating structure due to thermal processes, which include resonance frequency shift produced by structure heating by RF power and coolant temperature variation. A simplified block diagram of an RF power system of a linear accelerator, which provides stable accelerating field, is shown in Fig. 6.

The RF system includes a highly stable fast frequency adjustment synthesizer (1), ferrite isolators (2), p-i-n attenuator (3), a pulsed RF amplifier (4) and a klystron (5), the modulator (6), directional couplers (7, 14), a circulator (8) with a matched loads (9), the accelerating structure (10) with an antenna (11), a phase shifter (12), a phase detector (13), an RF detector (15), the frequency and amplitude controller (16).

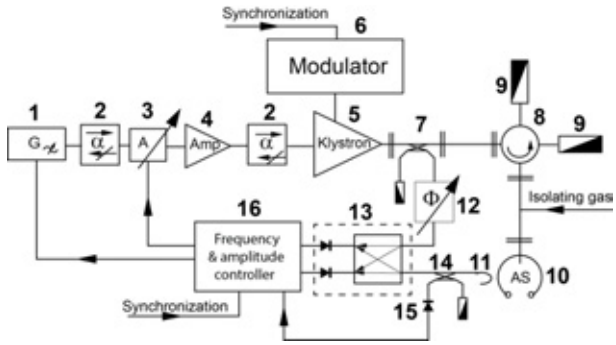

Figure 6: Simplified scheme of RF system.

The stability of the output power of the klystron from pulse to pulse is provided by a high voltage pulse amplitude stability, which for solid state modulator is ~0.1% [12]. Stabilization of the accelerating field is provided by two feedback loops: a fast loop for synthesizer frequency adjustment and a slow loop for adjustment of output klystron power. Adjusting the synthesizer frequency is performed by the controller of the resonance frequency and amplitude for each pulse of the accelerator basing on the signal of the phase detector, the sign and the amplitude of which is determined by the deviation of the frequency of synthesizer from the accelerating structure frequency. Slow adjustment of the accelerating field amplitude is achieved by means of p-i-n attenuator, installed at the input of pulsed RF amplifier.

CONCLUSION

We have designed compact 45 MeV linac with the magnetic mirror capable to produce 100 mA pulsed beam current with a single 10 MW klystron.

REFERENCES

[1] L. Alvarez, Patent US4756866 A, 1988
[2] W.P. Trower, NIM B79 (1993) 589-592
[3] A.Karev et al., Patent US8681939 B2, 2014
[4] V. Shvedunov et al., NIM A 550 (2005) 39–53
[5] A.N.Ermakov et al., in Proc. RuPAC-2012, 538-540
[6] A.A. Kolomensky, in Proc. HEACC 1967, p.46-48
[7] S.O. Schreiber et al., IEEE NS-22 (1975) p.1060
[8] A.V. Aloev et al., NIM A624, (2010) p. 39–46
[9] PARMELA code, originally developed by K. Crandall
[10] K. Halbach et al., Particle Accelerators 7, pp. 213-222 (1976).
[11] K.L. Brown et al., TRANSPORT code, SLAC-91, 1983, 143 p.
[12] www.sc-nova.com

ISBN 978-3-95450-170-0

THE X-RAY SYSTEM WITH SUB-SYSTEM OF SHAPING OF FAN-SHAPED BEAM AND ITS APPLICATION IN THE CUSTOMS INSPECTION SYSTEMS

A.M. Fialkovskiy, Y.N. Gavrish, P.O. Klinovskiy, K.V. Kotenko, V.P. Malyshev, D.A. Solnyshkov,
JSC "D.V. Efremov Institute of Electrophysical Apparatus", St Petersburg, Russia

Abstract

The analytical survey of X-ray sources based on linear electron accelerators applied in the customs inspection systems (IDK) was carried out on the grounds of requirements to customs inspection systems.

The test results of the linear electron accelerator IDK-6/9 MeV which allows to generate the X-ray mode with energies of 6 and 9 MeV are given in this article.

The questions of unification of linear electron accelerators for different IDK are also studied.

It is proved that the D.V. Efremov Institute of Electrophysical Apparatus (JSC "NIIEFA") has the necessary scientific and technical potential and is ready to work out and to produce the X-ray sources for Automobile, Sea and Railway Inspection Systems (IDK). In addition to that the JSC "NIIEFA" is ready to organize the serial production of X-ray sources for inspection systems.

INTRODUCTION

Integration of the Russian Federation into the world economic processes leads to the significant increasing of cargo traffic through its territory. The work-load of the Customs has also increasedgreatly. The most serious problem is an inspection of large-sized cargos; air, sea and railway containers; vehicles and refrigerators

The effective solution is possible with using of the customs inspection systems (IDK). The operating principle of the IDK is based on scanning of monitored objects by a narrow fan-shaped beam of bremsstrahlung with the following recording of a received shadow image and its computer reconstruction by a special software**.**

ANALYSIS OF REQUIREMENTS

As a result of analysis of different IDK types and taking into account the customs problems the Customs of the Russian Federation formed technical requirements for different IDK types: stationary (with energy 8-9 MeV), easy-to-build (relocated) (with energy 5-6 MeV) and mobile (with energy 2,5-4 MeV). This conception was fulfilled within the framework of the Federal target program "The State border of the Russian Federation (2003-2010)".

The experience of creating of IDK in «Ilek» as well as the analysis of development tendencies of IDK of leading world manufacture sallow to form new uniformed requirements for IDK andX-ray sources. The main characteristic sof IDK are given in Table 1.

Table 1: IDK maincharacteristics

Parameter	Mobile	Relocated	Stationary
Penetration capability forsteel	260 mm	400 mm	410 mm
Detection of steel wire without a barrier, diameter not more than	2,0 mm	0,7 mm	0,5 mm
Detection of steel wire behind a 100 mm steel barrier, diameter not more than	5 mm	1.5 mm	1,5mm
Detection of steel wire behind a 250 mm barrier, diameter not more than	-	7 mm	6 mm
Contrast sensation	3%	1%	1%
Carrying capacity, pcs	80 pcs	25 pcs	25 pcs
«Dual energy» mode	+	+	+

The realisation of the parameters given in Table 1 (especially Penetration capability and «dual energy» mode) [1]) requires the accelerators with energy up to 9-10 MeV with a possibility of energy changing. The parameters are given in Table 2.

THE LINEAR ELECTRON ACCELERATOR IDK-6/9 MEV

The linear electron accelerator IDK-6/9 MeV is used as asource of the X-ray bremsstrahlung. It was developed for using in customs control systems of large-sized cargos and vehicles [2].

The base operating mode of the accelerator is 6 MeV of the bremsstrahlung which provides penetration capability for steel more than 300 mm. If necessary the accelerator can be switched to an operating mode with energy 9 MeV of the bremsstrahlung. It provides the possibility to divide studied objects in accordance with a criterion organics/non-organics using the method of "two

ISBN 978-3-95450-170-0

energies". The transit time from the mode 6 MeV to 9 MeV is 15 sec.

Table 2: Parameters of accelerators with a possibility of energy changing DK maincharacteristics

Parameter	Manufactures		
	Varian, USA	Nuctech, China	JSC «NIIEFA», RF
Energy of accelerated electrons, low	6 MeV	6-7 MeV	6 MeV
Energy of accelerated electrons, upper	9 MeV	9 MeV	9 MeV
Absorbed dose for 1 m in different modes, Gy/m×minute			
6 MeV	1	10	2
9 MeV	3	30	5
6/9 MeV	0,5 (6 MeV) 1 (9 MeV)		
Pulse frequency	300 Hz		300 Hz
Focal spot	2 mm	-	2 mm

The accelerating structure working on a stationary wave is used in the accelerator. The structure length is 950 mm. The accelerating structure is powered from a UHF generator that works on a magnetron MG6090. The operating vacuum in the accelerating structure is provided by two magnet-discharged pumps placed near the electron source and near thetarget.

The triode circuit with its own modulators is used in the electron source. This decision optimized the bremsstrahlung level on the scale of recieving detectors independently of the accelerator mode.

The frequency automatic adjustment system adjusts the magnetron accelerating structure operating frequency which is changed during the operating as the equipment is heated. The system minimizes the pulse level of the reflected UHF capacity.

The development of the «dual energy» mode is completed at present. The alternation of the bremsstrahlung pulses with energies 6 and 9 MeV is provided by changing of load of the accelerating structure by accelerated electron current beam with the help of an additional grid modulator of the triode electron source.

Bremsstrahlung generator is controlled in automatic and semi-automatic modes. The control system is designed with a programmable logical controller which allows to use a flexible interface and wide range of peripheral equipment and algorithmic solutions. Also it allows to simple integration of the generator control system into the complex external control system.

OPPORTUNITIES "NIIEFA" AS THE IDK EQUIPMENT MANUFACTURER

Equipment for the production of "NIIEFA" allows you to perform, manufacture, assembly, testing and commissioning of the accelerators and systems based on them. The quality system for all kinds of activities for the production of particle accelerators complies with ISO 9001-2001.

JSC "NIIEFA" is ready to participate in the development of new IDK and commercially supply the following IDK equipment:

- X-ray systems based on linear electron accelerators with fan-beam collimators;
- Detector systems with electronic data collection system;
- Software of data collection, archiving, imaging;
- Software of data collection, archiving, imaging;
- Software of data collection, archiving, imaging;
- Automatic control systems, systemsof monitoring and diagnostics;
- Gantry systems and / or systems of moving of the inspected object;
- Set of auxiliary equipment (shielding doors, automatic control systems, systems of the television surveillance, systems radiation safety, etc.) to ensure safe and smooth operation of the IDK.

REFERENCES

[1] S.A. Ogorodnikov, V.I. Petrunin, "Radioscopic System with the Dual Energy for Customs Inspection of Large-Scale Vehicles and Containers," XVII Conference on Charged Particle Accelerators, Protvino, Russia, October 2000

[2] V.P. Malyshev, A.V. Sidorov, P.O. Klinovskiy, K.V. Kotenko, B.O Bolshakov, V.S. Smekalkin, The IDK-6/9MeV Linear Electron Accelerator and its Application in the Customs Inspection System, XXIII Russian Particle Accelerator Conference (RuPAC 2012), 24-28 September 2012, St. Petersburg, Russia.

ISBN 978-3-95450-170-0

HISTOGRAM BASED BREMSSTRAHLUNG RADIATION SOURCE MODEL FOR THE CYBERKNIFE MEDICAL LINEAR ACCELERATOR

G.E. Gorlachev, Burdenko Neurosurgery Institute, Moscow, Russia
A.V. Dalechina, A.I. Ksenofontov, National Research Nuclear University MEPhI (Moscow Engineering Physics Institute), Moscow, Russia

Abstract

The accuracy of dose calculations is of fundamental importance in treatment planning of radiation therapy. The dose distributions must be calculated and verified by an accurate algorithm. The Monte Carlo simulation (statistical method, based on random sampling) of radiation transport is the only method that makes it possible to perform high-precision dose calculations in the case of a complex geometry. The main bottleneck for the application of this method in practical planning of radiation therapy is the lack of a general virtual source model of the accelerator radiation source. There are several approaches that have been described in the literature [1].

The goal of this work is to build a source model, based on histogram distributions, to represent the 6 MV photon beams from the CyberKnife stereotactic radiosurgery system [2] for Monte Carlo treatment planning dose calculations. The transport of particles in treatment head of CyberKnife was simulated. Energy, radial and angular distributions were calculated. Source model was created on the base of the cumulative histograms. This approach provides producing an unlimited number of particles for the next dosimetric planning. Results of source modelling were verified in comparison with full-scale simulation without model. Good agreement was shown with calculations using the source model of the linear accelerator treatment head.

INTRODUCTION

The human body consists of tissues and cavities with different physical and radiological properties. Conventional, deterministic dose algorithms cannot provide accurate calculation dose distributions in some difficult cases, particularly in heterogeneous patient tissues. The method Monte Carlo is the most accurate method for patient dose calculations in radiotherapy. This method allows to simulate processes of material-radiation interaction inside the radiotherapy units and in the patient body [1]. The MC method, as applied to radiation transport problems, has been described by Rogers and Bielajew as follows: “The Monte Carlo technique for the simulation of the transport of electrons and photons though bulk media consists of using knowledge of the probability distributions governing the individual interactions of electrons and photons in materials to simulate the random trajectories of individual particles’’ [1]. The one of the drawbacks of Monte Carlo simulation as applied to radiation transport has been long calculation times. However, the development computer technologies has significantly reduced calculation times. MC treatment planning algorithms become widespread in the radiotherapy community. The other aspect, which has great influence on using MC method in routine clinical practice, is the general virtual model of the linear accelerator treatment head. The general virtual model has to permit to apply algorithm of dose calculations for any accelerator and substantially improve accuracy. In addition, beam modelling can effect considerable savings in computing time and disk space [3]. A beam model is any algorithm that delivers the location, direction, and energy of particles to the patient dose-calculating algorithm [1]. Accurate source model is an essential requirement for accurate dose calculation within the patient’s body. There are three possible approaches, described by different authors: direct use of phase space information from the accelerator treatment head simulation, development of multiple-source models, particles are grouped by the location of their last interaction and then scored at the phase-space plane leading to subsources [1]. Fluence distributions for each subsource may be reconstructed from the phase-space data in the form of correlated histogram distributions. Other approach is measurement-driven models. Information for the model can be deconvolved from measured data. The goal of this work is to characterize the 6 MV photon beams from the Cyber Knife treatment head and develop the source model to accurately represent and reconstruct the beam. We have developed source model based on a phase space data, which contains histogram distributions.

MATHERIALS AND METHODS

CyberKnife

The CyberKnife system used a flattering-filter-free 6MV Linac accelerator mounted on robotic arm (Kuka, Augsburg, Germany) with 6 degrees of freedom (rotation and translation). The CyberKnife has been used to treat prostate, lung, brain, spinal cord, liver or pancreas with millimetric conformity [4]. Circular treatment fields, ranging from 60 to 5 mm field size in diameter at source detector distance (SSD) of 80 sm. are created using either 12 fixed collimators or an Iris variable aperture collimator. In this work, the 800 MU/min version installed in Department of Radiology and Radiosurgery of N.N. Burdenko Neurosurgical Institute, mounted with fixed collimators was studied.

ISBN 978-3-95450-170-0

Monte Carlo Simulations

Our own Monte Carlo system for radiation transport was used to simulate the 6 MV photon beam from the CyberKnife. Schematic of the treatment head of the CyberKnife is shown in Figure 1.

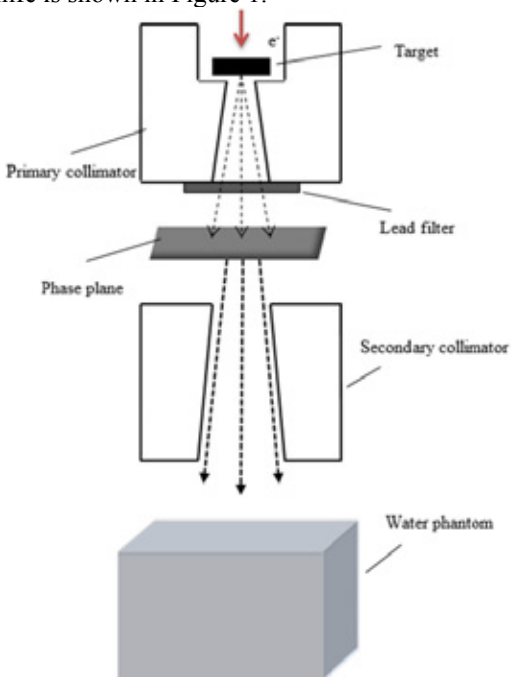

Figure 1: Schematic of the treatment head of the CyberKnife.

Geometry and materials used in the simulation based on the accelerators manufacture's specification. This code is completely written in C++ language. Internally the system uses well established EGS4 physics and principles of transport. Geometry and score classes can be easily extended to a new tasks. We have built following geometrical modules for provide simulations of the linear accelerator treatment head: CYLINDER (target), CYLINDER (aluminum plug), RING (primary collimator), CYLINDER (aluminum filter), CONICALHOLE (conical part of primary collimator), CYLINDER (lead filter), RING (first circular shield), CONICALHOLE (collimator), RING (secondary circular shield), PLANEFILTER (phase space detector), CONICALHOLE (secondary collimator), and SLAB (water phantom). Simulation conditions were specified by two XML-files. One describes geometry of the treatment head, the other – the radiation sources and simulation parameters. The application displays a scene of the simulation in 3D VRML-format for the control of the results and the visualization. The scheme of the location of the various components of the treatment head's simulation is shown in Figure 2.

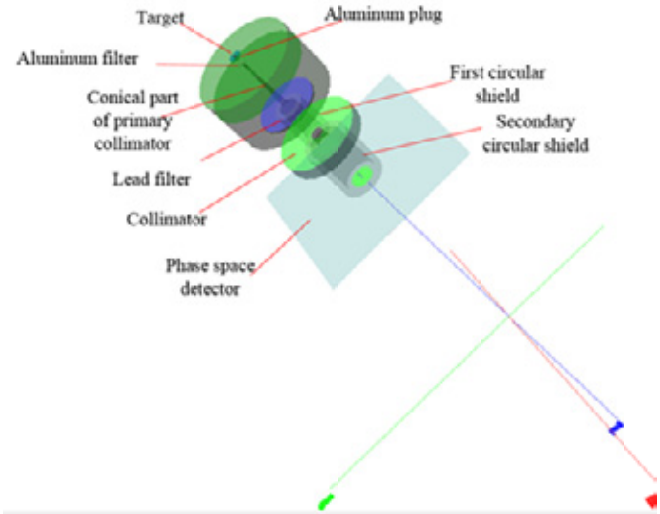

Figure 2: Schematic of treatment head modeling.

Source Model

We have used phase-space information from the accelerator treatment head simulation for develop source model. This approach is to perform the full-scale simulation of radiation transport in the treatment head and creation the phase space, containing required data (position, angle, energy) for each particle crossing the plane of the phase space, perpendicular to the beam axis. Plane model of the source was located after the primary collimation of the head of the CyberKnife.

The source model is created by calculating the energy, radial and angle histogram distributions. Couse of radial symmetry each particle hitting the phase space plane is defined by four coordinates: energy, distance to central axis and two angles. Code registers all photons crossing the plane of the source model. The indexes of the radius, the energy and the angle, referred to a line passing through a centre position of incidence of the electron beam on the target, and the azimuth, defined as the angle to a plane crossing through the axis of the beam and the point of the intersection with the plane of the particle source are determined. The one- dimensional radial histogram is formed. Then two-dimensional energy histogram, three- dimensional angle histogram and four-dimensional azimuth histogram are formed. In order to improve histogram sampling accuracy special parameters transformations were used to make distributions more uniform. Results are saved in format of the finished file of the source model. After that particles are generated from this file. We need about nine megabytes to store model's data. This small volume allows to distribute tasks between users and server components of the treatment planning systems easily.

RESULTS

The comparison between particle distributions from the source model and distributions from the direct simulation without model is shown closely to ideal transcript of the

ISBN 978-3-95450-170-0

radiation fluence by source model. Results are shown in Figure 3.

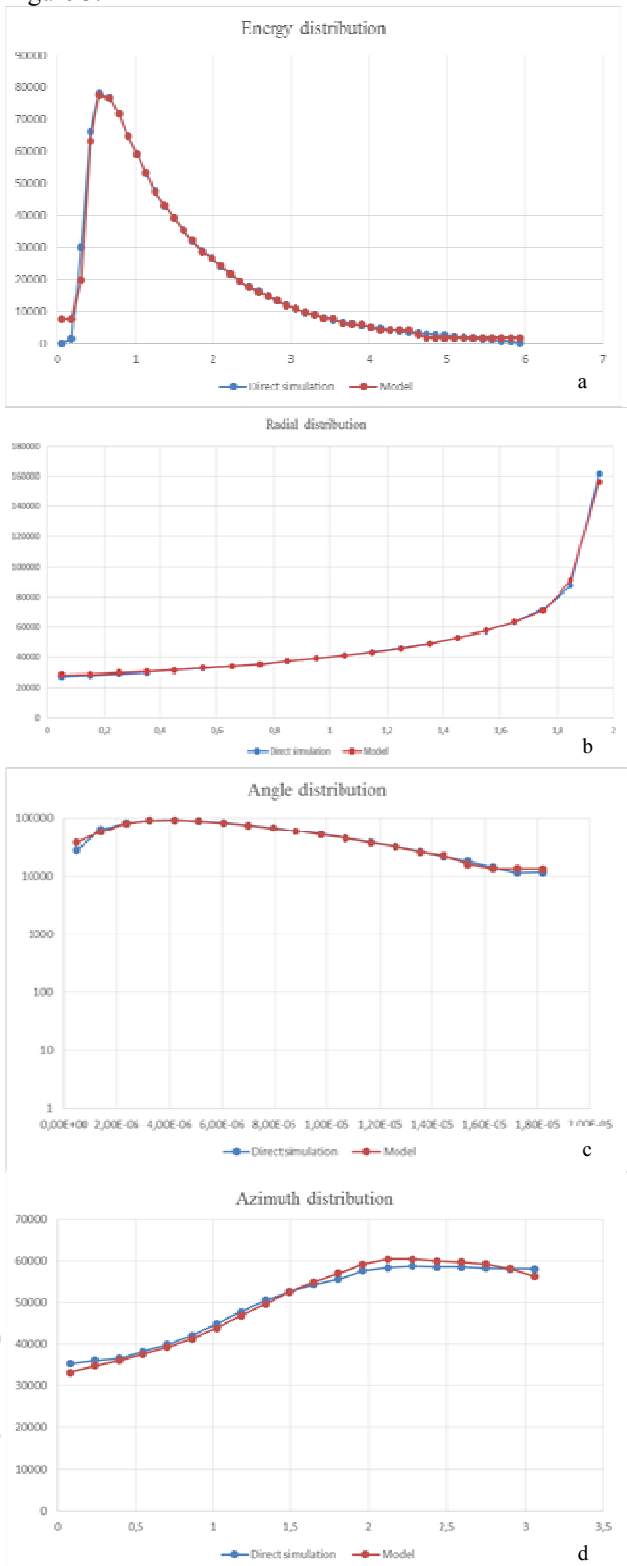

Figure 3: Mean energy (a), radial (b), angular (c) and azimuthal (c) distributions calculated directly from electron beam hitting target (blue lines) and from the source model (red lines). Excellent agreement demonstrate high reproducibility of particles phase space by the model.

Applied method has shown good correlation with results of direct simulation. Furthermore significant speed-up of calculation time has been demonstrated by use the source model.

CONCLUSION

There are many approaches, which allow to model source of radiation with high accuracy. Most of them can be applied to any accelerator if the detail information about the technical parameters and accurate dose measurements are provided. There are many ideas and unconcluded questions concerning influence different components of accelerator and accelerated beam's parameters on dose distributions.

The virtual bremsstrahlung source model of CyberKnife was developed. The application of the histogram based bremsstrahlung radiation source model stays in a good agreement with results of direct simulation. One can see that suggested method has a number of practical advantage in comparison to storage of particles' histories for future clinical calculations. The source model based on histograms is the groundwork for the development of a commissioning procedure to derive source model parameters.

REFERENCES

[1] Chetty I.J. et al. Report of the AAPM Task Group No. 105: Issues associated with clinical implementation of Monte Carlo, based photon and electron external beam treatment planning. Med. Phys.2007; 34. № 12. P. 4818–4853.

[2] Francescon P., Cora S., Cavedon C. Total scatter factors of small beams: A multidetector and Monte Carlo study. Med. Phys. 2008; V. 35 (2). p. 504–513.

[3] Deng J. et al. Modelling 6 MV photon beams of a stereotactic radiosurgery system for Monte Carlo treatment planning. Phys. Med. Biol.2004; V 49. P. 1689 - 1704.

[4] Mognier C. et al. Determination of the k Q c l i n , Q m s r f c l i n , f m s r correction factors for detectors used with an 800 MU/min CyberKnife® system equipped with fixed collimators and a study of detector response to small photon beams using a Monte Carlo method. Med. Phys. 2014; 41 (7). doi: 10.1118/1.4881098.

ISBN 978-3-95450-170-0

MAGNETIC BUNCHER ACCELERATOR UELV-10-10-T-1 FOR STUDYING FLUORESCENCE AND RADIATION-PHYSICAL RESEARCHES

Yu.S. Pavlov, B.B. Dobrohotov, B.A. Pavlov, O.N. Nepomnyaschy, V.A. Danilichev,
IPCE RAS, Moscow, Russia

Abstract

Accelerator UELV-10-10-T-1 is equipped with special system of injection and magnetic buncher with the purpose of generation picoseconds the beam duration 50 ps with the current 150 A at energy 10 MeV for studying fluorescence and radiation-physical researches. For maintenance of the magnetic bunching the accelerator works in the mode of the reserved energy when duration of the pulse of injection (2,5 nanoseconds) is much less than time of filling of a wave guide energy (100 nanoseconds). At a pulse microwave of capacity 10 MW the energy which has been saved up in the wave guide, makes about 2 J. It provides an opportunity of a cutting collimator separately chosen bunch after scan of "package" by a rotary magnet. After an output from the accelerator the package electrons from 3-5 bunches acts in magnetic buncher consisting of two electromagnets. In buncher the beam is scanning as "fan", and then focused. At a current of the beam 30 A in the pulse duration 2,5 nanoseconds distinction on energy between the adjacent bunches makes of 300 keV, that provides an opportunity of the cutting collimator the separate chosen bunch after space scanning with a rotary magnet. At a magnetic bunching electrons in "head" of a bunch have the big energy and are transported on trajectories with the big radius than "tail" electrons. Thus "compression" of the bunch on time is attained and accordingly the charge of a bunch increases.

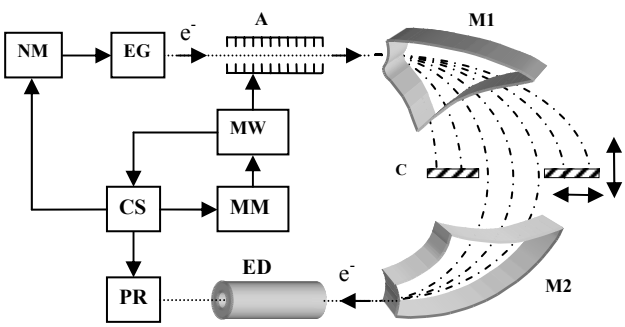

Fig. 1: A function chart of system of formation picoseconds pulses on accelerator UELV-10-10-T-1. NM - nanosecond modulator; EG - an electronic gun; A - the accelerator; M1 - a rejecting magnet; M2 - a focusing magnet; C - collimator; ED - the electro-optical detector of parameters of the beam; PR the pulse registrar; CS - the circuit of synchronization; MM - the modulator magnetron; MW - magnetron.

Accelerator UELV-10-10-T-1 is equipped with special system of injection and magnetic buncher with the purpose of generation picoseconds beam for studying fluorescence and radiation-physical researches [1-7]. The basic connections between the equipment of system of formation of accelerator UELV-10-10-T-1 are submitted on a function chart (see Fig. 1).

MAGNETIC BUNCHER TECHNOLOGY

Appearance of system of formation is shown in Fig. 2. The principle of action of system of formation is based on features of work of the accelerator electrons in a mode of use of the reserved energy. In such accelerator at sufficient loading the current arises significant reduction of energy electrons between the next bunchs, as is used for allocation of a separate clot from an initial pulse with the help of a dividing electromagnet.

Duration of bunch makes approximately 0,1 periods of the microwave of fluctuations of the generator of the accelerator (~ 50 ps).

Fig. 2: Appearance of system of formation picoseconds pulses on accelerator UELV-10-10-T-1.

For maintenance of a magnetic grouping the accelerator works in a mode of the reserved energy when duration of a pulse of injection (2,5 ns) is much less than time of filling of a wave guide energy (100 ns). At pulse power of the microwave 10 MW the energy which has been saved up in a wave guide, made about 2 J. At a pulse current more than 10 A distinction energy the next clots makes about 200 keV. It provides an opportunity of a cutting collimator separately chosen clot after scanning of "package" by a rotary magnet. After an output from the accelerator the bunch electrons as a package from 3-5 clots acts in magnetic buncher consisting of two electromagnets. In buncher the beam is scanning as "fan", and then focused.

Magnetron with capacity 10 MW in a pulse allow "to reserve" in the wave guide energy up to 2 J and to spend her for small time of injection electrons (2,5 ns) in

ISBN 978-3-95450-170-0

comparison in time filling of the wave guide (100 ns) is insignificant. In a case when the pulse of injection (1,5 ns) is much less than time of filling of a wave guide microwave power (~ 100 ns) the accelerating field essentially varies at passage of clots through a wave guide (see Fig. 3). The first clots will select more energy, than the subsequent, that leads to broadening power spectrum of the beam.

Effect broadening a spectrum usually various methods try to minimize. In our case, on the contrary, it is necessary "to widen" the spectrum to simplify a problem of allocation of one bunch. At big enough current of a beam (30 A) in an initial pulse duration of 2,5 ns the difference energy the next clots is equal 300 keV.

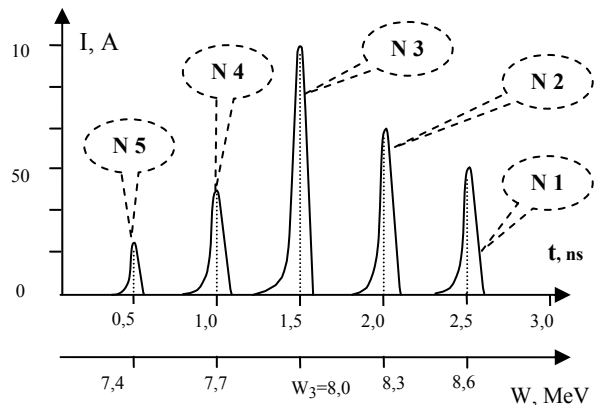

Fig. 3: Intrapulse structure of a bunch on accelerating frequency of 1886 MHz. The period of following of clots 530 ps

Compression Picoseconds Bunch

Distinction on energy between the next bunches provides an opportunity of a cutting collimator the separate chosen clot after spatial scanning pack with a rotary magnet (see Fig. 4). The current in windings of electromagnets is adjusted in limits 6-8A. At a current 7A collimator on an output of a magnet cuts out one of clots.

The bunch gets out of the middle of a package because of the greater difference in energy between bunches and the maximal current of the bunch. The allocated bunch is passed through the second electromagnet for a bunching of a beam, "clearing" of a gamma-background and is issued in the channel of transportation an atmosphere through foil window. Thus "parasitic" brake radiation from collimator is withdrawn aside from the experimental radiation-chemical equipment. The effect of a magnetic bunching is reached due to a difference of a course electrons inside a bunch. Electrons in "head" of a bunch have the big energy and are transported on trajectories with the big radius than "tail" electrons.

Thus "compression" of a bunch on time is reached and accordingly the charge of a clot (see Fig. 5, 6) increases.

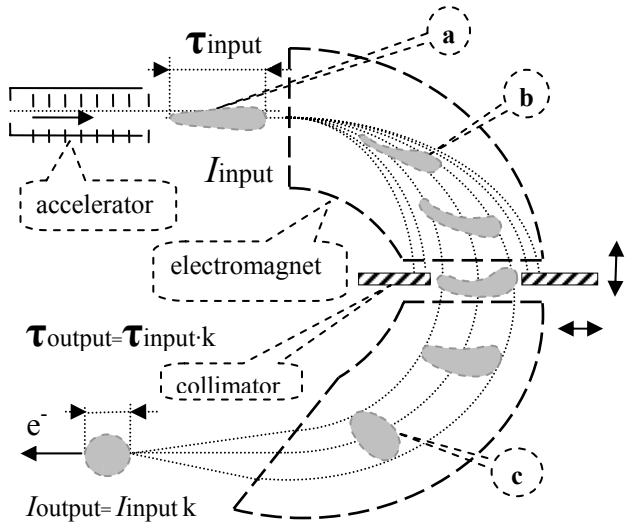

Fig. 4: Magnetic buncher and the circuit of its work: a) - intrapulse structure of the bunch; b) - a clot up to a magnetic bunching; c) - the bunch after a magnetic bunching.

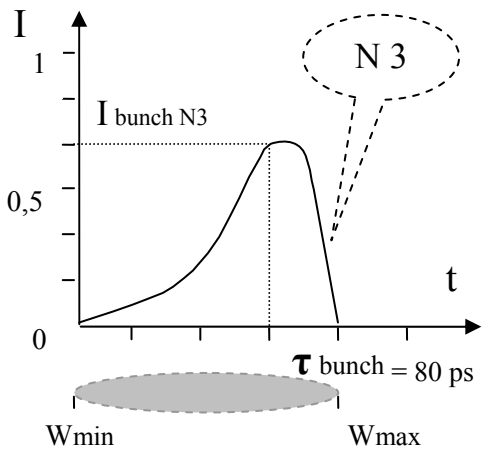

Fig. 5: A bunch № 3 up to a magnetic bunching.

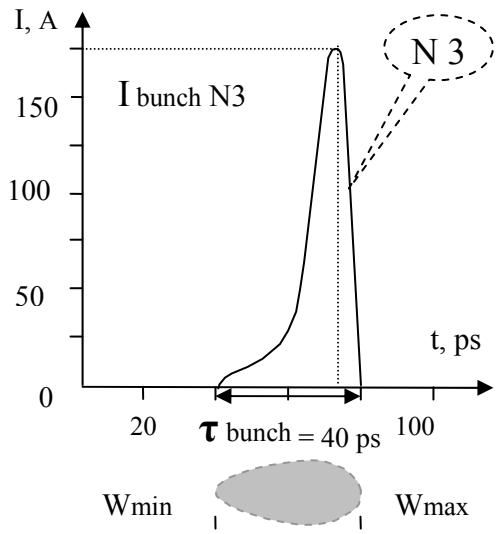

Fig. 6: A bunch № 3 after a magnetic bunching.

ISBN 978-3-95450-170-0

DIAGNOSTICS OF A BEAM

On Fig. 7, 8 pulses on an output of accelerator UELV-10-10-T-1 are shown.

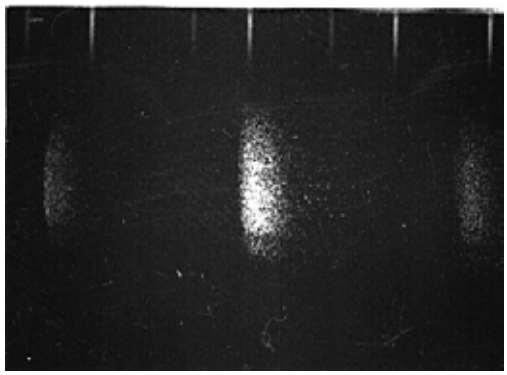

Fig. 7: Photoregisterogramma picoseconds a pulse.

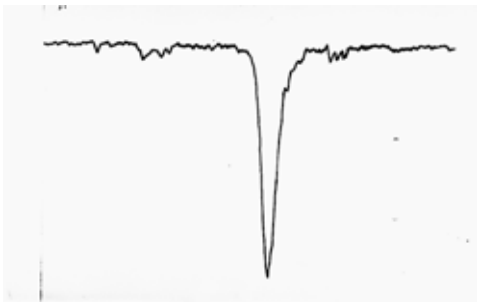

Fig. 8: Microdensitogramma picoseconds a pulse (50 ps, 150 A).

Picoseconds pulses from the accelerator are absorbed in a researched sample. In experimental pulse installation simultaneously through a sample light radiation from xenon lamps in a direction perpendicular to a beam electrons is passed. In a sample light is in part absorbed. Light past through a sample with the help of mirror optical system decays on a spectrum and is analyzed. Researches are carried out on spectrophotometer to diagnosing installation. (see Fig. 9).

Fig. 9: Appearance of system spectrophotometer to diagnosing installation.

REFERENCES

[1] Yu. S. Pavlov, V.P. Klimashin, O.N. Nepomnyaschy, "Spectrophotometer installation for research of radiating processes in solid bodies", Works of XXIV International conference "Radiating physics of a solid body", Moscow, FGBNU "SRI PMT", July 2014, pp. 526-535 (2014) (in Russian).

[2]. A.K. Pikaev, P.Ya. Glazunov, Yu.S. Pavlov. "Radiation centre of institute of physical chemistry in Moscow", Radiat. Phys. Chem., Vol. 42, Nos. 4-6, pp. 887-890 (1993).

[3] Yu. S. Pavlov., V. V. Dobrohotov, O.N. Nepomnyaschy. "Electro-optical methods measurement of parameters powerful electronic beams for radiation technologies", Questions of a nuclear science and technics, Series "Technical physics and automation", Vol. 58, Moscow, Tsniiatominform, pp. 135-143 (2004) (in Russian).

[4] Yu. S. Pavlov, "System of formation and metrics picoseconds pulses of a current of a beam on linear accelerators for studying quick-flashing processes in radiobiology and radiation chemistry", Reports of 4 All-Union meeting on application of accelerators of the charged particles in a national economy, Vol. 2, Leningrad, NIIEFA, pp. 66-74 (1982) (in Russian).

[5] Yu. S. Pavlov, N.G. Solovjev, P.J.Glazunov, O.N. Nepomnyaschy, V.N. Polkovnikov, "Research of thin structure of pulses of a current of a beam waveguide the accelerator electronic", Questions of a nuclear science and technics, Series "Technics of physical experiment", Vol. 2 (14), Kharkov, KIPT, p. 86 (1983) (in Russian).

[6] Yu. S. Pavlov, N.G. Solovjev. "Formed and measurement picoseconds beams of the charged particles", Works 8 All-Union meetings on accelerators of the charged particles, Vol. 2, Dubna, JINR, pp. 63-67 (1983) (in Russian).

[7] Yu. S. Pavlov. "Device for formation high-current picoseconds beams of the charged particles". Patent Russian № 793348. The bulletin of inventions USSR, № 47 (1985), (in Russian).

ISBN 978-3-95450-170-0

NEUTRON RADIATION MONITORING OF THE THERAPEUTIC PROTON BEAM TRANSPORTATION

V. Skorkin, INR RAS, Moscow, Russia

Abstract

A monitoring system online controls a therapeutic proton beam by measuring a secondary neutron radiation from the beam losses. The system consists of neutron detectors in the transport path passage from Linac to the facility of proton therapy and terminal controller connected to the computer. The neutron detectors measure a level of the secondary neutron radiation in real time along of the transport channel, near the formative elements.

INTRODUCTION

A result of the proton beam loss is formed neutron secondary radiation. The neutrons in the transport channels can be registered with help of fast neutron detectors. A level of secondary neutron radiation in the transport path of the proton beam is proportional to the average beam current and beam losses [1]. Fig. 1 shows the neutron radiation in the transporting channel at the average beam current of 0.7 mA to 35 mA.

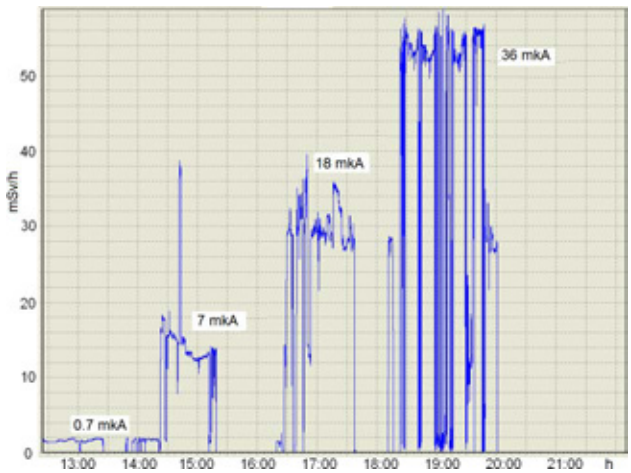

Figure 1: Diagram of the neutron radiation dose power measured in the beam transport channel.

The information about the neutron radiation intensity allows you to determine beam loss in different parts of the transport channel. The neutron monitor of the proton beam transport allows you to measure the temporal variations of the beam intensity in local areas transporting channels. These changes arise are due to changes in operating mode of the channels or instability of the elements forming the beam transport channels.

MONITORING THERAPEUTIC BEAM

The system monitoring the beam transport includes a terminal controller, which is connected to the computer. The neutron detectors are located along the ion guide, near the formative elements of the transport channels and the target of the proton therapy facility. The layout of neutron detectors of the system monitoring the proton beam transportation in Complex of proton therapy is illustrated in Fig. 2.

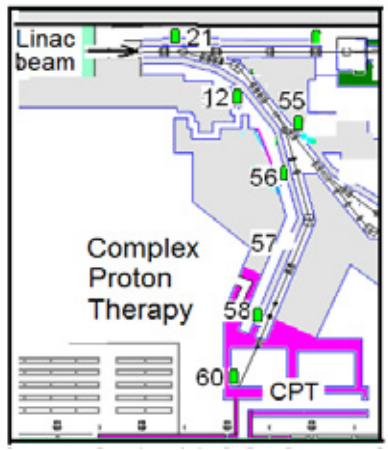

Figure 2: Complex of proton therapy.

The detectors in the transport channels are used for the beam loss measurements. Software module monitoring system determines and shows the dose power of the secondary neutron radiation in real time. The changing of the intensity of the beam of protons due to the unstable form of the elements in the medical channel caused by blocking is shown in Fig. 3.

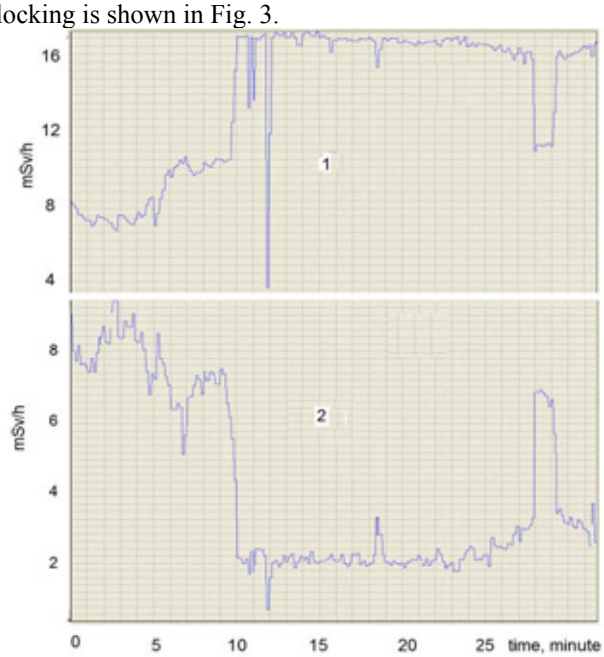

Figure 3: Diagram of the neutron radiation intensity in the beam transport channel. 1 – neutron background near the bending magnet; 2 - neutron background in front of the collimator.

ISBN 978-3-95450-170-0

The intensity of neutron radiation in the medical channel is changed by overlapping the therapeutic beam using emergency and working shutters. The neutron radiation intensity changes the beam covering the beam emergency workers or shutter. The monitoring system allows you to monitor this process (Fig. 4).

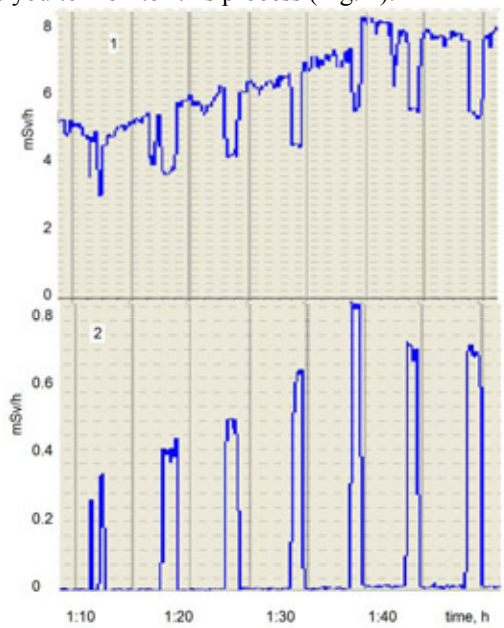

Figure 4: The profile of the neutron background in the medical channel (1) and in the procedural of proton therapy (2).

The diagrams observed correlation between the levels of neutron radiation in both sections of the proton beam transport due to the presence or absence of the beam in the procedural of proton therapy.

CONCLUSION

The system monitors the beam transport and reduces background radiation and activation equipment. The monitoring system determines the intensity and temporal structure of the therapeutic beam and to detect mode and instability of the formative elements.

Neutron radiation measured by the monitoring system can receive timely information about the losses of the beam and correction of operational parameters which form the transport channel devices to improve the quality of beam.

REFERENCES

[1] M.I. Grachev, V.A. Kljushnikov, S.I. Kuptsov et al. The automatic radiation control system of the INR linear accelerator (Troitsk) // *Proceedings of RuPAC XIX*. Dubna, 2004, p.483-484.

ISBN 978-3-95450-170-0

SMALL-SIZE HIGH-PERFORMANCE ARSA ACCELERATORS FOR ON-LINE TESTING FOR ECB RADIATION HARDNESS

S.L.Elyash, S.P.Pukhov, A.V.Rodigin, A.L.Yuryev, RFNC-VNIIEF, Sarov, Russia

Abstract

At present an extent of electrical engineering item tests for pulsed ionizing radiation (IR) hardness has abruptly increased. Solving of such problems with the help of only powerful simulators seems impossible due to significant time and material costs. Results of studies, performed in RFNC-VNIIEF, RISI and other organizations [1], have shown that optimal combination of small-size high-performance accelerators ARSA and powerful simulators allows a significant reduction of terms and costs for radiation tests, an increase of fidelity and self-descriptiveness of the results obtained.

As opposed to IC test simulation methods using laser radiation, ARSA accelerator employment allows approaching of the process inspection conditions to the real-life environment [2].

BRIEF DESCRIPTION OF ARSA ACCELERATOR

ARSA is a small-size pulsed electron direct-action accelerator with oil insulation [3, 4], see fig. 1. It consists of a high-volt unit 1 with accelerating tube 4, located in the sealed container, charger 2 and a control board 3. A specific feature of a ten-cascade Marx generator used in the accelerator is a pulsed charging of reservoir capacitors. Cascade current is switched with the aid of metal-ceramic pressurerized spark gaps [5].

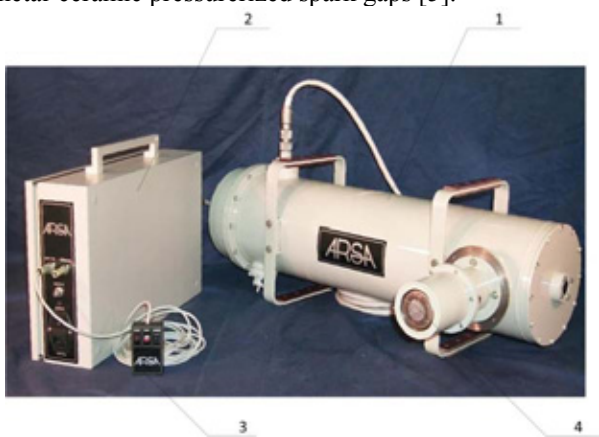

Figure 1: Small-size pulsed accelerator ARSA.

A sealed-off accelerating tube with a through target represents a vacuum diode with an explosive-emission cathode and titanium anode. Anode of 50 μm thickness is an output window for electron beam. To generate bremsstrahlung radiation onto the outer tube window surface there is mounted a target made of 50 μm thick tantalum foil and 2 mm thick aluminum filter for absorption of electrons passed through the window and target. Edge type cathode of diameter 10 mm supplies a homogeneous radiation spot.

A PULSED FIBER-OPTIC MONITOR-DOSIMETER WITH A DETECTOR CHANNEL FOR RADIATION PULSE SHAPE MONITORING

For the purposes of on-line monitoring of small-size pulsed ARSA accelerators' dose a fiber-optic monitor–dosimeter (MD) [6] has been developed, see fig. 2. It is structurally unified and used together with the accelerator's control panel. For MD one foresees also a possibility for autonomous operation in the mode of dose monitoring.

Figure 2: Fiber-optic monitor-dosimeter, combined with ARSA control panel.

MD represents a combination instrument, comprising:

- fiber-optic pulsed X-ray dose meter;
- pulse counter with nonvolatile memory for control over the facility life;
- storage device for each pulse dose values;
- pulse dose adder in a series;
- blocking device upon a specified dose is reached;
- port for reading of accumulated data into the computer.

Fiber-optic pulse dosimeter has a number of advantages:

- instant obtaining of measurement result as compared to the thermoluminescent dosimeter;
- high noise immunity, low detector's degradation as compared to meters based on semiconductor diodes;
- availability of new service-feature features (counter, adder, nonvolatile memory, port), due to employment of modern micro-processor.

A radiation detector in the device is scintillator CsI(Tl). The light is transferred from the detector to a photodetector through plastic fiber-optics of 1 mm diameter. A pin-photodiode is used as a photodetector. A peculiar feature of MD structure is a one-piece assembly

ISBN 978-3-95450-170-0

«scintillator-fiber-optic-photodetector», what increases measurement stability as compared to the multi-piece one.

In order to monitor shapes of X-ray pulses with lengths from units up to nanoseconds, a fast-acting fiber-optic scintillation detector is available in the MD set. The detector is characterized by increased noise immunity to magnetic pickups of pulsed physical facilities and does not require application of high-volt power supply sources. It contains a subnanosecond scintillator SPS-B18 [7] with diameter and height of 50 mm, dual plastic fiber-optic cable with a strand diameter of 1 mm, pin-photodiodes of ФД-271 type and a subnanosecond amplifier on a GaAs-field-effect transistor. «Cherenkov» background in the cable, approaching up to 16% of the useful scintillation light signal, is registered separately with the aid of a parallel fiber-optic channel (without a scintillator) and is subtracted from the detected signal on the amplifier input. The amplifier's output is connected to the registrator. ARSA X-ray pulse oscillogram, registered on the oscilloscope LeCroy Wavemaster-8500A with the aid of fiber-optic detector, is given in fig. 3.

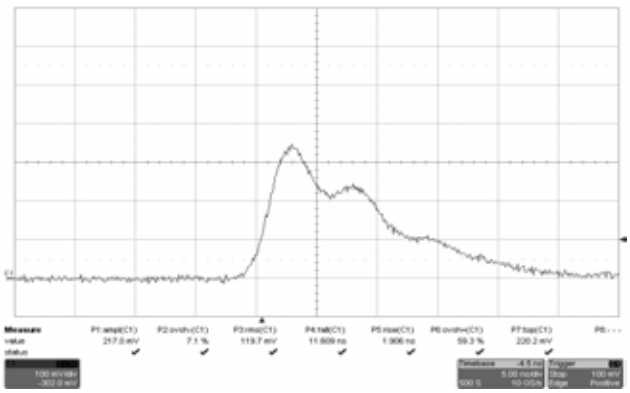

Figure 3: X-ray pulse shape of ARSA accelerator, registered with the aid of fiber-optic scintillation detector.

ARSA ACCELERATOR'S ADVANTAGES

A multi-year experience of ARSA accelerator's operation has revealed a number of their advantages with reference to other similar devices:

- high dose power (up to $5 \cdot 10^{10}$ cGy/s for X-ray radiation and up to $1 \cdot 10^{14}$ cGy/s for electron radiation),
- compact size and mobility,
- simplicity of operation and maintenance,
- good reproducibility of dose characteristics (±10 %),
- calculation of absorbed dose distribution in the irradiated object,
- varying of radiation type and parameters through a sealed tube change,
- long service life – up to 10^5 shots,
- rate of operation – hundreds of shots a day,
- ecology safety,
- electro-magnetic compatibility with electric equipment (developed level of electromagnetic interference in signal cables without special screening measures – not more than 0.2 V).

REFERENCES

[1] A.M. Chlenov, N.G. Mordasov, D.M. Ivashchenko, VANT, Phys. Rad. Exp. 1, pp. 5-10, (2010).
[2] S.L. Elyash, L.P. Profe, VANT, Phys. Rad. Exp. 3, pp. 132-136, (2002).
[3] S.L. Elyash, N.I. Kalinovskaya, Ye.N. Donskoy, et al., At. Energy 79, 6, pp. 462-464, (1995).
[4] S.L. Elyash., N.I Kalinovskaya, V.F. Goncharova, et al., Proceedings of the 7th International Conference on Electron-Beam Technologies EBT, Varna, Bulgaria, p. 591, (2003).
[5] E.A. Avilov, A.L. Yuryev, Prib. Tekh. Eksp. 2, p. 78, 2000.
[6] S.L. Elyash, A.V. Rodigin, V.A. Pikar', RF u. m. patent # 90575 (2009).
[7] T. Zoufal 1, K. Wick., Nucl. Phys. B 208, pp. 471-475, 2003.

ISBN 978-3-95450-170-0

DEPTH DOSE DISTRIBUTION OF THE BREMSSTRAHLUNG GENERATED BY THE BETATRON OB-4 IN DIFFERENT ENVIRONMENTS

I. Miloichikova, V. Ruchyeva, E. Shuvalov, S. Stuchebrov, TPU, Tomsk, Russia

Abstract

In the paper the dosimetric parameters measurement technique of the bremsstrahlung generated by betatron OB-4 is described. The radiation dose measurement results from the bremsstrahlung generated by betatron are shown. The depth dose distributions of the bremsstrahlung generated by betatron obtained with the help of the solid thermoluminescent detectors DTL-02 and the dosimeter UNIDOS E equipped with a PTW Farmer cylindrical ionization chamber type 30013 in the different environments (in the air, in the water and in the lead) are illustrated.

INTRODUCTION

Within a research framework of the development of the new methods to reduce radiation doses for the objects under radiographic analysis, it was proposed to use the pulsed irradiation source synchronized with the detecting device. Such X-ray visualization setups based on the pulsed X-ray generator RAP-160-5 were created in the Department of Applied Physics of the Tomsk Polytechnic University. The previous tests showed a significant radiation dose decline to the objects in comparison with conventional techniques [1, 2]. For estimation of the suitability of using the portable betatron OB-4 as a source of bremsstrahlung for visualization purposes it is necessary to investigate the dosymetric parameters of the device.

The research objectives are:

- to obtain the depth dose distribution in the air, lead and water of the pulsed bremsstrahlung generated by the betatron OB-4;
- to analyse the suitability of using the compact pulse betatron OB-4 as a source of bremsstrahlung for visualization purposes.

MATERIALS AND METHODS

Emitting source

The portable betatron OB-4 was used as a source of emission. This betatron is used as a pulsed source of bremsstrahlung. The material of the target is tungsten (0.6 cm thick). The maximum kinetic energy of the electrons is 4.0 MeV.

The general quantities of the portable betatron OB-4 are: the frequency of radiation impulse is 400 Hz; the duration of one pulse is about 15 μs [3].

Dosimetric equipment

The main problem associated with the dosimetry of the pulsed radiation is the response rate of the dosimeters. This problem can be solved by using the storage type of the detectors. The solid thermoluminescent dosimeters DTL-02 were used as dosimetric equipment for initial estimation of the radiation doses. The thermoluminescent material of the detectors is LiF: Mg, Ti. The dosimetric complex based on the thermoluminescent dosimeters DTL-02 is designed for the personal dosimetry. The dosimeters DTL-02 can work in the energy range of gamma radiation from 15 keV to 10 MeV, the dose range varies from 20 μSv to 10 Sv [4].

The dosimetry protocol for megavoltage photon beams (with nominal energies between 1.25 and 50 MeV) adopted by the AAPM is recommended to use the ionization chambers as the basis for measurements [5]. The universal dosimeter for radiation therapy and diagnostic radiology UNIDOS E equipped with a PTW Farmer chamber type 30013 was used in the experiments [6, 7].

The PTW Farmer cylindrical ionization chamber type 30013 is used for absolute photon and electron dosimetry. This chamber is waterproof and can be used in water phantoms. The main parameters of the cylindrical ionization chamber type 30013 are: the nominal photon energy range is from 30 keV to 50 MeV; the electron energy range is from 10 MeV to 45 MeV; the dose range varies from 0.1 mGy to 1 Gy; the sensitive volume is 0.6 cm^3 [7].

Experimental setup

The irradiation scheme is shown in the figure 1. The irradiation source (1) was placed in lead dome (2) with the output window. The detector (3) was positioned on the radiation axis opposite the output window.

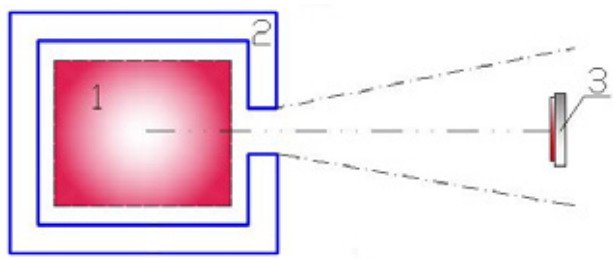

Fig. 1. The irradiation scheme: 1 – the portable betatron OB-4; 2 – the lead dome; 3 – the plane-parallel ionization chamber type 23342

For obtain the depth dose distribution in the lead of the bremsstrahlung generated by the betatron OB-4 the lead plates with the different thickness (0.3, 0.6, 0.8, 5.0 cm) was used.

For obtain the depth dose distribution in the water of the bremsstrahlung generated by the betatron OB-4 the

ISBN 978-3-95450-170-0

water phantom 41023 for horizontal beams was used. The external phantom dimensions are approximately $30 \times 30 \times 30$ cm^3. The entrance window in one of the walls has the thickness of 3 mm (the walls material is PMMA) and the size of 150×150 mm^2 [8].

Depth dose distribution technique of the pulsed bremsstrahlung of the betatron

According to the experimental setup the thermoluminescent detectors and the cylindrical ionization chamber were used for the dose measurements of the pulsed bremsstrahlung generated by betatron.

The thermoluminescent dosimeter DTL-02 was used for the dose measurements in the air of the pulsed bremsstrahlung generated by betatron. The measurements were carried out by three different DTL-02 dosimeters at the equal distance between the radiation source and the detector. The dose rate values were calculated.

In the second part of the experiment the dose and the dose rate measurements in the three different arias: in the air, in the lead and in the water were carried out by the universal dosimeter UNIDOS E equipped with the cylindrical ionization chamber type 30013.

The measurement mode of the dosimeter UNIDOS E was "LOW". The dose rates measurement operating mode of the ionization chamber type 30013 is 0.6 mGy/min – 0.5 Gy/min [7]. The cylindrical ionization chamber type 30013 was used with the special buildup cap.

In the experiment in the air the distance between the radiation source and the detectors was varied from 30 to 100 cm in increments of 10 cm.

For obtain the depth dose distribution in the lead of the bremsstrahlung generated by the betatron OB-4 the lead plates were arranged on the radiation axis close by the output window, the detector was positioned opposite the lead plates.

For obtain the depth dose distribution in the water of the bremsstrahlung generated by the betatron OB-4 the water phantom 41023 for horizontal beams was used. The phantom arranged on the radiation axis opposite the output window at the distance equal to 50 cm, the detector was positioned inside the phantom. Because of the water phantom plastic wall is greater than 0.2 cm thick, all depths was scaled to water-equivalent depths. For a PMMA wall, in photon or electron beams the effective wall thickness is given by the measured thickness in cm times 1.12 [5].

RESULTS AND DISCUSSIONS

In the Fig. 2 the dose rate distribution in the air of the pulsed bremsstrahlung generated by betatron depend on the distance between the betatron OB-4 and the detector using the solid thermoluminescent dosimeters DTL-02 and the cylindrical ionization chamber type 30013 are presented. The dose rate measurement for the different distance between the radiation source (betatron) and the detector are average over three different DTL-02 dosimeters.

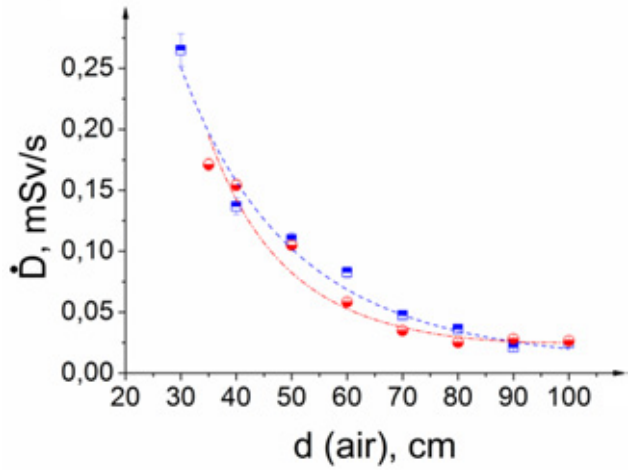

Fig. 2. The depth dose distribution in the air of the pulsed bremsstrahlung generated by betatron: – the solid thermoluminescent dosimeters DTL-02 measurement results; - - - - the approximation results of the solid thermoluminescent dosimeters DTL-02 measurements; – the cylindrical ionization chamber type 30013 measurement results; —·—·— - the approximation results of the cylindrical ionization chamber type 30013 measurements.

The Fig. 2 shows that the dose rates measurement obtained using the thermoluminescent detectors and the cylindrical ionization chamber are in a good agreement with each other. These points to the fact that the cylindrical ionization chamber can be used for routine dosimetry of the pulsed bremsstrahlung generated by betatron.

The insignificant divergences between the obtained curves in the Fig. 2 can be explained by the fact that there are some angular divergence of the betatron beam and dispersion of the high-energy part of the gamma spectrum. In this case, it is proposed to use the collimator for future dosimetry measurements. Nevertheless, it is evident that the obtained dependences are well approximated by exponential curves. That is in agreement with the theory.

The obtained data (Fig.2.) shows the sufficient equability of the accelerator beam, which indicates the suitability of the betatron OB-4 for the visualization purpose.

The depth dose distribution in the lead and in the water of the pulsed bremsstrahlung generated by betatron obtained with the help of the cylindrical ionization chamber type 30013 are presented in the Fig. 3 and the Fig. 4 correspondingly.

The profile of the depth dose distribution in the lead (Fig.3.) has an enough linear character for the adsorber thickness up to 3 cm, which indicates the suitability of the accelerator in the nondestructive testing goals.

The profile of the depth dose distribution in the water (Fig.4.) has a linear character and demonstrates the suitability of the pulsed bremsstrahlung generated by betatron OB-4 for visualization biological objects with

ISBN 978-3-95450-170-0

thicknesses up to 25 cm, which is typical of the human body size.

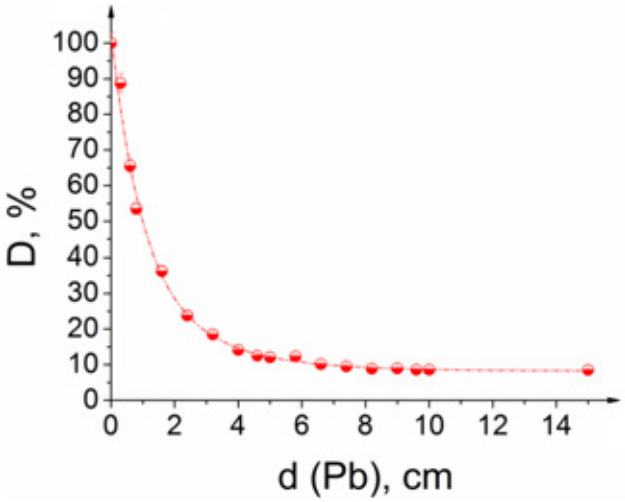

Fig. 3. The depth dose distribution in the lead of the pulsed bremsstrahlung generated by betatron: ◒ – the cylindrical ionization chamber type 30013 measurement results; –·–·– - the approximation results of the cylindrical ionization chamber type 30013 measurements.

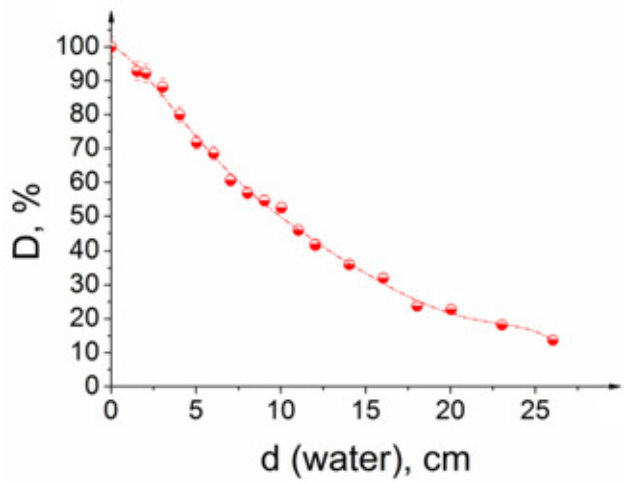

Fig. 4. The depth dose distribution in the water of the pulsed bremsstrahlung generated by betatron; ◒ – the cylindrical ionization chamber type 30013 measurement results; –·–·– - the approximation results of the cylindrical ionization chamber type 30013 measurements.

SUMMARY

The obtained date show the advisability of using the solid thermoluminescent dosimeters DTL-02 and the universal dosimeter UNIDOS E equipped with a PTW Farmer chamber type 30013 for the dosimetric parameters measurements of the pulsed bremsstrahlung generated by electron accelerator with energy of 4 MeV.

After the dosimetric equipments selection the radiation dose of the pulsed bremsstrahlung generated by betatron OB-4 was estimated. The obtained data show that the bremsstrahlung generated by betatron OB-4 can be used for the visualization purposes of the objects in the nondestructive and medical examinations.

ACKNOWLEDGEMENT

This work was partly supported by Competitiveness Enhancement Program of Tomsk Polytechnic University.

REFERENCES

[1] S. Stuchebrov, A. Batranin, D. Verigin, A. Wagner, “Setups for tomographic imaging with submillimeter spatial resolution”, J. of Phys.: Conf. Ser. 517 (2014) 012046.

[2] S. Stuchebrov, A. Batranin, D. Verigin,Y. Lukyanenko, M. Siniagina, A. Vagner, “Estimation of Radiation Doses in X-Ray Visualization of Biological Objects”, Advanced Materials Research 880 (2014) 53-56.

[3] *Technical specification: “Inductive cyclic accelerator OB”* (Tomsk: Betta Pljus, 2010), 15 (in Russian).

[4] *Technical specification ZhBIT2.805.006RJe: “Thermoluminescent dosimeters DTL-02”*, Version_2_05.10.2012, (Moscow: Doza, 2012), 13 (in Russian).

[5] P.R. Almond, P.J. Biggs, B.M. Coursey, W.F. Hanson, M.S. Huq, R. Nath, D.W.O. Rogers “AAPM’s TG-51 protocol for clinical reference dosimetry of high-energy photon and electron beams”, Med. Phys. 26 9 (1999) 1847-1870.

[6] UNIDOS E Universal Dosemeter; http://www.ptw.de/unidos_e_dosemeter_ad0.html?&cId=3965.

[7] *User Manual Ionization Chamber Type 30010, 30011, 30012, 30013 D596.131.00/03 2006-09 Hn*, (Freiburg: PTW, 2013), 16.

[8] Water Phantom 41023 for Horizontal Beams; http://www.ptw.de/water_phantom_horizontal_beams20.html.

ISBN 978-3-95450-170-0

STATUS OF EXPERIMENTS ON SURFACE MODIFICATION OF MATERIALS ON THE ACCELERATOR HIP-1

B.B. Chalykh, A.V. Kozlov, R.P. Kuibeda, S.V. Andrianov, D.A. Aparin, P.A. Fedin, N.N. Orlov, A.A. Nikitin, A.A. Bogachev, A.A. Aleev, A.A. Andreev, G.N. Kropachev, N.A. Iskandarov, A.A. Golubev, NRC KI SSC of RF ITEP, Moscow, Russia
S.V. Rogozhkin, T.V. Kulevoy, NRC KI SSC of RF ITEP, Moscow, Russia; NRNU MEPHI, Moscow, Russia

Abstract

Ion implantation is an effective method for materials surface modification for various technological applications. The most common examples of its use are an increase of the durability, corrosion resistance, heat resistance for various industrial steels and special alloys for applications in biology and medicine, strengthening and changes in the morphology of the surface layers of polymers. Work in this direction is underway at the accelerator HIP-1 in ITEP. To provide the experiments, the beams of iron, vanadium and titanium generated by vacuum-arc metal ion source, as well as ion beams of nitrogen generated by duoplasmatron ion source are used. Several sets of experiments for the modification of the surface features were carried out. The transmission electron microscopy (TEM) and tomographic atom-probe microscopy (TAP) were used for samples analysis after ion beam treatment.

INTRODUCTION

Ion implantation is widely used as a method for modification of materials in order to improve their physical and chemical parameters. The ions used can be divided into light ones (typically nitrogen, carbon, oxygen and boron) and heavy ones (chrome, titanium, and tungsten). For biomedical applications, it is effective to use silver ions, copper and other elements to improve the bactericidal properties of steels, titanium alloys, CoCr alloys without losing their strength and corrosion resistance [1]. To improve the wear resistance and durability of industrial steels, implantation of nitrogen ions is used widespread [2, 3]. It is shown that the hardening depends not only on the dose of implanted nitrogen, but also on the chemical composition of the material to be modified and formed as a result of nitride complexes [4]. Furthermore, implantation of high doses of carbon (about 8×10^{17} ions / cm ^{2}) allows achieving a significant increase in durability by forming a carbon layer on the product surface [5]. Improvement of the corrosion resistance can be obtained by implantation of chromium and rare earth metals ions [6]. Since the implantation of different chemical element ions into material can significantly modify the properties of their structure in sub-surface layers, the use of composite beams may be the best technology in the preparation of materials for specialized applications.

To provide experimental activity, the beams of iron, vanadium and titanium generated by vacuum-arc metal ion source, and beams of nitrogen generated duoplasmatron were accelerated in the heavy ion HIP-1 (Heavy Ion Prototype). Several sets of experiments for the modification of the surface features were carried out. The results of the first experiments of surface modification by ion beams are presented.

FACILITY AND EXPERIMENT

The scheme of RFQ HIP-1 is shown on Fig.1. The accelerator assembly consists of the 100 kV terminal (1), low energy beam transport (LEBT) line with two electrostatic Einzel lenses (3) and diagnostic chamber (2), 27 MHz RFQ section and channel with 3 magnetic quadruple lenses (L1,L2,L3) and diagnostic station (5) at the output of the accelerator.

The accelerator allows the two types of experiments: at "low energy" when the irradiation of samples is carried out at the output of the injector inside the diagnostic chamber A (fig.1. pos.2) for further study by transmission electron microscopy (TEM) and tomographic atomprobe microscopy (TAP). Another type is the samples irradiation by "high energy" beams at the output of the accelerator (fig.1. pos. 5) for the further samples testing by transmission electron microscopy [7].

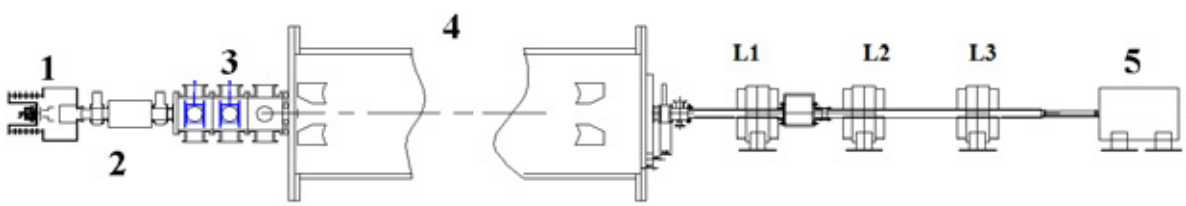

Figure 1: ITEP RFQ HIP-1. 1 - injector, 2 - diagnostic chamber A, 3 - electrostatic lens, 4 - RFQ, 5-diagnostic chamber B, L1,L2, L3 –quadruple lenses.

ISBN 978-3-95450-170-0

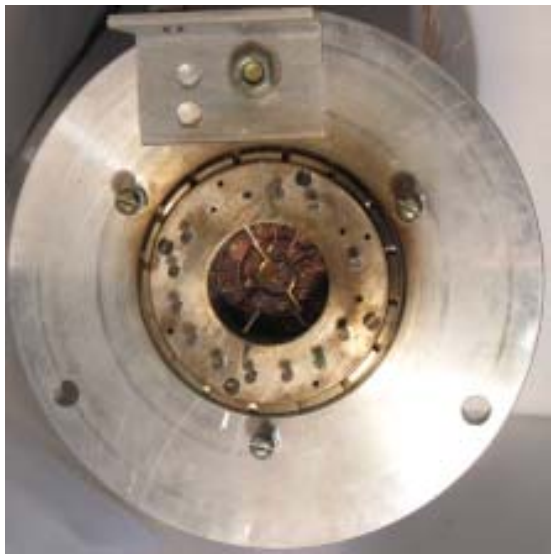

Figure 2: Target holder for TAP samples.

In the experiments at the output of the injector (acceleration of ions performed by electrostatic tube) the final energy of the ion beam is up to Z • 75 kV, where Z - ion charge. For the experiments with material surface treatment an existing target holder (Figure 2), established for the irradiation of the samples prepared for the following investigation by the atomic probe microscope is used. Those samples have a shape of needles with the cap radii about 100 nm. The additional target block was constructed and installed for another kind of samples irradiation. As samples the cylinders with the diameter of 3 mm and the thickness of 0.1 mm are used. The block enables simultaneous installation up to seven samples for ion beam irradiation (Figure 3). Irradiations at the output of the injector are held by Fe^{2+} ions with energy of 150 keV, and by the N^{1+} ion with energy of 75 keV.

For the experiments with high energy, a target assembly with samples heating system is used (Figure 4).

Figure 3: Target holder for TEM samples.

The construction of the sample holder allows samples irradiation with heating to a temperature of ~ 700^0C. The set-up of the sample holder consists of the copper heating block 2, sample holder assembly 1, placed on the butt copper block, two stainless steel rings 3 fixing the construction inside the water cooling screen 4 [8].

During irradiation, it is vital to control the samples temperature with tolerance ± 3^0C in the range from 300 to 500^0C. Heating of the samples is currently being implemented with the use of a proportional-integral-derivative controller (PID controller) TRM101. For the implementation of sample heating, in a copper holder (Figure 4. Pos 2) the axial blind hole was drilled for installation of the heating elements of 200 W. To control the samples temperature, two thermocouples were installed in the longitudinal blind holes located at the same distance but opposite side from heating element. One thermocouple is used to provide the PID regulation, while the second thermocouple is used as a control one

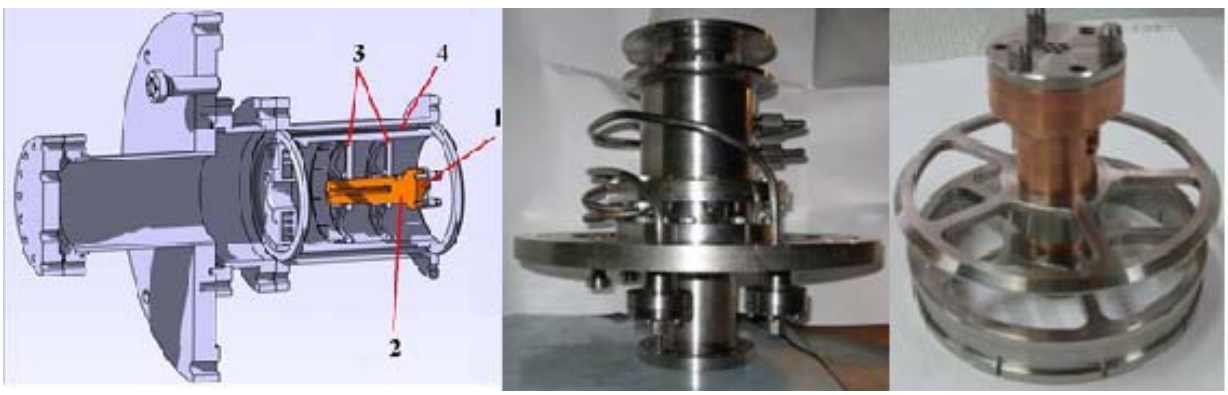

Figure 4: A) Target chamber construction: 1 – sample holder; 2 – copper ingot; 3 – stainless steel rings, 4 – water cooling system. B) Photo of system of sample holder C) Photo of copper ingot and stainless steel rings

ISBN 978-3-95450-170-0

Figure 5 shows a graph of samples heating up to 300°C. The desired temperature is reached in about 20 minutes, the temperature stability of the sample holder after the release in normal mode is better than ± 1°C. The maximum overheating is less than 2^0C. The heating test showed required stability of temperature and revealed new opportunities for further experimental works when heating is sufficient.

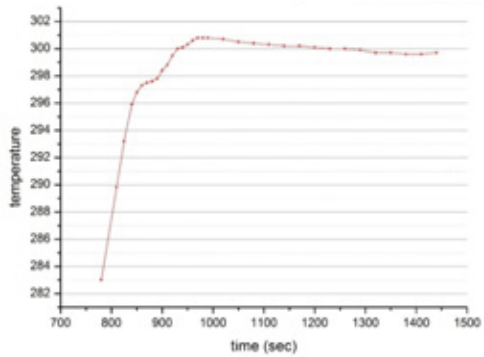

Figure 5: A plot of the T (t).

The first experiments on the irradiation of the samples of ADS Eurofer 97 steel by the Fe^{2+} ions accelerated up to 101 keV/n with simultaneous heating to a temperature of 300^0C was carried up to total flux of 1×10^{15} ions/sm^2. The final dose is ~3 DPA. After irradiation, samples were investigated by using at TEM. Results are shown in Fig.6.

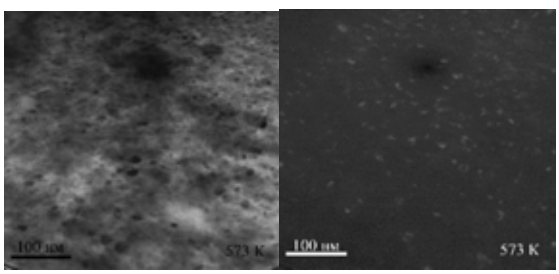

a b

Figure 6: Layout of papers. Photography of irradiated sample, obtained with TEM.

Results are presented in two different modes light field (Fig.6.a) and dark field (Fig.6.b). In Fig.6.a one can see that the carbide formation (black dots) with size of ~ 30 nmare is present in irradiated steel. White dots presented on Fig.6.b are appeared to be the result of clusters formation process. This result is in a good agreement with results of [9] taken as a reference to test the method we develop.

CONCLUSIONS

In ITEP the experiments for material surface modification is underway at the accelerator HIP-1. To provide the experiments, the beams of iron, vanadium and titanium generated by vacuum-arc metal ion source, as well as ion beams of nitrogen generated by duoplasmatron are used. Several sets of experiments for the modification of the surface features were carried out. The transmission electron microscopy (TEM) and tomographic atom-probe microscopy (TAP) were used for samples analysis after ion beam treatment.

REFERENCES

[1] Wan Y.Z., Raman S., He F., Huang Y. Surface modification of medical metals by ion implantation of silver and copper // Vacuum. – 2007. - V.81. - pp. 1114-1118.

[2] Martínez R., García J.A., Rodríguez R.J., Lerga B., Labrugere C., Lahaye M., Guette A. Study of the tribological modifications induced by nitrogen implantation on Cr, Mo and W // Surf. Coat. Tech. – 2003. - V. 174-175. - pp. 1253-1259.

[3] García JA, Guette A, Medrano A, Labrugere C, Rico M, Lahaye M, et al. Nitrogen ion implantation on group IVb metals: chemical, mechanical and tribological study // Vacuum. – 2002. - V. 64. - pp. 343-351.

[4] García J.A., Rodríguez R.J. Ion implantation techniques for non-electronic applications // Vacuum. – 2011. – V. 85. - pp. 1125-1129.

[5] Sánchez R., García J.A., Medrano A., Rico M., Martínez R., Rodríguez R., et al. Successive ion implantation of high doses of carbon and nitrogen on steels // Surf. Coat. Tech. – 2002. - V. 158-159. - pp. 630-635

[6] Arenas M.A., de Damborenea J.J., Medrano A., García J.-A., Rodríguez R. Corrosion behaviour of rare earth ion-implanted hot-dip galvanised steel // Surf. Coat. Tech. – 2002. - V. 158-159. - pp. 615-619

[7] The advanced nanostructure steel is modification by gas ions in nuclear technology. S.L Andrianov, P.A Fedin, R.P Kuibeda, A.V. Kozlov, A.A. Nikitin,B.BChalykh, A.L. Sitnikov T.V. Kulevoy ITEP, Moscow, Russia

[8] Setting the output channel of accelerator hip-1 for imitational experiments for study of radioactive resistance reactor materials R.P. Kuybida, T.V. Kulevoy, B.B. Chalykh, A.I. Semennikov, G.N. Kropachev, I.A. Stoyakin, A.O. Cheritsa, A.D. Fertman, A.A. Aleev, A.A. Nikitin, N.N. Orlov, S.V. Rogozhkin // VANT - 2012 №4(80) pp.68-70

[9] D. Kaoumi, J. Adamson, M. Kirk - Microstructure evolution of two model ferritic|martensitic steels under in situ ion irradiation at low doses (0-2 dpa), Journal of Nuclear Materials 445 (2014) 12–19

ISBN 978-3-95450-170-0

METHOD OF MEASURING FAST NEUTRON FLUENCE USING THE PLANAR SILICON DETECTORS

A.I. Shafronovskaia, N.I. Zamyatin, A.E. Cheremukhin, LHEP JINR, Dubna, Russia
(on behalf of the QUINTA Collaboration)

Abstract

The technique reported of fast neutron fluence measurements using silicon detectors. One of the main macroscopic effects at radiation damage of silicon detectors by fast neutrons is increase of the reverse current. The increment of the reverse current detector is a linear dependence on fast neutron fluence and is determined by the formula (Eq. 1):

$$\Delta I = \alpha_I \times F \times V, \quad (1)$$

where $\Delta I = (I_{irrad.}-I_{nonirrad.})$ (A) – the measured increment of the reverse dark current after irradiation of the detector normalized to temperature of +20˚C, $\alpha_I = (5\pm0.5)\times10^{-17}$ (A/cm) – current constant radiation damage of silicon for neutrons with energy 1 MeV, F (cm^{-2}) – equivalent fluence of fast neutrons with energy 1 MeV, V=d×S (cm^3) – the volume of the detector at the full depletion voltage. The experimental results of measurements of fast neutron fluence with silicon detectors are obtained on the pulsed fast neutrons reactor (IBR-2, channel #3) and on the experimental facility QUINTA JINR, Dubna.

MECHANISM OF RADIATION DAMAGES BY FAST NEUTRONS OF SILICON (SI-DETECTORS)

Fast neutrons with energy of E_n>100 keV are create in volume of silicon radiation damages in the form of violations of a crystal lattice (knocking-out by a neutron of primary atom from lattice site and then created a cascade of defects already beaten out atoms).

Reverse thermogeneration current of the detector grows linearly [1] with increasing fast neutron fluence (see Eq. 1).

The physical meaning of the constant α_I are following: when irradiated silicon detector volume 1cm^3 neutrons with an energy of 1 MeV and a fluence value of 1 n/cm^2 current of the detector is increased due to radiation damage to 5×10^{-17} A at +20˚.

RADIATION DAMAGE OF SILICON DETECTORS UNDER IRRADIATION WITH FAST NEUTRONS (E_N> 100 KEV)

What Happens in Irradiated Silicon

Knocking-out of atom of Si from a crystalline grid with formation of vacancy (V) and interstitial atom Si (I).

V and I to form - electrically active deep centers (VV, VO, VP, IC, I VP, etc.).

Effects of Deep Centres (see Fig. 1)

- Thermal generation / recombination of carriers in volume leads to an increase in reverse (dark) current of the detector, leading to increased noise and power dissipation on the detector.
- Capture (e-h)-pair reduces the primary ionizing charge collection efficiency and, consequently, to reduce the signal from the ionizing particles.
- Compensation impurity results in a change of volume resistivity values of the detector and to change the operating voltage (voltage of full depletion of the detector), respectively.

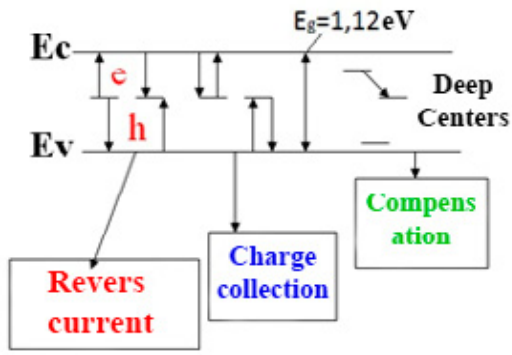

Figure 1: Effects of deep centers.

Fig. 2 shows function of defect formation of D(E) in MeV×mb, (Ougouag) and the function NIEL-FN-522 in keV×cm^2/g, (van Ginneken) [2].

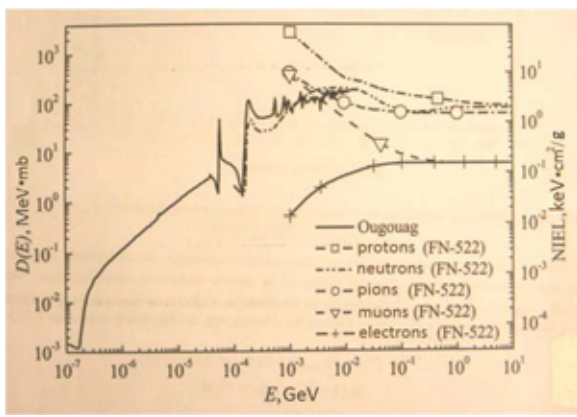

Figure 2: Function of defect formation of D(E) and the function NIEL-FN-522.

ISBN 978-3-95450-170-0

Table 1. Energy of offset of atom of Ed and minimum energy E_0^{min} of electrons and neutrons (protons) necessary for creation of defect of offset.

Semiconductor materials	Displaceable atom	Ed, eV	E_0^{min},keV	
			e	n (p)
Ge	Ge	12-20	320-530	0,17-0,29
Si	Si	11-22	115-330	0,18
GaAs	Ga	9,0	230	0,13
	As	9,4	260	0,14
CdTe	Cd	5,6	235	0,13
	Te	7,8	340	0,18
$Cd_{0,8}Zn_{0,2}Te$	Cd	5,6	235	0,13
	Te	7,8	340	0,18
C (diamond)	C	80	530	0,29

WHY IS USEFUL SI-DETECTORS NOT FOR ITS INTENDED PURPOSE (MEASURING OF ENERGY IONIZING PARTICLES), AND FOR MEASUREMENT FAST NEUTRON FLUENCE IN DC MEASUREMENT MODE OF RADIATION DEFECTS

Pin-diode structure with full depletion has strictly fixed sensitive volume (with an electric field) – space charge region (SCR).

Value of volume of the space charge region is determined by the thickness of the detector and area (p-n)-junction.

Thickness detector (crystal) measured with high accuracy (2%), and the square of transition is known from topology of detector with micron accuracy.

Modern technology of planar Si-detectors allows you to receive extremely low reverse current, defined the charge carrier lifetime in detector's volume (surface leakage to neglect).

Increment the reverse current of detector by fast neutron irradiation will be determined only by radiation defects in sensitive volume of the detector (SCR), which is known with high accuracy.

Si-detector as a detector for DC measurement, caused by radiation defects (without preamplifier, see Fig. 3).

METHOD OF MEASUREMENT OF THE EQUIVALENT 1 MEV FAST NEUTRON FLUENCE USING SI-DETECTORS

- Measurement of the thickness of detectors, visual inspection.
- Before irradiation screening detectors with good parameters to measure IV and CV characteristics of the detectors ($U_{bd}>2\times U_{fd}$; $I_d=a\times U_d^{1/2}$, i.e. there is no surface currents).
- Packaging, labels, entry into the database.
- The location and fixation detectors in specified positions on the physical installation and irradiation with astronomical time recording the start and end of irradiation.
- Removal of detectors after irradiation and storage in a freezer at t = –15˚.
- Measurement of IV and CV after irradiation, detectors put into storage in the freezer.
- Correction of the measured currents to t = +20˚.
- Calculation of the value of the equivalent 1 MeV neutron fluence by Eq. 1, tabulation and graphing.

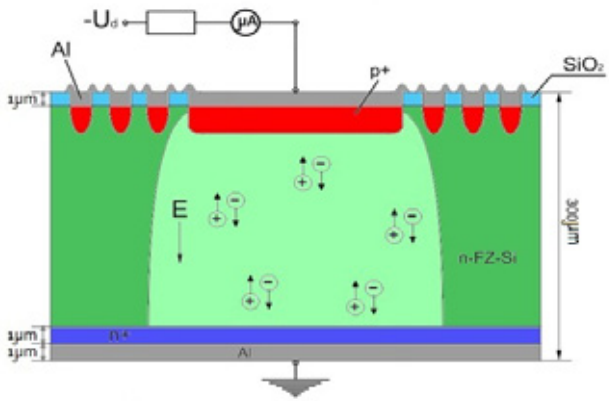

Figure 3: Si-detector without preamplifier.

Figure 4 shows the experimental IV characteristics for the detector before- and after- irradiation by fast neutrons. From the measured IV characteristics (+20˚) obtained the value of the equivalent fluence of 1 MeV neutrons equal to $\Phi = 2{,}86\times10^{10}$cm^{-2}.

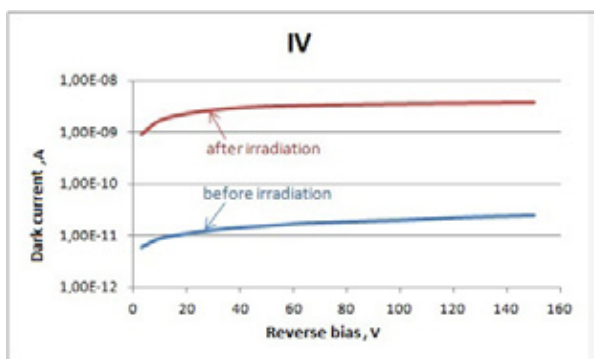

Figure 4: IV characteristic of the detector active area 13 mm^2 and a thickness of 300 μm before- and after-irradiation by fast neutron on QUINTA (as an example).

ISBN 978-3-95450-170-0

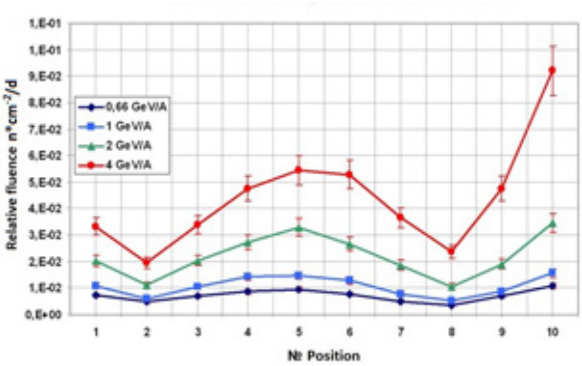

Figure 5: Corrected to 1 MeV neutron fluence (1 deuteron) on the surface of the "QUINTA" for different Ed.

CONCLUSION

- Experiments show that the value of radiation damage by fast neutron Si-detectors can measure equivalent fluence 1 MeV neutron for the unknown spectrum.
- Linear dependence of volume current of detector from fluence fast neutron allows you to measure fluence in the range from 10^8 cm^{-2} to 10^{16} cm^{-2}, the sensitivity of the method depends on the volume of the detector (the higher volume, the higher sensitivity).
- This way of measuring the fluence allows you to get the experimental result within 2-3 hours after extraction of detectors out of zone irradiation.
- Accuracy of method defined by accuracy current constant damages $\alpha_I=5\times10^{-17}\pm10\%$ ($A\times cm^{-1}$), at 20˚.
- To improve the accuracy of the measurement is necessary for calibration of detectors on the mono energy neutrons.

REFERENCES

[1] I.A.Golutvin et al., "Radiation hardness of silicon detectors for collider experiments", preprint E14-95-97, Dubna (1995).

[2] Van Ginneken A. Non ionizing energy deposition in silicon for radiation damage studies: Fermi Nat. Accelerator Lab. Report FN-522, (1989).

ISBN 978-3-95450-170-0

RESULTS OF LIA-2 OPERATION

P. Logachev, A. Akimov, P. Bak, M. Batazova, A. Batrakov, D. Bolkhovityanov, A. Eliseev, G.Fatkin, A. Korepanov, Ya. Kulenko, G. Kuznetsov, A. Pachkov, A. Panov, A. Starostenko, D. Starostenko, BINP SB RAS, Novosibirsk, Russia
A. Akhmetov, S. Hrenkov, P. Kolesnikov, E. Kovalev, O. Nikitin, D. Smirnov, RFNC-VNIITF, Snezhinsk, Russia

Abstract

Recent results of LIA-2 operation are presented. High quality of intense electron beam has been achived in design intervals of energy and current. All key elements of accelerator based on domestic technology successfully passed through long term operational tests.

INTRODUCTION

Linear induction accelerators are widely used now for x-ray flash radiography of high optical density objects [1]. This particular application of linear induction accelerators is very exigent to high current electron beam quality. The value of electron beam emittance determines the minimum electron beam spot size on the target, and thus the space resolution of this method. The first experimental results of LIA-2 operation at BINP were presented three yeas ago [2]. Now this accelerator is successfully used for X-ray flash radiography in RFNC VNIITF [3]. High quality electron beam produced by LIA-2 together with proved reliability of new technical solutions [4], [5], [6] make a good base for full scale 20 MeV radiographic LIA project.

FEATURES OF LIA-2 OPERATION IN RADIOGRAPHIC REGIME

The radiographic regime of LIA-2 operation restricts unfortunately the maximum electron beam energy and current. This phenomenon connected with X-ray conversion target explosion and ballistic penetration of small tantalum drops into accelerating bit-slice HV insulator and LIA-2 diode. This leads to significant breakdown strength reduction both in accelerating tube and diode (see Fig. 2). Thus reliable LIA-2 operation with X-ray conversion target explosion can be held up to 1.6 MeV and 1.5 kA of electron beam energy and current. The maximum energy and current for reliable operation without target explosion were obtained at the level of 2 MeV and 2 kA. It corresponds to design values. X-ray conversion target is placed at 3.9 m from the cathode. Electron beam energy deposition in 0.5 mm thick tantalum target for 1.6 MeV, 1.5 kA, 200 ns can be calculated as 230 J (1 MeV of energy loss per electron). It corresponds to 5000 K of melted target part on Fig.1 and about 1 bar of saturated vapor pressure of tantalum. There is a maximum size of hole in the target for fixed beam energy, current and pulse duration (in the case of increasing of the beam diameter on the target, the hole does not appear). For this particular case the maximum diameter of the hole is equal to 6 mm (see Fig. 1 and 4).

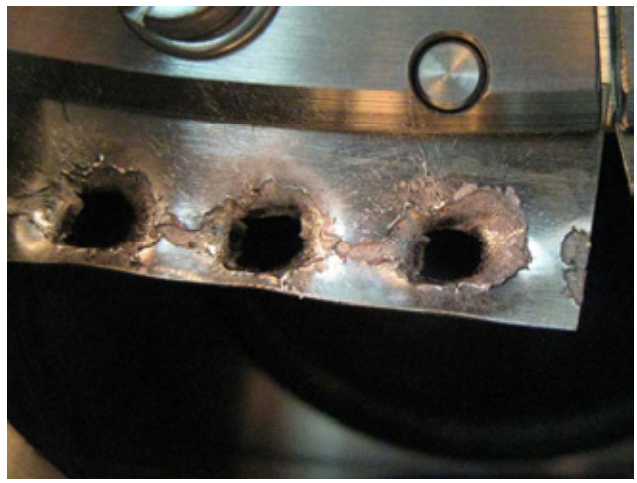

Figure 1: Maximum hole diameter in 0.5 mm thick tantalum target for 1.6 MeV, 1.5 kA , 200 ns electron beam.

In the case of the best focusing of electron beam on the target the minimum hole diameter is 1 mm (see Fig. 4) and peak tantalum temperature is about 200000 K. This is target explosion.

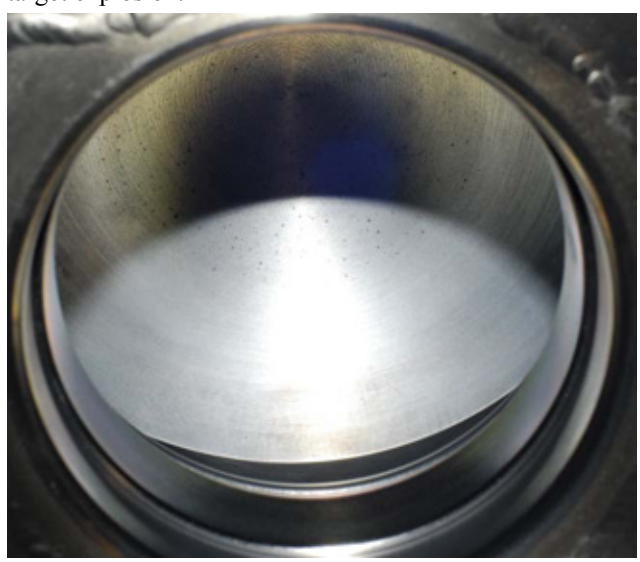

Figure 2: Damage of the central part of LIA-2 cathode by tantalum drops from the target. View on the cathode through the anode aperture.

The damage of the cathode central part due to target explosion (see Fig. 2) leads to emission degradation from

ISBN 978-3-95450-170-0

the cathode centre and thus to significant changes of diode optics.

This effect increases the beam spot size on the target and brings us to change the cathode after about 3000 radiographic pulses.

ELECTRON BEAM SIZE MEASUREMENT ON THE TARGET

In the case of Gaussian transverse distribution of power dissipation in the target

$$\xi = \xi_0 e^{-\frac{r^2}{2\sigma_r^2}} \qquad (1)$$

(here σ_r is electron beam transverse sigma on the target, ξ – surface density of power dissipation in the target) one can get the total energy deposition Q_0 per pulse:

$$Q_0 = 2\pi\sigma_r^2\xi_0 = \text{const} \qquad (2).$$

For LIA-2 radiographic operation case (1,6 MeV, 1,5 kA, 200 ns, 0,5 mm Ta target) Q_0=230 J. Let us assume that power density on the border of solid metal and hole in the target made by electron beam keeps constant upon electron beam radius on the target. This assumption is based on the dominance of local conditions in the process of metal melting and evaporation. The reality is more complicated. Power deposition in the target is not uniform also in longitudinal direction. It happens due to significant initial angle of beam divergence after focus plane and due to multiple scattering in the target, so the tantalum vapor pressure on the front side of the target is higher then one on the back side. It leads to appearance of big average force in the direction of electron beam propagation. This force increases the diameter of the hole in the target in comparison with the case of uniform longitudinal beam power deposition in the target. This effect is seen clearly on the holes of the target, holes borders are turned out in the direction of electron beam propagation. So the suggested model provides an upper estimation of electron beam transverse size on the target.

$$\xi_e = \xi_0 e^{-\frac{r_e^2}{2\sigma_r^2}} = const \qquad (3),$$

where ξ_e - edge value of surface power density on the target, r_e . is the target hole radius.

Simple combination of equations (2) and (3) shows that there is a maximum r_e for fixed values of Q_0 and ξ_e. This r_e corresponds to the maximum possible hole diameter for fixed value of Q_0. Thus ξ_e can be derived from maximum $r_{e\,max}$ and Q_0:

$$\xi_e = \frac{Q_0}{\pi r_{e\,max}^2 e} \qquad (4),$$

where e=2.718282…

Combining equations (2) and (3) one can obtain:

$$\frac{\pi r_e^2 \xi_e}{Q_0} = \frac{r_e^2}{2\sigma_r^2} e^{-\frac{r_e^2}{2\sigma_r^2}} \qquad (5).$$

Solving nonlinear equation (5) one can get transverse electron beam size σ_r as a function of target hole diameter ($2r_e$). Electron beam radius (FWHM/2) can be determined as $r_b = \sigma_r\sqrt{2\ln 2}$.

Fig. 3 represents r_b as a function of target hole diameter for different values of maximum target hole diameter.

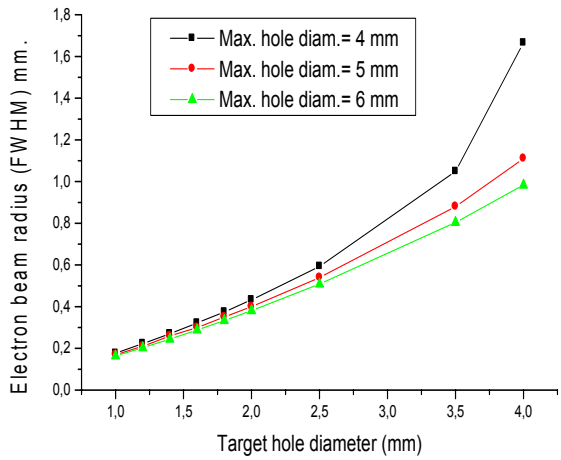

Figure 3: The dependences of electron beam radius (FWHM) upon the target hole diameter for different values of maximum target hole diameter..

In the range of target hole diameters between 1 and 1,5 mm. the solution of equation (5) is not very sensitive to the maximum target hole diameter. Fig. 4 shows minimum (1 mm) and maximum (6 mm) target hole diameters for 1.6 MeV, 1.5 kA, 200 ns LIA-2 electron beam and 0.5 mm thick tantalum target.

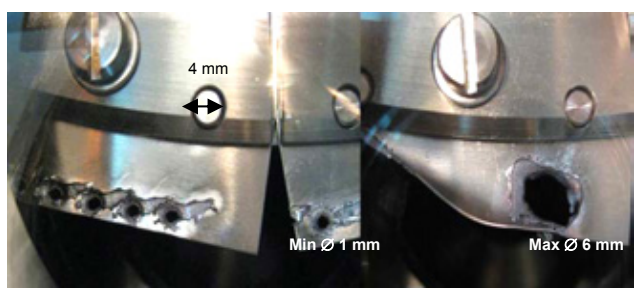

Figure 4: Minimum (1 mm) and maximum (6 mm) target hole diameters for 1.6 MeV, 1.5 kA, 200 ns LIA-2 electron beam and 0.5 mm thick tantalum target.

ISBN 978-3-95450-170-0

Finally, using Fig. 3, one can get transverse electron beam radius (FWHM) 0.17 mm for 1 mm target hole diameter.

BEAM EMMITTANCE ESTIMATION

The beam emittance estimation can be performed using the electron beam convergent angle just before the target. Electron beam structure for LIA-2 was calculated precisely by UltraSAM code developed in BINP [7]. The result is presented on Fig. 5 and 6.

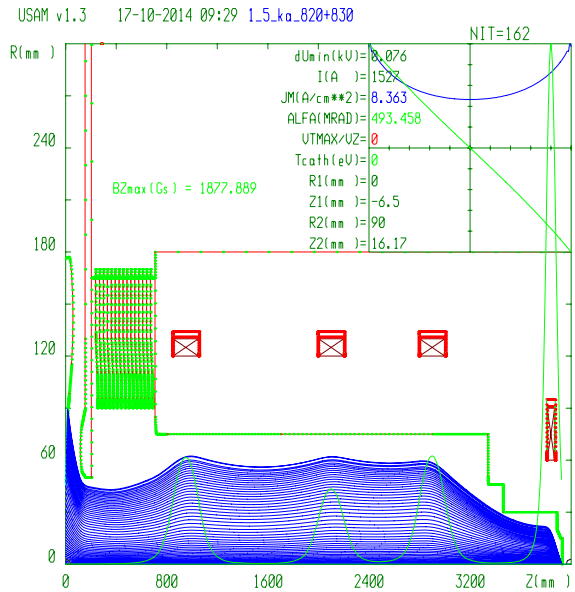

Figure 5: Electron beam envelope in LIA-2 for 1.6 MeV, 1,5 kA from the cathode to the target. UltraSAM simulation.

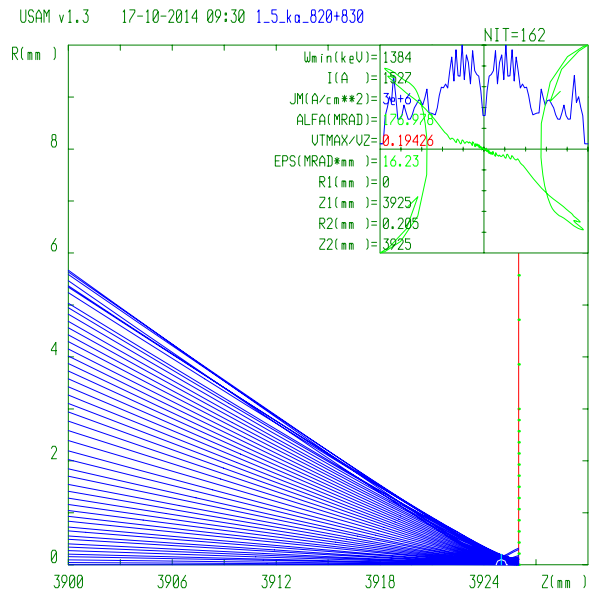

Figure 6: Electron beam envelope near the target for 1.6 MeV, 1,5 kA. UltraSAM simulation.

For this particular case the beam convergent angle on the target is 219 mrad, thus LIA-2 normalized beam emittance is less than 117 π mm•mrad.

ACKNOWLEDGMENTS

This work is supported by State corporation “Rosatom” and Ministry of education and science of RF.

REFERENCES

[1] K. Takayama, R. J. Briggs (editors) Iduction Accelerators, Springer, 2011, ISSN 1611-1052.

[2] P. V. Logachev et al., “Performance of 2 MEV, 2 Ka, 200 ns linear induction accelerator with ultra low beam emittance for X_ray flash radiography,” in *Proc. of 2nd Int. Particle Accelerator Conference (IPAC’2011)* (San Sebastian, Spain, 2011).

[3] A. Akhmetov, S. Khrenkov, P. Kolesnikov, E. Kovalev, O. Nikitin, D. Smirnov,LIA-2 and BIM accelerators as part of radiographic complex at RFNC-VNIITF. RuPAC-2014, October 6-11, 2014, Obninsk, Russian Federation.

[4] A. V. Akimov, V. E. Akimov, P. A. Bak, et al., “A pulsepower supply of the linear induction accelerator,”Instrum. Exp. Tech. **55** (2), 218 (2012).

[5] P. V. Logachev, G. I. Kuznetsov, A. A. Korepanov, et al., LIA_2 linear induction accdelerator, Instrum. Exp. Tech. **56** (6), 672 (2013).

[6] A. V. Akimov*a*, P. V. Logachov*a*, A. A. Korepanov*a*, F. V. Averin,O. V. Savinova*b*, G. L. Mamaev*c*, S. L. Mamaev , Magnetic Cores Made of an Amorphous Tape for the Induction Accelerator. Instruments and Experimental Techniques, 2012, Vol. 55, No. 2, pp. 268–273. © Pleiades Publishing, Ltd., 2012.

[7] A. Ivanov, M. Tiunov, ULTRASAM - 2D Code for Simulation of Electron Guns with Ultra High precision Proc. 8th European Particle Accelerator Conference (EPAC 2002), Paris, France, 3-7 June 2002, p.1634-1636.

ISBN 978-3-95450-170-0

EXPERIENCE IN RESEARCH, DEVELOPMENT, CONSTRUCTION AND COMMISSIONING OF NORMALLY CONDUCTING ACCELERATING STRUCTURES

L.V. Kravchuk, V.V. Paramonov *, INR of the RAS, Moscow, 117312, Russia

Abstract

The experience and results of research, development, construction and start of normally conducting accelerating structures for high intensity hadron linear accelerators at medium and high energii is summarized. Created methods and obtained results provided construction and start of operation of accelerating system in INR H- linac with designed energy 600 MeV. The research results allow generalize the properties of high energy structures and develop methods and criteria for improvements. Basing on research results, the high energy accelerating structure, which surpasses analogues in the total list of parameters, is proposed and tested.

INTRODUCTION

Instead of progress in development of superconducting structures for high energies, the normal conducting structures have the high value for high energy intense hadron linacs. The report presents briefly the main steps and INR results in this activity.

DAW CONSTRUCTION FOR INR LINAC

INR activity in accelerating structures originates from construction of accelerating system for high energy part of INR linac, Fig. 1. This system consists of 27 four-tanks cavities, operating at $f_a = 991$ MHz. DAW tanks contain from $N_m = 18$ to $N_m = 27$ DAW modules, see Fig. 3a. The total number of DAW modules in the system is ~ 2400 and the system length is $\approx 300m$.

DAW structure, invented by V.G. Andreev, [1], for INR linac was developed and tested in RTI AS USSR and the framework technology was established. The first three steps – hot sludge to $\approx 500mm$ blanks from $170mm$ OFC rods, pre-forming with stamping and draft pre-turn were performed in industry under INR and RTI monitoring. Another steps of construction, starting from accurate processing and continuing through RF tuning, brazing of DAW tanks and finishing with system commissioning, were performed by INR in-house. For mass production, all steps in construction, such as reasonable and motivated tolerances for DAW modules treatment, fast and precise RF tuning of DAW tanks, HOM displacement and so on, were optimized and improved. In the DAW construction there were no DAW modules lost due to non-compliance.

Figure 1: DAW accelerating structure in the INR linac.

Individual RF tuning for frequencies of operating f_a and coupling f_c modes for DAW modules in not required, due to coupling coefficient $k_c \sim 40\%$ of the structure. DAW tanks were tuned in assembly of N_m modules. Coupling mode can not be exited in DAW tanks and to close the stop band non direct methods for stop band width $\delta f = f_c - f_a$ definition are required. Due to large k_c, DAW dispersion curve in the f_a vicinity is essentially not linear and linear approximation from nearest modes $\delta f = f_u^{(1)} + f_d^{(1)} - 2f_a$, tolerable for structures with $k_c \sim 5\%$, Side Coupled Structure (SCS) and Annular Coupled Structure (ACS), results in $\delta f \sim 1MHz$. High order approximations for δf definition were developed for DAW tanks tuning, [2], resulting in $\delta f \leq 100kHz$. Basing on DAW particularities, the optimized procedure for tanks tuning was developed, [3], minimizing number of tuning operations.

The High Order Modes (HOM) with field variations on

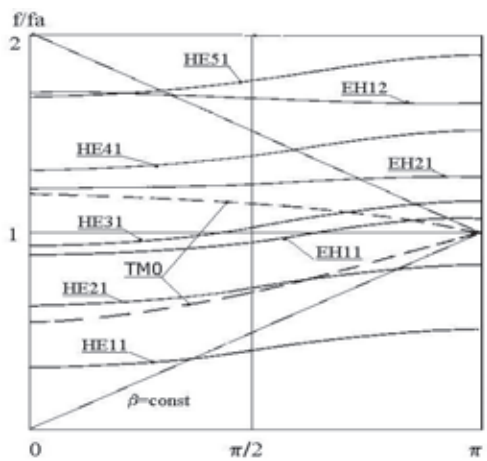

Figure 2: HOM dispersion diagram for the DAW, $\beta = 0.43$.

* paramono@inr.ru

ISBN 978-3-95450-170-0

azimuth in f_a nearest vicinity for DAW were found in experiments and later classified in simulations [4], [5]. Calculated in 2D approximation dispersion diagram for DAW, $\beta = 0.43$ is shown in Fig. 2. All time in f_a vicinity exit EH_{11} and HE_{31} modes. Different methods for HOM displacement were considered [6], resulting in T-slots addition in disks, Fig. 3a. T-slots are selective resonant elements,

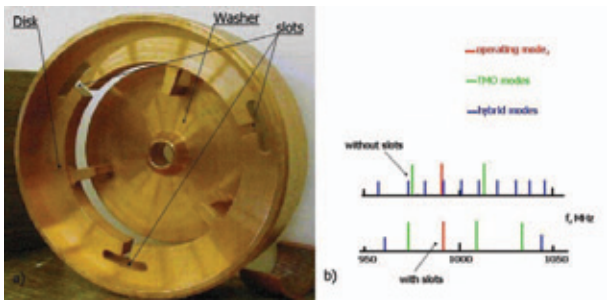

Figure 3: DAW module with T-slots (a) and modes spectrum in f_a vicinity without and with T-slots, (b).

which are tuned close to the operating frequency f_a, have no coupling with operating mode, weak coupling with another TM_0 modes, and a strong coupling with HOM. The result of T-slots interaction with HOMs in DAW is shown in Fig. 3b.

The beam break up in multi-sectional ion linac has very high current threshold, [7], and cumulative emmitance growth due to beam interaction with HOMs for the designed current 50 mA is less than the same effect due to focusing elements misalignment, [8].

The distribution of electric field in large DAW and DTL cavities were performed by bead pull technique. To reduce random errors in measurements for large multi gap cavities, the size of spherical bead should be reasonably large. If bead diameter is comparable with accelerating gap length, the classical Slatter formula [9], derived for uniform infinite field, becomes a first approximation. The study of systematic error for bead pull measurements has been performed, [10], and bead diameters were chosen to limit systematic error to $\leq 0.2\%$ for measurements in DTL cavities and to $\leq 0.1\%$ in DAW cavities.

The total set of 110 DAW tanks was constructed and tuned to operating frequency with average, over set, value of standard deviation for E_z distribution $\approx 0.65\%$, [11]. All 27 DAW cavities four DAW tanks and three coupling bridges also were tuned for operating frequency and deviation of average E_z value between tanks $\leq 0.5\%$, [12]. Cavities were conditioned for operating level of RF power. The methods to pass fast the multipacktor discharge areas were developed in mass commissioning. The first beam acceleration was obtained in 1991.

METHODOLOGICAL DEVELOPMENTS

In the development and construction of accelerating structures the adequate software serves as cost reducing tool of numerical experiments. Maintenance of DAW construction stimulated development, in collaboration with IHEP and JINR, the set of very fast and precise finite elements multi tasks software, [13], for simulations in 2D approximation. To maintain structure commissioning, the software for multipacting discharge study has been developed, [14]. For complete analysis of accelerating structures, operating with heavy RF power dissipation, the closed chain for simulations of RF parameters, dissipated RF power in the structure surface, flow and heat exchange simulation in cooling channels, thermal stress and deformations in the structure body and resulting changes in RF parameters, was developed [15] basing on ANSYS software. Very powerful tools for structures development are managing add-ins over software for data libraries storage, [16].

For generalization of physical processes description in

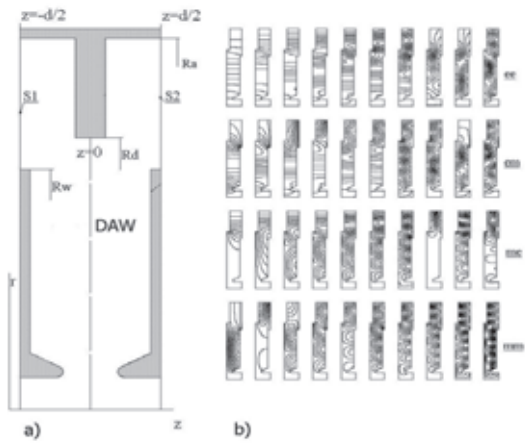

Figure 4: The geometry of one DAW period (a) and electric field distributions for 0 and π modes, simulated in different combinations of boundary conditions **ee, mm, em me** (b).

different structures, the method of field description in periodical structures was developed, [17] and realized in an additional code. Let us consider just one period of the structure, for example, DAW in Fig. 4a. Using powerful modern software, let us simulate and store for sets of field distributions and frequencies in different combinations of boundary conditions (electric **e** and magnetic **m**) for 0 and π modes **ee, mm** and **em, me**, respectively, Fig. 4b. In structures with mirror symmetry just one half of the period is sufficient for such simulations. Considering the travelling wave with the phase advance θ at the period d, let us expand the real and the imaginary components of travelling field in the sets over stored basis of 0 and π modes with unknown coefficients c_n in such expansion, $\Re e\vec{E} = \sum_n^{Nee} c_n^{ee}\vec{E}_n^{ee} + \sum_n^{Nem} c_n^{em}\vec{E}_n^{em}$, $\Im m\vec{E} = \sum_n^{Nme} c_n^{me}\vec{E}_n^{me} + \sum_n^{Nmm} c_n^{mm}\vec{E}_n^{mm}$. Applying Floquet boundary conditions at the period ends, $z = 0, z = d$ and using variational approach we obtain the symmetrical

ISBN 978-3-95450-170-0

eigenvalue problem

$$A(\theta)C - k^2BC = 0, \quad (1)$$

where $A(\theta), B$ are square matrices with elements representieng interaction of fields of basis elements, [17]. Specifying θ and solving problem (1) we define both frequency and field distribution for any $0 \leq \theta \leq \pi$. The equation (1) is the dispersion equation of the structure under consideration. The detail view of matrices $A(\theta)$ and B in (1) depends on the symmetry of the considered structure. All high energy structures, schematically shown in Fig. 5 have operating π mode and mirror symmetry plane in the middle of accelerating gap. Instead of quite different geometry and technical solutions, all these structures have the common dispersion equation (1), [18]. Even restricted with four modes, this

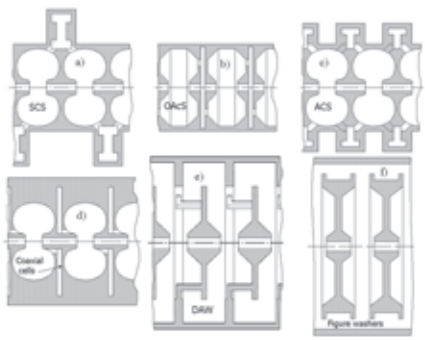

Figure 5: High energy compensated accelerating structures

equation describes well operating dispersion curve for all compensated high energy structures, including non symmetrical DAW curve. Considering just nearest vicinity of operating point f_a and restricting just with two interacting modes accelerating $\vec{E}_a$ and coupling $\vec{E}_c$, we obtain the local dispersion equation,

$$(f_a^2 - f^2)(f_c^2 - f^2) - (\frac{f_a f_c k_c sin\xi}{2})^2 = 0, \xi = \pi - \theta \quad (2)$$

which is valid for all compensated structures, and derive the expression for group velocity β_g (or coupling coefficient k_c).

$$\beta_g = |\frac{\pi\beta \int_{V_1}(\epsilon_0 \vec{E}_a \vec{E}_c - \mu_0 \vec{H}_a \vec{H}_c)dV}{4W_0}| = \frac{\beta\pi k_c}{4}, \quad (3)$$

The behaviour for mode frequencies and field distributions in the vicinity of operating mode were investigated in details illustrating both particularities of structures and common relationships too, [19]. The changes in field distributions and another parameters of these modes during structure tuning becomes clearly seen. Basing on the developed approach the coupling mode excitation due to beam loading [20], transient and tuning errors were studied, resulting in some deviations, which are more sensible physically, from the results, obtained by coupled circuits model [21]. Possibility of multipactoring discharge in coupling cells for slot coupled SCS, ACS and OAcS due to coupling mode excitation was studied [22] and methods for k_c increasing with the minimal Z_e drop by slot shape optimization were formulated [23]. For structures operating with heavy RF power dissipation criteria for thermo-mechanical stability were summarized, [24].

These developments are valid for a wide family of accelerating structures and provide complete set of approaches, recommendations and limitations in the research, development and improvement of accelerating structures. Joint with understanding of practical problems, it provides the reliable base for another developments.

COLLABORATING ACTIVITY

The results and experience of INR activity in investigation, construction and commissioning was implemented during construction and commissioning of warm part of the SNS linac, [25]. The total set of obtained results, developed methods and approaches was used in the development of physical design of ACS structure for J-PARC linac. Invented in USSR, ACS was strongly improved in KEK during JHP program under leadership of Y. Yamazaki for operating frequency $f_a = 1296MHz$.

For J-PARC operating frequency $f_a = 972.0MHz$ previous JHP ACS has been deeply reconsidered. The total set of developed methods and approaches has been applied for cells optimization and mutual fitting, coupling slots arrangement and cooling study in order do not lose, only improve, achieved performances and to provide RF efficient, compact, balanced cost effective design ensuring reliable stable operation in linac, [26, 27]. The optimized ACS cells for J-PARC linac are shown in Fig. 6. Later some improvements were introduced in cells design for cost reduction in mass production, [28] and total 21 ACS cavities, consisting each of two ACS tanks and one bridge cavity, were constructed. With the robust design and high quality of manufacturing, all ACS cavities were conditioned for operating parameters relatively fast, [29], and stable operate now in J-PARC linac.

Figure 6: ACS half cells for J-PARC linac

CDS DEVELOPMENT

The Cut Disk Structure (CDS) initially was proposed for electron linac, $\beta = 1$, [24],[30]. Topologically CDS looks,

ISBN 978-3-95450-170-0

Fig. 7, very similar to well known slot coupled OAcS, see Fig. 5, but realizes quite another concept. The shape of accelerating CDS cells is optimized for the maximal Z_e value, and coupling cell is formed so, that magnetic field H_c has no own space in coupling cell and is extruded into accelerating cell, with necessity resulting in large β_g value, according (3), without associated, for coupled slot structures, Z_e drop.

CDS concept was proven in the cold model measurements,

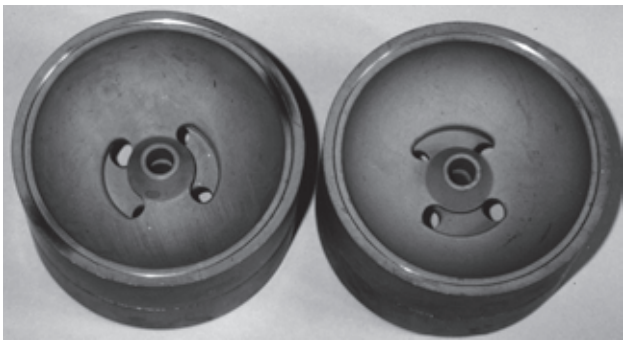

Figure 7: CDS cells for cold model test.

showing calculated $k_c = 0.22$ and Z_e/Q values, [31]. For further developments we adopt four windows CDS option with windows opening $\sim 45^o$ in order to improve vacuum conductivity, increase Z_e value, further reduce possibility of multipactor discharge in coupling cells. Basing on CDS, the booster cavity to increase electrons energy in the Photo Injector Test Facility (PITZ), DESY, Zheuthen, was developed in INR, [31] to operate with $\beta = 1$, $f_a = 1300MHz$, designed accelerating gradient up to $14MeV/m$ and dissipation heat load up to $17kW/m$, Fig. 7. In cavity development and construction all set of our methods and approaches was used. For higher structure reliability for four windows CDS option the cooling circuit design without brazed water-vacuum joints was developed. The booster cavity, Fig. 8, was constructed in DESY, tuned, conditioned [32] and now is in operation at the PITZ beam line, [33].

With operating PITZ booster cavity CDS operational reliability is proven.

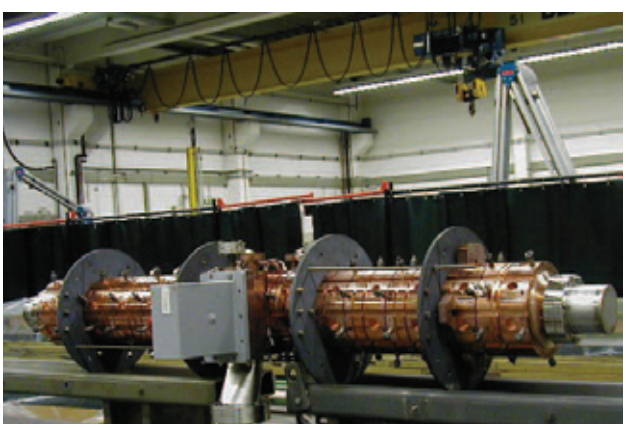

Figure 8: CDS booster cavity for PITZ

Due to design idea, transverse CDS dimensions are defined by accelerating cell radius $R_c \sim 0.37\lambda$. Comparison of different structures in transverse dimensions is shown in Fig. 8a for the same operating frequency f_a and same β. Due to small R_c, CDS has no HOM problem. The nearest HOM modes are placed at frequencies $\sim 1.5 f_a$. Also with smaller dimensions, CDS is cheaper in the construction, starting from smaller amount of row OFC material and continuing with relaxed requirements to treatment with modern NC machines. Expected CDS parameters were estimated and for lower β value, assuming proton acceleration from energy $\sim 100MeV$, [35]. Assuming the application in the intense proton linac with the heat loading $\sim 15kW/m$, resulting in the necessity of cooling channels in the walls between accelerating and coupling cells and the total thick web, the calculated Z_e values are shown in Fig. 8b. In for windows CDS option with slots opening $\sim 45^o$ the quite sufficient value $k_c \sim 0.15$ obeys naturally. The big CDS coupling windows, Fig. 8a replace the part of the accelerating cell surface with the high RF loss density. It explains higher Z_e value for high energies. For lower $\beta \leq 0.55$ for the present CDS design the original disadvantage the thick web determine Z_e reduction, as compared to another structures in Fig. 8a. Results of simulations show, if accelerating structure is applied for for proton acceleration from $100MeV$ to $\geq 400MeV$ the present CDS in total overlaps another structures in RF efficiency. Also, as recent estimations show, that with more complicated cell shape, but realistic for modern NC tools, we can improve CDS efficiency for low β, eliminating this disadvantage.

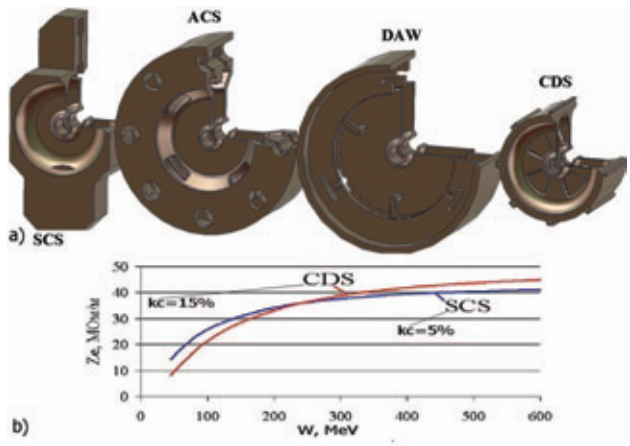

Figure 9: Structures comparison in dimensions (a) and efficiency (b).

The small transverse dimensions allow CDS application for relatively low operating frequency $f_a = 352MHz$, [36]. For such applications CDS efficiency and field stability can be decisive arguments. The summarized comparison of CDS parameters in values and in relative ranking, with another structures, is given in the Table 1.

As one can see, in the total set of parameters, both physical

ISBN 978-3-95450-170-0

Table 1: Thermo-mechanical effects

Structure	SCS	ACS	DAW	CDS
$Z_e/Z_{eSCS}, \%$	100	~ 99	~ 95	$85-107$
$k_c, \%$	~ 5	~ 5	~ 45	~ 15
$P_h, kW/m$	~ 10	≤ 60	≤ 6	≤ 35
R_c/λ	0.7	0.7	0.7	0.37
Vacuum cond.	$2-4$	$2-4$	1	$2-4$
HOM, rank	2	3	4	1
RF tuning				
before braz.	indiv.	indiv.	total	total
after braz.	a/c	no/c	no/no	a/no
water-vac.	yes	yes	yes	no

and technological, CDS represents the balanced optimized option. This structure is promising candidate for applications in attractive normal conducting linacs.

SUMMARY

In the INR research activity in normal conducting accelerating structures the complete set of methods, approaches for investigation, development and construction of accelerating structures was developed. Results of this activity are realized in the constructed, tuned, commissioned and operating accelerating system of the INR hadron linac, are implemented in the design, construction and commissioning of similar linacs in foreign laboratories. Guiding this basements results, attractive proposal for different future application is generated, investigated and tested.

ACKNOWLEDGMENT

The authors warmly tank a lot of our colleagues in INR, MRTI, DESY, KEK, J-PARC, SNS for good collaborations in accelerating structures development and construction.

REFERENCES

[1] V.G. Andreev, Journal of Technical Physics, v. 41, n. 4, p. 788-795, 1971, (in Russian)

[2] L. Kravchuk, V. Paramonov et.al., IEEE Trans. on Nucl. Sci., NS-32, n.5, p. 2818-2820, 1985

[3] L. Kravchuk, G. Romanov, Preprint INR AS USSR, P-0334, Moscow, 1984 (in Russian).

[4] V. Paramonov, Journal of Technical Physics, v. 43, n. 5, p. 956, 1983, (in Russian)

[5] V. Andreev, L. Kravchuk, V. Paramonov et.al., NIM, A, v. 204, p. 285, 1983

[6] V. Andreev, L. Kravchuk, V. Paramonov et.al., IEEE Trans. on Nucl. Sci., NS-32, n.5, p. 3575, PAC 1985, 1985

[7] P. Ostroumov, L. Kravchuk, V. Paramonov et.al., Proc. Linac 1984, p. 392, 1984

[8] P. Ostroumov, L. Kravchuk, V. Paramonov et.al., IEEE Trans. on Nucl. Sci., NS-32, n.5, p. 2368, PAC 1985, 1985

[9] L. Maier, J. Slatter, Journal of Applied Physics, v. 23, n,1, p.68, 1952

[10] L. Kravchuk, P. Ostroumov, V. Paramonov et.al., Proc. Linac 1990, p. 120, 1990

[11] S. Esin, L. Kravchuk, V. Paramonov et.al., Proc. Linac 1988, p. 657, 1988

[12] S. Esin, L. Kravchuk, G. Romanov et.al., Proc. EPAC 1990, p. 506, 1990

[13] I. Gonin, V. Gorbul, V. Paramonov, Proc. EPAC 1990, p. 1249, 1990

[14] L. Kravchuk, G. Romanov, S. Tarasov, Proc. Linac 1993, p. 465, 1992

[15] S. Joshi, V. Paramonov, A. Skasyrskaya, Proc. Linac 2002, p. 216, 2002

[16] V. Paramonov, Proc. Linac 1996, p. 493, 1996

[17] V. Paramonov, I. Gonin, Proc. Linac 2000, p. 804, 2000

[18] V. Paramonov, Proc. Linac 2002, p. 410, 2002

[19] V. Paramonov, Proc. Linac 2000, p. 401, 2000

[20] V. Andreev, V. Paramonov, IEEE Trans. on Nucl. Sci., NS-32, n.3, p. 1702, PAC 1985, 1985

[21] E.A. Knapp et.al.,Rev. Sci. Instr., v. 38, n.11, p. 22,1967

[22] V. Paramonov, S. Tarasov, Proc. Linac 1998, p. 971, 1998

[23] V. Paramonov, Proc. Linac 2008, p. 61, 2008

[24] V. Paramonv, Proc. of the 15-th RuPAC, Protvino, IHEP, v. 1, p. 156, 1996 (in Russian).

[25] S. Handerson, L. Kravchuk et.al., NIM,A, v. 763, p. 610-673, 2014

[26] V. Paramonov, KEK Report 2001-14A, KEK, 2001

[27] H. Ao, V. Paramonov, Y. Yamazaki et.al., Proc. Linac 2002, p. 234, 2002

[28] H. Ao, Y. Yamazaki, V. Paramonov et.al., Proc. Linac 2008, p. 915, 2008

[29] H. Ao et.al., Proc. Linac 2014, THPP089, 2014

[30] V. Paramonov. Proc. PAC1997, v.3, p.2959, 1997.

[31] V. Paramonov, L.V. Kravchuk, V.A. Puntus. Proc. Linac1998, p. 579, 1998.

[32] V. Paramonov, N. Brusova, Proc. Linac2004, p. 204, 2004.

[33] A. Naboka, V. Paramonov, F. Stephan et.al., Proc. Linac2010, p. 241, 2011

[34] M. Krasilnikov, F. Stephan, V. Paramonov et.al., Phys. Rev. ST Accel. Beams v. 15, n. 10, 100701, 2012

[35] V. Paramonov, Proc 22 RuPac2010 p. 65, 2010

[36] V. Paramonov, Proc. Linac2014, MOPP125, 2014

ISBN 978-3-95450-170-0

STATUS OF THE NUCLOTRON

A. Sidorin, N. Agapov, A. Alfeev, V. Andreev, V. Batin, O.Brovko, A. Butenko, D.E. Donets, E.D. Donets, E.E. Donets, A. Eliseev, A. Galimov, E. Gorbachev, A. Govorov, E. Ivanov, V. Karpinsky, H. Khodzhibagiyan, A. Kirichenko, V. Kobets, A. Kovalenko, O. Kozlov, K.Levterov, V. Mikhailov, V. Monchinsky, A.Nesterov, A. Philippov, S. Romanov, N. Shurkhno, G.Sedykh, I. Slepnev, V.Slepnev, A. Smirnov, G. Trubnikov, A. Tuzikov, B. Vasilishin, V. Volkov, JINR, Dubna, Moscow Region, Russia.

Abstract

Since last RuPAC five runs of the Nuclotron operation were performed. Diagnostic and control systems were improved. Commissioning of new quench detection system was completed. Deuteron beam was accelerated up to maximum design energy corresponding to 2 T of the dipole magnetic field. Stochastic cooling of coasting deuteron, coasting and bunched carbon beams was obtained. First run with new heavy ion source was performed. Results of these and other works are presented.

INTRODUCTION

The Nuclotron is used presently for fixed target experiments on extracted beams and experiments with internal target. The program includes experimental studies on relativistic nuclear physics, spin physics in few body nuclear systems (with polarized deuterons) and physics of flavours. At the same time, the Nuclotron beams are used for research in radiobiology and applied research.

Five Nuclotron runs (#46 ÷ #50) at total duration of about 4000 h were performed in the period from November 2012 till June 2014. About 70% of the runs were spending for experiments with accelerated beams (cooling down and preparation of the machine required about 25%). For more efficient usage of the beam time, during the run #49 the regime with two parallel users was realized routinely: experiment with internal target at the first plateau and beam extraction at the second one.

Improvement of the cryogenic complex performance, better cooling conditions of the magnetic system, modernization of quench detection system permitted gradual increase of the beam energy. As result during the run #48 (December 2013) the carbon beam was accelerated and extracted at maximum design energy corresponding to dipole magnetic field of 2 T.

Deuteron, lithium, carbon and argon beams were delivered for the experiments. Increase of the beam intensity and widening of the ion species are related with construction of three new ion sources: SPI (Source of Polarized Ions), LIS (Laser Ion Source), Krion-6T (ESIS type heavy ion source) [1]. New powerful laser was tested for the carbon beam generation during the run #48. For the first time Krion-6T was operated at the Nuclotron during the run #50.

Development of slow extraction system resulted in realization of acceptable quality of the extracted beam in the interval of the spill duration from 60 ms to 20 s.

In addition to the implementation of the current physics program the Nuclotron having the same magnetic rigidity as the future NICA collider [2] and based on the same type of the magnetic system is the best facility for testing of the collider equipment and operational regimes. Development works for NICA performed during recent Nuclotron runs include the testing of elements and prototypes for the MPD (Multy Purpose Detector which will be operated at the collider) using extracted deuteron beams; operational tests of the automatic control system based on the Tango platform, which has been chosen for the NICA facility; tests of diagnostic equipment for the Booster – small superconducting synchrotron constructing in the frames of the NICA project to improve the Nuclotron performance.

Simulation of the collider magnetic system operational conditions was performed at the Nuclotron during runs #45-47 (in years 2012-2013). This presumed test of the Nuclotron systems in the operational mode with long plateau of the magnetic field. In the run #45 the circulation of accelerated up to 3.5 GeV/u deuteron beam during 1000 seconds was demonstrated. During the runs #46 and #47 such a regime was used for test of stochastic cooling at the Nuclotron, which is an important phase of the NICA collider cooling system design.

In this report we are concentrated on the most important results of these works.

DEVELOPMENT OF THE ION SOURCES

The new LIS is based on commercially available Nd-YAG laser LPY 7864-2 providing output energy of 2.8 J at wave length of 1064 nm [3]. The new laser was investigated at test bench (Fig. 1) during outman 2013 and thereafter it was used at the Nuclotron run.

During the run the source and the LU-20 (linac using for injection into the Nuclotron) operation was optimized at acceleration of C^{5+} and C^{6+} ions. The current of C^{6+} beam reach to about 1.5 mA at the linac output. The pulse duration was of about 3 μs. Routinely the injector was operated in C^{5+} mode because of larger output beam current (up to 3 mA) and slightly longer the pulse duration - about 4 μs (the beam revolution period in the Nuclotron is about 8 s at injection energy). The carbon

ISBN 978-3-95450-170-0

beams were delivered to both the Nuclotron users and stochastic cooling experiments during about two weeks.

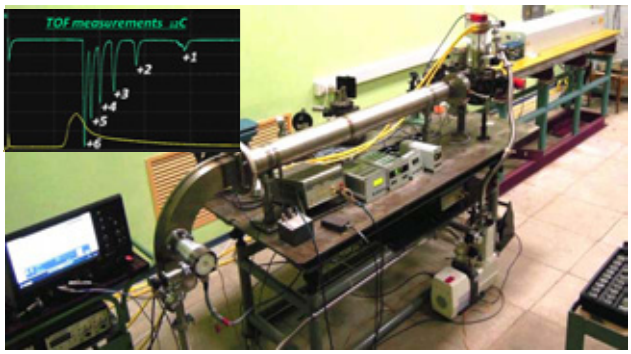

Figure 1: Nd-YAG laser at the test bench.

Krion-6T is a prototype of the heavy ion source which will be used for operation at new heavy ion linear accelerator – the HILac. Construction and assembly of Krion-6T were completed in spring 2013 and full-scale tests in reflex mode of operation had been started at a test bench. After reaching of 5.4 T of the solenoid magnetic field in a robust operation (the design value is 6 T) the $Au^{30+} \div Au^{32+}$ ion beams have been produced at intensity of about $6 \cdot 10^8$ particles per pulse. The required ionization time is 20 ms. The obtained parameters are close to the HILac requirements.

In difference with the heavy ion source used at the Nuclotron before the magnetic field and electron beam energy are sufficiently increased. Design of a few elements is changed also. Therefore, after investigations at the test bench, the source was optimized for production of ions with charge to mass ratio of $q/A \geq 1/3$ in order to provide complex test of all its systems at existing injection facility. In May 2014 the source was installed at high-voltage platform of the LU-20 fore-injector (Fig. 2).

Figure 2: Krion-6T at high-voltage platform of LU-20 fore-injector [3].

During about 250 h of operational time the source systems and linac were optimized for generation of different ion species. As result the Ar beams were accelerated and delivered for experiments.

NUCLOTRON TESTS STOCHASTIC COOLING FOR NICA

Application of the beam cooling methods (electron and stochastic) in the NICA collider rings has the purposes of beam accumulation using cooling-stacking procedure and luminosity preservation during experiments. During 2011-2013 the elements of the stochastic cooling chain for test at the Nuclotron were designed, constructed and installed at the ring. Main parameters of the system are the following: bandwidth 2-4 GHz, optimal beam kinetic energy 3.5 GeV/u, system (and notch filter) delay accuracy 1 ps, N_{ion}~1e9. This work performed in close collaboration with the Forschungszentrum Jülich (FZJ) is also important to FZJ for testing elements of the stochastic cooling system designed for the High-Energy Storage Ring (HESR, FAIR) [4]. In March 2013 (run #47) the effect of the longitudinal stochastic cooling using notch-filter method had been demonstrated at the Nuclotron for the first time (Fig.3). Experimentally obtained characteristic cooling time is in good agreement with simulation results. The beam cooling system includes ring-slot couplers as pick-up and kicker (designed at FZJ), unique optical notch-filter and a full remote-controlled automation of measurements and adjustments [5].

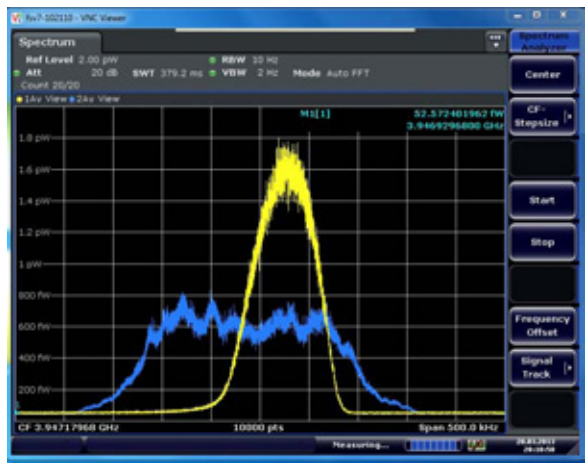

Figure 3: A longitudinal Schottky spectrum of the 3 GeV/u deuteron beam at 3500th harmonics of the revolution frequency, showing the initial spectrum (blue curve) and after 8 minutes of cooling (yellow curve). The beam intensity is 2×10^9 ions.

The experimental investigation of stochastic cooling was a complex test of machine performance. During the experiment, the cryogenic and magnetic systems, power supply, cycle control and diagnostic equipment were operated stably in a mode in which the circulation time of the accelerated beam at the flat-top of the magnetic field was gradually increased from a few tens of seconds up to eight minutes.

The safe operation of the magnetic system was guaranteed by a new quench-detection system commissioned during the runs #46-47. It permits a prompt

ISBN 978-3-95450-170-0

change in the number of detectors, uniform work with the group and individual detectors and implementation of the total reservation of the line controlling the energy evacuation system. The system provides monitoring of the status of all of its components, as well as signal-testing of external systems, and also indicates malfunctions [6].

The next step of the stochastic cooling experiments was dedicated to test of a bunched beam cooling (such a regime corresponds to luminosity preservation during collider experiment). Partial modernization of the Nuclotron RF accelerating system permitted to prolong the RF pulse duration up to about 25 s. Thereafter during the run #48 (December 2013) the stochastic cooling effect had been successfully demonstrated in both for coasting and bunched carbon beams (Fig.4) [7]. In the last case the bunching factor (ratio between peak and mean current) was about 5.

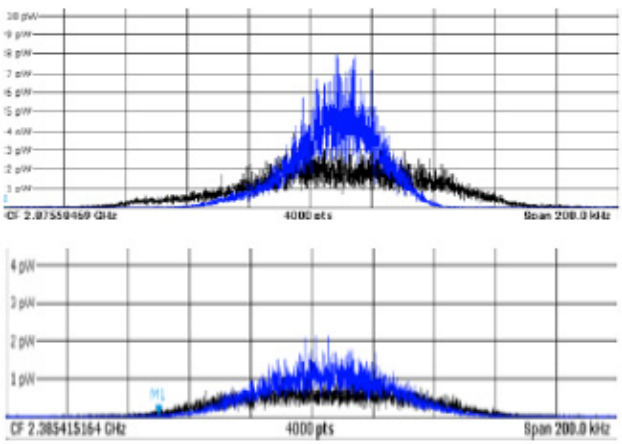

Figure 4: Experimental results of beam stochastic cooling of coasting $_{12}C^{6+}$ and bunched $_{12}C^{6+}$. Schottky beam spectra: black – initial beam, blue – cooled beam.
Upper: coasting beam, I~2e9 ions, E=2.5 Gev/u, $dP/P_{initial}$=0.15e-3, dP/P_{final}=0.07e-3, $\tau_{cool} \sim 27$ sec.
Below: bunched beam, I~2e9 ions, E=2.5 Gev/u, $dP/P_{initial}$=0.2e-3,dP/P_{final}=0.13e-3, $\tau_{cool} \sim 64$ sec.

CONTROL SYSTEM DEVELOPMENT

NICA facility will consists of two linacs, two synchrotrons, collider rings equipped with two detectors and a few beam transport lines. To operate this equipment a modern automatic control system is necessary. The concept of the NICA control system based on Tango platform was presented for international machine advisory committee (MAC) in October 2012. MAC approved the choice of the designer team and recommended to test a fragment of the system as soon as possible. Minimum set of equipment was prepared to the run #46 (December 2012) and since this period the new control system is under active development.

The Tango control system is a free open source device oriented controls toolkit for controlling any kind of hardware or software and building SCADA systems. It is used for controlling synchrotrons, lasers and physics experiments in over 20 sites. It is being actively developed by a consortium of research institutes. Addition argument for the Tango usage is that this system has been chosen as a basis for the control system of the FAIR facility, which is developed in very close co-operation with NICA.

Tango introduction to NICA has started with Nuclotron. Several subsystems (beam injection control [8], beam slow extraction control) have been converted to the Tango-based structure. For instance, the upgraded Nuclotron injection control and diagnostics system was put into operation during the run #47of in March 2013. It has demonstrated high reliability, operation convenience and fulfilled the injected beam quality requirements. Both hardware and software parts of the system were fully redeveloped. As example the client application for the injection system control is presented in the Fig. 5.

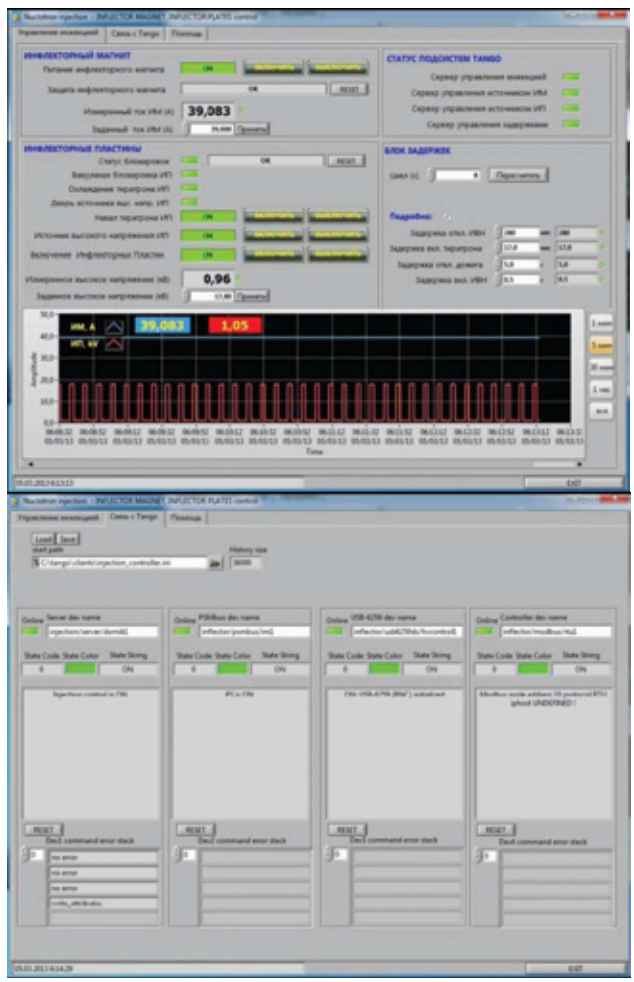

Figure 5: Injection control client application.

Several Tango-based subsystems are being developed now [9]. The software implementation using Tango framework allowed to reduce the development time significantly and confirmed the usage of Tango concept as a basis for the future NICA control system.

ISBN 978-3-95450-170-0

To implement the Tango control system as a control system of the NICA accelerator complex the 4 main tasks there were performed:

1) The control equipment database was designed and created.
2) The web-tool for using and managing of the control equipment database was developed.
3) Servers were purchased and configured.
4) The necessary toolbox for development, storing, documenting and using of Tango-based software was set up.

NEAREST PLANS

Nearest Nuclotron run is scheduled for February – March 2015. It will be dedicated to experiments with light ions in accordance with the JINR topical plans. In the frame of stochastic cooling development we plan to test time of flight method for longitudinal cooling. Test of the new source of polarized ions (SPI) is in progress at a test bench. The first run of the SPI operation at the Nuclotron dedicated to polarized deuteron beam production and acceleration is scheduled for the end of 2015 after commissioning of the new RFQ pre-accelerator for LU-20 [3]. The beginning of the HILac commissioning will be started in this year. The systems of the Nuclotron Booster are under construction in cooperation with Budker institute of nuclear research (Novosibirsk) and scientific centers from member states of JINR [10-14]. Serial production of the Booster magnets will be started this year [15].

CONCLUSION

Main result of the Nuclotron development during last years is stable and reliable operation of all the systems proving beam quality required for users. The operational time is optimized in accordance with the JINR topical plans with account the plan of the NICA construction. For more efficient usage of the beam time, the regime with two parallel users was realized routinely: experiment with internal target at the first plateau and beam extraction at the second one.

The beam time dedicated to the machine development is used for enhancement of the Nuclotron performance for current physics program realization and for tests of the equipment, diagnostics and operational regimes of the new NICA accelerators.

One of the key processes required for the NICA collider operation – the stochastic cooling – is under active experimental investigation at the Nuclotron.

Two new ion sources of the NICA injection facility - the LIS and Krion-6T - was tested at existing accelerator complex. As result in nearest runs we expect an increase of the beam intensity and widening of the ion species.

The segment of the NICA control system based on Tango platform was successfully tested at the Nuclotron, and presently the system is under active development.

REFERENCES

[1] A.V.Butenko et al, “Development of the NICA injection facility”, Proceedings of IPAC2013, Shanghai, China.
[2] G. Trubnikov et al., “Heavy ion collider facility NICA at JINR (Dubna): status and development”, Proc. ICHEP'12, Melbourne, Australia.
[3] A.V.Butenko et al, “Development of NICA injection complex”, Proceedings of IPAC2014, Dresden, Germany.
[4] R. Stassen, et al., “The stochastic cooling system of HESR”, COOL’11, Alushta, Ukraine.
[5] N.Shurkhno et al, Study for stochastic cooling at Nuclotron, JINR, Proceedings of COOL13, Murren, Switzerland.
[6] E.Ivanov et. al. Quench Detector for Superconducting Elements of the NICA Accelerator Complex, These proceedings.
[7] G.Trubnikov et al., Status of the NICA project at JINR, Proceedings of IPAC2014, Dresden, Germany
[8] E.Gorbachev et.al., Upgrade of the Nuclotron injection control and diagnostic system, Proceedings of ICALEPCS2013, San Francisco, CA, USA.
[9] G.Sedykh, E.Gorbachev, The equipment database for the control system of the NICA accelerator complex, Proceedings of ICALEPCS2013, San Francisco, CA, USA.
[10] A. Fateev, The Power Supply System of Electrostatic Deflecting Plates for Accelerating Complex NICA Booster, These proceedings.
[11] G.Kurkin et. al., RF System of the Booster of NICA Facility, These proceedings.
[12] A. Styuf, Fast Digital Phase meter for Booster of NICA Project, These proceedings.
[13] G. Fatkin, Controller for RF Stations for Booster of NICA Project, These proceedings.
[14] V. Parkhomchuk, Low Energy Cooler for NICA Booster, These proceedings.
[15] S. Kostromin, Facility for Assembling and Testing of SC Magnets for NICA and FAIR projects, These proceedings.

ISBN 978-3-95450-170-0

ACCELERATOR COMPLEX BASED ON DC-60 CYCLOTRON

M. Zdorovets#, I. Ivanov, M. Koloberdin, S. Kozin, V. Alexandrenko, E. Sambaev, A.Kurakhmedov, A. Ryskulov, Institute of Nuclear Physics, Astana, Kazakhstan

Abstract

DC-60 heavy ion accelerator [1], put into operation in 2006, according to its specifications - spectrum, charge and energy of accelerated ions, has the high scientific, technological and educational potential. The highest possible universality both by spectrum of accelerated ions and acceleration energy and regimes was built in DC-60 heavy ion accelerator designing. The ne interdisciplinary research complex based on DC-60 cyclotron makes it possible to create a highly-developed scientific-technological and educational environment in the new capital of Kazakhstan. This article is a review of the DC-60 heavy ion accelerator and the works carried out based on the cyclotron.

INTRODUCTION

DC-60 accelerator is a dual cyclotron, which is capable of charged particles acceleration up to kinetic energies in MeV/nucleon, expressed in the following relation: $E = 60(z_i/A)^2$, where z_i - accelerated ion charge, A - atomic weight of ion. Relation (z_i/A) in formula must be within the following limits: $(z_i/A) = (1/6 \div 1/12)$, that impose constraints on charge of accelerated ions.

Prototypes ECR heavy-ion source are sources DECRIS-2 and DECRIS-3 [2] which is used in the DC-60 accelerator. On the "ECR - surface" is used magnetic field configuration «minimum B» for the plasma confinement and electronic heating. This configuration is obtained as a result of the superposition of an axial field of magnetic mirror and a radial field of a sextupole magnet. Two single coils with an iron yoke form an axial magnetic field, and the radial magnetic field is created by an NdFeB permanent sextupole of a magnet.

The operating frequency of UHF the ECR generator is 14 GHz. The flash chamber of source is insulation meant for a voltage up to 25 kV. The extraction of ions is performed two elements Plasma electrode and the mobile extraction electrode.

For the beam transport from the ECR ion source to the cyclotron created a powerful system of axial injection of beam, which is consisting of:

- focusing element;
- energy-analysing magnet;
- detecting of elements;
- bunchers;
- vacuum pumps;
- electrostatic inflectors.

The entrapment of phase to accelerate in the center of the cyclotron is 30° ÷ 35°. This means that no more than 10% of ion of the desired charge will be involved in the acceleration process. To increase efficiency the entrapment of the beam by axial injection systems is installed the bancher with a sine wave, which includes the beam particles in the desired range of phases and increases the capture coefficient to 30÷50 %. Turn of the beam from the vertical axial injection channel in the median plane of the cyclotron using the electrostatic spiral of inflector.

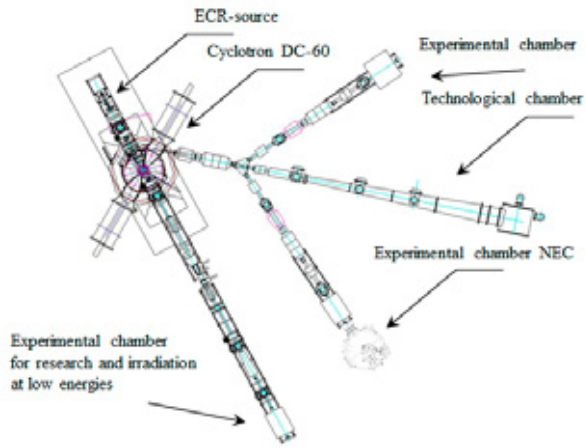

Figure 1: The scheme of the DC-60 accelerator complex.

The upper energy of the accelerated ions is 1.75 MeV/nucleon. The variation of the energy of ions in the range from 0.35 to 1.75 MeV/nucleon is provided by changes in the charge of the accelerated particles and magnetic field of the cyclotron.

High frequency system has a variation of the frequency in the band 12 - 18 MHz and provides the acceleration of ions on harmonics 4 and 6.

The electrostatic deflector with the electric field strength of 75 kV/cm is used for the beam extraction from the cyclotron which located in the cavity of the magnet. The beam transport channels from the cyclotron to the target chamber include the standard system focusing and rotation of the accelerated ions. Thus, range of ions accelerated on DC-60 cyclotron is ^{6}Li to ^{132}Xe, variation of ion energy is over the range 0.35 to 1.75 MeV/nucleon.

CYCLOTRON OPERATION

Since 2006 to 2014 many experimental works in the domain of nuclear and atomic physics, radiation physics of solid and nanotechnology have been carried out at the DC-60 cyclotron. The data of beam time in a period of 2006 - 2014 of operation of the accelerator is shown in Fig. 2.

#mzdorovets@gmail.com

ISBN 978-3-95450-170-0

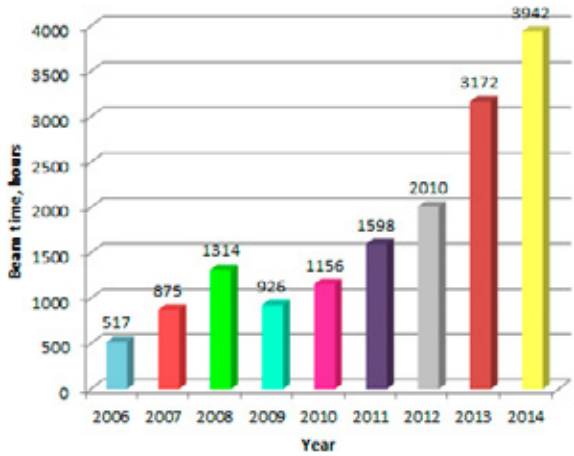

Figure 2: Total cyclotron beam time in the years 2006 - 2014.

As seen in Figure 2, there is an increase of the cyclotron beam time year by year, and in 2014 the work of the cyclotron is started its maximum. At the same time, about a third of the time is accounted for by the production of track membranes.

Over the last eight years of operation of DC-60 heavy-ion accelerator which used-on of the modes of operational of ion ^{6,7}Li, ^{12}C, ^{13}C, ^{14}N, ^{16}O, ^{20}Ne, ^{32}S, ^{40}Ar, ^{84}Kr и ^{132}Xe in the energy range 0.35 - 1.75 MeV/nucleon. For every the acceleration performance characteristic and resonance curves, radial beam profiles which carried out to optimize each system cyclotron [3] were measured. This work is carried out in the section "Fine-tuning technology of new ions in the DC-60 accelerator" of the program "Implementation of comprehensive research investigation in physics, chemistry, biology and advanced technologies on the basis of a heavy ion DC-60 accelerator", financed from the republican budget.

In 2014 work to the production lithium ions in the ECR source and further acceleration of ions on a cyclotron successfully completed. After the development of the technology of producing ions from solids using gateway solids feed to the ECR source, opens the possibility of using a number of prospective (not accelerated earlier) ion beams, such as ^{11}B, ^{40}Ca, ^{48}Ti, ^{56}Fe, ^{58}Ni, ^{98}Mo, etc.

Table 1 shows the main modes of operation of the accelerator and received the beam current of accelerated ions on the ECR source and the current external beam of ions from the cyclotron in the transport channel. All modes of operation of the cyclotron shown in Table 1 were optimized for long and stable operation. These values are ion beam current at the ECR source and extracted from the cyclotron are not as big as possible. Of all the modes of the most-coveted the acceleration modes with the maximum possible of energy, is a 1.75 MeV/nucleon.

Table 1: Current characteristics of accelerated ion beams

Ion	A/Z	Energy, MeV/nucl.	Beam current ECR, μA	Extracted beam current, μA
$^{7}Li^{1+}$	7	1.32	110	2.2
$^{12}C^{1+}$	12	0.40	63	0.6
$^{12}C^{2+}$	6	1.00	147	1.7
$^{12}C^{2+}$	6	1.25	150	1.5
$^{12}C^{2+}$	6	1.50	170	2.1
$^{12}C^{2+}$	6	1.75	140	1.7
$^{13}C^{2+}$	6.5	1.25	18.1	0.7
$^{13}C^{2+}$	6.5	1.50	19.9	0.6
$^{13}C^{3+}$	4.3	1.75	16.3	0.5
$^{14}N^{2+}$	7	0.4	84	0.9
$^{14}N^{2+}$	7	1.0	134	1.5
$^{14}N^{3+}$	4.6	1.4	325	2.0
$^{14}N^{3+}$	4.6	1.5	320	2.7
$^{14}N^{3+}$	4.6	1.75	120	1.9
$^{16}O^{2+}$	8	1.0	90	1.08
$^{16}O^{3+}$	5.3	1.25	85	1.1
$^{16}O^{3+}$	5.3	1.4	112	0.9
$^{16}O^{3+}$	5.3	1.5	95	0.8
$^{16}O^{3+}$	5.3	1.75	86	1.1
$^{20}Ne^{3+}$	6.67	1.08	106.0	1.03
$^{20}Ne^{3+}$	6.67	1.4	95.8	1.56
$^{20}Ne^{4+}$	5	1.75	76.4	2.0
$^{32}Se^{6+}$	5.33	1.75	61.1	0.8
$^{40}Ar^{4+}$	10	0.48	44.6	0.67
$^{40}Ar^{4+}$	10	0.64	37.2	0.84
$^{40}Ar^{5+}$	8	0.58	24.2	0.4
$^{40}Ar^{7+}$	5.7	1.1	42.7	1.2
$^{40}Ar^{7+}$	5.7	1.75	45.1	1.0
$^{84}Kr^{9+}$	9.3	0.4	47.6	0.25
$^{84}Kr^{10+}$	8.4	0.7	49.8	0.4
$^{84}Kr^{12+}$	7	1	34.3	1.7
$^{84}Kr^{15+}$	5.6	1.4	26.2	1.9
$^{84}Kr^{15+}$	5.6	1.75	28.6	2.1
$^{132}Xe^{14+}$	9.42	0.6	11.8	0.14
$^{132}Xe^{15+}$	8.8	0.4	10.7	0.25
$^{132}Xe^{17+}$	7.7	1	21.2	0.40
$^{132}Xe^{20+}$	6.6	1.5	22.6	0.46
$^{132}Xe^{22+}$	6	1.75	16.5	0.32

When accelerating ions of xenon and krypton are received intense beams of ions on the ECR source and even more so after the acceleration and the output from the cyclotron is quite low is shown in Fig.2. In the design of accelerator has been paid a lot of attention averaging charging ion beams on the ECR source, and thus justifies the selection of the microwave generator at a resonant frequency of 14 GHz. The production high intensities of highly charged ions on the ECR source is required under current conditions of operation of the cyclotron. In 2015 it is planned to modernize the ECR source and replacement of a RF generator with frequency variation of 18 GHz, so on the DC-60 accelerator will be able to produce large

ISBN 978-3-95450-170-0

currents of highly charged ions without reducing a current ion beams with a smaller charger.

EXPERIMENTAL TASKS CARRIED OUT ON CYCLOTRON

A facility based on DC-60 cyclotron is fully debugged production irradiation of polymeric materials (PET) the films with thicknesses in the range of 12 - 23 microns to create a track-etched membranes with pore density of $5 \cdot 10^5$ to 10^9 cm^{-2} [4].

The investigation in the field of nuclear physics is carried out by measuring the elastic scattering cross section of light nuclei on nuclei 1-p shell near the Coulomb barrier [5, 6], measuring the output section of the characteristic X-ray emission in the interaction of heavy ions with atoms of the target [7], the measurement of the neutron yield in the interaction accelerated heavy ions of average energy with easy targets [8].

The investigation in the field of radiation physics of solids is carried out by measuring the effect of irradiation with charged particles of low and medium energy on the structure and physic-mechanical properties of the alloy with a shape memory effect, the investigation of resistance to radiation of a structural materials with protective coatings and working medium of a dosimetric instrument, the development of techniques of modeling the interaction of heavy ions at high energy with structural materials of space technology [9-14].

The research to test the modes of chemical etching of the polymer material, modification of membrane surfaces [15], creating a smart filter, template synthesis of highly ordered metallic nanostructures arrays et al are carried out in the area of track-etched membranes [16].

SUMMARY

A facility based on DC-60 cyclotron has been created for scientific and applied research, as well as for nanotechnologies application. During work from 2006 to 2014 beams of ^{6,7}Li, ^{12}C, ^{13}C, ^{14}N, ^{16}O, ^{20}Ne, ^{32}S, ^{40}Ar, ^{84}Kr и ^{132}Xe were accelerated in energy range from 0.35 to 1.75 MeV/nucleon. The beam parameters have been investigated, technological polymer film irradiation was provided and track membranes were fabricated.

With the implementing techniques of producing ions using the sluice feed solids in the ECR source significantly expand the range of accelerated ions. With an increase in the spectrum of the accelerated elements will increase the possibility of staging, find and solve new problems and experiments in the field of experimental nuclear physics, radiation physics of solids and various applications.

REFERENCES

[1] B. Gikal et al., DC60 heavy ion cyclotron complex: First beams and project parameters, Physical of particles and nuclei letters, V5(7), pp. 642-644.

[2] V. Kutner et al., Operation and Resent Development of ECR Ion Sources at the FLNR (JINR) Cyclotrons, Proceedings of 15th International Conference on Cyclotron and their Applications, Caen, France, (1998), pp. 405-408.

[3] Ivanov I.A. et al., Testing of the acceleration mode $^{132}Xe^{22+}$ ions with an energy of 1.75 MeV / nucl. at the DC-60 cyclotron, Bulletin of ENU, 97, pp. 189-196.

[4] Mashentseva A. et al., Osnovy membrannykh tekhnologiy. Polucheniye i issledovaniye svoystv trekovykh membrane, Astana: Master PO, 186 p.

[5] Burtebayev N. et al., Detailed study for 16O elastically scattered from ^{16}O at energies 20, 24 and 28 MeV, International Journal of Modern Physics E22 (8), 1350058.

[6] Gridnev K.A. et al., Investigating the $^{16}O + {}^{12}C$ reaction over a wide range of energies, Bulletin of the Russian Academy of Sciences: Physics 75 (7), pp. 961-963.

[7] Gorlachev I. et al., X-ray production cross section for K-, L- and M-shell by 14 MeV and 19.6 MeV nitrogen, Nuclear Instruments and Methods in Physics Research B, Vol. 330, pp. 86-90.

[8] B. Gikal et al., Secondary fusion reactions in the bombardment of light-element targets with low-energy heavy ions, Physics of particles and nuclei letters, Vol. 11, № 4, pp. 462 – 466.

[9] Uglov V.V. et al., Stability of Ti-Zr-N coatings under Xe-ion irradiation, Source of the Document Surface and Coatings Technology 204 (12-13), pp. 2095-2098.

[10] Kislitsin S.B. et al., Blistering and α γ phase transitions at annealing of stainless steel C12Cr18Ni10Ti irradiated by low energy alpha-particles, Problems of Atomic Science and Technology (2), pp. 17-22.

[11] Russakova A. et al., Color center accumulation in LiF crystals under irradiation with MeV ions: Optical spectroscopy and modeling, Nuclear Instruments and Methods in Physics Research, Section B: Beam Interactions with Materials and Atoms, 313, pp. 21-25.

[12] Dauletbekova A. et al., Color centers and nanodefects in LiF crystals irradiated with 150 MeV Kr ions, Nuclear Instruments and Methods in Physics Research, Section B: Beam Interactions with Materials and Atoms 286, pp. 56-60.

[13] Dauletbekova A. et al., F center creation and aggregation in LiF crystals irradiated with 14N, 40Ar, and 84Kr ions, Nuclear Instruments and Methods in Physics Research, Section B: Beam Interactions with Materials and Atoms 326, pp. 311-313.

[14] Li W. et al., Effect of orientation on ion track formation in apatite and zircon, American Mineralogist 99, Issue 5-6, pp. 1127-1132.

[15] Korolkov I.V. et al., The effect of oxidizing agents/systems on the properties on track-etched PET membranes, Polymer Degradation and Stability 107, pp. 150-157.

[16] Mashentseva A. et al., Synthesis, Structure, and Catalytic Activity of Au/Poly(ethylene terephthalate) Composites, Acta Physica Polonica A 125, Issue 6, pp. 1263-1266.

ISBN 978-3-95450-170-0

THE STATUS OF THE FACILITIES OF KURCHATOV`S SYNCHROTRON RADIATION SOURCE

V. Korchuganov, A. Belkov, Y. Fomin, E. Kaportsev, M. Kovalchuk, Yu. Krylov, I. Kuzmin, V. Moiseev, K. Moseev, N. Moseiko, D. Odintsov, S. Pesterev, A. Smygacheva, A. Stirin, S. Tomin, V. Ushakov, V. Ushkov, A. Valentinov, A. Vernov, NRC Kurchatov Institute, Moscow, 123182 Russia

Abstract

The first electron beam had been received 20 years ago in a storage ring SIBERIA-2 - a dedicated synchrotron radiation source in the Kurchatov Institute and, also, the official opening of the SR source for the experiments marks 15th anniversary in year 2014. The report focuses on the development of the SR source accelerator complex systems in 2014.

INTRODUCTION

The electron accelerators complex of the Kurchatov`s SR source includes: a for-injector - the 80 MeV linear accelerator; the 450 MeV storage ring Siberia-1 with the natural emittance 800 nm·rad; the 2.5 GeV storage ring Siberia-2 with the natural emittance 78-100 nm·rad; two electron-optical channels – EOC-1 and EOC-2. Official opening of the Kurchatov SR source took place 1.09.1999.

KSRS FACILITIES WORK

The work of Siberia-2 on experiments is mainly carried out using SR from bending magnets in photons energy range (4-40) keV and spectral flux (10^{13}-10^{11}) ph/s/mrad/0.1%BW during the week runs in a round-the-clock mode. Within one week 9 working 12-hour shifts are presented.

Figure 1: Experimental time at Siberia-2 in 2000-2013.

Diagram in Fig.1 shows the integral time devoted for SR experimental work at Siberia-2 in 2000 – 2013 years. Table 1 presents a statistics of SR source Siberia-2 work at SR experiment in 2013 and on June 2014. Note that in 2014 the SR source spent relatively much time in standby and adjustment mode due to stops for the works of firms according contracts (opening shielding walls, new beam lines installation, etc).

The purpose of works on 2013-2014 is both modernization of the existing equipment and introduction of new diagnostics systems mainly on Siberia-2 storage ring.

Table 1: Statistics of Siberia-2 on 2013-June 2014.

Period	2013	Jan.-June 2014
Max. electron current	112 mA	128 mA
Life time (100mA)	41.8 hrs	38.5 hrs
Operation time	3480 hrs	2371 hrs
Experiment	2257 hrs / 50%	1074 hrs / 38%
Injection	10%	11%
Tuning / Other works	17% / 23%	16% / 35%

DEVELOPMENT OF KSRS ON 2014

Siberia-2 New High Voltage Generators

The important aim was to replace old generators of the injection kickers based on the HV gas-filled electric discharge devices and the HV forming lines (20 ns, <55 kV) on the new compact LV generators (≤3 kA, 25 kV) working only with solid electrical components and without SF_6 gas using.

After the testing in 2011-2012 of the prototype two new generators based on pseudo-spark switches (a thyrotron TPI1-10k/50) and RLC resonant circuits with a semi-sinusoidal form of currents were produced on “Pulse Systems” Ltd. (Ryasan). The final scheme of new generators is shown in Fig.2.

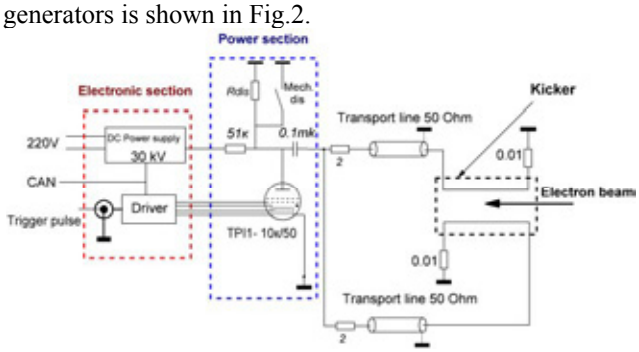

Figure 2: The scheme of new generators.

To guarantee a stable operation of the generators we have increased the working pulse duration till 1 μsec making 2.5 times longer than revolution period and have reduced the voltage on capacitance.

The calculation without taking into account any collective excitations showed that in the case long pulse shouldn’t affect the injection efficiency [2], see Fig.3.

ISBN 978-3-95450-170-0

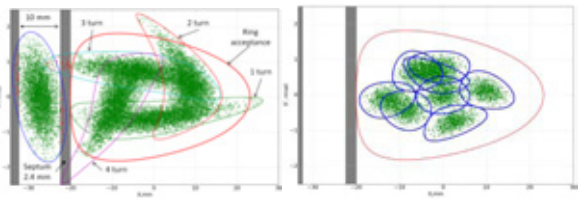

Figure 3: Horizontal phase trajectories of the injected and the stored bunches at the injection moment

Nevertheless, the maximum injection efficiency factor is limited near 50-70% (with 10 kV - on "kicker" and 7 kV- on "pre-kicker) due to the excitations of multibunch instabilities by long pulses of kickers. To avoid the excitations we shall continue the generator scheme modernization to shorten the pulse duration.

Siberia-2 RF System Modernization

The RF system includes two generators and three accelerating cavities, two of which are powered by one common generator. In January 2014 four new and more reliable powerful tetrodes of TH781 type with the pirographite grids (THALES, France) were installed in the output cascades of two RF generators instead of the old GU-101A type tetrodes [1].

Now we investigate the feature of stabilization system of voltages and phases of two coupled cavities. We observe that with electron current growing the RF voltages on accelerator gaps of the coupled cavities change oppositely (when keeping the summarized voltage). This reduces the voltage of one (of two) coupled cavity till the level which is do not stabilized and stops the electron storage. To continue the storage process we must increase the sum RF voltage and, so, to decrease injection effectiveness. The RF measurements and the calculation with a theoretical coupled cavity model have proved that the existing errors in the lengths of the feeders, in the matching of the cavities with the feeders and the waveguide are the reasons of an incorrect distribution of RF voltages between the cavities, limits the accumulation of electron beam current and leads to an increase of the generator load. To solve this problem most directly but rather costly each cavity should be powered by an individual generator and tuned separately by an individual feedback system. Other (difficult) way is to make a new feedback system for the independent stabilization of the voltages and phases of two cavities powered by one RF generator.

New System "Orbit" at Siberia-2[3]

The main purpose of new system "Orbit" is an improvement of the electron orbit diagnostics providing continuous measurements and carrying out turn-by-turn measurements of the electron beam trajectory during injection process. In addition, it will be a part of fast feedback system which will damp the distortions of the closed orbit.

The closed orbit correction system of Siberia-2 contains up to 48 vertical correctors, 48 horizontal correctors and 24 BPMs. In 2013 the BPMs were supplied with the new high-precision electronic equipment and software product for measurement of an equilibrium orbit transverse coordinates. The electronics of "Libera Brilliance Instruments" was mounted in the 4 racks inside of the Siberia-2 tunnel, each containing 6 "Libera Brilliance" units and 1 Libera Clock Splitter" unit. A new accelerator physics framework "Ocelot" was integrated with the new orbit correction system for high level beam control. Spatial resolution of new system "Orbit" with measurement time of 5 milliseconds for beam average current value 5-300 mA makes 1μm. The first results of orbit measurements and corrections are shown at BPMs azimuths at energy in Fig.4.

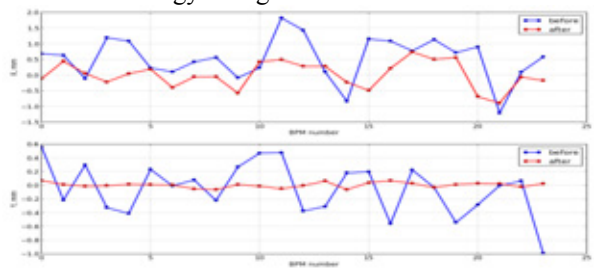

Figure 4: An orbit before (blue) and after (red) correction. H.:rms 880/420 μm; V.:rms 380/38 μm.

RMS of vertical orbit distortion is about 40 μm after correction. For horizontal plane the situation is worse due to the irregular locations of BPMs in betatron phase and the lack of correctors and BPMs in horizontal plane. In our case the currents of some correctors must be more than 13A when maximum sources current is 5A at 2.5 GeV. To minimize the horizontal orbit distortion the number of BPMs is planed to be increased in future.

Feedbacks for Instabilities Suppression

Longitudinal and transverse feedback systems for damping the beam excitations in Siberia-2 will be commissioned to the end of 2014. As a kicker for suppression of coherent synchrotron excitations a special small RF cavity is intended with own frequency of 950 MHz and a quality factor of 10 [4]. It was introduced in the straight section of ring in 2013. The longitudinal kicker reflectivity measurement and resulting reflectivity dependence on the frequency of the excitation are shown in Fig.5.

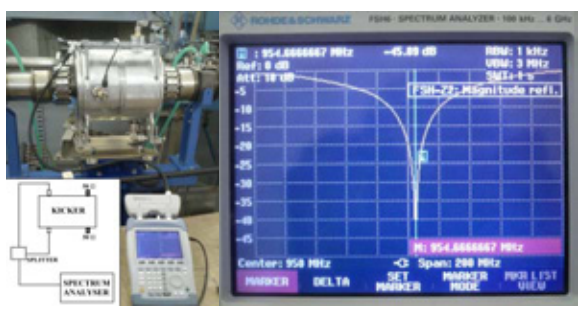

Figure 5: The reflectivity measurement of longitudinal kicker at the Siberia-2 straight section.

ISBN 978-3-95450-170-0

As transverse kickers for suppression of coherent betatron oscillations in X- and Y- plane the strip lines existing on Siberia-2 ring are used. The digital electronics, broadband amplifiers (25 W and 50 W) and a pickup - electrodes, phase detectors, the modulator, RF control were installed in the rack.

Siberia-2 New Station of Optical Supervision

The six diagnostic systems station of optical supervision (SOS) was mounted outside to biological protection of Siberia-2 by April, 2013.

For first measurements [5] of the vertical beam size the double slit interferometer was applied with a slit separation of 15mm and 20mm. The interference patterns for two different vertical beam sizes (σ_y =60μm; 90μm) and their intensity distribution cross-sections are presented in Fig. 6a, 6b.

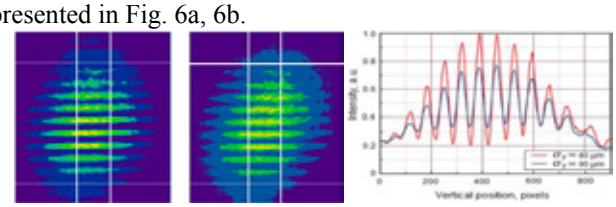

6a) 6b)

Figure 6a: Interference patterns for vertical beam sizes of 60μm (left) and 90μm (right). Figure 6b: The light intensity was integrated at the region between the vertical lines in Fig.7a.

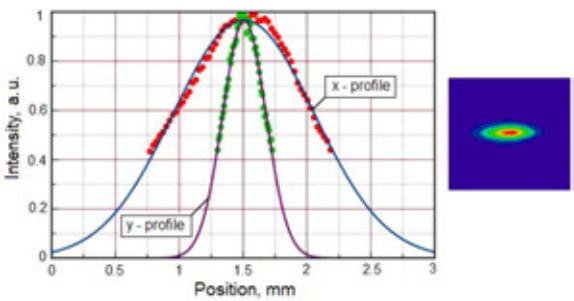

Figure 7: Beam image and its x, y - projections fitted by Gaussian curves.

The beam image was monitored and a fit of its projections by Gaussian curves are presented in Fig. 7. Comparison of the results obtained enables us to determine the value of apparatus function for transverse beam measurement system as $\sigma_{inst} \approx 80$μm. This rather large value can be explained by the poor quality of the first cooled mirror (which will be replaced by new one in December 2014). By means of comparison of the beam size measurements with slit separation of 15mm and 20mm we estimate the resolution of double slit interferometer as $\sigma_{int} \approx 5$μm.

New Power Supplies for Magnetic Correctors

In 2012 the replacement of old power supplies for the magnetic correctors by the new more exact ones developed by "Marafon" (Moscow) [1] was started. In 2013 the all set of the 269 bipolar and unipolar units were made with a new control system and computer programs. The testing shows rather high long time current stability ($2 \cdot 10^{-4}$, 6A and 20A).

New Control System

Upgrade of CS consists in changeover of the old equipment of CAMAC on trunk - modular hardware in the VME standard and the organization of new architecture. CS is conditional subdivided into the upper and lower levels, server level and the periphery. ***The lower level of CS*** realizes a collection of diagnostic information and an execution of control algorithms by the executive systems of the accelerator complex. ***Server level of CS*** includes application servers and the server of management system of a database (DBMS). ***The top level of CS*** includes automated workplaces of operators and other users. The full-function monitoring system and controls - CitectSCADA [6] works at the top level.

Work with 7.5T SC Wiggler

The first experiment started on "X-Ray structure analysis" (RSA) station with SR of existing 7.5T SCW in October 2013.

New SR Beamlines and Experimental Station

In 2013 the beamline and the station PHASA were run in operation. In 2014 we started the commissioning of the SR beamline and the station "Photo Electron Spectroscopy – PES".

CONCLUSION

We are sure that continuous efforts in the solution of the scientific and technical problems will lead to high-quality improvement of the KSRS.

REFERENCES

[1] V.Korchuganov, A.Belkov, Y.Fomin at al., "The development of synchrotron radiation source of NRC "Kurchatov Institute", RUPAC2012.

[2] V.Korchuganov, S.Tomin, New Injection System of Siberia-2 Light Source, IPAC 2014.

[3] Ye.Fomin, V.Korchuganov, N.Moseiko, A. Valentinov, NRC KI, Russia and R.Hrovatin, P.Leban, IT, Slovenia, "New Electron Beam Reference Orbit Measurement System at Dedicated Synchrotron Radiation Light Source Siberia-2", RUPAC2012.

[4]V. Korchuganov, A. Smygacheva, A. Valentinov, at al., NRC KI, Russia and D. Tinta, R. Hrovatin, R. Cerne, IT, Slovenia, "The Feedback System for Damping Coherent Betatron and Synchrotron Oscillations of Electron Beam at Dedicated SRS Siberia-2", ICALEPCS-2013, San Francisco, CA.

[5] A.Stirin, G.Kovachev, V.Korchuganov at al., NRC KI, O. Meshkov, V. Dorohov, A. Khilchenko at al., BINP, "New Station for Optical Observation of Electron Beam Parameters at Electron Storage Ring Siberia-2", IPAC14, Drezden.

[6] E.Kaportsev, A.Valentinov,Y.Krylov, Y.Efimov, "Modernization of the Automated Control System in the Kurchatov Synchrotron Radiation Source. The using of CitectSCADA", RUPAC2014.

ISBN 978-3-95450-170-0

THE NSLS-II BOOSTER DEVELOPMENT AND COMMISSIONING

V. Kiselev for the BINP and BNL teams [1]
BINP, Novosibirsk 630090, Russia

Abstract

National Synchrotron Light Source II is a third generation light source constructed at Brookhaven National Laboratory. The project includes highly optimized 3 GeV electron storage ring, linac pre-injector and full-energy injector-synchrotron. Budker Institute of Nuclear Physics has built a turnkey booster for NSLS-II. The main parameters of the booster, its characteristics and the results of commissioning are described in this paper.

INTRODUCTION

The tender on the designing, production and commissioning of the NSLS-II booster was started in January 2010. Budker Institute of Nuclear Physics won this tender in May 2010. The booster was designed, produced and delivered in full to BNL by September 2012. During 2013 the booster was assembled and all equipment was tested. The authorization to start the commissioning of the injector was received in November 2013. The BNL and BINP teams started beam injection into the Booster on December 8. The first turn was closed soon by tuning the LTB and BR orbit correctors. The beam was accelerated to 3 GeV by the end of 2013. The commissioning of the booster was successfully completed in February 2014.

BOOSTER DESIGN

The conceptual design of the booster has been done by BNL [2].

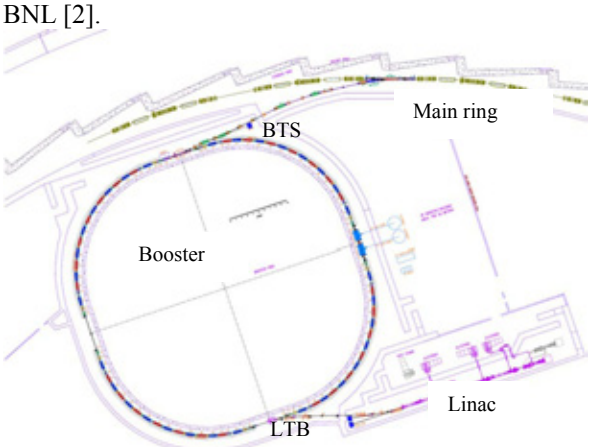

Figure 1: Schematic layout of the full energy booster.

The booster should accelerate the electron beam continuously and reliably from minimal 170 MeV injection energy to a maximal energy of 3.15 GeV and average beam current of 20 mA. The booster shall be capable of multi-bunch and single bunch operation. The main parameters of the designed booster are summarized in Table 1. The lattice provides rather low horizontal emittance of 37.4 nm·rad at the energy of extraction.

Table 1: NSLS-II Booster Main Parameters.

Energy, MeV	200	3000
Circumference, m	158.4	
Number of periods	4	
Repetition rate, Hz	1 Hz / 2 Hz	
Bunch number	1; 80-150	
RF frequency, MHz	499.68	
Betatron tunes: ν_x/ν_y	9.646 / 3.411	
Natural chromaticity: ξ_x/ξ_y	–9.5/–13.5	
Corrected chromaticity: ξ_x/ξ_y	1.25 / 2.05	
Momentum comp. factor, α	0.00882	
Hor. Emittance: ε_x, nm rad	0.17	37.4
Energy spread, σ_E/E	$0.55\cdot10^{-4}$	$8.31\cdot10^{-4}$
Energy loss per turn, U_0, keV	0.0135	685.8
Damping times: (τ_x τ_s), s	15.6; 7.8	0.0046; 0.0023

Lattice

The optical structure of the booster synchrotron consists of four quadrants. Two opposite straight sections of the ring contain elements for injection and extraction of the beam. Other two sections are intended for RF resonators and diagnostics. 60 magnets with combined functions magnetic field are set in the ring. The core of dipoles is a sector with parallel edges. For compensation of natural chromaticity of the structure the dipole magnets create sextupole component of a field. Separate quadrupole lenses provide adjustment of betatron working point during acceleration of particles and optimum acceptance of the structure. For correction of lattice chromaticity the separate sextupole lenses are inserted. Optical functions are shown in Figure 2.

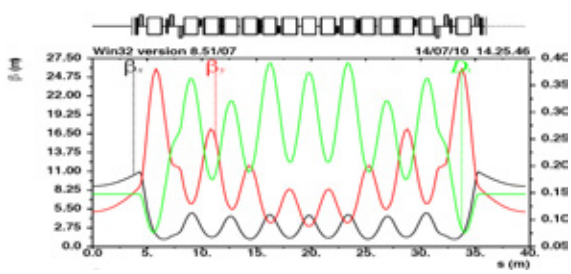

Figure 2. The betatron and dispersion functions for the lattice quadrant.

ISBN 978-3-95450-170-0

Beam Diagnostics

For successful commissioning and effective operation of the projected NSLS-II Booster, a set of beam diagnostic instruments has been designed. Fluorescent screens (8 pieces) are used for the Booster commissioning and troubleshooting. Closed orbit is measured using electrostatic BPMs (32 pieces) with turn-by-turn capability. The circulating current is measured using a DC current transformer and fill pattern by a fast current transformer. The synchrotron radiation monitor provides routine measurements of transverse beam profiles and beam sizes. Betatron tunes are measured using two pairs of striplines, the first pair is for beam excitation and the second one – for beam response measurement [3, 4].

Magnetic System

All booster magnets were made at BINP. The main parameters of the designed booster magnets are summarized in Table 2.

Table 2: Booster magnets parameters

Magnets	Total Number	Magnetic length, m	Magnetic force for 3 GeV		
			T	T/m	T/m2
BF Dipoles	28	1.24	0.46	8.2	36
BD Dipoles	32	1.30	1.13	-5.6	-43
Quadrupoles	8+8+8	0.30		20.4	
Sextupoles	16	0.12			±400
Correctors	20+16	0.13	0.1		

The BINP workshop has designed and produced all dies for magnet laminations with the accuracy up to 5 μm on the critical surfaces. The BF and BD dipoles have complicated end chamfers (Fig. 3), which were chosen so as to have minimal distortion field at the extraction energy.

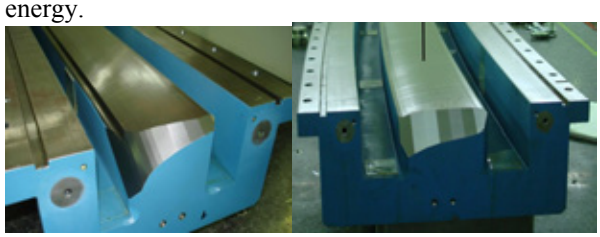

Figure 3. The BF and BD dipoles end chamfers.

The BF and BD dipole magnets were measured with the Hall sensors. The measurement method and results are described in the papers [5]. Magnetic properties of all magnets are better than the original requirements throughout the range of the energy: difference of integrated parameters between dipoles should not exceed: for integral of a field <0.1%, for integral of a gradient <0.5% and for sextupole field component <5% [6].

Injection and Extraction System

Four fast ferrite kickers and a pulse eddy-current type septum magnet are installed in the long straight section. The kicker and septum magnets are placed out of vacuum.

The booster extraction system consists of four slow orbit bumpers, AC septum, DC septum and a kicker. The main parameters of the injection and extraction system magnets are summarized in Table 3. After production, all the above-described elements were magnetically measured and long-term tested with the pulsed power supplies developed by BINP [7, 8].

All elements satisfy the requirements presented for them.

Table 3: Main parameters of IES magnets

Magnets	n	Magnetic length, m	Field T	Angle mrad	Pulse μs
Injection System for 200 MeV					
Kicker	4	0.207	0.055	17	0.3
Septum(AC)	1	0.75	0.112	125	100
Extraction System for 3 GeV					
Bump	4	0.17	0.46	7.8	1500
Kicker	1	0.83	0.073	6.1	0.3
Septum(AC)	1	0.6	0.8	48	150
Septum(DC)	1	1.2	0.89	106	-

COMMISSIONING

Thanks to the good quality of the booster magnets and precise booster alignment, commissioning of the booster passed without any problems. The first turn was closed soon by tuning the LTB and BR orbit correctors. The beam was monitored using the beam flags and BPMs in the single-pass mode. After achievement of the captured beam, the orbit at injection was corrected and the beam was accelerated. The diagram represents the measurements of the orbit during acceleration. The force of correctors during ramping was not changed (Fig. 4).

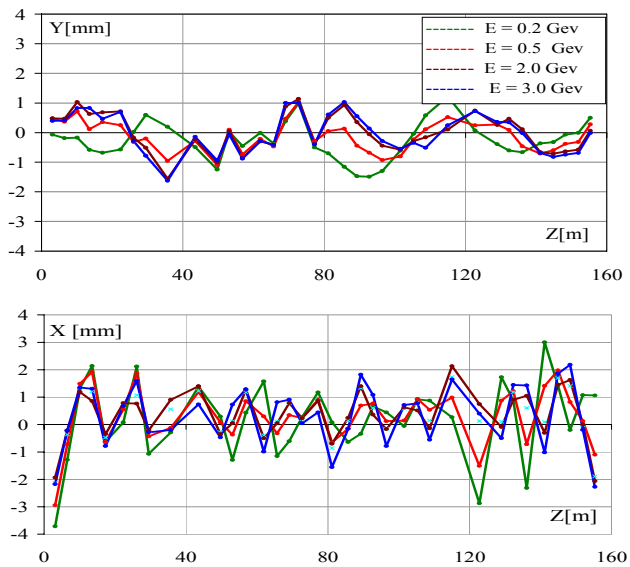

Figure 4. Vertical and horizontal orbit of beam along the whole ramp.

ISBN 978-3-95450-170-0

As can be seen from Figure 4, the beam orbit remains constant during the ramp with accuracy of ± 1 mm in the vertical plane and ± 2 mm in the horizontal without additional correction.

Thereafter the optical model of the magnetic structure was improved towards better booster ring parameters using the data of the final booster survey and the results from beam position monitors. The optical functions and betatron tunes were corrected throughout the ramp. As a result, the betatron frequences over the entire ramp remained constant (Fig. 5).

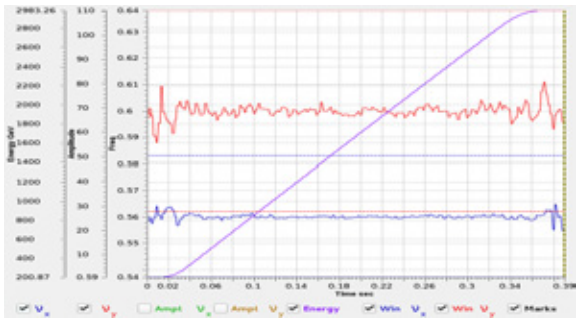

Figure 5: The horizontal (blue) and vertical (red) tunes along the whole ramp (purple).

This reduced beam losses during the ramp to below 5%. Besides, an additional adjustment of the optical functions of the linac-to-booster transport line was carried out, which resulted in increasing efficiency of particle capture and acceleration up to ~ 95 % (Fig.6).

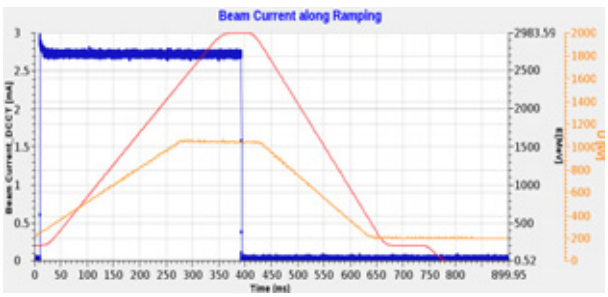

Figure 6: The beam current from DCCT (blue), the beam energy according dipole magnet currents (red) and the RF cavity voltage (orange) during 1Hz-cycle.

Emittance Measurement

Emittance value was derived from a spot of the synchrotron light [9]. The BR-A1SLM output port is located close to the DS straight section, in a region with minimal dispersion. Synchrotron light is emitted from the BR-A1BD8 dipole magnet. Using operating machine currents, Twiss parameters at the source are estimated to be β_x = 5.8 m, β_y = 23.8 m, and η_x=0.1 m. At extraction energy the measured emittances were ε_x=33 nm and ε_y=4nm.

The transverse stability of extracted beam was checked. Beam position stability was measured using the flag disposed in the extraction channel (BTS). Transverse beam stability better than ± 30 μm was observed at the repetition rate of 1 Hz during 1 hour.

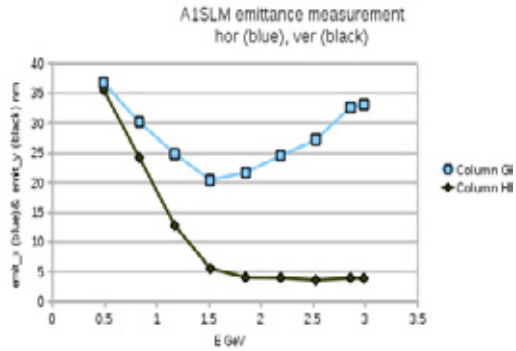

Fig. 7. Horizontal and vertical emittance during the acceleration cycle as determined by the profile of the synchrotron light seen by the BR-A1SLM monitor.

CONCLUSION

The NSLS-II 3-GeV booster synchrotron has passed the acceptance testing and the machine performance closely corresponds to the project requirements. The booster is a robust machine that will be an effective injector for the NSLS-II storage ring. The booster commissioning was successfully completed in February 2014. All booster systems work according to the design. The commissioning of NSLS-II Storage Ring was started in March 2014 and stored beam was achieved on April 5, 2014.

REFERENCES

[1] **BINP team**: A.Akimov, O.Anchugov, A.Batrakov, O.Belikov E.Bekhtenev, P.Cheblakov, A.Chernyakin A.Derbenev, A. Erokhin, S.Gurov, S.Karnaev, G.Karpov, R. Kadyrov, V.Kiselev, V.Kobets, V.Konstantinov, V.Kolmogorov, A.Korepanov, E.Kuper, V.Kuzminykh, E.Levichev, V.Neyfeld, I.Okunev, V.Petrov, M.Petrichenkov, A.Polyansky, D.Pureskin, A.Rakhimov, S.Ruvinskiy, T.Rybitskaya, L.Schegolev, A.Semenov, D.Senkov, S.Serednyakov, S.Shiyankov, D.Shvedov, S.Sinyatkin, A.Sukhanov, A.Zhuravlev
BNL New York, USA team: G.Bassi, A.Blednykh, E.Blum, W.Cheng, J.Choi, J.De Long, R.Fliller, F.Gao, W.Guo, Y.Hidaka, S.Kramer, S.Krinsky, Y.Li, M.Maggipinto, D.Padrazo, B.Podobedov, J.Rose, S.Seletskiy, O.Singh, V.Smaluk, T.Shaftan, W.Wahl, G.Wang, F.Willeke, L.Yang, X.Yang, L.Yu, E.Zitvogel, P.Zuhoski.
[2] T.Shaftan et al., NSLS-II Tech. note 0061 (2009).
[3] V.Smalyuk et al., DIPAC'11, MOPD01, p. 29 (2011).
[4] E.Bekhtenev et al., RUPAC'12, WEPPD029, (2012).
[5] I. Okunev et al., IPAC'13, THPME032, p. 3579 (2013).
[6] S.Sinyatkin et al., IPAC'13, THPME029, p. 3570 (2013).
[7] A. Zhuravlev et al., IPAC'13, THPME033, p. 3582 (2013).
[8] D. Shvedov et al., IPAC'13, THPME033, p. 717 (2013).
[9] S.Gurov et al., IPAC'14, MOPRO088, (2014).

ISBN 978-3-95450-170-0

SUPERCONDUCTING MULTIPOLE WIGGLERS FOR GENERATION OF SYNCHROTRON RADIATION

N. Mezentsev, Budker INP, Russia

Abstract

Superconducting (SC) multipole wigglers are very powerful instruments for generation of synchrotron radiation of high intensity. Use of a superconducting wire for creation of a sign alternating lateral magnetic field has the big advantages in comparison of permanent magnets and conventional electromagnets. Superconductivity use allows to create much higher magnetic field at the same field period and the vertical aperture for a beam. The high magnetic field allows not only to increase intensity, but also to expand spectrum of synchrotron radiations.

The first superconducting wiggler has been made and installed on the VEPP-3 electron storage ring as a generator of synchrotron radiation in 1979. Nowadays tens of the wigglers are successfully working in the various synchrotron radiation centers and more than 10 of them were developed and made in Budker INP.

The description of magnetic properties of the wigglers, parameters of both cryogenic and vacuum systems and their technical decisions are resulted in the report.

INTRODUCTION

Multipole superconducting wigglers are installing on synchrotron radiation (SR) sources to improve user properties of radiation by increasing of rigidity and intensity of SR. The magnetic system of multipole wiggler represents an array of superconducting dipole magnets creating sign alternate lateral magnetic field. Electron beam passing through this array generates SR in each magnet which the radiation intensity is summarised from all magnets practically in the same solid angle. Use of such magnetic systems is rather effective and cheap enough way of increase in intensity and rigidity of radiation. Spectral properties of radiation from such magnetic structure depend on parameter $K = 0.934 \cdot B[T] \cdot \lambda[см]$, where B and λ - amplitude and magnetic field period. For K~1 - the radiation spectrum has undulator property, for K>> 1 - the radiation spectrum transits to spectrum of synchrotron radiation. To expand opportunities for carrying out of experimental works and thus to prolong a life, expensive installations as electron storage rings superconducting insertion devices (SC ID) may be installed into straight sections of the storage rings to change spectral, angular, and polarizing properties of SR. These devices, as a rule, have zero first and second magnetic field integrals along electron orbit, and, therefore, they are not basic elements of the electron storage rings, and their status does not affect working reliability of all ring.

The magnetic system using superconducting magnets with NbTi/Cu or Nb_3Sn/Cu wires creates much higher field in comparison with use of conventional or permanent magnets. However use of superconductors demands use of a cryostat for maintenance of low temperatures of magnetic system.

MAGNETIC SYSTEM OF SC WIGGLERS

Magnetic Field Distribution and Field Integrals

Magnetic field of a superconducting multipole wiggler represents a periodic, sign-variable field (1) which begins and ends by special compensating end magnets.

$$\begin{aligned} B_z &= B_0 \cos(k_0\sigma)\cos(k_x\chi)\cosh(k_z z) \\ B_\chi &= -\frac{k_x}{k_z} B_0 \cos(k_0\sigma)\sin(k_x\chi)\sinh(k_z z) \\ B_\sigma &= -\frac{k_0}{k_z} B_0 \sin(k_0\sigma)\cos(k_x\chi)\sinh(k_z z) \end{aligned} \quad (1)$$

Where: $k_0 = 2\pi/\lambda_0$, $k_x = 2\pi/\lambda_x$, $k_z = 2\pi/\lambda_z$ - characteristic magnetic field variation in longitudinal and lateral directions.

The end magnets are used for creation of the first and second field integrals of the wigglers equal to zero for indemnification of a beam orbit distortion which is created by the basic wiggler field.

$$I_1 = \frac{1}{B\rho}\int_{-L/2}^{L/2} B_z(s)ds = 0 \qquad I_2 = \int_{-L/2}^{L/2} ds' \int_{-L/2}^{s'} \frac{B_z(s'')}{B\rho} ds'' = 0 \quad (2)$$

Field integrals of the wiggler with odd pole number can be compensated by two end magnets with a field of ½ of the main field or four end magnets with the fields, equal ¼ and ¾ of the main field..

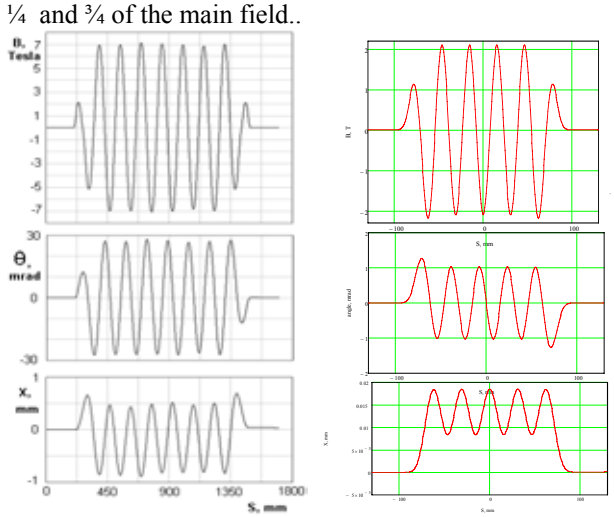

a) b)

Figure 1: Magnetic field distribution and behaviour of the first and second field integrals with the end magnets of a) ¼ and ¾ and the end magnets of ½ of the main field.

ISBN 978-3-95450-170-0

The second field integral is equal to zero automatically (if the first field integral is zero) for a wiggler with odd number of poles. The first field integral is provided with a separate power feeding of the end poles. Contrariwise for a wiggler with even pole number the first field integral is automatically equal to zero, and the second integral is controlled by separate power supply connected to the end poles.

Focusing Properties and Nonlinear Field Components

High field SC ID is a focusing element in magnetic structure of the storage ring and creates betatron tune shifts and structural functions changes. Horizontal and vertical betatron motion inside SC ID may be described by the following equations:

$$x'' + K_x \cdot x = 0 \qquad (3)$$
$$z'' + K_z \cdot z = 0$$

where the where coefficients of magnetic strength K_x, K_z are equal to:

$$K_x = \frac{B_z^2}{(B\rho)^2} + \frac{1}{B\rho}\left(x'\frac{\partial B_z}{\partial s} - \frac{\partial B_z}{\partial x}\right), K_z = -\frac{1}{B\rho}\left(x'\frac{\partial B_z}{\partial s} - \frac{\partial B_z}{\partial x}\right) \quad , \qquad (4)$$

where: $B\rho$ –electron beam rigidity.

Edge focusing completely compensates focusing by magnetic field in horizontal direction and the main focusing action of SC wiggler occurs in vertical direction.

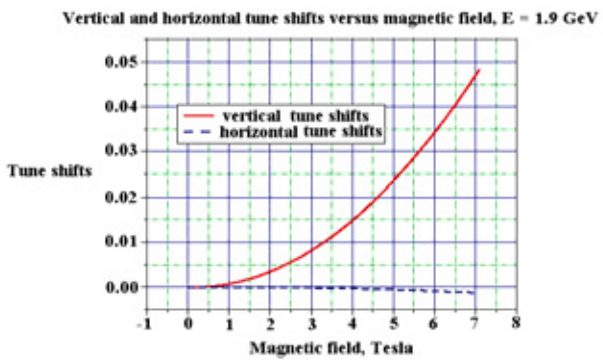

Figure 2: Example of tunes behaviour versus magnetic field in the 7 Tesla SC wiggler of BESSY ring.

Integral values of nonlinear components of the magnetic field of multipole wigglers with length *L*, at conditions that orbit distortion is much less than characteristic pole sizes and assuming $k_x / k_0 << 1$ may be written as:

$$\int_L B(s)ds = \frac{B_0^2 \cdot k_x^2}{2B\rho \cdot k_0^2} \cdot \delta \cdot L \qquad (5)$$
$$\int_L G(s)ds = \left(\frac{B_0^2}{2B\rho} + \frac{B_0^2 \cdot k_x^2}{2B\rho \cdot k_0^2}\right) \cdot L$$
$$\int_L S(s)ds = -\left(\frac{B_0^2}{B\rho} + \frac{B_0^2 \cdot k_x^2}{2B\rho \cdot k_0^2}\right) \cdot k_x^2 \cdot \delta \cdot L$$
$$\int_L O(s)ds = -\left(\frac{3B_0^4}{8B\rho^3} + \frac{3B_0^2 \cdot k_x^2}{2B\rho} + \frac{3B_0^4 \cdot k_x^2}{8B\rho^3 \cdot k_0^2}\right) \cdot L$$

where: δ – horizontal orbit displacement relative SC wiggler axis.

Orbit displacement δ leads to occurrence of nonzero first field integrals and nonzero integral of a sextupole field component. In case $k_x = 0$ (two-dimensional field at infinitely wide poles of magnets) field integrals and sextupole field component are equal to zero, but gradient and octupole field components are nonzero values:

$$\int_L G(s)ds = \left(\frac{B_0^2}{2B\rho}\right) \cdot L \qquad (6)$$
$$\int_L O(s)ds = -\left(\frac{3B_0^4}{8B\rho^3}\right) \cdot L$$

WIGGLERS USED AS GENERATORS OF SYNCHROTRON RADIATION

The Budker INP has fabricated more than one dozen of different wigglers, which may be divided into three groups: high field wigglers, medium field wigglers and short period wigglers (see Tables 1,2,3).

High Field Superconducting Multipole Wigglers

This type of the wigglers are installing on SR sources with relative low electron energy on purpose to expand a photon energy range to more hard X-ray. As a rule one wiggler may give a SR beam for 3 or more independent beamlines (Figure 3). This kind of the wiggler to be installed on a storage ring with electron energy of 6-8 GeV can give the chance to development of new researches, including possibility of creation of bright sources of positrons and neutrons. (On SR sources with electron energy 1-2 GeV it also can be used as a source of terahertz undulator radiations).

Table 1: List of the high field wigglers

	Magnetic field, normal	Poles number (main + side)	Pole gap, mm	Period mm
7Twiggler BESSY-II	7.0	13 + 4	19	148
7.5Twiggler SIBERIA	7.5	19 + 2	19	164
7.5Twiggler CAMD LSU	7.5	11+4	25.2	193.4

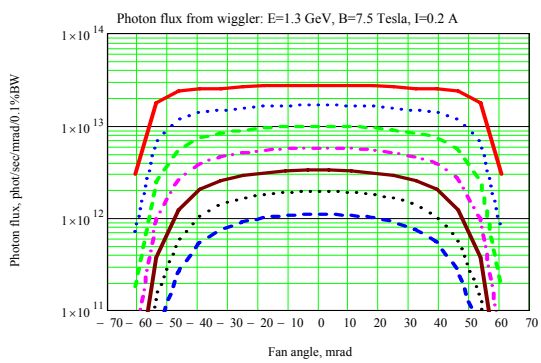

Figure 3: Spectral – angle photon flux distribution from 7.5 Tesla 15 pole SC wiggler for CAMD LSU.

ISBN 978-3-95450-170-0

In spite of the fact that undulation parameter

$$K = 0.934 * B_0(T) \cdot \lambda(cm) \quad (7)$$

takes on values 100-140 for this group of the wigglers, the photon spectrum has an undulator properties in low photon energy range (Figure 4).

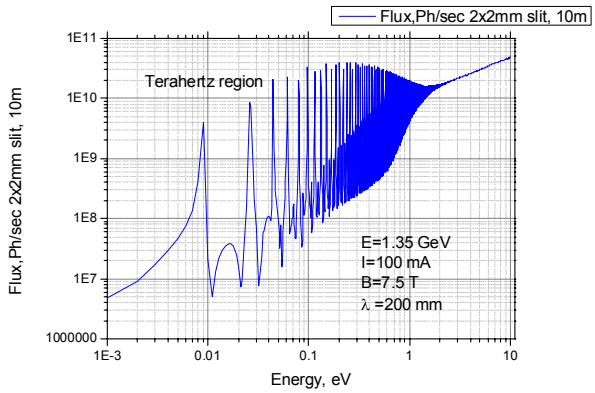

Figure 4: Low photon energy spectrum of radiation from 7.5T wiggler CAMD LSU .

Medium Field and Medium Period Wigglers

This type of the wigglers is most popular for installing on SR sources with 2-3 GeV electron energy on purpose to create very high photon flux of hard X-ray in range 10-100 keV. As a rule one wiggler may give a SR beam for 1 beamline which is equipped by many techniques and can be used in different investigations.

Table 2: List of the medium magnetic field SC wigglers

	Magnetic field, normal	Poles number (main + side)	Pole gap, mm	Period mm
3.5T wiggler ELETTRA,	3.5	45 + 4	16.5	64
3.5 T wiggler DLS	3.5	45 + 4	16.5	60
4.2 T wiggler CLS	4.2	25 + 2	14.5	48
4.2 T wiggler DLS	4.2	45 + 4	13.8	48
4.1 T wiggler LNLS	4.1	31 + 4	18.4	60
4.2 T wiggler ASHo,	4.2	59+4	15.2	50.5
2.5 T wiggler KIT	2.5	36+4	19	46.88

As a rule beamlines of this type wiggler are very long (more than 100 m). For example, beamlines of the SC wigglers in CLS (Canada) and ASHo (Australia) are used for biomedical imaging and therapy. The SC wigglers in DLS (England) are used for investigation of extreme conditions of materials and for Joint engineering, environmental and processing.

Main magnetic element of the superconducting wigglers with medium period is a magnetic pole with 2-sections horizontal racetrack coil (Figure 5). Superconducting NbTi/Cu wire with diameter of 0.9mm and critical current 650A at 7 Tesla magnetic field was used. Two section coil with optimal currents in the sections gives 15% increasing maximum field in comparison with an one section coil with the same sizes.

Figure 5: Main element of the medium field SC wigglers.

Short Period Wigglers

This type of the wigglers has a K-value about 5-7 and its spectrum properties are very close to undulators. The wiggler installed on SR sources with 2-3 GeV electron energy creates photon flux of very high brightness of X-ray in range of 6--50 keV.

Table 3: List of SC wigglers with short period

	Magnetic field, normal	Poles number (main + side)	Pole gap, mm	Period mm
2 T wiggler CLS	2.0	61 + 2	13.5	<34>
2.1T wiggler ALBA-CELLS	2.1	117+ 2	12.6	30

Figure 6: Assembling of 2 Tesla SC multipole wiggler for ALBA-CELLS (Spain).

Table 3 shows the information about short period wigglers. The wiggler for CLS made by the SC wire in the diameter of 0.9 mm, and the ALBA-CELLS wiggler made of the wire of 0.5mm. These wigglers are very close to the SC undulators with a large K-value (K~6) and the spectrum in the low photon energy range has undulator characteristics whereas at the higher photon energy the spectrum is the SR spectrum (see Figure **8**). Achievement of such advanced parameters of wire is caused by reduction of copper percentage in a conductor down to 30%. Thus the enhanced attention needs to be given for protection of windings since the using of such wire increases the risk of destroying of superconducting wire during a quench. Superconducting coils of the wiggler are protected from damaging during quench by shunts with resistance of 0.1 Ohm and cold diodes.

ISBN 978-3-95450-170-0

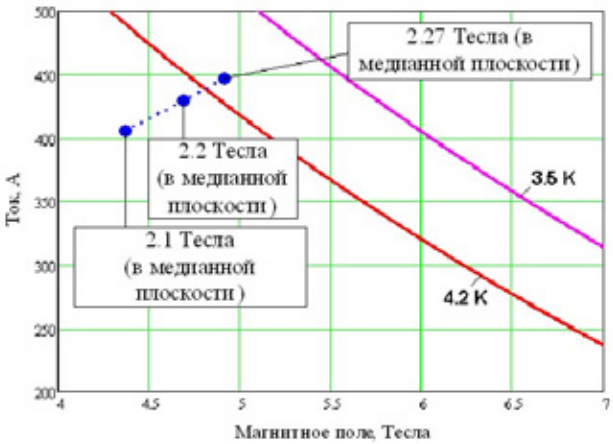

Figure 7: Load curves of the SC wire at different temperature and operation points.

Despite of rather small level of a magnetic field 2.1 T on median plane, the field on the coils reaches the value of 4.7 T and the superconducting wire is close to a critical condition (Figure 7). The experience acquired with the short period superconducting multipole wigglers on the base of the racetrack type coils gives the assurance that such technology can be successful for creation of superconducting undulators with the period down to 16 mm and without any length limitation of the undulator.

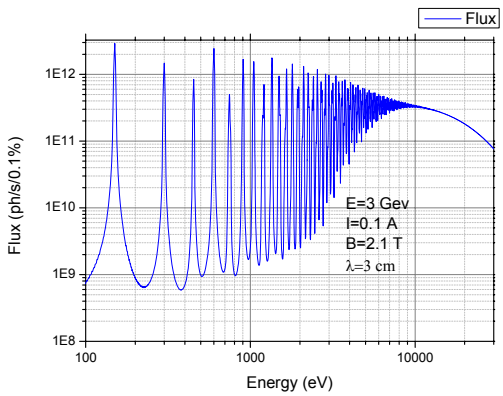

Figure 8: Spectrum photon flux through 1x1 mm^2 at 30m from 2T SC multipole wiggler ALBA CELLS.

CRYOGENIC SYSTEM OF THE WIGGLERS

The cryostat for the superconducting wigglers has been designed and made in Budker INP for continuous autonomic work in conditions of the limited access and raised radiation. The superconducting magnet is immersed into a vessel with liquid helium. The vacuum chamber for electron beam is passing through the magnet and it is a part of the vessel having liquid helium temperature. To provide zero liquid helium consumption, four 2-stage cryocoolers are used which intercept thermal load from thermal screens and current leads and from the copper liner passing inside the vacuum (Figure **9**).

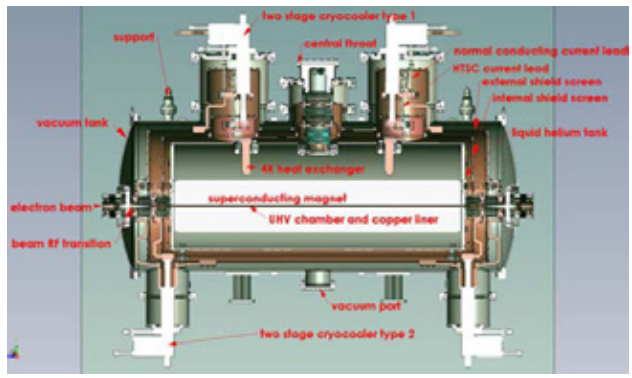

Figure 9: Sketch of the cryostat for SC wigglers.

Two cryocoolers with stages of 4K and 50K (type 1) and two cryocoolers with stages of 10K and 50K (type 2) are used for this aim. Stages with temperature ~50K of all cryocoolers are used for cooling external shield screen intercepting of heat coming through electron vacuum chamber, radiation from warm walls of housing and heat coming from normal conducting current leads due to its heat conductivity and Joule heat. Type 1 cryocoolers are assembled together with current leads block, consisting of normal conducting part and high-temperature superconductors (HTSC) (Figure 10).

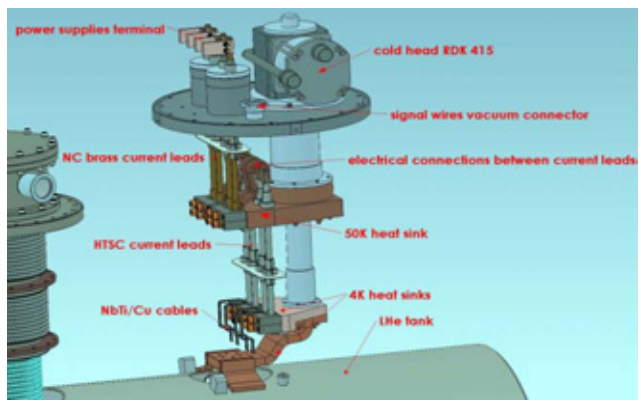

Figure 10: Current leads assembling with cryocooler type 1.

The second stages of type 2 cryocoolers are used for cooling down of 20K shield screen and for interception of released heat in the copper liner when electron beam is passing through the liner. The copper liner represents a copper tube in length about 2 m which is inserted into the electron beam vacuum chamber. The gap between the liner and the vacuum chamber is kept with use of special supports made of a material with small heat conductivity (Figure 11). Released heat in copper liner stimulated by electron beam (image current, electron clouds, synchrotron radiation etc.), is withdraw to type 2 cryocoolers using high heat conductivity of copper. Cooling time of the all system is about 24-36 hours and depends on magnet weight. Insulating vacuum at steady state of the magnet at liquid helium temperature corresponds to 10^{-7} - 10^{-8} Torr. The second stages of cryocoolers type 1 are equipped with copper heat

ISBN 978-3-95450-170-0

exchangers which are situated in gas helium inside liquid helium tank.

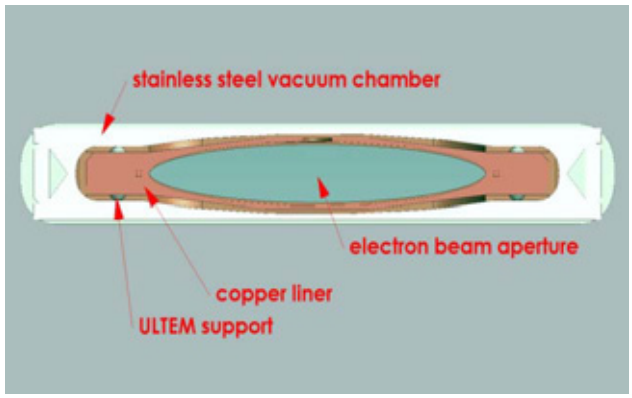

Figure 11: Cross section of UHV chamber and copper liner.

These heat exchangers liquify helium gas effectively reducing the magnet temperature and pressure in the helium tank. The equilibrium temperature can be decreased down to 3.0-3.6K and, accordingly, pressure in a tank can decrease till 0.3-0.5 bar under condition of isolation the helium tank from environment. Isolation should be reliable enough to prevent danger of air leak into helium tank from environment and creation of ice blockade during long term work with the lowered pressure in the helium tank. Temperature of HTSC current leads is in a range of 40-50K at different operating modes with or without currents in the wiggler coils. Protection of HTSC current leads from overheat and combustion is based on the temperature sensors located in junctions of normal conducting current leads with HTSC current leads. If temperature rise to higher level than 60K in these parts wiggler control system send a command to go slowly magnetic field down. If the temperature is above 65K then hard ware interlock sends a signal for switching-off of the power supplies.

CONCLUSION

The superconducting wigglers and the cryostats described above have proved to be so reliable and effective that it is possible to ensure a reliable and independent operation for a long time in a mode of limited access. Depending on the overall performance change of the cryocoolers with time the magnet temperature can change within 3.2-4.2K. Above 10 superconducting wigglers with this kind of cryostats are successfully working in various centres of synchrotron radiations (CLS (Canada), DLS (England), LNLS (Brazil), ELETTRA (Italy), BESSY (Germany), CAMD (USA), Siberia (Russia), ASHo (Australia), ALBA-CELLS (Spain), KIT (Germany).

As a plan for the next step of the superconducting magnet developing is further improvement of the superconducting magnets quality used as light sources, design and fabrication of the SC undulators with a short period (16-25 mm) and further upgrading of the cryogenic systems to the systems with indirect cooling of magnets.

REFERENCES

[1] Barkov, L. M. et al. (1978). A proposal to install a superconductive wiggler magnet on the storage ring VEPP-3 for generation of the synchrotron radiation. *Nuclear Instruments and Methods*, 152, pp. 23–29.

[2] Mezentsev, N. and Perevedentsev, E. (2005). Survey of superconducting insertion devices for light sources. http://accelconf.web.cern.ch/AccelConf/p05 /PAPERS/ TOAA003.PDF

[3] Batrakov A. et al. Superconducting Insertion Devices for Light Sources at Budker INP, Ninth International Conference on Synchrotron Radiation Instrumentation. AIP Conference Proceedings, Volume 879, pp. 305-310 (2007).

[4] Eric Walen, Nikolay Mezentsev, Superconducting wigglers, Synchrotron radiation news, May/June 2011, Vol24, №3, p.3-9.

[5] Nikolay Mezentsev, High field superconducting magnets for generation of synchrotron radiation, Pan Stanford publishing, ”SYNCHROTRON RADIATION AND STRUCTURAL PROTEOMICS”, V.3 Pan Stanford Series on Nanobiotechnology.

[6] Berger D. et al. A Superconducting 7T multipole wiggler for BESSY II: Main challenges and first field measurements. http://accelconf.web.cern.ch/AccelConf/e02/PAPERS/TU PLE030.pdf

[7] Zangrando D. et al. A Superconducting 3.5T multipole wiggler for ELETTRA storage ring. http://accelconf.web.cern.ch/AccelConf/e02/PAPERS/TU PLE044.pd

[8] Borovikov V. et al. Superconducting 7 Tesla wiggler for LSU-CAMD. Journal of Synchrotron Radiation (1998), Vol.5 Part 3, p.440-442.

[9] Zolotarev K.V. et al. High magnetic field superconducting magnets fabricated in Budker INP for SR generation. RuPAC XIX, p.40-44. http://accelconf.web.cern.ch/AccelConf/r04/papers/THFI0 1.PD

[10] Khrushchev S. et al. 3.5 Tesla 49-pole Superconducting Wiggler for DLS. RuPAC 2006.

[11] Khruschev S.V. et al, 27-Pole 4.2 T wiggler for biomedical imaging and therapy beamline at the Canadian light source. NIM A603 (2009), p. 7-9.

[13] S.V. Khrushchev et al, Superconducting 119-pole wiggler for ALBA light source. IPAC 2011, http://www.ipac2011.org/pre_press/THPC172.PDF

ISBN 978-3-95450-170-0

PRODUCTION OF SUPERCONDUCTING EQUIPMENT AT IHEP

S. Kozub, A. Ageyev, I. Bogdanov, E. Kashtanov, P. Slabodchikov, V. Sytnik,
P. Shcherbakov, L. Shirshov, L. Tkachenko, S. Zinchenko, IHEP, Protvino, Russia

Abstract

The report overviews the recent SC-related R&D and production activity at IHEP. The scope of the paper extends over the items to follow. Two superconducting magnetic systems of Electron Lens for the Tevatron collider were developed, manufactured and successfully brought into operation. 42 cryogenic electrical feed boxes of various types for the Large Hadron Collider were developed, produced and commissioned. Results of development of fast-cycling SC magnets for the FAIR project are discussed. Operational experience acquired with the largest in Russia cryogenic system for cooling with a superfluid helium of SC RF separator for the beam transfer line #21from the U-70 machine is presented. Test-and-trial results with HTS current leads and dipole magnet employing Bi2223 as well as racetrack coils made of second-generation HTS are reviewed.

LOW TEMPERATURE SC MAGNETS

New generation of high energy proton accelerators is based on superconducting (SC) magnets. Cooperation with international scientific accelerator centers was developed in last 15 years. In 1999 – 2000 and 2002 – 2003 two SC magnetic systems of Tevatron Electron Lens for Fermilab, USA were developed and produced. These systems were placed in the TEVATRON accelerator (Fig.1) and operated up to now.

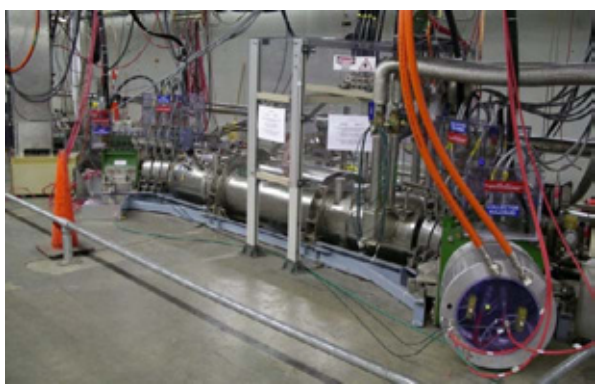

Figure 1: SC magnetic system of Tevatron Electron Lens.

The system consists of seven SC and ten copper magnets [1]. The main SC solenoid has 6.5 T nominal magnetic field, 2.5m length, 152 mm coil inner diameter. The solenoid coil was wound by the Rutherford type cable from 10 SC wires of 0.85 mm diameter. A turn number of the solenoid is 7238 and the nominal current is 1800 A. Six SC steering dipoles were placed over the solenoid. Two dipoles of 1840 mm length were arranged in the centre and four dipoles of 250 mm length in the end parts of the solenoid. The central dipole created 0.2 T magnetic field at 50 A current and the end dipole had 0.8 T at 200 A. All dipoles were wound by a cable, transposed from 8 SC wires of 0.3 mm diameter.

The system has gun and collector solenoids with 250 mm inner diameter, 474 mm outer diameter, 300 mm length, which create 0.4 T magnetic field in the aperture. Copper corrector coils are placed inside these solenoids. Three bending electron beam solenoids with 390 mm inner diameter, 500 mm outer diameter, 72 mm length are set between the cryostat and the gun solenoid as well as the same between the cryostat and the collector solenoid. A turn number of the solenoid is 48 at the nominal current 357 A. The gun, collector and bending coils of the solenoids are wound from copper cable with 8.25×8.25 mm^2 cross section having 5.5 mm diameter hole for cooling.

From 2002 IHEP collaborated with GSI, Darmstadt, Germany. SC fast cycling magnets were developed and produced for the SIS300 accelerator of the FAIR project (Facility for Ions and Antiprotons Research) [2]. The high field fast cycling dipole model is shown in Fig. 2 and its parameters are presented in Table 1.

Figure 2: SIS300 high field fast cycling dipole model.

Table 1: Parameters of the SIS300 SC fast cycling dipole

Magnetic field, T	6
Operating current, kA	6.72
Field ramp rate, T/s	1
Number of layers	2
Strand number in cable	36
AC losses (calc.), W/m	4.7
In the coil	3.4
In the iron yoke	1.3
Stored energy, kJ	260
Inductance, mH	11.7
Coil inner diameter, mm	100
Length of SC coil, m	1
Mass of magnet, ton	1.8

ISBN 978-3-95450-170-0

A special design of SC wire and cable with stainless steel core was developed for this dipole. 6.8 T magnetic field in aperture of the dipole was reached and the magnetic field did not reduced up to 1.2 T/s ramp rate [3]. The dipole with these parameters is unique in a world practice. Fig. 3 presents the training curve and Fig. 4 shows quench currents for different ramp rates of the dipole.

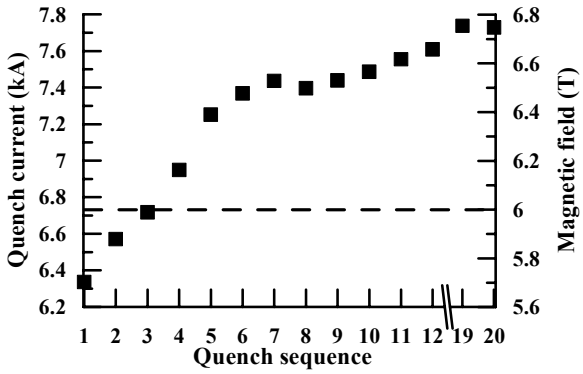

Figure 3: Training curve of the dipole.

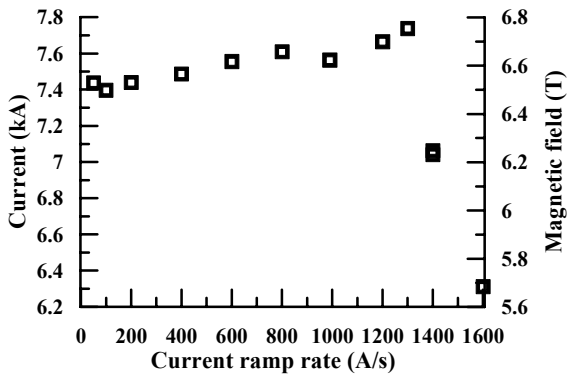

Figure 4: Ramp rate dependence of the dipole.

A prototype of the SIS300 fast cycling quadrupole was produced and tested in 2011. Design parameters of the quadrupole are 45 T/m central gradient, 10 T/m/s ramp rate, 125 mm inner diameter and 1 m effective length [4]. Fig. 5 shows a general view and Table 2 presents main parameters of the quadrupole.

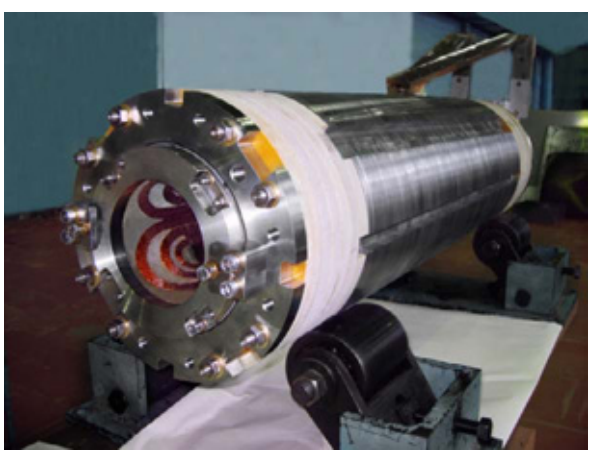

Figure 5: SIS300 fast cycling quadrupole prototype.

Table 2: Parameters of the SIS300 quadrupole prototype

Parameter	Value
Central gradient, T/m	45
Rate of central gradient, T/m/s	10
Operating current, kA	6.26
Maximum magnetic field on coil, T	3.51
Temperature margin in SIS 300 cycle, K	1.54
Stored energy, kJ	3.8
Inductance, mH	2
Number of turn in coil	80
Inner diameter of coil, mm	125
Thickness of collars, mm	22
Thickness of iron yoke, mm	52
Effective length, m	1

Fig. 6 presents training of the SIS 300 quadrupole prototype. The quench current of the magnet reached 8.2 kA in the first quench and 8.734 kA in fifth quench that corresponds to 39% current margin.

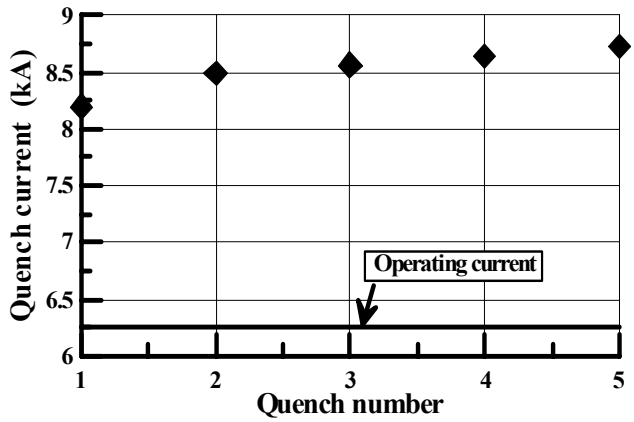

Figure 6: Quench current versus quench number of the SIS 300 quadrupole prototype.

Measurements of the quench current of the quadrupole at various ramp rates showed that the quench current was higher than 8.5 kA up to 5 kA/s (2.8 T/s) ramp rate.

Prototypes of the SIS300 fast cycling corrector magnets were developed [5]. Main requirements to these magnets are presented in Table 3.

Table 3: Requirements to SIS300 corrector magnets

Type of corrector	Force	*L*, m	*t*, s
Chromaticity sextupole	130 T/m^2	0.78	0.21
Resonance sextupole	325 T/m^2	1	0.5
Steering magnet:			
Vertical dipole	0.5 T	0.65	2.27
Horizontal dipole	0.5 T	0.65	2.27
Multipole:			
Quadrupole	1.8 T/m	0.65	2.25
Sextupole	60 T/m^2	0.65	2.18
Octupole	767 T/m^3	0.65	2.24

In the Table 3: *L* is the magnet length, *t* is a time of powering to the nominal magnetic force. The inner

ISBN 978-3-95450-170-0

diameter of the magnets is 250 mm, the operating current is up to 250 A.

SC quadruplet of the final focus system will be used for Proton Microscope for FAIR as a large-aperture, high-gradient proton imaging lens. For strong transverse focusing, a special final focus system (FFS) has to be installed at the end of the HEDgeHOB beam line. In order to provide a focal spot of the order of 1 mm, a large focal angle is needed therefore FFS will use four large-aperture high-gradient quadrupole magnets which IHEP develops at present [6]. The quadrupole cross-section is shown in Fig. 7 and its parameters are presented in Table 4.

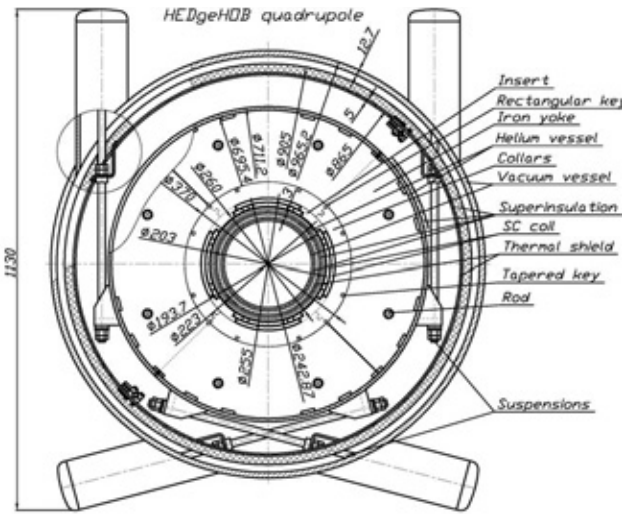

Figure 7: Cross-section of HEDgeHOB quadrupole.

Table 4: Main parameters of large-aperture high-gradient quadrupole

Central gradient, T/m	37.6
Inner diameter, mm	260
Maximal field, T	5.9
Operating current, kA	5.73
Total magnetic force/octant, kN/m	1454
Total energy in the magnet, kJ/m	613.5
Inductance, mH/m	36.5
Length of magnet, m	1.89

CRYOGENIC EQUIPMENT FOR SC SYSTEM

In frame of collaboration with DESY, Germany in 1997 IHEP produced the cryogenic helium vacuum heat exchanger for cooling 10 g/s helium flow from 300 to 2 K temperature [7], which is shown in Fig. 8.

In 2004 – 2007 years 42 Cryogenic Electrical Feed Boxes of various types for powering of SC magnets of Large Hadron Collider (Switzerland) were developed, produced and put into commission [8]. These boxes have 2600 HTS current leads with operating current from 25 to 12500 A. DFBA type box is shown in Fig. 9.

Figure 8: Cryogenic helium vacuum heat exchanger (10g/s helium flow, 300-2 K temperature range).

Figure 9: DFBA Cryogenic Electrical Feed Box for LHC.

In 2007 the largest in Russia cryogenic system for cooling SC devices by superfluid helium was put in operation at IHEP for a separated kaon beam. The system cools two SC RF cavities by superfluid helium at 1.8 K temperature [9]. The design refrigeration capacity of the cryogenic system is 280 W at 1.8 K and it should deliver 5 g/s of liquid helium per the each cavity. Main parts of the system are a satellite refrigerator and the KGU–500 cryogenic plant (Fig. 10), a cryogenic transfer line with distribution box, pumping group. The satellite refrigerator consists of a cryogenic helium vacuum heat exchanger (Fig.8), intercooling helium bath and two small helium heat exchangers, placed near each SC RF cavity. The equipment was developed and produced by IHEP. The liquid helium plant of the KGU-500 type to feed the satellite refrigerator is commercially produced by GELIYMASH company, Moscow, and it has liquefaction rate of 150 l/hr.

ISBN 978-3-95450-170-0

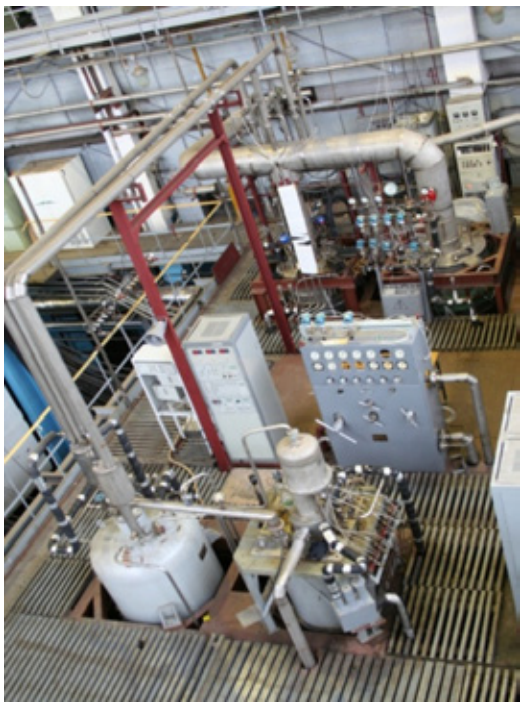

Figure 10: Cryogenic plant and large helium heat exchanger of superfluid refrigerator system of 21 channel.

To reach 1.8 K the pumping group is to pump helium tanks down to 1.64 kPa. The pumping group is arranged in 3 stages: 8 Roots blowers of the 2DVN-1500 type of the first stage compress helium from 1.5 kPa to 2.5÷3.0 kPa, 8 Roots blowers of the 2DVN-500 type of the second stage compress helium to 4.0÷5.0 kPa, and the third stage of 8 slide-valve pumps of the AVZ-180 type finally compress helium up to 103 kPa.

The control system of the cryogenic system includes 240 channels of data collection and remote control, 72 electronic modules, 5 computers for inputting and outputting information in two control rooms.

Successful operation of the cryogenic system allowed one to supply necessary parameters of SC RF cavities and record more than ten millions of kaon decay events.

HIGH TEMPERATURE SC DEVICES

At the same time activity for application of high temperature superconductor (HTS) for accelerator equipment production in collaboration with Bochvar institute was begun. In 1998 – 2000 first in Russia 600 A HTS current leads on basis of Bi2223 were developed and successfully tested in the frame of contract with CERN, Switzerland [10]. The first current lead had 33 HTS tapes with Ag+10%at.Au matrix, the second one had 16 HTS tapes and the third current lead had 14 HTS tapes with Ag+1%at.Au matrix (Fig. 11).

These current leads consisted of resistive part, cooled by 20 K helium gas, and HTS part, cooled by helium vapor. The resistive part consisted of 2300 copper wires of 0.13 mm diameter, which were placed into a stainless tube of 11 mm inner diameter and 500 mm length. The HTS part was 400 mm length. The third current lead had characteristics qualified by LHC: Heat leak to liquid helium was 0.08 W at 600 A current; a resistance of joint of resistive part with HTS was 220 nΩ and that of HTS with NbTi wire was 6 nΩ; a helium flow cooled the resistive part was 0.04 g/s; a pressure drop of the helium flow was 5 kPa.

Figure 11: 600 A HTS current leads.

The next step in application of HTS is development of first in Russia HTS dipole in 2000 – 2001 [11]. The dipole has 280x345 mm^2 cross section and 590 mm length (Fig. 12). 1 T magnetic field was reached at 25 A current and 65 K temperature in 21×70 mm^2 aperture of the dipole. “Racetrack” type coil was wound by 3.8×0.25 mm^2 HTS tape which consists of Bi2223 filaments in silver matrix. The coil was placed into yoke from electric steel.

Figure 12: HTS dipole magnet.

One of the applications of new high-temperature superconductor materials (HTS) is coils for synchronous electrical machines. The use of YBCO 2G HTS tapes (HTS-2G) allows increasing of magnetic flux density in the air gap that will increase the output power and reduce the dimensions of the motor. Such motors with improved

ISBN 978-3-95450-170-0

characteristics can be successfully used in transportation as traction motor. IHEP in collaboration with Moscow Aviation Institute designed, produced and tested HTS-2G racetrack coils for a prototype of the 50 kW synchronous motor with radial magnetic flux [12]. The HTS coils were made according to the technology of double pancake. The coil was wound on the 30 XGCA steel core (Fig. 13).

Figure 13: Four-layer racetrack coil from HTS-2G tape.

HTS coil length was 330 mm, the inner and outer diameters were 43 and 69 mm. Critical current measurements of four-layer racetrack coils from "SuperPower" HTS-2G are shown in Table 5 [13].

Table 5: Critical current of eight four-layer racetrack coils from "SuperPower" HTS-2G tapes at 77 K

Coil number	Critical current, A	
	1 μV/cm	10 μV/cm
1	38.1	41.5
2	31.4	35.4
3	34.2	38.3
4	36.3	40.3
5	31.5	35.2
6	32.8	36.4
7	34.1	37.5
8	35.9	39.6

One can see the critical current of these coils was equal to 32 – 38 A at 1 μV/cm and 35 – 41 A at 10 μV/cm. Thus, the developed production technology has allowed manufacturing these racetrack HTS coils without significant degradation of their critical current.

CONCLUSION

IHEP has meaningful experience and equipment for development and production of accelerator magnets on basis of Low Temperature Superconductors and High Temperature Superconductors as well as cryogenic system for cooling superconducting devices and systems.

At present IHEP is developing FFS superconducting large-aperture high-gradient quadrupole magnets and racetrack coils from HTS-2G tape.

REFERENCES

[1] I. Bogdanov et al. Test Results of the Magnetic System for the Tevatron Electron Lens. — European Particle Accelerator Conference EPAC 2002, Paris, France, 2002, p.p.2433-2435.

[2] A. Ageyev, I. Bogdnov I., S. Kozub, et al. Development fast cycling superconducting magnets and cryogenic system for SIS300 accelerator. Atomic energy. February 2012. V.112, N2, pp. 76-84.

[3] S. Kozub, I. Bogdnov I., V. Pokrovsky, et al. SIS 300 Dipole Model, IEEE Transaction on Applied Superconductivity, V20, N3, June 2010, pp. 200-203.

[4] S. Kozub, I. Bogdanov, E. Kashtanov, et al. "SIS300 fast-cycling superconducting quadrupole prototype", IEEE Transactions on Applied Superconductivity, Volume: 22 number 3, June 2012, p.p. 4001104.

[5] L. Tkachenko et al. Development of Quadrupole, Steering and Corrector Magnets for the SIS300, IEEE Transaction on Applied Superconductivity, V20, N3, June 2010, pp. 159- 163.

[6] L. Tkachenko, I. Bogdanov, S. Kozub, V. Sytnik, S. Zinchenko, V. Zubko, "Development of Wide-Aperture Quadrupole Magnets for Plasma Experiments in the FAIR Project", Proceedings of ASC2012, Portland, USA. ,IEEE Trans. on Applied Superconductivity, V. 23, Issue 3, Part 2, 2013.

[7] E.Kashtanov et al. Large Low Pressure Heat Exchanger for the TTF Cryogenic System. Proc. of ICEC-18, Mumbai, India, 2000, February, p.315-318.

[8] A. Perin et al. Design, production and first commissioning results of the electrical feedboxes of the LHC, Proc. of CEC-ICMC 2007 conference, Chattanooga, Tennessee USA July 16-20, 2007.

[9] A. Ageyev et al. Starting -Up and Adjustment Works on Cryogenic and Vacuum System of the Superconducting Radio-Frequency Separator, Proc. of RUPAC, 2008, p. 282.

[10] I. Bogdanov et al. Design and Test of High Temperature Superconductor Current Lead. IEEE Transactions on Applied Superconductivity, March 2000, V. 10, N 1, p.p. 1485-1488.

[11] I. V. Bogdanov et al. Test Results of HTS Dipole. — Proc. of XVII Int. Conf. on Magnet Technology, MT-17. Geneva, Swiss 2001.

[12] D. Dezhin, R. Ilyasov, S. Kozub, K. Kovalev, L. Verzhbitsky. "Synchronous motor with HTS-2G wires". Proceedings of EUCAS 2013, Genoa, Italy, September, 2013.

[13] S. Kozub, I. Bogdanov, D. Dezhin, et al. "HTS racetrack coils for electrical machines". Proceedings of 13th Cryogenics 2014 (Prague, Czech), 2014. ISBN:978-2-36215-002-9. IIRN:2014/1.

ISBN 978-3-95450-170-0

INR RAS LINAC PROTON INJECTOR 100 Hz PRR OPERATION MODE

E.S. Nikulin#, A.S. Belov, O.T. Frolov, L.P. Nechaeva, A.V. Turbabin, V.N. Zubets,
Institute for Nuclear Research of RAS, Moscow, 117312, Russia

Abstract

The injector provides linac by 400 keV protons with energy stability ±0.1%, pulsed ion current – up to 100 mA, 50 Hz pulse repetition rate (PRR) with 200 μs duration. PRR of the injector has been doubling with goal of linac average beam current increasing [1, 2]. Main stages and results of the injector modernization are presented.

Tests conducted earlier [3] have shown that pulse shape of the accelerating voltage produced by the high-voltage pulse generator (HVPG) at 100 Hz PRR has been distorted (Fig. 1).

It is seen that the high voltage (HV) value change in last forty microseconds of pulse duration is approximately 3% of the total pulse amplitude. This is unacceptable because the specified voltage change during pulse for the proton injector is ±0.1%.

Besides achieving a desired shape of HV pulse at 100 Hz PRR we have revealed two additional problems to be solved: first - instability of pulse amplitude and shape, associated with presence of a second 50 Hz series of pulses ("doubling of pulses") and second - overheating of the HVPG individual components and elements. This report contains, basically, the information relating to achievement of desired HV pulse shape. The HVPG circuit diagram is shown in Fig. 2.

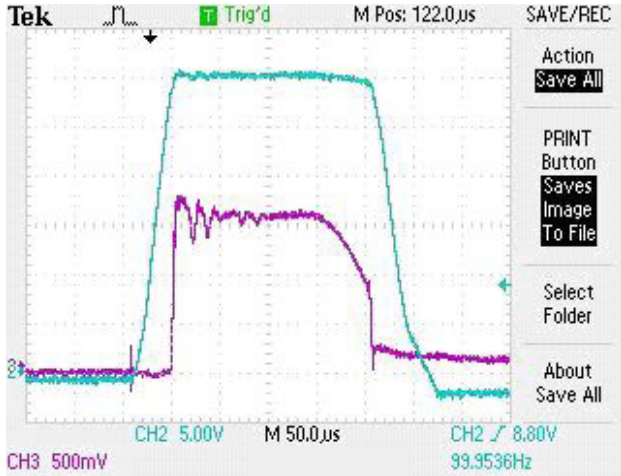

Figure 1: Oscillogram of the HVPG pulse at 100 Hz PRR (the pulse with smaller amplitude is the top of the HV pulse on a larger scale).

The HVPG consists of: 400 kV pulse transformer (PT-400), multi-cascade discriminator (MD) which stabilizes amplitude of HV pulses, sub-modulator that provides pulses with amplitude up to 20 kV to the PT-400 primary winding. The HVPG structure also includes three-phase 0 ÷ 380 V, 100 kVA auto transformer; step-up 380 V / 22 kV, 100 kVA transformer; the stabilization system of accelerating voltage which is intended to compensate the HVPG power supply slow changes, and the pulse top tilt compensation system.

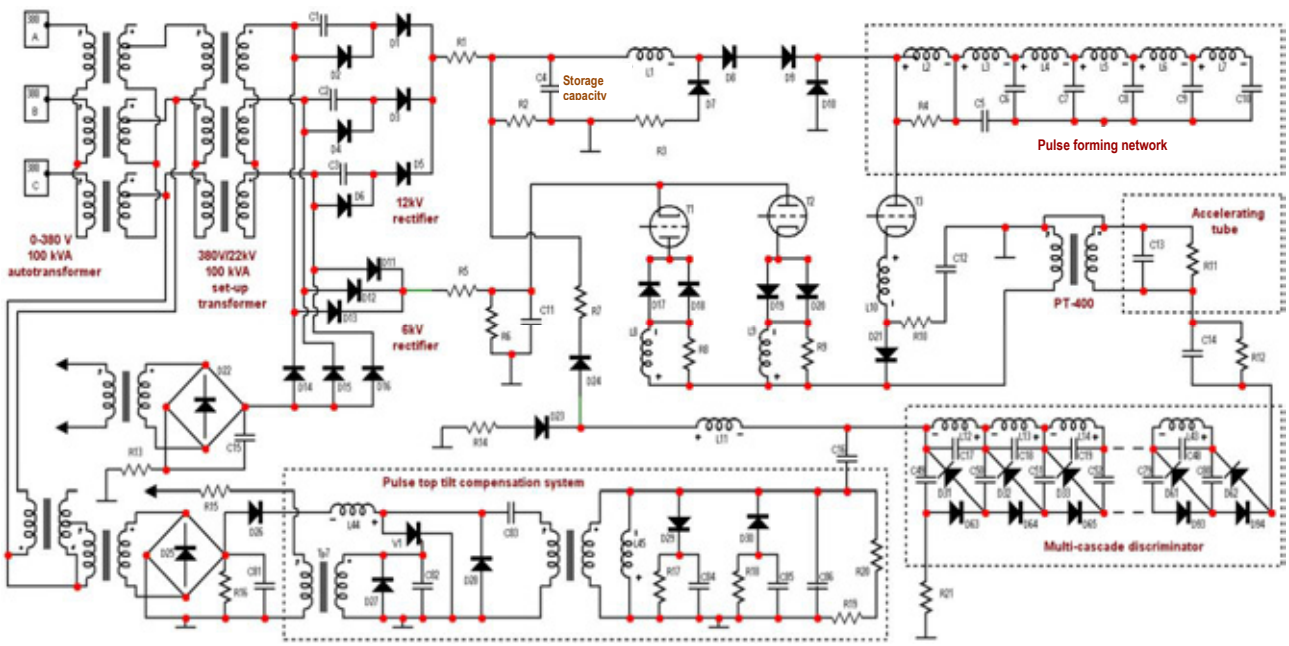

Figure 2: The proton injector HVPG electrical circuit.

#nikulin@inr.ru

ISBN 978-3-95450-170-0

HVPG voltage pulse is measured using the precision capacitive voltage divider embedded in the PT-400. Switching of the sub-modulator voltage pulses is carried out with high-voltage thyratrons.

The HVPG is developed in the 1970's at the D.V. Efremov Scientific Research Institute of Electrophysical Apparatus (NIIEFA, St. Petersburg) [4].

The HVPG operates as follows: C_4 storage capacitor of 11 μF is charged up to 12.5 kV by full-wave doubler. C_{11} leading edge shaper storage capacitor of 2.5 μF is charged up to 6 kV by six phase rectifier.

The pulse forming network (PFN) capacitors are charged in a quasiresonant way from C_4 storage capacitor through 8 H choke to a voltage of about 1.6 Uc_4.

When T_2 thyratron is opened then C_{11} capacitor is discharged through D_{19}, D_{20} diodes and L_9, R_9 buffer circuit to the PT-400 primary winding. As a result, the forced charge of constructive capacitance connected with the PT-400 secondary winding is occurred and the pulse leading edge of 40 μs base duration and of 400 kV amplitude is formed.

The trailing edge of pulse is formed by T_1 thyratron triggering. The charge which is stored in the constructive capacitance of the injector equipment is recurred in C_{11} capacity.

HV pulse voltage is applied to the accelerating tube which has the capacitive-resistive (water) voltage divider (R_{11} and C_{13}) as well as to the MD via R_{12} resistor and C_{14} capacitor.

The top of 200 μs HV pulse is formed during the PFN discharge to the PT-400 primary winding through T_3 thyratron, L_{10} choke and D_{21} diode assembly. Parameters of $C_5 \div C_{10}$ capacitors and $L_2 \div L_7$ inductances and the amount of the PFN cells are selected so as to provide the required 200 μs discharge current pulse duration.

Let us assume that HV pulse is supplied to the MD. If amplitude of the PT-400 open-circuit pulse voltage exceeds sum voltage of $C_{49} \div C_{80}$ capacitors, then $D_{31} \div D_{62}$ diodes are opened and $C_{49} \div C_{80}$ capacitors are connected in series, giving the stable (as a first approximation) 400 kV total voltage during HV pulse top. Current via the MD is limited by inner HVPG impedance and is proportional to difference between the PT-400 secondary winding open-circuit voltage and the MD voltage. This current charges the capacitors and the MD voltage slightly increases during the pulse.

$L_{12} \div L_{43}$ series-connected chokes are connected in parallel to $C_{49} \div C_{80}$ capacitors during the pulse top. Choke currents increase under influence of the U_{Ci} pulse voltage, which value is determined by relation:

$$I_{Ci} = (U_{Ci}\,\Delta T) / L_{MD}$$

where: I_{Ci} - current change in the i^{th} MD choke during the pulse, ΔT- pulse duration, L_{MD} - choke inductivity.

Between pulses MD state is changed:

- $D_{31} \div D_{62}$ diodes are closed, $D_{63} \div D_{94}$ diodes are opened and serial connection of $C_{49} \div C_{80}$ capacitors during pulse top is switched into PFN type circuit.
- an energy stored during pulse top in the MD chokes and capacitors is recurred to C_4 storage capacitor. Herewith some energy is lost, mainly in R_7 resistor.

Advanced analysis of the HVPG circuit has been performed with the software package Micro-Cap 9.0 [5]. It makes possible to receive information about processes in the HVPG which is not available by means of direct measurements when using the real HV equipment.

In particular it has been found that voltage of the MD capacitors is redistributed during a pulse: voltage of $C_{65} \div C_{80}$ capacitors ("upper" MD capacitors) decreases relative to the middle MD capacitor voltage, while voltage of $C_{49} \div C_{64}$ capacitors ("lower" MD capacitors) increases. Calculations show that C_{49} capacitor voltage reaches 18 kV, while C_{80} capacitor voltage is about 7 kV. I.e., the non-uniformity of the capacitors voltage distribution reaches a significant value. It leads to a redistribution of total current between capacitor and choke in each cascade. "Lower" choke currents reach higher values during pulse than "upper" choke currents and currents through cascade capacitors are changed in contrary. This can result in disruption of normal operation of the MD if any "lower" cascade capacitor current decreases to zero value before the end of 200 μs pulse top duration.

A cascade capacitor voltage has been decreased to the C_4 capacitor voltage value if transition processes are ending before next HV pulse beginning. The example of simulation at 100 Hz PRR with 7 H choke inductivity is shown in Fig. 3.

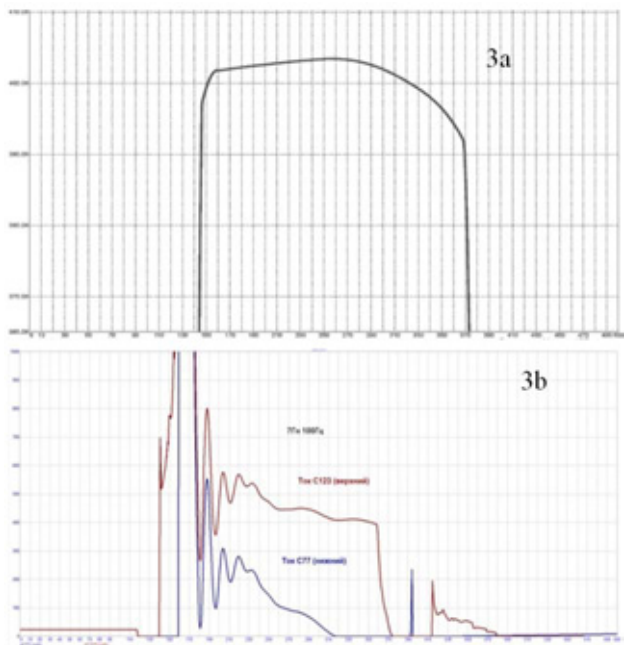

Figure 3: Simulation results for HV pulse top (3a) and for "upper" and "lower" MD capacitors current shape (3b, upper and lower curve, respectively).

Simulation results show that when the HVPG operates at 100 Hz PRR with 7 H choke inductivity then there is a "decline" with a voltage difference of about 10 kV. It begins at 115th μs. The current of "lower" MD capacitor

ISBN 978-3-95450-170-0

decreases to zero value at 155th μs in such a way (Fig. 3b): between 115th and 155th μs the zero current of capacitor signifies a closure of corresponding "direct" diode and violation of normal MD operation, which leads to appearance of "decline".

Fig. 4 shows similar curves for 20 H choke inductivity.

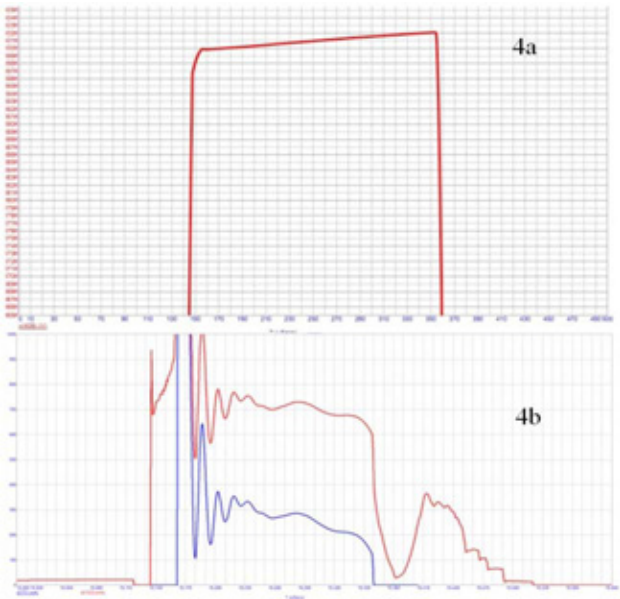

Figure 4: Simulation results with choke inductivity of 20 H.

We do not observe the HVPG pulse top "decline" (Fig. 4a) as well as vanishing of the MD "lower" capacitor current (Fig. 4b) when increasing choke inductivity up to 20 H.

The MD chokes were replaced by the new ones which have parameters as follows: L = 20 H, operating voltage – 25 kV, magnetic core - type of PL40h45-120.

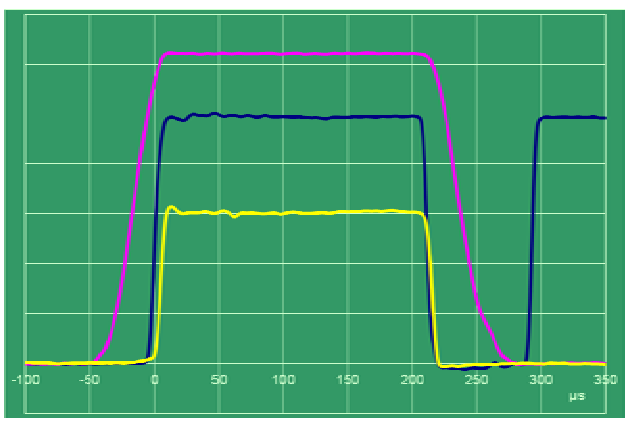

Figure 5: Oscillograms of the HVPG pulse at 100 Hz PRR (the yellow pulse with smaller amplitude is the top of HV pulse on a larger scale). Also there are (dark blue) the beam current curve and 100 mA calibrator pulse (on the right).

The oscillogram of HV pulse at 100 Hz PRR is shown in Fig. 5. From the tests carried out it follows that the changes have improved stability during HV pulse flattop at 100 Hz PRR to a desired value of ±0.1%.

CONCLUSION

The model of the high-voltage pulse generator is developed. We have achieved the satisfying accuracy and reliability of the simulation results.

The analysis has identified a number of necessary HVPG constructive changes. Its realization has allowed us to get 100 Hz PRR proton injector operation mode with 200 μs pulse duration, energy instability less than ±0.1% and ion beam current up to 100 mA.

ACKNOWLEDGMENTS

Work is supported by PhEI, Obninsk, contract # № 7-2011/5722 under the auspices of Russian Federation Ministry of Education and Science. We would like to thank A.V. Feshenko and V.L. Serov for support and help. The crucial assistance of A.V. Turbabin and Yu.Ya. Gavrilyuk in construction of the equipment is gratefully acknowledged.

REFERENCES

[1] A.N. Drugakov, A.V. Feschenko, A.I. Kvasha, A.N. Naboka, V.L. Serov. Investigation of INR DTL RF system operation of 100 Hz repetition rate // *Proceedings of RuPAC-2012, St.Peterburg, Russia, September 24-28, p. 296.*

[2] A.V. Feschenko, A.I. Kvasha, V.L. Serov. Some peculiarities of the INR DTL RF system operation at doubling of average RF power level // *Problems of atomic science and technology. Series "Nuclear Physics Investigations" (91). 2014, №3, p. 32.*

[3] V.I. Derbilov, S.K. Esin, E.S. Nikulin, O.T. Frolov, V.P. Yakushev. Average proton beam current increasing at the MMFL injector // *Problems of Atomic Science and Technology. Series "Nuclear Physics Investigations" (42). 2004, №1, p. 13.*

[4] Yu.V. Belov, etc. // *Proceedings of VIII All-Union Conference on charged particle accelerators, Dubna, 1983, v. 2, p. 159.*

[5] Micro-Cap 9.0, Electronic Circuit Analysis Program. Spectrum Software. 1021, South Wolfe Road, Sunnyvale, CA, 94086, www.spectrum-soft.com.

ISBN 978-3-95450-170-0

CW 100 keV ELECTRON RF INJECTOR FOR 40 mA AVERAGE BEAM CURRENT

V.N. Volkov, V.S. Arbuzov, K.N. Chernov, E.I. Kolobanov, S.A. Krutikhin, G.Ya. Kurkin, E.A. Kuper, I.V. Kuptsov, S.V. Motygin, V.N. Osipov, V.K. Ovchar, V.V. Repkov, V.M. Petrov, I.K. Sedlyarov, G.V. Serdobintzev, S.S. Serednjakov, M.A. Scheglov, S.V. Tararyshkin, A.G. Tribendis, I.A. Zapryagaev, BINP SB RAS, Novosibirsk, Russia
I.V. Shorikov, A.V. Telnov, N.V. Zavyalov, RFNC-VNIIEF, Sarov, Russia

Abstract

CW 100 keV electron RF gun for 40 mA average beam current was developed, built, and commissioned at BINP SB RAS. The RF gun consists of normal conducting 100 MHz RF cavity with a gridded thermo cathode unit, CW 16 kW generator with GU-92A tetrode in the output stage, and a set of LLRF electronics. The gun was tested up to the design specifications at a test bench that includes a diagnostics beam line.

The design features of different components of the gun are presented. Preparation and commissioning experience is discussed. The beam test results are summarized.

INTRODUCKTION

A 100 MHz RF electron injector was designed and manufactured at BINP for continuous wave (CW) powerful accelerator in RFNC-VNIIEF [1]. This compact accelerator, similar to the type of «RHODOTRON» [2], is designed for continuous production of short electron bunches with energy of 1.5 ÷ 7.5 MeV with power of 300 kW and higher.

Each bunch passes through a single accelerating cavity of the accelerator several times. After each pass, the beam is turned in the bending magnets. In order to preserve the transverse dimensions of the electron bunches within the aperture after passing through the bends, the bunches should have small enough energy spread (<1%) and be quite short (<0.2 ns).

An advantage of RF guns compared with static guns is the absence of cathode back bombardment with accelerated ions of residual gas ionized by an electron beam. This allows having a long lifetime of the cathodes and operating the gun continuously in the vacuum of 10^{-6} ÷ 10^{-7} Torr. Also, this enables raising the gun voltage and thus increasing the energy of the electron beam from 30-40 keV to 100 keV proportionally to the beam current to the power of 2/3, in-accordance with the Poisson law.

Furthermore, calculations showed that the increased voltage in the RF injector in combination with the effect of the longitudinal beam bunching therein provides a reduction in the energy spread of up to 0.3% (rms) in the first passage of the accelerator and the bunch shortening by up to 18 times.

RF INJECTOR

A grid-controlled thermo-cathode RF gun is based on high frequency quarter wave coaxial 100 MHz cavity shortened by a capacitance. The cavity is fed through an inductive input RF power coupler from 16 kW RF generator (based on tetrode GU-92A with a 500 W transistor preamplifier). The generator is powered by high DC voltage (8 kV) source situated in a separate rack. The control system consists of two parts: i) the control system for the cathode-grid unit consisting of a block inserted into the cavity and the blocks in the control rack, ii) control units for the cavity RF system located in the same rack. Detailed description of similar RF systems is given in [3].

The average beam current is regulated by the bunch repetition frequency and bunch charge adjustment. Bunch length is determined by the bunching effect. Maximum surface RF electric field (4 MV/m at 100 kV) is concentrated at the edges of the focusing electrode (see Fig.1), so field emission dark current from these places does not get into the beam line. Main characteristics of the RF injector are in Table 1.

Table 1: Main characteristics of the RF injector

Average current of the RF injector, mA	>40
Electron energy, keV	50÷100
Bunch duration (FWHM), ns	0.5÷2
Maximum repetition rate, MHz	100
Generator RF power, kW	<16
Operating vacuum, Torr	$<10^{-6}$

RF cavity (see Fig.1) has a bimetallic cylindrical body (1) with a diameter of 500 mm and a length of 550 mm. There is a water-cooled cylindrical electrode (2) inside the cavity with the gridded thermo-cathode unit (3) mounted on its end. The space between the focusing electrode (4) and the end wall of the cavity (5) is the accelerating gap.

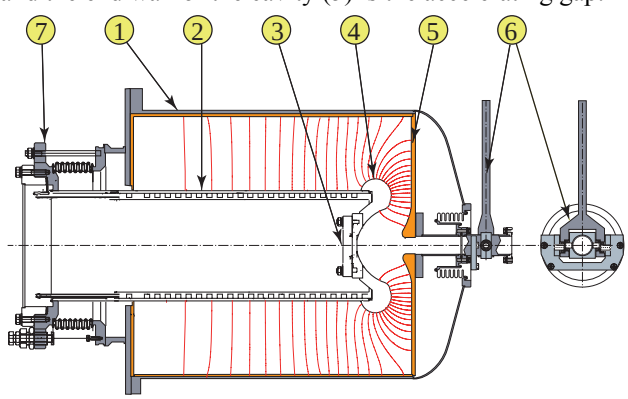

Figure 1: Sketch of the cavity RF gun with the force lines of the accelerating RF field.

ISBN 978-3-95450-170-0

At one end of the cavity there is a device for fixing the electrode and preset of the resonance frequency (7). The control electronic unit (modulator) of the cathode-grid assembly is inserted into the electrode. At the other end the cavity has a frequency tuner (6). The tuning is done by the cavity end wall deformation (5).

For the cavity manufacturing technologies were used such as electron beam welding, diamond machining on a CNC lathe, thermo-diffusion brazing in a vacuum oven of bimetallic housing (copper-to-stainless steel), copper plating inside the stainless steel housing and silver plating outside the copper housing. The cavity went through degassing heat treatment followed by an RF conditioning.

CATHODE–GRID UNIT, MODULATOR

RF gun is equipped with a replaceable cathode-grid unit produced in Russia on the basis of metal-ceramic triode RF tube GS-34 with an oxide cathode. The grid electrode of the cathode-grid unit is electron beam welded to a special flange having a vacuum seal of Conflat® type (see Fig. 2). The design is compatible also with a cathode-grid assembly from the EIMAC [4] company.

The cathode has a diameter of 12 mm. Thin grid of a "parquet" type is located at a distance of 80 μm from the cathode surface. The cathode unit provides electron bunches with maximum current of 1.5 ÷ 2.5 A, duration of 1 ns, and repetition rate up to 100 MHz.

Figure 2: Flange welded grid-cathode assembly.

The electronic equipment for cathode current control is located in a special cylindrical container (see Fig. 3), which is inserted into the electrode of the cavity and electrically connected to the cathode assembly using the triple collet.

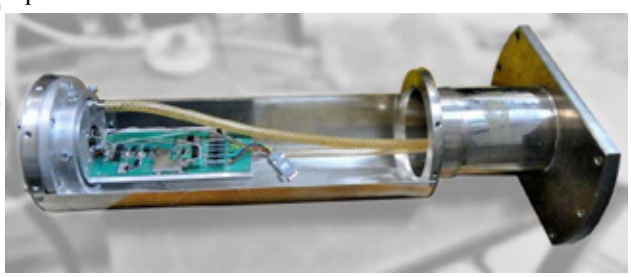

Figure 3: Plug-in container with the modulator unit.

This block works on the basis of the microwave FET transistors operating in the switching mode. This block generates pulses of 1.2 ns with adjustable amplitude of 0 ÷ -120 V and an adjustable repetition rate of 0.003 ÷ 100 MHz. Pulses are synchronized with the accelerating voltage of 100 MHz frequency. The bias DC voltage is adjustable between 30 ÷ 130 V. The unit is controlled from a computer via the communication interface of CAN-Bus type.

NUMERICAL SIMULATION

Numerical start-to-end calculations of the electron beam dynamics of RF injector were carried out for all stages of electron bunch formation: in the accelerating gap of the RF gun taking into account micron grid sizes [8], and in diagnostic beam line (see. Fig.4). Codes SAM, SLANS, ASTRA [5, 6, and 7] were used for the calculations.

Numerical calculations of the beam dynamics in the RF field of the grid-cathode assembly and in the accelerating gap of RF gun for different RF phases were performed taking into account the pulsed unlocking voltage applied to the cathode. The 1.2 ns pulse comes at the rising slope of RF voltage in the phase interval of 31 ÷ 55 degrees, at the amplitude of 50 and 100 kV voltage across the gap, and with the bunch charge of 0.4 nC.

The maximum acceleration is at the phase of 55 degrees. At lower phases the effect of longitudinal bunching appears. For example, when the phase is 31 degrees (the minimum possible phase before the bunch charge is limited) bunches get shortened by 1.5 times at the output of the RF gun (0.25m), and 2.3 times over a drift length of 2 m (see Table 2).

Table 2: Bunch characteristics of 100 kV RF gun

Distance from the cathode, m	0.25	0.25	2
RF phase at emission	55°	31°	31°
Bunch length (rms), mm	47.9	33.7	20.4
Energy spread (rms), keV	1.6	4.3	1.08
Emittance (rms), mm · mrad	10.5	9.5	21.5
Energy, keV	100	96.3	96.3

Calculations of beam dynamics in the diagnostic channel (see Fig.4) includes beam tracking through three focusing coils (2, 6) down to the target (8) made as the transition radiation sensor.

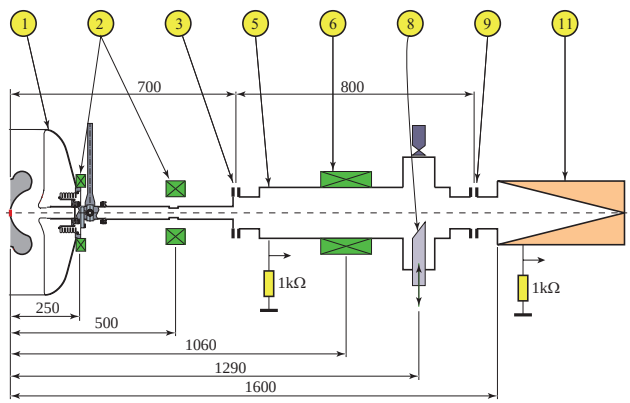

Figure 4: Sketch of the diagnostic channel. Numbering of callouts is common with Fig. 5.

ISBN 978-3-95450-170-0

STAND FOR RF GUN TESTING

A test stand for testing the RF gun with electron beam is shown in Fig. 5. The RF gun was installed on a support with cooling water manifolds; the diagnostic channel was placed on a separate support. The 16 kW RF generator, the high-voltage rack, the rack with LLRF electronics and the modulator of grid-cathode unit are also located in the stand. The stand is controlled remotely via a CAN-Bus interface.

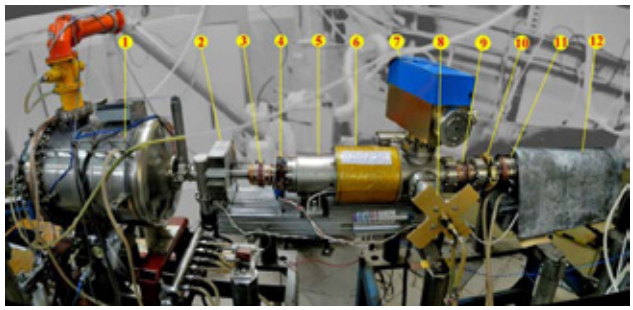

Figure 5: Diagnostic beam line. 1 - RF gun; 2 - focusing solenoid; 3 - first beam current sensor; 4 – beam steerer; 5 - vacuum chamber of 160 mm in diameter; 6 - solenoid; 7 - vacuum ion pump; 8 - movable target; 9 - the second beam current sensor; 10 - rotating beam steerer; 11 - 30 kW beam dump; 12 - lead radiation shielding.

TEST RESULTS

Calculations of the beam dynamics in the diagnostic channel (see Fig. 4) shows that the spot size on the target is substantially proportional to the emittance. When the beam emittance is 10 π·mm·mrad the spot should have a diameter of 5 mm (see Fig. 6). Exactly the same spot was observed in the experiments on the test bench (see Fig. 7).

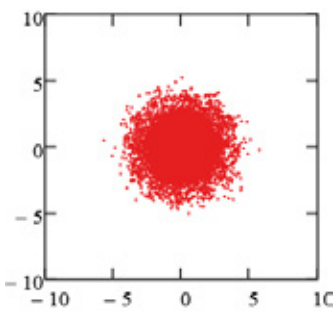

Figure 6: Numerically calculated beam spot on the target, $\sigma_{x,y}$ = 1.35 mm.

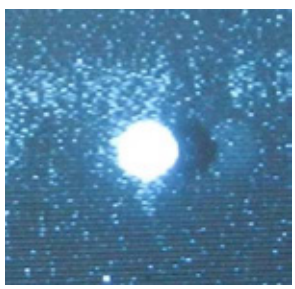

Figure 7: The spot image on the target from the video camera.

Forms of pulses from two current sensors depend on the emission phase in the grid-cathode unit. When the pulses have equal amplitudes then this corresponds to the operating phase of the maximum acceleration. When the second pulse is higher and shorter than the first one then the effect of the longitudinal bunching (shortening) over the drift space of 820 mm takes place; it means that RF phase is less than the operating phase (see Figs. 8a, 8b).

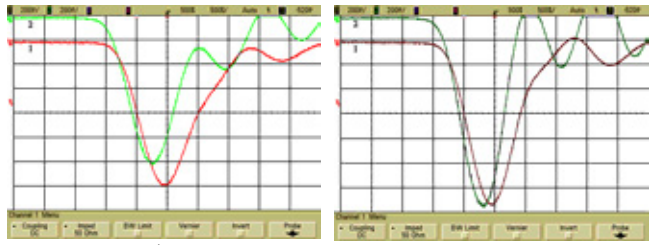

a) b)

Figure 8: Image of sensor signals for different emission phases: a) 55 °, b) 31 °. Resolution of horizontal axis is 0.5 nsec/cell.

Average current of 40 mA was obtained in the whole energy range of 50-100 keV. Continuous test runing during 8 hours at the beam energy of 100 keV, average current of 40 mA, and 100 MHz bunch repetition frequency was completed successfully.

Although the diagnostic beam line did not go through a degassing heat treatment, the vacuum in the cavity and the diagnostic system was 10^{-9} Torr without the beam. Vacuum deteriorates when the beam current increases. Setting the vacuum interlock threshold to $2 \cdot 10^{-7}$ Torr, we had to limit the beam current to 20 mA in the beginning. Within a few days it became possible to raise the current up to 40 mA due to gradual degassing of the vacuum diagnostic chamber.

CONCLUSION

CW 100 keV electron RF gun with 40 mA average beam current was developed, built, and successfully commissioned up to full design specifications at BINP SB RAS. The injector, as has been proven by the tests, is capable to operate reliably with high average beam current above 40 mA at up to 100 kV beam energy and 100 MHz bunch repetition frequency even in a poor vacuum of $10^{-6} \div 10^{-7}$ Torr. The injector will provide the required electron beams for the accelerator with the output beam power of 300 kW and above.

REFERENCES

[1] N.V. Zavyalov, et al.// Problems of Atomic Science and Technology. 2006 №2 Series: Nuclear Physics Investigations (46), – P.8-10.
[2] Y. Jongen, et al. EPAC96, Espanya, 1996, p.2687.
[3] V.S.Arbuzov, et al. // Physics Problems of High Energy Density. Proceedings of XII Chariton Thematic Science Symposium, Sarov, 2010, c. 28-32.
[4] http://www.cpii.com/eimac/index.html, Corporate Web site.
[5] Ivanov A. V., Tiunov M. A. // Proc. EPAC2002, Paris, 2002, p.1634.
[6] D.G. Myakishev, V.P. Yakovlev // Proceedings of the Particle Accelerator Conference, New York. – 1999. -- pp. 2775-2777.
[7] K. Floettmann, ASTRA User`s Manual, http://www.desy.de~mpyflo/Astra_docomentation.
[8] V. Volkov, et al. Proceedings of PAC09, Vancouver, BC, Canada, 2009.

ISBN 978-3-95450-170-0

STATUS OF LINACS WITH HIGH-FREQUENCY QUADRUPOLE FOCUSING LU-30 AND LU-30M IN IHEP

O.K.Belyaev, J.A.Budanov, V.P.Golubkov, A.J.Evstifeev, S.E.Zavjalov,
I.D. Kuzmin, E.V.Mazurov, S.A.Strekalovskikh, N.A.Chyornyj, IHEP, Protvino, Russia

Abstract

There are two RFQ DT proton linacs, named the LU-30 and LU-30M, in the SRC IHEP of NRC "Kurchatov Institute" that are presently in operation. Both are the unique machines employing radio-frequency quadrupole focusing up to 30 MeV at exit. The LU-30 machine now runs as a proton injector to the booster RC PS U-1.5 that feeds the main PS U-70 ultimately. The LU-30M is now run in a stand-alone test operation mode. Such a parallel functioning of these two accelerators allows to use the LU-30M as an experimental facility enabling R&D on new technical decisions and upgrades for the ageing LU-30. On the other hand, the routine operation of the workhorse LU-30 allows for testing of the technical decisions proposed under a heavy non-stop operation during the U-70 runs for fixed-target physics.

INTRODUCTION

The IHEP proton linacs, LU-30 and LU-30M, are the unique machines with Radio–Frequency Quadrupole (RFQ) focusing up to 30 MeV at exit [1, 2]. LU-30 was made as an experimental model. Since 1985 LU-30 has been operating as a proton injector to the booster RC PS U-1.5 on the packet-pulse mode, about 2500 hours per year with downtime (5÷7) %.

The LU-30M was developed from an experience of creation and operation of the LU-30. Emittance of the LU-30M beam reduced to a tenth and the beam transport along the LU-30M is higher then in the LU-30 as figure 1 shows.

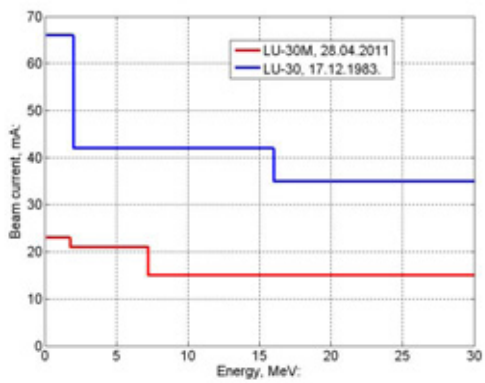

Figure 1: Beam transport in the LU-30 and LU-30M.

The other beam parameters of LU-30M are the same as the LU-30 parameters, except for the beam intensity, which is lower the project level yet. There are substantial differences in design of the accelerators:

- a modification of the electrodes of the initial part (RFQ) LU-30M allowed to halve the RFQ length;
- using the sector H-cavities in the main part LU-30M (RFQ DTL, [2]) some compensation of the decrease in accelerating rate was achieved by realizing the growth in the accelerating voltage along the accelerator;
- a modular design of the anode HV power supplies was developed for higher reliability of the RF-system [3].

Now accelerator LU-30M runs in a stand-alone test operation mode. This mode allows of using LU-30M as an experimental facility enabling R&D on new technical decisions and upgrades for increasing reliability and quality of ageing LU-30.

VACUUM BREAKDOWNS

During LU-30 operation it was noted that the breakdown frequencies for initial and main parts (RFQ, RFQ DTL) LU-30 are almost identical, but the field strength at the surface of the electrodes of this parts differs sufficiently (225 kV/cm and 380 kV/cm). Analytical treatment of the experimental dependence of the relative quality factor on the field strength at the electrodes for RFQ and RFQ DTL showed pronounced distinction between coefficients of local field enhancement for RFQ and RFQ DTL (1100 and 93 accordingly) [4]. This distinction may testify to the various factors that lead to breakdowns. According to paper [5], the values more than 200 can be explained by the presence of films and nonmetallic inclusions on the electrode surface and the smaller values – by the micro irregularities. As a result, we conclude that the products of the ion gun operation may be responsible for the pollution of the RFQ electrodes and the reduced breakdown strength.

BEAM CONDITONING

An injection system with collimators avoiding pollution of the RFQ electrodes by the ion source impurities has been developed. The optics not only effectively separates the impurities but also matches the proton beam to the RFQ in transversal motion. Figure 2 shows it schematically. A diaphragm with a hole of 3 mm in diameter is installed between two magnetic lenses (solenoids), nearby the proton beam crossover. A cylinder of 3.5 mm in diameter is placed in the middle of the second lens to separate the part of the impurity flow coming through the diaphragm hole. In addition the optics filters the transversal phase volume of the proton beam by

ISBN 978-3-95450-170-0

rejecting unconditioned protons. The root-mean-square ellipses of the transversal phase beam volume are presented in figure 3, the required and measured correspondingly.

On testing of the injection system at the LU-30M linac, a possibility of increasing the RFQ electrode field strength (to 450 kV/cm or 3.4 of Kilpatrick criterion) has been demonstrated. For reliable operation LU-30 this injection system will be placed at the input of RFQ LU-30.

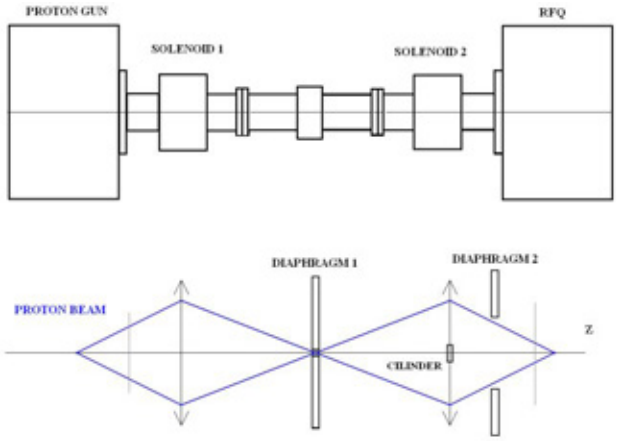

Figure 2: Optic scheme of the matching channel.

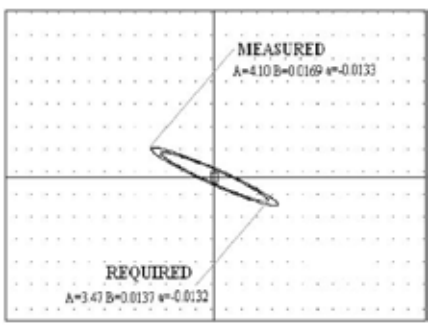

Figure 3: Root-mean-square ellipses of the transversal phase volume of the beam at the RFQ input (grid: 0.98 mm by 43.61 mrad).

FREQUENCY TRIM MODERNIZATION

The frequency trim of resonators at LU-30 and LU-30M is implemented by turning of the copper rings in magnetic field in vacuum. A 90º turn of the ring changes frequency up to 8÷25 kHz, depending on the Q-factor and size of the ring. Turning of the LU-30 rings is carried out by mechanical system with the powerful electric motor through a vacuum seal with plastic plugs and rubber collars. Such a system has the backlash and the susceptibility to mechanical deterioration.

A new system of the ring turning with SHDR-711 step motors and a metallic corrugation vacuum isolation has been developed and tested for LU-30M. Application of the system for LU-30 demanded some modification with using the powerful PL57HD76 step motor and modifying the control electronics, the design of mechanics etc. On figure 4 mechanisms of frequency trim for LU-30M and LU-30 are shown.

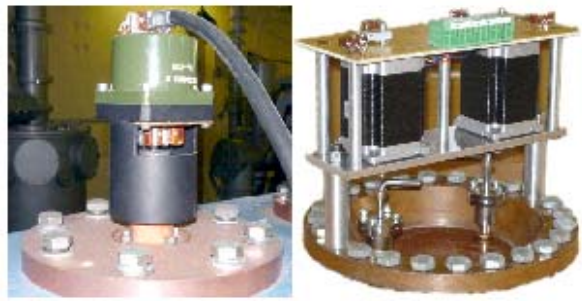

Figure 4: LU-30M (left), LU-30 frequency trim mechanics.

The control system of step motors is connected to the personal computer by means of the developed interface. The control program is created in language LabView that allows to supervision of the position of tuning rings to within 1°, and also operatively to change the program of adjustment of frequency. The system of frequency trim with step motors has been installed at LU-30M and LU-30 RFQ. We are preparing now to install it at the RFQ DTL LU-30.

TUNING OF RF BLOCKAGE

During the exploitation of the LU-30 and LU-30M a low efficiency of blocking of the high voltage (HV) modulator circuits against radio frequency (RF) was discovered. Having passed through the modulator outlet, RF voltage could disturb normal work of the low voltage modulator electronics and the measuring system. Since the high power RF systems of the LU-30 and LU-30M were identical, a common cause of the low blocking efficiency was supposed. A scheme of the HV input is shown in Figure 5.

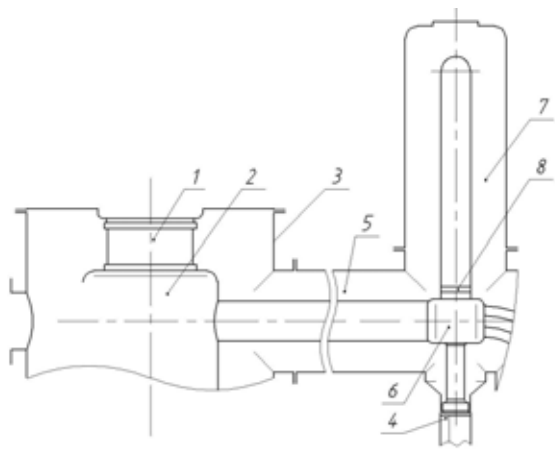

Figure 5: Scheme of the HV input.

The anode circuit consists of the GI-27AM triode (1), an anode block (2), the body (3), the HV modulator cable (4), a coaxial line (5) and rejection filter, that consists of a

ISBN 978-3-95450-170-0

clutch (6), the quarter–wavelength coaxial line (7) and the adjustment ring (8).

A theoretical and experimental studies show that the poor blocking is the result of the difference between the RF system operating frequency 148,5 MHz and the rejection filter resonance frequency (markers 1 and 2 in the figure 6). The filter frequency has been tuned at LU-30M by adjustment of the ring size (8). As a result pronounced frequency difference disappeared (figure 7).

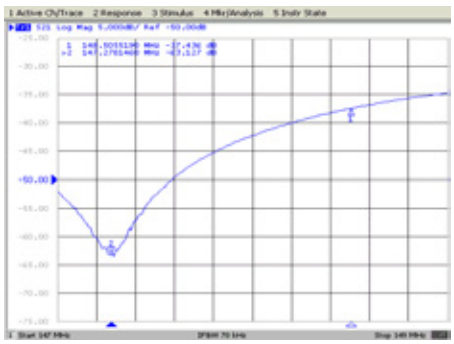

Figure 6: Frequency response characteristic before tuning.

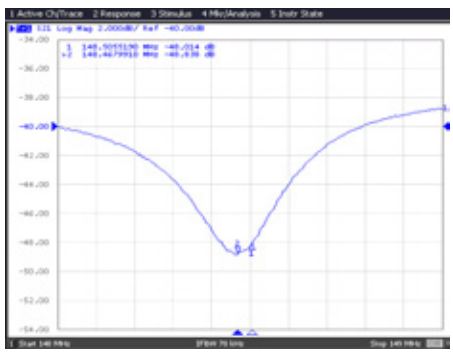

Figure 7: Frequency response characteristic after tuning.

Figure 6 and figure 7 show, that the decreasing of the frequency difference from 1.23 MHz to 48 kHz increases the blocking level of the RF filter from 37 dB to 60 dB. The same works are planned for the high power RF-system at the LU-30. The study [6] shows the necessity of the interference filtration to increase the electronic system reliability at the accelerator complex.

DROOP COMPENSATION

The observed accelerating voltage drooping at the resonators during the beam passing can be partially offset by increasing the output signal of the low power cascade. For that reason a 200 W amplifier was developed and tested. It's based on the UM145-300 "Pallet" module and controlled by an impulse generator.

Figure 8 shows the increase in pulse amplitude of the amplifier's output signal that corresponds to the beam's passage duration of 10 μs. Testing the system of voltage drooping compensation at the LU-30 is under way now.

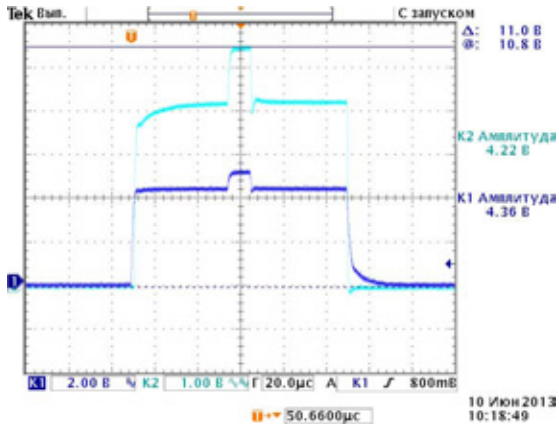

Figure 8: Oscillograms of the power amplifier: output RF impulse (up) and generator impulse (down).

CONCLUSION

It's shown in the paper that simultaneous functioning of two similar accelerators (one operates as a proton injector, another works in the standalone test mode) expands possibilities of increasing the reliability and the beam quality by carrying over the LU-30 the new technical decisions after its testing at the LU-30M. The LU-30M is used as an experimental facility. On the other hand, the routine operation of LU-30 allows a long-term testing of the technical decisions in heavy conditions.

REFERENCES

[1] A.A. Egorov, V.A. Zenin, S.A. Ilievsky et. al. "Start-up of the Linear Accelerator Protons URAL-30", IHEP preprint 1979-79-151, Serpukhov, Russia (1979).

[2] Yu. Budanov, A. Maltsev, I. Maltsev et. al. RFQ Drift-Tube Proton Linac in IHEP - Proceed. of 22-nd Int. Linear Accelerator Conference LINAC-2004, Luebeck, 2004, vol. 1, pp. 285-287. CD ROM Proc. ID: TUP01

[3] A.A. Evstifeev, A. Vorobiev. The Habits of Development Power Modular Grid for Supply RF-System Linear Accelerator of Ions: IHEP Preprint 2008-9. – Protvino, Russia (2008).

[4] O.K. Belyaev, V.E. Borodin, V.B. Stepanov. "Enhancement of the Breakdown Strength in Accelerators with Radio-Frequency Quadrupole Focusing". Instruments and Experimental Techniques, Vol. 44, No. 4, 2001, pp. 444–448.

[5] J.W. Wang, "Properties of Periodic Accelerating Structures for Linear Colliders". SLAC-339, VC-28(A), July 1989

[6] J. Galambos. "SNS performance and the next generation of high power accelerators". –Proceedings of PAC 2013, Pasadena, CA USA, pp.1443-1447.

ISBN 978-3-95450-170-0

GEOMETRY OF QUADRUPOLE MAGNET FOR THE U-3.5 ACCELERATOR IN THE OMEGA PROJECT

L. Tkachenko, S. Kozub, P. Shcherbakov,
Institute for High Energy Physics, Protvino, Moscow region, Russia

Abstract

Accelerating complex of intensive beams of charged particles (project Omega) is being developed at IHEP. The main part of this complex is 3.5 GeV ring accelerator. The basic parameters of the quadrupole magnet for this ring are: 5.564 T/m central gradient in the 102.9 mm radius of the "good field"; the injection gradient is 1.222 T/m; the gradient ramp rate is 334 T/m/s. Different profiles of the poles were considered for the purpose of selecting the most optimal 2D and 3D geometries of the magnet. The basic parameters of the optimal geometries are presented.

INTRODUCTION

IHEP (Protvino, Russia) is developing an accelerating complex of charged particles of high intensity (project OMEGA [1]). This complex is designed to create megawatt power beams. The OMEGA project consists of a new cascade of high-intensity accelerators, which includes a linear accelerator of H^- ions and protons with energy of 400 MeV, followed by a rapid cycling synchrotron with energy of 3.5 GeV. Basic parameters and preliminary optimization of the geometry of the main dipole were presented in [2]. Further the 2D and 3D geometry optimization for the main quadrupole in the 3.5 GeV ring is considered.

THE OMEGA PROJECT

The OMEGA project involves the construction of Accelerator Complex for Intense Hadron Beams. This multipurpose mega-project is being discussed at IHEP [1, 3] and is shown in Fig. 1. The proposal outlines a long-term plan to develop the accelerator and experimental facilities on the IHEP grounds for fixed-target research within and beyond the scopes of elementary particle physics. The base-line design foresees construction of a pulsed facility that will exceed 1 MW of proton beam average power, will have a pulse rate of 25 Hz, pulse width ≤ 1.5 μs, clear staging, site-specific integration and upgraded plans, and reduced technical risk (through use of proven technologies). The facility comprises of a non-superconducting 400 MeV linear accelerator LU-400 followed by a 3.5 GeV rapid cycled proton synchrotron (RC PS) U-3.5. At a later stage, the U-3.5 is engaged as a new injector to the existing U-70 PS, or its updated successor. A particular stage of the project addresses either applied or fundamental science (Fig. 1). Stage-1 assumes construction of a short-pulse accelerator-driven 1 MW neutron source for applied research (material and life sciences).

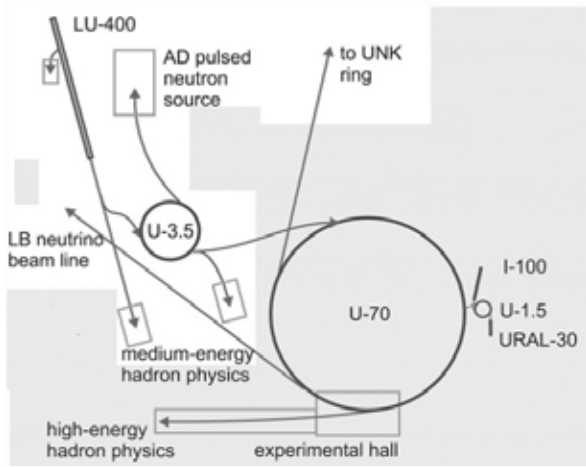

Figure 1: Tentative layout of the OMEGA facility.

Table 1: Specifications of U-3.5 (Project).

Specification	Value
Energy (kinetic), E, GeV:	0.4–3.5
Orbit length, L, m:	445.11
Magnetic rigidity, $B\rho$, T·m:	3.18–14.47
Compaction factor, α:	0.0173
Transition gamma, γ_t:	7.60
Intensity, N, ppp:	$7.5 \cdot 10^{13}$
Ramping time, t_R, s:	0.020
Cycle period, T, s:	0.040
Average beam current, μA:	300
Beam power, P, MW:	>1
RF harmonic, h:	9
Radio frequency, f_{RF}, MHz:	4.322–5.925
Net RF voltage, V_{RF}, kV/turn:	720
Lattice period:	FODO (90°)
No. of periods:	36
No. of super periods:	6
Betatron tune (H/V):	9.15/7.20

The goal for the next stage-2 is to develop the second direction of fast extraction from the U-3.5 to feed a new experimental zone dedicated to intense-beam medium-energy hadron physics. At a later stage the U-3.5 is engaged as a new injector to the existing U-70 PS, or its updated successor. To this end, the orbit length and RF harmonic number of the U-3.5 amount to 3/10 of those in the U-70. It facilitates, at most, a 3-train bunch-to-bucket transfer from U-3.5 to the U-70 ring thus yielding a beam pattern 3 × (9 filled + 1 empty) bunches there. Apart from the lower-energy mode of a 3.5 GeV proton beam stretcher delivering slow spills, the U-70 will accelerate

ISBN 978-3-95450-170-0

intense beam to higher energies. The core of the OMEGA Project constitutes a new 3.5 GeV rapid cycled proton synchrotron U-3.5, ramped at 25 Hz (sinusoidal) and yielding $7.5 \cdot 10^{13}$ ppp. Other specifications of the machine are listed in Table 1.

REQUIREMENTS TO QUADRUPOLE

The RCS quadrupole of U-3.5 is characterized:

- The central gradient is 5.564 T/m;
- The injection gradient is 1.222 T/m;
- The gradient ramp rate is 334 T/m/s;
- The repetition field frequency f is 25 Hz;
- The radius of the good field region is 102.8 mm;
- Integral field multipole b_6^{int} must be less than $|2| \times 10^{-4}$.

MATERIALS

Current-carrying elements should be developed so that reduction of the large dynamic losses in the cable is taken into account, as well as possibility of manufacturing the cable or its acquisition. For further calculations we selected the cable, which was designed for the J-PARC and SCNS projects [4, 5]. It was made of 33 aluminum wires of 3.2 mm diameter, which were wound on a 10 mm diameter tube for water cooling. Then the bare winding is formed into a square with a 20 mm side. The coils in all types of magnets consist of $N = 16$ turns. The total current $I_T = NI_{op}$ (I_{op} is the operating current) is equal to 36.38 kA. M250-50 steel [6] is selected for an iron yoke. It is characterized: the maximal magnetic permeability is >7500; the coercive force is 33 A/m; the saturation magnetization is 2.05 T; the sheets are 0.5 mm thick.

2D GEOMETRY OPTIMIZATION

The magnet cross section is shown in Fig. 2. The main task of optimization is to minimize the overall dimensions of the cross section keeping the low order multipoles within the required limits. In the magnet design the computer code MULTIC [7] was used. The field quality in the aperture is formed by poles of the magnet, the profile of which can be made either by a hyperbola, or a circular arc. Two parameters can be used for goptimization: the pole width, which is defined by horizontal coordinate of the bottom pole corner x_p, and a thickness of the iron yoke ΔFe. Note that the x_p influences both on the multipole b_6 and the normalized gradient b_2, while ΔFe mainly affects only on b_2. The normalization is performed on a central gradient at infinite permeability in the iron yoke. Fig. 3 and Fig. 4 present dependences of normalized gradient and multipole b_6 on coordinate x_p for two profiles of the pole and two radii of aperture r_{ap}. For each curve in Fig. 4 there is an optimal $x_p = X_{opt}$, at which $b_6 = 0$ and it has a linear dependence on r_{ap} within [105 mm, 130 mm]:

$$X_{opt} = 0.31413 + 1.52543\ r_{ap} \text{ (hyperbola)};$$
$$X_{opt} = -0.01305 + 1.52377\ r_{ap} \text{ (arc)}.$$

Figure 2: General view of the quadrupole magnet.

Results, presented in Fig. 3 and Fig. 4, were calculated at $\Delta Fe = 200$ mm. Dependence of normalized gradient b_2 on ΔFe is shown in Fig. 5. Taking into account that the yoke should have holes and cutouts for mounting, it is necessary to choose the thickness not less than 140 mm.

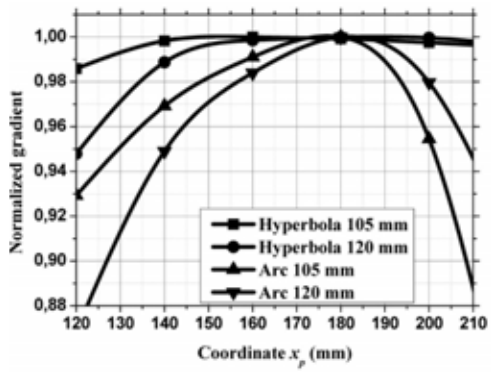

Figure 3: Normalized gradient versus coordinate x_p.

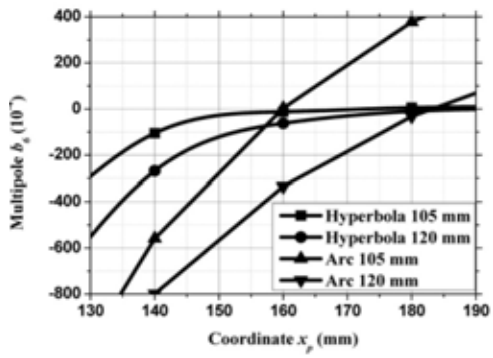

Figure 4: Multipole b_6 gradient versus coordinate x_p.

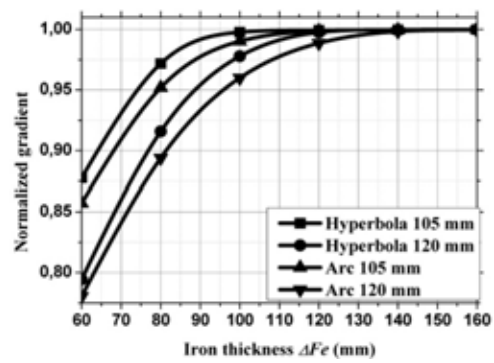

Figure 5: Normalized gradient versus iron thickness.

ISBN 978-3-95450-170-0

3D GEOMETRY OPTIMIZATION

The general view of the magnet is shown in Fig. 6.

Figure 6: General view of the magnet.

Further we will consider only the 120 mm aperture. The final its diameter will be made after the determination process sizes, in particular, a vacuum chamber. Since the magnet is too short, then the integral multipole b_6^{int} will be suppressed by an appropriate choice of the central multipole b_6 using parameter $x_p = X_{opt}$, at which $b_6^{int} = 0$. Fig. 7 – Fig. 10 present dependences of X_{opt}, the normalized gradient, lower central multipoles and the normalized effective length $L_{eff}^{(n)}$ on a geometric length L_g of the magnet. Here $L_{eff}^{(n)} = L_{eff}/L_g$, L_{eff} is a real effective length of the magnet. The integral multipole b_{10}^{int} is lesser 2×10^{-4} for the hyperbola and changes from -18×10^{-4} to -30×10^{-4} for the arc versus the magnet length. Fig. 8 shows that the pole in the arc form has significantly smaller geometric length, which can chose in 700 mm, as well as overall dimensions, while a minimum length with a hyperbolic pole is at least 1800 mm.

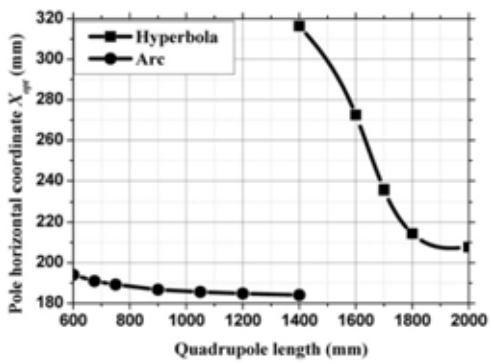

Fig. 7: Dependences of X_{opt} on a geometric length.

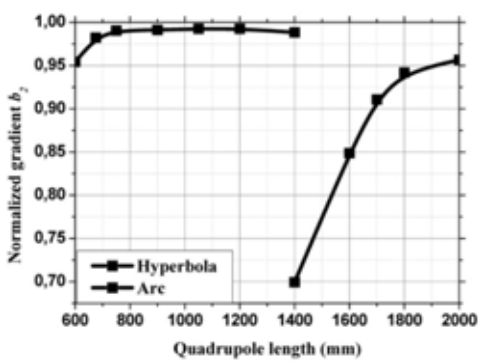

Figure 8: Dependences of the central normalized gradient on a geometric length.

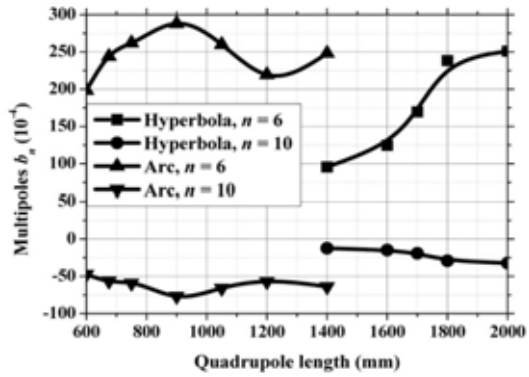

Figure 9: Dependences of the central lower multipoles on a geometric length of the magnet.

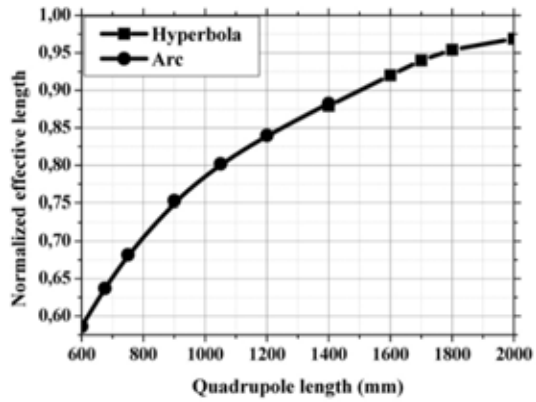

Figure 10: Dependences of the normalized effective length on a geometric length of the magnet.

CONCLUSION

Comparative characteristics of two types of the poles have been considered. Based on these calculations the final 2D and 3D geometries will be performed after formulation of the requirements on the field and integral field values as well as other technological and geometric parameters such as a beam tube, vacuum chamber etc.

REFERENCES

[1] http://www.ihep.ru/ihep/journal/IHEP-2-2010.pdf
[2] L. Tkachenko et al. “Design of Dipole Magnet for the Omega Project”. IEEE Transactios on Applied Superconductivity, Vol. 24, No3, June 2014, 4100305.
[3] S. Ivanov on behalf of IHEP staff. “Accelerator Complex U-70 of IHEP: Present Status and Recent Upgrades”. RUPAC-2010, Protvino, 2010, pp.27–31.
[4] http://hadron.kek.jp/ ~ accelerator/TDA/tdr2003.
[5] “Physics Design and Technology Development of CSNS Accelerator", 2-nd CSNS IATAC Review Meeting, IHEP, CAS, January, 2010, Beijing, China.
[6] I. Bogdanov et al. “Study of Electrical Steel Magnetic Properties for Fast Cycling Magnets of SIS100 and SIS300 Rings.” EPAC’2004, Lucerne, Switzerland, 2004, pp. 1741-1743.
[7] L.M Tkachenko. Code Package MULTIC for Calculation of Magnetic Field with an Arbitrary Configuration. IHEP preprint 92-28, 1992 (in Russian).

ISBN 978-3-95450-170-0

STUDY OF SUPERCONDUCTING ACCELERATING STRUCTURES FOR MEGAWATT PROTON DRIVER LINAC

K.A. Aliev, M.A. Gusarova, A.M. Fadeev, M.V. Lalayan, S.M. Polozov, N.P. Sobenin,
O.L. Verjbitskiy National Research Nuclear University MEPhI (Moscow Engineering Physics Institute), Moscow, Russia
T.V. Kulevoy, National Research Nuclear University MEPhI (Moscow Engineering Physics Institute) and Institute of Theoretical and Experimental Physics, Moscow, Russia

Abstract

The preliminary design of megawatt level proton accelerator-driver is carrying out by collaboration between Russian scientific centers MEPhI, ITEP, Kurchatov Institute. This project was supported in 2013 by the Ministry of Science and Education of Russia. The linac general layout includes SC Spoke-cavities at middle energy range and elliptical cavity at high energy one. The usage of QWR and/or HWR at 10-30 MeV was also discussed. Due to electrodynamics models of all structures types were designed and the electrodynamics characteristics were studied. QWR, HWQ and Spoke-cavities were proposed to operate on 324 MHz and elliptical cavities on 972 MHz. The main electrodynamics simulation results will present in report. The multipactor study results will also discussed.

INTRODUCTION

The study of high-power proton linac for 1.0 GeV was performed by collaboration of MEPhI, ITEP and Kurchatov institute researchers in 2013. Such linac was developed to understand the possibility of accelerator driven system (ADS) design in Russia.

The linac will consist of an RFQ, RF focusing sections and SC modular configuration sections. A number of QWR and HWR were also studied for 20-50 MeV energy range as an alternative of RF focusing sections. The SC part of developed linac can include QWR, HWR, Spoke-cavities and elliptical cavities due to. Medium energy cavities will operate on 324 MHz and elliptical one on 972 MHz [1, 2].

The results of noted above structures models design will discuss bellow. All simulations have been performed using CST Microwave Studio [3].

QWR AND HWR CAVITIES

The aim of the QWR and HWR optimization is to increase the beam energy gain and to have optimal power consumption at the same time. The beam energy gain is defined by the time-factor and the accelerating gradient. As it follows from the time-factor T definition, its maximum value is gained when the gap length is minimized. But the gap length decrease leads to higher gap capacity and, therefore, to lower shunt impedance, which is another important optimization target. The optimal value of the accelerating gap length g to the period length d equal to 1/3 could be taken [4], since its further decrease slightly improves the time-factor and the optimal particle velocity is only by 3 % higher than the optimal geometrical velocity β_g. Another QWR feature that affects the beam energy gain is the accelerating gradient. The accelerating gradient is estimated by the ratio B_p/E_a, where B_p is the magnetic field pick value and E_a is the accelerating field amplitude. Therefore, the ratio must be minimized for higher gradients. B_p/E_a depends on the inner and outer QWR conductor radii ratio R_i/R_o. The solution of the equation $\ln(R_o / R_i) = 1$ gives the optimal value of R_i/R_o [4] and it is equal to 0.36. The QWR effective shunt impedance R_a/Q_o defines how effectively RF field energy converts to the accelerating gradient. According to the "sphere in cylinder" approach offered in [5] the ratio R_i/R_o=0.12 yields the maximum shunt impedance (see Fig. 1). High shunt impedance and relatively low accelerating gradient results in a resonator with optimal power consumption, while a low B_p/E_a parameter resonator has an extreme accelerating gradient. When simulating a 324MHz QWR the value R_i/R_o=0.3 is chosen in favour of a higher accelerating gradient. Geometrical and RF characteristics of the QWR are presented in Table 1.

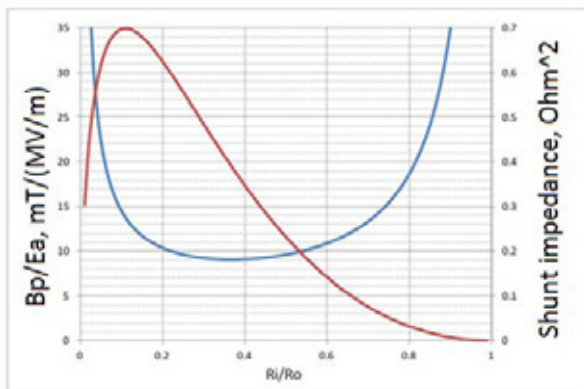

Figure 1: B_p/E_a and shunt impedance in QWR versus R_i/R_o.

The same analysis was performed for HWR also. To develop the electrodynamics model and determine the approximate geometric parameters of the HWR we assume the average value of the relative phase velocity β=0.25. The shape of the resonator should be optimized to minimize ratios B_p/E_a and E_p/E_a and get the maximum value of R_a/Q_o. Characteristics of the HWR are also presented in Table 1.

ISBN 978-3-95450-170-0

Table 1: Geometrical and RF characteristics of the QWR and HWR.

Parameter	QWR	HWR
f, MHz	324	324
β_g	0.25	0.25
E_p/E_a	6	2.3
B_p/E_a, mT/(MV/m)	10	5.1
R_a/Q_o, Ohm	608	140
Cavity height, mm	266	338
Central conductor length, mm	184	-
R_i, mm	30	60
R_o, mm	100	320
g, mm	39	60
d, mm	117	150

SPOKE-CAVITIES

Main geometrical parameters used for RF design and optimization of spoke cavities are shown in Figure 2. The main goal of the RF design is to provide a lower heat load and a higher accelerating gradient, which are determined by a higher R_a/Q_0. Also peak surface fields should be minimized.

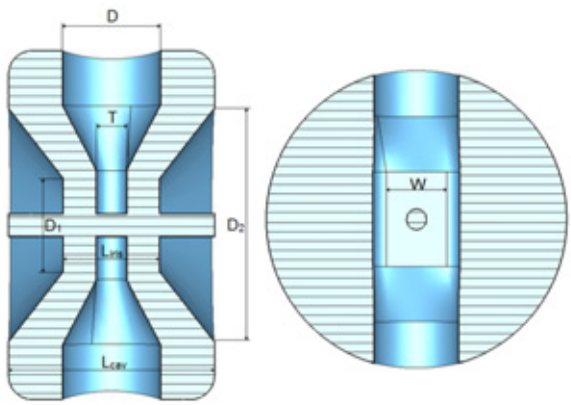

Figure 2: Cross-section of the spoke cavity with the geometrical parameters.

Accelerating electric field E_a is defined as:

$$E_a = \Delta W(\beta_0)/\beta_0\lambda\,. \quad (1)$$

where $\Delta W(\beta_0)$ is the energy gain at the optimal velocity and λ is the free-space wavelength of the accelerating mode. In our case β=0.2 and the operating frequency is f=324 MHz. The length from iris to iris is $2/3\beta\lambda$. The diameter of the cavity is of order of $\lambda/2$. To achieve a lower peak electric field the spoke width W and gap ratio T/L_{iris} were optimized. Simulation results are presenter in Figure 3.

The diameter of the spoke base D is optimized to get a lower B_p/E_a. The variation of B_p/E_a and R_a/Q_o is depicted in Figure 4. Also parameters D_1 and D_2 should be optimized. The diameter of small bottom D_2 is more sensitive to B_p/E_a, while the diameter of large bottom D_1 is more sencitive to B_p/E_a. Moreover blend edges will help to decrease the peak surface fields. The Geometric and RF properties of the spoke cavity are given in Table 2.

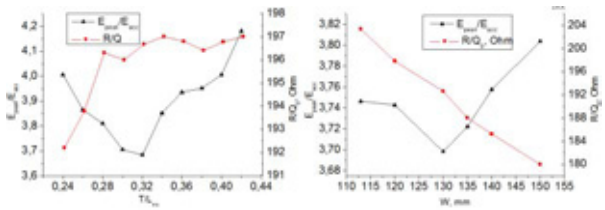

Figure 3: E_p/E_a (black) and R_a/Q_o (red) versus T/L_{iris} and W.

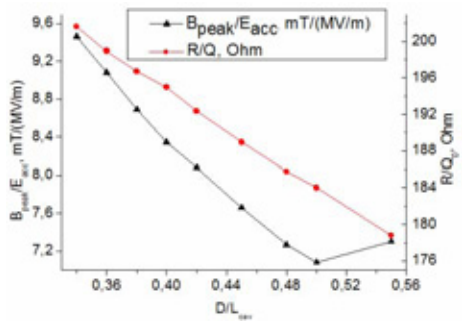

Figure 4: B_p/E_a (black) and R_a/Q_o (red) versus D/L_{cav}.

Table 2: Geometric and RF properties of the spoke cavity.

Parameter	Value
f, MHz	324
β_g	0.2
E_p/E_a	3.86
B_p/E_a, mT/(MW/m)	6.76
R_a/Q_o, Ohm	192
L_{iris}, mm	123.4
R_{cav}, mm	225
L_{cav}, mm	263.4

ELLIPTICAL CAVITIES

Multi-cell cavities based on modified disk-loaded waveguide shape are widely used for particle acceleration in 0.5-1.0c velocity range. Cavities with TESLA-shape design are the only known choice for superconducting accelerators dedicated for fault free operation. Wide experience gained by laboratories

First question presented by the cavity development is the cell number. It is known that multicell cavities require less power couplers and give rise to active length because of drift tubes number reduction. Contrariwise cavities of just a few cells typically show better performance because of easier quality control on material and production [6]. Usually cavities of 5 to 9 cells are used, but 7 to 9 cell ones are common for electron while 5 to 6 cells - for proton accelerators. SNS project using 5 cell cavities is the example of good performance facility. The beam dynamics simulation also shows that 5 cell cavities are optimal for high rate of the energy gain and 100 % current transmission [1]. This 5-cell design was chosen as basis for this study (Fig. 5).

In order to provide acceleration in whole energy range needed for ADS systems three phase velocity cavities were considered, namely 0.6, 0.7 and 0.8c. Operating frequency of all three cavities operated on π mode were

ISBN 978-3-95450-170-0

tuned to 972.6 MHz. Field flatness better than 99.3% was reached by end cells modification. Cavity electrodynamical characteristics are summarized in Table 3. Cavity for 0.6*c* has maximal surface field overvoltage factor due to lower period length. Surface magnetic field does not limit cavity performance because much lower than known limits.

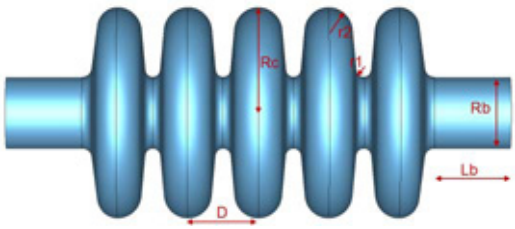

Figure 5: Five cell elliptical accelerating cavity.

Table 3: Electrodynamical parameters of elliptical cavity.

Parameter	β=0.6	β=0.7	β=0.8
coupling, %	3.53	2.35	1.57
$r_{sh\ eff}$, MOhm/m	5.39	7.79	10.44
r_{sh}, MOhm	12.5	16.24	20.84
Q	$1.17 \cdot 10^{10}$	$1.23 \cdot 10^{10}$	$1.79 \cdot 10^{10}$
E_{max}/E_{acc}	3.92	3.06	2.38
H_{max}/E_{acc}	0.0012	0.0011	0.001

Dispersion curves on fundamental mode being close to each other are presented in Figure 6.

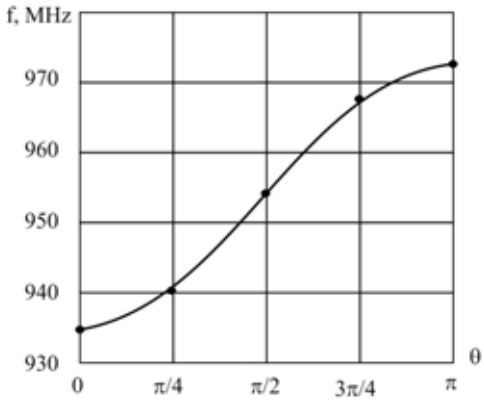

Figure 6: Dispersion curve for five cell elliptical accelerating cavity.

MULTIPACTOR SIMULATIONS

The results of calculation multipactor for elliptic superconducting accelerating cavities with phase velocity β_{ph}=0.6, 0.7, 0.8 are shown in Figure 7. As it could be seen from figure structures for β_{ph}=0.6 and 0.7 show very close accelerating field strength ranges with stable trajectories of 1st and 2nd order observed. They are equal to 0.86–3.1 MeV/m and 1.05–3.8 MeV/m correspondingly. But the structure for β_{ph}=0.8 features stable trajectories maintain up to 6 MeV/m. Electrons hitting surface have an energy of 180 eV at 4 MeV/m.

Geometry modification with flattened equator area or small hump added is known remedy for this kind of trajectories suppression [7]. But this solution demands special research on modified cavity electrodynamical parameters to be done.

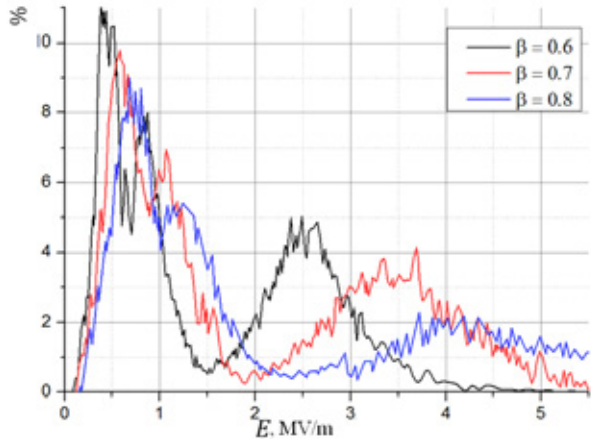

Figure 7: Particle number growth rate vs. field strength dependence

CONCLUSION

Results of electrodynamics models development and study and cavities design for superconducting part of 1 GeV linac were discussed. The tuned models of 324 MHz QWR, HWR and Spoke-cavities and 972 MHz 5 cell elliptical cavities were presented.

ACKNOWLEDGMENT

This work is supported in part by the Ministry of Science and Education of Russian Federation under contract No. 14.516.11.0084.

REFERENCES

[1] T.V. Kulevoy, S.M. Polozov, A.V. Samoshin et al. Beam dynamics simulation for the 1 GeV high power proton linac. Proc. of LINAC'14, THPP105 (in Press).

[2] T.V. Kulevoy, S.M. Polozov, A.V. Samoshin et al. Beam Dynamics Simulation in High-Power High-Energy Accelerator-Driver of the Proton Beam. Proc. of BDO-2014, pp. 49-50.

[3] www.cst.com

[4] V. L. Zvyagintzev. PhD Thesis. Moscow, MEPhI, 2013.

[5] J.R. Delayen. NIMA, 1987, 259, pp. 341-357.

[6] Didenko A.N., Kaminskiy V.I., Lalayan M.V., Sobenin N.P. Superconducting accelerating cavities. ISBN 978-5-726209531, MEPhI press, 2008.

[7] S. Kazakov, I. Gonin, V.P. Yakovlev. Multipactor simulation in SC elliptical shape cavities, FNAL, Batavia, IL 60510, USA.

ISBN 978-3-95450-170-0

STUDY OF NORMAL CONDUCTING ACCELERATING STRUCTURES FOR MEGAWATT PROTON DRIVER LINAC

A.E. Aksentyev, A.A. Kalashnikova, M.V. Lalayan, S.M. Polozov, S.E. Toporkov, National Research Nuclear University MEPHI (Moscow Engineering Physics Institute), Moscow, Russia
T.V. Kulevoy, National Research Nuclear University MEPhI (Moscow Engineering Physics Institute) and Institute of Theoretical and Experimental Physics, Moscow, Russia

Abstract

The preliminary design of a megawatt level proton accelerator-driver is carried out by collaboration between Russian scientific centers MEPhI, ITEP, Kurchatov Institute. This project was supported in 2013 by the Ministry of Science and Education of Russia. The linac general layout includes an RFQ section and section(s) with radiofrequency focusing. The different types of RF focusing were studied due to this project: RF crossed lenses, modified electrodes RFQ, axi-symmetrical RF focusing. All such focusing can be realized by IH-type cavities. The design of a segmented vane RFQ (SVRFQ) with coupling windows and IH- and CH-type normal conducting cavities is discussed in this report. All cavities operate at 162 MHz. The main results of the electrodynamics simulation are presented.

INTRODUCTION

The study of a high-power proton linac for 1.0 GeV was performed by a collaboration of MEPhI, ITEP and Kurchatov institute researchers in 2013. Such a linac was developed to understand the possibility of design an accelerator driven system (ADS) in Russia.

The linac will consist of an RFQ, RF focusing sections and SC modular configuration sections [1, 2]. The segmented vane RFQ (SVRFQ) with coupling windows was designed for beam bunching and low energy acceleration. Original design of elliptical coupling windows was proposed. IH- and CH- cavities were simulated and its electrodynamics characteristics were optimized.

The results of the modeling of the aforementioned structures are discussed below.

SVRFQ CAVITY

A 4-vane RFQ [3] with magnetic coupling windows is considered. The windows decrease the resonant frequency, minimize mode coupling in the RFQ and result in a smaller and more easily tuned accelerator. Specifically the following characteristics are being tuned: 1) separation of quadrupole and dipole modes' frequencies (Δf), 2) ratio of the maximal surface electric field in the resonator to the accelerating field on axis (overvoltage). The accelerating potential between the RFQ electrodes is limited by 1.2-1.5 of Kilpatrick limit units for the CW mode (~130-150 kV). The tuning is performed by variation of 1) the radius of the accelerating channel aperture (a), 2) electrode tip blend radius (VR_b) and 3) the distance between the end of a vane and the tank back wall – back end length (*BBL*). The parameters are shown in Figure 1.

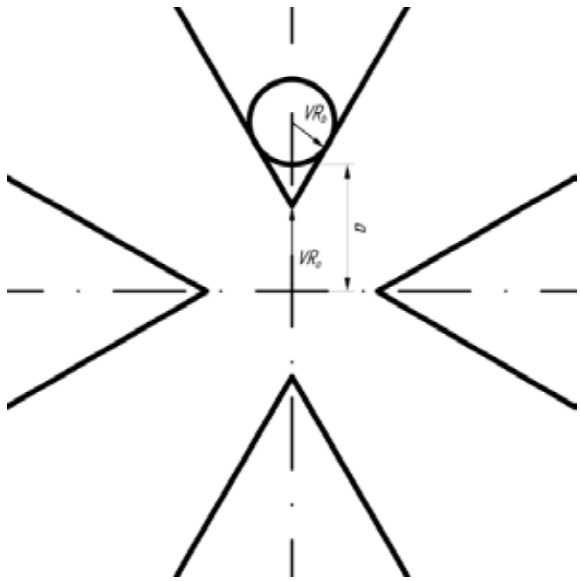

Figure 1: The SVREQ channel geometrical characteristics.

Base parameters of the optimized and tuned SVRFQ channel were discussed in [4]. Let us discuss, now, the influence of each of channel characteristics to the ratio of the surface electric field to the accelerating field and separation of the quadrupole and dipole modes' frequencies.

Aperture Radius, VR_o

The dependence of mode separation and the overvoltage (in Kilpatrick limit units, Kp [5]) against channel aperture radius variation is presented in Figures 2 and 3 respectively. These pictures show that mode separation is proportional to the overvoltage.

Blend Radius, VR_b

From Figure 4 one sees that variation of blend radius VR_b affects channel aperture: increase of VR_b is equivalent to that in VR_0. Expectedly, the mode separation plots in both cases are similar; yet it is clear that direct variation of electrode offset VR_o has greater effect on mode separation.

ISBN 978-3-95450-170-0

Back End Length, BBL

The effect of this characteristic's variation on the separation of modes is minimal, which is seen in Figure 5.

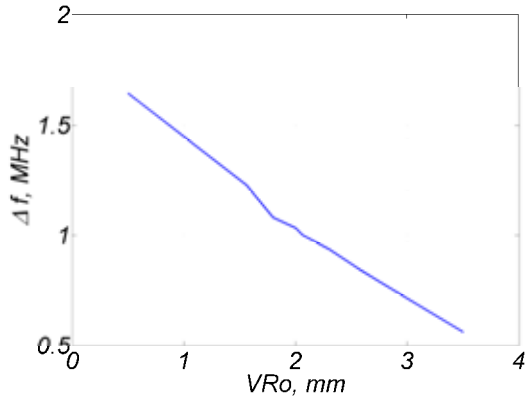

Figure 2: Mode's separation vs. aperture radius.

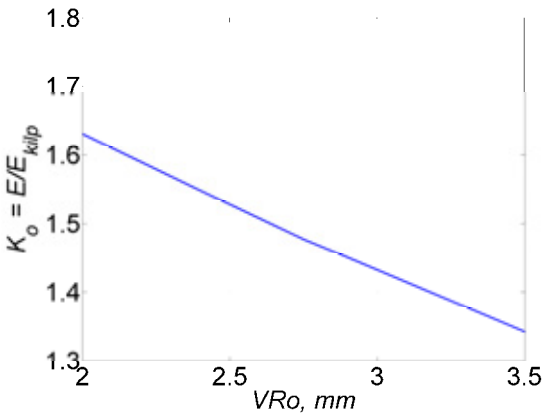

Figure 3: Overvoltage vs. aperture radius.

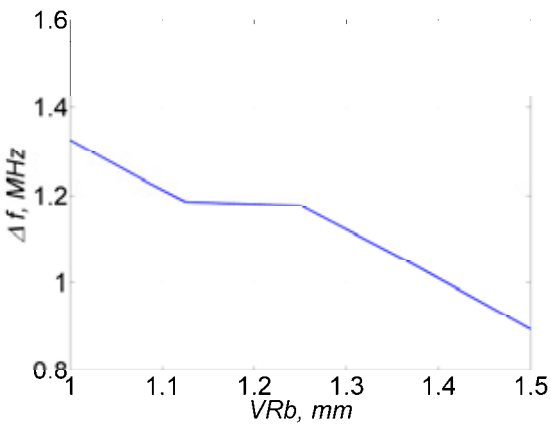

Figure 4: Mode's separation vs. blend radius.

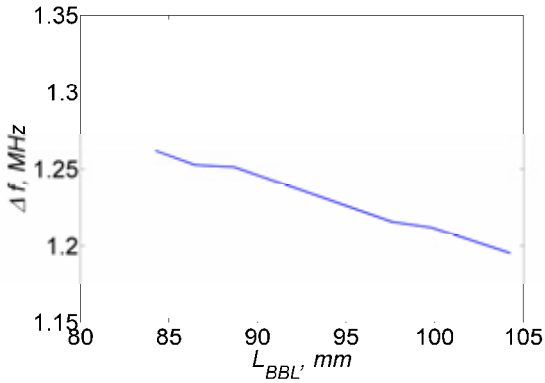

Figure 5: Mode separation vs. end region length.

Optimal Channel Geometrical Characteristics

Channel geometrical characteristics that satisfy 162 MHz resonant frequency, maximal surface electric field 1.721 Kp and mode separation 1.3 MHz are summarized in the Table 1.

Table 1: Optimal Channel Geometrical Characteristics of CVRFQ Channel

Parameter	Value, mm
Blend radius, VR_b	1.085
Aperture radius, a	5.3
End length, *BBL*	94

IH- AND CH- CAVITIES

The IH- and CH- resonators were designed for beam acceleration from 2.28 MeV to 4.73 MeV energy range. As mentioned earlier, the operating frequency of the inter-digital structure is equal to 162 MHz but for CH cavity it was changed to 324 MHz band (2-nd harmonics) since it operates at higher operating mode H_{210}. Each type of cavity works in the π-mode regime, has constant period D along the axis and acceleration gap between drift tubes $t=D/2$.

During investigation there were two main goals: 1) to optimize main electrodynamic characteristics (especially effective shunt impedance); 2) to reach uniform accelerating field distribution on the cavity axis (field flatness better than 95%). To reach these goals, design of both cavity types (CH- and IH-) consists of vanes (or pylons, see Fig. 6). It should be mentioned that the end wall of each pylon has an electrical contact with the tank sidewall. Therefore 4 magnetic fluxes around the vanes are combined in one common flux. This technique allows us to reach the uniform field distribution without critical drop of the Q-factor and shunt impedance.

ISBN 978-3-95450-170-0

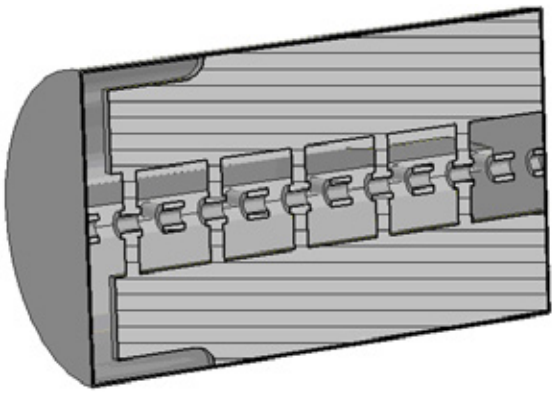

Figure 6: CH - tank layout.

During optimization, different CH- and IH- resonator models were considered. Main variable parameters are presented in Table 2.

Almost all models were optimized to the uniform field distribution (some extra cases with 13 gaps, big aperture and period length have field regularity equal to 92-93%). Some of results are summarized in Table 3 and the example of the optimized field distribution is presented in Figure 7.

Table 2: CH- and IH- resonator models design parameters.

Parameter	Value
Number of periods	7; 9; 11; 13
Aperture diameter, mm	15; 20; 30
Beam velocity, $\beta=v/c$	0.07; 0.08; 0.09; 0.10

Table 3: The results of CH- and IH- resonator's optimization.

Cavity type	CH	CH	IH	IH
β	0.10	0.09	0.08	0.08
Number of periods	9	7	13	11
Aperture diameter, mm	15	20	20	15
f, MHz	324	324	162	162
Effective shunt impedance, MOhm/m	83	67	145	154
Transit time factor	0.835	0.811	0.841	0.854
Q-factor	14000	11800	15500	15600
Field flatness, %	95	96	95	95

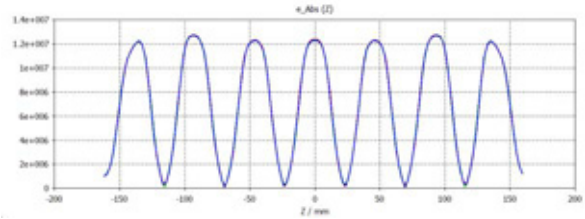

Figure 7. Typical field distribution for 7 gaps model.

CONCLUSION

Results of the electrodynamics models' development and study, and cavity designs for the normal conducting part of a 1 GeV linac were discussed. The initial section design based on a segmented vane RFQ (SVRFQ) with coupling windows was proposed. The problems of quadrupole and dipole modes' separation and electric field overvoltage were studied and discussed. The IH- and CH- resonators were designed for beam acceleration at medium energies. Both resonator types were optimized to enlarge the effective shunt impedance and Q-factor.

ACKNOWLEDGMENT

This work is supported in part by the Ministry of Science and Education of Russian Federation under contract No. 14.516.11.0084.

REFERENCES

[1] T.V. Kulevoy, S.M. Polozov, A.V. Samoshin et al. Beam dynamics simulation for the 1 GeV high power proton linac. Proc. of LINAC'14, THPP105 (in Press).

[2] T.V. Kulevoy, S.M. Polozov, A.V. Samoshin et al. Beam Dynamics Simulation in High-Power High-Energy Accelerator-Driver of the Proton Beam. Proc. of BDO-2014, pp. 49-50.

[3] V.A. Andreev. Patent US5483130, 1996.

[4] A.Y. Aksentyev, T.V. Kulevoy, S.M. Polozov. Proc. of IPAC'14, pp. 3286-3288.

[5] W.D. Kilpatrick. Rev. of Sci. Instr. V. 28, № 10, 1957, pp. 824 – 826.

ISBN 978-3-95450-170-0

STUDY OF POSSIBILITY OF 600-1000 MeV AND 1 MW PROTON DRIVER LINAC DEVELOPMENT IN RUSSIA

A.E. Aksentyev, K.A. Aliev, I.A. Ashanin, Yu.A. Bashmakov, A.A. Blinnikov, T.V. Bondarenko, M.A. Gusarova, A.N. Didenko, M.S. Dmitriyev, V.V. Dmitriyeva, V.S. Dyubkov, A.M. Fadeev, A.D. Fertman, A.A. Kalashnikova, V.I. Kaminsky, E.R. Khabibullina, Yu.D. Kliuchevskaia, A.D. Kolyaskin, M.V. Lalayan, S.V. Matsievskiy, S.M. Polozov, V.I. Rashchikov, E.A. Savin, A.V. Samoshin, Ya.V. Shashkov, A.Yu. Smirnov, N.P. Sobenin, S.E. Toporkov, O.L. Verjbitskiy, V.L. Zvyagintsev, A.V. Ziiatdinova, National Research Nuclear University MEPhI (Moscow Engineering Physics Institute), Moscow, Russia
T.V. Kulevoy, S.V. Rogozhkin, National Research Nuclear University MEPhI (Moscow Engineering Physics Institute), Moscow, Russia and Institute of Theoretical and Experimental Physics, Moscow, Russia
V.F. Batyaev, G.N. Kropachev, D.A. Liakin, Yu.E. Titarenko, Institute of Theoretical and Experimental Physics, Moscow, Russia
P.N. Alekseev, V.A. Nevinitsa, National Research Center "Kurchatov Institute" , Moscow, Russia
S.Yu. Stark, LNL INFN, Legnaro, Italy

Abstract

Alternative nuclear energetic's technologies as fast reactors and accelerating driven systems (ADS) are necessary to solve a number of problems as U-238 or thorium fuel reactor and nuclear wastes transmutation. ADS subcritical system should consist of megawatt-power proton accelerator, neutron producing target and breeder. A number of ADS projects are under development in EU, Japan, USA, China, S.Korea at present. Superconducting linacs or their complexes with high energy storage synchrotron are under design in main projects as a megawatt power proton beam driver. In Russian Federation the complex design for accelerator-driver was carried down more than ten years ago.

INTRODUCTION

A number of ADS projects are under development in EU (EUROTRANS including MYRRHA, EFIT, AT-ADS, Trasco ets. [1-2]; MERIT [3]; ThorEA [4]), Japan (OMEGA, KART, [5]), PRC [6], S.Korea (HYPER [7]), India [8], USA [9-10]. The review of main projects was done in [11].

It should be noted that complex study of driver linac in Russia was carried down more than ten years ago in cooperation of ITAP, IHEP and Moscow Radiotechnikal Institute [12-14]. Blanket studies are carried now in IPPI. The new OMEGA project at IHEP which includes a high power 400 MeV proton linac should be also noted.

The new approach to the ADS complex is now under development in framework of the project carried out by collaboration between Russian scientific centers MEPhI, ITEP, Kurchatov Institute. This project was supported in 2013 by the Ministry of Science and Education of Russia. A brief results observation for accelerator part of the project is presented in this paper. It includes accelerator-driver general layout, beam dynamics simulation, electrodynamics simulations of accelerating cavities and analysis of technological background in Russia.

ACCELERATOR-DRIVER GENERAL LAYOUT

The conceptual design of the linac is presented in Figure 1. The linac will consist of an RFQ for beam bunching and low energy acceleration (up to 2 MeV), RF focusing section(-s) for medium energies (up to 30-50 MeV) and SC modular configuration sections for higher energies. SC QWR and HWR were also discussed for 20-50 MeV range. Several different types of RF focusing linacs were discussed for the medium energies. They are RF crossed lenses [15], modified electrode profile RFQ [16], axi-symmetrical RF focusing (ARF) [17]. The conventional modular configuration linac [18] based on spoke-cavities and 5-cell elliptical cavities were designed for high energies. The linac layout has three intermediate energy output beam lines which can be used already during the linac construction to different experiments with neutron production targets or for radiation testing of reactor construction materials.

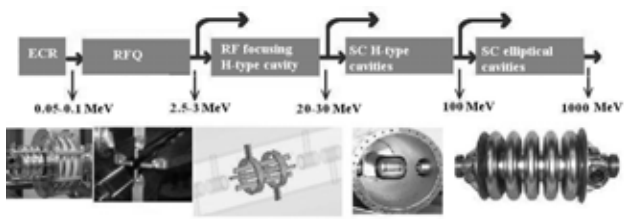

Figure 1: The linac general layout.

Note that such driver linac layout is now conventional and similar designs are proposed in main ADS projects as [1, 2, 6, 7]. The idea to use RF focusing sections for medium energy range is the main difference of our scheme.

ISBN 978-3-95450-170-0

BEAM DYNAMICS SIMULATION RESULTS

The designed 2 MeV RFQ section operates on 162 MHz. The section length is 2.4 m and the accelerating potential between electrodes equal to 120 kV was used [19]. Such potential limit is caused by needs to limit the surface field by 1.2-1.5 of Kilpatrick criterion value for CW mode. The injection velocity is 0.01c. The current transmission coefficient is equal to 96 % for zero current beam and slowly decrease to 94 % for 20 mA.

The different types of RF focusing sections as RF crossed lenses, modified electrode profile RFQ and axi-symmetrical RF focusing were studied for medium energy region with short SC cavities system. Results of beam dynamics simulation were presented in [20-21]. A method of ion focusing in linac by RF decelerating fields of crossed lenses (RFCL) permits to obtain energy-independent focusing strength and high acceleration rate. The RFCL linac having the FOODOO focusing periods was considered and it was shown that the stability of proton motion can be realized for 2-30 MeV energy range. The design parameters are the following: energy 2÷32.64 MeV, operating frequency162 MHz, peak field on surface 250 kV/cm (1.8 Kp), field amplitudes in the accelerating and decelerating gaps 100 kV/cm, focusing period 3βλ (FOODOO), number of focusing periods 8, number of lenses in period 2÷6, pulse current limit 60 mA, acceleration rate 4.4 MeV/m, linac length 7.0 m, normalized acceptance of the RFCL channel is 0.33 π cm·mrad, which is three times more than the beam emittance from the RFQ.

Beam dynamics in ARF section was also studied. It was shown that the rate of the energy gain can reaches to 2.5 MeV/m and section can be very compact. But the transverse emittance growth is very serious (more than 70 % with 10 mA initial beam current).

The modified electrode form RFQ can be also used as the second section to accelerate the beam in 2-15 MeV energy range, averaged rate of the energy gain is equal to 1.3 MeV/m. It should be noted that such sections provide the lowest transverse emittance growth: about 5 % for 1 mA and 70 % for 100 mA.

Beam loses are absent for all three RF focusing types.

The high energy linac section consisting of independently phased SC cavities (spoke and elliptical type) and focusing solenoids was studied. The synchronous phase slipping is the serious difficulty in such linac because it provides to longitudinal stability degradation and energy gain decreasing. The phase slipping factor was limited by 20 % for this project [21]. It was shown that linac should consist of five groups of identical cavities with phase velocities 0.31, 0.36, 0.48, 0.65 and 0.875 (see Fig. 2). First group are 2-gap (or 3-gap) spoke cavities with 324 MHz operating frequency, other groups – 5-cell elliptical cavities operating on 628 or 972 MHz. Total length of SC linac part is 173 m, it consist of 158 cavities. The solenoid fields necessary for focusing not exceeds 2.6 T and the beam loses are absent.

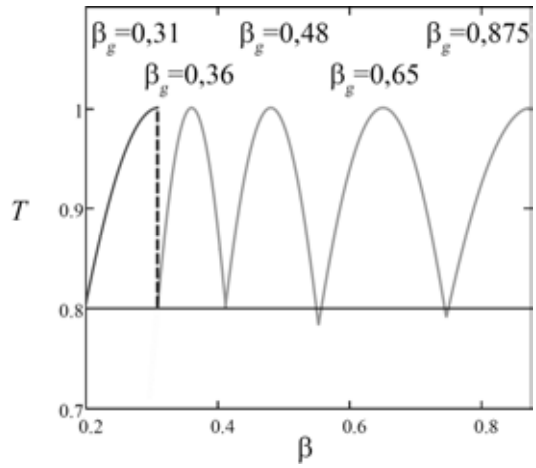

Figure 2: Slipping factor T versus beam velocity β in the high energy stage.

ELECTRODYNAMICS SIMULATIONS OF ACCELERATING CAVITIES

The linac will consist of an RFQ, RF focusing sections and SC modular configuration sections as it was noted above. RFQ and RF focusing section should be realized on CW normal conducting design

The segmented vane RFQ (SVRFQ) with coupling windows was simulated for beam bunching and low energy acceleration. Original modification of elliptical coupling windows was proposed. IH- and CH- cavities were simulated and it's electrodynamics characteristics were optimized. The magnetic coupling windows CH-cavities were studied. The normal conducting cavities design is detailed discuss in [22].

The SC part of developed linac can include spoke-cavities and elliptical cavities and QWR, HWR also if superconducting variant for 20-50 MeV energy range will be discussed further. Medium energy cavities (spoke, OWR and HWR) will operate on 324 MHz and elliptical one on 972 MHz [1, 2]. The detailed discussion of SC cavities electrodynamics simulation is presented in [23].

ANALYSIS OF TECHNOLOGICAL BACKGROUND

All technologies needed for contemporary accelerators construction were developed in our country till 1990th. But large numbers of technologies were lost during 20 last years. The minimal list of technologies which are necessary for accelerator-driver manufacturing are presented in Table 1 and the present state of such technologies at Russia is illustrated. Modern RF power sources and RF superconductivity looks most critically. Only last 2-3 years RF SC technology development starts in JINR [24] and first cavity was designed and manufactured. The design of modern RF sources in Russia is in inchoative stage. Now we also have very serious problem with human resources and there training.

It should be recommended to become accelerator-driver activities immediately and to realize such project step by

ISBN 978-3-95450-170-0

step starting CW RFQ as it was now planning in EU [1], China [6] or India [8] projects.

Table 1: Technological background in Russia analysis.

	R&D	Prototype	Industrial technology
Beam dynamics, engineering design	yes	yes	yes
ECR ion sources	u.d.*	u.d.	no
Normal conducting cavities	yes	yes	u.d.
SRF	u.d.	no	no
Permanent magnets	yes	yes	no
SC magnets	yes	yes	u.d.
Contemporary RF feeding systems	u.d.	no	no
Beam transport	yes	yes	u.d.
Diagnostics and control	yes	yes	u.d.

*under development

CONCLUSION

The brief results observation for high power high energy accelerator-driver design is presented in this paper. Results of beam dynamics simulation, electrodynamics simulations of accelerating cavities and analysis of technological background in Russia are discussed.

ACKNOWLEDGMENT

This work is supported in part by the Ministry of Science and Education of Russian Federation under contract No. 14.516.11.0084. Especial thanks to Dr. A.S. Plastun for modified electrode profile RFQ study.

REFERENCES

[1] H. Abderrahim. Abstracts of Intern. Topical Meeting on Nucl. Res. Applications and Utilization of Accelerators, p. 3, 2009.
[2] L. Mansani, C. Artioli, M. Schikorr et al. Nuclear Technology, 180:2, pp. 241-263, 2012.
[3] K. McDonald, R. Bennett, O. Caretta et al. Proc. of PAC'09, pp 795-799, 2009.
[4] S. Steer. Report of ThorEA Roadmapping Activity. ThorEA Report, 2010.
[5] K. Kikuchi, S. Saito, K. Tsujimoto et al. Nucl. Instrum. Meth. A, v. 562, 2, pp. 646—649, 2006.
[6] J. Tang, S. Fu, L. Ma. Proc. of HB'10, pp. 38-42, 2010.
[7] W. Park, T. Song, B. Lee, C. Park. Nucl. Eng. Design, v. 219, 3, pp. 207-223, 2003.
[8] T. Basak, S. Rao, P. Singh et al. BARC Newsletter, 285, pp. 140-152, 2007.
[9] S. Henderson. DOE Study Report. International Workshop on Accelerator-Driven Sub-Critical Systems & Th Utilization, 2010.
[10] R. Sheffield, E. Pitcher ICFA Beam Dynamics Newsletter, 49, pp. 16-38, 2009.
[11] S.M. Polozov, A.D. Fertman. Atomic Energy, 113, 3, pp. 192-200, 2013.
[12] B.P. Murin, G.I. Batskikh, V.M. Belugin et al. Proc. of the Second Intern. Conf. on Accelerator-Driven Transmutation Technologies and Applications, 1996, v. 2, p. 1047.
[13] V.A. Andreev, A.I. Balabin, I.V. Chuvilo et al. Ibid., p. 1020.
[14] B.P. Murin, G.I. Batskikh, V.I. Belugin et al. Proc. of EPAC'00, 2000, pp. 954-956.
[15] A.I. Balabin, G.N. Kropachev. Nuclear Instruments and Methods in Physics Research A, 459, pp. 87-92, 2001.
[16] A.S. Plastun, A.A. Kolomiets. Proc. of LINAC'12, pp. 41 – 43, 2012.
[17] Masunov E.S., Vinogradov N.E. Physical Review Special Topics – Accelerators and Beams, Vol. 4, 070101, 2001.
[18] Polozov S.M., Samoshin A.V. Problems of Atomic Science and Technology. Series: Nuclear Physics Investigations, 3 (91), 2014, p. 143-146.
[19] A.E. Aksentyev, T.V. Kulevoy, S.M. Polozov. Proc. of IPAC'14, pp. 3286-3288.
[20] T.V. Kulevoy, S.M. Polozov, A.V. Samoshin et al. Beam Dynamics Simulation in High-Power High-Energy Accelerator-Driver of the Proton Beam. Proc. of BDO-2014, pp. 49-50.
[21] T.V. Kulevoy, S.M. Polozov, A.V. Samoshin et al. Beam dynamics simulation for the 1 GeV high power proton linac. Proc. of LINAC'14, THPP105 (in Press).
[22] A.E. Aksentyev, A.A. Kalashnikova, M.V. Lalayan et al. Study of normal conducting accelerating structures for megawatt proton driver linac. Proc. of RuPAC'14, THPSC04.
[23] K.A. Aliev, M.A. Gusarova, A.M. Fadeev et al. Study of superconducting accelerating structures for megawatt proton driver linac. Proc. of RuPAC'14, THPSC05.
[24] N.S. Azaryan, Ju. Boudagov, D.L. Demin et al. Proc. of IPAC'13, pp. 2393-2395.

ISBN 978-3-95450-170-0

DEVELOPMENT AND TESTING OF POWERFUL HIGH-VOLTAGE ELECTRON ACCELERATOR FOR ENERGY-INTENSIVE INDUSTRIES

N.G. Tolstun, A.V. Efremov, A.S. Ivanov, A.N. Kuzhlev, V.P. Maznev, A.I. Machecha,
V.P. Ovchinnikov, D.E. Pavluhov, M.P. Svinin, D.A. Solnyshkov,
JSC "D.V. Efremov Institute of Electrophysical Apparatus", St. Petersburg, Russia

Abstract

The report describes the results of the development and testing of the Electron-23 high-voltage high-power accelerator rated for an accelerating voltage of 1 MV and beam power up to 500 kW at the "NIIEFA" testing facilities.

The accelerator is intended for industrial processing of flue gases from thermal power stations with the aim to reduce concentrations of nitrogen and sulfur oxides. It may also be used for other energy-consuming processes, such as treatment of wastewaters for their decontamination or processing of natural gases for their conversion into engine fuel. [1]

BRIEF DESCRIPTION OF THE ACCELERATOR

General view of the accelerator with the beam forming and extraction device is schematically shown in Fig.1.

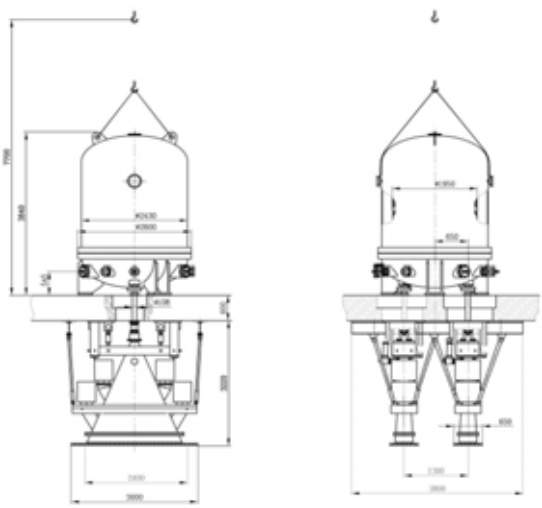

Figure1: General view and main parameters of the «Electron-23» accelerator.

The high-voltage (HV) generator, electron source and accelerating tube (AT) are placed inside a metal vessel filled with a pressurized insulating gas. A three-phase transformer-rectifier with a closed magnetic core and parallel feeding of cascades is used as a HV generator of the accelerator «Electron–23». Such a high-voltage source has a wall-plug-efficiency higher than 90% and practically no restrictions on power. The magnetic core of the HV generator is a construction symmetrical in space and consisting of 3 vertical rods and 2 horizontal annular yokes closing the magnetic flux. Three primary windings are located on the core rods, encircled with electrostatic screens and are star-connected with a power supply. Three secondary windings consist of separate coils located coaxially with primary windings. Each three coils of the secondary winding are located at one level on different magnetic core rods. They are star-connected and together with 6 diodes form a 3-phase bridge rectifying cascade [2, 3]. In the DC voltage, all twenty seven cascades are connected in series.

The majority of the accelerator components facing the HV gap is made of insulating materials with a high-resistive conducting coating. As a rule, these elements are made of stainless steel to prevent short-circuiting around the magnetic core of the HV generator; for this reason their construction is technologically complicated. The use of insulating materials with a high-resistive coating allows us to simplify the construction and considerably reduce the manufacturing cost of these elements.

A diode-type electron source with a lanthanum hexaboride emitter of 13 mm diameter is used in the accelerator. Emitter holders are made of anisotropic pyrolytic graphite that prevents chemical interaction of the emitter with emitter-holders and provides reduction of the filament power of the electron source down to 100 W [4]. The 1st electrode of the AT serves as the electron source anode. The source filament is fed from a special winding located on the magnetic core of the HV generator. The electron beam current is controlled and stabilized from the low voltage side.

The AT consists of alternating ceramic insulators and metal electrodes forming a vacuum-tight connection. A resistive voltage divider is placed outside the tube on its electrodes. A distinctive feature of the accelerator' design is location of the AT in parallel with rods of the HV generator magnetic core inside a common vessel. Such an engineering solution allows overall dimensions to be decreased, but, requires shielding of the AT against stray magnetic fields produced by the HV generator. To achieve this, electrodes of the AT are made of permalloy, and a distance between them is rather small (12, 5 mm), resulting in the reduction of the stray magnetic field on the AT axis approximately by a factor of 100 [5].

General view of the AT installed in the accelerator is shown in Fig. 2. The accelerator design also enables installation of one more AT in the same high-pressure vessel. Tests of the machine were carried out with a single tube.

The irradiation field forming system consists of an electromagnetic lens, beam scanning device and device for the beam extraction to the atmosphere. The beam scanning device comprises longitudinal and transverse

ISBN 978-3-95450-170-0

scanning electromagnets for the beam fast transport to any of 4 extraction windows. The magnetic core of the beam scanning device is made of ferrite, which excludes its corrosion in aggressive ozone environment.

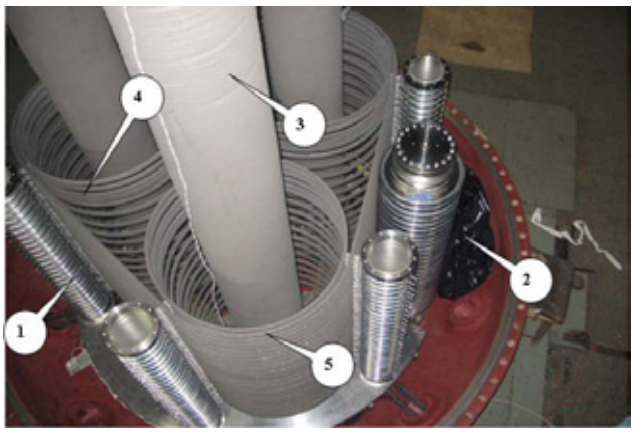

Figure 2: Support columns (1), AT with electromagnetic screens (2), magnetic cores of the HV rectifier primary winding phases (3), gradient rings (4) and electromagnetic screens (5).

The device for the beam extraction to the atmosphere is made separate from the accelerator vacuum chamber (see Fig. 3) and is electrically isolated from it. Electric signal from this device is fed to a unit visualizing the beam position in extraction windows. Four water-cooled extraction windows with a supporting grid are installed at the flange and are closed with metal foil.

Figure 3: Beam extraction device of the «Electron-23» accelerator at a test facility in NIIEFA.

The accelerator is supplied from the 3×380 V, 50 Hz mains and is connected directly to it without any voltage regulators. When the accelerator is switched on, firstly a 10 kVA autotransformer is used to increase high voltage up to a nominal value of 1100 kV. After that, the accelerator is re-switched to be fed directly from a power transformer; and the autotransformer is off.

The accelerator is equipped with an industrial computer-based automatic control system. Design technical parameters of the «Electron-23» accelerator are given in Table1.

Table1: Parameters of the «Electron-23» accelerator

Parameter	Value
Range of accelerating voltage control, MV	0,8-1,0
Accelerating voltage instability (excluding 50 Hz ripples), %, not more than	±5
Electron beam current, mA	0-500
Electron beam current instability, %, not more than	±2
Accelerator rated power, kW	500
Electron beam scanning length, cm	240
Non-uniformity of electron beam current linear density 10 cm from extraction foil, %, not more than	±10
Electron beam scanning frequency, Hz	≥300
Electron beam wall-plug efficiency at 500 kW rated power, %	≥90
Annual operating time, %	≥90

ADJUSTMENT AND TESTING RESULTS

As already mentioned above, in the process of the accelerator testing it was supplied from the power transformer without any voltage regulator. The open-circuit voltage in this case is 1100 kV; the leakage current is not more than 3 μA. When operating under load, (HV) depends on the load current; the load characteristic is shown in Fig.4. A max attained load current is 420 mA and it is limited by the beam extraction device; at this current the voltage drop is 210 kV, i.e. 19 % of its initial level.

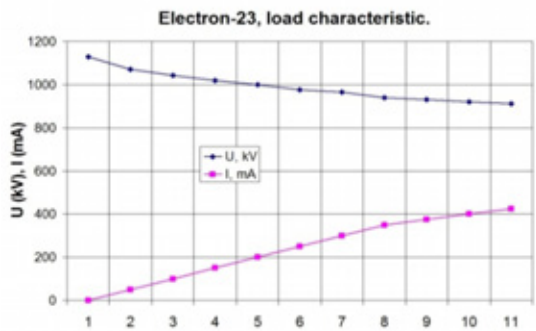

Note: without energy regulation

Figure 4: Load characteristics of the accelerator.

The accelerator operation on an industrial facility without voltage regulation is possible only if it operates in one mode, for example, when processing flue gases of thermal power stations. Advantages of such a solution are lower cost and higher efficiency.

However, in most cases, the use of a voltage regulator is necessary; note that they are commercially produced for a power of up to 1,8 MW.

In the process of the accelerator testing, HV rectifiers of SDL-130 type failed from time to time because of occasional breakdowns of the HV structure. After analyzing the mechanism of the rectifiers' failures, a

ISBN 978-3-95450-170-0

protection method developed for accelerators of the ELV series (INP, named after Budker) was applied [6]. According to this method, protection chokes were calculated, manufactured and installed in 14 cascades nearest to the HV part of the rectifier. After this no more failures of HV rectifiers were observed.

The beam current instability for one hour of operation does not exceed 1% of its preset value. No failures in the operation of the electron source and its power supply system were observed.

The AT in the idle regime provides safe operation without voltage breakdowns of up to 1200 kV level. As the AT in this accelerator is located in stray magnetic fields of the HV generator, the beam passage through the tube and in the vicinity of it was of special interest, particularly with the load increasing. In the process of the accelerator testing with the 420 mA beam current, the influence of the magnetic stray fields on the beam was not observed. No beam current presence was also registered on the AT electrodes.

In the course of the adjustment works at beam currents of 5-50 мА, it turned out that the beam trajectories looked like some curved lines instead of straight ones, and their shapes differed in different extraction windows. This fact did not allow the extraction window area to be properly used and hindered increasing of the electron beam current. Under the tests, 3 factors responsible for the scanned beam position distortion were found:

- when the beam entered the scanning device not in the center, the beam trace in extraction windows was in the form of an arc. This distortion was corrected by placing correcting electromagnets on the electron guide.
- the stray magnetic field produced by ion pumps also influences the electron beam trajectory. To reduce this influence, magnetic screens were mounted around the ion pumps.
- the influence of the variable magnetic field produced by power current-carrying cables on the beam position was observed at load currents in the HV generator primary windings higher than 500 A. To lessen this influence, each phase cables were laid in pairs. That allowed the beam distortion to be reduced by several times.

As a result of the works performed, the width of the scanned beam in extraction windows was enlarged to 40 mm, which allowed the beam current to be increased up to 420 mA.

Various types of foils were tested in the beam extraction device. Initially we used an Al foil of the AMD type of 80 μ thickness and Ti foil of the VT-1 type of 50 μ thickness. With the AMD foil, we attained the electron beam current close to the design value. However, because of low corrosion resistance and mechanical strength of Al, such a current can be obtained only for a short period of time. With the Ti foil, a beam current of up to 250 mA was obtained in the long-term mode at an accelerating voltage of 960–1100 kV.

Under real conditions the accelerator should operate for a long time without foil replacement. Thus, to provide the 500 мА beam current, one more AT with an electron source should be placed inside the high-pressure vessel, and the accelerator should also be equipped with one more system for the beam extraction to the using Ti foil.

CONCLUSIONS

Based on the results of adjustment and testing of the «Electron-23» HV accelerator, the following conclusions can be drawn:

1. The AT can be located in parallel with the rods of the 3-phase transformer-rectifier magnetic core inside a common vessel. When shielding the AT with electrodes made of permalloy, the influence of magnetic stray fields on the beam passage through the AT was not observed at beam currents of up to 420 мА.
2. The usage of components made of insulating materials with a high-resistive coating in the HV structure provides its necessary electric strength, allows us to simplify the accelerator design and reduce the cost of its manufacturing. Power of 250 kW was attained on the accelerator with a single beam extraction device.
3. The 500 kW power can be provided by installing one more AT inside the same high-pressure vessel and by inserting one more beam extraction device. It was shown that these measures will allow safe operation of the accelerator in energy-intensive industrial radiation processing.

REFERENCES

[1] A. G. Chmielewsky, Electron Accelerators for Environmental Protection, Reviews of Accelerators Science and Technology, Vol. 4 (2011), pp. 147-159.
[2] B.I. Albertinsky, M.P. Svinin, Cascade Generators. M., 1980, 194 pp.
[3] M.P. Svinin, Calculation and Designing of High-Voltage Electron Accelerators for Radiation Processing, M. Energoatomizdat 1989, 142 pp.
[4] A.K. Yevseev, V.P Maznev, V.P. Ovchinnikov. Cathode-Heating Unit. RF Patent №246503, priority of 15.03.2010.
[5] A.S. Ivanov, V.P. Ovchinnikov, M.P. Svinin, N.G. Tolstun, "Electromagnetic Electron Irradiation Field Shaping Systems for Industrial HV Accelerators", Proceedings of the EPAC94, London, June 27-July 1, 1994, World Scientific, V.3, pp.2655-2657
[6] N.K. Kuksanov. DC Electron Accelerators with Power of Hundreds kW. Doctoral Thesis, Novosibirsk, 1993, 127 pp.

ISBN 978-3-95450-170-0

SINGLE FREQUENCY HIGH INTENSITY HIGH ENERGY NORMAL CONDUCTING HADRON LINAC*

V.V. Paramonov#, V. N. Leontiev, INR of the RAS, Moscow,
A.P. Durkin, MRTI, Moscow, A.A. Kolomiets, ITEP, Moscow

Abstract

Considering both the beam quality and the possibility of practical realization, the scheme and parameters for 400 MeV H- linac are discussed. The concepts for beam emittance preservation, both transverse and longitudinal, starting from RFQ, following with PMQ focusing DTL and finishing with high energy CCL part are realized. Several focusing schemes are analyzed for DTL and CCL parts. The pulse beam current is limited to the safe value 40 mA and the average current up to 2 mA is supposed by Duty Factor (DF) of 5%. The operating frequency 352 MHz for all linac parts provides the full unification for RF system of the whole. Expected beam parameters are summarized.

INTRODUCTION

From the beam dynamics issue the smooth continuous acceleration with the minimal number of simple transitions between linac parts is the best case. There is no accelerating structure for effective H- ions acceleration in the total energy range from ~100 keV to ~ 400 MeV and different structures are used in different linac parts, operating at different frequencies. The matching of longitudinal motion is rather complicated. matching for transverse motion is still required. It can be strongly simplified [1] for the single operating frequency f_0 in the whole linac. The scheme of proposed linac includes well known structures. RFQ is an inevitable part in the linac front end and Coupled Cell Linac (CCL) is mostly effective for high energy part. The mostly developed and effective structure for intermediate part is the Drift Tube Linac (DTL). The recent progress demonstrates both RFQ operating f_0~(300-400) MHz and developed CCL for the same frequency range. CERN Linac4 realizes single frequency concept up to H- energy 160 MeV. Below parameters of such linac are estimated for higher output energy. Much more details of this consideration are given in [2]. All simulations for beam dynamics are performed by using LIDOS and TRANSIT codes [3].

LINAC FRONT END

For high power high energy linac the problem of particle losses is of primary importance. The care for emittance growth preservation should be paid starting from ion source and low energy beam transport to RFQ. For RFQ essential parameters are the transverse emittance growth and output longitudinal emittance. The output beam should be bunched without tails in the phase space, which will be transformed further in the beam halo.

To have the initial beam formation, RFQ with f_0=352,2 MHz and output energy W_1=3.0 MeV was estimated [2] assuming voltage 95.0 kV and the maximal electric field E_{smax}=1.85 E_k with the cavity length 3.65 m. For the beam current I_b=40 mA simulations shows transverse emittance growth ~10% and total longitudinal emittance as 0.914 π MeV·deg. For output beam the phase space portraits are shown in Fig. 1. Comparison with the recently achieved results for the J-PARC RFQ, f_0=324 MHz [4], and for SNS RFQ f_0=402.5 MHz, [5] shows the accepted parameters as reliable and RFQ cavity construction for DF=5% as realistic.

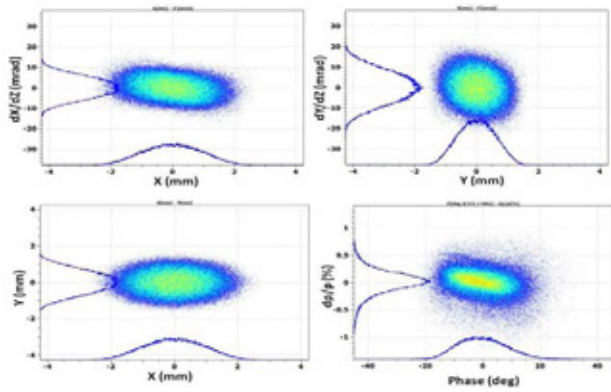

Figure 1: The phase space distributions of particles at the RFQ exit.

MEBT1

The transport line MEBT1 has the length ~2.31 m and is required for matching between RFQ and DTL, placement of chopper and beam diagnostic hardware. The line consists from eleven quads, chopper and beam absorber. To reduce the bunch lengthening along axis, line is equipped with two bunching cavities. The design parameters for MEBT1 elements are quite conservative [2]. Simulations show the transverse emittance growth as ~30% and longitudinal one as ~6%. It id in good coincidence with similar parameters in the existing linacs – SNS, J-PARC and Linac4. The phase space portraits for beam at the MEBT1 exit are shown in Fig. 2.

DTL PART

For DTL with f_0=352,2 MHz application of Permanent Magnet Quads (PMQ) is motivated by higher RF efficiency. RF parameters of DTL cells were studied [2] in the wide range of dimensions. To provide the higher RF efficiency and the safe E_{smax} value <1.3 E_k, one should start with small aperture diameter 2a and drift tube cone angle θ in the DTL beginning and increase it to the DTL

*Work supported by IHEP Contract № 0348100096313000178
#paramono@inr.ru

ISBN 978-3-95450-170-0

end. The accepted configuration of DTL cells are shown in Fig. 3 for the middle cells in each DTL tank.

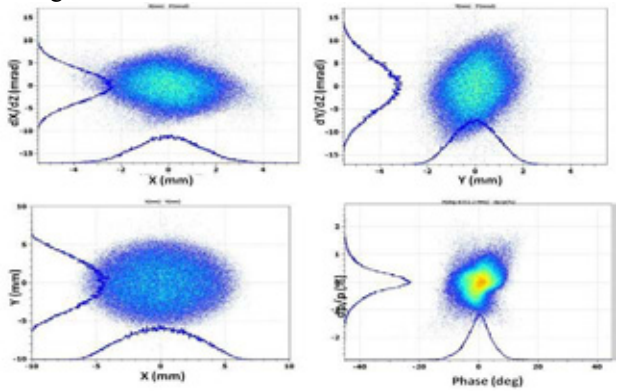

Figure 2: The phase space distributions of particles at the MEBT1 exit.

Two competitive focusing lattices were studied finally – FFDD and FHDH, where H means the empty drift tube without PMQ. Both these schemes have similar total sensitivity to PMQ misalignments and provide similar size for beam envelope. FFDD scheme requires lower focusing gradient and is more easy for beam dynamics understanding. This scheme is realized in Linac 4 for DTL. FHDH scheme requires higher, but realistic gradient, and has twice less PMQs. This scheme has very attractive advantages for the linac technology. In empty tubes correctors and BPMs, similar to SNS DTL, can be placed, improving DTL flexibility for beam transport. Inter tanks space could be arranged more simply. But simulations show indications for some local degradation in the transverse stability in the energy range (3-10) MeV. Particles cross this range fast and without significant deterioration for beam quality, but this point requires additional study. Currently we base on FFDD scheme.

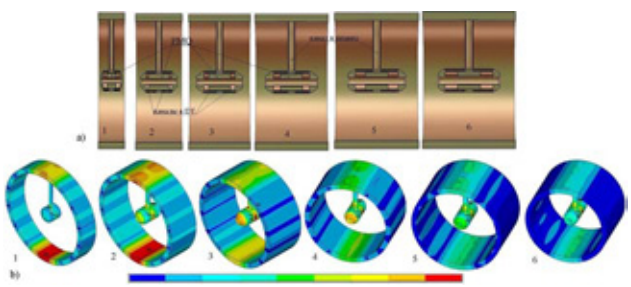

Figure 3: The DTL cells with PMQ in drift tubes (a) and the temperature distribution at the surface for accelerating rate 2.0 MV/m, DF=6% (b).

The PMQ length is accepted as ~40 mm for the first DTL tank and as ~90 mm for all following tanks. The diameter of drift tubes is 90 mm for all tanks. The DTL part consists of six tanks and accelerating rate is ~ 2 MeV/m is accepted preliminary, from costs estimation for accelerating structure and RF sources. The length of tanks L is limited either by 10λ from field stability reasons, or by RF power P_t~2.1 MW at the tank RF window. Conservative value E_{smax} <1.22 E_k is realized by drift tubes shape optimization without significant reduction in the shunt impedance value Z_e. Main parameters for DTL tanks are summarized in the Table 1. Due to similar purposes and assumptions, very similar parameters are independently chosen for ESS DTL, [5]. The technology of construction both for DTL tanks and drift tubes with PMQ, for example, is described in [6].

Table 1: The main parameters of DTL tanks.

	W_{out}, MeV	N_{dt}	2a, mm	ϕ_s, deg	P_{cu}, MW	P_t, MW	L, m
DTL1	18.18	65	20	-30	0.95	1.54	7.399
DTL2	35.86	45	22	-30	0.98	1.67	8.613
DTL3	53.47	35	24	-25	1.08	1.76	8.535
DTL4	71.12	30	26	-25	1.27	1.95	8.513
DTL5	88.23	26	28	-25	1.45	2.11	8.208
DTL6	102.98	22	30	-25	1.54	2.13	7.490

The beam envelope growth along DTL is ~ 40% and the maximal beam radius 5.3 mm is at DTL exit, providing very good aperture/(beam size) ratio, preventing particles losses from beam halo, formatted due to space charge forces together with hardware and tuning errors. At the DTL exit transverse particle distributions are shown in Fig. 4 and transverse emittance growth along DTL is ~ 10%, according simulations. In longitudinal direction we have well formed bunch with the total phase length ~ 15 degree and momentum spread ~0.6%.

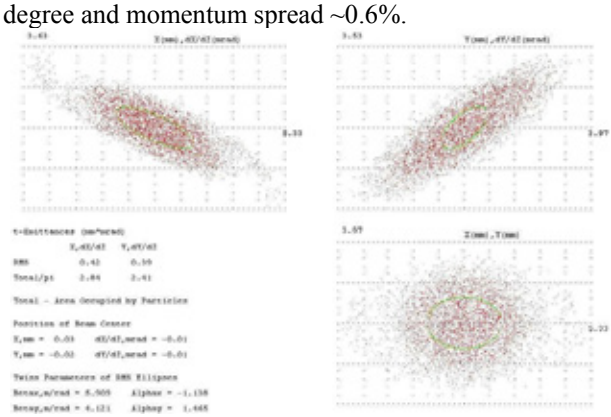

Figure 4: The transverse distributions of particles at the DTL exit.

With PMQ application, DTL RF efficiency in energy range ~80 MeV is high enough and there are no cost effective reasons to develop and introduce additional accelerating structure between DTL and CCL. Transition energy to the CCL part is ~ 103 MeV.

MEBT2 AND CCL PART

At transition energy ~ 103 MeV the beam lengthening is negligible at the length 3.04 m and MEBT2 contains just four EMQ with conservative gradients and beam diagnostic hardware.

For f_0=352.2 MHz CCL structures have much more weak Z_e dependence on aperture radius a (in mm), as compared to CCL at f_0~900 MHz. Comparing FODO, FDO and FDFO focusing with EMQ, we have selected FDO scheme to provide, together with CCL aperture ~ 40

ISBN 978-3-95450-170-0

mm, the higher transverse acceptance with realistic focusing gradient ~30 T/m. Due to operating frequency CCL longitudinal acceptance is large by definition.
For f_0=352,2 MHz application CCL must have reasonable transverse dimension and just two structures look now acceptable – PiMS, realized in CERN Linac 4 [7], Fig. 5a and CDS, Fig. 5b, developed in INR. CDS has higher Z_e value and the qualitative advantage in field stability, looks more labour-intensive in construction, but it is easy in RF tuning. Detailed PiMS and CDS comparison is in [8,2].

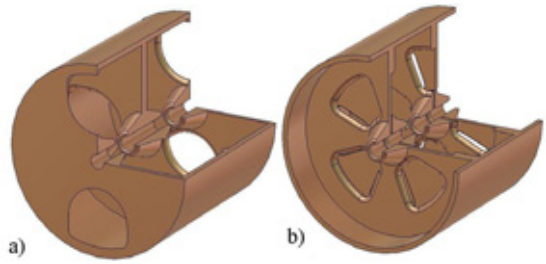

Figure 5: Accelerating structures, acceptable for f_0=352,2 MHz, PiMS (a) and CDS (b).

CCL part has the high canal acceptance and different options are considered, [2]. With RF power dividing one klystron feds two or four CCL tanks, forming together RF unit. For accelerating rate ~2 MeV/m the total number of CCL cells in one RF unit is ~30. To reduce cost, all CCL cells inside one RF unit are identical. Tanks are placed so, that reference particle cross the tanks centres at the prescribed phase ϕ_s. By fitting a geometrical β of cells in the unit, the maximal phase slip over tanks is minimized. We use actively both large CCL acceptance and small phase length of the bunch. For further cost reduction due to RF system simplification, the unit with two tanks, containing 15 CCL cells each, is studied in more details and beam envelopes along CCL part are shown in Fig.6.

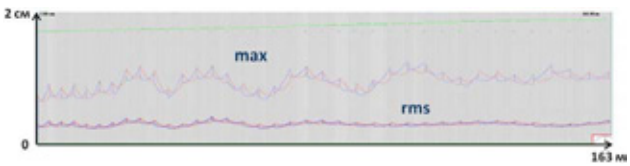

Figure 6: The beam envelope in CCL.

The transverse emittance growth along CCL is ~40% and longitudinal one – at 2.5%. The CCL part consists of 18 RF units and the total linac length this case is ~ 221 m.

RF SOURCES

The most appropriate RF source for designed linac is the klystron TH2179, [10], accepted also for CERN Linac 4. With the combination of pulse RF power 2.8 MW and average power 210 kW is allows operation with DF =7.5% and high efficiency 55%. Having the designed RF pulse length τ=1.5 ms, this klystron was tested for ESS DTL with τ>2.3 ms. Another required RF hardware, listed in [2], is already developed and tested in CERN Linac 4.

BEAM POWER

In present hadron linacs I_b is restricted with safe and realistic value ~(40-50) mA. Required beam power is by DF increasing. With high heat load for structure, the special care should be to thermal deformations. For DTL and CCL cells thermal effects were studied, [2,8], for DF=6% operation. The temperature distributions for DTL cells are shown in Fig. 3b. The operating frequency shift ~-60 kHz will be compensated by fast movable tuners in DTL and CCL tanks. It is more fast and precise method to control frequency for high heat load, when cooling water just remove heat from cavity. Operation with DF=5% is not unique. Operating SNS linac has DF=6%. For J-PARC linac, operating now with DF=3%, structures are designed to withstand with DF=15%, and for CERN Linac4 – with DF=10%.

CONCLUSION

The single frequency solution for the high power high energy hadron linac results in the comfortable conditions for beam dynamics with sufficient reserve. High beam quality allows optimal solutions and safe regimes for hardware operation. Unified RF system is cost effective in design, construction and maintenance. Required parameters for all linac parts are confirmed in the world wide practice. It is promising and cost effective direction for development and construction of such type normal conducting linacs.

REFERENCES

[1] M.Promé, Conceptual studies for a high-power proton linac, Linac1994, p.146, 1994.
[2] INR Report, Reg. N 01201371258, on IHEP Contract N 0348100096313000178, Moscow, 2014.
[3] B.I. Bondarev, A.P. Durkin et.al., A Computing System for Ion Linac Accelerating/Focusing Channels. Linac 1992, p. 734, 1993.
A. Kolomiets et.al., TRANSIT Code for Beam Dynamic Simulation, these proceedings, TUPSA07.
[4] Y. Kondo, et. al., Beam Test of a New RFQ for the J-PARC Linac., Linac2014, MOPP091, 2014.
[5] A. Aleksandrov et. al., Status of a New 2.5 MeV Test Facility at SNS. Linac2014, THPP108, 2014.
[6] R. De Prisco et. al., ESS DTL Status – Redesign and Optimization. IPAC2014, p. 3314, 2014 .
[7] S. Ramberger et. al., CERN Linac4 DTL Manufacturing. Linac2014, THPP036, THPP038, 2014.
[8] G Favre et. al., Manufacturing of Linac 4 Pi Mode Structure at CERN, IPAC2011, p. 1774, 2011.
[9] V. Paramonov, Comparison of Normal Conducting High Energy Accelerating Structures for a Moderate Operating Frequency. Linac2014, MOPP125, 2014.
[10] http://thalesgroup.com

ISBN 978-3-95450-170-0

THE PROJECT OF THE HV AXIAL INJECTION FOR THE DC-280 CYCLOTRON AT THE FLNR JINR

G.G.Gulbekian, B.N.Gikal, V.V.Bekhterev, S.L.Bogomolov, A.A.Efremov, I.A.Ivanenko, N.Yu.Kazarinov, I.V.Kalagin*, V.N.Melnikov, N.F.Osipov, S.V.Prokhorov, A.V.Tikhomirov, M.V.Khabarov, Flerov Laboratory of Nuclear Reaction, Joint Institute for Nuclear Research, Dubna, Moscow reg., 141980 Russia

Abstract

The project of the high-voltage (HV) axial injection for the DC-280 cyclotron which is being created at the FLNR JINR is presented. The injection system will consists of a Permanent Magnet ECR ion source and a Superconducting ECR ion source, beam analyzing magnets, focusing solenoids, beam choppers, a polyharmonic buncher, 75 kV DC accelerating tubes, a commutating electrostatic deflector and a spiral inflector. One part of the injection system is situated on the HV platform, another part is on the grounded yoke of the DC-280 magnet. The injection system will allow one to inject efficiently ions of elements from Helium to Uranium with the atomic mass to charge ratio in the range of 4÷7.5 providing acceleration of ion currents with intensity more than 10 pμA.

INTRODUCTION

At present time the project of Super Heavy Element Factory is being realized at the FLNR JINR [1]. The project implies design and creation of the DC-280 cyclotron (Figure 1) which has to provide intensities of ion beams with middle atomic masses (A~50) up to 10 pμA. The DC-280 will be equipped with high voltage injection system. The injection system has to provide ion transportation from the ECR-ion source to the cyclotron centre and capture into acceleration not less than 50% of ions with the atomic mass to charge ratio of A/Z=4÷7.5. Our experience in modernization of U-400 cyclotron [2] and creation of the DC-110 cyclotron [3] demonstrates that at ion energies of E_{inj}=15÷20 keV/Z (energy per single ion charge) the injection efficiency essentially depends on the ion beam current. At the ion beam currents of 80÷150 eμA the efficiency of capture into acceleration reaches 30÷35%, but for the ion currents less than 10 eμA increasing of the efficiency to 50÷60 % has been observed. The reason of it may be lowering influence of the ion beam space charge and decreasing the beam emittance, especially at low level of the microwave power in the ECR source. To improve the injection efficiency we will increase the injection energy up to E_{inj}=100 keV/Z, since the emittance and the space charge effects have to be decreased. The similar problem has been decided at Ganil, France by means of using the high voltage platform (HVP) equipped with the ECR-4 ion source [4]. Besides, we would like to create the injection with low electrical power consumption. In the last decade some of HVP in the world were equipped with the ECR with low power consumption, for example 300 kV HVP with the superconducting PK-ISIS ECR at "Pantechnik", (France) [**5**], 320 kV HVP with the permanent magnet ECR at IMP, Lanzhou, China [**6**].

* *kalagin@nrmail.jinr.ru*

LAYOUT OF THE AXIAL INJECTION

The high-voltage axial injection of the DC-280 will consist of two HVP. Every HVP will be equipped with an ECR ion source, a focusing solenoid, Einzel lenses and a magnet for ion separation and analyzing. The high voltage accelerating tube will be installed At the edge of the HVP to increase the ion energy up to 100 keV/Z. Both HVP will be placed on standoff insulators above the DC-280 magnet. The insulators will be fastened to the grounded metal platform which leans on the DC-280 magnet yoke (Figure 1).

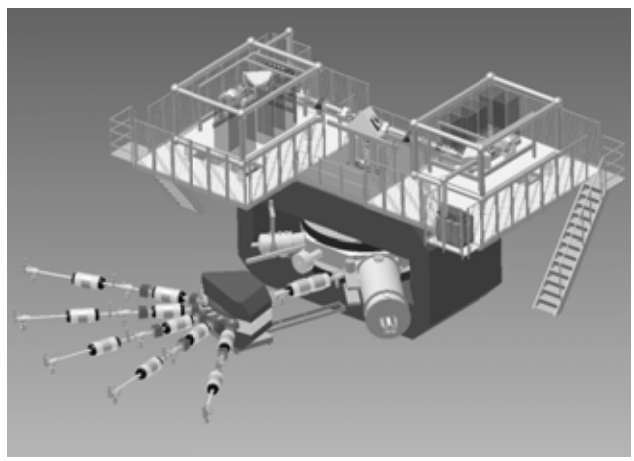

Figure 1: Layout of the DC-280 assembling.

HIGH VOLTAGE PLATFORM

We plan to limit the HVP power consumption to 50 kW to minimize maintenance charges and sizes of isolating transformers. The maximal HV on the HVP will be 75 kV. Every platform will have peripheral tube railings for equalization of the electrical potentials. Water cooling of the magnetic elements will be provided through water tube coils (head, drain) having the maximal total current leakage of 1 mA. When the HV is switched off the service personal can walk around the HVP for maintenance. The scheme allows us to work with every ECR source independently.

ISBN 978-3-95450-170-0

ECR ION SOURCES

To satisfy the HVP power consumption requirements, the electrical power of every ECR ion source has to be less than 10 kW. At that, the first ECR ion source has to produce high intensities (15÷20 pμA) of ions with medium masses (for example, $^{48}Ca^{7+,8+}$), the second one has to produce the high charged heavy ions, such as $^{238}U^{39+,40+}$. Therefore we will create two types of ECR ion sources: the DECRIS-PM source with permanent magnets [7] and the DECRIS-SC superconducting one [8].

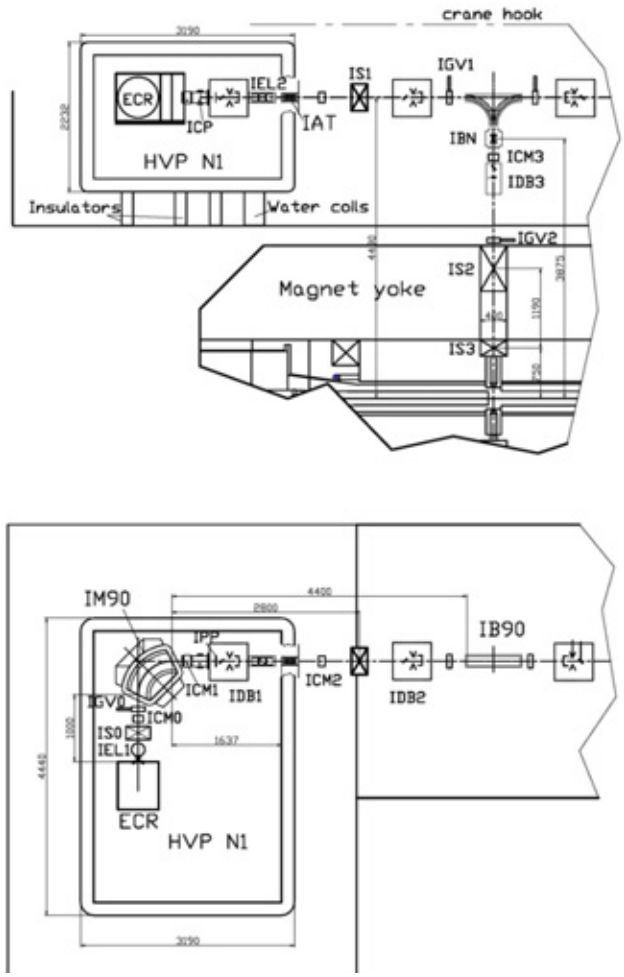

Figure 2: The scheme of the axial injection channel, front view and view from above.

Where: ECR- DECRIS-PM or DECRIS-SC are the ion sources; IM90 is the analysing magnet; IB90 is the bender; IEL1, IEL2 are the Einzel lenses; IS0,IS1,IS2,IS3 are the focusing solenoids; IAT is the accelerating tube; ICM0÷ICM3 are the steering magnets; IPP is the pepper-pot; ICP is the beam chopper; IDB1÷IDB3 are the diagnostic boxes; IBN is the polyharmonic buncher; IGV0, IGV1, IGV2 are the vacuum gate valves.

BEAM TRANSPORT AND FOCUSING

The scheme of the axial injection channel is shown in Figure **2** (only the HVP N1). The ion beam will be extracted from ECR with the energy of 25 keV/Z. After extraction the ion beam will be focused by the IEL1 Einzel lens and by the IS0 solenoid to the IM90 analysing magnet input. The ion charge spectrum will be analyzed by means of magnetic field variation in the IM90 and by the IS0 with measuring the ion current by Faraday cup (FC) in the IDB1 diagnostic box. After analyzing and separation the ion beam will be focused by IEL2 Einzel lens at the input of the IAT acceleration tube (NEC 2JA000260). The ion energy can reach 100 keV/Z after acceleration. Increasing the ion energy allows us to decrease of the ion beam emittance and space charge influence [**9**]. After the IAT the ion beam is matched with the acceptance of the IB90 electrostatic deflector (bender) with help of the IS1 solenoid. The IB90 bends the ion beam in the vertical direction to the cyclotron center. After the IB90, the ion beam longitudinal density will be modulated by the IBN polyharmonic buncher. Two solenoids (IS2, IS3) will match the ion beam emittance with the acceptance of the spiral inflector, which will turn the beam to the cyclotron median plane.

In our numerical calculations we supposed that compensation of the full space charge (by slow electrons accumulated in a beam) is absent in the channel parts with electrostatic elements, such as: the Einzel lenses, the IB90, the IAT, and also after the IBN. The calculation was carried out for $^{48}Ca^{8+}$ ion beam with the injection energy of 80 keV/Z (Fig. 3). The results show that this acceleration allows us to decrease the ion beam emittance in about 1.5 times. (Fig. 4) The calculated efficiency of the ion transport from the ECR to the DC-280 median plane is equal to 100%.

Of cause, the real transport efficiency will depend on many reasons: real value of the space charge compensation in the low energy part (it can be less than 60% so far as it depends on the beam parameters and vacuum conditions [10]), quality of the IM90, the IB90 and the inflector. To improve quality of the elements the special calculations have been carried out, including 3-D calculation [11], [12].

POLYHARMONIC BUNCHER

To increase the accelerating efficiency the polyharmonic buncher IBN will be installed in the vertical part of the channel at the distance of 388 cm from the cyclotron median plane. A prototype of the buncher could be the multiple cavity buncher [13]. The buncher consists of drift tube having the diameter of 5 cm at the length of $\beta\lambda/2$=7.8 cm and harmonic grids. The RF voltage is applied to the tube with the frequency equal to the cyclotron accelerating one (first harmonic, f=7.32÷10.38 MHz). Two thin tungsten grids are installed at the edges of the drift tube. Harmonic grids (for the second and the third harmonics) are situated before and after the drift tube. Two grounded grids are installed in the gaps to exclude interference between the tube and the harmonic grids,. All the grids have spacing of 0.8 cm. The numerical simulation has shown that longitudinal beam density will be increased in 8÷10 times.

ISBN 978-3-95450-170-0

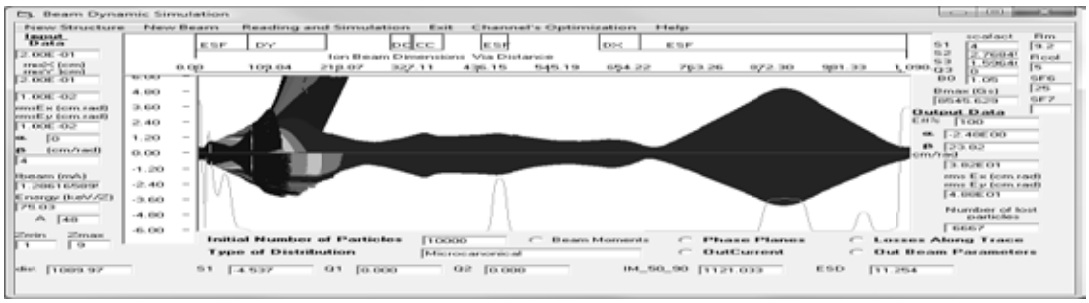

Figure 3: $^{48}Ca^{8+}$ ion trajectories along the injection line.

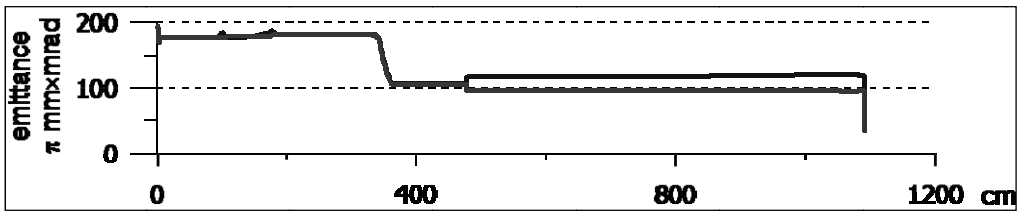

Figure 4: Behaviour of the emittance of $^{48}Ca^{8+}$ ion beam along the injection line. The ion beam emittance has been decreased in about 1.5 times after acceleration to 80 keV/Z. The IAT was situated at 370 cm from the ECR.

DIAGNOSTIC SYSTEM

The beam diagnostics placed in the special boxes IDB1÷IDB3 will consist of the FC, slit collimators and luminophors with TV cameras for beam intensity and profile monitoring. Decreasing the beam intensity in about 10 times can be made by means of the beam modulation by the ICP beam chopper, or using the IPP pepper-pot. It is necessary to measure parameters of high intensity beam in the DC-280 extraction channels.

VACUUM SYSTEM

The system is zoned on HVP and GP parts. Four turbopumps (total pumping speed of G_{Σ}=2720 l/s) will be installed at HVP and four turbopumps (G_{Σ}=1880 l/s) will be installed at GP. The expected average vacuum will be about $(4\div6)\cdot10^{-8}$ mbar to provide the ion losses of 2÷4% for $^{48}Ca^{7+,12+}$ and of 10÷15% for $^{238}U^{40+}$.

CONCLUSION

The project of the HV axial injection for the DC-280 cyclotron has been created at the FLNR JINR. The injection has to provide the DC-280 with the ion beam intensities more than 10 pμA for A/Z=4÷7.5.

REFERENCES

[1] G.Gulbekyan et al. "Development of FLNR JINR Heavy Ion Accelerator Comple[x in the Next 7 Years. New DC-280 Cyclotron Project" in Proc. of IPAC2011, San Sebastián, Spain, WEPS082, p. 2702, (2011).

[2] Yu.Ts. Oganessian et al. "Status report of the U400 Cyclotron at the FLNR JINR" in Proc. of APAC2004, Gyeongju, Korea, p.52÷54 (2014).

[3] Gikal B.N. et al. "Development, Creation and Start-Up of DC-110 Heavy Ion Cyclotron Complex for Industrial Production of Track Membranes", Part. Nucl., Lett. V. 11, No. 2(186). pp. 233÷253 (2014).

[4] C.Barue "The new high-voltage platform of the injector C01 PFI1 project" Technical report on operating accelerators 2003÷2004, GANIL R 05 01, (2004). http://hal.in2p3.fr/docs/00/03/14/59/PDF/GANIL_R_05_01.pdf

[5] "High Voltage Platform with ECR ion source", PANTECH-NIK S.A., Bayeux, France. http://www.pantechnik.com/ #!systems/vstc3=model-3---platform

[6] L.T. Sun, J.Y. Li, Y.C. Feng, Y. Cao "The High Charge State All-Permanent Magnet ECRIS Operated on 320 kV HV Platform" Proc. of ECRIS08, Chicago, IL USA, MOCO-B05, pp.23÷26 (2008).

[7] V.Bekhterev, S.Bogomolov, A.Efremov, N.Konev "Development of the magnetic system for new DECRIS-PM ion source", Proc. of ECRIS-14, Nijniy Novgorod, Russia (2014).

[8] S.Bogomolov el al." Resent Development in ECR Ion Sources at FLNR JINR" Proc. of RUPAC2012, Saint-Petersburg, Russia, pp. 203÷207 (2012).

[9] Yu. Ts. Oganessian et al." Modernization of the U-400 Axial Injection System", Proc. of RuPAC2004, Dubna, October 4-9, pp. 261÷262 (2004).

[10] D.Winklehne et al. "Space Charge Compensation Measurements in the injector beam lines of the NSCL coupled cyclotron facility", Proc. of Cyclotrons2013 Int. Conf., Vancouver, Canada, pp. 417÷419 (2013)

[11] I.Ivanenko, N.Kazarinov "Magnets of Injection and Extraction Systems of Cyclotron DC280", these Proceedings, RuPAC-2014, Obninsk, Russia (2014).

[12] I.Ivanenko "The Beam Vertical Focusing at Injection on the Centre of Isochronous Cyclotron", Proc. of 20th Int. Workshop on Beam Dynamics and Optimization (BDO), 30 June÷4 July, Saint Petersburg, Russia (2014).

[13] E.A. Wadlinger "Buncher System Parameter Optimization", IEEE Transactions on Nuclear Science, Vol. NS-280, N3, pp. 2630÷2632. (1981).

ISBN 978-3-95450-170-0

THE PROJECT OF BEAM TRANSPORTATION LINES FOR THE DC-280 CYCLOTRON AT THE FLNR JINR

G.G.Gulbekyan, B.N.Gikal, G.N. Ivanov, I.V.Kalagin*, V.I. Kazacha, N.Yu. Kazarinov, M.V. Khabarov, V.N. Melnikov, N.F. Osipov, A.V. Tikhomirov, Y.G. Teterev,
Joint Institute for Nuclear Research, FLNR, Dubna, Moscow region, Russia

Abstract

The project of beam lines for carrying out physical experiments at the DC-280 cyclotron which is being created at the FLNR JINR is presented. The commutating magnet with variable magnetic field induction up to 1.5 T gives us possibility to bend ion beams in five directions providing ion transportation through beam lines to five experimental setups. The beam focusing in the beam lines is provided by set of quadrupole lenses having the gradients up to 7.7 T/m. The beam lines are intended for the efficient ion transportation of elements from Helium to Uranium with the atomic mass to charge ratio in the range of 4-7.5 at energies from 4 up to 8 MeV/amu. The ion beam power will reach the value about 3 kW. The water cooled current aperture diaphragms will be installed into all beam lines to prevent the tube damage. The beam diagnostics consists of the Faraday caps (FC), slit collimators, sector aperture diaphragms and ionization beam profile monitors.

INTRODUCTION

DC-280 cyclotron designed at the Flerov Laboratory of Nuclear Reaction (JINR, Dubna) is intended for carrying out fundamental and applied investigations with ions from He to U (masses from A = 2 up to 238) produced by the ECR-source. The energy of the ions extracted from the cyclotron may vary from 4 up to 8 MeV/amu. The main parameters of the DC-280 cyclotron are given in **[1]**.

Utilization efficiency of the accelerator is determined in many respects by quality of the transportation system for the extracted ions. Widely branched system of the beam lines allows one to carry out numerous investigations. This work is devoted to the design of the beam lines for transportation of the extracted heavy ions from the cyclotron to physical targets. Lay-out of the beam lines for heavy ion transportation is shown in Fig. 1.

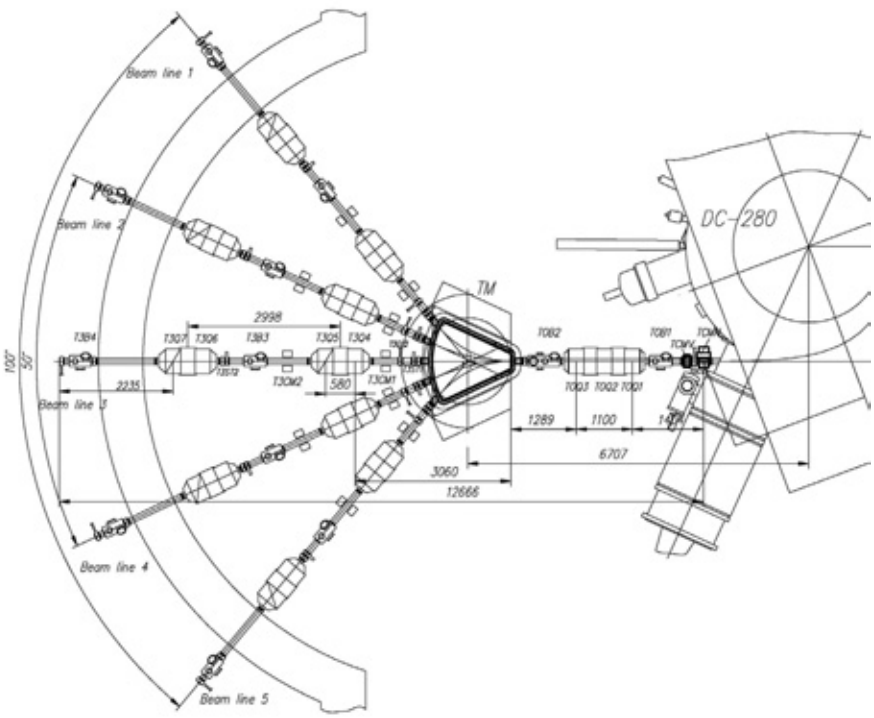

Figure 1: Lay-out of the beam lines for heavy ion transportation.

Where: **TM** is the bending magnet (±50º), TCMH,TCMV are the horizontal and vertical steering magnets at DC-280 extraction,T**x**Q**y** are the magnetic quadrupoles, T**x**CM**y** are the two-plane dipole steering magnets, T**x**B**y** are the diagnostics boxes, T**x**ST**y** are the beam stoppers, T**x**GV**y** are the vacuum gate valves (where: **x** is the beam line number, **y** is the element number).

kalagin@nrmail.jinr.ru

ISBN 978-3-95450-170-0

DESCRIPTION OF BEAM LINES

The particularity of the beam line system is using one commutating magnet (TM) to bend ion beams to five experimental beam lines, similar to the scheme used at RCNP of Osaka University **[2]**. Every physical setup will be separated from others by concrete walls. After TM the water-cooled beam stoppers will be installed into every beam line to prevent damage of the T**x**GV**2** vacuum gate valve (stopper T**x**ST**1)** and wrong beam transportation to the setups that are prepared to work (stoppers T**x**ST**2**, x=1÷5**)**. The scheme allows beam users to prepare experimental equipment in parallel with beam experiments in the neighbor beam lines, also it is preferable in respect to the cost optimization in comparing with wide spread beam lines.

The common part of all beam lines lies from the center of the TCMH magnet (horizontal steering magnet at the extraction point) to the TM bending magnet input (the beam line 0). The beam tracing to the TM input is carried out by means of the quadrupole triplet T0Q1÷T0Q3. The scheme of the TM bending magnet is shown in Fig. 2 (ABCD outline).

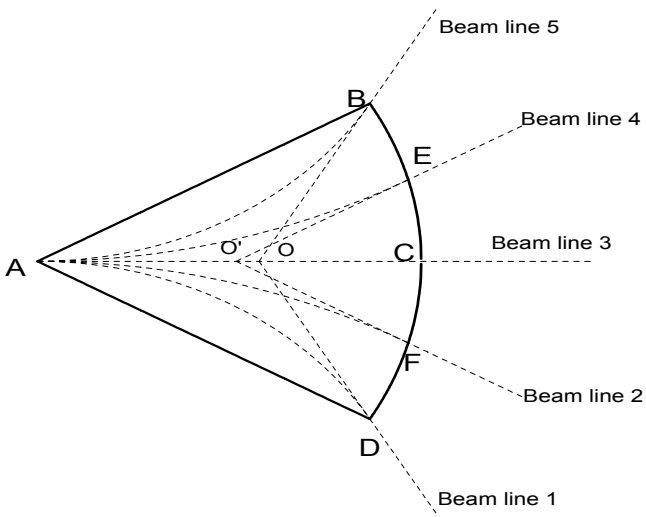

Figure 2. Scheme of TM bending magnet.

The TM has the magnetic field induction up to 1.36 T which bends the ion beam at the angles of $\pm 50^0$ (in the beam lines 1 and 5) and at the angles of $\pm 25^0$ (in the beam lines 2 and 4). When the TM is switched off the ion beam is traced along the beam line 3. Two more quadrupole doublets focusing the ion beam on a target are placed in every beam line behind the TM.

The edge angle at the TM input is ε_{in}=0. The 3D calculations of the TM magnetic field were carried out in [**3**]. The calculation results showed that the edge angles at TM output ε_{out} are equal to $+20.5^0$ for the beam lines 1 and 5, and to $+11.5^0$ for the beam lines 2 and 4. The radius of curvature of the magnetic pole (AC) is equal to 154.1 cm.

It is supposed that quadrupoles with the following parameters will be used in the beam lines: the effective length is l_{eff} = 35 cm ; aperture diameter is D = 11 cm; distance between the quadrupole centers in the doublets is Δ = 58 cm; the maximum gradient is G_{max} = 7.7 T/m.

The expected ion beam power in the beam lines will be up to 3 kW. Correspondingly the powerful beams can damage the beam lines. To protect the vacuum tubes against damage, the water cooled current aperture diaphragms (32 pieces) will be installed along all beam lines. They will combine function of vacuum seals and water cooled ring protectors.

CALCULATION RESULTS

Calculations of the extracted ion beam tracing were carried out with the help of COSY INFINITY code **[4]** for the ion beam parameters given in Table 1. They correspond to 3 points on the cyclotron working diagram. The following designations are used in the Table 1: W is the ion beam kinetic energy, $\alpha_x, \beta_x, \alpha_y, \beta_y$ are Twiss parameters, $\varepsilon_{x,y}$ are the RMS values of horizontal and vertical emittances, D_x and D_x' are the values of the horizontal dispersion function and its derivative.

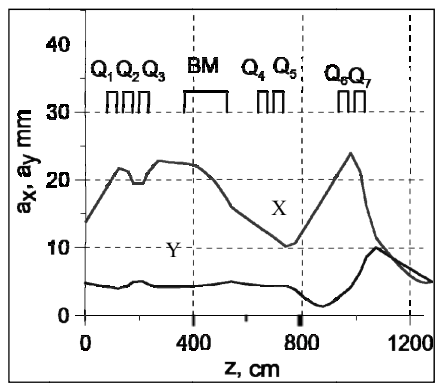

Figure 3. Transportation of $^{48}Ca^{9+}$ ions in beam line 1.

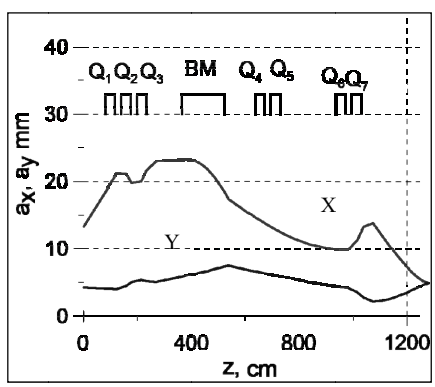

Figure 4. Transportation of $^{238}U^{43+}$ ions in beam line 2.

ISBN 978-3-95450-170-0

Table 1. Parameters of the extracted heavy ion beams.

Ion type	B_0 T	W MeV/u	α_x	β_x cm/rad	α_y	β_y cm/rad	ε_x π·cm·rad	ε_y π·cm·rad	D_x cm	D'_x
$^{40}Ar^{10+}$	0.65	4.0	-17.82	3005.9	-0.018	2214.5	$2.871\ 10^{-4}$	$1.334\ 10^{-4}$	123.8	0.426
$^{48}Ca^{9+}$	1	5.43	-10.4	1738.0	0.222	1600.1	$2.826\ 10^{-4}$	$1.27\ 10^{-4}$	170.8	0.6026
$^{238}U^{42+}$	1.3	7.7	-6.646	1200	-0.121	814.5	$2.852\ 10^{-4}$	$1.284\ 10^{-4}$	196.7	0.6399

It was also supposed that relative spread of ion momentums $\Delta p/p$ was equal to ±0.2% and the ion beam current was equal to 10 pμA. The values of the vertical dispersion function D_y and its derivative D_y' were considered to be equal to zero.

In the carried out calculations one took into account the influence of the initial ion longitudinal momentum spread $\Delta p/p$ [**5**]. For that one calculated the behavior of the dispersion function D_x along the beam trajectory and took into account contribution of the initial ion momentum spread to the behavior of the horizontal beam dimension.

Quadrupole gradients in the beam lines were chosen so that the beam diameter on the target to be equal to 10 mm and the dispersion function D_x to be close to zero. In the beam lines 4 and 5 the ion beam is deflected in the direction opposite to the beam circulation in the cyclotron.

As an example of the calculation results, the dependences of the horizontal α_x and vertical α_y ion beam half dimensions versus the beam line length z for the beam lines 1, and 2 are shown in Fig. 3 ($^{48}Ca^{9+}$**)** and Fig. 4 ($^{238}U^{43+}$), where BM is the commutating magnet TM, Q1÷Q7 are the quadrupoles.

BEAM POSITION CORRECTION

The system of beam position correction in the beam lines will consist of the horizontal and vertical steering magnets (TCMH, TCMV) at the cyclotron exit and two two-plane dipole steering magnets (T**x**CM1, T**x**CM2, **x**=1÷5) with length of 50 cm each, located after the TM.

BEAM DIAGNOSTICS

The main part of beam diagnostics will be situated in 12 diagnostics boxes (TxBy, **x**=1÷5, **y**=1÷4). The Faraday caps will be placed in every diagnostics box together with ionization beam profile monitors (IBPM) [**6**] they will be used to measure the ion currents and to determine the ion beam transverse position, the beam profile and intensity distribution in the beam cross section.

The slit collimators will be situated in the T0B2. They will be used to restrict the beam transverse distribution and intensity if it is necessary.

Stationary installed four sector aperture diaphragms will be situated in the beam lines before and after the TM and at the end of every beam line (16 pieces). They will be used for rough estimation of the beam position in the beam lines and for protection of the beam line components from damage due to incorrect beam adjustment.

Two pickup electrodes [**7**] will be placed into the beam line 0. The distance between pickups is equal to 2.4 m. They will be used for measuring the ion beam energy.

The beam intensity will be decreased in 10 times by using the beam chopper system in the DC-280 injection line to measure ion currents by the FC. That allows us to prevent damage and excessive activation of the FC. In routine operation the ion beam current can be controlled by vacuum calibrated IBPM.

VACUUM SYSTEM

The beam line will be pumped by turbo pumps with the pumping speed of 150 l/s installed at the diagnostic boxes and two turbo pumps with the pumping speed of 500 l/s installed at the TM vacuum chamber. The estimated average pressure in the beam lines is about $1 \cdot 10^{-6}$ Torr, the vacuum beam losses will be not more than 5 %.

CONCLUSION

The project of beam lines for efficient transportation of heavy ion beams extracted from the DC-280 cyclotron to five experimental setups was designed.

REFERENCES

[1] G. Gulbekyan et al., "Development of FLNR JINR Heavy Ion Accelerator Complex in the Next 7 Years. Project of New DC-280 Cyclotron", Proc. of PAC-2011, San-Sebastian, Spain, p.p. 2700÷2702 (2011).

[2] H. Ikegami, "Annual Report of Research Center for Nuclear Physics", Osaka University, Japan, p. 76 (1976).

[3] I. Ivanenko, N. Kazarinov, "Magnets of Injection and Extraction Systems of Cyclotron DC280", these Proceedings, RuPAC-2014, Obninsk, Russia (2014).

[4] K. Makino and M. Berz, "COSY INFINITY version 9", NIM, v. 258, p.p. 346÷350 (2005).

[5] V. Alexandrov et al., "Multi-Component Ion Beam Code — MCIB04", Proc. of XIX Russian Particle Accelerator Conference (RUPAC-2004), Dubna, Russia, p.p. 201÷203 (2004).

[6] Yu. G. Teterev et al, "A beam diagnostics system operating on non contacting method under heavy radiation conditions", IEEE Transactions of Nuclear Science, Vol. 58, N1, pp.170÷1 76 (2011).

[7] G.G.Gulbekian et al., "A system for beam diagnostics in the external beam transportation lines of the DC-72 cyclotron", in Proc. of DIPAC2003 Int. Conf., Mainz, Germany, pp. 155÷157 (2003).

ISBN 978-3-95450-170-0

MAGNETS OF INJECTION AND EXTRACTION SYSTEMS OF CYCLOTRON DC280

N.Kazarinov#, I.Ivanenko, JINR, Dubna, Russia

Abstract

The design of two magnets of the cyclotron DC280 is presented. The magnets are the parts of injection and extraction systems the cyclotron. The design is based on three-dimensional calculation of the magnet field carried out by using OPERA 3D program code. The influence of the magnetic fields nonlinearities on ion beam dynamics is analyzed.

INTRODUCTION

The isochronous heavy-ion cyclotron DC-280 is a basic part of the Super Heavy Element Facility – the new accelerator complex of Joint Institute for Nuclear Research [1]. The DC-280 cyclotron will produce high-intensity beam of accelerated ions in the range from helium to uranium. The maximum design value of a current of ion beams will be 10 pmcA and the maximum kinetic energy will be 8 MeV/u.

In this report the design of two magnets IM90 and TM50 of SHEF is presented. The analyzing magnet IM90 is a part of high voltage injection system of DC-280 cyclotron [2]. The switching magnet TM50 is placed in extraction beam lines [3] of the facility. Depending on the magnitude of the magnetic field in magnet, the particles move on five orbits corresponding to different bending angles (0, ±25 and ±50 degrees) of the ion beam. The design is based on three-dimensional calculation of the magnet field carried out by using OPERA 3D program code [4]. The 3D computational models of the magnets are shown in Fig.1.

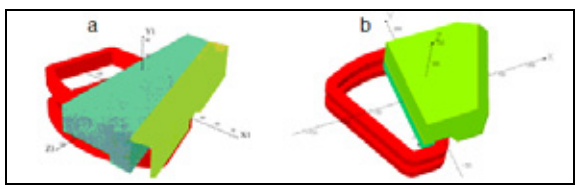

Figure 1: 3D models of IM90 (a) and TM50 (b) magnets

The 3D macro-particle beam dynamic simulation in the magnets was done in the curvilinear coordinates system connected with reference orbit, defined for computational field map. This simulation was carried out by using MCIB04 program code [5].

Inhomogeneities of the magnetic field distribution in the vicinity of the reference orbit were evaluated by Fourier analysis of the magnetic field map.

The optimum value of the basic geometrical characteristics of the magnets influencing on the form of the field distribution are found.

#nyk@lnr.jinr.ru

REFERENCE ORBITS OF THE MAGNETS

The reference orbits of the magnets are shown in Fig.2,3. In the case of IM90 magnet the initial approximation for the angular width of the magnet pole (84.75 degrees) found by using the results of [6] gave a good agreement of the effective bending radius (497.4 mm) and it design value (500 mm).

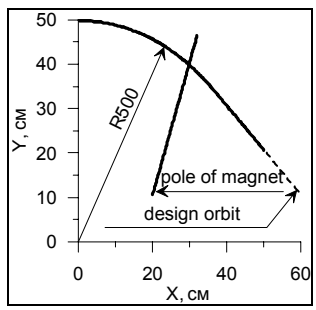

Figure 2: Reference orbit of IM90 magnet

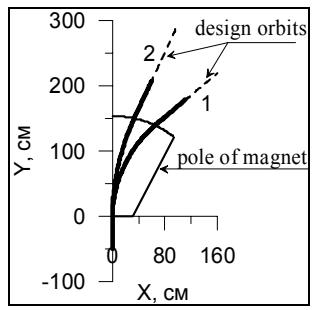

Figure 3: Reference orbits of TM50 magnet

The magnetic fields distributions at reference orbits are shown in Fig. 4-6.

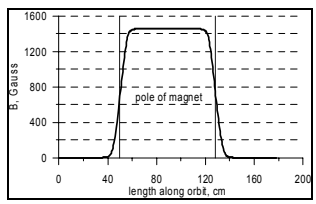

Figure 4: Bz field along reference orbit of IM90 magnet

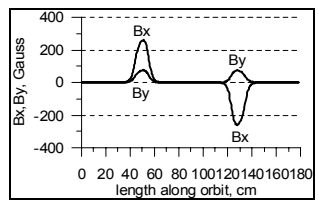

Figure 5: Bx,y field at 2 cm higher reference orbit of IM90 magnet

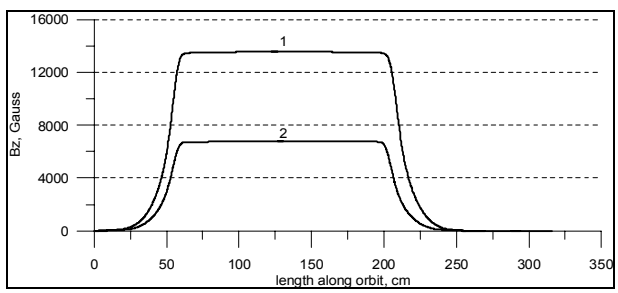

Figure 6: Bz field along reference orbits of TM50 magnet

MAGNETIC FIELD INHOMOGENEITIES

Inhomogeneities of the magnetic field distribution in the vicinity of the reference orbit were evaluated by Fourier analysis of the magnetic field map:

ISBN 978-3-95450-170-0

$$B_z = B_0 \sum_{n=0}^{\infty} b_n(r,s) r^n Cos(n\varphi) \quad (1)$$

Here (r,φ) is a polar coordinates of point in the curvilinear system connected with reference orbit, B_0 is the value of magnetic field in the midpoint of trajectory.

Dependence of the amplitudes of the first $b_1(r,s)$ and second $b_2(r,s)$ harmonics on the length along the orbit s at different radii r for the magnet IM90 is shown in Fig.7,8.

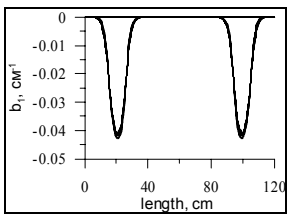

Figure 7: Quadrupole $b_1(r,s)$ component of magnetic field of IM90 magnet

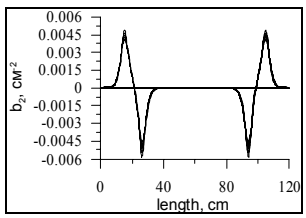

Figure 8: Sextupole $b_2(r,s)$ component of magnetic field of IM90 magnet

The same dependencies for the magnet TM50 are shown in Fig.9-12.

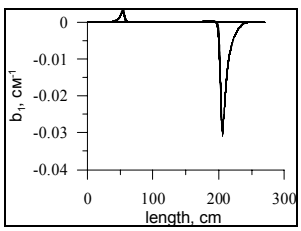

Figure 9: Quadrupole $b_1(r,s)$ component of magnetic field of TM50 magnet. Orbits 1,5

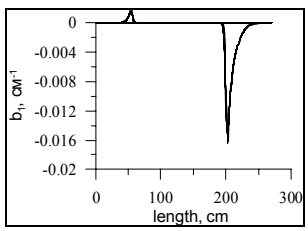

Figure 10: Quadrupole $b_1(r,s)$ component of magnetic field of TM50 magnet. Orbits 2,4

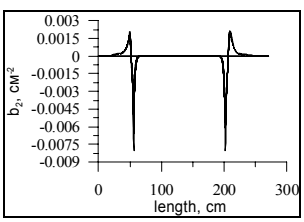

Figure 11: Sextupole $b_2(r,s)$ component of magnetic field of TM50 magnet. Orbits1,5

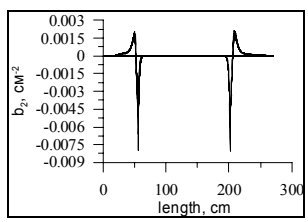

Figure 12: Sextupole $b_2(r,s)$ component of magnetic field of TM50 magnet. Orbits2,4

BASIC CHARACTERISTICS OF MAGNETS

In the case of IM90 magnet the optimum value of the basic geometrical characteristics influencing on the form of the field distribution are found. Selected geometric pole edge angle of the magnet (26.0 degrees) ensures symmetry of focusing on both transverse coordinates. The optimum value of the distance from the pole boundary to the magnetic screen (70 mm) reduces the effect of sextupole nonlinearity to an acceptable level. The growth of RMS emittance of the beam due to sextupole nonlinearity is not greater than 12.5%. The plots of the beam envelopes and emittance are shown in Fig.13,14.

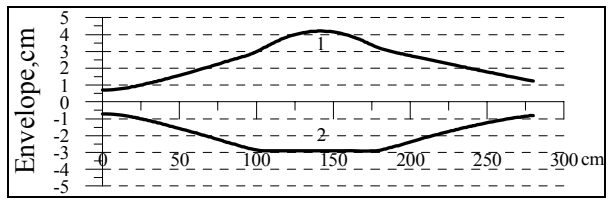

Figure 13: Envelopes of the ion beam for horizontal (1) and vertical (2) motion

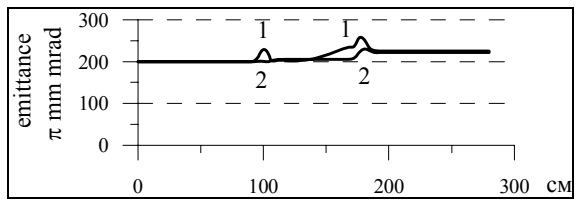

Figure 14: Emittances of the ion beam for horizontal (1) and vertical (2) motion

Particle distributions in the various phase planes at the image point of the IM90 magnet are shown in Fig.15.

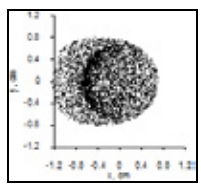

Figure 15a: Plane (x,y)

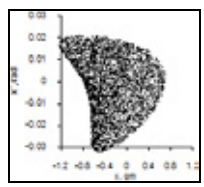

Figure 15b: Plane (x,x′)

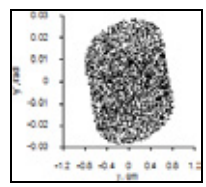

Figure 15c: Plane (y,y′)

Using of the focusing solenoid installed at the entrance of the magnet significantly reduces the effect of sextupole nonlinearity on the dynamics of particles. In this case the growth of RMS emittance is not greater than 2.8%.

In the case of TM50 magnet the actual bending angle θ for the orbit does not coincide with the design value φ. This is explained by a violation of symmetry of vertical magnetic field with respect to the mid-point of trajectory. The parameters of the orbits in TM50 magnet are contained in Table 1.

Table 1. Orbits parameters

Orbit number	Design bending angle φ, degree	Actual/ design bending radius, mm	Actual/ design exit edge angle, degree	$\lvert\theta-\varphi\rvert$, mrad
1,5	± 50	1887/1823	20.5/25	0.443
2,4	± 25	3699/3560	11.5/12.5	0.365

ISBN 978-3-95450-170-0

The envelopes of the ion beam transported through TM50 magnet are shown in Fig.16,17.

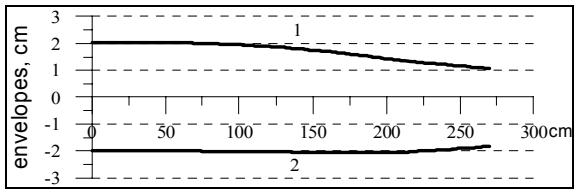

Figure 16: Horizontal (1) and vertical (2) beam envelopes at orbits 1,5

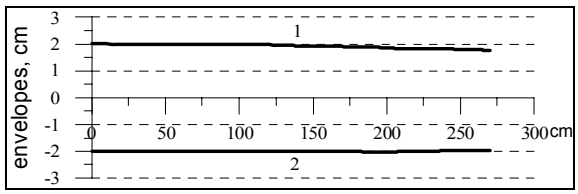

Figure 17: Horizontal (1) and vertical (2) beam envelopes at orbits 2,4

The emittances of the beam are shown in Fig.18,19.

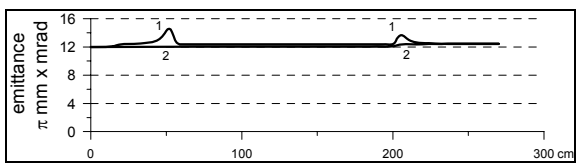

Figure 18: Horizontal (1) and vertical (2) beam emittances at orbits 1,5

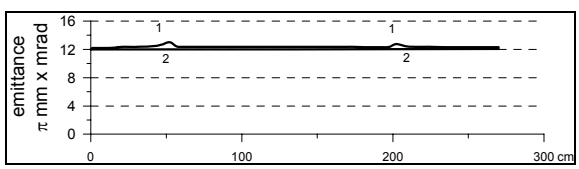

Figure 19: Horizontal (1) and vertical (2) beam emittances at orbits 2,4

RMS emittance of ion beam is increased by 3.4% for orbits 1,5 and 2.6% for orbits 2,4 due to sextupole nonlinearity of magnetic field.

CONCLUSION

Simulation of the dynamics of ion beams in the injection [2] and extraction [3] beam lines by means of the calculated three-dimensional maps of the magnetic field has shown the possibility of using the magnets IM90 and TM50 while creating the corresponding channels.

REFERENCES

[1] G.Gulbekyan, B.Gikal, I.Kalagin, N.Kazarinov. Status Report and Future Development FLNR JINR Heavy Ions Accelerators Complex, Proceedings of 11-th International Conference on Heavy Ion Accelerators Technology, HIAT09, 8-12 June 2009, Venezia, Italy, p.p. 59-63.

[2] G.G.Gulbekian, B.N.Gikal, V.V.Bekhterev, S.L.Bogomolov, A.A.Efremov, I.A.Ivanenko, N.Yu.Kazarinov, I.V.Kalagin, V.N.Melnikov, N.F.Osipov, S.V.Prokhorov, A.V.Tikhomirov, M.V.Khabarov. The Project of the HV Axial Injection for the DC-280 Cyclotron at the FLNR JINR, These proceedings, RuPAC'14, Obninsk, Russia (2014)

[3] G.G.Gulbekyan, B.N.Gikal, G.N. Ivanov, I.V.Kalagin, V.I. Kazacha, N.Yu. Kazarinov, M.V. Khabarov, V.N. Melnikov, N.F. Osipov, A.V. Tikhomirov, Y.G. Teterev. The Project of Beam Transportation Lines for the DC-280 Cyclotron at the FLNR JINR, These proceedings, RuPAC'14, Obninsk, Russia (2014)

[4] OPERA-3D Reference Manual, Oxford OX5 1JE, England, October 2012.

[5] V.Alexandrov, N.Kazarinov, V.Shevtsov, Multi-Component Ion Beam code – MCIB04. In: Proceeding of XIX-th Russian Particle Accelerator Conference, RUPAC2004, 4-9 October, Dubna, Russia, p.p.201-203.

[6] H.Hubner, H.Wolnik, The design of magnetic field elements, NIM, 86(1970), p.p. 141-148.

ISBN 978-3-95450-170-0

NSLS-II BOOSTER VACUUM SYSTEM

V.A. Kiselev, V.V. Anashin, S.M. Gurov, A.M. Semenov*, Budker Institute of Nuclear Physics SB RAS, Novosibirsk, Russia
A.A. Krasnov, Budker Institute of Nuclear Physics SB RAS, Novosibirsk, Russia and Novosibirsk State University, Novosibirsk, Russia

Abstract

NSLS-II - one of the latest third-generation SR sources - is currently under commissioning at the Brookhaven National Laboratory. In order to improve the operation efficiency in a continuous mode with maximum brightness, the injectors of these SR sources are operated continuously at the energy of up to the energy of the main ring (linac or synchrotron booster) [1]. The full injection energy allows adding electrons to the travelling electrons in a storage ring rather than to regulate a magnet system. This operating mode is often named "Top-Up". NSLS-II consists of a linear accelerator with the electron energy of up to 200 MeV, a synchrotron booster with the energy of 3 GeV, and a main storage ring. The status and review of the NSLS-II Booster vacuum system are presented in this paper.

INTRODUCTION

Since 1992, the first specialized storage rings (3rd generation SR sources) with a large number of straight sections of a sufficient length for installation of undulators (or wigglers) and more perfect systems of the storage ring parameter stabilization have been built.

In the first specialized SR sources, electrons were injected into the storage ring at a low energy, then the energy was increased, stabilized, and experiments were carried out. The beam current decreased with time, SR intensity dropped. The cycle with energy decrease, electron storage and energy increase was repeated in 1-2 hours. This was the mode of NSLS-I operation. NSLS-I booster was designed for acceleration of electrons from the energy of 120 MeV up to 700 MeV, the energy of storage rings was 800 MeV (vacuum ultra-violet spectrum) and 2.8 GeV (hard X-rays).

For today, mostly 3rd-generation SR sources are in operation and under construction in the world. One of latest sources scheduled for starting-up in 2015 is NSLS-II (Brookhaven National Laboratory, USA). Main parameters of the NSLS-II Synchrotron are presented in [1].

VACUUM SYSTEM DESCRIPTION

The perimeter of the booster vacuum chamber is 158.4 meters. 8 all-metal electropneumatical gate valves (actuation time ~ 2-3 sec) are installed in the ring for isolation of certain sections of the booster vacuum chamber. The booster consists of 4 arc sections (about 31 m each) and 4 straight sections (8 m each). All vacuum chambers are made of 316 L stainless steel, with Conflat flanges. The vacuum chamber aperture in arc sections is an ellipse of 41x24 mm (molecular conductivity of the chamber is about 3.2 l·m/sec); and the aperture of the majority of the chambers in straight sections is an ellipse of 62x22 mm (molecular conductivity of the chamber is about 4 l·m/sec). After manufacturing all vacuum chambers were exposed to special chemical treatment to reduce the outgassing rate [2].

For smoothness of the vacuum chamber and reduction of electron beam losses, special transitions from elliptical cross-section (24x41 mm) to circular cross-section (46 mm diameter) were produced, places for pumping were made from a one-piece tube with cut-out slots for pumping, besides, some bellows in straight sections were supplied with RF contacts having the shape of the vacuum chamber.

Residual gas pressure after accumulation of current integral of an order of 1 A·h should be not worse than 1E-7 Torr. Vacuum is provided with Gamma Vacuum ion-pumps (71 pieces) with pumping speed of 45 l/sec, placed at an average distance of 2.3 meters from each other. Two inverted-magnetron cold cathode gauges are installed in each section for vacuum measurements, and convection-enhanced Pirani gauges (MKS) are planned for forevacuum measurements. Detection of residual gas spectrum and of micro-leaks is carried out by means of MKS mass-spectrometers. Fig.1 shows the arrangement of the main components of the booster vacuum system.

RESULTS OF THE WORK PERFORMED

A rather strong synchrotron radiation results in an additional radiation-induced desorption of the residual gas molecules from the vacuum chamber walls and can cause a significant mechanical stress in vacuum chamber due to a non-uniform heating.

Despite a pulse operation mode of the booster (SR intensity duty ratio is 1/7 at a 2Hz repetition frequency), gas desorption under the influence of photons on vacuum chamber walls will exceed thermal desorption.

A relatively low SR power (maximum power is 44 W/m in BD bending magnets) does not require any special radiation absorbers. However, such radiation can cause mechanical stresses in vacuum chamber.

*A.M.Semenov@inp.nsk.su

ISBN 978-3-95450-170-0

As it was found, synchrotron radiation power density on the vacuum chamber wall is about 44 W/m, this results in a non-uniform heating of the chamber in places of SR direct effect by 60 degrees Celsius (calculated Δ□ = 62 ° C).

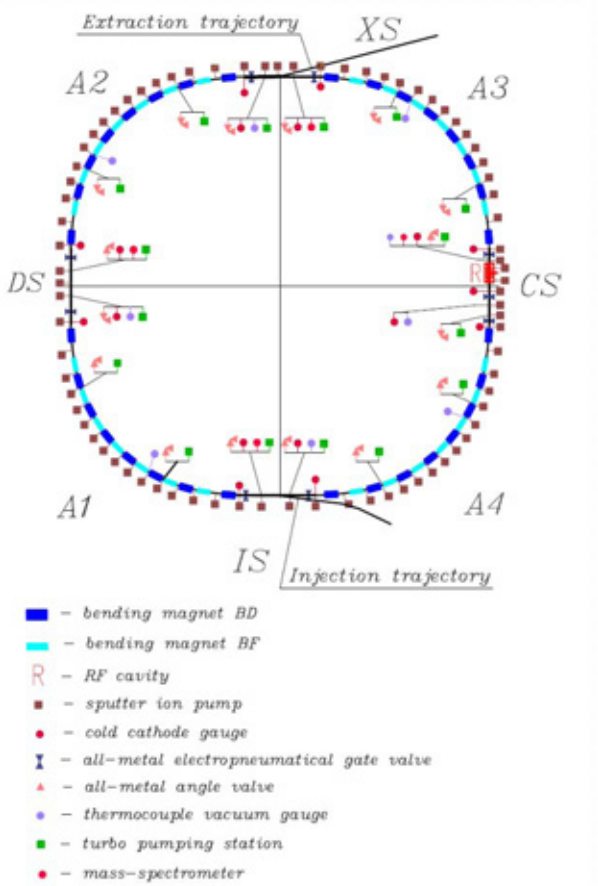

Figure 1: Layout of the NSLS-II booster vacuum system.

Heating of a narrow strip of the chamber (≈ 1 mm) causes mechanical stress of the chamber of about 114.5 MPa at permissible value of no more than 150 MPa that is a reliable safety factor.

BOOSTER COMMISSIONING

To the commissioning of the booster the whole vacuum system was assembled, leak-checked and was under vacuum. A residual gas pressure level in each section before commissioning of the booster is represented in Fig.2. In December, 2013 commissioning of the booster was started and, two days after, the first electron beams were obtained. The maximum electron energy (3 GeV) was successfully achieved in a month after start of the commissioning. The SR-induced dynamic pressure after the beginning of operation with electrons at a 3GeV energy is shown in Fig. 3.

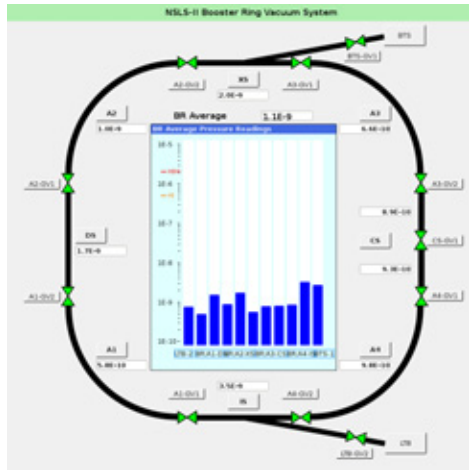

Figure 2: Residual gas pressure level in each section without a beam.

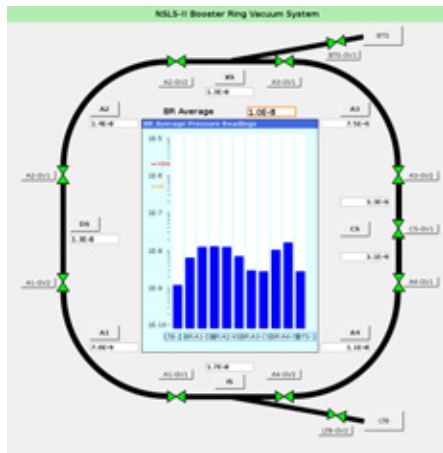

Figure 3: Residual gas pressure level in each section with a beam.

Table 1 gives a comparative analysis between the calculation and the experimental data. Some discrepancies in the experimental data and calculations are caused by the fact that, at calculations, the average vacuum in the whole section is considered, while the experimental data can be obtained only with indications of the pressure gauges placed at the points of connection of ion pumps.

Theoretical forecasting of the vacuum level for arc sections at the locations of pumping ports agrees with the data obtained at the accelerator, but for the straight sections this statement strongly depends on location of the pressure gauge as, with distance from the radiation source, the quantity of the photons causing additional outgassing reduces linearly.

ISBN 978-3-95450-170-0

Table 1. Comparative analysis between the calculation and the experimental data. Pressure (Torr)

		Arc section	Diagnostics	Extraction	Injection
Calculation (average)	Without beam	2.5E-8	3.7E-8	2.8E-8	3.8E-8
	With beam	4E-8 at 1.4 Ah	5.6E-8 at 1.4 Ah	5.8E-8 at 1.4 Ah	4.9E-8 at 1.4 Ah
Experiment	Without beam	9E-10	1.7E-9 Torr	2E-9 Torr	3.5E-9 Torr
	With beam	1E-8	1.3E-8	1.3E-8	1.7E-8

REFERENCES

[1] F. Willeke. Status of NSLS-II, Proceedings PAC'11, New York, NY, USA, 2011.
[2] LHC-BINP-LC-PR-001.

ISBN 978-3-95450-170-0

EFFECT OF THE VERTICAL VELOCITY COMPONENT ON PROPERTIES OF SYNCHROTRON RADIATION

O.E. Shishanin, Moscow State Industrial University, Moscow, Russia

Abstract

This subject determines more precisely characteristics of synchrotron radiation when the charge particle moves on the spiral in physical devices and a space. For this purpose the Bessel functions of a high order are approximated to within the second approach. It is discussed that the vertical component of velocity in alternating magnetic fields of accelerators significantly changes the spectral and angular distributions of the radiation intensity.

Theory of synchrotron radiation when the electron has a spiral trajectory considered by many authors (see, for example, [1]). In this paper we find a more accurate synchrotron radiation formulas for the spiral and circular motiom of electron in a constant and homogeneous magnetic field. For this purpose, first of all we define the asymptotic representation of the Bessel functions. Previously, several asymptotic expressions for the Bessel functions with large index were obtained [1] - [3]. Based on these methods we have extended the calculations up to the second order of accuracy [4].

However, we can take the integral representation of the Bessel functions

$$J_\nu(y) = \frac{1}{2\pi}\int_{-\pi}^{\pi} e^{i\nu\varphi - iy\sin\varphi}d\varphi.$$

When the circular motion, it will $y = \nu\beta\sin\theta$, where $\beta = v/c$ (v is the electron velocity) and θ is the spherical angle of radiation. Following Schwinger [5], we assume φ as a small parameter because the radiation is removed from the small part of the orbit in a certain direction.

To study the problem with a spiral trajectory there is a need to replace β by

$$\beta_0 = \sqrt{(\beta^2 - \beta_3^2)/(1-\beta_3^2)}$$

and $\sin\theta$ by

$$\sin\theta_0 = (\sqrt{1-\beta_3^2}\sin\theta)/(1-\beta_3\cos\theta);$$

$c\beta_3$ here is the velocity component along the magnetic field. Thus, we have

$$J_\nu(\nu\beta_0\sin\theta_0) = \frac{1}{2\pi}\int_{-\pi}^{\pi} e^{i\nu(\varphi - \beta_0\sin\theta_0\sin\varphi)}d\varphi.$$

Expanding the right-hand side in terms of φ and introducing a new variable as $\varphi = pt$, where

$$p = \sqrt[3]{6/(\nu\beta_0\sin\theta_0)}\cdot t,$$

we get

$$J_\nu(\nu\beta_0\sin\theta_0) = \frac{p}{2\pi}\int_{-\infty}^{\infty} dt e^{i(xt+t^3)}[1 - i\frac{\nu}{120}(\frac{6}{\nu})^{5/3}t^5]$$

with $x = p(1-\beta_0\sin\theta_0)\nu$. Here the integral limits were extended to infinity because φ is small.

Then we use the following expressions:

$$\int_0^\infty \cos(t^3+xt)dt = \frac{\sqrt{x}}{3}K_{1/3}(x_1),$$

$$\int_0^\infty t^5\sin(t^3+xt)dt = \frac{x^3}{27\sqrt{3}}K_{2/3}(x_1) - \frac{4}{27}x^{3/2}K_{1/3}(x_1),$$

where $x_1 = 2(x/3)^{3/2}$. In the first equality we took into account the terms of order

$$\varepsilon = 1 - \beta_0^2\sin^2\theta_0.$$

Finally for asymptotics of the Bessel function and its derivative, we obtain

$$J_\nu(\nu\beta_0\sin\theta_0) \approx \frac{\sqrt{\varepsilon}}{\pi\sqrt{3}}[K_{1/3} + \frac{1}{10}\varepsilon(K_{1/3} - 2\mu K_{2/3})], \quad (1)$$

$$J'_\nu(\nu\beta_0\sin\theta_0) \approx \frac{\varepsilon}{\pi\sqrt{3}}[K_{2/3} + \frac{1}{5}\varepsilon(2K_{2/3} - (\frac{1}{\mu}+\mu)K_{1/3}], \quad (2)$$

where $\mu = \nu\varepsilon^{3/2}$ and $\mu/3$ is an argument of functions K_i. The neglected terms are of the order ε with respect to the main term.

Formulas for spectral and angular distributions in the case of the spiral motion we can get a direct calculation or by the Lorentz transformations. Then for the components of the linear polarization of the radiation intensity(in the orbital plane and perpendicular to it, respectively) we get

$$dW_\sigma(\nu,\theta_0) = W_1\beta_0^2 J'^2_\nu(\beta_0\nu\sin\theta_0)\sin\theta_0 d\theta_0, \quad (3)$$

$$dW_\pi(\nu,\theta_0) = W_1\cot^2\theta_0 J^2_\nu(\beta_0\nu\sin\theta_0)\sin\theta_0 d\theta_0, \quad (4)$$

where

$$W_1 = \frac{3}{2}W_0\nu^2\varepsilon_0(1+\beta_3\cos\theta_0), W_0 = \frac{2}{3}\frac{e_0^4H^2}{m_0^2c^3}, \varepsilon_0 = 1-\beta_0^2.$$

Radiation frequency ω will be

$$\frac{e_0H}{mc}\cdot\frac{\nu}{1-\beta_3\cos\theta_0},$$

where H is the magnetic field strength. Using asymptotics, right-hand sides of (3) and (4) can be written as

$$\frac{1}{3\pi^2}W_1\beta_0^2\varepsilon^2K^2_{2/3}[1+\frac{2}{5}\varepsilon(2-(\frac{1}{\mu}+\mu)K_{1/3}/K_{2/3})]\sin\theta_0 d\theta_0, \quad (5)$$

ISBN 978-3-95450-170-0

$$\frac{1}{3\pi^2}W_1\cot^2\theta_0\varepsilon K_{1/3}^2[1+\frac{1}{5}\varepsilon(1-2\mu K_{1/3}/K_{2/3})]\sin\theta_0 d\theta_0. \quad (6)$$

We note that at a fixed frequency in (4) and (6) π - component is equal to zero when $\theta = \pi/2$. At this angle σ - component has a maximum. Integrating these expressions over angle θ_0 we obtain spectral formulas

$$W_\sigma(\nu) = W_2[\int_y^\infty K_{5/3}(x)dx + K_{2/3}(y) - \frac{1}{20}\varepsilon_0(7K_{2/3}(y)$$

$$+(16\mu_0 + \frac{11}{\mu_0})K_{1/3}(y) + 5\int_y^\infty K_{1/3}(x)dx)],$$

$$W_\pi(\nu) = W_2[\int_y^\infty K_{5/3}(x)dx - K_{2/3}(y) + \frac{1}{20}\varepsilon_0(7K_{2/3}(y)$$

$$+\frac{3}{\mu_0}K_{1/3}(y) - 15\int_y^\infty K_{1/3}(x)dx)],$$

where

$$W_2 = \frac{\sqrt{3}}{4\pi}W_0\nu\varepsilon_0^2, \quad y = \frac{2}{3}\mu_0, \quad \mu_0 = \nu\varepsilon_0^{3/2}.$$

It is clear that small corrections to the known formulas are proportional ε_0.

Then we take into account that at high ν the change of radiation frequency almost continuously. It gives us the opportunity to perform integration in the last formulas. Thus, we find the radiation intensities for components of linear polarization

$$W_\sigma = \frac{7}{8}W_0\frac{1}{\varepsilon_0}(1 - \frac{8}{7}\varepsilon_0), \quad W_\pi = \frac{1}{8}W_0\frac{1}{\varepsilon_0}. \quad (7)$$

Summing (7) we obtain total intensity

$$W = \frac{2}{3}\frac{e_0^2H^2}{m_0^2c^3}\frac{\beta^2 - \beta_3^2}{1-\beta^2}. \quad (8)$$

Found formulas apply also for the electron motion in a circle with a relativistic velocity if instead of β_0 and $\sin\theta_0$ take β and $\sin\theta$, respectively; in addition, it is necessary to put $\beta_3 = 0$. In this case, the important spectral formula applicable for accelerators becomes

$$W(\nu) = \frac{\sqrt{3}}{2\pi}W_0\frac{\nu}{\gamma^4}\{\int_{y_1}^\infty K_{5/3}(x)dx -$$

$$\frac{1}{\gamma^2}[\frac{1}{5}(\frac{2\nu}{\gamma^3} + \frac{\gamma^3}{\nu})K_{1/3}(y_1) - \frac{1}{2}\int_{y_1}^\infty K_{1/3}(x)dx]\},$$

where lorentz-factor $\gamma = 1/\sqrt{1-\beta^2}$, $y_1 = (2\nu)/(3\gamma^3)$.

In the case of electron motion in a spiral requires special consideration of the use of the asymptotics (1) and (2). First of all it is necessary that $\beta_3 \ll \beta$; if β_3 is close to β, it will be produced only basic tone and the integration over a quasi-continuous spectrum is meaningless. On the other hand, the asymptotics with corrections for the spiral motion can be used in the case when $\beta_3 > \varepsilon_0$; for $\beta_3 < \varepsilon_0$ terms in the spectral and angular distributions, which are proportional to $\varepsilon_0^2\beta_3^2$, will be less than the rejected terms proportional to ε_0^4. For $\beta_3 < \varepsilon_0$ is necessary to restrict the asymptotics for circular motion.

We now turn to an alternating magnetic fields of accelerators and storage rings. For example, in the case of an axially symmetric magnetic field we have a simple solution for the vertical oscillations of the form

$$z = B\cos(\sqrt{n}\omega_0 t + \delta),$$

where B is the amplitude of oscillations, δ is the initial phase, n is the field gradient, frequency $\omega_0 = (e_0H)/(mc)$. Study the problem of radiation has led to the fact that along with parameter $\cos\theta$ should be considered a derivative of the vertical movement, which defines the tangent of sloping angle. We must bear in mind new value

$$v_z/c|_{t=0} = \alpha\cdot\cos\delta, \qquad \alpha = \sqrt{n}B/R.$$

In the corresponding formulas it is necessary to carry out averaging over phase δ.

By this we take into account the scatter of the particle beam during the injection and difference of electron amplitudes in the cross section. Vertical betatron oscillations change the behavior of spectral and angular curves [6]. Intensity of π - component in the orbital plane is not equal to zero; maximum of σ - component decreases.

Quantity α varies for different machines. For storage rings, as is known,

$$z = \sqrt{\frac{\beta_z A_z}{\pi}}\cos(\int\frac{ds}{\beta_z} + \delta),$$

where A_z is the emittance, β_z is the betatron function. In this case we have [7]

$$\alpha = \sqrt{\frac{A_z}{\pi}}[\frac{1}{\sqrt{\beta_z}}\sqrt{1 + (\frac{1}{2}\frac{d\beta_z}{ds})^2}]_{\varphi=0}.$$

Here the azimuth angle is fixed at the point where the radiation is emitted; the derivative is found as the ratio of the legs of the triangle.

REFERENCES

[1] A.A.Sokolov, I.M.Ternov, Radiation from Relativistic Electrons, AIP, New York, 1986.

[2] G.N.Watson, Theory of Bessel Functios, Cambridge University Press, 1944.

[3] V.A.Fock, Doklady AN SSSR 1(1934)96 (in Russian).

[4] O.E.Shishanin, Vestnik of Moscow University, physics, astronomy, 4(1969)103 (in Russian).

[5] J.Schwinger, Phys.Rev. 75(1949)1912.

[6] V.Ch.Zhukovsky, O.E.Shishanin, JETP 34(1972)729.

[7] O.E.Shishanin, JETP 90(2000)725.

ISBN 978-3-95450-170-0

HORIZONTAL EMITTANCE REGULATION AT SIBERIA-2

A.G.Valentinov, V.N.Korchuganov, Yu.V.Krylov, Yu.L.Yupinov, NRC Kurchatov Institute, Moscow, Russia

Abstract

Synchrotron radiation (SR) brightness is the most valuable parameter of every SR light source. It depends greatly on horizontal emittance of an electron beam. That's why all modern SR light sources have designed emittance of several nanometers. A horizontal emittance of SIBERIA-2 now equals to 98 nm [1]. It can be decreased by two ways. First way is to find another working point (betatron tunes) with lower emittance. Maximal possible current values of existing power supplies must be taken into account. Injection efficiency may become worse because of smaller dynamic aperture (DA) due to stronger sextupoles. Second way is to rebuild magnetic structure keeping the same betatron tunes. Advantages of this method are good injection efficiency and proved energy ramping process. Modification of the magnetic structure may be done at high energy with more stable electron beam. But the second way is not allowed to reach as lower emittance level as in the first way.

Theoretical and practical aspects of these two ways are described in the report. Magnetic structures with dispersion-free straight sections and smooth horizontal dispersion function are presented. Also structure with higher emittance is described in order to reach higher injection efficiency.

INTRODUCTION

Brightness of synchrotron radiation from dedicated SR sources depends strongly on horizontal emittance ε_X of an electron beam. Modern 3rd generation storage rings have ε_X value of about several nanometers. Today SIBERIA-2 storage ring operates with ε_X = 98 nm at 2.5 GeV, so minimization of its value is very actual.

It may be performed by two ways. First way is to find new working point and to change magnetic structure at injection energy 0.45 GeV. Limitations imposed by power supplies (after energy ramping) must be taken into account in this case. Another problem is smaller DA in structures with smaller emittance, so injection efficiency may be decreased. Second way to minimize ε_X consists in reorganization of magnetic structure in old working point at 2.5 GeV after energy ramping. Established processes of injection and energy ramping are advantages of this way. Adjustment of magnetic structure takes place at high energy where stability of electron beam is much higher. But resulting emittance in the second way cannot be so small like in the first one.

NEW WORKING POINTS

ε_X minimization leads to stronger focusing, natural chromaticity growth and as a consequence stronger sextupoles for chromaticity compensation. Nonlinear magnetic fields in sextupole lenses excite resonances which restrict DA. It leads to lower injection efficiency, lower beam lifetime, beam losses during energy ramping. For these reasons magnetic structure in new working points must keep (or improve) machine parameters: injection rate, high stored current, small energy ramping time etc.

SIBERIA-2 structure contains 6 families of quadrupoles (see Fig.1). Lenses F1 and D1 create achromatic bend, F2 determines betatron functions behavior in bending magnets, other lenses in dispersion-free straight section define values of betatron tunes. Sextupoles for chromaticity correction are situated near F1 and D1 quadrupoles. Injection takes place in horizontal plane from inner part of the ring right before F1. Betatron tunes usually equal to Q_x = 7.77, Q_z = 6.70.

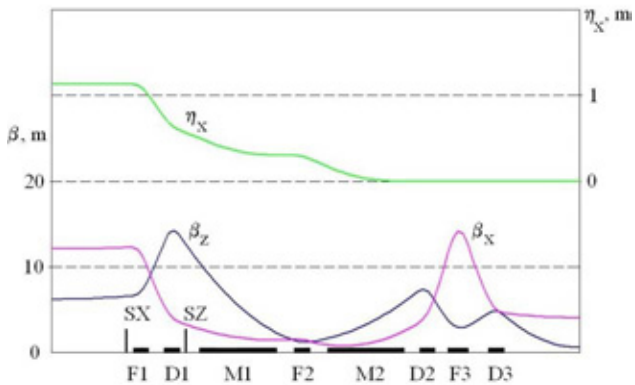

Figure 1: Betatron functions on one-half of the SIBERIA-2 cell (10.34 m = 1/12 of ring circumference). F, D – quadrupoles, M – bending magnets, S – sextupoles.

New magnetic structure may contain achromatic bend or not.

Magnetic Structure with Achromatic Bend

In this case gradients of F1 and D1 must correlate to keep achromatic bend, so emittance is strongly depends on F2 gradient. ε_X minimum value corresponds to F2 gradient 3.6 m^{-2} instead of 2.8 m^{-2} in present structure. New structure has betatron tunes Q_x = 7.85, Q_z = 3.79 and ε_X = 66 nm (all calculations were made by code OPTICK). DA calculations for injection point demonstrate reduction of available aperture from Ax = 27 mm (present structure, horizontal plane, ±40 mm physical aperture) to Ax = 19 mm in the new structure. We tried to inject beam into this structure and discovered two times less injection efficiency than in the old structure. As one can see later, this working point have not great advantages in comparison with present one. General properties of the structure are presented in Table 1.

ISBN 978-3-95450-170-0

Magnetic Structure without Achromatic Bend

There are fewer limitations for quadrupole gradients in this case. Smaller ε_x may be achieved because of optimal behavior of the betatron functions in bending magnets. Maximum possible power of quadrupoles and sextupoles must be taken into account. Magnetic structure with ε_x = 17 nm and betatron tunes Q_x = 9.71, Q_z = 5.62 was discovered (Fig.2). But phase conditions near injection point are disturbed and normal injection is impossible without serious transformation of the injection system. Dynamic aperture is much less than in the previous structure. Also it is worth noting that this structure is not suitable for high-field wigglers.

General parameters of new SIBERIA-2 structures at 2.5 GeV are presented in Table 1.

Table 1: SIBERIA-2 parameters for old and new magnetic structures

Structure:	Present	New, with achromatic bend	New, no achromatic bend
Betatron tunes, Q_x, Q_z	7.77, 6.70	7.85, 3.79	9.71, 5.62
Natural chromaticities, ξ_x, ξ_z	-17.7 -12.9	-15.5 -11.6	-21.4 -19.7
Horizontal emittance, nm	98	66	17
β_x, β_z at injection point, m	12.1 6.2	12.1 6.0	12.9 6.7
η_x at injection point, m	1.13	0.82	0.54
Momentum compaction	0.0104	0.0083	0.00424
Horizontal DA at injection point, mm	27	19	14

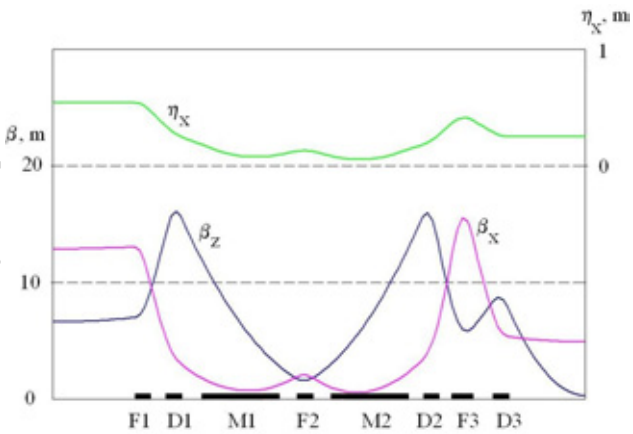

Figure 2: SIBERIA-2 betatron functions in the case of distributed dispersion. F, D – quadrupoles, M – bending magnets.

PRESENT WORKING POINT

In this case emittance decreasing procedure looks completely different. Advantages of this method are stable processes of beam storing at 0.45 GeV and energy ramping up to 2.5 GeV with minimal losses of the beam (2-3%). Structure adjustment takes place at high energy where betatron and synchrotron oscillations' damping is much stronger.

Magnetic Structure with Achromatic Bend

Horizontal emittance in this situation strongly depends on F2 gradient, like in new working point. Minimum ε_x value of 72 nm is achieved when F2 gradient is equal to 3.6 m^{-2}. Optical functions demonstrate behavior similar to Fig.1, excluding smaller dispersion function. General parameters of the structure are presented in Table 2. Structure readjustment experiments were successfully made. Adjustment time was about 1 minute, no beam losses are observed. Beam lifetime was 15% less than in initial structure because of smaller dynamic aperture.

Magnetic Structure without Achromatic Bend

ε_x value of 41 nm can be achieved for structure with distributed dispersion in present working point. Adjustment time was also 1 minute without beam losses. Beam lifetime was 30% less in this case. Structure parameters are presented in Table 2.

Magnetic Structure Enlarged Emittance

Magnetic structure with enlarged emittance value up to 135 nm (for 2.5 GeV) was also tested at injection energy. Record injection efficiency of about 90% was achieved after correction of closed orbit distortions and chromaticity. Beam storing process takes less time because of weaker sextupoles and large dynamic aperture (see Table 2).

Such strategy can be applied to other working points. If low injection efficiency is observed one can find structure with enlarged emittance for given working point and use it at injection energy. After beam storing and energy ramping it will be possible to decrease emittance to minimum possible value. For example, magnetic structure with ε_x = 17 nm may be used now only this way.

CONCLUSIONS

Different methods of the horizontal emittance decreasing at SIBERIA-2 storage ring are described. New magnetic structures for different working points were studied theoretically. Opportunities of the readjustment of SIBERIA-2 magnetic structure were tested experimentally at 2.5 GeV for present working point. Injection into new structure with decreased emittance and new working point was received. Possibility to improve injection efficiency for the structure with enlarged horizontal emittance was demonstrated.

ISBN 978-3-95450-170-0

Table 2: Different SIBERIA-2 structures' parameters for old working point $Q_x = 7.77$, $Q_z = 6.70$ at 2.5 GeV.

Structure:	**Decreased emittance, achromatic bend**	**Decreased emittance, without achromatic bend**	**Enlarged emittance, achromatic bend**
Natural chromaticities, ξ_x, ξ_z	-21.8 -15.6	-16.6 -12.3	-14.4 -11.5
Horizontal emittance, nm	68	41	135
β_x, β_z at injection point, m	14.7 5.7	15.1 5.1	11.7 4.1
η_x at injection point, m	0.81	0.62	1.36
Momentum compaction	0.0083	0.0081	0.0119
Horizontal DA at injection point, mm	20	21	30

REFERENCES

[1] V.Korchuganov, M.Blokhov, M.Kovalchuk et al. "The status of the Kurchatov center of SR", Nuclear Instruments and Methods, A 543 (2005) pp. 14-18.

ISBN 978-3-95450-170-0

ELECTRON EMISSION AND TRAPPING IN NON-UNIFORM FIELDS OF MAGNET STRUCTURE AND INSERTION DEVICES AT SR SOURCE SIBERIA-2

V.N. Korchuganov, V.I. Moiseev, N.V. Smolyakov, NRC KI, Moscow, Russian Federation

Abstract

In vacuum chamber of SR source, scattered photons provide high intensity flows of photo emitted electrons along the magnetic field lines. The unperturbed electrons reach the opposite walls. The relativistic bunches influence the trajectories of low energy electrons. These electrons can be trapped by non-uniform magnetic field. The low energy electron distributions change the operating settings of the storage ring. For Siberia-2 case, the low energy electrons are evaluated both in quadrupole lenses and in superconducting wiggler on 7.5 T field. The qualitative description of the trapped electrons behaviour was developed. In calculations, the analytical solution was obtained and used for estimations of single impact of relativistic bunch.

INTRODUCTION

The electron storage ring Siberia - 2 is 124 m in length with electron beam energies from 450 Mev up to 2.5 Gev. Beam life time is about 20 -30 hours in regular mode at the electron beam currents above 100 mA. Siberia-2 storage ring is equipped with a superconducting wiggler with magnetic field up to 7.5 Tesla.

This study is initiated by ultrasound measurements at walls of the Syberia-2 vacuum chamber [1]. Ultrasound signals increase with the beam current but appear only if the beam current exceeds some threshold. In this report, an analytical approach is developed for describing trapping and storage of the low energy secondary particles in spatially non-uniform magnetic fields.

In adiabatic approximation, the low energy particle can be considered as a small magnetic dipole with invariant momentum magnitude and oppositely directed to the external magnetic field. Particles oscillate along the magnetic field lines. Relativistic electron beam bunches circularly move in the storage ring. They periodically kick the secondary electrons by its electric field. Being strongly kicked, the secondary electrons move towards storage ring vacuum chamber. We have derived here the analytic expression for transversal component of the secondary electron momentum, which they acquire due to electromagnetic interaction with the electron beam bunch.

LOW ENERGY PARTICLES IN SLOW VARYING SPATIALLY NON UNIFORM MAGNETIC FIELDS

In uniform magnetic fields, particle trajectories are the regular spirals consisting of the circular transverse motion and the longitudinal motion along the magnetic field line. The transverse motion parameters are illustrated in Table 1 for electrons with 1 eV kinetic energy.

Table 1: Transvers motion parameters for 1 eV electrons

Field, T	0.01	0.1	1
Radius, mm	0.34	0.034	0.0034
Frequency, GHz	0.28	2.8	28

Adiabatic Approximation

In spatially non-uniform slowly varying magnetic field, the equations of particle motion can be averaged over the transverse circular motion of the particles (adiabatic approximation [2]). This approximation provides good results if the transverse trajectory radii are much smaller the radii of magnetic lines curvature. Time averaging procedure is illustrated at Fig.1. Spatial variation of magnetic field $\vec{B}$ initiates the normal field component B_n which relates the transverse to longitudinal motions:

$$m\frac{dv}{dt}=\frac{qV}{2\pi r}\oint B_n dl\,, \qquad m\frac{dV}{dt}=-\frac{qv}{2\pi r}\oint B_n dl\,.$$

These equations can be transformed to

$$\frac{dv}{dt}=\frac{vV}{2B}\frac{dB}{ds}\,, \qquad \frac{dV}{dt}=-\frac{v^2}{2B}\frac{dB}{ds}\,. \tag{1}$$

Directional derivative $\frac{dB}{ds}$ is the magnetic field gradient along the magnetic field line. In mentioned above transformations, resulted from Maxwell equation $div\vec{B}=0$ relation $\oint B_n dl=\frac{dB}{ds}\pi r^2$ is used.

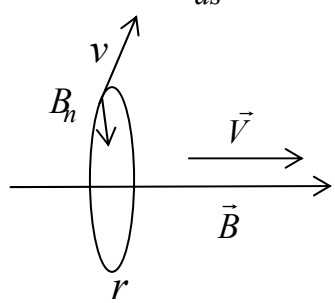

Figure 1: Sketch of an electron motion in magnetic field.

Two values are conserved in adiabatic approximation (1):

$$v^2+V^2=const\,, \qquad v^2/B=const\,. \tag{2}$$

Low Energy Particles in Quadrupole Plane field

The magnetic field may be considered as a planar one in the vicinity of the quadrupole lens centre, see Fig. 2.

*This work was partially supported by the Russian Federation program "Physics with Accelerators and Reactors in West Europe (except CERN)" and by grant of the Russian Ministry of Education and Science (agreement No. 14.587.21.0001).

ISBN 978-3-95450-170-0

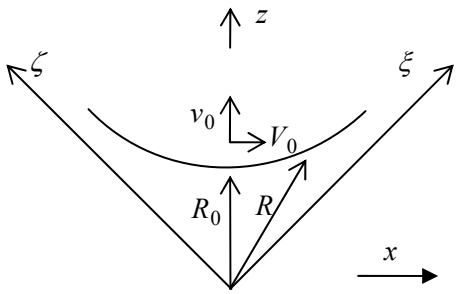

Figure 2: Particle motion in quadrupole magnetic field.

In Cartesian coordinate system (ξ, y, ζ), planar field $\vec{B}$ can be described as

$$\vec{B} = \left(\frac{B_w}{a_w}\xi, 0, -\frac{B_w}{a_w}\zeta \right),$$

where a_w is the radius of the vacuum chamber and B_w is the magnetic field magnitude at the chamber walls. The magnetic field lines are hyperbolas. The field magnitude B is proportional to the distance R from the quadrupole axis:

$$B = \frac{B_w}{a_w} R \ . \qquad (3)$$

In adiabatic approximation, particle moves along magnetic field line with R_0 shortest distance from the quadrupole axis (Fig. 2). The current particle position at this line is determined by distance R from quadrupole axis. At shortest distance R_0, particle has transversal v_0 and longitudinal V_0 components of its velocity, see Fig. 2. The relative transverse velocity $k = v_0/V_0$ is of considerable importance in particle dynamics under considiration.

It follows from relations (2) and (3) that the longitudinal velocity V is equal to:

$$V(R,k) = \pm V_0 \sqrt{1 + k^2 - k^2 \frac{R}{R_0}} \ . \qquad (4)$$

It can be easily found from Eq. (4) that in this case the particle anharmonically oscillates [3] along the magnetic field line with amplitude $R_{\max}$, which is equal to:

$$R_{\max} = R_0 + \frac{1}{k^2} R_0 \, . \qquad (5)$$

This relation illustrates the restricting role of the transverse motion – the more the relative transverse velocity, the less the amplitude of particle oscillations.

The longitudinal velocity (4) and the geometry of hyperbola give the following differential equation for radial oscillations:

$$\frac{dR}{dt} = \pm V_0 \sqrt{\left(1 + k^2\left(1 - \frac{R}{R_0}\right)\right)\left(1 - \frac{R_0^4}{R^4}\right)} \, .$$

The period T of adiabatic oscillations is equal to:

$$T = 4\frac{R_0}{V_0} \int_1^{1+1/k^2} \frac{p^2 dp}{\sqrt{\left(1 + k^2(1-p)\right)\left(p^4 - 1\right)}} \, .$$

Corresponding adiabatic oscillations frequency FC(k) is shown at Fig. 3 as a function of the relative transverse velocity k ($V_0 = 10^5$ m/s and $R_0 = 0.01$ m are taken for example). We mention that this dependence is almost linear in relative velocities exceeding approximately one.

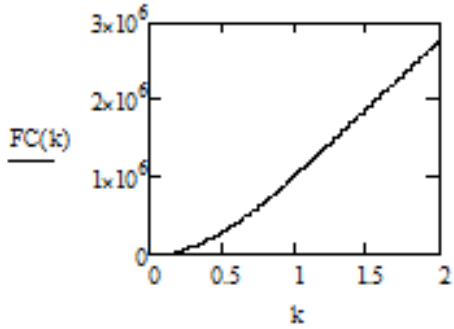

Figure 3: Adiabatic oscillation frequency.

Particles Space Distributions in Quadrupole

Steady-state space distribution functions can be constructed on the basis of the following two aspects. Firstly, along the magnetic field line the linear density is varying inversely to the longitudinal velocity of particles. Secondly, along the magnetic field line, the space density is proportional to the magnetic field magnitude. The space distribution function $\rho(R_0, R)$ can be written as

$$\rho(R_0, R) = \rho(R_0, R_0)\frac{R}{R_0} \int_{\sqrt{\frac{R_0}{a_w - R_0}}}^{\sqrt{\frac{R_0}{R - R_0}}} \frac{K(k)\cdot dk}{\sqrt{1 + k^2(1 - \frac{R}{R_0})}} \, .$$

In this expression, $K(k)$ is the particle distribution with relative velocities k, the upper and the lower limits of integration choose the particles reaching distance R but not reaching the walls. For example, the distribution $K(k) = k/\left(1+k^2\right)^{\frac{3}{2}}$ gives the particle space density

$$\rho(R_0, R) = \rho(R_0, R_0)\sqrt{1 - \frac{R}{a_w}} \, .$$

This density is almost uniform if the ratio R/a_w is small enough and the walls influence can be neglected.

ELECTRON BEAM BUNCH ACTION ON SECONDARY ELECTRONS

An electron beam bunch, moving along the storage ring equilibrium trajectory, interacts with the secondary electrons, which are trapped by the non-uniform magnetic field, via its electromagnetic field. As a result of interelectron repulsive force, the secondary electron

ISBN 978-3-95450-170-0

located at the point $\vec{X} = \{x, 0, z\}$ will acquire an additional transverse momentum $\Delta\vec{p}$ in the vacuum chamber wall direction, see Fig. 4.

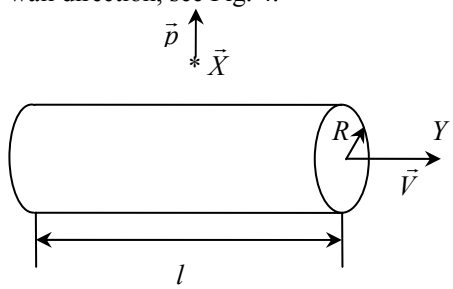

Figure 4: Sketch of cylindrical bunch action on electrons.

The secondary electron motion is given by the equation:

$$\frac{d\vec{p}(\tau)}{d\tau} = e\vec{E}(\tau). \qquad (6)$$

Here $e < 0$ is an electron charge, $\vec{E}(\tau)$ is time (τ) dependent electric field. We suppose that the repulsive push, made by high-energy electron from the storage ring beam bunch, is very short due to relativistic effects. If so, we can ignore the secondary electron drift during the kick. Integrating Eq. (6), we get the expression for the momentum increment acquired by the secondary electron:

$$\Delta\vec{p} = e\int_{-\infty}^{\infty}\vec{E}(\tau)d\tau \qquad (7)$$

For calculating of electric field $\vec{E}(\tau)$ generated by a relativistic electron, approximate expressions in the wave zone (far-field approximation) are usually employed. In our case the secondary electrons can be arbitrary close to the high-energy beam electrons, and exact expressions for electromagnetic fields should be used.

Let us consider the electric field of an electron moving along trajectory $\vec{r}(t)$, with velocity $\vec{v}(t)$, reduced velocity $\vec{\beta}(t) = \vec{v}(t)/c$ and reduced acceleration $\dot{\vec{\beta}}(t)$. The electric field is given by the exact expression [2]:

$$\vec{E}(\tau) = \frac{e}{cD(t)}\cdot\frac{[\vec{n}(t)\times[(\vec{n}(t)-\vec{\beta}(t))\times\dot{\vec{\beta}}(t)]]}{(1-(\vec{n}(t)\cdot\vec{\beta}(t)))^3} + \\ + \frac{e}{D^2(t)\gamma^2}\cdot\frac{\vec{n}(t)-\vec{\beta}(t)}{(1-(\vec{n}(t)\cdot\vec{\beta}(t)))^3} \qquad (8)$$

Here, the vector $\vec{D}(t) = \vec{X} - \vec{r}(t)$ with absolute value $D(t)$ represents the distance between the emission point points from the instantaneous position of the electron to the observer. The quantities $\vec{n}(t)$, $\vec{\beta}(t)$, $\dot{\vec{\beta}}(t)$ and $D(t)$ on the right-hand side of Eq. (8) are to be evaluated at the retarded time t which must obey the equation [2]:

$$c\tau = ct + R(t) \qquad (9)$$

Integrating Eq. (8) over τ and using Eq. (9), we get the following relation:

$$\int_{-\infty}^{\infty}\vec{E}(\tau)d\tau = e\int_{-\infty}^{\infty}\left(\vec{D}(t)/D^3(t)\right)dt. \qquad (10)$$

We mention in passing that Eq. (10) is an exact result of integration, if only the electron from the high-energy beam is infinitely far at $\tau = \pm\infty$. In our case the variable $\vec{D}(t)$ in Eq. (10) depends only weakly on the electron trajectory details, and we can consider the case of straight - line moving high-energy electron in (10):

$$\vec{r}(t) = \{r_{x0}, r_{y0} + c\beta t, r_{z0}\}. \qquad (11)$$

Substituting Eq. (11) into Eq. (10), we get from Eq. (7):

$$\Delta\vec{p} = \frac{2e^2\vec{\rho}}{c\beta\rho^2}, \qquad (12)$$

where $\vec{\rho} = \{x - r_{x0}, 0, z - r_{z0}\}$.

For simplicity, we will consider cylindrical bunch with radius R, length l and total number of electrons N, see. Fig. 4. Integrating Eq. (12) over the cylindrical bunch volume, we find that the electron beam bunch impact with the secondary electron changes the transversal momentum of the latter by the value:

$$\Delta\vec{p} = \left(2Ne^2\vec{X}\right)/\left(c\beta R^2\right), \qquad |\vec{X}| \le R, \qquad (13)$$

$$\Delta\vec{p} = \left(2Ne^2\vec{X}\right)/\left(c\beta|\vec{X}|^2\right), \qquad R \le |\vec{X}|. \qquad (14)$$

Maximum value for $|\Delta\vec{p}|$ is achieved at $|\vec{X}| = R$ and is equal to $|\Delta\vec{p}| = \left(2Ne^2\right)/\left(c\beta R\right)$. It corresponds to the secondary electron energy change of about of 5.4 keV for the Siberia-2 storage ring: electron beam current is equal to 5 mA at one-bunch mode and $R \cong 0.5\ mm$.

CONCLUSION

In this report we considered the theoretical background for non-relativistic secondary electrons accumulation and storage and its interaction with the relativistic electron beam. The phenomenon seems rather clear for theoretical description. At the same time comprehensive numerical simulations should be carried out in the future.

REFERENCES

[1] V.I. Moiseev et al, Ultrasound Measurements at Siberia-2 Vacuum Chamber, Proceedings of the 7th Annual Workshop on ESLS. -Berlin: BESSY, 1999, p.289.

[2] L.D. Landau and E.M. Lifshitz, The Classical Theory of Fields, Volume 2 of A Course of Theoretical Physics, (Pergamon Press, 1971), 374.

[3] L.D. Landau and E.M. Lifshitz, Mechanics, Volume 1 of A Course of Theoretical Physics, (Pergamon Press, 1969), 165.

ISBN 978-3-95450-170-0

ANALYSIS OF HIGH ORDER MODES DAMPING TECHNIQUES FOR 800 MHZ SINGLE CELL SUPERCONDUCTING CAVITIES*

Ya.V. Shashkov, N.P. Sobenin, National Research Nuclear University MEPhI
(Moscow Engineering Physics Institute), Moscow, Russia
M.M. Zobov, LNF-INFN, Frascati (Rome), Italy

Abstract

The High Luminosity LHC upgrade program foresees a possibility of using the second harmonic cavities working at 800 MHz for the collider bunch length variation. Such harmonic cavities should provide an opportunity to vary the length of colliding bunches. In order to supply the required harmonic voltage several single cell superconducting cavities are to be used. Different cavity designs and several higher order mode (HOM) damping techniques are being studied in order to reduce the cavity HOM impact on the beam stability and to minimize parasitic power losses. In this paper we analyze and compare the HOM electromagnetic characteristics and respective wake potential decay rates for cavities with grooves, fluted and ridged beam pipes. The problem of Lorentz force detuning is also addressed.

INTRODUCTION

At present the project aimed at Large Hadron Collider luminosity upgrade (HL-LHC) is being developed at CERN [1]. The luminosity increase is expected to be accomplished by increasing the currents of circulating beams, by reducing transverse beam sizes at the interaction points (applying smaller betatron functions) and using crab cavities to compensate the geometric luminosity loss in beam collisions [2].

The project considers also a possible implementation of harmonic cavities in addition to the main accelerating cavities working at 400 MHz to increase or to shorten the bunches [3-7]. In order to achieve the desired results a combination of the existing main RF cavities and harmonic cavities operating at 800 MHz is being studied.

In this paper we study electromagnetic characteristics of HOMs for a single cell 800 MHz superconducting cavity. Different techniques for the HOM damping such as beam pipe grooves, fluted beam pipes, ridged beam pipes etc. are investigated and compared.

HIGHER ORDER MODES DAMPING

Basic Design

An initial design of the harmonic cavity has been obtained by scaling (reducing) all the sizes of the LHC accelerating cavity operating at 400 MHz by a factor of 2 [8]. The cavity view is shown in Fig. 1. It is assumed in [8] that higher order modes damping is carried out, as in the case of the LHC accelerating cavity, with four couplers: two dipole and two broadband couplers. These couplers break the cylindrical symmetry of the electromagnetic field in the structure which gives rise to the transverse component of the electric field (kick-factor) causing a negative impact on the performance of the accelerated beam. Besides, the transient beam loading compensation in LHC requires a very high power main coupler [9]. Placing the robust main coupler and the HOM couplers on the same beam pipe may complicate the final design. That's why different HOM damping techniques were investigated.

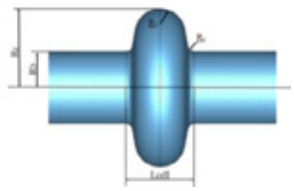

Figure 1: Accelerating cavity.

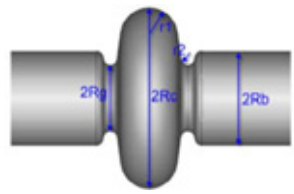

Figure 2: Cavity with grooved beam pipes.

We started our analysis by calculating the resonance frequency and the effective resistance to quality factor Q ratio (parameter R/Q_0) for the cavity shown in Fig. 1 by varying the drift tube radius. It was found that the most dangerous dipole HOM are TE_{111} and TM_{110}. The frequency of these dipole HOMs lie below the cut-off frequency of the TE_{11}wave and therefore cannot propagate along the drift tube [10]. HOMs couplers should be placed as close as possible to the accelerating cavity for the effective damping of such trapped modes.

Beam Pipe with Grooves

Another way to damp the HOMs is to cover the inner surface of the drift tubes with a dissipative material and let the HOMs propagate toward the absorbing load. This method is effective if the higher order mode frequencies become lower than the beam pipe cut-off frequency. Such a task can be accomplished by using grooved structures [11], i.e. cavities with grooves, as shown in Fig. 2.

The main advantage of the grooved structure is its cylindrical symmetry providing the same level of effective damping of HOMs with different polarizations. The absence of HOM couplers makes the design simpler and eliminates eventual negative impact of the couplers on beam dynamics due to the field distortion at their locations.

The results of simulations with ABCI code [12] clearly demonstrate that by choosing the beam pipe radius and the groove geometry in a proper way we have managed to obtain a truly "single mode" cavity. Figure 3a shows the simulated cavity shape, while Figs 3b shows respectively

*Work supported by RFBR grant 13-02-00562/14 and by the EU FP7 HiLumi LHC - Grant Agreement 284404

ISBN 978-3-95450-170-0

the dipole wake potential. We should not expect multibunch instabilities since the wake field decays completely at the distance of 15 m that corresponds to the actual bunch separation of 50 ns in LHC.

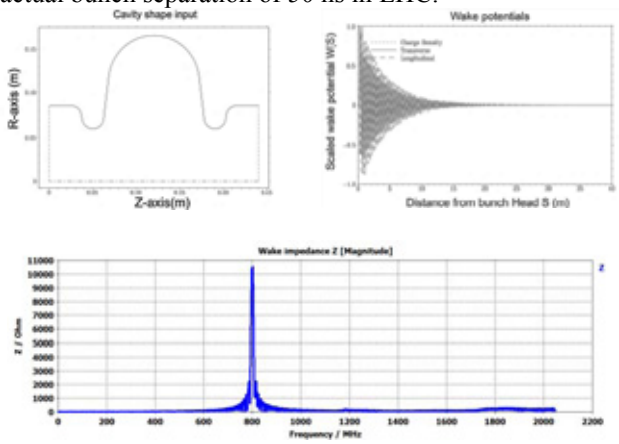

Figure 3: Wakefield results for the structure with grooved beam pipe (a. Structure profile, b. Wake potential, c. Monopole impedance).

Fluted Beam Pipe

Structure with fluted beam pipes [13] is demonstrated in Figure 4.

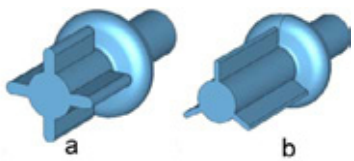

Figure 4: Structure with 4 (a) and 3 (b) flutes.

The effect of the fluted beam pipe size on cutoff frequencies of the TM_{01}, TE_{11}, TE_{21} waves was investigated with MWS program [14]. It was found that the sizes of the edges do not change the cutoff frequency of the wave TM_{01} but have a strong influence on the cutoff frequency of TE_{11} and TE_{21}waves and hence the damping of the TE_{111} , TM_{110}, TE_{211} , TM_{210} modes. It was found that the configuration with 3 flutes instead of 4, as in [13], has higher damping efficiency for quadrupole modes.

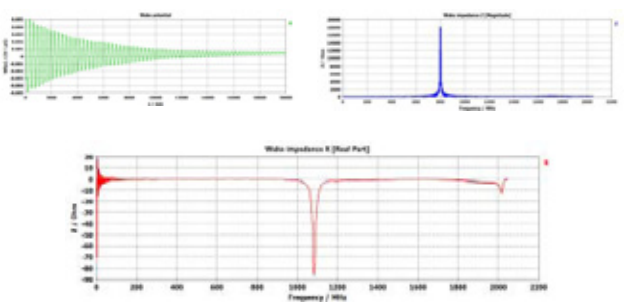

Fig 5. Wakefield results for the structure with fluted beam pipe (a. Dipole Wake potential, b. Monopole impedance, c. Dipole impedance).

In this structure Q_{ext} are below 100 for all HOMs except for a few modes with low R/Q ratio and the wake potential decays very fast (fig 5a). Respectively there are no sharp peaks on monopole (fig 5b) and dipole (fig 5c) impedance graphs except the one corresponding to the operating mode.

Ridged Beam Pipe

The fluted beam pipe damping efficiency could be improved if we reverse flutes inward the beam pipe (fig 6). In this case the cut off frequencies for quadrupole and dipole modes decrease and this allows reducing the beam pipe radius. The calculated wake field decays for this structure is presented in fig 7a.

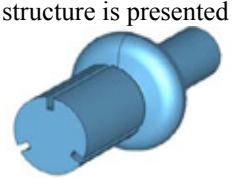

Figure 6: Structure with ridged beam pipe.

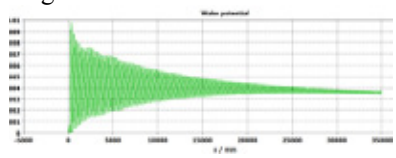

Figure 7a. Wake potential.

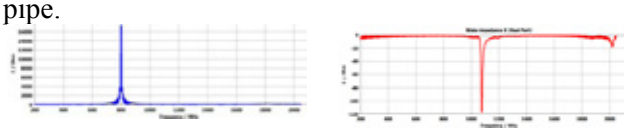

Fig 7b-c. Wakefield results for the structure with ridged beam pipe (7b. Monopole impedance, 7c. Dipole impedance).

As it can be seen the wake potential decays very fast also in this case. On the other hand, the cut-off frequency of E_{010} mode is also lower for this configuration which can lead to a deeper penetration of the working mode towards the load. To prevent decreasing Q_0 of the working mode beam pipe length can be chosen longer than that in fluted bam pipe case. Sharp peaks on the HOM monopole (fig 7b) and dipole (fig 7c) impedance graphs are not observed.

LORENZ FORCE DETUNING

Lorenz force frequency detuning was investigated for the discussed HOMs damping methods. As an example deformations of the grooved structure due to the influence of the Lorentz force are shown in Figure 8.

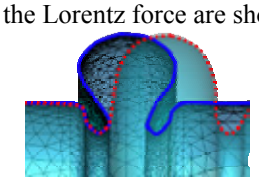

Figure 8: Grooved structure deformations due to the influence of the Lorentz force (dotted line – structure, solid line– deformed structure).

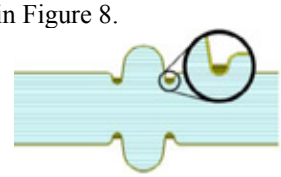

Figure 9: Structure with grooves and stiffeners.

The ratio of frequency detuning to the square of the electric field strength can be considered as a quality

ISBN 978-3-95450-170-0

criterion for the influence of the Lorentz force on the structure. The Lorentz force sensitivity can be decreased by increasing the cavity wall thickness or by adding of specific stiffeners schematically depicted in Fig. 9 to the structure design [15].

The calculations were carried out for the structure consisting of copper with Young's coefficients 120 kN/mm^2 (Table 1). One end of the cavity beam pipe is considered rigidly fixed during the calculations of frequency detuning.

Table 1. Lorenz force frequency detuning

Structure type (beam pipe/beam pipe outer radius, mm)	Copper structure $\Delta f/\Delta E^2$, Hz
Smooth structure(75)	-6.3
Grooved structure(75/105)	-6.3
Grooved structure with stiffners (75/105)	0.2
Fluted beam pipe structure (75/120)	-6.1

Table 1 shows that the $\Delta f/\Delta E^2$ ratio is smallest for the structure with grooves and stiffening ribs.

COMPARISON OF DESIGN SOLUTIONS

Table 2 shows that each of the considered methods of HOMs damping has its own advantages and disadvantages.

Table 2. Comparison of characteristics of calculated structures

	Grooved structure	Fluted beam pipe structure	Ridged beam pipe
Q_{ext} in single cell cavity	$<10^2$	$<10^2$	$<10^2$
Lorenz force detuning $\Delta f/\Delta E^2$, Hz	0.2	-6.8	-6.8
Symmetrical structure	Yes	No	No
Additional	Easy in manufac-turing	Quadrupole modes damping	Quadrupole modes damping

In our opinion, the structure with grooves seems to be a more suitable candidate for the 800 MHz cavity design since: a) it has simplest azimuthally symmetric geometry; b) there are no dangerous HOM created in the structure; c) no dedicated HOM couplers are required; d) an eventual multipacting discharge in the equatorial region at rather low accelerating gradients can be cured by an additional purification of the cavity surface and subsequent training; e) the Lorentz force detuning can be significantly reduced by inserted ring stiffeners in the grooves.

In the following we also consider a possibility to combine several such structures in a chain of non-communicating cavities in order to place them in a single cryostat.

CONCLUSION

We have compared four different HOM damping techniques for the 800 MHz harmonic cavity. In our opinion, the solution with grooves is preferable due to its cylindrical symmetry, design simplicity and absence of dangerous HOMs. We have also proposed to combine two such cavities connected by smaller radius beam pipe in a single cryostat [16].

REFERENCES

[1] L. Rossi, LHC upgrade plans: options and strategy, IPAC2011, p.908.

[2] O.Bruning, F.Zimmermann, Parameter space for the LHC luminosity upgrade, IPAC2012, p. 127.

[3] O. Bruning et al., LHC Luminosity and Energy Upgrade: A Feasibility Study, LHC Project Report 626, 2002.

[4] F. Ruggiero and F. Zimmermann, Luminosity Optimisation near the Beam-Beam Limit by Increasing the Bunch Length or Crossing Angle, CERN-SL-2002-005-REV (AP), 2002.

[5] F. Ruggiero and F. Zimmermann, Possible Scenario for an LHC Upgrade", CARE-Conf-05-002-HHH, Proc. of the HHH 2004 Workshop, Geneva, November 2004.

[6] T. Linnecar and E. Shaposhnikova, An RF System for Landau Damping in the LHC, LHC Project Note 394, 2007.

[7] D. Shatilov, M. Zobov, On the Possibility of Utilizing Flat Longitudinal Beam Profiles to Increase the Luminosity in Collisions with Large Piwinski Angle, 14/04/2012 (unpublished)

[8] Ficcadenti F. et al., LHC Landau Cavity Design // BE-RF CERN, BR section meeting, March 29, 2012

[9] P. Baudrenghien, T. Mastoridis, Power requirement for the harmonic cavities in the full-detuning scheme, CERN BE-RF 2nd LHC Harmonic Cavity meeting, May 27th ,2013.

[10] N.Sobenin, B.Zverev, ElectrodynamicCharacte-ristics of Accelerating Cavities, Foundation for International Scientific and Education Cooperation. Gordon and Breach Science Publishers S.A. 1999

[11] S. Kurokawa, Present Status of KEK-B Project, EPAC, p. 448 (1996).

[12] http://abci.kek.jp/

[13] H. Padamsee et al., Accelerating Cavity Development for the Cornell B-Factory, CESR-B, Accelerator Science and Technology. vol. 2, 1991, p. 786 – 788.

[14] https://www.cst.com/

[15] R.Mitchell,K.Matsumoto,G.Ciovati,etal.,Lorentzforcedetuning for the SNS cavities,LLRFWorkshop, 2001.

[16] Ya. Shashkov et al., Comparison of higher order modes damping techniques for array of single cell cavities, this proceedings, This Proceedings.

ISBN 978-3-95450-170-0

HIGHER ORDER MODES DAMPING FOR 9-CELL STRUCTURE WITH MODIFIED DRIFT TUBE

A. Mitrofanov, Ya.Shashkov, N. Sobenin, National Research Nuclear University MEPhI (Moscow Engineering Physics Institute), Moscow, Russia,
V. Zvyagintsev, TRIUMF, Canada, Vancouver

Abstract

This paper is focused on HOM damping in 9-cell superconducting cavities. We are considering HOM propagation outside from the cavity ridged and fluted drift tubes. The analysis of the influence of the parameters of the drift tube on the HOM damping was conducted. The considered methods were analysed and compared.

INTRODUCTION

Development of accelerating structures for modern types of accelerators, such as Energy recovery linacs (ERLs), requires special attention to higher order modes (HOMs) damping. HOMs excitation could create high losses on the cavity walls, beam instability and beam break up (BBU). HOMs couplers are often used in such structures for HOM damping but they could lead to violation of the axial symmetry of the accelerating field and create transverse field components (kick-factor) that can negatively affect on the beam emittance. Also these devices are subject for multipactor discharge and all kinds of pollution. Here we are studying different options of beam pipes to provide better HOMs propagation from the cavity, assuming that they will be dissipated away from the cavity.

INITIAL DESIGN

As a reference point for simulation HOMs propagation was taken 9-cell 1300 MHz superconducting electron accelerating cavity (Fig. 1) [1]. In order to estimate efficiency we decided to calculate HOM electrodynamics characteristics for the structure without couplers and put at the end of drift tubes RF port boundary conditions, representing ideal loads away from the cavity.

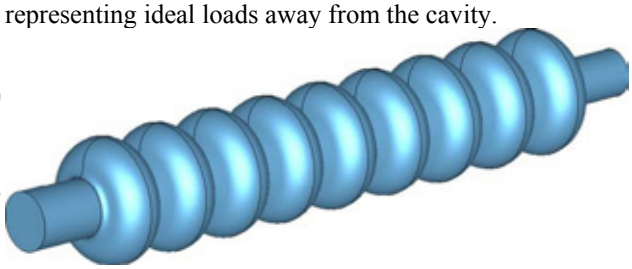

Figure 1: Superconducting 9-cell cavity model.

In order to estimate HOM frequency range, we calculated dispersion characteristics (Fig. 2) for E_{010} modes and HOMs. The most dangerous HOMs for the structure are dipole modes H_{111}, E_{110}, EH_{11}; quadrupole modes H_{211} and E_{210} and monopole mode E_{011}.

*Work supported by RFBR grant 13-02-00562/14

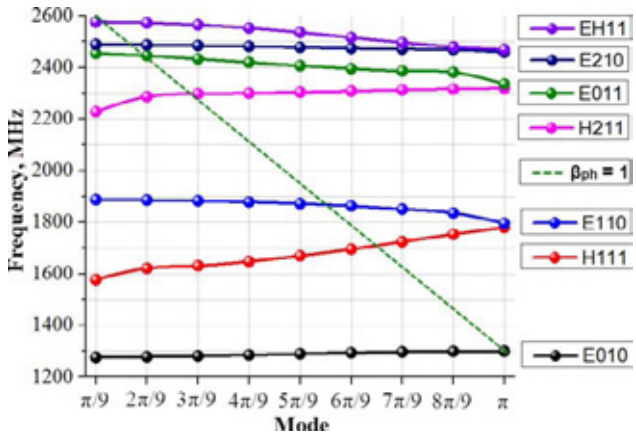

Figure 2: Dispersion characteristics for main wave and for HOMs and β-phase = 1 line.

β-phase = 1 line is shown on the dispersion characteristic on fig 2. Intersection points of dispersion characteristics with β-phase = 1 line (synchronous point) represent modes with the largest interaction between particles and waves and those points needs an additional attention.

External Q-factor values for HOMs and operational mode are presented on Fig 3. Q_{ext} values were calculated in CST Microwave Studio [2].

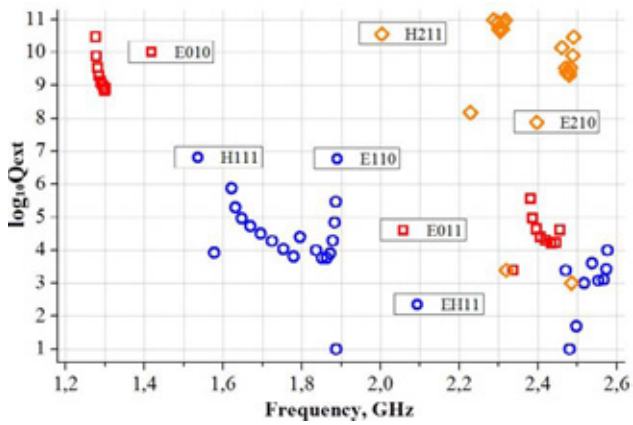

Figure 3: External Q-factor calculations results for HOMs in 9-cell elliptical cavity with beampipes loaded with RF ports. Square (red) – monopole waves, circle (blue) – dipole waves, diamonds (orange) – quadrupole waves.

Comparison of the results with results for similar structures [3] showed that Q_{ext} for operating mode is nearly the same, three orders higher for dipole modes, 4-5 order higher for quadrupole modes and for 2nd monopole HOM it's two times higher.

ISBN 978-3-95450-170-0

FLUTED BEAM PIPE

We decided to simulate the 9-cell structure with fluted beam pipes that was successfully applied for HOMs damping in single cell cavities [4].

Fluted beam pipes are presented on Fig. 4. Quantity and form of those flutes can be chosen on purpose to get more damping of HOMs. The best results for damping of dipole and quadrupole HOMs were obtained for a structure with fluted beam pipes with 3 flutes [5]. The structure with 4 flutes has the problem with quadrupole HOMs damping with certain polarization.

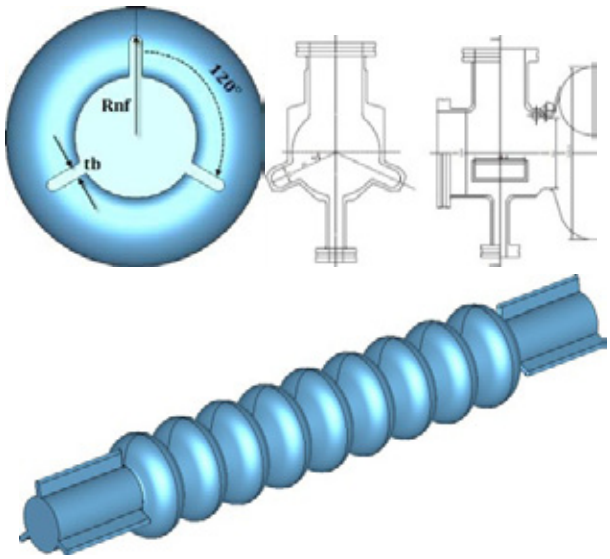

Figure 4: Upper left: fluted beam shape with 3 inhomogeneities; upper right: schematic view of eccentric-fluted beam pipe, designed for KEK-ERL model-2 [6]; bottom: fluted beam pipe cavity model.

The main advantage of fluted beam pipe is that H_{21} cut-off frequency is below of the quadrupole HOMs band. This is true not only for quadrupole but also for dipole HOMs. The operational mode remains trapped in the structure due to high cut-off frequency of E_{01} mode. Cut-off frequency values for different modes in fluted beam pipe are presented in Table 1. Field distribution in fluted beam pipe for E_{01}, H_{11} and H_{21} waves are presented on Fig 5.

Table 1. Cut-off frequencies for different mode in fluted beam pipe

H_{11}	1330
E_{01}	1972
H_{21}	2004

In order to get the same cut-off frequency cylindrical beam pipe beam pipe radius should be 65.5 mm for H_{11} wave and 72.8 mm for H_{21}, however it will cause reduction for E_{01} cut-off frequency (on 248MHz and 396MHz correspondingly). It could create to negative effect for shunt impedance of operating mode.

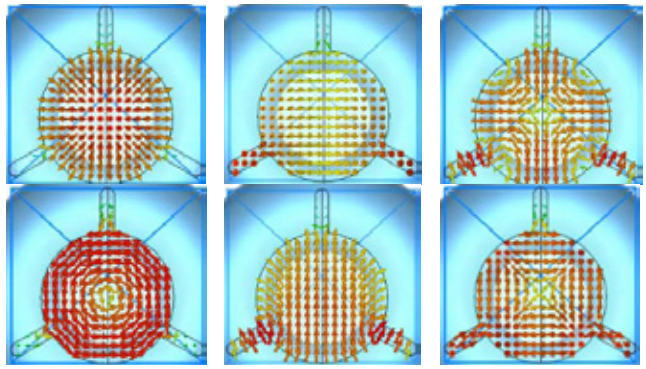

Figure 5: Electric (first line) and magnetic (second line) fields distribution in fluted beam pipe for E_{01}, H_{11} and H_{21} waves.

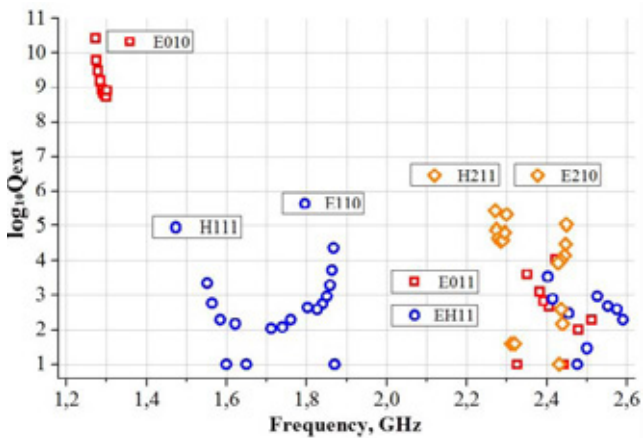

Figure 6: External Q-factor calculations results for 9-cell elliptical structure with fluted beam pipes loaded at the ends with RF ports. Square (red) – monopole waves, circle (blue) – dipole waves, rhombus (orange) – quadrupole waves. Beam pipe length 300 mm, inner radius 54 mm, flutes radius 90 mm

Comparing Q_{ext} results for the 9-cell structure with fluted (Fig. 6) and for cylindrical beam pipes (Fig. 3) and results obtained for the similar structures [3], we can conclude that this method is very effective because of we see reduction of Q_{ext} values were reduced by two orders of magnitude monopole and dipole and by five orders for quadrupole HOMs.

RIDGED BEAM PIPE

Another structure that provides conditions for HOMs propagation is ridged beam pipe structure (Fig. 7). The ridged beam pipe geometry is symmetrically opposed to fluted beam pipe. Typically it has 3 grooves in beam pipe, evenly distributed on azimuth on 120º angle.

After the change initial design to fluted and ridged beam pipe structures we used standard method [7] of modifying geometry of end cells for field flatness of operating mode (Fig 8).

ISBN 978-3-95450-170-0

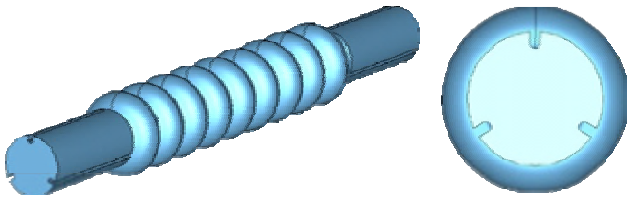

Figure 7: Ridged beam pipe 9-cell cavity model.

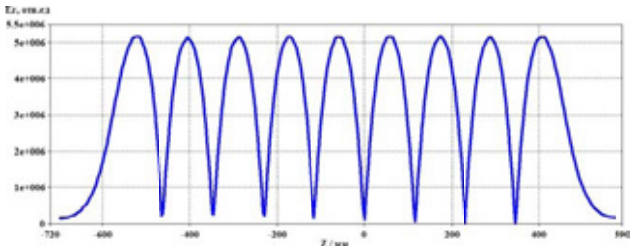

Figure 8: Electric field distribution for operational mode in symmetrical 9-cell cavity.

Results for Q_{ext} in 9-cell structure with ridged beam pipes are presented on Fig 9.

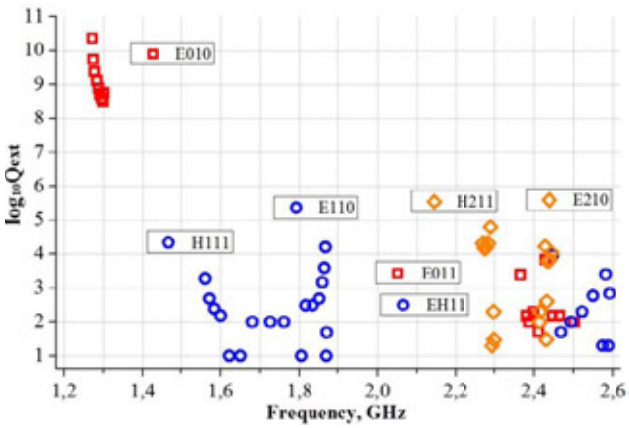

Figure 9: External Q-Factor calculations results for 9-cell elliptical structure with ridged beam pipes. Square (red) – monopole waves, circle (blue) – dipole waves, rhombus (orange) – quadrupole waves. Beam pipe length 350 mm, inner radius 56,5 mm, ridged outer radius 75 mm.

We found that the results for ridged beam pipe are even better than for fluted beam pipe. All the dipole and monopole modes have Q_{ext} values > 10^4, quadrupole modes > 10^5.

CONCLUSIONS

Propagation of HOMs from 9-cell structure was compared for cylindrical, fluted and ridged beam pipes. The comparison has been done based on calculated external quality factor Q_{ext} in the models with beam pipes loaded with RF ports at the ends. In the result the fluted and ridged beam pipes shown Q_{ext} for HOMs 2-6 orders of magnitude less than cylindrical pipes. Such a way fluted and ridged beam pipes provide much better HOM propagation then cylindrical.

We are planning to proceed development of HOM dampers for 9-cell structure based on this result.

REFERENCES

[1] V.Zvyagintsev, et al. 'Nine-Cell Elliptical Cavity Development at TRIUMF' / Proceedings of SRF-11 Conference, Chicago, USA.
[2] https://www.cst.com
[3] T. Galek, et al. 'Study of Higher Order Modes in Multi-Cell Cavities for Bessy-VSR Upgrade' / Proceedings of IPAC-2014, Dresden, Germany.
[4] Ya.Shashkov, N.Sobenin. 'Comparison of Higher Order Modes Damping Techniques for 800 MHz Superconducting cavity' / Proceedings of IPAC-2014, Dresden, Germany.
[5] Ya.V. Shashkov et al, Comparison of higher order modes damping techniques for 800 MHz single cell superconducting cavities, Nuclear Instruments and Methods in Physics Research A, 767, (2014), pp 271–280.
[6] K. Umemori, et al, 'Design of L-Band Superconducting Cavity Recovery Linacs' / Proceedings of APAC-2007, Indore, India.
[7] N.Sobenin, B.Zverev, Electrodynamic Characteristics of Accelerating Cavities, Foundation for International Scientific and Education Cooperation, Gordon and Breach Science Publishers S.A., 1999.

ISBN 978-3-95450-170-0

SUPPRESSION OF MECHANICAL OSCILLATIONS IN QUARTERWAVE 106 MHZ RESONATOR

I.I.Petrushina, I.V. Rybakov, M.A. Gusarova , Ya.V. Shashkov, National Research Nuclear University (Moscow Engineering Physics Institute), Kashirskoe shosse, 31, Moscow, Russia
V.L.Zvjagincev, TRIUMF, Canada's National Laboratory for Particle and Nuclear Physics, Vancouver, Canada

Abstract

Analytical calculations and numerical simulations have been done for mechanical eigenmodes of quarter wave superconducting resonators with operating frequency of 106 MHz and 80 MHz. A possibility of frequency shift of mechanical modes in 106 MHz resonator has been estimated by application of the damper. We have optimized the damper's position for suppression efficiency. We have also compared the numerical and experimental results.

INTRODUCTION

Superconducting quarter wave resonators (QWR) are used very often in particle accelerators at relatively low particle velocities $\beta < 0.15$. They operate in frequency range from 70 to 160 MHz. The structure of commonly used superconducting QWRs is enough sensitive for mechanical vibrations because of their length of 0.5-1 m made from 2-3 mm thin sheets of Nb. Superconducting cavities inside of cryomodule affected by various factors such as vibrations from environment and vacuum pumps, instant impacts from valves, oscillations of liquid He pressure. Hence, a wide spectrum of mechanical oscillations is applied to the cavity and could excite mechanical oscillations deforming the cavity geometry and providing substantial deviations of resonant frequency. It causes instabilities in cavity operation. There are several ways to mitigate this problem:

- To keep mechanical resonances in higher frequencies region to be far away from strong industrial noise components of 50-60 Hz
- To make cavity structure more rigid to reduce sensitivity for vibrations
- To make operational bandwidth of the cavity higher than frequency deviation caused by mechanical vibrations
- To use mechanical damper [1] to dissipate energy of mechanical vibrations.

The most effective way of microphonics suppression is to develop mechanical dampers for the cavities.

This paper is focused on investigation of mechanical oscillations in 106 MHz [2] superconducting QWR with mechanical damper. The cavity design presented in Fig. 1.

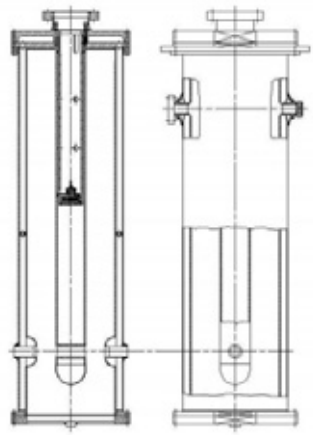

Figure 1: Design of the 106 MHz superconducting Nb QWR with mechanical damper.

ANALYTICAL CALCULATIONS

Inner conductor of the QWR is the most sensitive part to mechanical impacts. Frequencies of mechanical modes f_i of the inner conductor can be roughly estimated by using an approach of a thin-wall cylinder fixed at one edge [3].

$$f_i = \frac{\alpha_i^2 \cdot \sqrt{\frac{E \cdot I}{\mu}}}{2 \cdot \pi \cdot L^2} \qquad (1)$$

where E is Young's modulus; L = 685 mm is the length of the inner conductor; μ is the mass of the inner conductor per unit length; α_i is the intrinsic constant of oscillation (α_1 = 1.875, α_2 = 4.694 for the first and second modes, respectively); $I = \frac{\pi}{4}\left(r_o^4 - r_i^4\right)$ is the moment of inertia of a thin-wall cylinder with radii of r_i and r_o.

According to these formulae, the frequencies of the lowest mechanical modes are f_1 = 46.5 Hz and f_2 = 291.2 Hz for the resonator with an operating frequency of 80 MHz; and f_1 = 72.7 Hz and f_2 = 455.7 Hz for the resonator with an operating frequency of 106 MHz. According to [3], the frequencies of the first two modes of the inner conductor of 80 Hz resonator are f_1 = 45 Hz and f_2 = 284 Hz. The difference between results might be explained due to approximation of the theoretical model which did not take into account a complicated shape of the inner conductor.

ISBN 978-3-95450-170-0

NUMERICAL SIMULATIONS

Numerical simulations of mechanical oscillations of the 106 MHz quarterwave resonator have been done with two codes: ANSYS [4] and Comsol Multiphysics [5]. The upper plate of the QWR (see Fig. 1) is fixed for assembly in the cryomodule and was treated as a fixed plane. The parameters of Nb used in simulations are presented in Table 1.

Table 1: Parameters of niobium used in simulations.

Material	Young's modulus, GPa	Poisson coefficient	Density, kg/m^3
Niobium	105	0.38	8570

Mechanical eignefrequencies of the first five lowest mechanical oscillations obtained from numerical simulations in ANSYS and COMSOL are very close and are presented in Table 2. Figure 2 shows damper deformations for the first two modes simulated in Comsol.

Table 2: Main mechanical modes in 106 MHz QWR

Mode	Frequency f_i, Hz	
	ANSYS	Comsol
1	66.85	66.68
2	157.2	156.89
3	429.5	415.19
4	431.8	431.22
5	552.6	544.4

The first and the fourth modes shown in the table appear to be the first and second modes of the resonator's inner conductor (Figure 2a), while the remaining ones correspond to the outer conductor (Figure 2b).

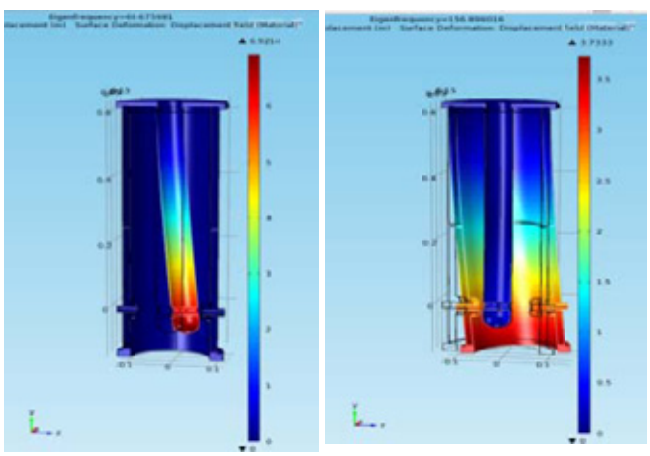

a) f_1 = 67 Hz *b)* f_2 = 157 Hz

Figure 2: Main mechanical modes in 106 MHz QWR.

Frequencies obtained from analytic and numerical simulations are in good agreement; the difference of 8-9% is due to the approximation of the cavity shape.

The simulation results for 80 MHz superconducting QWR are presented in Table 3. The frequencies of the first two modes for the inner conductor obatined numerically in ANSYS and compared to analytical calculations [3].

Table 3: Frequencies of the first two modes of the inner conductor

Mode	Frequency f_i, Hz	
	ANSYS	By [3]
1	44.76	45
2	281.20	284

The results are very close and the difference is less than 1%. The approximation works better for 80 MHz QWR rather than for 106 MHz QWR because the impact of cylindrical part of the geometry is dominating in the result.

DAMPER SIMULATIONS

Design of the mechanical damper for 106 MHz QWR is presented in Fig. 4. The damper [3] consists of the stainless steel cone on the stainless steel bottom, brass load is placed on the top of the cone and three fingers are used for contact between cone and the inner conductor internal surface. The finger's vibrations transfer to the inner conductor and to the cone. In the result the vibrations convert to damper's sliding on the bottom. Thus, the energy of vibrations convert to friction.

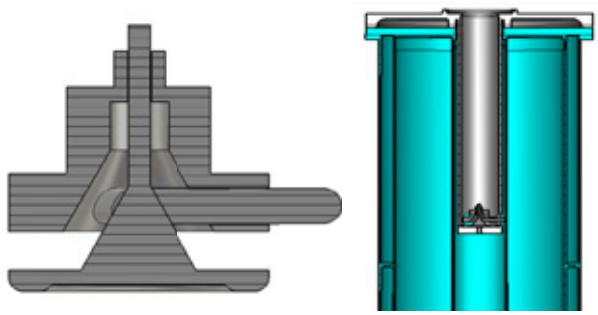

a) b)

Figure 3: Geometry of damper (a) and its position in resonator (b).

Mechanical model of the 106 MHz QWR inner conductor with damper was created for simulations in Comsol.

The first results of the numerical simulations of damper, integrated on the tube and assembled inside of the QWR inner conductor, show that the inner conductor frequency is of 75.5 Hz (Fig.5) which is 12% above the value of the first mechanical mode of the inner conductor without damper.

ISBN 978-3-95450-170-0

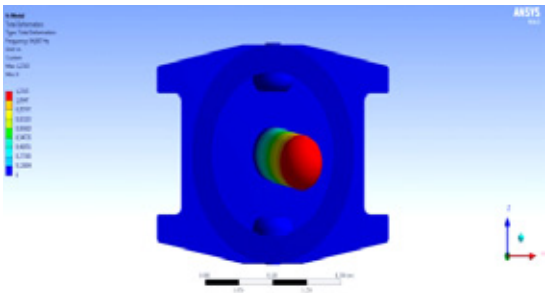

Figure 4. The lowest mechanical mode of the inner conductor with damper.

To achieve the maximum displacement of the lowest mode frequency, optimization of the damper's position, we have changed the length of cylindrical base of the damper. Simulations in ANSYS were done for the models with the damper's base lengths from 100 mm to 600 mm. Figure 6 shows the plot of the inner conductor first mode frequency as a function the length of the damper's base.

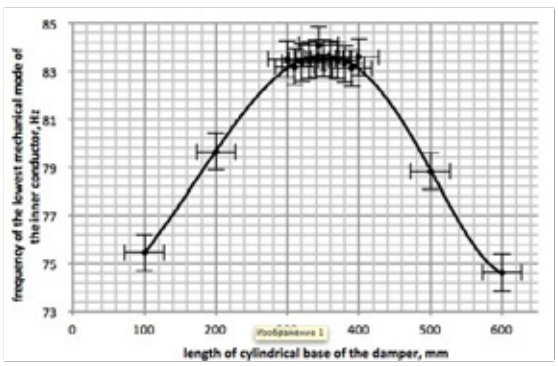

Figure 5: Plot of the inner conductor first mode frequency as a function of the length of the damper's base.

The hughest frequency of the inner conductor first mode was obtained for the damper's base length of 343.5 mm . It equals to 84.1 Hz which is 20.7% above the value of the frequency in the structure without damper application.

SUMMARY

Analytical and numerical simulations of the mechanical modes in 80 MHz and 106 MHz resonators have been done. The comparison of mechanical frequencies of 80 MHz resonator obtained using analytical calculations,numerical simulations and previously obtained data was done. The mentioned techniques provide the reasonable agreement. The highest frequency displacement of the first inner conductor mode o is achieved by the application of a damper. The studies will be continued for damper efficiency optimization.

REFERENCES

[1] A. N. Didenko, V. I. Kaminsky, M. V. Lalayan, N. P. Sobenin. Superconducting accelerating resonators (in Russian).

[2] A. Facco et al. The superconducting medium beta prototype for radioactive beam acceleration at TRIUMF, Proceedings of the 2001 Particle Accelerator Conference, Chicago.

[3] A. Facco et al. Mechanical mode damping in superconducting low β, Proceedings of the 1997 Workshop on RF Superconductivity, Abano Terme (Padova), Italy.

ISBN 978-3-95450-170-0

INFLUENCE OF THE DIFFERENT GEOMETRIC PARAMETERS OF SUPERCONDUCTING ELLIPTICAL CAVITIES ON THE MULTIPACTOR

I.I.Petrushina, M.A. Gusarova, National Research Nuclear University (Moscow Engineering Physics Institute), Kashirskoe shosse, 31, 115409, Moscow, Russia

Abstract

The results of numerical simulations of multipacting discharge in different superconducting elliptical cavities are presented in this paper. The influence of aperture radius, equator shape, iris shape and frequency and electron trajectories for different geometrical parameters of elliptic structures are considered.

INTRODUCTION

Multipacting simulations were carried out using MultP-M code [1] which provides information about threshold values of accelerating gradient, character and parameters of an electron trajectories and shows the areas of the structure where multipacting discharge occurs. As the result of simulations we obtain a dependence of the of secondary electrons number increase within the cavity vs. accelerating gradient. Example of such graph for various aperture radii is shown in Figure 1.

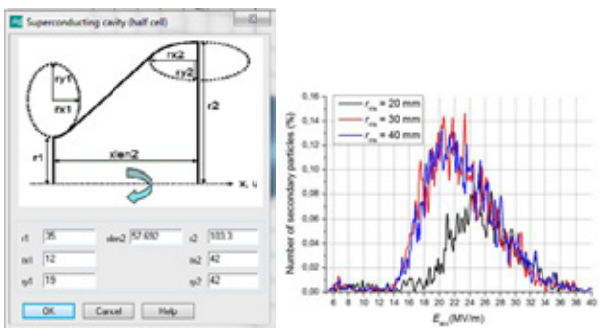

Figure 1: Basic shape of the 1.3 GHz SC cell (left) [2] and the number of secondary electrons as a function of accelerating gradient (right).

This plot doesn't allow obtaining precise values of accelerating gradient when multipacting discharge can occur. The next step of discharge prediction is a detailed analysis of an electron motion.

INFLUENCE OF THE APERTURE RADIUS

Detailed investigation of an electron motion shows that stable multipacting trajectories (1st order at equator region) are obtained in a wide range of an accelerating gradients from 4.3 to 38 MV/m. One can see from Figure 2 that the range of accelerating gradient becomes narrower for larger iris aperture dimensions..

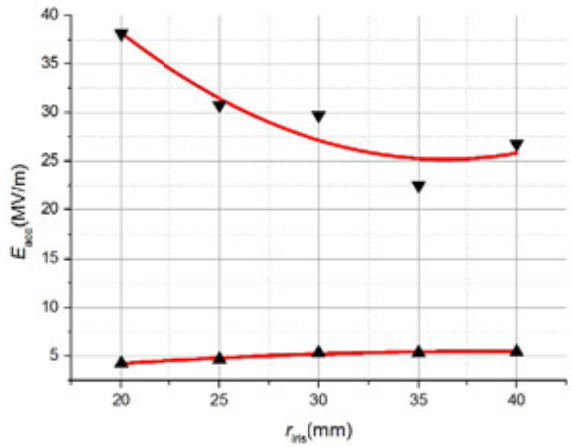

Figure 2: Threshold values of Eacc for various radii.

Q-curve plot (Fig.3) obtained during the vertical test of the standard cell geometry with r_{iris}= 35 mm shows that Q-value starts decreasing at 5-6 MV/m of accelerating gradient which is close to the simulation result.

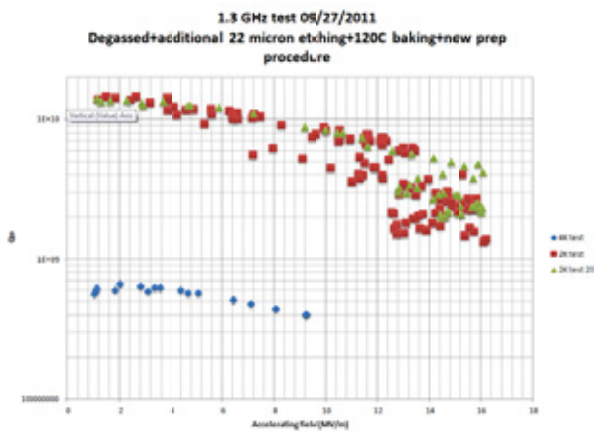

Figure 3: Experimental Q-curve for the standard geometry riris=35 mm. Courtesy of TRIUMF [3].

An example of stable 1st order trajectory is shown in Figure 4. Dependence of main parameters of such trajectories (energy and amplitude) as functions of. accelerating gradient for various aperture radii is presented in Figures 5 and 6.

ISBN 978-3-95450-170-0

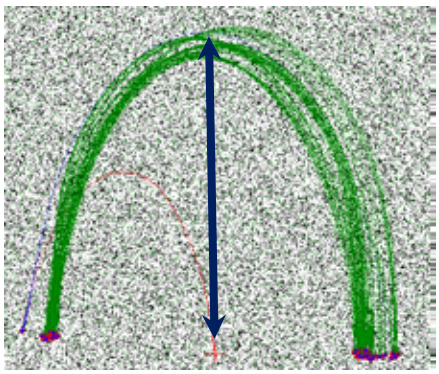

Figure 4: Trajectory amplitude.

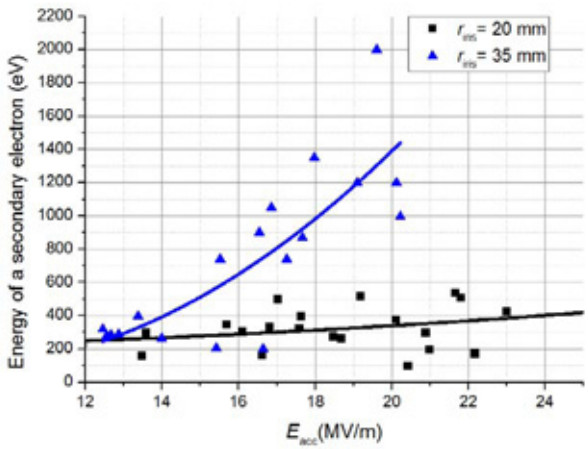

Figure 5: Energies of a secondary electrons as a function of accelerating gradient for aperture radii 20 and 35 mm.

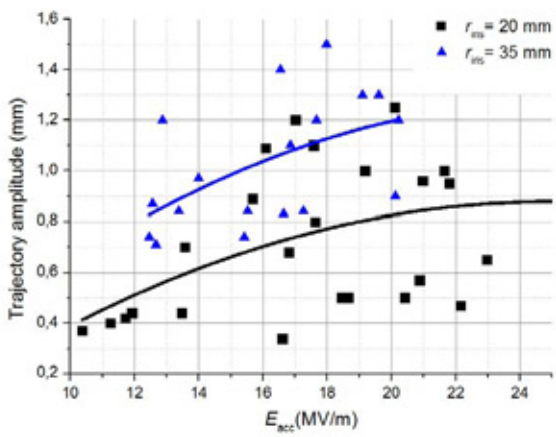

Figure 6: Trajectory amplitudes as a function of accelerating gradient for aperture radii 20 and 35 mm.

One can see that the larger is aperture radius, the higher is energy of an electron and bigger is trajectory amplitude. This fact explains narrow multipacting region for large apertures.

INFLUENCE OF THE EQUATOR SHAPE

We have obtained the dependence of the cell's equator shape on multipacting discharge development for 3 types of cells: standard cell, Low Loss cell, and standard cell with equator dome radii $r_{x2} = r_{y2} = 43$ mm.

The results of simulations show that standard geometry undergoes multipacting in the most narrow region of the accelerating gradient due to the higher electron energy.

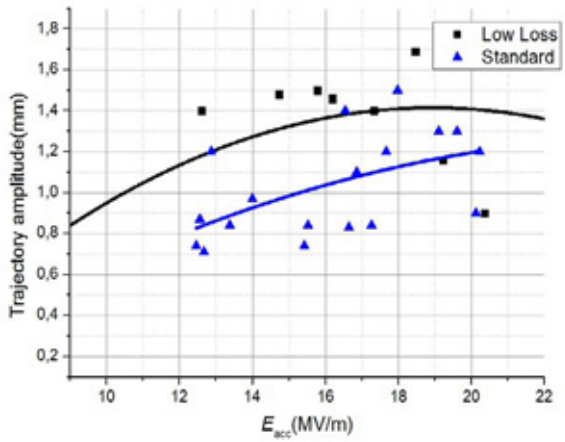

Figure 7: Trajectory amplitudeas a function of accelerating gradient for Low Loss and standard geometries.

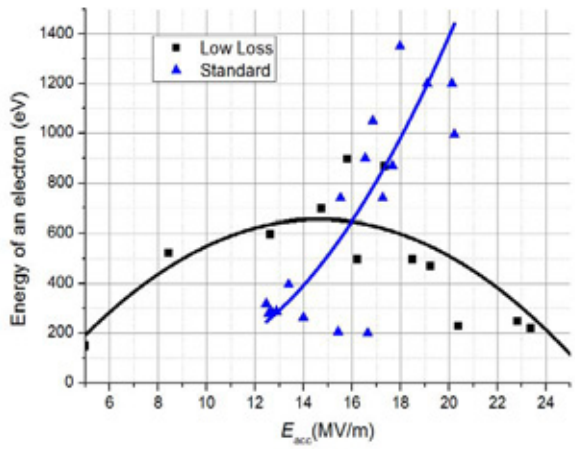

Figure 8: Energy of secondary electrons as a function of accelerating gradient for Low Loss and standard geometries.

INFLUENCE OF THE IRIS SHAPE

We have done simulations for structures with various radii of the iris ellipse: r_{x1} = 12 mm, r_{y1} = 19 mm (standard), r_{x1} = 12.5 mm, r_{y1} = 21 mm and r_{x1} = 10 mm, r_{y1} = 21 mm. The results show that r_{x1} has practically no influence on multipacting ranges. Lower threshold values are almost the same for all structures. Upper threshold value of accelerating gradient is higher for the structure with r_{y2}=21 mm.

ISBN 978-3-95450-170-0

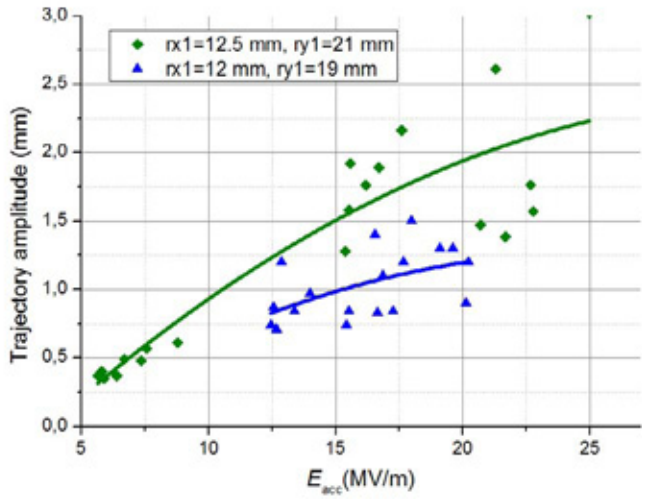

Figure 9: Trajectory amplitude as a function of. accelerating gradient for Low Loss and standard geometries.

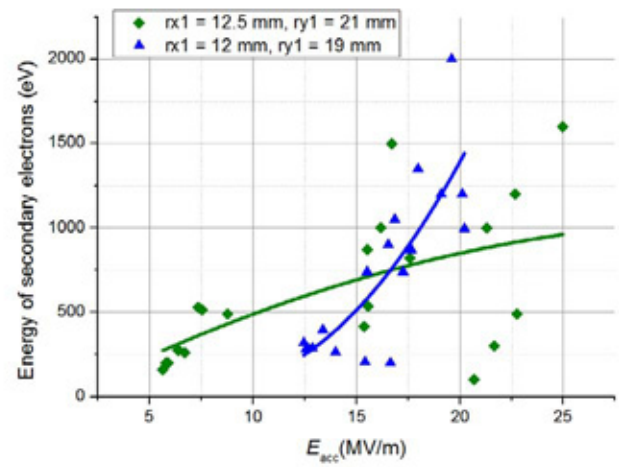

Figure 10: Energy of secondary electrons as a function of accelerating gradient for Low Loss and standard geometries.

SUMMARY

We were able to obtain stable 1st order multipacting trajectories in SC elliptical cells in a wide region of accelerating gradient, roughly at 5-30 MV/m.

The smaller is the aperture radius, the wider is the range of accelerating gradient at which cell suffers from multipactor discharge.

Low Loss cavity and cavity with a wider equator (r_{x2}=r_{y2}=43 mm) suffers from multipacting discharge in a wider range (4.7–29.3 MV/m in comparison with 5.4-22.5 for regular cell).

Larger radii of the iris ellipse have little influence on the multipacting discharge development.

REFERENCES

[1] Gusarova M.A., Petrushina I.I., Khuduakov S., The new possibility of MultP-M code, Proceedings of IPAC'14.

[2] http://www.cst.com

[3] P. Kolb et al., 1.3 GHz SRF CAVITY TESTS FOR ARIEL AT TRIUMF, Proceedings of SRF2013, Paris, France.

[4] Jacek Sekutowicz,TM Class Cavity Design, Proceedings of SRF2013, Paris, France.

ISBN 978-3-95450-170-0

MULTIPACTOR IN ELLIPTICAL CAVITIES 800 MHz

I.I. Petrushina, M.A.Gusarova, National Research Nuclear University (Moscow Engineering Physics Institute), Kashirskoe shosse, 31, 115409, Moscow, Russia

Abstract

The studies of the multipacting discharge possibility in elliptic single-cell cavities at 800 MHz with three types of hifger order modes couplers were done. The ranges of the field gradients where the conditions for the occurrence of first order multipacting discharge in the equatorial region, as well as the HOM field levels were determined.

INTRODUCTION

It is known that the equator area in the elliptical shape cavities is of the greatest risk in terms of multipactor discharge development where the first and the second orders stable trajectories could exist. In addition, HOM damping components such as corrugations, ribs and chokes can create additional resonance conditions for the development of a secondary electrons avalanche. The results of the multipactor discharge obtained using the three-dimensional modeling code MultiP-M 3D [1] have been published recently [2]. The number of particles percentage increase as a function of the field gradient for three resonator geometries smooth, fluted beam pipe and demountable damped structure are presentedin Figure 1.

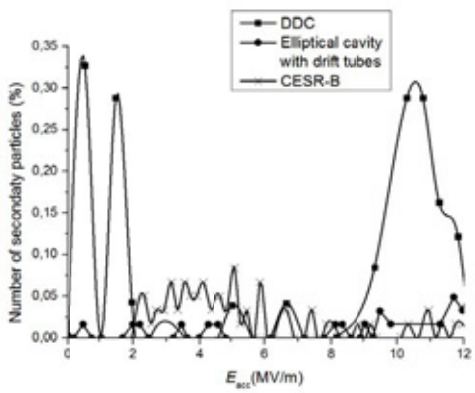

Figure 1: The number of particles percentage increase in the structure as a function of the field gradient for three resonator geometries smooth, fluted beam pipe and demountable damped structure.

For the mentioned structures, the first order trajectories in the equatorial region at low accelerating field gradientsof 2–4 MV/m (the numbers may vary slightly depending on the structure type), are of the highest danger of the multipactor discharge. Such trajectories can be eliminated by an additional purification of the cavity surface and subsequent surface conditioning. Beam pipe geometry doesn't provide any additional resonance conditions to start an avalanche of secondary electrons, except for the notch filter in demountable damped cavity (DDC) structure.

In this paper, we will examine in details the design of DDC and will provide the calculation results of the avalanche increase coefficient for that structure. The calculation was performed in CST Particle Studio [3].

MULTIPACTING DISCHARGE IN DDC

The model and the niobium secondary emission yield (SEY) plot that wereused in simulations are presented in Figures 2 and 3. The calculation of the number of particles increase in the structure as a function of time and different field gradients for demountable damped structure was done for 40 RF periods. The results of this calculation are shown in Figure 4.

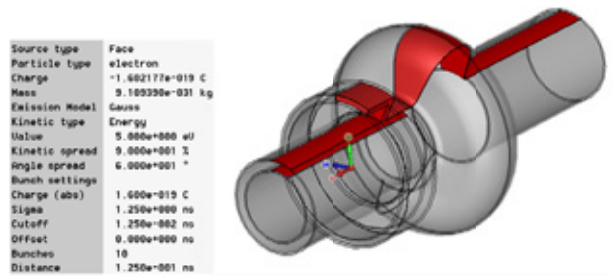

Figure 2: Demountable damped cavity (DDC).

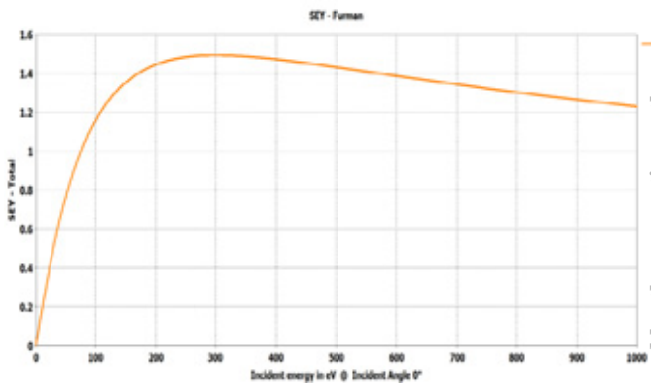

Figure 3: SEY plot for niobium.

ISBN 978-3-95450-170-0

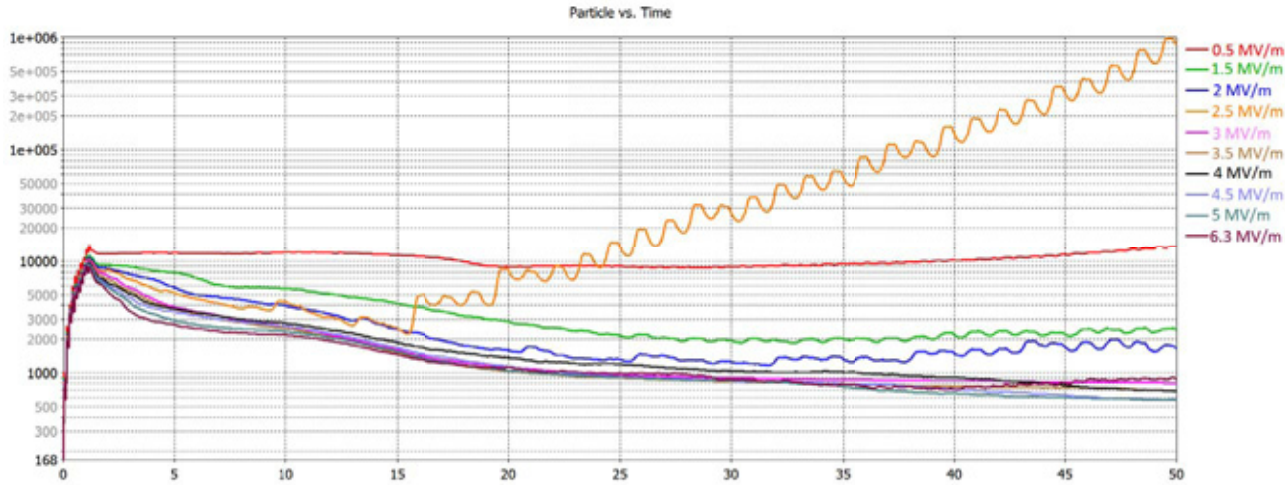

Figure 4: Number of particles increase in the structure as a function of time and different field gradients for demountable damped structure.

Figure 4 shows that the trajectories of electrons are observed in a wide range of accelerating gradients. According to the simulation results, we have calculated the avalanche growth rate (1) for different levels of the accelerating gradient – see Figure 5.

$$N = N_0 e^{\alpha t} \qquad (1)$$

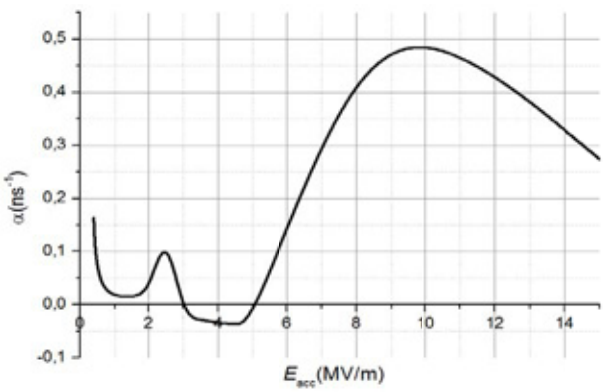

Figure 5: Avalanche growth rate at different levels of the accelerating gradient in demountable damped structure.

The areas with the remaining electron trajectories after 40 RF periods are presented on Figure 5 for different accelerating gradients.At low accelerating gradients, the stable trajectories are observed in the notch filter. The trajectories that remain active after 40 RF periods haveα = 0.16. The particle growth is also observed at the equator and coaxial parts, but is less intense.At high accelerating field gradient of about 7 MV/m, the stable trajectories with α = 0.41are observed in the equator area/. For accelerating gradients higher than 15 MV/m, the trajectories with α = 0.27 are also observed in the equator area of the accelerating cavity..

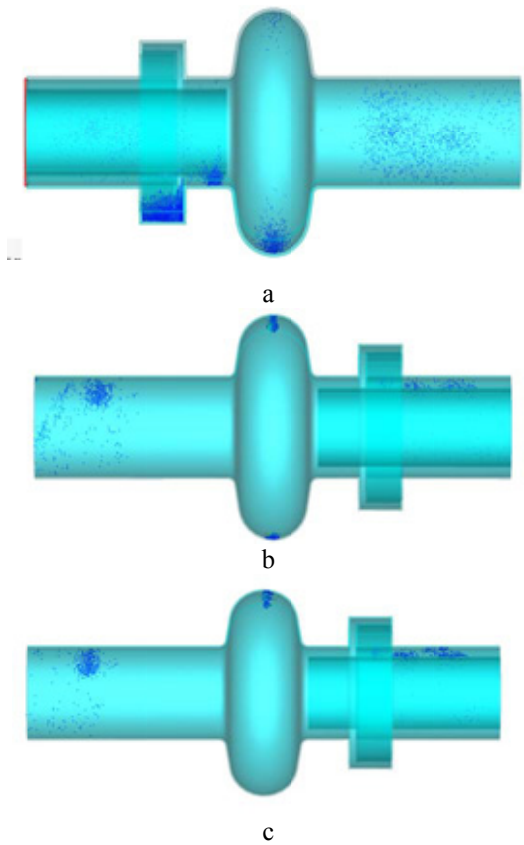

Figure 6: Regions of secondary electrons that remain active after 40 RF cycles. a) at 0.4 MV/m; b) at 7.5 MV/m; c) at 15 MV/m.

ISBN 978-3-95450-170-0

SUMMARY

The results provided by MultP-M code [2] are in agreement with the results of calculations in CST PS [3]. For low accelerating gradients stable multipacting trajectories are observed in the notch filter and coaxial line of demountable damped structureare. Rate of of its avalanche growth is $\alpha < 0.15$. Such trajectories which correspond tosoft multipactor discharge can be eliminated by an additional purification of the cavity surface and subsequent conditioning. At higher accelerating field gradients of about 7 MV/m, the avalanche growth rate increases up to $\alpha = 0.41$. The operating gradient of this structure is 10 MV/m, so obviously the multipacting discharge can possibly become a problem after reaching the this field level.

REFERENCES

[1] Gusarova M.A. et al. Multipacting simulation in accelerator RF structure // Nuclear Instrument and Methods in Physics Research A. 599. P. 100. 2009.

[2] Ya. Shashkov et al, Comparison of higher order modes damping techniques for 800 MHz single cell superconducting cavities, Nuclear Instruments and Methods in Physics Research A 767, 2014, pp 271–280.

[3] http://www.cst.com

[4] Ya. Shashkov et al, Analysis of Higher Order Modes Damping Techniques for 800 MHz Single Cell Superconducting Cavities, This proceedings.

ISBN 978-3-95450-170-0

UPGRADE OF BPM SYSTEM AT VEPP-4M COLLIDER

E.A. Bekhtenev, BINP, Novosibirsk, and Novosibirsk State University, Russia
G.V. Karpov, BINP, Novosibirsk, Russia

Abstract

Developed in BINP wideband beam position monitor (BPM) electronics has been installed at the VEPP-4M electron-positron collider. The VEPP-4M operates with two electron and two positron bunches. Wide bandwidth of new electronics (200 MHz) allows the separate measurements of electron and positron bunches with time interval between bunches up to 18 ns. 18 BPMs located near four meeting points are supplied with new electronics. The electronics can measure the position of each of four bunches. BPM system works at two modes: slow closed orbit measurements and turn-by-turn measurements. We present details of system design and operation.

INTRODUCTION

Basic scenario of high energy experiments at VEPP-4M provides operation with two electron and two positron bunches [1]. Beam position measurements near four meeting places require high time resolution of BPM electronics. Such electronics with analog bandwidth 200 MHz has been developed and tested at BINP [2]. At present 18 BPMs near four meeting places at VEPP-4M are supplied with new electronics. Positions of these BPMs are shown in Fig.1.

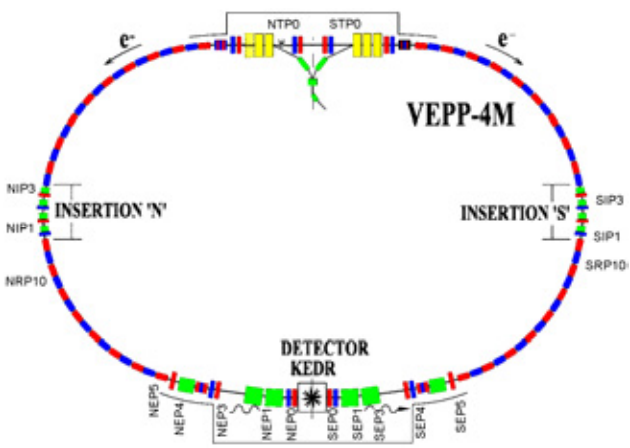

Figure 1: Positions of BPMs with new electronics.

Time intervals between signals of electron bunch and positron bunch for the part of BPMs located close to places of meeting of bunches are given in Table 1.

New electronics design utilizes signal peak sampling with high bandwidth digitizer [2].The main problem for achieving of required accuracy of a few tens microns is separation the BPM signals of electron and positron bunches. This problem has been solved with two ways: increasing of analog bandwidth to 200 MHz and digital compensation of the first bunch signal to second bunch signal. Two sets of new electronics have been successfully worked since 2010 year at BPMs NEP0, SEP0. At the end of 2013 year other 16 BPMs are supplied with new electronics. Special software for new BPM system control on base of EPICS has been developed.

Table 1: Time intervals between signals of electron and positron bunches for the part of BPMs

BPM	Time interval, ns
SIP2	2.27
STP0	18.07
NTP0	18.25
NIP3	20.09
NEP0	22.48
SEP0	22.66
NIP1	26.11
SIP1	26.38

BPM ELECTRONICS DESIGN

Functional diagram of the new BPM electronics is presented in Fig.2.

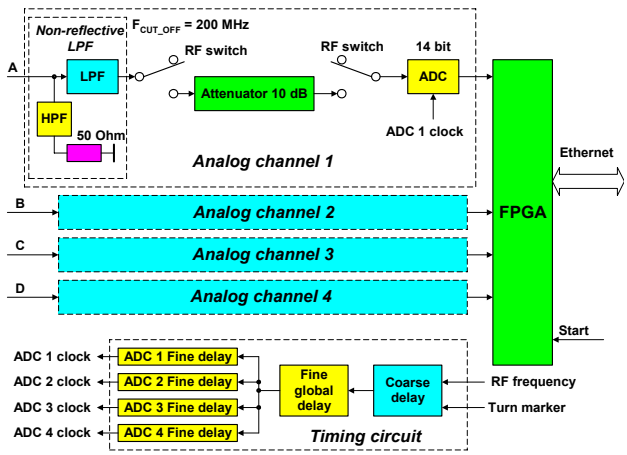

Figure 2: Functional diagram of new BPM electronics.

The electronics consists of four identical analog channels, FPGA, Timing circuit and Ethernet interface. All electronics occupies 1U 19" chassis.

The bandwidth of analog electronics is defined by non-reflective Low Pass Filter (LPF) with cut-off frequency of 200 MHz. Each analog channel has no amplifiers. Linearity and gain temperature stability are defined essentially by ADC.

ISBN 978-3-95450-170-0

Clock frequency of ADC is revolution frequency F_0. Each turn ADC digitizes one of four bunch signals. Timing circuit provides ADC samples at the top of BPM signal. Timing circuit is a three-stage delay. The first stage (coarse delay) is 8-bit programmable counter MC100EP016 with clock frequency of 181.8 MHz (RF frequency). After applying of turn marker the counter is preset by code defining coarse delay and then starts. Delay step of the first stage is one period of RF frequency ~5.5 ns. Delay range is $1/F_0$ – 5.5 ns.

The second stage (fine global delay) is 10-bit programmable delay chip MC100EP195B. It provides 10.24 ns delay range with 10 ps delay step. The third stage consists of four chips MC100EP195B, each chip for one of four ADC. As a result timing circuit provides total programmable delay range exceeding period of revolution frequency F_0 with delay step of 10 ps. Measured time jitter of ADC clock is ~10 ps. Choosing of measured bunch is made by setting of corresponding delay code. Measurement of four bunches is carries out with multiplexing of four delay codes.

Beam position is measured each turn. Turn-by-turn data are recorded to memory (with capacity of 8192 turns) and accumulated in Accumulator (inside FPGA). Accumulated data for specified number of turns form slow acquisition data (SA data).

MEASUREMENT ACCURACY

Beam position measurement accuracy is defined by 5 main parameters:

1) Resolution of turn-by-turn data
2) Resolution of slow acquisition (SA) data
3) Dependence of measurement result on temperature
4) Beam-current dependence
5) Dependence of measured beam position of the second bunch on the beam current of the first bunch

Dependence of the result on temperature is caused by two main reasons:

- Inequality of the Low Pass Filters, RF switches and attenuators
- Delay instability.

Delay instability is defined by delay instability of the chips MC100EP195B (10-20 ps/°C). For excluding of measurement error caused by delay instability of different chips delay scanning with step of 10 ps around the signal top in the range ±40 ps is carry out. After completing of the scanning the maximal signal for each channel is chosen.

Beam-current dependence is defined only by ADC nonlinearity because no other active elements are used.

For reducing of measurement error caused by overlapping of electron and positron signals program compensation of the signal "tail" is implemented in the system. "Tail" of the first bunch signal on the peak of second bunch signal for time interval between signals ~18 ns is about 0.5-1%. Such "tail" value without compensation can cause position measurement error of the second bunch up to 0.5 mm. Pickup voltage of the second bunch is calculated with formula:

$$U_{2C} = U_{2M} - k \times U_{1M},$$

where U_{2M} and U_{1M} – are measured pickup voltages of second and first bunches correspondingly,

k – is measured relative amplitude of the "tail" of the first bunch on the peak of the second bunch.

The k value is measured experimentally one time and then is used for "tail" compensation. In the Fig.3 signal of the first bunch (result of delay scanning) and its "tail" in the location of second bunch are represented. Dots indicate position of the signal top.

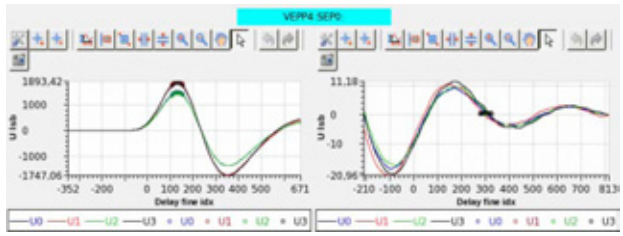

Figure 3: Signal of the first bunch (left picture) and its "tail" in the location of second bunch (right picture).

Such compensation decreases position measurement error of the second bunch caused by "tail" of the first bunch approximately in 10-20 times (besides of BPM SIP2 for which time interval between signals is 2.27 ns).

Accuracy parameters are given in Table 2.

Table 2: BPM system parameters defining accuracy of measurements for beam current 1÷10mA ($K_X \approx 43$ mm, $K_Z \approx 42$ mm)

Resolution of slow measurements (SA data)	μm	3-6
Resolution of turn-by-turn data	μm	15-30
Beam-current dependence	μm	40-60
Error for the second bunch caused by first bunch "tail" when electron and positron beam currents are equal (besides of BPM SIP2)	μm	< 100
Dependence on temperature	μm/°C	< 2

BPM CONTROL SYSTEM

Structure of BPM control system is represented in Fig.4.

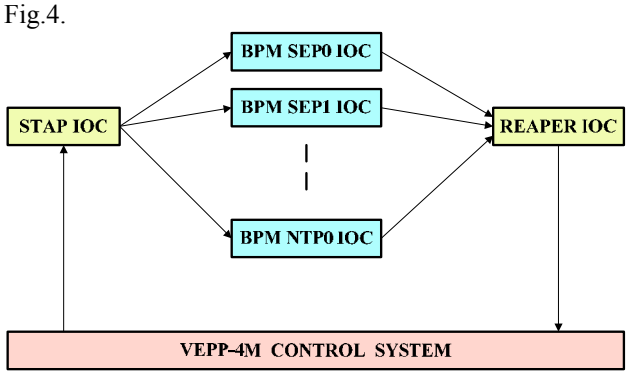

Figure 4: Structure of BPM control system.

ISBN 978-3-95450-170-0

BPM control system is developed on base of EPICS. BPM electronics (BPM Processor module) for each BPM is controlled by its own IOC (Input/Output Controller). For connection of these 18 IOC with existent VEPP-4M Control system special two IOC: STAP IOC and REAPER IOC have been made. Main mode of BPM system operation is periodical (1 time in a sec) orbit measurements. Time of orbit measurement cycle T_{MEAS} is ~600 msec. During the time T_{MEAS} delay scanning in the range ±40 ps with finding of signal maximum is carry out for each of four bunches. Remained 400 msec IOC performs delay scanning (with large delay step) inside the whole separatrix and scanning along all 222 separatrixes. Another mode of operation is external trigger mode with obtaining of turn-by-turn data. Before beam injection or kicking every BPM IOC receives from STAP IOC information about injected beam (or about kicking). BPM IOC stops orbit measurements. Each BPM Processor is waiting of external trigger pulse synchronized with beam injection or kicking. After coming of the external trigger pulse BPM Processor fills turn-by-turn buffer and then started slow orbit measurements. In Fig. 5, 6 turn-by-turn data and its spectrum obtained after injection of the beam are shown.

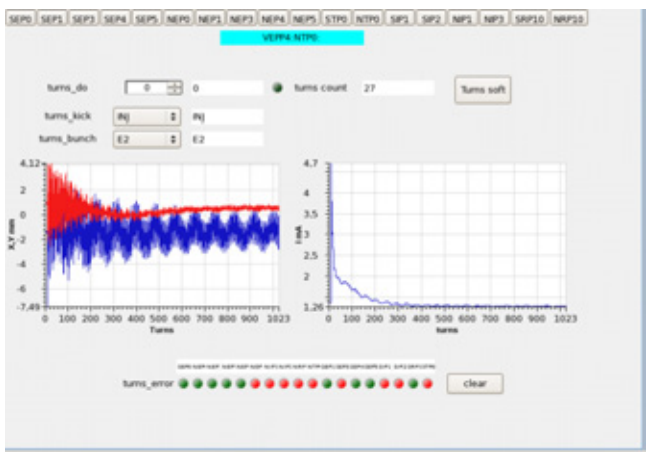

Figure 5: Turn-by-turn beam position measurements obtained after injection of the beam.

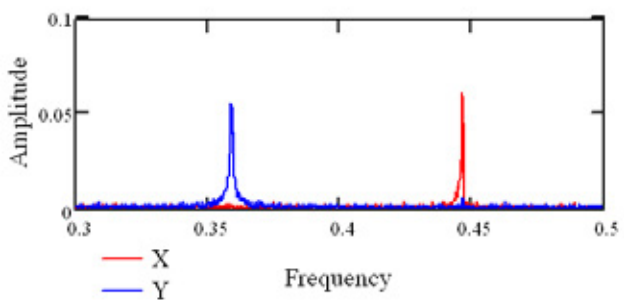

Figure 6: Spectrum of turn-by-turn measurements.

Additional mode of BPM system operation is "Post mortem" mode. In this mode turn-by-turn buffer is filled continuously (works as circular buffer). When beam current becomes lower specified value I_{MIN} writing to the turn-by-turn buffer is stopped. It allows looking of beam behavior before its abrupt losses or death. This mode is actively used for the tuning of VEPP-4M feedback system.

SUMMARY

At present 18 complete sets of new BPM electronics are manufactured and installed at VEPP-4M storage ring. All software for this electronics has been written. New electronics allows separate electron and positron orbit measurements during experiments with colliding beams. Ability of turn-by-turn beam position measurements also facilitates storage ring study and tuning.

ACKNOWLEDGEMENT

The work is supported by the Ministry of Education and Science of the Russian Federation, NSh-4860.2014.2.

REFERENCES

[1] V. Kiselev et al. "Particle and Accelerator Physics at the VEPP-4M Collider". This proceeding.
[2] E. Bekhtenev et al. "Wideband BPM Electronics for the VEPP-4M Collider", Proceeding of RuPAC-2010, Protvino, Moscow region, p. 245-247.

ISBN 978-3-95450-170-0

EXTENDING VEPP-5 CONTROL SYSTEM BY MIDDLEWARE FOR INJECTION/EXTRACTION AUTOMATION

Gusev E.A., Bolkhovityanov D.Yu., Frolov A.R., BINP, Novosibirsk, Russia
Emanov F.A.*, BINP, Novosibirsk, Russia; NSU, Novosibirsk, Russia

Abstract

CX and EPICS are used at VEPP-5 Injection complex. Each system is in charge of some part of accelerator devices. Middleware layer was added in order to make data processing and facility-level control actions more straightforward. Middleware is separated from clients layer by means of additional CX-server. Architectural approach is considered on the example of injection/extraction automation.

INTRODUCTION

In order to provide electrons and positrons for colliders VEPP-5 injection complex [1] in the Budker Institute of Nuclear Physics is being built. This complex includes linear accelerator-based electron-positron source (preinjector) and damping ring. There are two existing injection complex beam users VEPP-4 and VEPP-2000. Charm-Tau Factory project claims the complex to provide positrons [2].

VEPP-4 and VEPP-2000 colliders will require both electron and positron beams with relatively low injection rate. In order to supply users injection complex will switch between users (further switch user) and switch between electrons and positrons (further switch particles type). It is required to store electrons and positrons in damping ring and transfer beam to users on complicated schedule. All mentioned above control actions compose injection complex main loop (machine loop) which is easier to implement by software in this case. Basic-level control was implemented by CX and EPICS software control systems. In order to create facility-level control for injection complex it is required to use both systems. Injection complex synchronization system is in charge of machine loop implementation. Synchronization system hardware was changed in order to support selected operation model.Software and hardware design based on the following principles is discussed:

- existing software and hardware infrastructure is used,
- software is suitable for regular machine operation,
- few copies of any GUI application started on the same or different computers are allowed,
- developers work is minimized.

DESIGN

Requirements

Requirements for injection/extraction automation arise from complex tasks to serve colliders. Let's consider colliders injection loops. VEPP-4 injection cycle consists of the following stages: storage to VEPP-3 up to 4^{11} particles, 2^{10} particles/injection, time between injections at least 1 second; acceleration to experiment energy, transfer to VEPP-4 and change VEPP-3 polarity, process duration about 7 minutes; then those stated above are repeated for other particles. Beam for VEPP-2000 is to be injected to BEP. 1.1^{11} 1.4^{11} particles are required to be injected at once. BEP uses 30 s to accelerate, transfer particles and change polarity. VEPP-2000 is expected to require 8 injections of each type of particles as initial collider filling. Refill is to be done in 30-50 s with usual amount of electrons and positrons.

According to beam users working schedule it is required to change machine settings from electrons to positrons or from one user to another one every 30 seconds. Highly automated control has to be implemented to meet this tight machine schedule. Currently injection complex operates with engineering software which presents full set of measurement and control points. Regular machine operation requires dramatic reduction of information amount presented to operator.

In order to avoid additional radiation load on equipment no beam should be accelerated without reason. Continuous start mode with masking was previously used for preinjector. Equipment in this mode can emit undesirable start signals since mask command execution time can be larger than time to next start. Preprogrammed number of starts mode ("counter mode") has to be implemented for preinjector beam systems. Continuous starts mode is being used for high power RF systems since it keeps constant thermal state of accelerating structures.

Start signals for extraction are provided by RF matching system in order to transfer beam to user. Currently this system is under development. Internal start possibility being presented for extraction and transfer channels is required for testing and tuning. RF matching system will continuously generate starting signals. Therefore synchronization hardware has to pass single start on request ("single-pass mode"). Internal starting signals can be provided by any continuous-mode channel of start generator.

Let's summarize requirements for the machine control system changes:

- "counter mode" must be implemented for preinjector beam systems,
- "single pass mode" must be implemented for extraction signals,
- automatic control software must organize user requests processing, beam storage and transfer with all

* F.A.Emanov@inp.nsk.su

ISBN 978-3-95450-170-0

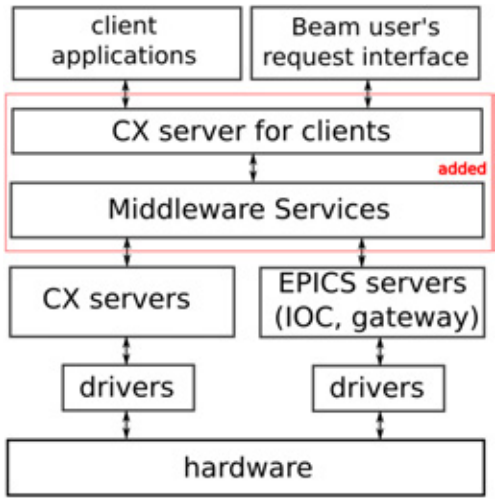

Figure 1: Injection complex software structure with middleware.

required operation mode changes,

- few copies of operator applications can be launched.

General solutions

In order to meet the requirements operator applications have to be isolated from closed-loop control code. Since CX and EPICS are used in control system we have to create common server side processing infrastructure. A logical middleware layer and additional CX-server is proposed to be added (see Fig. 1). Middleware layer consists of client-space services which implement facility-level control, closed-loop control and data processing. Top-level CX-server is in charge of communication with clients. Currently services can be implemented with C/C++ when throughput is crucial or with python for fast development. GUI applications are communicating with control system via CX only and don't implement any closed-loop control. This allows few copies of application to be started and makes GUI programs development more straightforward.

INJECTION/EXTRACTION AUTOMATION

Device level control for injection complex was implemented earlier including hardware, drivers, servers and engineering GUI applications. Specified above requirements lead us to implement some hardware and software changes. Let's brief discuss equipment and programs involved to injection and extraction control with emphasis on made changes.

Hardware

One turn injection with pre-kick of a stored beam is used in a damping ring. Injection system consist of four kickers (see Fig. 2) and their high voltage generators [5]. Currently injection system can reliably operate with up to 12.5 Hz repetition rate. Generators controlled by synchronization

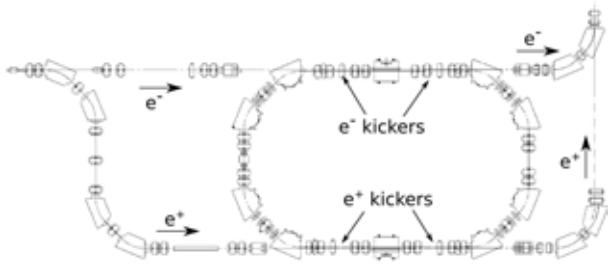

Figure 2: Damping ring kickers placement layout.

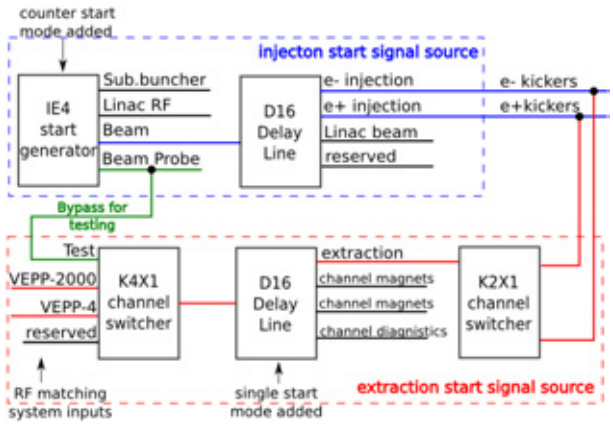

Figure 3: Kikers start signals sources layout.

system (providing start signals), CAC208 DAC/ADC (generator voltage settings) and fast ADC (generator waveform acquisition). Channel switchers are used to select which pair of kickers is operated.

Part of synchronization system shown on Figure 3 is in charge of carrying out injection and extraction actions. Other automation hardware defines operation mode. Synchronization system is hosted in CAMAC and controlled with EPICS. Start generator IE4 signals are used to inject the beam to damping ring. Extraction involves signals from shared with beam users RF matching system. Test extraction can be done with bypass from beam probe channel which continuously generate starts at 1 Hz repetition rate. This generator has 4 channels to support operation of all complex pulsed devices: 50 Hz channel for subharmonic buncher, 1 Hz channel for slow devices, 50Hz/N channel for RF system and, 50HZ/N/M for beam and injection systems. RF system and beam systems channels were separated to keep accelerator thermal mode while beam acceleration is not required. In order to meet mentioned above requirements "counter mode" was added to IE4 start generator beam channel and single pass mode was added to first D16 delay line in extraction circuit.

Damping ring beam current is measured with direct current current transformer (DCCT). Closed-loop injection control based on DCCT data is to be implemented. DCCT current is measured with CAC208 and provided via CX-server.

ISBN 978-3-95450-170-0

Software

Injection and extraction automation is a machine main loop implementation. The problem consists of following tasks: machine operation mode changes, procedures (inject, extract,...), create facility-level data, process user requests and schedule tasks, bring data to top-level CX-server. Middleware services were created for each task (see Fig. 2). There are following basic kinds of services: gateway, data processor, aggregator, action and control loop. Let's describe their features.

- Gateway with simple data processing capabilities was implemented in general way and is suitable for many cases.
- Data processors are individually designed. DCCT data processor and magnetic system failure trackers are implemented to date. It is planned to create failure and readiness trackers for all control devices.
- In order to simplify facility-level actions and control loops they should operate with facility-level data. Aggregators are used to provide facility-level data. And, or and sum aggregators are implemented to date.
- Actions and control loops are individually designed but have few common features. In order to generalize run control and interrupts processing actions and control loops must support at least start, stop, continue and reset state commands which are sent via clients CX.

Common services design points:

- Corresponding hardware-side data can conflict with client-side data. When service is starting hardware considered as reliable data source. In a runtime service solve data conflict on it own.
- Service settings that can be changed run-time are transferred by CX server. SDDS [4] files are used for other settings.
- CX and EPICS both have client libraries for C and Python. If it's possible Python should be used to implement service in object-oriented way.

Currently Python wrappers for QT, CX and EPICS CA were used for implementation of all services. This way was tested to be good for all non-vector channels. Vector channels processing will require C/C++ implementation.

ACKNOWLEDGMENT

Authors are grateful to A.V.Makeev for his work on initial version of python wrapper of CX client libraries and all the people who taken a part in VEPP-5 injection complex project.

The work was supported by the Ministry of Education and Science of the Russian Federation, NSh-4860.2014.2

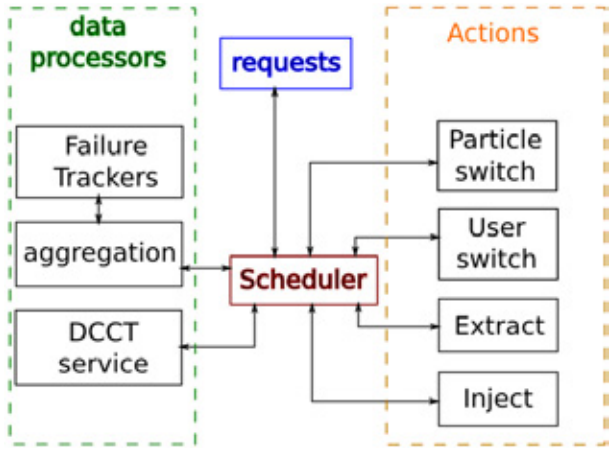

Figure 4: Injection/extraction control services.

REFERENCES

[1] Physical project VEPP-5. BINP SB RAS. 1995.

[2] A. E. Bondar, Project of a Super Charm-Tau Factory at the Budker Institute of Nuclear Physics in Novosibirsk, Physics of Atomic Nuclei, 2013, Vol. 76, No. 9, pp. 10721085.

[3] D.Bolkhovityanov, "VEPP-5 Injection Complex Control System Software", 2007, Ph.D. thesis

[4] M. Borland, L. Emery, "The Self-Describing Data Sets File Protocol and Toolkit," Proceedings of the 1995 ICALEPS Conference, October, 1995, Chicago, Illinois.

[5] A.I.Butakov, B.I. Grishanov, F.V. Podgorny, Injection system to damping ring of an electron-positron injection complex VEPP-5, Proceedings of RuPAC XIX, Dubna 2004.

ISBN 978-3-95450-170-0

DISTRIBUTED BEAM LOSS MONITOR BASED ON THE CHERENKOV EFFECT IN OPTICAL FIBER

Yu.I. Maltseva*, V.G. Prisekin, BINP SB RAS, Novosibirsk, Russia
F.A. Emanov, BINP SB RAS and NSU, Novosibirsk, Russia
A.V. Petrenko, BINP SB RAS, Novosibirsk, Russia; CERN, Geneva, Switzerland

Abstract

A distributed beam loss monitor based on the Cherenkov effect in optical fiber has been implemented for the VEPP-5 electron and positron linacs and the 510 MeV damping ring at the Budker INP. The monitor operation is based on detection of the Cherenkov radiation generated in optical fiber by means of relativistic particles created in electromagnetic shower after highly relativistic beam particles (electrons or positrons) hit the vacuum pipe. The main advantage of the distributed monitor compared to local ones is that a long optical fiber section can be used instead of a large number of local beam loss monitors. In our experiments the Cherenkov light was detected by photomultiplier tube (PMT). Timing of PMT signal gives the location of the beam loss. In the experiment with 20 m long optical fiber we achieved 3 m spatial resolution. To improve spatial resolution optimization and selection process of optical fiber and PMT are needed and according to our theoretical estimations 0.5 m spatial resolution can be achieved. We also suggest similar techniques for detection of electron (or positron) losses due to Touschek effect in storage rings.

INTRODUCTION

VEPP-5 Injection Complex [1] now is under commission and will supply BINP RAS colliders with electron and positron beams. The VEPP-5 Injection Complex consists of 270 MeV driving electron linac, 510 MeV positron linac and dumping ring. Since the Complex is not equipped with any operational beam loss monitor system we proposed to use a distributed beam loss monitor based on the Cherenkov effect in optical fiber.

This type of beam loss monitor has been developed at several facilities such as FLASH (DESY), SPring-8 (RIKEN/JASRI), CLIC Test Facility (CERN) [2–4]. The monitor overview is given by T. Obina [5]. The basic idea behind optical fiber beam loss monitor (OFBLM) is to detect a burst of the Cherenkov radiation (CR) generated in optical fiber by means of relativistic particles created in electromagnetic shower after highly relativistic beam particles (electrons or positrons) hit the vacuum pipe. Some of the Cherenkov photons propagate through the fiber and can be detected by PMT (Fig. 1).

Compared with other distributed beam loss monitors such as long ionization chamber and scintillating fiber, the OFBLM has the following advantages: fast response time (< 1 ns) which allows to detect multi-turn beam losses in a storage ring, near zero sensitivity to background signal (mainly gamma radiation) and synchrotron radiation, unlike scintillating fiber. Moreover, optical fiber is insensitive to magnetic field, but it is susceptible to radiation damage (except quartz fiber), which limits fiber lifetime. Another disadvantage of the OFBLM is an issue with its calibration.

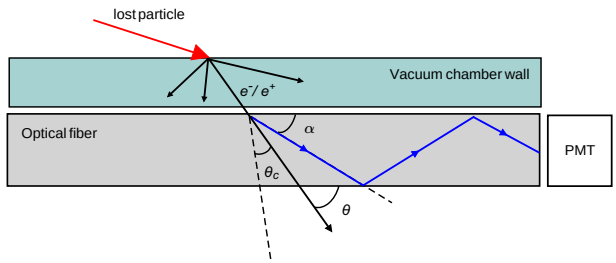

Figure 1: Scheme of beam loss monitor.

PRINCIPLE OF BEAM LOSS MONITOR

The following physical processes determine the OFBLM spatial resolution.

Electromagnetic Shower

For electromagnetic shower simulation G4beamline code [6] was used. Angular distribution of secondary electrons and positrons relative to beam direction was obtained (Fig. 2).

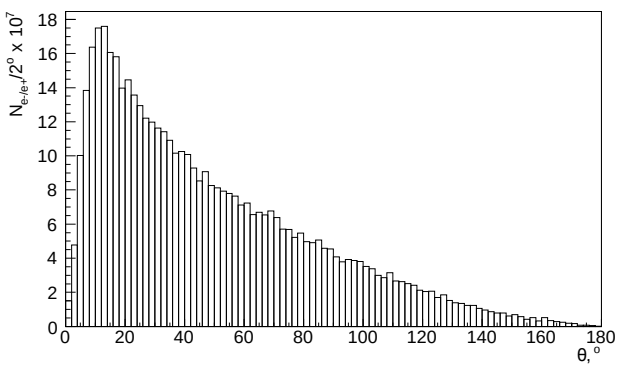

Figure 2: Angular distribution of secondary e-/e+ relative to beam direction passing through optical fiber. 270 MeV electron beam with 10^{10} electrons hits 2 mm steel vacuum pipe with 1° incident angle. Fiber is placed at the loss point. Total number of charged particles is $0.5 \cdot 10^{10}$.

* Yu.I.Maltseva@inp.nsk.su

ISBN 978-3-95450-170-0

For the CR to be generated kinetic energy of charged particle traveling through a dielectric medium must be:

$$E > E_0 \left(\frac{n}{\sqrt{n^2 - 1}} - 1 \right) \quad (1)$$

where E_0 – particle rest energy, n – medium refractive index. To obtain such particles from electromagnetic shower with energies satisfying eq. (1), lost particle energy must be greater than 10 MeV for electron (or positron) beams and greater than 5 GeV for proton beams.

Cherenkov Radiation

The Cherenkov radiation is an electromagnetic radiation emitted in a cone around the moving charged particle with cone semi-angle θ_c:

$$\cos\theta_c(\lambda) = \frac{1}{\beta n(\lambda)}$$

where λ – radiation wavelength, β – particle velocity ($\beta = v/c$), n – medium refractive index. Neglecting refractive index dispersion, the number of the Cherenkov photons from a single electron or positron per particle path length in a medium is given by:

$$\frac{dN}{dx} = 2\pi\alpha \sin^2\theta_c \int_{\lambda_1}^{\lambda_2} \frac{d\lambda}{\lambda^2} \quad (2)$$

where α is the fine structure constant, λ_1 and λ_2 determine spectrum range. According to eq. (2), the greater part of the Cherenkov photons is emitted in the UV range of the spectrum. For relativistic electron passing through plastic optical fiber ($n = 1.492$) the CR in visible spectrum (400 nm < λ < 700 nm) will be generated with 30 photons per mm and emission semi-angle θ_c about 48°.

Besides the CR, optical transition radiation [7] can be detected by PMT. However, the number of optical transition radiation photons was estimated to be 10^4 times less than the number of the CR photons and thus can be neglected.

Signal Propagation

The emitted Cherenkov radiation propagates through optical fiber by means of total internal reflection. This is the case when light (see Fig. 1) propagates with angle α relative to the fiber axis lower than:

$$\alpha \le \alpha_{max} = \arcsin(NA/n_{co})$$

where NA – optical fiber numerical aperture, n_{co} – refractive index of optical fiber core. For example, for optical fiber with $NA = 0.47$ and $n_{co} = 1.492$, $\alpha \le 18°$. This leads to secondary charged particles passing through optical fiber with angle θ between 30° - 66° and 114° - 150° relative to the fiber axis will generate the Cherenkov radiation which is able to be trapped in optical fiber. This results in trapping of about 33% and 5% of generated radiation, respectively. Consequently, downstream signal sensitivity is 7 times higher than upstream one.

MONITOR SPATIAL RESOLUTION

Monitor spatial resolution depends on light dispersion in optical fiber, PMT and electronics resolution. There are two main dispersion types in fiber: modal and chromatic. Modal dispersion originates from the fact that light rays with different trapping angles travel the same distance with different times. Chromatic one is caused by different propagation times for different light wavelengths. When transmitting signal through optical fiber of length L each dispersion contribution to pulse broadening can be estimated as:

$$t_{mod}/L = 1/cn_{co}(1/\cos\alpha_{max} - 1),$$

$$t_{chr}/L \approx 1/c(n_{co}(\lambda_1) - n_{co}(\lambda_2)).$$

In multimode optical fiber with step-index profile signal lengthening is effected mainly by modal dispersion, in multimode optical fiber with graded-index profile chromatic one is dominant and modal one is negligible. In singlemode fiber there is no modal dispersion, but its lower pulse distortion comes at the expense of lower signal sensitivity. For step-index multimode fiber which was used in our tests $t_{mod}/L = 0.25$ ns/m, $t_{chr}/L = 0.05$ ns/m, i.e. modal dispersion contributes 5 times greater to monitor spatial resolution then chromatic dispersion. Therefore, to make spatial resolution smaller graded-index multimode optical fiber or singlemode one should be used as well as PMT and electronics with small time resolution. Micro-channel plate PMT is a good candidate.

The Cherenkov signal can be detected at either downstream or upstream end of the fiber. In case of multiple losses originated from successive magnet elements 5 times better spatial discrimination between losses can be achieved by signal detection at the upstream end of the fiber compared with the downstream one. This is due to the fact that beam velocity βc is greater than speed of light in optical fiber c/n. Despite upstream signal sensitivity is 7 times lower than downstream one, the former is preferable.

EXPERIMENTAL RESULTS

A prototype of the OFBLM was made using 20 m and 60 m long plastic step-index multimode fibers Avago Tech. HFBR-RUS500Z (1 mm core diameter, $n_{co} = 1.492$ and $NA = 0.47$). To detect the CR signal at the downstream end of the fiber FEU-85 PMT (300-600 nm spectral sensitivity range) was used. The prototype of the OFBLM was installed in the VEPP-5 electron linac and tested in a controlled manner by dumping beam with dipole correctors. The experimental results are shown in Fig. 3.

As one can see from Fig. 3a) FWHM of the signal approximately corresponds to 3 meters for 20 m long optical fiber and 1.5 m beam length. For single bunch (4 mm) using graded-index multimode optical fiber or singlemode one and micro-channel PMT will allow us to achieve 0.5 m monitor spatial resolution limited mostly by ADC characteristics. In Fig. 3b) for 60 m long optical fiber besides controlled beam loss at the end of the 4th RF-structure one can see beam losses in multiple locations along linac.

ISBN 978-3-95450-170-0

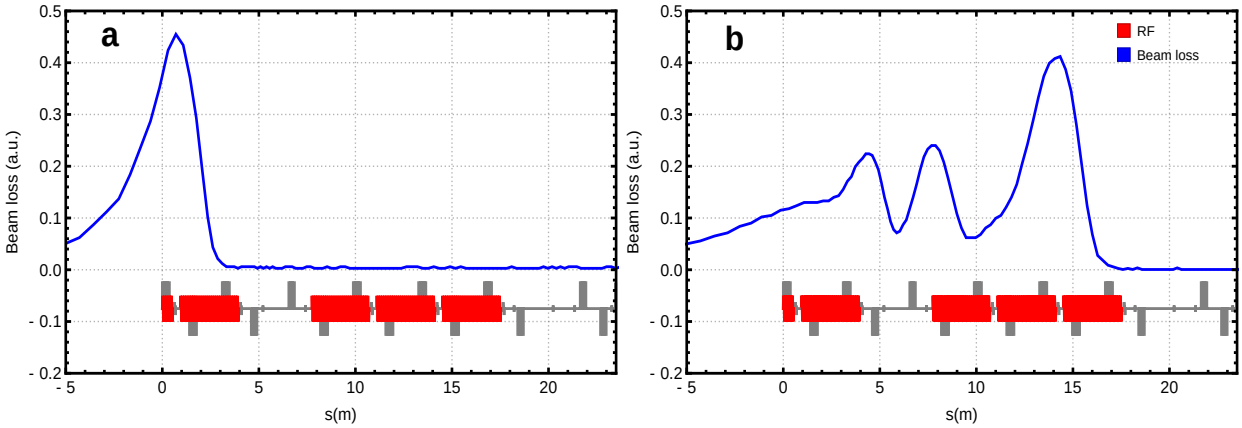

Figure 3: Beam losses: a) beam was dumped at the end of the 1st RF-structure, 20 m fiber was used; b) at the end of the 4th RF-structure, 60 m fiber was used.

TOUSCHEK EFFECT

In storage rings besides irregular beam losses there are beam lifetime losses due to Touschek effect [8] (loss mechanism driven by large-angle Coulomb scattering within the high charge bunch). This effect results in losses of scattered particles with energy variation exceeding the energy acceptance of the ring. For the VEPP-5 dumping ring with 28 m circumference and $2 \cdot 10^{10}$ electron bunch charge the beam lifetime is roughly 10 min and the average number of lost electrons per turn is 2. According to our theoretical estimations, the OFBLM can detect a single electron (or positron) hitting the vacuum pipe with probability about 1% for the VEPP-5 beam parameters. Hence, using two optical fibers placed on both sides of vacuum chamber the monitor can detect 10^8 Touschek events. It's sufficient to obtain precise distribution of the beam losses due to Touschek effect in a storage ring.

CONCLUSION

The distributed beam loss monitor based on the Cherenkov effect in optical fiber has been tested in the VEPP-5 electron linac. 3 m monitor spatial resolution for 20 m long optical fiber was obtained. Using graded-index multimode optical fiber or singlemode one and micro-channel plate PMT 0.5 m spatial resolution can be achieved. To achieve better spatial discrimination between successive losses one should detect the light signal at the upstream end of the fiber. The monitor ability to detect single particle losses and high signal-to-noise ratio make it possible to use the monitor for detection of electron (or positron) losses due to Touschek effect in storage rings.

REFERENCES

[1] K.V. Astrelina et al. "Production of Intense Positron Beams at the VEPP-5 Injection Complex", Journal of Experimental and Theoretical Physics, Vol. 106, Issue 1, p. 77 (2008)

[2] F. Wulf, M. Körfer, "Beam Loss and Beam Profile Monitoring with Optical Fibers", Proc. DIPAC09, Basel, Switzerland (2009) 411

[3] X.-M. Maréchal et al. "Beam Based Development of a Fiber Beam Loss Monitor for the Spring-8/XFEL", Proc. DIPAC09, Basel, Switzerland (2009) 234

[4] S. Mallows et al. "Fiber Based BLM System Research and Development at CERN", Proc. HB2012, Beijing, China (2012) 596

[5] T. Obina, "Optical Fiber Based Loss Monitor for Electron Storage Ring", Proc. of IBIC2013, Oxford, UK (2013) 638

[6] `http://www.muonsinternal.com/muons3/G4beamline`

[7] V.L. Ginzburg, "Transition Radiation and Transition Scattering", 16th International Cosmic Ray Conference, Vol. 14, p. 42 (1979)

[8] C. Bernardini et al. "Lifetime and Beam Size in a Storage Ring", Phys. Rev. Lett. 10, 407 (1963)

ISBN 978-3-95450-170-0

MODERNIZATION OF VEPP-2000 CONTROL SYSTEM*

Yu.A. Rogovsky#, D.E. Berkaev, O.V. Gorbatenko, Yu.M. Shatunov, BINP SB RAS and Novosibirsk State University, Novosibirsk, Russia
A.P. Lysenko, A.L. Romanov, A.I. Senchenko, P.Yu. Shatunov, BINP SB RAS, Novosibirsk, Russia

Abstract

Electron-positron collider VEPP-2000 delivered data for the high energy physics since the end of 2009. In the summer of 2013 the long shutdown was started dedicated to the deep upgrade of the wide range of subsystems. The main goal of the improvements is to reach or exceed design luminosity in the whole energy range from 200 MeV to 1000 MeV per bunch.

The hardware of the accelerator complex consists of high current main field power supplies, low current power supplies for steering and multipole magnets, pulsed power supplies for channel's elements, RF subsystems, BPM and some other special subsystems (such as vacuum, temperature, etc.). The control system is based on CANbas, CAMAC and VME devices. The wide range of software corresponding to specific hardware subsystems forms complicated interacting system that manages all parts of the VEPP-2000 accelerator facility. Automation software is running on several TCP/IP connected PC platforms under operating system Linux and uses client-server techniques.

The paper presents general overview and changes made in architecture, implementation and functionality of hardware and software of the VEPP-2000 collider control system.

VEPP-2000 PROJECT

VEPP-2000 electron positron collider [1] was commissioned and spent three successful runs 2010-2013 collecting data at whole energy range of 160÷1000 MeV per beam [2].

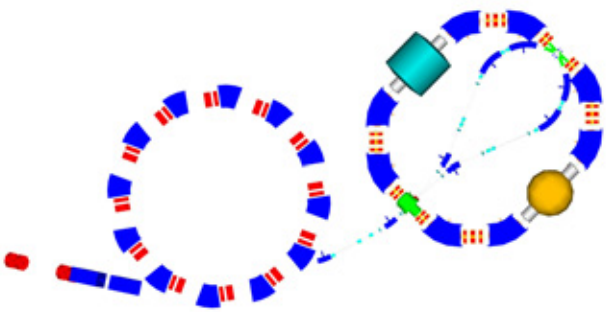

Figure 1: VEPP-2000 facility layout.

During this work VEPP-2000 used the injection chain of its predecessor VEPP-2M which has worked at BINP over 25 years in energy range up to 1.4 GeV in c.m.s. and has collected of about 75 pb^{-1} integrated luminosity. That machine worked at lower energy (< 700 MeV) and showed luminosity 30 time lower than designed value of 10^{32} $cm^{-2}s^{-1}$ for VEPP-2000 at 1 GeV. As a result the positron production rate was not enough to achieve beams intensity limited only by beam-beam threshold. This restriction will be cured by link up via 250 m beamline K-500 [3] to the new injection complex VEPP-5 capable to produce intensive electron and positron high quality beams at energy of 450 MeV. The layout of the VEPP-2000 complex is presented in Fig. 1. The complex consists of Booster of Electrons and Positrons (BEP) and the collider itself with two particle detectors, Spherical Neutral Detector [4] and Cryogenic Magnetic Detector [5], placed into dispersion-free low-beta straights. The main design collider parameters are listed in Table 1.

Table 1: VEPP-2000 Main Parameters (at E = 1 GeV)

Parameter	**Value**
Circumference (C)	24.3883 m
Energy range (E)	200 ÷ 1000 MeV
Number of bunches	1 × 1
Number of particles per bunch (N)	1×10^{11}
Betatron functions at IP ($\beta^*_{x,y}$)	8.5 cm
Betatron tunes ($\nu_{x,y}$)	4.1, 2.1
Beam emittance ($\varepsilon_{x,y}$)	1.4×10^{-7} m rad
Beam–beam parameters ($\xi_{x,y}$)	0.1
Luminosity (L)	1×10^{32} cm^{-2} s^{-1}

CONTROL SYSTEM OVERVIEW

The architecture of VEPP-2000 software [6] is based on three-layer structure (see Fig. 2). Specialized services (hardware layer) control one or several CAN or CAMAC buses and allow client applications to have access to hardware. The main application of Middleware layer is VCAS (VEPP-2000 Channel Access Server). Third level is presented with GUI applications, which provides to facility operator powerful and convenient instrumentation for beam tuning and diagnostics of possible systems malfunctioning. For the high loaded data channels like control systems of magnetic structure of storage and collider rings it is possible direct communication between GUI and hardware layers. Another important application in the middleware layer in specially designed Log Server.

*Work supported by: 1) Ministry of Education and Science of the Russian Federation, Nsh-4860.2014.2; 2) partly supported by: RFBR grant 14-02-31501
#Yu.A.Rogovsky@inp.nsk.su

ISBN 978-3-95450-170-0

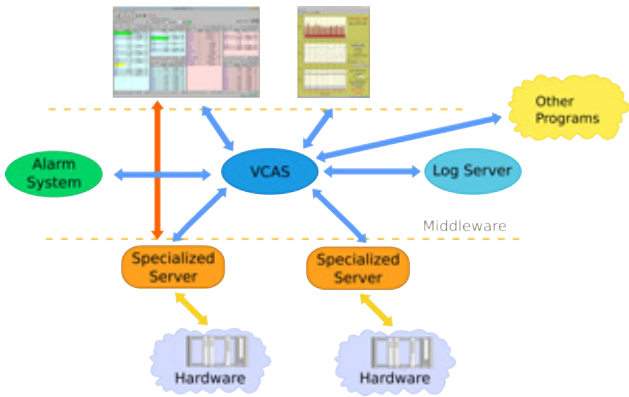

Figure 2: VEPP-2000 Software scheme.

Alarm System

VEPP-2000 collider is a complicated system it's state is characterized by sousands of parameters. Sometime it is difficult to find out system diviation in time. To solve this problem Alarm System was developed. Alarm system is rule based. Every rool could depend on many channels. Alarm system is written in javascript and based on asynchronyos IO library Node.js. Web user interface are embedded in system and provides on-line rule editor. Such approach provides flexible way for rule definition and allows to reduce number of elements to maintain.

Logging Server

The Logging system [7] is aimed at and saving and tracking of parameters changes. It is build on client-server architecture. Logging server is core element. System was deployed in 2011. After one year and a half of successfull operation new version of logging server was developed. Main goal was to improve maintainability. To achieve this goal custom made subsystem and modules were reimplemented with standart or widely used libraies and frameworks. For example network custom made submodule was replaced with Netty based. To provide more simple way for extending logging server with new storage backends and data types server's structure also was revised (see Fig. 3).

At present time the following backends are implemented:

- ***In memory*** – all data stored in memory.
- ***RDB*** – storage relation database as backend
- ***BDB*** – BerkeleyDB JE
- ***Sync*** – synchronize data from source to destination

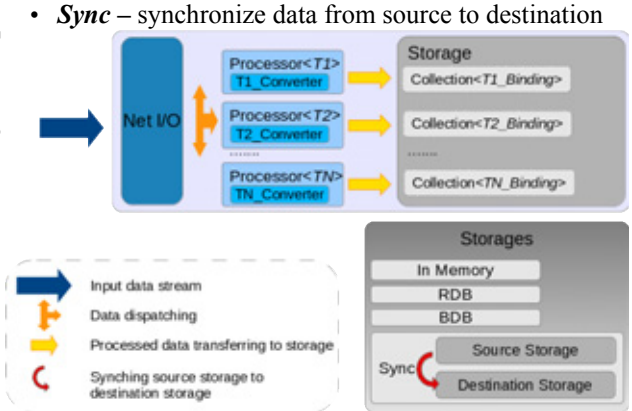

Figure 3: Logging Server structure.

Supervision subsystem

Distributed nature of control system make it necessary to control started services and to monitor resource consumption. To accomplish this task dedicated service was constructed. It base on Supervisord process manager. Custom plugins were developed for resource consumption monitoring per process and entire machine mode. To aggregate informatiom from different machines, Qt based end user apllication was developed.

Beam Position Monitor

Before 2012 2013 working season the Beam Position Monitor System (electrostatic BPM) was equipped with new electronics designed and produced at BINP. New design allows combining the preamplifier and ADC in a single device located nearby from pickup electrodes. Pickup station (shown at Fig. 4) has 4 inputs for analogous signals from pickup electrodes and 3 inputs for from VEPP-2000 timing system (RF frequency, revolution frequency, external trigger). Each input signal from pickup passes through 420 MHz lowpass filter, low noise tunable attenuator (dynamic range 20 dB) and digitized with 14 bit ADC. Wide bandwidth of electronics allows the separate measurements of electron and positron bunches with time interval between bunches up to 20 ns.

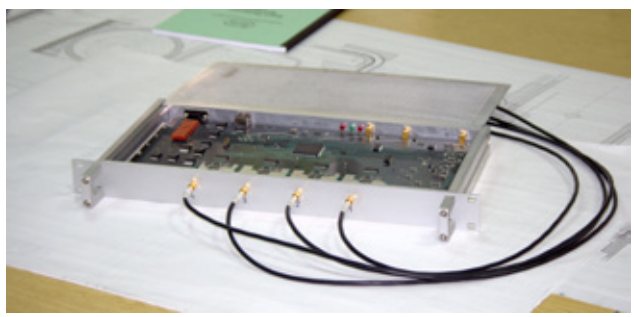

Figure 4: Pickup station.

New system is capable to store up to 8192 points per channel with turn by turn resolution (at revolution frequency) in memory for future use so called fast acquisition, and up to 1024 points with averaging slow acquisition.

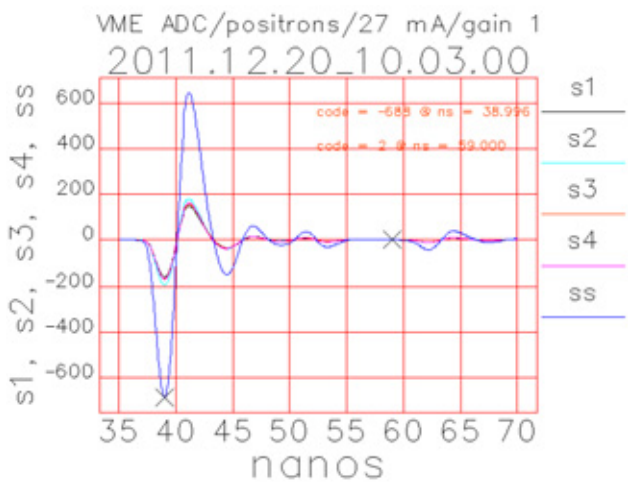

Figure 5: Signal from pickup electrodes.

ISBN 978-3-95450-170-0

The VME interface allows to have 8192 turns of the beam history at 5 Hz frequency and beam position (2048 averaging) at 10 Hz. This bandwidth is fully limited by VME bus and should be improved in new Ethernet interface (prototype will be commissioned until end of 2014). Our estimates show bandwidth limited only by Ethernet capabilities. Fig.5 shows digital output of pickup station while single bunch flew through BPM (picture taken with stroboscope method by varying digital delay between ADC clocks and revolution frequency).

Specroscope

For BPM's data visualization special software "Spectroscope" was developed. Spectroscope provide visualization for beam turn-by-turn position, oscillation spectrum and spectrogram. Frequency diagram is also provided. Spectroscope is written in Python with extensive usage of Pyqtgraph, PyQt and NumPy libraries (Fig. 6).

Figure 6: Spectroscope user interface.

NMR

In 2013 the system of energy determination with use of NMR gauges was upgraded with new processing modules. These modules are made in 19 inch 1U form factor and include all the needed electronics onboard. The new system allows to provide measurements of all NMR channels simultaneously. The processing power of the module's CPU is enough to make all the calculations in time comparable to the measurement time. It made possible to reduce the program architecture of the system to just two levels – client and server. The whole time of the energy determination now is just 5 seconds in contrast to 40 seconds with previous system. This value is satisfactory for VEPP2000 as it is more than 10 times less than the typical ramping time.

CONCLUSION

During the 2010-2013, VEPP-2000 control system have been proved as reliable and consitent. Nevertheless, system development and enhancment are still under way. Significant efforts were made to increase accuracy, to reduce time lags, to provide more useful information and as a result to improve user experience.

Some efforts all ready resulted in new electronics and software for NMR and BPM subsystem, what significantly reduce required time for facility tunning. Some of them, like Alarm System and Supervisor Subsystem will reduce complexity of facility control.

The control system of VEPP-2000 is flexible system and allows very fast development of a new, more powerful application.

REFERENCES

[1] Yu. Shatunov et al., "Project of a New Electron-Positron Collider VEPP-2000", EPAC'2000, Vienna, Austria, p.439
[2] Yu.Rogovsky et al., "Status and Perspectives of the VEPP2000 Complex", RuPAC'14, Obninsk, Russia, October 2014, TUY01.
[3] Ilya Zemlyansky et al., "Electron and Positron Beams Transportation Channels to BINP Colliders", RuPAC'14, Obninsk, Russia, October 2014, FRCA03.
[4] "SND Project", http://wwwsnd.inp.nsk.su
[5] "CMD-3 Project", http://cmd.inp.nsk.su
[6] A. Senchenko et al., "VEPP2000 Collider Control System", PCaPAC'12, Kolkata, India, December 2012, FRCB04, http://www.JACoW.org.
[7] A. Senchenko, D. Berkaev, "VEPP2000 Logging System", PCaPAC'12, Kolkata, India, December 2012, WEPD14, http://www.JACoW.org

ISBN 978-3-95450-170-0

DEVELOPMENT OF AUTOMATION SYSTEM OF THE ION SOURCE

A. Koshkarev, Novosibirsk State University, Novosibirsk, Russia
P. Zubarev, A. Sanin, U. Belchenko, A. Kvashnin, Budker Institute of Nuclear Physics, Novosibirsk, Russia

Abstract

To operate a source of negative hydrogen ions an automatic distributing control system was developed. This system consists of master controller (Slab C8051F120) and a set of peripheral local controllers (PLC) based on microcontroller Slab C8051F350. Using an optical link between PLC and master controller there was created a system resistant to high-voltage breakdown of the ion source.

To control the system, a special programming language has been created. It includes procedures for checking the necessary parameters, setting the value of the physical quantities to simplify the experiment, verifying the lock status and protection. This system provides two programmable timers, as well as procedures in emergency situations, such as: lack of water, poor vacuum. It can be operated in semi-automatic mode, if the script asks operator about preferable actions and then continues the script depending on the response. All scripts are performed in master controller, and this makes system very rapid (for example system response time is 1 ms).

INTRODUCTION

One of the most important stages in the development of new facilities is to automate and connect all control units together. To achieve this goal, the automation of power supply units in the new ion source injector was carried out. The ion source injector is located in a research facility BNCT. This method of treatment is very effective against a number of currently incurable radioresistant tumors, such as glioblastoma multiforme and metastatic melanoma [1, 2]. Frequent changes of control commands and their parameters during experiments cause serious problems. Therefore, the scripting language consisting of control commands was developed. It allows operator to implement all sorts of automatic control algorithms and conduct experiments with minimal outer control. Automation, conducted within the framework of this work, simplifies significantly the operation of the facility.

SUBJECT AREA

The ion injector comprises several high-voltage power sources, temperature and vacuum level nodes, requiring remote control and data capture.

Power sources are controlled by identical and interchangeable modules of programmable logic controller (PLC), receiving commands from a personal computer through a switch. Each PLC has a microcontroller and several analog and digital channels, which are connected via serial interfaces SPI & I2C with the PLC microcontroller. The microcontroller allows operator to test devices on the board if they are connected with each other. In conditions of high electromagnetic noise the distributed control system with sufficient independence of modules increases the reliability of the entire control system.

The structure of the control system is shown in Fig. 1.

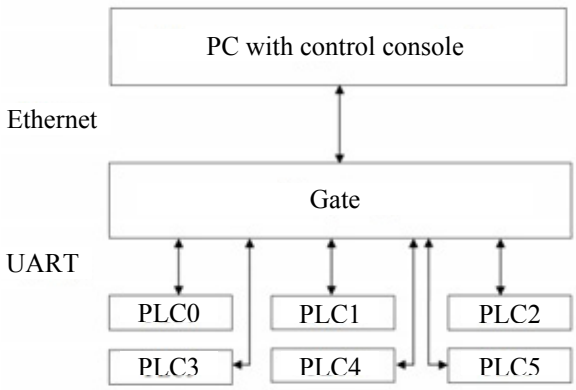

Figure 1: Structure of the control system.

ALGORITHMS

Commands are usually repeated during the experiment and for convenience to operator algorithm scenarios have been developed. Operator can create a certain set of commands once and then these commands can be repeatedly applied. Command can be as unconditional execution of some action, and also it can be a check of channel status. After checking it is possible to jump to another line in the scenario.

The switch algorithms allows user to apply two modes: manual and automatic. In manual mode, the operator can change the values of PLC. On the other hand, automatic mode allows user to run the script, which will perform the control over the experiment without operator. A block diagram of the basic algorithm is presented in Fig. 2.

The developed switch algorithms allow user to control automatically the ion source. Link between the management console and the switch is not required. Accordingly, if the operator console suddenly loses contact with the switch, the experiment will not stop, and the switch will continue to capture the critical parameters of the experiment. If these values are exceeded, the switch takes some measures that were initially set by the user.

SCENARIO

Scenarios – a set of strings that contain parameters such as the block number, channel number, the command, the value of the team and its priority.

The sequence of operations required depends on checking of states and transitions. Therefore, an internal

ISBN 978-3-95450-170-0

control programming language was created – scripting language. To measure the time intervals the internal timer of microcontroller was used, which hosted four logical timers with a period of one millisecond. All script parameters are translated into physical quantities, so the operator can control experiment simply. Scenarios allow us to describe the action in emergency situations, such as a lack of cooling water, poor vacuum, etc. If this happens, the console informs the operator about the error. Scenario processes by the switch and that allows user to instantly respond to emergencies and not waste time waiting for a response from the PC.

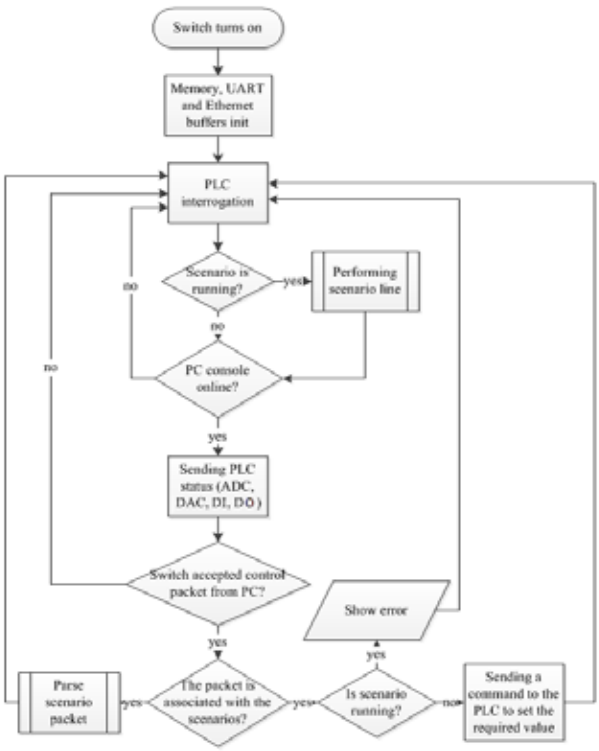

Figure 2: The basic algorithm of the switch.

Block number denotes the index card PLC, which will use certain equipment. The channel number indicates what kind of equipment can be used. User can choose ADC, DAC, digital inputs (DI, 1 bit ADC) or digital outputs (DO, 1 bit DAC). The command can be either set the value or values of the comparison device with the parameters specified by the user. Execution priority specifies how the command will be executed: normally, rapid or emergency. After the command with normal priority it is exhibited a delay in one second. Rapid command is executed without delay. Command checking emergency are executed before each execution line in the script: on stage startup script host controller stores the row numbers and emergency script before executing the next line in the script ensures rapid implementation of all emergency lines.

User has an opportunity to write the values in the array of intermediate calculations, for example for the implementation of various filters.

Automatic control is realized by algorithms which are stored as data files in the controller memory. Microcontroller has built-in memory, but depending on the complexity of the scenarios it may not be enough. To solve this problem, the anchor controller is equipped with an external memory to 32 KB.

For transmission lines in the script, you must first compile them using the built-in compiler, and only then operator can transmit control commands to the switch. All lines of the script have the same number of parameters. Each parameter – a signed 32-bit number.

HARDWARE

The programming code implements the developed algorithms and allows switch to receive pre-programmed in the console operator scenarios, to change values on the PLC through the console and send the values of recorded parameters to the operator. Program code was written in C language with the help of SiLabs utility.

The switch

The switch is a "bridge" between the Ethernet channel and the UART interface. It also processes its own programming language, which allows operator to organize the automatic control equipment. Switch hardware:

- microcontroller C8051F120;
- RAM memory K6X4008T1F 32 KB;
- Internet module CP2201;
- two-channel UART buffer SC16IS752.

The PCL

The PLC board is used as a direct control unit, which interacts with high-voltage power sources. Every PLC contains 8 ADC (16 bit, 0-5 V), 4 DAC (16 bit, 0-10 V), 8 DI and 8 DO. Every PLC communicates with a switch through opto fiber lines. After the switch is turned on, it queries all PLC one by one. All data transfers between these devices according to a certain algorithm, which allows switch to send the unlimited length of the packet data. PLC hardware:

- microcontroller C8051F350;
- 8 16-bit ADC with a range from 0 to 5 V;
- 4 16-bit DAC with a range from 0 to 10 V;
- 16 optocouplers SFH628A;
- Instrumentation amplifiers INA129;
- 16 I / O ports I2C PCA9539.

PC CONSOLE

Control of source of negative ions is performed using the program created in LabView environment.

The program allows user to work on manual and automatic control. The user is provided with a special language that provides the implementation of various management scenarios, as well as the handling of emergencies.

The attendant console is implemented so-called "scenario editor", allowing user to create scenarios. The

ISBN 978-3-95450-170-0

editor allows you to save the script in computer memory and load them into the program. It also allows you to select a control channel by its name. All names must be assigned to a special configurator, which is composed of the management console. Before sending the script to the switch user have to compilated it by program means. During compilation program check all the lines in the script, conversion of physical quantities in the codes for DAC / ADC and the conversion of all the rows in a clear view of the switch.

TESTING

System has passed a series of tests. The connection between the electronic devices and the management console was established. A long-term test was performed: operators program sends a command to PLC0 through the switch to set the voltage on DAC0. Then delay set in a quarter of a second. After this values are read from all ADC (ADC and DAC are connected with each other), and after this received data are sent to the console. As a result, the operator gets the same value that he exhibited at the outset (precision is ±1%). Testing was conducted for three hours, any failures were not found.

RESULTS AND DISCUSSION

The developed and tested control system allows operator to perform experiments with minimal operator control, that improved the operational characteristics of the facility, including the protection of the patient from operator errors. At the same time this system allows operator to interact with the elements of the installation without much effort.

The universality of the implementation of this system makes it possible to integrate it into other hardware and control systems. Simplicity of replacing of burned-out modules allows to repair the ion source in a few minutes. Also, when you connect the adapter for PLC, which was developed earlier, it is possible to apply this management system in any other assigned tasks (for example, the inclusion of a teapot for dinner, and control of water temperature in a pan).

ACKNOWLEDGMENTS

The study was performed by a grant from the Russian Science Foundation (Project No.14-32-00006) with support from the Budker Institute of Nuclear Physics.

REFERENCES

[1] Bayanov B.F., Belov V.P. et al. Accelerator based neutron source for the neutron-capture and fast neutron therapy at hospital // Nuclear Instr. and Methods in Physics Research. Section A. – Vol. 413. – 1998. – P. 397–426.

[2] Neutron Capture Therapy: Principles and Applications. Eds.: W. Sauerwein, A. Wittig, R. Moss, Y. Nakagawa. Springer, 2012. 533 p.

ISBN 978-3-95450-170-0

CONTROLLER FOR RF STATIONS FOR BOOSTER OF NICA PROJECT

G.A. Fatkin, M. Yu. Vasilyev, Budker Institute of Nuclear Physics, Novosibirsk and Novosibirsk State University, Novosibirsk, Russia
A.M. Batrakov, I.V. Ilyin, A.M. Pilan, G. Ya. Kurkin, Budker Institute of Nuclear Physics, Novosibirsk, Russia

Abstract

Intellectual Controller for RF stations based on CPU module SAMA5D31-CM for Booster of NICA Project is presented. Controller measures magnetic field using induction coil and provides corresponding real-time tuning of frequency according to non-linear law with 20 μs period and better than $2 \cdot 10^{-4}$ accuracy. Controller also allows setting up and monitoring parameters of RF stations. The tester module that generates a sequence of events and signals imitating acceleration cycle is alo presented.

INTRODUCTION

RF System for Booster of NICA Project (JINR, Dubna) [1] are created at Budker Institute of Nuclear Physics [2]. It consists of two resonators, two RF stations including power amplification cascades and low-voltage electronic, intellectual controller and tester module. RF system provides ~10 kV acceleration voltage in required frequency range (0.5-5 MHz) on cavity gaps.

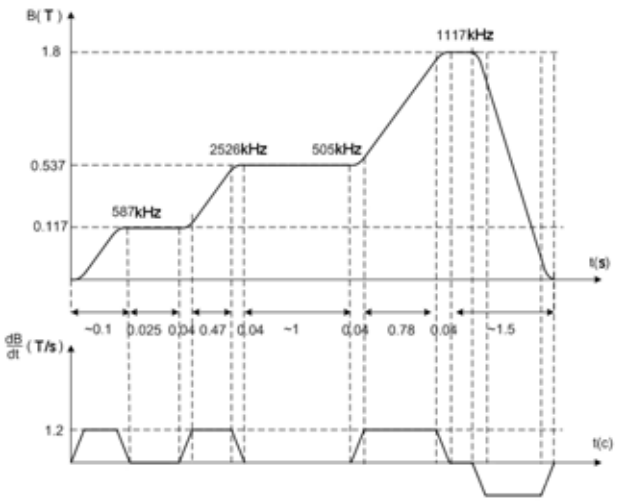

Figure 1: Booster magnetic field and acceleration frequencies.

This article describes the intellectual controller and tester module. Primary function of controller is generation of master frequency depending on the current value of magnetic field. Inaccuracy of frequency setting must not be worse than $2 \cdot 10^{-4}$. The graphic of magnetic field in booster and corresponding acceleration frequencies for nuclotron injection mode are presented at fig. 1. Magnetic field increase rate in this mode is around 1.2 T/s. Several other acceleration modes are planned including autonomous mode (rising frequency from 0.5 to 5 MHz in 2 s).

Controller also manipulates low voltage electronics, measures and generates all signals necessary for the functioning of RF sections (see tab. 1). Controller must also have means to be integrated in booster control system.

Table 1: Main controller signals

Signal	Channels	Sample Rate	Resolution
Input Signals			
Master frequency	2	50 kHz	24
V resonator	2	50 kHz	12
I anode	2	1 kHz	10
Synchronization	7	N/A	N/A
Output Signals			
Field sensor	1	50 kHz	18
V resonator	2	50 kHz	12
V preamplifier	2	5 kHz	12
I anode	4	1 kHz	12
V rectifier	6	1 Hz	12
V filament	2	1 Hz	12

Currently most of booster elements are in design and manufacturing stages. That is the reason why tester module is created. It imitates signal from magnetic field sensor and necessary synchronization pulses in different acceleration modes. Tester module is intended to allow regular RF system checks at the installation. Both developed devices are 19" 3U modules and are placed in RF stations electronics rack.

CONTROL ARCHITECTURE

The scheme on fig. 3 shows interaction of controller and tester modules with booster instrumentation and RF stations electronics.

Signals from magnetic field sensor and synchronization pulses are provided to the tester module Tester module allows to interchange between imitation and through-pass modes. Signal from magnetic field sensor is integrated and resulting magnetic field value B is used to calculate frequency according to the following formula:

$$F(B) = \frac{c^2 / L Z / A_n \rho 1 / 10^6 B}{\sqrt{m_n^2 + (Z / A_n \rho c / 10^6)^2 B^2}} \quad (1)$$

ISBN 978-3-95450-170-0

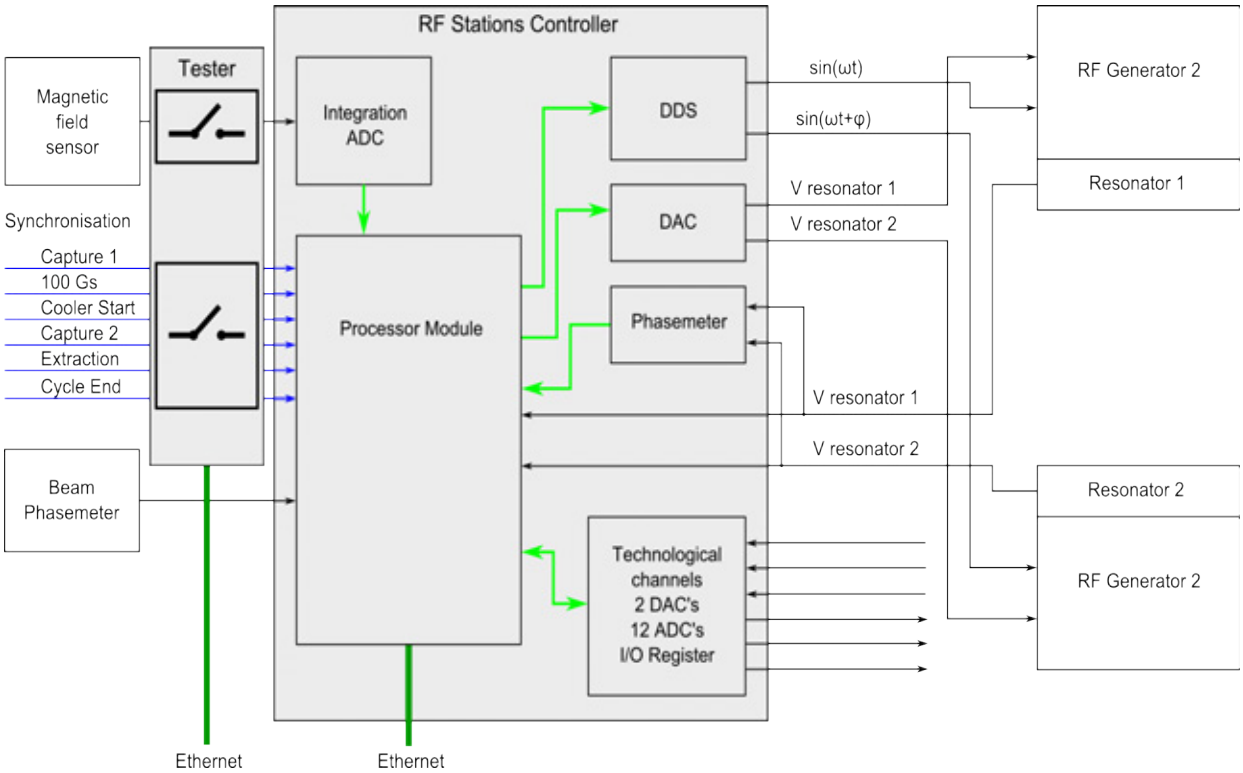

Figure 2: Control architecture.

In (1), B – is the resulting field value and all other symbols represent static parameters of installation. Calculated value is used to generate two master frequency sinusoidal signals. These signals are generated with specified phase difference defined by distance between resonators. In future it is intended to provide suppress synchrotron oscillations by variation of this phase according to signal from designed beam phase measurement system.

SOFTWARE

Both tester and controller modules are managed over the Ethernet interface using text-based command protocol over telnet. RS-232 interface is provided for reprogramming and debug.

Apart from adequate embedded programs, testing software was developed. This software will also serve as a reference for implementation of corresponding modules in NICA booster control system.

CONTROLLER MODULE

Observing tab. 1 one may conclude that controller module must supply 3 high rate (50 kHz) output channels and measure 6 output channels with same rate. Most calculations and data conversions require floating-point arithmetic. It is also necessary to arrange data interchange between several independent measurement and control devices. E.g. to generate master frequency controller must receive data from measuring ADC, convert, correct and integrate the resulting value to attain field value then calculate frequency according to formula (1), convert it again and finally send this data to DDS. At the same time a lot of other signals must be changed and measured: resonator voltages, cathode currents, preamplifier voltages etc.

Two main approaches are used for creation of such complex high rate systems: FPGA and high-end micro-controllers. The reasons for choosing micro-controller approach were following: need of floating point arithmetic, complex logic with different modes of operation that will require expansion and finally variety of interfaces (I2C, SPI, Ethernet, RS232).

Controller structure is shown on fig. 3. It is based on Atmel SAMA5D31 micro-controller. Availability of on-board 1 MHz 12 bit 8-channel ADC was a significant advantage. Usage of SAMA5D31-CK SO-DIMM board allowed to significantly accelerate and simplify PCB design.

It must be noted though that we had to give up usage of any (even real-time) operational system to provide necessary reaction rate (20 μs cycle). Apart from such bare-metal approach we had to significantly optimize our program code. Another restriction we had to establish is following: interaction with booster control system using Ehternet protocol is available only between cycles, while in-cycle Ethernet controller is turned off.

Apparently an ideal approach is using SOC with FPGA and ARM kernel e. g. CYCLONE V SOC. But when we started this work, boards like MITYSOM-5CSX on SODIMM were still unavailable. And PCB layout of

ISBN 978-3-95450-170-0

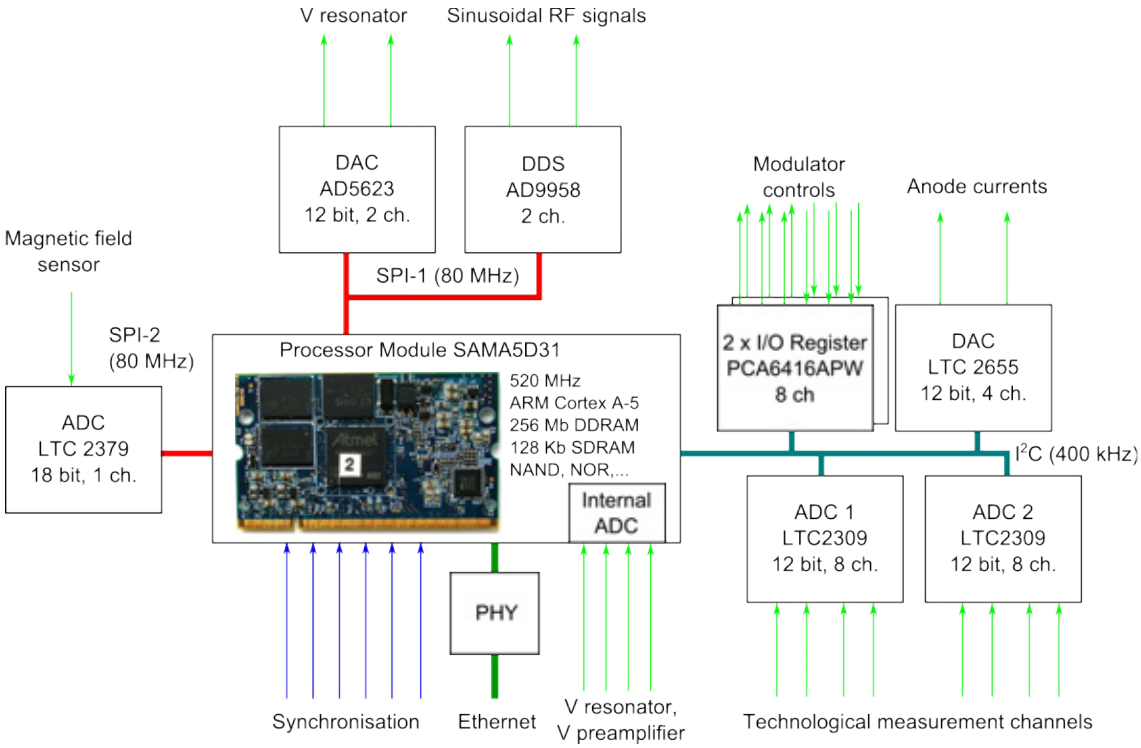

Figure 3: Controller module structure.

CYCLONE V SOC is quite problematic in itself and was considered more tedious than program optimization.

TESTER MODULE

Imitation of the signal from induction magnetic field sensor and generation of synchronization pulses sequence according to the booster mode is the main task of this auxilary module. Resulting imitated signal and it's integral (magnetic field) is shown or fig.3.

For the operational check of RF stations tester has a multiplexor that allows to disconnect controller module from booster systems and check it's operational capability. Generally, tester will be in through-pass mode when real signals from booster are provided to the controller inputs.

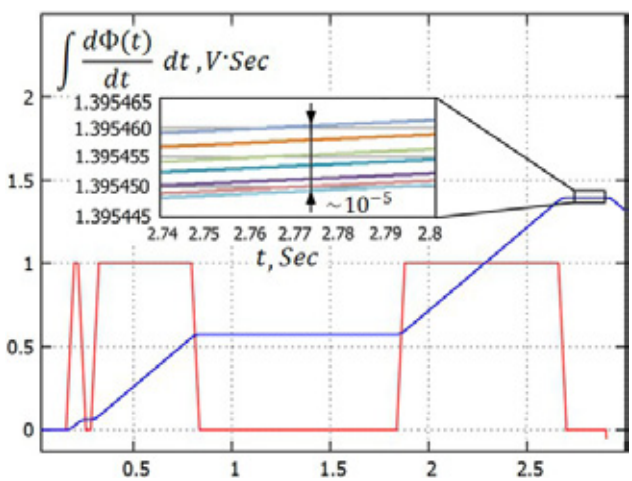

Figure 4: Imitation of magnetic field sensor signal.

Particular attention was paid to precision of imitation circuit design. Resulting noise of integral (magnetic field) at the end of acceleration cycle is shown on fig. 4. This resulting noise is $\pm 5 \cdot 10^{-6}$, attained signal noise is ±5 μV and temperature stability is 5 ppm/°C. Imitator circuitry is based on DAC8331.

Intellectual part of tester module is based on LPC2478 processor and provides control of DAC, synchronization pulses generation, multiplexor control and Ethernet interface for inter-operation with booster control system.

CONCLUSION

Controller and tester modules were designed manufactured and tested in work with RF stations. Usage of SAMA5D31-CK board allowed to achieve necessary speed and algorithm modification easiness. Processor had almost reached it's performance capacity though. And bare-metal programming is not very comfortable. In future similar works it is more appropriate to use more powerful multi-core processors like TI AM355x or CYCLONE V SOC chips. This will allow to use real-time operational system and further ease software development.

REFERENCES

[1] Eliseyev A.V., Meshkov I.N. and others, “Longtitudal Dynamics of AU-197**(32+) and AU-197**(79+) Beams in the NICA Collider Injection Chain”, PEPAN Letters, vol 78, no7 2010. p.774-780

[2] Kurkin G. Ya. and others, “RF System of the Booster of NICA Facility”, TUCB02 RUPAC'14, these proceedings

ISBN 978-3-95450-170-0

MEDIA SERVER FOR VIDEO AND AUDIO EXCHANGE BETWEEN THE U-70 ACCELERATOR COMPLEX CONTROL ROOMS

I.V. Lobov, V.G. Gotman, IHEP, Protvino, Russia

Abstract

The media server was developed that implements the exchange of video and audio streams between control rooms for U-70 technological subsystems. Media server has the possibility of making changes into the intermediate video images to embed current technological information. The media server is implemented as a set of threads of execution, one for each video format conversion module. The media server is a chain of successive transformations of video and audio streams from one format to another: H.264—Y4M—THEORA formats for video, PCM—VORBIS formats for audio. The final video and audio streams are encapsulated into the OGG container stream which is translating into the local network. OGG container has been chosen because of its completely open, patent-free technology and full support in HTML5. Any Web browser with full HTML5 support may be used as OGG stream consumer. The browser client program has written with tag <video> utilization. This allows for client to work on different platforms (Linux, Windows) and get rid of third-party video plug-ins.

INTRODUCTION

The aim of the work was to develop a dispatching system for the organization of audio and video-sharing between different U-70 technological subsystems in IHEP. Requirements for the dispatching system were as follows:

- Simple and convenient instrument of organizing the conversations and conferences.
- The client software must run on different operation systems.
- The software must use open-source free algorithms and libraries.
- Do not use any special designed programs (plug-ins) on the client side.
- The ability to modify the intermediate video images in real time scale.
- To record the video and audio tracks into archive with a possibility of quick search of the desired fragments.
- The ability to transmit media information in conjunction with digital technology data.

DISPATCHING SYSTEM STRUCTURE

The solution of the task lies in the following main ideas (see Fig. 1):

- The dispatching system will use the IP-cameras with video and audio transmit ability instead of connecting to the PC webcams.
- The media server will provide data transmission from IP-cameras to the clients in form of media streams. Thus, instead of a set of programs for different client's operation systems only one dispatching program will be written in.
- To use the benefits of the HTML5 for the client access to the server.

IP-camera which makes your participation in the conference does not need to be connected to the client computer. Thus the client computer does not transmit any media-streams to the server. It simply receives the media-streams. At first, the client makes a connection to the server. Next, the server connects to an IP-camera and starts to receive the media-stream. Finally, the client begins to receive the media-stream from the server.

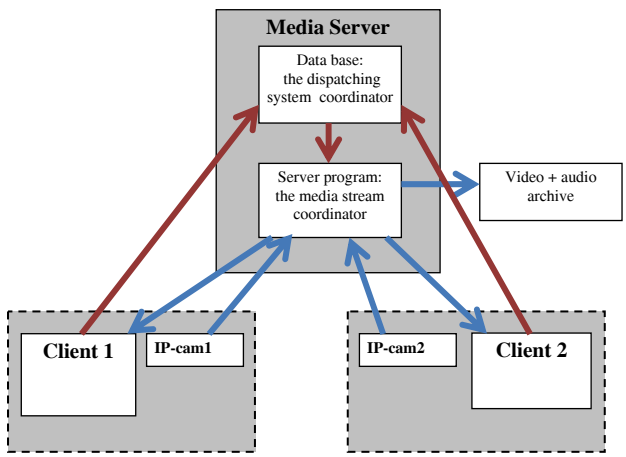

Figure 1: The scheme of the data flow (blue arrows) and the control flow (red arrows).

SOFTWARE INSTRUMENTS AND MEDIA FORMATS STANDARDS

Programming Tools

The server part of the dispatching system was written in Visual Studio 2012.

The libraries used in the project:

- JM 18.6,H.264/AVC Software, Karsten Suehring [1].
- libogg, version 1.3.2, Xiph.Org [2,3].
- libtheora, version 1.1.1, Xiph.Org [4].
- libvorbis, version 1.40, Xiph.Org [5].

The client part was written in HTML5 + JavaScript.

ISBN 978-3-95450-170-0

Media Exchange Standards

RTSP—Real Time Streaming Protocol designed to control streaming media servers [6].
RTP over H.264—Real time Transport Protocol designed to transmit H.264 video streams in real time scale [7].

Media Data Formats and Standards

H.264, MPEG-4 Part 10 or AVC (Advanced Video Coding)—licensed video compression standards designed to achieve a high compression ratio while maintaining high video quality [1].

YUV—image color model, in which the color appears as three components: the luminance (Y) and two chrominance components (U and V). Luminance component Y contains a "black and white" grayscale image, and the remaining two components contain the information required to restore the color. YUV is convenient model for image recognition and intermediate image replacement by changing the desired pixels. YUV model will help in the future augmented reality implementation which is intended to use in the dispatching system [1].

OGG—open standard multimedia container format, it is the main file and stream format for multimedia codecs funded by Xiph.Org [2].

THEORA—free video codec for video compression with losses developed by the Xiph.Org [4].

VORBIS—free audio compression format with losses [5].

The OGG format with VORBIS and THEORA content is quite promising because of 1) free licensing and 2) the ratio between sound and image quality and file size which is the best among peers. The last factor is quite critical for local networks when a large amount of packages is used for media exchange. Owing to these, the OGG format was selected as a container for the audio and video transmission to the client.

SERVER PROGRAM DESCRIPTION

The server software is designed for transmitting data streams between clients as shown in Fig. 2.

The transmission of the media from IP-camera to a web browser is a chain of successive media transformations from one format to another. The chain for media transformation from IP-camera to the client is performed by the server program. The server program connects to an IP-camera, takes video and audio RTP-packets from the camera. Then the received media information is analyzed and altered (if necessary). Finally the media information is sent to the client.

The server program consists of the software modules which transform the information as follows:

- Module "MAIN"—establishes a connection to IP-camera via RTSP and receives the data in real time via RTP.
- Module "YUV"—converts the compressed video format H.264 into uncompressed image format YUV for further analysis.
- Module "OGG"—performs the transcoding of the pair "Uncompressed video format YUV + Audio format PCM [8]" into the THEORA and VORBIS formats with subsequent encapsulation into an OGG container.
- Module "TRAN"—transmits the OGG packets to the client. The module connects to the database and reports on its readiness for data transmission.

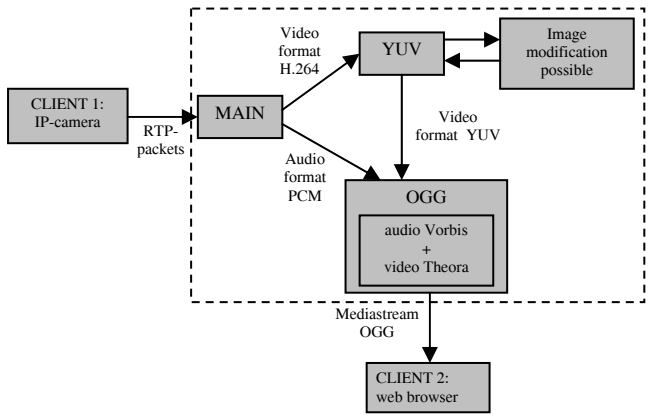

Figure 2: The data flow.

Program Organization as a Set of Threads

Program modules are implemented as separate threads, one thread for each client. The data exchange between threads is performed by means of intermediate buffers and semaphores in order to synchronize the intermediate buffer's reading and writing. The semaphores are needed to prevent the possibility of data corruption when threads use the intermediate buffers.

Four threads are used to transfer video and audio data from a camera to a client. Thus, the data exchange between two clients requires eight threads. The same software procedures are used for both clients. This imposes a requirement of using only re-entrant software. In other words, it is necessary to use only two types of variables:

- Local variables in procedures;
- In case of using global variables they should be organized in the form of two-dimensional arrays.

Description of the MAIN Module

The main module of the server is started as a thread for each client. It connects to the camera via RTSP. MAIN module generates three threads (YUV, OGG, TRAN) for processing and transmitting information to the client browser. The task of MAIN is to take RTP packets from the camera, analyze them and identify the types of the packets (audio or video, single or fragmented).

Each RTP packet contains the NAL units of different types [7]:

- SPS—the Sequence Parameter Set.
- PPS—the Picture Parameter Set.
- IDR—I frame.
- NONE-IDR—B- frame (move).

ISBN 978-3-95450-170-0

The flow of the MAIN is implemented in infinite loop which accepts incoming packets from the camera.

For video data, MAIN checks the packet loss, and if the package was lost, the buffer is filled with the last full frame received. In case no packet loss the buffer is filled with all of the packets had come between two consecutive packets containing SPS. Once the buffer is full, the flow is stopped and the video data is copied to the YUV module. When the copy is finished the flow continues.

In the contrary, audio data is sent directly to the OGG module.

Description of the YUV Module

This software module is implemented in the form of an infinite loop waiting for data from the main program module (MAIN). After receiving the data, the YUV decodes them from a compressed format H.264 to uncompressed YUV format and transmits the transcoded data to the OGG module.

Description of the OGG Module

The first step of the OGG module is to initialize OGG header with THEORA and VORBIS content. OGG module writes the header to the output buffer and begins to wait for data from the YUV module, as well as the TRAN module readiness. Upon the receiving the uncompressed video data from YUV module, the OGG module breaks them into frames. One uncompressed frame makes IDR-frame while the others make NONE-IDR frames (move). At the same time the OGG module waits for the uncompressed PCM audio data from the MAIN and encodes it in a compressed format VORBIS.

Finally, when the THEORA and VORBIS formats are encoded into OGG container packets, the output is written to the intermediate buffer for the TRAN module processing.

Description of the TRAN Module

The TRAN module is waiting a request from the client to join. After joining the TRAN module gets the data from intermediate OGG buffer, divide it into packets with 1400 bytes length and sends them to the client.

CLIENT PROGRAM DESCRIPTION

The client program is implemented in the form of a window containing the video and control buttons as shown in Fig. 3. It connects to the database and sets the "online" flag for other clients. At the same time it reads the "online" flags from all other clients and the server.

The operator can connect to other clients and establish connection with them. He can press the corresponding button addressed to the desired remote client. After getting answer the remote connection is established and the video picture comes alive.

The connection buttons use 3 colors:

- Green—the client (server) is online.
- Red—the client (server) is offline.
- Yellow—operator requests the connection.

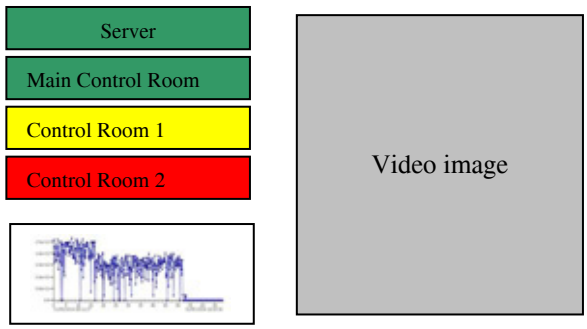

Figure 3: The scheme of the client interface.

CONCLUSIONS

Upon the development process of the media server software a number of technical problems was resolved:

- Initially the chain of video stream consecutive format conversions resulted in data loss. The solution founded—a media server was organized as a set of multiple interacting threads of execution.
- Initially the audio and video streams were gradually diverging from each other due to the differences in timing principles (audio is transmitting in frequency units while video is transmitting in video frames). The peculiar method of the audio and video stream synchronization was developed—to use the independent timing scheme, same for audio and video.
- Initially the image was transferred choppy due to the inconstant number of frames per second getting from the camera. The problem was solved by counting the actual number of frames per second.

A dispatching system scheme for U-70 Accelerator Complex was developed and implemented. An optimal method for the video and audio streams conversion was achieved via threads of execution. As a consequence the video and sound streams have no transcoding losses whereby the media is played smoothly and correctly.

REFERENCES

[1] Karsten Suehring et al., H.264/AVC Software Coordination; http://iphome.hhi.de/suehring/tml/
[2] S. Pfeiffer., The Ogg Encapsulation Format Version 0, RFC 3533; http://xiph.org/ogg/doc/rfc3533.txt
[3] I. Goncalves et al., Ogg Media Types, RFC 5334; http://xiph.org/ogg/doc/rfc5334.txt
[4] Xiph.Org Foundation, Theora Specification; http://theora.org/doc/Theora.pdf
[5] Xiph.Org Foundation, Vorbis I specification; http://xiph.org/vorbis/doc/Vorbis_I_spec.pdf
[6] R. Lanphier et al., Real Time Streaming Protocol, RFC 2326; http://www.ietf.org/rfc/rfc2326.txt
[7] Y.-K. Wang et al., RTP Payload Format for H.264 Video, RFC 6184; http://tools.ietf.org/html/rfc6184
[8] J. Salsman et al., The Audio/L16 MIME content type, RFC 2586; http://tools.ietf.org/html/rfc2586

ISBN 978-3-95450-170-0

U-70 ACCELERATOR COMPLEX: CENTRALIZED ACCESS TO IP-DEVICES WITH EMBEDDED WEB-SERVER

Yu.Milichenko, E.Takaeva, V.Voevodin, IHEP, Protvino, Russia

Abstract

The paper describes our efforts to organize centralized access to IP-devices of specific types. Each device includes proper embedded web-server and is connected to an accelerator department network. Today there are tens of the devices are used to give pictures online.

A device access is carried out by user understandable device names with the aid of accelerator department web-server. Some arisen problems due to increasing number of device users are pointed. Possible manifold forms of on screen presentation of pictures derived from devices are presented.

NEW DEVICES

At last time an accelerator specialists are using increasing number of various digital devices to solve specific tasks of visual monitoring. At present there are tens of the devices. The devices should to be connected to local computer network and they give possibility to user to access them by means of web browser.

The types of devices in use are some models of digital multi-channel oscilloscopes, video recorders, IP-cameras, video encoders. The devices are installed in a control and technical rooms of different buildings.

All devices, mentioned above, provide users with online pictures. Web browser may be used to get the digital picture and set some operational parameters of a device, for example, time of the picture renovation. For U-70 accelerator complex this time usually is set to be equal to 10s.

The pictures from video devices first of all give possibilities to see processes of beam injection from linacs, acceleration and beam transfer from booster to main ring. Some of devices used to observe most significant objects, such as radiation dangerous zones, corridors, technological halls and etc.

As a rule, a multi-channel oscilloscope serves signals of a certain technological system or process. It gives possibility to observe processes of acceleration regimes tuning, the quality of a technological system operation.

NETWORKING OF DEVICES

The first devices were directly connected to the same open network together with an accelerator department office PCs. But fast increase in the number of devices and appearance of certain maintenance problems required some centralization and severe discipline to access and control the devices.

The next problems have appeared after short time of operation:

1. Each PC got access to each device and possibility for tuning it up – led to curious situations.
2. Outsiders of accelerator department had direct access to the all devices by printing IP address.
3. A user should to remember set of IP addresses of all the devices he is interested in.
4. Some devices stopped the web service due to exceeding of simultaneously opened web-sessions limit.
5. Some old models of devices do not support classless IP addressing – possible decisions were discussed with support services of the manufacturers.

To solve the problems a network redesign was necessary [1]. It was decided to organize protocol-based virtual network (VLAN) on top of the accelerator department physical office local area network [2]. It became new internal local domain 192.168.0.0/16 including all devices mentioned above. Except devices VLAN combines only those computers, which are installed in the control or technical rooms and assigned to view images from the devices or tuning up them. The usual computer of the office LAN can't access the devices if it is not a member of the VLAN.

CENTRALIZED ACCESS

The centralized access meant for deriving online pictures only. To set operational parameters of the device is possible if user enters directly to web browser the device IP address as web page address.

To centralize and simplify an access to the distributed devices the accelerator department web-server is used. The server was included in the VLAN to get direct access to the devices. It supports two schemes to organize access to the devices from user computers. In both cases the web-server is used as a reference book – a user selects from the corresponding to the scheme list of devices. Each selection list includes names of all available and accessible devices and some comments.

In the first scheme the user web-browser after device selecting request communicates with selected unit directly, so increasing number of clients of the remote device web-server. This scheme is used to access all devices in scale of VLAN only and is showed in Figure 1.

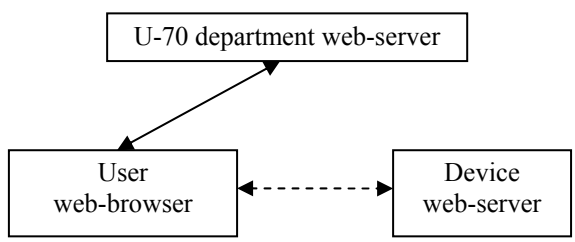

Figure 1: First scheme of device centralized access.

ISBN 978-3-95450-170-0

The second scheme is used to view images from oscilloscopes only. In this case after oscilloscope selecting the accelerator department web-server communicates with selected device, derives picture periodically and forwards it to the web-browser of user. Figure 2 shows the scheme of network interrogations.

In this case accelerator department web-server is the only client of each oscilloscope web-server. The picture once received from selected device is sent to all interested users.

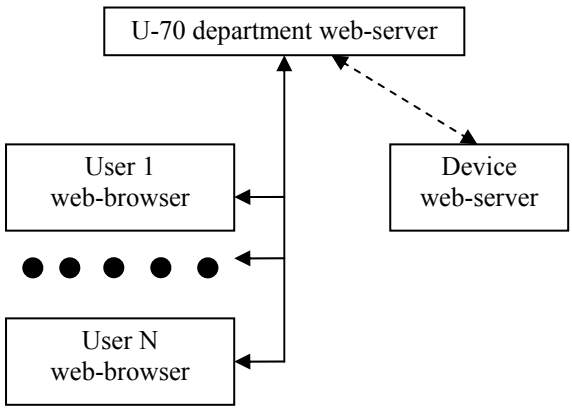

Figure 2: Second scheme of device centralized access.

The second scheme allows access to images created by oscilloscopes from outside of the VLAN, for example from home computers.

SCREENS AND WINDOWS

There is some number of forms to present online pictures on a monitor screen. Usually separate web-browser window is used for each picture (see Figure 3).

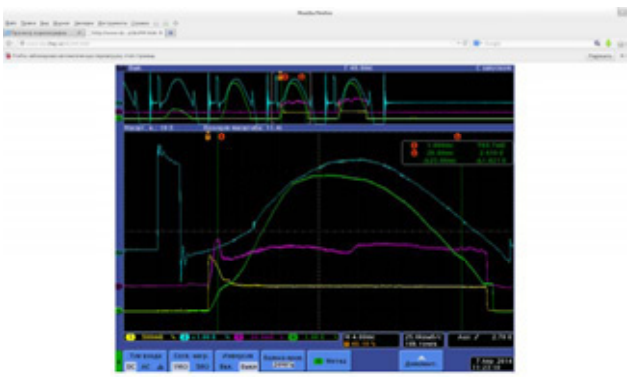

Figure 3: Web-browser window with one picture.

As a rule this form is used by users from their office personal computers taking an opportunity of second scheme of device centralized access.

The first scheme of device access supports possibility to visualize up to four pictures from different source devices inside one window simultaneously. The possibility was realized by framing HTML content [3]. Figure 4 is the example of this form.

Figure 4: Web-browser window with four pictures.

Now a typical control room maintains computer monitors with a large screen. Depending on current task to solve a user may layout all necessary windows with corresponding pictures on the screen. He can use any of device access schemes. The Figure 5 shows a screen with five online pictures from remote oscilloscopes.

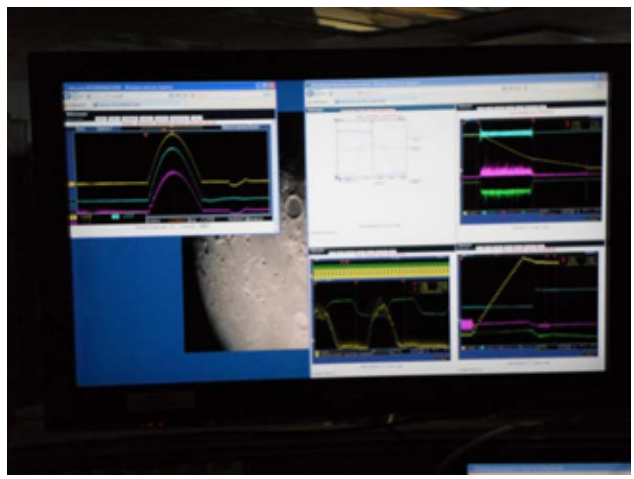

Figure 5: Screen with web-browser windows.

In control room user may see a set of significant signals on screens of local real oscilloscopes and on computer monitors with pictures from remote devices. The corresponding devices may be installed in other building of any accelerator of the U-70 complex.

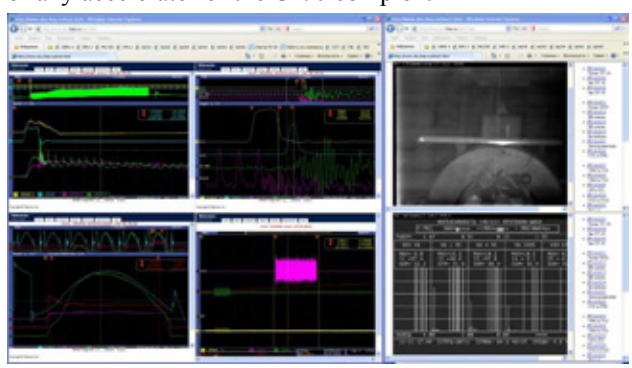

Figure 6: Two web-browser windows on one screen with four frames each.

The Figure 6 shows screen with two web-browser windows. The left window contains images received from

ISBN 978-3-95450-170-0

four different oscilloscopes. The right one presents two images from cameras and two lists of device selection.

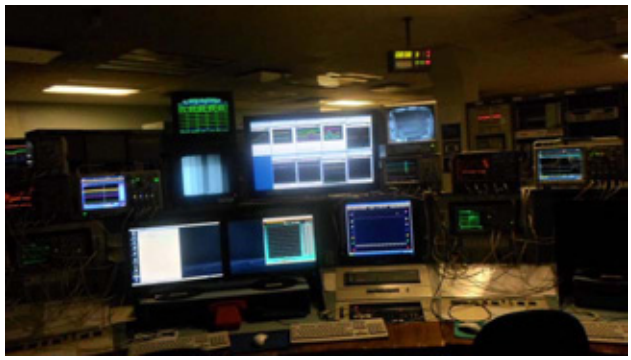

Figure 7: Overview of the booster control room consol.

General view of booster control room consol is presented in Figure 7.

CONCLUSIONS

Engineers are responsible for technological instrumentation may to form their current screens to detect malfunctions of hardware in use.

An operator solving tasks of technological system parameters adjustment, control physical processes related to beam dynamics, creates set of windows with pictures are good for making decisions on optimization of current accelerators regimes.

For example, tuning of beam ejection from booster and beam transfer to main ring require to form at least two windows with digital multi-channel oscilloscopes pictures.

The first one to observe:

- Forms of changes of the magnetic field of booster circular electromagnet.
- Forms of changes of the RF field of accelerating cavities.
- Signal of orbit middle radius change.
- Intensity signal of accelerating beam.

The second one is necessary to view mutual synchronization of accelerating beam and timing of pulse and bump systems to eject beam from booster and inject it to main ring.

So, the centralized access to distributed IP-devices is a new tool, giving a user possibility to select the most significant for current moment information in form of pictures. User may use the computer monitor space in a most efficient way to solve his tasks. He can do selections and screen forming on-the fly.

Historically there are control rooms distributed over accelerators and beam lines of the U-70 accelerator complex. One can see current state of the significant parameters over the whole accelerator complex from any control rooms consol.

Today this facility became integral part of whole toolset to control the beam quality during the U-70 accelerator complex run.

REFERENCES

[1] N. Olifer, V. Olifer “Computer Networks: Principles, Technologies and Protocols for Network Design”, Wiley & Sons, England, 2005.

[2] G, A. Donahue “Network Warrior”, O’Reilly Media Inc., 2007. http://www.safaribooksonline.com

[3] Frames in HTML Documents; http://www.w3.org.

ISBN 978-3-95450-170-0

DIGITAL SIGNAL PROCESSING ALGORITHMS FOR LINAC LOW-LEVEL RF SYSTEMS

D.Liakin, S. Barabin, A.Orlov, ITEP, Moscow

Abstract

A set of LLRF systems had been designed for various applications of resonant RF devices such as accelerators or beam deflectors [1], [2]. This report presents compact signal detection algorithms, used in most of developed systems. Application-specific extension of the signal processing procedure allows the system be synchronized to external self-excited oscillator.

SIGNAL AND SYSTEM PARAMETERS

Linear accelerator of charged particles use a resonant principle, where the EM field energy from period to period converted into the energy of accelerated particles. For conversion efficiency, it is important to keep the resonance condition during the system operation cycles. In addition, systems of several resonators need certain and accurate phase difference between oscillations in different resonators. The signal, taken from high-Q resonator, occupies narrow frequency range, defined by the resonator characteristic, shown as an example in Fig. 1. Systems with dynamic phase control use a resonator model to build an efficient feedback transfer function. There is always a trade-off between efficiency on one hand, and resource cost of the signal processor on the other. Normally a first order model describe the resonator very well. However, as it is seen in Fig. 1 the difference is visible.

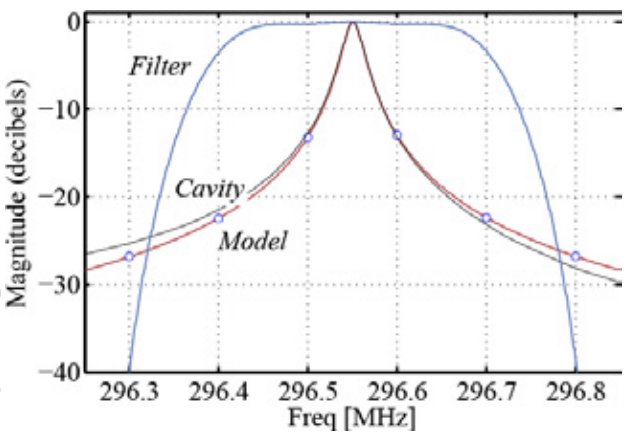

Figure 1: The frequency characteristics of the cavity, 1st order cavity model and overall frequency response of the digital processing unit.

The signal detection needs another compromise. Fig. 1 shows the frequency response of the signal processor. Besides, it shows how ineffective is a resonator as a filtering device. To keep the efficiency the signal processor must reduce the system's sampling rate down to reasonable low value. For that, it wastes the signal power outside of 500 kHz band.

THE BASE ALGORITHM

Fig. 2 presents the general process used to handle RF signals. The carrier frequency of the RF is higher than the sampling frequency of an ADC or system clock frequency of an FPGA-based digital signal processor (DSP). Because of this the ADC operates in IF mode, working as frequency down converter. The intermediate frequency signal is an input signal for the DSP.

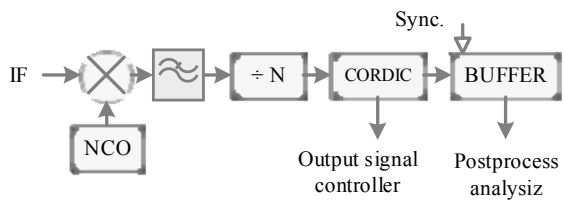

Figure 2: The signal evaluation in the digital domain.

As it is shown in Fig. 2, the first stage of the DSP performs an additional frequency conversion. The system set up defines precisely the frequency shift by a frequency tune word (FTW) of the numerically controlled oscillator NCO. The following low-pass filter suppress image and carrier frequencies existing at the down converter output. The output of the filter is a complex amplitude slowly varying in time. The cost of algorithm is important. To keep the efficiency and effective use of the FPGA resources the data needs to be rarefied according the system bandwidth. Due to the slow signal, the DSP reduces the data rate by factor N, normally down to 1 MSPS. Until this DSP uses a fixed-point arithmetic and Cartesian representation of complex amplitudes. The COordinate Rotation DIgital Computer module converts complex data to the vector form. Then the DSP store the amplitude and phase of the signal in separate buffers.

Fig. 3 gives an example of a system, where the original signal 1 is taken from the master self-excited generator, is used for synchronization of EM-field in the resonator of the novel just designed acceleration section. For successful operation, the digital controller must synchronize two system within 50-microsecond interval after the master-generator start. A distinctive feature of the described system is an oscillation of the amplitude and phase at the rising edge of the reference signal's pulse.

ISBN 978-3-95450-170-0

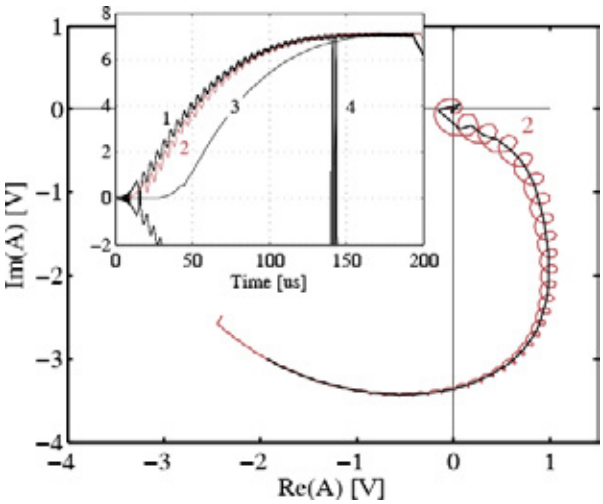

Figure 3: Original signal envelope (1) and some of DSP signals.

Different low-pass filters give different result. A wide-band system response, shown as curves 2 in Fig. 3, follows the oscillation of the master-generator. A narrow-band system (curve 3) produce smooth signal, but the delay time is critical.

NON-PARAMETRIC METHODS

The algorithm described above uses a continuous data stream to produce a decimated data. There are some situation, which require more detailed signal observation. The system uses a short time interval (shown with marker 4 in Fig. 3) to store a portion of raw data for further off-line analysis. The main way of the raw data treatment is a fast Fourier transform.

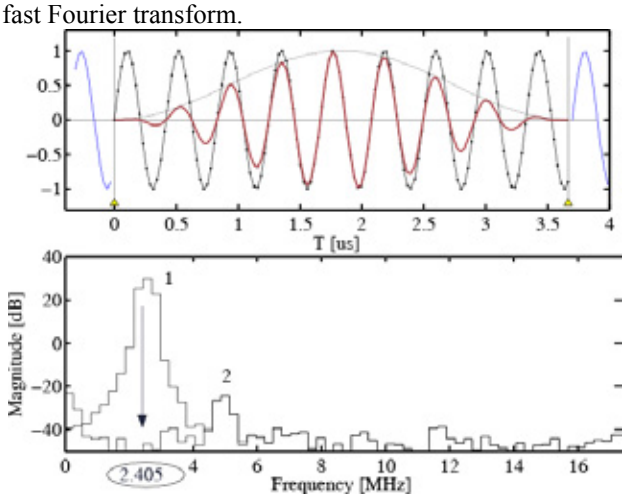

Figure 4: Raw data and 'momentary' FFT spectrum.

Fig. 4 on top shows captured data and a window function used for sharpening of the spectral lines. As it is seen in the bottom of Fig. 4, even pure sinusoidal signal produces a pattern of spectral lines instead of the single peak. The signal processor uses most significant lines of the pattern to determine final values – phase and amplitude of the signal. The window function smoothly sew up the data patterns, but also waste some signal strength and produces a phase error (see Fig. 5).

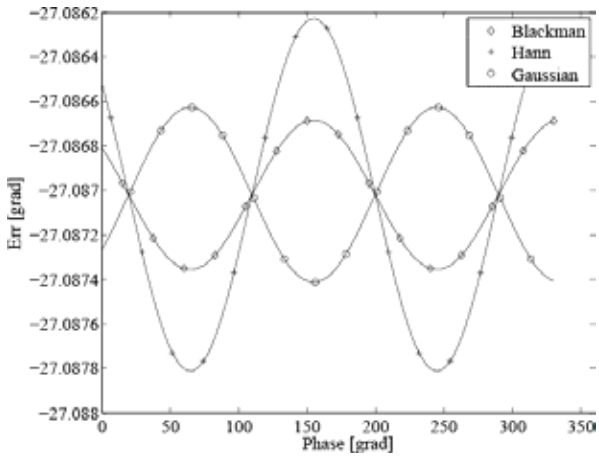

Figure 5: Phase error for the set of window functions.

Fortunately, the phase error due to the window function has only small fraction, depending on phase. Significant frequency dependent phase shift error plays no role due to the relative nature of phase measurements.

PARAMETRIC METHODS

The parametric least squares method used to solve the broadening of the spectrum lines problem. We know that the actual signal is a sin and therefore looking for the most appropriate parameter set of function

$$A_i = \zeta_0 + \zeta_1 * \cos(2 * pi * \zeta_2 * iT_{ADC} + \zeta_3),$$

having minimal power of residual signal:

$$P_{res} = K \sum_{i=1}^{N} (A_i - Y_i)^2,$$

where Y – stored ADC data, K-normalizing factor.

For systems, using a reference generator, the parameter ζ_2, or reference frequency, is known. The method works well for signals with large signal-to-noise ratio, which is true in considered cases. Fig. 4 shows the spectrum of the residual signal. A sine signal of 2.405 MHz absorbs all energy of the pattern 1. The spectrum of the residual signal is shown in Fig.4.

On the other hand, method is not so good for complicated signals with weak fractions, like the second signal harmonic in Fig. 4. Use of simplex or gradient LS-methods to determine parameters of peak 2 will not give an accurate result in the presence of strong harmonic 1. Other methods are too inefficient to be implemented in front-end electronics.

EXAMPLE. EIGHT-CHANNEL SIGNAL PROCESSOR

Fig. 6 shows a structure of an FPGA-based eight-channel signal processor used in multichannel reference generator with automatic phase control option. In general,

ISBN 978-3-95450-170-0

Fig. 6 corresponds to Fig. 2. It includes a frequency converter, a three-stage digital decimation filter consisting of two Hogenauer's filters (CICa and CICb) and FIR-filter of 20th order, CORDIC and the data buffer. For better efficiency, the system uses a time multiplexing of data streams. The data rate from the ADC is 4.6(6) times lower than processor's clock, and single decimation filter CICa is able sequentially handle the data from four ADCs. Then the time multiplexer unites all eight channels into one stream to the input of CICb. As a result, the signal processor uses only 20 embedded FPGA DSP blocks. Ten of them are dedicated to the 128-point fast Fourier transform, four used in frequency converters, and five – in FIR filter. The Blackman window-modulator takes the last DSP block.

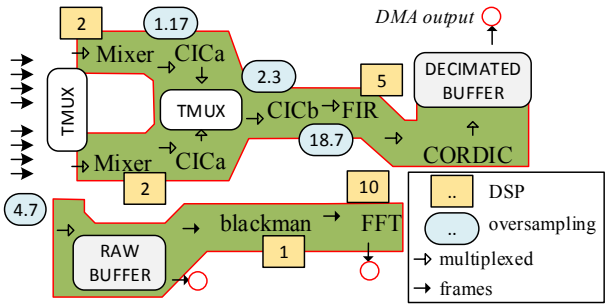

Figure 6: Eight-channel signal processor.

In addition to the signal processing part the FPGA implements timing and synchronization elements, peripheral control functions and interface to the auxiliary microprocessor including the direct memory access.

CONCLUSION

ITEP has developed a set of RF signal processors for low-level RF applications. The digital core of developed modules provides a great flexibility in signal generation and control. The 'standard' streaming algorithm of the input RF data processing is suitable in most of applications.

REFERENCES

[1] A.V. Butenko et al. 'Development of NICA injection complex', proc. IPAC2014
[2] S.Minaev et al. 'Multi-cell RF deflecting system for formation of hollow high energy heavy ion beam', proc. IPAC10, Kyoto, Japan.
[3] Alexander D. Poularikas, Discrete random signal processing and filtering primer with MATLAB,CRC Press, Boca Raton, FL, 2008

ISBN 978-3-95450-170-0

A DIGITAL LOW-LEVEL RF SYSTEM FOR RESONANT BEAM DEFLECTOR OF LAPLAS EXPERIMENT

D. Liakin, S. Barabin, A. Orlov, ITEP, Moscow, Russia

Abstract

A two-resonator heavy ion deflecting system is a part of LAPLAS experiment [1]. ITEP built and put into operation a lightweight prototype of a deflector. Developed high performance radio-frequency control unit provides all necessary options for successful operation in LAPLAS or ITEP installations. The LLRF includes a two-channel reference generator based on a digital signal processing core and resonant frequency control modules, also powered by an appropriate DSP.

RF DEFLECTOR

ITEP develops a radio-frequency deflector of high-energy heavy ion beams as a prototype of the system, assigned to plasma physics experiment in FAIR (Darmstadt, Germany). The operating prototype, shown in Fig.1, consist of two resonators forming orthogonal electromagnetic fields to deflect the beam in vertical and horizontal planes and provide a cylindrical impact volume in solid target body.

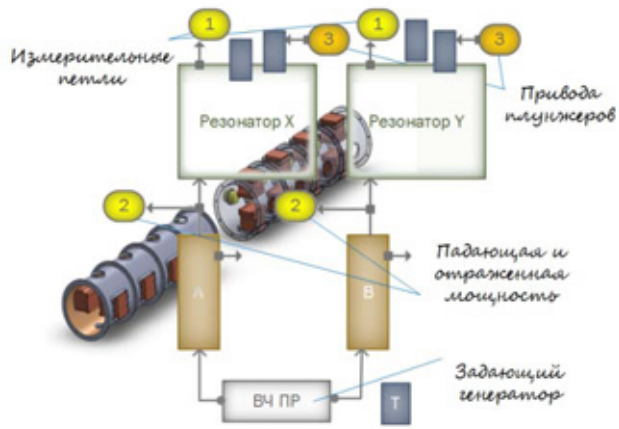

Figure 1: RF system of the beam deflector.

LOW-LEVEL RF SYSTEM

Fig. 2 shows the LLRF divided into the measurement and generator parts. The LLRF system of the deflector operates in conventional way, similar to LLRF systems of resonant accelerators. As a reference generator, it issues two coherent RF signals, shown as outputs A and B in Fig. 3. When required, the amplitude of signals could be independently set within full-scale range. The ability of the phase difference control between channels is a key option of the reference generator. The phase is adjustable in the 360-degree range. The feedback controller allows phase correction on pulse-by-pulse base.

The model of the RF system of the deflector use three independent parameters describing the system: resonant frequencies and a phase difference between two resonators. The system uses a set of control signals to stabilize the model near the optimal statement. The main criteria of the proper system operation are accurate phases and amplitudes of EM fields, estimated by measuring of signals taken from control loops 1_X and 1_Y in Fig. 1. Signals 2_X and 2_Y from reflectometers are used while checking the matching criterion.

Fig. 2 presents the structure of the crate of the LLRF module.

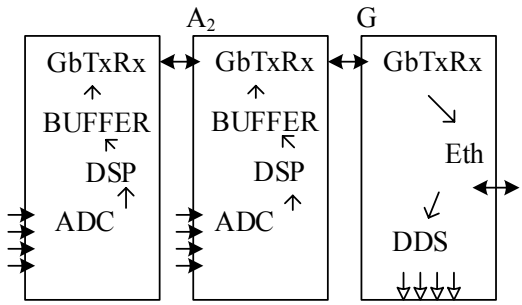

Figure 2: The structure of the LLRF module.

The crate unites two similar four-channel ADC modules A1 and A2, capable simultaneously digitize RF signals in the IF mode, and vector signal synthesizer G with pair of independent two-channel outputs of sinusoidal signals.

GENERATION OF REFERENCE SIGNALS

As shown in Fig. 3, the output signals are generated using the frequency up converter scheme.

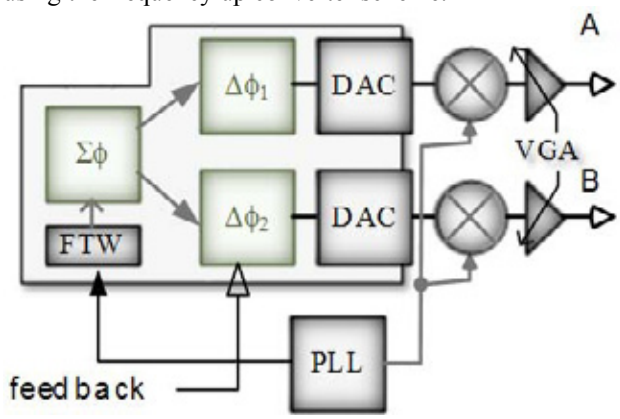

Figure 3: The reference generator.

Two-channel DDS generates synchronized signals of intermediate frequency. The frequency depends on frequency tune word (FTW) and frequency of the synchronization clock taken from on-board PLL-based synthesizer. The PLL's voltage controlled oscillator (VCO) generates the frequency of 1740 MHz. The clock

ISBN 978-3-95450-170-0

signal of ¼ of the VCO feed the DDS. The integrated two-channel DDS on single chip is an optimal solution because it provides flexible signal generation combined with seamless synchronization mechanism and simple control interface. 14-bit phase words $\Delta\phi_1$ and $\Delta\phi_2$ define phases of output signals with less than 0.025° step.

Two outputs of PLL serve as local oscillators (LO) for up converters. This configuration define the output frequency of generator as follows:

$$f_{OUT} = \left(\frac{FTW}{2^{32}} \frac{1}{N_1} + \frac{1}{N_2} \right) f_{VCO} \qquad (1)$$

where N_1 and N_2 are frequency division coefficients for the DDS synchronization and LO outputs of the PLL. As it follows from the formula 1, the required output frequency may be obtained in several ways, and this allows an additional optimization in terms of intermodulation components.

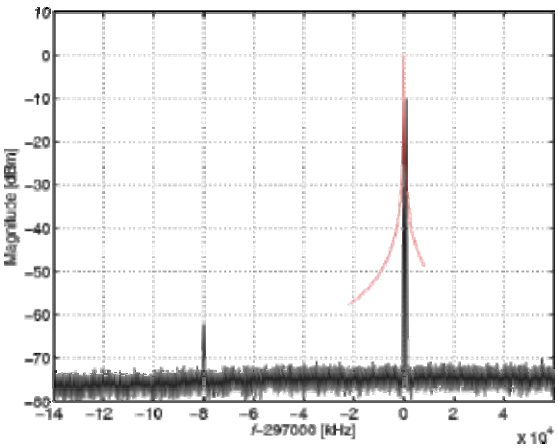

Figure 4: The output spectrum of the reference generator.

Fig. 4 shows the measured spectrum at the generator output. In the figure, the spectrum superposed the frequency characteristic of a resonator. One can see the nearest peak of the spurious signal, which is pretty far out of the system central frequency.

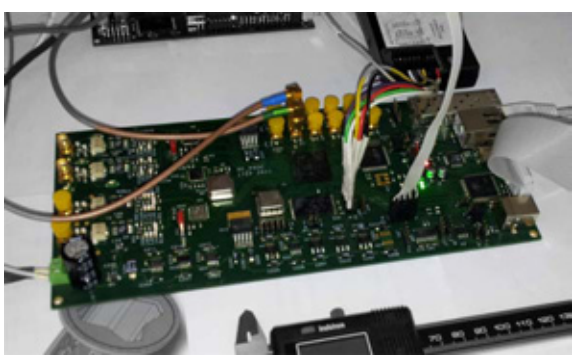

Figure 5: The PCB of the reference generator.

Fig. 5 shows the assembled printed board of the reference generator. Analog components: DDS, mixers, filters, transformers and variable gain amplifiers occupy the left side of the board. The FPGA microchip and supplemental components are placed in the central area to have shortest paths to analog circuits and high-speed serial interface connectors, placed on top of the PCB. The FPGA implements a control logic for board periphery configuration, for the signal processing and for local data exchange between the generator and ADC modules. The long-distance communication use a lightweight ARM microprocessor to provide the remote control and data delivery to the host computer over TCP/IP protocols. The microprocessor and communication related stuff take the right side of the PCB. Fig. 5 shows the board connected to the FPGA and ARM JTAG programmers.

Table 1 gives main parameters of the vector reference generator.

Table 1. main parameters of the vector reference generator.

Operating frequency f_0.	MHz	297
Frequency range. (not less)	MHz	f_0±0.5
Frequency tune step.	kHz	<0.1
Long-term frequency stability.	kHz	±3
Amplitude range.	dBm	-52÷-3
Amplitude range with VGA	dBm	-31÷18
Phase range.	Degree.	0÷360
Phase tune step.	Degree.	<0.2

SIGNAL MEASUREMENTS

Fig. 6 presents the image of the assembled printed board of the ADC module. The aim of the module is a digitizing of a narrowband signals modulated by 297MHz. Used AD converter has a data rate limited by hundred samples per microsecond, and therefore pair of two-channel 16-bit analog to digital converters operates in intermediate frequency mode.

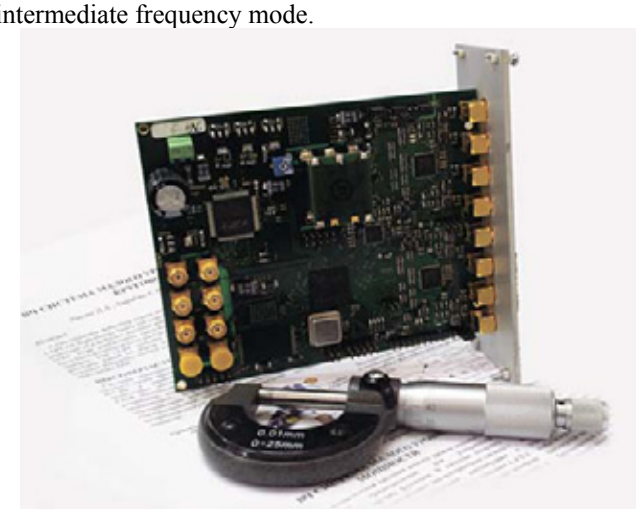

Figure 6: The ADC module.

As it is shown in Fig. 7 the ADC has a sampling rate lower than the input signal carrier frequency and operates as a zero-order hold undersampling device. As a result, the ADC shifts the 12.25 MHz-wide band around the input signal to low frequencies. The shift is equal to

ISBN 978-3-95450-170-0

frequency of 12th harmonic of the sampling clock. The RF system of the deflector, resonators and power RF amplifiers, have a narrow spectrum with no power in the near of the ADC clock harmonics with order other than 12. In addition, an analog pass band filter reduces all possible out of band EMI components of the signal. Consequently, the output of the ADC provides clear and oversampled digital signal with intermediate frequency of 3 MHz. Report [2] describes further data evaluation in details.

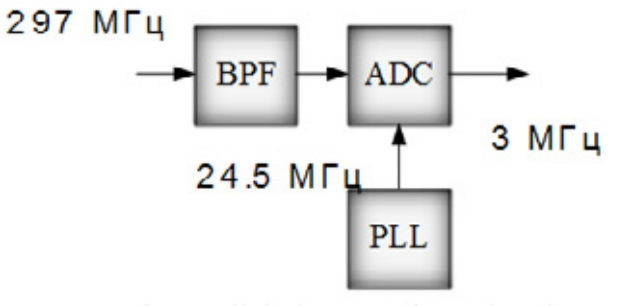

Figure 7: Analog to digital conversion using the IF mode.

SYSTEM INTEGRATION

A high-speed serial interface integrates the reference generator and ADC boards into the single joint module. Fig. 8 shows a logical structure of the whole system. The ADC or detector (D) boards acquire control signals and present the data to the generator (G) block. Detector modules have an interface to the general stepper controller module to adjust the resonant frequency of deflecting resonators using mechanical tuners T.

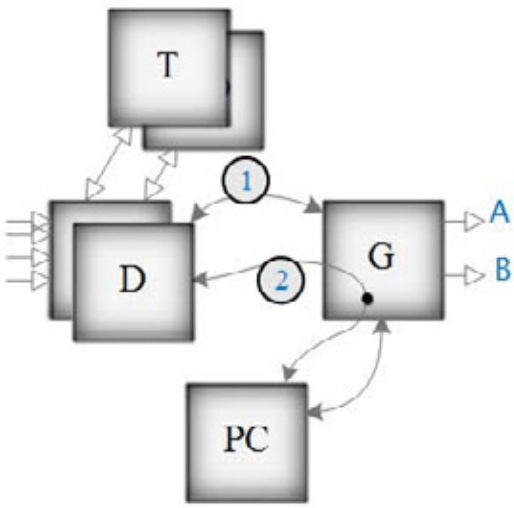

Figure 8: The logical structure of the LLRF.

As it is shown in Fig. 8, LLRF is able to operate as standalone device (branch 1) or could be taken under control by the remote host computer PC (branch 2).

FIRMWARE

The firmware part of the LLRF system includes FPGA and microprocessor microcode for each board, described above. Roughly, the FPGA is logically divided into interface modules, peripheral control modules, timing elements and signal processor. The signal evaluation algorithms is described in [2].

CONCLUSION

Fig. 9 shows the photo of the LLRF module developed for the ITEP version of the RF deflector. At the beginning of 2014 the module was used during the comissioning of the RF deflector.

Figure 9: LLRF module.

Parameters of the developed LLRF allows using it also in RF system of LAPLAS. The operating frequency of klystrons of 354 MHz lies within the range of ADCs and frequency converters. To change the frequency, it would be enough to replace input and output pass-band filters. Then the actual frequency change will be obtained by adjusting of parameters of the formula 1, and tuning of the DSP algorithms.

REFERENCE

[1] S.Minaev et al. 'Multi-cell RF deflecting system for formation of hollow high energy heavy ion beam', proc. IPAC10, Kyoto, Japan.
[2] D.Liakin et al. 'Digital signal processing algorithms for linac low-level RF systems', this proc.

ISBN 978-3-95450-170-0

QUENCH DETECTOR FOR SUPERCONDUCTING ELEMENTS OF THE NICA ACCELERATOR COMPLEX

E. Ivanov, A. Sidorin, Z. Smirnova, L. Svetov,
JINR, Dubna, Moscow Region

Abstract

A universal quench detector is designed for new superconducting accelerators of the NICA accelerator complex under construction at JINR. The presence of a two channel digital input permits the detector to be used both for comparing voltage across two nearest magnets by a bridge scheme and for separating a resistive constituent of the voltage across a controlled element.

INTRODUCTION

The Nuclotron quench-detection system was modernized in the frames of the Nuclotron upgrade project and commissioned during the runs #46-47 [1]. The detectors are based on a comparison of voltage drops across two identical elements connected in series to the supply circuit using a measuring bridge. The bridge circuit was chosen as the simplest one from the viewpoint of technical implementation. The system (Fig. 1) permits a prompt change in the number of detectors, uniform work with the group and individual detectors and implementation of the total reservation of the line controlling the energy evacuation system. The system provides monitoring of the status of all of its components, as well as signal-testing of external systems, and also indicates malfunctions. The self-diagnostic is provided by apply of pulse signals into measurement circuits between the magnetic field cycles.

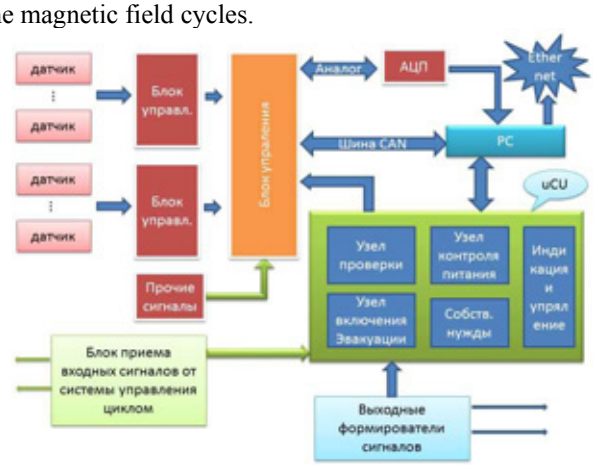

Figure 1: Block-diagram of the Nuclotron quench detection system.

Additionally, the system to control quench detectors allows all cases of protection operation to be analyzed, which yields the experimental material for further development of the detector construction. First and foremost this refers to revealing the reasons and excluding the cases of protection operation when elements do not enter the normal state. The new system permitted safe operation of the magnetic system in the regimes with long plateau of the magnetic field and operation at maximum designed magnetic field. As result, for instance, successive experiments on stochastic cooling and the beam acceleration up to maximum design energy were realized [2].

Further development of the accelerator complex is related with the realization of the NICA (Nuclotron based Ion Collider fAcility) project that presumes creation of two new Super-Conducting (SC) acceleration facilities: booster synchrotron (Booster) and collider rings, and SC transfer line from the Booster to the Nuclotron [3].

The Booster is the fast cycling synchrotron with magnetic system similar to the Nuclotron one. The Booster quench detection system can be based on the same technical solutions and the bridge scheme of the quench detector seems to be optimum.

The collider rings will be operated in the mode of a storage ring (slow beam acceleration is presumed as a reserve option only). The continuous operation is the basic regime for the SC transfer line. Two main detectors of the collider utilize the SC solenoids in a continuous mode. The quench detection is necessary for the test-bench under construction for serial production and tests of the SC magnets for NICA and FAIR facilities where different regimes of the operation are presumed.

In the mentioned cases a method of the quench detection based on separation of a resistive constituent from the measured signal by comparison with the certain reference signal can be more efficient than the bridge one. This method is rather universal: as a reference signal one can use a derivative of the magnetic field with respect to the time that determines the inductive constituent of the voltage drop. It is also possible to use the time derivative of the current flowing through the controlled element. In this case a derivative of the field is defined from the known dependence of the element inductance on the current. A difference in signals of the voltage drop across the controlled element and a signal of the derivative of the field (calculated and analyzed by the electronic circuit) indicates that the normal state is being entered.

In the continuous operation the scheme of the malfunction diagnostic has to be modified also: application of pulse signal in the measurement circuit is impossible in this case.

For use at the NICA accelerator complex and at the bench for testing SC devices, a universal quench detector was developed that is suitable for implementation in both detection schemes required.

ISBN 978-3-95450-170-0

UNIVERSAL QUENCH DETECTOR

The universal quench detector (Fig. 2) consists of two isolated channels, each of which can receive an analog signal with a maximum amplitude of ~10 V. The channel sensitivity is regulated within wide limits by the input scaling amplifiers; therefore, a signal from both the bridge (~100 mV) and the inductive element (~10 V) can be a source signal for the circuit. Next, the input signals are transformed to the digital series code by the 12-bit ADCs and through the optical isolator they are transmitted to the processor module that analyzes them. The analysis can be performed using the signal amplitude and time characteristics as well as by comparing signals between each other for separating a resistive constituent. The control and reception of ADC data by the microprocessor is implemented through the digital high-speed isolators.

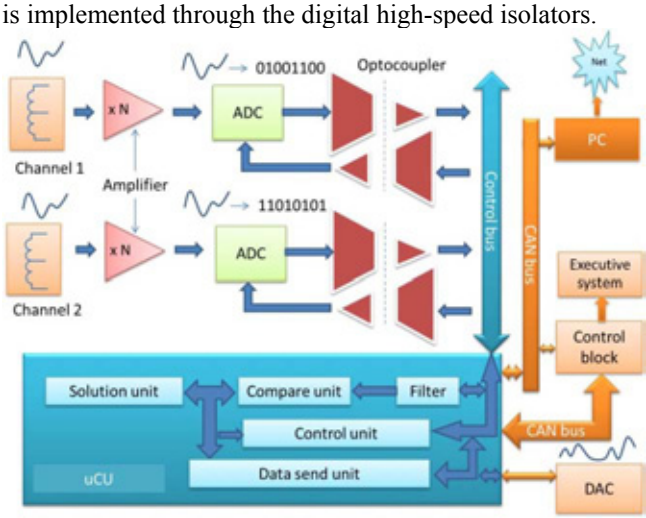

Figure 2: Block diagram of the universal quench detector.

Printed circuit board (Fig. 3) made on Eurocard 3U module with using SMD components high degree of integration [4] .

Figure 3: Printed circuit board of the quench detector

The direct connection of an inductive element made it also possible to improve the system of checking circuits of communication and detector, which now can check the galvanic coupling of all connections in the detector without the delivery of pulse signals (Fig. 4). When the testing voltage is supplied to the non-inverting input of the operational amplifier, a voltage at the amplifier output is caused by the R–R divider and equals a half of the testing value if there is no break or it equals the testing voltage if a break exists. By measuring the amplifier output voltage, it is easy to determine the integrity of communication circuits.

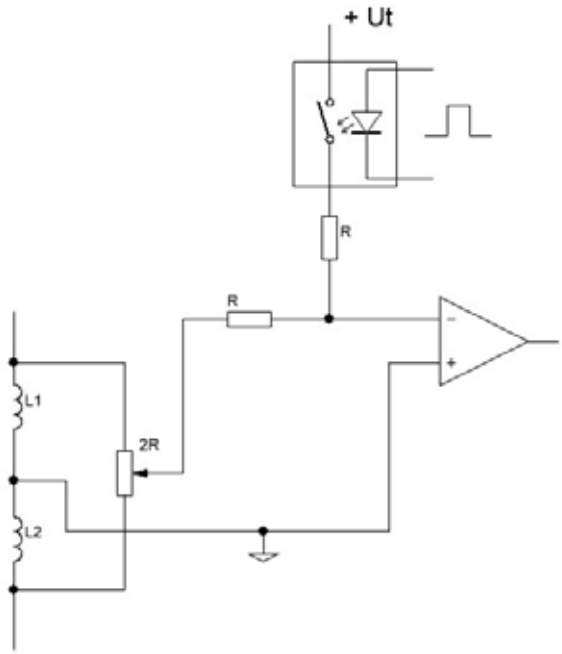

Figure 4: The system of checking circuits of communication and detector.

SUPPRESSION OF INTERFERENCES

The experience of the Nuclotron operation shows that there are places in the accelerator ring where the great noisiness of the detector input signal was noted. It is connected with disposition of powerful loads and other facilities radiating interferences near the controlled element and communication lines. The situation at the NICA collider can be sufficiently worse: the voltage at the RF stations will be of the order of 1 MV and powerful kickers will be used for the beam injection.

To suppress the noises from surrounding equipment, the method for digital filtering of input signal is used in the new detector.

Strict demands are made to the digital filter:
- realtime operation with a single sampling with a period of 4.8 μs
- minimum time delay of a signal
- absence of phase distortions
- minimum response to a jump of input signal
-simple algorithm of implementation.

According to the given criteria, a lowpass filter implemented using the “movingaverage” method was chosen. The application of the filter has shown good results for a real signal from the quench detector (Fig 5).

ISBN 978-3-95450-170-0

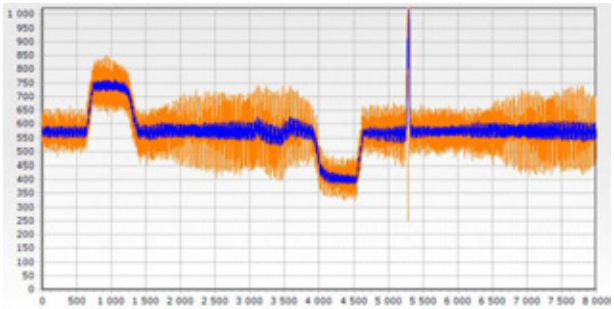

Figure 5: Signal from the quench detector at the filter input (yellow curve) and output (blue curve). Units of measure are the same as in indicated along the vertical axis; the entire scale corresponds to 3.3 V and the zero level is approximately 500. The time in hundreds of milliseconds is laid along the horizontal axis; i.e., the entire scale is 800 ms.

The degree of noise suppression is regulated by varying the filter coefficient using a program. It is possible to thus adjust the detector individually for each particular placement of it in the accelerator ring. It should be remembered that the filter introduces a time delay into the initial signal (depending on the coefficient, from 500 μs to 2 ms); therefore, it is necessary to correct the detector in its application.

CONCLUSIONS

On the basis of the experience of operation of the quench detection system of the Nuclotron SC synchrotron with account of demands from new SC elements of the NICA facility, the new universal quench detector is developed. The validity of the signal processing concept and the absence of fundamental errors in circuitry construction were checked on the detector mockup. Now a prototype is fabricated and tested during the Nuclotron run and at the test bench for the magnet production. Beginning of the quench detector serial production of s is scheduled for 2015.

REFERENCES

[1] E. V. Ivanov, G. V. Trubnikov, A. O. Sidorin, and Z.I. Smirnova, “System of quench detection in superconducting magnets of the Nuclotron accelerator complex,” Phys. Part. Nucl. Lett. 10 (4), 374 (2013), E.Ivanov, A.Sidorin, G.Trubnikov, «The quench detection system for superconducting elements of Nuclotron acceleration complex», proceedings of RuPAC2012, Saint-Petersburg.

[2] A.Sidorin et. al., Status of the Nuclotron, these proccedings.

[3] V. Kekelidze, R. Lednicky, V. Matveev, I. Meshkov, A.Sorin, and G. Trubnikov, “NICA Project at JINR,” Phys. Part. Nucl. Lett. 9 (4–5), 313 (2012).

[4] E. V. Ivanov, L. A. Svetov, and Z. I. Smirnova, Quench Detector for Superconducting Elements of the NICA Accelerator Complex, Physics of Particles and Nuclei Letters, 2014, Vol. 11, No. 4, pp. 486–490.

ISBN 978-3-95450-170-0

EXPERIMENTAL STUDY OF THE SCATTERING OF 7.4 – MEV ELECTRONS INTERSECTING A FOIL AT AN ANGLE OF 5º – 60º TO ITS SURFACE

A.V. Koltsov, A. V. Serov , LPI, Moscow, Russia
I. A. Mamonov, MEPhI, Moscow, Russia

Abstract

Angular distributions of electrons incident of a planar target at a small angle to its surface have been measured. Electrons have been injected from a microtron with a particle energy of 7.4 MeV. The dependence of the characteristics of beams on the initial energy and direction of injection of particles, as well as on the material and thickness of the target, has been considered. The intersection and reflection of electrons in the target have been investigated. The angle between the trajectory of the particles and the surface of the target was varied in the range of 5º - 60º. Aluminum, lead, and copper foils have been tested. The thickness of the foils was varied from 50 μm to 600 μm.

INTRODUCTION

The solution of some applied problems implies the knowledge of the characteristics of the scattering of particles incident on the surface at an angle much smaller than a right angle. One of such problems is the problem of the excitation of transition radiation by electrons intersecting a dihedral angle [1] or a conical surface [2]. The transition surface can be a thin layer of a certain material (Mylar, metal). In this case, the characteristics of radiation should depend not only on the initial parameters of the beam but also on a change in these parameters when intersecting the thin layer, i.e., on the material and thickness of the intersected surface, as well as on the direction of motion of particles. The smaller the angle between the direction of motion of particles and the surface, the stronger the effect of the properties of the transition surface on scattering. The motion of beams injected at a small angle to the surface was studied in [3]. The aim of this work is to analyse the effect of the direction of injection of particles on the parameters of the beam intersecting metallic foils with various thicknesses.

SETUP OF THE EXPERIMENT

The layout of the experiment is shown in Fig. 1. The z axis is taken along the trajectory of particles and the x axis lies in the horizontal plane. The charge e_d intersecting the target leaved it at the angle of refraction θ_d with respect to the initial direction of motion, whereas the charge e_r reflected by the target moved at the angle φ_r to the plane of the target. The point x_b in Fig. 1 is the point at which a straight line in the plane of the target intersects the plane of the detector. The coordinate x_b is determined by the distance *L* from the target to the detector and the angle of injection α. According to the geometry of the experiment, the coordinates of particles e_d intersecting the target on the plane of the detector satisfy the condition $x > x_b$ and the coordinates of reflected particles e_r satisfy the condition $x < x_b$.

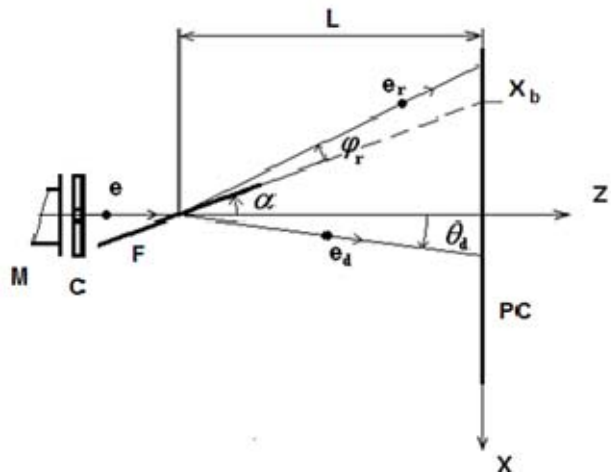

Figure 1: Geometry of the experiment.

In the experiments, it is used 7.4 MeV electron bunches from the microtron. Electrons were extracted to the atmosphere through a 100 μm aluminum foil on the flange of microtron M. Lead collimator C and foil F were placed behind the flange. The 50 mm thick collimator had a hole with a diameter of 3 mm. The foil was rotated with respect to the vertical (y) axis by the angle α. The distribution of electrons was measured by multiwire proportional chamber PC consisting of three 64 × 64 mm frames. The chamber allowed measurements of the distributions of particles in the horizontal (x) and vertical (y) directions. The chamber was located at a distance of L ~ 150 - 300 mm from the point of intersection of the foil by the beam. A signal from the proportional chamber was fed to an oscilloscope. Charged particles passing through the layer of the substance undergo numerous collisions; consequently, the spatial distributions of passed and reflected particles are approximated well by a Gaussian distribution. The direction at which the distribution has a maximum was taken as the motion direction of refracted and reflected beams of particles.

EXPERIMENTAL RESULTS

The typical oscillograms of the signals of the chamber are shown in Fig. 2. The first and second pulses of the oscillograms describe the horizontal and vertical distributions of particles, respectively. Figure 2 shows the distributions for the cases where (a) copper foil with a

ISBN 978-3-95450-170-0

thickness of $\delta = 50$ μm is placed behind the collimator at the angle of $\alpha = 90$ ° to the *z* axis and (b) the same with the $\alpha = 10$ °. The comparison of the figures shows that the intersection of the foil in case $\alpha = 10°$ leads to split of the beam to refracted and reflected ones and to the shift of the maximum of the horizontal distribution (Δx_d and Δx_r in Fig. 2b). This indicates that the intersection of the foil changes the direction of motion of a particles bunch relatively to the initial direction. The trajectory of the refracted beam deviates by an angle of $\theta_d = \text{arctg}(\Delta x_d/L)$. The angle φ_r of reflected beam is $\varphi_r = \text{arctg}(\Delta x_r / L) - \alpha$. The position of the maximum of the vertical distribution hardly changes. Therefore, the refraction of the trajectory occurs only in the horizontal plane.

The measurements were performed with a copper, aluminum and lead foils with a thickness from $\delta = 40$ μm to 600 μm. The angle α between the trajectory of injected particles and the surface of the foil varied in the experiments from 5° to 60°.

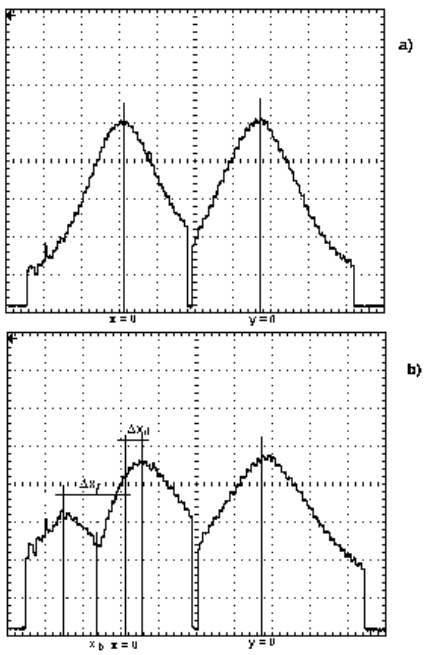

Figure 2: Transverse distributions of electrons intersecting a 50 μm cooper foil at an angle of $\alpha = 90°$ (a), 10° (b) to its surface. L = 100 mm.

The experiment results make it possible to plot the dependence of the angle refraction θ_d at a given angle of injection α. (Fig. 3). The measurement results for the copper foil with a thickness of $\delta = 50$ μm, for the aluminum foil with a thickness of $\delta = 600$ μm and the lead foil with a thickness of $\delta = 70$ μm are shown by squares, triangle and circles respectively. It can be seen that the angle refraction θ increases with a decrease in α.

There have been investigated dependences $\theta_d(\alpha)$ for different thicknesses of copper foil. These dependences are shown in the Fig.4. Increase of thickness of the target leads to increase of refraction angle θ_d. Moreover changes of thickness of the target influence the behaviour of curve $\theta_d(\alpha)$.

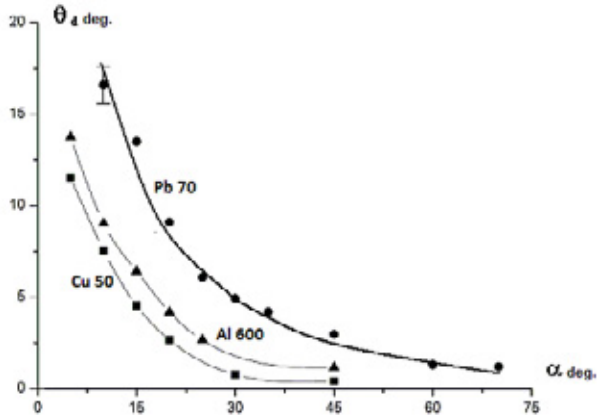

Figure 3: Angle of refraction of the trajectory θ_d versus the angle of injection α. 50 μm copper, 600 μm aluminum and 70 μm lead foils. Notes for curves indicate the foils materials and their thicknesses in microns.

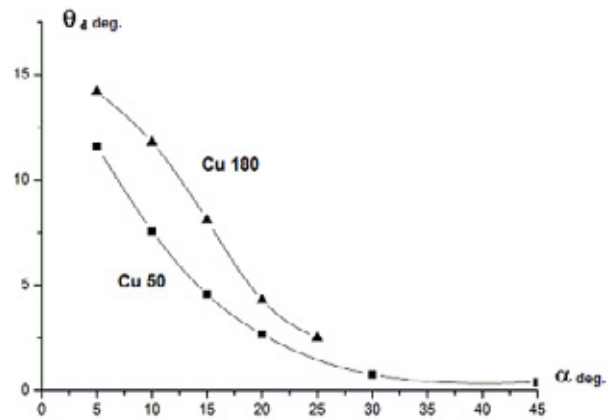

Figure 4: Angle of refraction of the trajectory θ_d versus the angle of injection α. 50 μm and 180 μm copper foils. Notes for curves indicate the foils materials and their hicknesses in microns.

t

It has been also analyzed the effect of the angle of injection on the direction of motion of reflected electrons. The results of the corresponding measurements are shown n Fig. 5. It can be seen that the direction of motion of reflected particles changes slightly in certain angular ranges (α ~ 12° -- 17°).

Notice that for small foil thickness δ reflected angle φ_r is less than the injection angle α. Increase of thickness of the target leads to increase of reflected angle.

Figure 6 shows dependences of the angle of reflection of the beam φ_r on the thickness of the intersected foil δ at angle of injection $\alpha = 10°$. It can be seen that for $\delta < 300$ μm the reflection of the trajectory of the beam increases with the thickness of the target. For $\delta > 300$ μm the reflection of the trajectory of the beam changes slightly.

ISBN 978-3-95450-170-0

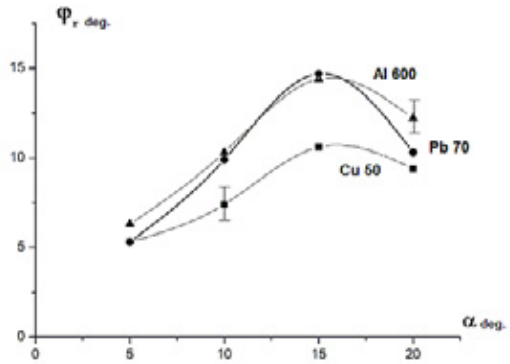

Figure 5: Angle of reflection of the trajectory φ_r versus the angle of injection α. 50 μm copper, 600 μm aluminum and 70 μm lead foils. Notes for curves indicate the foils materials and their thicknesses in microns.

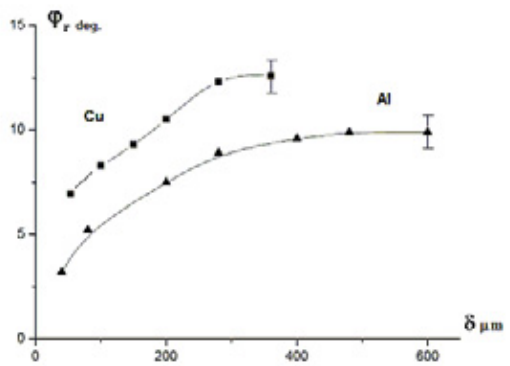

Figure 6: Angle of reflection of the trajectory φ_r versus the foil thickness δ. α = 10°. Copper and aluminum foils.

The experimental data indicate that the intensity and direction of motion of the refracted and reflected beams can be changed by modulating the thickness of the target or the angle at which the plane of the target is intersected.

REFERENCES

[1] A. V. Serov, JETP. **108** (4), 593 (2009).
[2] A. V. Koltsov, A. V. Serov, JETP. **116,** (5), 732 (2013).
[3] A. V. Koltsov, A. V. Serov, JETP Lett. **99** (1), 1 (2014).

ISBN 978-3-95450-170-0

A PULSE GENERATOR OF X-RAY QUANTS FOR REMOTE RADIATION MONITORING

B.Yu. Bogdanovich, A.V. Nesterovich, A.E. Shikanov,
National Research Nuclear University "MEPhI", Moscow, Russia
B.D. Volchansky, A.V. Ilyinsky, D.R. Khasaya, E.A. Shikanov,
OOO «SPEKTR» Integrated monitoring systems, Moscow, Russia

Abstract

The report presents the development of compact UT, which improved definition x-ray image is ensured by using a diode system with a coaxial geometry acceleration of electrons to the anode electrode internal target and explosive emission cathode. UT used to run a specially designed high-voltage pulse transformer-based "Tesla" with surge sharpener. Describes the design and block diagram interface generator X-ray quanta. Feature is the high stability of the generator is not dependent on the voltage, battery charge. Presented the results of experimental testing of the generator X-ray quanta. Also shows the waveform duration x-ray pulses in the presence of the lead filter and without it.

Modern complex industrial facilities (nuclear reactors, elements of pipeline and rail transports, power plants turbines, heat exchangers, aircraft, etc.) require the implementation of remote penetrant monitoring. At the same time, such monitoring systems are subject to the increased requirements for transportation, portability, expressness of changes.

The best solution for this kind of problems is the application of portable mono-block instruments based on pulse x-ray acceleration tubes (AT). The weight and dimensions of mono-block radiator, the power supply and control panel allow to transfer them easily and quickly mount to take effective measurements. Such radiation sources concerning small dimensions should provide the average exposure rate as ~10 mR/s within the distance of ~m from the target with the minimum area of target's radiating surface. Given parameters are obtained by generating the x-ray quants in the vacuum diode AT operating in the pulsed-periodic mode with the current amplitude of accelerated electrons ~kA, the pulse duration ~(1-10) ns and the maximum energy of electrons with several hundred keV. For this purpose, the Experimental Plant of Pulse Technique (EPPT) - the subsidiary of OOO «SPECTR»-IMS, with the assistance of Institute for Nuclear Research of the National Academy of Sciences of Ukrainian and NRNU MEPhI, has designed a small-sized AT in which the enhancement of the x-ray image clarity was provided by the diode system with the coaxial geometry of an electrons' acceleration to the internal anode electrode - target [1-2].

This electrodes' geometry allows to produce a cathode plasma spreading to the anode and acting as an intensive source of electrons. The electric field intensity in the anode region can reach up to ~108 V/m.

While operating pulse generators of x-ray quants in the field, high requirements are imposed on the mechanical and dielectric strength of AT. And therefore in order to enhance these indicators, the special high voltage ceramic insulator was suggested to be used. By means of computer simulation and physical modelling at a demountable vacuum stand information has been received on optimal geometrical dimensions of a diode acceleration system [3] that formed the basis for designing AT. Fig.1 shows its schematic section and general view.

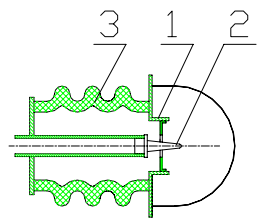

a)

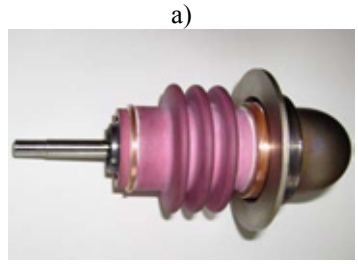

b)

Figure 1: Acceleration tube and its triggering circuit: a) the schematic section of AT. 1- cathode; 2- anode; 3- ceramic corrugated insulator; b) the general view of AT.

Obtained relations of geometric dimensions for a diode system are defined by the following system of inequalities [4]:

$5.10^{-4}\text{m} \le \rho \le 10^{-3}\text{m}$, $5\rho \le r_K \le 10\rho$, $0.2\ r_K \le r_A \le 0.5\ r_K$, $0.4\ r_K \le h \le 1.4\ r_K$,

where ρ- the rounding radius at the anode end, r_K– the radius of a hole in the cathode, r_A- the radius of an anode circular section with the plane passing through the

ISBN 978-3-95450-170-0

front end of a cathode, h- the distance from the front end of a cathode disk to the front end of an anode.

The special pulse high voltage source based on the Tesla coil with a spark gap-peaker was used for triggering AT. It was mounted with AT in a sealed pressure-resistant case filled with the insulating gas under the pressure of 15-20 atm. The basis for an insulating medium was the elegas (SF_6).

Fig. 2 depicts the switching diagram of a high voltage circuit.

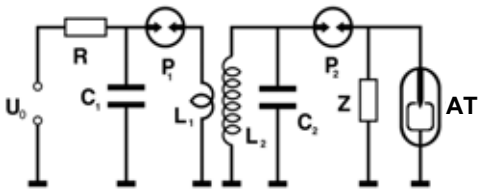

Figure 2: The triggering circuit of AT: R- the charging resistance; C_1- the tank capacitor; P1- the spark gap of primary circuit; $L_{1,2}$- the inductance of primary and secondary windings of Tesla coil ; C_2- the capacitor of secondary circuit of Tesla coil; P_2- the spark gap; Z- reactance for initial galvanic coupling of the spark gap - peaker with the ground and matching the primary and secondary windings of Tesla coil.

The tank capacitor charges via a specially designed by EPPT small-sized source of direct-current voltage U_0. Fig.3. shows the block diagram of generator interface. The distinctive feature of this generator is a high stability, regardless of the line voltage or of the battery charge. This is achieved by the division of a voltage increase into two stages. Due to the feedback there is no-load loss protection and short circuit protection in a generator.

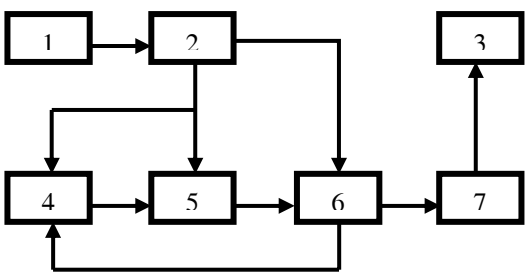

Figure 3: The block diagram of x-ray quants generator. 1- the supply-line filter, 2- the power supply unit, 3- the high voltage unit , 4- the control unit, 5- the pulse generator, 6- the power amplifier, 7- the voltage multiplier.

The pulsed-periodic launch of AT could be performed in both the auto generated mode and armed mode with a given frequency. In the latter case instead of an uncontrolled gas-filled double-electrode spark gap P_1 there can be used a controlled vacuum or gas-filled spark gap provided with an additional ignition electrode.

When launching AT in the auto generated mode, the tank capacitor C_1 is being charged. Reaching the breakdown of the spark gap at the voltage capacitor, the circuit is closed and the capacitor is discharged into the primary winding of a transformer. Due to the current flowing through the primary low-inductive winding, in the secondary winding there arises a high voltage which increases to the response voltage ($U_м$) of a spark gap - peaker P_2. As a result, the anode of AT acquires potential $U_м$. To ensure the galvanic coupling of the right electrode of the spark gap - peaker with the ground in a circuit, the resistance Z is introduced which also ensures to maintain the voltage on the anode of AT during the generation of x-ray quants owing to the inductive component. In addition parameters of resistance are selected so as to provide the optimal conditions for power transmission to the accelerated electron stream .

The enhancement of a primary discharge circuit in the part of the tank capacitor and the spark gap was carried out during the development of the instrument. The original design of the capacitor with three plates was suggested, i.e. consisting of two combined capacitors in series.

Tests of AT working model have shown that with the amplitude of accelerating voltage of 300kV the amplitude of electron current and the pulse duration at half maximum comprised about 2 kA и 2ns respectively that is in agreement with estimated data and the dose at 0.5 m away exceeded 1mR per pulse .

The obtained radiation-monitoring performance of the instrument provides an opportunity for operating it both in the mode of exposing films and in the mode of using the photoelectric converters with subsequent encoding in the analog-to-digital converter and computational signal processing .

Fig. 4. shows experimental dependencies of the dose rate in the air on the distance R between the target and the observation point and on the power W stored in the tank capacitor.

Given dependencies are built using the least squares method according to measurements data of an exposure rate taken for 50 pulses of AT response at a response frequency 10Hz in different places at different values of W. There was also the enhancement of the AT triggering circuit parameters. The average percentage error of approximation measured by the residual principle did not exceed 15%.

Also in collaboration with All-Russia Research Institute of Automatics (VNIIA) named after N.L. Dukhov investigations of the lead screen influence on the x-ray radiation pulse form were carried out using a semiconductor detector with a temporal resolution of at least 1,5 ns. Fig.5 shows oscilloscope pictures of voltages from the detector.

The sensor was positioned 2 sm away from AT. The sensor was connected to the digital oscilloscope.

ISBN 978-3-95450-170-0

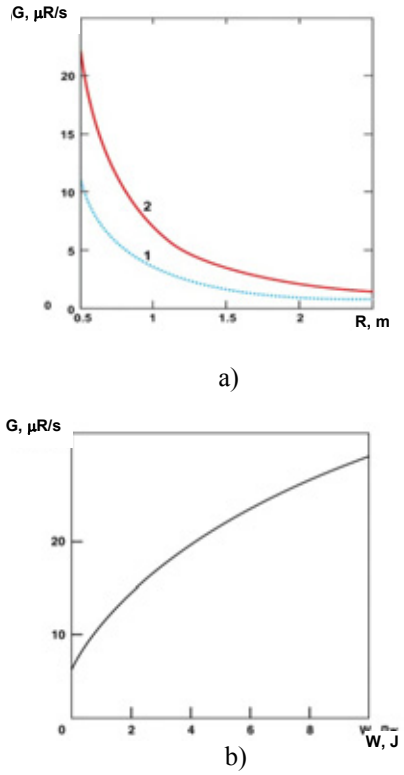

Figure 4: The measurement results of the dose rate of generated radiation – G: a) dependencies G(R), taken for values W=1 J- curve 1 и W=7 J- 2; b) dependence G(W).

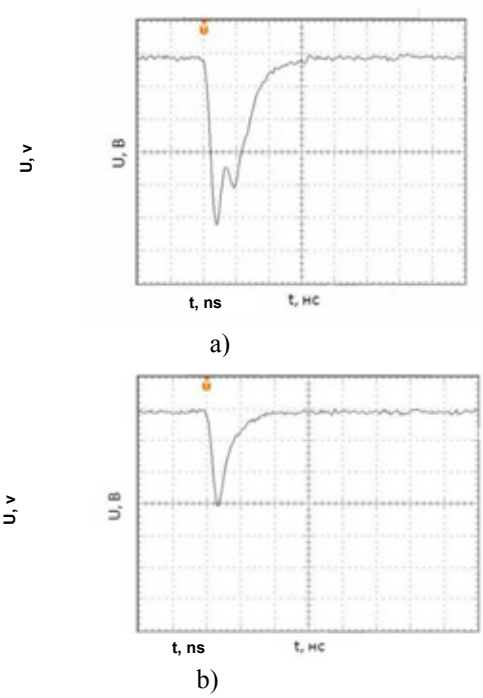

Figure 5: a) The oscilloscope picture taken without the screen. b) The oscilloscope picture taken with the lead screen of 1mm thick.

From oscilloscope pictures it can be clearly seen the reduction of a signal amplitude with the lead screen at AT. In addition pulse durations at half maximum do not exceed 3ns. This fact allows to use designed pulse sources of x-ray radiation analizing high-speed processes.

REFERENCES

[1] Yu.A. Bystrov, S.A. Ivanov, 1976, Uskoriteli i rentgenovskie pribory [Accelerators and X-ray Instruments],Vyssh. shk., Moscow, 208 p.

[2] E. G. Aleksandrovich, N.V. Belkin, M.A. Kanunov and A.A. Razin, 1972, Malogabaritnaya impul'snaya rentgenovskaya trubka s samovosstnavlivau-shchimsya avtokatodom, [A small-sized pulse x-ray tube with self-regenerating field-emission cathode], PTE (Journal; Intruments and Experimental Techniques), No 6, pp. 198-199.

[3] B. A. Myagkov, A. E. Shikanov and E. A. Shikanov, 2009, Razrabotka i issledovanie impul'snogo generatora rentgenovskogo izlucheniya, [Development and investigation of a pulsed x-ray generator], Atomnaya Energiya(Atomic Energy), vol. 106, issue 2, pp. 114- 117.

[4] E. A. Shikanov, Malogabaritnaya uskoritel'naya trubka dlya generatsii rentgenovskikh kvantov, [A small-sized acceleration tube for x-ray quants generation], Patent RU for utility model No.71817 from 03.10.2007.

ISBN 978-3-95450-170-0

DEVELOPMENT OF THE SOFTWARE FOR THE ACCELERATING FIELDS IN LINEAR STRUCTURES MEASUREMENT

E. Savin, M. Lalayan, A. Smirnov, National Research Nuclear University «MEPhI», Moscow, Russia
A. Zavadtsev, OOO «Nano Invest», Moscow, Russia

Abstract

The software which allows controlling the whole installation to measure electric fields in the linear structures has been developed. The installation consists of linear structure, step motor drive, motor controller, a probe which moves on the string throw the structure to perturb the field to use the perturbation measuring method, network vector analyzer and the PC. He software interface is user-friendly, user only needs to write down the length of the structure, a desired step of the probe and push the start button. As a result user can obtain the picture of electric field on the structure axis. It is possible to choose between two measuring methods: by S11 of by S21.

METHOD DESCRIPTION

Information about electrical field amplitude and phase distribution along the axis of the accelerating or deflecting section can be obtained from the measurements, based on non resonant perturbation theory. According to this theory, change of the complex reflection coefficient on the entrance of the structure, when the small perturbing body is in the structure, is proportional to the square of the electric field amplitude in the point where perturbing body is placed:

$$\Delta S_{11} = S_{11}^{pb} - S_{11}^{0} = CE^2, \qquad (1)$$

where S_{11}^{pb} – is a complex coefficient of the reflection on the structure entrance with perturbing body,

S_{11}^{0} – is a complex coefficient of the reflection on the structure entrance with perturbing body,

E – is a complex amplitude of the electrical field in the point of the perturbing body комплексная амплитуда напряженности электрического поля в точке размещения тела,

C – is a complex coefficient.

RF field is perturbed by the probe moving along the structure axis. For the accelerating structure with a longitudinal field, the probe geometry is a needle. And for the deflecting structure with a transverse field – it is a flat disk.

Using the measurement results, it becomes possible to calculate reflecting coefficient change $\Delta S_{11}^{(n)} = S_{11}^{pb(n)} - S_{11}^{0}$ (where n – it is a cell number) and find the ratio between complex amplitudes of electric field in the centers of the neighbor cells.

$$\frac{E_{n+1}}{E_n} = \left[\frac{\Delta S_{11}^{(n+1)}}{\Delta S_{11}^{(n)}}\right]^{\frac{1}{2}}. \qquad (2)$$

Let the complex amplitude in the first cell is equal $E_1 = 1$, i.e. its amplitude is equal 1 and phase is equal 0. Then we get following expressions for the complex amplitudes in the cells centers

$$E_{n+1} = E_n\left[\frac{\Delta S_{11}^{(n+1)}}{\Delta S_{11}^{(n)}}\right]^{\frac{1}{2}}, \qquad (3)$$

$$E_1 = 1.$$

So, as a result of the reflecting coefficients measurements we get the following data:

$S_{11}^{0} = a^{(0)} + jb^{(0)}$ – a complex reflection coefficient with the probe outside the structure (j-is the imaginary unit),

$S_{11}^{pb(n)} = a^{(n)} + jb^{(n)}$ – a complex reflection coefficient with the probe inside the center of the n-cell.

Using the measurement results we can calculate the reflection coefficient change

$$\Delta S_{11}^{(n)} = S_{11}^{pb(n)} - S_{11}^{0} = CE_n^2 = C|E_n|^2 \exp(j2\varphi_n)$$

, where $|E_n|^2$ – is a square of electric field amlitude in the middle of the n-cell, φ_n – is a starting phase of electric field amlitude in the middle of the n-cell.

THE INSTALLATION CONSISTANCE

The installation consists of the followings components:

- Directly the measured structure with the thread with probe.
- Step-motor, which controls the thread moving.
- Controller, which is connecting the step-motor with the computer.
- Network analyzer, which is measuring the reflection coefficient and the structure frequency in the defined time moments. It is also connected PC.
- PC with the describing software.

THE INTERFACE

The software is developed in the Lab VIEW, which allows creating the comfortable and intuitive interface. On the Fig. 1is presented the main window, in which displays

ISBN 978-3-95450-170-0

the main data: time, date, the structure name. Also it is possible to plot the field distribution, using previously measured and saved data array, while pushing the "Load from Disk" button.

After pushing the «New Measurement» button, user is prompted to input the measurement parameters (see Fig.2). In the case of required data precision it is possible to choose one of two types of measurement:

• «Regular measurement step». In this case it is required to input the probe step value. The data from analyzer will be read after the each step. This method allows obtaining the smooth field distribution, but the measuring time will be long.

• «Set coordinates manually». The probe is stopping only in previously defined coordinates that allows measuring faster in cases when, for example, it requires to make sure about zero field value in coupling cells centers or in field distribution uniformity in the accelerating cell centers.

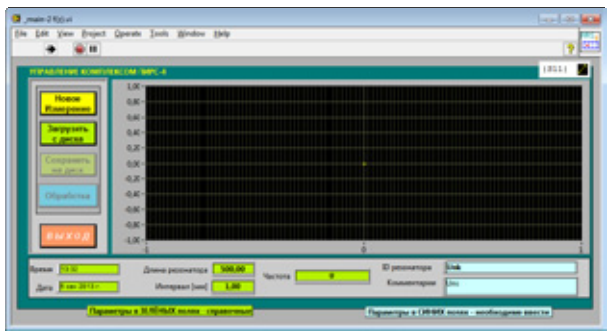

Figure1: Program main window.

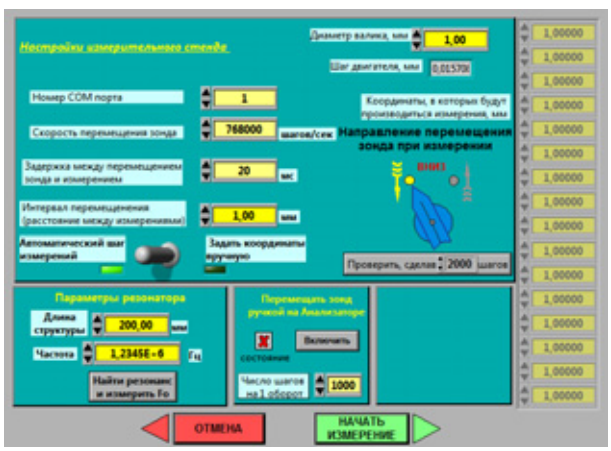

Figure 2: "New measurement" window.

After the measure type selecting, step motor parameter setting and the structure resonant frequency measure, the program proceeds to the main measurements (see Fig.3). In this window the momentum picture of the complex reflecting coefficient and the progress line are displayed. Also it is possible to select the possibility of probe returning in the initial coordinate after measurement end.

When the measurement is done, it is possible to save the obtained data array (real and imaginary parts of reflecting coefficient in the each coordinate). Then this array is proceeding in postprocessor (see Fig. 4). There is a possibility to view the field amplitude and phase along the axis and also to find the cells centers.

The postprocessor allows recalculating of the thermal drift influence. It needs specification of points, where the plot was placed outside the structure before and after measurement.

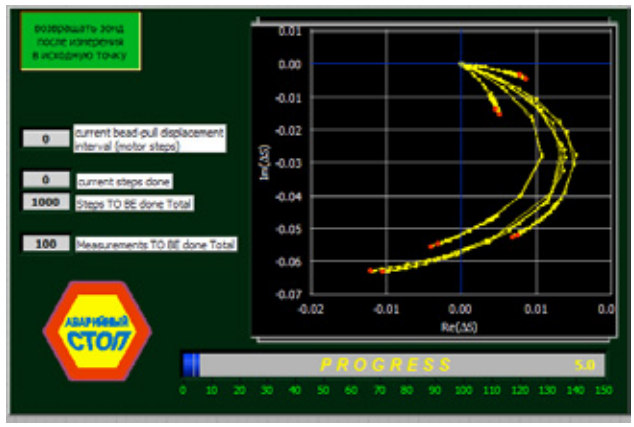

Figure 3: Measurement process.

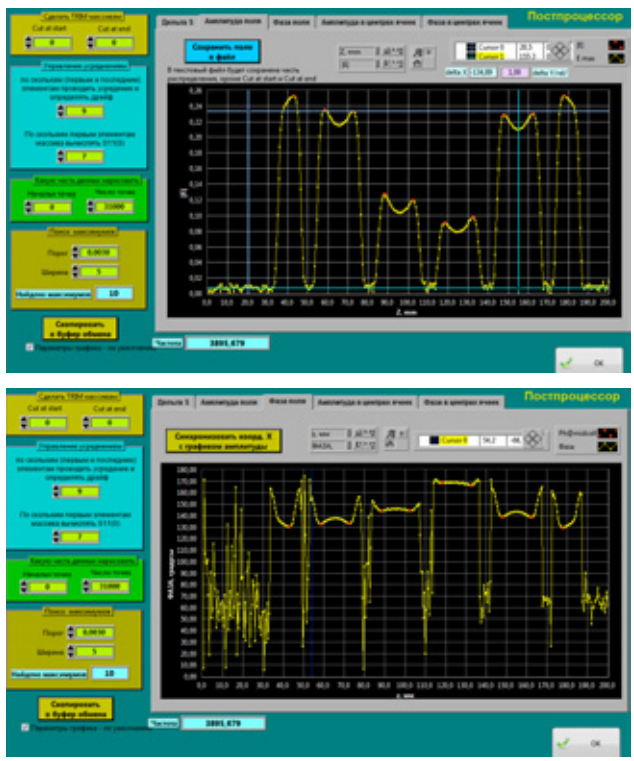

Figure 4: Postprocessor.

THE PROGRAM PART

The measuring complex operating and treatment of the obtaining results program algorithm allows measuring of the electromagnetic fields distribution as by the change of the reflection coefficient and the shift of the resonant frequency. Both methods have their own features and well complement each other. The first of these algorithms is

ISBN 978-3-95450-170-0

based on mathematical apparatus, shown above. Justification of second is well known [3].

The used code is graphical (see Fig.5), that's why it always easy to add new functions or to delete excess.

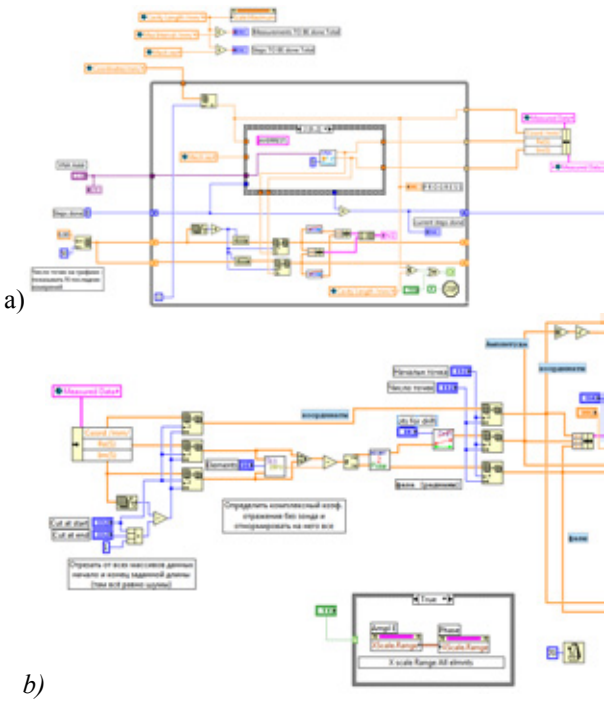

a)

b)

Figure 5: The part of the graphical code, describes the measurement (a) ad postprocessor (b) processes.

CONCLUSION

This article describes the theory on which is based the work of the program for the accelerating or deflecting linear structure electric field axis distribution measurement. The principle of program operating and its interface is described.

At the moment, purchased, configured and successfully tested all the components of the measuring unit.

REFERENCES

[1] J.C. Slater. Microwave Electronics. New York, Van Nostrand.

[2] D. Alessini, et al. About non resonant perturbation field measurement in standing wave cavities. Proceedings of EPAC08, Genoa, Italy, 2008.

[3] N.P. Sobenin, B.V. Zverev. Electrodynamic Characteristics of Accelerating Cavities. Foundation for International Scientific and Education Cooperation, London, England, 1999.

[4] P. Goudket, et al. Comparison of the Stretched-wire, Bead-pull and Numerical Impedance Calculations on 3.9 GHz Dipole Cavities. Proc. of EPAC08. Genoa, Italy, 2008.

ISBN 978-3-95450-170-0

CONTROL SYSTEMS FOR RADIOGRAPHY AND CARGO INSPECTION RF ACCELERATORS

A.N. Ermakov, A.N. Kamanin, V.G. Sayapin, V.I. Shvedunov, D.S. Yurov,
Skobeltsyn Institute of Nuclear Physics, Lomonosov Moscow State University, Laboratory of Electron Accelerators MSU, Ltd, 119992 Moscow, Russia
I.V. Shvedunov, Laboratory of Electron Accelerators MSU, Ltd, 119992 Moscow, Russia

Abstract

Based on “open technologies” approach to design of control systems for radiography and cargo inspection electron RF accelerators constructed at Laboratory of Electron Accelerators MSU is described. The control system consists of a number of specialized controllers each responsible for separate accelerator subsystem connected via Ethernet interface and Modbus/TCP protocol with control computer which in turn is connected with control panel computer, modulator, power supplies etc. each having its own digital interface. Each controller contains one or several special boards conditioning external analogue and discrete signals and universal microcontroller part providing controller operation and network connection. Both control computer and control panel computer are based on BlueShark SOM (System on a Module) amd run Linux operating system. Custom SCADA-like system has been developed to provide proper accelerator operation and operator interface with support for different levels of access to accelerator parameters.

INTRODUCTION

The radiography accelerator UELR-8-2D with beam energy regulated in the range 3-8 MeV and dose rate from 0.5 to 15 Gy/min and cargo inspection accelerator UELR-6-1-D-4-01 with pulse to pulse energy switching between 3.5 and 6 MeV, with repetition rate 400 Hz and dose rate 4 Gy/min were developed and put into operation with the participation of Lomonosov Moscow State University and "Research and Production Enterprise "Toriy" stuff [1]. A compact control system located in the X-ray head cabinet in the vicinity of controlled objects is necessary for proper operation. The control system is built on the hierarchical principle (fig. 1). The top-level computer is connected by Ethernet network and RS232 interface to the operator panel and several subsystem controllers. Subsystem controllers are custom devices implemented using microcontrollers except for klystron modulator which is ready-made device. The control application running on the top-level control computer uses Modbus/TCP protocol to communicate with subsystem controllers that perform data acquisition, actuation and real-time critical tasks. The control application also communicates with the klystron modulator using modulator's own proprietary serial line protocol [2]. The system relies on hardware interlocks to ensure safe operation. The top level computer can query interlocks via Accelerator Controller and other controllers. Accelerator Controller also uses klystron modulator's hardware interlock inputs to prevent klystron failure in situations such as vacuum loss or cooling system malfunction.

CS STRUCTURE AND OPERATION

All the accelerator systems (fig. 1) are combined into several subsystems: interlocks and alarm signal processing system and synchronization controller (accelerator controller); RF system and cooling system sensors; klystron and accelerating structure ion pumps; sulfur hexafluoride gas delivery system; electron gun supply control; dose rate with ion chamber measurements; cooling module and accelerator power supply control.

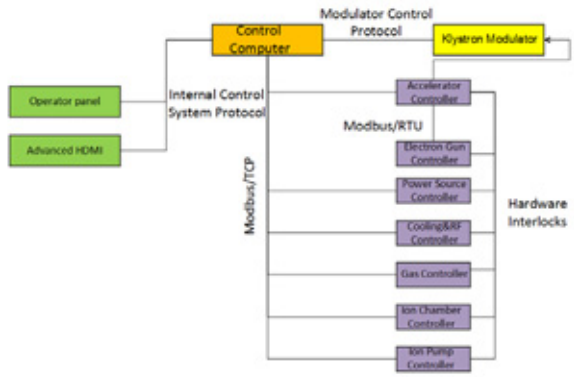

Figure 1: Control system structure.

Each subsystem contains a programmable controller which has the functions of receiving the primary sensor signals, transmitting control signals to actuators, controlling the system operation by incorporated algorithms and communicating with the host computer. The control system also includes a control computer, a network switch and the power source for its own needs.

Operator communicates to the monitor and control system using the control panel located in the control room and connected to the host computer via Ethernet interface. The accelerator network is also connected to the local enterprise network via a router. It can also be connected to a PC running the advanced HMI client program, which provides full access to the host computer and controllers. Local network provides access to the host computer and the individual controllers by the remote terminal over the Internet or private network.

Control computer functions are (1) providing the power supply accelerator on/off procedures and accelerator operation; (2) storing and loading operating parameters of

ISBN 978-3-95450-170-0

the subsystems; (3) maintaining the event lo and accumulation of statistical information related to accelerator operation; (4) to ensure operation in a remote location via the Internet

All controllers except the modulator controller communicate with the host computer via an Ethernet interface by the Modbus/TCP protocol. The RS-232 interface is used for communication with the modulator controller using proprietary ScandiNova protocol. The cooling module operates in standalone mode. To power on the cooling module the accelerator control system sends a signal of +24 V. The control computer and controllers are located in the X-ray head cabinet and connected via a network switch. The top level computer and operator panel are separate ARM-based machines running Debian GNU/Linux operating system. Optionally additional computers running Advanced HMI client software can be connected to the system. The control application is implemented using custom Lisp-based domain specific language (DSL) based on Hierarchical Finite State Machine (HFSM) formalism. The system has a number of states (fig. 2, on the left) that correspond to the states of klystron modulator (on the right). The control application's primary task is executing operator's commands by driving subsystems and the modulator in such way that they can function together correctly. Other tasks performed by the top level control application include maintaining the event log, support for maintenance tasks such as isolating gas replacement and relatively slow-running control tasks such as stabilization of acceleration section frequency. When an emergency situation is detected the system enters special "Fault" state which requires operator intervention.

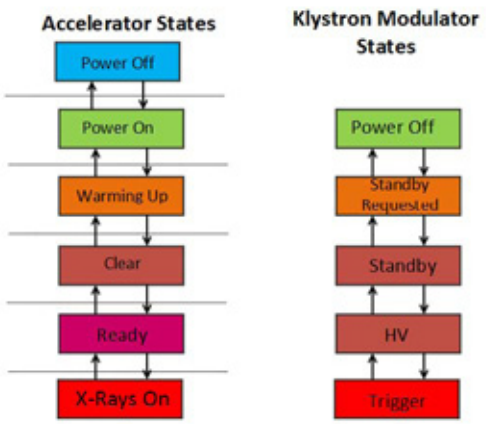

Figure 2: A diagram of control system states with corresponding modulator states.

The control computer provides the following three modes of the accelerator – operator interaction. (1) Production and maintenance works mode. (2) Single exposure beam energy, dose rate, integral dose settings, power on/off, X-ray on/off, emergency stop, the interlock status view. (3) Radiography operation mode, as well as shutdown and emergency shutdown of the accelerator.

The control panel allows the operator to perform all the necessary operations using keys and on-screen menu (fig. 3). The current state of the accelerator, energy and dose values, interlocks information is displayed on the console screen. The built-in speaker is used for sound notifications.

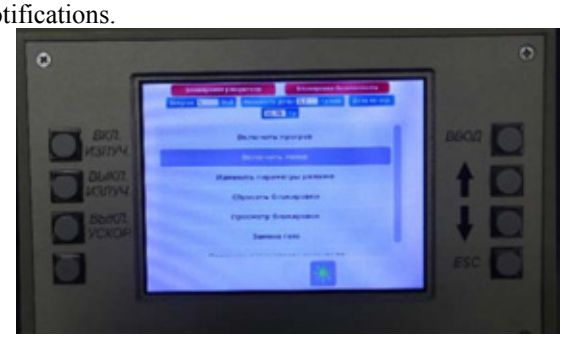

Figure 3: The control panel screen.

The controllers and control computer placement is shown on fig. 4.

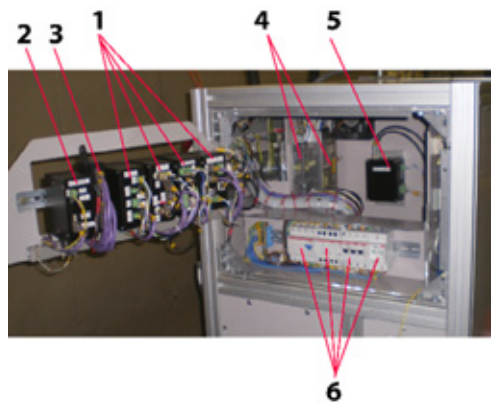

Figure 4: The controllers and control computer placement. 1 – controllers, 2 – control computer, 3 – network switch, 4 – power supplies 24 V, 5 - ion pumps power supply, 6 – switches and contactors.

SUBSYSTEMS CONTROLLERS

All controllers of the control system are based on LPC17xx series ARM microcontrollers [3]. It consists of three functional blocks implemented on a separate printed circuit boards (Fig. 5).

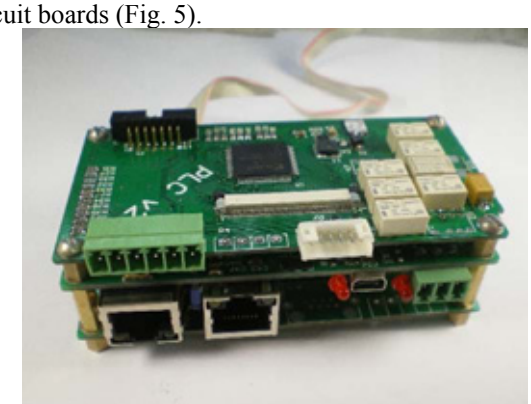

Figure 5: The accelerator controller without a box.

ISBN 978-3-95450-170-0

The controller consists of a CPU board, a synchronization board and an instrumental board. The CPU board function is receiving and transmitting data and commands from/to the control computer, communicating with DACs and ADCs located on the instrumental board via SPI and I2C interface, receiving and transmitting digital and analogue normalized signals from/to the instrumental board. The Ethernet controller is located on the CPU board and allows to communicate with control computer by Modbus/TCP protocol. A flash memory chip is also located on the CPU board. It allows to store the parameters required for controller operation. For example, there are amplifier normalizing factors, controlled device settings and so on. The instrumental board function is to normalize, receive and transmit signals from/to external sensors and devices. For example, the RF and cooling system controller structural diagram is shown on fig. 6. Figure 7 shows the placement of a controller of the RF and cooling system in the X-ray head cabinet.

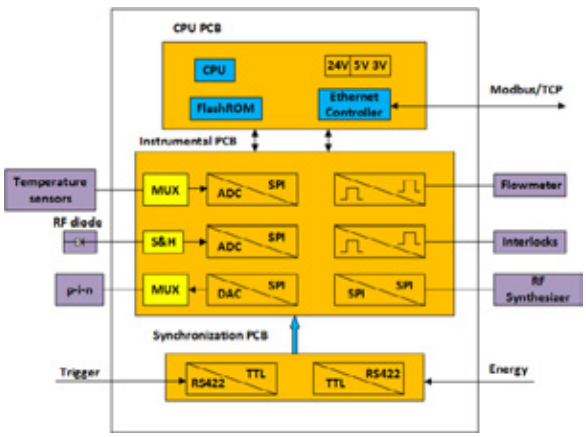

Figure 6: RF and cooling system controller structure.

In this case the sample-and-hold circuit used measure the RF field envelope amplitude, the p-i-n attenuator control circuit, the flow relays circuit, the circuit of flowmeter, temperature sensors signal processing, the interlock and RF pre-amplifier control optically isolated circuit are located on the instrumental board. The synchronization board is used to receive the trigger signal from accelerator controller via optically isolated RS-422 interface and to convert it to TTL. This signal synchronizes operation of the above-mentioned sample-and-hold and RF amplifier control circuits. The accelerator controller treats the hardware level interlock signals from the accelerator hall safety system, the modulator, the electronic key, subsystem controllers and from accelerator cabinet switches. In order to provide the interlock signal to the modulator and RF system the accelerator controller communicates with external safety system via standard +24V signals and open/close “dry” contacts.

The controller software utilizes a common Modbus/TCP stack based on uIP and FreeModbus library [4]. Each controller has its own IP address and supports several simultaneous Modbus/TCP connections. This can be used to debug the controllers without stopping the main control program. Coil and holding register values that represent controller settings are stored in controller EEPROMs. A special protocol used for coils (writable single-bit registers) that represent interlocks so that interlock signals are never missed by the control program. The control application maintains a database that maps controlled device parameters to Modbus registers. In case of communication problems with subsystem controllers the control system enters the fault state with corresponding operator notification.

Figure 7: RF and cooling system controller.

CONCLUSION

We have designed and manufactured the control system of accelerators for radiography and cargo inspection. The authors are grateful to Mr. A.V. Nalivaev for support of this work.

REFERENCES

[1] A.N.Ermakov et al., in these Proc.
[2] www.sc-nova.com
[3] www.nxp.com
[4] http://www.freemodbus.org

ISBN 978-3-95450-170-0

AUTOMATED CONTROL SYSTEM OF THE TARGET SYSTEM FOR PET RADIONUCLIDES' PODUCTION

P.A. Gnutov, M.L.Klopenkov, R.M.Klopenkov, A.N.Kuzhlev, A.A.Melnikov, A.P. Strokach,
JSC "D.V.Efremov Institute of Electrophysical Apparatus", St. Petersburg, Russia
B.V. Zabrodin, the St. Petersburg State Polytechnical University

Abstract

An automated control system of target system for production of PET-radionuclids has been designed. The system allows on-line obtaining of the data on the status of the target system and remote control of loading, irradiation and evacuation of the activity to synthesis modules.

According to algorithms available in the software, this system makes possible emergency situations to be prevented and incorrect actions of the operator to be blocked.

INTRODUCTION

Nowadays, the method of positron-emission tomography (PET) is widely used for diagnostics and in medical-biological investigations. This method is the most informative when observing the processes occurring in a human organism [1].

Short-lived and ultra-short lived radionuclides with the lifetime from 13 min to 2 hours are used for PET investigations. Such radionuclides can be produced on proton accelerators located directly in clinics. Cyclotrons of the CC-series [2, 3] designed and manufactured in NIIEFA in its radiation characteristics as well as in overall dimensions completely meet the requirements imposed today on cyclotrons intended for PET. However, until recently, these machines were not equipped with target systems.

At present, our Institute has delivered the 1st model of completely automated target system with the CC-18/9M cyclotron to JSC "NIITFA", Moscow. Fig.1 shows the general view of the target system with the cyclotron.

Figure 1: General view of the target system and cyclotron.

This target system is designed for 5 targets, 3 water and 2 gas, however, delivery with any set of targets is possible. The target system was tested at a beam current of 50 μA, and the target pressure was not more than 8 barr, which confirms a high efficiency of this system. In future, this will allow us to increase the intensity of the proton beam for production of radionuclides. When irradiating $H_2{}^{18}O$ with beams of accelerated 18 MeV protons, the calculated activity yield was 280 mCi/μA.In measurements, the activity yield of 200 mCi/μA was obtained for a 3-ml water target. Below in Table 1 are given activity yields of commercial target devices of leading world manufacturers.

Table 1: Activity yields bading world manufacturers

Manufacturing Companies	**Activity Yield**
IBA	240 mCi/μA
NIIEFA	200 mCi/μA
Triumf	200 mCi/μA[4]
Kirams	180 mCi/μA[5]
Syntra	137mCi/μA

Characteristics of the target system produced in NIIEFA satisfy the world requirements for yield ranges of such systems. In future, when testing the system we plan to increase the target pressure up to 20 barr, which will allow the beam current increase up to 100-120 μA.Works have been started on widening the assortment of water targets; production of 1-ml, 2-ml and an experimental 5ml targets are planned.

AUTOMATED CONTROL SYSTEM OF THE TARGET SYSTEM

The automated control system (ACS) of the target system consists of an operator's workstation and controller unit.

The Mitsubishi GT1275 panel was chosen for the control console of the operator's workstation, which allowed a high-quality user-friendly intuitive operator interface to be designed in the Russian language (see Figs. 2 and 3).

This interface allows remote loading of targets with target materials, unloading of the activity to hot cells and rinsing the target and capillaries connecting the target with hot cells. In the left part of the window, the execution of these programs can be observed in real time, i.e. valves' position, readiness of hot cells, filling of

ISBN 978-3-95450-170-0

syringe and target can be seen. In addition, all necessary data are displayed in real time:

- Availability of water and helium cooling
- Target pressure
- Helium pressure in the loop
- Helium flowing in the loop
- Time of target irradiation
- Time for activity unloading

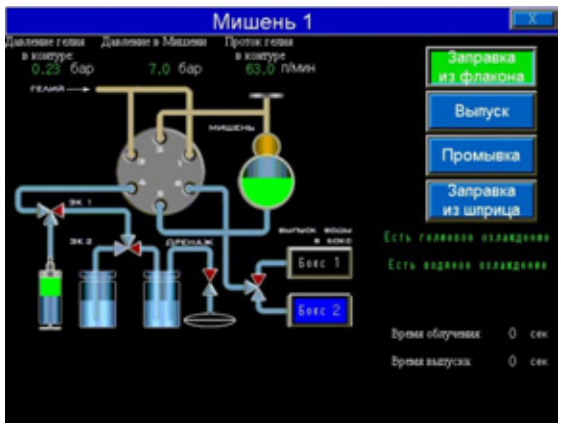

Figure 2: Window for operation with water target.

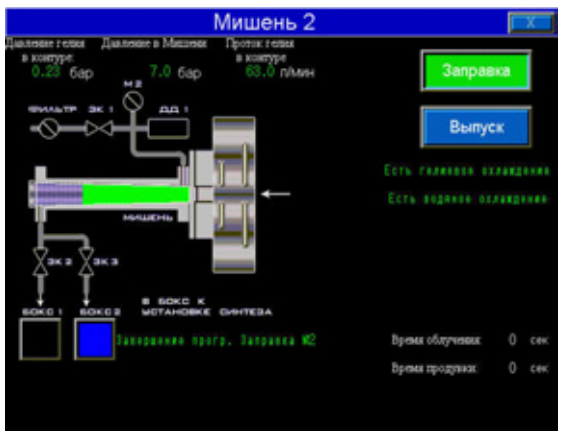

Figure 3: Window for operation with gas target.

The information about the termination of the program and failure messages are displayed at the bottom of the window. The control program interface is developed in the GT Designer3, which is included in a standard delivery set of the Mitsubishi software.

The controller block is the host device of the automated control system. It serves for acquisition, processing and analysis of the data on the status of the target system. The controller prevents emergency situations and disables incorrect operator's actions in accordance with an algorithm of the controller software.

The Mitsubishi FX3UC was chosen as a controller of the automated control system. Reliability, simple maintenance, high performance, relatively low cost and small size were governing factors for its choice. It was also taken into account that automatic control systems of the CC-series cyclotrons are also built on the basis of Mitsubishi FX controllers. Choice of these controllers makes simpler maintenance of both systems and reduces the time needed for the software development due to application of practical experiences used in ACS of the cyclotrons.

The control program of the target system was developed in the GX IEC Developer 7.03. The label diagram language (LD) was chosen as a programming language. Visualization of the status of the system and its components makes much more simpler both programming and putting into operation as well as troubleshooting in the equipment connected to the controller. In addition, use of functional units in the program makes it universal and allows the number and type of installed targets to be changed sufficiently simply.

CONCLUSIONS

When designing the ACS of the target system, the main criterion was reliable long-term operation of the equipment maximally simple in control and widely using visualization means. This ACS of the target system can be to be operated by personnel without special training in the field of ACS for sophisticated engineering systems. Due to control of target remote replacement, the efficiency of using the "beam on" time of the cyclotron is higher, and radiation exposure of the attending personnel is lower. On finishing the irradiation process, a target is removed from under the beam and replaced for another loaded target ready for irradiation. The produced activity of the 1st targetis unloaded to hot cells, and then this target is loaded with new target material. The ACS developed provided stable operation of the target system, which allowed us to obtain he activity yield ranges competitive on the world market.

REFERENCES

[1] B.V. Zabrodin, V.N. Lomasov, A.V. Motorny. Radionuclide Visualization Methods Teaching Guide. St.Petersburg, the St.Petersburg State Polytechnical University, 2006. 75 pp.

[2] P.V. Bogdanov, A.A. Budtov, M.F. Vorogushin, A.V. Galchuck, V.I. Ponomarenko, A.V. Sidorov, S.A. Silaev, A.P. Strokach, S.E. Sychevsky. Designing the CC-12 Cyclotron VANT, series "ElectrofizicheskayaApparatura", № 5 (31), St.Petersburg, 2010, pp. 1.

[3] P.V. Bogdanov, I.N. Vasilchenko, S.V. Grigorenko, E.A. Lamzin, V.P. Kukhtin, Yu.I. Stogov, A.P. Strokach, S.E. Sychevsky, N.F. Shilkin. The CC-18/9 Cyclotron Project Development and Implementation VANT, series "ElectrofizicheskayaApparatura", № 5 (31), St. Petersburg, 2010, pp.21-32.

[4] M. Stokely, B. Wieland. A high current pet target and compact beamline Bruce Technologies Inc., Chapel Hill, NC 27514, USA M.P. Dehnel, T.M. Stewart, D-Pace Inc., PO Box 201, Nelson BC, CANADA, V1L5P9 (2009).

[5] Report of the 3rd Research Coordination Meeting on "Improved High Current Liquid and Gas Targets for Cyclotron Produced Radioisotopes" (2009).

ISBN 978-3-95450-170-0

SYSTEM FOR REMOTE TARGET REPLACEMENT OF THE TARGET SYSTEM FOR THE CC-SERIES CYCLOTRONS

R.M. Klopenkov, E.N. Abramov, Yu.N. Gavrish, M.L. Klopenkov, K.A. Kravchuck, G.V. Muraviev, A.P. Strokach, JSC "D.V. Efremov Institute of Electrophysical Apparatus", St. Petersburg, Russia

Abstract

An automated system for remote replacement of target devices of the target system for cyclotrons of the CC-series has been designed. The system allows 1 of 5 available targets to be positioned under the beam of the cyclotron at the operator's choice. Such a technical solution allows us to have sufficiently smaller overall dimensions of the equipment and less time for servicing water and gas targets.

Separate system for target replacement is provided for each beam extraction, which allows the cyclotron to be equipped with 10 different target devices, and makes possible simultaneous irradiation of 2 targets.

INTRODUCTION

Nowadays, positron-emission tomography (hereinafter PET) is the most effective method for diagnostics of a wide spectrum of diseases including oncologic cases. This diagnostic method applies radiopharmaceticals, i.e. substances labeled with radionuclides, which are actively used in various metabolic processes occurring in a human organism.

To produce radionuclides, beams of accelerated particles are used to bombard targets containing target materials. [1]

In clinics and in commercial production of radioisotopes, of the first priority are the operational stability of radiopharmaceuticals' production systems, compactness of their size, multifunctionality, easy maintenance, low radiation exposure of the attending personnel and updating flexibility to meet the requirements of modern medicine and market [2].

In JSC "NIIEFA", energetic works are now underway on designing and preparation of serial equipment for production of radionuclides. Three models of cyclotrons for 12 MeV [3], 18 MeVB [4] and 30 MeV [5] as well as target systems for these machines have been designed and constructed.

At the end of 2013 in JSC "NIITFA", Moscow, a system for the production of radionuclides for PET on the basis of the CC-18/9M cyclotron was installed. At the stage of testing of the system, we managed to obtain the target yield ranges comparable with those of the latest-generation equipment of leading producers in the world. The main tasks to be solved when designing target systems are the reliability, easy maintenance-repair and versatility of the target system [6].

SYSTEM FOR TARGET REMOTE REPLACEMENT

To meet the demanding requirements of customers on widening the functionality of the target system, work on designing a system for targets' remote replacement was done. This system is intended for automatic setting of a chosen target under the beam of the cyclotron. The use of this system will allow: optimization of the cyclotron system configuration and minimization it's overall dimensions because of possibility to refuse part of ion transport system; possibility to furnish the cyclotron with larger number of targets; remote taking out of target devices from under the beam to reduce the induced activity before its removal and maintenance/repair.

The system for targets' remote replacement consists of 2 systems: a system for disconnection of a vacuum-tight joint between target devices and the ion tube of the cyclotron and system for the transport of target devices (see Fig.1).

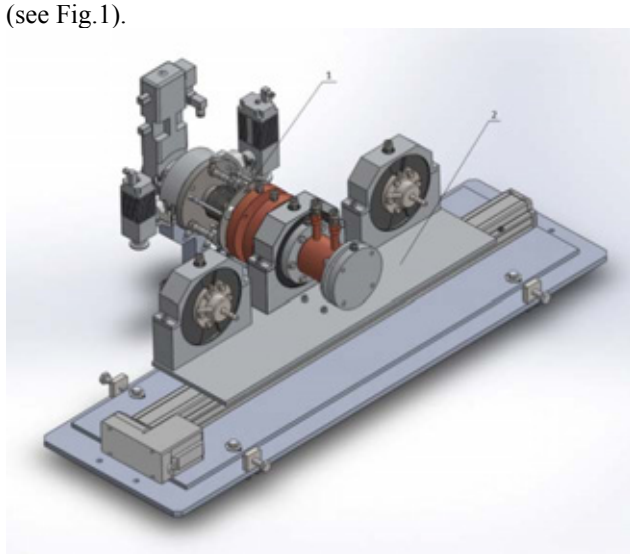

Figure 1: System for targets' remote replacement: 1- system for disconnection of the vacuum-tight joint between target devices and the ion tube of the cyclotron; 2- system for transport of target devices.

The first system provides remote disconnecton and connection of the vacuum-tight joint between the end flange of the ion tube and the target device flange. This operation is performed with 3 pneumatic cylinders compressing an intermediate bellow.

The system for transport of target devices consists of a linear electric drive with a step motor and target devices fixed on it. It makes possible transportation of a chosen

ISBN 978-3-95450-170-0

target device and makes it coincident with the ion tube axis accurate to ± 0.1 mm.

The process of a target device replacement is as follows:

1. A vacuum gate valve separating the ion tube of the cyclotron and the vacuum volume of the system for target remote replacement is closed. Air is in-leaked into the volume of the system for targets' remote replacement through a pneumatically-driven leak valve.
2. The vacuum joint between the ion tube and installed target device is disconnected when the intermediate bellow is compressed with 3 pneumatic cylinders.
3. The chosen target device is made coincident with the ion tube axis.
4. The vacuum joint between the chosen target and the ion tube is re-connected.
5. The volume of the system for targets' remote replacement is pumped out with the forevacuum pumping system of the cyclotron.
6. The gate valve is opened, and the system volume is pumped out with the high-vacuum pumping system of the cyclotron.

The use of standard collimator units and helium cooling systems allows the system for targets' remote replacement to be furnished with a set of target devices of different types and volumes produced in NIIEFA.

CONCLUSION

The system for targets' remote replacement allows us the following:

- to furnish the cyclotron with a set of targets of different types and yield ranges.To optimize the cyclotron system configuration and to minimize it's overall dimensions because of possibility to refuse part of ion transport system;
- to reduce the radiation exposure of the attending personnel.

This innovation technology can be applied:

- in commercial production of radionuclides and for widening the range of isotopes produced;
- when locating cyclotron systems in places limited in size.

REFERENCES

[1] JA B.V. Zabrodin, V.N. Lomasov, A.V. Motorny. Radionuclide Visualization Methods //Teaching Guide.St. Petersburg; St. Petersburg State Polytechnical University, 2006.75 pp.

[2] A.N. Syed M. Qaim Development of Cyclotron Radionuclides for Medical Applications: From Fundamental Nuclear Data to Sophisticated Production Technology.

[3] P.V. Bogdanov, A.A. Budtov, M.F. Vorogushin, A.V. Galchuck, V.I. Ponomarenko, A.V. Sidorov, S.A. Silaev, A.P. Strokach, S.E. SychevskyDesigning the CC-12 Cyclotron// VANT, series «ElectrofizicheskayaApparatura», № 5 (31), St. Petersburg, 2010, pp. 11-20

[4] P.V. Bogdanov, I.N. Vasilchenko, S.V. Grigorenko, E.A. Lamzin, V.P. Kukhtin, Yu. I. Stogov, A.P. Strokach, S.E. Sychevsky, N.F. Shilkin. The CC-18/9 Cyclotron project Development and Implementation // VANT, series «ElectrofizicheskayaApparatura», № 5 (31), St. Petersburg, 2010, pp.21-32.

[5] P.V. Bogdanov, A.A. Budtov, I.N. Vasilchenko, M.F. Vorogushin, S.V. Grigorenko, V.G. Mudroly, S.A. Silaev, Yu.I. Stogov, A.P. Strokach, S.E. Sychevsky, N.F. Shilkin. The MCC-30/15 Compact Cyclotron for Medicine with Variable Energy of Accelerated Ions // VANT, series «ElectrofizicheskayaApparatura», № 5 (31), St. Petersburg, 2010, pp.32-43.

[6] E.N. Abramov, Yu.NGavrish, P.A. Gnutov, M.L. Klopenkov, R.M. Klopenkov, K.A. Kravchuck, A.N. Kuzhlev, A.A. Melnikov, V.G. Mudrolyubov, G.V. Muraviev, A.P. Strokach , B.V. Zabrodin, A.V. Regel. Target System for the CC-Series Cyclotrons Designed and Manufactured in NIIEFA // Problems of Atomic Science and Technology, 2013, V. 6(88), Series "Nuclear Physics Investigation" (61), Pp. 201-204.

ISBN 978-3-95450-170-0

MODERNIZATION OF THE AUTOMATED CONTROL SYSTEM IN THE KURCHATOV SYNCHROTRON RADIATION SOURCE USING SitectSCADA

E. Kaportsev, A. Valentinov, V. Dombrovsky, V. Korchuganov, Yu. Krylov, K. Moseev, N. Moseiko, S. Schekochikhin, RRC Kurchatov Institute, Moscow, Russia
Yu. Efimof, CJSC RTSoft, Moscow, Russia

Abstract

The running cycle of Kurchatov Synchrotron Radiation Source (KSRS) includes the injection of electrons with energy 80 MeV from the linear accelerator in the booster storage ring Siberia-1, the accumulation of a electron current up to 400 mA and, then, electron energy ramping up to 450 MeV with the subsequent extraction of electrons in the main ring, storage ring Siberia-2, and accumulation there up to 300 mA, and at last the energy ramping up to 2.5 GeV. [1]

Several years ago, a modernization of the current system of automated control systems (ACS) has started. Modernization has affected the most important parts of the system - the system of data collection and monitoring system. Used advanced solutions based on CAN and VME and modular complexes National Instruments. Currently begins implementation of the SCADA system of Sitect.

In this paper the stages of implementation of the SCADA control system. Showing part of the system, which is already widely used, as well as parts of the system, which is scheduled to launch in the near future.

DESCRIPTION AND OPERATION OF ACS

Appointment of ACS

The current system of automated control systems (ACS) accelerating-storage complex (UNK) "Siberia" - a synchrotron radiation source and the center of collective use of NRC "Kurchatov Institute" was created over 20 years ago on the basis of control equipment in the CAMAC standard. [2] It is physically and obsolete and do not meet modern requirements for speed, accuracy of measurements and speed of data transmission.

Control apparatus of the new ACS UNK with embedded processors, as well as to powerful servers with the operator's computer and network equipment has developed software at all levels of the ACS. [3] All of this should be used to create a modern system of ACS ESC "Siberia" which should significantly increase the speed control parameter stability and reliability of the SR source.

Structural diagram of ACS "Siberia"

Hardware complex (TCC) ACS ESC "Siberia" has a hierarchical structure.

The first (lower) level is the level of local systems. At the level of local systems of CCC ACS UNK transferred command of the actuators, and the level of local systems in CCC ACS UNK receives signals from the sensors parameters of field equipment.

The second level is the level of control. The second level includes a cabinet controller and control panels that form the management team of the actuators, as well as receiving signals from the sensors parameters of field equipment.

The third level is a local area network (LAN), combining the second level control cabinets with cupboard fourth server - the server level. Used for data transmission copper and fiber optic cable lines.

The fourth level includes a cabinet server provides storage and management of data communications between the control cabinets belonging to the third layer structure, on the one hand, and data on the LAN of the upper level, on the other hand.

The fifth level is the top-level LAN, server cabinet combines the fourth level and workstations (AWP) of the sixth level. To transfer data to the LAN using copper and fiber optic cable lines and LAN switches.

The sixth layer is a set of workstations, comprising the following ARM professionals:

- Operator workstation CitectSCADA
- ARM Developer CAN
- ARM developers CitectSCADA
- ARM Developer VME

Structural diagram of ACS "Siberia" is shown on Fig.1.

HARDWARE COMPLEX OF ACS

The composition of program-technical complex (PTC) ACS ESC "Siberia" includes the following products:

- cabinets and equipment;
- basic software (SCADA-system, operating systems);
- application software;
- Spare parts for the warranty period of the PTC.

ISBN 978-3-95450-170-0

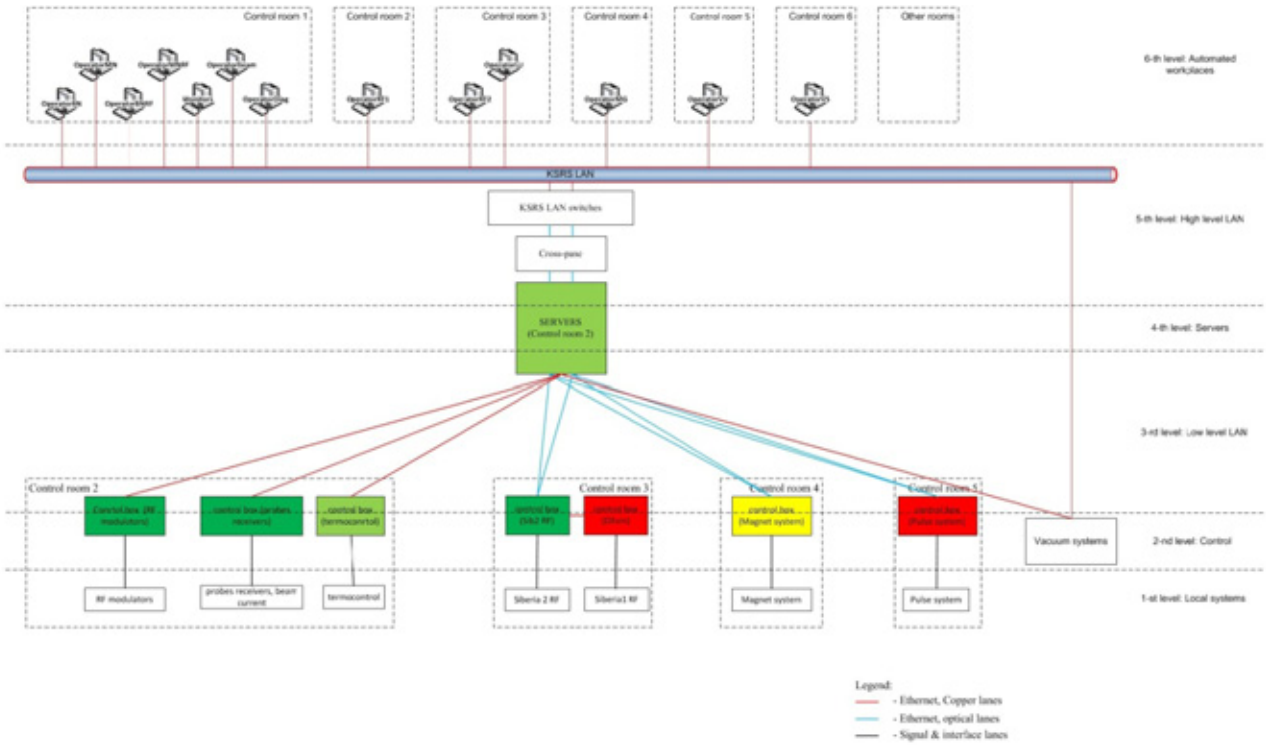

Figure 1: Structural diagram of ACS "Siberia".

ACS is also working with the controllers of local management systems that are part of the following process units:

Controllers of local management systems of Siberia-1:
- RF System;
- Magnetic system;
- Pulse system;
- System synchronization;

Controllers of local management systems of Siberia-2:
- RF System;
- Magnetic system;

Vacuum system Server [4];
- MS SQL Server;

Controllers of local control and local devices:
- System temperature control;
- System diagnostics beam.

SOFTWARE

Software for imaging systems ACS "Siberia", is a series of applications developed in the environment of CitectSCADA 7.2 SP4. These applications are part of the software, as I / O servers and workstation operators control subsystems UNK "Siberia."

The visualization system has the following composition of applications:

- application UNK_Termocontrol;
- application UNK_Magnit;
- application UNK_Vacuum;
- application UNK_VCH;
- application UNK_Diagnostic;
- application UNK_Config;
- application UNKSibir;

Each application contains a graphical information management subsystems UNK "Siberia."

UNK_Config - contains configuration information, as well as variable input / output control on all subsystems. Annex UNK_Config configured redundancy, both servers and I / O devices.

Appendix UNK_Config includes 2 clusters:
- DIAG_TERM_VACUUM;
- Control actuators;

UNK_Termocontrol - contains graphic characters for displaying temperature values on the flanges of the cavity of the linear accelerator, temperature gun linear accelerator, temperature correctors, lenses and bending magnets, small storage, EOC -1 and six superperiod large drive.

UNK_Magnit - contains graphics to display current values TPV power sources, power supply voltage values shunts TPV, setpoint current power sources for TPV bending magnets and large lens drive, as well as the currents of power supplies, the current values of the load, the voltage in the load, temperature transistors, inductors, current setpoint sources of supply for proofreaders large and small storage and EOC - 1.

UNK_Vacuum - contains graphic symbols to display the status of the pumps of the vacuum system, the currents and voltages. Just UNK_Vacuum application keeps a record of currents and voltages in the system vacuum pumps CitectHistorian 4.3 storage history. If

ISBN 978-3-95450-170-0

necessary, it is possible to view the historical data in the form of trends.

UNK_VCH - contains graphics to display the RF system. Current cathodes heated, currents and voltages of screen and control grids, RF voltages on the anodes, and the inputs and outputs of stages generators G1 and G2. Otobrazhaetznacheniya voltages and phase resonators 1,2 and 3, the currents and voltage feeders resonators incident and reflected waves. It is possible to adjust the position of the phase shifters, as well as provisions setting fifth stages generators G1 and G2.Displays the status of locks and keeps a log of alarm and warning messages to the operator.

UNK_Diagnostic - contains graphic characters for displaying states of samplers and receivers diagnostic system is also possible to control the position of probes and receivers.

All applications are included as projects in **UNKSibir** (Fig. 2), which runs on all the workstations and servers for system visualization. UNK_Sibir has access to all the applications included in it and can display any video frame of each subsystem management

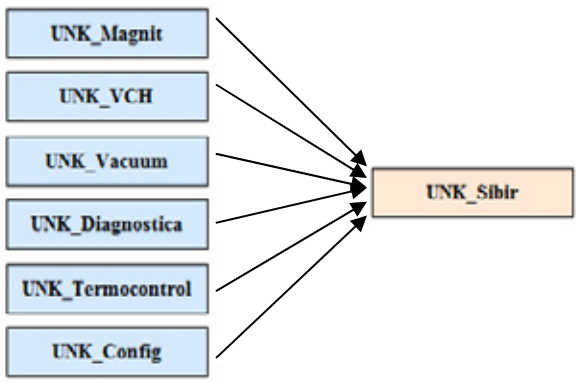

Figure 2: Application Structure CitectSCADA.

CONCLUSION

Currently installed and commissioned rack servers, temperature control, diagnosis, and monitoring of the RF generator. The structure of the database control channels and archive parameters of the complex, debugged software for thermo control and thermal stabilization, vacuum control, control of receivers and SI probes beam position. During the development of the control system is the operating cycle of SRS, which includes server and mainframe systems magnetic RF system.

REFERENCES

[1] V.Korchuganov et al., Kurchatov Synchrotron Radiation Source Facities Modernization. Proceedings of RuPAC XXII, Protvino, Russia, 2010.

[2] E.Kaportsev et al., The Expanded Program Tools for KSRS Operation with Archivation of Data. Proceedings of RuPAC XXII, Protvino, Russia, 2010.

[3] E.Kaportsev et al., Modernization of the automated control system in the Kurchatov synchrotron radiation source. Proceedings of RuPAC XXIII, S.-Petersburg, Russia, in 2012.

[4] N.Moseiko et al., Modernization of the Vacuum System of Synchrotron Radiation Sources at the National Research Centre Kurchatov Institute. Physics of Particles and Nuclei Letters, 2012, vol.9, No.4-5, pp.456-460.

ISBN 978-3-95450-170-0

ELECTROSTATIC PICK-UPS FOR DEBUNCHED BEAMS AT INR LINAC

S. Gavrilov, P. Reinhardt-Nickoulin, I. Vasilyev
Institute for Nuclear Research of Russian Academy of Sciences, Moscow, Russia

Abstract

Pick-ups are one of the most widespread non-destructive diagnostics at charged particle accelerators. These detectors, also known as beam position monitors, are generally used for the center-of-mass position measurements of bunched beams. The paper describes the research results for infrequent case of debunched beams operation. Measurement peculiarities and distinctive features of electronics are presented. The results of test bench-based measurements and 3D finite element simulations are discussed.

INTRODUCTION

The main idea of pick-ups is to measure the charges induced by the electric field of the beam charged particles on an insulated conductive plates [1]. For a bunched beam the measurement is performed using radio frequency methods [2]. However in case of a debunched beam it is transformed into measurement of quasi-steady-state charge during a macropulse. The name "electrostatic pick-up" is better suited for this application, which became urgent recently at multipurpose research center (MRC) based on the linear accelerator of INR RAS. For some time passed the beam is accelerated up to 209 MeV of 600 MeV and is transported near $L_{Drift} \approx 400$ m to the research facilities without acceleration. Due to the momentum spread ($\Delta p/p \approx \pm 3.5 \cdot 10^{-3}$ at the base) the beam bunch structure ($T_{Bunch} \approx 200$ ps, $f_{RF} = 198.2$ MHz) is lost and the measurements are done for the debunched coasting beam [3].

THEORY FORMALISM

INR electrostatic pick-ups consist of two pairs of cylindrical signal split-electrodes with so-called "linear-cut" (Figure 1). Projection of the cut between adjacent electrodes on the vertical and horizontal planes is a diagonal line. Three guard rings at ground potential minimize asymmetric fringe field effect and reduce cross-talk between pairs.

It is known, that in linear-cut pick-ups induced charges are proportional to the actual plate length at the beam center-of-mass position [1].

In ideal 2D electrostatic approximation for cylindrical split-electrodes with inner radius R beam positions are determined by Difference of the charges over their Sum (DoS) [4]. In practice, because of the capacitive coupling between the adjacent electrodes and asymmetry of the electric field at their edges, positions are:

$$X = K_X \frac{\Delta Q_{Horizontal}}{\sum Q_{Horizontal}} + \delta_X, Y = K_Y \frac{\Delta Q_{Vertical}}{\sum Q_{Vertical}} + \delta_Y,$$

where K_X, K_Y – "pick-up constants" (the smaller the K, the larger the DoS for the same beam position), and δ_X, δ_Y – so-called "pick-up offsets" of the geometrical center with respect to the electrical center, defined by $\Delta Q = 0$.

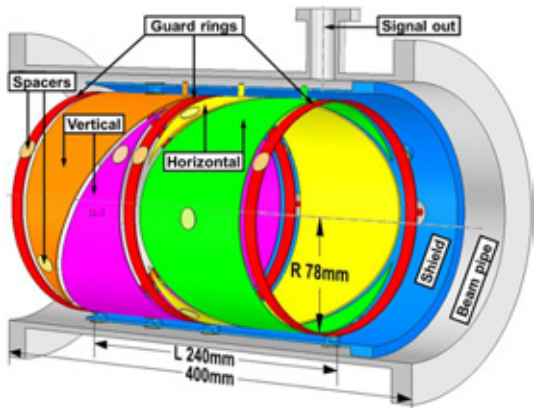

Figure 1: 3D-design of INR electrostatic pick-up.

BENCH-BASED CALIBRATION

Prior to the beam operation it is necessary to map the relationship between the beam position and the DoS, which is actually measured. A simple test bench was assembled for this purpose. The test bench consists of a copper pipe (10 mm diameter) placed between two grid dielectric plates at either sides of the pick-up. The copper pipe rests in two corresponding holes in the front and back grid plates and can be manually positioned accurate within ±0.5 mm. A signal generator produces a voltage pulse (500 mV, 100 μs, 50 Hz) at the pipe, imitating the debunched proton beam.

Electronics

Pick-up-based measurements require a conversion of beam-induced charge on detector plates to voltage. Generally, plate charge Q_p is integrated on the total pick-up capacitance C_p, producing voltage $V_p = Q_p/C_p$. Then voltage amplifier (Figure 2a) is used to provide gain. C_p is composed of a pick-up plate-to-ground capacitance (~110 pF for INR pick-ups) plus the capacitance of the interconnecting cable.

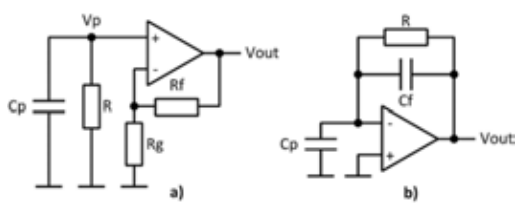

Figure 2: Pick-up electronics operation modes: (a) voltage amplifier, (b) charge amplifier.

ISBN 978-3-95450-170-0

Alternatively it is possible to perform conversion and amplification in one step by means of charge amplifier (Figure 2b). Unlike floating potentials of the electrodes in case of voltage amplifier, charge amplifier actively keeps the electrodes at zero potential. Its output voltage is always $V_{out} = -Q_p/C_f$ and depends on feedback capacitance C_f only, so pick-up calibration can be done with an arbitrary cable length.

For the same V_{out} voltage amplifier has lower noise than charge amplifier but this difference diminishes for large gains. Charge amplifier using operational amplifier with JFET inputs and C_p = 110 pF, C_f = 10 pF, R = 100 MΩ was built for the test bench. With second stage gain of 10 and input referred noise of 16 nV/√Hz, the output noise is 15 mV peak-to-peak.

High value resistor R defines DC gain and provides a path for the bias current to flow. In parallel with C_p or C_f it forms a high pass filter that causes pulse droop. Small droop can be assumed as linear for compensation by simple baseline restoration algorithm after digitization.

Pulse droop is about 10% for 100 μs beam pulse and component values mentioned above. Besides plate-to-ground capacitances C_p there is a capacitance, which consists of plate-to-plate capacitance of the detector (a few pF for INR pickup) and mutual capacitance between the signal wires.

The RF component of the signal due to the residual modulation of the beam is outside the amplifier bandwidth. Therefore, in a first approximation, the output signal of the amplifier corresponds to a steady component of the beam electric field, which is determined by the average pulse current of the beam. The convenient feature of DoS-measurement is that common mode hum is subtracted from the weaker signal corresponding to beam position and does not spoil it.

Test Results

Results of bench-based measurements for horizontal plane (Figure 3a) show expected DoS linearity across the whole aperture of the pick-up, though the sum and the difference are nonlinear per se. Deviations from the linear fit are smaller than ±0.5%. Constant K_X = 75.3 mm is 3.5% better than 2D-ideal approximation and is primarily caused by variation of beam pipe shape and size near the electrodes in spite of guard rings presence [4]. The offset δ_X = 2.7 mm is observed. For vertical plane $K_Y = K_X$, but the offset δ_Y = 4.1 mm.

As expected, the obtained results are independent of the total pick-up capacitance. The pick-up operation as a current monitor is complicated because of considerable nonlinearity of the sum signal.

Taking into account electronics noise ±7.5 mV of the sum and the difference signals, one can estimate the pick-up resolution (precision) ΔX specifying the ability to measure small beam position displacements $X_{real} = X_{measured} \pm \Delta X$ (Figure 3b). It is about ±0.5 mm around the work region for the electrodes signals induced by 0.5 V voltage at the test pipe.

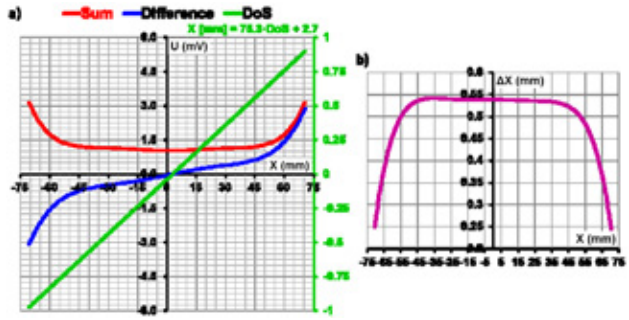

Figure 3: (a) Bench-based calibration results for horizontal plane. (b) Position resolution.

The pick-up accuracy specifies the beam position offset relative to the known fixed origin, for instance the symmetry axis of a quadrupole doublet, and is mainly determined by the pick-up offsets (δ_X, δ_Y) as well as mounting tolerances.

SIMULATION-BASED CALIBRATION

Conductive wires or pipes are usually used as beam imitators for test bench-based measurements. However it is obvious, that conductive object with uniform surface distribution of a fixed voltage cannot be an equivalent of a beam charged particles distribution. Therefore we need a complementary method for pre-tests based on 3D finite element simulations, for example, using ANSYS code.

Firstly, electrostatic equivalence between the model and a real pick-up must be established. For this purpose the bench-based measurements with copper pipe are reproduced in simulations. The results are in good mutual agreement: linear dependences $X[mm] = 75.3 \cdot DoS + 0.5$ for horizontal plane and $Y[mm] = 75.3 \cdot DoS - 0.8$ for vertical plane. Offsets δ in the simulation results indicate slight asymmetry of the electric field caused by asymmetric positions of the electrodes with respect to the shield edges. The greater quantities of experimental offsets are determined by manufacturing mechanical tolerances. Also results independence of the total pick-up capacitance is confirmed.

Beam Position Measurements

A debunched beam is simulated as five nested coaxial vacuum-material "pipes" with the outer radius 5/4/3/2/1·σ_{beam} = 2 mm and the central cylinder with radius 0.5·σ_{beam}. To decrease the edge effects the simulation region of the beam and beam pipe are extended up to 690.5 mm. The total charge corresponds to 10 mA pulse proton current (typical beam current).

The 2D Gaussian distribution of charged particles in cross section of the real beam is approximated by percentage discretization of the total charge into the σ-charges with following uniform distribution of these σ-charges inside volumes of congruent components of the beam model. Simulations show that a beam "surface" voltage distribution (Figure 4) differs considerably from the uniform surface voltage distribution of a conductive pipe, and this difference increases with a beam offset.

ISBN 978-3-95450-170-0

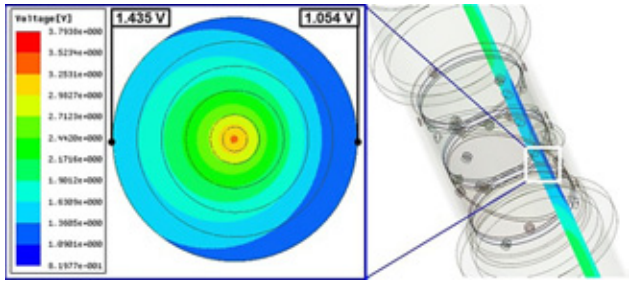

Figure 4: Voltage distribution in the beam with σ_{beam} = 2 mm and position (X_C = 60, Y_C = 0).

This effect provides expected qualitative changes of the electrodes responses. The sum and the difference signals dependences lose non-linear tails, so current measurement becomes possible, whereas the DoS dependence is retained perfectly (Figure 5a).

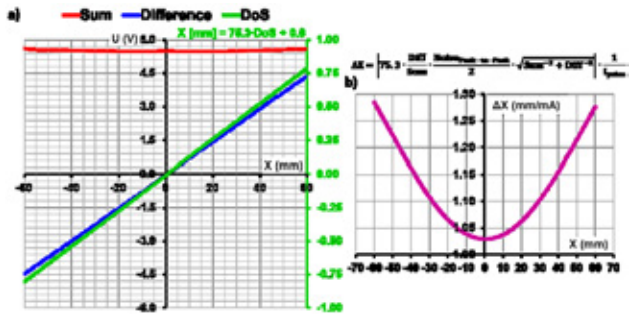

Figure 5: (a) Simulation-based calibration results for horizontal plane. (b) Position resolution.

Besides, the resolution increases together with the beam position offset, but $\Delta X < 130$ μm across the whole aperture for a typical pulse current of 10 mA (Figure 5b). Consequently, bench-based measurements with conducting pipe are suitable for DoS calibration, but can obscure extra pick-up applications.

Extra Measuring Capabilities

Because position, RMS size and pulse current of the beam can be varied during the accelerator operation, it is necessary to compare results for different typical cases.

The comparison of electrodes responses for different position offsets shows that the horizontal-vertical coupling is within the measurement errors (Figure 6).

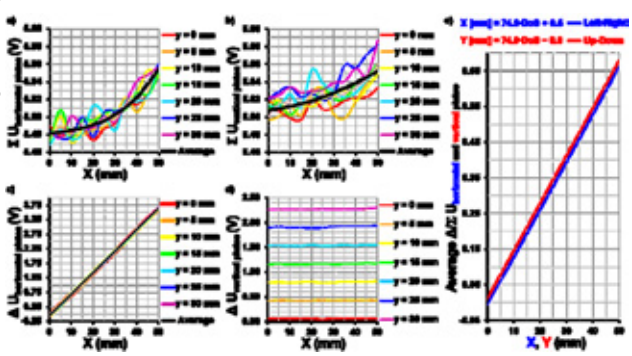

Figure 6: Results for different position offsets.

The comparative simulations for different σ_{beam} with the same total charge show consistency of the results. Besides the electrode responses are directly proportional to the beam pulse current as expected.

As a result, current monitor mode of the pick-up operation is confirmed. The simulated sum signal for 10 mA beam pulse current is about 5.5 V. Consequently, the resolution of current measurements with ±7.5 mV electronics noise is about 30 μA, that enable to cover the entire range of beam pulse current at INR accelerator.

The sum signal deviations because of the beam position and RMS size are less than 0.5%. The relative error of current measurements is less than 3% and is mainly determined by a small nonlinearity of the sum signal dependence. The current measurement capabilities can be used for beam losses monitoring of high-intensity beams at long sections between two electrostatic pick-ups.

CONCLUSIONS

Linear-cut electrostatic pick-ups can serve as multipurpose non-destructive diagnostics for debunched beams. The research for INR RAS linac shows, that for typical beam parameters pick-ups enable to measure beam center-of-mass position with the resolution about 0.2 mm, which corresponds to about 0.1% of the aperture. The initial accuracy can be worse by an order of magnitude and is mainly determined by mechanical tolerances.

Signal-to-noise ratio is limited by total detector capacitance, therefore it is necessary to use a preamplifier, either of voltage or charge type, connected to pick-up with short cable. Charge amplifier is more convenient, because its output signal is independent of total detector capacitance and pick-up calibration can be performed with arbitrary cable length.

Beam current measurements are confirmed and quantified by 3D electrostatic finite element simulations as more beam-similar calibration method, than a test bench with conducting pipe, imitating a beam. The resolution of current measurements is determined by electronics noise of the sum signal and is about 30 μA. The relative error of current measurements is mainly determined by nonlinear variations of the sum signal because of beam position and size and can be decreased down to 0.5% according to simulated dependences.

REFERENCES

[1] P. Forck, P. Kowina, D. Liakin, Beam position monitors, CERN Accelerator School, 2008.

[2] T. Bogey et al., LogAmp electronics and optical transmission for the SPS beam position measurement system, 2013 JINST 8 C12008.

[3] V. Moiseev, Study of low energy operation for INR proton storage ring, Probl. Atom. Sci. Tech. 5 (2008) (in Russian).

[4] B. Pine, Position monitoring on the ISIS synchrotron, in proceedings of CARE-Conf-06-087-HHH.

ISBN 978-3-95450-170-0

DEVELOPMENT OF REMOTE CONTROL SYSTEM FOR H-MINUS IONS SOURCE OF INR LINAC

O.M. Volodkevich, V.N. Zubets, Yu.V. Kiselev, V.S. Klenov
Institute for Nuclear Research, Russian Academy of Sciences, Moscow, Russia

Abstract

A system of remote control of surface – plasma source of negative ions for INR LINAC was designed, constructed and put into operation.

The INR LINAC negative ions injector is based on the accelerating tube at energy of 400 keV and surface – plasma source of negative ions. Galvanic isolation and spatial separation of elements that are at potential 400 kV in the power rack of the ion source and the host computer are carried out by means of fiber-optic USB-interface extender from firms Icron. A set of multifunctional units from National Instruments allows to monitor the oscilloscope signals with up to 50 Ms/s and to control the ions source power settings. The data acquisition devices programming performed in a LabView graphical environment. Algorithm and LabVew code for fast and safe "conditioning" of the ion source discharge gap and extractor gap from arcing and breakdowns were developed.

INTRODUCTION

Negative ions injector for INR LINAC is based on the accelerating tube at energy of 400 keV [1]. In this scheme, an ions source with its power supply system is located under pulsed potential of 400 kV. Ions source is a surface-plasma source developed at INP SB RAS (Novosibirsk) [2]. In this source the increase of the negative ions yield achieved by reducing the work function of the electrodes by deposition on its surface the layer of alkali metal (cesium).

A characteristic feature of the source is the presence of several modes, which have different discharge voltage, discharge current and the output of negative ions."Pure hydrogen" mode of operation is characterized by high discharge voltage (400 V - 600 V) and low discharge currents (1 A - 10 A).The appearance in the discharge of cesium vapor causes decrease in discharge voltage (to 100 V - "low-voltage operation") and increase in the discharge current up to ~ 100 A. Furthermore, in the discharge gap may develop arcs with very low discharge voltage ~ (20 - 40) V and high current. Arcs can lead to significant erosion of the electrodes and are characterized by the absence of negative ions current at the output of the source.

Extraction of the negative ions from the plasma of a gas discharge occurs through the emission hole in the anode by apposition of extracting voltage with amplitude of 16 - 20 kV to the extracting gap with size of about 1.5 mm. Breakdowns in this gap can cause increased erosion of the electrodes and are also characterized by lack of output current of negative ions. Such breakdowns occur with the source electrodes training and during normal operation of the source.

The transition from "high-voltage" discharge mode in the "low-voltage" mode can occur quite quickly. The change in the discharge voltage is an indication of the emergence of cesium in discharge and is usually accompanied by a change in the intensity of H-minus beam.

This rather complex behavior of the discharge and the dependence of the negative ions yield from the history of the source, cause the urgent need for a reliable detailed control of key parameters of the source, which works with a pulse repetition rate up to 50 Hz. To do this, the operator is required to monitor the pulse waveforms of discharge current and discharge voltage, extracting voltage, extracted current of the H-minus ions and others, as well as to control a variety of continuous signals.

The use of the ions source in the injector of LINAC requires some additional conditions on the control system. In particular, it should be possible to integrate it into the control system of the linear accelerator and to choose the different places for the entrance to the source control system, including from the main control room of the LINAC.

STRUCTURE OF THE CONTROL SYSTEM

The control system is based on the connection of multi-function ADC / DAC units to the host computer via the USB-interface. The control system includes multi-function ADC / DAC unit NI USB 6363s, digital oscilloscope unit NI USB 5132, the control computer and fiber-optic extension of the USB-interface Ranger 2224. Block - diagram of the control system is shown at Figure 1.

ISBN 978-3-95450-170-0

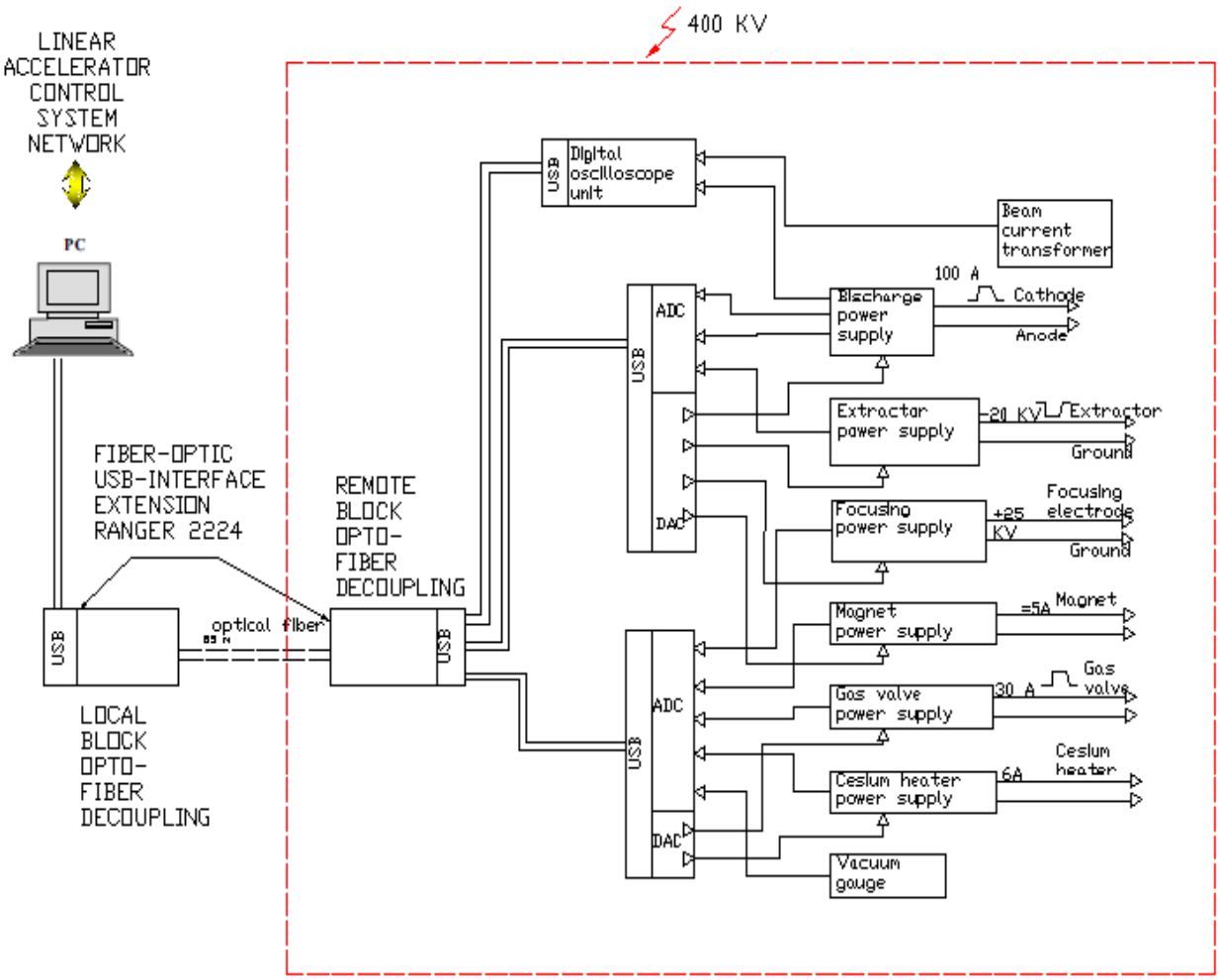

Figure 1: The block diagram of the remote control system of negative ions source.

This system allowed galvanically isolate and spatially spread at considerable distance (about 80 m) equipment of control system and host computer of the ion source operator. In this case, retains all the advantages of working with devices via USB-interface. The system provides a connection in the USB 2.0 standard at 480 MB/s, which allows you to connect a digital 2-channel oscilloscope with a bandwidth of up to 50 Ms/s, and the required set of ADCs and DACs.

PROGRAMMING

The data acquisition devices programming performed in a graphical environment LabView (2010 version). Using programmable blocks allowed to begin the development of the algorithm to control the blocks of power supply system of the ion source with the aim of lifting the parameters to the desired level, "conditioning" of the discharge gap and extractor, maintaining the specified parameters for a long time unattended.

In the development of the control algorithm, experimental work has been done to find the most optimal speed for changes of settings both in regular way to put ion source in the operating mode and in the case of an "emergency" situations. In the result "conditioning" of the ion source and putting it to the operating mode by using this algorithm and developed program allows it to increase the stability and reproducibility of the parameters, reduces the response time to changing conditions in the gas discharge (occurrence of breakdown, rapid transitions from "low-voltage" discharge mode to "high-voltage" and others). In particular, the program's reaction to the appearance of breakdowns in extracting gap and subsequent recovery of operating mode is shown in Fig. 2.

The example of the programmable transition of ion source in the operating mode with the adjustable parameters of the discharge current (Id) and extracting voltage (Uo) shown in Fig3.

ISBN 978-3-95450-170-0

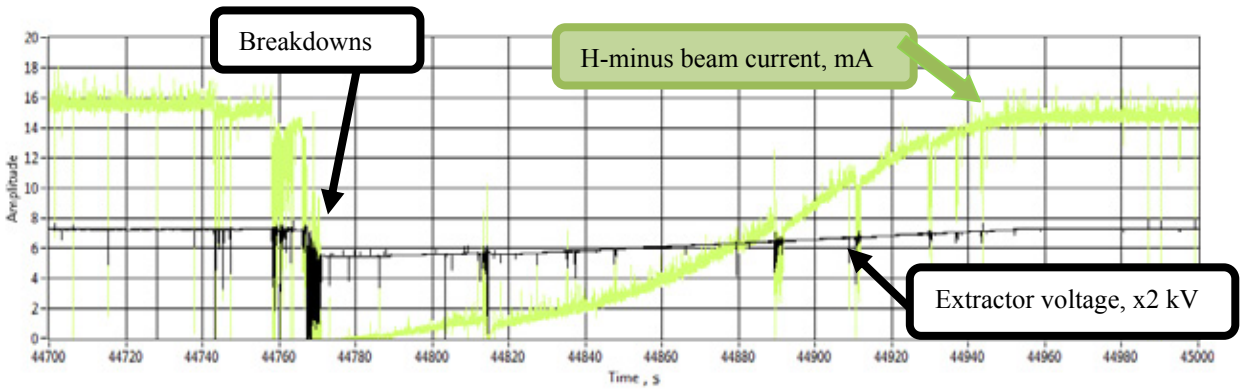

Figure 2: Example of processing by control program breakdowns in the extracting gap voltage (Uo) and restore the beam current (I-).

As characteristic of the quality settings of the ion source can serve relative standard deviation of the measurements of the pulsed ion beam current of H-minus ions. A value of pulse signals in each pulse is obtained by averaging 20 measurements with a period of 5 ms for the middle part (100 ms) of pulse.

The relative standard deviation in the values of pulsed H-minus beam current was achieved by this program less than 1% of the mean pulse current.

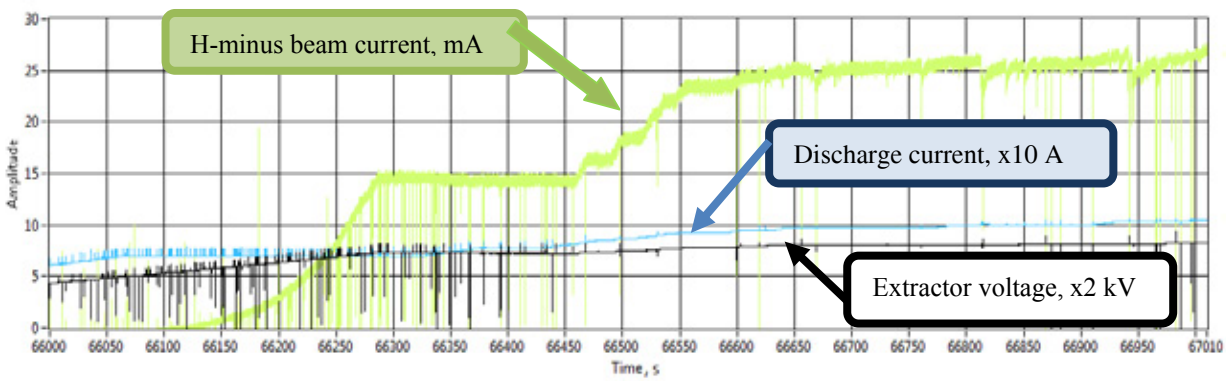

Figure 3: Example of lifting extracting voltage (Uo) and discharge current (Id) by control program and reaching the H-minus ion beam (I-) current 26 mA.

CONCLUSION

The remote control system of negative ions source can adequately control the operating modes of the source, ensuring the completeness of the resulting information on the control computer screen. System allows for programmable control of the ADC units for the purpose of "conditioning" of the ions source, outputting it to the operating mode and maintain over long periods of time."Conditioning" of the ion source using software control of power settings allow you to achieve the stability of the ion beam at the output of the source of better than +-1%.

REFERENCES

[1] A.S. Belov, V.I. Derbilov, S.K. Esin,e.a., “H- injector for Moscow meson factory LINAC”. Problems of atomic science and technology.Series: 52 Nuclear Physics Investigations (46), 2006. № 2.p.52-54.

[2] G.I. Dimov, G.E. Derevyankin, and V.G. Dudnikov, “A 100-mA negative hydrogen-ion source for accelerators”, IEEE Trans. Nucl.Sci.24, p. 1545 (1977).

[3] O.M. Volodkevich, V.N. Zubets, Yu.V. Kiselev, V.S. Klenov, “Remote control system for H-minus ions source of INR LINAC”, Problems of atomic science and technology. Series: 52 Nuclear Physics Investigations (68), 2013 №6, p53.

ISBN 978-3-95450-170-0

USE OF FAST MAGNETIC BEAM RASTER SYSTEM FOR INR ISOTOPE PRODUCTION FACILITY

O.Volodkevich, S.Bragin, A.Feschenko, O.Grekhov, Yu.Kiselev, V.Kokhanyuk, V.Mikhailov, A.Mirzojan, V.Serov, Institute for Nuclear Research of RAS, Moscow, Russia

Abstract

Fast magnetic beam raster system for INR isotope production facility is developed and implemented. The system enables to increase the isotope production efficiency by providing a possibility of using a higher intensity proton beam on the target of the isotope production facility. First experimental results of system application for irradiation of the targets are presented.

INTRODUCTION

Interaction of the pulsed proton beam with the irradiated target results in fast (during the beam pulse) local heating of the target material. So the target material density is decreased, consequently, the efficiency of beam interaction with the target is decreased too. This effect causes limitation of beam intensity on the target and restricts the possibilities of isotope production. The problem can be solved by reducing the beam density on the target. But one cannot just increase the cross section of the beam for the existing configuration of the irradiation facility and beam extraction line. Increasing of beam cross section is provided by fast circular or elliptical scan of the beam on the target. Thus, the heating of target material is reduced, consequently, the beam intensity and irradiation efficiency can be increased. Fast beam scanning on the target is done by the Beam Fast Scan System (BFSS), which has been developed [1] and installed upstream the target. Target irradiation is carried out at beam energies from 100 MeV up to 158.6 MeV.

THE STRUCTURE AND PARAMETERS OF THE SYSTEM

Beam scanning is performed by means of its deflection in two mutually perpendicular alternating magnetic fields having the same frequency and quarter period phase shift. Mutually perpendicular alternating magnetic fields are created by two windings. Each winding consists of two symmetrical coils connected in series. Winding X deflects the beam in the horizontal direction, winding Y deflects the beam in the vertical direction. Frequency of fast beam scanning is about 5 kHz. One scan cycle takes one beam pulse of 200 μs. The angle of beam deflection in this system has been calculated according to the results of magnetic field calibration for windings X and Y. It equals to 1.5 mrad at nominal winding current and beam energy of 158 MeV. Corresponding deflection of the beam on the target is equal to 4.5 mm in both planes. This system gives the possibility to vary the beam size and the beam scan radius on the target in wide range. BFSS consists of electromagnetic windings and control system.

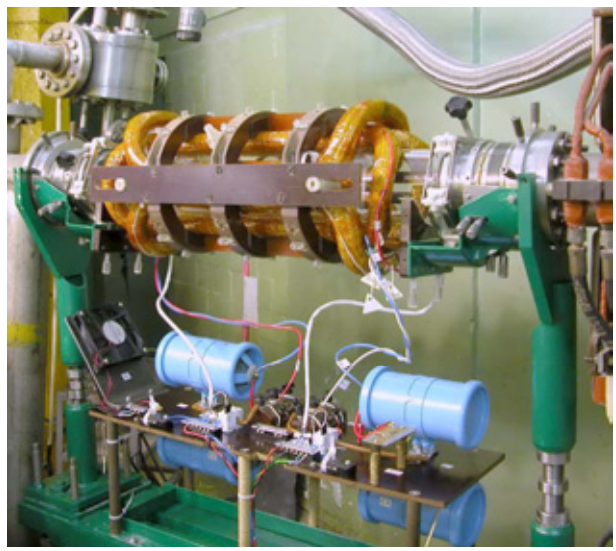

Figure 1: Windings assembly with the capacitor bank.

The windings are designed for vertical and horizontal deflection of the beam and are arranged one above the other on the outside of a glass chamber, which is a part of beam transportation line (Fig. 1). Each winding is included in parallel resonant circuit. The main characteristics of the system are given in Table 1.

Table 1: The main parameters of the system

Supply voltage	~220V,50Hz
Power consumption	≤ 500 W
Resonant circuit X	
Amplitude of deflecting magnetic field	71.5 G
Amplitude of nominal current	4.4 A
Effective magnetic length of winding	40.7 cm
Number of turns of the winding	309
Inductance of the winding	36 mH
Resonant circuit Y	
Amplitude of deflecting magnetic field	55.7 G
Amplitude of nominal current	3.8 A
Effective magnetic length of winding	52.3 cm
Number of turns of the winding	282
Inductance of the winding	36 mH
Control	
Number of channels	2
Output signal shape	Sinusoidal
Range of frequency adjustment	4.6÷5.0 kHz
Maximum output current	10 A
Current adjustment range	0÷10 A
Phase adjustment range	±90°

ISBN 978-3-95450-170-0

The BFSS installation, tuning and testing were carried out in 2013.

Frequency tuning of BFSS resonant circuits was done by adjustment the position of the windings and by regulating procedure with ferrite rods.

The pressure of the residual gas in vacuum chamber can affect the operation of BFSS. Such influence has been observed during the tests. It is concerned with the ionization of residual gas in vacuum chamber and the occurrence of high-frequency discharge, which leads in turn to a change in the resonant frequencies of the circuits. This effect occurs at the pressure of the residual gas higher than 10^{-5} Torr and it was visually observed by the residual gas glow inside vacuum chamber (Fig. 2). Therefore, it is necessary to maintain a high vacuum in order to avoid the appearance of discharge.

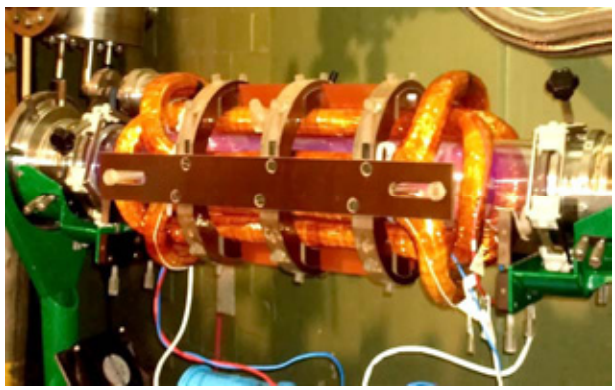

Figure 2: Residual gas glow at low vacuum.

The software for BFSS control has been created on the basis of LabView package. It is integrated into the control system of linear accelerator.

Operator can continuously monitor the BFSS operating mode. BFSS control interface, which provides the possibility to monitor and to control the parameters of the system is shown in Fig. 3.

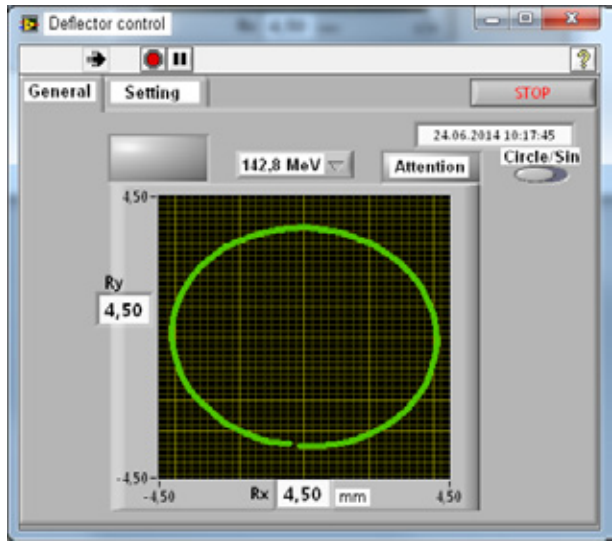

Figure 3: BFSS control interface.

BFSS winding current should provide a specified amplitude of the magnetic field and the value of beam deflection on the target. If the current drops below a predetermined threshold, the interlock system locks the beam passage through the accelerator. It is necessary to avoid the damage of the target at too high density of the beam.

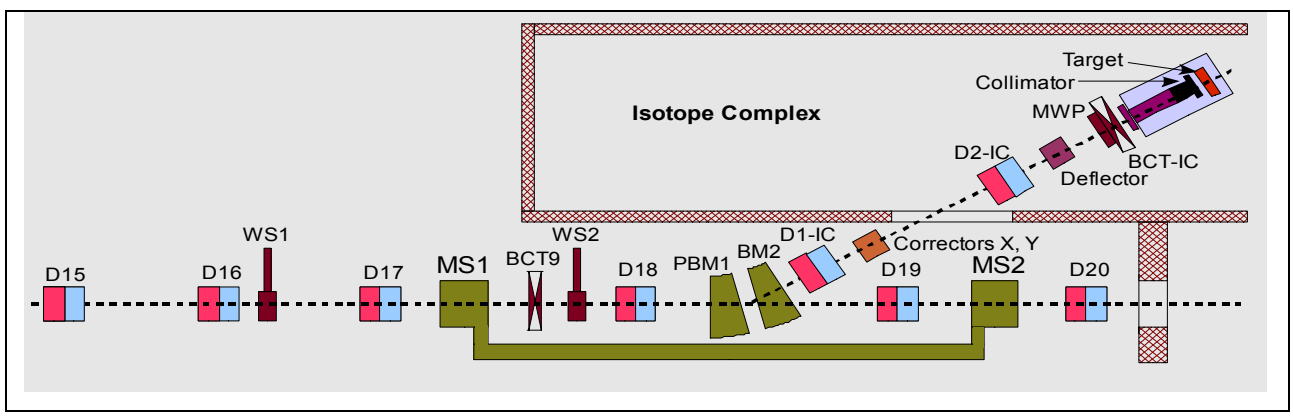

Figure 4: Layout of beam transportation channel in the area of beam extraction to isotope complex. D-quadrupole doublets; PBM1, BM2-bending magnets; MS1, MS2-longitudinally matching sections; BCT-IC, BCT9-beam current transformers; WS1, WS2-wire scanners; MWP-multiwire profilometer.

ISBN 978-3-95450-170-0

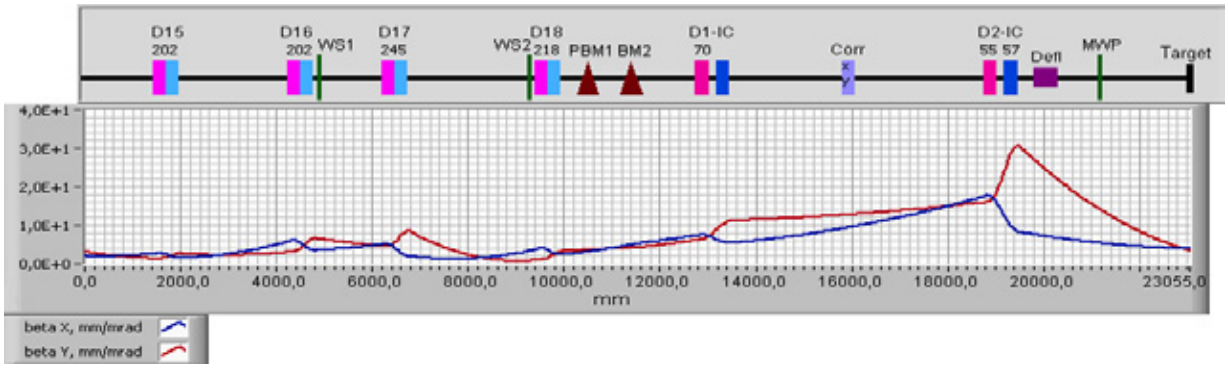

Figure 5: Lattice of beam extraction line and tracing of characteristic β-functions.

RESULTS

Study of BFSS operation with proton beam of INR linac was carried out in 2014. First experimental results were obtained.

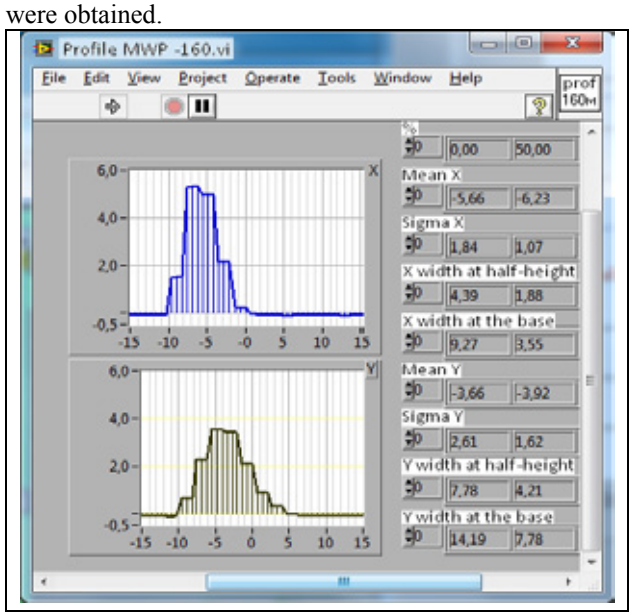

Figure 6: Characteristic beam profiles at MWP.

Table 2: Calculated and measured amplitudes of beam scanning along horizontal (R_x) and vertical axis (R_y)

Beam energy	143 MeV
Current in winding X	2.05 A
Current in winding Y	1.80 A
Calculated R_x on the target	±2.2 mm
Calculated R_y on the target	±2.2 mm
Measured R_x on the target	±2.35 mm
Measured R_y on the target	±2.2 mm

Equipment layout and behavior of characteristic β-functions (beam envelope is proportional to $\sqrt{\beta}$ in the area of beam extraction to isotope complex target [2] are shown in Fig. 4 and Fig. 5. Amplitudes of beam scanning on the target were calculated according to the results of magnetic field calibration for both windings. Experimental results of beam center deflection on the target were determined by beam center measurements at MWP. MWP is located in the drift space between deflector and the target. Characteristic beam profiles are shown in Fig. 6.

Beam scanning amplitudes R_x, R_y measured at MWP location are ±0,85 mm and ±0,80 mm respectively. These results can be used for determination of beam center deflections on the target, since the beam deflection on the target is 2.75 times higher than its deflection at MWP location. Comparative results for calculation and measurement are shown in Table 2.

In isotope production session at INR linac five targets have been irradiated by 143 MeV proton beam in almost continuous operation mode. BFSS has been used as fast beam deflector. It successfully and smoothly worked during the entire sessions. Targets irradiation was carried out at following beam parameters: σ_x≈2.6 mm, σ_y≈2.2 mm – rms beam sizes on the target; R_x≈2.6 mm, R_y≈3.6 mm - amplitudes of beam scanning on the target.

CONCLUSION

The first experimental results of using the BFSS system for INR isotope production facility confirmed the possibility to change the sizes of the beam and the amplitudes of beam scanning on a target within a wide range. BFSS has proven its reliability and flexibility. BFSS will be further used in isotope production sessions at INR linac.

REFERENCES

[1] O.Grekhov, I.Zhelezov, V.Mikhailov, V.Serov, A.Feschenko. “Development of Fast Magnetic Beam Raster System for INR Isotope Production Facility”, Problems of Atomic Science and Technology, Series «Nuclear Physics Investigations», 2013, № 6 (88), p. 86-89.

[2] S.Bragin, A.Feschenko, O.Grekhov, Yu.Kiselev, A.Mirzojan, V.Moiseev, I.Vasilyev, O.Volodkevich., “Proton Beam Monitoring and Forming on the Target of Isotope Complex at INR Linac.”, Problems of Atomic Science and Technology, Series «Nuclear Physics Investigations», 2010, № 2 (66), p. 96-100

ISBN 978-3-95450-170-0

SIMULATION AND OPTIMIZATION OF ION OPTICAL EXTRACTION, ACCELERATION AND H⁻ ION BEAM MATCHING SYSTEMS

B.A.Frolov#, National Research Centre "Kurchatov Institute" State Research Center of Russian Federation – Institute for High Energy Physics, Protvino, Moscow Region, Russia
V.S.Klenov, V.N.Mihailov, O.M. Volodkevich, Institute for Nuclear Research, Russian Academy of Science, Moscow, Russia

Abstract

The source of negative hydrogen ions for the implementation of multiturn charge-exchange injection to increase the intensity of IHEP buster is developed. Surface-plasma ion source with Penning discharge is selected as a source of H-minus ions. A high-current extraction system with downstream electron dumping has been designed. A three-dimensional ion optical code IBSimu has been utilized for simulation and optimization the extraction system and ion beam acceleration to energy of 100 keV. A magnetic low energy beam transport line consisting of two solenoids has been designed to match the beam with RFQ. TRACE 2D code was used to optimize LEBT. A deflecting magnet with small angular deflection (10^0) has been installed between solenoids to eliminate forward tracing of neutral atoms from ions source to RFQ.

INTRODUCTION

The beam intensity increase is one of the main tasks of modern proton accelerators' development. In the leading acceleration centers of the world the charge-exchange injection H-minus (H^-) ions to accelerators is being used for this purpose. Such methodology is planned to be used in the IHEP booster storage ring which will allow to several times raise the intensity of U-70 complex acceleration (up to 10^{13} protons per cycle). It will be necessary to develop the highly effective and reliable source of H-minus ions. The collaboration of IHEP and INR is developing the H-minus ions source which should produce the H- beam with the following parameters: H-minus current ≥ 50 mA, pulse duration – 25 μs, repetition rate -25 Hz, energy of ions -100 keV, normalized rms emittance ≤ 0.25 π mm·mrad, e/H^- ratio < 5. Basing on the experience of working with the negative ions source in INR RAS [1] and BINP SB RAS [2], and also on the analysis of publications about the work of negative ions sources in BNL [3] , ISIS [4], FNAL [5], CERN [6] the surface-plasma source with the Penning gas-discharge chamber with axially symmetric emission aperture at the ion source output was chosen as a source of H-minus (H^-) ions. To extract ions from plasma, accelerate and form the beam with minimal aberrations and match the optical parameters of ion beam with the RFQ entrance the high effective ion-optical system (IOS) and low energy beam transportation system (LEBT) are needed. The numeric modeling results of IOS of extraction, acceleration and H^- beam matching are described below.

EXTRACTION AND ACCELERATION SYSTEM

The three-electrode IOS is used to extract ions from plasma and accelerate to the energy of 100 keV. It is formed by plasma, extraction and acceleration electrodes. Plasma electrode works as gas discharge anode and the gas-discharge chamber of source itself is under potential of 100 kV. Emission aperture diameter equals to 3 mm. Extraction voltage is 20 kV, extracting electrode diameter is 4 mm. The acceleration of negative hydrogen ions up to energy of 100 keV happens in the second gap. The lengths of extracting and accelerating gaps were chosen basing on the detailed calculation series on the condition of getting minimal rms emittance at the matching line entrance. The drift space of 140 mm before the matching line entrance is provided after the accelerating electrode. It is meant for gas evacuation, magnet corrector and diagnostic device allocation. Penning gas-discharge chamber is located in the magnetic field with the induction of around 0.1-0.15 T. The ion source magnetic field protrudes to the extraction and acceleration area. The negative ions are deflected from the axis by the gas-discharge chamber magnetic field in the extraction and acceleration gaps. Therefore the corrector is required to compensate the H^- beam deflection.

The three-dimensional code IBSimu (Ion Beam Simulation) was used for the H^- beam extracting, focusing and accelerating simulation [7]. Self-consistent procedure of plasma sheath calculation takes into account fast and thermal positive ions, negative ions and electrons. IBSimu is used in several acceleration centers (like CERN, SNS , etc.) for modeling of negative ions extraction from plasma and beam transportation processes. IBSimu describes the experimental results with good accuracy [8].

The extraction system was simulated with ion source producing H- beam current of 50 mA and co-extracted electrons current of 150 mA. In simulation the ions and electrons transverse temperature was set to 2 eV, plasma potential to 10 eV, the initial energy of particles to 5 eV, number of each sign particles to 30 000. The electron component was deflected from the ion beam on the extraction electrode by the source residual magnetic field. The simulation has been carried out with gas-discharge

#bfrolov.ihep@list.ru

ISBN 978-3-95450-170-0

chamber peak magnetic field of 0.1 T The dipole field was used to correct the H^- beam deflection. Two SmCo permanent magnets ($10\times20\times10$ mm^3) with the axis peak induction of 0.098 T for vertical x-direction are situated at z=35 mm and create the corrector dipole field. The source and the corrector magnetic fields were calculated with ANSYS and the magnetic field data were imported in IBSimu.

The Figure 1 shows the ions (red) and electrons (yellow) trajectories in IOS considering the source and corrector magnetic fields. The gas-discharge chamber magnetic field quite properly separates the electron flux from ion beam. Setting the corrector before the beam matching line helps to minimize the ion beam deflection angle. The corrector magnetic field almost returns the H^- beam back to axis (the beam horizontal deflection from axis is in order of 0.3 mm). Second dipole is needed to achieve the beam near-zero off-axis displacement and near-zero angular deflection.

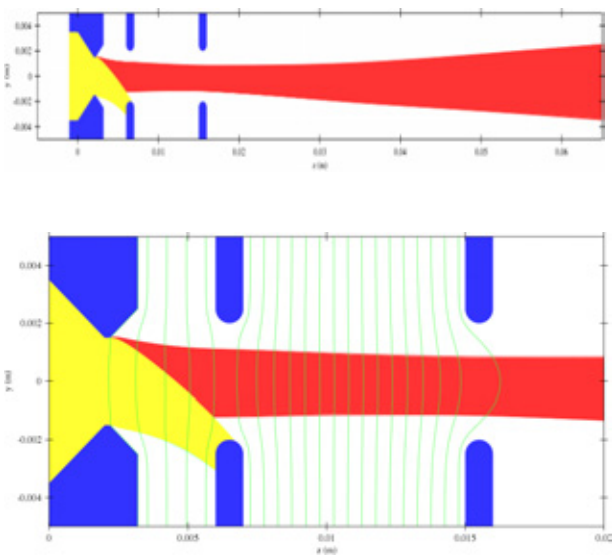

Figure 1. Trajectories of H^- ions (red) and electrons (yellow) from 3D simulation of the IOS. The co-extracted electron beam with the energy of 20 keV is deflected on the extraction electrode by a source magnetic field.

Fig.2 and Fig.3 show the beam phase space distribution in horizontal y- plane and vertical x-plane at z = 65 mm. The simulation of IOS showed that the beam emittance varies only slightly in the drift space after the acceleration electrode (ε_y = 2.50 π mm·mrad and ε_x = 2.433 π mm·mrad at z= 2 mm and ε_y= 2.466 π mm·mrad and ε_x = 2.463 π mm·mrad at z = 65 mm). The calculated normalized 4*rms emittance of ε = 0.14 π mm·mrad is approximately close in magnitude to the experimentally measured Penning source emittance in the operating mode without fluctuations of discharge parameters ("noiseless" operating mode) [9]. Source adjustment to get such operating mode should be done by optimizing hydrogen and cesium supply and the source magnetic field value.

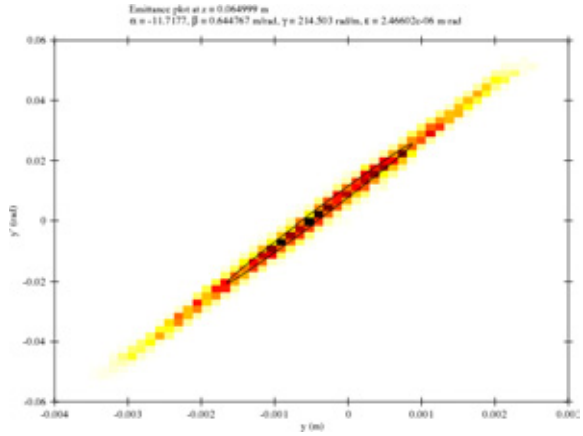

Figure 2.Transverse emittance plot in y-plane from 3D simulation shown on figure 1.

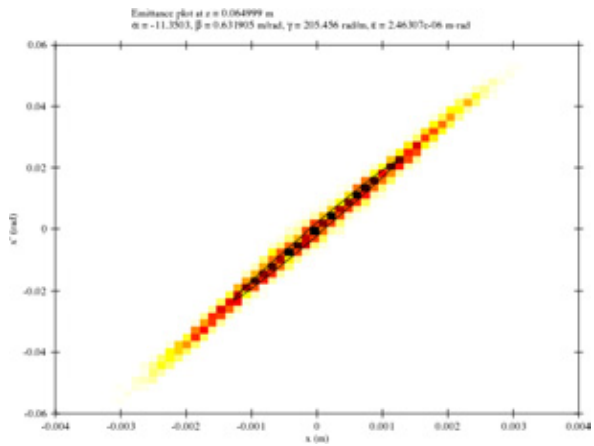

Figure 3.Transverse emittance plot in x-plane from 3D simulation shown on figure 1.

TWO-SOLENOID MAGNETIC LEBT

The emittance requirements at the entrance of the RFQ are the Twiss parameters A=2.3 and B=0.14 and 4*rms normalized emittance □ ≤ 1π mm·mrad at an injection energy of 100 keV. As a first step to select set of LEBT elements, the ion beam transportation through the matching channel up to RFQ entrance was simulated by code TRACE-2D. [10]

As the forward tracing of neutral cesium atoms from the emission aperture of ions source to RFQ entrance should be eliminated, the beam-bending magnet should be added in matching channel. Several variants of arrangement for matching channel of beam with the linear accelerator LU-30 entrance were investigated, including the channel with the quadrupole lenses, with two or one solenoid lens and with beam-bending magnet in different allocations and with different parameters of deflection angles, radius and field index. For the matching channel with quadrupole lenses it resulted hard to provide the beam matching with the accelerator entrance at sensible channel geometry (length and diameter) due to quite serious angle difference which the beam acquires at the drift space before the channel entrance.

ISBN 978-3-95450-170-0

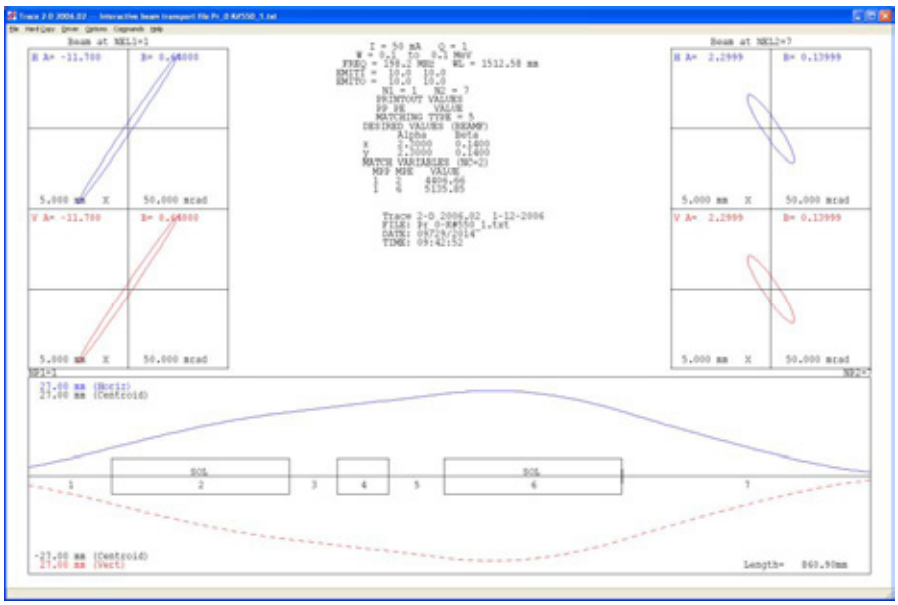

Figure 4. The beam envelope profile for two-solenoid magnetic LEBT (2, 6) with beam-bending magnet (4).

The channel of two solenoids is more convenient in adjustment and beam matching. Basing on the several parameters the variant with two solenoid lenses and beam-bending magnet with small deflection angle of 10^0 was chosen. Two correctors also included in the channel. Such LEBT structure helps to get the beam with the required parameters at the RFQ entrance and allows you to have a sufficiently large drift space before the RFQ entrance for gas evacuation and diagnostic device allocation. The Figure 4 shows the beam envelope for "noiseless" operating mode in horizontal and vertical planes. The Twiss parameters and emittance were taken from the IOS simulating at z=65 mm. The magnetic field induction on the lenses axis is around 0.441 T and 0.514 T in the first and second lenses accordingly, the channel diameter does not exceed 55 mm for the beam passing with no losses.

CONCLUSION

Simulation of IOS has been carried out with source peak magnetic field of 0.1 T. The adjustment of source magnetic field will be needed to generate ion beam in "noiseless" operating mode. Therefore the second dipole with auxiliary winding is required to compensate the beam deflection caused by the change of the source magnetic field. In the future IOS simulation will be carried out by taking into account the second dipole and with various values of the source magnetic field. LEBT will be also simulated using the large particles method and the complete IOS and LEBT modeling will be carried out by using IBSimu code.

REFERENCES

[1] A.S. Belov, O.T. Frolov, V.S. Klenov, V.P. Yakushev, Rev. Sci. Instrum., **63** (4), pp. 2622-2624, (1992).

[2] Yu.I. Belchenko, A.I. Gorbovsky, A.A. Ivanov et.al., "Upgrade of CW Negative Hydrogen Ion Source" , AIP Conf. Proc.,1515, 448-455 (2013).

[3] J. G. Alessi, "Performance of the Magnetron H^- Source on the BNL 200 MeV Linac", AIP Conf. Proc., **642**, pp. 279-281, (2002).

[4] J. Lettry, J. Alessi, D. Faircloth, A. Gerardin, T. Kalvas, H. Pereira and S. Sgobba, "Investigation of ISIS and Brookhaven National Laboratory ion source electrodes after extended operation", Rev. of Sci. Instr., **83**, 02A728 (2012).

[5] C.Y. Tan, D.S. Bollinger, K.L. Duel, J.R. Lackey, W.A. Pellico, "The FNAL injector upgrade", Proceedings of 2011 Particle Accelerator Conference, New York, NY, USA WEP115, pp. 1701 – 1703, (2011).

[6] J. Lettry et. al., "Status and operation of the Linac ion source prototypes", Rev. Sci. Instrum., **85**, 02B122, (2014).

[7] T. Kalvas, O. Tarvainen, T. Ropponen, O. Steczkiewicz, J. Ärje et. al., "IBSIMU: A three-dimensional simulation software for charged particle Optics", Rev. Sci. Instrum., **81**, 02B703 (2010).

[8] T. Kalvas, R.F. Welton,O. Tarvainen, B.X.Han and M. P.Stockli, "Simulation of H^- ion source extraction system for the Spallation Neutron Source with Ion Beam Simulator", Rev. Sci. Instrum., **83**, 02A705 (2012).

[9] G.E. Derevjankin, V.G. Dudnikov, V.S. Klenov "About ion optical characteristics of H^- ion beams produced by surface-plasma sources", Rus. Physics JTP, v. **48**, №.2, p. 404. (1978).

[10] K. R. Crandall, D. P. Rusthoi, "TRACE 3-D Documentation", **LA-UR-97-886,** Los Alamos National Laboratory, Los Alamos, New Mexico.

ISBN 978-3-95450-170-0

PRODUCTION OF METAL ION BEAMS FROM ECR ION SOURCES BY MIVOC METHOD*

S. Bogomolov, A. Bondarchenko, A. Efremov, K. Kuzmenkov, A. Lebedev, K. Lebedev, V. Lebedev, V. Loginov, N. Yazvitsky, JINR, Dubna, Moscow Region, Russia
Z. Asfari, B.JP. Gall, IPHC, Strasbourg Cedex 2, France

Abstract

The production of metal ion beams with ECR ion sources using MIVOC method is described. The method is based on the use of metal compounds having a high vapor pressure at room temperature: for example, $C_2B_{10}H_{12}$, $Fe(C_5H_5)_2$ and several others. Intense ion beams of B and Fe were produced at the FLNR JINR cyclotrons using this method. The main efforts were went into production and acceleration of ^{50}Ti ion beam at the U-400 cyclotron.

The experiments on production of ^{50}Ti ion beam were performed at the test bench with the natural and enriched compounds of titanium $(CH_3)_5C_5Ti(CH_3)_3$. In the experiments at the test bench the beam currents of $^{50}Ti^{5+}$ - 80 mkA and $^{48}Ti^{11+}$ - 70 mkA were achieved at different settings of the source. After successful tests two 3 weeks runs with Ti-50 beam were performed at the U-400 cyclotron for the experiments on spectroscopy of super heavy elements. The intensity of the injected beam of $^{50}Ti^{5+}$ was about of 50-60 μA, during experiment the source have shown stable operation. The compound consumption rate was determined to be about of 2.4 mg/h, corresponding to ^{50}Ti consumption of 0.52 mg/h.

INTRODUCTION

The most heavy target, with which it is possible to carry out experiments on the synthesis of super heavy elements in heavy-ion reactions is ^{249}Cf, and the further progress in the area of the elements with Z > 118 requires the production of intense beams of accelerated neutron-enriched isotopes such as ^{50}Ti, ^{58}Fe, ^{64}Ni and others. The use of each new isotope for production of the accelerated beam requires investigations directed on optimization of the ECR source operation mode and development of technique for material feed into the source.

The method of solid materials feed into an ECR ion sources strongly depends on the specific properties of materials.

Several methods for production of ions of solids from ECR sources have been developed. Solid material can be evaporated by resistor or inductive oven, which is inserted into the source chamber [1]. Refractory metals can be sputtered by plasma ions [2] or inserted into the plasma and heated by energetic plasma electrons ("insertion technique") [3].

The other possibility for production of ions of solids is the feeding of the plasma with an organometallic compound through the Metal Ions from VOlatile Compounds (MIVOC) method [4].

*Work supported by Russion Foundation for Basic Research under grant number 13-02-12011

PRODUCTION OF IONS OF METALS BY MIVOC METHOD

MIVOC method is based on the use of organometallic compounds having a high vapor pressure at room temperature: for example, $C_2B_{10}H_{12}$, $Fe(C_5H_5)_2$ and several others.

First time in FLNR the MIVOC method was used for production of intense beam of $^{11}B^{3+}$ required for generation of secondary beams of ^{6}He and ^{8}He at the U400M cyclotron [5]. The compound $C_2B_{10}H_{12}$ which has the vapor pressure of about 1÷2 Torr at the room temperature has been used. The ion source operated stable without addition of support gas.

The maximal current of $^{11}B^{3+}$ up to 200 eμA was produced from DECRIS-2 [6] ion source. The material consumption measured at 100 eμA current of $^{11}B^{3+}$ constitutes 2,2 – 2,8 mg/h.

Later this method was successfully applied for production of iron, cobalt and chromium ion beams using the ferrocene, cobaltocene and chromocene as a working substances. The results, obtained at the test bench are presented in the Table 1.

Table 1: Intensity (eμA) of Metal Ion Beams Produced by MIVOC Methods at the Test Bench (* - intensity optimisation)

	Fe	Co	Cr
6+	43	57	70*
7+	93	80	60
8+	125	86	37
9+	172	80*	17
10+	145*		7
11+	114	82*	
12+	73	25	
13+	45		

At the U-400 cyclotron the beam of ^{58}Fe was accelerated using the same technique. The intensity of injected $^{58}Fe^{7+}$ beam was 40÷50 eμA (6 ÷ 7 pμA), and the $^{58}Fe^{23+}$ beam intensity at the target constitutes 15 ÷ 17 eμA (~ 0.7 pμA). The consumption of ^{58}Fe constitutes about of 1,5 mg/h.

PRODUCTION OF TITANIUM ION BEAM

The experiments on production of Ti ion beams were carried out at many laboratories with the use of different methods.

The production of Ti ion beams by evaporation from the resistor oven was studied at GSI [7]. The evaporation

ISBN 978-3-95450-170-0

of pure titanium requires the temperature between 1750 °C and 1800 °C. During the experiments more than 50 eμA of $^{50}Ti^{8+}$ were produced with high level of beam stability. The oven life time of 6 days was obtained.

The experiments on production of Ti ion beams by evaporation from the induction oven were carried out at ANL [8]. The beam of $^{50}Ti^{12+}$ with the intensity of 5.5 eμA was produced during seven days.

The MIVOC method was first adopted for production of Ti ion beam by JYFL group [9]. Commercially available $(CH_3)_5C_5Ti(CH_3)_3$ compound was used as a working substance. In the case of $^{48}Ti^{11+}$ion beam the intensity of 45 eμA was produced.

The consumption of the compound was measured to be 47 mg giving the value of 0.22 mg/h for the consumption of titanium. The ion beam was very stable during the period of 282 h.

So, from the point of view beam intensity, stability, reliability and material consumption the MIVOC method seems very promising for providing ^{50}Ti ion beam for long term experiments on synthesis of super heavy elements. But, the compound is sensitive to air, moisture, temperature and light that needs cautious handling when loading the material for use. The synthesis of this compound is rather complicated especially with the use of enriched titanium which is available in a small, about several grams, quantity.

Test Experiments

First time the ^{50}Ti ion beam was accelerated at the U-400 cyclotron in 2005. The task was to provide about of 30 enA of ^{50}Ti beam at the target for experiments on the fission physics. The natural $TiCl_4$ (5.2 % of ^{50}Ti) was used as a working substance. The intensity of ^{50}Ti ion beam, extracted from the cyclotron constitutes about of 200 enA, the source was running stable during two weeks.

But the use of $TiCl_4$ do not provide the intensity required for the experiments on the synthesis of super heavy elements.

Taking into account the problems with synthesis and handling of $(CH_3)_5C_5Ti(CH_3)_3$ we decided to try to find the other compounds, suitable for MIVOC method. The titanium isopropoxide ($Ti\{OCH(CH_3)_2\}_4$) and cyclopentadienyl cycloheptatrienyl titanium ($C_5H_5TiC_7H_7$) were tested, but no noticeable titanium current were observed, just a few microamperes of Ti^{5+}. The ($C_5H_5TiC_7H_7$) compound was later used at IMP [10] with LAPECR2 source for production of titanium ions by oven method. During the test, 24 eμA of Ti^{11+} has been achieved with 250 W 14.5 GHz microwave power.

The commercially available compound was tested with DECRIS-4 [11] and DECRIS-2 sources. The sources were optimized for production of Ti^{5+}, similar results were produced with both sources – about of 50÷60 μA. In the experiments with the modified ECR4M [12] source at the test bench about of 80 μA of Ti^{5+} were produced. In all experiments no support gas and no control of MIVOC chamber temperature were used. The operation of the sources was stable and reproducible.

Production of Titanium-50 Ion Beams

The development of titanium-50 beam production was performed in the frame of collaboration between IPHC (Strasbourg, France) and JINR.

After several years of chemistry developments at IPHC the $C_5(CH_3)_5Ti(CH_3)_3$ compound was synthesized using 92.57 % enriched ^{50}Ti. A two step chemistry was done starting from $TiCl_4$ going to $C_5(CH_3)_5Ti(CH_3)_3$ through an intermediate $C_5(CH_3)_5TiCl_3$ organic compound with quite high efficiency.

First isotopicaly enriched beam of ^{50}Ti by MIVOC method was produced in 2011 at the University of Jyväskylä. After optimization, up to 19.4 eμA of $^{50}Ti^{11+}$ was extracted from the JYFL 14 GHz ECRIS2 ion source [13, 14].

The compound from natural titanium, synthesized at IPHC, was also tested at GANIL [15]. An intensity of 20 eμA for $^{48}Ti^{10+}$ was maintained for 4 days, with regulation the temperature of the MIVOC chamber. The consumption of 1.5 mg/h for the MIVOC compound has been deduced, i.e. 0.23 mg/h for ^{48}Ti.

First natural material synthesized at FLNR by IPHC group was tested in October 2013 with ECR4M ion source at the test bench. After optimization, very stable ^{48}Ti beams were produced with intensities up to 70 eμA for the 11^+ charge state (6.2 pμA) and 75 eμA for the 5^+ charge state (15.0 pμA). Figure 1 shows the charge state distribution of ^{48}Ti ion beam with the source settings for optimum production of $^{48}Ti^{11+}$.

Following these very promising results, a 92.57 % enriched compound was synthesized and tested with ECR4M at test bench. Under similar conditions up to 80 eμA of $^{50}Ti^{5+}$ beam was extracted, corresponding to 16.0 pμA. Figure 2 shows the charge state distribution of ^{50}Ti ion beam with the source settings for optimum production of $^{50}Ti^{5+}$.

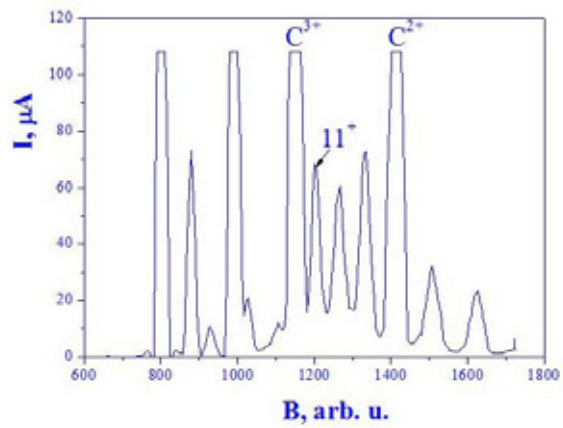

Figure 1: Ti ion spectrum, produced by MIVOC method from the ECR4M source at microwave power of 300 W.

ISBN 978-3-95450-170-0

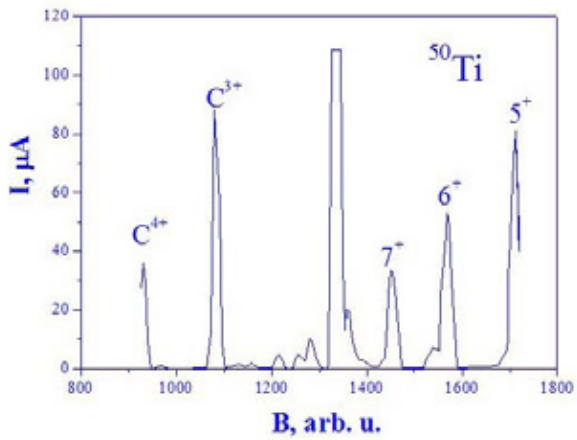

Figure 2 : ^{50}Ti ion spectrum, produced by MIVOC method from the ECR4M source at microwave power of 30 W.

This beam was then produced with the DECRIS-2m [16] source and accelerated at the U400 cyclotron. A very stable $^{50}Ti^{5+}$ beam with the intensity of 55 eμA (11.0 pμA) was injected in the cyclotron. Extracted titanium-50 ion beam with the intensity of 0,49 pμA was used on target for several weeks in October-November 2013. This beam was very stable with wery low, about of 0.6 mg/h titanium consumption.

Next run with titanium-50 ion beam was performed at the U-400 cyclotron during April-May 2014. By then the DECRIS-2m source at the U-400 cyclotron was replaced by ECR4M source. During three weeks the intensity of $^{50}Ti^{5+}$ beam was maintained at the level of 55÷62 eμA. The material consumption was similar to the previous run with DECRIS-2m ion source.

Table 2 summarise the results of titanium ion beam production at different Laboratories by MIVOC (JYFL, GANIL, FLNR) and oven (GSI, ANL, IMP) methods.

Table 2: Intensity (eμA) of Titanium Ion Beams Produced at Different Laboratories by MIVOC and Oven Methods

	JYFL	GANIL	FLNR	GSI	ANL	IMP
$^{48}Ti^{5+}$			79			
$^{48}Ti^{10+}$		20				
$^{48}Ti^{11+}$	45		68			24
$^{50}Ti^{5+}$			82			
$^{50}Ti^{8+}$				50		
$^{50}Ti^{11+}$	20					
$^{50}Ti^{12+}$					5.5	

CONCLUSION

During last years significant progress was achieved in production of intense multiply charged ion beams of metals from ECR ion sources by MIVOC method.

The MIVOC method was successfully used for production and acceleration of titanium-50 and iron-58 ion beams at the U-400 cyclotron.

This method provides intense ion beams with long term stability, and is quite promising for experiments on synthesis of super heavy elements.

ACKNOWLEDGMENT

This work was supported by Russian Foundation for Basic Research under Grant number 13-02-12011.

REFERENCES

[1] D. J. Clark, C. M. Lyneis, J. Phys. (Paris) Colloq. 50 (1989), C1–759.
[2] R. Harkewicz, P. J. Billquist, J. P. Greene et al., Rev. Sci. Instrum., 66, (1995), p. 2883.
[3] R. Geller, P. Ludwig, G. Melin, Rev. Sci. Instrum. 63 (1992) 2795–2800.
[4] H. Koivisto, J. Drentje, M. Nurmia, Rev. Sci. Instrum., 69, (2). 1998, p. 785.
[5] Bogomolov S.L., Efremov A.A., Kutner V.B. et al. Proc. of the 14th Int. Worshop on ECRIS, CERN, Geneva, Switzerland, 1999, p.71-73
[6] A. Efremov, V. Bekhterev, S.L. Bogomolov et al., Rev. Sci. Instrum., 1998, v.69, N2. p. 662.
[7] K. Tinschert, R. Lang, J. Mäder et al., WEPP15, Proceedings of ECRIS2012, Sydney, Australia.
[8] R.Vondrasek, R.Scott, R.Pardo High energy physics and nuclear physics (HEP & NP) A Series Journal of the Chinese Physical Society (C) vol.31, Supp.I, July, 2007, p. 101.
[9] H. Koivisto et al., NIM B, 187 (2002), p.111.
[10] W. Lu, J. Y. Li, L. Kang et al., Rev. Sci. Instrum. **85**, 02A947 (2014).
[11] M. Leporis, V. Bekhterev, S. Bogomolov et al., Rev. Sci. Insrum., **77**, 03A301, 2006.
[12] S. Bogomolov, V. Bekhterev, A. Efremov et al., FRYOR01, Proceedings of RUPAC2012.
[13] J. Rubert, J. Piot, Z. Asfari et al., NIM B 276 (2012), p. 33.
[14] H. Koivisto, O. Tarvainen, V. Toivanen et al., FRYA03, Proceedings of ECRIS2012, Sydney, Australia.
[15] P. Jardin, O. Bajeat, C. Barué et al., FRYA01, Proceedings of ECRIS2012, Sydney, Australia.
[16] V.N. Loginov, V.V. Bekhterev, S.L. Bogomolov et al., Nukleonika 2003, Volume 48(Supplement 2), p. S89.

ISBN 978-3-95450-170-0

HYDROGEN NUCLIDES ACCELERATION FROM LASER PLASMA IN THE DIODE WITH MAGNETIC INSULATION OF ELECTRONS

K.I. Kozlowski, E.D. Vovchenko, V. L. Shatokhin, A.E. Shikanov, National Research Nuclear University "MEPhI" (Moscow Engineering Physics Institute), Moscow, Russia

Abstract

The results of an experimental investigation of the deuterons acceleration from laser plasma in a compact magnetically insulated ion diode are reported. The experiments were done in a pulsed mode ($U \leq 300$ kV, $I_{max} \leq 600$ A, $\tau \leq 500$ ns) at a pressure of 0,01 Pa. The deuterium laser plasma was produced at the anode during irradiation of a TiD target with a laser pulse (wavelength $\lambda = 1060$ nm and intensity $q \sim 5 \cdot 10^{14}$ W/m^2). The positive accelerating voltage was created by means of a 20 stage Marx generators with air spark gap-switched circuit. The ion diode has an axially symmetric geometry of the anode-cathode gap. A hollow cylindrical cathode made of a permanent magnet with induction on an axis up to 0,4 T. Magnetic insulation of electrons in the accelerating gap leads to suppression of the electronic components of the total current in 4-5 times.

INTRODUCTION

Plasma diodes are widely used for producing intense beams of electrons and ions with currents up to 100 kA and energy 100÷500 keV. Such high-energy dense beams of charged particles are applied in various fields of science and technology (for example, in ion implantation materials, injection of charged particle accelerator, neutron and x-ray radiation). In this work we discuss only the ion diodes developed for the generation of neutron radiation.

Currently, new technologies are being developed on the basis of compact pulsed neutron generator (PNG), such as screening and detection of dangerous substances and items, neutron logging oil and mineral deposits, neutron activation analysis [1]. Much attention in this research is given to the hydrogen nuclides acceleration on the basis of vacuum and gas-filled pulse diode and the optimization of their design, aimed at increasing resource and neutron yield. In this case work with the sealed designs on tritium gives an increase in the neutron yield by two orders of magnitude, however due to of high radiation danger their application is extremely limited. The main part of basic researches is carried out on a deuterium.

Good prospects for the development of compact PNG provides the use of the diode with magnetic insulation of the electrons and the laser-plasma source of deuterons [2, 3]. In environments with strong magnetic fields, the electrons move along the trajectories of the cycloid, not already captured the anode plasma and does not overlap the accelerating gap. According to preliminary estimates in such laser-plasma diode can be achieved density of the ion current up to 10^6 A/m^2. Such scheme has high efficiency for radial extraction of deuterium ions from the side surface of a laser-induced plasma cloud and provides higher emission characteristics compared to the vacuum-arc ion sources. It is simple and convenient to install the laser target on the high-voltage electrode. In addition, the laser-plasma diode allows to vary the initial parameters of the plasma by changing the intensity of the laser radiation.

Neutron generators on the basis of laser deuterons sources began to be developed for a long time, about 30-40 years ago [4, 5] (in MEPhI, JINR (Dubna), All-Union Scientific Research Institute of Nuclear Geophysics and Geochemistry, some other research centers). However, these experimental studies have significantly limited the absence of laser technology with high performance. At the same time had no active development of the idea of magnetic insulation of electrons. The main part of neutron generators based on the laser-plasma diode with magnetic insulation of electrons remained as experimental models. Now, this work is continued in National Research Nuclear University MEPhI again, due to the possibility of using compact new lasers and new super-strong permanent magnets.

THE EXPERIMENTAL SET-UP

Experimental investigations carried out on the model of laser-plasma diode with direct acceleration of deuterium ions from anode laser plasma to the cathode-target, forming neutrons (DD reaction). The diode has an axially symmetric geometry of electrodes (Fig. 1) with the internal high-voltage anode and the external hollow cylindrical cathode. At the anode is installed laser TiD target. Electrodes are established in the vacuum chamber equipped with means of pumping for obtaining residual pressure to $5 \cdot 10^{-2}$ Pa. For connection of the high voltage anode with Marx generator is used the vacuum electrical connector. It isolator is designed for an operating voltage up to 500 kV.

In the diode, for the purpose of increase in ion acceleration effectiveness, the scheme with magnetic insulation of electrons is applied. The magnetic field is created by the permanent magnet which is at the same time the cathode of the diode. The cathode has a form of the hollow cylinder with an internal radius of 0,02 m and 0,06 m high. The required induction value B was estimated from a comparison of the Larmor radius r_L of accelerated electrons with the distance between the plasma anode and cathode. From a condition of

$$r_L = [(2mU)/(eB^2)]^{1/2} < 5 \cdot 10^{-3} \text{ m}, \quad (1)$$

where $U = 300$ kV − the accelerating voltage, m and e − the mass and elementary charge of electron, follows $B \approx$

ISBN 978-3-95450-170-0

0,4 T. Realization of a stationary magnetic field with such induction value is possible, for example, at a choice of a magnetic material based on of NdFeB.

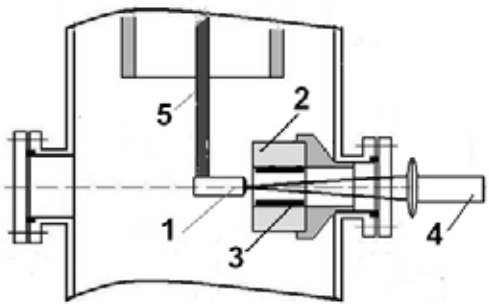

Figure 1: Laser-plasma diode. 1 − the anode with a laser TiD target; 2 – the hollow cylindrical cathode (NdFeB); 3 – place target, forming neutrons (DD reaction); 4 − laser radiation; 5 – vacuum electrical connector

A compact YAG laser with a wavelength $\lambda = 1060$ nm was used for produce of laser plasma. It has energy of 0,1 J and the duration of the laser pulse of 7 ns in giant pulse formation mode. These characteristics correspond to intensity $q \sim 5 \cdot 10^{14}$ W/m^2. The laser pulse was detected using the photocell (FEC−09) and a digital oscilloscope. Amplitude of the accelerating voltage was determined by means of a sphere spark gap and the table of breakdown voltages [6]. High-voltage divider was used for monitoring of temporary characteristics of pulse voltage.

Discharge current was measured by Rogovsky coil which was developed for work in the conditions of an intensive electromagnetic disturbance. Rogovsky coil has sensitivity 10 A/V in a mode of a current transformer.

The pulse Marx generator of high voltage was applied in experiments. It consists of a 20 step-section with air spark gap-switched circuit. The energy about 0,5 J was accumulated at a charge voltage of 15 kV in each from 20 step-section. The output voltage has amplitude up to $U = 300$ kV without loading ($R_H = \infty$), front duration less than 100 ns and the time constant τ_{RC} = 75 μs. At connection as loading of a laser plasma diode three different modes of its work were experimentally investigated.

EXPERIMENTS AND ANALYSIS

Mode 1 − testing of the diode system without laser radiation. Researchers showed that without of laser plasma the high-current discharge does not develop. In this case Marx generator works only for very large loading, and its output voltage practically is not distorted. The slight decrease in amplitude to $0,9U$ is observed in experiments. It can be explained as formation in the vacuum volume of the low-current discharge due to ionization of residual gas in the conditions of enough strong electric (≈ 20 MV/m) and magnetic (≈ 0,3 MA/m) fields. In the conditions of higher vacuum these ionization processes probably can no considered.

Mode 2 − main accelerator mode in laser-plasma diode with magnetic insulation of electrons. It is the mode high-current discharge and it is observed only with formation of laser plasma on anode. Waveforms of accelerating voltage and the discharge current are shown in Fig.2. They show that the Marx generator has a mode of aperiodic discharge capacity on the plasma load. In this case, resistance of the plasma R_p is limited from below by the value of the critical resistance of discharge circuit $R_c = (L/C)^{1/2} = 300\ \Omega < R_p$, where $C = 230 \cdot 10^{-12}$ F, $L = T^2/(4\pi^2 C) = 5$ μH, and the oscillation period $T = 2\pi \cdot (LC)^{1/2} = 220$ ns was determined from experience in the short circuit in the Marx generator.

On the other hand for high current discharge the resistance of plasma should not be large. The resistance of the plasma R_p is limited from above by the value $R_{max} = kU/I$, where discharge current I was determined from experience (see Fig. 2b) and the factor k takes into account that the voltage U decreases as the capacity is discharged. Because the duration of the discharge current is much smaller than the time constant τ_{RC}, the capacity does not have time to discharge. This is confirmed experimentally, since the amplitude of the accelerating voltage decreases only to a value $0,8U$ ($k = 0,8$). Maximum discharge current has been measured by the Rogowski coil and amounted to the value $I = 150$ A. Then $R_p < R_{max} = 0,8U/I \approx 1600\ \Omega$ and the resistance of the plasma can be estimated by the average $R_p = (R_c + R_{max})/2 \approx 1$ kΩ.

For aperiodic discharge capacity C in a circuit containing inductance L and resistance R_p, the temporal behavior of the current is described by the expression

$$i(t) = (U/L) \cdot (p_1 - p_2)^{-1} [exp(p_1 t) - exp(p_2 t)], \qquad (2)$$

where p_1 and p_2 − roots of the characteristic equation corresponding to this process. Effect of a non-linear dependence of R_p from the current $i(t)$, the calculation of transient processes is quite complicated. However for the limiting case when roots of p_1 and p_2 are real and equal each other (i.e. when $R_p = R_c$) expression for current becomes simpler

$$i(t) = -(U/L) \cdot t \cdot exp(-t/t_p), \qquad (3)$$

where $t_p = 2L/Rc = 30$ ns − the time to reach the current of the maximum values. Then the maximal value of calculated current $i_p \approx (U/L) \cdot (t_p/e) \approx 670$ A. Comparison of values $i_p \approx 670$ A and $I \approx 150$ A and estimation $300 < R_p \approx 1000 < 1600\ \Omega$ qualitatively confirm the correctness of the current measurement.

To synchronize the pulse of acceleration voltage with the process of moving laser plasma was used "optical" scheme. 25% of the total laser energy is gone in the first spark gap of Marx generator, causing its breakdown and switching in other sections. In this case the delay of the pulse voltage relative to the laser pulse, as a rule, did not exceed 100÷200 ns.

ISBN 978-3-95450-170-0

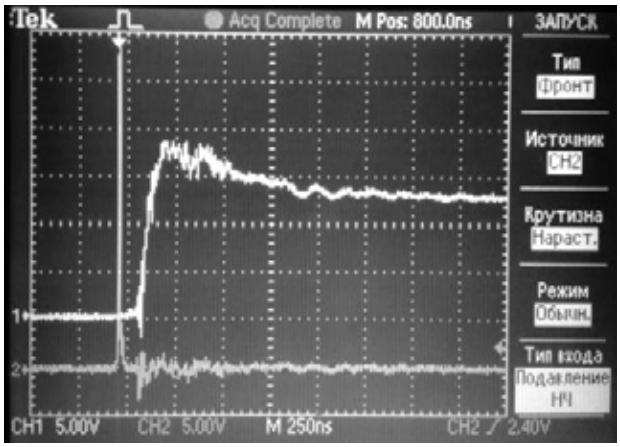

a) the accelerating voltage (the top beam) and a laser pulse (the lower beam)

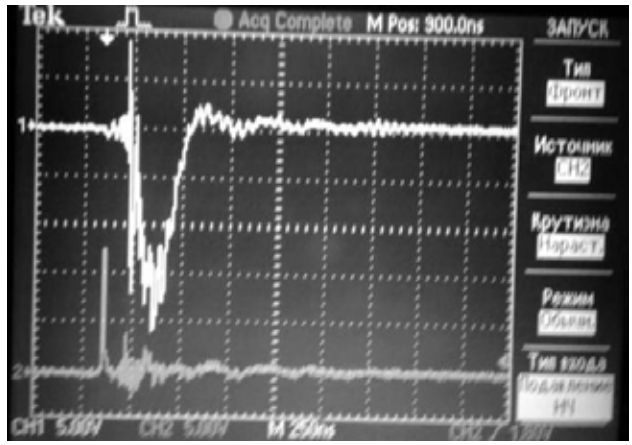

b) discharge current (top beam) and laser pulse (lower beam)

Figure 2: Marx generator in mode 2 (sweep speed −250 ns /div)

Mode 3 − monitoring of effectiveness of magnetic insulation of electrons. In this mode of diode operation also the laser initiation was carried out, but without magnetic field. Instead of the cathode of the permanent magnet was mounted non-magnetic Al cathode with the same dimensions. The total current of the diode with the non-magnetic cathode is increased to 600 A in comparison with the mode 2, and amplitude of the accelerating voltage is decreased to 0,5U. It means that without magnetic field the current of electrons is significantly increased and it is caused by development of the emission process on the cathode. In turn, it leads to increase in conduction of a discharge gap and decrease in the accelerating voltage. In this case Marx generator still worked in the mode of an aperiodic discharge, however it is rather close from border of transition to the mode of oscillations.

CONCLUSION

Data of electric measurements for all modes of a laser plasma diode are summarized in Table 1. Comparison of these data allows making the conclusion that application of magnetic insulation of electrons is proved, and discharge current in the mode 2 (see Fig. 2b) generally is determined by current of ions.

Table 1: Summary of Modes

	Mode 1	Mode 2	Mode 3
Laser initiation	−	+	+
Magnetic field	+	+	−
Voltage	0,9 *U*	0,8 *U*	0,5 *U*
Discharge current	−	150 A	600 A

Thus, the experiments showed the possibility of effective ion acceleration to energy of 300 keV, when these ions were extracted from the plasma anode. The plasma is created on the anode by the radiation of a pulsed laser and allows producing ion beams with a current of more than 100 A and a current density of ~10 A/cm^2. Acceleration modes with the insulation of the electron by the field of the permanent magnet were obtained for laser-plasma diode with coaxial geometry of electrodes. It is planned to increase the accelerating voltage up to 500 kV and the energy of the laser pulse up to 1 J.

REFERENCES

[1] Portable generators of neutrons and technology on their basis / Reports edited by Yu.N. Barmakov. Moscow: VNIIA, 2013, − 620 pages.
[2] Didenko A.N. Rashchikov V. I. Ryzhkov V. I. Shikanov A.E. // PROBLEMS OF ATOMIC SCIENCE AND TECHNOLOGY, 2012, No. 4, p. 129−132.
[3] Ananyin O. B., Kozlowski K. I., Shikanov A. E. Tsybin A. S. // Atomic energy, 2013, T. 115, вып. 2, p. 115-118.
[4] Ananyin O. B., Bespalov D. F. Bykovsky Yu. A. etc.// Works of All-Union Scientific Research Institute of a Nuclear Geophysics and Geochemistry, 1975, вып. 23, p. 33.
[5] Bespalov D. F., Bykovsky Yu., A. Kozlowski K. I. etc. //PTE, 1978, No. 6, p. 19−21.
[6] Technique of high voltage / Textbook edited by G. S. Kuchinsky, SPb: Prod. PEIPK, 1998. – 700 pages.

ISBN 978-3-95450-170-0

HYDROGEN NUCLIDES EXTRACTION FROM PULSE PLASMA FORMATION

B.Yu. Bogdanovich, A.V. Nesterovich, A.E. Shikanov, V.L. Shatohin,
National Research Nuclear Universety «MEPhI», Moscow, Russia

Abstract

The features of hydrogen nuclides extraction from vacuum-arc plasma and laser sources by electric field research results are presented in the report. Such sources can be used in accelerators injection systems and in neutron generators. These processes, found, are strongly influenced by electrostatic oscillations in the plasma boundary, which position continuously varies, in addition to the ions thermal motion. Such movement kinematics determined by the velocity field in plasma formation and its concentration reducing because of the ions extraction. On the basis of this model it shows that plasma boundary moves initially in the direction to the ejection electrode, then stops and begins quickly move back. An equation for the nuclides emission current density from hydrogen plasma surface for their quasiplanar extraction geometry is obtained.

At present sources of hydrogen nuclides based on an arc discharge in a vacuum or a laser-produced plasma are used in pulse neutron generators (PNG) [1,2]. PNG contains a small-sized pulsed ion diode placed in a sealed vacuum containing hollow cylindrical anode and cathode. Between them deuterons are accelerated to the maximum energy not exceeding 150 keV by a pulse electrostatic field. The operating pressure in diode's volume comprises about 10^{-2} Pa.

The reactions $T(d,n)^4He$ and $D(d,n)^3He$ undergoing inside the target located in the cavity of a cathode electrode are used for obtaining neutrons. The target represents a metal film effectively dissolving hydrogen (Ti, Sc, Zr), evaporated onto a metal substrate and containing occluded deuterium or tritium.

Fig. 1 shows the schematic section in one embodiment of the vacuum arc deuteron source (VADS) described in works [1,3].

The anode and cathode of the source in question are made of deuterated zirconium.

The processes of deuterium plasma formation are defined by properties of an arc discharge in a vacuum [3,4]. The formation of an arc is preceded by high voltage discharge in the interelectrode space. During the build-up of the discharge current under the influence of a self-generated magnetic field, pinching of the discharge channel occurs in the cathode and anode regions where current densities can exceed 10^{10} A/m^2. Fast local heating of electrodes, deuterium desorption and evaporation of the metal carrier (Zirconium) take place in the pinch zones. And in this medium the formation of an arc occurs. An ignitor discharge over the surface of a hollow disk shaped insulator is used for the enhancement of an arc.

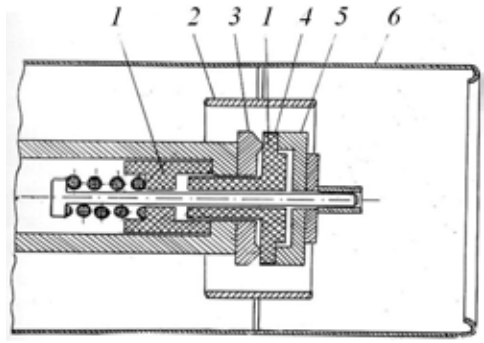

Figure 1: A three-electrode VADS: 1- insulators; 2- anode; 3- cathode; 4- semiconducting coating ; 5- igniter electrode; 6- shielding electrode

This discharge arises due to intensive field emission in the region of the triple point (insulator-metal-vacuum) characterized by abnormally high value of the electric field intensity. The breakdown of a vacuum gap between cathode and igniter electrode leads to the heating of the cathode's part followed by deuterium desorption. As a result, a partially ionized cloud of deuterium vapour rapidly spreading into the space between the cathode and anode of an ion source is formed.

The process of an arc formation is accompanied by the establishment of anode and cathode spots in the regions of its pinching over a period of time about 10^{-8} c.

The temperature of electrode spots can reach several thousand degrees. This provides a continuous deuterium desorption and evaporation of the metal carrier. After filling the discharge gap by metal pairs, they become the base medium of arcing since the ionization potential of the metal carrier is sufficiently lower than the deuterium potential. Therefore it should be assumed that the main suppliers of deuterons to VADS are not the body of an arc but its cathode and anode spots. Plasma is injected by electrode spots of an arc in the form of jets moving at a velocity of shock wave propagating in a vacuum. Estimates and the experimental data show that this velocity is equal to ~10^4 m/s [5].

The emission of laser jets by the electrode spots is a random process. There is also a significant variance of laser jets directions from pulse to pulse. However, as a result of internal anode reflections of a VAT (Vacuum acceleration tube) diode system, a laser jet is partially symmetrized.

One of the factors that shall affect the current value of deuterons extracted from VADS is the atomic weight of the metal carrier. To illustrate this effect it can be easily drawn an analogy to a simpler laser deuteron source (LDS) [1,6], which can be regarded as a physical model

ISBN 978-3-95450-170-0

of VADS. The work [7] revealed an increasing relative yield of deuterons from a laser source with the increase in atomic weight of the metal carrier of a plasma-forming target. This is due to an decreasing the velocity of plasma expansion with the increase in atomic weight of the metal carrier, this provides better conditions for the competition of the ionization processes in an expanding plasma over the recombination processes[1].

The formation of a voltage pulse on an igniter electrode of an ion source is initiated synchronously with the formation of a high voltage pulse on the accelerating diode gap.

The extraction of deuterons from VADS and their subsequent acceleration are generally carried out in a quasi stationary state when a flight time of a deuteron in the diode gap and a characteristic time of a voltage change are substantially less than a pulse duration of the deuteron current.

The kinetic energy of a deuteron T on the cathode is proportional to potential differences U between the anode and cathode electrodes: $T=eU$, where e- is the elementary electrical charge. The maximum attainable energy is defined by the dielectric strength of a diode system and does not exceed 0.15 MeV. Deuterons in a extending plasma cloud fly at the forefront getting ahead of heavier ions of the metal carrier.

Two factors are responsible for the process of extracting deuterons from the VADS plasma. The first factor is the thermal agitation of deuterons determining the dependence of the thermocurrent density on the time t at the VADS output [1, 8]:

$$j_T(t) = en(t)\langle V_\perp(t)\rangle \quad (1)$$

where

$$n(t) \approx \frac{N_d}{\pi R_A^{\,2}(b_0 + V_d t)} \quad (2)$$

- the electron density in the region of a plasma edge, V_d is the initial velocity of a plasma front determined by the velocity of shock wave propagating in a vacuum ~10^4, N_d is the total number of deuterons in plasma at the cooling stage of its ionization state depending on the energy stored in the tank capacitor of an ion source circuit: $W_i = \frac{C_i U_i^{\,2}}{2}$. Here C_i~(10^{-8}-10^{-7})F is the tank capacitor in the VADS circuit, U_i~kV- its charge voltage. The cooling of an ionization state corresponds to the stage of plasma extension when a balance between the processes of recombination and ionization in its volume is established and further the number of deuterons remains more or less constant. The parameter b_0~$10a_0$ estimates the characteristic initial size of plasma formation corresponding to the completion of its ionization state cooling similar to LDS [9], a_0- the characteristic size of an electrode spot, R_A- the radius of an anode electrode,

$$\langle V_\perp(t)\rangle = 0.4\sqrt{2e\theta(t)/M_d} \quad (3)$$

- the average, according to the Maxwell distribution, projection on normal to a plasma surface of deuteron's thermal velocity; M_d - the mass of deuteron; θ- the plasma temperature on the energy scale, eV.

Fig. 2 depicts the set of experimental dependencies N_d (C_i,U_i), obtained for VADS with electrodes from $ZrD_{1.3}$ during the measurement of VAT current characteristics and built after processing the experimental data by the method of least squares.

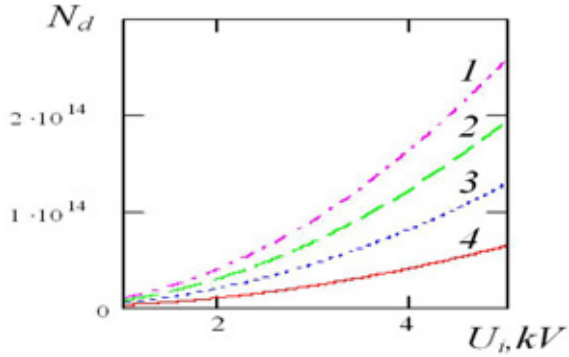

Figure 2: The characteristic set of experimental dependencies $N_d(U_i)$: 1- C_i=4.10^8 F; 2- 3.10^8 F; 3- 2.10^8 F; 4- 10^8 F;

Fig. 3 shows the results of the experiment on the neutron production.

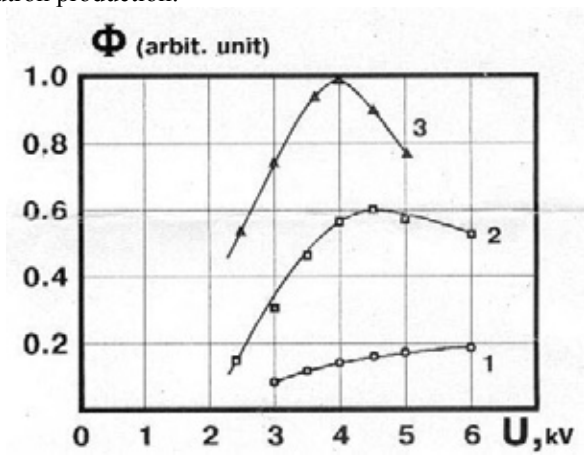

Figure 3: The characteristic set of neutron yield dependencies of PNG per a pulse (RVU) - $\Phi(U_i)$:
1- C_i=2.5·10^{-8} F; 2- 5·10^{-8} F; 3- 10^{-7} F

The monotonic disturbance of curves 2 and 3 can be explained by a limited store of energy in the tank capacitor of a high voltage circuit.

The measurement error calculated using Student's distribution with the 0.95 confidence level did not exceed 20%.

By taking a single-atomic plasma and its adiabatic expansion we find the following expression for temperature-time dependence:

$$\theta(t) \approx \theta_0\left(1 + \frac{V_d t}{b_0}\right)^{-2/3}, \quad (4)$$

where θ_0 - the initial plasma temperature.

The second factor is related to Langmuir waves in the region being adjacent to a plasma edge [10].

ISBN 978-3-95450-170-0

Forming a plasma jet in the region of an electrode spot, every particle of plasma will account for about an equal share of kinetic energy:

$$\frac{mV_e^2}{2} \approx \frac{M_d V_d^2}{2} \approx \frac{M_{Zr} V_{Zr}^2}{2}. \quad (5)$$

Here m, V_e; M_{Zr},V_{Zr} - the masses and maximum velocities of electrons and zirconium ions respectively.

At first electrons in the region of a plasma edge are emitted getting ahead of deuterons and forming a double layer. After being stopped, they turn back accelerating in the region of a deuteron front and rush into the depth of a plasma cloud exposing deuterons and forming a new double layer with the opposite polarization. After being stopped, electrons accelerate in the field of this double layer and run ahead again. This process is further repeated. That is the mechanism of Langmuir waves in the region of a plasma edge.

The initial length of polarization L_0 at the completion stage of an ionization state cooling can be estimated, taking into account (2), from the equation of potential (electrostatic) and kinetic energies of electrons constituting the mentioned double layer and constraints of the plasma quasi-neutrality. As a result, we have the following expression:

$$L_0 \approx \frac{V_d R_A}{e} \sqrt{\frac{\pi \varepsilon_0 M_d}{2} \frac{h_0}{N_d}}, \quad (6)$$

where ε_0 - the electric constant.

The frequency of Langmuir waves at any given time t can be estimated using the well-known formula [11]:

$$\omega_л(t) = e\sqrt{\frac{n(t)}{m\varepsilon_0}} \approx \frac{e}{R_A}\sqrt{\frac{N_d}{\pi m \varepsilon_0 (b_0 + V_d t)}}. \quad (7)$$

To estimate the change of a polarization length L in the process of a plasma expansion an adiabatic invariant can be used: $L^2\omega_л$. As a result, we have:

$$L(t) \approx L_0\left(1 + \frac{V_d t}{b_0}\right)^{1/4}. \quad (8)$$

At the negative phase of Langmuir waves in the region of a plasma formation front

$$\frac{N_d L(t)}{b_0 + V_d t}$$

deuterons are exposed which can be involved in the process of acceleration. The time-averaged density of an emission current related to Langmuir waves can be estimated:

$$j_{Л}(t) \approx \frac{eN_d L(t)\omega_л(t)}{\pi^2 R_A^2 (b_0 + V_d t)}. \quad (9)$$

Therefore, the total density of a VADS emission current according to formulae (1)-(4) и (6)-(9) will be defined as follows:

$$j_э(t) = j_T(t) + j_{Л}(t) \approx$$

$$\approx \frac{eN_d}{\pi R_A^2 b_0}\left(0.4\sqrt{\frac{2e\theta_0}{M_d}} + \frac{V_d}{\pi}\right)\left(1 + \frac{V_d t}{b_0}\right)^{-5/4}\left[1 + \left(1 + \frac{V_d t}{b_0}\right)^{-1/12}\right]$$

REFERENCES

[1] B.Yu. Bogdanovich, A.V. Nesterovich, A.E. Shikanov, M. F. Vorogushin and Yu. A. Svistunov, 2009, Distantsionnyi radiatsionnyi kontrol' s lineinymi uskoritelyami. Tom 1. Lineinyi uskoritel' dlya generatsii tormoznogo izlucheniya i neitronov, [Remote Radiation Monitoring with Linear Accelerators, vol. 1. Linear Accelerators for Generation of Bremsstrahlung and Neutrons], Energoatomizdat, Moscow, 272p.

[2] Sbornik materialov Mezhdunarodnoi nauchno-tekhnicheskoi konferentsii "Portativnye generatory neitronov i tekhnologii na ikh osnove, Vserossiisky nauchno-issledovatel'skii institut avtomatiki (VNIIA) im. N.L. Dukhova, Moskva [Collection of materials of International Scientific and Technical Conference "Portable Neutron Generators and Technologies Based on Them"], 2005, All-Russia Research Institute of Automatics, Moscow, pp.203-206

[3] S. P. Sukhoveev, May 1979, O vakuumnoi podzhigaemoi duge mezhdu elektrodami iz ZrD, [Externally ignited vacuum arc between ZrD electrodes], Zhurnal Tekhnicheskoi Fiziki, vol. 49, pp. 1027-1029

[4] Vakuumnye dugi, [Vacuum arcs], A collective monograph ed. J.Lafferty, 1982, Mir, Moscow, 430p.

[5] I.G. Kesaev, 1968, Katodnye protsessy elektricheskoi dugi, [Cathode Processes in an Electric Arc], Nauka Publ, Moscow, 245p.

[6] I.I. Vergun, K.I. Kozlovsky, Yu.P. Kozyrev, A.S. Tsybin and A.E. Shikanov, Issledovanie intensivnogo lazernogo istochnika deitronov, [Investigation of an intensive laser source of deuterons], Zhurnal Tekhnicheskoi Fiziki, vol.49, No. 9, p.2003–2006

[7] V.M. Gul'ko, N.F. Kolomiets, A.E. Shikanov and K.I. Yakovlev, 1991, Issledovanie sostava plazmo-obrazuyushchikh mishenei lazernykh deitronnykh istochnikov dluya malogabaritnykh uskoritel'nykh trubok, [Investigation of the plasma-forming targets composition of laser deuteron sources for small acceleration tubes], Kvantovaya elektronika, vol. 18, No4, pp. 485-486.

[8] M.D. Gabovich, 1972, Fizika i tekhnika plazmennykh istochnikov ionov, [Physics and technology of plasma ion sources],Atomizdat, 304 p.

[9] Y.A. Bykovsky and V.N. Nevolin, 1985, Laser Mass Spectroscopy (in Russian),Energoatomizdat, Moscow? 1985.

[10] A.N. Didenko, V.I. Rashchikov, V.I. Ryzhkov and A.E. Shikanov, 2011, Osobennosti izvlecheniya vodorodnykh ionov iz impul'snykh plazmennykh obrazovanii, [Peculiarities of hydrogen ion extraction from pulsed plasma plumes], Pis'ma v ZTF(Letters to the Technical Physics Journal), vol.37, issue 21, pp.70-75.

[11] D.A. Frank-Kamenetsky, 1968, Lektsii po fizike plasmy, [Lectures on Plasma Physics] Atomizdat, Moscow, 288 p.

ISBN 978-3-95450-170-0

NEUTRON ACCELERATING TUBES WITH MICROWAVE DEUTERONS SOURCE USING ELECTRON-CYCLOTRON RESONANCE EFFECT

Didenko A.N., Bogdanovich B.Y., Nesterovich A.V., Shikahov A.E.,
Kozlovskiy K.I., Prokopenko A.V., Shatokhin V.L.
National Research Nuclear University (Moscow Engineering Physics Institute)
Moscow, Russia

Abstract

The physical principles of increased efficiency neutron accelerating tubes based on the microwave sources of heavy hydrogen nuclides, using the electron-cyclotron resonance effect (ECR) are considered. The authors' theoretical results consist of electromagnetic oscillations generation in the working volume of the ion source of the accelerating tube with the boundary excitation of a microwave discharge. Resonator and waveguide modes for ECR-plasma excitation are examined. Features of neutron generation in these accelerator neutron tubes based on microwave source of heavy hydrogen nuclides are analyzed. The algorithm is developed and numerical simulation of neutron pulse formation in neutron generators based on microwave source is done taking into account target shape and the possible deuterons resonant recharge. Frequency dependences of the energy flux density transmitted from an alternating electromagnetic field to the electron component of the plasma are obtained. They depend on the constant longitudinal magnetic field induction and pressure in the discharge chamber. The results of these studies could form the basis for the efficient domestic portable neutron generators development based on accelerating tubes with microwave hydrogen nuclides sources.

Modern development of several areas of science and technology requires a new generation of compact electro-physical neutron sources - neutron generators [1, 2]. The main units of neutron generator are accelerating tube, high-voltage source, as well as of its operation and energy supply systems. Accelerating tube consists of an ion source of heavy hydrogen, the target, accelerating and focusing electrode system. In an accelerating tube for receiving hydrogen ions Penning sources with heated, cold or hollow cathodes, duoplasmatron, sources with high-frequency and superhigh-frequency (microwave) discharges, vacuum-arc discharge or laser plasma could be used [2-4]. The results of studies related to the development and production of neutron generators with the microwave oven sources of nuclides of hydrogen, in which the effect of an electron-cyclotron resonance (ECR) is realized, were published at [5-6].

The presence of the ECR and the magnetic constriction of the discharge allow to the increase of energy input into the plasma to achieve and maintain a high degree of ionization k (70%) with electron temperature θ (up to 10 eV) and the ion concentration n (to ~ 10^{19} m^{-3}). Thus intense beams of nuclides hydrogen with output source current density 0.1 – 10 kA/m^2 are formed;

$$j = \left(\frac{e^3}{2\pi M}\right)^{1/2} n\left(\frac{\theta}{A}\right)^{1/2}. \quad (1)$$

where e - elementary electric charge, M - the mass of a proton, A - the atomic mass of a nuclide of the hydrogen extracted from plasma.

Plasma generation in a microwave ion source is carried out in the course of cyclotron acceleration of electrons in the field of electrodynamics cavity or waveguide. Thus dynamics of an electron in considered local area of the resonator will be defined by the following differential equation:

$$m\frac{d^2\mathbf{r}}{dt^2} = -m\omega_e^2\mathbf{r} - e\mathbf{E}\cos 2\pi ft - e\left[\frac{d\mathbf{r}}{dt}, \mathbf{B}\right] - m\nu\frac{d\mathbf{r}}{dt}, \quad (2)$$

where m - electron mass, $\mathbf{r}$ - radius vector in the local coordinate system, $\mathbf{E}$, $\mathbf{B}$ - vectors of the electric field and the magnetic field at a given point of the resonator, f - microwave generator frequency, ν - the average electron collision frequency. The influence of an alternating magnetic field in equation (2), as shown by computer simulations carried out, can be neglected, if the power of the microwave generator does not exceed 1 kW. Equation (2) can be solved by an equivalent system of differential equations. To the electrons of the plasma which are in the set unit of volume, energy of an electromagnetic field will be transferred in unit of time ($J \cdot m^{-3} \cdot s^{-1}$):

$$q(f, p, b, z) = en\mathbf{E}(z)\left\langle\frac{d\mathbf{r}}{dt}\cos 2\pi ft\right\rangle.$$

This function has a resonant character. On Fig.1,2 as an example, shows the calculated dependencies $q(f,p,1,0)$ and $q(f,0.25,b,0)$. The point z = 0 corresponds to the center of the discharge space. The calculation of these temperature dependencies of was chosen at $\theta \approx 10$ eV. Such temperature is typical for ECR plasma, obtained as a result of the probe measurements (see, for example [7]). On these curves can be clearly seen two peaks. Their presence is a consequence of the ECR. Calculations show that the presence of two such peaks occurs at commensurability of Larmor and Langmuir frequencies.

ISBN 978-3-95450-170-0

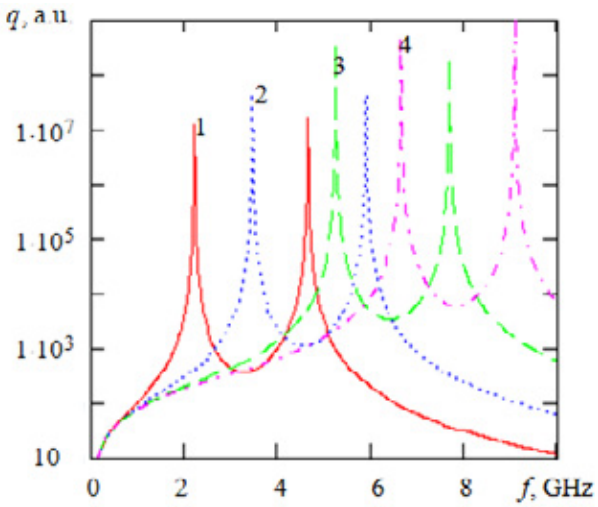

Figure 1: Dependencies of the energy flux density, in arbitrary units, obtained for b = 1 and p =: 1- 0.25; 2 - 0.5; 3 - 1.0; 4 - 1.5 Pa.

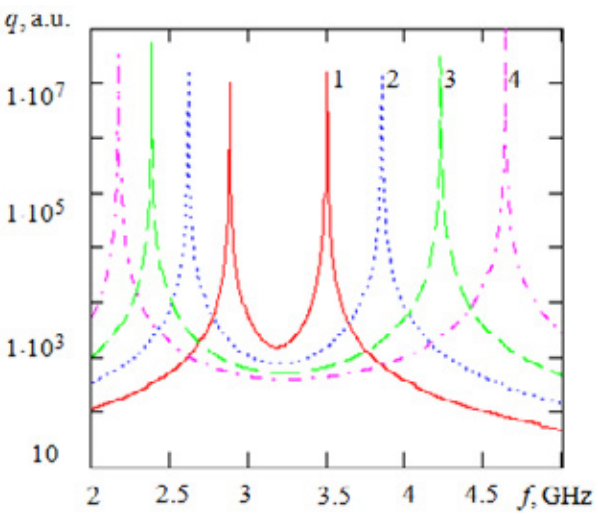

Figure 2: Dependencies of the energy flux density, in arbitrary units, obtained for p = 0.25 Pa and b =: 1- 0.25; 2 - 0.5; 3 - 0.75; 4 - 1.0.

There are two possible options of ECR discharge excitation. In the first case [5-6] of the microwave power from the generator (magnetron) by a rectangular waveguide through ceramic plate, which is the waveguide window, was supplied into a cylindrical cavity, where the electric discharge with the ECR effect is occurred. For this purpose in the cavity by means of system of ring magnets create a longitudinal magnetic field. It is necessary to notice that in other case plasma can be obtained in a mode of a running wave. In this source the waveguide segment has to be used instead of the cavity. Extraction of deuterons is carried out through an exhaust outlet in a resonator edge.

Another option of realization of a source of hydrogen nuclides using the ECR effect provides the location of the discharge area between the two electrodes [7]. One of them is the central conductor of the coaxial line connected with the microwave generator, and the second - the central conductor of a coaxial loop with the short-circuited plunger which length is. In this loop input impedance selected so as to compensate for the reactive component of the complex impedance of the plasma. The magnetic field in this case is formed by two coaxial coils with the magnetic shield.

The average power transmitted from the microwave field to the electrons per unit of volume of plasma formation, in both these cases can be estimated as follows:

$$\langle q(f,p)\rangle \approx \frac{1}{L}\int_0^L dz q[f,p,b(z),z],$$

where L - the longitudinal dimension of the plasma formation. The dependence $b(z)$ can be calculated using the algorithm described in [8], and for obtaining dependence of $E(z)$ it is possible to use modeling of electromagnetic fields in the cavity of deuterons source. Considered ion sources operate at authorized power frequency of 2.45 GHz. ECR condition providing requires a longitudinal constant magnetic field with induction in the center of working area of a source 87.5 mT.

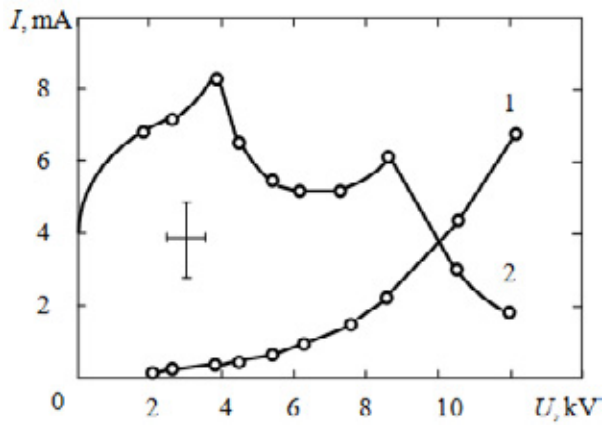

Figure 3: .Dependences of the deuterons current taken in the accelerating gap of the neutron generator (a curve 1) and the current getting on the extracting electrode (a curve 2) from voltage on the extraction electrode.

For higher current densities of hydrogen nuclides at the exit of a source and their transport to the neutron generator target in addition to the high emission parameters of plasma effective ion-optical systems of extraction of ions are required. Volt-ampere characteristics (VAC) of ion streams formation systems between the working volume - extracting electrode were carried out in MEPhI. Thus selection of ions was done from plasma boundary situated in the plane of the emission aperture, and the geometry of the ejection

ISBN 978-3-95450-170-0

electrode corresponded to Pierce optics. Fig. 3 shows the corresponding VAC characteristics.

Computer simulations of working chambers of neutron generators was carried out, the modern package of applied programs which is based on differential methods of the numerical solution of the Masksvell equations with given boundary conditions are certainly was used. Parameters of electric and magnetic fields intensity, Q-factor, resonant and frequency dependences for considered neutron generators were calculated.

Cylindrical resonator working chamber has the following geometric dimensions - diameter 90 mm, length 100 mm, the aperture to the output beam of deuterium ions 60 × 6 mm^2. The resonator is made of stainless steel. The simulation shows that the structure of the electric and magnetic fields in the working chamber of the ion source corresponds to TE_{111} - mode, at a frequency of 2.45467 GHz. That's roughly the same as the default value for the frequency of magnetrons for power ECR discharge ion sources. The electric field in this kind of oscillation transverse axis of the resonator, on a sinusoid is maximum in the center and falls down at the ends. Calculation of parameters of intensity, Q-factors and electric fields is executed at frequency 2.45 GHz. Microwave power is supplied from rectangular waveguide WR-340. At the inlet into the chamber a thin membrane of alumina ceramics is established. It provides to support low pressure of deuterium in the chamber. Maximum electric field strength in the center of the cavity at a microwave power supply 400 W corresponds to $E = 4.5 \cdot 10^5$ V/m. This field strength is sufficient for ignition and microwave discharge burning in a deuterium plasma at pressures of less than 1 Pa. Calculated value of the induction of the microwave magnetic field was more than an order less than the induction of a constant magnetic field, which allows us to neglect the variable component of the magnetic field in equation (2).

Calculation of electrodynamics characteristics of the waveguide working chamber showed that a strong cross electric field arises in the chamber at the end wall bordering the alumina ceramics used as vacuum microwave window. Geometric dimensions of the chamber: diameter 40 mm, length 50 mm. Deuterium ions outlet aperture of diameter 2 mm is made axially at the end wall of the working chamber. Working chamber material is stainless steel. Value of the electric field amplitude on the axis of the chamber at a distance of 1 mm from the ceramic wall in the microwave power supply ≈ 300 W is $E = 2.9 \cdot 10^5$ V/m, also suggests the possibility of ignition and sustained discharge in deuterium at low pressure. Discharge has to ignite near the ceramic inlet. Deuterons diffuse toward the outlet, which has about few millimeters in diameter and locates in the center of the end of the working chamber.

Based on this analysis the choice of geometry of the working chamber of deuterons microwave source in the form of the rectangular cavity made on the basis of standard waveguides of section (for example the WR-340, WR-430 and WR-284 type) with the main wave of TE_{101} - mode was made. In this type of oscillations the electric field structure coincides with that in the cylindrical cavity TE_{111}-mode.

Numerical calculation for a cavity with dimensions of 72 mm × 34 mm × 114.83 mm showed that the maximum value of electric field amplitude in the cavity made of stainless steel at the power of magnetron of ≈ 400 W at frequency of 2.45 GHz and Q-factor - 2400 is $E = 4.56 \cdot 10^5$ V/m. For cavity with sizes of 86.36 mm × 43.18 mm × 86.17 mm – $E = 4.25 \cdot 10^5$ V/m, and for the cavity with sizes of 90 mm × 45 mm × 82.96 mm – $E = 4.15 \cdot 10^5$ V/m. For effective power supply system of microwave chambers of ion sources it is supposed to use magnetrons of continuous action with power up to 1 kW, which can be regulated by anode current of the magnetron.

REFERENCES

[1] B.Yu. Bogdanovich, A.V. Nesterovich, A.E. Shikanov, M.F. Vorogushin, and Yu.A. Svistunov, Remote Control of Radiation from Linear Accelerators, Vol.2: Complexes of Radiation Control (Mashinostroenie, Moscow, 2012), 284.

[2] Portable generators of neutrons and technology on their basis / Reports edited by Yu.N. Barmakov, Moscow, VNIIA, 2013, 620.

[3] B. Yu. Bogdanovich, A. V. Nesterovich, A. E. Shikanov, M. F. Vorogushin, and Yu. A. Svistunov, *Remote Control of Radiation from Linear Accelerators*, Vol. 1: *Linear Accelerators for Generation of Bremsstrahlung and Neutrons* (Energoatomizdat, Moscow, 2009), 272.

[4] A.S. Tsybin, A.E. Shikanov, Izv. Vuzov USSR, Physics (1985) p. 3-31.

[5] Waldmann O., Ludewigt B. Development of a permanent-magnet microwave ion source for a seald-tube neutron generator, Lawrence Berkeley National Laboratory, 1 Cyclotron Road, Berkeley, CA 94530.

[6] Oing Ji. Compact Permanent Magnet Microwave-Driven Neutron Generator. Lawrence Berkeley National Laboratory, 1 Cyclotron Road, MS5R0121, Berkeley, CA 94720.

[7] Nesterovich A., Abramenko N., Bogdanovich B. "Ion microwave source for linear accelerator", Proceedings of 17th Particle Accelerator Conference, vol. 1-3, 1998, pp. 2773- 2774.

[8] R.V. Dobrov, V.I. Ryzhkov, D.D. Ponomarev, S.V. Syromukov, A.E. Shikanov, Problems of Atomic Science and Technology, 2011, №1(28), p.26–31.

ISBN 978-3-95450-170-0

ION SOURCE DEUTERON BEAM ACCELERATION IN GAS-FILLED ION-OPTIC SYSTEM

V.I.Rashchikov, NRNU(MEPHI), Moscow, Russia

Abstract

Computer simulation of deuteron beam from ion source acceleration in gas-filled neutron tube has been fulfilled. Fully relativistic electromagnetic particle-in-cell finite difference, time-domain cod SUMA [1-2] has been used to investigate the ionization and knock on processes and there influence on deuteron beam and output neutron flow parameters. When deuteron and ionized particles space charge self-field forces become the same order of magnitude as external one, virtual cathode may occurs. It is happens because of injected from ion source deuterons cannot overcome their own space charge potential wall and move in transverse direction. However, electrons, produced by ionization, are trapped within the deuteron beam space charge potential wall and decrease it significantly. Thus, space charge neutralization of deuteron beams by electrons, may considerably increase target current and, as a result, output neutron flow. The data obtained were compared with experimental results.

COMPUTER SIMULATION

To design neutron tube with assigned flow value and other parameters such as size, service life and so forth, preliminary computer simulation should be fulfilled. PIC code SUMA was used for ion optic system modeling and investigation of ionization processes influence on deuteron beam dynamics and output data of gas-filled neutron tubes. The code is a 2.5 dimensional time dependent model that may self-consistently describe the charged particles dynamics at various coordinate systems.

As a sample typical gas-filled pulse neutron tube has been studied (see Fig. 1).

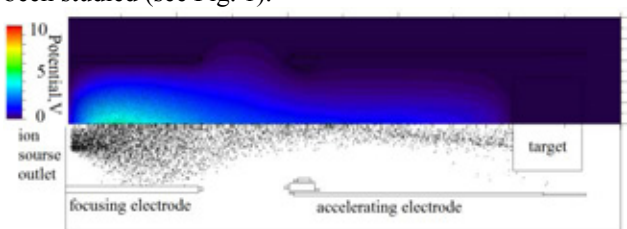

Figure 1: Deuterons distribution (lower) and their self-field potential (upper) in neutron tube.

Accelerated electrode is under -85kV potential, target -83kV, focusing electrode is grounded.

Preliminary ion source deuteron beam parameters has been obtained experimentally. For this purpose alone Langmuir probes, multi-electrode energy analyzer and Faraday cup were used. We obtain following deuteron beam parameter: longitudinal energy 1.7±0.4 keV, current ~150μA for initial gas pressure $0.5 \cdot 10^{-3}$ Torr. Moreover, some beam density distribution measurement were fulfilled. Nevertheless, it was not enough data for computer simulation. Therefore, the attempt to solve inverse problem was made. As the result to be obtained the experimental deuteron current density distribution on target shown on Fig. 2*a* was used.

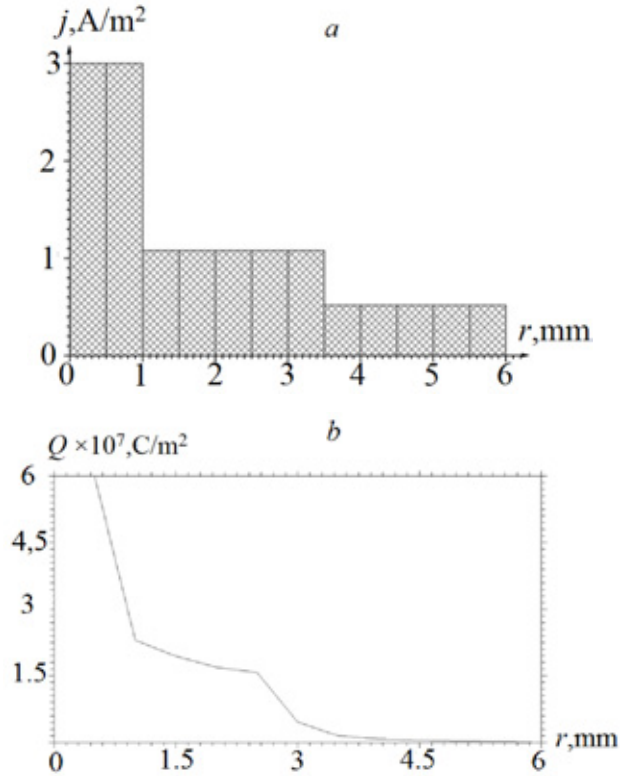

Figure 2: Current density (experimental, *a*) and charge distributions (simulation, *b*) on the target.

Experimental data were rebuild from target depth erosion and target sputtering calculation.

Computer simulation shows that for the following input beam data, experimental and calculated distributions are closed to each other: longitudinal energy 1.9±0.1 keV and transverse energy distribution ~120 eV, current ~150μA (see Fig.2*b*).

Passing through the gas, deuteron beam produce plasma, which consist of electron and slow ion. Their densities under considered gas pressure range approximately equal each other (see Fig. 3.) [3].

ISBN 978-3-95450-170-0

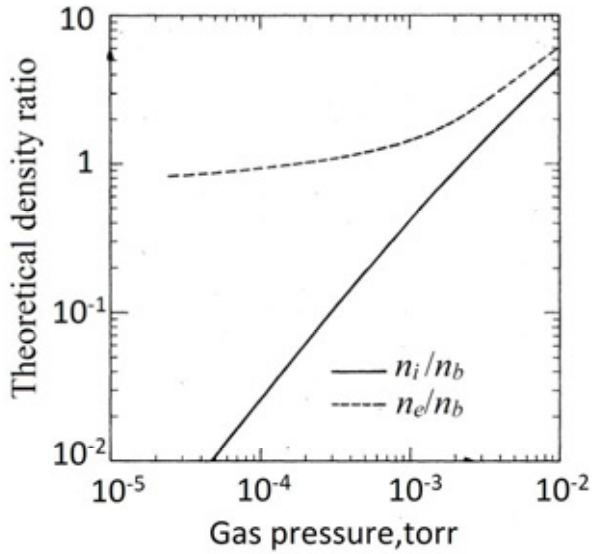

Figure 3: Ratio of electron or ion density as a function of pressure.

Deuteron and ionized particles own space charge forces for this current value are considerably less than that of the external one (see Fig. 4.).

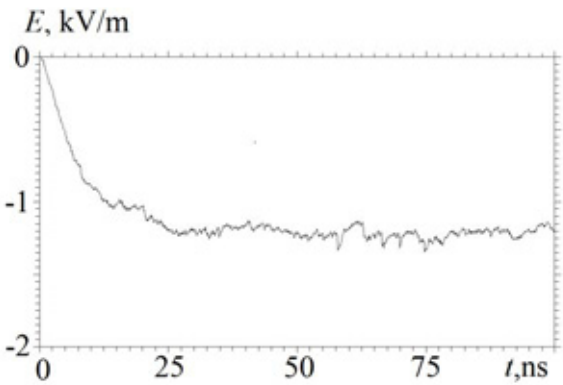

Figure 4: Longitudinal electric self-field time dependence near the cathode.

The value of decelerating deuteron space charge self-field is about 1kV/m, that three order of magnitude less than external accelerating field. Therefore, they cannot effect on deuteron beam propagation. Figure 5 shows that electric field is accelerating for the deuteron elsewhere in the tube.

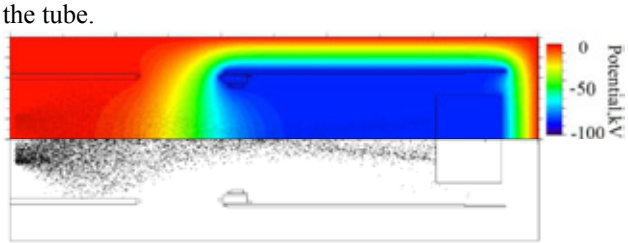

Figure 5: Deuterons distribution (lower) and total field (external and self-field) potential (upper) in neutron tube.

The electrons knocked on from the target by accelerated deuterons cannot pass through the accelerating electrode – target potential wall and cannot effect on deuteron beam propagation either (see Fig. 6).

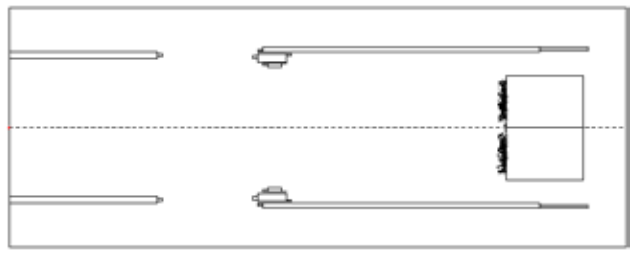

Figure 6: Knocked on electrons distribution.

Current gain leads to deuteron and ionized particles self space charge forces increases and become the same order of magnitude as external one. If we are not taking into account ionization processes, deuteron beam propagation for current 150mA shown on Fig. 7*a*.

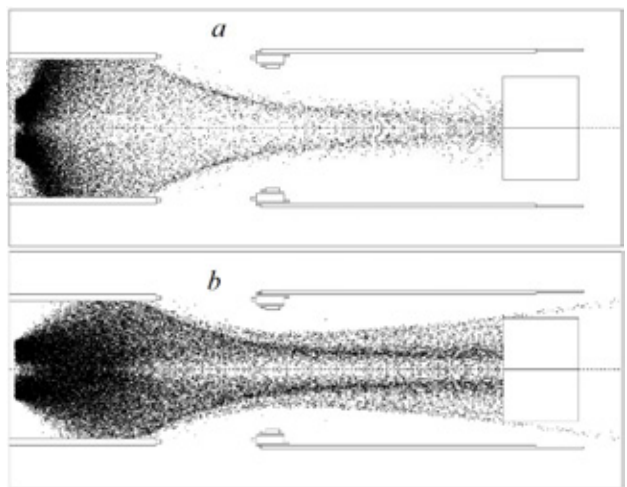

Figure 7: Deuterons distribution without (*a*) and with (*b*) ionization.

Injected from ion source deuterons cannot overcome own space charge potential wall and form a virtual cathode – positive potential value (see Fig. 8).

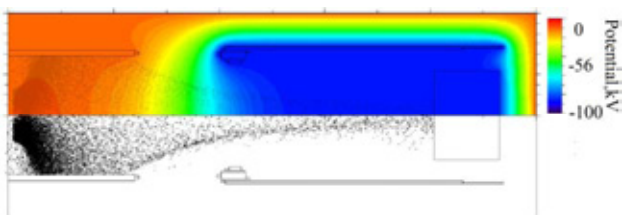

Figure 8: Virtual cathode forming.

Significant part of them leave the region in radial direction and get off to focusing electrode. Target current become four time less than injection one.

If we take into account ionization processes deuteron beam propagation changes considerably (see Fig.7*b*). Electrons, produced by ionization, are trapped within the deuteron beam space charge potential wall and cannot

ISBN 978-3-95450-170-0

leave the interaction region (see Fig. 9*a*), as they did for current 150μA (see Fig. 9*b*).

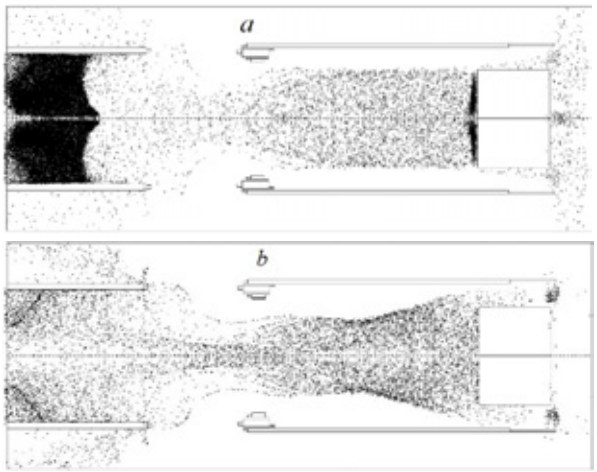

Figure 9: Electrons distributions for current 150mA (*a*) and 150μA (*b*).

Electron accumulation result in decreasing of the potential wall effective depth and deuteron target current rising. Figure 10 shows longitudinal electric field time dependence on the tube axis near the left border for cases without (*a*) and with (*b*) ionization taking into account.

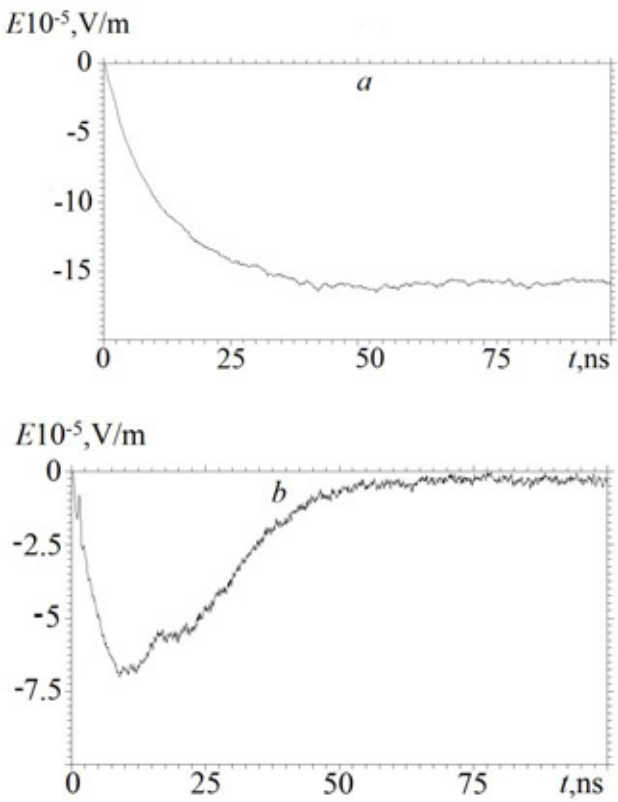

Figure 10: Longitudinal electric field time dependence without (*a*) and with (*b*) ionization taking into account.

The value of deuteron current increases almost three times that result in identical neutron flow increased approximately the same value [4].

$$\Phi = \frac{sn}{e\tau}\sum_i q_i \int_0^{W_i} dW \frac{\sigma(W)}{F(W)},$$

where s – target stoichiometry coefficient, n – target nuclei concentration, e – elementary electric charge, q_i - deuteron charge with energy W_i, $\sigma(W)$- nuclei reaction cross-section on the target, $F(W)$ - deuteron bremsstrahlung loss in the target, τ- pulse duration.

Moreover, own longitudinal electric field rise near the target leads to reduction of accelerating electrode – target potential wall and, as a result, additional knocked on electrons may appear in the region.

Influence of low energy ion, produced by ionization, is not so significant. Slow ion rather quickly obtain radial velocity and move to the tube periphery (see Fig. 11).

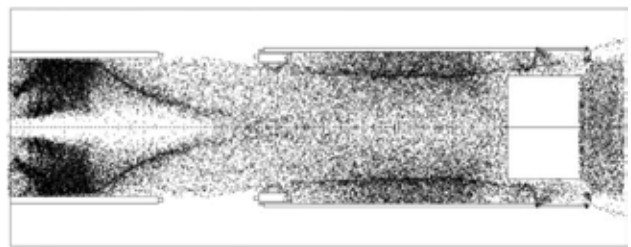

Figure 11: Slow ion distributions in the tube.

Thus, space charge neutralization of deuteron beams by electrons, produced by ionization, may considerably increase target current and, as a result, output neutron flow.

REFERENCES

[1] V. I. Rashchikov, Problems of Atomic Science and Technology. Series: Nuclear Physics Investigations, No. 10 (18), pp. 50 -53, 1990.

[2] A.N. Didenko, V.I. Rashchikov, V.E. Fortov, Technical Physics, Vol. 56, No. 10, pp. 1535–1538, 2011

[3] A.J.T. Holmes, Phys. Rev. A. , Vol. 19, No. 1, pp. 389-407, 1979.

[4] A.N. Didenko, V.I. Rashchikov, V.I. Ryzhkov et al., Atomic Energy, Vol. 112, No. 3, pp. 182 -184, 2012

ISBN 978-3-95450-170-0

DYNAMICS OF PLASMA-BEAM FORMATIONS IN THE ACCELERATION GAP OF THE PULSE NEUTRON GENERATOR-BASED VACUUM NEUTRON TUBE

A.V. Agafonov, The Lebedev Physical Institute of the Russian Academy of Sciences, Moscow, Russia
S.G. Kladko, S.P. Maslennikov, E.Y. Shcolnikov, NRNU MEPhI, Moscow, Russia

Abstract

The analysis of dynamics of plasma flows containing deuterium, zirconium ions and electrons in the accelerating gap of the pulse neutron generator-based vacuum neutron tube (VNT) [1] is presented in the paper. The investigations have been carried out using the code KARAT [2] for the two-dimensional non-stationary mode. The limiting currents of each component for the real accelerating gap geometry have been determined. The differences between the values of these currents and those ones determined by the Child-Langmuir equation have been demonstrated.

The analysis of plasma emitter dynamics in the gap has been performed by the model of VNT with the accelerating voltage amplitude of 120 kV and the pulse duration of 1.2 μs. It has been shown that the value of the current entering the gap from the source of ions can be very different from the current value at the target. To increase this value the accelerating gap partition using the conductive grid which is transparent for a beam and has several geometric configurations has been proposed. The ring configuration of the emitter has been considered for the same purposes. The calculations have shown that the combination of these two methods described above can allow transporting the current of deuterons from the anode grid to the target without losses.

INTRODUCTION

All set of physical processes accompanying the operation of VNT can be structured as follows. Firstly, these are processes in the vacuum arc discharge including in particular the production of an erosion mass from the discharge gap electrodes. Secondly, these are processes accompanying the expansion of plasma products emitted by a vacuum arc. Thirdly, this is the transmission of a plasma flow through the anode grid of VNT and the acceleration of deuterium ions in the accelerating gap and, fourthly,these are the processes in the target accompanied with the generation of neutrons.

Modelling of the plasma dynamics in the accelerating gap has been carried out using the code KARAT. Initial data for plasma parameters were obtained from the designed model of VNT [3]. A voltage supply to the accelerating gap has been modelled using a TEM wave, therefore the diode has been shown as a shorted coaxial transmitting line. All computational region is divided into cells, a set of which forms a rectangular grid. The basic parameters for choosing the size of a grid unit cell are the Debye length λ_D and the collisionless skin depth. The above mentioned values of plasma parameters are:

$$\lambda_D = 2,35\times10^{-4}\,см, \qquad \frac{c}{\omega_{pe}} = 1,68\times10^{-1}\,см. \tag{1}$$

where ω_{pe} – the electronplasma frequency

The increase in the number of cells extends the running time. As a non-stationary process is under consideration and the Debye length is more statistic parameter, in this case, the collisioness skin depth is the characteristic scale. On that basis, the number of divisions is selected in such a way that a unit cell is a square with a side of 1,24 * 10^{-2}sm. The time step for every iteration is automatically selected by a code and comprises 1,87*10^{-4}ns that is agreed with the period of electron component oscillations of this plasma ~ 10^{-2} ns.

To estimate the space-charge limited current in a planar diode with the distance d between electrodes and the emitting surface of R, the Child-Langmuir equation can be used:

$$I_{CL} = \left(\frac{R}{d}\right)^2 \frac{\sqrt{2}}{9} \frac{mc^3}{e} \left(\frac{\varphi_a}{mc^2/e}\right)^{3/2} \tag{2}$$

where φ_a - the voltage across the diode, m – the mass of accelerated particles.

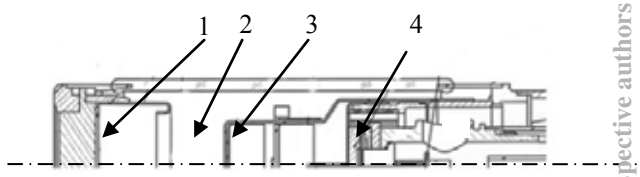

Figure 1: The design of VNT: 1 - the target, 2 – the accelerating (cylindrical) electrode, 3 – the anode grid, 4 – the ion source.

The code KARAT has been used to calculate limiting currents of each plasma component in the real geometry of the accelerating gap.

The design of typical VNT developed in All-Russia Research Institute of Automatics named after N.L. Dukhova is shown in Fig. 1. The plasma flowing comes from the ion source (4). The accelerating gap itself represents a space between the anode grid (3) and the target electrode (2).

ISBN 978-3-95450-170-0

It was assumed that through the anode grid of radius 1sm in the gap there were emitted one-component beams of deuterons, electrons, zirconium ions which were accelerated by direct voltage of 100kV and the current of which knowingly exceeded relevant maximum values. The current flow has been fixed at the target electrode. The results of calculations are presented in the table.

Table 1: The results of current calculations

	e	d	Zr
Partial current (maximum value), A	6,3	6,3	$6,3*10^{-2}$
Limiting current, calculated by the formula (2), A	57,8	$9,5*10^{-1}$	$1,4*10^{-1}$
Limiting current modelling, A	100	1,8	$2,6*10^{-1}$

The "partial current" in the Table 1 refers to the current entering the accelerating gap of VNT.

As shown in Table 1, values of limiting currents in modelling have been greater than in calculations using a formula (2). This is due to the fact that the emitter (the anode grid) size is commensurate with the accelerating gap size. In this case the field amplification effect arises due to the edge effect on the emitter surface. As a result of an excess of the partial current over the limiting one, the plasma starts to penetrate into the accelerating gap.

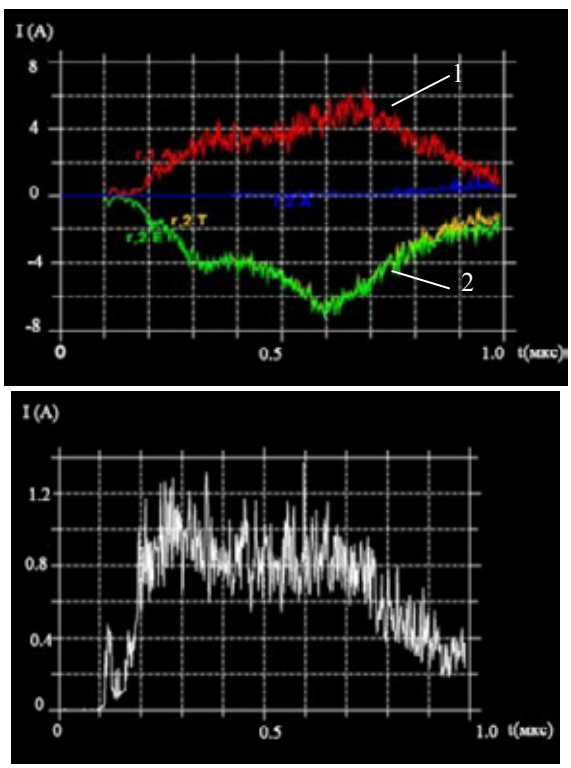

Figure 2: The dependence of currents in the accelerating gap on the time: a – the current on the surface of a cylindrical electrode(1) и the current emitted from the anode grid(2), b – the current on the target.

The dynamics of a plasma emitter can be properly described as follows.As a consequence of an excess of the partial current over the limiting one, the plasma expands in the accelerating field for ions and emits positively charged particles from its surface. This plasma expansion takes place before reaching such an effective distance from the anode grid at which the limiting current of ions will be equal to the partial one. Thus if the partial current is greater than the limiting one, the partial current is removed from the outer edge of the plasma at any time and a fraction of particles accumulates in the plasma emitter. And if the partial current is less than the limiting one, in contrast, the plasma gives off a part of a stored charge together with the limiting current.

Data based on the modelling confirm the described above physics (Fig.2.). As seen in Fig.2., before the emitter comes to a standstill while moving to the target, less partial current is removed from it, whereas at the reverse movement - more partial current. This is due to removing the excess charge which was accumulated in the plasma. As follows from Fig. 2, about 20% of the deuteron current injected into the gap reaches the target. Most of particles settles on the cylindrical target electrode and on the dielectric case of VNT. As the plasma penetrates into the accelerating gap, the fraction of the current on the targetdecreases.

The enhancement of the accelerating gap geometry implies seeking such a design which contributes to obtaining the maximum deuteron current on the target. The way to achieve this objective is by increasing the limiting current for the accelerating gap and, consequently, decreasing the plasma penetration in the accelerating gap. This can be achieved by the insertion of a grid transparent for particles in the gap and by the division of the accelerating gap into two accelerating regions. In addition the grid transparent for particles will be located at the end of the target electrode and be under its potential. As a result, the accelerating gap will be divided into two gaps: of acceleration and of drift region. This way allows reducing the effective acceleration distance at the same accelerating voltage.

Another way is by developing such a gap design at which the emitting surface (the anode grid) represents a ring. In this case the limiting current value increases due to the electric field intensity increase on the surface of the emitter. Moreover, with this emitter geometry there will not be the spacial charge in the paraxial region.

As calculations have shown, in this case the current on the target increases up to 35% from the injected current, whereas previously this figure comprised 20% from the total current on the accelerating electrode.

It should be noted that the use of a ring emitter of the same area leads to the same effect.

The application of this emitter topology allowed increasing the current share on the target up to 45%. In comparison with the contiguous emitter of the same area the increasing of a current can be explained by reducing the spatial charge action due to decreasing the emitter size in cross direction.

ISBN 978-3-95450-170-0

With regard to the use of a grid in the accelerating gap, Fig. 8 shows the design of the accelerating gap with an additional grid, whose surface represents a fructum of cone. In addition the length of the accelerating gap is reduced by 2 times.

The reduction of the accelerating gap size due to the insertion of an additional grid leads to the decrease of the plasma penetration rate in the accelerating gap. On the other hand, the grid surface generates the electric field, the radial component of which leads to the focusing effect. The results of calculations are presented in Fig. 3.

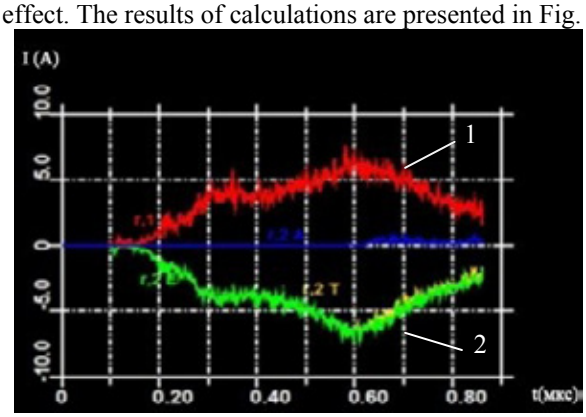

a)

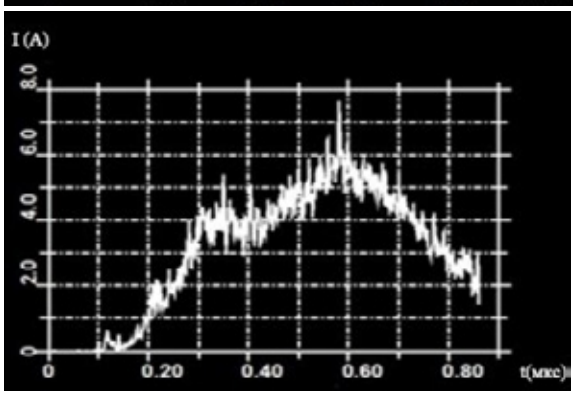

b)

Figure 3: The oscilloscope pictures of currents for the partitioned gap: a - the current on the surface of a cylindrical electrode (1) and the emitted (partial) current of deuterium (2), b –the current on the target.

As seen in Fig.3, such a gap design allows increasing the current share on the target up to 90%.

Calculations have shown that the use of the gap design with the cone-shaped grid and the ring emitter allows transmitting practically all deuterons passing through the anode grid.

CONCLUSION

The analysis of dynamics of plasma flows in the accelerating gap of VNT has shown the possibility of a substantial increase of deuterons' current on the target in comparison with its standard operation procedure. Currently, All-Russia Research Institute of Automatics named after N.L. Dukhova develops and carries out the experiments of different designs of the accelerating gap on the dynamics of ion flows.

Works supported by Ministry of Sciense and Education RF. Agreement № 14.575.21.0049 (RGMEFI57514X0049)

REFERENCES

[1] Yu.N. Barmakov, E.P. Bogolyubov and G. A. Smirnov, 2004, Portativnye generatory neitronov: ot sozdaniya - k sovremennomy sostoyaniyu i perspektivam razvitiya// sbornik materialov Mezhdunarodnoi nauchno-tekhnicheskoi konferentsii "Portativnye generatory neitronov i tekhnologii na ikh osnove" [Portable neutron generators: from the establishment to the current state and perspectives of development/Collection of materials of the International Scientific and Technical Conference "Portable neutron generators and technologies based on them"],All-Russia Research Institute of Automatics named after N.L. Dukhova VNIIA, Moscow .

[2] V.P. Tarakanov User's Manual for Code KARAT// Springfield, VA, Berkeley Research Associates, Inc. 1992, p 127.

[3] S.P. Maslennikov, N.A. Pastukhov,A.V. Chebotarev, E.Y. Shcolnikov, M.A. Gorbunov and D.I. Yurkov, 2014, Fizicheskaya model vakuumnoi neitronnoi trubki impulsnogo generatora, [Physical model ofthe vacuum neutron tube of a pulse neutron generator], Journal "Nuclear physics and engineering", vol.5, No3, pp 229-236.

ISBN 978-3-95450-170-0

THE NG-10 NEUTRON GENERATOR FOR PRODUCTION OF NEUTRON FLUXES IN CONTINUOUS AND PULSE MODES

D.A. Solnyshkov#, A.V. Antonov ,G.G. Voronin, A.N. Kuzhlev,
N.P. Mikulinas, A.V. Morozov, JSC "D.V. Efremov Institute of Electrophysical Apparatus",
St. Petersburg, Russia

Abstract

The neutron generator is designed for a neutron yield of 1x1011 n/s in the continuous operation mode. It consists of an ion accelerator with an accelerating voltage continuously adjustable in the range of 120-150 keV and beam current of atomic deuterium ions up to 2 mA and a set of target devices, in which Ti-T and Ti-TD targets of different diameters are used. In addition to a high and stable in time yield of neutrons when operating continuously, the generator also provides the pulsed mode over a wide range of pulse widths and repetition rates. By modulating the discharge current of the ion source, the neutron generator is switched into the pulsed mode. A unique system of the discharge power supply allows operation both in continuous and pulse modes. In this case, a smooth adjustment of the pulse width and repetition rate is possible. Switching from the pulse mode to DC can be promptly made from the host computer.

A wide range of available neutron sources and instruments for measuring neutron flux parameters calls for creation of systems of apparatus for calibration and certification of such products. The NG-10 neutron generator designed in NIIEFA can be used as an apparatus producing reference neutron fluxes in such systems. In addition to a high and stable in time neutron yield in the continuous mode, such a generator will ensure the pulse operating mode when pulse durations and repetition rates vary over a broad range.

This generator can be widely used for the neutron-activation analysis in different fields of science and engineering as well as in highly efficient systems intended for control of fissionable substances, detection of explosives, toxic substances and drugs. The NG-10 neutron generator is designed for a neutron yield of 1x1011 n/s in the continuous operating mode. It includes an ion accelerator with an accelerating voltage continuously adjustable in the range of 120-150 keV and beam current of atomic deuterium ions up to 2 mA and 4 target devices, in which Ti-T and Ti-TD targets of different diameters are used.

An ion beam produced by a duoplasmatron - type source is accelerated up to 150 keV in a sectionalized accelerating tube, separated in mass with an electromagnetic mass-separator and then is focused to a target with a doublet of quadrupole electromagnetic lenses. General view of the ion accelerator is shown in Fig. 1.

#d-soln@luts.niiefa.spb.su

The power supply system of the ion source is installed in a high-voltage terminal and consists of a unit for data receive and transfer, hv sources of extraction and focusing voltage and power supply unit housing power supplies of the discharge, electromagnet, cathode filament and Pd leak valve.

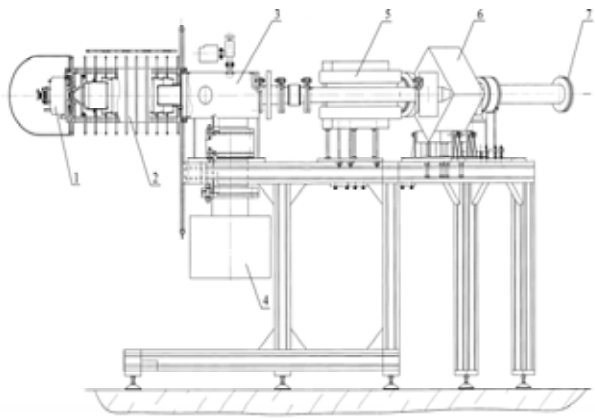

Figure 1: Ion Accelerator. General View. 1-ion source, 2-accelerating tube, 3-vacuum chamber, 4- ion pump, 5-electromagnetic mass-separator, 6- quadrupole lens, 7-target device.

All power supply systems are stabilized and operate at a frequency of 40-50 kHz, which allows its overall dimensions to be reduced and the ion beam current stability of about 1% to be attained. Power supplies under high potential are controlled through fiber-optic communication lines.

By modulating the discharge current of the ion source the neutron generator is switched into the pulse mode. For this purpose a unique system of the discharge power supply was designed, which allows operation both in continuous and pulse modes. In this case smooth adjustment of the pulse width and repetition rate is possible. Switching from the pulse mode to DC and vice versa can be promptly made from the host computer. The structural diagram of the discharge power supply is shown in Fig. 2.

The discharge power supply is a serial pulse current controller based on V1, V3 components and operating at a frequency of 40 kHz. Choke L1 serves to smooth current ripples and to store energy. The current from the controller output enters a load through the connector X1.Transistor V4 is connected in parallel with the current controller output. In the continuous mode of the power supply this transistor is cut off and does not affect its operation. When switched into the pulse mode, the

ISBN 978-3-95450-170-0

transistor V4 is modulated in frequency and duration with pulses applied from the generator through a light guide.

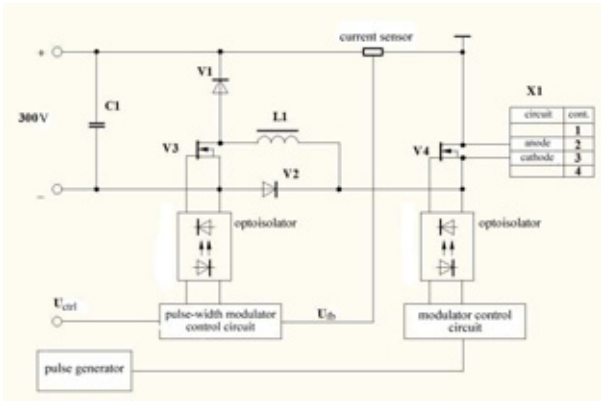

Figure 2: Structural diagram of the discharge power supply.

When the transistor is on, the power supply output is short-circuited, and the output voltage is 0. During the pulse, the transistor moves into the cut-off mode, and an energy stored in the choke L1 is transferred to the load as a current pulse. Diode V2 limits the load voltage to be not higher than the supply voltage by delivering the rests of the energy stored in chokes to an input capacitor C1. Power transistors V3 and V4 are controlled via optical drivers A1 and A2, which generate voltages pulses of necessary amplitude and growth rate and ensure galvanic isolation between power and control circuits. Pulses controlling the power transistor V3 of the pulse controller are generated with the control card A3. The width of these pulses is proportional to an error signal obtained by summing a reference signal arriving to the control system input with a feedback signal from the current meter D1. Pulses controlling the modulator transistor V4 are generated with the card A4of the optical receiver.

To supply power to devices under high voltage, a compact isolation transformer was designed. The secondary winding of the transformer consists of 4 turns of a hv cable with an insulation designed for 160 kV placed inside ferrite cores located uniformly around the winding perimeter. The transformer operates at a frequency of 50 kHz, and its design allowed its overall dimensions and weight to be significantly reduced. Photo of a high-voltage structure of the neutron generator at a test-facility in NIIEFA is shown in Fig. 3.

The vacuum system of the generator is based on the НМД-0,4ion pump. A dry forevacuum pump is used for preliminary pumping. The НМД-0,4pump is separated from the vacuum volume of the accelerator with a fast gate valve. The target device is connected to the accelerator vacuum system through a fast vacuum valve, which allows replacement of targets without the vacuum break in the accelerator. All vacuum valves are pneumatically driven; the process is controlled from the host computer. Necessary pressure in the pneumatic line is provided with a compressor, a part of the facility.

A set of targets devices, in which targets with diameter less than 10, 16, 18, 23 mm can be used, was designed for the generator. Targets with the 45mm diameter, which can be used at a high beam power, are installed in a special target device, which performs circular travel of a target relative to the ion beam.

Figure 3: High-Voltage Structure of the Neutron Generator.

The automatic control system made on the basis of an industrial computer is intended for the acquisition of the data on the status of the neutron generator and its separate devices and systems and its visualization on the display as well as for solving routine tasks of choosing and setting operating modes of the accelerator and tuning the working parameters of separate devices. The automatic control system consists of a control cabinet, units for data receiving and transfer and operator workstation. The control cabinet houses controller blocks with expansion modules, input/output analog modules, transmitter-receiver of the optical channel for data transfer and power supply units for electronics. The unit for data receiving and transfer houses a controller with an expansion module, galvanic isolations of analog signals and transmitter-receiver of the optical communication link. The operator workstation consists of an industrial computer with 2 monitors. The automatic control system allows the generator interaction with systems for measuring the neutron flux parameters.

The automatic control system of the NG-10 neutron generator is built on the basis of the Fastwel CPC109 controller, three Fastwel IO CPM704 controllers and the Advantix panel-type industrial computer. The software of the automatic control system consists of the five following programs:

- program of the host controller (Fastwel CPC109);
- program to control the injector (Fastwel IO CPM704);
- program to control the vacuum system of the neutron generator (Fastwel IO CPM704);
- program to control the neutron generator (Fastwel IO CPM704);
- host computer program (Advantix)

ISBN 978-3-95450-170-0

The Fastwel CPC109 controller program functions under an operational system compatible with the MS-DOS 6.22, and CPM704 controllers' programs function in the Fastwel IO special environment. The host computer functions under the MS Windows7. Fig. 4 shows the structure of the automatic control system.

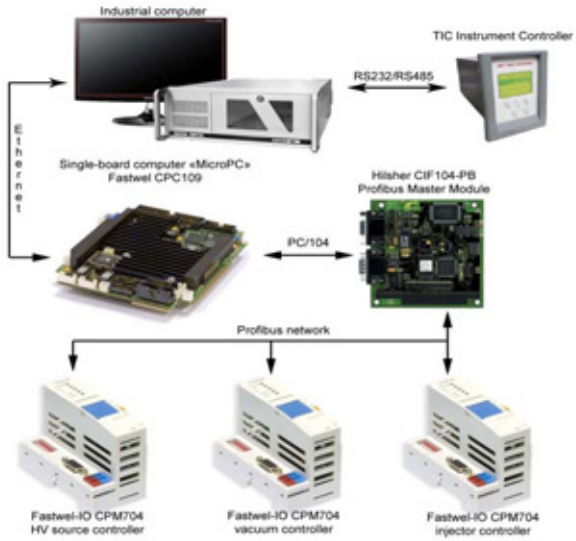

Figure 4: Structure of the Automatic Control System.

Controllers' programs are automatically loaded and are not directly controlled by the operator. Information about their states and control commands are transmitted in the network based on the Ethernet and Profibus protocols via the host computer program. A DB Viewer program is provided for viewing analog parameters of the system.

The host computer program is intended for:

- setting the operation mode of the neutron generator;
- control and preventing of accidents when the neutron generator is brought to its operating conditions and in the process of operation ;
- keeping constant input parameters of the neutron generator in the process of operation;

The program is loaded automatically after the loading of the computer operational system or, if necessary, by an icon located on the desktop of the MS Windows 7. General view of the user interface is given in Fig. 5.

The main window of the program consists of two sections. In the upper part of the window there are a panel to change-over pages of the control systems, setting buttons, unlocking buttons, button for logbook and the exit button. In the lower panel are located digital indicators of the main parameters of the neutron generator and indicators of the door, water and oil interlocks (1).The most part of the window is occupied by the panel with switched-over pages of the NG sub-systems (2).

Figure 5: Main window of the program.

As a result of an experimental tryout and optimization of the neutron generator and its separate systems, we successfully solved problems of generation and forming of 2μs - 100 ms pulsed ion beams with a smooth regulation of the pulse width. The pulse repetition rate can be changed from single pulses to tens of kHz. In the process of the accelerator tests, a beam of atomic ions with a current of up to 2 mA and beam diameter of 5-10 mm was formed on target.

So, in recent years in NIIEFA have been designed 4 modifications of neutron generators [1, 2], which produce neutron yields from 1010 up to 2×1012 n/s in the continuous mode and are equipped with pulsed mode systems allowing production of pulse neutron fluxes both in microsecond and nanosecond ranges of the pulse width.

REFERENCES

[1] G.G. Voronin, D.A. Solnyshkov. et al. "The НГ-12-2 Neutron Generator" Proceed. of the XI International Conference on Charged Particle Accelerators Applied in Medicine and Industry, (ICAA 05), St. Petersburg, 2005. pp. 278-281.

[2] V.P. Bagrievich, G.G. Voronin, D.A. Solnyshkov et al. "Neutron Generators for Production of Neutron Fluxes in Continuous and Pulse Modes", Voprocy Atomnoi Nauki i Tekhniki, № 5 (31), St. Petersburg, 2010, pp.155-159.

ISBN 978-3-95450-170-0

IMPROVEMENT OF THE BEAM TRANSMISSION IN THE CENTRAL REGION OF WARSAW U200P CYCLOTRON

O. Steczkiewicz#, J. Choinski, P. Gmaj, HIL, Warsaw, Poland
V. Bekhterev, I. Ivanenko, JINR, Dubna, Moscow Region, Russia

Abstract

To date, Warsaw U200P cyclotron exploited a mirror inflector to feed heavy ions extracted from ECR ion source (10 GHz, 11 kV) to the central region of the cyclotron. However, in such configuration very low transmission was reachable after many optimizations. Additionally, the new ECR ion source (14,5 GHz, 14-24 kV) was installed, which offers energies exceeding the energy acceptance of the currently operated inflector and central region. To avoid these obstacles, we have developed a spiral inflector and redesigned central region of the cyclotron. It was a very challenging task, bearing in mind limited volume of central region in our compact machine, to carve these elements suitably for decent versatility of ion beams offered by Warsaw cyclotron. This project was executed in the collaboration with FLNR in Dubna, Russia. The cyclotron equipped with the new central region works in the "constant orbit" regime. Here we present the results of both computational simulations and measurements of the beam transmission in upgraded central region.

COMPUTATIONAL SIMULATIONS

Introduction

The basic informations of U200P cyclotron are described in Refs. [1,2]. U200P cyclotron is an isochronous cyclotron (with four – sectors magnetic structure) equipped with two 45 degrees dees. The range of RF system's frequency is from 12 MHz to 18 MHz. The ions are accelerated using second and third harmonic with the range of the dee voltages from 50 kV to 70 kV. The scope of ions, which can be accelerated in U200P cyclotron is from A/q=4 to A/q=6,7, where A is a mass number and q is a charge state of the ion. The average magnetic field in the cyclotron amounts to 2T. The measured form of the magnetic field map used in all calculations and simulations is shown in Figure 1.

Spiral Inflector

A spiral inflector consists of two coaxial, spirally twisted electrodes, placed in the magnetic field.

According to the scope of the accelerated ions and the range of the injection voltage of the ECR ion source (14kV – 24kV), following parameters of the spiral inflector were chosen. To avoid the sparking effect the maximum potential on each electrode has to be not higher than 10kV. The height of the inflector is limited by the existing geometry in the central region of the cyclotron and equal to 40mm. The electric radius, which corresponds to the energies of the ions produced in the ion source, amounts to 25mm. Taking into account the electric radius and the maximum voltage on the electrode, the aperture of the inflector has to be equal 10mm. The width of the electrodes amounts to 20mm, due to the fact, that the ratio between the width and the spacing of the electrodes should be equal 2 to minimise the fringe field effect. According to all above mentioned parameters, the appropriate magnetic radius of the designed spiral inflector should amount to 2,16 cm. The main influence on the trajectory of the ions inside the spiral inflector and at the first accelerating gap has a minimum and the maximum injection voltage (14kV and 24kV) and the adequate level of the magnetic field in the cyclotron centre.

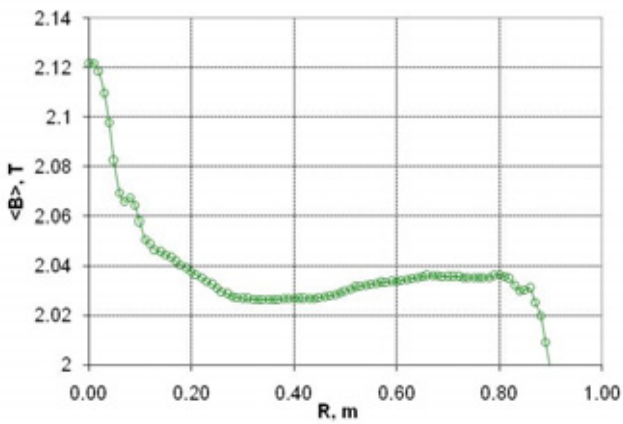

Figure 1: Magnetic field map of U200P cyclotron.

Calculations

All calculations were done for two extreme regimes for U200P cyclotron, which means the minimum and the maximum injection voltages and A/q ratio. These two cases are listed below:

- $^{16}O^{4+}$; U_{inj} = 23,3kV; U_{dee} = 65kV; B_0 = 2,037T; 2h; f = 15,33MHz
- $^{20}Ne^{3+}$; U_{inj} = 14kV; U_{dee} = 65kV; B_0 = 2,037T; 3h; f = 14MHz.

The spiral inflector and the new central region is designed to work in the "constant orbit" regime. Each ion has the same trajectory in the spiral inflector and before the first acceleration gap, which is secure by varying the injection voltage of the ion source and the potential at the inflector's electrodes. For both calculation regimes the transverse emittance at the entrance of the spiral inflector was defined as 150 π mm mrad.

ISBN 978-3-95450-170-0

In order to design the spiral inflector and the new central region different code were used. Two of them are well known codes developed by TRIUMF in Vancouver (Relax 3D and Casino). Remaining code is developed by JINR in Dubna. They are listed below:

- Relax 3D [3] – electrostatic field calculations,
- Casino [4] – trajectory of the ions inside the inflector,
- Centre [5] - trajectory of the ions after the inflector.

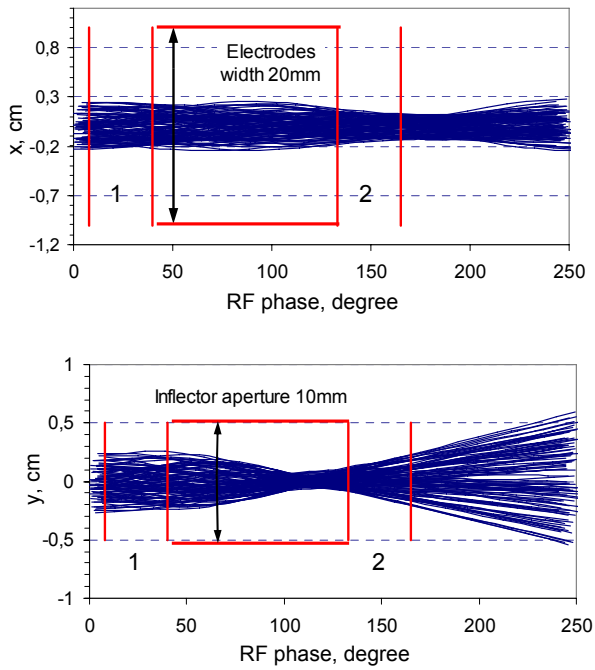

Figure 2: Trajectory of $^{16}O^{4+}$ inside the spiral inflector.

The calculated trajectory of $^{16}O^{4+}$ beam inside the spiral inflector is shown in Figure 2. The beam in the horizontal direction is focused and well defined inside and at the exit of the inflector. The defocusing at the exit of the inflector can be observed in the vertical plane. At an early date such inconvenience can be eliminate by using special shape of the electrodes [6] or adding some focusing system before the first accelerating gap.

The trajectory of $^{16}O^{4+}$ beam through the first accelerating gap and at the first few orbits is shown in Figure 3. On this drawing the hitherto used central region geometry, but with the spiral inflector instead of mirror one is shown. On the basis of these simulations the new compact central region without additional pillars and the appropriate pullers (noses of the dees) were designed.

MEASUREMENTS

The electrodes of the spiral inflector and the view of the central region with new elements are shown in Figure 4 and Figure 5 respectively.

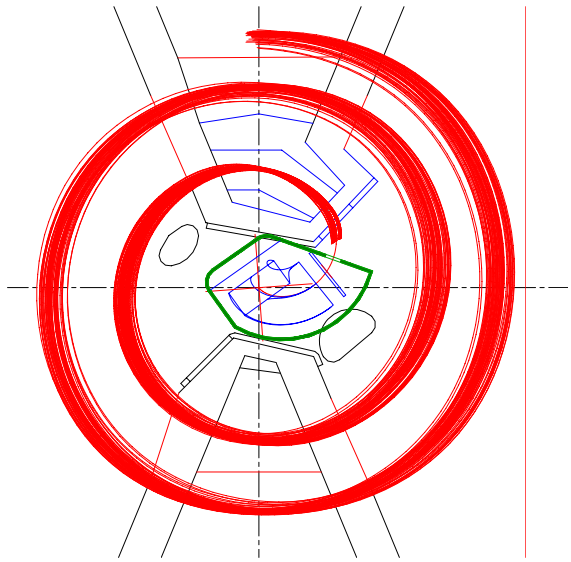

Figure 3: Trajectory of $^{16}O^{4+}$ through the first accelerating gap.

Since installation in February 2014 few experiments with new system were done. All beams, which were produced up to this time in the new ECR ion source, where successful injected to the cyclotron and accelerated to the extraction orbit (82cm). Few examples of the accelerated beams with received currents after few turns (first legible position of the probe – 12,5 cm) are listed below:

- $^{4}He^{1+}$ - 24μA (300μA before the inflector's entrance)
- $^{20}Ne^{3+}$ - 18,8μA (160μA before the inflector's entrance)
- $^{12}C^{3+}$ - 18μA (100μA before the inflector's entrance)

Figure 4: The electrodes of the spiral inflector.

ISBN 978-3-95450-170-0

CONCLUSION

After taking into account all the physical constraints imposed by the ion source and the existing structure of the cyclotron the spiral inflector and the new central region for U200P was designed and installed. First experiments show, that all elements work correct. The efficiency of the transmission at the first few orbits could be increased through the elimination of the defocusing of the beam in the vertical plane at the exit of the inflector.

Figure 5: New central region of U200P cyclotron.

REFERENCES

[1] http://www.slcj.uw.edu.pl/
[2] J. Choinski, Ph. D. Thesis, University of Warsaw, 2003
[3] H. Houtman, F.W. Jones, C.J. Kost, Comput. Phys. 8 (4) (1994) 469
[4] F.B. Milton et al., CASINO user guide and reference manual, TRIDN-89-19, Vancouver, Cyclone Version 8.4, TRI-DN-99-4, 1989
[5] G. Gulbekian, I. Ivanenko, "Design of the central region of the new multi-purpose cyclotron U400R", HIAT'09, http://www.jacow.org
[6] G. Gulbekian, I. Ivanenko, "U400 Cyclotron Spiral Inflector with Beam Vertical Focusing Effect", IPAC'10, Kyoto, Japan, 2010

ISBN 978-3-95450-170-0

COOLING STORAGE RING CR OF THE FAIR FACILITY - STATUS AND PERSPECTIVES*

Yu. Rogovsky#, D. Berkaev, A. Kasaev, E. Kazantseva, I. Koop, A. Krasnov, A. Semenov, P. Shatunov, D. Shwartz, A. Starostenko, BINP SB RAS, Novosibirsk, Russia
U. Blell, C. Dimopoulou, A. Dolinskii, O. Gorda, U. Laier, H. Leibrock, S. Litvinov, I. Schurig, U. Weinrich, GSI, Darmstadt, Germany

Abstract

In 2014 BINP takes full responsibility on the design and construction of the Collector Ring of the FAIR facility. Still few work-packages remain be on the supervision of GSI' team. In this paper the current status of the CR project is presented and future plans are discussed.

INTRODUCTION

The Collector Ring (CR) at FAIR [1,2] is a dedicated storage ring which will fulfill the following tasks (next column). Its layout and location of subsystems are shown in the Fig. 1, parameters are presented in the Table1.

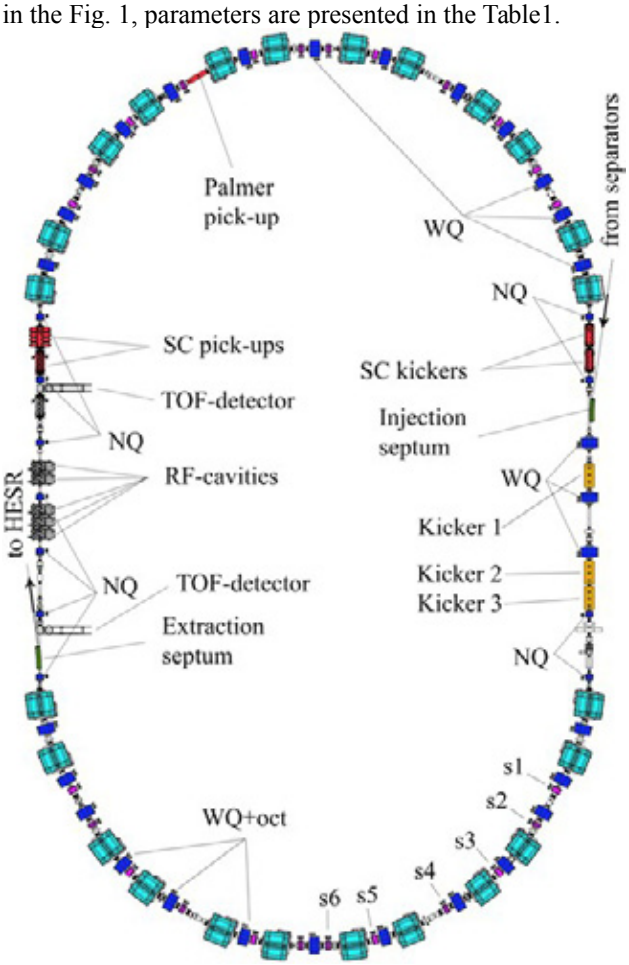

Figure 1: Layout of CR ring.

Main tasks for Collector Ring operations:

- Stochastic cooling of antiprotons coming from the antiproton separator, to be delivered to the HESR (later to RESR) storage ring.
- Stochastic cooling of rare isotope beams (RIB) coming from the Super-FRS fragment separator, to be delivered to RESR.
- TOF measurements of masses of short-lived secondary rare isotopes in the isochronous mode.

Table 1: Main parameters of Collector Ring

Circumference	**221.45 m**		
B·ρ	13 Tm		
Mode	**p-bar**	**RIB**	**Isochronous**
Max. N	10^8	10^9	$1\text{-}10^8$
Kinetic energy	3 GeV	740 MeV/u	400-790 MeV/u
Lorentz γ	4.20	1.79	1.43 – 1.84
Transition γ_{tr}	3.85/4.84	2.71/2.95	1.43 – 1.84
Slip factor |η|	0.011	0.178	0
Acceptance	240	200	100
Max Δp/p	±3%	±1.5%	±(0.22–0.62)%

LATTICE

The lattice of the CR consists of two 180 degree arcs separated by two long straight sections. Because of the large acceptance of the CR, it is important to use large aperture magnets only where they are needed. In order to minimize both the production and operating costs, wide aperture quadrupole magnets with useful aperture 400mm by 180 mm are used for the injection section and in the arcs of the CR. The narrow quadrupole magnets with reduced horizontal good field region (useful aperture 180 mm by 180 mm) are installed only in the straight sections.

A list of magnetic elements includes:

- 24 dipole magnets
- 29 wide aperture quadrupoles (WQ) and 11 narrow aperture quadrupoles (NQ) will be used.
- 6 families of sextupoles (s1-s6) will be applied to control the chromaticity and the dispersion in the arcs.
- 3 families of octupole correctors embedded into wide quadrupoles (WQ+oct) are needed for corrections of mass measurement accuracy.
- Orbit correctors in dipoles and in drifts

According to the list of tasks, there were developed 2 basic optical schemes: one for antiproton beam cooling,

*Work is supported by SAEC "Rosatom" and Helmholtz Association
#rogovsky@inp.nsk.su

ISBN 978-3-95450-170-0

the second for rare ions plus 3 different variants for the isochronous operation mode. In all cases the thorough optimization of the dispersion and beam amplitude functions was made. Results are presented in Fig. 2. Another care was paid to provision of needed phase advances between pickups and kickers of the stochastic cooling system.

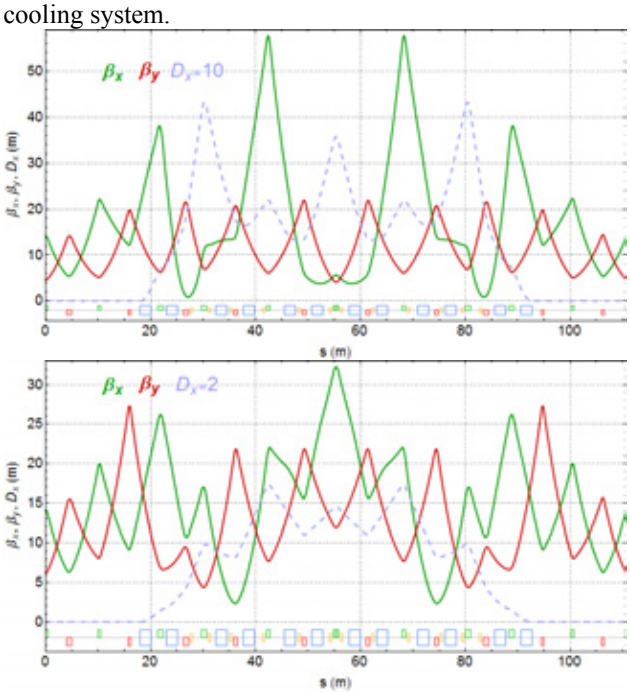

Figure 2: Lattice functions p-bar and RIB mode.

The main element of CR is a bending magnet. Its view is shown in the Fig. 3-4 and main parameters are listed below:

- Laminated, lamination thickness 1 mm
- Sector shape poles and coils
- Bending angle 15^0
- Maximum field 1.6 T
- Bending radius 8.125 m
- Pole gap 170 mm
- Useful aperture 380 by 140 mm
- Field homogeneity $\pm 1 \cdot 10^{-4}$ (at 1.6 T)
- Design ramp rate 1 T/s
- Maximum current 1396 A

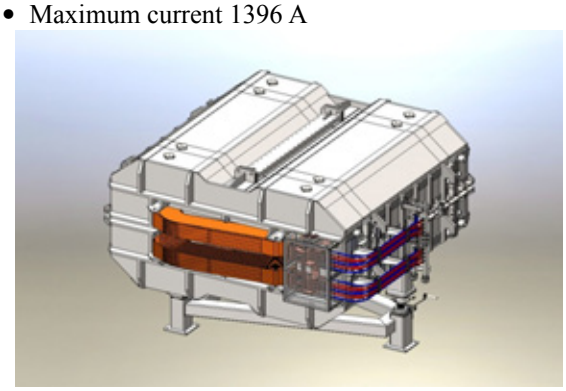

Figure 3: 3d model of the CR dipole magnet.

Main parameters of quadrupoles are listed in Table 2.

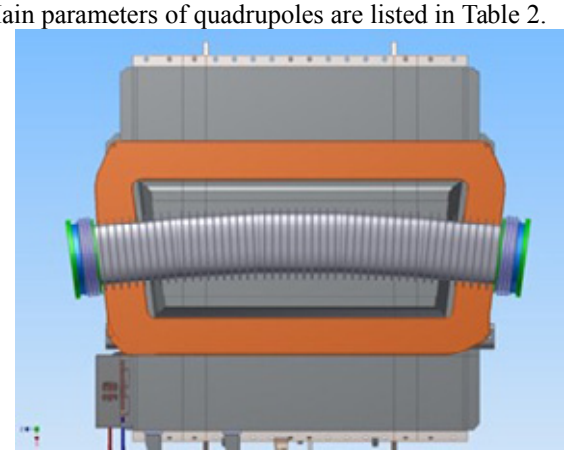

Figure 4: Half of the dipole yoke with the 2 mm thick elliptical vacuum chamber with ribs.

Table 2: The reference parameters of quadrupoles

Quadrypole type	WQ	NQ
Effective length, m	1.0	0.5
Maximum gradient, T/m	4.9	9.0
Useful aperture, mm×mm	400×180	180×180
Field homogeneity	$\pm 5 \cdot 10^{-4}$	$\pm 5 \cdot 10^{-4}$

NONLINEAR EFFECTS

Special feature of CR storage ring is the large 6D acceptance. The initial emittance of injected antiprotons will be as large as 240 mm·mrad in both transverse directions, while momentum spread amounts to ±3%. Thus, it is important to study carefully different chromatic and nonlinear effects.

Six sextupole magnet families are foreseen for compensation of linear chromaticity. The closed orbit distortion for the off-energy particle can be written as

$$\delta x(s) = D \cdot \delta + D_1 \delta^2 .$$

The second-order dispersion function D_1 is presented in Fig. 5. Chromaticity of lattice functions was also examined. Accurate calculations made by 6D SAD code [3] for lattice functions of off-energy particles with momentum deviation of ±3% are shown in Fig. 6.

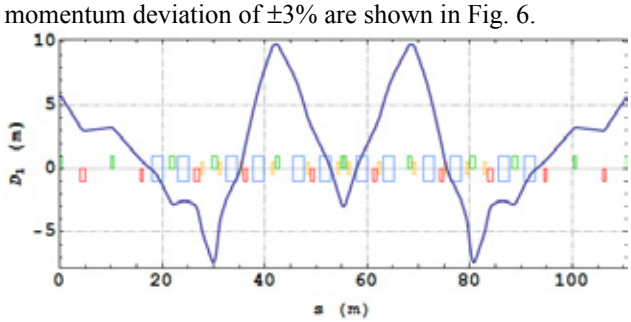

Figure 5: Second order dispersion (p-bar mode).

The beam size with mentioned above chromatic aspects taken into account are shown in Fig. 7. Chromatic

ISBN 978-3-95450-170-0

sextupoles is an essential source of nonlinear magnetic fields that can result in the instability of betatron motion for large enough oscillations amplitudes.

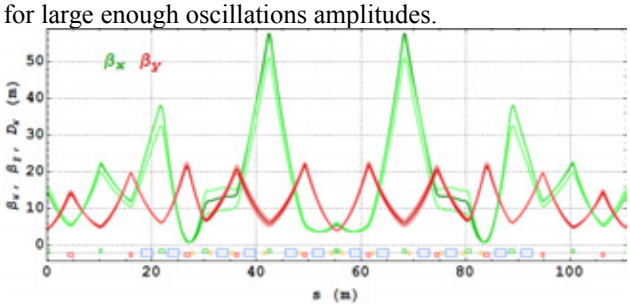

Figure 6: Lattice functions for on-enegy particle (dark) and off-energy particles (light).

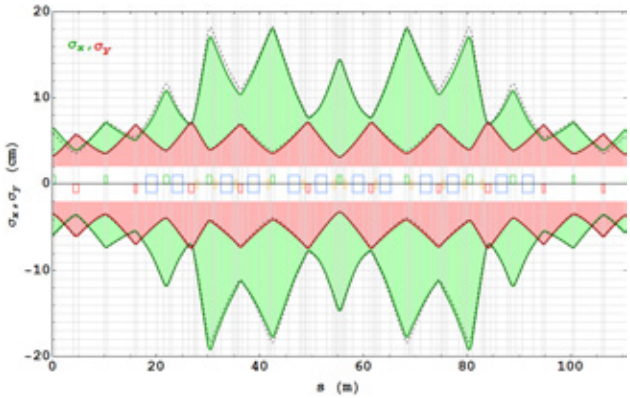

Figure 7: Beam size along one half of the ring.

The Dynamic Aperture (DA) simulated numerically by the use of PTC tracking module of the MAD-X code [4]. Particle trajectories are integrated over 1000 turns. Fringe field and the higher-order harmonics [5] have been included in the computation. Results are shown in the Fig. 8.

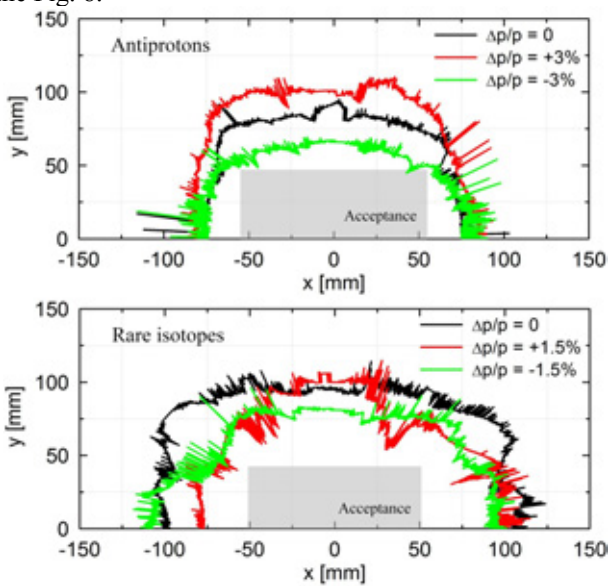

Figure 8: MAD-X dynamic aperture simulation results.

ISOCHRONOUS MODE

Precise determination of rare isotope masses requires the absolute accuracy of $dT/T=10^{-6}$ in the TOF measurements of the revolution time [6]. 3 families of quadrupoles and 3 families of octupole correctors embedded into the wide quadrupoles (WQ+oct) in the arcs (totally 12 magnets of each type) can be applied to correct the impact of field errors and fringe field of the magnets on the measurement accuracy, see Fig. 9.

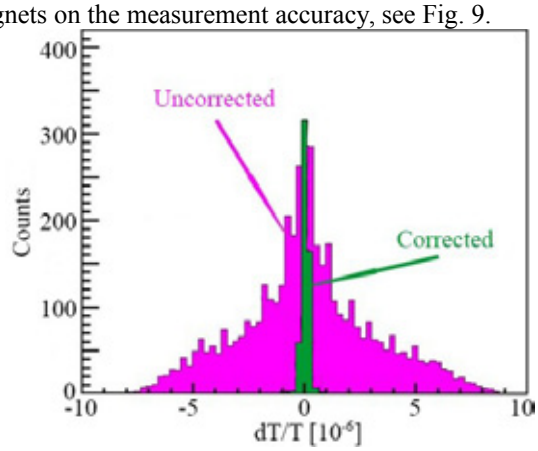

Figure 9: Effect of sextupole and octupole corrections on TOF distribution.

INJECTION-EXTRACTION

Injection system consists of 3 pulsed bipolar magnetic kickers (Kicker 1, Kicker 2 and Kicker 3) and the pulsed injection septum magnet. Full aperture kickers are needed to guarantee the large injection acceptance. Maximum kick angle of 7 mrad for each kicker is required for the injection [2]. Maximum kicker voltage is 70 kV. Maximum current is 6140 A. Rise/fall time is 318 ns. Maximum pulse length is 1.5 μs. Same kickers are used for extraction. The septum magnet design is under development.

CONCLUSION

A great variety of optical schemes were developed for different operation modes of the CR. Many linear and nonlinear dynamics studies were performed up to now. No show-stoppers were found on this way. Still, many technical problems and solutions need to be solved in nearby future.

REFERENCES

[1] A. Dolinskii et al., COOL'07, Bad Kreuznach, TUA2C08 (2007).
[2] CR Technical Design Report, GSI. Darmstadt, 2014.
[3] SAD code homepage, http://acc-physics.kek.jp/SAD/sad.html
[4] The MAD-X code, http://cern.ch/madx.
[5] A. Dolinskii et al., IPAC'11, San Sebastian, WEPC054 (2011).
[6] S. Litvinov et al., EPAC'06, Edinburgh, TUPLS054 (2006).

ISBN 978-3-95450-170-0

TIME DEPENDENCE OF ION BEAM TRANSVERSE PHASE-SPACE PORTRAIT ORIENTATION DURING LINAC PROTON INJECTOR PULSE

O.T. Frolov, A.S. Belov, S.E. Golubovskyi, E.S. Nikulin, V.N. Zubets,
Institute for Nuclear Research of RAS, Moscow, 117312, Russia

Abstract

It is shown that turn-on transients of the 400 kV column intermediate electrode potential is one of main processes responsible for change of beam phase-space portrait orientation during 200 μs, 50 Hz proton injector high voltage accelerating pulse. It has been found that significant variation of this potential takes place due to transition process during a pulse in the resistive-capacitive voltage water divider of the accelerating tube. The divider capacitors matching procedure has been performed. The beam emittance measurement results presented have shown significant decrease of a beam transverse phase-space portrait orientation change during injector pulse with the accelerating tube voltage divider being compensated.

The INR RAS linac proton injector provides a pulsed beam with the following parameters:
peak current – (65÷100) mA; duration – 200 μs; pulse repetition rate – 50(100) Hz; energy of ions – 400 keV. Schematic drawing of the accelerating tube is shown in Fig. 1. A beam of hydrogen ions is generated in the duoplasmatron type ion source.

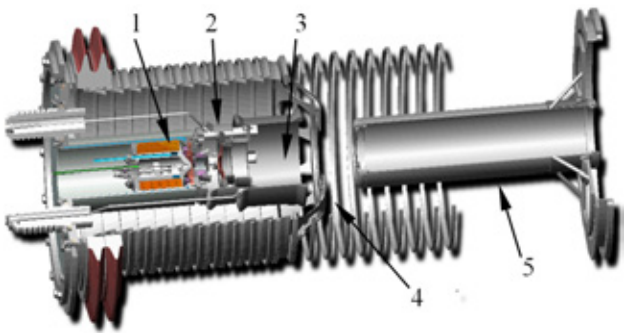

Figure 1: Schematic drawing of the accelerating tube: 1 - ion source, 2 – extracting electrode, 3 - focusing electrode, 4 - intermediate electrode, 5 - grounded electrode.

A beam is accelerated in the tube of about 1600 mm long with external surface being positioned in the open air. For decreasing of influence of coulomb repulsion of ions in beam a total length of inner accelerating gaps in vacuum have to be a minimal one, so the ion source and the grounded electrode are deeply in the tube (Fig. 1). The column has two inner accelerating gaps with a summary length of 220 mm: a) the first accelerating/focusing gap (100 mm) in which an ions have reached an energy about 95 keV; b) in the second gap (120 mm) an ions have been accelerated to an energy of 400 keV. The intermediate electrode (IE) is positioned at joint between two gaps. Focusing electrode and IE diaphragm represent electrostatic lens which determine the beam focusing/crossover location at LEBT channel entrance when focusing electrode potential being changed.

A high accelerating voltage is distributed along the tube by means of water divider with a total resistance about 1.5 MΩ. At nominal voltage of 400 keV a current through the divider is about 0.27 A; this value more than 3 times exceeds usual beam current of 80 mA. This is important for reliable distribution of voltage along the tube and full elimination of high voltage breakdowns. The IE is connected with the divider point where high accelerating voltage is divided in approximate ratio of 1:3.

Emittance measurements for ion beam at the injector exit show significant phase-space portrait orientation change during 200 μs injector high voltage pulse [1, 2].

Study of ion beam transport in the proton injector has been performed using Trak and SpaceCharge package developed at Field Precision LLC [3]. The numerical simulation takes into account plasma boundary formation at ion source expander, space charge effects for ion beam extracting, accelerating and transporting.

It has found that the causes of observed position/shape phase portrait changes during high voltage injector pulse can be as follows: instability of high voltage pulse; possible changes of the injector ion beam current; dynamic of ion beam space charge compensation process; the IE potential changes.

As a result of some efforts which have been made in recent times with the aim to decrease the injector accelerating voltage instability the latter is now not worse than ±0.085% (see Fig. 2). Pulse-to-pulse voltage instability does not exceed ±0.04% [4]. So the summary instability equals value of ±0.125% or less.

The beam transport simulation performed shows that such a change of high voltage amplitude during pulse has no influence on the ion beam transverse phase-space portrait orientation.

Influence of ion beam current changes on phase-space portrait orientation is especially important in the case of "noisy" mode of an ion source operation because of ion beam current fast variations which can reach tens percent of maximal value during a pulse. However, the present duoplasmatron source has "noiseless" operation mode [5]. As we can see from Fig. 2, beam current transients up to ±8% result in notable change of beam phase-space portrait orientation when beam current is about 65 mA.

Additionally to improve stability of beam current during a pulse and pulse-to-pulse stability the transistor stabilized arc modulator (instead of the thyristor unit based on pulse forming network) with no more than ±0.5% dis-

ISBN 978-3-95450-170-0

charge current instability along a pulse has been developed and placed in operation. As a result, stability of beam current pulse plateau (see Fig. 3) has been improved [2].

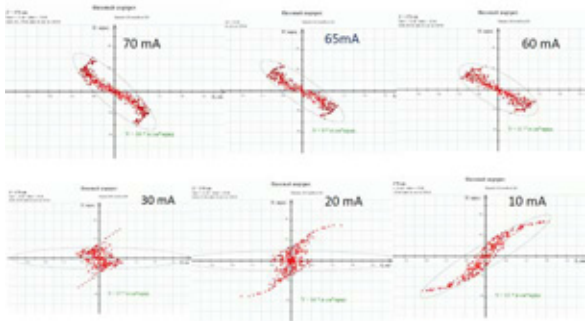

Figure 2: Influence of beam amplitude on position/shape of the injector exit beam phase portrait.

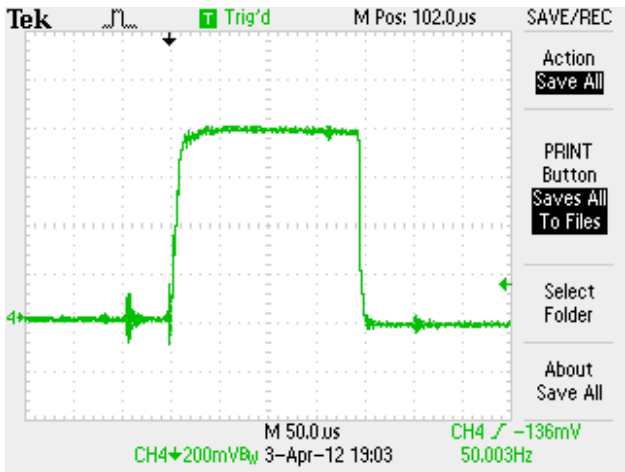

Figure 3: The ion beam current shape at the injector exit.

It is known that process of ion beam space charge compensation can lead to change of phase-space portrait orientation [6].

In our injector space charge compensation of the ion beam is prevented by electric fields of the accelerating tube beam forming system (extraction and focusing). These fields eliminate accumulation of electrons arising both due to ionization of residual gas molecules and hitting of ions with beam transport line apertures and walls.

It has been found that main process leading to a change of ion beam phase space portrait orientation at the injector exit is turn-on transient of the 400 kV accelerating tube IE potential.

Simulation have shown that change of the IE potential for a value less than 1% already leads to significant changes in the injector beam properties. The example of calculation results for different IE potential is shown in Fig. 4.

C_2 and C_1 capacities are the sum of each outer gap interelectrode capacity of the tube (~200 pF) and additional capacitors installed at each gap in front of and behind the IE. The additional capacitor values have been chosen to compensate influence of C_3 capacities between each electrode of the tube and "ground".

Equivalent schematic diagram of the tube resistive-capacitor voltage divider is shown in Fig. 5.

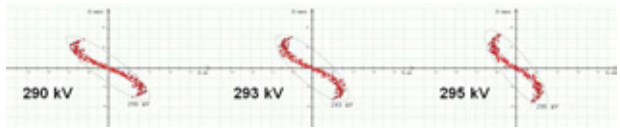

Figure 4: Influence of the IE potential value on position/shape of the injector exit beam phase portrait.

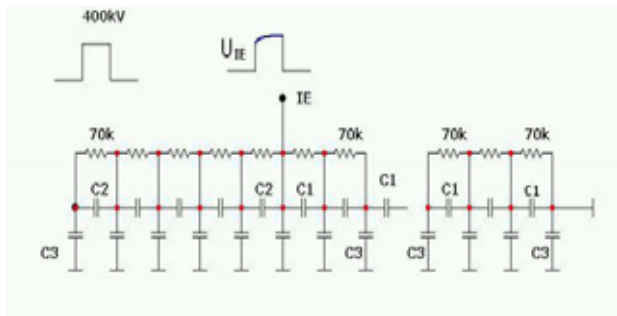

Figure 5: Equivalent schematic diagram of the tube resistive-capacitive voltage divider.

During matching procedure C_2 capacities have been changed more than once and every time the IE potential pulse shape has been measured. These measurements have been performed with the help of especially designed low capacity voltage divider at reduced injector pulse voltage (50 kV). Examples of the measurement results are shown in Fig. 6.

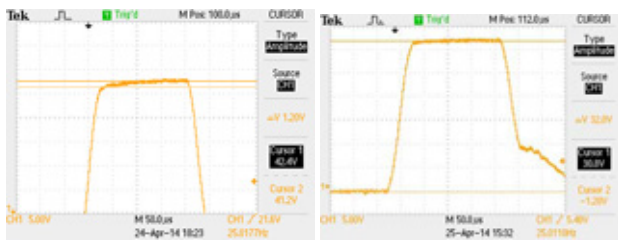

Figure 6: The IE voltage pulse shapes at reduced injector pulse voltage (50 kV). Left curve: C2 = 1200 pF; right curve: C2 = 1400 pF, C1 = 1000 pF.

Additional capacitors of 1200 pF, 20 kV have been chosen for the first five outer gaps of the tube before the IE as a result of matching procedure.

Studies of phase portrait parameters changes along 200 µs accelerating voltage pulse have been carried out. The duoplasmatron arc modulator has produced 25 µs duration beam which has been injected into the accelerating tube with multiple of 25 µs different delays relative to beginning of high voltage pulse plateau. It has been found that:

a) beam phase portrait changes its orientation during 200 µs pulse length in the case of noncompensated divider;

b) within the accuracy of measurements there is no change of orientation in the case of the compensated tube

ISBN 978-3-95450-170-0

divider. Some of emittance measurement results are shown in Fig. 7.

Normalized emittance for 63% of 65 mA beam has been measured of value no more than 0.06π cm•mrad and 0.15π cm•mrad for 90% of beam in case of the compensated divider.

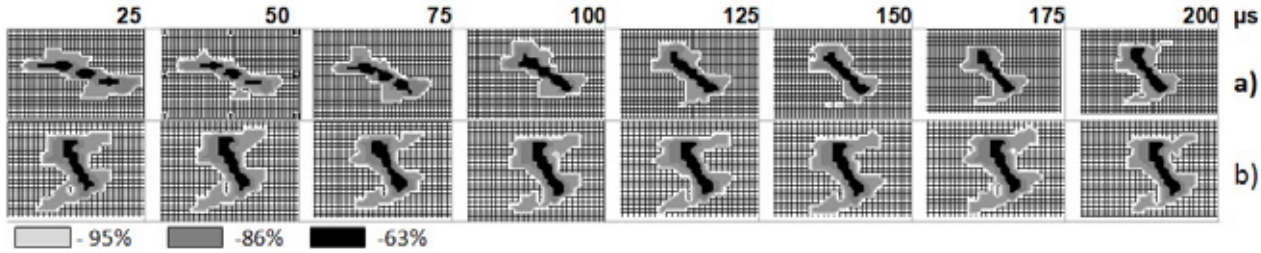

Figure 7: Beam phase portraits when scanning along 200 μs high voltage injector pulse plateau duration: a) noncompensated divider; b) compensated divider. Contours of black, dark-grey and light-grey regions contain 63%, 86% and 95% of beam current, correspondingly.

CONCLUSION

Analysis of the processes that can lead to a transverse phase-space portrait orientation change at the proton injector exit during beam pulse results in belief that the main processes are: possible changes of the ion beam current and turn-on transient of the 400 kV accelerating tube intermediate electrode potential.

Due to both installation of the compensated accelerating tube divider, using of duoplasmatron "noiseless" operation mode, stabilizing of ion source discharge current and improvements conducted to increase accelerating voltage stability a transverse phase-space portrait orientation change does not observed during beam pulse within the accuracy of measurements. A satisfactory agreement of beam parameter measurements and numerical simulation has been achieved.

ACKNOWLEDGMENTS

We are grateful to A.V.Feschenko and V.L.Serov for useful discussions, A.V.Turbabin and Yu.V.Kiselev for participation in emittance measurements.

REFERENCES

[1] A.S. Belov, O.T. Frolov, E.S. Nikulin, V.P. Yakushev and V.N. Zubets. Study of proton injector beam transverse phase space variations during accelerating voltage pulse. Proc. of RUPAC-2012, St.-Petersburg, Russia, p. 397. http://www.accelconf.web.cern.ch/accelconf/r12/papers/tuppb036.

[2] A.S. Belov, O.T. Frolov, E.S. Nikulin, V.P. Yakushev and V.N. Zubets. The INR of RAS Proton Linac Injector Beam Study // Problems of atomic science and technology. Series "Nuclear Physics Investigations" (79), 2012, №3, p. 44 (in Russian). http://vant.kipt.kharkov.ua/ARTICLE/VANT_2012_3/article_2012_3_44.pdf

[3] Field Precision LLC, http://www.fieldp.com/trak.html

[4] V.N. Zubetz, V.I. Derbilov, S.K. Esin, O.T. Frolov, E.S. Nikulin and V.P. Yakushev. The stabilization system of 400-750kV pulsed accelerating voltage // Problems of atomic science and technology. Series "Nuclear Physics Investigations" (34), 1999, №3, p. 52.

[5] A.S. Belov, O.T. Frolov, E.S. Nikulin, V.P. Yakushev and V.N. Zubets. Study of the INR RAS Linac Pulsed Duoplasmatron // Proc. Of RUPAC-2010, Protvino, Russia, p. 289. http://www.accelconf.web.cern.ch/accelconf/r10/papers/thchb01.

[6] J. Hurd, A. Browman. Transverse phase space time dependence of LAMPF's high intensity H+ beam //IEEE Trans. on NS, v. NS-28, 1981, № 3, p. 2658.

ISBN 978-3-95450-170-0

ELECTRON AND POSITRON BEAMS TRANSPORTATION CHANNELS TO BINP COLLIDERS*

I.M. Zemlyansky#, D.E. Berkaev, V.A. Kiselev, I.A. Koop, A.V. Otboev, A.M. Semenov, A.A. Starostenko, Budker Institute of Nuclear Physics, Novosibirsk, Russia

Abstract

There are two accelerator complexes VEPP-2000 and VEPP-4M in BINP. There is preparatory work for building of new accelerator – Super Charm-Tau Factory. As an injector of positrons for Super c-τ Factory the existing injection complex VEPP-5 will be used. Existence of the powerful injection complex provokes the desire to use it for needs of the working accelerator complexes VEPP-2000 and VEPP-4M. Replacement of the existing injection subsystems with the injection complex VEPP-5 will allow us to increase the speed of accumulation of positrons at the accelerator complexes VEPP-2000 and VEPP-4M in 1000 and 100 times respectively. For VEPP-2000 this improvement has a great significance as the existing conversion system doesn't provide the demanded quantity of positrons for designed luminosity of a collider $1x10^{32}$ $cm^{-2}s^{-1}$.

In the article the short review of transportation channels from the injection complex VEPP-5 to the accelerator complexes VEPP-2000 and VEPP-4M, time sequence of an injector's work for both complexes are given. The transportation channel from the injection complex VEPP-5 to the booster ring BEP of the accelerator complex VEPP-2000 is described in details.

BINP COLLIDERS AND INJECTION COMPLEX

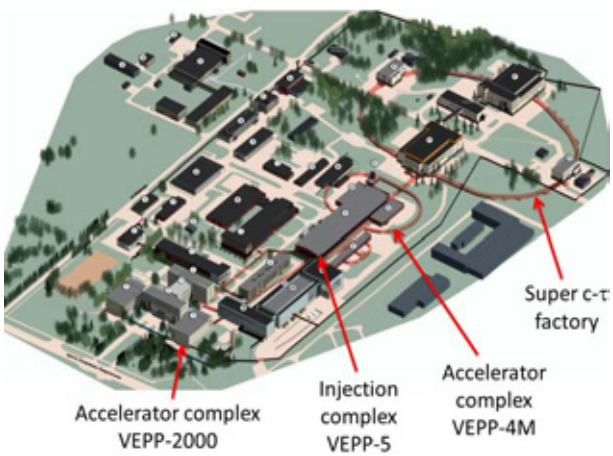

Figure 1: Colliders and Injection Complex in BINP.

In Figure 1 the arrangement of colliders and the injection complex in the territory of BINP is shown. Their detailed schemes are submitted in Figures 2-4.

The existing injection system of VEPP-2000 provides $2x10^7$ positrons per second that allows us to reach luminosity $5x10^{30}$ $cm^{-2}s^{-1}$ at energy 1GeV in one bunch. Achievement of designed luminosity $1x10^{32}$ $cm^{-2}s^{-1}$ requires $1x10^8$ positrons per second.

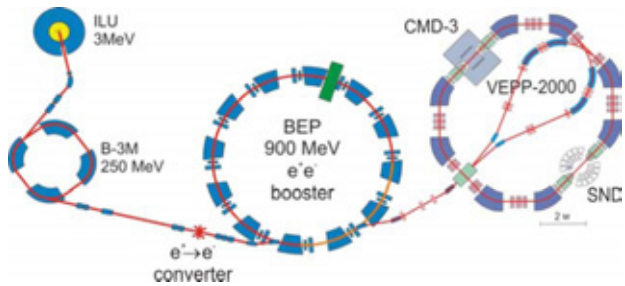

Figure 2: Accelerator Complex VEPP-2000.

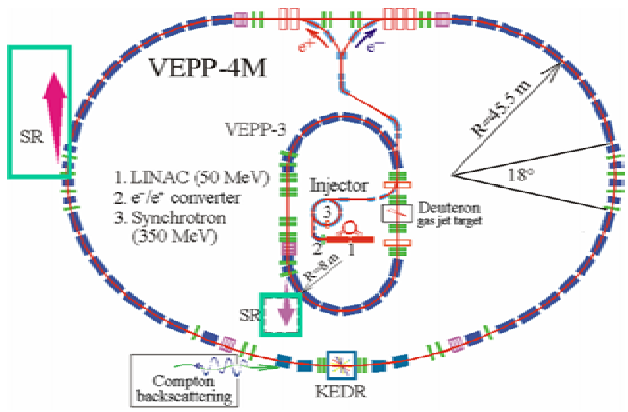

Figure 3: Accelerator Complex VEPP-4M.

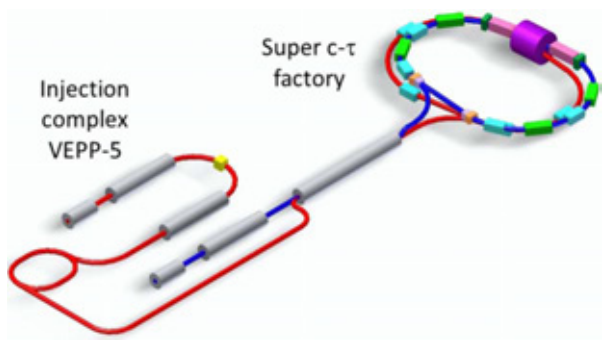

Figure 4: Super Charm-Tau Factory and Injection Complex VEPP-5.

The existing injection system of VEPP-4M makes $2x10^8$ positrons per second that allows us to reach luminosity $2x10^{30}$ $cm^{-2}s^{-1}$ at energy 1.8 GeV in one bunch. Achievement of the future designed luminosity $8x10^{31}$ $cm^{-2}s^{-1}$ at energy 5.5 GeV in one bunch requires $2x10^{10}$ positrons per second.

*Work supported by the Ministry of Education and Science of the Russian Federation, NSh-4860.2014.2
#I.M.Zemlyansky@inp.nsk.su

ISBN 978-3-95450-170-0

For future Super c-t Factory with designed luminosity $1x10^{35}$ $cm^{-2}s^{-1}$ $6x10^{11}$ positrons per second will be required.

The Injection complex VEPP-5 parameters are: energy 510 MeV, number of positrons $2x10^{10}$ per second, energy spread $5.1x10^{-4}$, emittances ϵ_x $2.3x10^{-6}$ cm·rad ϵ_z $5x10^{-7}$ cm·rad. These are enough for needs of VEPP-2000 and VEPP-4M. Super c-t Factory requires more productivity of the injector. Improvement of the injection complex will be made along with construction of Super c-t Factory.

OPERATION: INJECTOR VEPP-5 FOR VEPP-2000 & VEPP-4M

Work at VEPP-4M: accumulation of electrons in a booster ring VEPP-3 to current 200 мА in one minute; energy rise to 1.8 GeV in 10 minutes; transportation of electrons to collider VEPP-4M; a polarity reversal of booster ring VEPP-3 in 2 minutes; accumulation of positrons to 200 мА; transportation to VEPP-4M collider, once again electrons and positrons. After injection to the collider of two bunches of electrons and two bunches of positrons, there is a rise to the energy of experiment from 1 to 5.5 GeV per bunch. Receiving four bunches and energy rise takes 1 hour. After that experiment runs 3 hours.

Work of the accelerator complex VEPP-2000 differs from VEPP-4M. The collider of VEPP-2000 can work for experiment constantly as its booster ring BEP is capable to change the energy in all range of experiments from 0.16 to 1 GeV per bunch. After receiving electrons, BEP boost them to the energy of experiment in 10 seconds. After transportation of electrons to VEPP-2000 collider, the booster reverses polarity in 20 seconds. Then BEP takes positrons, increases their energy, transports to collider ring, reverses polarity and so on.

TRANSPORTATION CHANNEL FROM INJECTIOR VEPP-5 TO BOOSTER BEP

Geometry and optics

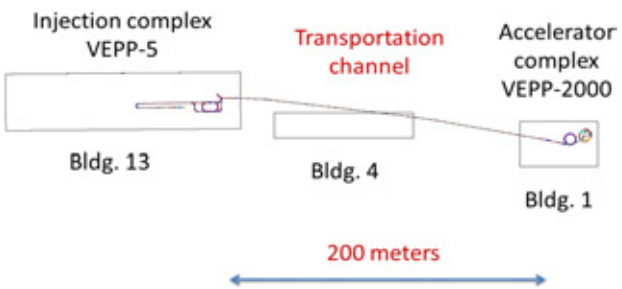

Figure 5: Location of the transportation channel in the BINP.

The transportation channel layout is presented in Figure 5. The detailed geometry and lattice functions are shown in Figures 6-13.

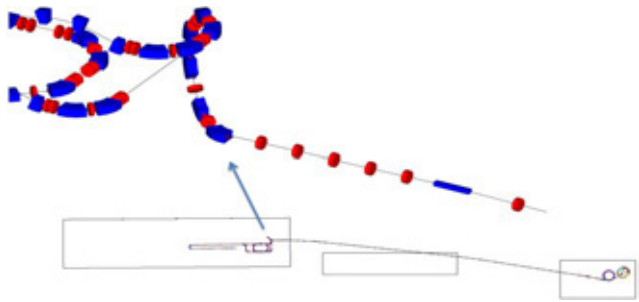

Figure 6: Descent from the storage ring of VEPP-5.

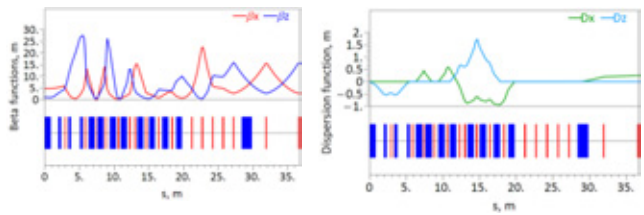

Figure 7: Lattice functions of descent.

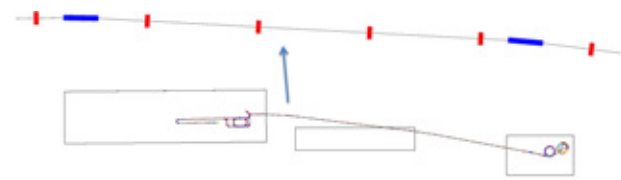

Figure 8: First horizontal bend.

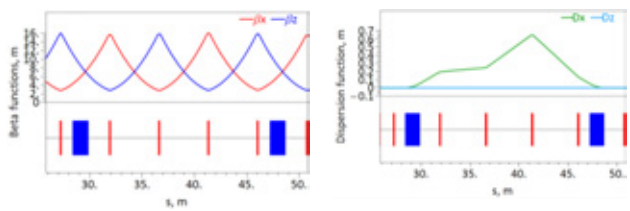

Figure 9: Lattice functions of first horizontal bend in regular part.

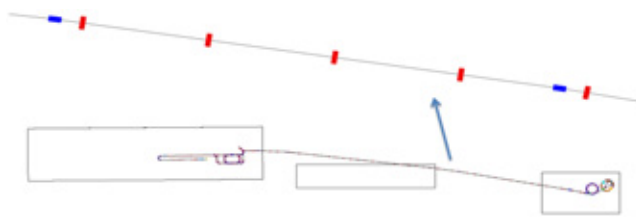

Figure 10: Second horizontal bend.

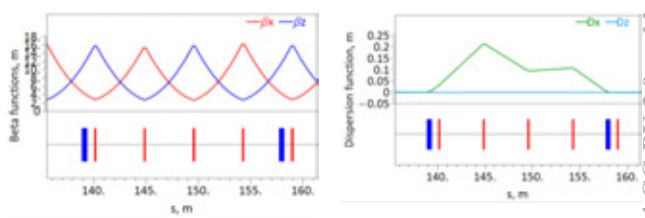

Figure 11: Lattice functions of second horizontal bend in regular part.

ISBN 978-3-95450-170-0

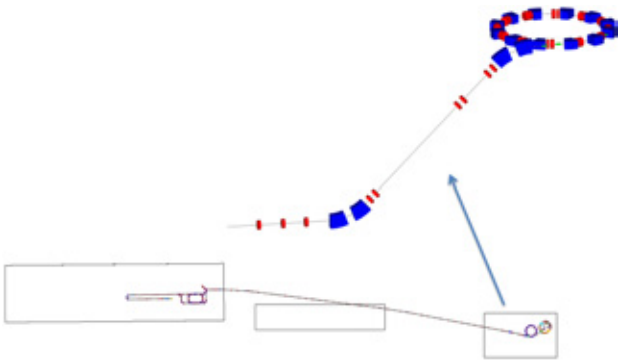

Figure 12: Ascent to booster BEP.

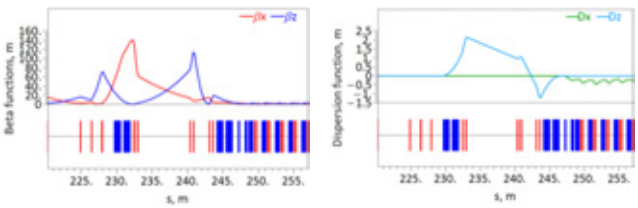

Figure 13: Lattice functions of ascent.

Beam Diagnostics and Vacuum

For beam diagnostics two types of sensors are used: 12 luminophor probes and 23 image current monitors. Probes used for the first beam-pass, they are not transparent for the beam. Monitors are used for supervision of bunches at the time of the beam-pass. They are located after the dipole correctors with betatron phase advance of $2/3\pi$. It allows us to observe effectively the influence of dipole correctors on a bunch trajectory.

At present the vacuum is 10^{-8} Torr, for this purpose 8 pumps NMD-016 are installed.

Magnets and Power Supply

Magnets and power supplies of the transportation channel are listed in Table 1. The first three power supplies are in production. Other power supplies and all magnets are already manufactured.

PERSPECTIVE

Work of beam-pass from Injection complex VEPP-5 to the booster BEP is planned to carry out from December, 2014 to March, 2015. Experiment on collider VEPP-2000 is planned to begin in May, 2014.

ACKNOWLEDGMENT

Thanks to V.V. Anashin, L.N. Arapov, A.M. Batrakov, O.V. Belikov, D.B. Burenkov, A.S. Churkin, B.A. Dovzhenko, K.V. Dyakov, Yu.I. Koysin, I.E. Korenev, A.A. Krasnov, N.N. Lebedev, E.B. Levichev, P.V. Logatchev, S.A. Mishin, M.I. Nepomnyaschykh, A.A. Novikov, A.V. Pavlenko, A.V. Polyansky, R.Z. Pronik, V.P. Prosvetov, O.A. Proskurina, V.V. Rashenko, A.L. Romanov, S.I. Ruvinsky, S.V. Seleznev, L.E. Serdakov, A.N. Skrinsky, V.P. Cherepanov, Yu.M. Shatunov, V.A. Shishkin, D.B. Shwartz, G.G. Shumakov, V.D. Yudin, Yu.M. Zharinov, V.K. Zhurba.

Table 1: Magnets and Power supplies

Element	Parameters	Power supply
2 horizontal magnets, 1-st bend	H=0.08T, L=0.5m	1 DC, UM-20, I=20A
2 horizontal magnets, 2-nd bend	H=0.08T, L=1.5m	1 DC, UM-20, I=20A
4 vertical magnets of the ascent to the booster BEP	H=0.7T, L=1m	1 AC, GID-3000, W=3kJ
1 horizontal magnet before the septum magnet in the booster BEP	H=1.7T, L=0.3m	1 AC, W=2.4kJ
1 septum magnet of the booster BEP	H=1.7T, L=0.4m	1 AC, W=2.4kJ
42 lenses of regular part	G=2.5T/m, L=0.2m	8 AC, GID-25, W=25J
17 lenses of matching parts	G=10-20T/m, L=0.2m	17 AC, GID-25, W=25J
12 dipole correctors in 12 lenses	Hmax=0.2T, L=0.1m	12 AC, GID-25, W=25J
27 dipole correctors	Hmax=0.2T, L=0.1m	27 DC, PS-3-A, I=3A

REFERENCES

[1] Yu. Rogovsky et al., “Status and Perspectives of the VEPP-2000 Complex,” TUY01, these proceedings.
[2] V.A. Kiselev et al., “Particle and Accelerator Physics at the VEPP-4M Collider,” TUZ01, these proceedings.
[3] A.E. Bondar et al., “Project of a Super Charm-Tau factory at the Budker Institute of Nuclear Physics in Novosibirsk,” Physics of Atomic Nuclei, Volume 76 (September 2013), Issue 9, pp 1072-1085.
[4] A. Starostenko et al., “Status of Injection Complex VEPP-5,” TUY02, these proceedings.
[5] A.P. Lysenko et al., “Program of numerical simulation of accelerator structures RING,” BINP, Novosibirsk.
[6] A.N. Dubrovin, “Program of magnetic calculations MERMAID,” BINP, Novosibirsk.

ISBN 978-3-95450-170-0

PROBLEMS AND PROSPECTS OF THE TANDEM ACCELERATOR WITH VACUUM INSULATION*

D. Kasatov, A. Koshkarev, A. Kuznetsov, A. Makarov, Yu. Ostreinov, I. Sorokin, I. Shchudlo, S. Taskaev#, Budker Institute of NuclearPhysics, Novosibirsk, Russia,

Abstract

A tandem accelerator with vacuum insulation for development of the technique of boron neutron capture therapy (BNCT) is proposed and constructed. The accelerator is characterized by rapid acceleration of charged particles. The article describes the problems of the new type of accelerator, both solved and remain to be solved. Also research plans and prospects for the use of the accelerator are presented and discussed.

INTRODUCION

Presently, Boron Neutron Capture Therapy (BNCT) is considered to be a promising method for the selective treatment of malignant tumours [1]. The results of clinical trials, which were carried out using nuclear reactors as neutron sources, showed the possibility of treating brain glioblastoma and metastasizing melanoma incurable by other methods. The broad implementation of the BNCT in clinics requires compact inexpensive sources of epithermal neutrons. At BINP the source of epithermal neutrons based on Vacuum Insulation Tandem Accelerator (VITA) and neutron generation through $^{7}Li(p,n)^{7}Be$ reaction was proposed [2], created and operated [3-5].

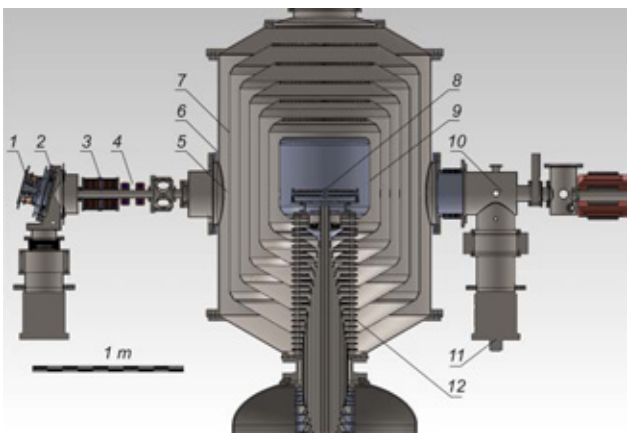

Figure 1: Vacuum insulation tandem accelerator. 1 – H^- ion source, 2 – diaphragm, 3 – magnetic lenses, 4 – corrector, 5 – a temporary location of the beam detector, 6 – accelerator, 7 – electrodes, 8 – high voltage electrode, 9 – stripper, 10 – high energy beam transport, 11 – turbo molecular pumps, 12 – bushing insulator.

General view of the accelerator is shown in Fig. 1. Negative hydrogen ions are injected and accelerated up to 1 MeV by potential applied to the electrodes, then H^- turn into protons in the gas stripping target and at last the protons are accelerated up to 2 MeV by the same potential. Pumping of the stripping gas is carried out by cryogenic and turbomolecular pumps through the jalousies. The potential of the high-voltage and five intermediate electrodes is supplied by a high-voltage source through the bushing insulator which has a resistive divider.

PROBLEMS

The main problem of accelerators is high-voltage strength of vacuum gaps. Because of the large square of the electrodes, great energy is stored in the gaps and the inevitable breakdowns could lead to the gap detraining. The high-voltage strength of 45-mm and 66-mm vacuum gaps was studied. It was found out that the breakdowns at stored energy of 50 J did not lead to the gaps detraining. The stored energy in this accelerator did not exceed 26 J. Training by breakdowns allowed to obtain the required voltage of 1 MV [6].

Another problem of accelerators is strong input electrostatic lens. To provide passage of the beam through the stripping target it was necessary to refocus the beam before the lens without a significant increase in the emittance. To study H^- beam injection, the 22-channel detector has been produced and mounted in front of the first accelerating electrode. It has been determined that the best agreement with the numerical calculation is achieved by assuming the full compensation of the space charge in the transport channel and setting the transverse ion temperature equal to 1 eV at the plasma boundary of the ion source. This study described in detail in [7] resulted in better focusing of the beam required for acceleration of the beam without significant losses.

On the accelerator, stationary proton beam with 2 MeV energy, 1.6 mA current, 0.1% energy monochromaticity and 0.5% current stability was obtained [8]. To conduct BNCT, it is planned to increase the beam parameters to at least 2.5 MeV and 3 mA.

Not good enough vacuum conditions in the beginning of the acceleration of the ion beam seem to be the main current problem. Injected beam ionizes residual and stripping gas mainly in the area before a strong input lens. The born electrons are accelerated to the full voltage of 1 MV and absorbed by construction materials lead to significant power bremsstrahlung [9]. The resulting positive ions were registered by the detector mounted on inlet flange of the accelerator at beam periphery [10]. The magnitude of the current of charged particles reaches 25 % of the current of the accelerated ion beam. Probably, it is the presence of a beam of charged particles in the

* Work is financially supported by the Russia through the Ministry of Education and Science of Russia (project RFMEFI60414X0066)
# taskaev@inp.nsk.su

ISBN 978-3-95450-170-0

accelerating gap that limits high voltage reliability of the gap and does not allow increasing the proton beam current.

To reduce the flow of charged particles and to improve the vacuum conditions, two solutions are proposed.

The first proposal is to install a cooling aperture and to put a cryopump at the input of the accelerator. This will allow reducing significantly the gas flow from the ion source to an accelerating gap.

The second proposal is to reduce the gas flow to the accelerating gap from the gas stripping target. It is proposed to tilt the stripping target, to place permanent magnets in the space between the target and the input aperture of the high voltage electrode [11] and to put the turbo molecular pump inside the high-voltage electrode. This will make it possible not only to reduce the gas flow to the accelerating gap, but also to reduce the flow of ultraviolet radiation and suppress the flow of positive argon ions from weakly ionized plasma inside the stripping tube.

It was found that the high-voltage strength of the accelerator is limited by the high-voltage strength of the outer surface of the glass rings of the vacuum part of the bushing insulator. To raise the voltage to 1 MV to 1.25 MV a new bushing insulator is under manufacturing, the glass rings in it are replaced by polycarbonate rings with corrugated outer surface.

PROSPECTS

The main advantage of VITA is high rate of acceleration – about 25 keV/cm for singly charged ions. This makes an accelerator compact.

In the paper [12], we propose a radical improvement of the accelerator concept. It is proposed to abandon the separate placement of the accelerator and the power supply and connecting them through the bushing insulator. The source of high voltage is proposed to be located inside the accelerator insulator, high voltage and intermediate electrodes mounted on it (Fig. 2). This will reduce the facility height from 7 m to 3 m and makes it really compact and attractive for placing in a clinic.

Also Fig. 2 shows the first proposed orthogonal beam shaping assembly (BSA) [13]. Such orthogonal neutron beam can be used to easily direct the beam to the patient at any angle. This solution is “à la gantry” for proton therapy. The change of direction of therapeutic neutron beam is ensured by the rotation of the whole BSA or its part containing moderator about the axis of proton beam propagation.

Obtaining of 2.5 MeV 3 mA proton beam and implementation of the embedded power supply and orthogonal BSA will make it possible to create a source of epithermal neutrons suitable for BNCT.

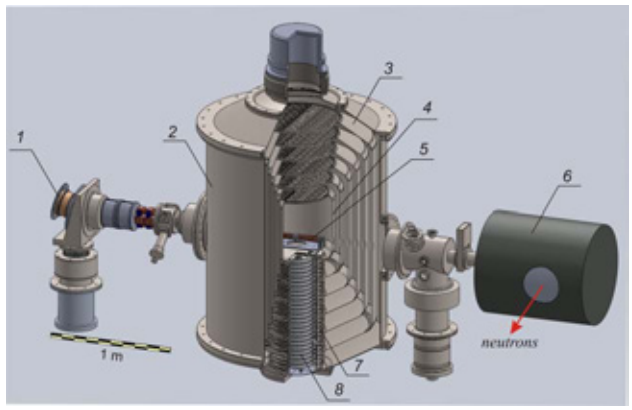

Figure 2. Neutron source for BNCT. *1* – negative hydrogen ion source, *2* – accelerator, *3* – intermediate electrodes, *4* – high voltage electrode, *5* – gas stripping target, *6* – beam shaping assembly, *7* – insulator, *8* – high voltage sectioned rectifier.

REFERENCES

[1] Neutron Capture Therapy: Principles and Applications. Eds.: W. Sauerwein, A. Wittig, R. Moss, Y. Nakagawa. Springer, 2012, 533 p.
[2] B. Bayanov, et al., NIM A 413 (1998) 397.
[3] A. Kuznetsov, et al., Tech. Phys. Lett. 35 (2009) 346.
[4] A. Kuznetsov, et al., NIM A 606 (2009) 238.
[5] L. Mostovich, et al., Bulletin of Experimental Biology and Medicine 151 (2011) 264.
[6] I. Sorokin, S. Taskaev, Instr. Experim. Techn. 57 (2014) 377.
[7] A. Makarov, et al., “Optimization of the negative hydrogen ion beam injection into the tandem accelerator with vacuum insulation”, Proc. RUPAC 2012 Saint-Petersburg Russia, WEPPD038 (2012) 623.
[8] D. Kasatov, et al., “Obtaining of 2 MeV 1.6 mA proton beam on a tandem accelerator with vacuum insulation”, JINST (2014).
[9] D. Kasatov, A. Makarov, I. Shchudlo, S. Taskaev, “Measurement of the spatial distribution of gamma radiation on accelerator-tandem with vacuum insulation”, these proceedings.
[10] D. Kasatov, A. Makarov, I. Shchudlo, S. Taskaev, “Studying of the accompanying charged particles in the tandem accelerator with vacuum insulation”, these proceedings.
[11] A. Makarov, Yu. Ostreinov, S. Taskaev, P. Vobly, “Modification of the argon stripping target of the tandem accelerator”, these proceedings.
[12] I. Sorokin, S. Taskaev, “A new concept of a Vacuum Insulation Tandem Accelerator”, Appl. Radiat. Isot. (2015).
[13] V. Aleynik, et al., Appl. Radiat. Isot. 88 (2014) 177.

ISBN 978-3-95450-170-0

DYNAMICS OF PROCESSES IN SUBCRITICAL REACTOR DRIVEN BY LINEAR ACCELERATOR*

A.G. Golovkina#, I.V. Kudinovich, D.A. Ovsyannikov, Yu.A. Svistunov
Saint-Petersburg State University, Saint-Petersburg, Russia

Abstract

In this paper dynamics of processes in accelerator driven subcritical reactor (ADS) is considered. ADS operates at subcritical level and the necessary neutron supply comes from the interaction of a charged particles beam with a heavy atom nucleus (spallation reaction). Mathematical model of dynamics of subcritical reactor controlled by linear accelerator is presented. Calculation results of transient processes in the reactor core taking into account fuel feedback. The reactor power level control is carried out through the regulation of linac current impulses frequency.

INTRODUCTION

The subject of research in the paper is subcritical reactor driven by proton linac. Currently, research in this field purposes is carried out in many scientific centers all over the world. They are focused on the problem of ADS design for transmutation of radioactive waste and safe energy production. The proposed projects are mostly supposed the use of accelerator with output energy about 1-2 GeV, that substantially defines the facility high price. In this paper proton linac with lower beam characteristics [1] (E = 300 MeV, I = 5 mA, duty factor 10%, W = 1.5 MW) is considered as an ADS driver.

The ADS control strategy should differ from traditional critical reactors control. In traditional reactors the reactivity effects are compensated by neutron absorber that guarantees the reactor maintenance in the critical condition. But there is no control impact on the subcritical reactor reactivity in ADS, the system power level is regulated only by accelerator.

POSSIBLE CONTROL SCHEMES FOR ADS WITH PROTON LINAC

Thermal power for the reactor core is defined by the following formula

$$N_T = \frac{E_f S k_{ef}}{\nu(1-k_{ef})}, \qquad (1)$$

where E_f - energy, released per a fuel nuclei fission, k_{ef} .- effective multiplication factor, S – external neutron source generation intensity:

$$S = \frac{I_p m_0}{e},$$

where I_p – the accelerator average current, m_0 – neutron yield (the average number of neutrons generated in the target by one accelerated charged particle, depends on charged particles beam energy, target composition and sizes), e – the charge of an accelerated particle.

ADS Power Level Regulation

The ADS power level control can be realized by variation of external neutron source generation intensity which depends on the average accelerator current and charged particles beam energy.

The average current regulation is possible because of pulse current value or pulse repetition rate variation.

Pulse current can be increased by raising current at the exit of plasma ion source (for example, because of increasing the emissive aperture diameter), but the beam emittance grows meanwhile, system of beam formation for injection to the acceleration channel gets more complicated, transient processes in resonators and beam dynamics change. That is the accelerator design and adjustment becomes more complicated in comparison to accelerator with fixed output parameters.

Increasing of average current by increasing pulse repetition rate is a simpler decision because particle dynamics in accelerating tract doesn't change. The effect is achieved due to the control system of rf and injector feed lines.

Increasing of proton energy can be fulfilled by activating additional resonators at the end of the accelerating channel. In should be noted that when the resonators are turned off, the beam output characteristics will get worse.

Thus, the most suitable way to control ADS is the accelerator average current variation by pulse repetition rate change.

It should be noted that because of resonators high quality factor the transient processes in them will have quite large duration. As well known, the process of rf electrical field amplitude stabilization is characterized by the following expression:

$$E = E_\infty\left(1-\exp\left(-t/\tau\right)\right),$$

where $\tau = Q/\pi f$ – magnitude which characterize transient (taking into account generator impact); t -time, Q – quality factor, E_∞ – steady value of rf field in resonator (for $t \to \infty$).

The field stabilization time can be comparable with the current pulse duration or exceed it in several times. This can lead to the additional short pulsations of source neutron power.

*Work was partly supported by SPbSU, grant No. 9.38.673.2013
#golovkina.a@gmail.com

ISBN 978-3-95450-170-0

Subcritical Reactor Feedbacks

The ADS subcritical reactor dynamics depends on outer and inner feedbacks (Fig. 1). The inner feedbacks are determined by the reactor core physical characteristics, the external ones reflect the reactor connection with the power plant (coolant flow, coolant temperature at the entrance).

For stable ADS working at the constant power level, the reactor core should have the negative fuel and coolant temperature inner feedback and the negative mean reactivity coefficient. These conditions ensure the reactor self-control and the average temperature maintenance.

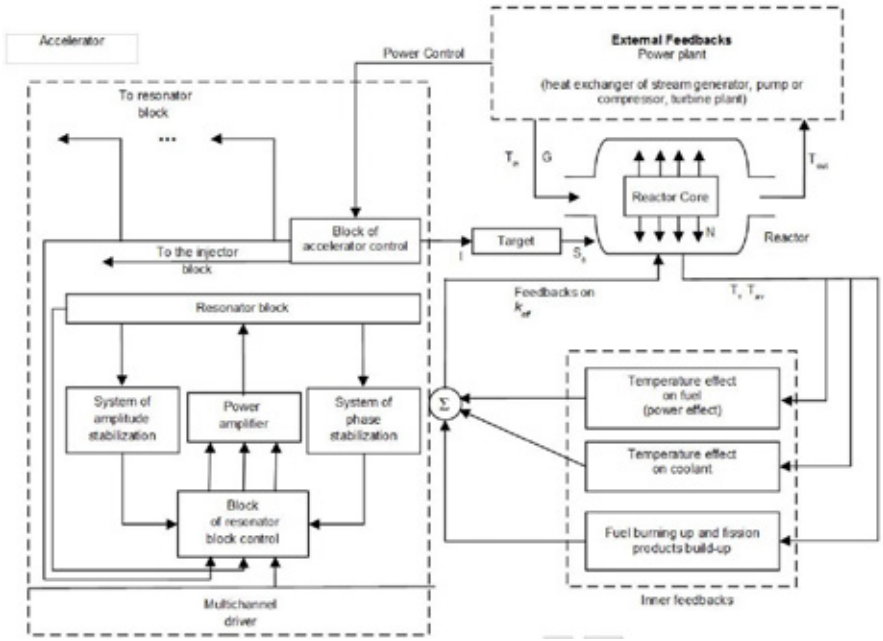

Figure 1: ADS structural scheme with feedbacks.

ADS PARAMETERS CHANGE IN TIME IN STEADY-STATE CONDITION

The law of linear accelerator current variation in time looks like periodic impulses, so it can cause steady-state power level oscillation in the subcritical reactor core. Thereby, kinetics of subcritical reactor with periodical external neutron source should be investigated; the influence of power level oscillation on the fuel elements temperature condition should be estimated.

The ADS reactor core power level change is described by the point kinetics equations for subcritical reactor with the external neutron source:

$$\frac{dN(t)}{dt} = \frac{\rho-\beta}{l}N(t) + \sum_{i=1}^{6}\lambda_i c_i(t) + Q(t),$$
$$\frac{dc_i(t)}{dt} = \frac{\beta_i}{l}N(t) - \lambda_i c_i(t). \qquad (2)$$

Here $N(t)$ – reactor core power level (W), c_i - power of nucleus sources, bearing delayed neutrons, β – effective part of delayed neutrons; λ_i – decay constant for nucleus, bearing delayed neutrons,; l_0 – average prompt life time; $\rho = (k_{ef} - 1)/kef$ – reactivity coefficient, determined by Doppler effect; $l = l_0/k_{ef}$, $Q(t)$ - external neutron source intensity.

The average prompt lifetime l_0 depends on neutron energy spectra in the reactor core and changes from $5\cdot10^{-7}$ sec (for fast reactors) to $5\cdot10^{-4}$ sec (for thermal reactors). The effective part of delayed neutrons is $\beta = 0.0068$ for U^{235}.

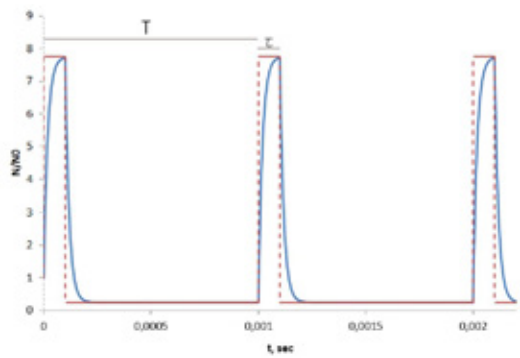

Figure 2: The dependence of accelerator current and ADS reactor power on time.

ADS subcritical reactor kinetics depends on accelerator current pulse period and duration $q(t)$ (Fig. 2). If pulse period considerably less than the average prompt lifetime in the reactor, then the neutron source can be treated constant with the intensity equals to the average (time) value of $q(t)$. This condition is fulfilled in cyclotrons.

The micro pulses period in the linear accelerator ($T = 5\cdot10^{-9}$ sec) is considerably less than the prompt life

ISBN 978-3-95450-170-0

time. However the macro pulses period of the accelerator proposed for ADS ($T = 5 \cdot 10^{-3}$ sec) exceed the prompt lifetime in the reactor. Thus, the additional neutron source intensity in ADS with linac can be described as the sequence of rectangular pulses with a period and pulse duration corresponding to the accelerator current period and macro-pulse duration and with pulse amplitude corresponding to the average current value in the macro-pulse [2]:

$$q_{av} = \frac{Q^{\max}\tau}{T}.$$

Inner feedbacks specify the dependence of power level dynamics in the reactor core on the fuel elements temperature. Because of reactor core heat capacity the time constant, characterizing the fuel rods temperature change, is not less than 0.01 sec. Thus, the subcritical reactor dynamics taking into account the influence of inner feedbacks can be described by quasi-static approximation for prompt neutrons – instantaneous step approximation [3]. In this case the system, describing the ADS subcritical reactor dynamics with external neutron source looks like:

$$\begin{aligned}
&N = \frac{\left(\sum_i \lambda_i c_i + Q\right) l}{\beta - \rho},\\
&\rho = \rho_{cp} + \alpha_T \left(T_T - T_{cp}\right),\\
&\frac{dc_i}{dt} = \frac{\beta_i}{l} N - \lambda_i c_i,\\
&M_T C_T \frac{dT_T}{dt} = N_T - hF\left(T_T - T_{TH}\right),\\
&M_{TH} C_{TH} \frac{dT_{TH}}{dt} = 2GC_{TH}(T_{ex} - T_{TH}) + hF\left(T_T - T_{TH}\right),
\end{aligned} \tag{3}$$

where $M_т$ – the fuel elements in the reactor core mass; $M_{тн}$ – the coolant mass, $T_т$ –fuel elements temperature; $T_{тн}$ –coolant temperature, $N_т$ – reactor thermal power; G – coolant mass flow; F – fuel elements heat exchange area, α_T – Doppler coefficient (fuel) , h – heat-transfer coefficient, $Q=pq_0$ – average source intensity, p – normalization coefficient.

Constants in (3) corresponds to fast reactor BN-350 characteristics (N=1 GW), initial conditions: $N(0)$=0, $c_i(0)$.

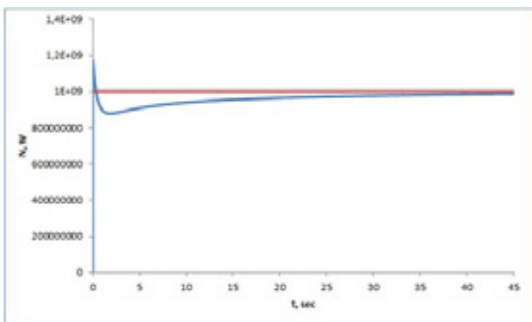

Figure 3: The ADS reactor power level change in time.

In Fig. 4, 5, as an example, calculation results of parameters change during fast subcritical reactor start-up and reactor going to power rating level, are presented. On the basis of the presented model power level change in the ADS subcritical reactor core ($k_{ef} = 0.98$, fuel composition corresponds to BN-350) driven by linac ($T = 10^{-3}$ sec; $\tau = 10^{-4}$ sec) is calculated (Fig. 3).

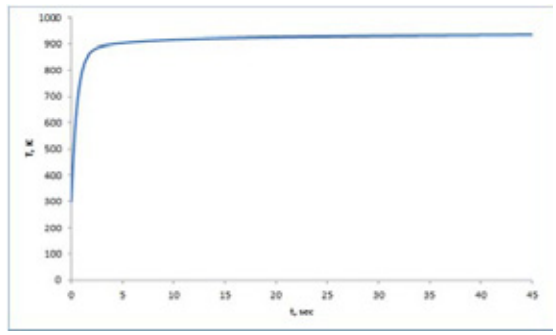

Figure 4: The fuel temperature change in time.

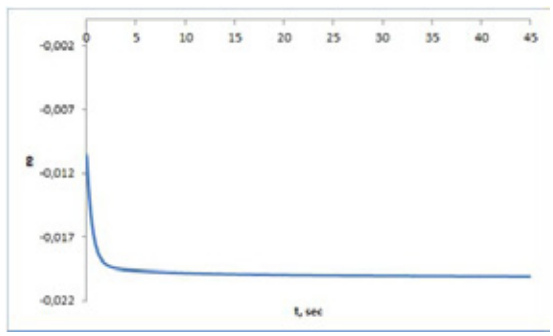

Figure 5: The reactivity coefficient change in time.

CONCLUSION

For ADS control it is necessary to regulate the external neutron source intensity and therefore charged particles beam characteristics.

The most convenient way to control ADS is the average current variation by pulse repetition rate change.

In the steady ADS operation condition neutron flux density in the reactor core changes periodically with a period corresponding to the impulse period in accelerator. The fuel elements temperature is almost constant in time because of their thermal inertia.

At the ADS start-up, driven by linac with the constant average current, a short-time power surge higher the power rating level is possible, but the fuel temperature doesn't exceed its rated value.

REFERENCES

[1] A.G. Golovkina, et al. "Project of Low-Energy Accelerator Driven Power Plant", RuPAC'12, St. Petersburg, September 2012, p. 224-226 (2012).

[2] A.G. Golovkina, et al. Dynamics of Accelerator Driven Subcritical Reactor, BDO'14, St. Petersburg, July 2014, doi: 10.1109/BDO.2014.6890020 (2014).

[3] D.L. Hetrick, *Dynamics of Nuclear Reactors*, (Chicago: Univ. Chicago Press, 1971).

ISBN 978-3-95450-170-0

ACCELERATORS APPLICATION FOR RADIATION PROCESSING OF FOODSTUFFS

A.Yu. Gracheova, M.A. Zaviyalov, V.V. Kondratenko, V.P. Filippovich, Russian Research Institute of Canning Technology, Vidnoye, Moscow area, Russia
Yu.S. Pavlov, Institute of Physical chemistry and Electrochemistry RAS, Moscow, Russia
A.V. Prokopenko, National Research Nuclear University (MEPhI), Moscow, Russia

Abstract

During last couple decades in Russia an interest in the electron-beam sterilization technology has been significantly renewed. The electron beam irradiation occurs at electron energies in the range from 3 up to 10 MeV with dose of 30 kGy. A special research interest is an exploring the possibility to reduce electron energy and dose characteristics upon foods irradiation. The aqueous suspensions with Escherichia coli and Staphylococcus aureus have been used as the research objects.

Whole treatment process has been carried out on an industrial electron accelerator UELV-10-10-C-70 located in the A.N. Frumkin Institute of Physical chemistry and Electrochemistry at the Russian Academy of Sciences. Beforehand partially filled and sealed 10 ml vials containing the sample suspensions with microorganisms have been installed on an accelerator line in two different positions: vertical and horizontal. The samples were irradiated with doses of 3, 5, 7 and 10 kGy. Microbiological investigations of irradiated objects have been carried out in accordance with the Russian State Standards 30726-2011 and GOST 10444.2-94 by the most probable number of colony forming units (CFU) method.

As an investigative result, the microorganism radioresistance index D10 has been determined. It makes it possible to evaluate amount of these microorganism types upon contaminated foodstuffs irradiation. It has been established that during exposure the horizontal position of the vials was more effectively. It may be explained due to simultaneous influence of two different though interrelated reasons: the direct radiation and radiation-induced ozone.

In recent years, Russia has been a renewed interest in radiation technologies. The application of radiation technologies at agriculture and food industry is a global trend [1]. Radiation sterilization technology and food processing have a high degree of efficiency, high performance, accuracy of dosing radiation and possibility to irradiate packaged products. Radiation processing occurs without significant heating of the product, which allows to sterilizethermolabile objects. Radiation facilities have low operating costs and compliance with accepted environmental standards. According to the International Commission on Radiological Protection every year on Europe market receives more than 200 000 tons of irradiated foods.

In the USSR, feasibility studies on radiation processing of food began with the beginning of the 60s of the last century. The studies were conducted at the 'A.N. Bach Institute of Biochemistry' of Academy of Sciences, in research institutes of Union Academy of Agricultural Sciences of the USSR, 'Institute of Nutrition' of Academy of Medical Sciences and 'F.F. Erisman Research Institute of Hygiene'. At that time, the lead organization for the study of radiation effects on the food served Institute of Canning and Vegetable Drying Industry (now Russian Research Institute of Canning Technology), which had gamma-installation based on the activity of the ^{60}Co irradiator 300 Curie. The investigations [2, 3] have shown promising applications of radiation method to prolong the shelf life of food products. At [4] it was shown the relevance and timeliness of the use of electron-beam sterilization technology using high current electron accelerator.

In contrast to sterilization by gamma radiation, electron radiation does not use radioactive isotopes. Electron accelerators have appeared in the 50s of the last century, but their use at that time was not economically justified. With the development of technologies for the creation of high-current electron accelerators (energy, beam current and pulse duration increase) value of electron beam sterilization decreased to quite an acceptable level. This has caused interest in the electron beams from the food industry. Irradiation occurs when the energy of the electrons in the range of 3 to 10 MeV. At these energies electrons no education isotopes in food and the penetration depth of the electrons is sufficient for their penetration into the product packed in containers ready for shipment.

High dose rates of electron irradiation allows to influence them for several seconds as opposed to hours of exposure to the product with gamma radiation. Short-term impact of accelerated electrons reduces the possible effects of oxidation product. This minimizes radiation and thermal disturbances in products and packaging material. Accelerators it is possible to vary the energy of the electrons and bremsstrahlung. Reduction of energy leads to the minimization of damage to the products during radiation treatment. In addition, the cost of operation of the accelerator and the capital cost of the creation of radiation-accelerator center is much smaller.

In Russia since 1980 designed and built for industrial radiation processes over 200 accelerators (excluding accelerators for medicine, fault detection and imaging). At the moment are in operation for more than 80 linear electron accelerator. In [5] provides an overview of the

ISBN 978-3-95450-170-0

developed and used electron accelerators for radiation processing plants. The advantages of linear electron accelerators are:

- Ability to control the parameters of the installation;
- The directionality of energy transfer;
- The service life of more than 20 years without major repairs;
- Reduced requirements for permits and protection;
- The problem of "nuclear proliferation";
- The low cost of the process of irradiation on the accelerator.

One of the industrial electron accelerators for radiation processing electron is in the A.N. Frumkin Institute of Physical chemistry and Electrochemistry RAS. Accelerator UELV-10-10-C-70 is a multi-purpose source of ionizing radiation and intended for use in industrial radiation processes [6-8]. Currently this accelerator is used in research on electronic sterilization model media with solutions of microorganisms. Using this accelerator is possible to develop technical requirements and regulations of processing agricultural products and products of its processing.

Currently, at the international level is set a number of documents regulating of radiation treatment of food products. This accelerated the introduction of radiation treatment abroad. Russia, unlike in European Union and the United States is at early stage of formation of the market of radiation technologies processed products. One of the major problems in the development of this sector is outdated legal framework, as well as partial or complete absence of the required standards for irradiation of certain foods. Also technical regulations and specifications of radiation treatment are not developed. Preparation of modern regulatory framework in Russia is engaged Ltd. «Center Atommed" [9]. The need for development and improvement of regulatory framework of radiation food processing technology due to the following factors:

- presence and growth of dissemination of radiation technologies in the market consumption of food and agricultural products;
- need to introduce standardizing requirements for products obtained with the use of radiation technologies (defined by general health, sanitation, hygiene, consumer and other requirements);
- necessity ensure reproducible model of radiation effects in the process of product life cycle (requirements for reproducibility of the dose of irradiation conditions, modes of storage products, etc.);
- need to ensure radiation safety radiation facilities and production lines;
- requirements of unification project, design and equipping of radiation facilities, systems for monitoring and control exposure.

Strict requirements for managing necessitated the adoption of general international standard ISO 14470:2011. This standard ensures compliance with the latest requirements under irradiation of food, which is used to improve the quality and safety of food processing. The standard is intended for manufacturers, the operators on the irradiation, regulators activities, customers, and most importantly – consumers. The main objectives of ISO 14470: 2011 are as follows:

- Ensure that the requirements of food irradiation in accordance with current standards and practices;
- Provide technical regulations between the client and the operator of the irradiation;
- Create documentation and control systems for processing of food irradiation.

Currently, the Russian legal framework of industrial radiation technologies is divided into the following levels: legal level of control (changes in the number of federal laws, government regulations and the preparation of technical regulations), technical level (licensing, standardization and training sanitary rules and norms) and technological level (development orders, manuals, technical manuals, regulations and sets of documents). The basic standard for radiation processing of food products developed as part of the project documentation for the customs union of Russia, Belarus and Kazakhstan on the basis of pre-existing norms of radiation safety and standards adopted by the European Union.

In preparation for establishment of draft technical regulations in 2013 at A.N. Frumkin Institute of Physical chemistry and Electrochemistry RAS on the accelerator UELV-10-10-C-70 in conjunction with the Russian Research Institute of Canning Technology conducted a series of studies on the irradiation of sealed ampoules with model solutions with microorganisms by an electron beam with different irradiation doses. Modeling environments allow to determine the impact of the alleged doses and installradioresistance of traditional microorganisms. Of great interest is relatively low irradiation doses up to 10 kGy.

Accelerator UELV-10-10-C-70 has the energy of the electron beam 10±0,4 MeV electron radiation dose rate at distance 1 m from the exhaust flange window 3 kGy/s. Accelerator used a circular conveyor for transporting irradiated samples before scanning electron beam. Monitoring the radiation dose carried out by means detectors based on single-use polymer films and spectrophotometer. Range measurement of absorbed dose varies at the range from 5 to 50 kGy and the error does not exceed 12%. Smaller doses can be estimated by interpolating the results obtained.

In the fourth quarter of 2013 at the accelerator UELV-10-10-C-70 was exposure of sealed vials with model solutions of microorganisms. Vials have diameter of 10 mm and height of 60 mm. Gram-negative rod-shaped bacterium E. coli with the size of 1.1-1.5 × 2.0-6.0 mm and grammopozetiv coca Staphylococcus aureus spherical shape with a diameter of 0.5-1.5 mm are studed. In the study used daily cultures of these microorganisms dissolved in meat-peptone broth. Single irradiation of microorganisms carried by electrons with doses of 3, 5, 7, 10 kGy at two vials positions. In each experiment were used 3 ampoules with microorganism to reduce statistical

ISBN 978-3-95450-170-0

errors. Microbiological examination of irradiated and control samples were carried out on the day after exposure. Control vials were stored under the same conditions as irradiated.

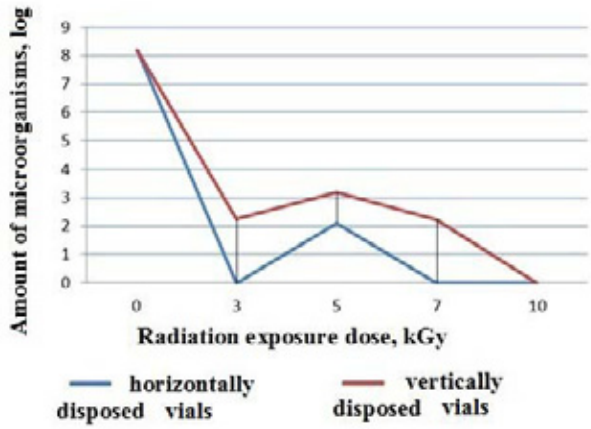

Figure 1: Microbiological characterization of the irradiation effect at E. coli.

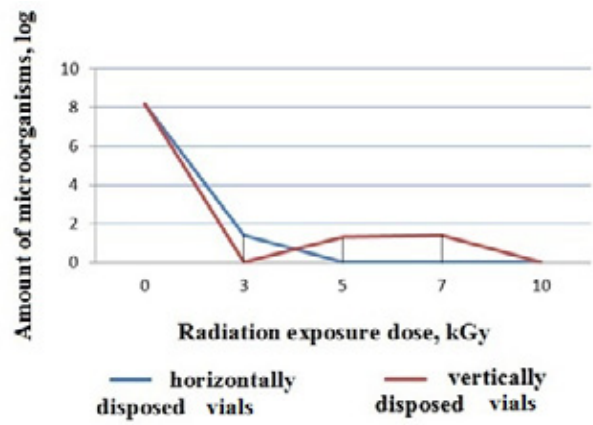

Figure 2: Microbiological characterization of the irradiation effect at S. aureus.

Microbiological investigations of irradiated objects have been carried out in accordance with the Russian State Standards 30726-2011 for E. coli and standard GOST 10444.2-94 for S. aureus. According to standards of the cultivation of microorganisms on dry nutrient agar should be 24 hours at 37° C. Studies were carried out by the most probable number of colony forming units (CFU) method. The results were taken into account in each test sample for two reps. The results of the study are presented in Fig. 1 for E. coli, and Fig. 2 for S. aureus. Figures present in logarithmic scale content surviving organisms from absorbed dose. It has been established that cultures of E. coli and S. aureus, exposed to radiation die by 80-100%. It has been established that during exposure the horizontal position of the vials is more effectively is more effective in comparison with the vertical. It may be explained due to simultaneous influence of two different though interrelated reasons: the direct radiation and radiation-induced ozone.

In the work shows the current trends of radiation processing technology of food production using particle accelerators in Russia. The urgency of establishing legal documentation is shown and terms of reference for further research are defined. The possibility of using the existing radiation accelerators for food irradiation is determined. In the course of research on the accelerator UELV-10-10-C-70 established the lethal dose for suspensions of microorganisms. This allows to estimate the dose required for irradiated foods at radiation sterilization.

REFERENCES

[1] Food preservation by radiation // Radiation and agricalture, URL: http://www.iaea.org/Publications /Magazines/Bulletin/Bull233/23305783336.pdf – 2011, (dateaccessed 13.12.13). (in Russian).

[2] Metlitski L.V., Rogachev V.I., Khrushchev V.G. // Radiation processing of food products. M.: "Economy", 1967.159 p. (in Russian).

[3] Frumkin M.L., Kowalski L.P., Gelfand S.Y. // Technological basics of radiation processing of food products. M: Food industry, 1973. 408 p. (in Russian).

[4] Gelfand S.Y., Zaviyalov M.A., Petrov A.N., Prokopenko A.V., Philippovich V.P. // Modern aspects of food radiation processing. / Storage and processing of farm products, №2, 2013, pp. 25-31. (in Russian).

[5] Pavlov Y.S Russian industrial electron beam technology in 2014. Works of XXIV International conference "Radiating physics of a solid body", Moscow, FGBNU "SRI PMT", July 2014, pp. 22-33 (2014) (in Russian).

[6] Pavlov Y.S., Ershov B.G., Fomenko Y.L., Polyakov A.A. // Implemented and developed radiation technology at IPCE RAS. Problems of Atomic Science and Technology.Ser. Technical Physics and Automation. Release 67 (part 1). Moscow, JSC "NIITFA", 2013, p. 27-41. (in Russian).

[7] Pavlov Y.S., Ershov B.G., Dobrohotov V.V., Pavlov V.A. The radiation system for studying radiation-chemical transformations of materials and the development of radiation technologies at IPCE RAS. V All-Russian conference "Actual problems of high energy chemistry."Proceedings of the conference. M. RCTU, 2012, p. 80-82. (in Russian).

[8] A.K. Pikaev, P.Ya. Glazunov, Yu.S. Pavlov. "Radiation centre of institute of physical chemistry in Moscow", Radiat. Phys. Chem., Vol. 42, Nos. 4-6, pp. 887-890 (1993).

[9] Draft standards irradiation // Atommed company, corporation Rosatom. [Moscow, 2013]. URL: http: //Atommedcenter.ru (date accessed 28.11.2013). (in Russian).

ISBN 978-3-95450-170-0

List of Authors

Bold papercodes indicate primary authors

— A —

Afonin, A.G. THPSC21
Agafonov, A. THPSC52
Agapov, N.N. THX03
Ageev, A.I. THZ03
Ahmanova, E.V. TUCA04, **TUPSA23**, TUPSA24
Akhmetov, A.R. **WECA07**, THX01
Akimov, A. THX01
Aksentyev, A.E. THPSC04, THPSC05
Aleev, A.A. WEPSB48
Alekseev, P.N. **WEPSB26**
Alekseev, P.N. THPSC05
Alenitsky, Yu.G. **TUPSA31**
Alexander, A.A. WEPSB17
Alexandrenko, V.V. THCA01
Alexeev, N.N. **TUZ02**, TUPSA08
Alexey, P.G. WEPSB03
Alfeev, A.V. THX03
Aliev, K.A. THPSC03, THPSC05
Alimov, A.S. WECA08, WEPSB39
Altsybeyev, V.V. TUCA03, **TUPSA22**
Anashin, V.S. WECA12
Anashin, V.V. THPSC11
Andreev, A. A. WEPSB48
Andreev, V. THX03
Andreev, V. TUZ02, TUPSA08
Andrey, O.A. WEPSB03
Andrianov, S.L. **TUPSA27**, **TUPSA28**, WEPSB27, **WEPSB48**
Antonov, A.V. THPSC53
Aparin, D. WEPSB48
Apel, P.Yu. WECA09
Arbuzov, V.S. THCE02
Artemenko, S.N. WEPSB12, WEPSB13
Asfari, Z. THPSC47
Ashanin, I.A. **TUPSA20**, THPSC05
Aulenbacher, K. TUCA02
Averyanov, G.P. TUPSA13, **TUPSA35**
Avgustinovich, V.A. WEPSB12, WEPSB13
Ayzatsky, N. THPSC54

— B —

Baev, V.K. **TUPSA11**
Bagova, S.Z. **WEPSB34**
Bak, P.A. **TUPSA33**, THX01
Bakhmutova, A.V. WEPSB25
Balabin, A.I. **TUPSA08**
Barabin, S.V. THPSC33, THPSC34
Barnes, C.W. WEPSB25
Bashmakov, Y.A. **TUPSA13**, THPSC05
Batazova, M.A. THX01
Batin, V. THX03
Batrakov, A.M. TUCB02, TUPSA29, THX01, THPSC29
Batyaev, V.F. THPSC05
Bazanov, A.M. TUCB01
Bazhal, S.V. WEX01
Beckmann, F. THPSC30
Beketov, E.E. WEPSB19
Bekhtenev, E.A. **THPSC23**
Bekhterev, V. THPSC08, THPSC55
Belchenko, Y.I. THPSC28
Belkov, A. THY02
Belov, A. **THCE01**, FRCA02
Belyakova, T.F. TUPSA32
Berkaev, D.E. TUY01, THPSC27, FRCA01, FRCA03
Blell, U. FRCA01
Blinnikov, A.A. WEPSB36, THPSC05
Bogachev, A.A. WEPSB48
Bogdanov, A.V. TUPSA16, TUPSA30, WEPSB25
Bogdanov, I. THZ03
Bogdanovich, B.Y. TUPSA11, THPSC37, **THPSC49**, THPSC50
Bogomolov, S.L. WECA09, THPSC08, THPSC47
Bokor, J. WEPSB31
Bolkhovityanov, D. THX01, THPSC25
Bondarchenko, A.E. THPSC47
Bondarenko, T.V. THPSC05
Borisov, O.N. WECA09
Bragin, S. TUPSA21, THPSC45
Britvich, G.I. TUPSA38, WEPSB19
Britvich, G.I. THPSC21
Brovko, O.I. THX03
Bruker, M.W. TUCA02
Bryazgin, K.A. WEPSB15
Bryzgunov, M.I. TUY03, TUCA01, TUCA02
Bubley, A.V. TUY03, TUCA01
Budkin, V.A. TUPSA13
Buleiko, A.B. WEPSB04
Butenko, A.V. TUCB01, WEPSB01, THX03
Buyanov, G.O. **WEPSB03**
Buzmakov, V.A. WECA09

— C —

Chalykh, B.B. TUPSA28, WEPSB27, WEPSB38, WEPSB48
Cherepenko, A. TUPSA33
Chernov, K.N. THCE02
Chertishchev, I.A. THPSC54
Chesnokov, Y.A. THPSC21
Chikhachev, A.S. **TUPSA25**
Choinski, J. THPSC55
Comunian, M. WEPSB27, WEPSB38

ISBN 978-3-95450-170-0

— D —

Dalechina, A.V. **WEPSB42**
Danilichev, V.A. WEPSB43
Didenko, A.N. THPSC05, **THPSC50**
Dietrich, J. **TUCA02**, TUCA01
Dimopoulou, C. FRCA01
Dmitriev, S.N. WECA09
Dmitriyev, M.S. THPSC05
Dmitriyeva, V.V. TUPSA13, TUPSA35, WEPSB37, THPSC05
Dobrohotov, V.V. WEPSB43
Dolbilov, G. **WEPSB29**, **WEPSB30**
Dolinskyy, A. FRCA01
Dolya, S.N. WEPSB28
Domarov, E.V. **WEPSB15**
Dombrovsky, V. THPSC42
Donets, D.E. THX03, WEPSB01
Donets, E.D. THX03
Donets, E.E. THX03
Dorofeev, G.L. TUPSA02
Dourkine, A.P. THPSC07
Dovbnya, A.N. THPSC54
Drivotin, O.I. **TUPSA15**
Drobin, V.M. TUPSA02
Drobin, V.M. TUPSA23
Drozdovsky, A.A. **TUPSA16**
Drozdovsky, S.A. TUPSA16
Durkin, A.P. TUCA03
Durum, A.A. THPSC21
Dyubkov, V.S. **TUPSA10**, **WEPSB37**, THPSC05

— E —

Efimov, S.V. WEPSB25
Efimov, Y.V. THPSC42
Efremov, A.A. WECA09, THPSC08, THPSC47
Efremov, A.V. THPSC06
Egorov, A.S. WEPSB20, WEPSB21, **WEPSB23**
Eliseev, A.A. THX01
Eliseev, A.V. THX03
Elyash, S.L. **WEPSB45**
Emanov, F.E. **THPSC25**, THPSC26
Emeljanov, M.A. WECA11
Ermakov, A.N. **WECA08**, WEPSB40, **THPSC39**
Ermolaev, S.V. **WEX04**
Eseev, M.K. **TUCA04**, TUPSA23

— F —

Fadeev, A.M. **WEPSB36**, THPSC03, THPSC05
Fadeev, S. WECA06, WEPSB15
Fateev, A.A. **TUPSA34**, WECA09
Fatkin, G.A. TUCB02, THX01, **THPSC29**
Fedin, P.A. TUPSA28, WEPSB48
Fertman, A. THPSC05
Feschenko, A. TUPSA21, WEX04, THPSC45
Fialkovskiy, A.M. WEPSB41
Fomin, Y.A. THY02
Frejdovich, I.A. WECA08
Frolov, A.R. WECA05, THPSC25
Frolov, B.A. **THPSC46**
Frolov, O.T. THCE01, **FRCA02**

— G —

Galchuck, A.V. WECA11
Galimov, A.R. TUCB01, THX03
Gall, B.J.P. THPSC47
Gavrilin, R. TUPSA16, WEPSB38
Gavrilov, S.A. **THPSC43**
Gavrish, Yu.N. WEX03, WECA11, **WEPSB41**
Gikal, B. TUPSA32, **WECA09**, WECA12, THPSC08, THPSC09
Gmaj, P. THPSC55
Gnutov, P.A. THPSC40, THPSC41
Gogolev, A.S. THPSC21
Golovkina, A.G. **FRCB02**
Golubev, A. TUZ02, TUPSA16, TUPSA26, TUPSA30, **WEX02**, WECA02, WEPSB25, WEPSB38, WEPSB48
Golubovskiy, S.E. FRCA02
Goncharov, A.D. TUY03, TUCA01, WECA05
Gorbachev, E.V. TUPSA34, THX03
Gorbatenko, O.V. THPSC27
Gorda, O.E. FRCA01
Gorev, S.A. **WEPSB12**, WEPSB13
Gorlachev, G.E. WEPSB42
Gorokhov, S.A. WEPSB19
Gotman, V. THPSC31
Govorov, A. WEPSB01, THX03
Grekhov, O.V. WEX04, THPSC45
Gremyachkin, D.E. WEPSB20
Grigorenko, S.V. WECA11, WEPSB11
Grigoriev, V.I. WECA11
Gulbekyan, G.G. TUPSA32, WECA09, WECA12, **THX04**, **THPSC08**, **THPSC09**
Gurov, S.M. THPSC11
Gusarova, M. **WEPSB06**, **WEPSB07**, THPSC03, THPSC05, **THPSC18**, **THPSC19**, **THPSC20**
Gusev, Ye.A. THPSC25

— H —

Hofmann, A. TUCA02
Horodek, P. TUPSA23, **WEPSB32**
Hrenkov, S.D. WECA07, THX01
Hseuh, H.-C. THPSC11

— I —

Ignatev, I.G. **WEPSB46**
Igumnov, V.S. WEPSB12, **WEPSB13**
Il'inskiy, A.V. **THPSC37**

ISBN 978-3-95450-170-0

Ilyin, I.V. THPSC29
Ishkanov, B.S. WECA08, WEPSB39, WEPSB40
Iskandarov, N.A. WEPSB48
Ivanenko, I.A. **TUPSA32**, WECA09, THPSC08, THPSC10, THPSC55
Ivanov, A.V. WECA10
Ivanov, E.V. THX03, **THPSC35**
Ivanov, G.N. WECA09, THPSC09
Ivanov, I.A. THCA01
Ivanov, S.M. WEPSB36
Ivanov, S.V. **TUX02**
Ivanova, N. WEPSB19

— K —

Kalagin, I.V. WECA09, WECA12, THPSC08, THPSC09
Kalashnikova, A.A. THPSC04, THPSC05
Kalinin, V.A. WEPSB19
Kamanin, A.N. WECA08, THPSC39, WEPSB40
Kamerdzhiev, V. TUCA01, TUCA02
Kaminski, V.L. WEPSB12, WEPSB13
Kaminsky, V.I. THPSC05
Kantsyrev, A.V. TUPSA30, WEX02, WECA02, WEPSB25
Kaportsev, E.V. THY02, **THPSC42**
Karamysheva, G.A. **WEPSB28**, WEPSB31
Karev, A.I. WEPSB40
Karpinsky, V. THX03
Karpov, G.V. TUPSA29, THPSC23, THPSC24
Kasaev, A.S. TUY01, FRCA01
Kasatov, D.A. **TUPSA36**, TUPSA37, WEPSB16, FRCB01, WEPSB17
Kashtanov, E. THZ03
Kats, M.M. **WEPSB24**
Kazacha, V.I. WECA09, THPSC09
Kazantseva, E.S. FRCA01
Kazarinov, M.Y. WEPSB31
Kazarinov, N.Yu. WECA09, THPSC08, THPSC09, **THPSC10**
Khabarov, M.V. WECA09, THPSC08, THPSC09
Khabibullina, E. **WEPSB38**, THPSC05
Khankin, V.V. WECA08, WEPSB40
Khasaya, D.R. THPSC37
Khodzhibagiyan, H.G. THX03, THZ02
Khokhriakov, I.A. **THPSC30**
Khoroshkov, V.S. WECA03
Khudyakov, S. WEPSB07
Kirichenko, A. THX03
Kirsanov, B.N. WECA10
Kiselev, V.A. **TUZ01**, **THCB01**, THPSC11, FRCA03
Kiselev, Yu.V. WEX04, THPSC44, THPSC45
Klachkov, A.P. WEPSB03
Klementiev, V.V. WECA08
Klenov, G.I. **WECA03**
Klenov, V.S. **THPSC44**, THPSC46
Klinovskiy, P.O. WEPSB41
Kliuchevskaia, Yu.D. **WEPSB35**, THPSC05
Klopenkov, M.L. WECA11, THPSC40, THPSC41
Klopenkov, R.M. **THPSC40**, **THPSC41**
Klyuev, V. WECA05
Kobets, A.G. TUCA04, TUPSA24, TUPSA23, WEPSB32
Kobets, V. **WEPSB01**, **WEPSB02**, THX03
Kogut, D.A. **WECA06**, WEPSB15
Kokhanyuk, V.M. WEX04, THPSC45
Kolesnikov, P.A. WECA07, THX01
Kolesov, I.V. WECA09
Kolobanov, E.I. THCE02
Koloberdin, M.V. THCA01
Kolomiets, A. TUZ02, TUPSA07, THPSC07
Koltsov, A.V. THPSC36
Kolyaskin, A.D. THPSC05
Kondratiev, B. TUPSA28
Konstantinov, E.S. WECA05
Koop, I. TUY01, FRCA01, FRCA03
Korchuganov, V. THPSC13, THPSC14, THPSC42, **THY01**, **THY02**
Korepanov, A.A. TUPSA33, THX01
Koryakin, S.N. WEPSB19
Koshelev, A.V. WEPSB19
Koshkarev, A.M. **THPSC28**, WEPSB17
Kostin, M.Y. TUPSA38, WEPSB19
Kostin, M.Yu. THPSC21
Kostromin, S.A. WEPSB28, **THZ02**
Kostyrev, V.A. WECA09
Kotenko, K.V. WEPSB41
Kovalchuk, M.V. THY02
Kovalenko, A.D. THX03
Kovalev, E.O. WECA07, THX01
Kozlov, A.V. TUPSA28
Kozlov, O.S. THX03
Kozlovskiy, K.I. THPSC48, THPSC50
Kozodaev, A.M. TUZ02
Kozub, S. THZ03, THPSC02
Krasik, Y. WEPSB25
Krasnov, A.A. THPSC11, FRCA01
Kravchuk, L.V. WEX04, THX02
Kropachev, G. WEPSB27, WEPSB38, WEPSB48, THPSC05
Kruchkov, Ya.G. TUCB02
Krutikhin, S.A. TUCB02, THCE02
Krylov, Y.V. THY02, THPSC13, THPSC42
Ksenofontov, A.I. WEPSB42
Kubankin, A.S. THPSC21, THPSC22
Kudinovich, I.V. FRCB02
Kuibeda, R.P. TUPSA28, WEPSB27, WEPSB38, WEPSB48
Kukhtin, V.P. TUPSA32
Kuksanov, N.K. WECA06, WEPSB15
Kulenko, Ya.V. THX01
Kulevoy, T. TUZ02, TUPSA26, TUPSA28,

ISBN 978-3-95450-170-0

	WEPSB06, WEPSB27, WEPSB38, WEPSB48, THPSC03, THPSC04, THPSC05
Kulikov, E.A.	**TUPSA02**
Kuper, E.A.	THCE02
Kuptsov, I.V.	THCE02
Kurakin, V.G.	**TUPSA18**, **TUPSA19**
Kurkin, G.Y.	**TUCB02**, THCE02, THPSC29
Kutnykova, L.A.	WECA05
Kuzhlev, A.N.	WECA11, WEPSB11, THPSC06, THPSC40, THPSC41, THPSC53
Kuzmenkov, K.I.	**THPSC47**
Kuznetsov, A.S.	**WEPSB17**, FRCB01
Kuznetsov, G.I.	THX01
Kuznetsov, S.V.	**TUPSA01**
Kvashnin, A.N.	THPSC28
Kyrpotin, A.N.	TUY01

— L —

Lagutin, A.	**WEPSB14**
Laier, U.	FRCA01
Lalayan, M.V.	WEPSB04, WEPSB07, THPSC03, THPSC04, THPSC05, THPSC38
Lamonov, S.V.	WECA08
Lamzin, E.A.	TUPSA32
Lang, P.M.	TUPSA30, WEPSB25
Larin, P.O.	TUPSA12
Lebedev, K.V.	THPSC47
Lebedev, N.	THPSC47
Lebedev, N.I.	TUPSA34
Lebedev, V.Ya.	THPSC47
Leibrock, H.	FRCA01
Leonov, A.I.	WECA10
Leontiev, V.N.	THPSC07
Levterov, K.A.	THX03
Liakin, D.A.	THPSC05, **THPSC33**, **THPSC34**
Litvinov, S.A.	FRCA01
Liverovskij, A.K.	WEPSB11
Lobov, I.	**THPSC31**
Logachev, P.V.	**THX01**
Loginov, V.N.	THPSC47
Lomovcev, A.M.	WECA09
Lukyantsev, A.	WEPSB19
Lychagin, A.A.	WEPSB19
Lysenko, A.P.	TUY01, THPSC27

— M —

Machecha, A.I.	THPSC06
Maisheev, V.A.	THPSC21
Makarov, A.N.	TUPSA36, TUPSA37, **WEPSB16**, WEPSB18, FRCB01
Makonin, S.	WEPSB19
Malinowski, H.	TUPSA02
Maltseva, Y.	**THPSC26**
Malyshev, V.P.	WEPSB41
Mamonov, A.N.	WECA10
Mamonov, I.A.	THPSC36
Mariam, F.G.	WEPSB25
Markov, N.V.	**WECA02**, WEPSB25
Maslennikov, S.	THPSC52
Matsievskiy, S.V.	TUPSA05, TUPSA09, WEPSB08, THPSC05
Matyushin, A.	WEPSB19
Maximov, A.V.	WEPSB19
Mazmanishvili, A.S.	THPSC54
Maznev, V.P.	THPSC06
Melnikov, A.A.	THPSC40, THPSC41
Melnikov, V.N.	WECA09, THPSC08, THPSC09
Melville, G.P.	**WECA01**
Merrill, F.E.	WEPSB25
Meshkov, I.N.	TUCA04, TUPSA23, TUPSA24, WEPSB32
Mezentsev, N.A.	**THZ01**
Mezhov, I.I.	WEPSB11
Mikhailov, V.A.	THX03
Mikhailov, V.N.	THPSC45, THPSC46
Mikulinas, N.P.	THPSC53
Milichenko, Yu.V.	**THPSC32**
Miloichikova, I.	**WEPSB47**
Milyutkin, V.	WEPSB19
Mironov, V.I.	WECA09
Mirzojan, A.N.	TUPSA21, WEX04, THPSC45
Mitrofanov, A.A.	THPSC17
Mitrofanov, K.V.	**WEPSB20**, **WEPSB21**
Mitrofanov, S.	**WECA12**
Mitrofanov, V.F.	WEPSB20, WEPSB23
Moiseev, V.A.	**TUPSA21**, WEX04
Moiseev, V.I.	THY02, **THPSC14**
Moisio, M.F.	TUPSA27
Monchinsky, V.	WEPSB01, THX03
Morozov, A.V.	THPSC53
Morozov, N.A.	WEPSB28, WEPSB31
Moseev, K.	THPSC42
Moseiko, N.I.	THY02, THPSC42
Motygin, S.V.	TUCB02, THCE02
Mudroliubov, V.G.	WECA11
Muraviov, G.V.	WECA11
Mytzin, G.V.	WEPSB31

— N —

Nazhmudinov, R.M.	**THPSC21**, **THPSC22**
Nechaeva, L.P.	THCE01
Nemytov, P.I.	WECA06, WEPSB15
Nepomnyaschy, O.N.	WEPSB43
Nesterov, A.	TUCB01, THX03
Nesterovich, A.	TUPSA11, THPSC37, THPSC49, THPSC50
Nevinnitsa, V.A.	THPSC05
Nikishkin, V.I.	WECA11
Nikitaev, V.G.	WEPSB37
Nikitin, A.A.	TUPSA28, WEPSB48
Nikitin, O.A.	WECA07, THX01

ISBN 978-3-95450-170-0

Nikolaev, I.B. TUPSA29
Nikolaev, V.I. TUZ02
Nikulin, E.S. THCE01, FRCA02
Novikov, S.A. WEPSB12, WEPSB13

— O —

Odintsov, D.G. THY02
Oleg, O. WEPSB25
Oleinik, A.N. THPSC22
Orlov, A.Y. THPSC33, THPSC34
Orlov, N.N. WEPSB48
Orlov, O. TUCA04, TUPSA23, TUPSA24, WEPSB32
Osadchuk, I.O. TUPSA13
Osipov, N.F. WECA09, WECA12, THPSC08, THPSC09
Osipov, V.N. THCE02
Ostankov, A.P. WEPSB19
Ostreinov, Y.M. **WEPSB18**
Otboev, A.V. FRCA03
Ottmar, A.V. TUPSA33
Ovchar, V.K. THCE02
Ovchinnikov, V.P. THPSC06
Ovchinnikova, L.Yu. WECA08, WEPSB40
Ovsiannikov, A.D. TUCA03
Ovsyannikov, D.A. **TUCA03**, TUPSA22, FRCB02

— P —

Pachkov, A.A. THX01
Pakhomov, N.I. WECA08, WEPSB39, WEPSB40
Panasyuk, V.M. TUY03, TUCA01
Panov, A. THX01
Panyushkin, V.A. **TUPSA30**, WEPSB25
Paramonov, V.V. **THX02**, **THPSC07**
Parkhomchuk, V.V. TUY03, TUCA01, TUCA02, WECA05
Paschenko, S.V. WECA12
Pashchenko, S.V. WECA09
Pavlenko, A.V. **TUPSA29**
Pavlov, V.A. WEPSB43
Pavlov, Y.S. **WEPSB43**
Pavluhov, D.E. THPSC06
Pavshenko, Yu.N. WECA08
Perevedentsev, E. TUY01
Pesterev, S.G. THY02
Petrenko, A.V. THPSC26
Petrov, V.M. THCE02
Petrozhitskii, A.V. WECA05
Petrushina, I.I. WEPSB06, THPSC18, THPSC19, THPSC20
Philippov, A.V. THX03
Pikalov, V.A. TUPSA38, **WEPSB19**
Piksaikin, V.M. WEPSB20, WEPSB21, WEPSB23
Pilan, A.M. TUCB02, THPSC29
Plastun, A.S. **TUPSA07**, WEPSB06
Polkovnikov, M.K. WEPSB19
Polozov, S.M. **TUPSA12**, TUPSA20, WEPSB06, WEPSB35, WEPSB36, **THPSC03**, **THPSC04**, **THPSC05**
Polukhin, V.A. TUY03
Ponomarenko, V.I. WECA11
Prisekin, V.G. THPSC26
Prokhorov, S.V. THPSC08
Prokopenko, A.V. THPSC50
Prosvetov, V.P. TUY01
Pukhov, S.P. WEPSB45
Putmakov, A.A. TUY03

— R —

Raevsky, V.G. WEPSB40
Rashchikov, V.I. THPSC05, **THPSC51**
Rastigeev, S. **WECA05**
Razbash, A.A. **WECA10**
Reinhardt-Nickoulin, P.I. THPSC43
Repkov, V.V. THCE02
Reshetnyak, N.G. **THPSC54**
Reva, V.B. **TUY03**, **TUCA01**, TUCA02
Řežvykh, K.A. WEX01, **WEPSB22**
Rodigin, A.V. WEPSB45
Rodionova, M.E. TUPSA30, WEPSB25
Rogovsky, Yu. A. **TUY01**, **THPSC27**, **FRCA01**
Rogozhkin, S.V. TUPSA28, WEPSB48, THPSC05
Romanov, A.L. TUY01, THPSC27
Romanov, S. THX03
Romanov, V. **WEX01**
Romas'ko, V.P. THPSC54
Roncolato, C. R. TUPSA27
Roudskoy, I. TUPSA16, WECA02
Rubtsova, I.D. **TUPSA14**
Ruchyeva, V. WEPSB47
Rudakov, A.Yu. TUPSA23, TUPSA24
Ryaskov, A.A. WEPSB11
Rybakov, I.V. THPSC18

— S —

Sabirov, B.M. **THPSC15**
Sakharov, V.P. WEPSB39
Salimov, R.A. WECA06, WEPSB15
Sambayev, Y.K. THCA01
Samoshin, A.V. TUPSA20, THPSC05
Samsonov, E. TUPSA31, WEPSB28
Samylin, B.F. WEPSB20, WEPSB21, WEPSB23
Sanin, A.L. THPSC28
Satov, Yu.A. TUZ02
Savin, D.A. THPSC21
Savin, E.A. **TUPSA04**, **TUPSA05**, **TUPSA06**, **TUPSA09**, **WEPSB08**, THPSC05, **THPSC38**
Savin, S.M. TUPSA16
Sayapin, V.G. WECA08, THPSC39
Scheglov, M.A. THCE02
Schegolev, V.A. TUZ02

ISBN 978-3-95450-170-0

Schurig, I. FRCA01
Sedlyarov, I.K. THCE02
Sedykh, G.S. THX03
Seleznev, V.S. WEPSB19
Seleznev, V.V. TUPSA23
Semchenkova, O.V. WECA09
Semennikov, A.I. WEPSB25
Semenov, A.M. **THPSC11**, FRCA03
Semenov, A.V. FRCA01
Senchenko, A.I. TUY01, THPSC27
Serdobintsev, G.V. THCE02
Serednyakov, S.S. THCE02
Sergey, S. **THPSC52**
Serov, A.V. **THPSC36**
Serov, V.L. WEX04, THPSC45
Shafronovskaia, A.I. **WEPSB49**
Shaftan, T.V. THPSC11
Shakun, N.G. WEPSB31
Shashkov, Ya.V. **WEPSB09**, THPSC05, **THPSC16**, **THPSC17**, THPSC18
Shatokhin, V.L. TUPSA35, THPSC48, THPSC49, THPSC50
Shatunov, P.Yu. TUY01, THPSC27, FRCA01
Shatunov, Y.M. TUY01, THPSC27
Shchagin, A.V. THPSC21, THPSC22
Shcherbakov, A.A. **THCB02**
Shcherbakov, P.A. THZ03, THPSC02
Shchudlo, I.M. TUPSA36, **TUPSA37**, WEPSB16, FRCB01
Shestov, L. TUPSA30, WEPSB25
Shikanov, A.E. THPSC37, **THPSC48**, THPSC49, THPSC50
Shirshov, L.S. THZ03
Shishanin, O.E. **THPSC12**
Shkolnikov, E. THPSC52
Shokin, V.I. TUPSA24
Shorikov, I.V. THCE02
Shul'ga, N.F. THPSC21
Shumshurov, A. TUZ02
Shurkhno, N. THX03
Shuvalov, E. WEPSB47
Shvedunov, I.V. WECA08, THPSC39, WEPSB40
Shvedunov, N.V. WECA08, WEPSB40
Shvedunov, V.I. WECA08, WEPSB39, THPSC39, **WEPSB40**
Shwartz, D.B. TUY01, FRCA01
Sidorin, A.A. TUCA04, TUPSA23, **TUPSA24**, WEPSB32
Sidorin, A.O. **THX03**, WEPSB01, THPSC35
Simonov, A.S. WECA08
Sitnikov, A. **TUPSA26**, TUPSA28, WEPSB48
Skachkov, V. TUPSA30, WEPSB25
Skasyrskaya, A.K. WEX04
Skorkin, V.M. **WEPSB44**
Skrinsky, A.N. TUY01
Skuratov, V.A. WECA12
Slabodchikov, I. THZ03
Slepnev, I. THX03
Slepnev, V. THX03
Smirnov, A.V. **TUCB01**, TUPSA02, THX03
Smirnov, A.Yu. THPSC05, THPSC38
Smirnov, D.S. WECA07, THX01
Smirnov, V.L. **TUPSA17**
Smirnova, Z.I. THPSC35
Smolyakov, N.V. THPSC14
Smygacheva, A.S. THY02
Sobenin, N.P. TUPSA05, TUPSA09, WEPSB08, WEPSB09, THPSC03, THPSC05, THPSC16, THPSC17
Sokolov, I.D. TUPSA04
Sokolov, V.A. WECA09
Solnyshkov, D.A. **THPSC53**
Sorokin, I.N. FRCB01
Sotnikov, A.Y. WEPSB19
Starikov, D.A. TUPSA15
Stark, S. THPSC05
Starostenko, A.A. **TUY02**, THX01, FRCA01, FRCA03
Starostenko, D.A. THX01
Steczkiewicz, O. **THPSC55**
Stogov, Yu.I. WECA11
Strekalovskikh, S.A. **THPSC01**
Strokach, A.P. WEX03, **WECA11**, WEPSB11
Stuchebrov, S. WEPSB47
Styuf, A.S. **THPSC24**
Sumaneev, O.V. **TUPSA38**
Svetov, L.A. THPSC35
Svinin, M.P. THPSC06
Svishchev, V.V. TUPSA29
Svistunov, Y.A. **WEPSB11**, TUCA03, FRCB02
Syresin, E. **WECA04**, WEPSB28, **WEPSB31**
Sytchevsky, S.E. TUPSA32
Sytnik, V. THZ03

— T —

Takaeva, E.V. THPSC32
Tararyshkin, S.V. THCE02
Taskaev, S.Yu. TUPSA36, TUPSA37, WEPSB16, WEPSB18, **FRCB01**
Telnov, A.V. THCE02
Teterev, Yu.G. WECA12, THPSC09
Tikhomirov, A. WECA09, THPSC08, THPSC09
Titarenko, Y.E. THPSC05
Tiunov, M.A. WEPSB17
Tkachenko, L. **THZ03**, **THPSC02**
Tolstun, N.G. **THPSC06**
Tomin, S.I. THY02
Toporkov, S.E. **WEPSB04**, **WEPSB05**, THPSC04, THPSC05
Tretyakova, T. TUPSA07
Tribendis, A.G. THCE02
Troshina, M.V. WEPSB19

ISBN 978-3-95450-170-0

Trubnikov, G.V. **TUX01**, THX03
Tsvetkov, V.F. WEPSB11
Tsygankov, S.S. WECA11
Turbabin, A.V. THCE01
Tuzikov, A. THX03
Tyutyunnikov, S.I. WEPSB33

— U —

Udrea, S. WEPSB25
Uglov, S.R. THPSC21
Ulin, S.E. WEPSB37
Ulyanenko, S.E. WEPSB19
Ushakov, V. THY02
Ushkov, V.L. THY01, THY02

— V —

Valentinov, A.G. THY02, **THPSC13**, THPSC42
Varentsov, D. TUPSA30, **WEPSB25**
Vasilishin, B. THX03
Vasilyev, I.V. THPSC43
Vasilyev, M.Yu. THPSC29
Veresov, O.L. WECA11, WEPSB11
Verevochkin, V.A. WECA09
Verjbitskiy, O. THPSC03, THPSC05
Vernov, A. THY02
Visotski, S.A. TUPSA26, WEPSB38
Vladimirov, I.Yu. WECA08, WEPSB40
Vobly, P. WEPSB18
Voevodin, V.P. THPSC32
Vogel, V. TUPSA33
Vokhmyanina, K.A. THPSC22
Volkov, V. **THCE02**
Volkov, V. THX03
Volodkevich, O. TUPSA21, THPSC44, **THPSC45**, THPSC46
Vorogushin, M.F. **WEX03**
Voronin, G.G. THPSC53
Vorontsov, V.A. **TUPSA03**
Vorozhtsov, S.B. TUPSA17
Vovchenko, E.D. THPSC48

— W —

Weinrich, U. FRCA01
Weyrich, K. TUPSA30, WEPSB25
Wilde, C. WEPSB25

— Y —

Yakovenko, S. TUCA04, TUPSA23
Yanenko, V.V. TUPSA16
Yanovich, A.A. THPSC21
Yazvitsky, Yu. THPSC47
Yudin, I.P. **WEPSB33**
Yupinov, Y.L. THPSC13
Yurov, D.S. WECA08, THPSC39, **WEPSB39**, WEPSB40
Yur'yev, A.L. WEPSB45
Yushkov, Yu.G. WEPSB12, WEPSB13

— Z —

Zabrodin, B.V. THPSC40
Zaplatin, N.L. TUPSA31
Zarubin, A. TUZ02
Zavadtsev, A.A. TUPSA06, TUPSA09, WEPSB08, THPSC38
Zavialov, M.A. **FRCB03**
Zavyalov, N.V. THCE02
Zdorovets, M.V. **THCA01**
Zemlyansky, I.M. TUY01, **FRCA03**
Zharinov, Yu.M. TUY01
Zhuikov, B. WEX04
Ziiatdinova, A.V. **WEPSB27**, THPSC05
Zinchenko, S. THZ03
Zobov, M. WEPSB09, THPSC16
Zolotukhina, N.A. TUPSA33
Zubarev, P.V. THPSC28
Zubareva, A.N. WEPSB25
Zubets, V. THCE01, THPSC44, FRCA02
Zuev, Yu. WEPSB11
Zvyagintsev, V. THPSC05, THPSC18, THPSC17

ISBN 978-3-95450-170-0

ISBN 978-3-95450-170-0

Institutes List

Allrussian Electrotechnical Institute
Moskow, Russia
- Chikhachev, A.S.

Belarusian State Agrarian Technical University
Minsk, Belarus
- Lagutin, A.

BelSU
Belgorod, Russia
- Kubankin, A.S.
- Nazhmudinov, R.M.
- Oleinik, A.N.
- Shchagin, A.V.
- Vokhmyanina, K.A.

BINP SB RAS
Novosibirsk, Russia
- Akimov, A.
- Alexander, A.A.
- Anashin, V.V.
- Arbuzov, V.S.
- Bak, P.A.
- Batazova, M.A.
- Batrakov, A.M.
- Bekhtenev, E.A.
- Belchenko, Y.I.
- Berkaev, D.E.
- Bolkhovityanov, D.
- Bryazgin, K.A.
- Bryzgunov, M.I.
- Bubley, A.V.
- Chernov, K.N.
- Domarov, E.V.
- Eliseev, A.A.
- Emanov, F.E.
- Fadeev, S.
- Fatkin, G.A.
- Frolov, A.R.
- Goncharov, A.D.
- Gorbatenko, O.V.
- Gurov, S.M.
- Gusev, Ye.A.
- Ilyin, I.V.
- Karpov, G.V.
- Kasaev, A.S.
- Kasatov, D.A.
- Kazantseva, E.S.
- Kiselev, V.A.
- Klyuev, V.
- Kogut, D.A.
- Kolobanov, E.I.
- Konstantinov, E.S.
- Koop, I.
- Korepanov, A.A.
- Koshkarev, A.M.
- Krasnov, A.A.
- Kruchkov, Ya.G.
- Krutikhin, S.A.
- Kuksanov, N.K.
- Kulenko, Ya.V.
- Kuper, E.A.
- Kuptsov, I.V.
- Kurkin, G.Y.
- Kuznetsov, A.S.
- Kuznetsov, G.I.
- Kvashnin, A.N.
- Kyrpotin, A.N.
- Logachev, P.V.
- Lysenko, A.P.
- Makarov, A.N.
- Maltseva, Y.
- Mezentsev, N.A.
- Motygin, S.V.
- Nemytov, P.I.
- Nikolaev, I.B.
- Osipov, V.N.
- Ostreinov, Y.M.
- Otboev, A.V.
- Ottmar, A.V.
- Ovchar, V.K.
- Pachkov, A.A.
- Panasyuk, V.M.
- Panov, A.
- Parkhomchuk, V.V.
- Pavlenko, A.V.
- Perevedentsev, E.
- Petrenko, A.V.
- Petrov, V.M.
- Petrozhitskii, A.V.
- Pilan, A.M.
- Polukhin, V.A.
- Prisekin, V.G.
- Prosvetov, V.P.
- Putmakov, A.A.
- Rastigeev, S.
- Repkov, V.V.
- Reva, V.B.
- Rogovsky, Yu. A.
- Romanov, A.L.
- Salimov, R.A.
- Sanin, A.L.
- Scheglov, M.A.
- Sedlyarov, I.K.
- Semenov, A.M.
- Semenov, A.V.
- Senchenko, A.I.
- Serdobintsev, G.V.
- Serednyakov, S.S.
- Shatunov, P.Yu.
- Shatunov, Y.M.
- Shchudlo, I.M.
- Shwartz, D.B.
- Skrinsky, A.N.
- Sorokin, I.N.
- Starostenko, A.A.

ISBN 978-3-95450-170-0

- Starostenko, D.A.
- Styuf, A.S.
- Svishchev, V.V.
- Tararyshkin, S.V.
- Taskaev, S.Yu.
- Tiunov, M.A.
- Tribendis, A.G.
- Vasilyev, M.Yu.
- Vobly, P.
- Volkov, V.
- Zemlyansky, I.M.
- Zharinov, Yu.M.
- Zolotukhina, N.A.
- Zubarev, P.V.

BNL
Upton, Long Island, New York, USA
- Hseuh, H.-C.
- Shaftan, T.V.

CERN
Geneva, Switzerland
- Petrenko, A.V.

Cyclotron Company Ltd.
Obninsk, Russia
- Ivanov, A.V.
- Kirsanov, B.N.
- Leonov, A.I.
- Mamonov, A.N.
- Razbash, A.A.

DELTA
Dortmund, Germany
- Dietrich, J.

DESY
Hamburg, Germany
- Cherepenko, A.
- Vogel, V.

Federal State Unitary Enterprise, Laboratory of Electron Accelerators MSU, Ltd
Moscow, Russia
- Frejdovich, I.A.
- Klementiev, V.V.
- Lamonov, S.V.
- Pavshenko, Yu.N.
- Shvedunov, I.V.
- Simonov, A.S.

FZJ
Jülich, Germany
- Kamerdzhiev, V.

GSI
Darmstadt, Germany
- Blell, U.
- Dimopoulou, C.
- Dolinskyy, A.
- Gorda, O.E.
- Laier, U.
- Lang, P.M.
- Leibrock, H.
- Litvinov, S.A.
- Rodionova, M.E.
- Schurig, I.
- Shestov, L.
- Varentsov, D.
- Weinrich, U.
- Weyrich, K.

HIL
Warsaw, Poland
- Choinski, J.
- Gmaj, P.
- Steczkiewicz, O.

HIM
Mainz, Germany
- Aulenbacher, K.
- Bruker, M.W.
- Dietrich, J.
- Hofmann, A.

HZG
Geesthacht, Germany
- Beckmann, F.
- Khokhriakov, I.A.

IERT
Kharkov, Ukraine
- Kobets, A.G.

IHEP
Moscow Region, Russia
- Afonin, A.G.
- Ageev, A.I.
- Bogdanov, I.
- Britvich, G.I.
- Chesnokov, Y.A.
- Durum, A.A.
- Frolov, B.A.
- Gorokhov, S.A.
- Gotman, V.
- Ivanov, S.V.
- Ivanova, N.
- Kalinin, V.A.
- Kashtanov, E.
- Koshelev, A.V.
- Kostin, M.Y.
- Kostin, M.Yu.

ISBN 978-3-95450-170-0

- Kozub, S.
- Lobov, I.
- Lukyantsev, A.
- Maisheev, V.A.
- Makonin, S.
- Matyushin, A.
- Maximov, A.V.
- Milichenko, Yu.V.
- Milyutkin, V.
- Ostankov, A.P.
- Pikalov, V.A.
- Polkovnikov, M.K.
- Savin, D.A.
- Seleznev, V.S.
- Shcherbakov, P.A.
- Shirshov, L.S.
- Slabodchikov, I.
- Sotnikov, A.Y.
- Strekalovskikh, S.A.
- Sumaneev, O.V.
- Sytnik, V.
- Takaeva, E.V.
- Tkachenko, L.
- Voevodin, V.P.
- Yanovich, A.A.
- Zinchenko, S.

INFN/LNF
Frascati (Roma), Italy
- Zobov, M.

INFN/LNL
Legnaro (PD), Italy
- Comunian, M.
- Moisio, M.F.
- Roncolato, C. R.
- Stark, S.

INP NNC RK
Almaty, Kazakhstan
- Alexandrenko, V.V.
- Ivanov, I.A.
- Koloberdin, M.V.
- Sambayev, Y.K.
- Zdorovets, M.V.

Institute of Archaeology and Ethnography, Siberian Branch of the Russian Academy of Sciences
Novosibirsk, Russia
- Kutnykova, L.A.

IPCE RAS
Moscow, Russia
- Danilichev, V.A.
- Dobrohotov, V.V.
- Nepomnyaschy, O.N.
- Pavlov, V.A.
- Pavlov, Y.S.

IPCP
Chernogolovka, Moscow region, Russia
- Zubareva, A.N.

IPHC
Strasbourg Cedex 2, France
- Asfari, Z.
- Gall, B.J.P.

IPPE
Obninsk, Russia
- Bazhal, S.V.
- Egorov, A.S.
- Gremyachkin, D.E.
- Mitrofanov, K.V.
- Mitrofanov, V.F.
- Piksaikin, V.M.
- Řežvykh, K.A.
- Romanov, V.
- Samylin, B.F.

ITEP
Moscow, Russia
- Aleev, A.A.
- Alekseev, P.N.
- Alexeev, N.N.
- Andreev, A. A.
- Andreev, V.
- Andrianov, S.L.
- Aparin, D.
- Bakhmutova, A.V.
- Balabin, A.I.
- Barabin, S.V.
- Batyaev, V.F.
- Bogachev, A.A.
- Bogdanov, A.V.
- Chalykh, B.B.
- Drozdovsky, A.A.
- Drozdovsky, S.A.
- Fedin, P.A.
- Gavrilin, R.
- Golubev, A.
- Iskandarov, N.A.
- Kantsyrev, A.V.
- Kats, M.M.
- Khoroshkov, V.S.
- Kolomiets, A.
- Kondratiev, B.
- Kozlov, A.V.
- Kozodaev, A.M.
- Kropachev, G.
- Kuibeda, R.P.
- Kulevoy, T.
- Liakin, D.A.
- Markov, N.V.
- Nikitin, A.A.
- Nikolaev, V.I.
- Orlov, A.Y.
- Orlov, N.N.

ISBN 978-3-95450-170-0

- Panyushkin, V.A.
- Plastun, A.S.
- Rogozhkin, S.V.
- Roudskoy, I.
- Satov, Yu.A.
- Savin, S.M.
- Schegolev, V.A.
- Semennikov, A.I.
- Shumshurov, A.
- Sitnikov, A.
- Skachkov, V.
- Titarenko, Y.E.
- Tretyakova, T.
- Visotski, S.A.
- Yanenko, V.V.
- Zarubin, A.
- Ziiatdinova, A.V.

JIHT RAS
Moscow, Russia
- Kuznetsov, S.V.

JINR/DLNP
Dubna, Moscow region, Russia
- Dolya, S.N.
- Horodek, P.
- Meshkov, I.N.
- Smirnov, V.L.
- Vorozhtsov, S.B.
- Zaplatin, N.L.

JINR/VBLHEP
Dubna, Moscow region, Russia
- Bazanov, A.M.
- Brovko, O.I.
- Butenko, A.V.
- Donets, D.E.
- Dorofeev, G.L.
- Drobin, V.M.
- Kulikov, E.A.
- Nesterov, A.
- Philippov, A.V.
- Sedykh, G.S.
- Sidorin, A.O.
- Smirnova, Z.I.
- Svetov, L.A.
- Yudin, I.P.

JINR
Dubna, Moscow Region, Russia
- Agapov, N.N.
- Ahmanova, E.V.
- Alenitsky, Yu.G.
- Alfeev, A.V.
- Andreev, V.
- Apel, P.Yu.
- Batin, V.
- Bekhterev, V.
- Bogomolov, S.L.
- Bondarchenko, A.E.
- Borisov, O.N.
- Butenko, A.V.
- Buzmakov, V.A.
- Dmitriev, S.N.
- Dolbilov, G.
- Donets, D.E.
- Donets, E.D.
- Donets, E.E.
- Drobin, V.M.
- Efremov, A.A.
- Eliseev, A.V.
- Eseev, M.K.
- Fateev, A.A.
- Galimov, A.R.
- Gikal, B.
- Gorbachev, E.V.
- Govorov, A.
- Gulbekyan, G.G.
- Horodek, P.
- Ivanenko, I.A.
- Ivanov, E.V.
- Ivanov, G.N.
- Kalagin, I.V.
- Karamysheva, G.A.
- Karpinsky, V.
- Kazacha, V.I.
- Kazarinov, M.Y.
- Kazarinov, N.Yu.
- Khabarov, M.V.
- Khodzhibagiyan, H.G.
- Kirichenko, A.
- Kobets, A.G.
- Kobets, V.
- Kolesov, I.V.
- Kostromin, S.A.
- Kostyrev, V.A.
- Kovalenko, A.D.
- Kozlov, O.S.
- Kuzmenkov, K.I.
- Lebedev, K.V.
- Lebedev, N.I.
- Lebedev, N.
- Lebedev, V.Ya.
- Levterov, K.A.
- Loginov, V.N.
- Lomovcev, A.M.
- Malinowski, H.
- Melnikov, V.N.
- Meshkov, I.N.
- Mikhailov, V.A.
- Mironov, V.I.
- Mitrofanov, S.
- Monchinsky, V.
- Morozov, N.A.
- Mytzin, G.V.
- Orlov, O.
- Osipov, N.F.
- Paschenko, S.V.
- Pashchenko, S.V.

ISBN 978-3-95450-170-0

- Prokhorov, S.V.
- Romanov, S.
- Rudakov, A.Yu.
- Sabirov, B.M.
- Samsonov, E.
- Seleznev, V.V.
- Semchenkova, O.V.
- Shafronovskaia, A.I.
- Shakun, N.G.
- Shokin, V.I.
- Shurkhno, N.
- Sidorin, A.A.
- Sidorin, A.O.
- Skuratov, V.A.
- Slepnev, I.
- Slepnev, V.
- Smirnov, A.V.
- Sokolov, V.A.
- Syresin, E.
- Teterev, Yu.G.
- Tikhomirov, A.
- Trubnikov, G.V.
- Tuzikov, A.
- Tyutyunnikov, S.I.
- Vasilishin, B.
- Verevochkin, V.A.
- Volkov, V.
- Yakovenko, S.
- Yazvitsky, Yu.

KhNU
Kharkov, Ukraine
- Shul'ga, N.F.

Laboratory of Electron Accelerators MSU, Ltd, Physics Department, Lomonosov Moscow State University
Moscow, Russia
- Ovchinnikova, L.Yu.
- Vladimirov, I.Yu.

LANL
Los Alamos, New Mexico, USA
- Barnes, C.W.
- Mariam, F.G.
- Merrill, F.E.
- Wilde, C.

LPI RAS
Moscow, Russia
- Agafonov, A.

LPI
Moscow, Russia
- Bashmakov, Y.A.
- Karev, A.I.
- Koltsov, A.V.
- Kurakin, V.G.
- Raevsky, V.G.
- Serov, A.V.

M.V. Lomonosov Moscow State University (MSU), Skobeltsyn Institute of Nuclear Physics
Moscow, Russia
- Alimov, A.S.
- Kamanin, A.N.
- Khankin, V.V.
- Pakhomov, N.I.
- Sayapin, V.G.
- Shvedunov, N.V.
- Shvedunov, V.I.
- Yurov, D.S.

Macquarie University
North Ryde, Australia
- Melville, G.P.

MEPhI
Moscow, Russia
- Aksentyev, A.E.
- Alexey, P.G.
- Aliev, K.A.
- Andrey, O.A.
- Ashanin, I.A.
- Averyanov, G.P.
- Baev, V.K.
- Bagova, S.Z.
- Bashmakov, Y.A.
- Blinnikov, A.A.
- Bogdanovich, B.Y.
- Bondarenko, T.V.
- Budkin, V.A.
- Buleiko, A.B.
- Buyanov, G.O.
- Didenko, A.N.
- Dmitriyev, M.S.
- Dmitriyeva, V.V.
- Dyubkov, V.S.
- Fadeev, A.M.
- Fertman, A.
- Golubev, A.
- Gusarova, M.
- Il'inskiy, A.V.
- Ivanov, S.M.
- Kalashnikova, A.A.
- Kaminsky, V.I.
- Khabibullina, E.
- Khasaya, D.R.
- Khudyakov, S.
- Klachkov, A.P.
- Kliuchevskaia, Yu.D.
- Kolyaskin, A.D.
- Kozlovskiy, K.I.
- Kulevoy, T.
- Lalayan, M.V.
- Larin, P.O.
- Matsievskiy, S.V.

ISBN 978-3-95450-170-0

- Mitrofanov, A.A.
- Nesterovich, A.
- Nikitaev, V.G.
- Osadchuk, I.O.
- Petrushina, I.I.
- Plastun, A.S.
- Polozov, S.M.
- Prokopenko, A.V.
- Rashchikov, V.I.
- Rybakov, I.V.
- Samoshin, A.V.
- Savin, E.A.
- Shashkov, Ya.V.
- Shatokhin, V.L.
- Shikanov, A.E.
- Smirnov, A.Yu.
- Sobenin, N.P.
- Sokolov, I.D.
- Toporkov, S.E.

MEPHI
Moscow, Russia
- Ulin, S.E.

MEPhI
Moscow, Russia
- Verjbitskiy, O.
- Vorontsov, V.A.
- Vovchenko, E.D.
- Ziiatdinova, A.V.
- Zvyagintsev, V.

MNIRTI
Moscow, Russia
- Dourkine, A.P.
- Klenov, G.I.

MRRC
Obninsk, Russia
- Beketov, E.E.
- Koryakin, S.N.
- Lychagin, A.A.
- Troshina, M.V.
- Ulyanenko, S.E.

MRTI RAS
Moscow, Russia
- Durkin, A.P.

MSIU
Moscow, Russia
- Shishanin, O.E.

MSU SINP
Moscow, Russia
- Shvedunov, I.V.
- Shvedunov, N.V.
- Yurov, D.S.

MSU
Moscow, Russia
- Alimov, A.S.
- Ermakov, A.N.
- Ishkanov, B.S.
- Kamanin, A.N.
- Khankin, V.V.
- Ovchinnikova, L.Yu.
- Pakhomov, N.I.
- Sakharov, V.P.
- Shvedunov, V.I.
- Vladimirov, I.Yu.
- Yurov, D.S.

N.N. Burdenko Neurosurgical Institute
Moscow, Russia
- Gorlachev, G.E.

NAFU
Arkhangelsk, Russia
- Eseev, M.K.

Nano
Moscow, Russia
- Zavadtsev, A.A.

National Research Nuclear University (MEPhI)
Moscow, Russia
- Maslennikov, S.
- Sergey, S.
- Shkolnikov, E.

NIIEFA
St. Petersburg, Russia
- Antonov, A.V.
- Belyakova, T.F.
- Efremov, A.V.
- Emeljanov, M.A.
- Fialkovskiy, A.M.
- Galchuck, A.V.
- Gavrish, Yu.N.
- Gnutov, P.A.
- Grigorenko, S.V.
- Grigoriev, V.I.
- Klinovskiy, P.O.
- Klopenkov, M.L.
- Klopenkov, R.M.
- Kotenko, K.V.
- Kukhtin, V.P.
- Kuzhlev, A.N.
- Lamzin, E.A.
- Liverovskij, A.K.
- Machecha, A.I.
- Malyshev, V.P.
- Maznev, V.P.
- Melnikov, A.A.

ISBN 978-3-95450-170-0

- Mezhov, I.I.
- Mikulinas, N.P.
- Morozov, A.V.
- Mudroliubov, V.G.
- Muraviov, G.V.
- Nikishkin, V.I.
- Ovchinnikov, V.P.
- Pavluhov, D.E.
- Ponomarenko, V.I.
- Ryaskov, A.A.
- Solnyshkov, D.A.
- Stogov, Yu.I.
- Strokach, A.P.
- Svinin, M.P.
- Svistunov, Y.A.
- Sytchevsky, S.E.
- Tolstun, N.G.
- Tsvetkov, V.F.
- Tsygankov, S.S.
- Veresov, O.L.
- Vorogushin, M.F.
- Voronin, G.G.
- Zuev, Yu.

NRC
Moscow, Russia
- Alekseev, P.N.
- Belkov, A.
- Dombrovsky, V.
- Efimov, Y.V.
- Fomin, Y.A.
- Kaportsev, E.V.
- Korchuganov, V.
- Kovalchuk, M.V.
- Krylov, Y.V.
- Moiseev, V.I.
- Moseev, K.
- Moseiko, N.I.
- Nevinnitsa, V.A.
- Odintsov, D.G.
- Pesterev, S.G.
- Smolyakov, N.V.
- Smygacheva, A.S.
- Tomin, S.I.
- Ushakov, V.
- Ushkov, V.L.
- Valentinov, A.G.
- Vernov, A.
- Yupinov, Y.L.

NRNU
Moscow, Russia
- Dalechina, A.V.
- Ksenofontov, A.I.
- Mamonov, I.A.

NSC/KIPT
Kharkov, Ukraine
- Ayzatsky, N.
- Chertishchev, I.A.
- Dovbnya, A.N.
- Mazmanishvili, A.S.
- Reshetnyak, N.G.
- Romas'ko, V.P.
- Shchagin, A.V.
- Shcherbakov, A.A.
- Shul'ga, N.F.

NSU
Novosibirsk, Russia
- Bekhtenev, E.A.
- Emanov, F.E.
- Fatkin, G.A.
- Kasatov, D.A.
- Koshkarev, A.M.
- Pavlenko, A.V.
- Reva, V.B.
- Rogovsky, Yu. A.
- Starostenko, A.A.

RAS/INR
Moscow, Russia
- Belov, A.
- Bragin, S.
- Ermolaev, S.V.
- Feschenko, A.
- Frolov, O.T.
- Gavrilov, S.A.
- Golubovskiy, S.E.
- Grekhov, O.V.
- Kiselev, Yu.V.
- Klenov, V.S.
- Kokhanyuk, V.M.
- Kravchuk, L.V.
- Leontiev, V.N.
- Mikhailov, V.N.
- Mirzojan, A.N.
- Moiseev, V.A.
- Nechaeva, L.P.
- Nikulin, E.S.
- Paramonov, V.V.
- Reinhardt-Nickoulin, P.I.
- Serov, V.L.
- Skasyrskaya, A.K.
- Skorkin, V.M.
- Turbabin, A.V.
- Vasilyev, I.V.
- Volodkevich, O.
- Zhuikov, B.
- Zubets, V.

RFNC – VNIIEF
Sarov, Russia
- Pukhov, S.P.
- Rodigin, A.V.
- Shorikov, I.V.
- Yur'yev, A.L.

ISBN 978-3-95450-170-0

RFNC-VNIITF
Snezhinsk, Chelyabinsk region, Russia
- Akhmetov, A.R.
- Hrenkov, S.D.
- Kolesnikov, P.A.
- Kovalev, E.O.
- Nikitin, O.A.
- Smirnov, D.S.

RRC
Moscow, Russia
- Korchuganov, V.

RRICT
Vidnoye, Russia
- Zavialov, M.A.

Saint Petersburg State University
Saint Petersburg, Russia
- Starikov, D.A.
- Svistunov, Y.A.

SSU
Sumy, Ukraine
- Ignatev, I.G.

St. Petersburg State Polytechnic University
St. Petersburg, Russia
- Zabrodin, B.V.

St. Petersburg State University
St. Petersburg, Russia
- Altsybeyev, V.V.
- Drivotin, O.I.
- Golovkina, A.G.
- Kudinovich, I.V.
- Ovsiannikov, A.D.
- Ovsyannikov, D.A.
- Rubtsova, I.D.

STU
Bratislava, Slovak Republic
- Bokor, J.

Technion
Haifa, Israel
- Efimov, S.V.
- Krasik, Y.
- Oleg, O.

TPU
Tomsk, Russia
- Artemenko, S.N.
- Avgustinovich, V.A.
- Gogolev, A.S.
- Gorev, S.A.
- Igumnov, V.S.
- Kaminski, V.L.
- Miloichikova, I.
- Novikov, S.A.
- Ruchyeva, V.
- Shuvalov, E.
- Stuchebrov, S.
- Uglov, S.R.
- Yushkov, Yu.G.

TRIUMF, Canada's National Laboratory for Particle and Nuclear Physics
Vancouver, Canada
- Zvyagintsev, V.

TU Darmstadt
Darmstadt, Germany
- Udrea, S.

United Rocket and Space Corporation, Institute of Space Device Engineering
Moscow, Russia
- Anashin, V.S.

VNIIEF
Sarov, Russia
- Elyash, S.L.
- Telnov, A.V.
- Zavyalov, N.V.

ISBN 978-3-95450-170-0

Participants List

Институт ядерной физики им. Г.И. Будкера, Новосибирск
Бехтенев Евгений Алексеевич
Волков Владимир Николаевич
Еманов Федор Александрович
Землянский Илья Михайлович
Касатов Дмитрий Александрович
Киселев Владимир Афанасьевич
Когут Дмитрий Анатольевич
Кошкарев Алексей Михайлович
Кузин Максим Витальевич
Кузнецов Александр Сергеевич
Логачев Павел Владимирович
Макаров Александр Николаевич
Мезенцев Николай Александрович
Остреинов Юрий Михайлович
Павленко Антон Владимирович
Растигеев Сергей Анатольевич
Рева Владимир Борисович
Роговский Юрий Анатольевич
Скринский Александр Николаевич
Старостенко Александр Анатольевич
Таскаев Сергей Юрьевич
Фатькин Георгий Александрович
Щудло Иван Михайлович

ОИЯИ, Дубна
Аленицкий Юрий Григорьевич.
Ахманова Екатерина Всеволодовна
Гикал Борис Николаевич
Гульбекян Георгий Герасимович
Долбилов Геннадий Варламович
Иваненко Иван Анатольевич
Иванов Евгений Владимирович
Казаринов Николай Юрьевич
Калагин Игорь Владимирович
Кобец Андрей Геннадиевич
Кобец Валерий Васильевич
Костромин Сергей Александрович
Кузьменков Константин Игоревич
Куликов Евгений Александрович
Мешков Игорь Николаевич
Митрофанов Семен Вячеславович
Орлов Олег Сергеевич
Сидорин Алексей Анатольевич
Сидорин Анатолий Олегович
Смирнов Александр Валентинович
Смирнов Виктор Леонидович
Смирнов Виталий Олегович
Сыресин Евгений Михайлович
Трубников Григорий Владимирович
Фатеев Анатолий Александрович
Хородэк Павел Ришард
Юдин Иван Павлович
Яковенко Сергей Леонидович

НИЯУ МИФИ, Москва
Багова Сузана Зауровна
Башмаков Юрий Алексеевич
Буянов Григорий Олегович
Гусарова Мария Александровна
Далечина Александра Владимировна
Дюбков Вячеслав Сергеевич
Кладко Сергей Геннадьевич
Козловский Константин Иванович
Лалаян Михаил Владимирович
Николаев Алексей Станиславович
Осипов Андрей Андреевич
Полозов Сергей Маркович
Пономаренко Алексей Гаврилович
Топорков Сергей Евгеньевич
Фадеев Алексей Михайлович
Шатохин Вадим Леонидович
Шашков Ярослав Васильевич
Шиканов Александр Евгеньевич

Институт ядерных исследований, Троицк
Васильев Иван Андреевич
Володкевич Ольга Михайловна
Гаврилов Сергей Александрович
Ермолаев Станислав Викторович
Кленов Виктор Сергеевич
Кравчук Леонид Владимирович.
Моисеев Василий Александрович
Никулин Евгений Семенович
Парамонов Валентин Витальевич
Серов Валерий Львович
Скоркин Владимир Михайлович
Фещенко Александр Владимирович
Фролов Олег Тимофеевич

ГНЦ ИТЭФ, Москва
Андрианов Станислав Леонидович
Алексеев Николай Николаевич
Алексеев Петр Николаевич
Богданов Антон Валентинович
Голубев Александр Александрович
Дроздовский Александр Андреевич
Зиятдинова Альбина Валерьевна
Кац Марк Моисеевич
Лякин Дмитрий Алексеевич
Панюшкин Всеволод Алексеевич
Пластун Александр Сергеевич
Ситников Алексей Леонидович

Институт геофизических и радиационных технологий международной академии наук высшей школы, Москва
Ильинский Андрей Викторович

НИИЯФ МГУ, Москва
Ермаков Андрей Николаевич
Овчинникова Любовь Юрьевна
Юров Дмитрий Сергеевич

Физический институт им. П.Н. Лебедева, Москва
Куракин Вячеслав Григорьевич

Институт физической химии и электрохимии им. А.Н. Фрумкина, Москва
Павлов Юрий Сергеевич

ISBN 978-3-95450-170-0

ГНЦ ИФВЭ НИЦ «Курчатовский институт», Протвино
Готман Владислав Георгиевич
Иванов Сергей Владиславович
Пикалов Владимир Александрович
Стрекаловских Сергей Александрович
Ткаченко Леонид Михайлович
Фролов Борис Александрович

Московский государственный индустриальный университет, Москва
Шишанин Олег Евстропович

Всероссийский электротехнический институт им. В.И. Ленина, Москва
Чихачев Алексей Сергеевич

ОАО «НИИЭФА», Санкт-Петербург
Ворогушин Михаил Феофанович
Клопенков Роман Михайлович
Солнышков Дмитрий Адольфович

Санкт-Петербургский государственный университет, Санкт-Петербург
Головкина Анна Геннадьевна
Дривотин Олег Игоревич
Рубцова Ирина Деонисовна

НИЦ «Курчатовский институт», Москва
Валентинов Александр Геннадьевич
Капорцев Евгений Валерьевич
Корчуганов Владимир Николаевич
Крылов Юрий Викторович
Моисеев Валерий Иванович
Мосейко Николай Иванович

Научно-исследовательский институт технической физики и автоматизации, Москва
Ярош Валерий Евгеньевич

Северный (Арктический) федеральный университет им. М.В. Ломоносова, Архангельск
Есеев Марат Каналбекович

РФЯЦ ВНИИЭФ, Саров
Старобыкин Кирилл Валерьевич
Тельнов Александр Валентинович
Эльяш Света Львовна

Белгородский государственный национальный исследовательский университет, Белгород
Нажмудинов Рамазан Магомедшапиевич

РФЯЦ ВНИИТФ, Снежинск
Хренков Сергей Дмитриевич

Национальный исследовательский политехнический университет, Томск
Горев Станислав Андреевич
Милойчикова Ирина Алексеевна

ОИВТ РАН, Москва
Кузнецов Сергей Вячеславович

ЗАО «Циклотрон», Обнинск
Абрамов Игорь Александрович
Закуркин В.В.
Иванов Александр Васильевич
Кирсанов Борис Николаевич
Кудин Дмитрий Иванович
Леонов Анатолий Ильич
Мамонов Александр Николаевич
Павлихин Виктор Евгеньевич
Разбаш Анатолий Анатольевич

ВНИИТеК, Видное
Завьялов Михаил Александрович
Кондратенко Владимир Владимирович
Филиппович Виталий Павлович

ГНЦ РФ-ФЭИ, Обнинск
Бажал Сергей Владимирович
Бондаренко Иван Петрович
Войтенков Дмитрий Александрович
Глотов Александр Иванович
Говердовский Андрей Александрович
Грудзевич Олег Теофильевич
Гурбич Александр Фаддеевич
Дмитриева Ольга Константиновна
Журавлев Борис Васильевич
Кобец Ульян Александрович
Колесников Денис Владиславович
Конобеев Юрий Васильевич
Кононов Виктор Николаевич
Кононов Олег Евгеньевич
Куприянов Борис Васильевич
Манохин Василий Николаевич
Митрофанов Константин Вячеславович
Образцов Сергей Михайлович
Павленко Олеся Александровна
Печенкин Валерий Александрович
Пиксайкин Владимир Михайлович
Порываев Владимир Юрьевич
Прусаченко Павел Сергеевич
Пучков Александр Валентинович
Резвых Константин Анатольевич
Романов Валентин Александрович
Рябов Валерий Александрович
Савостин Вадим Валентинович
Свирин Михаил Иванович
Хромылева Татьяна Александровна
Хрячков Виталий Алексеевич
Чалый Юрий Романович

МРТИ РАН, Москва
Кленов Геннадий Иванович

Иностранные участники
Дитрих Йорген, TU Dortmund, Helmholtz Institut Mainz, Germany
Здоровец Максим Владимирович, ИЯФ, Астана, Казахстан
Стечкевич Ольга, Heavy Ion Laboratory University of Warsaw, Poland

ISBN 978-3-95450-170-0